Guangxin Li · Yunmin Chen · Xiaowu Tang *Eds.*

Geosynthetics in Civil and Environmental Engineering

Geosynthetics Asia 2008
Proceedings of the 4th Asian Regional Conference on Geosynthetics in Shanghai, China.

ZHEJIANG UNIVERSITY PRESS
浙江大学出版社

Springer

Guangxin Li
Yunmin Chen
Xiaowu Tang

Geosynthetics in Civil and Environmental Engineering

Geosynthetics Asia 2008
Proceedings of the 4th Asian Regional Conference on Geosynthetics in Shanghai, China

Guangxin Li
Yunmin Chen
Xiaowu Tang

Geosynthetics in Civil and Environmental Engineering

Geosynthetics Asia 2008
Proceedings of the 4th Asian Regional Conference on Geosynthetics in Shanghai, China

With 1,173 figures

ZHEJIANG UNIVERSITY PRESS
浙江大学出版社

Springer

EDITORS:

Prof. Guangxin Li
Dept. of Hydraulic Engineering
Tsinghua University
Beijing, 100084
China
E-mail: ligx@mail.tsinghua.edu.cn

Prof. Yunmin Chen
Department of Civil Engineering
Zhejiang University
38 Zheda Road, Hangzhou 310027
China
E-mail: chenyunmin@zju.edu.cn

Prof. Xiaowu Tang
Department of Civil Engineering
Zhejiang University
38 Zheda Road, Hangzhou 310027
China
E-mail: tangxiaowu@zju.edu.cn

ISBN 978-7-308-05919-0 **Zhejiang University Press, Hangzhou**
ISBN 978-3-540-69312-3 **Springer Berlin Heidelberg New York**
e-ISBN 978-3-540-69313-0 **Springer Berlin Heidelberg New York**

Library of Congress Control Number: 2008928540

Co-published by Zhejiang University Press, Hangzhou and Springer-Verlag GmbH Berlin Heidelberg

Springer is a part of Springer Science+Business Media
springer.com

Cover design: Frido Steinen-Broo, EStudio Calamar, Spain
Printed on acid-free paper

Preface

The 4th Asian Regional Conference on Geosynthetics (Geosynthetics Asia 2008) was held on 17-20 June 2008, in Shanghai, China. The previous Asian Regional Conferences on Geosynthetics were held in Banaglore, India, 1997; Kuala Lumpur, Malaysia, 2000; and Seoul, Korea, 2004. Geosynthetics Asia 2008 was organized by the Chinese Chapter of International Geosynthetics Society (CCIGS) and the Chinese Technical Association on Geosynthetics (CTAG) with the support of the Shanghai Investigation Design and Research Institute (SIDRI), Zhejiang University, and Shanghai Hejie Tech & Trading Co. Ltd., under the auspices of the International Geosynthetics Society (IGS) and the Chinese Hydraulic Engineering Society (CHES).

China presently has numerous large-scale infrastructure developments in the planning stage or under construction. Some of the projects include the Development of Western Regions, the South to North Water Diversion, the 2008 Beijing Olympic Games, the 2010 Shanghai World-Expo. Geosynthetics Asia 2008 provided an excellent opportunity for the exchange of information amongst academia, professional engineers, and industrial suppliers of geosynthetics.

Under the conference theme, “Geosynthetics in Civil and Environmental Engineering”, a total 238 abstracts were submitted and 157 papers were collected in addition to the Special Lecture, the Mercer Lecture, 3 Keynote Lectures, and 8 Invited Reports. The topics of the research papers were related to fundamental principles and properties of geosynthetics, testing and test standards, physical tests and centrifuge tests, reinforcement, soil improvement and ground improvement, filter and drainage characteristics, landfill engineering, geosystem usage, transportation applications, geosynthetics-pile support systems and geocell usage, hydraulic applications, ecological techniques and case histories. The papers were from 22 countries and regions (i.e., Australia, Austria, Brazil, Canada, China, France, Germany, Greece, Hong Kong China，India, Iran, Italy, Japan, Jordan, Korea, Malaysia, Singapore, Thailand, Turkey, USA, Vietnam, and West Pacific). The Technical Committee of Geosynthetics Asia 2008, under the support of the Paper Review Board organized by persons from Zhejiang University, Tsinghua University, Tianjin University, Hohai University, Tongji University, and Shanghai University. The Technical Committee followed the guidelines of the International Geosynthetics Society (IGS) to ensure that a high technical standard was maintained for all papers. The Organizing Committee of Geosynthetics Asia 2008 would like to express their sincere gratitude to the Shanghai Investigation Design and Research Institute, Zhejiang University, Chinese Production Base on Geosynthetics—Lingxian, Shandong, Tai’an Modern Plastic Co. Ltd, Key Laboratory of Port Geotechnical Engineering of the Ministry of Communications, PRC, and CCCC-Tianjin Port Engineering Institute Ltd, for their generous financial support.

It is our desire that the Proceedings of the 4th Asian Regional Conference on Geosynthetics provide an opportunity for the exchange of views among the academicians, technocrats, and professional engineers. It is our belief that all sectors will benefit through the sharing of knowledge and experience related to the design and use of geosynthetics.

Professor Guangxin LI

Chairman of Organizing Committee of Geosynthetics Asia 2008

Advisory Committee

Dr. Ing. Daniele A. Cazzuffi (Italy, IGS Immediate Past President)
Prof. Fumio Tatsuoka (Japan, IGS President)
Prof. Jorge Zornberg (USA, IGS Vise-President)
Prof. Masashi Kamon (Japan, IGS Asian Activities Committee President)
Mr. Gao Anze (Chinese Hydraulic Engineering Society)
Mr. Liu Zongyao (Chinese Technical Association on Geosynthetics)
Prof. Wang Zhenghong (Beijing University of Technology)
Mr. Bao Chenggang (Yangtze River Scientific Research Institute)
Mr. John W. Cowland (Strategy/Membership Committee Chairman)
Mr. Mike Sadlier (Australasian Chapter President)
Dr. G.V. Rao (Indian Chapter President)
Mr. Gouw Tjie Liong (Indonesian Chapter President)
Dr. Hiroshi Miki (Japanese Chapter President)
Dr. Sam-Deok Cho (Korean Chapter President)
Dr. Chew Soon Hoe (South East Asian Chapter President)
Prof. Dennes T. Bergado (Thai Chapter President)
Dr. Rong-Her Chen (West Pacific Regional Chapter President)

Organizing Committee

Prof. Li Guangxin (Tsinghua University)
Mr. Shi Xiaoqiang (Shanghai Investigation, Design & Research Institute)
Mr. Chi Jingkui (Chinese Chapter of IGS)
Ms. Bai Jianying (Chinese Technical Association on Geosynthetics)
Asso. Prof. Chen Lun (Tsinghua University)
Prof. Tang Xiaowu (Zhejiang University)
Dr. Dave T.T. Chang (Chung Yuan University)
Mr. John W. Cowland (Strategy/Membership Committee Chairman)

Technical Committee

Prof. Yan Chi (Tianjin University)
Prof. Chen Yunmin (Zhejiang University)
Mr. Shi Xinming (Ministry of Railways)
Mr. Tian Junfeng (Ministry of Transportation & Communication)

Conference Secretary

Mr. Chi Jingkui (Vice President of Chinese Chapter of IGS)
Prof. Tang Xiaowu (Secretary of Chinese Chapter of IGS)

Paper Review Board

A. Arulrajah（Australia）
S.R. Lo (Australia)
J.G. Zhang (Australia)
P.C. Lodi (Brazil)
M.S. Mok (Canada)
J.F. Chen (China)
L. Chen (China)
W.D. Deng (China)
Z.L. Dong（China）
Y.Y. Fei (China)
S. J. Feng (China)
D. Gao (China)
Y.X. Jie (China)
G. Lin（China）
Y. X. Liu (China)
L.H. Li (China)
Z. Y. Liu (China)
X.M. Qu (China)
Y.M. Shu（China）
X.W. Tang (China)
H.M. Wu (China)
C. Xu (China)
S.F. XU (China)
C. Yan (China)
Q.R. Yan (China)
H. P. Yang (China)
J. Zhang（China）
M.X. Zhang (China)
C. Duquennoi (France)
D.K. Atmatzidis (Greece)
H. Zanzinger (German)
J.W. Cowland (HongKong, China)
S. Kazempoor (Iran)
D. Cazzuffi (Italy)
Y.J. Du（Japan）
T. Harada (Japan)
S. Imaizumi (Japan)
T. Inui (Japan)
H. Ishimori (Japan)
T. Mukunoki (Japan)
M. Nishimura (Japan)
N. Yasufuku (Japan)
X. Zhang (Japan)
Omar Al-Hattamleh (Jordan)
T.W. Yee (Malaysia)
H.B. Ng (Thailand)
A.A. Javadi (United Kingdom)
M.C. Lu (U.S.A)

And others

Organized by

Chinese Chapter of International Geosynthetics Society

Chinese Technical Association on Geosynthetics

Under the auspices of

International Geosynthetics Society

Chinese Hydraulic Engineering Society

Under the auspices of

Shanghai Investigation Design and Research Institute

Zhejiang University

Shanghai Hejie Tech & Trading Co. Ltd.

Contents

Fundamental Principles and Properties of Geosynthetics

Testing and Test Standards

Physical Tests and Centrifuge Tests

Reinforcement

Soil Improvement and Ground Improvement

Filter and Drainage Characteristics

Landfill Engineering

Geosystem Usage

Transportation Applications

Geosynthetic-Pile Support Systems Sand Geocell Usage

Hydraulic Applications

Ecological Techniques and Case Histories

Fundamental Principles and Properties of Geosynthetics

INVESTIGATING THE RELATIONSHIP BETWEEN CREEP AND WATER FLOW CAPACITY OF GEOSYNTHETICS

C. Duquennoi[1], R. Gallo[2] and A. Thomas[3]

ABSTRACT: It has been evidenced in literature that time-dependant decrease of thickness under compressive loading affects the water flow capacity of geosynthetics. Jarousseau and Gallo (2004) introduced a new method to estimate the long-term flow capacity of drainage geocomposites based on an estimation of the thickness reduction factor.

We propose to apply the same method to different families of geosynthetics used for drainage purposes. Two standard tests are used: EN 1897: Geotextiles and geotextile-related products – Determination of the compressive creep properties and EN ISO 12958: Geotextiles and geotextile-related products – Determination of water flow capacity in their plane.

For each geosynthetic, compressive creep properties are first determined. The long-term thickness reduction factor is derived from this first test. The stress-strain curve of the geosynthetic is then used to evaluate the stress corresponding to the reduced long-term thickness. This equivalent stress is finally applied to the water flow capacity test. A relationship is shown between creep strain and flow capacity reduction factor. We also show the magnitude of errors committed when using instantaneous water flow capacity without long-term effect correction.

KEYWORDS: water flow capacity, creep, reduction factor, drainage

INTRODUCTION AND STATE OF THE ART

The effect of compressive stress on the hydraulic properties of geosynthetics has been investigated since the pioneering work of Gourc et al. (1982) and Mc Gown et al. (1982). It is now well documented that increasing the compressive stress reduces such essential properties as thickness and hydraulic conductivity, thus impacting the resulting transmissivity or in plane flow capacity of geosynthetics.

Creep of geosynthetics, on the other hand, has been investigated since the 1990s, mostly in relation to tensile properties and reinforcement applications (Sawicki and Kazimierowicz-Frankowska 1998).

Koerner (1994) is one of the first authors to consider compressive creep as one of the possible reduction factors affecting the long-term design of drainage geosynthetics, in addition to immediate compressive stress.

Giroud et al. (2000a) carried this work further on in defining a limited number of reduction factors (RF) applying to generic drainage geocomposites: immediate compression (RF_{IMCO}), long-term creep (RF_{CR}), immediate intrusion of boundary material (RF_{IMIN}), long-term intrusion of boundary material (RF_{IN}), etc. The long-term on-site transmissivity of the geosynthetic is then evaluated by dividing the transmissivity as measured in the laboratory by the pertinent reduction factors. The closer the laboratory conditions are to the site conditions, the fewer the reduction factors. The magnitude of each reduction factor reflects the influence of the considered phenomenon on transmissivity of the geosynthetic. In the same article, Giroud et al. (2000a) give orders of magnitudes for each possible reduction factor. They range in between 1.0 and 2.0 for geocomposites with a geonet transmissive core, which are fairly non-compressible products.

In a second article of the same issue (Giroud et al. 2000b), the authors concentrate on parameters affecting the thickness of geosynthetics, both on the short- and long-term, and propose a simple relationship between thickness reduction and hydraulic transmissivity reduction, using Koseny-Carman's law relating porosity to hydraulic conductivity. Using this method enables one to use a simple compressive creep test to derive the transmissivity reduction factor due to long-term creep.

Giroud's theoretical work has been confirmed by Palmeira and Gardoni (2002). The authors showed the accuracy of Giroud's equations to estimate non-woven geotextile permeability from physical properties such as porosity or fiber density. They also showed that transmissivity of such compressible products under high

[1] Hydrosystems and Bioprocesses Research Unit, Cemagref, FRANCE. Email: christian.duquennoi@cemagref.fr
[2, 3] Idem

instantaneous stress levels (up to 2000 kPa) can be reduced by a factor of 2 to 3 orders of magnitude, leading to RF_{IMCO} values much higher than those proposed by Giroud et al. (2000a) for non-compressible geocomposites and low stress levels.

Chai et al. (2004), conducting long term (200 days) hydraulic tests under confinement up to 50 kPa, confirmed that long-term drainage capacities where better preserved (lower values of RF_{IMCO}, RF_{CR}, RF_{IMIN} and RF_{IN}), by geosynthetics using stiff filters and a stiff and resisting core.

Jaisi et al. (2005) used Giroud's (2000b) method to estimate compression and creep reduction factors. The authors measured the thickness of various geonets and geocomposites after creep test and used Kozeny-Carman's law to deduce transmissivity reduction. RF_{IMCO} has been found to vary between 1.17 and 9.6, depending on the type of geosynthetic and the level of normal stress (up to 800 kPa). RF_{CR} on the other hand was notably smaller than RF_{IMCO}, and never greater than 1.28.

Müller-Rochholtz et al. (2006) introduced a method based on the use of two standardized tests and nomograms to deduce long-term flow capacity from thickness reduction. The authors showed the influence of filter creep and of hydraulic test boundary conditions, such as the use of compressible foam. The importance of the support system in hydraulic tests has also been underlined by Böttcher (2006). The author conducted long-term (up to 8 years) flow capacity tests under load and produced values for RF_{CR} and R_{FIN}.

The work presented herein is based on the method first developed by Jarousseau and Gallo (2004). In this first paper, the authors introduced their method and presented test results on four different types of geosynthetics. The overall reduction factor ($RF=RF_{IMCO} \times RF_{CR} \times RF_{IMIN} \times RF_{IN}$) was found to range between 1.2 and 4.2 depending on the type of geosynthetic tested and also on the level of normal stress.

In the following, we will first shortly introduce the theoretical basis of the method first developed in the above-mentioned paper and used in the present study. We will then present the new experimental program including 5 types of geosynthetics. These geosynthetics are different from the ones presented previously by Jarousseau and Gallo (2004) and are thought to complement the former study. We will eventually expose and discuss the obtained results.

OUTLINE OF THE METHOD

The method developed by Jarousseau and Gallo (2004) aims at the determination of long-term water flow capacity of geosynthetics (whether geotextiles or geo-composites) under compressive stress. It has been devised to fulfill a twofold objective:

—It has to be technically practical in order to be implemented in a testing laboratory, as part of a certification program for example. Thus, very long term methods such as Böttcher's (2006) could not be used because of the time required to produce results and the long term immobilization of the testing apparatus.

— It should benefit from the experimental and theoretical advances outlined in our introductory chapter. In particular, preference has been given to the direct measurement of hydraulic properties over their theoretical determination using Kozeny-Carman's or Giroud's equations. Special attention has thus been given to the hydraulic test itself, preferring the determination of flow capacity and the use of compressible foam plates to better approach in-situ confinement conditions.

A good compromise has been found by using standardized methods, both for the determination of creep properties (EN 1897) and for the determination of water flow capacity under compression (EN ISO 12958). The latter method prescribes the use of foam plates and is perfectly adequate to our method.

Moreover, it has to be underlined that the seating time prescribed in EN ISO 12958 is 6 minutes. A particular procedure has been designed to insure that the seating time for the thickness determination under compressive stress, following standard EN ISO 9863-1, is of the same order of magnitude, in order to avoid imprecision in the method.

It is thought that the sole source of imprecision is the present method is related to the fact that thickness determination is conducted between rigid plates, whereas water flow capacity is determined between compressible plates, as already underlined by Böttcher (2006).

Finally, since this method is not solely based on compressive creep determination but also on water flow capacity measurement between soft plates, it is thought to be a better representation of long term field conditions, including such effects as intrusion of filter material, without the drawbacks of hydraulic tests on the long term.

The overall method can be described by the following scheme:

MATERIALS AND DETAILED PROCEDURE

Five different types of geosynthetics have been chosen to be tested using the present method:

- GC1: Compressible geocomposite with random monofilament array core and 1 thermobonded unwoven filter,
- GC2: Compressible geocomposite with random monofilament array core and 2 thermobonded

unwoven filters,

- GNC: Non-compressible geocomposite with V-shaped monofilament array core and 2 thermo-bonded unwoven filters,
- NW1: Non-woven needle-punched compressible geotextile
- NW2: Non-woven needle-punched compressible geotextile reinforced with stitched cables.

All these five products have been tested using the following procedure:

Step 1: Long-term thickness is first determined using EN 1897. Each specimen is conditioned according to the standard and submitted to constant vertical load, in between two rigid steel plates as required by the standard. The test is conducted for 42 days and the long-term thickness is the one recorded at 42 days. In addition, thickness is also measured at 1, 2, 4, 15 and 30 minutes, 1, 2, 4 and 8 hours, 1, 2, 4, 7, 14 and 28 days, enabling the establishment of creep curves as the one presented in Fig. 1. Each creep test is conducted under a given compressive stress, adapted to the type of geosynthetic product. Being compressible products, GC1 and GC2 have been tested under 10 and 20 kPa respectively. NW1 and NW2 have been both tested under 100 kPa, whereas GNC has been tested under 200 kPa.

Step 2: Short-term thickness is determined versus compressive stress using EN ISO 9863-1. A sample of each product is placed in between rigid plates and a compressive load is applied. First, the nominal thickness is measured under 2 kPa after 30 s, and then thickness of the same sample is measured under 10, 20, 30, 50, 70, 100, 130, 150, 200, 250, 300 and 350 kPa. For each stress, thickness is measured after 30 s and after stabilization. Stabilization is deduced from successive measurements after 1 minute and 11 minutes. If the difference between these two successive measurements is less than 0.1 mm, stabilization time is 1 minute, otherwise the same procedure is applied between the thickness measured after 11 minutes and the one measured after 21 minutes. In all the cases presented herein, the difference of thickness between 1 and 11 minutes was not significant, which is in coherence with the 6 minute seating time used in water flow capacity testing as seen below.

Step 3: Based on these two tests, the level of compressive stress to be used for water flow capacity testing is determined: Long-term thickness from Step 1 is reported on the stress-thickness curve issued from Step 2 (see example shown on Fig. 1).

Step 4: Water flow capacity test is conducted using EN ISO 12958 under the compressive load determined in Step 3. This procedure guaranties that the hydraulic test is performed on a sample compressed at the same thickness as after creep. The apparatus used for this test is a constant-head device equipped with a vertical loading system. Each specimen is tested between two soft foam plates as required in the above-mentioned standard.

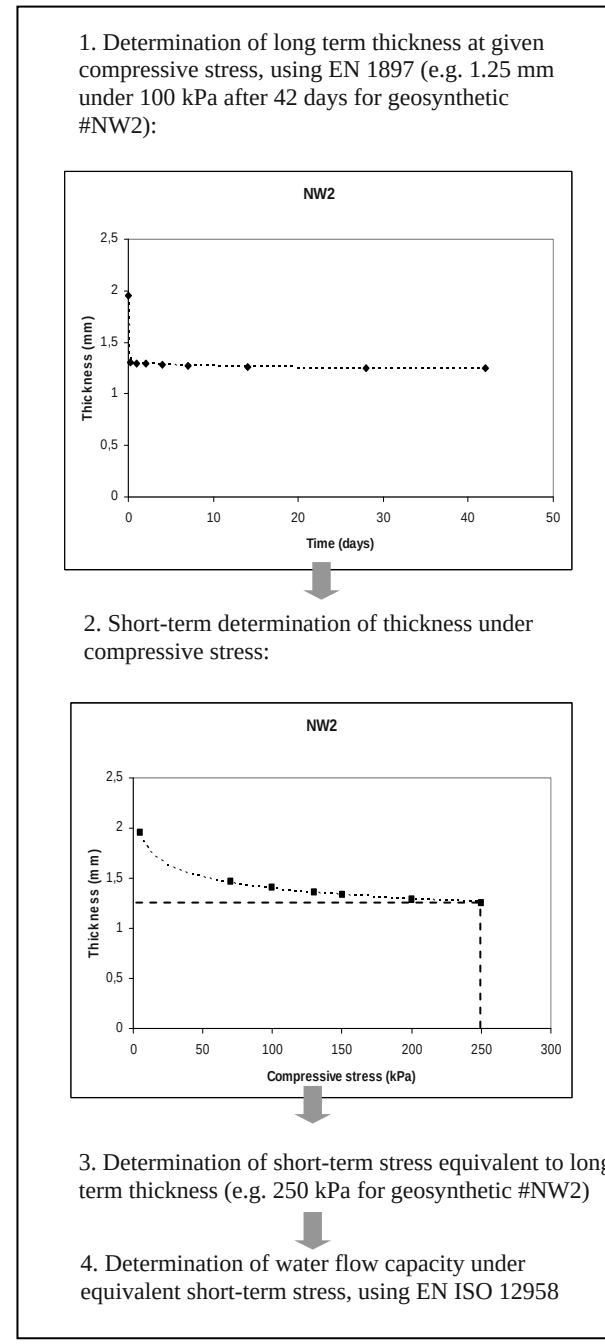

Fig. 1 Overall scheme of the method

RESULTS AND DISCUSSION

Results of Steps 1 and 2 are given on Figs. 2 and 3 for the 5 tested geosynthetics.

Results for the five types of geosynthetics, including

water flow capacity as determined using Step 4 of our method are synthesized in Table 1.

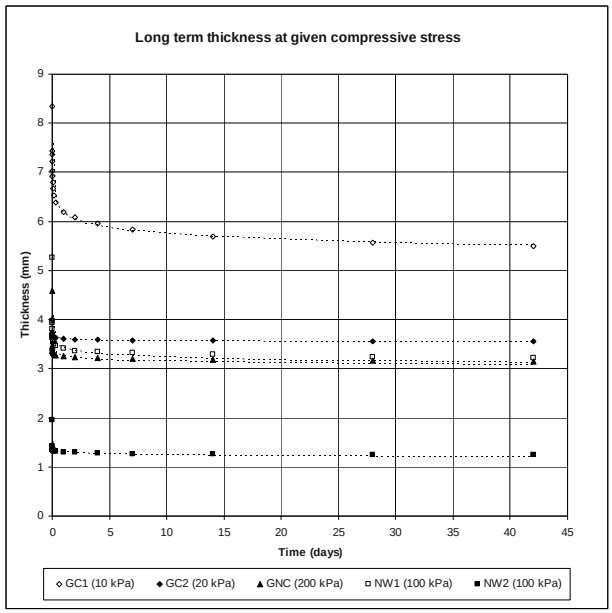

Fig. 2 Long-term thickness vs. time as obtained on 5 different geosynthetics and under given compressive stress, using Step 1 of our method

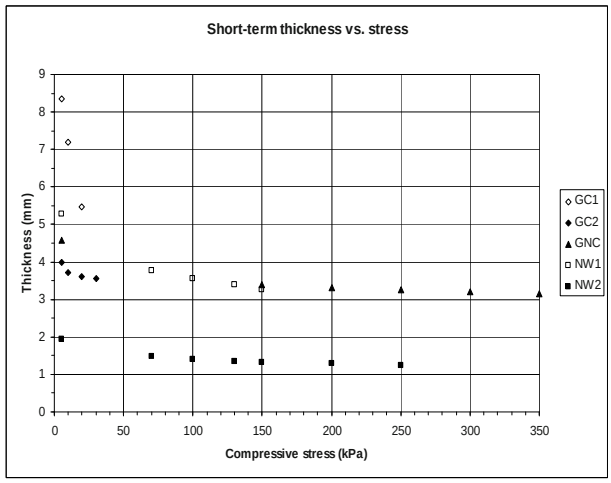

Fig. 3 Short-term thickness vs. compressive stress as obtained on 5 different geosynthetics using Step 2 of our method

It has to be noted that the long-term water flow capacity reduction factor computed in table 1 is a combination of long-term creep (RF_{CR}) and long-term intrusion of boundary material (RF_{IN}), i.e. $RF_{LT}=RF_{CR} \times RF_{IN}$ in our case.

It is immediately visible that the two non-woven geotextiles exhibit the highest creep strain as well as the highest RF_{LT}. Due to their different natures, the hierarchy of creep strain between these two geotextiles is not maintained in terms of hierarchy of flow capacity reduction factors.

Table 1 Main results of the testing method for 5 types of geosynthetic products

Product #	GC1	GC2	GNC	NW1	NW2
T_i, Initial thickness (mm)	8.34	4.00	4.59	5.27	1.95
T_{42}, Thickness at 42 days (mm)	5.49	3.55	3.15	3.22	1.25
Creep strain, $(T_i-T_{42})/T_i$ (%)	34.2	11.2	31.37	38.9	35.9
σ_1, stress used for creep test (kPa)	10	20	200	100	100
σ_2, stress used for water flow capacity test (kPa)	20	30	350	150	250
C_1, water flow capacity at σ_1 (l/m/s)	2.87	1.01	0.72	3.82	3.76
C_2, water flow capacity at σ_2 (l/m/s)	2.06	0.89	0.52	2.45	2.21
Long-term water flow capacity reduction factor, $RF_{LT}=C_1/C_2$	1.39	1.13	1.38	1.56	1.70

The three geocomposites exhibit the lowest creep strain as well as the lowest long-term flow capacity reduction factor. Between those three products, the hierarchy of flow capacity reduction factor matches perfectly the hierarchy of creep strain.

It has to be underlined that the two compressible geocomposites GC1 and GC2 have only been tested with very low stress levels, whether for creep test or for water flow capacity test.

Our method did not enable us to discriminate between such mechanisms as creep of the drainage core or long term intrusion of the filter, but rather shows the overall effect of long term deformation of the whole geosynthetic.

It is nevertheless important to remember that thickness determination, whether in long term (Step 1) or in short term (Step 2) tests, has been conducted between rigid plates, whereas water flow capacity is determined between compressible plates. This could be a source of imprecision which may need further investigation in future studies.

For all the tested products, long term deformation is a detrimental factor to long term flow capacity. Neglecting creep and long term intrusion of the filter can lead to important overestimation of flow capacity, from 13% up to 70% for the products tested herein.

CONCLUSIONS

A method for the determination of long term water flow capacity of geosynthetic products has been used on

three drainage geocomposites and two non-woven needle-punched geotextiles. The method includes three tests: determination of long term thickness under compressive stress (compressive creep test), determination of short-term thickness under compressive stress and determination of water flow capacity under equivalent short-term stress. Among those, the only long-term test is the creep test, giving the method an advantageous practical quality.

Long-term flow capacity reduction factors range between 1.13 and 1.70 and are consistent with creep strain of each product. These figures show that neglecting long-term deformation, whether of the drainage core or of the geotextile filters, can lead to overestimation of flow capacity up to 70%.

ACKNOWLEDGEMENTS

The authors wish to thank Nathalie Touze-Foltz for her useful help and suggestions.

REFERENCES

Böttcher RD (2006) Long-term flow capacity of geocomposites. Proc. 8th Int. Conf. on Geosynthetics, Yokohama: 423-426

Chai JC, Miura N, Nomura T (2004) Effect of hydraulic radius on long term drainage capacity of geosynthetics drains. Geotextiles and Geomembranes 22: 3-16

EN 1897 (2003) Geotextiles and geotextile-related products – Determination of the compressive creep properties. European Committee for Standardization

EN ISO 12958 (1999) Geotextiles and geotextile-related products – Determination of water flow capacity in their plane. European Committee for Standardization

EN ISO 9863-1 (2005) Geosynthetics – Determination of thickness at specified pressures – Part 1 – Single layers. European Committee for Standardization

Giroud JP, Zornberg JG, Zhao A (2000a) Hydraulic design of geosynthetic and granular liquid collection layers. Geosynthetics International 7(4-6): 285-380

Giroud JP, Zhao A, Richardson, GN (2000b) Effect of thickness reduction on geosynthetic hydraulic transmissivity. Geosynthetics International 7(4-6): 433-452

Gourc JP, Faure Y, Rollin A, Lafleur J (1982) Structural permeability law of geotextiles. Proc. 2nd Int. Conf. on Geotextiles, Las Vegas 1: 149-154

Jaisi DP, Glawe U, Bergado DT (2005) Hydraulic behaviour of geosynthetic and granular landfill drainage materials in the Sa Kaeo landfill, Thailand. Geotextiles and Geomembranes. 23: 185-204

Jarousseau C, Gallo R (2004) Drainage geocomposites: relation between water flow capacity and thickness in the long-term. Proc. 3rd European Geosynthetics Conf., Eurogeo3, Munich: 349-354

Koerner RM (1994) Designing with geosynthetics. 3rd edition. Prentice Hall

Mc Gown A, Kabir MH, Murray RT (1982) Compressibility and hydraulic conductivity of geotexiles. Proc. 2nd Int. Conf. on Geotextiles, Las Vegas 1: 167-172

Müller-Rochholtz J, Bronstein Z, Recker C, Diederich, R (2006) Influence of geotextile filters on the discharge capacity of geocomposite drainage materials in long term tests wit soil contact. Proc. 8th Int. Conf. on Geosynthetics, Yokohama: 427-430

Palmeira EM, Gardoni MG (2002) Drainage and filtration properties of non-woven geotextiles under confinement using different experimental techniques. Geotextiles and Geomembranes 20: 97-115

Sawicki A, Kazimierowicz-Frankowska K (1998) Creep behaviour of geosynthetics. Geotextiles and Geomembranes 16: 365-382

STUDY ON VERTICAL PERMEABILITY COEFFICIENT OF NONWOVEN GEOTEXTILE

L.F. Liu[1], R. H.Li[2] and J.K. Chi[3]

ABSTRACT: Permeability is one of the most important characteristics for nonwoven geotextiles used in filtration systems. Based on drag-force theory and Darcy's Law, the relation between fabric structure and permeability is theoretically discussed in this paper, and a mathematical model on the vertical permeability coefficient is also established. Comparison with experimental results shows that the theoretical model is accurate for heat-bonded nonwoven geotextiles.

KEYWORDS: permeability property, vertical permeability coefficient, drag-force model, nonwoven geotextiles

INTRODUCTION

In selecting geotextiles for civil engineering works, their characteristics, which are closely related to the type of application, have to be principally considered. Their permeability is especially important when they are used in filtration systems, and usually expressed by vertical permeability coefficient. This paper only sheds light on the vertical permeability coefficient of heat-bonded nonwoven geotextiles only.

There are many researches on the permeability of porous medium (Carman 1956; Mao and Russeull 2000a; Masounave et al. 1981; Rollin et al. 1982), which can be classified into two types according to their theoretical basics: one is based on capillary model, the other on drag-force model. As for the porous medium with high porosity, such as nonwoven geotextile, drag-force model is more applicable to study their permeability property according to former researchers' theoretical studies (Carman 1956; Cox 1970; Happel 1959; Mao and Russeull 2000a; Masounave et al. 1981; Piekaar and Clarenburg, 1967; Rollin et al. 1982; Scheidegger 1974). So, drag-force model is also introduced in this paper to analyse the theoretical vertical permeability of heat-bonded nonwoven geotextiles.

BACKGROUND

A solid boundary can act on liquid that have relative motion against it. The force is usually caused by the following two reasons: one is viscidity and velocity grade on the boundary, which causes the shear stress tangential with the boundary; the other is the change of pressure along the boundary, which cause the stress vertical to the boundary. Cumulating the two vectors of forces along the whole surface of the considered solid can get the composition of forces, in which the component along the direction of moving liquid can be defined as resistance (or drag-force). The resistance is equal to the vectorial resultant of friction component D_f and pressure component D_p, which can be expressed as follows respectively (Jacob 1983).

$$D_f = C_f \rho \frac{V_s^2}{2} A_f \tag{1}$$

$$D_p = C_p \rho \frac{V_s^2}{2} A_p \tag{2}$$

where C_f, C_p are drag-force coefficients of friction component and pressure component respectively; ρ is density of the liquid; V_s is velocity of the liquid; A_f, A_p are area of the selected reference planes.

Based on the two expressions above, Iberall (Jacob 1983) established a theoretical model for porous medium consisted of random distributed, cylindrical fibers with the same diameter. According to the theoretical model if all the fibers distributed in a plane vertical to the flowing direction of liquid, then the drag-force carried by a single fiber with unit length can be expressed as following:

$$f = 4\pi\mu V_0 \tag{3}$$

where f is drag-force carried by a single fiber with unit length; μ is dynamical viscidity of the liquid; V_0 is the average velocity of liquid in pores.

[1] Associate Professor, College of Textiles, Donghua University, CHINA. Email: lifangliu@dhu.edu.cn
[2] Postdoctor, School of Economics and Management, Tongji University, CHINA. Email: liruihai@126.com
[3] Professor, Shanghai Investigation Design & Research Institute, CHINA. Email:

THEORETICAL MODEL OF VERTICAL PERMEABILITY COEFFICIENT OF NONWOVEN GEOTEXTILE

The following assumptions are made before theoretical analysis: (1) the fibers in nonwoven geotextile are all cylindrical, with the same diameter and density; (2) All fibers are randomly distributed in plane of nonwoven geotextile, i.e. no fibers are aligned in the Z-direction. And nonwoven geotextile is homogenous; (3) The distance between fibers and the length of individual fibers are much greater than the fiber diameter, that is, nonwoven geotextile has high porosity; (4) liquid only move in the vertical direction of nonwoven geotextile plane; (5) The inertial forces of the fluid are negligible, i.e. the fluid has a low Reynolds number Re.

Presume that the mass per unit area of nonwoven geotextile is μ_g (kg/m^2), thickness is T_g (m), fiber diameter is d_f (m), fiber density is ρ_f (kg/m^3), so the density of nonwoven geotextile ρ_g (kg/m^3) can be got as

$$\rho_g = \frac{\mu_g}{T_g} \tag{4}$$

The total mass of fiber in unit volume is equal to the density of nonwoven geotextile. That is

$$\frac{\pi}{4} d_f^2 l \rho_f = \rho_g \tag{5}$$

where l is the specific length, i.e. the total length of fiber in unit volume of nonwoven geotextile.

With Eqs. 4 and 5, l (m) can be expressed by

$$l = \frac{4\mu_g}{\pi T_g \rho_f d_f^2} \tag{6}$$

According to the assumptions above, if fiber length is much greater than its diameter, the total drag-force acting on unit volume of nonwoven geotextile can be regarded as the sum of drag-force on every single fiber with unit length (Happel 1959), that is

$$F = f \cdot l = \frac{16\mu\mu_g V_0}{T_g \rho_f d_f^2} \tag{7}$$

where F is the total drag-force, N.

The pressure gradient in the flow direction due to the drag-force in unit volume of the fabric is equal to the pressure drop per unit length of flow resulting from the drag-force in this direction. So the following expression can be got:

$$\frac{\Delta P}{T_g} = F \quad \text{and} \quad \Delta P = \frac{16\mu\mu_g V_0}{\rho_f d_f^2} \tag{8}$$

where ΔP is the difference in hydraulic pressure across nonwoven geotextile, N/m^2.

Use a basic formulation in hydrodynamics $\Delta P = \rho g \Delta h$, the following expression can be obtained:

$$\Delta h = \frac{16\mu}{\rho g} \cdot \frac{\mu_g V_0}{\rho_f d_f^2} \tag{9}$$

where g is the acceleration of gravity, m/s^2; ρ is the liquid density, kg/m^3; Δh is the difference in water level across nonwoven geotextile, m.

The pores in nonwoven geotextile are flexuous and continuous, which make their actual length much greater than the thickness of nonwoven geotextile. Carman (1956) had researched on it and got that the former was about $\sqrt{2}$ times of the later, that is

$$V_0 = \sqrt{2} V \tag{10}$$

where V is the observed liquid velocity, m/s.

According to Darcy's Law, the vertical permeability coefficient of nonwoven geotextile can be expressed as (Nanjing Water-Conservancy and Science Academe 1991):

$$K = \frac{V T_g}{\Delta h} \tag{11}$$

where K is the vertical permeability coefficient of nonwoven geotextile, m/s.

With equations 9 — 11, the vertical permeability coefficient of nonwoven geotextile can be got as

$$K = \frac{\sqrt{2}\rho g}{32\mu} \cdot \frac{\rho_f d_f^2 T_g}{\mu_g} \quad \text{(m/s)} \tag{12}$$

In particular, when the liquid is water at 20℃, so $\rho = 998.2$ kg/m^3, $\mu = 1.004 \times 10^{-3}$ m/s, and $g = 9.8$ m/s^2, then the following equations can be obtained:

$$\begin{aligned} K &= \frac{4.31\rho_f d_f^2 T_g}{\mu_g} \times 10^5 \quad \text{(m/s)} \\ &= \frac{4.31\rho_f d_f^2}{\rho_g} \times 10^5 \quad \text{(m/s)} \\ &= \frac{4.31 d_f^2}{1-\varepsilon} \times 10^5 \quad \text{(m/s)} \end{aligned} \tag{13}$$

where ε is the porosity of nonwoven geotextile, %.

Equation 13 shows that the vertical permeability coefficient is directly related to the mass per unit area and thickness of nonwoven geotextile, as well as fiber density and diameter.

EXPERIMENTS

Three needle-punched nonwoven geotextiles marked 1#—3# and three heat-bonded nonwoven geotextiles marked 4#—6# are selected as samples respectively, as shown in Table 1. The fiber diameter of samples 1# and 4# are 20.1 um, and those of samples 2#, 3#, 5#, and 6# are

21.7 um respectively in Table 1. The specific parameters and vertical permeability coefficients at 20℃ of those samples are all tested using the method introduced in the testing handbook (Nanjing Water-Conservancy and Science Academe 1991). The results are also listed in Table 1, in which the vertical permeability coefficients of every sample are average value of five testing results. Moreover, based on Eq. 13, the theoretical vertical permeability coefficients of the six samples and their relative errors with the corresponding experimental values are also calculated and shown in Table 1.

Table 1 The specific parameters and vertical permeability coefficient of samples

	μ_g g/m^2	T_g mm	ρ_g kg/m^3	ε %	K_{ex} cm/s	K_{th} cm/s	R %
1#	400	4.76	84.03	93.9	0.352	0.285	19.0
2#	410	5.72	71.68	94.8	0.514	0.390	24.1
3#	159	3.72	42.74	96.9	0.787	0.655	16.8
4#	400	4.53	88.30	93.6	0.286	0.272	4.89
5#	400	4.61	86.77	93.7	0.343	0.322	6.1
6#	160	3.65	43.84	96.8	0.671	0.634	5.5

In table 1, K_{ex} is the experimental value of the vertical permeability coefficient, while K_{th} is the theoretical value; R is the relative error of K_{ex} and K_{th}.

The results in Table 1 show that the relative errors of K_{ex} and K_{th} of samples $4^{\#}$~$6^{\#}$ are all less than 7%, however samples $1^{\#}$~$3^{\#}$ are much greater, especially that of sample $2^{\#}$, which reach to 24.1%, which indicate that the theoretical model in this paper is more suitable to heat-bonded nonwvoen geotextiles. This is mainly because that, some fibers in the needle-punched nonwoven can move with the needles and then distribute in the vertical direction of nonwoven plane, those fibers not only have less resistance to the water, but also guide water to flow quickly; However, all fibers are theoretically presumed to be distributed horizontally in nonwoven geotextile plane in this paper, which is the main reason that the experimental vertical permeability coefficients of samples $1^{\#}$—$3^{\#}$ are higher than the theoretical values in Table 1.

CONCLUSIONS

In this paper, the relation between nonwoven geotextile structure parameters and vertical permeability coefficient is theoretically studied on the base of drag-force model and Darcy's Law. A mathematical model expressing the relation of vertical permeability coefficient with nonwoven geotextile structure parameters is proposed and validated by experiments.

According to the analyses in this paper, the theoretical vertical permeability coefficient of nonwoven geotextile can be expressed as Eq. 12, which can simplified as Eq. 13 when the liquid is water at 20℃.

Experimental results show that the theoretical model in this paper is more suitable to heat-bonded nonwoven geotextiles, however not applicable to needle-punched nonwoven geotextiles.

ACKNOWLEDGEMENTS

The authors wish to thank Prof. C.Y. Chu from Donghua University, China, for his kind and efficient help to finish this paper.

REFERENCES

Carman PC (1956) Flow of Gases through Porous Media. Butterworths Scientific Publications. London

Cox RG (1970) The Motion of Long Slender Bodies in a Viscous Fluid. Part 1. J. Fluid Mech 44: 791-810

Happel J (1959) Viscous Flow Relative to Arrays of Cylinders. Amer. Inst. Chem. Eng. J 5: 174-177

Jacob B (1983) Hydrokinetics of Porous Medium (in Chinese, translated by Jingsheng Li and Chongxi Chen). China Architectural Industry Publisher, Peking

Mao N, Russeull SJ (2000a) Directional Permeability in Homogeneous Nonwoven Strucures PartI: The Relationship between Directional Permeability and Fiber Orientation. J. Text. Inst 91(2): 235-243

Mao N, Russeull S J (2000b) Directional Permeability in Homogeneous Nonwoven Strucures Part II: Permeability in Idealized Structures. J. Text. Inst. 91(2): 244-257

Masounave J, Rollin AL, Denis R (1981) Prediction of Permeability of Nonwoven Geotextiles from Morphometry Analysis. J. Microsc 121: 99-110

Nanjing Water-Conservancy and Science Academe(1991) Testing Handbook of Geosynthetics (in Chinese). Water Conservancy and Electricity Publisher, Peking

Piekaar HW, Clarenburg LA (1967) Aerosol Filters: Pore Size Distribution in Fibrous Filters. Chem. Eng. Sci. 22: 1399-1408

Rollin AL, Denis R, Estaque L, Masounave J (1982) Hydraulic Behaviour of Synthetic Nonwoven Filter Fabrics. Can. J. Chem. Eng. 60: 226-234

Scheidegger A.E (1974) The Physics of Flow through Porous media. University of Toronto Press. Toronto

DISCRETE ELEMENT MODELLING OF GEOGRID PULLOUT TEST

J. Zhang[1], N. Yasufuku[2] and H. Ochiai[3]

ABSTRACT: The pullout test was effective in order to study the interaction behavior between soil and geogrid in the reinforced zone. Therefore its resulting properties had important implications on the reinforced soil structure practice. It had been demonstrated by experimental studies that several parameters (geotechnical properties of soil, geogrid properties, applied vertical effective stress) influenced on the pullout behavior and pullout resistance. As a micro-mechanics study is difficult to carry out in traditional study, a discrete element modelling of pullout test was employed here to investigate the pullout behavior of geogrid embedded in a compacted granular soil. The discrete element modelling was used to investigate the interaction between the geogrid and compacted granular soil paying attention to the properties of geogrid, taking into account the compaction effect linked with porosity. Compared with the experimental results, the discrete modelling was favourable. The discrete element modelling was capable of evaluating the interaction between soil and reinforcement.

KEYWORDS: discrete element modelling, pullout test, interaction, porosity

INTRODUCTION

The behavior of reinforced soil structures is largely governed by interaction mechanisms developing between reinforcement and backfill soil. The pullout test is most commonly used in the reinforced soil practice, which is believed to be able to evaluate the reinforced mechanism in more detail. On the other hand, numerical analysis such as FEM is conducted to investigate the interaction effect of reinforced soil. However, the interaction effect on the geogrid reinforcement could not be investigated directly in these attempts. Soil is a kind of discrete material, the discrete element method (DEM) is based on discrete feature of soils. The soil particles act on reinforcement particles directly in DEM pullout test model without interaction unit as other analysis methods; therefore, the interaction could be reflected directly. Furthermore, the shear resistance involves an interface frictional resistance and bearing resistance developing against the front of transverse ribs. The contributions of frictional resistance and bearing resistance could also be evaluated in the DEM pullout test model respectively. The DEM hold much promise as a tool for investigating aggregate-geogrid composite systems (McDowell et al. 2006). This paper presents DEM simulation of geogrid pullout behavior using PFC^{2D}. The DEM Pullout test model evaluates the pullout mechanism in a microscopic view and interaction behavior paying attention to compaction effect linked with porosity.

MICROSCOPIC PARAMETERS OF DEM MODEL

The DEM soil sample used in this study differs from real tested soil, although their grading distributions are similar. A Mohr-Coulomb liked slip contact model for soil material is applied to enable close coupling of the simulation and soil physical behavior. Microscopic parameters of DEM soil sample are adjusted by numerical biaxial tests. Geogrid is modelled as bonded particle chain. And parameters for such geogrid are calibrated by simulating simple tension of geogrid in the air.

Fig. 1 provides the slip contact model for the DEM soil sample, consisting of normal contact and shear contact. As shown in Fig. 1, the normal contact included a normal spring and a divider; no tensile force is transmitted through the contact when the particles are separated. The shear contact includes a shear spring and a slider that provides a shear resistance controlled by the Mohr-Coulomb criterion. The normal contact is characterized by the normal contact stiffness k_n. The shear contact is characterized by the shear contact stiffness k_s and the shear strength is defined by the interparticle friction angle φ_μ.

[1] Ph.D Student, Department of Civil Engineering, Kyushu University, Fukuoka, JAPAN Email: soil19@civil.kyushu-u.ac.jp
[2] Associate Professor, ditto. Email: yasufuku@civil.kyushu-u.ac.jp
[3] Professor, ditto. Email: ochiai@civil.kyushu-u.ac.jp

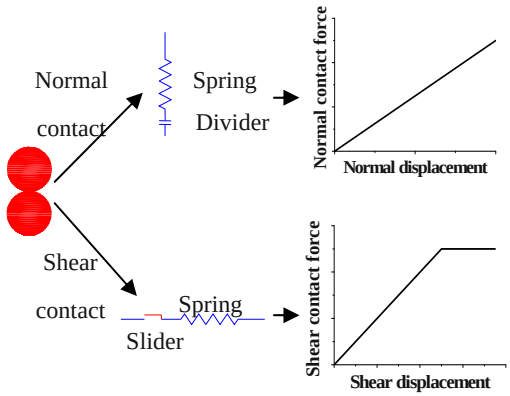

Fig. 1 Contact models of soil sample

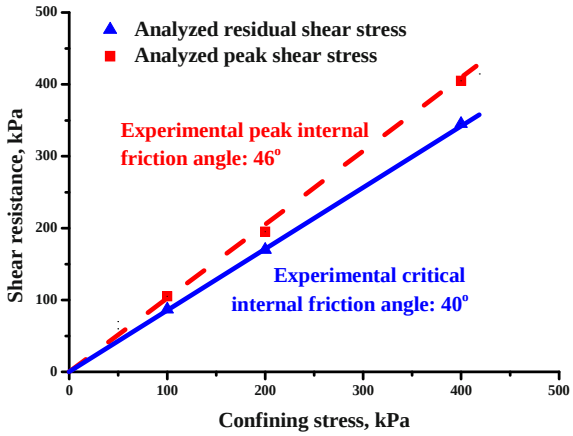

Fig. 2 Shear resistance of DEM soil sample

In order to couple with the microscopic parameters of DEM analysis with the nature of cohesionless soil assembly, the biaxial test is carried out to investigate the influence of microscopic parameters (k_n, k_s and φ_μ) on the macro behavior of soil sample.

The ball stiffness ratio (k_n / k_s) was shown that it did not have great effect on strain-stress behavior and shear strength of soil sample. Meanwhile, the normal contact stiffness was closely linked with Young's modulus of soil sample. And the interparticle angle had great influence on the shear strength of soil sample. The shear strength increased with the increase of the interparticle friction angle (Zhang et al. 2007).

Therefore, to determine the parameters of slip contact model of cohesionless soil, it could be assumed that the normal contact stiffness is equal to shear contact stiffness ($k_n = k_s$), and that the interparticle friction angle (φ_μ) is equal to the critical internal friction angle. The normal contact stiffness k_n is first estimated from a uniform array of particles, and then examined through biaxial simulation coupling with the Young's modulus of soil assembly. Fig. 2 shows that this procedure fit well with the tested soil sample.

The geogrid is modelled as disks bonded together by contact bond (Fig. 3). Considering that the geogrid pullout resistance is made up of frictional resistance and bearing resistance of transverse ribs, the junction of geogrid is simulated using a cluster of bonded particles to reflect the influence of bearing resistance (Fig. 3). Microscopic parameters for such geogrid are calibrated by simulating simple tension of geogrid in the air (Fig.4).

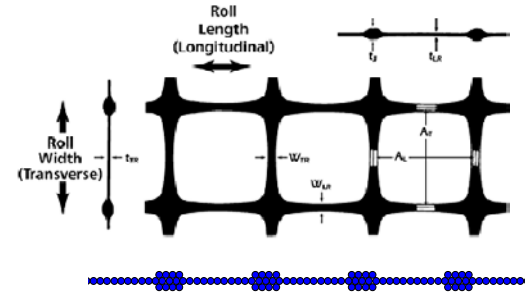

Fig. 3 DEM model of geogrid

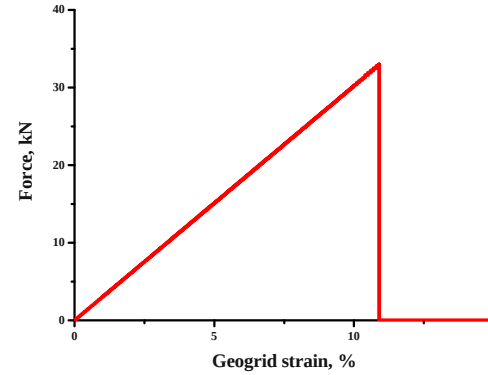

Fig. 4 Simple tension test for geogrid

Table 1 Microscopic parameters for DEM model of soil and geogrid

Soil model	Value	Geogrid model	Value
Density, g/m^3	2.63	Density, g/m^3	0.191
Normal stiffness, kN/m	2.0×10^5	Radius, mm	1.0
Shear stiffness, kN/m	2.0×10^5	Normal stiffness, kN/m	2.36×10^5
Friction angle	40.1°	Shear stiffness, kN/m	2.36×10^5
		Bond normal strength, kN	1.0×10^3
		Bond shear strength, kN	1.0×10^3
		Interface friction factor	0.843

IMPLEMENTATION OF THE PULLOUT TEST

Discrete element simulations of pullout test are performed in order to reproduce the response of geogrid embedded in gravel soil.

The DEM pullout test model is shown in Fig. 5, displaying a soil sample of disks and the location of embedded geogrid in a pullout box. Using servo-control,

the velocity of top wall is adjusted in a feedback loop to achieve a target vertical stress. The dimensions of the pullout test box are h (height) = 300 mm, w (width) = 370 mm and the geogrid length embedded in the soil sample is 180 mm.

Microscopic parameters of DEM pullout model are given in Table 1. The microscopic parameters for soil sample and geogrid are defined following the method mentioned above. And to avoid any dynamic effect, the pullout test is run under a low pullout rate of 0.0002mm/timestep.

The simulation results in terms of macroscopic behavior are presented in Fig. 6. The pullout resistance is calculated by: $\tau = F / 2BL_G$,where τ is the pullout resistance, F is the pullout force, B is the geogrid width, and L_G is the length of geogrid in the soil sample. The simulated pullout test result is close to the experiment results when displacement is small. They are different when pullout displacement increases. This difference might due to that the boundary condition of the front wall is hard to be simulated accurately when junction unit is pulled out.

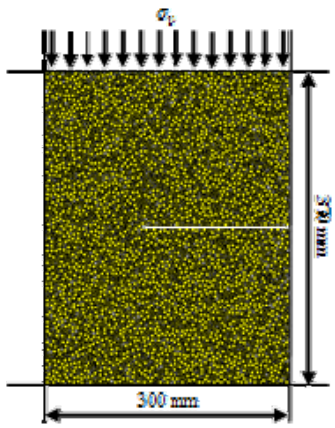

Fig. 5 DEM model of pullout test

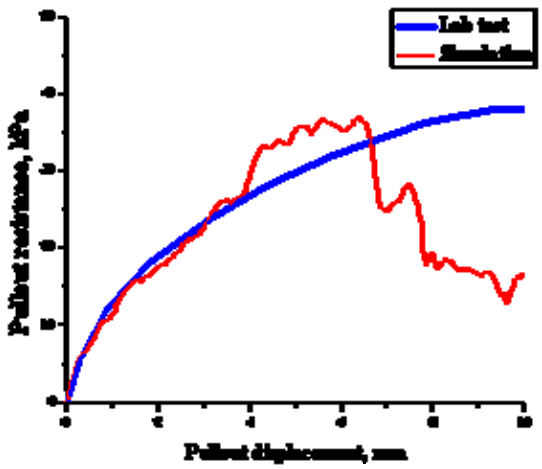

Fig. 6 Pullout resistance as a function of displacement

RESULTS AND DISCUSSIONS ON DEM ANALYSIS

Geogrid interaction with soil is a complex phenomenon. The stress transfer mechanism at soil reinforcement interface involves shear resistance and normal stress. The shear resistance components involve frictional resistances at the longitudinal ribs and transverse ribs and bearing resistance against transverse ribs.

The predicted components of shear resistance to pullout from DEM pullout test model are plotted in Fig. 7 against the pullout displacement expressed as percentage of the ultimate resistance. Although the analyzed components are something scattered, the tendency of the shear resistance components is clear. Initially, greatest transfer of shear resistance is taken by the longitudinal ribs friction. The component of longitudinal friction decreases as the increase of pullout displacement, while the component of bearing resistance increases and transverse component is comparatively stable. All three components mobilize from the beginning of load well tally with the theoretical analysis results of pullout mechanism (Ragui et al. 1994).

The effect of restrained soil dilatancy on soil reinforcement interaction under field conditions and pullout test was observed earlier. The dialatancy behavior is dramatically influenced by the compaction effect linking with the porosity of soil.

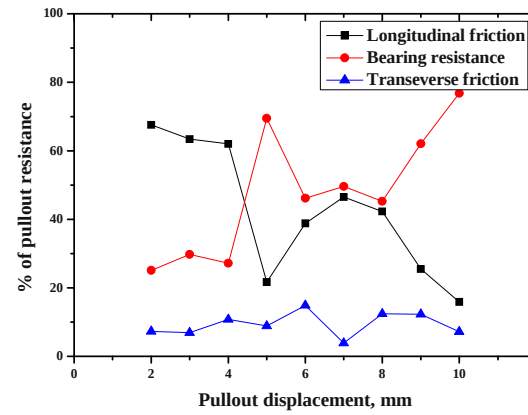

Fig. 7 Predicted components of resistance

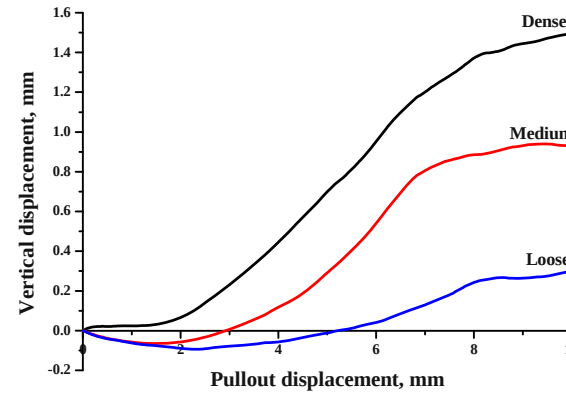

Fig. 8 Vertical displacement of top wall

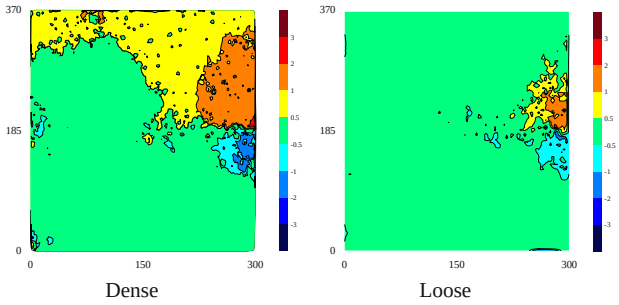

Fig. 9 Vertical displacement field

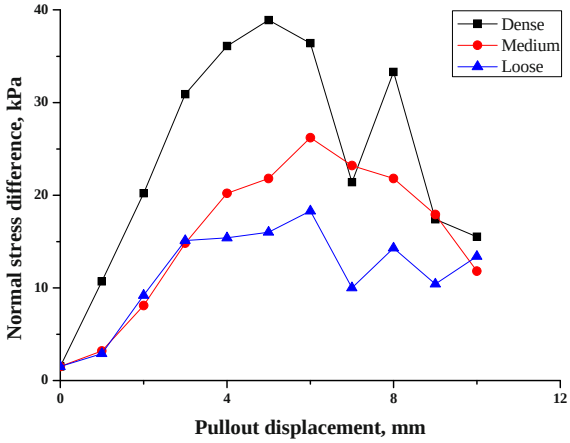

Fig. 10 Changes in normal stress during pullout

Fig. 8 indicated that the dilatancy behavior is more obvious in dense soil sample. It could also be proved in Fig. 9. It is clear in Fig. 9 that the dilatancy occurs in wider zones with greater magnitude in denser soil.

The extra normal stress applied on the embed geogrid aroused by dilatancy could be investigated in this DEM pullout test model. The normal difference in magnitude between actual normal stress and applied normal stress, due to the restrained dilatancy effect in DEM pullout test simulation under different density is given in Fig. 10. The restrained dilatancy effect is significantly linked with the density of soil sample. Initially, the normal difference increases as the increase of the pullout displacement, and then slowly decreases when the pullout displacement continuously increases. In general, the restrained dilatancy effect becomes greater as the soil sample become denser. This restrained dilatancy behavior is similar to previous experimental results (Hayashi et al. 1999).

CONCLUSIONS

Here presented a DEM model to simulate the pullout test. The DEM model of pullout test was demonstrated reasonable and helpful. Such DEM model was able to analyze the interaction between soil and geogrid directly. It is capable of evaluating the shear resistance components during pullout test, in accord with the theoretical analysis of pullout mechanism. And the DEM pullout model also could reasonably reflect the restrained dilatancy behavior during pullout, corresponding to previous experiment. It was shown that the density had great influence on the restrained dilatancy effect on soil reinforcement interaction during pullout test. The simulation results indicated that the restrained dilatancy effect was greater under soil density

REFERENCES

Hayashi S, Shahu JT, Watanabe K (1999) Changes in interface stresses during pullout tests on georgic strip reinforcement, Geotechnical Testing Journal, GTJ-ODJ 22(3):32-88

Liu SH, Sun D, Matsuoka H (2005) On the interface friction in direct test, Computers and Geotechnics 32:317-325

McDowell GR, Harireche O, Konietzky H, Brown SF, Thom NH (2006) Discrete element modelling of geogrid-reinforced aggregates, Proceedings of the Institution of Civil Engineers—Geotechnical Engineering 159: 35-48

Nejad FM, Small JC (2005) Pullout behaviour of geogrids, Iranian Journal of Science & Technology, Engineering 29:301-310

Wilson-Fahmy RF, Koerner RM, Sansone LJ (1994) Experimental behavior of polymeric geogrids in pullout, Journal of Geotechnical Engineering, ASCE 120(4):661-677

Zhang J, Yasufuku N, Ochiai H (2007) A few considerations of pullout test characteristics of geogrid reinforced sand using DEM analysis, Geosynthetics Engineering Journal 22:103-110

STUDY ON THE WHOLE STABILITY ANALYSIS METHOD FOR REINFORCED SOFT FOUNDATION OF EMBANKMENT WITH GEOFABRIC

H.X. Tang[1] and H.Q. Wang[2]

ABSTRACT: Based on full-scale test data, the sliding resistance and reinforcement effect are revealed using several different analysis methods. A new circular sliding surface passing the maximal vertical settlement point, which is the center point of the interface between embankment and geofabric, is put forward. An applied simplified circular failure analysis method, which can take the role of geofabric into account more reasonably for computing the factor of safety of the embankment with reinforced underlying layers, is brought forward also.

KEYWORDS: geofabric, reinforced underlying layer, full scale test, applied simplified circular failure analysis method

INTRODUCTION

Circular failure analysis method, which is usually adopted to calculate the safety factor against deep sliding of reinforced underlying layer of embankment with geofabric, is suspectable in engineering practice. Some problems can be concluded as follows (stated in Technical standard for applications of geosynthetics, GB50290-98) "At present, the safety coefficients are improved little with circular failure analysis method stated in the criterion for preventing deep sliding of reinforced underlying layer of embankment with geofabric, which doesn't agree with the actual effect. It shows that the circular arc analysis method doesn't reflect the whole effect of reinforced geofabric. So the analysis methods in existence are to be improved." Recently, some theory researches and analysis for engineering in practice have appeared(e.g., Chen et al. 1990; Xu 1991; Zhao et al. 1991; Xu and Hong 2000; Lin et al. 2000; Liu et al. 2003). Tang and Wang put forward a new circular sliding surface passing through the maximal vertical settlement point, which is the center point of interface between embankment and geofabric. With the new sliding surface, the resulting factors of safety of the embankment without or with one or two reinforced underlying layers is improved obviously and closer to actual situation than the old one (Tang and Wang 2006). With the example of the full scale test stated in Tang and Wang's paper, this paper will step further to talk about the safety of reinforced embankment with geofabric based on circular failure analysis method. As a result, an applied simplifid circular failure analysis method, which can take the role of geofabric into account more reasonably for computing the factor of safety of the embankment with reinforced underlying layers, is put forward.

FULL SCALE TEST

In the 1980's, a great deal of embankment against the seawater had been built in the seaport of Shengli Oil Field. But later, the project had to be shut down because some sections of embankment can not achieve the height of obstructing out the seawater due to their instability and collapse. The reason is that but the surface layer(sandy loam with thickness of 1.0 m—2.0 m) of embankment foundation has some bearing capacity, the lower part is soft layer of mucky loam with thickness of 2.6 m—9.3 m. The instability and failure of embankment is mainly related to the insufficient bearing capacity of soft layer. To get the essential data to examine the effect of the building plan, and to approve the experimental and numerical results, the field full scale failure tests are put up. The testing embankment with the foundation of 2.6 m—9.3 m thick soft layer of mucky loam is divided into four sections. The typical section is depicted in Fig. 3.

Here only the embankment with one reinforced underlying layer of geofabric spreading on the surface of its foundation is introduced. The filling material is sandy loam, with 0.3 m thick one layer. After rolling the dry density should be 1.55 g/cm^3. At the same time, the observation instruments such as border piles, surface settlement plates, displacement gauges of geofabric, magnetic probe extensometers, pore water pressure cells and so on are buried in the embankments and its foundations. In addition, the geological prospecting and vane shear test in field, and tensile tests of the strips with

[1] Doctor, School of Civil and Hydraulic Engineering, Dalian University of Technology, CHINA. Email: tanghx@dlut.edu.cn
[2] Professor, School of Civil and Hydraulic Engineering, Dalian University of Technology, CHINA. Email:hqwang@163.com

width of 5 cm selected in the longitude and latitude directions from the geofabric are carried out in laboratory. Fig. 1 illustrates the relationship between tensile force and tensile strain.

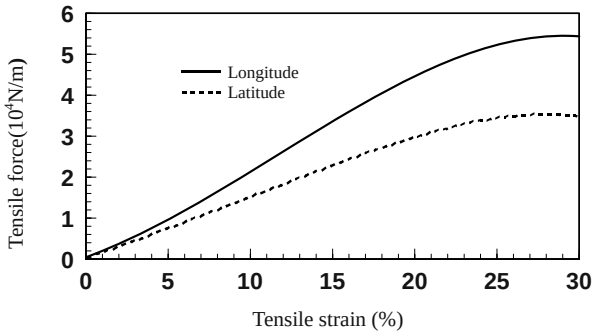

Fig. 1 The relationship between tensile force and tensile strain of geofabric

When the height of filling soil achieves 3.86 m, the horizontal displacement observed by border piles and the vertical settlement observed by surface settlement plates on the surface of foundation, and the tensile strain observed by displacement gauges of geofabric start to increase. When the height achieves 4.0 m, the observed numerical value increases rapidly. As horizontal displacement and vertical settlement increased from several decades to one hundred millimetres everyday, the embankment can be considered to enter the state of limit equilibrium. When the height achieves 4.78 m, a majority of embankment together with part of foundation slide towards one side and the whole instability occurs. At the same time the tensile strain of geofabric, the horizontal displacement and the vertical settlement on the surface of foundation increase to the maximum rapidly, then cease or start to decrease. The settlement contour line of section B is depicted in Fig. 2.

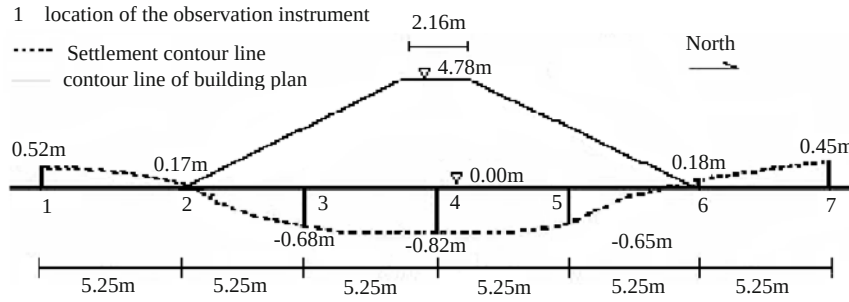

Fig. 2 The settlement contour line of the embankment with one reinforced underlying layer of geofabric

THE CALCULATION METHODS FOR DEEPLY SLIDING OF REINFORCED EMBANKMENT

Several different conditions are considered to calculate the factors of safety of reinforced embankment with geofabric based on circular failure analysis method.

The Results Based on Standard Circular Failure Analysis Method

The material parameters used in the analysis can be seen from Table 1. The depth of ground water is －1.5 m.

Table 1 Material parameters used in the analysis

Material types	Shear strength parameters
Embankment	$\varphi_1 = 32^\circ$, c=2kPa
The interface between soil and geofabric	$\varphi_1 = 30^\circ$, c=5kPa
Sandy loam of the upper layer of foundation	$\varphi_1 = 36^\circ$, c=35kPa
Mucky loam of the lower layer of foundation	$\varphi_1 = 0$, c=12.5kPa

According to the circular failure analysis method, the most dangerous arc of the embankment without reinforced geofabric is the arc AAAA, and the minimum factor of safety (K_1) is 0.852, as can be found from Fig. 3. The settlement of the embankment has been reckoned in.

According to technical standard for applications of geosynthetics, if the reinforcement effect and the sliding resistance moment of geofabric are reckoned in, the minimum factor of safety (K_2) is 1.047. The tension resistance moment strength supplied by geofabric near the failure surface is not reduced from the limit tension resistance strength according to technical standard, but adopted 3.6 t/m corresponding to the maximum of tensile strain (15.58%). The direction of the sliding resistance force is neither the tangent direction of sliding arc nor the original horizontal direction of the geofabric put on the surface of the ground, but the direction of ED, which is the figure of geofabric after settlement deformation.

The difference between these two factors of safety K_1 and K_2 is 0.195, which can be seen as the contribution of reinforced geofabric.

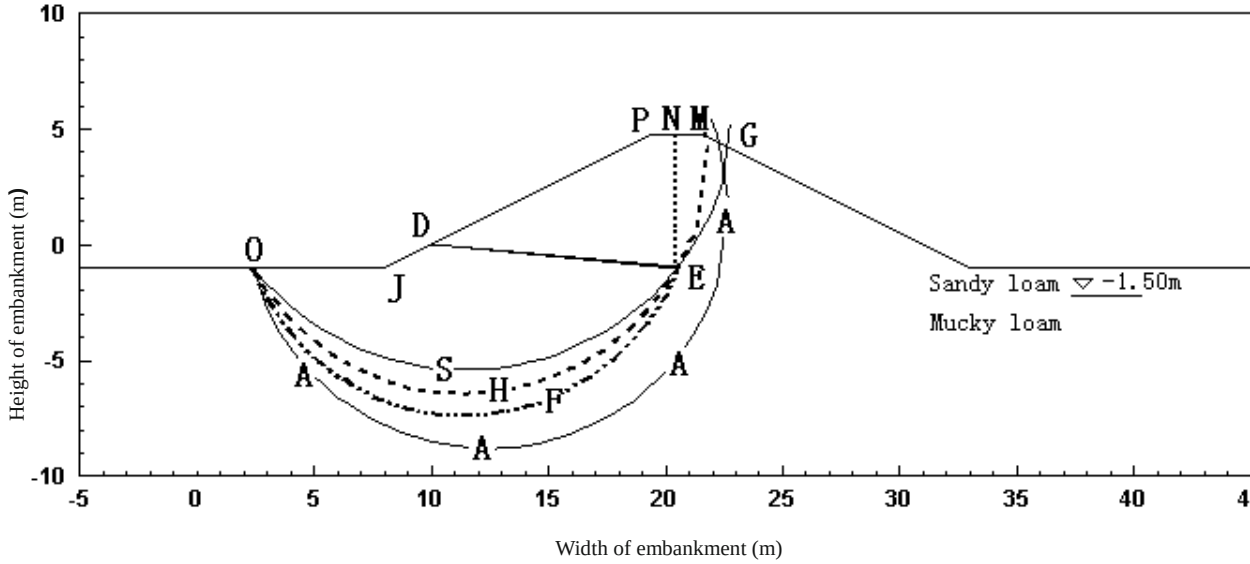

Fig. 3 The limit slip surfaces under different conditions

The Suggested Circular Failure Analysis Method

From Tang and Wang's opinion and the above analysis, it can be concluded that the preconditions of present method are:

(1)The embankment is symmetry and located on the horizontal uniformity foundation, so the maximal vertical settlement point, through which the potential sliding arc passes, is the center point of interface between embankment and geofabric, where the maximal extension deformation of geofabric may occur.

(2)The foundation will reach the limit state before the embankment. When too much deformation of geofabric occurs or the geofabric is torn up, the sliding failure will appear in the foundation first, then the embankment slides and failure takes place.

(3)The sliding resistance role of the geofabric is embodied by the resistance moment, which is supplied by geofabric after settlement deformation.

Limit the potential sliding arc passing through the point of maximal vertical settlement

The maximal vertical settlement point is the center point of interface between embankment and geofabric. The most dangerous arc of the embankment without reinforced geofabric is the arc MEHO, and the minimum factor of safety (K_3) is 0.990, as can be found from Fig. 3. The intersection point O of arc MEHO and the ground surface locates in the crack area which appears in full scale test. The factor of safety K_3 is greater than K_1, which reveals the indirect sliding resistance role of reinforced underlying layer.

The factor of safety under the condition of embankment sliding on the surface of geofabric ED

The potential sliding surfafce is the arc GED, and the minimum factor of safety (K_4) is 6.428, as can be found from Fig. 3. It indicates that this sliding type may not appear. But in fact, the whole sliding failure does occur in site test, that can only be interpreted that the foundation enters the limit equilibrium state first, which affects the safety of embankment on the foundation and induce the whole failure of embankment later. This phenomenon can not be reflected by the circular failure analysis method according to technical standard. It should be pointed out that point G locates in the crack area which appears on the embankment in full scale test.

The safety of the foundation under the embankment

The safety of the foundation under the embankment with the restriction of the sliding arc passing through the point of maximal vertical settlement, which is the center point of interface between embankment and geofabric. In this case, the potential sliding body of embankment GEDPN is considered as the loads acting on the foundation. The potential sliding surface is the arc EFO, and the minimum factor of safety K_5 is 0.917, as can be found from Fig. 3. It is noticeable that the height of the embankment should be reduced to 3.87 m when the factor of safety K_5 is 1.0, which corresponding to the whole failure analysis for the full scale test. The factor of safety K_5 is less than K_3, which means the failure of foundation occurs before the whole failure takes place.

The whole failure analysis for the embankment and the foundation based on circular failure analysis method

Affected by the sliding failure of foundation, the embankment on the foundation will slide down along the arc GE, with which the potential sliding arc ESO connected in the foundation can be gained, as can be found from Fig. 3. The minimum factor of safety K_6 of arc ESO is 0.984. The factor of safety K_6 is less than K_3, which means that the embankment slides down along the potential sliding arc GE other than ME.

The sliding resistance role of the geofabric

The sliding resistance role of the geofabric is embodied by the resistance moment, which is supplied by geofabric after settlement deformation. The tension resistance moment supplied by geofabric is the uplift force corresponding to the maximum of tensile strain (15.58%) multiplies the force arm. The uplift force is 0.098 t/m, which can be educed from geofabric ED. The force arm is the perpendicular distance from the centre of the circle ESO to the uplift force. Thus the tension resistance moment supplied by geofabric is worked out as 0.887 t·m, which can be added to the sliding resistance moment of the potential sliding arc ESO. The direction of the sliding resistance force is the direction of ED, which is the figure of geofabric after settlement deformation. Finally the minimum factor of safety K_7 gained is 1.004, which corresponds to the limit equilibrium state of the embankment.

AN APPLIED SIMPLIFIED CIRCULAR FAILURE ANALYSIS METHOD

The Sliding Resistance Role of the Geofabric Includes

(A)When the potential sliding arc is limited to pass through the maximal vertical settlement point, which is the center point of interface between embankment and geofabric, the factor of safety can be increased a little greater than that of ordinary analysis method.

(B)The factor of safety K_5 is less than K_3, which means that the whole failure occurs after the failure of foundation takes place. The height of the embankment should be 3.87 m only when the factor K_5 is 1.0, but the actual height of the embankment is 4.78 m, which is 0.91m higher than 3.87 m. Thus the role of geofabric is revealed.

(C)With the uplift force supplied by geofabric corresponding to the maximum of tensile strain, the factor of safety can directly be increased from 0.984 to 1.004.

Triaxial Shear Testing Results

It can be found from the triaxial shear test with one horizontal layer of geofabric in the middle of the soil sample in laboratory, that the failure surface doesn't run through the geofabric but be separated into the upper part and the lower part, and that the failure starts in the lower part. As can be seen form Fig. 4. So it can be concluded that the failure surface does not run through the geofabric continuously, and the lower part of failure surface should originate from the center of foundation surface.

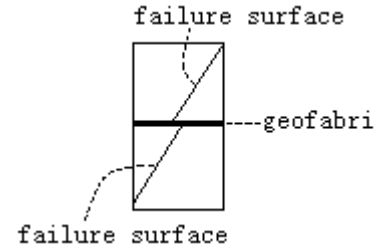

Fig. 4 Failure surface of triaxial shear test with one horizontal layer of geofabric

An Applied Simplified Circular Failure Analysis Method Taking the Role of Geofabric into Account

Firstly, the maximal vertical settlement of the center point of interface between embankment and geofabric with layerwise summation method is to be worked out. It can be seen as the approximate value of actual vertical settlement.

Secondly, the potential sliding arc, which may intersect the surface of embankment slope and the surface of the foundation, is worked out based on standard circular failure analysis method. The two intersection points together with the maximal vertical settlement point can be used to compute the center of a potential sliding arc. Then with the center and the maximal vertical settlement point, a potential sliding arc and the corresponding factor of safety are worked out.

Thirdly, the tensile strain can be chosen as 2/3 times the maximum of tensile strain or others according to site conditions. Then the tension force and the tension resistance moment supplied by geofabric can be worked out, but it should be guaranteed that pulling out force is not greater than the tension one.

Finally, the tension resistance moment supplied by geofabric can be added to the sliding resistance moment of the potential sliding arc. If the minimum factor of safety gained is greater than 1.0 and meets the standards, the reinforced plan is successful; otherwise the reinforced plan should be modified and checked up again until the safety of the embankment can be guaranteed.

CONCLUSIONS

Making use of the data of the full scale test, an applied simplified circular failure analysis method for computing the safety coefficient of the embankment with reinforced underlying layers was put forward. The simplified circular failure analysis method can take the role of geofabric into account more reasonably and should be reviewed and proved in actual situation thoroughly for considering the whole contribution to sliding resistance of reinforced underlying layer.

ACKNOWLEDGEMENTS

The authors are pleased to acknowledge the support of this work by the Young Teacher Foundation of Dalian University of Technology (2007).

REFERENCES

Chen H, Deng W, Zheng Y (1990) Non-linear FEM analysis of the stability of geotextile reinforced embankment. Selected Thesis of the 2nd Chinese Conference of Geosynthetics. Tianjin: The Press of Tianjin University: 296-303

Construction Engineering Headquarters of Shengli Oil Field, Civil Engineering Dalian University of Technology (1989) Study report of foreshore soft foundation transaction. Dalian: Dalian University of Technology

Chinese GB50290-98 (1998) Technical standard for applications of geosynthetics

Lin X, Zhou L, Wu J (2000) The application of geotextile-reinforced sand cushion in ground treatment of buildings. Chinese Journal of Rock and Soil Mechanics 21(3): 252-255

Liu H, Wu W, Gao Y (2003) Nonlinear finite element analysis of reinforced dike with geotextile. Chinese Journal of Rock and Soil Mechanics 24(4): 79-82, 87

Tang H, Wang H (2006) Sliding resistance mechanism and whole stability analysis for reinforced soft foundation of embankment with geofabric. Chinese Journal of Rock and Soil Mechanics 26(12): 1879- 1884

Xu S (1991) Analysis for geotextile reinforcement on soft groud under embankment. Journal of Fuzhou University-Natural Science Edition 13(2): 73-81

Xu S, Hong, C (2000) A stability analysis method for soft subgrade under embankment considering strengthened cushion. China Civil Engineering Journal 33(4): 88-92

Zhao J, Long G, Xu X, Yang C (1991) Analysis for the symmetrical failures of subgrade reinforced with geotextile and natural subgrade. Chinese Journal of Geotechnical Engineering 13(2): 73-81

STRESS RELAXATION BEHAVIORS OF NONWOVEN GEOTEXTILE COMPOSITES

H.Y. Jeon[1], B.W. An[2], H.J. Kim[3], Y.J. Kim[4] and G.Y. Cui[5], Y.S. Jang[6]

ABSTRACT: Stress relaxation behaviors of nonwoven geotextile and geomembrane which have protection, filtration and drainage, water barrier functions, respectively were analyzed. 'Theory of transition phenomena' was applied to interpret the stress relaxation behaviors of two geosynthetics. The initial and later relaxation times for stress relaxation behaviors of geosynthetics were derived from the constitutive equations. The initial relaxation behaviors of these geosynthetics were dependent on the additional strains and were especially faster with temperature. Finally, both relaxation times of geosynthetics were shorter with additional strain and temperature.

KEYWORDS: stress relaxation, additional strain, theory of transition phenomena, relaxation time

INTRODUCTION

Nonwoven geotextiles show the larger deformation till the fracture point beyond the yield strain and this means fracture mechanism of nonwoven geotextiles would be dependent on the unrecoverable plastic deformation after yield point.

In general, fracture mechanism of geogrids which have only the reinforcement function would be dependent on the deformation behaviors by creep deformation behaviors (Salman et al. 1997).

However, fracture mechanism of nonwoven geotextiles and geomembranes would be strongly affected by the stress decay phenomena as time-dependent behavior with additional strain (Soong 1995).

If these geosynthetic materials should be maintained the optimum and sufficient stress with additional strain during the service period, the stress relaxation behaviors must be examined with weather, temperature, additional strain under environmental condition.

In this study, the stress relaxation behaviors of nonwoven geotextiles and geomembranes with additional strain were analyzed through the interpretation by the effects of stress decay phenomena as time-dependent behavior.

EQUILIBRIUM THEORY OF STRESS RELAXATION

The stress relaxation behaviors of geosynthetic materials could be explained by "Equilibrium theory of transition phenomena", namely, Equilibrium state(I) before additional strain → Non-equilibrium state after additional strain → Equilibrium state(II) during stress relaxation.

This means that new equilibrium state would be occurred along the way of stress relaxation when the system transit from non-equilibrium state to equilibrium state as shown in Fig. 1.

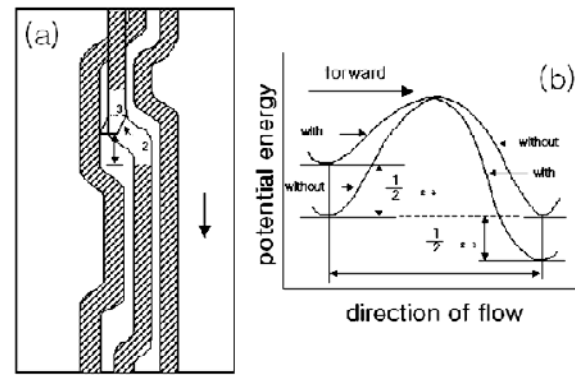

Fig. 1 Schematic diagram of equilibrium theory of transition phenomena

(a) simplified representation indicating voids or holes into which segments of molecules can jump, thus relaxing stress.
(b) diagram indicating how an applied stress alters potential energy barrier a flowing molecular segment must surmount as it flows from one equilibrium position to the next.

Fig. 1 (a) means the transition of polymer molecule segments which were deformed from the equilibrium state by additional strain and the surrounded parts by these segments would be considered as "relaxation sites."

[1] Professor, Division of Nano-Systems Engineering, Inha University, Incheon, KOREA, Email: hyjeon@inha.ac.kr
[2] Master Candidate, Dept. of Textile Engineering, Inha University Graduate School, KOREA, Email: warzero@naver.com
[3] Master Candidate, Dept. of Textile Engineering, Inha University Graduate School, KOREA Email: oveiz2u@nate.com
[4] Master Candidate, Dept. of Textile Engineering, Inha University Graduate School, KOREA, Email: pooh9868@hotmail.com
[5] Master Candidate, Dept. of Textile Engineering, Inha University Graduate School, KOREA, Email: cguiyue@hanmail.net
[6] Professor, Dept. of Civil and Environmental Eng., Dongguk University, Seoul, KOREA, Email: ysjang@dongguk.edu

Fig. 1(b) means the transition process that polymer molecule segments would approach the equilibrium state over the energy barrier by the applied stress of stress relaxation.

In here, the size of relaxation site could be represented with the multiplication of cross section area of relaxation site and distance between two different equilibrium state and potential energy barrier.

The transition process to equilibrium state could be driven by the stress of stress relaxation and the coefficient of transition rate, K_f, would be written as the function of relaxation stress, σ(t) in Eq. 1.

$$-\frac{d\log\sigma(t)}{dt}=K_f\bullet[e^{a_1\bullet\frac{\sigma(t)}{\sigma(0)}}-e^{a_2\bullet\frac{\sigma(t)}{\sigma(0)}}] \quad (1)$$

where a_1 is the relaxation site of the forward reaction in stress relaxation process and a_2 is the relaxation site of the recovery term during the forward reaction by the energy barrier change in stress relaxation process.

The later reaction of stress relaxation process could be interpreted by the simple Maxwell model application because this later reaction shows very slow and linear behavior.

However, the initial reaction of stress relaxation process is very fast and complicated and therefore, "Equilibrium Theory of Transition Phenomena" should be adopted if only the forward reaction could be considered.

From this assumption, the 2nd term of the Eq. 1 could be discarded and then we can rewrite the Eq. 1 as follows.

$$-\frac{d\log\sigma(t)}{dt}=K_f\bullet e^{a\bullet\frac{\sigma(t)}{\sigma(0)}} \quad (2)$$

The stress relaxation process could be represented the sum of two different reaction process; i) the initial relaxation mechanism of the fast and small relaxation stress and ii) the later relaxation mechanism of the slow and large relaxation stress.

For this case, the constitutive equation of the stress relaxation process is as follows.

$$\sigma(t)=\sigma_1\bullet e^{-\gamma_f\bullet t}+\sigma_2\bullet e^{-\gamma_b\bullet t} \quad (3)$$

$$\sigma(t)=\sigma_1\bullet e^{-\frac{t}{\tau_1}}+\sigma_2\bullet e^{-\frac{t}{\tau_2}} \quad (4)$$

$$(\text{where } \tau_1=\frac{1}{\gamma_f},\ \tau_2=\frac{1}{\gamma_b})$$

Therefore, the application of coefficient of transition rate, K_f, in the "Equilibrium Theory of Transition Phenomena" is very reasonable to interpret the fast and complicated initial relaxation reaction than that of relaxation reaction rate.

EXPERIMENTAL

Preparation of Samples

1,200 g/m^3, nonwoven geotextile of protection, filtration and drainage functions and 2mm HDPE geomembrane of water barrier function were used in this study.

Evaluation of Load-elongation Property

To determine the stress relaxation experimental conditions, the load-elongation test of nonwoven geotextile and geomembrane were done in accordance with ASTM D4595 and ASTM D638, respectively.

Evaluation of Stress Relaxation Behavior

For stress relaxation experiment, the additional strains were 2%, 5%, and 8% of yield elongation for nonwoven geotextile 20, 30, and 45% of yield elongation for geomembrane, respectively. The temperature condition is 25℃, 35℃, 45℃, 55℃, 65℃, 75℃, 85℃ and this was due to the consideration of the inner site condition of the real waste landfill in the hot season.

RESULTS AND DISCUSSION

Stress-strain Behaviors

Fig. 2 shows the load-elongation curves of the non-woven geotextile and it is seen that the yield elongation is about 50%.

Fig. 3 shows the load-elongation curves of the geo-membrane and it is seen that the yield elongation is about 80%.

From this, the needed additional strain could be determined for stress relaxation experiment.

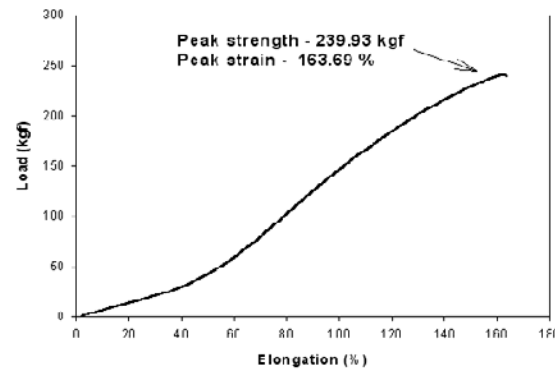

Fig. 2 Load-elongation curve of nonwoven geotextile

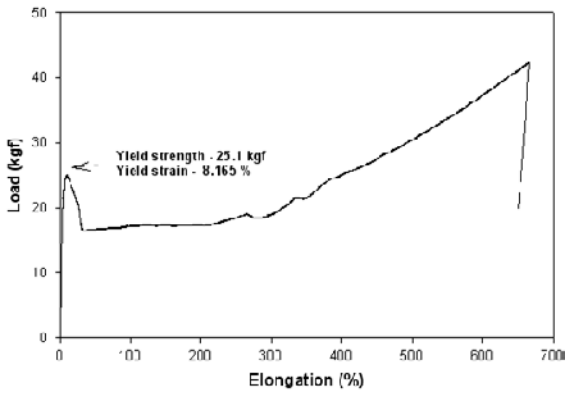

Fig. 3 Load-elongation curve of HDPE geomembrane

Stress Relaxation Behaviors

The stress relaxation behaviors of nonwoven geotextile were shown in Fig. 4.

In here, the initial relaxation behavior was fast with the larger additional strain and higher temperature.

The later relaxation behavior showed the same tendency with regardless to the additional strain but showed the little increase with higher temperature.

Fig. 5 shows the stress relaxation behavior of geomembrane and it is seen that they have the same tendency of nonwoven geotextile.

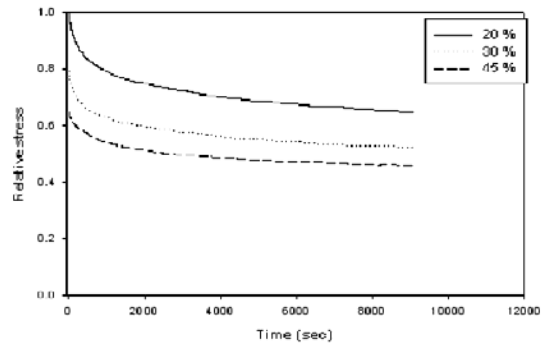

(a)

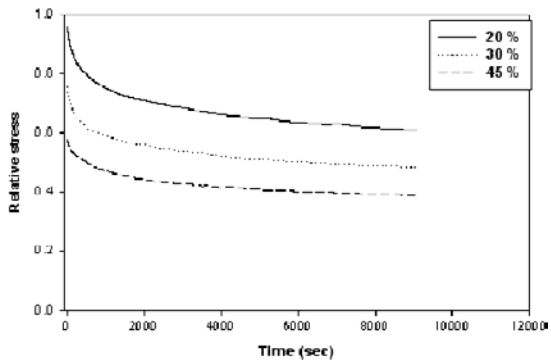

(b)

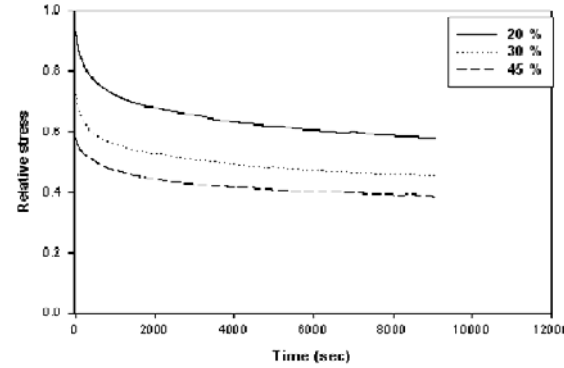

(c)

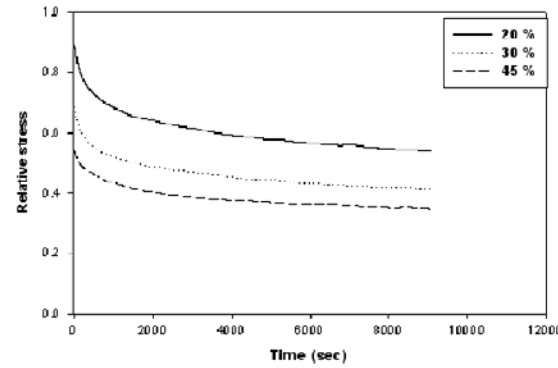

(d)

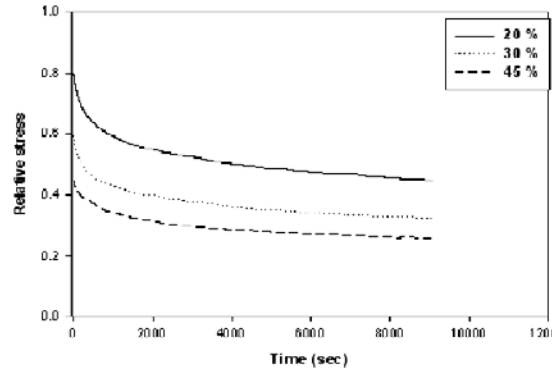

(e)

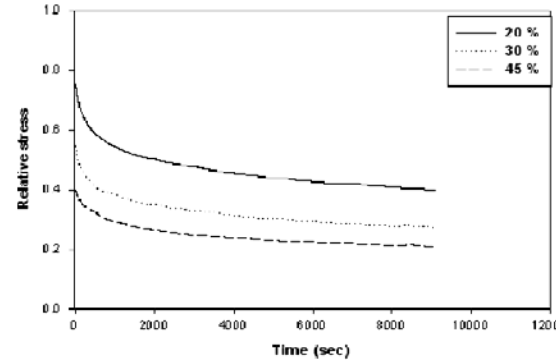

(f)

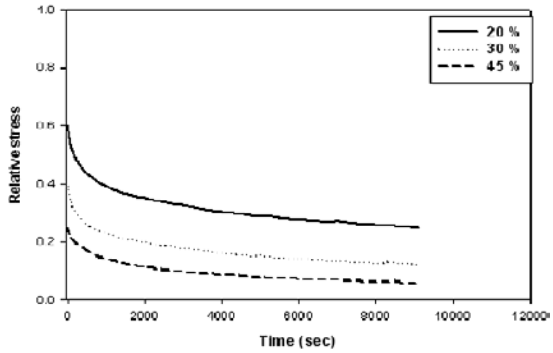

(g)

Fig. 4 Stress relaxation curves of nonwoven geotextile with additional strains
(a) 25℃ (b) 35℃ (c) 45℃ (d) 55℃ (e) 65℃ (f) 75℃ (g) 85℃

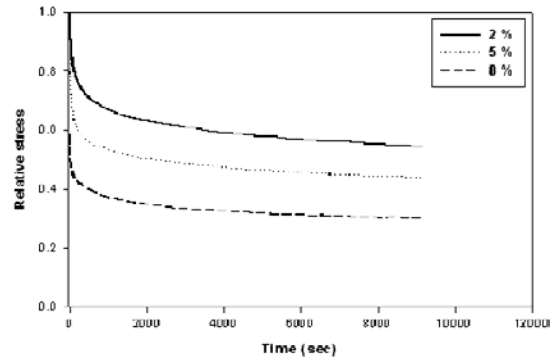

(a)

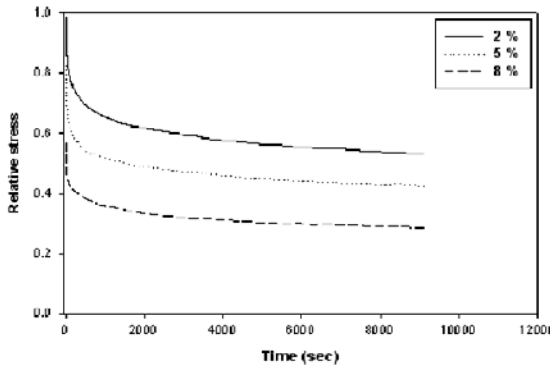

(b)

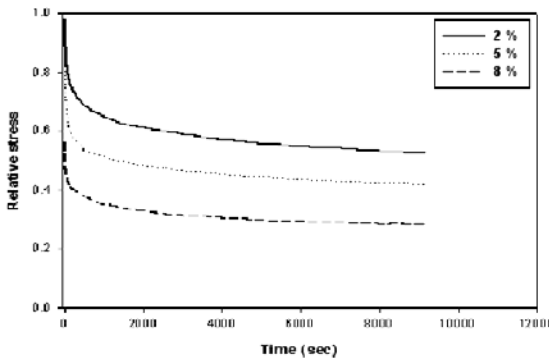

(c)

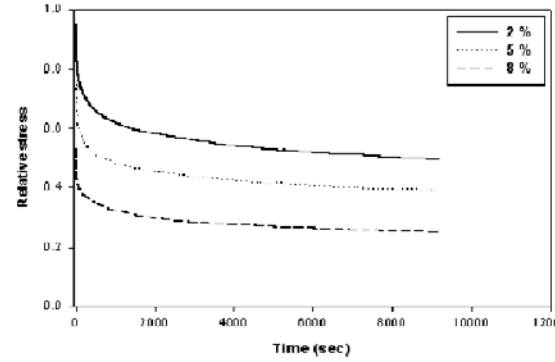

(d)

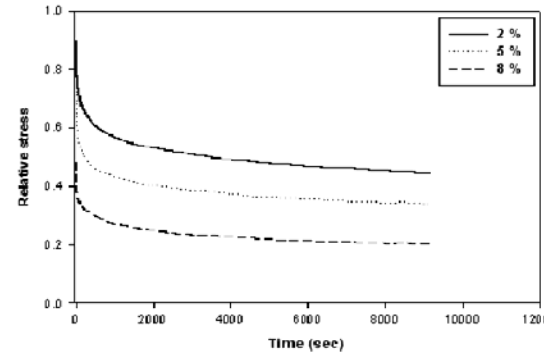

(e)

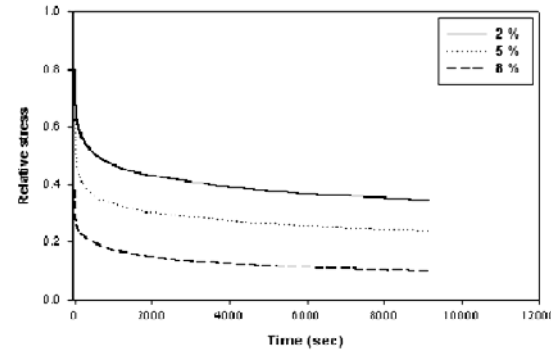

(f)

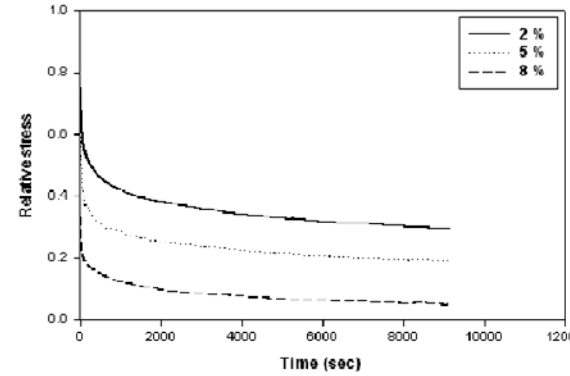

(g)

Fig. 5 Stress relaxation curves of geomembrane with additional strains
(a) 25℃ (b) 35℃ (c) 45℃ (d) 55℃ (e) 65℃ (f) 75℃ (g) 85℃

Stress Relaxation Times

The stress relaxation times of nonwoven geotextile and geomembrane were determined through the Eq. 4 and the experimental data of stress relaxation.

Table 1 show this result and the relaxation times of nonwoven geotextile and geomembrane were increased with larger additional strain and higher temperature for both initial and later relaxation reactions.

Table 1 Stress relaxation times of geosynthetics

Geosynthetics	Additional Strain(%)	τ_1(min)			τ_2(min)		
		25℃	55℃	85℃	25℃	55℃	85℃
Nonwoven Geotextile	2	6.7	6.1	5.2	357.4	351.5	343.6
	5	6.3	5.7	4.7	354.7	347.3	339.6
	8	5.8	5.2	4.2	352.3	342.8	332.7
Geo-membrane	20	1.8	1.2	0.6	133.4	131.5	130.4
	30	1.2	0.8	0.4	131.7	130.4	130.1
	45	0.8	0.5	0.2	130.4	130.2	129.9

The reason of the shorter relaxation times for nonwoven geotextile is due to the slippage phenomena effects of the aggregated fibers against the applied strain.

CONCLUSION

The stress relaxation process could be considered as the transition phenomena from one equilibrium state to another equilibrium state. Stress relaxation behaviors of nonwoven geotextile and geomembrane showed the fast initial relaxation behavior with larger additional strain and higher temperature. The later relaxation behavior showed the same tendency with regardless to the additional strain but showed the little increase with higher temperature. Finally, the initial and later relaxation times were shortened with the additional strain and temperature.

ACKNOWLEDGEMENTS

This work was supported by grant No. RTI04-01-04 from the Regional Technology Innovation Program of the Ministry of Commerce, Industry, and Energy (MOCIE).

REFERENCES

Salman A, Elias V, Jurean I, Lu S, Pearce E (1997) Durability of Geosynthetics based on Acceleraated Laboratory Testing, In Proc. of '96 geosynthetics conference, Long Beach, Califonia: 217-234

Soong TY (1995) Effects of Four Experimental Variables on the Stress Relaxation Behavior of HDPE Geomembranes, In Proc. of Geosynthetics'95 Conference, Nashville: 1139-1147

PREDICTION OF WEATHERABILITY OF GEOSYNTHETICS UNDER EXPOSURE CONDITIONS

H.Y. Jeon[1], W.S. Lyoo[2], Z.L. Shen[3] and K.Y. Lee[4]

ABSTRACT: Geotextile composites, improving the weatherability, were composed of recycled polyester geotextile combined with carbon black used as an ultraviolet stabilizer and polypropylene geotextile by needle-punching method, and were evaluated for such as physical properties, ultraviolet resistance, and chemical stability. Retention of tensile properties of nonwoven polypropylene geotextiles were decreased about 50% by the exposed condition with ultraviolet but those of geotextile composites were decreased slightly than polypropylene geotextiles. Geotextile composites which have heavier weights of polyester geotextile were more stable against ultraviolet rays and chemical degradation.

KEYWORDS: geotextile composites, ultraviolet resistance, chemical stability, retention of tensile properties

INTRODUCTION

Geotextile is used to reinforce the slope of the landfill, and is exposed to light degradation during the construction of the landfill and while refuse is being filled in the landfill (Baker 1997; Koerner et al. 1997; Artires et al. 1007).

When the refuse is completely filled, geotextile serves as drainage, filtration, and protection layer for geomembrane; however, it is then expected to degrade due to reactions with light, chemicals, and leachate solutions (Mathur 1994; Salman 1997).

About 90% of geotextile currently used in Korea is PP(Polypropylene) geotextile product with added carbon black as an ultraviolet ray's stabilizer or without any additives.

This research was conducted for the purpose of enhancing the stability of PP geotextile to ultraviolet rays. A composite geotextile, which was composed of PET geotextile with carbon black as an ultraviolet ray's stabilizer, and currently used PP geotextile and examined for its stability against ultraviolet rays and its resistibility to chemical degradation.

EXPERIMENTAL

Geotextile Composites

Three kinds of 700, 800, 1000 g/m^2 PP geotextile which does not have added carbon black and 2 kinds of cycled 200, 300 g/m^2 PET geotextile which contain carbon black were chosen as experimental geotextile composite materials, frequently applied in a waste landfill.

For the purpose of enhancing the stability of existing PP geotextile to ultraviolet rays, a geotextile composite was produced by combining recycled PET geotextile and PP geotextile, using a needle-punching method. Table 1 shows the specifications of geotextile composites used in this study.

Table 1 Specifications of geotextile composites

Composition / Geocomposite	PP/PET (g/m^2)
GC1	700/300
GC2	800/200
GC3	1000/200

Weatherability Test

The experiment to assess the stability of geotextile and geotextile composite was carried out by exposing these materials to irradiation according the ASTM D 4355 and G 155-05a.

A cycle of 102 minutes and then water-spraying for 18 minutes was used. These procedures were repeated for a total of 500 hours to compare and assess the stability before and after the exposure experiment.

[1] Professor, Division of Nano-Systems Engineering, Inha University, Incheon, KOREA Email: hyjeon@inha.ac.kr
[2] Professor, School of Textiles, Yeungnam University, Gyeongsan, KOREA, Email: wslyoo@ yu.ac.kr
[3] Master Student, Dept. of Textile Eng., Inha University, Incheon, KOREA, Email: shenzhelong813@hanmail.net
[4] Professor, Department of Civil Engineering, Dongseo University, Busan, KOREA, Email: civklee@gdsu.dongseo.ac.kr

Due to the lack of widely-accepted experimental procedure to assess the resistibility of geotextile to chemical degradation, EPA 9090 Test Method was applied for chemical resistance at 25℃ and 50℃ and then the immersed sample is subject to a tensile strength test in both machine direction (MD) and cross machine direction (CMD).

The resistibility of the experimental materials is then evaluated for their tensile strength according to the immersion duration by using ASTM D 5034 and the preservation of elongation.

The general refuse in a landfill gets disintegrated while being filled up and produces a strong acid leachate while other solid refuse gets oxidized and broken down can produce a strong alkaline leachate.

For this, buffer solutions of pH 3 and 12 and leachate from the real landfill site were used.

The change in tensile strength of geotextile was measured and evaluated in order to analyze its resistance to chemical degradation and the impact of ultraviolet rays.

RESULTS AND DISCUSSION

The initial tensile strengths of 3 kinds of geotextile composites produced by combining PET geotextile with carbon black and PP geotextile without carbon black by a needle-punching method.

The tensile strengths of geotextile composites were about 80%-85% of PP geotextile of equal weight to exhibit a slight difference compared to existing PP geotextile, and it is due to the combination of two materials.

Geotextile composites produced in order to enhance the stability of PP geotextile (PP GT) to ultraviolet rays displayed the following results of photo degradation experiment. (Table 2)

All three kinds of geotextile composites exhibited more than 80% of retention ratio of physical characteristics, manifesting a very significant enhancement in the stability to ultraviolet rays compared to existing PP geotextile.

Table 2 Strength retention after UV exposure

Geotextile		GC1	GC2	GC3	PP GT
Strength Retention (%)	MD	98.3	98.6	98.7	74.5
	CMD	98.5	98.8	98.7	78.4

When the total weight of geotextile composites was fixed and the concentration percentage of PET geotextile with added carbon black increased, the decrease in tensile strength and elongation due to photo degradation was markedly reduced.

When the weight of PET geotextile was fixed and the weight of PP geotextile was increased, the decrease in tensile strength and elongation due to photo degradation was markedly reduced according to the increased weight of PP geotextile.

This can be described by the fact that the concentration of fibers per unit volume of the geotextile composites increases with increased amount of PP geotextile, single straw fiber, thus, reducing the area exposed to the ultraviolet infiltration.

Nevertheless, a greater enhancement was achieved by increasing the weight of PET geotextile than that of PP geotextile in the geotextile composites.

The resistibility of geotextile composites to an acid condition of pH 3 is depicted in Figs. 1 and 2.

The tensile strength of geotextile composites showed a very similar reaction in acid buffer solution and exhibited about 10% decrease, showing a rather stability in an acid condition.

On the other hand, the percentage change in tensile strain of geotextile composites was about 10 20% as exhibited and shows the greater percentage decrease in tensile strain than in tensile strength.

Figs. 3 and 4 show the percentage change in tensile properties of geotextile composites immersed in an alkaline buffer solution of pH 12.

The tensile strength exhibited about 10%-20% decrease whereas the tensile strain showed about 20%-40% decrease.

The percentage changes in the tensile strength of geotextile composites immersed in a leachate, which was actually collected in a refuse dump, are shown in Figs. 5 and 6 whereas the percentage changes in tensile strain are depicted.

As seen before in the case of acid and alkaline reaction experiments, the tensile properties exhibited 10%-20% decrease, and, furthermore, the percentage changes at 50℃ were greater than those at 25℃.

From these chemical reaction experiments with three kinds of geotextile composites, it was found that the tensile strain was markedly decreased while the tensile strength showed about ±20% change, a rather stable result.

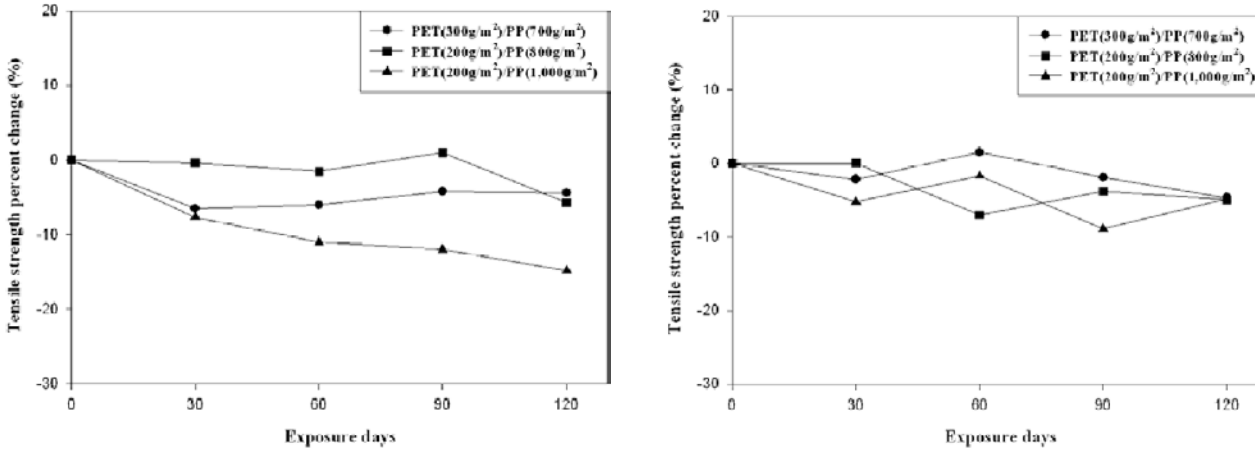

Fig. 1 Tensile strength percentage change of geotextile composites at pH 3, 25℃: (a) MD (b) CMD

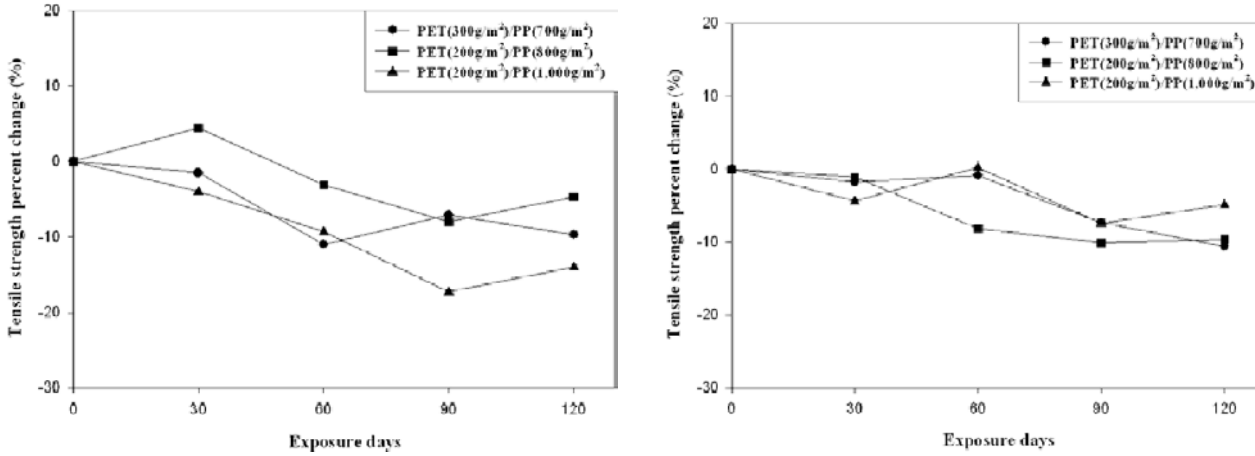

Fig. 2 Tensile strength percentage change of geotextile composites at pH 3, 50℃ : (a) MD (b) CMD

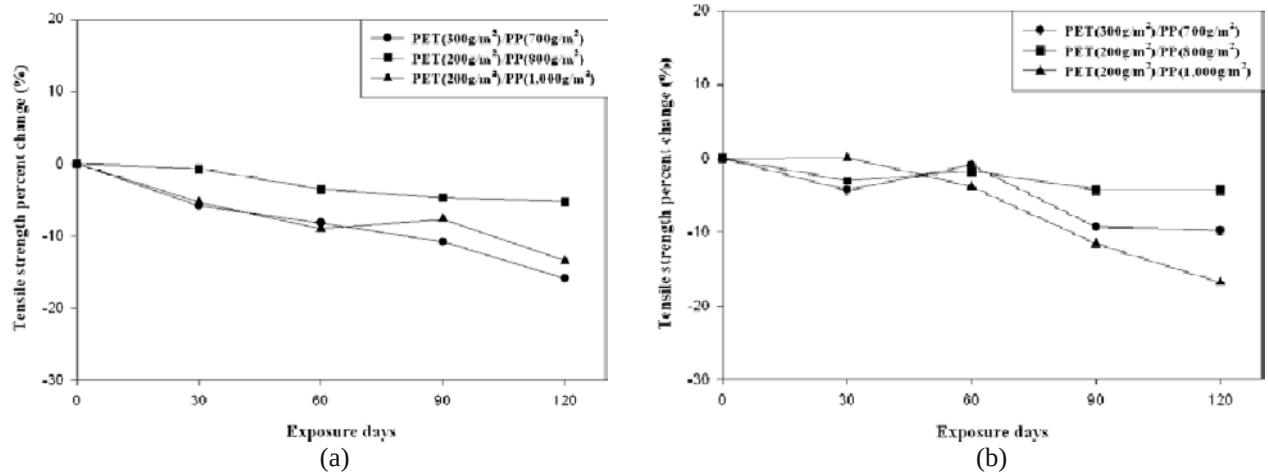

Fig. 3 Tensile strength percentage change of geotextile composites at pH 12, 25℃ : (a) MD (b) CMD

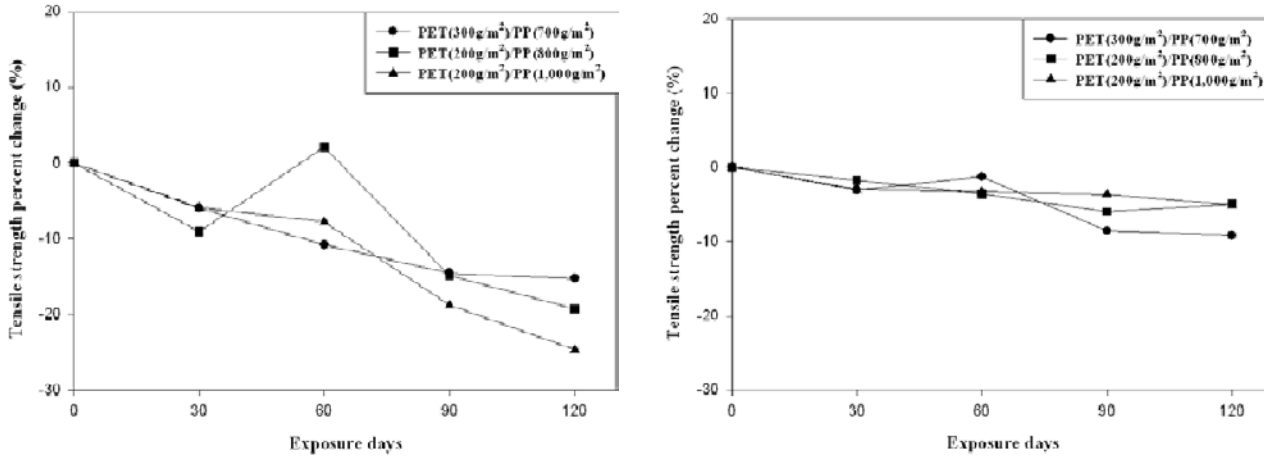

Fig. 4 Tensile strength percentage change of geotextile composites at pH 12, 50℃ :(a) MD (b) CMD

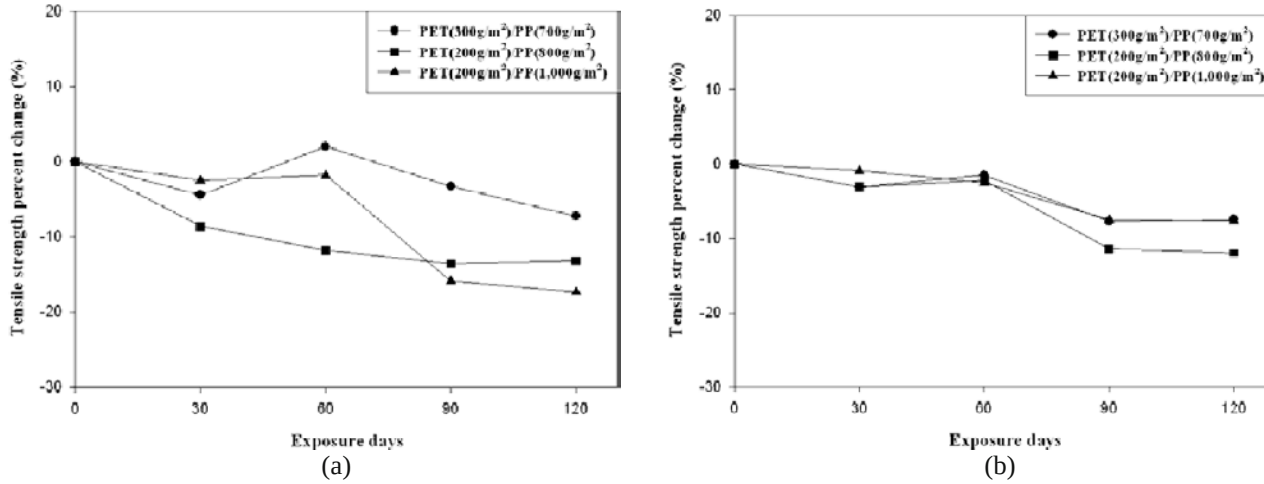

Fig. 5 Tensile strength percentage change of geotextile composites in leachate at 25℃: (a) MD (b) CMD

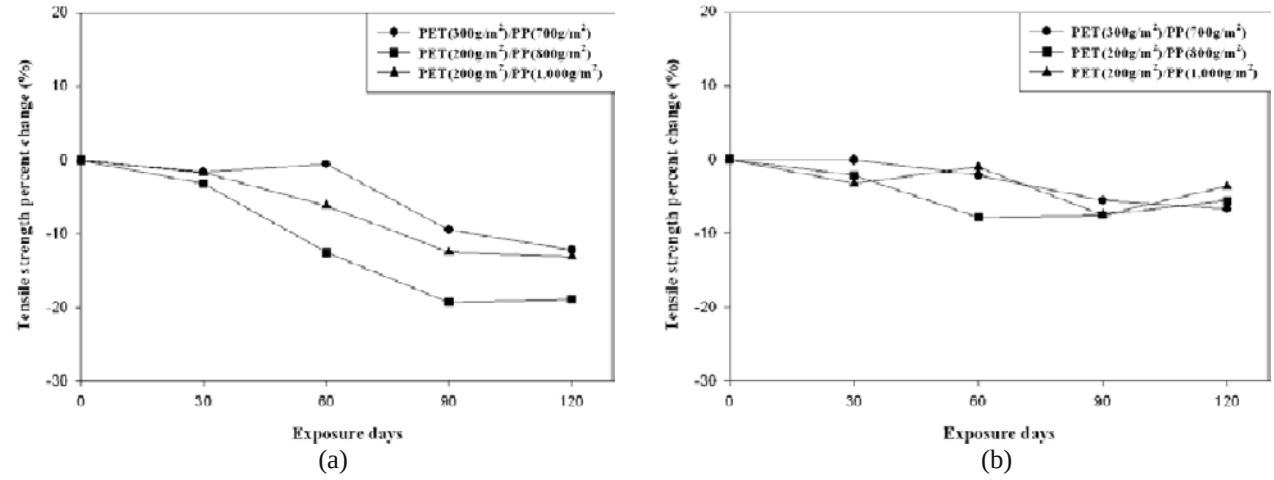

Fig. 6 Tensile Strength Percentage Change of Geotextile Composites in Leachate at 50℃ :(a) MD (b) CMD

CONCLUSIONS

The retention ratio of tensile strength of geotextile composites after being exposed to ultraviolet rays was about 80% and showed a greater stability to ultraviolet rays as the weight of PET geotextile in the geotextile composites increased.

Geotextile composites exhibited an increase in retention ratio of tensile strength as PP geotextile in the composites increased, after being exposed to ultraviolet rays.

The stability of geotextile composites under various chemical conditions showed 80%-90% retention ratio of tensile properties to exhibit a rather stable property while being immersed in an acid buffer solution of pH 3 and 12 and leachate, which was collected in a refuse dump.

In reality, the construction sites where geotextiles are used as water barrier liner are exposed to not only ultraviolet rays but day lights with heat, rains, temperature, humidity and oxygen, etc.

These environmental factors impact the overall characteristics of geotextiles simultaneously. Thus, future research to examine the weatherability of geotextiles to these factors is needed.

ACKNOWLEDGEMENTS

This work was supported by grant No. RTI04-01-04 from the Regional Technology Innovation Program of the Ministry of Commerce, Industry, and Energy (MOCIE).

REFERENCES

Baker TL (1997) Proceedings of '97 Geosynthetics Conference 3: 829

Koerner GR, Hsuan GY, Koerner RM (1998) J. of Geotechnical and Geoenvironmental Engineering 124:1

Artires O, Gaunet S, Bloquet C (1997) Geosynthetics International 4:393

Mathur A et al. (1994) Geotextiles and Geomembranes 13:591

Salman A et al. (1997) Proceedings of '97 Geosynthetics Conference 1: 217

ASTM International (2007) ASTM D 4355-07 Standard Test Method for Deterioration of Geotextiles by Exposure to Light, Moisture and Heat in a Xenon Arc Type Apparatus, West Conshohocken, PA, USA

ASTM International (2005) ASTM G 155-05a, Standard Practice for Operating Xenon Arc Light Apparatus for Exposure of Non-Metallic Materials West Conshohocken, PA, USA

EPA (1997) EPA 9090 test method, Environmental Protection Agency, USA

ASTM International (2007) ASTM D5034, Standard Test Method for Breaking Strength and Elongation of Textile Fabrics (Grab Test), West Conshohocken, PA, USA

Proceedings of the 4th Asian Regional Conference on Geosynthetics
June 17 - 20, 2008 Shanghai, China

ENVIRONMENTAL STRESS CRACK RESISTANCE OF GEOMEMBRANE BY NCTL TEST

H.Y. Jeon[1], Y.S. Jang[2] and K.Y. Lee[3]

ABSTRACT: The effects of acidic and alkaline solutions from wastes leachate on the machine properties of a 2.5 mm thick high density polyethylene (HDPE) geomembranes (GMs) were examined. Smooth/textured HDPE GM specimens were cut into machine direction (MD) and cross machine direction (CMD) which were immersed in the tanks of notched constant tensile load (NCTL) test apparatus containing acidic water (pH=4), alkaline water (pH=8) and incubated at 40 and 60°C respectively. The decline in stress crack resistance of HPDE GMs is evaluated using NCTL tester. In acidic and alkaline conditions, HDPE GMs performed the same stress crack resistance. The increase in temperature and the level of loading shows the decrease in stress crack resistance.

KEYWORDS: stress crack resistance, pH value, temperature, NCTL test

INTRODUCTION

HDPE geomembranes (GMs) in landfills are usually exposed under different chemical stress. The pH values of leachate depend on the waste age, varying typically between 4.5 and 7.5 in new landfill and between 6.6 and 7.5 in old landfills.

The general waste in a landfill site disintegrates during filling of the site and produces a strong acid leachate solution, while other solid waste becomes oxidize and can produce a strong alkaline leachate solution when broken down.

The period of this change could up to 3 months and a pH value of 8 was recorded for the final waste leachate solution.

The temperature of the landfills is also considerably higher than normal conditions, ranging from 20°C to 80°C (Koerner 2005; Giroud 2005; Grulec 2004).

There is no such data on the performance of HDPE GM with consideration of above situations.

In this study, buffer solutions were used to simulate the pH conditions in landfills while GMs were artificially notched to simulate the damage or crack of GMs in natural environments.

The tensile strength and slow crack resistance of HDPE GMs were determined with a temporal scale.

EXPERIMENTAL

Preparation of Geomembranes

Smooth and textured HDPE GMs of 2.5mm thickness were tested in this study, the appearance of surfaces and some properties under normal conditions of these GMs.

For tensile test and notched constant tensile load (NCTL) test, specimens were prepared according to ASTM Standard D 638 type IV and D 5379 respectively.

The notches were made by cutting a control notch of 20% of the thickness of each specimen by ASTM Standard D 5379.

Un-notched smooth and textured, notched smooth and textured specimens are referred to as UN-S, UN-T, N-S and N-T, and used thereafter throughout the text.

Performance Evaluation

Mechanical properties such as load at yield and elongation at yield were then recorded simultaneously according to ASTM Standard Test Method D 638.

NCTL test specimens were treated in solutions with pH values of 8 and 4 at temperatures of 40°C and 60°C.

The failure time of stress crack resistance were obtained by testing five specimens at each condition.

Tests of stress crack resistance were performed according to the ASTM standard D 5379 by using the constant stress loading type apparatus.

The applied stress levels were ranged from 25% to 60% of yield stress at increments of 5%.

RESULTS AND DISCUSSION

Mechanical Properties

Figs. 1 and 2 showed the average load at yield of tensile properties of N-S and UN-S HDPE GMs treated in pH solution for 1, 2, 3 and 4 months; (a) pH=4, (b)

[1] Professor, Division of Nano-Systems Engineering, Inha University, Incheon, KOREA. Email: hyjeon@inha.ac.kr
[2] Professor, Dept. of Civil and Environmental Eng., Dongguk University, Seoul, KOREA. Email: ysjang@dongguk.edu
[3] Professor, Department of Civil Engineering, Dongseo University, Busan, KOREA. Email: civklee@gdsu.dongseo.ac.kr

pH=7, (c) pH=8, (d) pH=12.

There were no obvious changes of the load at yield values at 20°C and 40°C during four months long treatment. HDPE GMs (notched and un-notched) retained the original values at these conditions.

This indicates that at lower temperature (20°C and 40°C), HDPE GMs (notched and un-notched) have excellent chemical resistance, machine resistance and good durability.

While the temperature increased, at the first two months, a slight decrease was observed in the load at yield values of N-S and UN-S HPDE GMs at 60°C and 80°C pH solutions but it decreased markedly in the third and fourth month in comparison with the load at yield values of HDPE GMs (notched and un-notched) treated in different pH solutions which showed no significant difference.

The load at yield values decreased while the strain increased when specimen were treated for more than two months which clearly indicates the excellent chemical resistance of HDPE GMs (notched and un-notched) at higher temperatures (60°C and 80°C), but decrease in machine resistance was observed with the increase in temperature and time.

Figs. 3 and 4 showed the average elongation at yield of tensile properties of N-S and UN-S HDPE GMs treated in pH solution for 1, 2, 3 and 4 months; (a) pH=4, (b) pH=7, (c) pH=8, (d) pH=12.

Treating the specimens for more than two months in the pH solution at 60°C, the elongation at yield values increased slightly but, it increased markedly at 80°C in the similar conditions.

This indicates that at higher temperature, HDPE GMs (notched and un-notched) have excellent chemical resistance but, the temperature and the time affect the machine resistance in the same manner as it has been discussed above.

Analysis of variance (ANOVA) was used to further evaluate whether any of the treatments had statistically significant effects on tensile test (Box G. et al. 1978). The p-statistic is used to determine the treatments which had statistically significant effect on tensile test.

A p-statistic, less than the significance level α indicates a statistically significant temporal trend. p-statistics higher than α=0.05 (no temporal trend in tensile test) exist for all exposure conditions.

For this analysis, each of the eight treatments pH=4, 7, 8 and 12; T=20°C, 40°C, 60°C and 80°C were treated as a group, and the tensile test data (load at yield and elongation at yield) for each treatment were compared with each other.

The ANOVA yielded p_{pH}=0.99 (four months, load at yield), whereas α =0.05 (p > 0.05). The ANOVA yielded p_T=1.47E-43 (four months, load at yield), whereas α=0.05 (p<0.05).

That is, statistically significant difference exists between the mean load at yield and elongation at yield corresponding to the T=20°C, 40°C, 60°C and 80°C treatments.

In Fig. 6, after tensile test the intact (UN-S) HDPE GM has been tensioned, there is no significant damaged at the surface of the intact (UN-S) HDPE GM.

After tensile test, intact (UN-S) HDPE GM retains impermeable to solid particles and water vapor.

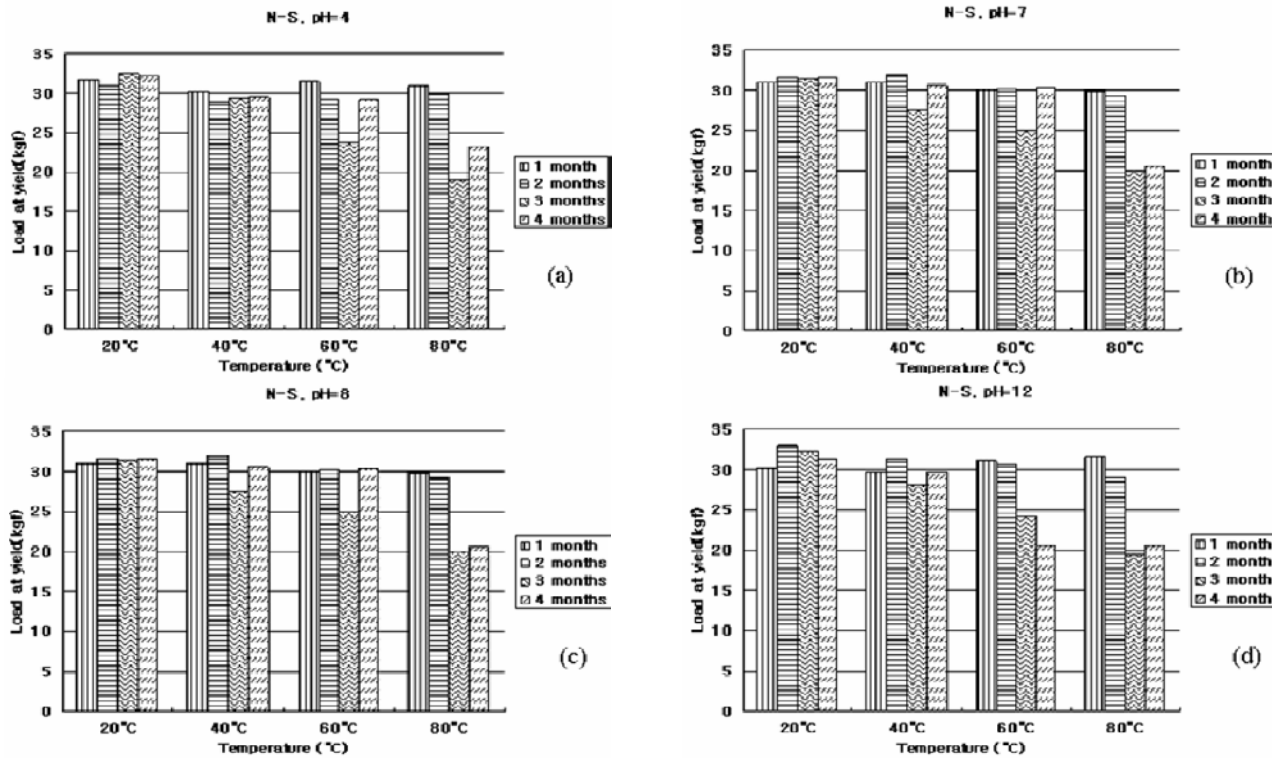

Fig. 1 Average load at yield of tensile properties of N-S HDPE GMs treated in pH solution for four months; (a) pH=4, (b) pH=7, (c) pH=8, (d) pH=12

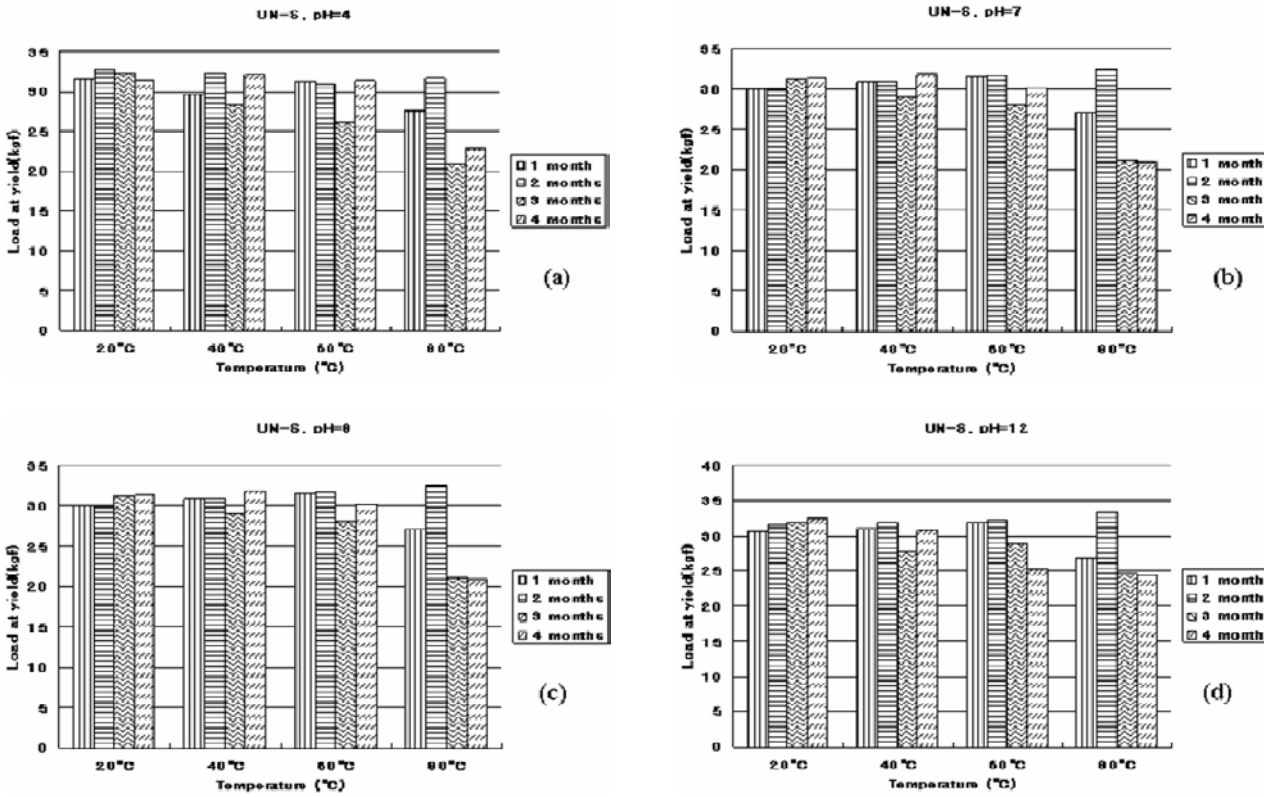

Fig. 2 Average load at yield of tensile properties of UN-S HDPE GMs treated in pH solution for four months; (a) pH=4, (b) pH=7, (c) pH=8, (d) pH=12

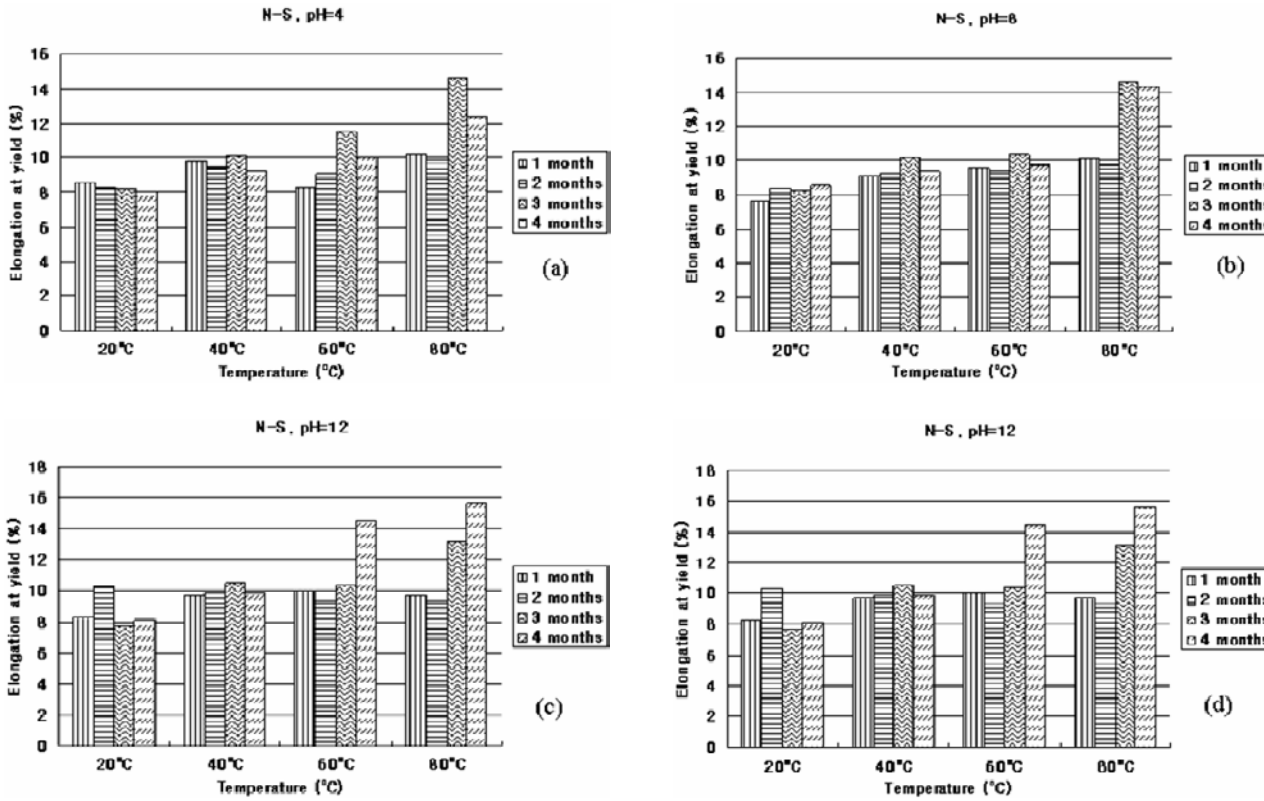

Fig. 3 Average elongation at yield of tensile properties of N-S HDPE GMs treated in pH solution for four months; (a) pH=4, (b) pH=7, (c) pH=8, (d) pH=12

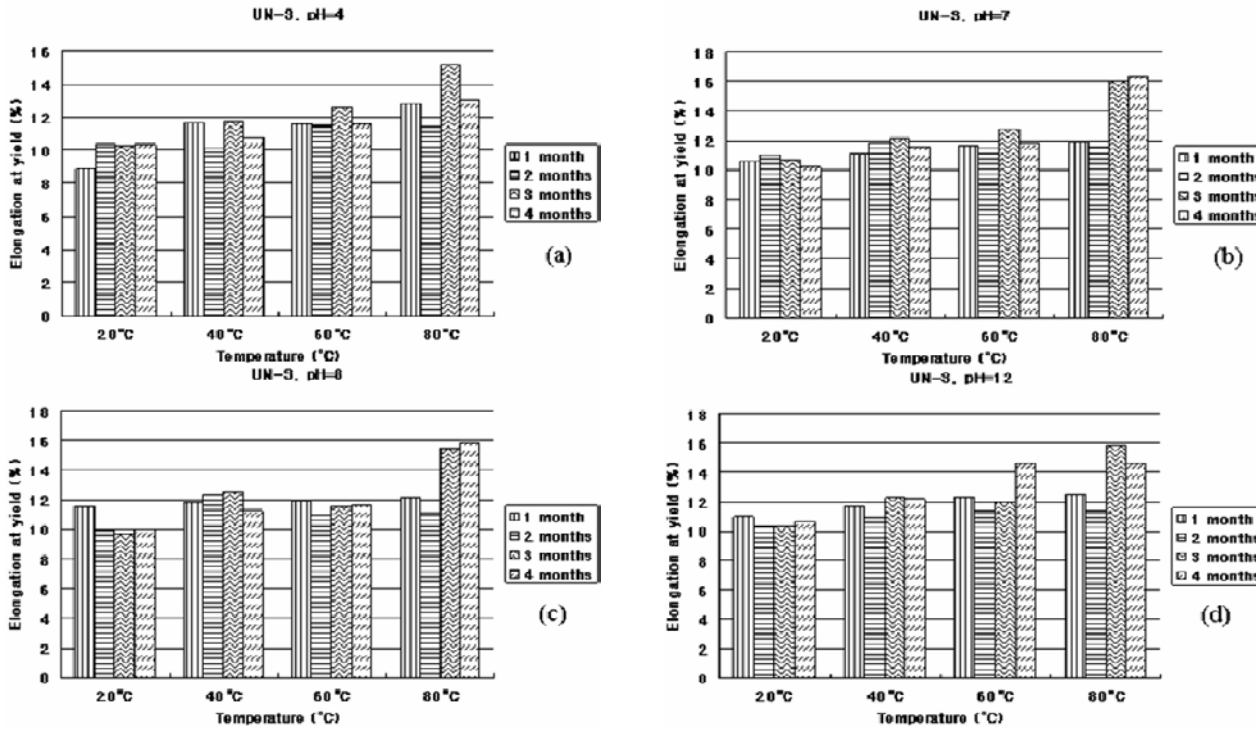

Fig. 4 Average elongation at yield of tensile properties of UN-S HDPE GMs treated in pH solution for four months; (a) pH=4, (b) pH=7, (c) pH=8, (d) pH=12

Stress Crack Resistance

Fig. 5 shows the percent yield stress versus failure time HDPE GMs immersion in acidic (pH=4) and alkaline (pH=8) solution at 40°C respectively. There is a significant difference of failure time between 40°C and 60°C. The failure times obtained at 40°C were longer than that of 60°C.

This indicates that high temperature imparted flexibility in HDPE GMs which in turn showed lower tensile strength. No obvious differences were observed between alkaline (Fig. 5 (b)) and acidic treatments (Fig. 5 (a)) of each kind of HDPE GMs specimens (CMD-S, MD-S, CMD-T and MD-T).

This suggests that different types of HDPE GMs have the similar stress crack resistance at the same temperature, in both acidic and alkaline conditions. Stress crack resistance times of the HDPE GMs under different conditions were summarized in Table 3.

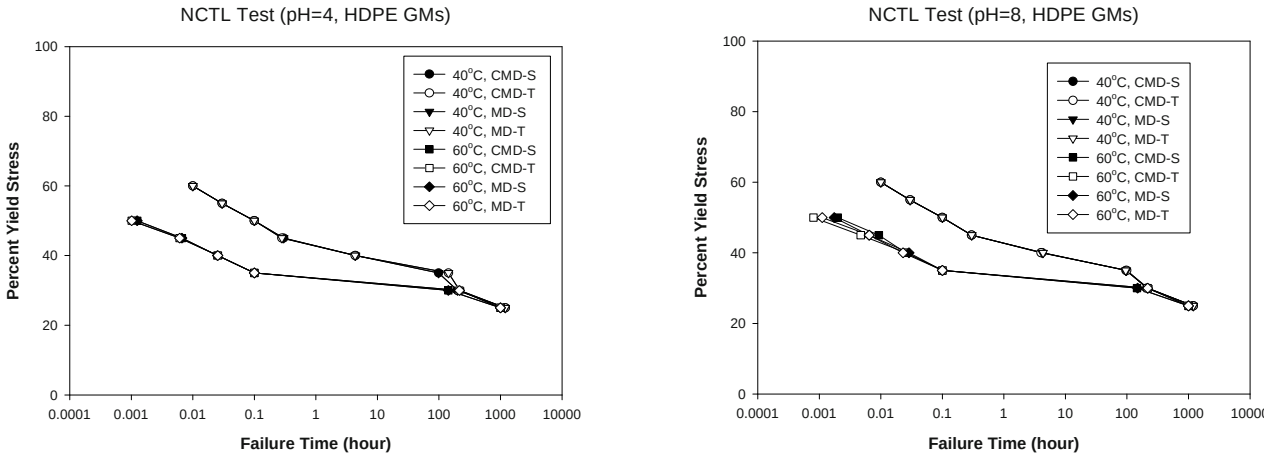

Fig. 5 Percentage yield stress versus the logarithm of the average failure time of high density polyethylene (HDPE) geomembranes (GMs) (CMD-S: cross machine direction smooth HDPE GM, MD-S: machine direction smooth HDPE GM, CMD-T: cross machine direction textured HDPE GM and MD-T: machine direction textured HDPE GM) at 40°C and 60°C: (a) Acidic solution (pH=4), (b) alkaline solution (pH=8))

Table 3 Stress crack resistance of HDPE GMs (hour)

HDPE GMs		40°C		60°C	
		pH=4	pH=8	pH=4	pH=8
Smooth	CMD	210	218	141	146
	MD	220	220	151	149
Textured	CMD	210	210	140	147
	MD	218	215	151	149

CONCLUSION

Damaged HDPE GMs showed excellent acidity-resistance as intact HDPE GMs. There is no statistically significant difference exists between the mean load at yield and elongation at load corresponding to the pH treatments whereas statistically significant difference was found between the mean load at yield and elongation at yield corresponding to the temperature treatments. In acidic and alkaline conditions, HDPE GMs performed the same stress crack resistance. The increase in temperature and the level of loading shows the decrease in stress crack resistance.

ACKNOWLEDGEMENTS

This work was supported by grant No. RTI04-01-04 from the Regional Technology Innovation Program of the Ministry of Commerce, Industry, and Energy (MOCIE).

REFERENCES

Koerner RM (2005) Designing with Geosynthetics, 5th ed., Prentice Hall, Eaglewood Cliffs, NJ, Chapter 5

Giroud JP (2005) Quantification of geosynthetic behavior, Geosynthetics International 12(1): 2-27

Grulec SB, Edil TB, Benson, CH (2004) Effect of acidic mine drainage on the polymer properties of an HDPE geomembrane, Geosynthetics International 11(2): 60-72

ASTM D 638-03 (2003) Standard Test Method for Tensile Properties of Plastics, ASTM International, West Conshohocken, PA, USA

ASTM D 5379-05 (2005) Standard Test Method for Shear Properties of Composite Materials by the V-Notched Beam Method, ASTM International, West Conshohocken, PA, USA

WEATHERING DEGRADATION OF POLYESTER AND POLYPROPYLENE GEOTEXTILES

P.C. Lodi[1], B.S. Bueno[2], O.M. Vilar[3] and N.S. Correia[4]

ABSTRACT: This paper presents results of physical and mechanical tests in polyester (PET) and polypropilene (PP) nonwoven geotextiles that were exposed to weathering conditions (solar radiation, humidity, wind, rain) after some specific periods of exposure (1, 2, 3 and 4 months). ASTM D5970 and Brazilian standards (NBR) recommendation were followed in this research. Results show variations in tensile properties and in the mass per unit area. Variations in the deformations were more significant in the PP geotextile when compared to the PET geotextile.

KEYWORDS: geotextiles, degradation, weathering exposure, mechanical properties

INTRODUCTION

Solar irradiance is a critical weathering variable for many materials and may cause color change, surface damage and numerous other deteriorations. Increasing the levels of irradiance represents a primary accelerating factor for different weathering test methods.

Since many geosynthetics may be exposed to UV radiation (sun light) evaluation of the effects of outdoor exposure is very important. Generally, UV stability is necessary: additives, antioxidants and UV stabilizers are mixed and added to the composition.

Geotextiles (GT) are very sensible to UV effects and continuous exposure results in lost of tensile properties and superficial deterioration of the material. Commercially, polyester (PET) and polypropylene (PP) are the most common types of nonwoven geotextiles. Generally, the PET shows good UV resistance when compared to PP.

This paper presents the results of tests on the tensile properties of PET and PP nonwoven geotextiles that were exposed to weather agents by 1, 2, 3 and 4 months.

NATURAL WEATHERING

Exposure laboratories typically measure "narrow bands" of solar spectra. The 300－800 nm narrow band includes both high energy UV light considered important for photodegradation, and visible light that may have an independent or synergistic effect on materials photo degradation. Often, exposure laboratories record the 300－400 nm or 295－385 nm UV region and report radiant exposure in MJ/m^2 total UV. Table 1 shows the wavelengths or wavelength ranges that cause photo-degradation of the polymers.

Table 1 Wavelengths (λ) of many polymers (modified from Suits and Hsuan 2003 and Agnelli 2002)

Polymer	λ (nm)	E* (Kcal/mol)
Polycarbonate (PC)	295-345	97－83
Polypropylene (PP)	335-360	97－77
Polyethylene (PE)	330-360	96
Polystyrene (PS)	318	90
Poly Vinyl Cloride (PVC)	320	89
Polyester (PET)	325	88

* photon energy ($E=28{,}5\times10^5/\lambda$)

The degradation of polyethylene (PE) or polypropylene (PP) is controlled by photo-oxidation via a series of free radical reactions (Suits and Hsuan 2003):

$$RH + O2 + h\lambda \rightarrow R\bullet + ROO\bullet + RO\bullet + OH\bullet \quad (1)$$

[1] Professor, Department of Civil Engineering, São Paulo State University (UNESP), Ilha Solteira, BRAZIL. Email: plodi@dec.feis.unesp.br
[2] Professor, Department of Geotechnical Engineering, University of State of São Paulo (USP) at São Carlos, BRAZIL. Email address: bsbueno@sc.usp.br
[3] Professor, Department of Geotechnical Engineering, University of State of São Paulo (USP) at São Carlos, BRAZIL. Email address: orencio@sc.usp.br
[4] Graduating student, Department of Civil Engineering, São Paulo State University (UNESP), Ilha Solteira, BRAZIL. Email address: nataliacorreia@uol.com.br

where RH is the polymer chain, hλ is the photon energy with h and λ representing Planck's constant and wavelength, respectively, and R•, ROO•, RO• e OH• are the free radical species with R representing the polymer chain. The oxidation reaction leads to chain scission in the polymer and yields a chemical product of carbonyl compound. The energy required to generate free radicals in polyolefins is lower than that to break a bond; subsequently, polyolefins are more susceptible to UV degradation than other types of polymers. Kay et al. 2004 says that the energy carried by a monochromatic ray is inversely proportional to its wavelength. The shorter the wavelength, the higher the potency of bonds cleavage (Fig. 1).

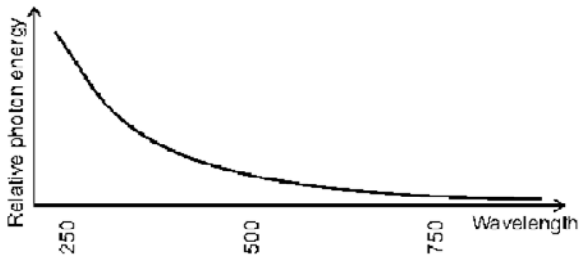

Fig. 1 Photon energy versus wavelength (Kay et al. 2004)

The ASTM D5970 procedure is commonly used like a guide in outdoor exposure to evaluate geotextile products. This method only evaluates ultraviolet degradation at a specific site in terms of expected life, not in terms of incident radiation and temperature. This test method evaluates geotextiles under site specific atmospheric conditions over an 18 month period. Geotextile coupons are attached to a test frame oriented 45° from the horizontal and facing due South at designated location for exposure times of 1, 2, 4, 8, 12, and 18 months. Exposure shall begin so as to ensure that material is exposed during the maximum intensity of ultraviolet light of the year. After each exposure time the appropriate coupons are brought into a laboratory for strength determination. The results of these tests are compared to the strength determined for the unexposed coupons. Researchers also may use exposure times other than specified in this test method.

In order to perform any type of comparison, the total solar radiant energy and solar UV radiant energy should be measured during the exposure duration. However, the effects of temperature and moisture cannot be incorporated into the comparison. The irradiance and the permeability to oxygen are the most important factors in the degradation of polymers by photo-oxidation; however, the temperature and moisture have also an influence on the rate of degradation.

Temperature's effect on material weathering includes thermal oxidation degradations, subsequent reaction rates and accelerating other weathering reactions. Increasing levels of temperature represents a primary accelerating technique for different weathering test methods. Temperature represents a critical weathering variable for many materials. In wet chemistry, a rise in 10°C often results in a doubling of reaction rates. Photolytic and hydrolytic weathering reaction rates also accelerate with rising temperatures.

Moisture cycling by humidity or liquid water creates mechanical stress cyclic loading in many materials. Absorbed water results in compressive stresses on the outside and tensile stresses in the bulk. Drying creates bulk compressive and surface tensile stress gradients. The daily fatigue due to the night's condensation and day's solar drying, in subtropical and tropical environments may interact with hydrolytic, thermal and photo degradations causing mechanisms significantly different than those observed in arid exposures. The effects of relative humidity, like liquid water, depend on material characteristics. Relative humidity often receives undue attention simply because exposure facilities report this data. In fact, the amount of water molecules available for materials degradation at the highest possible terrestrial relative humidities (vapor pressures) may represent order of magnitudes less than amount of water molecules available in liquid state depending on how the calculation is performed (Hardy 1983; Agnelli 1993; ASTM D5970).

MATERIAL AND METHODS

Two types of Polyester (PET) and Polypropylene (PP) nonwoven geotextiles were exposed and evaluated: PET (615 g/m^2) and PP (650 g/m^2).

Geotextiles (GT) were exposed according to ASTM D5970. Samples were placed in a panel located in the east-west axis. Sunlight reached the samples during the entire day. Climate conditions were monitored and the medium values obtained were: 26°C (temperature), 59 mm (precipitation), 65% (relative humidity), and 19 (MJ/m^2).day (intensity of global radiation). Fig. 2 shows the samples exposed to weathering.

Physical and tensile properties were evaluated and compared to intact material. Tests were carried out in accordance with ABNT standards (Brazil standards): ABNT NBR 12568 (mass per unit area) and ABNT NBR 12824 (tensile properties).

Fig. 2 Geotextiles samples exposed to weathering

RESULTS AND ANALYSIS

Table 2 presents the results obtained for both PET and PP geotextiles (intact and after exposure). Fig. 3 shows the percentual variation in mass per unit area. The results of tensile properties are presented in the Figs. 4 and 5 (the curves presented are medium values).

Results show that the mass per unit area decreases (≅ 8.0%) after 1 month and the variations were practically the same until the 3rd month concerning the PP geotextile. After 4 months the value was 2.77% (increase). PET geotextile showed higher variation (decreases) compared to PP: the largest value occurred after 2 months (≅ 19%). After 3 months the variation decrease to 10% and at the last time the variation increases again (15.77%). All these values show that the mass per unit area of the material presented some oscillations caused by the lost of additives, gain in mass per unit area (increase of humidity) or by the variability in the exposed samples.

For tensile properties, the values presented are medium values (machine and cross machine direction).

Both PET and PP geotextiles presented decreases in tensile resistance. PET GT presented highest variations when compared to PP GT. After 2 months the retention of the tensile resistance was about ≅ 69% and 63.71% after 4 months. PP GT presented very low variations: at the final time the retention was 93.06% (PP).

However, concerning the deformation, the behavior of PET and PP GT was very similar. Decreases in deformation occurred since the first month.

Table 2 Results obtained for PET and PP geotextiles (mass per unit area and tensile properties)

Geotextile	Condition	Mass per unit area (g/m^2)	CV (%)	Tensile Strength (N/m)		CV (%)		Elongation (%)		CV (%)	
				L	T	L	T	L	T	L	T
PET	Intact	615	7.48	28.92	35.44	4.76	4.19	65.50	66.44	4.33	7.09
	After 1 month	560	7.00	21.17	38.12	13.15	3.82	66.41	53.89	7.97	2.07
	After 2 months	500	7.00	13.31	32.37	3.35	4.74	55.77	38.01	1.90	6.87
	After 3 months	550	6.00	15.29	30.67	10.38	4.05	62.16	50.54	3.00	0.86
	After 4 months	518	6,00	12.31	30.07	1.38	1.86	66.29	45.43	4.75	1.28
PP	Intact	650	5.44	21.09	41.48	5.55	5.06	100.20	76.70	3.68	8.29
	After 1 month	600	5.00	25.31	32.30	3.83	6.57	57.15	50.66	1.39	4.76
	After 2 months	600	5.00	27.07	27.07	5.25	5.78	47.39	49.73	4.12	2.68
	After 3 month	600	5.50	23.98	31.80	3.49	7.54	60.77	62.19	3.30	6.48
	After 4 months	686	5.00	24.86	28.31	10.16	3.58	43.48	47.34	1.78	12.40

CV = Coefficient of variation; L = longitudinal or machine direction; T = transversal or cross machine direction

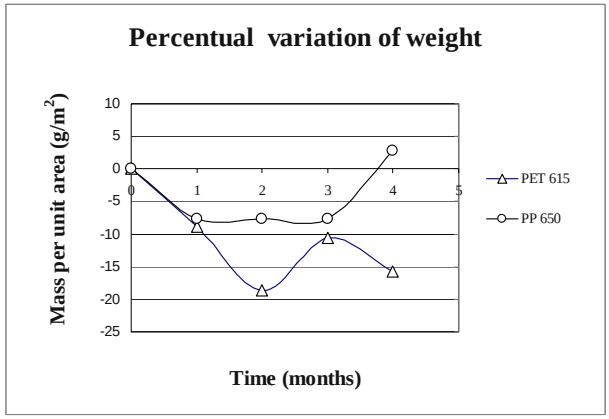

Fig. 3 Variation of mass per unit area

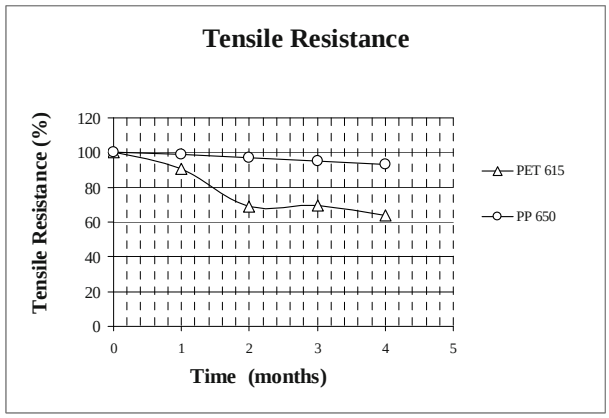

Fig. 4 Variation of the tensile strength

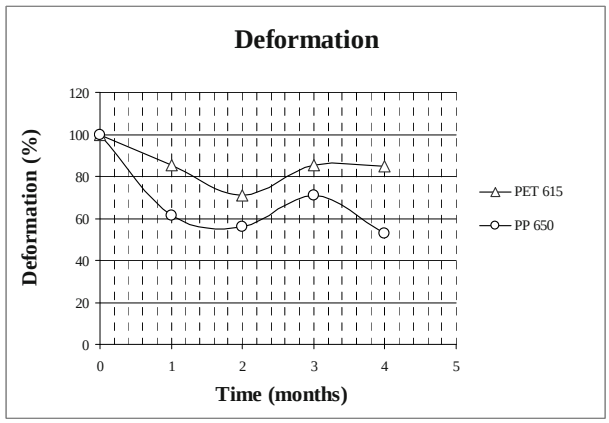

Fig. 5 Variation of the deformation

After the third month both PET and PP showed increases in the deformation variation. At the last time the variation decreased again. The final values of the retention observed were: 84.79% (PET) and 52.56% (PP). In spite of the behavior of the curves, the PP GT presented higher variations than the PET GT. At the first month the PP showed a high variation in deformation: the retention of the property was about ≅ 62%.

In general, both PET and PP geotextiles showed significant decreases in deformation and some variation in tensile strength (see Table 2). The variations in mass per unit area may explain the oscillations in tensile properties: the behavior was very similar showing to have a relation enters the variation of the mass per unit area and the variation of the resistance.

PP geotextiles showed the highest variation (decrease) in deformation: ≅50% after 4 months. Both PET and PP became stiffer than intact samples but the PP geotextile suffered the highest level of UV degradation: PP geotextile became more rigid than PET geotextile. At the first month the retention values of the deformations in PP (61.54%) were more significant than in the PET geotextile (85.56%). This occurs because PP is more susceptible to UV degradation than PET. PP polymers present low resistance to weathering when compared to PET polymers. Moreover, in the process of polymerization of the PP, the inclusion of starters is necessary to make the propylene reacts with another propylene in order to generate the polypropylene. These starters are cromophores and will remain in final polymer. These cromophores are absorbers of UV that more become the PP susceptible to UV when exposed. About PET, this susceptibility does not occur since the polymerization happens without the presence of these starters, because it is a reaction of an acid with an alcohol resulting in an ester. (Agnelli 2002).

CONCLUSION

Results of tensile properties and mass per unit area in PET and PP geotextiles exposed to weathering (solar radiation, humidity, wind, rain) after 720, 1440, 2160 and 2880 hours (1, 2, 3 and 4 months) were presented.

Some oscillation in mass per unit area occurred after exposure for both PET and PP geotextiles. PET GT presented the highest variation after 2 months.

In general, both PET and PP geotextiles showed variations in tensile resistance and expressive decreases concerning the deformation. The highest variation occurred in the PP geotextile which became more rigid than PET geotextile. Both PET and PP geotextile presented superficial levels of UV degradation.

ACKNOWLEDGEMENTS

The authors are thankful the OBER S.A. (Industry and Commerce, São Paulo, Brazil) for supplying materials and to the CNPq and Fapesp for the financial support.

REFERENCES

ABNT NBR 12568. Geosynthetics. Determination of mass per unit area, Brazilian Association of Technical Standard, Brazil (in Portuguese)

ABNT NBR 12824. Geotextiles. Determination of non-confined tensile—wide strip test, Brazilian Association of Technical Standard, Brazil (in Portuguese)

Agnelli JAM (2002) Characterization Tests of Polimeric Materials (in portuguese) — class notes, DEMA/ UFSCar, São Carlos: 200

ASTM D 1435. Standard Practice for Outdoor Weathering Plastics, American Society for Testing and Materials, West Conshohocken, Pennsylvania, USA

ASTM D 5970. Standard Practice for Deterioration of Geotextiles from Outdoor Exposure. American Society for Testing and Materials, West Conshohocken, Pennsylvania, USA

Hardy W B (1983) Light stabilization of polymers. Atlas Sun Spot 13(30): 3

Kay D, Blond E, Mlynarek J (2004) Geosynthetic durability: a polymer chemistry issue. Québec 2004, 57th Canadian Geotechnical Conference, Québec, Canadá:13

Suits LD, Hsuan YG (2003) Assessing the photo-degradation of geosynthetics by outdoor exposure and laboratory weatherometer. Geotextiles and Geomembranes, 21: 111-122, technical note, Elsevier Science Publishers Ltd

Proceedings of the 4th Asian Regional Conference on Geosynthetics
June 17 - 20, 2008 Shanghai, China

EVALUATION OF GEOMEMBRANE UV DEGRADATION USING MELT FLOW INDEX AND OXIDATIVE INDUCTION TIME TESTS

P.C. Lodi[1], B.S. Bueno[2] and O.M. Vilar[3]

ABSTRACT: Many factors such as the sunlight, intensity of radiation, temperature, and moisture may influence the degradation process of geosynthetics. UV stabilizers are used especially in polyolefin geomembrane to prevent the degradation process. In these geomembranes the service lifetime is initially governed by the consumption of antioxidants. Tests like MFI and OIT are a alternative to detect the oxidative degradation in polyolefins. This article evaluates HDPE geomembrane degradation after UV exposure through the results of MFI and OIT tests. Two kinds of geomembranes were evaluated: a black and smooth (0.8, 1.0, 1.5, 2.5 mm) and a white and textured (1.0 mm). MFI test showed some levels of superficial degradation (crosslink) in HDPE geomembrane.

KEYWORDS: geomembranes, UV exposure, MFI and OIT tests

INTRODUCTION

When synthetic polymers are exposed to sunlight bond cleavage and destructive oxidation occur, leading to the reducing in the molecular weight and consequently a diminished service life for the polymer. Embrittlement, discoloration, and sever loss of physical and tensile properties that take place with continued exposure are a real problem (Hardy 1983). Geosynthetics manufactures and the customers recognized that these deficiencies must be solved for the many outdoors applications of the polymeric materials.

When geosynthetics are used in exposed applications they may suffer UV rays action. Moreover, the natural sunlight contains UV radiation that may degrade all the polymers. The photochemical degradation is the main factor which the UV degradation is related. Other factors such as intensity of radiation, temperature, oxygen, moisture and contaminants in the atmosphere, such as nitrogen oxides and sulfur dioxides, may also influence the degradation processes.

To prevent the degradation process many UV stabilizers are used in geosynthetics, especially in polyolefins geomembranes which the service lifetime is initially governed by the consumption of antioxidants. Tests like MFI and OIT are a good tool to detect the oxidative degradation in these polymers.

In this sense, this paper presents the results of MFI and OIT tests after UV exposure on geomembranes (GM) of HDPE of two kinds: a black and smooth (0.8, 1.0, 1.5, 2.5 mm) and a white and textured (1.0 mm).

PHOTODEGRADATION OF POLYMERS

Kay et al. (2004) says that the photodegradation is a process similar to thermal degradation. The source of energy is supplied by radiation instead heat and the molecular bonds can be cleaved by radiation to form free radicals if the energy carried by the radiation is close to the energy of liaison.

A great explanation about the photodegradation in polymers is given by Suits and Hsuan (2003). The authors emphasize that when solar radiation strikes the polymer surface exposed, photons with energy similar, or higher, than the chemical bond strength of the polymer cause a series of reactions that can lead to polymer chain scission and eventual degradation of polymer properties. An example is given by the authors: the energies of 400–300 nm photons are 300 and 390 kJ/mol, respectively, whereas the strengths of C–C and C–H bonds are 420 and 340 KJ/mol, respectively. Thus, the UV energy of the sunlight is sufficient to break chemical bonds of polymers, with the shorter

[1] Professor, Department of Civil Engineering, São Paulo State University (UNESP), Ilha Solteira, BRAZIL.
Email: plodi@dec.feis.unesp.br
[2] Professor, Department of Geotechnical Engineering, University of State of São Paulo (USP) at São Carlos, BRAZIL.
Email address: bsbueno@sc.usp.br
[3] Professor, Department of Geotechnical Engineering, University of State of São Paulo (USP) at São Carlos, BRAZIL.
Email address: orencio@sc.usp.br

wavelengths being more severe.

The energy required to generate free radicals in polyolefins is lower than that to break a bond. In this sense, polyolefins are more susceptible to UV degradation than other types of polymers.

UV stabilizers are widely used in geosynthetics to reduce sensitivity of polymers to photo-oxidation by increasing the duration of the induction period. There are some types such as pigments, UV absorbers, quenchers and free radicals deactivators (such as HALS). Pigments and UV absorbers act as a screen, absorbing UV radiation before they cause damage. Quenchers deactivate excited states, removing the energy from liaisons that have been excited by photons and inhibiting the way of the formation of free radicals. HALS are primary antioxidant, which have the particularity to involve a cyclic, and regenerative stabilization process. They are very effective to protect polyolefin resins. Suits and Hsuan (2003) described three different groups of UV stabilizers: carbon black, UV screener, and antioxidants.

Researches results from Hsuan and Koerner (1998) shows the service lifetime of polyolefin geomembranes is initially governed by the consumption of antioxidants. The rate of antioxidant depletion is significantly faster under photo-oxidation than under thermoxidation. In this sense, antioxidants are mixed into the polymer to protect it from oxidation. Each antioxidant has a temperature range in which it functions most effectively. There are antioxidants which have their effective temperature range at higher temperature and are used as processing stabilizers (e.g. phosphites) and there are others which have their most effective temperature range at ambient temperature (e.g. HALS) or over a wide range of temperature (e.g. hindered phenols) and which are used as long-term stabilizers to provide protection during the low temperature service time (Mueller and Jakob 2000). A complete and great review on the process of oxidative degradation can be found in the papers of Rowe and Sangam (2002) and Hsuan and Koerner (1998).

MATERIAL AND METHODS

HDPE geomembranes of two kinds were tested: black smooth (0.8, 1.0, 1.5 and 2.5 mm) and white textured (1.0 mm).

The total time of UV exposure was 6 months. ASTM G154 was used like a guide. Cycles of 4 hours UV at 60 ± 3°C followed by 4 hours condensation at 50 ± 3°C were used. The lamps used were UV-B. This kind of lamp was used to verify the effects and the level of damage on the HDPE geomembranes.

OIT and MFI tests were performed in HDPE geomembranes after the last period to verify the oxidative degradation. The ASTM specifications were used: ASTM D1238 (Test Method for Flow Rates of Thermoplastics by Extrusion Plastometer Endurance of the Geomembrane Under Examination) and ASTM D3895 (Test Method for Oxidative-Induction Time of Polyolefins by Differential Scanning).

Melt Flow Index (MFI) Test

The MFI test (ASTM D1238) is a qualitative method to assess the molecular weight of the polymer. The MFI test may be used like an indicator of oxidation. The oxidative degradation of the polymer will induce either a cross-linking reaction or a chain scission reaction in the polymer resulting in changes in molecular weight. Cross-linking reactions results an increase in molecular weight, whereas chain scission reactions produce a decrease in molecular weight.

The MFI test measures the amount of molten polymer at 190ºC extruded through an orifice with a defined diameter under a load of 2.16 kg in 10 minutes. A high MFI value indicates a low molecular weight, and vice-versa.

Hence, the MFI value will decrease to cross-linking reactions and will increase to chain scission reactions (Hsuan and Koerner 1998). The apparatus utilized in MFI test is illustrated in the Fig. 1. This test is only carried in HDPE: the PVC contain s many volatiles and plasticizers in its composition.

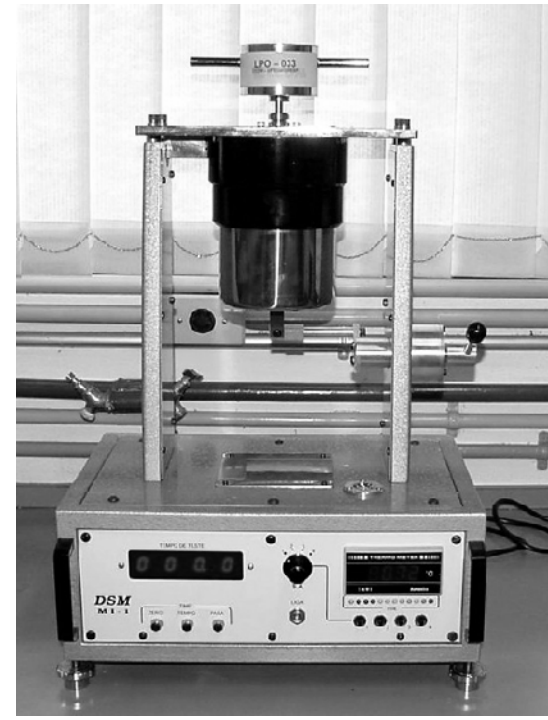

Fig. 1 MFI equipment test

Oxidative Induction Time (OIT) Test

OIT is the time required for the geomembranes test specimen to be oxidized under a specific pressure and temperature. Since the antioxidants protect the geomembrane from oxidation, the OIT value indicates the amount of antioxidant remaining in the test specimen (Hsuan and Koerner 1998).

The OIT tests were performed in accordance to ASTM D3895 (Standard Oxidative Induction Time—Sdt-OIT) which uses a differential scanning calorimeter (DSC) with a specimen test cell that can sustain a 35 kPa gauge pressure. The specimen is heated from room temperature to 200ºC at a heating rate of 20ºC/min under a nitrogen atmosphere. At 200ºC an isothermal condition is maintained for 5 min and the nitrogen gas is changed by the oxygen gas. The test is finished when an exothermal peak occurs (oxidation of material). The minimum OIT value required is 100 minutes. For instance, the Fig. 2 shows a result obtained in a HDPE geomembrane. In this case, the OIT value obtained was 8.11 minutes.

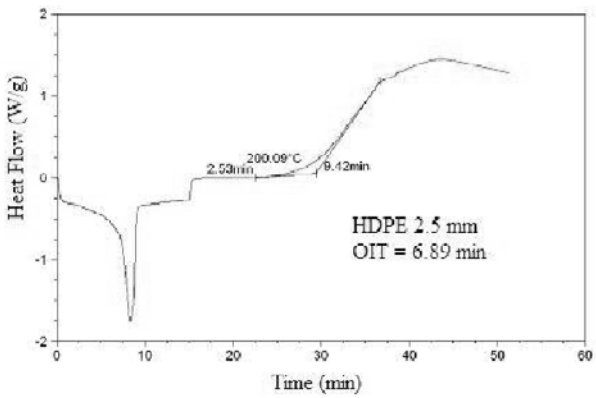

Fig. 2 OIT test (2.5 mm HDPE)

TESTS RESULTS AND ANALYSIS

MFI and OIT tests results are presented in Table 1 and 2, respectively. Table 1 shows the variation of the values of the exposed samples with relation to the values of the fresh samples.

The MFI results obtained shows that all HDPE geomembranes presented decrease in MFI values. However, these values are not so expressive: the biggest value observed was 4.89%. The white GM presented the lowest value: 2.80%. Decreases in MFI value are an indication of crosslink in polymer (crosslink after exposure is always an indicative of superficial degradation). This is a good fact since the level of degradation was not so critical. According to Rowe & Sangam (2002) when chain scission occurs and as the degradation progresses further, the geomembrane will become increasingly brittle and the tensile properties change to the point that cracking occurs in stressed areas. Once sufficient cracks have developed to signicantly increase flow through the geomembrane, the geomem-brane may be considered to have reached the end of the service life.

Table 1 MFI tests results

Condition	HDPE (mm)	MFI (g/10 min)	Variation (%)	Probably meaning
Intact	0.8	0.1778	-	-
	1.0	0.1710	-	-
	1.5	0.1530	-	-
	2.5	0.1460	-	-
	1.0 (W)	0.1680		
Exposed	0.8	0.1691	(-) 4.89	CL
	1.0	0.1650	(-) 3.50	CL
	1.5	0.1484	(-) 3.00	CL
	2.5	0.1433	(-) 1.85	CL
	1.0 (W)	0.1633	(-) 2.80	CL

W = white GM; (-) decrease; CL = Crosslink

Table 2 OIT tests results

Condition	HDPE (mm)	OIT (min)
Intact	0.8	12.55
	1.0	11.50
	1.5	12.00
	2.5	10.05
	1.0 (W)	100.00
Exposed	0.8	6.99
	1.0	11.00
	1.5	10.00
	2.5	12.24
	1.0 (W)	65.68

W = white GM

The intact white GM presented the minimum OIT value required (100 minutes) and showed a good value after the exposure (65.68 minutes).

The OIT tests values were very low to all intacts and exposed samples (black HDPE). The minimum value required was not achieved. However, according to Hsuan and Koerner (1998) the high temperatures employed in the Std-OIT test may bias the test results for certain types of antioxidants, such as HALS antioxidants. HALS antioxidants have a maximum effective temperature below of 150°C. According to GM13 (test method from GRI – Geosynthetic Research Institute) the Std-OIT is not recommended after UV exposures since the high

temperature of the Std-OIT test produces an unrealistic result for some of the antioxidants in the UV exposed samples. UV resistance is based on percent retained value regardless of the original HP-OIT (High Pressure) value. According to GM13 this value is 50%.

However, we must take in account the advantages and disadvantages of each method. The HP-OIT is not a common test, is expensive, has a longer testing time (up to 300 minutes), special testing cell and set up is required, and is specific for some OIT values (it can't detect short OIT values).

CONCLUSION

Some considerations about photodegradation of HDPE geomembrane, MFI and OIT tests were presented. Results of MFI and OIT after UV geomembrane exposure were evaluated to detect oxidative degradation.

MFI test showed some levels of superficial degradation (crosslink) in HDPE geomembranes. Although MFI is a qualitative test it may be an indicative that the degradation already started and what kind of phenomenon is occurring (crosslink or chain scission).

OIT tests showed low oxidation time values to both intact and exposed samples and were unable to detect if any oxidative degradation took place. More specialized tests, such as the HP-OIT (High Pressure) would be necessary to evaluate certain antioxidants packages eventually present in the geomembrane and clarify the oxidative properties of the tested geomembrane.

REFERENCES

ASTM D1238. Test Method for Flow Rates of Thermoplastics by Extrusion Plastometer Endurance of the Geomembrane Under Examination

ASTM D3895. Test Method for Oxidative-Induction Time of Polyolefins by Differential Scanning

ASTM G154. Standard Practice for Operating Fluorescent Light Apparatus for Exposure of Nonmetallic Materials, American Society for Testing and Materials, West Conshohocken, Pennsylvania, USA

GRI Test Method GM13 (2006). Standard specification for test methods, test properties and testing frequency for high density polyethylene (HDPE) smooth and textured geomembranes

Hardy WB (1983) Light stabilization of polymers. Atlas Sun Spot 13(30): 3

Hsuan YG, Koerner RM (1998) Antioxidant depletion lifetime in high density polyethylene geomembranes. Journal of Geo-technical and Geoenvi-ronmental Engineering ASCE :532–541

Kay D, Blond E, Mlynarek J (2004) Geosynthetic durability: a polymer chemistry issue. Québec 2004, 57th Canadian Geotechnical Conference, Québec, Canadá: 13

Mueller W, Jakob I (2000) Comparison of Oxidation Stability of various Geosynthetics. European Geosynthetics Conference (Eurogeo):13

Rollin AL (2004) Long Term Performance of Geotextiles. Geo Québec 2004, 57th Canadian Geotechnical Conference, Québec, Canada

Rowe RK, Sangam HP (2002) Durability of HDPE geomembranes, Review Article, Geotextiles and Geomem-branes 20: 77–95, Elsevier Science Publishers Ltd

Suits LD, Hsuan YG (2003) Assessing the photo-degradation of geosynthetics by outdoor exposure and laboratory weatherometer. Geotextiles and Geomembranes, 21: 111-122, technical note, Elsevier Science Publishers Ltd

Proceedings of the 4th Asian Regional Conference on Geosynthetics
June 17 - 20, 2008 Shanghai, China

UV EXPOSURE OF POLYMERIC GEOMEMBRANES

P.C. Lodi[1], B.S. Bueno[2] and O.M. Vilar[3]

ABSTRACT: The break of polymer chemical bonds may occur due to penetration of sun short wavelengths. In sanitary landfills for instance, ultraviolet radiation affects uncovered materials and can be dangerous during the installation of the liner and before the placement of the waste. Only the ultraviolet part of the light is harmful to the geosynthetic materials, moreover, each material is sensitive to a particular wavelength. This article evaluates the effects of UV degradation and condensation in black HDPE (1.0 and 1.5 mm) and white HDPE (textured – 1.0 mm) geomembrane that were tested in laboratory during 6 months. The tests were performed using a weatherometer assembled at EESC-USP in accordance to ASTM G154. The results have shown variations in punction and tear resistance after each period of exposure.

KEYWORDS: geomembranes, UV exposure, punction resistance, tear resistance

INTRODUCTION

The radiation of the sun, particularly the ultraviolet (UV) portion is mainly responsible for limiting the lifetime of materials exposed to the environment. Generally, UV radiation is characterized by photochemical degradation and thermal oxidation or a combination of these factors. Moreover, factors such as intensity of radiation, temperature, and moisture are the agents that cause aging in polymers.

To evaluate the UV degradation some kinds of lamps are used in laboratory simulations. They are compared with worst-case conditions or the solar maximum condition. Practice G151 provides general procedures to be used when exposing nonmetallic materials in accelerated test devices that use laboratory light sources. This practice (G151) also describes performance criteria for all exposure devices that use laboratory light sources. Detailed information covering exposures in devices that use carbon-arc, xenon-arc, and fluorescent UV light sources are found in Practices G152, G153, G154, and G155.

This paper presents results of the effects of UV degradation and condensation in HDPE (1.0 and 1.5 mm) geomembranes that were exposed by 6 months. White geomembrane (HDPE textured – 1.0 mm) were also evaluated. Proceedings of ASTM G154 were used like a guide.

UV DEGRADATION AND SIMULATION

The degradation with time of exposed specimens is mainly initiated by the ultraviolet rays (UV) of the solar radiation, heat and oxygen, besides other climatic factors as humidity, rain, nitrogen oxides, ozone and deposits of polluted air. The atmospheric pollution and acid rains also can speed up the degradation for UV (Rollin 2004).

The polymers present photodegradative sensitivity differentiated to several wave lengths (λ) of UV rays. These variations of sensitivity are due to the differences in the molecular structures and chemical compositions. Region UV can be subdivided in three bands of wave lengths: UV-A (315-400 nm), UV-B (290-315 nm) and UV-C (below of 290 nm). Some references divide the bands UV-A and UV-B in 280 nm. Band UV-B is main the responsible one for the photochemistry changes in polymers. The maximum sensitivity of some polymers, determined for the energies of dissociation of its chemical bonds, is positioned inside the region of radiation UV with wave lengths between 290 and 400 nm. The Poly Vinyl Chloride (PVC) presents value of λ equal to 320 nm while Polyethylene (PE) presents λ in the band of 330-360 (Agnelli 2002).

The single most significant component of simulated weather is the nature of the radiation source. The type and intensity of radiation to which the materials are

[1] Professor, Department of Civil Engineering, São Paulo State University (UNESP), Ilha Solteira, BRAZIL. Email: plodi@dec.feis.unesp.br
[2] Professor, Department of Geotechnical Engineering, University of State of São Paulo (USP) at São Carlos, BRAZIL. Email address: bsbueno@sc.usp.br
[3] Professor, Department of Geotechnical Engineering, University of State of São Paulo (USP) at São Carlos, BRAZIL. Email address: orencio@sc.usp.br

exposed are the determinant factors in accelerating degradation.

The type of radiation is described by the wavelengths emitted and their intensities, i.e., by the spectral power distribution (SPD) of the light source.

Fluorescent UV-A lamps are very used in laboratory simulations and the kinds more common are UVA-340 (used for simulation of the short and middle UV wavelength region of daylight) and UVA-351 (used for simulation of the short and middle UV wavelength region of daylight which has been filtered through window glass).

Thus, for simulations of direct solar UV radiation the UVA-340 lamp is recommended. Because UVA-340 lamps typically have little or no UV output below 300 nm (that is considered the "cut-on" wavelength for terrestrial sunlight), they usually do not degrade materials as rapidly as UVB lamps, but they may allow enhanced correlation with actual outdoor weathering. Tests using UVA-340 lamps have been found useful for comparing different nonmetallic materials such as polymers, textiles, and UV stabilizers. Fig. 1 illustrates the SPD of the UVA-340 lamp compared to noon, summer sunlight.

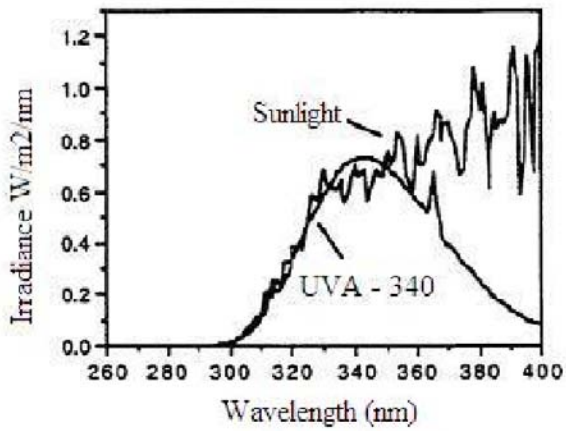

Fig. 1 Spectral power distributions of UVA-340 Lamp and sunlight (ASTM G154)

Fluorescent UV-B lamps have the spectral distribution of radiation peaking near the 313-nm mercury line. They emit significant amounts of radiation below 300 nm, the nominal cut on wavelength of global solar radiation that may result in aging processes not occurring outdoors. Use of this lamp is not recommended for sunlight simulation. There are two commonly available types of UVB-313 lamps. These are known commercially as the UVB-313 and the FS-40. These lamps emit different amounts of total energy, but both peak at 313 nm and produce the same UV wavelengths in the same relative proportions. In tests using the same cycles and temperatures, shorter times to failure are typically observed when the lamp with higher UV irradiance is used. Furthermore, tests using the same cycles and temperatures with these two lamps may exhibit differences in ranking of materials due to difference in the proportion of UV to moisture and temperature. The Fig. 2 illustrates the difference between the lamps. All UVB-313 lamps emit UV below the normal sunlight cut-on. This short wavelength UV can produce rapid polymer degradation and often causes degradation by mechanisms that do not occur when materials are exposed to sunlight. This may lead to anomalous results. Fig. 2 shows the spectral power distribution (SPD) of typical UVB-313 lamps compared to the SPD of noon, summer sunlight (ASTM G 154).

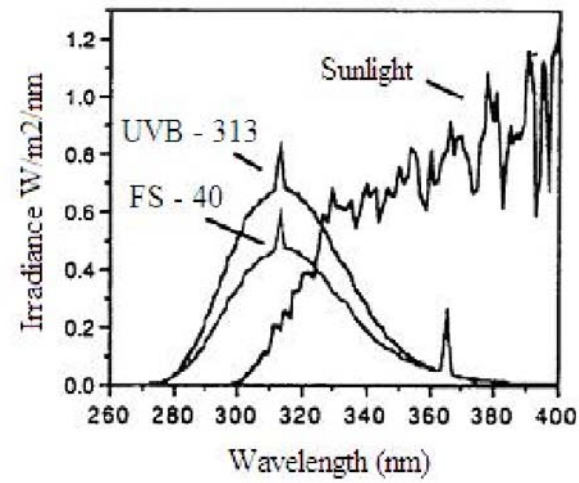

Fig. 2 Spectral power distributions of UVB Lamps and sunlight (ASTM G154)

Both the absorption of light, a necessary first step in the interaction of light with materials, and bond breakage, a critical primary effect of the absorbed radiation, are wavelength dependent. Generally, short UV wavelengths are absorbed by materials to a greater extent than longer wavelengths. In addition, the shorter the wavelength, the larger the energy of the photon associated with that wavelength and the greater the propensity to break the higher energy chemical bonds. Therefore, while the presence of shorter wavelengths than those present in sunlight can accelerate degradation, the mechanism and type of degradation will be altered compared with effects of solar radiation. Acceleration involving change in mechanism and type of degradation cannot be relied on to predict lifetimes under environmental conditions.

Results from accelerated exposure must be considered as representative of actual exposures only when the degree of correlation has been established for

the specific materials being tested and when the type of degradation is the same.

For exposure cycle for coatings and plastics the ASTM G154 suggests UVA 340 lamps (8 h UV at 60 ± 3°C) followed by 4 h condensation at 50 ± 3°C. Another cycle has been widely used for coatings: UVB 313 lamps (4 h UV at 60 ± 3°C) followed by 4 h condensation at 50 ± 3°C.

The light source is an important factor in laboratory tests of materials. Besides that the heat and moisture play a significant role in the effect of weather on materials through their effect on the secondary reactions following bond breakage by the absorbed radiation and are an important component of the laboratory accelerated tests. A great benefit of a laboratory simulation is the repeatability compared to what is essentially an uncontrolled and variable phenomenon, the actual weather. The weather factors can be manipulated independently. Thus, many weather factors that would be impossible to conduct outdoors can be reproduced in specific conditions.

MATERIAL AND METHODS

HDPE geomembranes of two kinds were tested: black smooth (1.0 and 1.5 mm) and textured white (1.0 mm).

The analyses were performed after 6 months of UV exposure. Equipment (Fig. 3) was assembled at the laboratory of the Engineering School of São Carlos (EESC-USP), Brazil. In this sense, recommendations of the ASTM G154 were used like a guide.

UV-B lamps (40 W) were used with the cycle of 4 hours UV at 60 ± 3°C followed by 4 hours condensation at 50 ± 3°C. This kind of lamps was used to verify the possible damage effects on the geomembranes after the exposure.

Physical properties, tensile, tear and punction resistance were evaluated and compared to intact material. Tests were carried out according to ASTM standards: ASTM D5199 (Measuring Nominal Thickness of Geotextiles and Geomembranes), ASTM D3776 (Mass Per Unit Area), ASTM D792 (Specific Gravity and Density of Plastics by Displacement), ASTM D4833 (Test Method for Index Puncture Resistance of Geotextiles, Geomembranes and Related Products), and ASTM D1004 (Test Method for Initial Tear Resistance of Plastic Film and Sheeting).

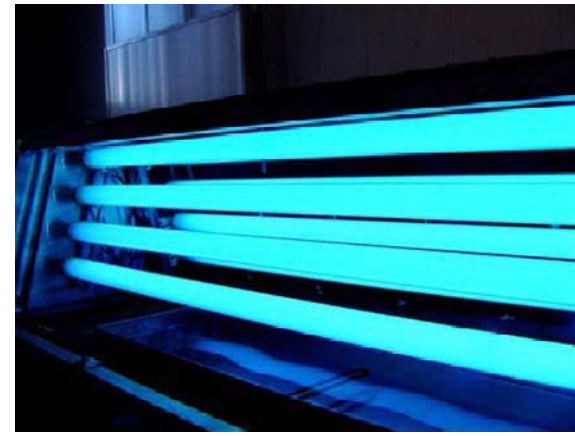

(a)

(b)

Fig. 3 UV equipment (a) UV lamps (b) Detail of exposed samples

TESTS RESULTS AND DISCUSSION

Physical properties presented small variations (nearest to 0.5% to 1%). Figs. 4—6 show results from tensile, tear and punction tests.

Some increases were verified in tensile resistance and deformability. Concerning to tensile resistance the average increases were by 20% (1.0 mm), 7% (1.5 mm) and 14% to HDPE textured.

The deformability presented some oscillation of 14% to HDPE (1.0 mm). On the other hand, variations to HDPE (1.5 mm) and the textured HDPE were not expressive.

The same trend was verified to the elasticity modulus. In this sense, the HDPE became more ductile. The white textured geomembrane presented small variations on its behavior. The deformability and stiffness remain the same values what it implies in a great efficiency against the UV rays.

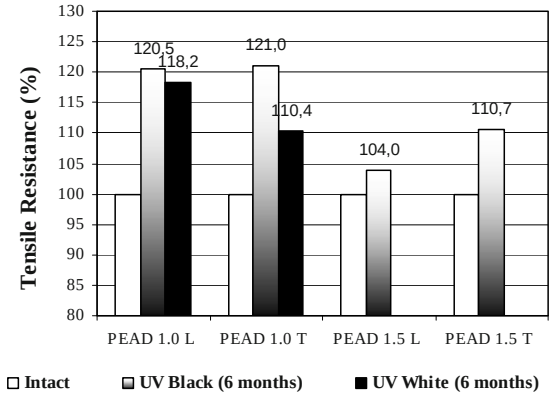

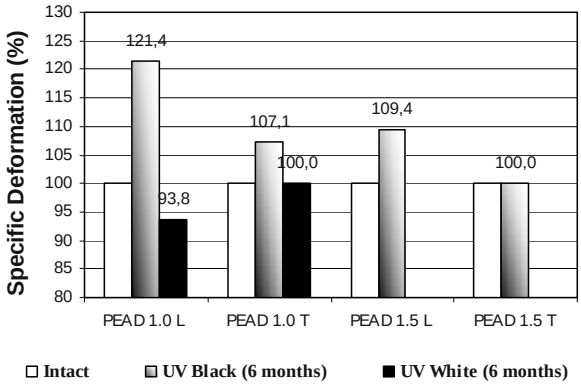

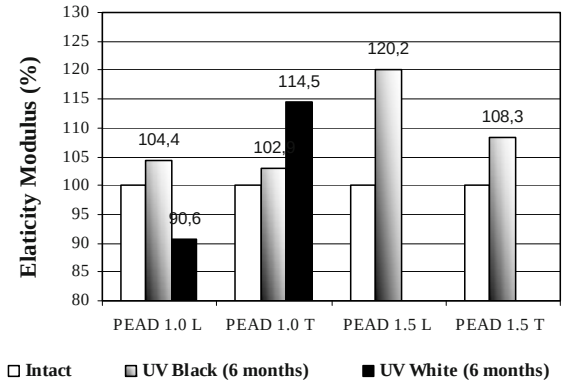

Fig. 4 Tensile properties

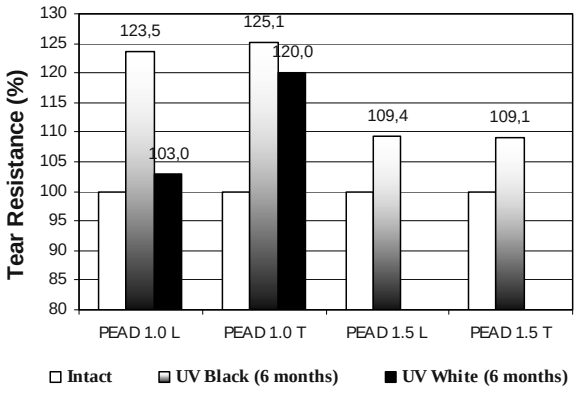

Fig. 5 Tear resistance

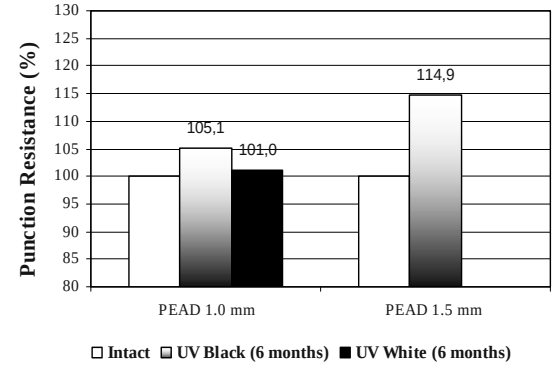

Fig. 6 Punction resistance

The tear resistance presented some increases: HDPE (1.0 mm): 23.5% (L) and 25.1% (T); HDPE (1.5 mm): 9.0% (L and T). The white HDPE also presented increases: 3% (L) and 20% (T).

Concerning to punction resistance the variations were not expressive to HDPE: 5.1% (HDPE 1.0 mm) and 14.9% (HDPE 1.5 mm). The white HDPE practically does not change the property values.

CONCLUSION

Some considerations about UV degradation, laboratory exposure, ASTM standards and kinds of lamps which commonly are used were presented.

In general, the results show that the tested geomembrane presented some variations in properties after exposure. Some variations were inexpressive and did not allow establishing a behavior trend of the material. The HDPE geomembrane has become more ductile than fresh samples and the white HDPE textured were more resistant to the UV effects.

REFERENCES

Agnelli JAM (2002) Characterization Tests of Polimeric Materials (in portuguese) — class notes, DEMA/ UFSCar, São Carlos: 200

ASTM D792. Specific Gravity and Density of Plastics by Displacement. American Society for Testing and Materials, West Conshohocken, Pennsylvania, USA

ASTM D1004. Test Method for Initial Tear Resistance of Plastic Film and Sheeting, American Society for Testing and Materials, West Conshohocken, Pennsylvania, USA

ASTM D3776. Standard Test Methods for Mass Per Unit Area (Weight) of Fabric, American Society for Testing and Materials, West Conshohocken, Pennsylvania, USA

ASTM D4364. Standard Practice for Performing Outdoor Accelerated Weathering Tests of Plastics Using Concentrated Sunlight, American Society for Testing and Materials, West Conshohocken, Pennsylvania, USA.

ASTM D4833. Test Method for Index Puncture Resistance of Geotextiles, Geomembranes and Related Products, American Society for Testing and Materials, West Conshohocken, Pennsylvania, USA

ASTM D5199. Measuring Nominal Thickness of Geotextiles and Geomembranes, American Society for Testing and Materials, West Conshohocken, Pennsylvania, USA

ASTM G23. Standard Practice for Operating Light Exposure Apparatus (Carbon-Arc) Type With and Without Water for Exposure of Nonmetallic Materials, American Society for Testing and Materials, West Conshohocken, Pennsylvania, USA

ASTM G26. Standard Practice for Operating Light-Exposure Apparatus (Xenon-Arc) Type With and Without Water for Exposure of Nonmetallic Materials, American Society for Testing and Materials, West Conshohocken, Pennsylvania, USA

ASTM G53. Standard Practice for Practice for Operating Light- and Water-Exposure, Apparatus (Fluorescent UV Condensation Type) for Exposure of Nonmetallic Materials, American Society for Testing and Materials, West Conshohocken, Pennsylvania, USA

ASTM G151. Standard Practice for Exposing Nonmetallic Materials in Accelerated Test Devices that Use Laboratory Light Sources, American Society for Testing and Materials, West Conshohocken, Pennsylvania, USA

ASTM G152. Standard Practice for Operating Open Flame Carbon-Arc Light Apparatus for Exposure of Nonmetallic Materials, American Society for Testing and Materials, West Conshohocken, Pennsylvania, USA

ASTM G153. Standard Practice for Operating Enclosed Carbon-Arc Light Apparatus for Exposure of Nonmetallic Materials, American Society for Standard Practice for esting and Materials, West Conshohocken, Pennsylvania, USA

ASTM G154. Standard Practice for Operating Fluorescent Light Apparatus for Exposure of Nonmetallic Materials, American Society for Testing and Materials, West Conshohocken, Pennsylvania, USA

ASTM G155. Practice for Operating Xenon-Arc Light Apparatus for Exposure of Nonmetallic Materials, American Society for Testing and Materials, West Conshohocken, Pennsylvania, USA

Rollin AL (2004) Long Term Performance of Geotextiles. Geo Québec 2004, 57th Canadian Geotechnical Conference, Québec, Canada

PROGRESSIVE FAILURE PROPERTIES OF SAND RETAINING WALL REINFORCED WITH DENTI-STRIP INCLUSIONS

M.X. Zhang[1], H. Zhou[2], C.C. Qiu[3] and T.J. Chen[4]

ABSTRACT: In conventional reinforced soils structures, the reinforcements are often laid horizontally in the soil. In this paper, a new concept of soil reinforced with denti-strip reinforcements is proposed. In the proposed method of soil reinforcement, denti-strip elements instead of conventional horizontal inclusions are placed in the soil. A fundamental difference between the denti-strip reinforcing elements presented in this paper and other forms of inclusions is that the soil enclosed within the H-V orthogonal reinforcing elements will provide passive resistances against shearing that will increase the strength and stability of the reinforced soil. A series of laboratory model tests were carried out on sand retaining wall reinforced with denti-strip reinforcements. Besides the horizontal displacements of the facing, the lateral earth pressures acted on vertical elements were measured. A microscopic measurement was performed to investigate the progressive failure process and failure models. The progressive failure of the sand within retaining wall reinforced with denti-strip reinforcements was recorded by digital video camera. Based on the image and graph disposal technique, the model of the initial shear failure and final shear failure was proposed. The failure surface and interaction mechanism of reinforced sand retaining wall were analyzed.

KEYWORDS: denti-strip inclusion, reinforced sand retaining wall, progressive failure, model test, failure surface

INTRODUCTION

The reinforced soil structures have been widely used in geotechnical engineering applications such as construction of road and railway embankment, since the principle of reinforced soil was proposed by Henri Vidal in 1963. Numerous papers have examined the reinforced soil structures, especially in horizontal reinforcement. Zhao (1996) calculated the failure loads on geosynthetic reinforced soil structures by limit equilibrium theory; Lesniewaka and Porbaha (1998) proposed a numerical simulation of scaled retaining wall by rigid-plastic approach; Andrzej (1999) analyzed the creep of geosynthtic reinforced soil retaining wall; Hatami (2001) discussed static response of reinforced soil retaining wall with non-uniform reinforcements; Yang et al. (2003) performed model test on reinforced earth retaining wall under repeated load; Taesoon and Siew (2005) proved the enhanced performance of reinforced soil walls by the inclusion of short fiber; Wang and Zhou (2005) presented an experimental study on the reinforced retaining wall for embankment; Gao et al. (2005) used model tests to study sliding rupture of reinforced earth retaining wall. The above researches have played an active role in the development of reinforced soil structures.

There are mainly two kinds of inclusions used in the reinforced soil retaining wall: strip inclusions (geobelts) and plane inclusions (geotextiles and geocells), which are often laid horizontally in the soil. Zhang et al. (2006, 2008) proposed a new concept of soil reinforced with three-dimensional (3D) elements and carried out triaxial tests and pull-out tests to study the strength of 3D reinforced soil and the interface behavior between 3D inclusions and soil. In this paper, a series of laboratory model tests were carried out on sand retaining wall reinforced with denti-strip reinforcements which were one kind of 3D inclusions. Based on model tests, the progressive failure properties and failure model were analyzed. The deformation character and interaction mechanism of reinforced sand retaining wall were also discussed.

CONCEPT OF DENTI-STRIP INCLUSION

The denti-strip inclusion consists of conventional horizontal element and particular vertical or 3D element. Besides the friction between horizontal inclusion and soil, the vertical or 3D inclusion will provide passive

[1] Professor, Department of Civil Engineering, Shanghai University, CHINA. Email: mxzhang@shu.edu.cn
[2] Postgraduate Student, Department of Civil Engineering, Shanghai University, CHINA. Email:h_zhou2000@163.com
[3] Postgraduate Student, Department of Civil Engineering, Shanghai University, CHINA. Email:qiuchengchun@sina.com
[4] Postgraduate Student, Department of Civil Engineering, Shanghai University, CHINA. Email:tjc284003717@163.com

resistances against shearing and form enclosed area in soil to increase the strength and stability of reinforced soil. Therefore the denti-strip inclusion is one kind of 3D reinforcing structures.

Adopt this concept in reinforced soil retaining wall and the model of reinforced soil retaining wall was developed in Fig. 1. In this model, the passive resistances on vertical inclusions will be against lateral deformation more effectively and the enclosed areas in soil will improve mechanical behaviors of reinforced soil retaining wall.

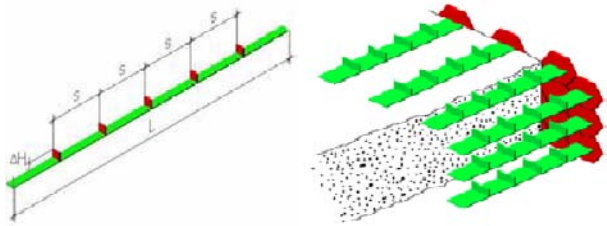

(a) single-sided denti-strip inclusion

(b) reinforced soil retaining wall

Fig. 1 Typical soil retaining wall reinforced with denti-strip inclusions

MODEL TEST

Sand Box

The model tests were performed in a cube sand box with a size of 62×80×110 cm. The sand box had a framework of angle iron. The side walls and base board were made of high strength plexiglass with the thickness of 10mm and 20 mm which were rigid enough against deforming. The front of sand box consisted of ten layers of facing panels and the total size of model retaining wall was 62×80×80 cm (Fig. 2(a)). During model tests the sand distribution and movement could be observed clearly through plexiglass side walls.

Experimental Materials

The denti-strip inclusions used in model tests were made of plexiglass with a high tensile strength ($[\sigma]_t$=40 MPa) and a low elongation ratio (δ=4%). Both horizontal and vertical reinforcements had a width of 15mm and a thickness of 3 mm and they were conglutinated together by chloroform. The denti-strip inclusions and facing panels were connected by bolts (Fig. 2(b)).

Uniform, clean, dry, river sand was used in model tests. The grain-size and physical parameters of sand are shown in Tables 1 and 2.

(a) model of reinforced sand retaining wall

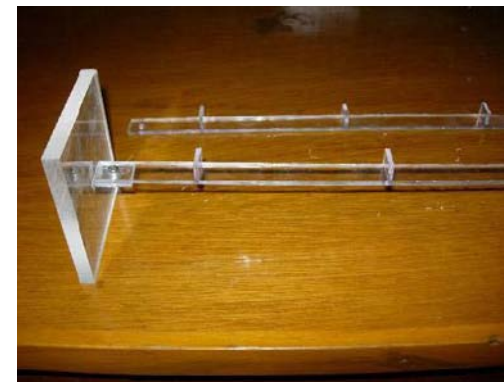

(b) denti-strip inclusion

(c) resistance strain gauge

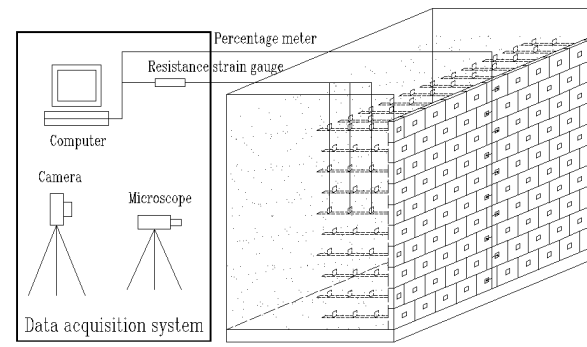

(d) data acquisition system

Fig. 2 Model test of sand retaining wall reinforced with denti-strip inclusions

Table 1 Grain size distribution of sand

Grain composition /%				
10-5	5-2	2-0.5	0.5-0.25	<0.25
3.2	14.85	50.67	24.15	7.13

Table 2 Physical parameters of sand

Specific gravity Gs	Unit weight γ/kN·m^{-3}	Moisture content ω/%	Void ratio e
2.643	15.99	0.15	0.5855

Table 3 Experimental cases of sand retaining wall reinforced with denti-strip inclusions

Case	Type	*l*/cm	ΔH/cm	*s*/cm
T25-0-0	horizontal	25	—	—
T25-0.5-10	denti-strip	25	0.5	10
T25-1.0-10	denti-strip	25	1.0	10
T25-1.5-10	denti-strip	25	1.5	10
T25-2.0-10	denti-strip	25	2.0	10
T35-0-0	horizontal	35	—	—
T35-0.5-10	denti-strip	35	0.5	10
T35-1.0-10	denti-strip	35	1.0	10
T35-1.5-10	denti-strip	35	1.5	10
T35-2.0-10	denti-strip	35	2.0	10
T45-0-0	horizontal	45	—	—
T45-0.5-10	denti-strip	45	0.5	10
T45-1.0-10	denti-strip	45	1.0	10
T45-1.5-10	denti-strip	45	1.5	10
T45-2.0-10	denti-strip	45	2.0	10

(T *l*-ΔH-*s*: *l* length of horizontal element; ΔH height of vertical element; *s* distance between vertical elements)

Experimental Scheme

A total of 15 model tests were carried out to investigate the effects of test parameters on the behaviors of sand retaining wall reinforced with denti-strip inclusions (Table 3). The test parameters mainly included: length of horizontal element (25, 35, 45 cm), height of vertical element (0.5, 1.0, 1.5, 2.0 cm) and distance between vertical elements (10 cm). Cases of simple horizontal reinforcements were also designed for comparison.

The test process was monitored by digital ergometer. Linear variable displacement transducers (LVDT) were used to record horizontal displacements of the facing. The lateral earth pressures acted on vertical elements were measured by resistance strain gauge (Fig. 2(c)). And a microscopic measurement was performed to investigate the progressive failure process and failure models. (Fig. 2(d))

TEST RESULTS AND DISCUSSIONS

Progressive Failure Property

In order to investigate the progressive failure process and failure models of the sand retaining wall reinforced with denti-strip inclusions, two digital video cameras were placed in front of and beside the sand box to record the whole failure process. Coloured powders were mixed with sand where denti-strip inclusions were placed, to help observe the failure surface. The main photographs taken during whole failure process of reinforced sand retaining wall was presented in Fig. 3.

(a) stage 1 (b) stage 2

(c) stage 3 (d) stage 4

Fig. 3 Failure process

The development of failure surface can been observed clearly in Fig. 3. Fig. 3(a) shows the initial failure. Based on the image, we can see the crest of failure surface which is about 33 cm away from the facing. After that the sand within active zone slipped quickly along the failure surface and the failure scale became larger (Fig. 5(b)). During this period, the potential failure surface was close to an arc. The failure reached a temporary stable state in Fig. 5(c) and the toe of failure surface located at the top of the third facing which was about 24 cm above the base. After a few seconds, the failure continued due to disturbance of initial failure to sand and the sand crashed facings of second and third layers. The final failure is presented in Fig. 5(d).

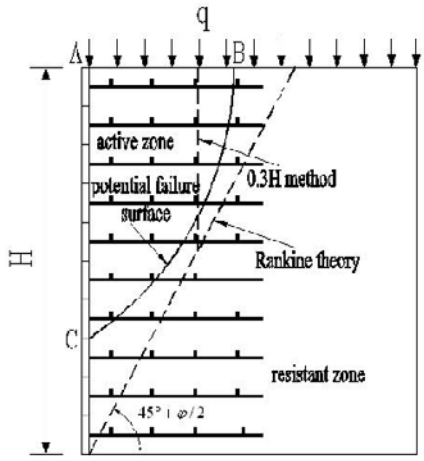

Fig. 4 Potential failure surface

Based on the images, the crest B and toe C were found and the potential failure surface was proposed in Fig. 4. The potential failure arc divided the section into active zone and resistant zone. In general, the resistant zone was larger than that of Rankine theory and 0.3 H method. Furthermore, the lower reinforcements (first to third layer) take part directly in the support of retaining wall. And the crest of potential failure surface indicates that the necessary reinforcement length was 0.413 H.

Lateral Earth Pressure

The lateral earth pressures acted on vertical elements of seventh layer were measured to study interaction mechanism of reinforced sand retaining wall. Based on the potential failure surface proposed in Fig. 4, the denti-strip inclusion was divided into active zone and resistant zone by the division which was 26.5 cm (0.332 H) away from the facing of seventh layer. The lateral earth pressures were analyzed considering both zones.

If the lateral earth pressure σ_p acted on the front of vertical element (see Fig. 5(a)) was positive, the resultant ones of both sides were determined. Fig. 5 showed the surcharges versus lateral earth pressures on dent-elements during loading.

In Figs. 5(b) and (c) there were three dent-elements in active zone and one in resistant zone, respectively. In active zone σ_a was always higher than σ_p and the resultant values were almost negative, which was in agreement with the movement of sand within the active

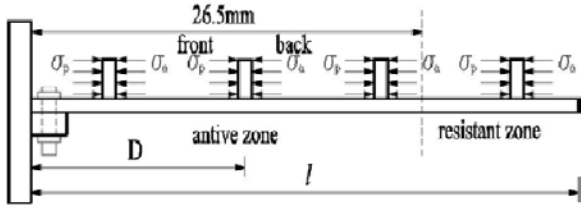

(a) lateral earth pressures on dent-elements

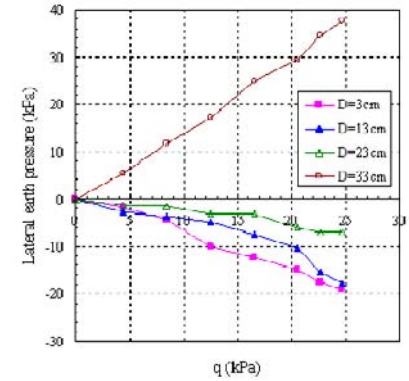

(b) 7th layer (l=35cm, ΔH=1.5cm)

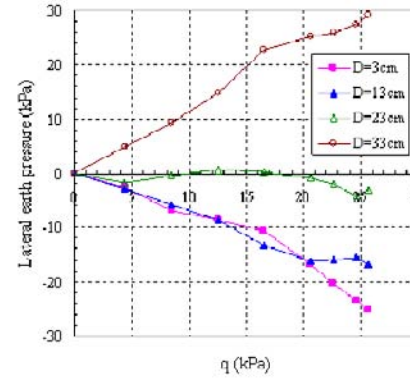

(c) 7th layer (l=35cm, ΔH=2.0cm)

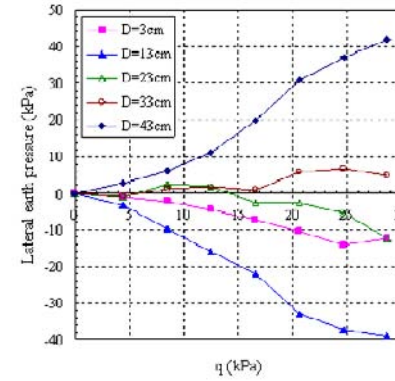

(d) 7th layer (l=45cm, ΔH=1.5cm)

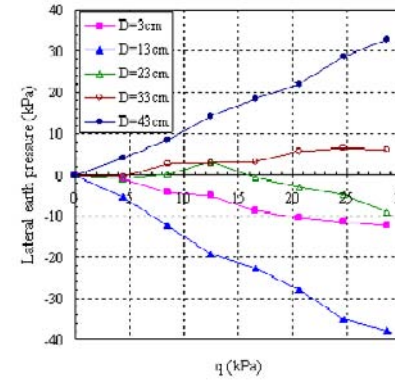

(e) 7th layer (l=45cm, ΔH=2.0cm)

Fig. 5 Curves of surcharges versus lateral earth pressures on dent-elements

zone. On the contrary, the lateral earth pressure σ_p was much higher than σ_a in resistant zone. And it showed that the the lateral earth pressure σ_p acted on the front of dent-elements gradually increased along the distance from the facing, especially in resistant zone. In general, the above distribution tendency still existed in Figs. 5(d) and (e). According to the limit equilibrium theory of reinforced soil retaining wall, the inclusions within active zone were not considered into calculation. Therefore, the dent-elements within resistant zone played an important role to support reinforced sand retaining wall. It can also be inferred that the active lateral earth pressure and passive one should be equal, if denti-element was placed at the potential failure surface. Therefore, denti-elements should be laid in resistant zone to increase the reinforcing effect of denti-elements and bearing capacity of retaining wall reinforced with denti-strip inclusions.

CONCLUSIONS

In this paper, a new concept of soil reinforced with denti-strip reinforcements was proposed. In order to study the progressive failure properties and interaction mechanism, a series of laboratory model tests were carried out on sand retaining wall reinforced with denti-strip inclusions. The following conclusions can be drawn from the results:

(1) The progressive failure progress consisted of initial shear failure and final shear failure with different interaction mechanism.

(2) Based on initial shear failure, a potential failure arc was proposed.

(3) The distribution of lateral earth pressures acted on dent-elements depends on its locations. It is quite different in active zone and resistant one.

ACKNOWLEDGEMENTS

The financial assistance from the National Natural Science Foundation of China under Grant No. 50678100 is herein much acknowledged.

REFERENCES

Andrzej Sawicki (1999) Creep of geosynthetic reinforced soil retaining wall. Ceotextiles and Geomembrances 17(1): 51-65

Gao JP, Yu MH, Hu CS,Chen ZD (2005) Large model experiment on sliding rupture of reinforced earth retaining wall. Journal of Changan University (Natural Science) 25(6): 6-9

Hatami K, Bathurst RJ, Pietro PD (2001) Static response of reinforced soil retaining walls with nonuniform reinforcement. The International Journal of Geo-mechanics 1(4): 477-506

Lesniewaka D, Porbaha A (1998) Numerical simulation of scaled retaining walls by rigid-plastic approach. J. Computers and Geotechnics 23(2): 113-129

Taesoon P, Siew AT (2005) Enhanced performance of reinforced soil walls by the inclusion of short fiber. Geotextiles and Geomembrances 23(4): 348-361

Wang X, Zhou SH (2005) An experimental study on the reinforced retaining wall for embankment. China Civil Engineering Journal 38(10): 119-128

Yang GL, Li HS, Wang YH (2003) Model test on reinforced earth retaining wall under repeated load. China Civil Engineering Journal 36(6): 105-110

Zhang MX, Javadi AA, Min X (2006) Triaxial tests of sand reinforced with 3D inclusions. Geotextiles and Geomembrances 24(4): 201-209

Zhang MX, Min X (2006) Behavior of sand reinforced with one-layer 3D reinforcement by triaxial tests. Chinese Journal of Geotechnical Engineering 28(8): 931-936

Zhang MX, Zhou H, Javadi AA, Wang ZW (2008) Experimental and theoretical investigation of strength of soil reinforced with multi-layer horizontal-vertical orthogonal elements. Geotextiles and Geomembranes 26 (1): 1-13

Zhao AG (1996) Failure loads on geosynthetic reinforced soil structures. Ceotextiles and Geomembrances 14 (6): 289-300

Proceedings of the 4th Asian Regional Conference on Geosynthetics
June 17 - 20, 2008 Shanghai, China

EVALUATION ON STRESS CRACKING RESISTANCES OF VARIOUS HDPE DRAINAGE GEONETS

M.S. Mok[1], E. Blond[2], J. Mlynarek[3] and H. Y. Jeon[4]

ABSTRACT: Specimens from each geonet were placed under various compressive loads in a vessel containing a solution of 10% surface-active agent and 90% water at a temperature of 50°C. Then the surface morphology study of the specimen was performed after 500 hours test duration. The results show that all of these geonets did not appear any kind of stress cracking in the condition of 400 kPa, which is a typical landfill's loading condition. However, in the case of bi-planar geonet there were some deposits on the surface of geonet's strand and it is expected that this phenomena is due to the results of chemical clogging. On the other hand, in the case of the tri-planar and circular type bi-planar geonets, it maintained very clean flow channels until the end of the test. For high normal pressure some environmental stress cracks were detected for the circular type bi-planar geonet. The results show that the resistance to the environmental stress cracking is related to its polymer density, crystallinity and also rigidity not its mechanical properties.

KEYWORDS: geonet, compressive loads, surface morphology, stress cracking, chemical clogging, flow channels

INTRODUCTION

Land filling, by all indications, will continue to be the predominant method of solid waste disposal. As the use of high density polyethylene (HDPE) geonets increase in landfill applications, it is required to evaluate their long-term properties in several chemical conditions. (Ward and Brown 1990; Carlson 1993)

Typically, the high crystallinity of polyethylene geonets provides an excellent chemical resistance to harsh chemical leachate, however can be problematic with regard to environmental stress cracking. (Qian and Brown 1993; Thomas 1998) Under low stresses in the circumstance of room temperature polyethylenes will fracture by slow crack growth. This mode of failure limits the lifetime of polyethylenes used in critical applications as drainage materials, lining under landfills. (Lagaron, Pastor, Kip 1999; Bobsein 1999)

Geomembranes and geonets are used as a barrier and drainage component in this system, respectively. With addition of carbon black which is an anti-oxidation material HDPE geomembranes and geonets are normally used in hazardous landfill system as a barrier and drainage respectively.

Many researchers and a lot of work about environmental stress cracking resistance for the geomembranes were done and many beneficial reports have already been published. (Peggs and Kannien 1995; Thomas and Deschepper 1993) However a few research results on the environmental stress cracking resistance for the geonet drainage material were performed. Therefore, in this study the resistance to environmental stress cracking (ESCR) was examined mainly in morphological issues for various geonets (bi-planar, tri-planar and circular type of bi-planar geonet) under condition of various normal pressures.

SPECIMEN & TEST METHODS

Total three types of geonets were test in this study. Sample A has 5.6 mm mean value of thickness and two layers which means bi-planar geonet. The cross sectional shape of strand of Sample A is more likely to a square. Sample B has average of 8.6 mm thickness and has 3 layers (tri-planar). Sample C is also bi-planar geonet however has circular type cross sectional shape and thicker than sample A. The raw material of all these samples is high density polyethylene (HDPE). Typical specifications of the samples are provided in Table 1.

Fig. 1 shows these samples. Short-term compressive deformation test was performed using the procedures set forth in Standard Test Method for Determining Short-term Compression Behavior of Geosynthetics (ASTM

[1] Researcher, CTT Group/SAGEOS, Saint-Hyacinthe, Quebec, CANADA, Email: munsungmok@gmail.com
[2] Director, CTT Group/SAGEOS, Saint-Hyacinthe, Quebec, CANADA, Email: eblond@gcttg.com
[3] CEO, CTT Group/SAGEOS, Saint-Hyacinthe, Quebec, CANADA, Email: jmlynarek@gcttg.com
[4] Professor, Division of Nano-Systems Engineering, Inha University, Incheon, KOREA, Email: hyjeon@inha.ac.kr

D6364) to evaluate basic mechanical properties of samples. Specimen is positioned between two rigid steel platens and compressed at a constant rate of 1.0 mm/min. To control an accurate temperature of specimen of 23°C heating platens were manufactured and its heating is 14°C/min. Also special test equipment for ESCR under compression was manufactured and this equipment is shown Fig. 2.

The specimens were immersed in a solution of 90% water and 10% I-gepal CO630 at a temperature of 50°C. The solution level was checked daily and de-ionized water used to keep the bath at a constant level.

And the solution was replaced every 2 weeks. 200, 400 and 700 kPa for sample A, 600, 1,000 and 1,200 kPa for sample B and 400, 600 and 800 kPa for C of load were subjected as compressive load using 6:1 arm lever loading system within considering their compressive strengths.

The immersion duration was 500 hours and during and after the test apparent observation and microscopic morphology was evaluated for the specimen.

Table 1 Typical specification of the samples

Property	Test method	Unit	Sample		
			A	B	C
Thickness	ASTM D5199	mm	5.6	8.6	8.2
Mass per unit area	ASTM D5261	g/m^2	920	1700	2300
Carbon black	ASTM D4218	%	2.3	2.2	2.3
Density	ASTM D1505	g/cm^3	0.942	0.944	0.940
Crystallinity	ASTM D2910	%	56	55	61

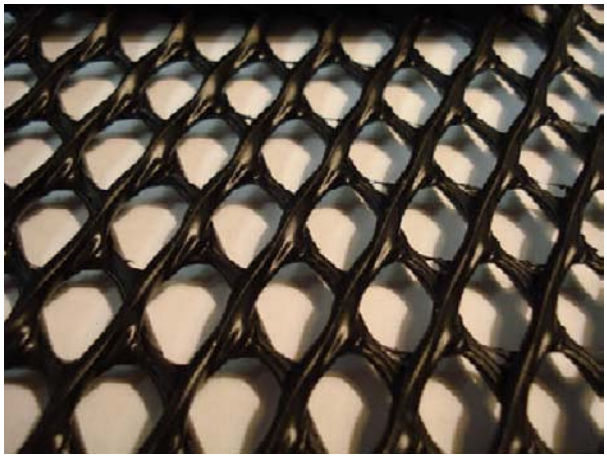

(a) Sample A

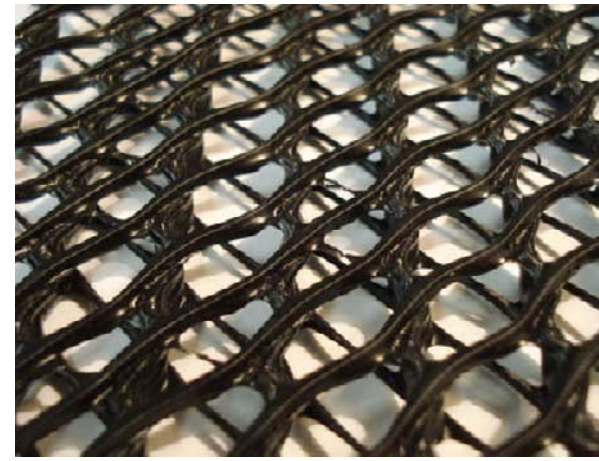

(b) Sample B

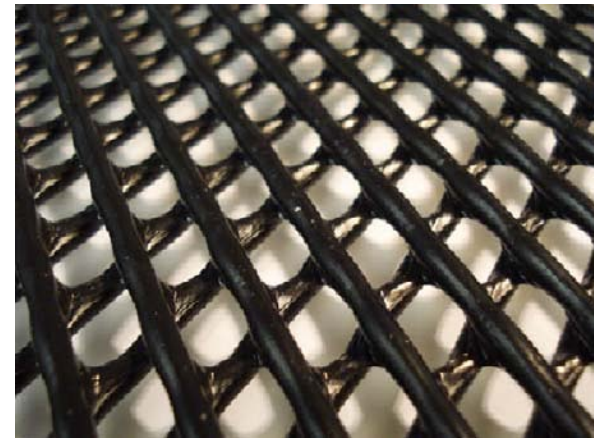

(c) Sample C

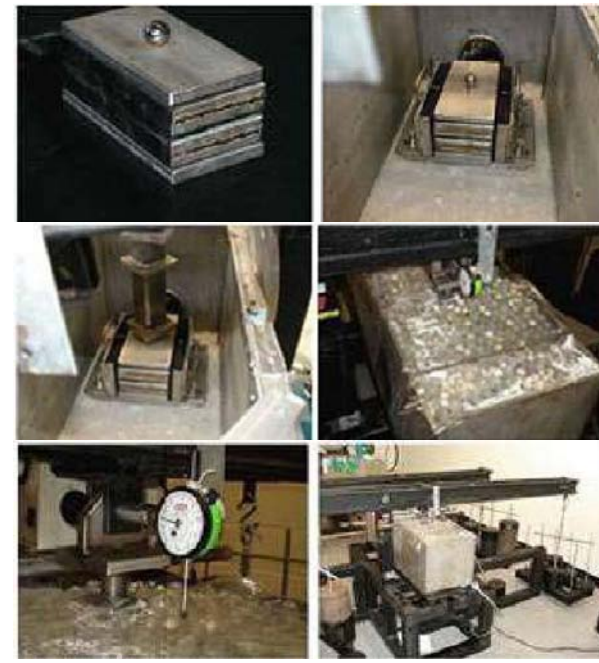

Fig. 2 Compressive environmental stress cracking test equipment

RESULTS & DISCUSSION

Considering the compressive strength and strain properties, the sample C has the stiffest behavior in these three Samples. Initial 5% elastic modulus is much higher than other samples. From this behavior of Sample C it is expected that sample C has rigid structure and has high crystallinity of over 60%. Table 1 confirms this phenomenon. In the other hand Sample A and C have more flexible behavior and low initial elastic modulus.

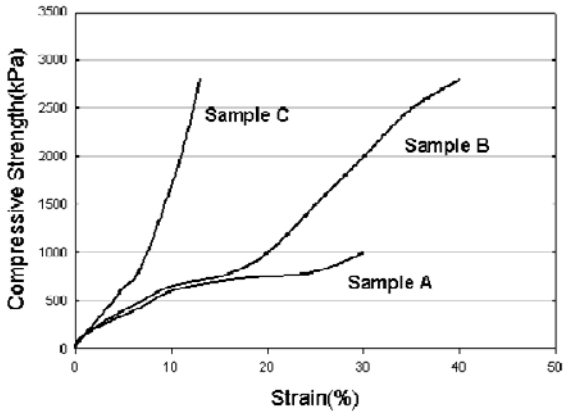

Fig. 3 Short-term compression test results

Figs. 4—9 exhibit the results of apparent observations and microscopic morphologies. Some kind of chemical clogging due to the I-gepal solution is expected for the Sample A because of its flow channel and thickness. This chemical clogging for the Sample A was confirmed by the apparent observation. Fig. 4 shows the results of apparent observations for Sample A. In this figure many deposits on the surface of the specimens were detected during and end of the test and it seems that these deposits which were induced from the chemical solution may occur clogging and therefore affect geonet's in-plane flow capacity. Also there is no chemical clogging on the surface of the specimen for Sample B and this fact was confirmed by apparent observation (Fig. 5).

Considering flowing pattern of the I-gepal solution through out the specimen, the I-gepal has zig-zag flow pattern and this courses some frictions with strands of sample A, therefore the chance of clogging is higher than the Sample B which has straight flow pattern. Also thin thickness compared to other samples can increase chance of any clogging. For the Sample C, the initial creep deformation was very low which means the initial modulus is higher than the other samples and therefore high modulus indicate more rigid than others. High rigidity has brittle failure pattern rather than ductile failure and this can induce a stress crack during the compressive creep test. Also it seems that the chemical act a stress cracking accelerator.

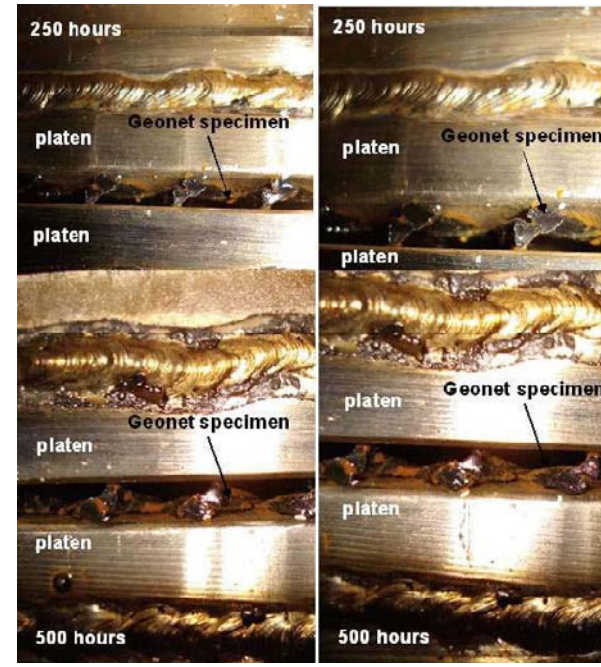

Fig. 4 Apparent observation during and end of the test for sample A (200kPa)

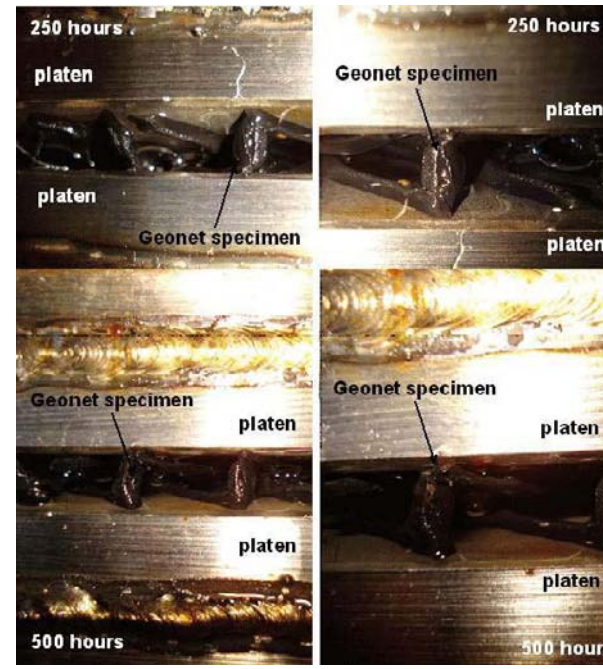

Fig. 5 Apparent observation during and end of the test for sample B (700 kPa)

Figs. 6—9 confirm this environmental stress cracking phenomenon. From these exhibitions it is clear that Sample A and Sample B which have relatively more flexible HDPE strand than Sample C didn't experience any kind of environmental stress cracking. For the Sample C which is more rigid and has high crystallinity (Table 1) likely has to chance of stress cracking. The microscopic morphologies indicate that the extent of

environmental stress cracking observed in the Sample C is related to its flexibility and crystallinity. And from the morphologies it seems that the stress cracks occurred at the junction point of the strands first and then propagate to strands with increasing normal pressure.

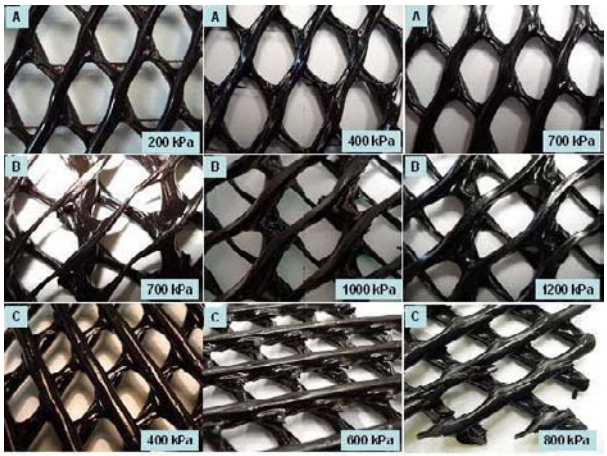

Fig. 6 Apparent observations end of the test for samples under various normal pressures

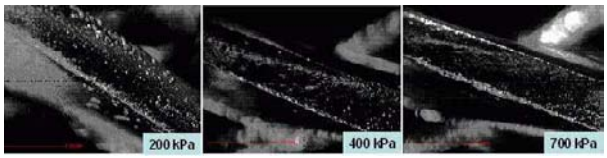

Fig. 7 Microscopic morphologies of Sample A after the test for various normal pressures

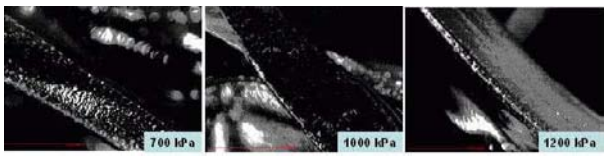

Fig. 8 Microscopic morphologies of Sample B after the test for various normal pressures

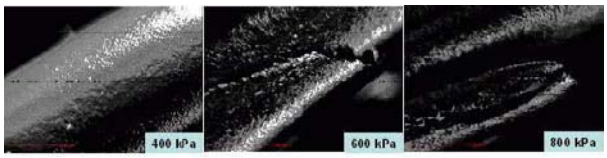

Fig. 9 Microscopic morphologies of Sample C after the test for various normal pressures

CONCLUSIONS

In this study long-term (500 hours) environmental stress cracking resistance for various geonets under various normal pressures were evaluated. The conclusions are as follows:

1. ESCR property is one of the most critical parameters for evaluating long-term chemical resistance of HDPE geonets which used in hazardous landfill systems.

2. Traditional bi-planar geonets which have square type strand and tri-planar geonet have very strong chemical and stress cracking resistance even high normal pressure.

3. Cylindrical type bi-planar geonets is more rigid material than other samples and it is very week to environmental stress cracking with increasing normal pressure

REFERENCES

Bobsein RL (1999) factors influencing SP-NCTL test results, Proceedings of the 13th GRI Seminar: 46-57

Carlson, DS, etc. (1993) laboratory evaluation of HDPE geomembrane seams, Geosyntheitcs 93, Vancouver, Canada: 1543

Lagaron JM, Pastor JM, Kip BJ (1999) Polymer 40: 1629-1636

Peggs ID, Kannien MF (1995) Geosynthetics International 2(1)

Qian R, Lu X, Brown N (1993) Polymer 34(22)

Thomas, RW (1998) evaluating the stress crack resistance of HDPE seams, 6th International Conference on Geosynthetics

Thomas RW, Deschepper BW (1993) stress crack testing of unnotched HDPE geomembrane and seams, Proceedings of the 7th GRI seminar Dec. 14-15

Ward AL, Lu X, Brown N (1990) Polymer Engineering and Science, Sep 30(18)

Proceedings of the 4th Asian Regional Conference on Geosynthetics
June 17 - 20, 2008 Shanghai, China

INFLUENCE OF SOLUTION CHARACTERISTICS ON SWELLING AND HYDRAULIC PERFORMANCE OF GEOSYNTHETIC CLAY LINERS

C. Xu [1], X.Y. Liao [2] and Z.B. Li [3]

ABSTRACT: The influence of solutions with different valence, concentration of cation and hydrated ionic radius on swelling characteristics and hydraulic properties of geosynthetic clay liner (GCL) were explored by free swell tests and hydraulic conductivity tests. The mechanical analyses on swelling and hydraulic performance of GCL were carried out. It is found that cation valence, concentration and hydrated ionic radius all have impacts on swelling and hydraulic performance of GCL. Test results indicate that the free swell of bentonite decreases and the hydraulic conductivity of GCL gradually increases with the increase of cation valence and concentration. Monovalent cation concentration can greatly influence the swelling amount and hydraulic conductivity of the GCL, however, the influence of the concentration of divalent and trivalent cations is negligible. As the radius of the hydrated ionic increases, the free swell of bentonite in monovalent cation solutions grows, and the hydraulic conductivity of GCL gradually decreases.

KEYWORDS: geosynthetic clay liners (GCL), solution characteristics, swelling features, hydraulic properties, mechanical analysis

INTRODUCTION

Geosynthetic clay liners (GCLs) have been incorporated into environmental engineering, hydraulic project and geotechnical engineering approximately since 1990s. There are three main advantages of GCL: low hydraulic conductivity, great adaptability to deformation and construction convenience. These synthetics are often used solely or combined with other seepage control materials (for instance geomembranes) as hydraulic barrier in projects. The characteristics of swelling and hydraulic performance of GCL are of important aspects to its application.

Several studies have been conducted to assess the swelling characteristics and hydraulic conductivity. Petvu and Rowe (1997) conducted a series of permeability tests on GCL with distilled water to study the influence of stress level on hydraulic conductivity of GCL, and found that there is a significantly inverse proportional relation between hydraulic conductivity of GCL and normal stress. LaGatta and Boardman (1997) found that the hydraulic conductivity of GCL increases as the tensile strain increased.

Ruhl and Daniel (1997) performed hydraulic conductivity tests of five kinds of GCLs using seven permeant liquids, including simulated MSW leachate, simulated hazardous MSW leachate, fly ash leachate, real MSW leachate, tap water, hydrochloric acid and sodium hydroxide. Lake and Rowe (2000) examined the hydraulic conductivity of GCL with 3g/L to 5g/L NaCl solutions, and found that the hydraulic conductivity may change with composition of source reservoir solutions. Shackelford and Benson (2000) discussed and tested the hydraulic conductivity of GCL permeated with non-standard liquids. The results showed that aggregate-size distribution and content of bentonite have important impacts on hydraulic conductivity as well as other factors such as thickness and void ratio of GCL, hydration conditions and test time.

Lin and Benson (2000) conducted tests to assess how wet-dry cycling affects the plasticity and swell of bentonite, as well as the hydraulic conductivity of GCL. Results showed that the hydraulic conductivity remained low during first four dry-wetting cycles while increased dramatically within five to eight cycles. Li Xian (2005) studied the characteristic of healing of GCL and its influence on hydraulic conductivity.

In this research, a series of solutions, with different valence and concentration of cation and different hydrated ionic radius, were employed to conduct free swell tests and hydraulic conductivity tests, the objective is to cognize the influence of solution features on swelling and hydraulic properties of GCL. The test results are also analyzed and discussed with hydration theory.

[1] Prof., Ph.D, Key Laboratory of Geotechnical Engineering, Tongji University, CHINA. Email: c_axu@mail.tongji.edu.cn
[2] Ph.D Student, Key Laboratory of Geotechnical Engineering, Tongji University, CHINA. Email: liaoxingyue@gmail.com
[3] Ph.D, Construction and Traffic Committee of Changning District, Shanghai, CHINA. Email: scraft_li@163.com

MATERIALS

All laboratory tests described in this paper were conducted on a needle-punched GCL manufactured by Yixing Non-Weavings Cloth Factory. The GCLs contained a minimum of 5.32 kg/m^2 of essentially dry, natural, granular sodium bentonite sandwiched between a 110g/m^2 woven geotextile as a carrier and a 220 g/m^2 nonwoven geotextile as a cover and held together by needle-punching. The free swelling volume of bentonite performed with tap water was 28.0 mL/2g. A series of X-ray diffraction tests showed that the bentonite was composed of 67% of montmorillonite, 14% of Kaolin Clay, 12% of Illite, 4% of Syenite and 2% of quartz. The properties and chemical composition of the bulk bentonite were listed in Table 1.

Five types of solutions (NaCl, KCl, $CaCl_2$, $ZnCl_2$ and $AlCl_3$) with seven different concentrations (0.005 mol/L, 0.0075 mol/L, 0.01 mol/L, 0.03 mol/L, 0.05 mol/L, 0.01 mol/L, 1.0 mol/L) were used as hydration and permeant media. Comparison of test result of NaCl solution and KCl solution helped to investigate the influence of monovalent cation and hydrated ionic radius on swelling and hydraulic properties of GCL, while test result of $CaCl_2$ solution, $ZnCl_2$ solution and $AlCl_3$ solution helped to understand the effects of bivalent and trivalent cation, respectively. In this research, tap water was used to conduct free swells test and hydraulic conductivity tests of GCL as reference.

APPARATUS AND METHOD

Free Swell Tests

According to ASTM D5890, the free swell tests of bentonite were conducted as follows:

The standard test method according to ASTM D5890 is applied to obtain the swell index of the bentonite. The test procedure in detail is as follows:

(1) Cut a piece of GCL, snip the needle-punched fiber and remove the bentonite.

(2) Mash the bentonite in the mortar and make 80% of it pass the sieve with the diameter of 0.075 mm, and dry the 80%.

(3) Fetch 90 ml hydration solution and pour into a 100ml measuring cylinder with a plug, weigh 2 g bentonite and add 0.1 g into cylinder each time, after the bentonite sediments on the bottom totally, add another 0.1 g.

(4) After the completion of step 3, pour a little hydration solutin along the side wall to flush the bentonite on the side wall of cylinder until the volume of the liquid is up to 100ml.

(5) Plug the measuring cylinder and measure the volume of the settled bentonite after 24 hour standing.

In order to eliminate the influence of the temperature, the standard test method for swell index of the bentonite in this study is carried out in the temperature of 20°±2°C.

Table 1 Properties and composition of bulk bentonite

Properties	Units	Values
Initial moisture	%	17.0
Initial thickness	mm	6.65－6.84
pH		9.89－10.67
Chemical component		
SiO_2	%	57.2
Al_2O_3	%	16.1
CaO	%	3.4
TiO_2	%	0.8
Fe_2O_3	%	5.7
Na_2O	%	3.3
K_2O	%	0.7
MgO	%	3.7
Ionic exchange ability		
Na^+	mmol/g	0.445
K^+	mmol/g	0.010
Ca^{2+}	mmol/g	0.159
Mg^{2+}	mmol/g	0.017

Hydraulic Conductivity Tests

The hydraulic conductivity test is carried out by the self-developed geosynthetic permeameter Geo-syn.

The instrument has the advantages of well-sealed, high seepage pressure and high precision. The test method and procedure in detail are as follows:

(1) Cut the GCL with the size of 15 cm×15 cm, put the rigid bearing plate in the middle of the sample, and mark the plate along the outer range by a color pen.

(2) Remove the plate, inject little hydration solution into the marked GCL with the pinhead syringe. Cut the GCL along the marked range by a sharp scissors after standing 2－3 minutes.

(3) Fix the upper and lower plate of the permeameter together, put a dry permeable stone with a diameter of 10cm and thickness of 1cm into the groove of the lower plate, and then place a piece of the filter paper with the same size on the permeable stone.

(4) Place the cutted GCL on the filter paper, and then place another filter paper, upper permeable stone in sequence.

(5) Install the pressure chamber and put on the pressure system. Apply a certain vertical stress, and read the dial indicator once an hour until the vertical deformation of the GCL is not more than 0.001 mm in 24 hours, then inject the hydration solution into the pressure

chamber.

(6) When the GCL sustained stable under the given vertical pressure, open the pressure chamber and take away the rigid bearing plate, permeable stone and the filter paper. The Na-bentonite mixed with the hydration solution is smeared in between the GCL and chamber wall carefully.

(7) Install the pressure chamber and inject full pemeatant. Put the pressure chamber into loading system and apply the vertical stress.

(8) After 24-hour standing, connect the pressure chamber, the measurement system and the permeaton pressure system. Apply the permeation pressure and then measure the volume permeated through GCL at different time breaks. Time is measured by the second counter with an accuracy of 0.01 s. Electrical conductivity (EC) and pH value is measured by the sensIONTM378 desktop multi-parameter determinator of HACH.

The permeability test is terminated when the standard of ASTM D6766 are satisfied, i.e., the difference between the continous quartic permeability coefficient is not more than 25% (when the permeability coefficient is not less than 10^{-8} cm/s) or if not more than 50% (when the permeability coefficient is less than 10^{-8} cm/s). The raito of the liquid volume infiltrated and exudated from the GCL is 0.75—1.25, the ratio of the pH value and electrical conductivity (EC) of infiltrated and exudated liquid are 0.9—1.1.

Considering the influence of the vertical stress and the infiltration pressure (hydraulic gradient) to the permeability test, the vertical stress and the permeation pressure in the test is remained a constant of 25 kPa or 50 kPa. In order to eliminate the influence of the temperature, the permeability test is carried out in the temperature of 20±2°C.

RESULTS AND DISCUSSION

Influence of Cation Valence

Influence on free swell feature

Influence of cation valence on free swell feature of bentonite was shown in Fig. 1, in which free swell volume of bentonite in tap water is showed as reference (DDW=28 mL/2g). Fig. 1 showed that: (1) Performed with equivalent concentration, free swell volume of bentonite decreases with the increase of cation valence. The sequence, based on the swell volume, is monovalent ions (Na^+, K^+)> bivalent ions (Ca^{2+}, Zn^{2+})> trivalent ion (Al^{3+}). The swell volume of betonite in any one above solution is smaller than that in tap water. (2) When the solution concentration was less than 0.05 mol/L, free swell volume of GCL was influenced significantly by cation valance. However, when the concentration is more than 0.05mol/L, the effect of cation valance is much less. When the concentration reaches 1.0mol/L, the influence of cation valance can be negligible.

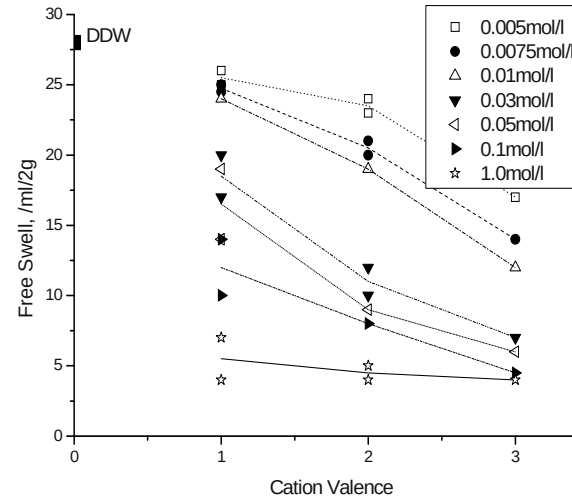

Fig.1 Influence of cation valence on bentonite free swell

Influence on hydraulic conductivity

The influence of cation valence on hydraulic conductivity is shown in Fig. 2. The hydraulic conductivity of GCL performed with tap water is also shown in Fig. 2 as reference (DDW=2.250×10^{-10} m/s). The following can be acquired: (1) Tested with equivalent concentration, the hydraulic conductivity of GCL increases along with cation valence. The sequence of hydraulic conductivity with different solutions is monovalent ions (Na^+, K^+)< bivalent ions (Ca^{2+}, Zn^{2+})< trivalent ion (Al^{3+}). The hydraulic conductivity of GCL with any one above solution is larger than that of tap water. (2) The effect of cation valence on hydraulic conductivity became weaker when the concentration getting higher. And when the concentration reached 1.0 mol/L, the influence of cation valance is negligible.

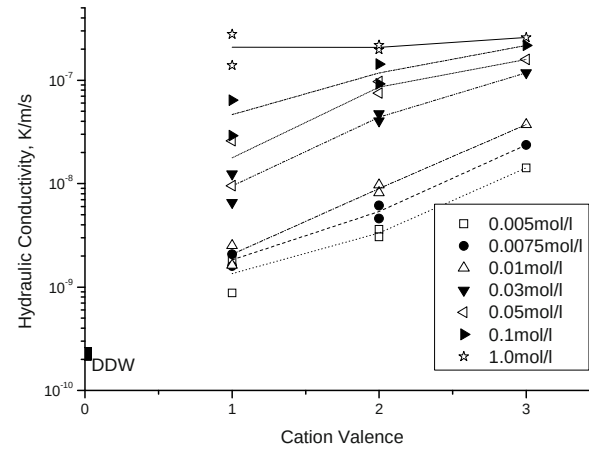

Fig.2 Influence of cation valence on GCL's hydraulic conductivity

Influence of Ionic Concentration

Influence on free swell feature

Fig. 3 shows the influence of concentration of cation on free swell volume of bentonite. Free swell volume of bentonite decreases apparently with the increase of concentration. The trend of curves in Fig. 3 is similar while cation valence is equivalent. The free swell volume of bentonite in different solutions remains in a relatively small range when concentration reaches as high as 1.0 mol/L. It is obvious that free swell characteristic of bentonite is influenced simultaneously by cation valence and ionic concentration, and the effect of cation valence is more evident with low ionic concentration.

Influence on hydraulic conductivity

Fig. 4 shows the influence of ionic concentration on hydraulic conductivity of GCL, the test result with tap water (DDW) is also presented. The hydraulic conductivity of GCL increases significantly with the increase of ionic concentration, and all test results are larger than DDW. The hydraulic conductivity is more sensitive to lower valence ions. It is also obvious that the test results converge to a much small range when concentration increases to 1.0 mol/L.

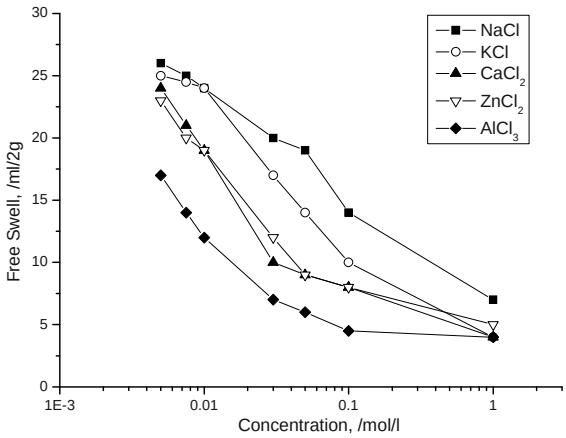

Fig. 3 Influence of concentration on bentonite's free swell

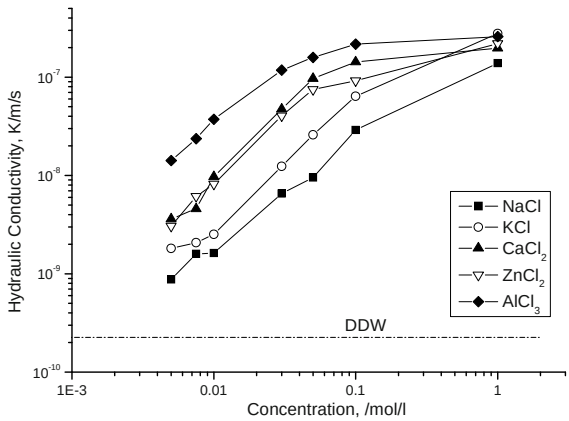

Fig. 4 Influence of concentration on GCL's hydraulic conductivity

Influence of Hydrated Ionic Radius

Influence on free swell feature

The hydrated ionic radius increase along with valence, for Na^+, K^+, Ca^{2+}, Zn^{2+}, Al^{3+}, the radius is 0.45 nm, 0.3 nm, 0.6 nm, 0.6 nm, 0.9 nm, respectively. The variance between Na^+ and K^+ will have effect on the test results. Free swell characteristic of bentonite is shown in Fig. 5.

The trend that free swell volume of bentonite decreases with the increase of hydrated ionic radius is similar for all tests excluding K^+ solution. The radii of Ca^{2+} and Zn^{2+} are equal so that the test results of $CaCl_2$ and $ZnCl_2$ solution with same concentration are very close, and even the same when concentration is 0.03 mol/L and 0.1 mol/L. Comparing the results of Na^+ and K^+, The free swell volume of bentonite increases along with hydration ionic radius. This phenomenon could be attributed to the permeant hydration of monovalent ionic. When permeant hydration happens, hydrated ions take relatively large space among structural layers of bentonite. Increasing the hydrated ion radius could result larger space, so the free swell volume becomes higher.

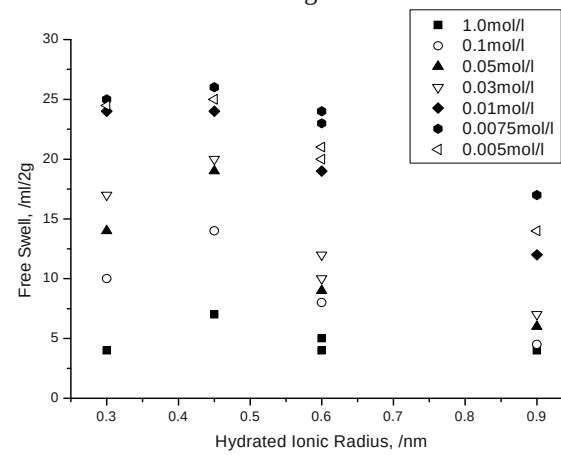

Fig. 5 Influences of hydrated ionic radius on bentonite free swell

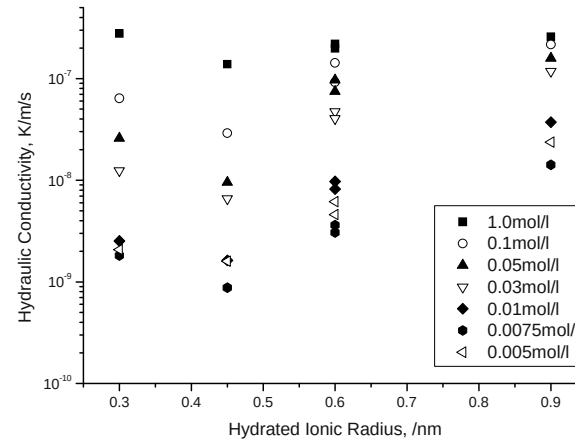

Fig. 6 Influences of hydrated Ionic radius on GCL hydraulic conductivity

Influence on hydraulic conductivity

Influence of hydrated ionic radius on hydraulic conductivity of GCL is shown in Fig. 6. Observation from the figure indicates that the hydraulic conductivity of GCL generally increases along with hydrated ionic radius, but the hydraulic conductivity of GCL with NaCl solution is smaller than that with KCl solution, though Na^+ radius is little larger than K^+ radius.

ANALYSIS ON SWELLING AND PERMEABILITY OF GCL

From the test results and discussions above, it is demonstrated the following rules: (1) The characteristics of solution, which include cation valence, ionic concentration and hydrated ionic radius, have great synthetically effect on free swell performance and hydraulic conductivity of GCL. (2) The hydraulic conductivity of GCL has contrary relationship with free swell characteristic of bentonite. For example, the hydraulic conductivity of GCL becomes larger, but the free swell amount of bentonite gets smaller with the increase of ionic radius.

According to the subsection hydration theory of bentonite proposed by Norrish and Quirk (1954), the process of hydration is divided into crystalline hydration and permeant hydration. When bentonite associated with water, the crystalline hydration happens immediately. Bound water of several numberator heights is produced on the structural layer surface due to electrostatic attraction. Permeant hydration happens just after crystalline hydration, and it would happen only when there is monovalent cation adsorbed on bentonite. On the contrary, when there is multivalent cation, permeant hydration could not happen. This procedure gets much more water absorbed on bentonite so that there is larger space between structural layers, which will induce larger swelling macroscopically. The above statement might explain the phenomenon that free swell volume of bentonite is the largest when tested with monovalent ionic solutions. The extent of permeant hydration is also influenced significantly by concentration. When hydration gets equilibrium, the number of water molecule layers absorbed among structural layers is anti-proportional to ionic concentration. This agrees the test results very well.

The bound water absorbed among structural layers of bentonite increases free swell volume as well as fills in the interspace of grain. This situation can decrease the hydraulic conductivity because the permeant path becomes twist.

CONCLUSIONS

The following conclusions could be drawn from the present study.

Free swelling of bentonite and hydraulic conductivity of GCL are influenced by several characteristics of solutions. When concentration reaches 1.0mol/L, the influence of cation valence and hydrated ion radius on free swelling and hydraulic conductivity is negligible.

The hydraulic conductivity of GCL is closely related to free swell volume of bentonite. It can be concluded that the hydraulic conductivity of GCL decreases with the increase of the free swell volume of bentonite.

The influence of cation valence, concentration and hydrated ionic radius on free swelling and hydraulic conductivity can be interpreted using the subsection hydration theory of bentonite combined with basic hydraulic mechanics.

REFERENCES

American Society for Testing and Materials (ASTM). D5890(2002) Standard test method for swell index of clay mineral component of geosynthetic clay liners. Philadelphia

American Society for Testing and Materials (ASTM). D6766(2002) Standard test method for evaluation of hydraulic properties of geosynthetic clay liners permeated with potentially incompatible liquids. Philadelphia

LaGatta M D, Boardman BT, Cooley BH et al. (1997) Geosynthetic clay lines subjected to differential settlement. Journal of Geotechnical and Geoenvironmental Engineering 123(5):402-410

Lake CK, Rowe RK (2000) Diffusion of sodium and chloride through geosynthetic clay liners. Geotextiles and Geomembranes 18:103-131

Li X (2005) Research on Anti-Seepage Characteristic of GCL and Liner System in Landfill. M.A. Thesis. Hohai University, Nanjing

Lin L C, Benson CH (2000) Effect of wet-dry cycling on swelling and hydraulic conductivity of GCLs. Journal of Geotechnical and Geoenvironmental Engineering 126(1):40-49

Norrish K, Quirk J (1954) Crystalline swelling of montmorillonites, use of electrolytes to control swelling. Nature 173:255-257

Petrov RJ, Rowe RK, Quigley RM (1997) Selected factors influencing GCL hydraulic conductivity. Journal of Geotechnical and Geoenvironmental Engineering 123(8):683-695

Petrov RJ, Rowe RK (1997) Geosynthetic clay liner (GCL)-chemical compatibility by hydraulic conductivity testing and factors impacting its performance. Canadian Geotechnical Journal 34:863-885

Ruhl JL, Daniel DE (1997) Geosynthetic clay liners permeated with chemical solutions and leachates. Journal of Geotechnical and Geoenvironmental Engineering 123(4):369-381

Shackelford CD, Benson CH, Katsumi T et al. (2000) Evaluating the hydraulic conductivity of GCLs permeated with non-standard liquids. Geotextiles and Geomembranes 18:133-161

Proceedings of the 4th Asian Regional Conference on Geosynthetics
June 17 - 20, 2008 Shanghai, China

POST-CONSTRUCTION TIME HISTORY OF TENSILE FORCE IN GEOGRID ARRANGED IN A FULL-SCALE HIGH WALL

W. Kongkitkul[1], D. Hirakawa[2], T. Sugimoto[3], S. Kawahata[4], T. Yoshida[5], S. Ito[6] and F. Tatsuoka[7]

ABSTRACT: To confirm a very low possibility of tensile rupture until the end of specified life time of polymer geogrids arranged in a full-scale reinforced soil retaining wall (21 m-high with a slope of 1:0.3 in V:H) constructed to support a taxi way of an airport, time histories of tensile force in the reinforcement were estimated based on those of measured tensile strain in the reinforcements in the wall. To this end, tensile tests were performed on the geogrids and their elasto-viscoplastic properties were evaluated. A constitutive model was developed based on the test results. The model was validated by that the model can accurately predict the tensile load-strain-time behaviour of the geogrids when subjected to arbitrary loading histories. The time histories of tensile force in the geogrids in the wall estimated from the measured tensile strains based on the model indicate that, even in the most severe case among those analysed, the tensile force will increase with time to a very limited extent, towards a value significantly lower than the tensile rupture strength at the end of life time. This result indicates that eventual creep rupture of the geogrids in the wall is not likely unless significant degradation takes place.

KEYWORDS: creep, geogrid, full-scale behaviour, model simulation, rate effect, tall wall

INTRODUCTION

Shizuoka prefecture is located about 150km southwest of Tokyo. By this distance, it was considered in the past that it is sufficient for passengers from Shizuoka to come to Tokyo by on-land transportation and then travel by plane domestically or internationally from Haneda and Narita airports in the Tokyo area. However, the number of passengers who have to travel by the above-mentioned method has largely increased recently. Therefore, a local airport becomes realistic and now under construction, since 2004, in a mountain area near the city of Shizuoka. In this construction, soil-reinforcing technologies for retaining walls, tiered-walls and slopes were used at many locations of the airport (Fujita et al. 2007; Takagi et al. 2007). As the most important structures, two high geogrid-reinforced soil retaining walls were constructed. One is to support a taxi way, having a height of 21 m with a slope of 1:0.3 in V:H (Fujinami et al. 2007; Fig. 1). This is one of the tallest geogrid-reinforced soil retaining walls ever constructed in Japan.

Due to the wall is very tall and will support a crucial structure (i.e., a taxi way), only selected good-quality backfill was used and very well-compacted. The average degree of compaction of the backfill reached about 98 % (Takagi et al. 2007). Furthermore, geogrid layer Nos. 3, 13 and 23 (Fig. 1) were selected to be equipped with electric-resistant strain gauges (Fig. 2) to obtain time histories as well as length-wise distributions of tensile strain during construction stage and, more importantly, for more than one year after the wall completion so far. In this study, the time histories of tensile force in these geogrid layers were estimated from the measured time histories of tensile strain not only until now but also by the end of life time of typical civil engineering structures (i.e., 50 years). This estimation was made based on a non-linear three-component model that can properly describe the elasto-viscoplastic properties of polymer geogrid. It is shown below that, even in the most severe case among those analysed, the tensile force mobilised by the end of typical life time (50 years) is significantly lower than the ultimate tensile strength and the tensile force even decreases with time in the other cases. These results indicate that the possibility of geogrid creep rupture is very low.

[1] Postdoctoral Fellow, Tokyo University of Science, JAPAN. Email: warat@rs.noda.tus.ac.jp
[2] Assistant Professor, ditto, JAPAN. Email: dhirakaw@rs.noda.tus.ac.jp
[3] Engineer, Shizuoka Prefecture, JAPAN
[4] Engineer, Nippon-koei Co., Ltd., JAPAN
[5] Supervisory Research Engineer, Kajima Corporation, JAPAN. Email: yt@kajima.com
[6] Engineer, Maeda-kosen Co., Ltd., JAPAN
[7] Professor, Tokyo University of Science, JAPAN. Email: tatsuoka@rs.noda.tus.ac.jp

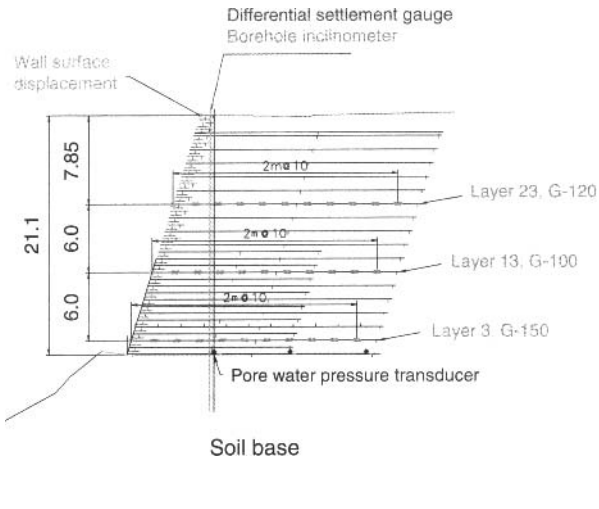

Fig. 1 Locations of geogrid layers equipped with electric-resistant strain gauges in a full-scale high wall; unit in m (after Fujinami et al. 2007)

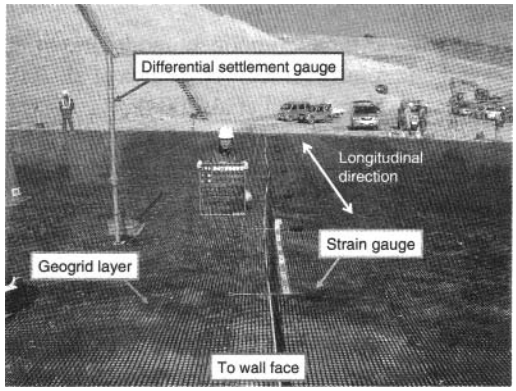

Fig. 2 Installation of electric-resistant strain gauges: the connection cables are extended toward the wall face for data acquisition (after Fujinami et al. 2007)

GEOGRIDS AND TEST RESULTS

As indicated in Fig. 1, geogrid layer Nos. 3, 13 and 23, installed with electric-resistant strain gauges, consist of types G-150, G-100 and G-120, respectively. These geogrids are made of Aramid fibre, having different densities of the fibre and therefore different tensile ultimate strengths, and coated with HDPE. Table 1 summarises their ultimate tensile strengths at a strain rate of 1.0 %/min obtained by using 22.4 cm-wide specimens, reported by the manufacturer.

Table 1 Ultimate tensile strengths of the geogrids

Geogrids' name	Layer No. (see Fig. 1)	Ultimate tensile strength (kN/m)
G-100	13	95
G-120	23	112
G-150	3	140

Figs. 3(a) and (b) respectively show the tensile load-strain ($T-\varepsilon$) relations and time histories of tensile strain from unconventional load-controlled tensile loading tests performed following the methods reported by Hirakawa et al. (2003) and Kongkitkul et al. (2004). That is, monotonic loading (ML) was performed at a load rate of 0.0018 kN/m/min and two 12-hour sustained loading were performed at tensile load (T) equal to 6.5 and 13 kN/m. Creep deformation is noticeable even at these low tensile load levels, far below the respective ultimate tensile strengths (Table 1). The simulations presented in these figures are explained later.

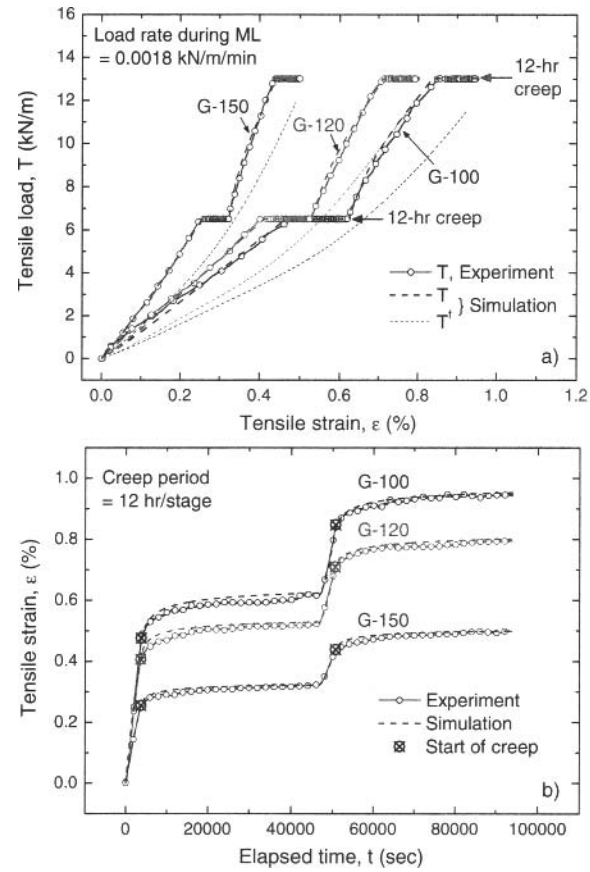

Fig. 3 In-air tensile test results and model simulations: (a) tensile load-strain relations; and (b) time histories of tensile strain

MEASURED GEOGRID TENSILE STRAINS IN THE WALL

Figs. 4(a),(b), (c) show time histories of the mobilised tensile strain for geogrid layer Nos. 3 (G-150), 13 (G-100) and 23 (G-120), respectively, in the wall. The origin of elapsed time was defined at the moment when the respective layers were placed. The general trend is that the increase in the tensile strains at such a high rate as during wall construction stopped when the wall was completed. At some locations in the respective geogrid layers, the geogrid tensile strains even started decreasing

with time. This trend of behaviour is similar to the one observed by performing plane strain compression (PSC) tests on geosynthetic-reinforced sand specimens as reported by Kongkitkul et al. (2007b). Furthermore, these observed strains are very low. The tensile loads obtained by substituting these strain values into the measured load-strain relations shown in Fig. 3(a) are substantially lower than the respective tensile rupture strengths listed in Table 1.

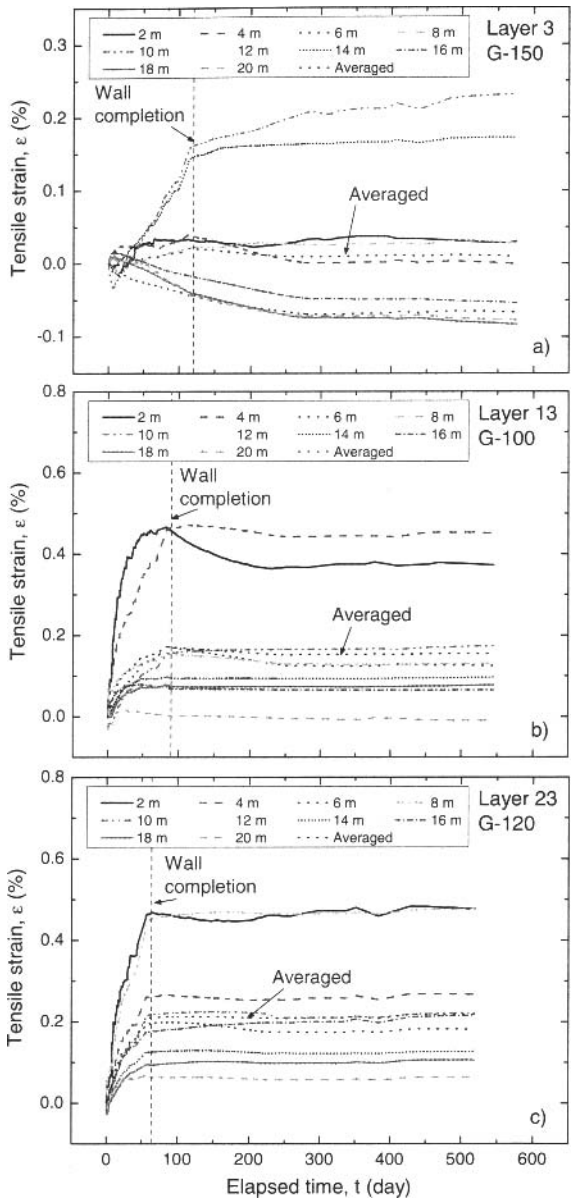

Fig. 4 Time histories of individual and average tensile strains of geogrids arranged in the wall at layer Nos.: (a) 3 (G-150); (b) 13 (G-100); and (c) 23 (G-120); the legends indicate the distances back from wall face

MODELLING OF GEOGRID PROPERTIES

Hirakawa et al. (2003) and Kongkitkul et al. (2004) showed that polymer geogrids are essentially elasto-viscoplastic materials and their load-strain behaviour can be properly described by the three-component model (Fig. 5): i.e., tensile load (T) is obtained by adding the viscous component (T^v) to the inviscid component (T^f) at the same irreversible strain (ε^{ir}) while the tensile strain rate ($\dot{\varepsilon}$) by adding the elastic component ($\dot{\varepsilon}^e$) to the irreversible component ($\dot{\varepsilon}^{ir}$) at the same T. They also reported the geogrid made of Aramid fibre exhibited Isotach viscosity, for which T^v is obtained as:

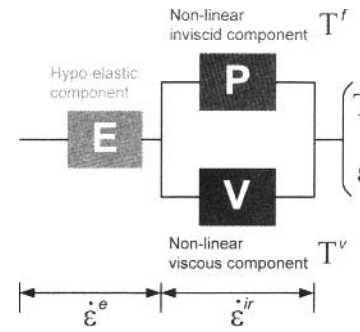

Fig. 5 Non-linear three-component model modified for geosynthetic reinforcement (Hirakawa et al. 2003; Kongkitkul et al. 2004)

$$T^v\left(\varepsilon^{ir},\dot{\varepsilon}^{ir}\right)=T^f\left(\varepsilon^{ir}\right)\cdot g_v\left(\dot{\varepsilon}^{ir}\right) \tag{1a}$$

$$g_v\left(\dot{\varepsilon}^{ir}\right)=\alpha^*\cdot\left(\dot{\varepsilon}^{ir}/\dot{\varepsilon}_0^{ir}\right)^{1+b^*} \tag{1b}$$

where $g_v\left(\dot{\varepsilon}^{ir}\right)$ is the viscosity function, a highly non-linear function of ε^{ir}; and α^*, b^* and $\dot{\varepsilon}_0^{ir}$ are constants. Eq. 1b was proposed by Di Benedetto et al. (1999) for simulation of creep deformation of sand and found relevant by Kongkitkul et al. (2007a) for the simulation of creep behaviour of geosynthetic reinforcements after the strain rate becomes extremely low. By back-analysis of the test results based on the elasto-viscoplastic model of Aramid fibre that was determined for short-term creep behaviour (Hirakawa et al, 2003), α^*= 0.18, b^*=-0.65 and $\dot{\varepsilon}_0^{ir}$ = 10^{-6} %/s were found equally relevant for all the studied geogrids. The elastic property determined by this previous study was also used in the present study. The $T^f-\varepsilon$ relations of the geogrids (i.e., the reference relations), which are the $T^f-\varepsilon$ relations at $\dot{\varepsilon}^{ir}=0$, were determined as shown in Fig. 3(a). Not only tensile load-strain relations (Fig 3(a)), but also the time histories of creep tensile strain (Fig. 3(b)) can be simulated very well by the model using these parameters.

GEOGRID STRAIN RATES IN THE WALL

The tensile strains mobilised at the completion of wall were largest at 10 m, 4 m and 8 m back from the wall face respectively in geogrid layer Nos. 3, 13 and 23. The time histories of these tensile strains as well as those of averaged tensile strain in the respective layers were analysed by the three-component model (Fig. 5) to obtain the time histories of tensile loads.

Fig. 6 shows the time history of tensile strain increment, defined zero at the wall completion, at 10 m back from the wall face in geogrid layer No. 3 (G-150), which is typical of those that exhibited an increase with time shown in Fig. 4. Due to a large scatter in the data, a smooth curve was fitted by the following exponential form, Eq. 2a, as shown in Fig. 6

$$\Delta\varepsilon = A_1 \cdot \left(1 - e^{-\Delta t / t_1}\right) + A_2 \cdot \left(1 - e^{-\Delta t / t_2}\right) \qquad (2a)$$

$$\Delta\varepsilon' = \frac{A_1 \cdot e^{-\Delta t / t_1}}{t_1} + \frac{A_2 \cdot e^{-\Delta t / t_2}}{t_2} \qquad (2b)$$

where A_1, A_2, t_1 and t_2 are constants. Eq. 2b is the differentiation of Eq. 2a. Eq. 2a was also used to fit the data of the selected locations as well as the averaged ones of the respective layers, as above-mentioned.

Figs. 7(a) and (b) show the time histories of tensile strain rate obtained from Eq. 2b (in full-log plot) respectively for the selected locations and the averaged ones of the respective layers. Note that, at 4 m back from the wall face in geogrid layer No. 13 and the averaged values in geogrid layer Nos. 3 and 13, the tensile strain rates are negative, as the respective geogrid strains decreased with time after the wall completion. In all the cases, the absolute value of geogrid strain rate decreases substantially with time. In the analysis shown below, the respective time histories of tensile strain were extended based on Eq. 2b to the end of design life for typical civil engineering structures (i.e., 50 years).

ESTIMATION OF GEOGRID TENSILE LOADS

The time histories of tensile load of the geogrids arranged in the wall were estimated by the three-component model from the fitted time histories of tensile strain rate extrapolated to 50 years. Figs. 8(a), (b) and (c) show the relationships between the estimated tensile load and the measured tensile strain before and after the wall completion at 10 m, 4 m and 8 m back from the wall face respectively in geogrid layer Nos. 3, 13 and 23. Figs. 9(a), (b) and (c) show similar relations obtained from the

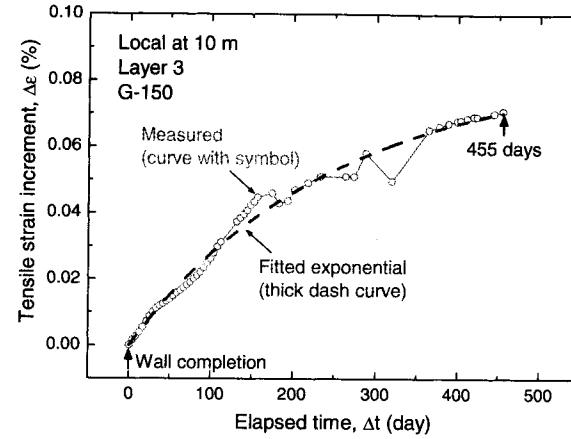

Fig. 6 Time history of tensile strain increment of G-150 geogrid measured at 10 m back from the wall face in layer No. 3 and its fitted relation

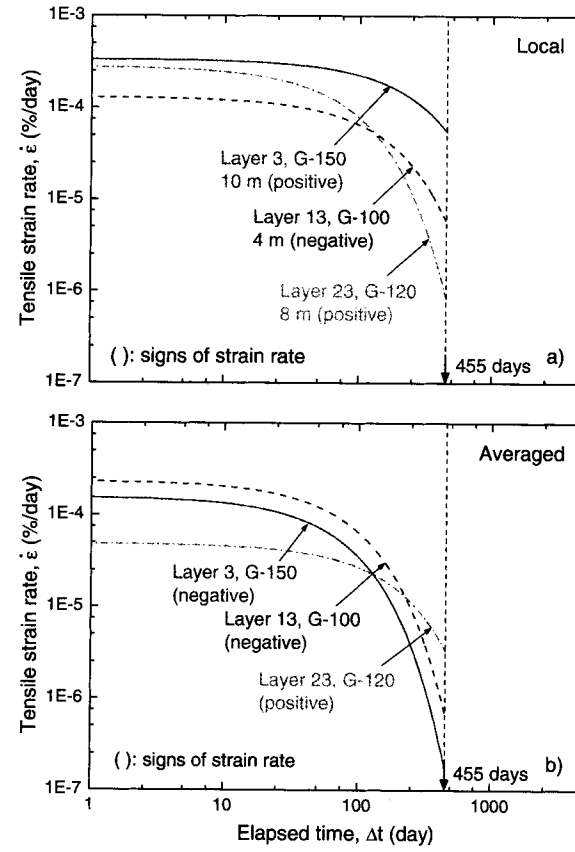

Fig. 7 Geogrid strain rate-elapsed time relations from the fitted time histories of tensile strain increment of geogrids arranged in the wall: a) local at the selected locations; and b) average in the respective layers

time histories of averaged tensile strain rate. The simulated $T - \varepsilon$ relations from the origin (0, 0), when the respective geogrid layers were arranged, until the wall completion presented in Figs. (8) and (9), were obtained from the measured time histories of tensile strain until the wall completion. The dotted curves represent the relations when ML had continued at the strain rate at the wall completion. The simulated relations after the wall

completion were obtained based on the respective time histories of tensile strain rate extended to 50 years. When the irreversible strain rate, $\dot{\varepsilon}^{ir}$, becomes negative via a neutral state (where $\dot{\varepsilon}^{ir} = 0$) from the loading condition (where $\dot{\varepsilon}^{ir} > 0$) in the simulation of the post-construction behaviour, the tensile load-strain behaviour enters an unloading branch (where $\dot{\varepsilon}^{ir} < 0$). Simulations under the unloading condition were made based on the respective reference relations under the unloading condition, which were determined following the method shown in Kongkitkul et al. (2004).

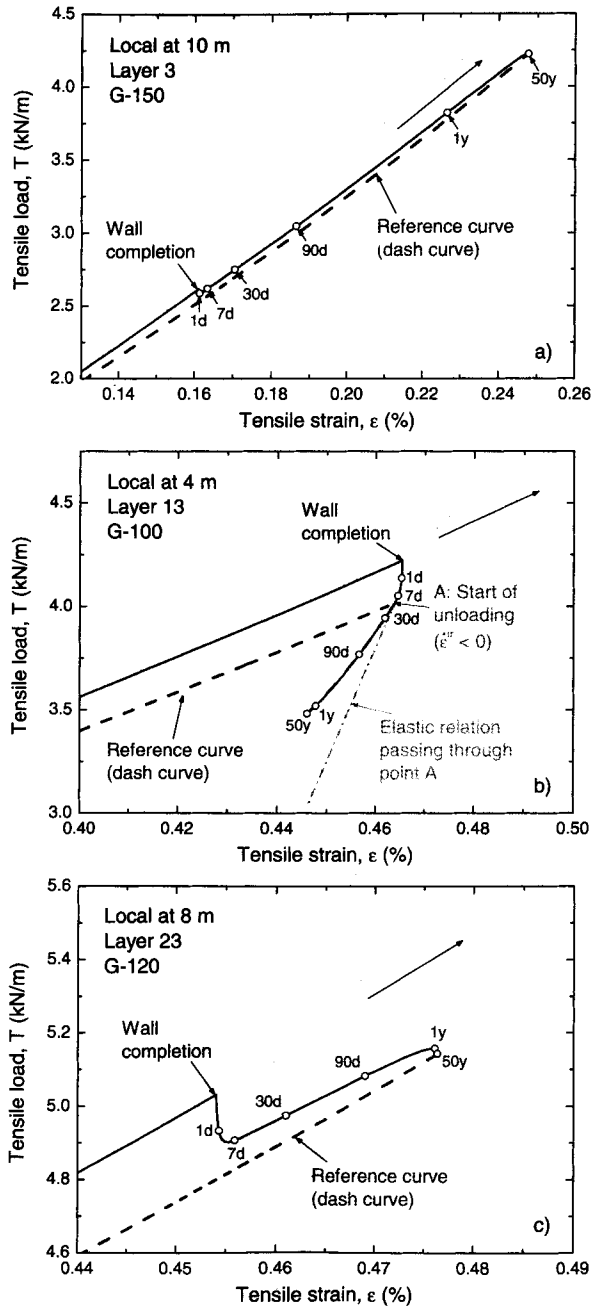

Fig. 8 Tensile load-strain relations of geogrid at the selected locations in the wall, predicted for 50-year service, in layer Nos.: (a) 3 (G-150); (b) 13 (G-100); and (c) 23 (G-120)

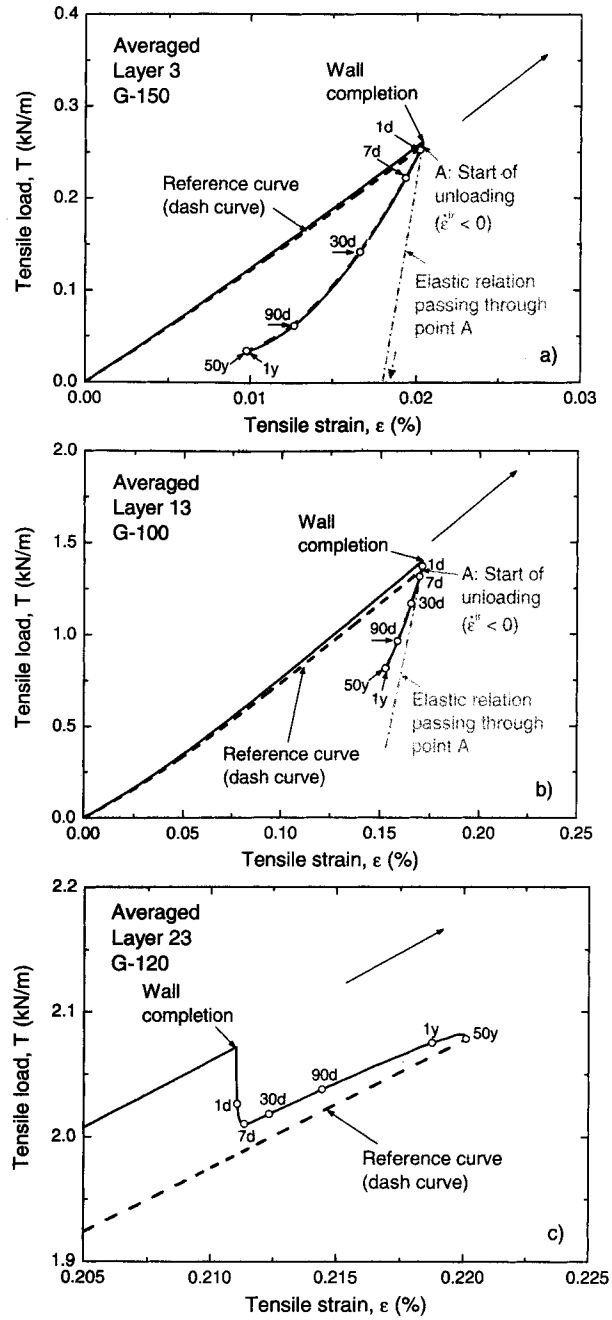

Fig. 9 Tensile load-strain relations of geogrid arranged in the wall averaged for all the locations, predicted for 50-year service, in layer Nos.: (a) 3 (G-150); (b) 13 (G-100); and (c) 23 (G-120)

Fig. 8(a) shows the $T-\varepsilon$ relation for the most severe case among those analysed, in which the tensile strain continues increasing with time (see Fig. 6), resulting in a continuous increase in the geogrid tensile load with time. Yet, the predicted tensile load after 50 years is only about 4.25 kN/m, substantially lower than the ultimate tensile strength. In Figs. 8(c) and 9c), the tensile strain rate increases with time similar to the case in Fig. 8(a) but it is at a large deceleration. As a result, the $T-\varepsilon$ relations exhibit firstly a sudden decrease, which is followed by a gradual increase in the tensile load with

time. Even at 50 years, the estimated tensile load is only slightly higher than the value at the wall completion. Fig. 10 shows the time history of tensile load estimated based on the measured tensile strain, corresponding to Fig. 9(c). In this figure, the trends of behaviour described above can be confirmed. It is also predicted that the tensile load is kept nearly constant after the elapsed time becomes about two years.

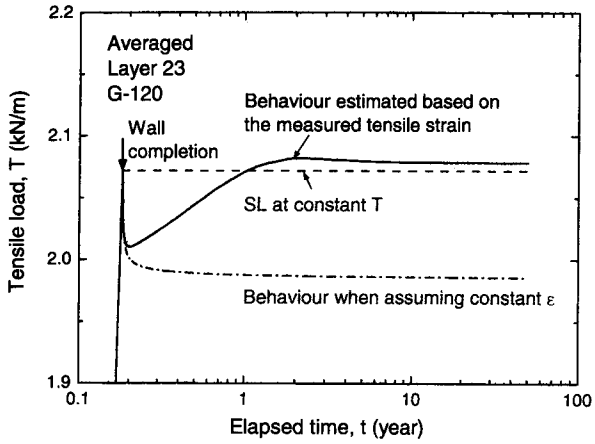

Fig. 10 Estimated time histories of tensile load of geogrid based on averaged strain in layer No. 23 (Fig. 9(c)) and the behaviours when assuming constant T and ε

On the other hand, in Figs. 8(b), 9(a) and 9(b), the tensile load decreases with time due to consistently negative strain rates during service (Fig. 7). In these cases, the tensile load decreases firstly under the loading condition (where $\dot{\varepsilon}^{ir} > 0$), then under the unloading condition (where $\dot{\varepsilon}^{ir} < 0$). As also seen from Figs. 8(b), 9(a) and 9(b) , when estimated assuming purely elastic response under the unloading condition in the simulation, the decrease in the tensile load is largely over-predicted.

Summarising the above, it is very likely that the geogrid tensile loads would not reach values close to the respective ultimate tensile strengths by the end of design life. In general, the geogrid tensile loads would increase to a very limited extent or even decrease during service. This trend of behaviour is due to the viscous properties of the geogrids as well as the backfill. The reduction of tensile strains in the geogrids with time is due likely to compressive creep strains in the horizontal direction of the backfill caused by the tensile force in the reinforcement. Therefore, the possibility of tensile creep rupture of geogrids arranged in this wall by the end of design life is very low. It should also be the case with those constructed using well-controlled backfill and following construction procedures as the wall described in this paper.

CONCLUSIONS

The analysis by the three-component model of the measured time histories of tensile strain of geogrids arranged in a tall wall supporting a taxi way of an airport indicated that the geogrid tensile loads would never increase to values close to the respective ultimate tensile strengths by the end of design life (i.e., 50 years). Therefore, the possibility of tensile creep rupture is very low.

REFERENCES

Di Benedetto H, Sauzéat C, Geoffroy H (1999) Modelling viscous effects for sand and behaviour in the small strain domain, Proc. 2nd Int. Symp. on Pre-failure Deformation Characteristics of Geomaterials, IS Torino 2: 1357-1367

Fujinami T, Sugimoto T, Nakamura Y, Kawahata S, Funuda H, Yoshida T, Ito M, Yoshidaatta N (2007) Application of reinforced soil wall to high embankment in Mt. Fuji Shizuoka Airport, Part III: Field observation, Proc. of the 42nd Japan National Conf. on Geotech. Eng., Nagoya 804: 1603-1604 (in Japanese)

Fujita Y, Sugimoto T, Koha T, Tsuda M (2007) Application of reinforced soil wall to high embankment in Mt. Fuji Shizuoka Airport, Part I: Design and planning, Proc. of the 42nd Japan National Conf. on Geotech. Eng., Nagoya 802: 1599-1600 (in Japanese)

Hirakawa D, Kongkitkul W, Tatsuoka F, Uchimura T (2003) Time-dependent stress-strain behaviour due to viscous properties of geogrid reinforcement, Geosynthetics Int 10(6): 176-199

Kongkitkul W, Hirakawa D, Tatsuoka F, Uchimura T (2004) Viscous deformation of geosynthetic reinforcement under cyclic loading conditions and its model simulation, Geosynthetics Int 11(2): 73-99

Kongkitkul W, Hirakawa D, Tatsuoka F (2007a) Viscous behaviour of geogrids; experiment and simulations, Soils and Foundations 47(2): 265-283

Kongkitkul W, Kanemaru T, Hirakawa D, Tatsuoka F (2007b) Relaxation of tensile load mobilised in geosynthetic reinforcement arranged in sand. Proc. of the 13th Asian Reg. Conf. on Soil Mech. and Geotech. Eng., Kolkata

Takagi H, Sugimoto T, Nakamura Y, Kawahata S, Funada H, Yoshida T, Ito S, Tatta N (2007) Application of reinforced soil wall to high embankment in Mt. Fuji Shizuoka Airport, Part II: Earthwork, Proc. of the 42nd Japan National Conf. on Geotech. Eng., Nagoya, 803: 1601-1602 (in Japanese)

Proceedings of the 4th Asian Regional Conference on Geosynthetics
June 17 - 20, 2008 Shanghai, China

EXPERIMENTAL STUDY ON CREEP PROPERTIES OF PLASTIC GEOGRID UNDER LOW TEMPERATURE

E.L. Wang[1], X.Y. Xu[2], B. Zhang[3], H. Zhong[4], Z.K. Gao[5] and J.D. Chang[6]

ABSTRACT: The creep properties of geogrid influence greatly the long-term service behavior of geogrid reinforced retaining structures. The comparing tests on the creep properties of plastic geogrid were carried out in the lab, with various load and temperature combinations. Based on the comprehensive comparison of the test results, the creep properties of plastic geogrid under low temperature and the changing characteristics of the load strain isochronous curve were studied ~~of~~, and the influence of the freeze-thaw cycling on the plastic geogrid creep properties was described.

KEYWORDS: plastic geogrid, creep test, low-temperature, creep properties

INTRODUCTION

The geogrid has network structure, after being buried in the earth, the soil can embed into the grid of grille, together with the friction between the soil and the grid surface and the passive hindrance function of the node when it is being tensioned, which restrain the lateral displacement of soil particles. In this way, the geogrid and soil together compose a compound material system, which greatly increases the stability of the soil body, in other words it takes the role of strengthening the ground.

Creep is a very important property of plastic geogrid, it refers to the phenomenon that under the invariable tension load effect, the strain grows along with the time. When the plastic geogrid is used in the reinforced soil structure, the allowable tensile strength of plastic geogrid is determined by many factors, such as creep, the destruction of chemical agents and the mechanical damage in paving and biological destruction. Above all things, the tensile strength reduction coefficient caused by creep is larger than others. For example, Wang found that under the effect of 40% load level, the biaxial oriented polypropylene geogrid was tensile failure after 1,196 h, with the strain up to 62% (Wang 1994). The creep properties of plastic geogrid is concerned with the raw material natures, the structural pattern of the product and the tensile load range, and it is also influenced by the environment, pressure and temperature. In cold regions, the limiting temperature in winter is lower than -20℃, and in summer over +20℃. Therefore, the reinforced material of reinforced soil structure is always be in negative temperature working condition in lengthy winter. However, the creep properties of plastic geogrid under low temperature (between -20℃ and 0℃) and the effect of freeze-thaw cycling on the stabilized reinforcement material are still not reported now, except for the creep tests of plastic geogrid under high temperature. In this paper the creep properties of plastic geogrid under low temperature was studied.

SUMMARY

The measurement of the tensile strength of plastic geogrid takes National Standard of People's Republic of China (GB/T 17689-1999 Geosynthetics-Plastic Geogrid) as reference. The creep test is carried out referring to the standard of ISO 13431:1999. Geotextiles and geotextile-related products — Determination of tensile creep and creep rupture behaviour.

[1] Senior Engineer, Heilongjiang of Seasonal Frozen Soil Region Engineering Frozen Soil Key Laboratory, Harbin 150080, CHINA; College of Civil Engineering, Harbin Institute of Technology, Harbin 150090, CHINA, Email: hljskywel@163.com
[2] Professor, College of Civil Engineering, Harbin Institute of Technology, Harbin 150090, CHINA, Email: xxyan@hit.edu.cn
[3] Professor of Engineering, Heilongjiang of Seasonal Frozen Soil Region Engineering Frozen Soil Key Laboratory, Harbin 150080, CHINA, Email: hljzhb@126.com
[4] Assistant Engineer, Heilongjiang of Seasonal Frozen Soil Region Engineering Frozen Soil Key Laboratory, Harbin 150080, CHINA, Email: zhonghua131@126.com
[5] Assistant Engineer, Heilongjiang of Seasonal Frozen Soil Region Engineering Frozen Soil Key Laboratory, Harbin 150080, CHINA, Email: jackie607@163.com
[6] Assistant Engineer, Heilongjiang of Seasonal Frozen Soil Region Engineering Frozen Soil Key Laboratory, Harbin 150080, CHINA, Email: king1903@163.com

Test Instruments

The plastic geogrid creep test adopts the homemade creep facility to survey and evaluate (Fig. 1). The corresponding testing load was applied by load-on system through lever system.

Fig. 1 Creep test facility

Test Materials

This test chose the uniaxial oriented plastic geogrid with the type of TGDG25 produced by certain factory in Shandong province. Table 1 shows its main technological and mechanics parameters.

Sample Preparation

The length of the sample includes 6 nodes (five sections), and its width includes 5 nodes (five longitudinal ribs). During the test, a large gauge length of 1,000 mm was taken. And the deformation of geogrid being tested was measured with steel rule, of which the accuracy is millimeter, so the precision is only 0.1%. The gauge line is 25mm away from the clamp, so as to avoid the influence of the gripping effect on deformation.

Gripping Method of Samples

The up and down gripper are 2 steel plates, the internal of which is located with the anti-skid groove and is tightened by bolt to grip the sample. During testing, the sample must keep balanced gripping, in order to avoid the stress asymmetry destruction of the sample after on-loading, and to prevent the sample skid in the jaw of gripper. One side of the gripper is fixed at the foundation plate and the other side is hanging on the lever loading system.

Test Environment

The low-temperature test is carried out at special low-temperature laboratory. The temperature range controlled is between -35℃ and +25℃, and the temperature control precision is ±1℃. Each time, 3 groups of samples were put on the creep tester and control the room temperature and humidity level, it should be sheltered from the direct sunlight and avoid aging by the ultraviolet irrigation.

TESTING PLAN AND PROCESS

Testing Plan

According to the correlation method of geosynthetics testing and the status of our lab, the load level that was chosen is 20%, 40% and 60% of tensile strength, respectively, and the environmental temperature is 20℃, 10℃, 0℃ and -20℃, respectively. Based on the analyses of the former testing results, it can be concluded that the effect of freeze-thaw cycling on the creep properties of geogrid is small. So the load level of creep test under the freeze-thaw cycling that was chosen is 5%, 10% and 20% of tensile strength, respectively. And then the creep test was carried out in 20℃, and after the deformation becoming stable, it was carried out under the freeze-thaw cycling by 10 times. The temperature range of freeze-thaw cycling is between -20℃ and 20℃.

Table 1 Main physical and mechanics parameters of plastic geogrid

Type	TGDG25			
Performance Parameters	Physical Parameters		Mechanics Parameters	
	Rib length (mm)	222	Breaking load (kN/m)	36.47
	Rib width (mm)	5	Elongation at rupture (%)	9.9
	Rib thickness (mm)	0.4	bearing capacity at 2% strain (kN/m)	10.98
	Node length (mm)	18.2	bearing capacity at 5% strain (kN/m)	23.43
	Node width (mm)	15	Sample width (mm)	90/ (5 rib)
	Node thickness (mm)	1.5		

Conditioning Treatment

Before the test, the samples should be put into laboratory and keep for 24 h, of which the humidity level is 65±2% and temperature is 20±2℃.

Loading and Strain Measurement

Weights were taken as tension load hanging on the lever system, and they were loaded at the same time.

During the experiment, the measuring period is gradually changed from short to long. The measure was taken at 0, 1 min, 8 min, 12 min, 30 min, 1 h, 2 h, 4 h, 8 h, 12 h, 24 h, and after this the measure was taken every 24 h interval until 1,000 h. The strain value is equal to the ratio of the elongation value between two gauge line and the original length of the sample.

TESTING RESULTS

Creep Regulations

The strain-time curve is the most important result of creep test. Fig. 2 shows the creep process curves under four temperature conditions and different load ranges.

Fig. 2 shows that under all the temperature conditions, the slope of strain-time curves of these three different load level increases with the increase of load. And it can be concluded that the creep properties of TGDG25

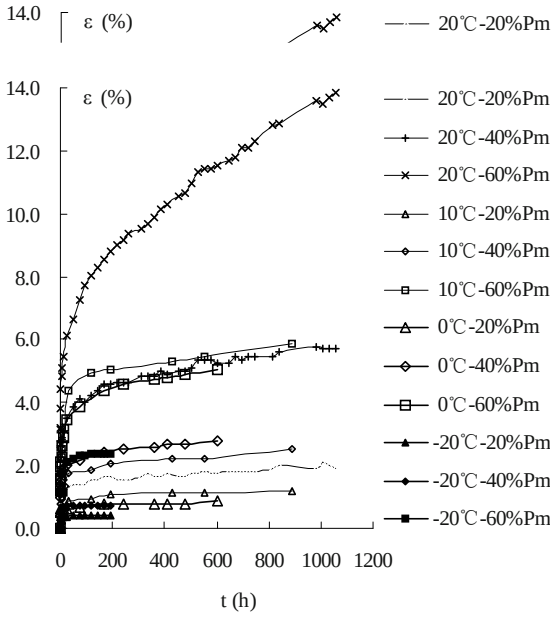

Fig. 2 Creep curves of TGDG25 plastic geogrid under different temperature conditions and different load levels

curves are more distinct under the temperature condition of 20℃, creep curve with fairly low load level (20%P_m) is comparatively flat at the beginning of loading, and then the strain value is enlarged quickly along with the increase of load, after a period of stabilization, it begins to deform again, but quickly it becomes stable.

The creep properties of polymer are influenced mainly by two important parameters.

The first parameter is glass transition temperature (T_g). It refers to the critical temperature of amorphous polymer changing from the glass state to high-elasticity state. The T_g of different polymer is different. For example, for PET, HDPE and PP the T_g is about 75℃, -80℃ and between 10 and 15℃, respectively. When the environmental temperature is lower than the T_g of polymer, the molecule of the non-crystal region in the polymer is at the freezing state, the molecular bond is difficult to be moved, so the creep property is low. Therefore the creep properties of polyester are far lower than polypropylene and polyethylene (Wang 2002).

The second parameter is stretching orientation. The stretching process of polymer can be divided into 3 stages. The first stage is elastic stage. When going through the yield point, enter into the second stage, the stress-strain curve is in a level. When the strain reaches a certain value, the stress grows along with strain. When entering into the third stage, the secondary creep is not obvious. Therefore, the polymer material should be stretched in place. What is called orientation is mean to the molecular bond oriented. In this condition, the polymer presents anisotropy. The intensity of the orientation direction is greatly increased.

The raw material of TGDG25 plastic geogrid is HDPE, the T_g of which is about -80℃. With the fall of environmental temperature, the molecular activity ability of the polymer non-crystal region is largely lowered, and the molecular bond is not likely to move, so comparatively large load is needed to change the oriented arrangement of molecular bond, that is why the influence of load on creep properties is more and more obvious with the lowering of temperature.

Fig. 3 shows the strain and temperature relation curves corresponding to the identical load and at the time of 1 min, 12 h and 1,000 h. Under the same load level, the strain value and temperature of 1min approximate linear relationship. However, the falling trend of 1,000 h curve is especially obvious from the temperature 20 ℃－10℃. It is clear that of the same load and at the same time period, the strain value is obviously reduced along with the fall of temperature, which shows that load has obvious influence on the plastic geogrid creep properties.

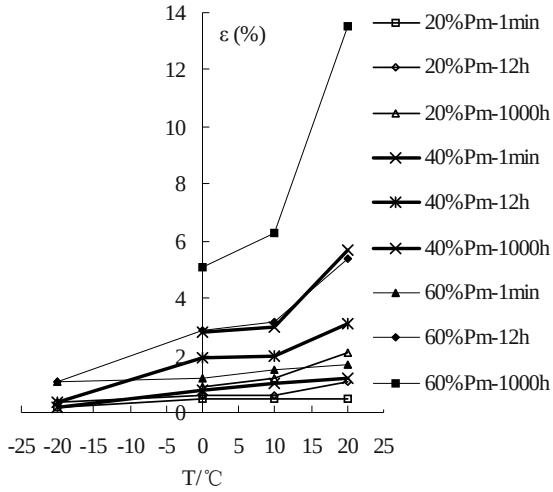

Fig. 3 The strain and temperature relation curves

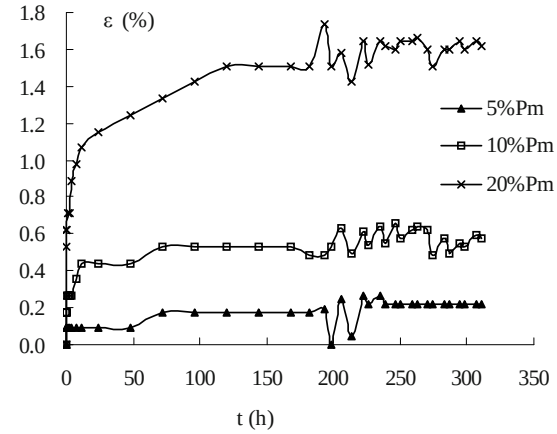

Fig. 4 Creep curves under freeze-thaw cycling conditions

Plastic Geogrid Creep Properties under Freeze-Thaw Cycling Conditions

At first, the creep test was carried out at the environment temperature of 20 ℃. After the deformation became stable, the creep tests were carried out under freeze-thaw cycling conditions, and the geogrid suffered 10 times freeze-thaw cycles. The loading level adopted is 5%, 10% and 20% of breaking load. Fig. 4 shows the creep process curve under different loading conditions.

Fig. 4 shows that at the temperature of 20℃, the creep curves of the plastic geogrid under fairly small load effect are accorded with the rules explained above. At 193 h, the creep curves with different loading level became stable basically. And then the temperature began to drop down. At 5%P_m load conditions, the creep of geogrid is very sensitive to the freeze-thaw cycling. During the first temperature fall period, the shrinking phenomenon is appeared. After two freeze-thaw cycles, the deformation became stable, the total strain value is slightly enlarged. At 10%P_m and 20%P_m load conditions, the creep of geogrid reacts slowly for freeze-thaw cycling. After one freeze-thaw cycling, the deformation grows up with different degrees at the temperature-rise period, and grows down at the temperature fall period. Finally, the stable values all have increased.

It is obvious that affected by freeze-thaw cycling, the further deformation is still going to be happen, though the creep have become stabilized under a certain load effect. Therefore, this should be considered in design and construction.

CONCLUSIONS

The creep properties of plastic geogrid under different temperatures are quite different. Under the condition of 20℃, when the ratio of elongation approach to 14% after 1,000 h, the deformation of 60% P_m load conditions still has no stable sign. However, under the condition of -20℃, only after 100 h, the deformation becomes stable and the ratio of elongation is less than 2.5%. Under low temperature conditions, the design value of plastic geogrid strength can be appropriately reduced, but the influence of freeze-thaw cycling on creep properties should be considered in design and construction.

REFERENCES

GB/T 17689-1999. National Standard of the People's Republic of China. Geosynthetics-Plastic Geogrid (GB/T 17689-1999)

ISO 13431:1999. Geotextiles and geotextile-related products—Determination of tensile creep and creep rupture behaviour. International Standard Organisation. Switzerland

Jiang XH, Chen JQ, Pang JY (2005) Test method for creep behavior of plastics geogrid. China Plastic 19 (3):87-89

Luan MT, Xiao CZ, Yang Q, Pei JJ (2005) Experimental study on creep properties and viscoelasticity constitutive relationship for geogrids. Rock and Soil Mechanics 26 (2):187-192

Wang Z (2002) The application research of geosynthetics at abroad. Hong Kong: Modern Knowledge Press

Wang Z (1994) The creep tests of geosynthetics. Chinese Journal Geotechnical Engineering 16 (6): 96-102

Yang GL (2001) Study on creep test of geosynthetic. Journal of China Coal Society 26 (2):132-136

Proceedings of the 4th Asian Regional Conference on Geosynthetics
June 17 - 20, 2008 Shanghai, China

THE USE OF BETA NUCLEATION TO IMPROVE THE PROPERTIES AND LOWER THE COST OF POLYPROPYLENE GEOGRIDS

P. Jacoby[1]

ABSTRACT: A unique masterbatch that can be used to produce extruded polypropylene sheet containing high levels of beta phase crystallinity is developed. When a perforated sheet is biaxially stretched to produce a geogrid, the stretching characteristics of the sheet are altered. This results in more polymer being drawn out of the nodal regions of the sheet thereby increasing the cross-sectional area for the reinforcing strands. The final geogrid has improved tensile strength as well as improved torsional rigidity. The improved physical properties of this geogrid made using beta nucleation allow the geogrid basis weight to be reduced leading to significant raw material and cost savings. The final geogrid also has a flatter profile with thinner nodal regions compared to that of a standard polypropylene geogrid. The presence of beta crystals in the extruded sheet also broadens the processing window during the orientation step. This allows the sheet to be drawn at lower temperatures and higher line speeds. This improved processing behavior results in productivity increases of up to 50%.

KEYWORDS: polypropylene, geogrid, beta, nucleation

INTRODUCTION

Polypropylene geogrids are widely used to reinforce roadbeds and to improve the performance of weak subgrades by distributing the loads over a wider area. Biaxial geogrids have similar strength properties across the width of the roll and across the length of the roll, and this balance of properties gives improved performance over a larger area.

These biaxial geogrids are produced by extruding a thick sheet of polypropylene using either a standard flat die or a specially designed die that extrudes a tube containing regularly spaced openings. In the case of a flat sheet, holes are produced in the sheet after the sheet has solidified. The flat extruded sheet of either process is then oriented in both the machine and transverse directions by reheating the sheet to a temperature below its melting point, and stretching it sequentially. The final geogrid product contains square or rectangular openings that are separated by highly oriented strands. A thickened section of unoriented polymer is located at the junction between the strands, and this is referred to as a node. Since the polymer in these nodes has largely random orientation, the nodes constitute areas of weakness. The junctions of the machine and cross direction oriented strands must be strong, since these junctions bear a considerable amount of the load when the geogrid is used to reinforce roadbeds.

Polypropylene is a polymorphic semi-crystalline polymer which can crystallize in more than one crystal form. The most common crystal form of polypropylene is the alpha, or monoclinic form, which melts at about 160^{o}C for Zeigler-Natta polymerized homopolymer. In an injection molded or extruded part over 95% of the crystals are typically of the alpha type. A less common form, known as the beta or hexagonal crystal form, generally comprises less than 5% of the crystals. The beta crystals have a melting point that is typically 12^{o}C－14^{o}C below that of the alpha form. The beta crystal phase is also more ductile than that of the alpha crystal phase, and it requires less force to orient a sheet containing mainly beta crystals compared to that of a sheet with containing only the alpha crystalline phase. This higher ductility means that extruded sheets containing high levels of beta crystallinity can be drawn at lower temperatures and at higher draw rates compared to that of sheets containing mainly alpha crystals. Another attribute of beta nucleation is the fact that when a beta crystalline sheet is stretched in the solid state, microvoids develop during the stretching process (Jacoby et al. 1994, 1995). These microvoids lead to a reduction in the density of the final oriented sheet or film.

There are many nucleating agents that are used in polypropylene, and all of these provide sites where crystals can grow as the as the molten PP cools. These agents typically nucleate the alpha crystal phase, and

[1] Vice President of Technology, Mayzo Corporation, USA., Email: pjacoby@mayzo.com

their addition to PP causes the rate of crystallization to increase leading to faster cycle times, and higher levels of crystallinity in the final part. This higher crystallinity results in higher stiffness and strength characteristics.

There are only a handful of nucleating agents that preferentially nucleate the beta crystal phase (Mathieu et al. 2002). Although there are many commercially available grades of alpha nucleated polypropylene, there are almost no commercially available beta nucleated PP grades. This situation has limited the number of commercial applications of beta nucleated polypropylene. We have developed beta nucleant masterbatches that can be added to non-nucleated polypropylene at the extruder hopper to produce extruded sheets that contain high levels of beta phase crystallinity.

EXPERIMENTAL

Materials

The extruded sheet was produced using Basell PRO-FAX® 7823, which is a polypropylene homopolymer with a melt flow rate of about 0.7 g/10 min. The beta nucleant masterbatch was identified as MPM 1106, and contained a proprietary beta nucleant in a polypropylene carrier resin having a melt flow rate of about 12 g/10 min. A carbon black masterbatch containing 30% carbon black was also used to produce the sheet samples. The additional level of the beta nucleant masterbatch was 2.7%, and the addition level of the carbon black masterbatch was 3%.

Processing

Extruded sheets were made on a 200 mm single screw extruder into which the different raw materials were fed using loss-in-weight feeders. The extruder had a typical output rate of 1050 kg/hour, and the molten polymer passed through a static mixer and a gear pump before being extruded from a flat sheet die onto a three-roll cooling stack. The molten polymer bead was nipped between the bottom and middle rolls, and the sheet wrapped around the middle and top rolls while it cooled and solidified. The bottom roll temperature was set at 96.7°C, the temperature of the middle roll was set at 112.8°C, and the temperature of the top roll was set at 111.7°C. The zone temperature settings on the extruder ranged from 190°C at the feed zone to 207°C at the die. The melt temperature reading at the die was 238°C. The line speed and roll gap nip were set to produce a final sheet thickness of 4.5 mm. The line speed was 3.25 meters/minute, and the final sheet width after the edges were trimmed off was 1.0 meter.

Prior to the orientation step, the sheet had circular holes punched in it, with a total of 105 holes across the width of the sheet, with a hole separation of 0.9 mm. This perforated sheet was oriented in the machine direction by passing it over a series of heated rollers moving at different speeds. The MD roll temperatures were set at 150°C for stretching all of these sheet samples. The fast roller was rotated at three times the speed of the slow roller, so that sheet was stretched at a 3:1 draw ratio in the machine direction. This sheet was then fed into a tenter frame (stenter) where it was gripped by clips on each side and stretched transversely to a final width of about four meters, representing a transverse draw ratio of 4:1. The initial air temperature settings in the stenter were set at 132 ºC–135 ºC. The line speed of the geogrid exiting the stenter varied from 13 meters per minute (standard conditions) to as high as 20 meters per minute.

Characterization and Testing

The beta crystal content of the final part is dependent on both the concentration of the beta nucleant masterbatch used to produce the part, and the thermal and processing history used during fabrication. Differential Scanning Calorimetry (DSC) testing is commonly used to assess beta nucleation, since the alpha and beta crystal phases have different melting points, so that their relative heats of fusion can be estimated. This technique is only qualitative, since there is some overlap between the two melting endotherms, and some recrystallization of beta into alpha crystals occurs during the heating scan.

A more quantitative way of characterizing the beta content is to measure it directly on an extruded sheet using wide angle x-ray diffraction (WAXD). The beta phase shows a particularly strong diffraction peak due to the (300) plane, while the alpha phase shows three strong peaks due to the (110), (130), and (040) planes. An empirical ratio of the intensity of these peaks known as the “K” value and defined [Turner-Jones 1964] as follows, was measured on selected sheet samples.

$$K = I(300)\beta/\{I(300)\beta + I(110)\alpha + I(130)\alpha + I(040)\alpha\} \quad (1)$$

Here K will vary from 0 for a sample with no beta crystals to 1.0 for a sample with only beta crystals. For most of the examples discussed in this paper, the K value for beta nucleated materials fell in the range of 0.6 – 0.9. It should be noted that in the case of the oriented geogrid, the WAXD measurements must be made on the extruded sheet before it has been oriented, since the orientation process converts the beta crystals to alpha crystals.

The tensile strength (kN/m) of the geogrids was measured at 2% elongation and 5% elongation using ASTM D6637. The torsional rigidity (kg-cm/deg) was measured as the resistance to in-plane rotational movement by applying a 20 kg-cm moment to the central junction of a 22.9 cm×22.9 cm specimen restrained at its perimeter (U.S. Army Corps of Engineers Methodology for measurement of Torsional Rigidity).

RESULTS AND DISCUSSION

A series of six geogrid samples were produced. Two of the samples contained no added carbon black and the remaining four samples contained 0.9% carbon black. One of the clear samples and three of the black samples were beta nucleated. A description of the samples is given in Table 1.

Table 1 Compositions and X-ray characterization of geogrid samples

Sample ID	Carbon Black (%)	Beta Nucleant	Sheet Thickness (mm)	X-ray K Value
1	0	No	4.50	0
2	0	Yes	4.50	0.83
3	0.9	Yes	4.50	0.69
4	0.9	Yes	4.15	Not Tested
5	0.9	Yes	3.84	Not Tested
6	0.9	No	4.50	0

We see from this table that the sheet samples containing the beta nucleant showed high levels of beta crystallinity as judged from the K values. The beta crystal content was somewhat lower in the black sheet, and this may indicate a small interference of the carbon black with the beta nucleant. After this work was done we developed a higher performance beta nucleant masterbatch that produced K values in excess of 0.85, even in the presence of carbon black.

After holes were punched in these sheet samples they were made into geogrids. The samples without the carbon black required slightly higher stretching temperatures to stretch them, compared to that of the black samples. The purpose for producing the non-pigmented samples was to facilitate the observation of the microvoids, since the microvoids scatter light and cause the final geogrid to take on a white/opaque appearance. This whitening was observed in Sample #2 but not in Sample #1, thereby confirming the presence of microvoids in Sample #2.

Another processing difference that we observed between the non-nucleated and the beta nucleated sheets was the width contraction that occurred after the MD stretching step. The MD-oriented beta nucleated sheets were approximately 6%—8% narrower in width compared to that of the non-nucleated sheets. This width contraction of beta nucleated sheets appears to be a general characteristic of this crystal phase, and has been observed in the production of oriented film made from beta nucleated sheet.

Table 2 Dimensions and geometry of geogrids

Sample ID & Type	Strand Width (mm)		Strand Thickness (mm)		Aperture Area (mm^2)	Node Thickness (mm)
	MD	TD	MD	TD		
1 (clear/no beta)	3.73	3.27	1.79	1.15	966	3.81
2 (clear/beta)	3.43	3.63	1.92	1.14	831	1.80
3 (black/beta)	3.60	3.77	1.87	1.22	868	2.29
4 (black/ beta)	3.68	3.73	1.62	1.04	899	1.95
5 (black/beta)	3.62	4.18	1.44	0.80	923	1.84
6 (black/ no beta)	3.22	3.12	1.70	1.11	961	3.41

Table 3 Physical properties of geogrids

Sample ID &Type	Basis Weight (g/m^2)	Tens. Strength @ 2% Elongation (kN/m)		Tens. Strength @ 5% Elongation (kN/m)		Ultimate Tens. Strength (kN/m)		Torsional Rigidity (cm kg/deg)
		MD	TD	MD	TD	MD	TD	
3 (beta)	309	7.9	13.0	13.2	23.3	24.3	36.4	8.7
4 (beta)	268	7.6	11.5	12.6	21.4	23.9	32.2	9.1
5 (beta)	254	7.6	11.6	12.8	21.3	23.4	31.0	8.0
6 (no beta)	313	6.0	9.0	11.8	19.6	19.2	28.8	6.5

We also observed that we were able to increase the line speed during the orientation process from the standard production rate of 13 meters per minute to as high as 20 meters per minute, without making any changes in the oven temperature settings. Typically a standard polypropylene geogrid cannot be produced at this high production rate without breaking during the stretching process. This 50% improvement in productivity is quite dramatic and can lead to significant cost reductions.

The dimensions and geometry of the final geogrids are given in Table 2.

A number of interesting features are evident from this data. Firstly we see a dramatic decrease in the thickness of the nodes when beta nucleation is used. We also see that the open area of the grid holes (aperture area) decreases when beta nucleation is used at constant extruded sheet thickness. The decrease in aperture area reflects the fact that more polymer was drawn into the oriented strands, and the overall size of the nodal region increased. As the starting sheet thickness is reduced going from sample 3 to 4 to 5, the aperture area gradually increased, since less polymer was available to be drawn into the strand regions The appearance of the actual geogrid samples 3 and 6 are illustrated in Fig. 1.

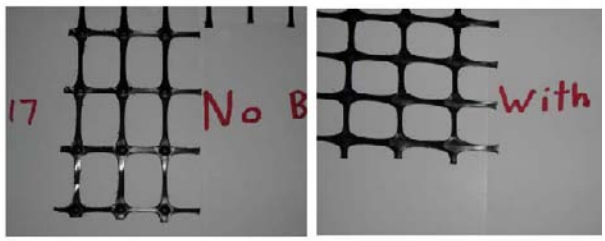

Sample #6 – No Beta Sample #3 – With Beta

Fig.1 Appearance of geogrids made with and without beta nucleation

The physical properties of the black geogrid samples are given in Table 3.

It can be seen from the data listed in Table 3 that the geogrids made from beta nucleated sheets of Samples 3, 4 and 5 all had tensile strength and torsional rigidity values that exceeded that of the non-nucleated control Sample 6. This strength and rigidity improvement was even seen for the sheets of Samples 4 and 5, where the initial extruded sheet thickness and final basis weight was lower than that of Sample 6.

We also measured the densities of the MD-oriented strands in Samples 1, 2, 3, and 4, and these values are given in Table 4.

Table 4 Density of MD Strands of Geogrids

ID & Type	1 (clear)	2 (clear β)	6 (black)	3 (black β)
Dens. (g/m^3)	0.907	0.871	0.911	0.876

The reduction in density of the strands from the beta nucleated geogrids is the result of the microvoiding that occurred during the MD stretching process. This density reduction also contributes to the increase in the cross sectional area of the oriented strands.

SUMMARY AND CONCLUSIONS

We have shown that beta nucleation can be used to improve the strength and rigidity of biaxially oriented polypropylene geogrids. These physical property improvements allow the basis weight of the geogrid to be significantly reduced resulting in raw material and cost savings. The processing performance of the beta nucleated extruded sheet is also dramatically improved allowing for increases in productivity of up to 50% compared to that of standard non-nucleated geogrids, and this also results in significant cost savings. The unique beta nucleant masterbatch that we developed can be added to conventional polypropylene resins at the extruder hopper in order to achieve these benefits of beta nucleation.

REFERENCES

Jacoby P et al., US Patent# 5,594,070 (1995); US Patent# 5, 317, 035 (1994)

Mathieu C, Thierry A, Wittmann J, Lotz BJ (2002) Polymer Sci., Part B: Polymer Physics, Vol. 40, 2504

Turner-Jones A, Aizlewood J, Beckett D, Makromol (1964) Chem: 75, 134, 9

Proceedings of the 4th Asian Regional Conference on Geosynthetics
June 17 - 20, 2008 Shanghai, China

EFFECTS OF Y TYPE PP FIBERS AND HYDROXYETHYL METHYLCELLULOSE (HEMC) ON DRY-SHRINKAGE OF CEMENT MORTARS

L.F. Liu[1], R.H. Li[2], X.J. Yang[3] and J.Z. Ren[4]

ABSTRACT: Dry-shrinkage has evident effect on the durability of cement mortars, so the research on it has great significance. The effects of Y type PP fibers, hydroxyethyl methylcellulose (HEMC), and the two admixtures together on the dry-shrinkage of cement mortars are studied in this paper. The dry-shrinkage is expressed by the length shrinkage of mortars at curing time of 2 d—180 d comparing to the length of mortar at 1d after casting. The experimental results show that HEMC and Y type PP fibers can reduce the dry-shrinkage of cement mortars, and the reduced extent increase with their increased amount (except for Y type PP fibers in volume fraction of 0.3%). Furthermore, the two together can obviously reduce the dry-shrinkage. However, either HEMC or Y type PP fibers or the two together all have limited effects on the dry-shrinkage.

KEYWORDS: cement mortar, dry-shrinkage, hydroxyethyl methylcellulose, Y type PP fibers

INTRODUCTION

Dimensional changes (shrinkage) of cementitious materials are of fundamental importance although they are not unacceptable in themselves but they are sometimes accompanied by development of slots that are unsightly and objectionable. These slots may develop into macro-scopical cracks even when taking standard precautions. Cracks can impair the serviceability, durability, or esthetics of cementitious materials, and are therefore of economic significance in construction industry. Various forms of shrinkage are associated with cementitious materials and since drying-shrinkage is among the most troublesome (Theodorakopoulos 1995; Kraft et al. 2004; Xiao et al. 2002), this paper shed light on it only.

Dry-shrinkage, which has evident effect on the durability of cement mortars, is a process where water is removed from cement mortars (concretes) by evaporation. The dry-shrinkage of cement mortars has close relation with its anti-cracking properties. Researches (Xiao et al. 2002) show that the netted cracks on surface of cement mortars (concretes) are mostly caused by dry-shrinkage. So the research on it has great significance. There are many researches on it up to the present (Sanjuan et al. 1997; Wiegrink et al. 1996; Cohen et al. 1990; Qi et al. 2003). However, the effects of Y type PP fibers and hydroxyethyl methyl cellulose are still waiting for discussing. So the function of Y type PP fibers, hydroxyethyl methyl cellulose and the two admixtures together on the dry-shrinkage of cement mortars, as well as their performance mechanisms, are studied in this paper.

EXPERIMENTAL

Materials

The cement used in this study is ordinary Portland cement, CEM 32.5R. The sand used is natured sand (100% passing 1.75mm sieve, 99.9% SiO2). No coarse aggregate is used. A white polymer powder, hydroxyethyl methyl cellulose MH10007 P4 (shorted for HEMC), produced by Clariant Ltd. Co., German, is used, which is called HEMC for short in this study. PP fibers are also used, whose physical properties are shown in Table 1 and shape of cross-section is shown in Fig.1.

Methods

Mortar specimens were mixed in a normal mixer for 3 minutes with mix proportions of cement: sand: water=1:3:0.54, adding Y type PP fibers or/and HEMC in the required amount if needed. In this study, the amount of Y type PP fibers is by volume fraction of mixture, and HEMC by weight of cement and sand. Then the mixture was casted according to Test Method

[1] Associate Professor, College of Textiles, Donghua University, CHINA. Email: lifangliu@dhu.edu.cn
[2] Postdoctor, School of Economics and Management, Tongji University, CHINA. Email: liruihai@126.com
[3] Doctor, School of Materials Science and Engineering, Tongji University, CHINA. Email: yangxiaojie@mail.dhu.edu.cn
[4] Engineer, Jinan Bairan Gas Pipeline Co., CHINA. Email: d99908lf@mail.dhu.edu.cn

for Strength of Hydraulic Cement Mortars GB177-85. After casting, the specimens were cured in an curing box with a constant temperature of 20±2℃, relative humidity of 95±5 % for 24h before demoulded. And then the demoulded specimens were cured to given time at a room with a constant temperature of 20±2℃, relative humidity of 60±5%. The length of specimens with curing time of 1 d, 2 d, 3 d, 4 d, 5 d, 6 d, 7 d, 10 d, 14 d, 21 d, 28 d, 35 d, 45 d, 60 d, 90 d, 120 d and 180 d after casting were measured respectively in this study. So the dry-shrinkage, expressed by the length shrinkage of mortars at 2 d—180 d comparing to the length of mortar at 1d, could be calculated. Three mortars were tested and averaged for every specimen.

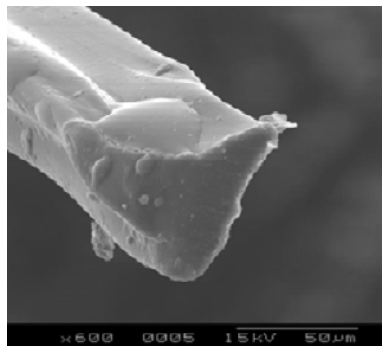

Fig. 1 Morphology of Y type PP fiber

Table 1 Physical property of polypropylene fibers

Shape of cross-section	*Y type*	*Length*/mm	15
Tensile strength/MPa	400	Diameter/um	48
Elastic modulus/GPa	8	Elongation/%	8

RESULTS AND DISCUSSIONS

Effect of Y Type PP Fibers

Fig. 2 shows the experimental results of dry-shrinkage of cement mortars modified with Y type PP fibers in different volume fractions.

As shown in Fig. 2, cement mortars modified by Y type PP fibers have lower dry-shrinkage than blank mortar. And the dry-shrinkage reduce with the increase of fibers amount within the range of 0—0.20%. For example, the dry-shrinkage of cement mortar with Y type PP fibers in the amount of 0.05% decrease by 7.6% than blank mortar at 180d after casting, while decrease by 22.0% when modified with Y type PP fibers in the amount of 0.20%. Those results illustrate that fibers will have obvious effects on cement mortars only when their volume fraction reach to a certain value. However, when the amount of Y type PP fibers get to 0.3%, the cement mortar will have a higher dry-shrinkage, but still decrease by 11.7% compared to blank mortars at 180d after casting.

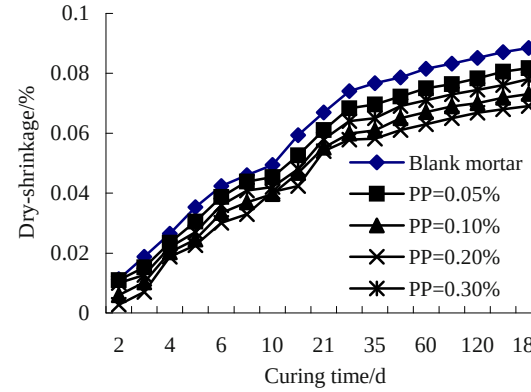

Fig. 2 Dry-shrinkage of cement mortars with Y type PP fibers

Effect of HEMC

Fig. 3 shows the experimental results of dry-shrinkage of cement mortars modified with HEMC in different amount

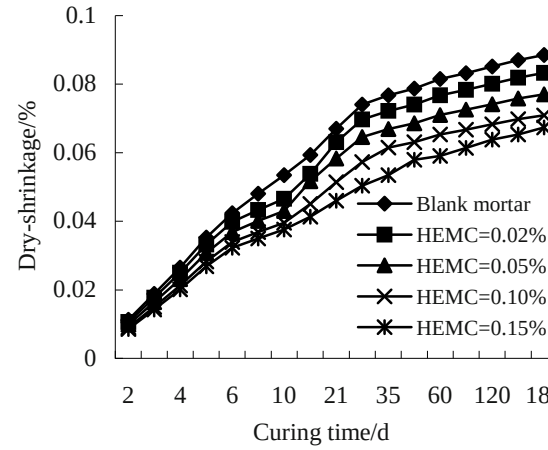

Fig. 3 Dry-shrinkage of cement mortars with different amount of HEMC

Adding HEMC into cement mortars can decrease their dry-shrinkage, and with the increase of HEMC their dry-shrinkage decrease, too, as shown in Fig. 3. The dry-shrinkage of cement mortar with HEMC in the amount of 0.02% decrease by 5.9% than blank mortar at 180d after casting, while decrease by 23.8% when the amount of HEMC reach to 0.15%.

Effect of HEMC and Y Type PP Fibers

Fig. 4 shows the experimental results of dry-shrinkage of cement mortars modified with HEMC and Y type PP fibers in different amount.

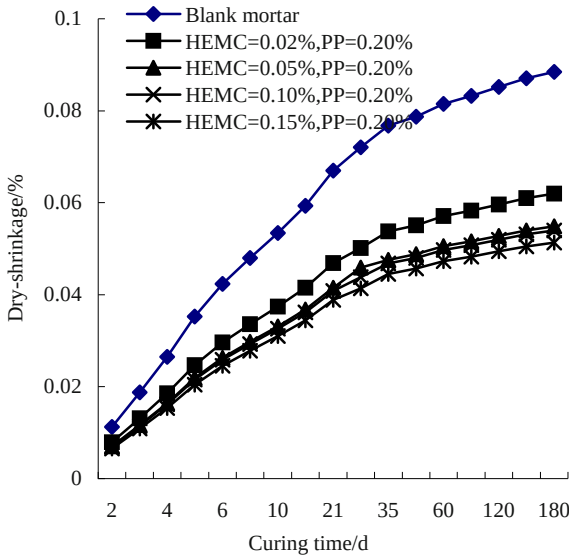

Fig. 4 Dry-shrinkage of cement mortars with HEMC and Y type PP fiber

As shown in Fig. 4, the addition of HEMC and Y type PP fibers together can obviously reduce their dry-shrinkage; furthermore, the effects aren't simply equal to the sum of decreased ratios when adding HEMC and Y type PP fibers individually, as shown in Table 2.

The results in Table 2 show that, the dry-shrinkage of cement mortars with HEMC and Y type PP fibers together are smaller than the sum of those of cement mortars with HEMC and Y type PP fibers individually, when the amount of HEMC is 0.02% or 0.05%. While the dry-shrinkage of cement mortars with HEMC and Y type PP fibers together are about equal to or greater than the sum of those of cement mortars with HEMC and Y type PP fibers individually, when the amount of HEMC is 0.10% or 0.15%. This shows that the adding amount of HEMC or Y type PP fibers exit a optimum value, and either HEMC or Y type PP fibers or the two together all have limited effects on the dry-shrinkage of cement mortars, which is also verified by the experimental results in Fig. 4.

Table 2 Decreased dry-shrinkage of cement mortars with Y type PP fibers and HEMC (at 180d)

Amount of HEMC	0.02%	0.05%	0.10%	0.15%
Mortars with HEMC only	5.9%	12.9%	19.9%	23.8%
Mortars with PP fibers only (PP=0.20%)	22.0%			
Mortars with HEMC and PP fibers (PP=0.20%)	30.0%	38.0%	39.1%	42.9%

MECHANISM

Two mechanisms can be identified by which Y type PP fibers reduce the dry-shrinkage of cement mortars. First, fibers can reduce differential settlement, increase the stiffness of cement mortars (Ma et al. 2004) which can reduce the extent of dry-shrinkage; secondly, fibers can redistribute water and replenish water at the surface to minimizing capillary stress effects, which can also reduce the size of pores in cement mortars, especially the harmful big pores whose diameter are above 100nm (Sooushian et al. 1995), as shown in Fig. 5. The smaller pores can have stronger ability to retain free water from migration, and even if the free water is evaporated the dimensional change thus caused are less obvious than bigger pores. So the extent of dry-shrinkage of cement mortars could be reduced.

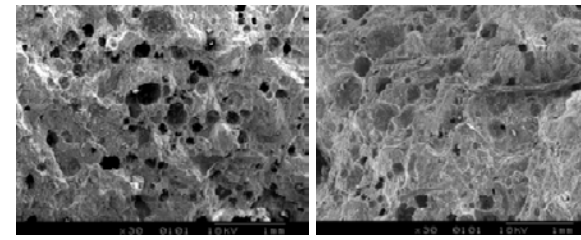

(a) (b)

Fig. 5 Pore distribution of cement mortars: (a) Blank mortar; (b) Modified by Y type PP fibers (PP=0.10%)

The space between fibers will decrease with the increased fibers amount added into cement mortars, which contribute to reducing the pores size thereby minimizing dry-shrinkage. However, if the volume fraction in which the fibers are mixed is high enough, such as 0.3% in this study, they will entangle with each other, being difficult to distribute evenly, and so decrease their effects, as illustrated in Fig. 2.

The mechanism that HEMC can reduce the dry-shrinkage lies in that HEMC can improve the water retention ability of cement mortars, as shown in the research of Wang, et al (Wang et al. 2000) that the water retention ability is increased by about 97% than blank mortar when the amount of HEMC is 0.02% by the weight of cement and ground granulated blast furnace slag (tested according to the German standard DIN 1855527). So the cement mortars can deeply hydrate and have higher stiffness, which reduce the extent of dry-shrinkage.

Adding HEMC and Y type PP fibers together into cement mortars can improve the water retention ability, minimizing the capillary stress of cement mortars caused by free water migration, at the same time, obviously reducing the pores size, so can evidently reduce the dry-shrinkage of cement mortars. However, as stated above, either HEMC or Y type PP fibers or the two together all have limited effects on the dry-shrinkage of cement mortars. Due to the combination of sand settlement and water evaporation that takes place after casting, especially within the first few hours, pores will unavoidably occur in hardened cement mortars. Furthermore, cement mortars in practice will suffer external temperature change, which can also bring shrinkage to them. Proverbially, cement mortars are anisotropic composites, the components in which have different shrinkage, so the formed pores inevitably have different sizes. Although HEMC and Y type PP fibers can reduce the pores size, they couldn't fully prevent the occurring of pores or their unevenly distribution in cement mortars. So the cement mortars still exist dry-shrinkage phenomenon though after modification.

CONCLUSIONS

Hydroxyethyl methyl cellulose shorted for HEMC in this study, as well as Y type PP fibers, can reduce the dry-shrinkage of cement mortars, and the reduced extent increase with their increased amount (except for Y type PP fibers in volume fraction of 0.3%). HEMC and Y type PP fibers together can obviously reduce the dry-shrinkage; furthermore, the effects aren't simply equal to the sum of decreased ratios when adding HEMC and Y type PP fibers individually. The amount of HEMC or Y type PP fibers exists an optimum value, and either HEMC or Y type PP fibers or the two together all have limited effects on the dry-shrinkage of cement mortars.

Y type PP fibers can reduce the dry-shrinkage because they can reduce differential settlement and pores size in cement mortars, and so reduce the dry-shrinkage of cement mortars. The reason that HEMC can reduce the dry-shrinkage lies in that they can improve the water retention ability and decrease the capillary stress of cement mortars. Their combined action can obviously reduce the dry-shrinkage. However, they couldn't fully prevent the occurring of pores or their unevenly distribution in cement mortars. So the cement mortars still exist dry-shrinkage phenomenon though after modification.

Continuing research is needed to draw a more specific conclusion on the effect mechanism of HEMC and Y type PP fibers on dry-shrinkage of cement mortars.

ACKNOWLEDGEMENTS

The authors wish to thank Prof. Peiming Wang from Tongji University, China, for his kind and efficient help to finish this paper.

REFERENCES

Theodorakopoulos DD (1995) Shrinkage behaviour of GRCthin sheets. Cem. Concr. Compos 17: 229-238

Kraft L, Engqvist H, Hermansson L (2004) Early-age deformation, drying shrinkage and thermal dilation in a new type of dental restorative material based on calcium aluminate cement. Cem. Concr. Res 34: 439-446

Xiao RM, Zhang X, Le JL (2002) Effect of binder on dry shrinkage of concrete. China Cem. Concr 5: 11-13

Ma SJ Moragues A (1997) Polypropylene-fiber-reinforced Mortar Mixes: Optimization to Control Plastic Shrinkage. Compos. Tech 57: 655-660

Wiegrink K, Marikunte S (1996) Shrinkage Cracking of High-Strength Concrete. ACI Mat. J 93(5): 409-415

Cohen MD, Olek J, Dolch WL (1990) Mechanism of plastic shrinkage cracking in Portland-cement and Portland cement-silica fume paste and mortar. Cem. Concr. Res 20:103-119

Qi C, Weiss J, Olek J (2003) Characterization of plastic shrinkage cracking in fiber reinforced concrete using image analysis and a modified Weibull function. Mat. Struct 36(7): 386-395

Ma Y, Zhu B, Tan M, Wu K (2004) Effect of Y type polypropylene fiber on plastic shrinkage cracking of cement mortar. Mat. Struct 37 (3): 92-95

Sooushian F, Mirza F, Alhozaimy A (1995) Permeability characteristic of polypropylene fibers reinforced concrete. ACI Mat. J 92(3): 291-295

Wang PM, Xu Q, Li WW (2000) Effect of hydroxyethyl methyl cellulose on properties of cement mortar. J. Build. Mat 3(4): 305-309

UNIFIED CONSTITUTIVE CURVES OF STRAIN-HARDENING MEDIUM AND STRAIN-SOFTENING MEDIUM

Q. Sun[1] and S.Q. Qin[2]

ABSTRACT: A constitutive curve - L-S curve is developed for both strain-softening and strain-hardening media. There are two factors, which are water and stress, to damage and soften the media. The stress-strain constitutive model is described by the Weibull's distribution law.

KEYWORDS: strain-softening medium, strain- hardening medium, L-S function, constitutive curve

INTRODUCTION

Various scholars have studied on the constitutive curves of strain-softening medium and strain- hardening medium (Li et al. 2006; Yuan et al. 2006; Qin et al. 1993; Phillips 1995; Qin et al. 2001; Qin et al. 2005), and presented some important models. In this way, a lot of achievements have been obtained. However, there are two problems in these constitutive curves.

One problem is that relation of the influencing factors, which is not allowed to neglect. For example, the pore water has two functions to the medium (Fig. 1).

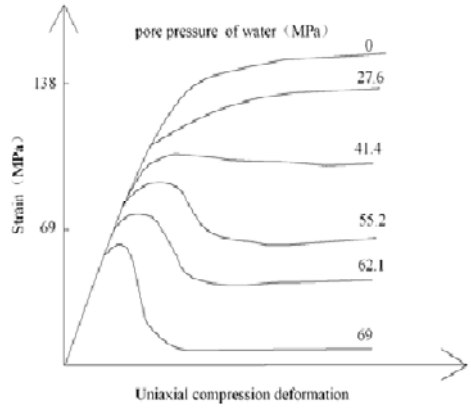

Fig. 1 Effect of pore-pressure on the brittle-ductile transition in limestone at a confining pressure of 6.9 MPa. Numbers on the curves are values of pore pressure in MPa (Robinson et al. 1979)

First is the mechanical effect which the hole stresses (or is called mechanics effect), the existence of the hole stresses reduced the medium effect stress, caused the effective shear strength to reduce. On the other hand, the corrosion, which is caused by mechanics and chemical effect, reduced the friction coefficient of shear belt medium. The other problem is that the constitutive curves only can be used to one medium which has the same character under different strain. However, the same medium may have different strain-stress characters (Fig. 2).

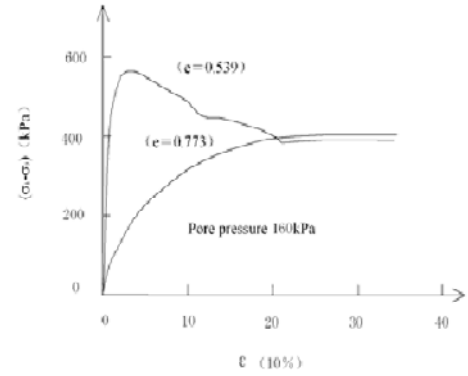

Fig. 2 Drained experimental curves of loose and compacted Sandboil sand soils

In this paper, the L-S Constitutive curve is presented. The characteristics of the L-S curve is also analyzed.

CONSTITUTIVE CURVES OF STRAIN-HARDENING MEDIUM AND STRAIN-SOFTENING MEDIUM

Constitutive Curve of Strain-hardening Medium

The shear stress-displacement relation, for the strain-hardening medium, can generally be assumed to be linear prior to failure. At failure, the strain-hardening medium is bisected and a sudden stress drop will take place. According to the above assumptions for the medium 1 (Fig. 3) can be written as (Qin 2005):

[1] Ph.D Student, Institute of Geology and Geophysics, Chinese Academy of Science, CHINA. Email:sunqiang04@126.com
[2] Professor, Institute of Geology and Geophysics, Chinese Academy of Science, CHINA. Email:qsqhope@sohu.com

$$\tau = \begin{cases} \dfrac{G_1 u}{h} (0 \le u \le u_h) \\ \tau_h + \dfrac{G_2 (u - u_h)}{h} (u > u_h) \end{cases} \quad (1)$$

Where u_b is the critical displacement corresponding to the failure of the rock block, u_2 is the displacement when the stepped or saw-toothed discontinuity inside the rock block is leveled out, G_{e1} and G_{e2} are the shear moduli space for $u < u_b$ and $u_b \le u \le u_2$, respectively, and h is the layer thickness of the intercalation.

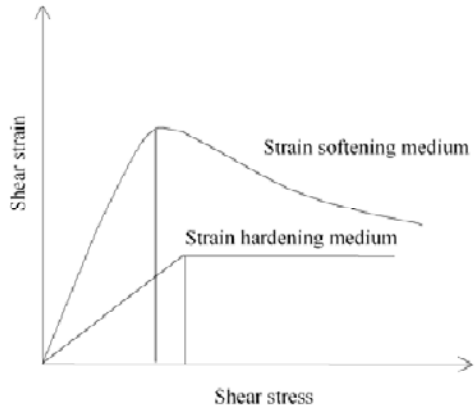

Fig. 3 Shear constitutive curves of strain-softening medium and ideally strain- hardening medium

Constitutive Curve of Strain-softening Medium

A simplified constitutive model of medium 2 can generally be expressed as a nonlinear function between the shear stress τ and the creep displacement u. Qin et al. (2001b) used a negative exponent distribution of strength to distribution is the strain-softening propery. However, the most commonly used distribution is the Weibull's distribution which describes very well the experimental data (Hudson and Fairhurst 1969), so the weibull's distribution law is adopted for the strain-softening media, i.e.

$$\tau = G_s \frac{u}{h} \exp\left[-\left(\frac{u}{u_0} \right)^m \right] \quad (2)$$

Where G_s is the initial shear modulus, u_0 is a measurement of average strength and m is the shape parameter.

L-S MODEL

Characteristics of L-S Model

It is presented the Liu-Sun (L-S) curve to the medium 1 and 2, which can be written as Eq. (3).

$$\tau = \frac{\tau_0}{h} \left(\frac{u}{u_0} \right) \exp\left[-\left(\frac{u}{u_0} \right)^{\frac{w}{w_0}+b} \right] \frac{m}{1 + n \times \exp\left[\dfrac{w}{w_0} \right]} \quad (3)$$

Where τ is the shear strain; τ_0 is the initial referenced manual of τ; u is the stress; u_0 is reference manual of u; w is water content (or compaction); w_0 is the initial manual of w; m, d and n are parameters of curve shape. One can get the m, d and n from test.

Non-dimensioned

Choosing non-dimensioned parameters $\bar{u}$ and $\bar{w}$, one can get equations. (4)-(6).

$$\bar{u} = \frac{u}{u_0} \quad (4)$$

$$\bar{w} = \frac{w}{w_0} \quad (5)$$

$$\tau = \frac{\tau_0}{h} \bar{u} \exp\left[-\bar{u}^{(\bar{w}+b)} \right] \frac{m}{1 + n \times \exp(\bar{u})} \quad (6)$$

Change of Parameter $\bar{w}$

$$\frac{\partial \tau}{\partial \bar{w}} = \begin{Bmatrix} -\dfrac{\tau_0}{h} \bar{u} \exp\left[-\bar{u}^{(\bar{w}+b)} \right] \dfrac{mn \times \exp(\bar{w})}{\left[1 + n \times \exp(\bar{w}) \right]^2} \\ -\dfrac{\tau_0}{h} \bar{u} \exp\left[-\bar{u}^{(\bar{w}+b)} \right] \dfrac{m}{1 + n \times \exp(\bar{w})} \bar{u}^{(\bar{w}+b)} \ln \bar{u} \end{Bmatrix} \quad (7)$$

$$\frac{n \times \exp(\bar{u})}{1 + n \times \exp(\bar{u})} < -\bar{u}^{(\bar{w}+b)} \ln \bar{u}, \ \frac{\partial \tau}{\partial \bar{w}} < 0 \quad (8)$$

$$\frac{n \times \exp(\bar{u})}{1 + n \times \exp(\bar{u})} > -\bar{u}^{(\bar{w}+b)} \ln \bar{u}, \ \frac{\partial \tau}{\partial \bar{w}} > 0 \quad (9)$$

One gets that the τ declines along with the increasing of water content, when $\bar{p}$ gets to some quantity, form Eqs. 8 and 9.

Relation between Stress and Distortion

$$\frac{\partial \tau}{\partial \bar{u}} = \frac{\tau_0}{h} \exp\left[-\bar{u}^{(\bar{w}+b)} \right] \frac{m}{1 + n \times \exp(\bar{w})} \left[1 - \bar{u}^{(\bar{w}+b)} (\bar{w} + b) \right] \quad (10)$$

$$\bar{u}^{(\bar{w}+b)} (\bar{w} + b) < 1, \ \frac{\partial \tau}{\partial \bar{u}} > 0 \quad (11)$$

$$\bar{u}^{(\bar{w}+b)}(\bar{w}+b)>1,\ \frac{\partial\tau}{\partial\bar{u}}<0 \tag{12}$$

One gets that the τ increases along with the increasing of water content, when $\bar{w}$ is a constant. However, when the equation (12) is satisfied, τ declines along with the increasing of $\bar{u}$.

Let
$$\bar{\tau}=\frac{\tau_0}{h} \tag{13}$$

$$\tau^*=\frac{\tau_0}{h}\frac{m}{1+n\times\exp[r-b+d]},\quad r=\bar{w}+b \tag{14}$$

One can get equation (15):

$$\begin{aligned}\tau&=\bar{\tau}\bar{u}\exp\left[-\bar{u}^r\right]\frac{m}{1+n\times\exp[r-b+d]}\\&=\tau^*\bar{u}\exp\left[-\bar{u}^r\right]\end{aligned} \tag{15}$$

CASE STUDY

In the equation (3), it can be seen that the water content and stress have impotent influence to the medium constitutive curve (Fig. 4). In Fig 4, the curves (a)-(c) are obtained by equation (3); the curves (d)-(f) are gotten from experiment (Wang ChengHua et. al. 2004).

Table 1 Parameters of Fig. 4

Items	b	m	n	h	τ_0	d	$\bar{w}$
(a)	0.30	0.9	0.9	1.0	90	0.0	0.02
(b)	0.28	0.9	0.9	1.0	300	0.0	0.04
(c)	0.43	0.9	0.9	1.0	1200	0.15	0.08

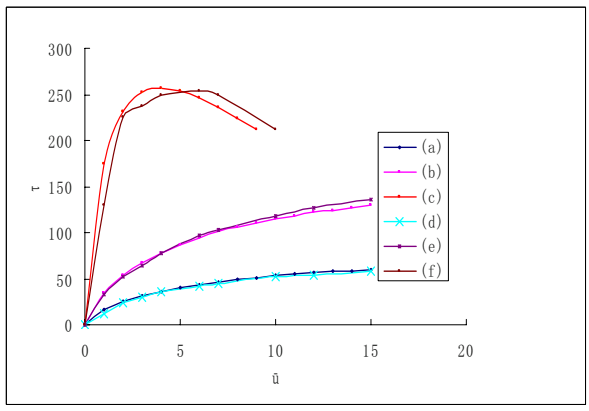

Fig. 4 Constitutive curves of Eq. 3

CONCLUSIONS

From the case study, it is found that the L-S curve had the good compatibility with the experimental situation.

The further work is to study the constitutive equation of medium and the mathematical model acted by the external environment to get better results.

REFERENCES

Gehle C, Kutter, HKJ (2003) Breakage and shear behaviour of intermittent rock joints. Int. J.Rock Mech. Min Sci: 687-700

Guo CQ (1995) The Stability Safety Factor of Rook Slope with Soft Inter layers. Water Resources and Hydropower Engineering: 27-30

Gye CC (2001) Unsaturated soil stiffness and post-liquefaction shear strength. PhD.Thesis, Georgia Institute of Technology, USA: 91

Jaeger JC, Cook NGW (1979) Fundamentals of rock mechanics (third edition). London: Chapman and Hall

Lajtai EZ (1967) The influence of interlocking rock discontinuities on compressive strength (model experiments). Felsmech Ingenieurgeol: 217-228

Li HZ, Liao HJ, Sheng Q (2006) Study on Statistical Damage Constitutive Model of Soft Rock Based on Unified Strength Theory. Chinese Journal of Rock Mechanics and Engineering: 1331-1336

Qin SQ, Jiao JJ, Wang SJ (2001a) A cusp catastrophe model of instability of slip-buckling slope. Rock Mechanics and Rock Engineering: 119-134

Qin SQ, Jiao JJ, Wang SJ (2001b) A Nonlinear Catastrophe Model of Instability of Planar-slip Slope and Chaotic Dynamical Mechanisms of Its Evolutionary Process. International Journal of Solids and Structures: 8093-8109

Qin SQ (2005) Nonlinear Evolutionary Mechanisms and Physical Prediction of Instability of Planar-slip Slope. Chinese Journal of Geotechnical Engineering: 1241-1248

Wang CH, Li GX (2004) Analysis of problem of pattern transition in stress-strain relations of soils. Rock and Soil Mechanics: 1185-1190

Yuan HP, Cao P, Xu WZ, Chen YJ (2006) Visco-elastop-lastic. Chinese Journal of Geotechnical Engineering. Constitutive relationship of rock and modified Burgers creep model: 796-799

Testing and Test Standards

CHARACTERISTICS OF SELF-HEALING OF GCL

X. Li[1], Y.M. Shu[2] and X.R. Wu[3]

ABSTRACT: GCL used as impervious liner may be damaged in the putting of large area. In order to quantitatively cognize the impervious ability of the damaged GCL, a series of penetrant tests of different punctured flaw have been done to know the relationship between ability of healing itself and damaged extent. Tests are done in the flexible wall permeator according to ASTM. By penetrated tests of different flaw samples, curve of permeability coefficient varies with time and diameters of the holes is gained, and the following conclusions are taken: the decrease of permeability coefficient of punctured sample mainly happens in the inceptive 2 days of test; the variety between permeability coefficient and different flaw is similar in each period of time; the permeability coefficients of flaw diameters between 0.002m and 0.004m increase obviously; and permeability coefficient decreases when thickness is restricted.

KEYWORDS: GCL, characteristics of self-healing, punctured flaw, permeability coefficient

INTRODUCTION

In the design and construction of modern solid waste landfill, many design engineers and environmental protection departments use GCL instead of CCL (Compacted Clay Liner) as impervious material. In the recent 10 years, GCL is widely used in the liner systems and cover systems. Liner or liner system is the most key section in the landfill system. The reliability of liner system is the element of whether leach ate collection system or leak detection system can make full use of prospective function. GCL wetted can hold very low permeability coefficient ($k<10^{-11}$ m/s) under the condition of tension, partial immerging and cycle of freezing and thawing. It has good characteristics like self-healing and so on (Bouazza 2002; Lake and Rowe 2000; Petrov and Rowe 1994). In recent years, there are several manufacturers in China have produced GCL, and it has already been applied in landfill and subway tunnel. Taking the large area construction of landfill into account, the GCL being laid may be damaged and it will injure the safety of impervious liner system. In order to have a quantitative cognition to characteristics of self-healing of flaw GCL and to supply evidence for the appraisal of impervious ability of flaw GCL, a series of penetrated tests of GCL with different sizes of flaw have been done, seeing about the relation between characteristics of self-healing and damaged extent.

TEST PROCEDURE

Testing Regulations and Apparatus

Testing regulations is based on ASTM D5887. Testing apparatus is the permeable apparatus with flexible wall for permeability as Fig. 1.

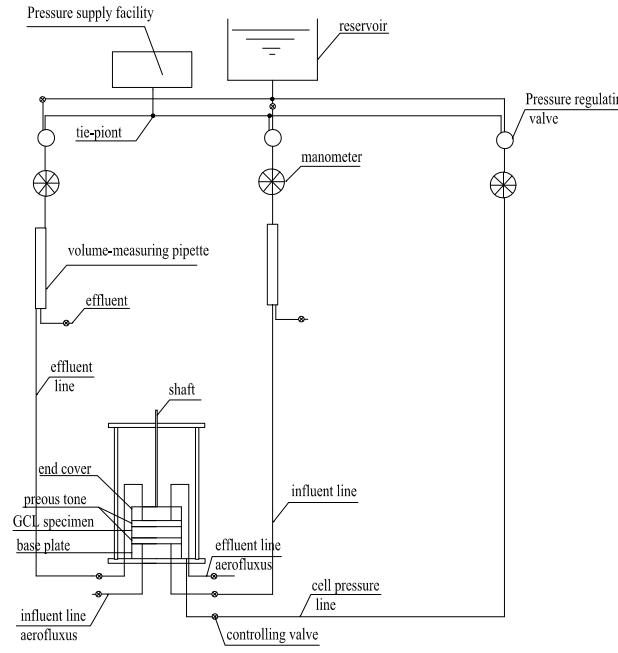

Fig. 1 Principle of permeable apparatus

[1] Engineer, Guangxi Electric Power industry Investigation Design and Research Institude, CHINA. Email:muyu-2000-2000@163.com
[2] Professor, Water Conservancy and Hydropower Engineering College of Hohai University, CHINA. Email:yimingshu2004@yahoo.com.cn
[3] Engineer, China Water Huaihe Engineering Co., LTD, CHINA. Email: wxr99021626@163.com

Testing Scheme

GCL samples are got from certain domestic product. The diameter of sample is 0.1 m, and a rounded hole is cut in the center of the sample in order to simulate punctured flaw. The sizes of flaw are 0.002 m, 0.004 m, 0.007 m and 0.01 m respectively shown as Fig. 2, and the samples when soaking for 23,47,101 minutes are shown as Figs. 3 — 5. Testing procedure is that the sample is placed in permeable apparatus, and the cell pressure is maintained of 550 kPa and backpressure of 515 kPa for a period of 12h to allow consolidation, swell, saturation and hydration to occur. Then the intake pressure at the base of the sample is raised to 530 kPa in order to form the upward flow through the test sample. Finally, the trend of permeability coefficient vs. time is tested till the seepage is stabilized.

Fig. 2 Samples with different sizes of flaw

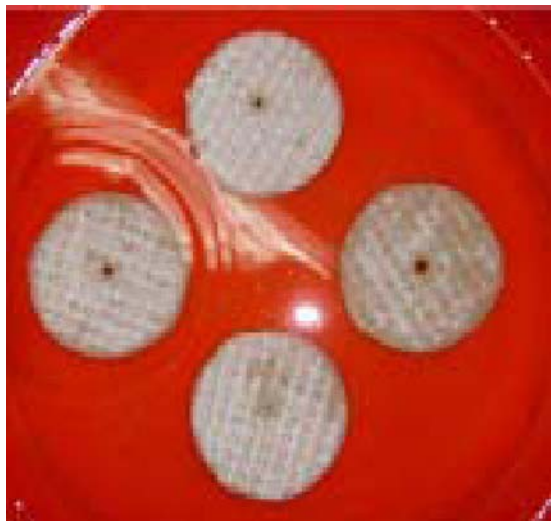

Fig. 3 Samples when soaking for 23 minutes

Fig. 4 Samples when soaking for 47 minutes

Fig. 5 Samples when soaking for 101 minutes

EXPERIMENTAL RESULTS

Large Variation of Permeability at Initial Hydration

The relationship between permeability coefficient (k) and time (t) with different diameters of flaw is curved as Fig. 6.

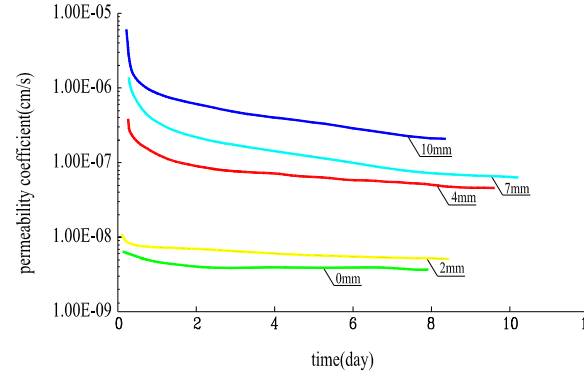

Fig. 6 Relationship k~t

As shown in Fig. 6, at experimental initial stage, the value of curve gradient about the permeability coefficient varied with time to variational sizes of flaw are greater than the ones in the latter progress.

At the initial stage of hydration, reduction of the permeability coefficient is depended on the area of flaw and the thickness of hydrated bentonite when the flaw heals; therefore the permeability coefficient of GCL reduces rapidly. Along with the increase of the flaw's size of sample, the time for healing become longer, and the time for which bentonites achieve to a certain thickness is longer. So the initial stage of hydration is longer. After the flaw of sample is wholly healed, the thickness of bentonites has achieved to the value at which GCL reaches seepage stabilization ultimately. But the pore spaces in the bentonites decrease as the effects of hydraulic expansibility and sanction in the thickness direction of bentonites. This process is quite slow, so gradient of the permeability coefficient is diminishing.

Relation between Permeability Coefficient and Different Sizes of Flaw

Comparing the permeability coefficient (k) of GCL specimen with variational sizes (d) of flaw when seepage is stabled, as shown in Fig. 7. It represent that the influence of the permeability coefficient of GCL specimen with smaller size of flaw is small when seepage is stabled. In a word, the permeability coefficient of GCL specimen with increscent sizes of flaw is increasing gradually when seepage is stabled, and when the seepage reach stable state, the relationship of the permeability coefficient of GCL specimen with variational sizes of flaw as follows:

$$y = 3\times10^{-9}\cdot e^{0.4934x} \tag{1}$$

where y=permeability coefficient of GCL, cm/s; x=size of flaw, mm; t=time, day. When the size of flaw is smaller than 0.002 m, the permeability coefficient is similar to that of non-defective; when the size of flaw is more than 0.006 m, the permeability coefficient is increasing rapidly; the permeability coefficient of GCL increases rapidly when the size of flaw is equal to or more than 0.01 m, and it has exceeded 2 order of magnitude.

Gradient of Permeability Coefficient Varied with Different Sizes of Flaw

By comparing the permeability coefficient of GCL specimens with variational sizes of flaw passing the same hydrating time, it is found that at the same time of day the curve shape with the permeability coefficient of GCL specimens to variational sizes of flaw hold in line basically, and this is similar to that of GCL when seepage reached stable state.

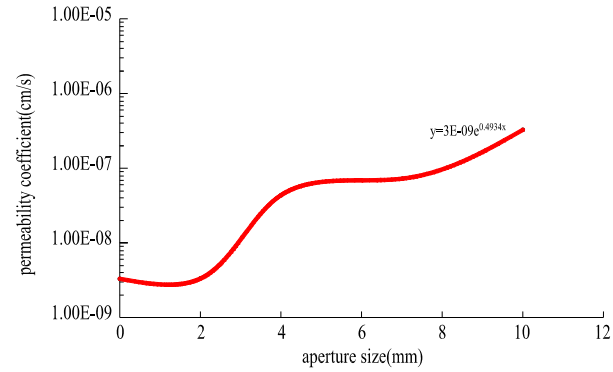

Fig. 7 k—d when seepage reach stable

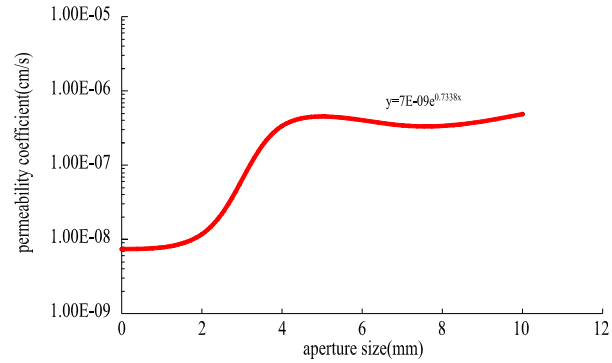

Fig. 8 k—d when hydration passed 1 day

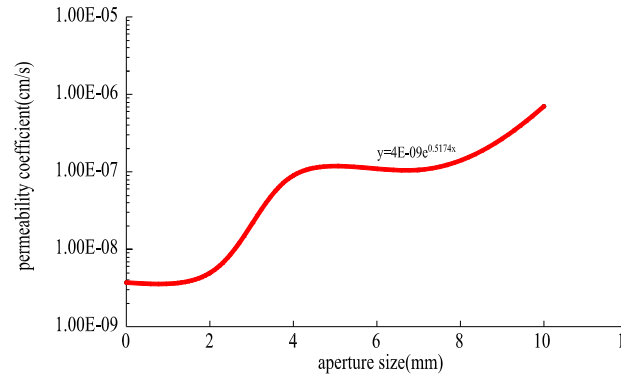

Fig. 9 k—d when hydration passed 2 days

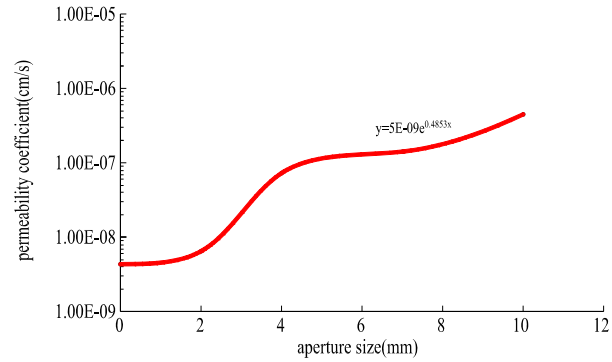

Fig. 10 k—d when hydration passed 4 days

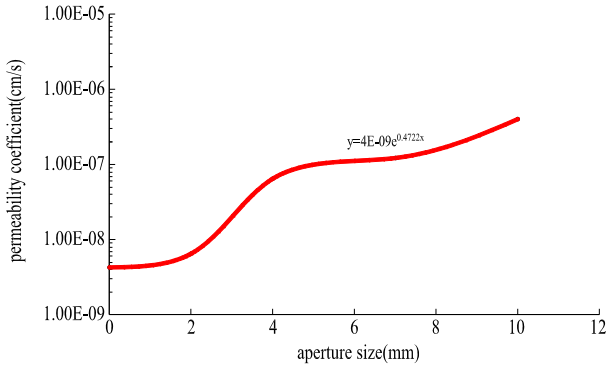

Fig. 11 k—d when hydration passed 6 days

As shown in Figs. 8-11, when y <0.002 m, the influence of the permeability coefficient of GCL specimens with sizes of flaw is small; when 0.002 m< y <0.0045 m, the influence of permeability coefficient of GCL specimens with sizes of flaw becomes remarkable; when 0.0045 m < y < 0.0067 m, the permeability coefficient of GCL specimens increases slowly along with increasing sizes of flaw, and when y >0.0067 m, the permeability coefficient of GCL specimens increases remarkably with. increasing sizes of flaw.

From trendlines of Figs. 8—11 the relation between the permeability coefficient of GCL specimens with size of flaw is power function, taking time into account, following expression is given

$$y = \left(5.0\times10^{-8}\cdot t - 0.1915\right)\cdot e^{\left(2\times10^{-12}\cdot t^2 - 2\times10^{-6}\cdot t + 0.285\right)x} \quad (2)$$

where y=permeability coefficient of GCL, cm/s; x=size of flaw, mm; t=time, day.

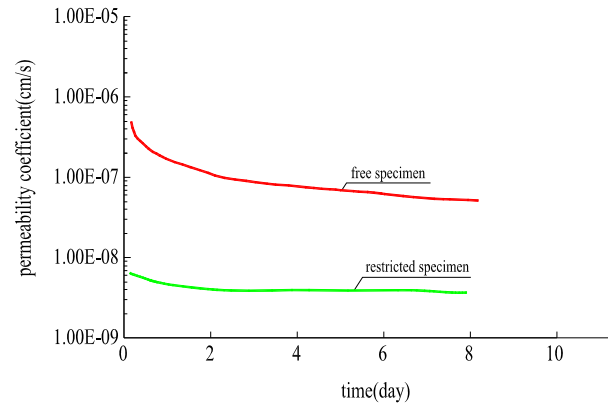

Fig. 12 Comparing between freedom and restriction of GCL

Permeability Coefficient When Thickness be Restricted

We also studied the permeability coefficient of GCL when thickness direction of the sample is restricted and free respectively at the same time. From Fig. 12 we can see that whether it was flawed or non-defective, the permeability coefficient of GCL which is restricted is one order of magnitude less than that of GCL which is free. The reason is that sanction has restricted the expanse of bentonite in the thickness direction. In addition, the time when seepage reached stable state through GCL which is restricted is shorter than that through GCL which is free.

Characteristics of self-healing of GCL are mainly dependent on the characteristics and thickness of bentonite. The better dilatability and thicker thickness of bentonites, the characteristic of healing itself of GCL is better. In addition, processing technics can also affect characteristics of self-healing of GCL. When the fluidity of hydrated bentonite of GCL is better, the speed of bentonite moving to flaw is faster; the initial stage of self-healing is shorter. Processing technology of GCL will affect the fluidity of bentonite, it will affect characteristics of self-healing of GCL.

The flaws are in the center of the samples in the test, so hydrated bentonites will flow toward the flaw. The thickness is thinner than those of GCL of non-defective, which affects the permeability coefficient further.

CONCLUSIONS

1) The decrease of permeability coefficient of flaw sample mainly occurs in the inceptive 2 days of test;
2) The variety between permeability coefficient and different flaw is similar in each stage of time;
3) When size of flaw is between 0.002 m and 0.004 m, permeability coefficient increases obviously;
4) Permeability coefficient decreases when thickness is restricted.

Actually, punctured flaw is quite small relative to the whole GCL sample, and the flaw just influences partial area around the hole. So that radius of influence of flaw with a certain area needs to be tested and verified. If the radius is greater than 0.1 m, the characteristics of self-healing of GCL are better than those in the test.

REFERENCES

Bouazza A (2002) Geosynthetic Clay Liners. Geotexiles and Geomembranes 20:3-17

Lake CB, Rowe RK (2000) Swelling Characteristics of Needlepunched Thermally Treated GCLs. Geotexiles and Geomembranes 18:77-101

Petrov RJ, Rowe RK (1994) Geosynthetic Clay Liner(GCL)—Chemical Compatibility by Hydraulic Conductivity Testing and Facters Impacting its Permance. Canadian Geotechnical J 34:863-885

Ruhl JL, Daniel DE (1997) Gesynthetic Clay Liners Permeated with Chemical Solutions and Leachates, J. of Geoth and Geoenvior. Eng., ASCE 123: 683-695

DEVELOPMENT AND IMPORTANCE OF TESTING AND SPECIFICATION OF GEOSYNTHETICS

J. Zhang[1]

ABSTACT: Geosynthetics industry is nothing short of excitement during the past three decades or so. Geosynthetics are now widely used on geotechnical, environmental, transportation, hydraulics, and other areas. The success can be largely attributed to the development of geosynthetic testing and specification and their standardization, which provide necessary material parameters and guidelines for the design and construction. Aside with this success, numerous failures were observed with geosynthetics and geosynthetics-related structures during the development course as well. A large number of these failures are associated with inappropriate use of material properties, the disagreement between practice and specifications, or lack/ignorance of material testing and specifications. This paper will discuss both the development and importance of testing and specification on geosynthetics.

KEYWORDS: Geosynthetics, testing, specification

INTRODUCTION

The last three decades have seen dramatic development in the geosynthetics industry. Innovation, standardization of testing and specification of geosynthetics have played and continue to play the critical role for the growth. The innovation represents the state-of-art and stands at the forefront of the development. The transition into state-of-practice through recognized testing and specification assures the realization of the development. From the point of view of a geotechnical engineer, it is imperative to obtain reliable material parameters and guidelines for adequate design and construction. Apparently, standardized testing is critical in selecting the proper geosynthetics material and providing basis for specifications. Currently, there are readily available testing methods for all geosynthetic products (i.e., geotextile, geomembrane, geogrid, geonet, GCL, geocomposite, and sometimes geopipe due to its similarity in material and function with geosynthetics) in all the functions (i.e., separation, reinforcement, drainage, filtration, and barrier). A number of guidelines and specifications on specific geosynthetics and their application were postulated by different regulators and research institutes. For a given application, project-specific material and installation specifications should be determined based on the guidelines. Thanks to these guidelines and specifications, only less than 0.1% of the number of the structures using geosynthetics experienced significant failures (Giroud 2005). For failed structures that have used geosynthetics, it was found that a major cause is that the specifications were not strictly followed. In order to achieve higher efficiency and accommodate the continual geosynthetics innovation, the existing testing, guidelines and specifications are subject to frequent reviews and updates.

DEVELOPMENT OF GEOSYNTHETICS TESTING

One way of tracing the development of geosynthetics testing is by reviewing the creation and growth of geosynthetics committee D35 affiliated with American Society of Testing and Materials (ASTM), whose standards are widely used around the globe.

As the earliest member in the geosynthetics family, geotextile took the pioneer role on testing and standardization. In 1977, the first meeting towards the standardization of geosynthetics was held in New York City. The discussion led to the formation of a subcommittee on geotextile (then named “filter fabrics”) under ASTM Textile Committee (D13) the following year. The true meaning of “geo-textile” was achieved when the geotechnical engineering community was involved in the standardization process. In 1980, ASTM Soil and Rock Committee (D18) and D13 formed a joint subcommittee D13.61/D18.19 known as Geotextiles and Related Products. The subcommittee became a full committee (D35) in 1984. Five years later, D35 changed its name to Committee on Geosynthetics. The Committee

[1] Ph.D, geotechnical engineer, The Shaw Group Inc., USA. Email: jingyu.zhang@shawgrp.com

on Geosynthetics consists of six technical subcommittees and five administrative subcommittees. The six technical subcommittees focus on the subjects of: mechanical properties (D35.01), endurance properties (D35.02), permeability properties (D35.03), GCL (D35.04), geosynthetic erosion control (D35.05), and geomembranes (D35.10). The first standard was approved and published in 1984, which was D4354, and named the "Practice for Sampling of Geotextiles for Testing". The current name is broadened to "Standard Practice for Sampling of Geosynthetics for Testing" with the last revision in 2004. Currently, there are 118 standards on geosynthetics (19 on mechanical properties, 20 endurance properties, 23 on permeability properties, 14 on GCL, 7 on geosynthetic erosion control, and 35 on geomembrane) published in the volume of 04.13 in ASTM book. Fig. 1 shows the growth of the approved and published standards by Committee D35 since its founding.

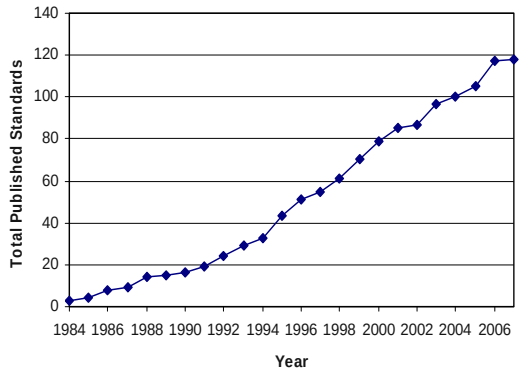

Fig. 1 The growth of the approved and published standards collected in ASTM D35

The wide-acceptance of these standards is based on the process by which they are developed. The approval of the standards is an agreement of all the involved parties: geosynthetics manufacturers and distributors, geotechnical engineers, government agencies, and researchers and academe. All the approved standards are subject frequent revisions.

Other than ASTM, the International Organization for Standards (ISO) is also very influential in the process of standardization. There are 26 standards on geosynthetics included by ISO. The testing standards from the ASTM and ISO are often equivalent. In order to avoid further duplication of efforts in standards development, the two committees, i.e., ISO/TC221 and ASTM D35, agreed to work together in 2002. There are a number of other organizations that have standards on geosynthetics testing methods, such as, British Standards Institute in UK, French Standards Organization in France, DIN Deutsches Institue für Normung e.V. in Germany, Australian Standards in Austria, to name a few.

SPECIFICATION OF GEOSYNTHETICS

For quality and convenience of practice, generic specifications are desired. The availability of standard testing on geosynthetics makes it feasible for generic specifications and guidelines, which are usually stipulated by government agencies, regulators, or research institutes. Generic specifications provide the criteria for material selection, design and installation/construction. AASHTO M288 Geotextile Specification will be used as an example for illustration below.

AASHTO M288 was a generic specification for geotextile application on drainage, separation, stabilization, silt fence, and prevention of reflective cracking in flexible pavement overlays. Firstly, three classes of survivability have been categorized based on installation conditions, and then the required geotextile properties will be set forth for the targeted function. For example, for the application of infiltration under severe survivability condition (Class 1), the specification is listed in the following table.

Table 1 AASHTO M288 infiltration geotextile property requirements

Property	Test method	Unit	Requirement		
			Percent in-situ soil passing 0.075 mm		
			<15	15—50	>50
Geotextile class	--	--	Class 1		
Permittivity	ASTM D4491	per sec	0.5	0.2	0.1
Apparent opening size	ASTM D4751	mm	0.43 MARV	0.25 MARV	0.22 MARV
Ultraviolet stability (retained strength)	ASTM D4355	%	50% after 500 hours of exposure		

This specification assures the proper function of the selected geotextile given a certain percent passing a 0.075mm sieve. For example, the required apparent opening size allows adequate flow of liquid as well as retains the soil particles from its upstream side.

The selected example is generic and simple to follow. It must be noted that generic specification only set forth the minimum required properties, and may not be adequate. Often, additional tests and more restrictive values may be necessary for a particular condition. The specification for a commercial geosynthetic is usually made available by its manufacturer.

IMPORTANCE OF TESTING AND SPECIFICATION

Performance inadequacy and failures of geosynthetics were observed for all their functions, especially for drainage, barrier, and reinforcement. A good example to demonstrate both the success and failure of geosynthetics is landfills. A study on the failures performed by Rudolph et al. (2002) indicates that most failures were caused by inadequate design and construction, which can be avoided by following strict specifications on both material selection and installation.

The following example will illustrate the importance of the specifications. For a typical landfill cap with 3H: 1V slope, a slope length (L) of 126 ft (38 m) between geocomposite daylights, and cover soil thickness (t) of 2 ft (0.6 m), the factor of safety (FS) was calculated under different interface and internal friction angles under different loading conditions.

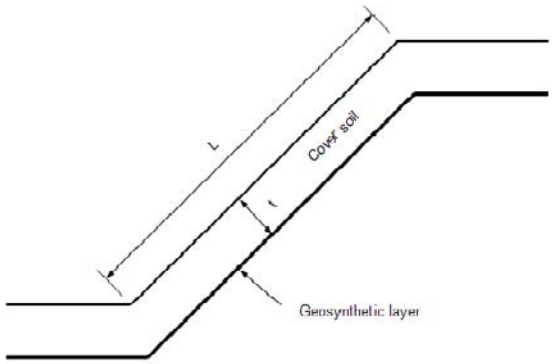

Fig. 2 Typical landfill cap system for the calculation example

In the given cap veneer, the design driving forces are gravity, equipment force during construction, and seismic load if the site is located in an earthquake-hazardous area (assume peak ground acceleration, i.e., PGA=0.2 g in this example). The generic specification assures that the design and construction lead to a capping system that generates no seepage in the cover soil, i.e., water head build-up is completely contained in the thickness of the selected geocomposite drainage layer. Table 2 summarized the calculated FS assuming different minimum interface friction angles under various loading conditions and drained condition.

Table 2 Sensitivity study on veneer stability of typical landfill cap under drained conditions (see example)

Weakest friction angle	FS at Different Loading Conditions			
	gravity	equipment pushing up	equipment pushing down	seismic (PGA= 0.2 g)
30^o	1.79	1.78	1.63	1.33
26^o	1.53	1.52	1.38	1.14
24^o	1.4	1.39	1.27	1.04
22^o	1.27	1.26	1.16	0.95
20^o	1.16	1.15	1.05	0.86
Target FS	1.4	1.3	1.3	1

The results above show that a minimum interfacial friction angle of 26^o is generally adequate for the veneer stability. However, the requirement could be lowered to 24^o if it is specified that equipment pushes the soil upslope during the construction. This practice has been widely-recognized and included in specification thanks to the work by Koerner and Soong (2005).

One of the critical components of the capping system is the performance of the drainage system. Inadequate design or improper construction could result in saturation of cover soil and seepage during a major storm event. Table 3 shows the difference made by the addition of seepage in the capping system stability. A minimum interfacial friction angle of 30^o is required for the desired FS if seepage induced in half of the cover soil thickness; and even higher value of interfacial friction angle would be required for the fully saturated case. If the geocomposite becomes clogged or under designed for a major storm, the cover soil could be saturated quickly, and seepage in the full thickness of the cover soil would occur. As a result, a FS could be decreased to less than unit indicating the failure along the geosynthetic layer. Furthermore, considering that the geosynthetics typically have the interface friction angles less than 30^o, the capping system will be jeopardized even if the material with highest interface friction angle is utilized.

Table 3 Sensitivity study on veneer stability of typical landfill cap under undrained conditions (see example)

Weakest friction angle	FS at under seepage load	
	half seepage	full seepage
30^o	1.3	0.87
26^o	1.1	0.74
24^o	1.01	0.68
22^o	0.93	0.62
20^o	0.84	0.57
Target FS	1.3	1.3

The example shows that if the specification is not strictly followed, e.g., the geocomposite does not function sufficiently or construction equipment pushes cover soil downslope, the FS would be decreased significantly.

Other concerns on specifications include the proper testing of the geosynthetics properties. The design and construction would be meaningless if the material properties were inaccurate. It should be noted that the test results published by geosynthetics manufacturers are generally index values, which should never be used for design purpose. The testing should be performed using product-specific materials under project-specific conditions by an accredited laboratory.

SUMMARY

The fast growth of geosynthetics in the past three decades would not occur without the corresponding establishment of standardized testing and specifications. ASTM Geosynthetics Committee D35 played a significant role in standardizing the testing methods. 118 standards are approved and published by D35 to date. Readily available specifications addressing specific geosynthetics and their applications were stipulated by government agencies and research institutes. Despite the great success, numerous failures were reported on structures using geosynthetics. Failures to strictly follow the testing, design, and installation specifications are considered to be the main cause. A calculation of typical veneer stability analysis showed the importance of the specification.

REFERENCES

Annual Book of ASTM Standards, Soil and Rock(II): Geosynthetics (2002) 04.09: 1005-1399

Jamie R, Robert MK (2006) Status of Adoption and Use of the AASHTO M288 Geotextile Specification Within U.S. State Department of Transportation. GRI Report No. 31

Rudolph B, Beth AG, David ED, Robert MK, Steve D (2002) Technical Guidance for RCRA/CERCLA Final Cover. USEPA

David S (2004) A Look Back at Geosynthetic Testing and Specification Standardization—A Celebration of 20 Years for ASTM International Committee D35 on Geosynthetics. Proceedings of the Symposium Honoring the Research Achievements of Professor R.M.Koerner. Drexel University, Philadelphia: 172-183

Gregory NR (2004) Geosynthetic Research Institute (GRI)—The Beginning. Proceedings of the Symposium Honoring the Research Achievements of Professor R.M.Koerner, Drexel University, Philadelphia: 149-157

Stark TD, Arellano D, Evans WD, Wilson VL, Gonda JM (1998) Unreinforced Geosynthetic Clay Liner Case History. Geosynthetics International 5(5): 521-544

Gross BA, Bonaparte R, Giroud JP (2002) Waste Containment Systems: Problems and Lessons Learned. Appendix F in Assessment and Recommendations for Optimal Performance of Waste Containment Systems. USEPA

Koerner RM, Soong TY (2005) Analysis and Design of Veneer Cover Soils, Geosynthetics International

Giroud JP (2005) Geosynthetics Engineering: Successes, Failures, and Lessons Learned. The Vienna Terzaghi Lecture. The Proceedings of 5 Osterreichische Geotechniktagung

Lara P, Elizabeth P (1998) Insurance-Construction Risk Management. GFR 22(7)

PERMEABILITY TEST AND SHEAR TEST ON GEOSYNTHETIC CLAY LINER

Y.X. Jie[1], Z.B. Fu[2], T. Peng[3] and G.X. Li[4]

ABSTRACT: Being nearly impervious, geosynthetic clay liner (GCL) can be used as an alternative of conventional compacted clay liner in many cases. According to the requirement of waterproof protection of Yungang Grotto, the authors conducted permeability test and shear test on GCL. A simple method was proposed to investigate the seepage coefficient of GCL, which can also be used to estimate the permeability of the composite comprising GCL and the surrounding soil. Shear test was made with a slab, friction angle of the interface between GCL and soil was measured.

KEYWORDS: geosynthetic clay liner (GCL), permeability, seepage coefficient, shear test, Yungang Grotto

INTRODUCTION

Geosynthetic clay liner (GCL) is a factory-made clay liner that consists of a layer of bentonite sandwiched between two geotextiles that are held together by needle punching, stitching, or adhesives. GCL has attracted considerable recent attention with respect to their use in geotechnical and geoenvironmental applications (Meer et al. 2007; Rowe et al. 2006; Wang 2002; Maubeuge et al. 2000; Fox et al. 2000; Boardman et al. 1996).

In order to protect the relic at Yungang Grotto, GCL was designed to be placed on the peak of the Grotto. To estimate the permeability and stability behavior of the GCL and the surrounding soil, the authors made a simple apparatus to conduct permeability test on GCL placed in surrounding soil. The authors also conducted shear test on GCL with a slab and a compass.

PERMEABILITY TEST

A schematic of the permeability test apparatus is given in Fig. 1. The cylinder is 28 cm in diameter and 65cm in height. A filter paper was placed on the bottom of the cylinder. On the filter was a sand layer. The thickness of the layer is 5 cm~14 cm. A clipped round GCL specimen was placed on the sand layer. Bentonite powder was filled in the gap between GCL and the cylinder. It was found that the swelling of the bentonite can well close the gap. Another 25 cm~30 cm thick sand layer was then put on the GCL as weighted layer.

After the sample preparation was finished, water was slowly immited into the cylinder till it reached the top. The cylinder was then sealed with the cover. The change of water head and seepage discharge could be measured with the burette, and the combined seepage coefficient of the composite was obtained. Seepage coefficient of GCL could be calculated after we measured the thickness of the saturated GCL and the seepage coefficient of the sand.

By this falling head test, the combined seepage coefficient k is (Chen et al. 1994; Wu 1976)

$$k = \frac{aL}{A(t_2 - t_1)} \ln \frac{h_1}{h_2} \tag{1}$$

where a and A are the cross-sectional area of the burette and the cylinder, respectively; L is the thickness of the combined layer; h_1 and h_2 are the water head at time $t_1$and t_2, respectively. For seepage through soil layers, the combined seepage coefficient k can be

$$k = \frac{L}{\frac{L_1}{k_1} + \frac{L_2}{k_2}} \tag{2}$$

where L_1 is the thickness of sand layer, L_2 is the thickness of GCL, $L = L_1 + L_2$, k_1 and k_2 are the seepage coefficients of the sand and the GCL, respectively. Then we can get the seepage coefficient of the GCL as follows:

$$k_2 = \frac{L_2}{L - \frac{k}{k_1} L_1} \times k \tag{3}$$

[1] Associate professor, Department of Hydraulic Engineering, Tsinghua University, CHINA. Email: jieyx@tsinghua.edu.cn
[2] Engineering, China Institute of Geotechnical Investigation and Suverying, CHINA
[3] Associate Professor, China Institute of Geotechnical Investigation and Suverying, CHINA
[4] Professor, Department of Hydraulic Engineering, Tsinghua University, CHINA. Email: ligx@tsinghua.edu.cn

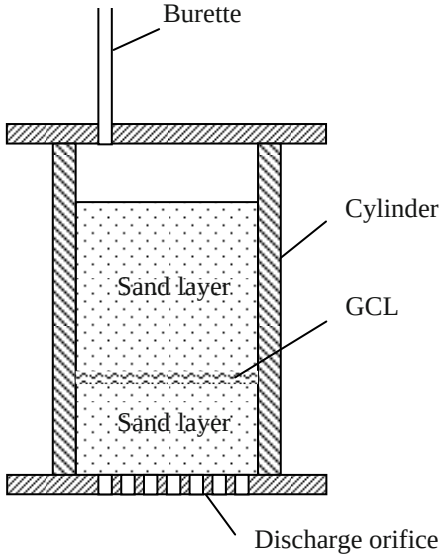

Fig. 1 Permeability test apparatus

The seepage coefficient of the sand layer used in the test was 2.41×10^{-3} cm/s (at 20℃). Test results of the seepage coefficient of GCL are presented in Table 1. Variation of seepage coefficient vs. time is shown in Fig. 2. Each test lasted for 24—43 days. GCL became a mud cake after the test (see Fig. 3)

Table 1 Test results of the seepage coefficient of GCL

Test	Specimen of GCL	Seepage coefficient (10^{-9} cm/s)	
		(1)	(2)
A1		5.6	6.1
A2		4.0	4.4
A3	Original	0.55	0.60
A4		1.67	1.78
B1		2.3	2.6
B2		0.99	1.06
A3P	Repeated	0.30	0.31
B1P	Repeated	2.64	2.75

Note:

(1) The seepage coefficients in column 1 were calculated from Eq. 3 after the combined seepage coefficients were obtained from Eq. 1. The coefficients in column 2 were directly calculated from Eq. 1 by assuming the seepage coefficient of sand being $k_1=\infty$;

(2) Test A3P used the repeated GCL specimen of A3 after test A3 finished and the specimen was air-dried for 24 days. The GCL used in B1P was the repeated specimen of B1 after being air-dried for 24days, too.

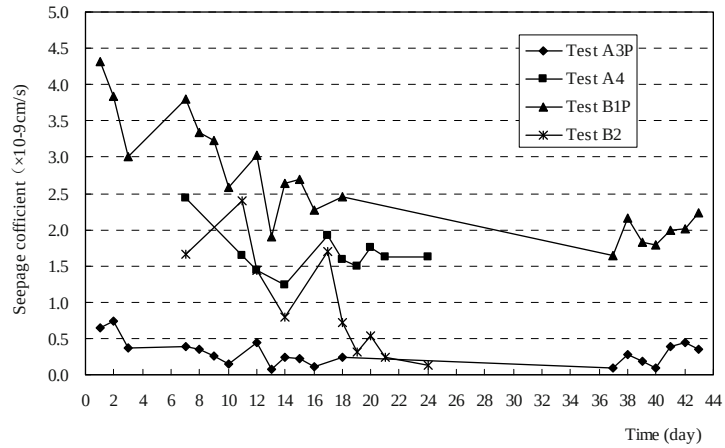

Fig. 2 Variation of seepage coefficient vs. time

(a) Side A (b) Side B

Fig. 3 GCL specimen after test

SHEAR TEST

Shear test was conducted to measure the shear strength of the interface between GCL and the soil from Yungang Grotto. The maximum dry density of the soil was 1.98 g/cm^3, and the optimum water content was 9.2%. the test apparatus included a wood slab of 100 cm ×90 cm×5 cm, an aluminum alloy frame of 60 cm× 60cm in area, a lifting chain, and a compass (error < 1°) to measure the slope angle when the soil begin to slide (see Fig. 4).

Fig. 4 Shear test apparatus

The procedure of the shear test was as follows:

(1) Placed the slab on the ground;

(2) Stapled the GCL on the slab;

(3) Placed the aluminum alloy frame on the GCL;

(4) Filled the soil in the frame and compacted to specified density;

(5) Lifted one side of the slab slowly till slide occurred. Then we measured the slope angle at different place of the slab. The average of the angle was thought to be the friction angle between GCL and the soil.

A block was stapled on one end of the slab to prevent the frame from destroy the floor. An iron pad was placed between the block and the frame. There was 2 cm wide spacing between the pad and the frame. So we could do two tests and got two angles with one specimen. Firstly we lifted the slab to make the soil in the frame slide for 2 cm. Then took off the pad after leveled the slab, and made another lift.

The specimen was prepared with three thicknesses (20 cm, 40 cm, and 60 cm) of the soil layer. The dry density of the soil was ρ_d=1.63 g/cm^3. The test results were shown in Table 2.

The test results demonstrate that the friction angle of the interface between GCL and the saturated soil is almost the same with that of the dry one. One of the reasons may be the “false” cohesion at the interface induced by the negative pore water pressure. The friction angle of the interface may decrease if the “false” cohesion is removed. So the stability of the slope changes little if the rainfall at Yungang Grotto just be moist the soil, while the stability may decline if seepage flow occurred in the soil along the slope.

Table 2 Results of shear tests

Test	Layer thickness (cm)	Water content	Slope angle at sliding (°)	
			1st	2nd
gBb-20	20		44.5	37.5
gBb-40	40		43.5	39.5
gBb-60	60		42.0	/
gBa-20	20		41.5	36.5
gBa-40	40		42.5	43.0
gBa-60	60	Air-dry	42.0	/
gJb-20	20	w=3.07%	42.5	37.5
gJb-40	40		44.5	42.0
gJb-60	60		43.0	/
gJa-20	20		44.0	37.5
gJa-40	40		44.5	/
gJa-60	60		40.5	/
sBa-40	40		44.5	45.5
sBb-40	40	Saturated	29	38
sJb-40	40		33.5	/
sJa-40	40		36	39

Note: “g” and “s” denote the soil is in air-dried and in saturated, respectively; “a” and “b” denote side A and side B of the GCL, respectively (see Fig. 3).

CONCLUSIONS

(1) Permeability test proposed in this paper is suitable for evaluating seepage coefficient of GCL. If the sand layer is replaced by the soil in-situ, one can measure the combined permeability of GCL and surrounding soil.

(2) The soil layer on the GCL must have certain thickness and be well compacted to constrain the dilation of the bentonite.

(3) Seepage coefficient of GCL may vary during the test. Generally 14 days are necessary for the measurement.

(4) The friction angle of the interface between GCL and the soil of Yungang Grotto is bigger than 36°, if no seepage flow occurred in the soil along the slope.

REFERENCES

Boardman BT, Daniel DE (1996) Hydraulic conductivity of desiccated geosynthetic clay liners. J. Geotech. Engrg. ASCE 122(3):204-208

Chen ZY, Zhou JX, Wang HJ (1994) Soil mechanics. Beijing: Tsinghua University Press

Fox PJ, Battista DJ, Mast DG (2000) Hydraulic performance of geosynthetic clay liners under gravel cover soils. Geotextiles and Geomembranes 18:179-201

Maubeuge KP, Witte J, Heibaum M (2000) Installation and monitoring of a geosynthetic clay liner as a canal liner in a major waterway. Geotextiles and Geomembranes 18:263-271

Meer SR, Benson CH (2007) Hydraulic conductivity of geosynthetic clay liners exhumed from landfill final covers. J. Geotech. Geoenviron. Engrg. ASCE 133(5):550-563

Rowe RK, Mukunoki T, Bathurst RJ (2006) Compatibility with Jet A-1 of a GCL subjected to freeze–thaw cycles. J. Geotech. Geoenviron. Engrg. ASCE 132(12):1526-1537

Wang Z (2002) Application and study of geosynthetics overseas. Hongkong: Modern Knowledge Press

Wu TH (1976) Soil mechanics (second edition). Boston: Allyn and Bacon, Inc.

LONG-TERM PROTECTION EFFICIENCY OF NONWOVEN POLYPROPYLENE GEOTEXTILES

D.K. Atmatzidis[1], D.A. Chrysikos[2], T.N. Blantzoukas[3] and A.T. Kondyli[4]

ABSTRACT: European Standard EN ISO 13719:2002 specifies an index test used to determine the efficiency with which a geotextile will protect a geosynthetic barrier against the mechanical long term effects of static point loads. Laboratory tests were conducted on 16 nonwoven needle-punched polypropylene geotextiles (mass per unit area 202 g/m^2—1,406 g/m^2, thickness 1.63 mm—10.06 mm) representing six different manufacturers and made of staple fibers or continuous filament. Based on local strain measurements, the protection efficiency values of the geotextiles were found to range between 25.0×10^3 and 66.7×10^3 kN/m^2. Good linear correlations (R^2=0.85—0.88) were obtained between protection efficiency and mass per unit area, average tensile strength and static puncture strength. Geomembrane protection under high external loads (1200 kPa) requires use of relatively heavy geotextiles (over 1,500 g/m^2). Selection of an appropriate geotextile depends on the anticipated magnitude of the external load and on the specified allowable geomembrane deformation.

KEYWORDS: geotextiles, geomembranes, protection efficiency, long-term loads

INTRODUCTION

Geomembranes are used as liners or barriers in order to control fluid or gas migration in a project, structure or system. Geomembranes may be damaged prior or during installation, during load application and during the life-time of a project. When a geomembrane is placed at the base of a fill of significant height, protection against the mechanical long term effects of static loads is necessary. Protection can be effectively provided by a geotextile in contact with the geomembrane on the side where the static loads are to be applied. Previous laboratory investigations (i.e. Laine et al. 1989; Motan et al. 1993; Saathoff et al. 1994; Brummermann et al. 1994; Zanzinger 1996; Zanzinger and Gartung 1998; Jones et al. 1999; Gallagher et al. 1999) utilized specially constructed equipment and applied static point loads on the geotextile-geomembrane system for significant time periods through natural aggregate or through geometrically specified elements.

Based on available information, it can be observed that:

(a) Nonwoven, needle-punched geotextiles can provide the required geomembrane protection.

(b) Some national standards require the use of geotextiles with very high mass per unit area of 2000 g/m^2 to 4000 g/m^2 (Heerten 1993; Seeger and Muller 1996) while other standards suggest lower values in the range of 350 g/m^2 to 550 g/m^2 (Corbet and Peters 1998).

(c) Field observations (Reddy et al. 1996, Reddy and Saichek 1998) indicate good protection with even lighter geotextiles (270 g/m^2).

(d) In general, the protection efficiency of nonwoven geotextiles increases with increasing mass per unit area and increasing mechanical properties. However, significant differences in the protection efficiency have been observed (Jones et al. 1999) between geotextiles with the same mass per unit area.

(e) Previous investigations tested a small number of geotextiles (up to four per reported investigation), employed different testing equipment and applied different testing procedures. Accordingly, a mostly qualitative synthesis of the results can be obtained.

European Standard EN ISO 13719, approved in 2002, specifies an index test to determine the efficiency with which a geotextile will protect a geomembrane against the mechanical long term effects of static point loads. The laboratory investigation reported herein is based on the application of these standard procedures in order to test a large number of geotextiles. Scope of the investigation is to supplement available data on the protection efficiency of nonwoven geotextiles and to evaluate the effect of their physical and mechanical properties.

[1] Professor, Department of Civil Engineering, University of Patras, GREECE. Email: dka@upatras.gr
[2] Lecturer, Department of Civil Engineering, University of Patras, GREECE. Email: dac@upatras.gr
[3] M.Sc. Student, Department of Civil Engineering, University of Patras, GREECE.
[4] M.Sc. Student, Department of Civil Engineering, University of Patras, GREECE.

MATERIALS AND PROCEDURES

According to EN ISO 13719, the protection efficiency test is conducted in a smooth sided steel cylinder with an internal diameter not less than 300 mm. The geotextile is placed on a soft sheet metal disc which serves to capture the geotextile deformations. The metal disc rests on a 25 mm thick rubber pad with a hardness of 50±5 Shore A. Load (300 kPa, 600 kPa and 1200 kPa) is applied through a simulated standard aggregate (20 mm diameter steel balls, 150 mm minimum depth) for 100h. The protection efficiency is calculated based on the average of the strains measured for the three largest depressions on the soft metal disc.

An overall view of the laboratory equipment used for conducting the tests reported herein is shown in Fig. 1. The steel cylinder had an internal diameter of 305 mm and a height of 300 mm. The rubber pad (Figure 2) had a hardness of 55 Shore A. The metal disc was made of lead and complied with the specifications set by the standard (testing shown in Fig. 3). Approximately 1500 steel balls were used to form a 150mm thick layer. The upper loading plate rested on a sand layer which was separated from the steel balls by a thin geotextile. Due to equipment limitations the highest applied load was 1100 kPa instead of the 1200 kPa specified by the standard. An appropriate dial gage and support device, shown in Fig. 4, was used to define the limits of the deformations and to measure vertical displacements on the lead plate.

For the purposes of the experimental investigation reported herein, geotextile specimens were taken from large size samples obtained from six different manufacturers. The size of the samples ranged from 4 m^2 to 12 m^2 with a width equal to the standard production roll width of each manufacturer. All geotextiles were nonwoven, polypropylene, needle-punched and were made of staple fibers (five manufactures) of continuous filament (one manufacturer). One geotextile series was thermally post-treated on both surfaces. All geotextiles were tested for mass per unit area (EN ISO 9864),

Fig. 1 Overall view of laboratory equipment

Fig. 2 Rubber pad hardness check

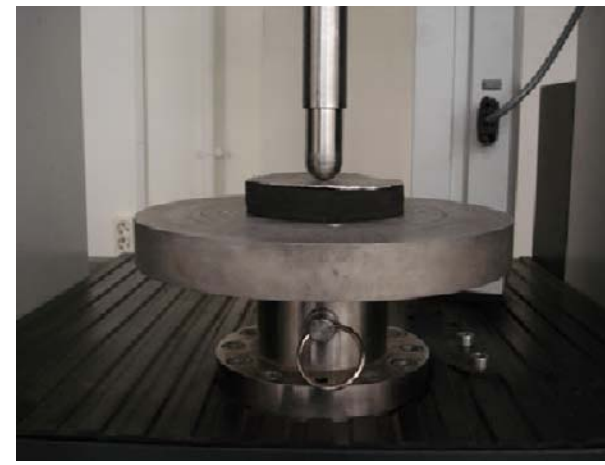

Fig. 3 Testing of lead plate

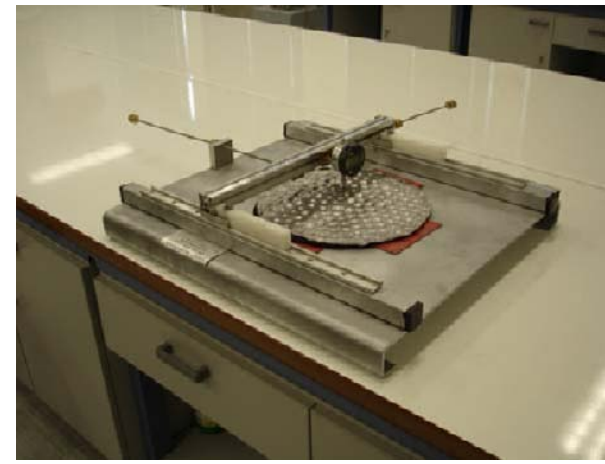

Fig. 4 Deformation measurement system

thickness (EN ISO 9863), wide-width tensile strength (EN ISO 10319) and static puncture strength (EN ISO 12236). All results are summarized in Table 1. To avoid the use of commercial names, a generic notation is used (i.e., M1) to identify manufacturer and geotextile series and letters to identify each geotextile in a series (i.e., a, b, c). All geotextiles were tested according to EN ISO 13719 to obtain protection efficiency values. To obtain base-line values, tests were also conducted without incorporating a geotextile in the apparatus.

Table 1 Geotextile properties

GTX	μ_A (g/m^2)	t (mm)	T_f (kN/m)	F_p (kN)
M2a	306.6	2.59	19.84	3.23
M2b	420.5	2.26	29.21	4.70
M2c	641.0	3.87	36.70	7.18
M4a	202.8	1.93	14.50	2.16
M4b	243.4	2.18	17.24	3.07
M4c	451.6	3.47	31.18	4.51
M6a	372.4	3.90	22.04	3.43
M6b	801.5	6.45	46.54	7.22
M6c	1406.6	7.99	85.35	16.37
M11a	814.8	6.76	32.71	4.62
M11b	1219.7	10.06	48.72	7.95
M13a	202.3	1.85	13.37	2.07
M13b	305.8	2.48	20.92	3.30
M17a	185.9	1.63	13.48	2.74
M17b	392.2	2.67	24.20	4.62
M17c	530.5	3.27	33.89	7.16

GTX: geotextile
μ_A: mass per unit area
t: thickness
T_f: average tensile strength in MD and CMD directions
F_p: static puncture (CBR) strength

RESULTS AND DISCUSSION

The average of the strains measured for the three largest depressions on the lead plate after each test were used to prepare stress-deformation graphs and obtain the index protection efficiency of each geotextile tested. Typical stress-deformation graphs are shown in Fig. 5. The required linear relationship was obtained with the constrain that the line passes through the origin of the axes in order to avoid disadvantages in terms of physical interpretation. In general, the linear correlations obtained were very good to excellent as judged by the correlation coefficient values, R^2, which ranged between 0.903 and

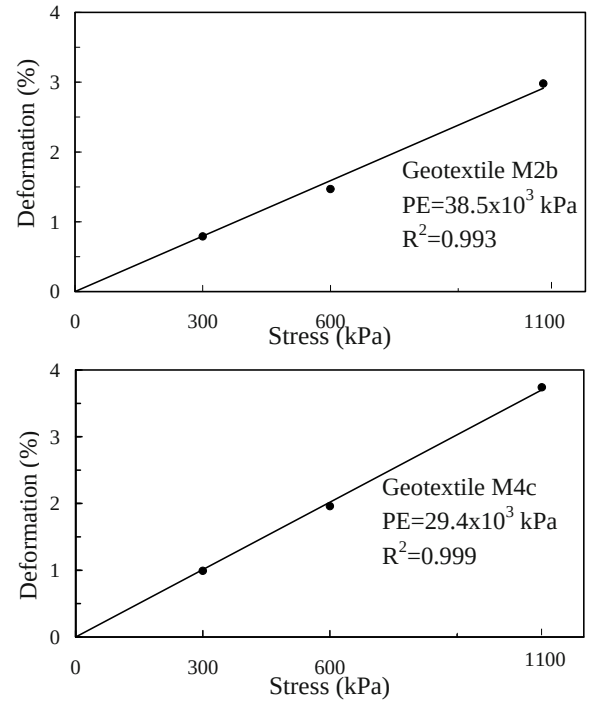

Fig. 5 Typical stress-deformation graphs

0.999. Measured deformations and computed protection efficiency are summarized in Table 2. Also presented in Table 2 are the results obtained from tests conducted without incorporating a geotextile in the apparatus and are considered as base-line values.

Table 2 Deformation and protection efficiency results

GTX	Deformation (%) for stress (kPa)			Protection efficiency ($\times 10^3$kPa)
	300	600	1100	
M2a	1.10	1.67	4.13	28.6
M2b	0.79	1.47	2.98	38.5
M2c	0.96	1.42	3.06	37.0
M4a	1.06	1.87	3.52	31.2
M4b	1.29	1.91	3.60	30.3
M4c	0.99	1.96	3.74	29.4
M6a	1.10	2.03	3.45	31.2
M6b	0.60	1.60	2.76	40.0
M6c	0.35	0.96	1.71	66.7
M11a	0.63	1.61	3.05	37.0
M11b	0.63	1.45	2.03	52.6
M13a	1.14	1.85	4.57	25.6
M13b	0.89	1.61	3.31	34.5
M17a	0.97	2.20	4.50	25.0
M17b	0.58	1.50	3.64	32.2
M17c	0.45	1.28	2.61	43.5
NoGTX	1.47	2.36	4.66	23.8

Effect of External Load

The loads applied on geomembranes are often dictated by the maximum allowable strains which are set by standards or specifications. It is frequently specified that tensile deformation under long-term loading should not exceed a value of 2%. From this perspective, it is of interest to examine the implications of the data generated during this investigation by assuming that the strains measured on the lead plate are those to be experienced by a geomembrane. Shown in Figure 6 is the range of measured deformations versus applied stress. It can be observed that, for low anticipated external load (300 kPa), all geotextiles tested provide positive protection regardless of their physical and mechanical properties. However, the degree of protection varies. If a safety factor is defined by the ratio of allowable deformation (2%) to measured deformation, then this factor has values ranging between 1.55 and 5.71. Similarly, for intermediate anticipated external load (600 kPa), most of the geotextiles tested provide positive protection with a safety factor between 1.02 and 2.08 while two geotextiles fail to provide the required protection. At high external loads (1100 kPa), only one of the geotextiles tested provided some protection with a safety factor of 1.17 while for the rest of the geotextiles tested the safety factor ranges between 0.98 and 0.44.

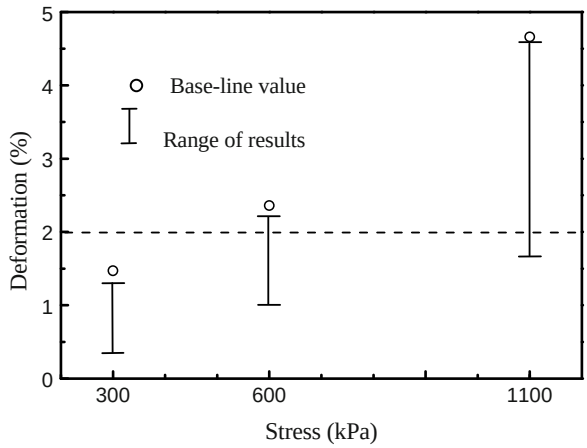

Fig. 6 Effect of applied load on deformation

The effect of geotextile mass per unit area on the measured deformations is shown in Fig. 7. It can be observed that, for the selected limiting deformation value of 2%, a relatively heavy geotextile with mass per unit area over 1500 g/m^2 should be employed in order to provide adequate protection if the external load is high (1100 kPa). However, for intermediate and low external loads (600kPa and 300 kPa) protection can be provided by geotextiles with mass per unit area as low as 200 g/m^2 depending on the specified degree of protection.

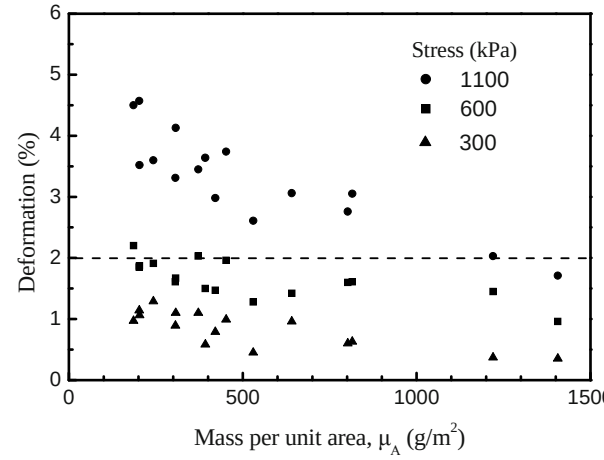

Fig. 7 Effect of geotextile mass per unit area on deformation

Correlations with Geotextile Properties

As a first order approximation, a linear relationship was used to obtain correlations between protection efficiency and geotextile physical and mechanical properties. The results obtained are shown in Fig. 8 and 9. It can be observed that the correlation with geotextile mass per unit area is qualitatively superior to the correlation with geotextile thickness. Correlations with major mechanical properties (tensile strength and static puncture strength) are, for all practical purposes, equivalent to the correlation with mass per unit area. This latter observation should be anticipated since excellent correlations between mass per unit area and mechanical properties have been documented for nonwoven polypropylene geotextiles (Atmatzidis et al. 2004). Finally, it should be noted that the experimentally obtained base-line value (23.8×10^3 kPa) is in good agreement with the values obtained by the linear correlations.

Using the overall correlation with mass per unit area, the expected protection efficiency was computed for each geotextile and the results were compared with the measured value. The resulting error ranged between ±10% and ±20% for 56% and 100% of the geotextiles, respectively. Accordingly, the linear relationship has an acceptable overall predictive capability. However, it should be pointed out that significant differences may be observed if comparisons of protection efficiency are made between individual geotextiles with similar mass per unit area (or similar mechanical properties). Such differences are in the range of up to 6×10^3 kPa and yield a ratio between the protection efficiencies of similar geotextiles (same mass and/or mechanical properties) in the range of up to 1.2.

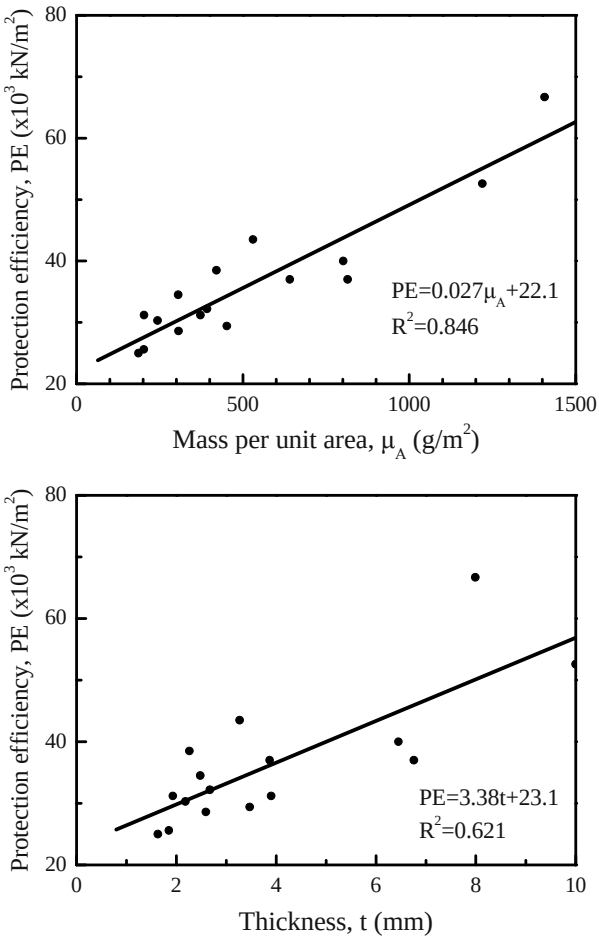

Fig. 8 Correlations of protection efficiency with geotextile physical properties

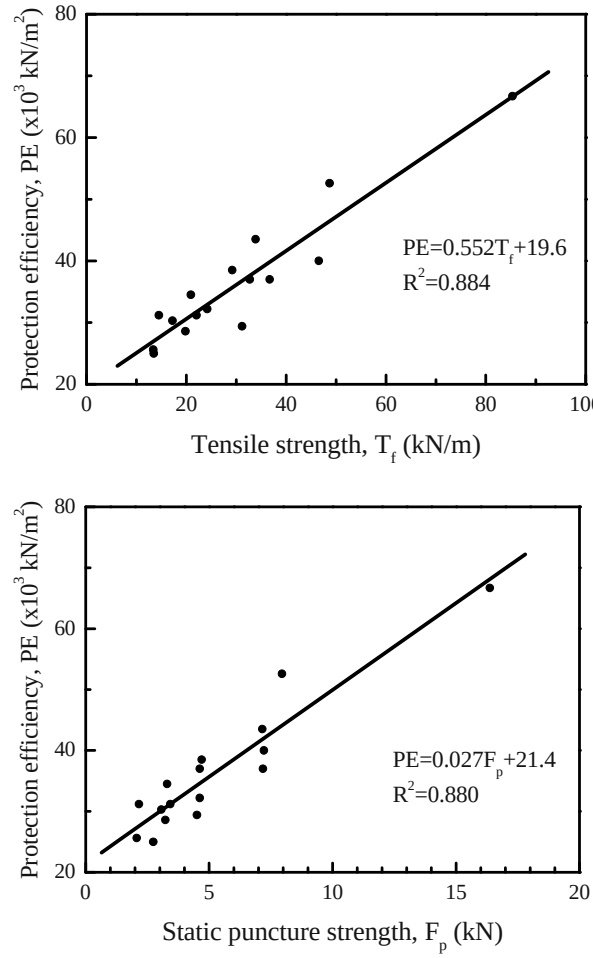

Fig. 9 Correlations of protection efficiency with geotextile mechanical properties

CONCLUSIONS

Based on the results obtained and the observations made during the limited experimental investigation reported herein, the following conclusions may be advanced with respect to the long term protection efficiency provided by nonwoven polypropylene geotextiles:

1. A good linear correlation exists between physical (mass per unit area) and mechanical (average tensile strength, static puncture strength) properties of nonwoven geotextiles and the protection they provide to other geosynthetics (i.e., geomembranes) against the long term effects of static point loads.

2. The protection efficiency index values obtained for geotextiles with similar physical and/or mechanical properties may differ by up to 20%.

3. Selection of a geotextile for long term protection depends on the magnitude of the anticipated external load and on the maximum allowable deformation of the protected geosynthetic.

ACKNOWLEDGEMENTS

The following manufacturers provided large-size samples: Bonar, Geofabrics, Naue Fasertechnik, Polyfelt, Synthetic Industries, TC Mirafi.

REFERENCES

Atmatzidis DK, Chrysikos DA, Missirlis EG (2004) Correlations between nonwoven polypropylene geotextile mechanical properties. Proc. 3rd European Geosynthetics Conference, Munich, Germany II: 587-592

Brummermann K, Blumel W, Stoewahse C (1994) Protection layers for geomembranes: effectiveness and testing procedures. Proc. 5th International Conference on Geotextiles, Geomembranes and Related Products, Singapore 3: 1003-1006

Corbet SP, Peters M (1996) First Germany/USA geomembrane workshop. Geotextiles and Geomembranes 14 (12): 647-726

Heerten G (1994) Geotextile and/or GCL protection systems for geomembranes. Geosynthetic Liner Systems: Innovations, Concerns and Designs, R.M. Koerner and RF Wilson-Fahmy, ed, IFAI, Philadelphia, PA, USA: 115-167

Gallagher EM, Darbyshire W, Warwick RG (1999) Performance testing of landfill geoprotectors: background, critique, development, and current UK practice. Geosynthetics International 6(4): 283-301

Jones DRV, Shercliff DA, Dixon N (2000) Difficulties associated with the specification of protection geotextiles using only unit weight. Proc. 2nd European Geosynthetics Conference, Bologna, Italy 2: 551-555

Laine DL, Miklas MP, Parr CH (1989) Loading point puncturability analysis of geosynthetic liner materials, Proc. Geosynthetics '89 Conference, San Diego, USA 2: 478-488

Motan ES, Reed LS, Lundell CM (1993) Geomembrane protection by nonwoven geotextiles. Geosynthetics '93 Conference, Vancouver, Canada: 887-900

Reddy KR, Saichek RE (1998) Performance of protective cover systems for landfill geomembrane liners under long-term MSW loading. Geosynthetics International 5(3): 287-307

Saathoff F, Sehrbrock U (1994) Indicators for selection of protection layers for geomembranes. Proc. 5th International Conference on Geotextiles, Geomembranes and Related Products, Singapore 3: 1019-1022

Seeger S, Muller W (1996) Requirements and testing of protective layer systems for geomembranes. Geotextiles and Geomembranes, Vol.14, No.7/8, pp. 365-376

Zanzinger H (1996) Efficiency of geosynthetic protection layers for geomembrane liners: performance in a large-scale model test. Geosynthetics International 6(4): 303-317

Zanzinger H, Gartung E (1998) Efficiency of puncture protection layers. Proc. 6th International Conference on Geosynthetics, Atlanta, Georgia, USA I: 285-288

Proceedings of the 4th Asian Regional Conference on Geosynthetics
June 17 - 20, 2008 Shanghai, China

STUDY ON CREEP STRENGTH TEST OF HIGH-STRENGTH GEOGRID

Q.R. Yan[1], W.D. Deng[2] and C.Z. Deng[3]

ABSTRACT: In this paper, indoor creep test under unconfined conditions was conducted for two typical types of high-strength geogrid, one of which was applied to practical roadbed engineering, where creep observation is taken for a continuous year. Test result shows that creep rate under unconfined conditions is almost 2 times of that under confined conditions if the high-strength geogrid are approximately under load level. At last, the paper proposed some suggestions on value taking range of creep strength reduction factor for high-strength geogrid.

KEYWORDS: creep, test, high-strength geogrid

INTRODUCTION

Geogrid creep is the key factor to determine whether reinforced soil could be used for construction of permanent engineering. Creep features influence long-time feature of reinforced structure, and creep or stress release may lead to change of internal stress status of the reinforced structure, which may result in unsteadiness or excessive deformation. Therefore, prediction of long-term creep for geogrid reinforced materials is critical to safety and economy of structures.

Creep features of geogrid are related to many factors such as category, temperature, damage, load and unconfined conditions of reinforced materials. That is why creep is so complicated. Studies show that creep of geogrid greatly influences reduction factor of tensile strength. For example, in AASHTO Standards 1996, reduction factor of creep strength for polypropylene and polythene materials reaches 4.0 — 5.0 and 2.5 — 5.0 respectively when geogrid synthetic materials are used for reinforcement. Excessive reduction factor and inconsistent cognition of reduction factor restrict application of geogrid in reinforced soil structures. As a result, this technical indicator is rarely used in reinforced soil structure design.

With improvement of manufacturing technique and quality of raw materials, tensile strength of geogrid is more and more strong. So creep reduction factor is expected to be applied in design of reinforced structures. From indoor creep test for typical TGDG 130 single polypropylene geogrid and CATISG70-70 biaxial polythene geogrid and from one-year actual creep measurement for TGDG130 geogrid on test section of Guangdong-Tianjin-Shanwei Expressway, we make some useful conclusions.

STYLE BASIC FEATURES OF TEST MATERIALS

According to tensile test, limit tensile strength for TGDG130 uni-axial polypropylene geogrid is 146 kN/m, where lower limit of 95% confidence is 143.6 kN/m and peak value is 7.11%; limit tensile strength for CATISG70 — 70 biaxial polythene geogrid is 7.8 kN, where lower limit of 95% confidence is 7.65 kN and peak value is 9.28%.

TEST METHOD

Test methods are as per Test Methods of Geo-synthetics for Highway Engineering (JTG E50-2006) and applicable regulations on Creep Testing and Evaluating Method on Plastic Geogrids (QB/T 2854-2007). Under environment of 20±2℃ and in relative humidity of 50%—70%, a constant dead load is applied to test piece, and the load is evenly distributed on the whole width of the test piece. Extension of the test piece is recorded continuously or within specified interval. The load should be applied for 1000 hours or longer. If there's any crack if the load is applied for less than 1000 hours, time at which such crack happens is recorded. Test principle and procedures are as follows:

First, conduct creep test under preset load at certain tensile strength percentage of the test piece to get time when test piece under load reaches 10% strain ($t_{10\%}$).

[1] Assistant Professor, Chongqing Communications Research & Design Institute, CHINA. Email: yanqiurong@ccrdi.cmhk.com
[2] Professor, Chongqing Communications Research & Design Institute, CHINA. Email: dengweidong@ccrdi.cmhk.com
[3] Assistant Engineer, Sichuan Chengnan Expressway Co., Ltd., CHINA. Email: dcz1218@sina.com

Second, plot relation curve of preset load (P/T_{av}) and time log value at 10% strain. Calculate design period linearly and determine preset load where 10% strain could be satisfied during the whole design period. Unusually design period will be 110 years or 10^6h.

Third, determine lower limit of 95% confidence P_{all} under load at 10% strain during the whole design period with the following formula.

$$P_{all} = T_{95\%} \times \left[\frac{P}{T_{av}} \right]_{10\%} \quad (1)$$

where, P is load applied in creep test, P/T_{av} is preset load in creep test; $(P/T_{av})_{10\%}$ is preset load at 10% strain during the whole design period in creep test, P_{all} is allowed load (under lower limit load of 95% confidence at 10% stress during design period), T_{av} measured value of tensile strength (mean of 5 test values as per Test Methods of Geosynthetics for Highway Engineering), $T_{95\%}$ is lower limit of 95% confidence for tensile strength, t is time of creep test and $T_{10\%}$ is time at 10% strain of creep test.

Forth, the test defines corruption of reinforced materials as per 10% strain.

TEST EQUIPMENT AND TEST CONDITIONS

The indoor creep test instrument is geo-synthetic materials and soil long-term deformation tester in Chongqing Communications Research & Design Institute. The tester is driven by lever. The loading part can be rotated from left and right. Vertical loading is assured via adjusting horizontal level of the lever. Test equipment is shown in Fig. 1.

Fig. 1 Geo-synthetic materials and soil long-term deformation tester

Loading bar with breadth of 200 mm is used for loading in creep test for TGDG130 geogrid and Uni-axial bar is used for loading in creep test for CATTSG70-70 geogrid.

Fig. 2 Test detail picture

TEST RESULT AND ANALYSIS

Indoor Creep Test Result for TGDG130

Indoor creep test for TGDG130 geogrid lasts for over 2000 hours. Take 5 levels of load as 10%, 20%, 40%, 50% and 60% of tensile strength. Test result is shown in Fig. 3.

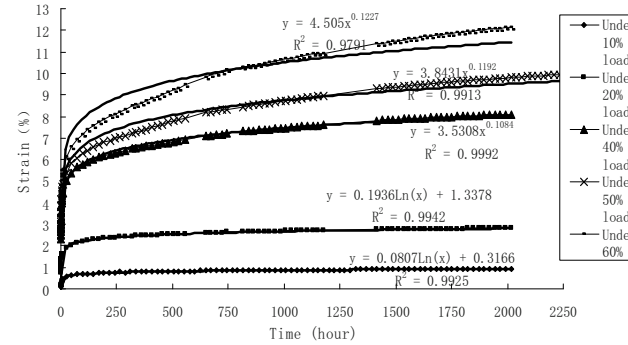

Fig. 3 Creep curve of TGDG130 geogrid

From Fig. 3 we can see that when load level is 50% and 60%, geogrid reaches 10% strain at 2352 h and 696 h. At load level below 40%, geogrid fails to reach 10% strain within test period. Based on the regression curve, geogrid will reach 10% strain at 14822.5 h. List of time when geogrid reaches 10% strain for each load level is as follows:

Table 1 Time for TGDG130 geogrid at 10% strain

Items	Time at 10% strain ($t_{10\%}$-h)		
P/T_{av}	60%	50%	40%
Test time at 20℃	696	2352	14822.5

Fig. 4 is plotted based on data in Table 1. Coordinate axis for load and time are in log form.

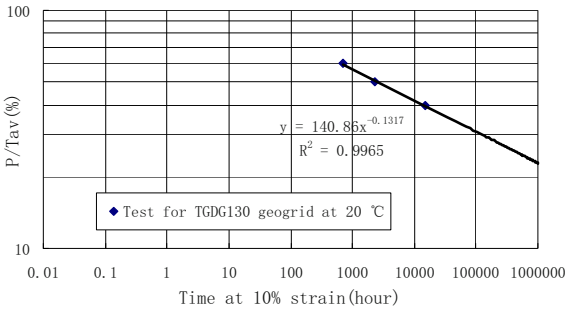

Fig. 4 Load-time curve for TGDG130 geogrid at 10% strain

As the two coordinate axes are in log form, linear relation shown in Fig. 4 could be defined with the following power function.

$$Y=140.86X^{-0.1317} \quad (2)$$

Where Y= (P/T_{av}), X= $t_{10\%}$. The function could be used to calculate value of $(P/T_{av})_{10\%}$ for the whole design period 10^6h.

$$Y=140.86\times1000000^{-0.1317}=22.8\% \quad (3)$$

Reduction factor RF_{CR} of indoor unconfined creep strength for TGDG130 polypropylene geogrid is calculated with the following formula.

$$RF_{CR}=1\div22.8\%=4.4 \quad (4)$$

According to tensile test result, limit tensile strength of TGDG130 polypropylene geogrid is 146 kN/m, lower limit of 95% confidence is 143.6 kN/m. At temperature of 20 ℃ and under long-term load during design period of 10^6 h, lower limit could be calculated with the following formula.

$$P_{all}=T_{95\%}\times\left[\frac{P}{T_{av}}\right]_{10\%} =143.6\times0.228=32.7\text{kN/m} \quad (5)$$

Result of Indoor Creep Test for CATTSG70-70 Geogrid

Take 4 levels of load for indoor creep test on CATTSG70-70 geogrid as 20%, 40%, 50% and 60% of tensile strength respectively. The test result is shown in Fig. 5.

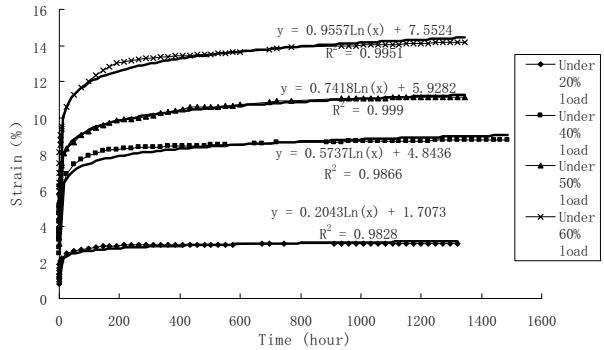

Fig. 5 Creep curve of CATTSG70-70 geogrid

According to test result shown in Fig. 5, time at 10% strain for each level is listed in the table below.

Table 2 Time at 10% strain for CATTSG70-70 geogrid

Items	Time at 10% strain ($t_{10\%}$-h)		
P/T_{av}	60%	50%	40%
Test time at 20℃	12.95	258.4	8007

Fig. 6 is plotted based on data in Table 2. Coordinate axis for load and time are in log form.

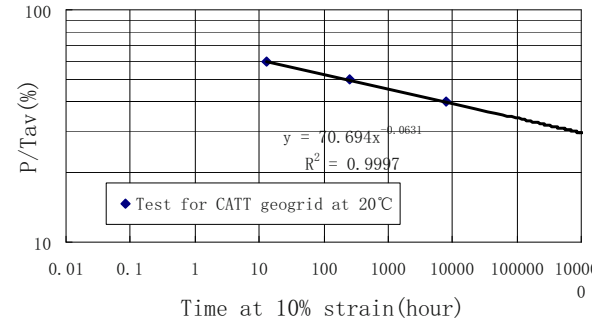

Fig.6 Load-time curve for CATTSG geogrid at 10% strain

Linear relation shown in Fig. 6 could be defined with following power function.

$$Y=70.694X^{-0.0631} \quad (6)$$

Where Y=(P/T_{av}), X= $t_{10\%}$. The function could be used to calculate value of $(P/T_{av})_{10\%}$ for the whole design period 10^6 h.

$$Y=70.694\times1000000^{-0.0631}=29.6\% \quad (7)$$

Thus, reduction factor RF_{CR} of indoor unconfined creep strength for CATTSG70-70 polyethylene geogrid is calculated with the following formula.

$$RF_{CR}=1\div29.6\%=3.4 \quad (8)$$

Limit tensile strength of CATTSG70-70 polythene geogrid strip is 7.8 kN, lower limit of 95% confidence is 7.65 kN. At temperature of 20 ℃ and under long-term load during design period of 10^6 h, lower limit value could be calculated with the following formula.

$$P_{all}=T_{95\%}\times\left[\frac{P}{T_{av}}\right]_{10\%} =7.65\times0.296=2.3\text{ kN} \quad (9)$$

Result of Creep Test for TGDG130 Geogrid in Practical Engineering

TGDG130 geogrid is used in cut-and-fill subgrade section in Guangdong-Tianjin-Shanwei Expressway, shown in Fig. 7. The subgrade fill for the section is fine grain (GF) and subgrade compactness is from 93%—95%.

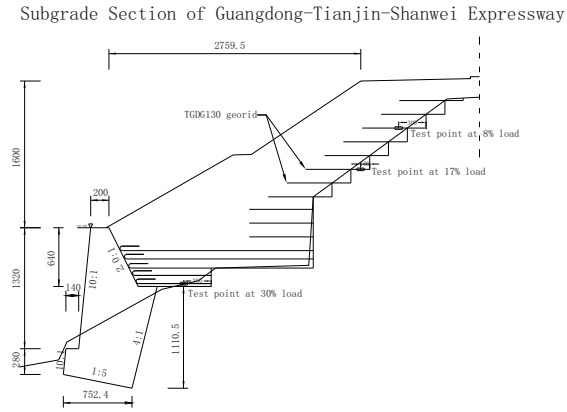

Fig. 7 Diagram of points where TGDG130 geogrid's creep in roadbed is measured

Subgrade filling of the section is proceeding rather fast. By September 14, 2005, balance weight platform of retaining wall was covered with first layer of geogrid. By September 30, 2005, top of road trough filling is completed. It is supposed that laid geogrid is under constant stress and stepping into creep stage. Based on strain test result of each test points on geogrid measures on September 30, 2005 and based on indoor tensile test curve for such geogrid, we could determine load level for the 3 creep test points to be 8%, 17% and 30% respectively.

From end of September 2005 to July 2006, we carried out about one-year creep test to the 3 test points. Creep result is shown in Fig. 8.

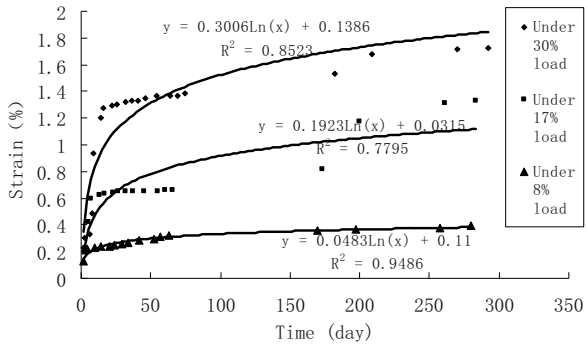

Fig. 8 Creep curve of TGDG130 geogrid in roadbed

Result Analysis

According to indoor creep test result, indoor creep reduction factor of TGDG130 polypropylene uni-axial geogrid is 4.4 and indoor creep reduction factor of CATTSG70-70 polyethylene biaxial plastic geogrid is 3.4. Difference in creep reduction factor which is based on different materials is not so obvious.

Studies show that creep rate of geo-synthetic materials becomes slow under confined conditions obviously compared with unconfined conditions, which is also approved in the test we conducted. Fig. 4 shows that TGDG130 geogrid under 10%, 20%, and 40% load will reach 1.43%, 4.01% and 15.79% strain respectively during 10^6 h under indoor unconfined conditions. However, the same type of geogrid which is in operation within subgrade under 8%, 17% and 30% load will only reach 0.78%, 2.69% and 4.29% strain respectively during 10^6 h.

CONCLUSIONS

First, with improvement of manufacturing technique and quality of raw materials, there's slight difference of creep reduction factor for geogrid made of different materials.

Second, based on indoor unconfined creep test and creep test under confined conditions in subgrade, log function and power function could be used in fitting of creep curve for TGDG130 polypropylene geogrid. When geogrid is under lower level of load, log function fitting performs well. On the contrary, when geogrid is under higher level of load (e.g. above 40% load), creep curve is relatively precipitous and power functions fitting performs well.

However, fitting function of creep curve for CATTSG70-70 polyethylene geogrid has nothing with load level. Log function could is enough to be used for fitting.

Third, creep rate under unconfined conditions is almost 2 times of that under confined conditions for TGDG130 geogrid approximately under load level.

Forth, based on test carried out and existing studies, range from 3.5 to 4.5 of creep reduction factor for high-strength geogrid should be safe regardless of raw materials. The creep reduction factor could be slightly reduced if confined conditions are taken into consideration in practical engineering.

REFERENCES

AASHTO Designation (1996) M288-97, Geotextile specification for highway application. Standard Specification for Transportation Materials and Method of Sampling and Testing, 8th Edition. AASHTO,U.S.A

Ministry of Communications of the People's Republic of China (2006) Test methods of geo-synthetics for highway engineering (JTG E 50-2006).China Communications Press, China

National Development and Reform Commission of the People's Republic of China (2007) Creep testing and

evaluating method on plastic georids (QB/T 2854-2007). China Light Industry Press, China

Wang Z, Li LH, WANG XQ (2004) Creep properties and testing methods of geosynthetics. Rock and Soil Mechanics 25(5): 723-727

Wu CS, Hong YS (1994) Creep behavior of geotextile under confining stress. Proceedings of 5th International Conference on Geotextiles, Geomembranes and Related Products. Singapore:1135-1138

Becker LDB, Nunes ALLS (2002) Confined creep of geotextile in a compacted sand fill. Proceedings of 7th International Conference on Geosynthetics. France: 1519-15 22

Proceedings of the 4th Asian Regional Conference on Geosynthetics
June 17 - 20, 2008 Shanghai, China

DEVELOPMENT OF THERMO-GRAPH INSPECTION FOR GEOMEMBRANE SEAM EVALUATION

H. Nakayama[1], T. Shimaoka[2] and S. Ueda[3]

ABSTRACT: This study attempted to develop of a method for detecting failures on welded seams between liner sheets. To identify the location of faulty seams, thermal images taken by a thermo graphic device were used to determine the unique temperature distribution on the faulty seam. It was shown that the real-time inspection for detecting faulty area was possible by taking thermal images of the seams while the sheets were welded by a self-propelled heat-welding machine. This method is more efficient compared to the conventional inspection method as that the seam can be examined with the welding work.

KEYWORDS: geomembrane, heat-welding, fault detection, thermal images

INTRODUCTION

For the construction of landfill liners, liner sheets are welded together. The seams between the sheets must be carefully inspected for faulty welds. There are various inspection methods such as air pressure testing and vacuum box testing. Air pressure testing, which can only be applied to seams joined by double fusion welding, is easy and effective, but does not indicate the exact location of the fault. Vacuum box testing is time-consuming if all the seams are to be inspected. A new viable method, which will complement the demerits of the existing methods, is therefore required.

In this study, a thermo graphic device was employed as a tool for real-time inspection that the thermal images taken by the device were used to identify faulty seam.

EXPERIMENTS

Fig. 1 is a sectional view of a welded seam, and temperatures in welding are also shown. Surfaces of the sheet to be welded are heated to 350－400℃ by a self-propelled heat-welding machine. This heat reaches upper surface of the seam and it makes the temperature increase to 70 － 80 ℃. On a faulty seam, surface temperature shows the unique distribution since its heat transfer rate is different from the normal seam. The thermal image of the welded seam is expected to provide an evidence to detect faulty area on the seam. A thermo graphic device used in this study has a sensor called microbolometer, and this makes images of the temperature distribution using infrared energy at the 7.5－13 μm wavelength. The detection accuracy of the temperature is 0.07℃, and the number of pixels of thermal image is 76800 (320×240), and the minimum pixel size in the close-up photographing is about 0.7 mm.

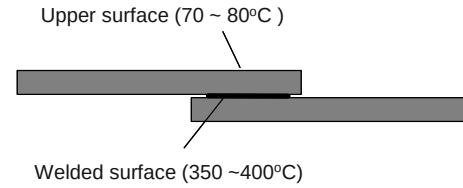

Fig. 1 Sectional view of a welded seam

Samples

High-density polyethylene (HDPE) sheets and flexible polymer alloy (FPA) sheets were welded together by single welding or by double fusion welding using a self-propelled heat-welding machine. To construct a faulty area on the seam, samples like following were made; (1) seams with scratch, (2) seams that a foreign object such as sheet piece or gum tape was held between the sheets, (3) a seam that the oil was applied.

[1] Associate Professor, Department of Urban and Environmental Engineering, Faculty of Engineering, Kyushu University, JAPAN. Email:nakayama@doc.kyushu-u.ac.jp
[2] Professor, Department of Urban and Environmental Engineering, Faculty of Engineering, Kyushu University, JAPAN. Email:shimaoka@doc.kyushu-u.ac.jp s
[3] Chief Director, Department of Environmental Engineering, Taiyokogyo Co.,Ltd., JAPAN. Email: US002917@mb.taiyokogyo.co.jp

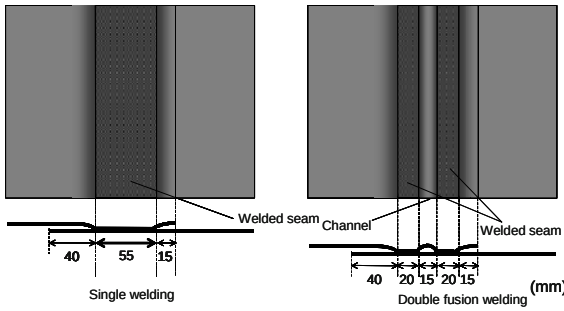

Fig. 2 Single welding and double fusion welding

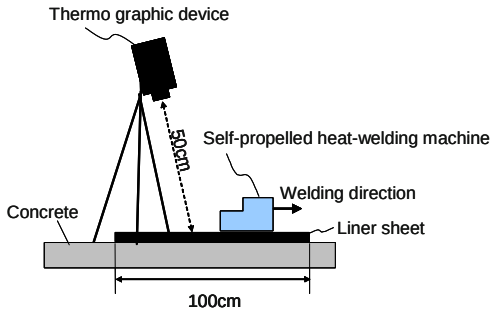

Fig. 3 Experimental equipment for thermo graph inspection

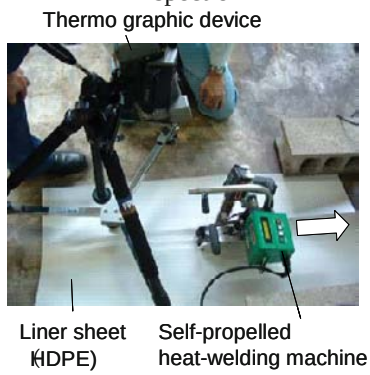

Fig. 4 A photo of experiment for thermo graph inspection

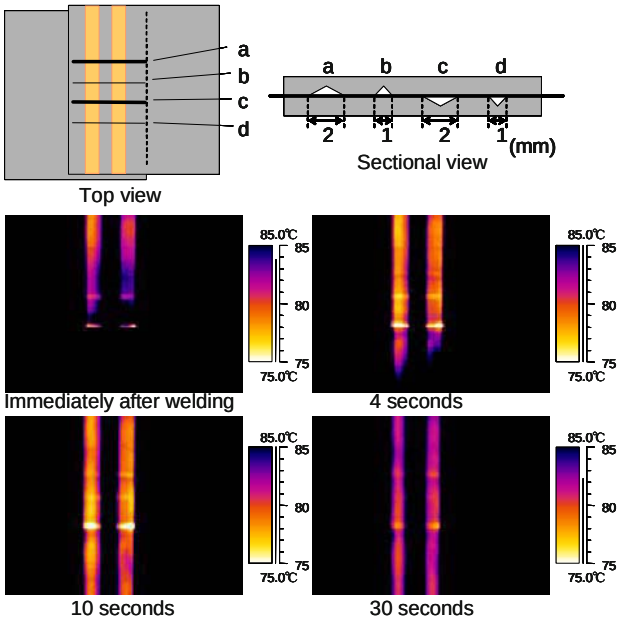

Fig. 5 Thermal images of the sheets with groove scratch

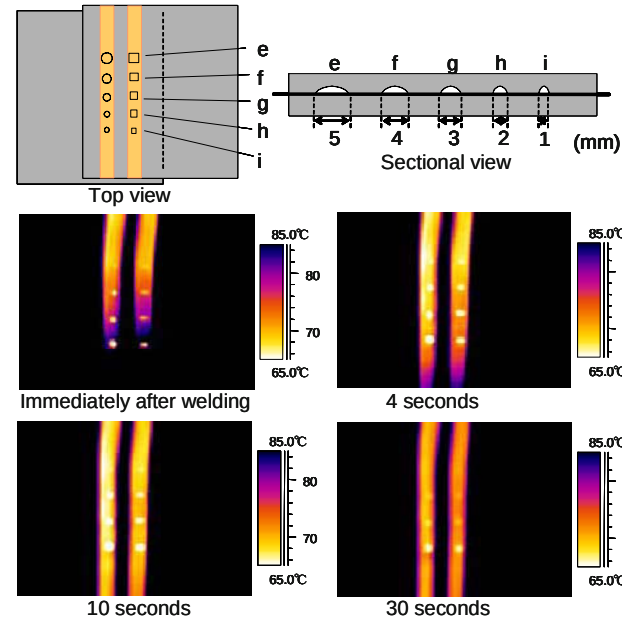

Fig. 6 Thermal images of the sheets with concaves

Experimental Equipment

Fig. 3 shows the experimental equipment required for thermo-graph inspection. In this experiment, 2 sheets with faulty area were welded together by self-propelled heat-welding machine. The temperature in welding was 350－400℃, and the welding speed was 1.0－1.5 m/min. When the sheets were welded, a thermo graphic device was used at 2-second intervals for 60 seconds to take images of the surface temperature. The experiment was conducted indoors in an environment where both the ambient and sheet temperatures were approximately 30℃.

RESULTS AND DISCUSSION

Samples with Faulty Seam Caused by Scratch on Sheet Surface

Fig.5 and 6 are the thermal images that were taken when the sheets, which have groove scratch and circular concaves, were welded. On those images, the welding machine welded sheets from the bottom to top of the image. In Fig. 5, the temperature of the faulty area was higher than the normal area, especially faulty area at the “a” position, where a scratch of 2 mm width and 1mm depth was made on the upper sheet, indicated apparently high temperature. On the other hand, since the temperature of the faulty area at the position of “d”, where a scratch of 1mm width and 1mm depth was made on the lower sheet, was almost same as the normal area, it could not be detected on the thermal image. Almost similar result was observed in Fig. 6.

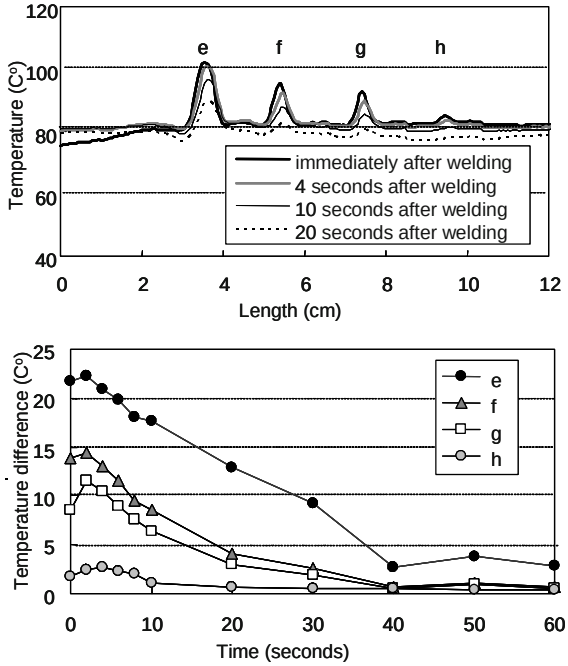

Fig. 7 Changes in surface temperature of the faulty and normal seams

Fig. 7 shows changes in surface temperature of the faulty and normal seams in the experiment. As shown in this figure, the temperature difference was at its largest 2—4 seconds after welding, then it gradually decreased.

Samples with faulty seam caused by insertion of foreign object

Fig. 8 and 9 show thermal images of faulty seams caused by insertion of foreign object. Unlike the case of the above-mentioned faulty seams with scratch, the temperature in the faulty area was lower than the normal area, since the heat capacity of the part where the foreign object located increased, and the heat transfer in boundary surface decreased.

Comparison of Thermo-graph Inspection and Air Pressure Testing, Vacuum Box Testing

Table 1 is the comparison of thermo-graph inspection and conventional air pressure testing and vacuum box testing on the experiments of inspection carried out in this study. All of the faulty area, which was detected by air pressure testing or vacuum box testing, was also detected by thermo-graph inspection. The thermo graph inspection can detect small faulty area that could not be detected by conventional testing.

CONCLUSIONS

This study describes a method for the detection of faulty seams using a thermo graphic device. The major results can be summarized as follows:

—The thermal images taken by the thermo graphic device can be used to determine the unique temperature distribution of faulty seams while sheets are welded by the heat-welding machine.

—The temperature of the faulty area caused by scratch was higher than the normal area, while the one caused by insertion of foreign object was lower than the normal area.

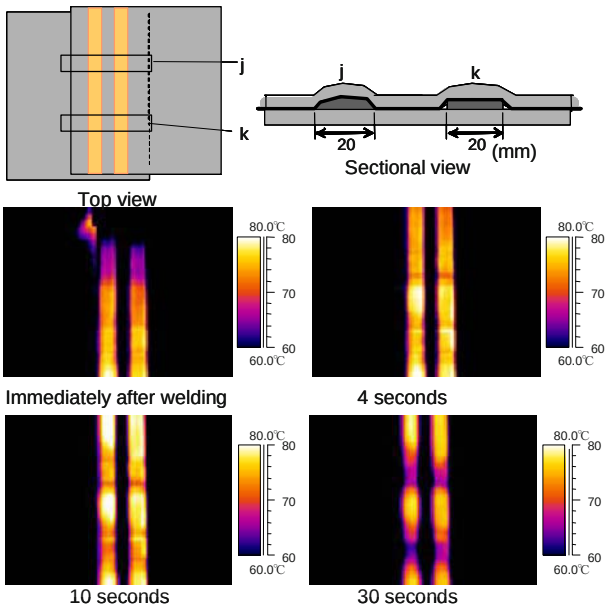

Fig. 8 Thermal images of the sheets with groove scratch

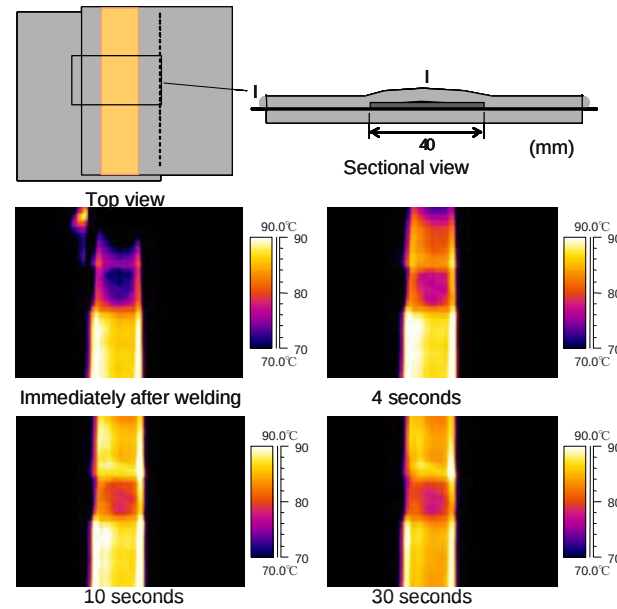

Fig. 9 Thermal images of the sheets with concaves

Table 1 Comparison of thermo-graph inspection and air pressure testing, vacuum box testing

type of fault	size(mm)				position of fault		material	result of detection			
								double fusion welding		single welding	
								thermal image	air pressure	thermal image	vacuum box
groove scratch	width	1	depth	1	upper sheet	backsurface	FPA	D	ND	-	-
	width	2	depth	1	upper sheet	backsurface		D	ND	-	-
	width	1	depth	1	lower sheet	surface		ND	ND	-	-
	width	2	depth	1	lower sheet	surface		D	ND	-	-
	width	1	depth	1	upper sheet	backsurface	HDPE	D	ND	-	-
	width	2	depth	1	upper sheet	backsurface		D	D	-	-
	width	1	depth	1	lower sheet	surface		ND	ND	-	-
	width	2	depth	1	lower sheet	surface		D	D	-	-
circular concave	diameter	1	depth	1	upper sheet	backsurface	HDPE	ND	ND	-	-
	diameter	2	depth	1	upper sheet	backsurface		D	ND	-	-
	diameter	3	depth	1	upper sheet	backsurface		D	ND	-	-
	diameter	4	depth	1	upper sheet	backsurface		D	ND	-	-
	diameter	5	depth	1	upper sheet	backsurface		D	ND	-	-
inesertion of sheet piece	width	20	thickness	2	lower sheet	surface	HDPE	D	D	D	D
	width	20	thickness	2	lower sheet	surface		D	ND	D	ND
insertion of gum tape	width	40	thickness	0.3	upper sheet	backsurface	HDPE	D	D	D	D
	width	40	thickness	0.3	lower sheet	surface		D	D	D	D
oil	width	30	-	-	lower sheet	surface	HDPE	-	-	ND	ND

—The thermo graph inspection can detect small faults that could not be detected by conventional air pressure testing and vacuum box testing in the experiments in this study.

ACKNOWLEDGEMENTS

The authors wish to thank the Mr. Aoyama of Taiyo Kogyo Corporation, Mr. Yuge of Mitsuboshi Belting Corporation and Mr. Washio of Sotou Corporation for their comments and for helping experiments.

REFFERENCES

Nakayama H, Shimaoka T, Inoue K, Komiya T (2004) Non-Destructive and In-situ Inspection of Seams Between Liner Sheets Using a Thermo Graphic Device, Proceedings of the Third Asian-Pacific Landfill Symposium 10: 131-137

The Technical Committee on Geomenbrane (2000) Japan Chapter of International Geosynthetics Society: Handbook on Design and Construction of Waste Landfill Site—Techniques for the Barrier System Construction

Japan Chapter of International Geosynthetics Society: (2000) The Introductory Book of Geosynthetics

Proceedings of the 4th Asian Regional Conference on Geosynthetics
June 17 - 20, 2008 Shanghai, China

UNDRAINED AND DRAINED TRIAXIAL TESTS OF FIBER-REINFORCED SAND

C.W. Chen [1] and J.E. Loehr [2]

ABSTRACT: A series of consolidated-undrained ($\overline{CU}$) and consolidated-drained (CD) type triaxial compression tests were performed on comparable unreinforced and fiber-reinforced specimens of Ottawa sand to evaluate the effective stress-strain-pore pressure and effective stress-strain-volume change behavior of fiber-reinforced sands. The results show that fibers increase the effective stress cohesion intercept (c') and effective stress friction angle (φ'). Also, c' and φ' determined for the reinforced specimens was observed to increase with strain. The c' from the $\overline{CU}$ tests are higher than those from the CD tests, whereas the φ' from the $\overline{CU}$ tests are slightly lower than those from the CD tests. In $\overline{CU}$ tests, loose reinforced specimens exhibited lower pore pressures than comparable unreinforced specimens. Loose and medium-dense reinforced specimens showed more dilation than comparable unreinforced specimens in CD tests. For Ottawa sands, the additional resistance due to the fibers is mobilized at smaller strains in drained tests than in undrained tests.

KEYWORDS: triaxial tests, fibers, reinforced soils, soil shear strength

INTRODUCTION

The behavior of fiber-reinforced soils has been studied by several investigators over the last two decades. Fiber-reinforced soil is becoming a viable soil improvement method for geotechnical engineering problems. Fiber-reinforced soils are currently being used or considered for applications that include stabilization of shallow slope failures (Gregory and Chill 1998), construction of new embankments with marginal soils, reduction of shrinkage cracking in compacted clay liners (Rifai 2000), and to reinforce roadway subgrades (Santoni et al. 2001).

Fiber-reinforced soil is a mixture of soil and synthetic fibers. Synthetic fibers can be made of different materials, shapes and lengths. Polypropylene and polyester are the most common materials used to manufacture fibers. Fibers can be flat or round and continuous or discrete. Discrete fibers are manufactured in several lengths, ranging from 13-mm to 76-mm, and are available in different types such as monofilament, fibrillated, tape, and mesh.

Significant research has been performed over the last few decades to evaluate basic shear strength properties and deformation characteristics of fiber-reinforced soils. Previous work has shown that an increase in fiber content generally increases the shear strength of soil. Most investigators have found that shear strength increases in direct proportion to fiber content or area ratio (Gray and Ohashi 1983; Gray and Al-Refeai 1986; Maher and Gray 1990; Ranjan et al. 1996; Bauer and Oancea 1999). However, Shewbridge and Sitar (1989) observed that increase in strength was not proportional to the reinforcement concentration.

Some previous research has shown that inclusion of fibers increases both the cohesion intercept and angle of internal friction values as compared to values for unreinforced soil (Kumar et al. 1999; Gregory and Chill 1998). However, Gray and Ohashi (1983), Gray and Al-Refeai (1986), and Ranjan et al. (1996) found that inclusion of fibers did not significantly affect the angle of internal friction, but rather that fiber-reinforced specimens exhibited bi-linear failure envelopes as a result of the existence of a critical confining stress below which the fibers tended to slip or pull-out. Consoli et al. (1998) observed an increase in the angle of internal friction but a decrease in the cohesion intercept. Bauer and Oancea (1999), and Consoli et al. (2003) found the friction angle to be barely affected by fiber inclusion whereas the cohesion intercept increased with increasing fiber content. As it can be seen, it is not clear that which statement is correct. Therefore, additional tests of fiber-reinforced soil are needed to confirm the response with different loading conditions.

[1] Coordinator of the Geosynthetic-Interaction Laboratory, TRI/ Environmental, Inc., 9063 Bee Caves Road, Austin, TX 78733, USA. Email: cchen@tri-env.com

[2] Associate Professor, University of Missouri-Columbia, Department of Civil and Environmental Engineering, EBE 2509, Columbia, MO, 65203, USA. Email: eloehr@missouri.edu

Table 1 Summary of Triaxial Tests Performed to Evaluate the Stress-Strain Behavior of Unreinforced and Reinforced Ottawa Sand Specimens

Type of Triaxial Testing	Fiber Content (%)	Effective Confining Stress							
		Loose Specimens				Medium-Dense Specimens			
		35 kPa	140 kPa	280 kPa	415 kPa	35 kPa	140 kPa	280 kPa	415 kPa
$\overline{CU}$	0.0	1	1	1	1	1	1	1	1
	0.4	1	1	1	1	1	1	1	1
CD	0.0	1	1	1	1	1	1	1	1
	0.4	1	1	1	1	1	1	1	1

TESTING MATERIALS AND PROGRAM

The soil used in testing program was Ottawa sand (Grade F-75), a well known laboratory-tested sand. The particles have a mean diameter (D_{50}) of 0.18 mm, a uniformity coefficient (C_u) of 1.7, a minimum void ratio (e_{min}) of 0.46, a maximum void ratio (e_{max}) of 0.77, and a specific gravity of 2.65 (ASTM D854). According to the Unified of Soil Classification System (ASTM D2487), Ottawa sand is classified as poorly graded sands (SP).

The fibers utilized consist of commercially available 51-mm long fibrillated polypropylene fibers of 3600-denier. The specific gravity of the fibers is 0.91 gr/cm^3 (ASTM D792). The ultimate tensile strength (ASTM D2256) and modulus of elasticity (ASTM D2101) of the fiber are 310-MPa, and 4,830-MPa, respectively.

An undercompaction process (Ladd 1978) was selected to produce homogeneous samples for the laboratory-testing program. Unreinforced and fiber-reinforced Ottawa sand specimens were prepared in a "loose" condition ($D_r \approx 10\%$) and in a "medium-dense" condition ($D_r \approx 55\%$).

All specimens were backpressure saturated at effective confining stresses of 17-kPa using the dry mounting method as specified in ASTM D4767. Skempton's (Skempton 1954) pore pressure coefficient, B, was measured during saturation. Specimens were allowed to saturate until measured B-values were reached at least 0.96 before consolidation and shear. Approximately 5 days were required to bring the B-value of the specimens to 0.96 or greater.

The strain rate used to shear the specimens in triaxial tests was 10 percent per hour (deformation rate of 12.5-mm per hour) to eliminate concern over strain rate when comparing on undrained and drained triaxial test results. Most specimens were sheared up to a maximum axial strain of 30 percent to permit the evaluation of the post-peak stress-strain behavior.

Table 1 summarizes the testing program undertaken to evaluate the stress-strain behavior of unreinforced and reinforced specimens. A total of sixteen consolidated-undrained triaxial compression tests with pore pressure measurements ($\overline{CU}$ tests) were performed to evaluate the stress-strain-pore pressure behavior of fiber-reinforced specimens under undrained loading conditions. A total of sixteen consolidated-drained triaxial compression tests (CD tests) were also performed for specimens prepared at loose and medium-dense states to evaluate the stress-strain-volume change behavior of fiber-reinforced specimens under drained loading conditions. All tests were performed on 63.5-mm diameter by nominal 124.5-mm tall specimens. Specimens isotropically consolidated to the target effective stresses of 35, 140, 280, and 415-kPa.

STRESS-STRAIN RESPONSE

Typical deviatoric stress versus triaxial shear strain behavior from $\overline{CU}$ and CD tests for unreinforced and reinforced specimens is shown in Figs. 1 and 2. The test results are plotted as deviatoric stress (q) versus triaxial shear strain (ε_q), where

$$q = \sigma_1 - \sigma_3 \tag{1}$$

in which σ_1 is the maximum principal stress and σ_3 is the minimum principal stress, and

$$\varepsilon_q = \varepsilon_a - \frac{1}{3}\varepsilon_v \tag{2}$$

in which ε_a is the axial strain and ε_v is the volumetric strain.

In undrained triaxial tests, the loose unreinforced specimens consolidated at greater effective stresses (e.g. 140, 280, and 415-kPa) reached a peak deviatoric stress at approximately 2 percent strain and then decreased with additional strain. In contrast, medium-dense unreinforced specimens at different effective consolidation stresses reached peak deviatoric stresses at strains of approximately 5%, but tended to level off or

decrease slightly at large strains. The loose and medium-dense fiber-reinforced specimens exhibited a strain-hardening behavior, but noticeable peak stresses were observed for medium-dense reinforced specimens at large strains (e.g. 20%) when consolidated to different effective confining stresses. The stress-strain responses of the fiber-reinforced sand specimens begin to deviate from that of the unreinforced specimens at 2%－6% strains for both the loose and medium-dense specimens.

As shown in Fig. 2, the loose and medium-dense

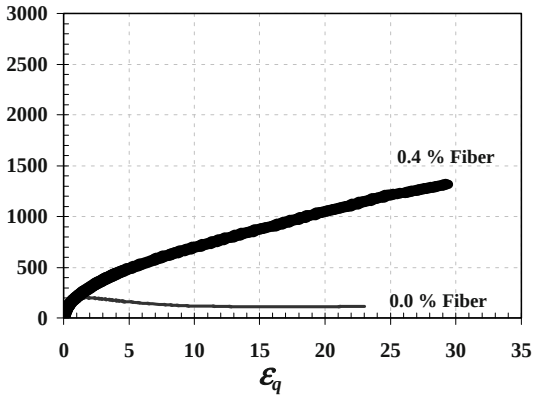

(a) Loose state (D_r≈10%)

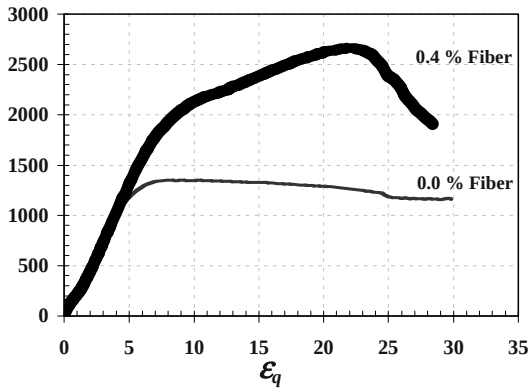

(b) Medium-dense state (D_r≈55%)

Fig. 1 Deviatoric stress (q) versus triaxial shear strain (ε_q) curves from $\overline{CU}$ tests for specimens consolidated to 140-kPa effective stress and prepared at: a) loose state, and b) medium-dense state

unreinforced specimens consolidated to different confining stresses tended to reach peak deviatoric stress levels at strains of approximately 1% and maintained stresses until large strains were reached. The loose and medium-dense reinforced specimens again exhibit strain-hardening response for all tests. At higher effective confining stresses (e.g. greater than or equal to 140-kPa) reinforced specimens also exhibited a peak stress at strains of 20% or greater. The stress-strain responses for fiber-reinforced loose and medium-dense specimens began to deviate from those of unreinforced specimens before 2 percent strain at all effective consolidation stresses. Note that reinforced sand specimens require significantly less strain (e.g. 5%) to begin mobilizing resistance in undrained tests (Fig. 1). Results of the drained tests show that some strain is also required to mobilize fiber resistance, but the amount of strain needed in drained tests (Fig. 2) is generally smaller (e.g. 1%－2%) than required in undrained tests for both loose and medium-dense reinforced sand. This is presumably due to the volume change that is allowed in drained tests. The level of strains needed to mobilize fiber resistance is even greater for other soils, more details can be found in Romero (2003) and Chen (2007).

PORE PRESSURE RESPONSE

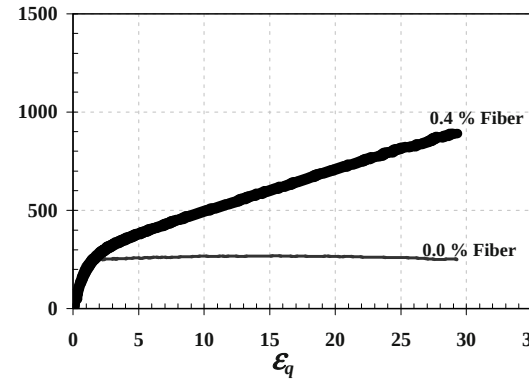

(a) Loose state (D_r≈10%)

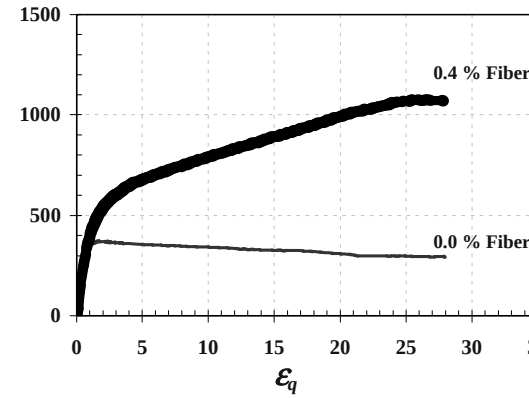

(b) Medium-dense state (D_r≈55%)

Fig. 2 Deviatoric stress (q) versus triaxial shear strain (ε_q) curves from CD tests for specimens consolidated to 140-kPa effective stress and prepared at: a) loose state, and b) medium-dense state

Observed changes in pore pressure observed in tests for both unreinforced and reinforced specimens are shown in Fig. 3.

The loose unreinforced specimens consolidated to lower effective stresses (e.g. 35-kPa) exhibited typical

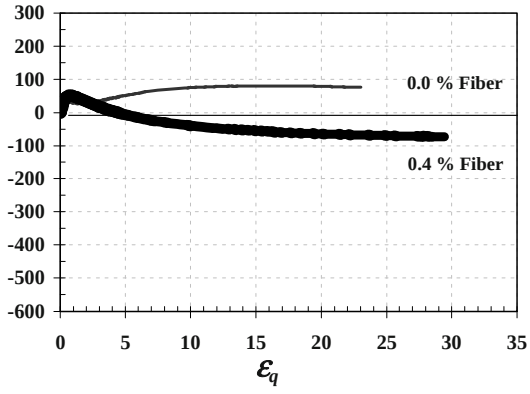

(a) Loose state ($D_r \approx 10\%$)

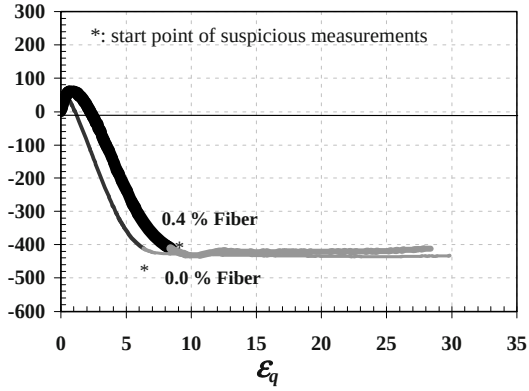

(b) Medium-dense state ($D_r \approx 55\%$)

Fig. 3 Change in pore pressure (Δu) versus triaxial shear strain (ε_q) curves from $\overline{CU}$ tests for specimens consolidated to 140-kPa effective stress and prepared at: a) loose state, and b) medium-dense state

"dense sand" behavior with the change in pore pressure decreasing rapidly at small strains and subsequently slowly decreasing until the end of the test. Unreinforced specimens consolidated at higher effective confining stresses (greater than or equal to 140-kPa) exhibited typical "loose sand" behavior with pore pressures increasing throughout the end of test. In contrast, medium-dense unreinforced sand specimens showed that the initial pore pressure changes increased within 1%, followed by significant decreases and the absolute pore pressure equal or less than zero before 10% strains. When pore pressure transducer measured less than the atmosphere pressure, cavitation has taken place. Pore pressure transducers cannot measure negative pressure accurately; therefore, the measured values do not represent the real readings in the soil when the absolute value of pore pressure is equal to or less than zero.

The loose reinforced specimens (Fig. 3a) generally show that the initial change in pore pressure increase at small strains (e.g. 2%), decrease with additional strains, and tend to level off at larger strains. Although the initial increases in pore pressure at lower strains are slightly higher for the reinforced specimens than for the unreinforced specimens, the differences in pore pressure change in terms of loose unreinforced and fiber-reinforced specimens became larger with increasing effective confining stresses up to 280-kPa.

The medium-dense fiber-reinforced specimens showed that initial changes in pore pressure increased at small strains (2%) followed by a significant decrease at absolute pore pressures equal to or less than zero before 10 percent strains. The amount of initial pore pressure increased as the effective confining stresses increased for the unreinforced sand specimens as well. Medium-dense reinforced specimens tended to have slightly higher pore pressures than unreinforced specimens before absolute pore pressure became equal to or less than zero.

VOLUMETRIC STRAIN RESPONSE

The typical volumetric strain versus triaxial shear strain response from CD tests for the unreinforced and reinforced sand specimens are shown in Fig. 4 for the samples prepared to "loose" and "medium-dense" state. The volumetric strain (ε_v) was calculated.

$$\varepsilon_v = \frac{\Delta V}{V_c} \tag{3}$$

where ΔV is the volume change measured during shearing and V_c is the specimen volume after the isotropic consolidation, which is

$$V_c = V_0 - \Delta V_c \tag{4}$$

where V_0 is the initial volume of specimen and ΔV_c is the volume change caused by consolidation and measured on the volume-change burette.

The unreinforced specimens exhibit volumetric strain response typical of loose and medium-dense behavior. The loose specimens consolidated to higher effective stresses (greater than or equal to 140-kPa) showed increasing compression with increasing consolidation stress. In contrast, the medium-dense unreinforced specimens showed initial compression at small strains followed by a significant dilation up to large strains. The initial compression increased with increasing effective confining stress; however, the amount of dilation decreased with increasing effective confining stress for medium-dense unreinforced specimens.

The loose and medium-dense reinforced specimens generally showed similar volumetric strain response to the unreinforced specimens. In same tests, reinforced

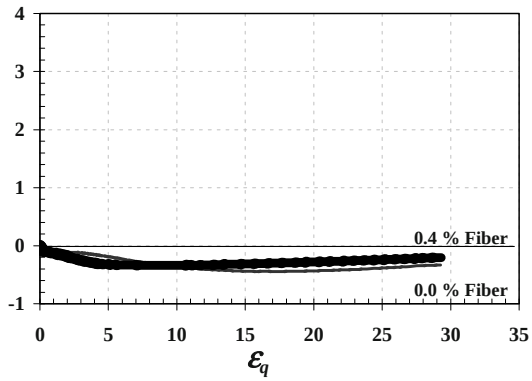

(a) Loose state (D_r ≈10%)

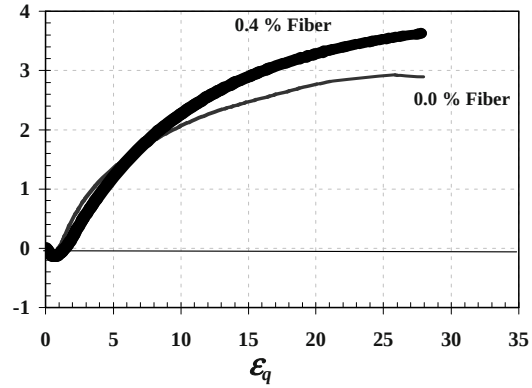

(b) Medium-dense state (D_r ≈55%)

Fig. 4 Volumetric strain (ε_v) versus triaxial shear strain (ε_q) curves from CD tests for specimens consolidated to 140-kPa effective stress and compacted at: a) loose state, and b) medium -dense state

specimens exhibited slightly more or less volumetric strain than unreinforced specimens, but the differences are small and appear to follow no consistent trend. The reinforced sand specimens tended to compress less (dilate more) than the unreinforced specimens when specimens were consolidated to higher effective stresses (e.g. greater than or equal to 140-kPa), which is a consistent observation in the undrained tests.

FAILURE ENVELOPES FOR TRIAXIAL TESTS

Failure envelopes were determined from peak effective principal stress ratio (PSR) failure criterion for $\overline{CU}$ and CD tests. Values of the Mohr-Coulomb strength parameters, effective cohesion intercept, c', and effective internal friction angle, φ', for the unreinforced and fiber-reinforced sand specimens from $\overline{CU}$ and CD tests are listed in Tables 2 and 3, respectively.

In undrained tests (Table 2), the shear strength of the unreinforced sand specimens prepared at loose state can be represented by an effective friction angle of 30°, and those prepared at medium-dense state can be interpreted by an effective friction angle of 34° for both failure criterions with zero effective cohesion intercept. The data show the effective cohesion intercepts of 87-kPa and the effective friction angle of 43° for loose reinforced sand specimens. A comparison of the Mohr-Coulomb strength parameters for the unreinforced and reinforced sand specimens show that fiber inclusion has a significant effect in improving not only the effective stress friction angles, but also the effective stress cohesion intercepts.

Table 2 Mohr-Coulomb Strength Parameters, c' and φ', Measured for Unreinforced and Reinforced Sand Specimens from $\overline{CU}$ Tests

Relative Density, D_r (%)	0.0% Fiber Content		0.4% Fiber Content	
	c' (kPa)	φ'(deg)	c' (kPa)	φ'(deg)
10	0.0	30.4	87	43.1
55	0.0	33.7	0[a]	43.5[a]

[a]: Suspicious result due to equipment limitation for pore pressure measurement.

In drained tests (Table 3), the shear strength of the unreinforced sand specimens compacted at a loose state is represented by an effective stress friction angle of 30°, while the shear strength at a medium-dense state is represented by an effective stress friction angle of 34°. The effective stress cohesion intercepts of fiber-reinforced sand specimens from the $\overline{CU}$ tests are higher than those from the CD tests, whereas the effective stress friction angle from the $\overline{CU}$ tests are slightly lower than those from the CD tests.

Table 3 Mohr-Coulomb Strength Parameters, c' and φ', Measured for Unreinforced and Reinforced Sand Specimens from CD Tests

Relative Density, D_r (%)	0.0% Fiber Content		0.4% Fiber Content	
	c' (kPa)	φ'(deg)	c' (kPa)	φ'(deg)
10	0.0	29.8	21	45.3
55	0.0	34.2	34	47.9

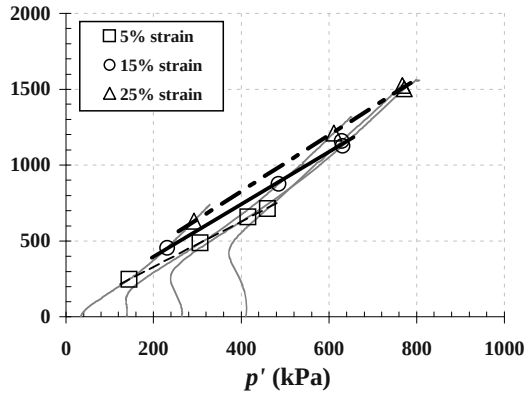

(c) $\overline{CU}$ tests

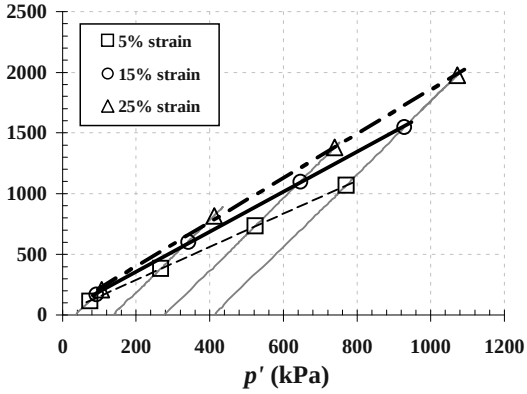

(d) CD tests

Fig. 5 Cambridge stress paths and failure envelpoes for limiting strains of 5, 15, 25 percent strain for loose specimens consolidated to 140-kPa effective stress and reinforced with 0.4% fiber: a) $\overline{CU}$ tests, and b) CD test

Peak effective principal stress ratio for the fiber-reinforced specimens under undrained and drained loading occurred at very large strain. The peak deviatoric stress in the fiber-reinforced Ottawa sand specimens were often not mobilized until reaching strains as large as 25%. Since such large strains are seldom tolerable, failure envelopes were also established at limiting strains of 5%, 15%, and 25% to evaluate the effects of the fibers inclusion on mobilized resistance at small strains. Fig. 5 show the Cambridge stress path diagrams and failure envelopes for the chosen limiting strains from $\overline{CU}$ and CD tests on reinforced loose specimens. Since peak stresses generally occurred at relatively low strains and maintain strength up to large strains for $\overline{CU}$ and CD tests, the effective stress friction angles for the unreinforced Ottawa sand specimens are identical for the chosen limiting strains. In contrast, the shear strength parameters computed for the reinforced specimens at chosen limiting strains are all different. For loose reinforced specimens in particular, both the effective stress cohesion intercepts and friction angles increased with increasing strains. This also indicates the strain hardening response for the loose fiber-reinforced Ottawa sand.

CONCLUSIONS

The results of the triaxial tests performed on loose and medium-dense Ottawa sand show that inclusion of fibers can improve the strength of soils under undrained and drained loading conditions. Shear strength parameters of effective stress cohesion intercept and friction angle increase significantly in the $\overline{CU}$ and CD tests, due to the addition of fibers. The effective stress cohesion intercepts from the $\overline{CU}$ tests are higher than those from the CD tests, whereas the effective stress friction angle in the undrained tests are slightly lower than those from the drained tests for fiber-reinforced sand specimens. It is noted the reinforcing fibers alter the pore pressure response of specimens tested under undrained loading conditions and the volume change response of specimens tested under drained loading condition. The loose reinforced specimens exhibited lower pore pressures than unreinforced specimens in undrained tests. The loose and medium-dense reinforced specimens showed less compression (more dilation) than unreinforced specimens at moderate and larger strains when they consolidated to higher effective stresses (e.g. greater than or equal to 140-kPa) in drained tests.

Resistance due to the fiber reinforcement is mobilized at lower strains in drained tests than in undrained tests. This suggests that volumetric strain plays an important role in mobilization of fiber resistance.

The peak deviatoric stress in the fiber-reinforced Ottawa sand specimens were not mobilized until reaching strains as large as 25%. While such large strains are rarely tolerable, failure envelopes established at limiting strains to evaluate the effects of the fibers inclusion on mobilized resistance at small strains is important for implementation of fiber-reinforced soil in engineering practice.

REFERENCES

American Society for Testing and Materials ASTM (2000) D792-00 standard test methods for density and specific gravity (relative density) of plastics by displacement. Annual Book of ASTM Standards, Volume 08.01, Philadelphia

American Society for Testing and Materials ASTM (2002) D854-02 standard test methods for specific gravity of soil solids by water pycnometer. Annual

Book of ASTM Standards, Volume 04.08, Philadelphia

American Society for Testing and Materials ASTM (1994) D2101 standard test methods for tensile properties of single man-made textile fibers taken from yarns and tows. Annual Book of ASTM Standards, Volume 07.01, Philadelphia

American Society for Testing and Materials ASTM (2002) D2256-02 standard test method for tensile properties of yarns by the single-strand method. Annual Book of ASTM Standards, Volume 07.01, Philadelphia

American Society for Testing and Materials ASTM (2000) D2487-00 standard practice for classification of soils for engineering purposes (Unified Soil Classification System). Annual Book of ASTM Standards, Volume 04.08, Philadelphia

Bauer G, Oancea A (1999) Soils reinforced with discrete synthetic fibers. Geosynthetics '99 — Specifying Geosynthetics and Developing Design Detail, IFAI, Boston, MA, 465-475

Chen CW (2007) A constitutive model for fiber-reinforced soils. Dissertation submitted in partial fulfillment for the requirements of the Doctoral Degree, University of Missouri-Columbia.

Consoli NC, Prietto PDM, Ulbrich LA (1998) Influence of fiber and cement addition on behavior of sandy soil. Journal of the Geotechnical and Geoenvironmental Engineering 124(12): 1211-1214

Consoli NC, Casagrande MDT, Prietto PDM, Thome A (2003) Plate load test on finer-reinforced soil. Journal of the Geotechnical and Geoenvironmental Engineering 129(10): 951-955

Gray DH, Ohashi H (1983) Mechanics of fiber reinforcement in sand. Journal of the Geotechnical Engineering 109(3): 335-353

Gray DH, Al-Refeai T (1986) Behavior of fabric- versus fiber-reinforced sand, Journal of the Geotechnical Engineering Division, ASCE, 112(8): 804-820

Gregory GH, Chill DS (1998) Stabilization of earth slopes with fiber reinforcement. Proceedings of the Sixth International Conference on Geosynthetics, Atlanta, Georgia, 1073-1078

Kumar R, Kanaujia VK, Chandra D (1999) Engineering Behaviour of Fibre-Reinforced Pond Ash and Silty Sand, Geosynthetics International, 6(6): 509-518

Ladd RS (1978) Preparing test specimens using undercompaction. Geotechnical Testing Journal, 1(1): 16-23

Maher MH, Gray DH (1990) Static response of sands reinforced with randomly distributed fibers. Journal of the Geotechnical Engineering 116(11):1661-1677

Ranjan G, Vasan RM, Charan HD (1996) Probabilistic analysis of randomly distributed fiber-reinforced soil. Journal of Geotechnical Engineering 122(6):419-426

Rifai SM (2000) Impact of polypropylene fibers on desiccation cracking and hydraulic conductivity of compacted clay liners. Dissertation submitted in partial fulfillment for the requirements of the Doctoral Degree, Wayne State University, Detroit, Michigan

Romero RJ (2003) Development of a constitutive model for fiber-reinforced soils. Dissertation submitted in partial fulfillment for the requirements of the Doctoral Degree, University of Missouri-Columbia

Santoni RL, Tingle JS, Webster SL (2001) Engineering properties of sand-fiber mixtures of road construction. Journal of the Geotechnical and Geoenvironmental Engineering 127(3): 258-268

Shewbridge SE, Sitar N (1989) Deformation characteristics of reinforced soil in direct shear. Journal of the Geotechnical and Geoenvironmental Engineering 115(8): 1134-1147

Skempton AW (1954) The pore pressure coefficient A and B. Geotechnique, 4, 143-47

ACCELERATED TESTING OF GEOSYNTHETICS FOR DESIGN AND MATERIAL CONFIRMATION SUPPORT

Sam R. Allen[1]

ABSTRACT: The characterization of geosynthetic products for design is critical for successful selection of products and realization of planned performance. Subsequent checking or verification of important design properties is also crucial to avoid suspect products and achieve the best possible material supply for a given project. While the testing for short term physical and mechanical properties is achieved readily, the verification testing of time-dependent or durability properties has traditionally been outside the scope of project specific testing programs due to the longer testing times required. This challenge has been especially daunting as users have become more aware that similar short term properties do not always suggest similar long term design properties. Recent developments in accelerated testing technologies are making what was once considered excessive and inappropriate, newly practical for responsive testing programs. This paper will outline some of these technologies and their use in today's testing programs.

KEYWORDS: accelerated testing, durability, stepped isothermal method, SIM

SHORT AND LONG TERM PROPERTIES

While the design function of a geomembrane material is almost always related to establishing a barrier based on immediate core material properties and manufacturing consistency, other geosynthetics that provide for drainage and reinforcement derive their performance from both as-manufactured structure and longer-term time-dependent properties. In addition, the longer term processes of material degradation that affect all geosynthetic materials may only be assessed with a respect for time-dependent durability properties. These longer term properties have been studied with variable approaches ranging from long-term test procedures lasting multiple months or years, to shorter term properties that serve to indicate or suggest a desirable longer term response. However, acceptable short term properties do not always correspond to desirable long-term properties.

THE CASE OF GEOSYNTHETIC DRAINS

Geonets and geocomposites are used routinely to achieve flow in the plane of the product in support of a variety of applications. Historically, short-term planar flow or hydraulic transmissivity has been tested to evaluate a product's suitability for the site-specific design function. It is well established that compressive loading active on the planar drain serves to reduce the product thickness and thus the planar flow achieved. Additionally, this compression is time-dependent in its impact on flow.

The GRI procedure GC8 (1996) provides a simple relationship for incorporating the influence of material compressive creep on hydraulic performance.

$$q_{allow} = q_{100}\left[\frac{1}{RF_{CR} \times RF_{CC} \times RF_{BC}}\right] \quad (1)$$

Where
q_{allow} = allowable flow rate (m2/sec)
q_{100} = flow rate at 100 hours from a transmissivity test
RF_{cr} = reduction factor for creep
RF_{cc} = reduction factor for chemical clogging and
RF_{bc} = reduction factor for biological clogging.

In this determination, both the 100-hour transmissivity test and the longer-term determination of the compressive creep reduction factor depend heavily on the product's resistance to angled or normal compressive loading. Product structure, upper rib orientation, density and thickness are all contributors to ultimate compressive strength and resistance. However, the table below shows two high density polyethylene products having similar thickness, different aperture and rib thickness structures and different densities, for which short term compressive strengths are similar but longer-term creep reduction factors are significantly different.

[1] Vice President of TRI/ Environmental, Inc, (TRI) Geosynthetic Services, 9063 Bee Caves Road, Austin, TX 78733, USA. Email: sallen@tri-env.com, ASTM D35 Chairman, IGS Council Member, ISO WG5 Durability Convenor

Geonet Product	1	2
Short Term Compression Strength (kPa)	955	1020
Horizontal to-the-plane (0°) - 1 year Creep Reduction Factor @ 35% stress level	1.21	1.32
Slope of 1 to 4 (14°) - 1 year Creep Reduction Factor @ 35% stress level	3.62	3.81

The greater shorter term compression strength did not correspond to greater longer-term resistance to compressive loading. For this reason, an understanding of the longer term compression behavior of drainage products is emphasized.

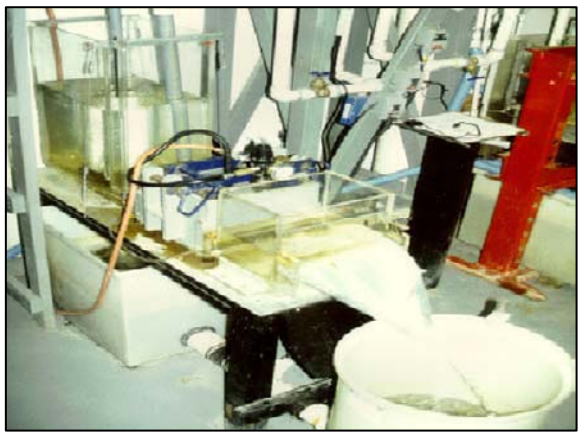

Fig. 1 Hydraulic transmissivity test

For the purpose of the 100-hour transmissivity value, ASTM D4716 test method or any other equivalent procedure is typically used. However, the test is usually performed using the same configuration of materials, load and gradient as that expected in the field. If the actual application involves a soil/geocomposite interface then the test is also per-formed with soil overlying the geocomposite. While the variability in flow properties across the roll width of a geonet or geocomposite is accounted for in a multiple specimen flow test, the 100 hour or 4+ day transmissivity test required has been per-formed with a single specimen as available test equipment and cost restraints limit a more representative test program with multiple specimens.

In addition to time burdensome time requirements associated with longer-term testing, material variability from variable raw material resources and manufacturing processing parameters impacts site specific performance parameters too. Because a given product style has been characterized for a compression creep reduction factor does not mean that that reduction factor is valid for all rolls having that brand name. Indeed, continued research in these areas has indicated significant impacts of even small changes of geonet and geocomposite structure and density to resulting behavior under compressive loading. These small fluctuations are not characterized in most single-value reduction factors.

In the schedules of geosynthetic material acquisition and installation, a multiple day testing program is of-ten not feasible, yet product dependent and time de-pendent resistance to compressive loading, and related hydraulic flow measurement are crucial to understanding geo-synthetic drain performance.

THE CASE OF GEOSYNTHETIC REINFORCEMENT

Reinforcement geosynthetics may include geogrids, woven geotextiles and strips, where the reinforcing component is made from polyester (polyethylene terephthalate), polypropylene, polyethylene, polyamides and polyvinyl alcohol.

As these geosynthetic materials serve as reinforce-ment when they assume load, and knowing they ex-perience elongation when loaded, the measurement of their strain behavior and its incorporation into design is required for successful design. In addition, many other in-situ conditions bear on the realized performance of the geosynthetic reinforcement including affects caused by installation damage, weathering and chemical degra-dation.

The traditional approach including these phe-nomenon in design is to place a multi-component reduction factor on short term measured tensile strengths. This allowable, or long-term strength, of a geosynthetic reinforcement may be determined in accordance with the following equation.

$$T_{al} = T_{ult}/RF \tag{2}$$

where: $RF=RF_{ID}\times RF_{CR}\times RF_{D}$ (3)

T_{al}=allowable strength—The long term tensile strength that will not result in rupture of the reinforcement during the required design life, calculated on a load per unit of reinforcement width basis

T_{ult}= the ultimate tensile strength of the rein-forcement determined from width width tensile tests (ASTM D 6637 or ISO 10319)

RF=a combined reduction factor to account for potential long-term degradation due to installation damage, creep, and chemical/biological aging

RF_{ID} = a strength reduction factor to account for installation damage to the reinforcement

RF_{CR} = a strength reduction factor to prevent long-term creep rupture of the reinforcement

RF_{D} = a strength reduction factor to prevent rupture of the reinforcement due to chemical and biological degradation.

The T_{ult} wide width tensile test is the most often used test performed to evaluate candidate products or verify an as-manufactured product for site-specific use. This is due to the relative simplicity of measurement and the rapid access to short term test results. However, the table below shows two coated polyester geogrid products having very similar mass/unit area, product structure and wide with tensile strength, but significantly different longer term creep-rupture reduction factors.

Geogrid Product	1	2
Ultimate Tensile Strength (kN/m)	106.3	104.5
114 year creep-rupture reduction factor (as percent of ultimate strength)	58.9	66.4

Again, the short term tensile strength did not correspond to the superior resistance to tension creep and rupture. This behavior is also seen routinely in the characterization of component polyester yarns investigated for use in geosynthetic flexible coated geogrids. While short term ultimate tensile strengths are important they do not provide sufficient information with which to select appropriate yearn candidates. The segregation between good, bad and excellent occurs only when longer term creep and durability properties are established.

TIME DEPENDENT DURABILITY TESTING

Geosynthetic durability testing technologies have enjoyed robust development during the past decade. However, in spite of representing perhaps the most important aspect of product performance, testing is still challenging due to relative sophistication of procedures and time dependency of test results and subsequent interpretation. Even in accelerated testing environments, the encouragement of oxidation, hydrolysis, stress crack resistance and other mechanisms of aging require time. Longer term aging experiments may require multiple years and numerous specimen populations to achieve experimental results worthy of durability assessment.

Still, significant among developments in durability testing are test procedures that both identify product components or properties significant to durability, and significantly reduce the time for assessment.

ACCELERATED TESTING AS A SOLUTION

While manufacturers and product development specialists are taking advantage of a new generation of accelerated testing technologies, the site-specific engineer is just beginning to realize the same significant benefits for site specific product assessment of time dependent properties. While reduction factors associated with design have traditionally been provided by the product manufacturer with a unique supporting report, the lot-specific production roll designated for a specific installation is now being proposed for full design assessment via reduction factor estimation.

This is made possible via accelerated testing technologies. Examples of these technologies include simple shorter term tests that assess durability, and the Stepped Isothermal Method (SIM) used to accelerate the creep and creep-rupture response.

ACCELERATED DURABILITY TESTING

All polymers are susceptible to environmental degradation due to weathering, including exposure to ultra-violet light, and chemical attack. These effects are further accelerated by elevated temperature and, for some polymers, by moisture availability and uptake. The durability of reinforcement geosynthetics is generally possible by their high degree of orientation and high molecular weights, while for polyolefins in particular, molecular stability (non-reactivity) is the principal reason for durability.

The accelerated testing procedures used to assess durability incorporate a host of acceleration mechanisms that present durability challenges to the tested product and measure its response. These procedures include the following.

Biological Resistance

ISO 12961, Geotextile and geotextile related products—Method for determining the microbiological resistance by a soil burial test (acceleration by aggressive microbiological activity and elevated temperature)

ASTM G160, *Standard Practice for Evaluating Microbial Susceptibility of Nonmetallic Materials by Laboratory Soil Burial* (acceleration by aggressive microbiological activity and elevated temperature)

UV and Oxidation Resistance

ISO 13438, *Geotextiles and geotextile-related products—Screening test method for determining the*

resistance to oxidation (acceleration by concentrated UV bandwidth exposure as well as elevated temperature)

ASTM D 3895, *Standard Test Method for Oxidative-Induction Time of Polyolefins by Differential Scanning Calorimetry* (acceleration by related durability parameter assessment—used in concert with aging procedure)

ASTM D 5885, *Standard Test Method for Oxidative Induction Time of Polyolefin Geosynthetics by High-Pressure Differential Scanning Calorimetry* (acceleration by related durability parameter assessment—used in concert with aging procedure)

ASTM D 4355, *Test Method for Deterioration of Geotextiles from Exposure to Ultraviolet Light and Water (Xenon-Arc Type Apparatus)* (acceleration by concentrated UV bandwidth exposure as well as elevated temperature)

ASTM D 7238, *Standard Test Method for Effect of Exposure of Unreinforced Polyolefin Geomembrane Using Fluorescent UV Condensation Apparatus* (acceleration by concentrated UV bandwidth exposure as well as elevated temperature)

ASTM D 5721, *Standard Practice for Air-oven Aging of Polyolefin Geomembranes* (acceleration by elevated temperature

Fig. 2 Fluorescent UV weatherometers

Stress Crack Resistance

ASTM D 5397, *Standard Test Method for Evaluation of Stress Crack Resistance of Polyolefin Geomembranes Using Notched Constant Tensile Load Test* (acceleration by elevated temperature and chemical accelerator)

Chemical Resistance

GRI GG7, *Carboxyl End Group Content of Polyethylene Terephthalate (PET) Yarns* (acceleration by related durability parameter assessment – leads to a default reduction factor)

GRI GG8, *Determination of the Number Average Molecular Weight of Polyethylene Terephthalate (PET) Yarns Based on a Relative Viscosity Value*. (acceleration by related durability parameter assessment – leads to a default reduction factor)

ISO 13439, *Geotextile and geotextile related products —Method for determining the resistance to hydrolysis* (acceleration by elevated temperature)

ISO 12960, *Geotextiles and geotextile-related products — Screening test method for determining the resistance to liquids* (acceleration by elevated temperature and chemical concentration)

ASTM D 5322, *Standard Practice for Immersion Procedures for Evaluating the Chemical Resistance of Geosynthetics to Liquids* (acceleration by elevated temperature)

Fig. 3 Chemical resistance exposure baths

COMPRESSION AND TENSION CREEP TESTING

The creep reduction factor, RF_{CR} as it is applied to both geosynthetic reinforcement and drainage design, often represents the most significant reduction factor in the determination of allowable strength and allowable flow. For purposes of this discussion, we will consider a case of tension creep as associated with reinforcement design.

When testing to predict the strengths intended to prevent the long-term rupture of a geosynthetic reinforcement, a testing laboratory is responding to **limit state** design requirements. However, creep testing is also performed to respond to specific job applications establishing limits on the total strain allowable over the service lifetime. In this case, a **strain limit** design and strength is desired to prevent excess strain over the intended service life.

A typical creep test involves the unconfined loading of a geosynthetic reinforcement with some percentage of its short term tensile strength. This loading of the specimen results in its elongating under load. The test is performed by monitoring this strain over time and reporting results accordingly.

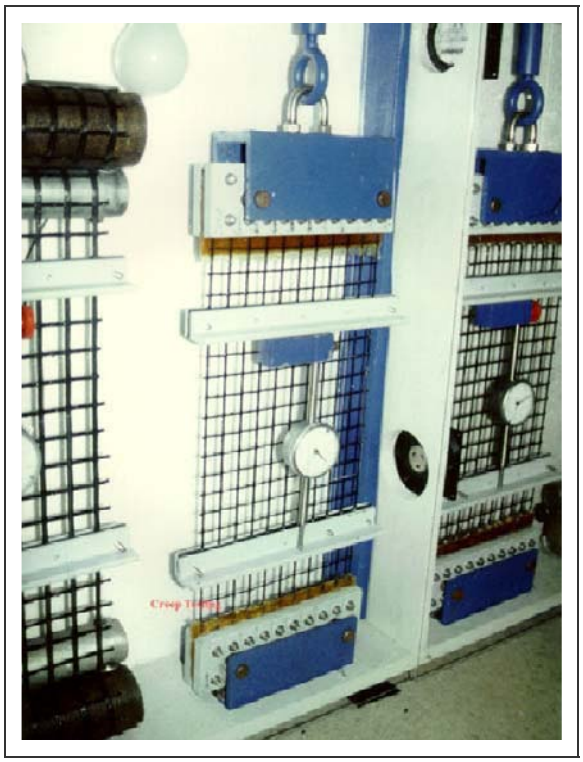

Fig. 4 TRI Laboratory tension creep test

Creep tests are performed in accordance with the following established procedures.

- ASTM D 5262, *Standard Test Method for Evaluating the Unconfined Tension Creep Behavior of Geosynthetics.*
- ISO 13431, *Geotextiles and geotextile-related products—Determination of tensile creep and creep rupture behaviour*
- ASTM D 6992, *Standard Test Method for Accelerated Tensile Creep and Creep-rupture of Geosynthetic Materials Based on Time-Temperature Superposition Using the Stepped Isothermal Method*

CONVENTIONAL ACCELERATED CREEP TESTING

Accelerated creep testing is based on the principles and practices of time temperature superposition (TTS). The fundamental notion of all TTS techniques is that elevating temperature accelerates the response to mechanical load. Deformations, such as creep strain, occur relatively rapidly when load is first applied, but the rate of increase decreases with time. The total strain and strain rate associated with creep is the study of creep and creep rupture, or maximum strain, tests.

The precise way that increasing temperature accelerates strain behavior governs how creep response can be “shifted” along a time scale. At test temperatures greater than the reference temperature, test time is shortened.

Even so, historical creep testing programs involved the testing of multiple specimens at various temperatures and loads resulting in individual tests consuming a few days to over 14 months. Collectively, the measurements could be used to determine design reduction factors.

Fig. 5 TRI laboratory compression creep test

THE SPECIAL CASE OF SIM

The single most significant development in the measurement of a geosynthetic’s response under load involves technology advancement with regard to creep and creep rupture characterization. The long term test durations and excessive expense associated with time dependent strain characterization was largely made insignificant. First proposed by Thornton et. al. (1997), the stepped isothermal method (SIM) for creep testing has been a significant contributor to more robust, frequent and site-specific creep characterization of geosynthetic reinforcements and planar drains.

The procedure was developed at TRI geosynthetics laboratories in Austin, Texas, USA and is currently

employed as a measurement technique in consensus based characterization guides and in site specific product verification testing programs. SIM has made it possible to quickly and affordably avoid products having suspect creep reduction factors on a site-specific level through immediate product rejection in the case of well established SIM use, or additional exploratory testing when SIM has not yet been completely related to in-application temperatures.

The SIM test consists of a series of timed isothermal creep tests performed at a sequence of increasing temperatures. As in an ordinary creep test the load is held constant and the creep strain in measured throughout the duration of the test. The number, heights and durations of temperature steps are designed to produce a master curve of creep compliance over a long term period defined by the test objective. For the geosynthetics community, long term design is generally 114 years for geosynthetic reinforcement applications, or 30 — 50 years based on landfill leachate collection drainage system applications.

What is accomplished in relatively short times (< 24 hours) is a master creep curve for the creep response of a specimen under a specific load. One may think of a single SIM test as “visiting” a portion of each of the component creep tests in a conventional testing program involving individual tests performed in their entirety under isothermal conditions.

While conventional time-temperature shifting of results obtained on specimens tested at elevated temperatures can provide improved predictions of longer-term performance at ambient temperatures, SIM has evolved this conventional approach to pro-vide shorter term, and more numerous predictions of creep and creep rupture behavior. The SIM test is standardized in ASTM D 6992, and its use in development of creep reduction factors is well established and referenced in the two guidance documents.

SIM FOR COMPRESSIVE CREEP

As with geosynthetic reinforcements, SIM is increasingly used to evaluate the compressive creep proper-ties and reduction factors for geosynthetic planar drains. In much the same way as a reinforcement is tested at loadings representing various percentages of its measured ultimate tensile strength, a geosynthetic drain is tested at loading representing various percentages of its measured ultimate compression strength.

Significantly, once a product is characterized for its retained thickness at some design life, a drain may be able to be compressed to that exact thickness in a short term controlled compression, then tested for flow testing at that thickness. What may be realized then is a thickness-dependent hydraulic transmissivity test.

For example, if SIM compressive creep testing of a HDPE bi-planar geonet has resulted in a retained thickness of 75 percent at an equivalent time of 30 years,

Fig. 6 TRI compression SIM incline test

then a series of short term thickness-dependent transmissivity tests may be performed by first compressing the geonet to 75% of its original thickness and then immediately measuring flow.

This approach was first proposed by Allen in 1999 and has been used in a variety of site specific testing programs which require rapid response design estimates of flow for product selection and design confirmation. SIM allows the thickness-load-time relationship to be characterized rapidly affording time-dependent transmissivity testing that is both accomplished in a short period of time, and with numerous specimens reflecting roll width variability.

CONCLUSION

The measurement of short term physical and mechanical properties does not always segregate the good, bad and superior geosynthetic products from each other. However, the development of accelerated testing technologies has afforded this segregation and has recently been made more practical for site-specific use.

Accelerated testing has afforded more robust product

development and independent site specific product design and verification. Especially useful and integral to these testing programs has been the standardization of SIM and the acknowledgement of the SIM as a useful application of TTS with testing schedule and economical benefits to the user.

REFERENCES

Thornton JS, Allen SR, Thomas RW, Sandri D (1997) Approaches for the Prediction of Long Term Viscolelastic Properties of Geosynthetics from Short-Term Tests. Geosynthetics ’97, Vol. 1, Indus-trial Fabrics Association International, Long Beach, California

Thornton J, Allen S, Siebken J (2000) Long Term Compressive Creep of High Density Polyethylene Geonet, Proceedings of EuroGeo 2

Baker TL, Thornton JS (2001) Comparison of Results Using the Stepped Isothermal Method and Conventional Creep Tests on a Woven Polypropyl-ene Geotextile, Geosynthetics ’01, Portland, Oregon

Allen SR (2003) Considerations on the Stepped Isothermal Method — A Breather on the Way to Widespread Use, GSI Conference Proceedings, Hot Topics in Geosynthetics—IV Waste Properties; Geotextile Tubes; Challenges 4: 272- 291

Narejo D, Allen SR (2004) Using Steeped Isothermal method for geonet creep evaluation. Proc. Of the 3rd EuroGeoconference, Munich, Ger-many, 539-544

Washington Department of Transportation Test Method T 925, 1) Washington State Department of Transportation Standard Practice T 925, Standard Practice for Determination of Long-Term Strength for Geosynthetic Reinforcement, 2006, http://www.ntpep.org/ProfileCenter/Uploads/WSDOT_T925_11-23-05.pdf

ISO CD 20432, Guide to the determination of long-term strength of geosynthetics for soil reinforcement, www.iso.org

Proceedings of the 4th Asian Regional Conference on Geosynthetics
June 17 - 20, 2008 Shanghai, China

CREEP TESTS OF GLASS FIBER REINFORCED PLASTICS

L.H. Li[1], L. Chen[2] and Z. Wang[3]

ABSTRACT: Glass fiber reinforced plastics (GFRP) is a new type of geosynthetics. A spiral anchor of GFRP is developed. Tensile tests and creep tests of GFRP anchor have been carried out. Creep test results show that creep properties of the GFRP are obviously different from that of conventional geosynthetics. Creep properties of the GFRP have not been affected by temperature change. There is no creep occurrence besides instantaneous strain when bearing load is smaller than 40% of the tensile strength. It can be concluded that creep properties of GFRP are perfect.

KEYWORDS: GFRP, spiral anchor, creep

INTRODUCTION

Glass fiber reinforced plastics (GFRP) is a new type of compound geotechnical materials manufactured by molding technology of pulling and extrusion. Glassfiber is used as reinforced material of GFRP and synthetic resin is parent material of GFRP mixed some auxiliary. GFRP has obvious merits such as high strength, lightweight, corrosion resistant and antifatigue etc. Other aramid fiber and carbon fiber are in common use. Common parent materials have unsaturated polyester resin, epoxide resin and vinylit resin etc. GFRP came out in the 1970s. GFRP is instead of conventional steel and wood in some special environment. GFRP has been widely used in architecture, bridge, underground, ocean and tunnel engineering, etc. GFRP was firstly used in Sweden in 1987. A great variety of FRP anchors later have been developed in Germany, Canada and Japan. A new type of GFRP anchor has been put forward by professor. Wang in Wuhan University. The GFRP anchor is made by glass fiber reinforced plastics. The whole spiral anchor structure consists of anchor slab, body of rod and anchor lock of GFRP. The long term mechanical properties of the GFRP anchor must be conserved when used in slope protection. Present applied research of GFRP is introduced in this paper.

The principal material of GFRP is high polymer of glass fiber. GFRP is a new type of geosynthetics. Creep properties of the GFRP anchor are important factors to determine long term work properties when reinforced in slope protection. Creep properties have intimate relation with stress level. The working stress of GFRP is different from that of steel anchor. Presently, there are creep studies on aramid fiber reinforced plastics (AFRP) and carbon fiber reinforced plastics (CFRP). But there is no creep study on GFRP.

ACI440 committee came into existence in American in 1991. A summary report on GFRP was publicized by the committee in 1996, which discussed background, constituent performance, test methods, design criteria, practical application and research area of GFRP. Concrete design and construction criterion on FRP were put forward by the ACI440 committee in 2001. Material nature, design and construction criterion on FRP have been represented because physical and mechanical properties of FRP are obviously different that of steel. CFRP is firstly developed by the Marshall-Vega company in American. Subsequently, GFRP is used in ocean structure, park, retaining wall, foundation of nuclear reaction, aerodrome runway, electron test site and tunnel etc.

FRP standard about express highway bridge was publicized in Canada in 1991. Light guide monitoring technology was exploited in 1995. The Taylor Bridge was built through Assiniboine River in Manitoba province in Canada in 1997. CFRP was used in girders of the Taylor Bridge. The bridge board and retaining wall material consist of FRP.

Application studies on FRP began in the 1970s in Japan. Many products about FRP were developed in 1987 including sheet, board, twisted line, flat and three-dimensional lattice products. The first part of world construction standard about FRP was established in Japan in 1993. FRP has been widely used in concrete bridge, suspension bridge, ocean pier, dock, tunnel, anchor block, retaining wall and magnetic suspension

1 Assistant Researcher, State Key Laboratory of Hydroscience and Engineering, Tsinghua University, Beijing 100084, CHINA. Email: lilihua466@163.com
2 Associate Professor, State Key Laboratory of Hydroscience and Engineering, Tsinghua University, Beijing 100084, CHINA. Email: lunchen@tsinghua.edu.cn
3 Professor, Department of Civil engineering, Wuhan University, Wuhan, CHINA. Email: wazh136@163.com

rail in Japan.

The first world twist highway bridge of FRP was built in 1986 in Germany. A cooperation project of Germany and Holland from 1991 to 1996 mainly was studied on FRP properties used in concrete structure. EUROCRETE project from 1993 to 1997 was studied on FRP about material development, durability, design criteria and economic viability etc.

Long term strength tests on AFRP show that stress relaxation of AFRP increases with temperature rising and stress relaxation in atmosphere is smaller than that of in liquor. AFRP presents excellent creep character in all environments when bearing load under 40% of the tensile strength (Saadamanesh and Tannous 1999). Some studies show that creep strain of CFRP is always zero when loading under 60% of the tensile strength (Patrick 2003).

Creep tests of the new GFRP anchor have been carried out in this paper, which undergoes four months. Creep test results have been analyzed and some conclusions have been given. The GFRP anchor has not any creep strain occurrence when applied loading under 40% of the tensile strength. The GFRP has perfect creep properties, which is obviously different from conventional creep properties of geosynthetics. The creep results of GFRP obtained from this paper conform to the creep research conclusions by other scholars on AFRP and CFRP. Creep test results can offer references for development and wide application of GFRP.

CREEP TEST OF GFRP ANCHOR

Tensile Test

The tensile test equipment is a compositive geosynthetic determinator with TZY-1 of the model number, which can automatic record tensile force and extension. Because of material self-particularity, glass fibre reinforced plastic easily appears slipping and pinching off during tensile test. Conventional clamping fixture used to check tensile strength of geosynthetics can not hold the anchor rod of glass fiber reinforced plastic during test. Therefore, a home-made clamping fixture is used according to material self-properties. Concave and convex canals matching to inside and outer radius of the anchor rod are fluted separately in the interspace of two clamping fixture. Samples inside and outer radius are 8 mm and 14 mm separately. Sample shape is columned and slender. Ten same samples are used to determine tensile strength and extensibility. Measurement metering length of samples is 100 mm. Rate of extension is 20 mm/min namely 20%/min of measurement metering length. Structural figure, photograph and tensile test picture of the GFRP anchor rod are showed in Figs. 1, 2 and 3.

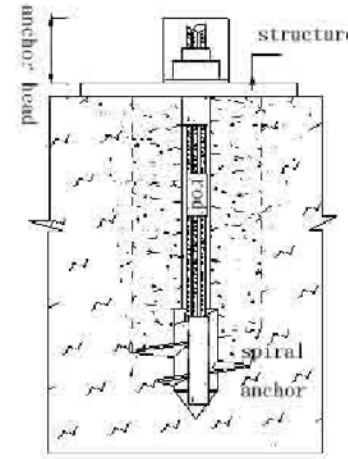

Fig. 1 Structure of the GFRP anchor

Fig. 2 The site photo of the GFRP anchor

Fig. 3 Tensile test of the GFRP anchor

Test data drawn from samples failure at gripping head and samples slipping during test are taken as ineffective data. Mean value of ten groups data is calculated results. Tensile force of the GFRP anchor rod is 5.4 kN and the extensibility is 5.1%. The mean square deviation and coefficient of variation are calculated in order to determine reliability of arithmetical mean. Tensile force is with 0.576 of the mean square deviation and 10.8% of the coefficient of variation. Extensibility is with 0.001 of the mean square deviation and 19.3% of the coefficient of variation.

Creep Test

Creep tests of the GFRP anchor rod are carried out. Different load levels are selected according to samples tensile strength during test.

(1) Sample Size and Strain Measurement

Creep test size is the same as tensile test size. Effective length is the clear distance between upper and lower clamping fixture. Measurement of extension strain is manual.

(2) Clamping Method of Samples

Conventional clamping fixture can not used to the GFRP anchor rod because of material special performance. Slipping and shearing failure often occurs. Six groups clamping fixtures are specially made. Each group clamping fixture is consisted of two small aluminum plates. Concave and convex canals at interspace of the two aluminum plates are fluted, which is matching to inter and outer radius. Two aluminum plates with concave and convex canals are gripped in conventional clamping fixture, which can avoid samples slipping and shearing failure.

(3) Samples Loading

Constant weights are adopted to feed during creep test. Three groups of creep tests are carried out because of limited condition. Three tensile loads are selected with 10%，20% and 40% of the tensile strength. Samples and clamping fixtures are vertical hanging. Tensile load is applied once by weights.

(4) Test Environment

Tests are carried on in testing laboratory. Indoor temperature is recording test temperature.

(5) Time-interval Observation

Measurement when starting is strictly according to the standard specification of geosynthetics. Subsequently, reading once every day.

(6) Test Results and Analysis

The loading level of the first creep test is 10% of the tensile strength with 209 mm of the initial measure length. The instantaneous creep strain is 3 mm when applied. But subsequently we can not observe any creep strain during four months. The loading level of the second creep test is 20% of the tensile strength with 216 mm of the initial measure length. The instantaneous creep strain is 4mm when applied. The loading level of the third creep test is 40% of the tensile strength with 204 mm of the initial measure length. The instantaneous creep strain is 5 mm when applied. There is also no creep strain occurrence of the second and the third tests during four months. But the sample applied 40% of the tensile strength failures at the end of the fourth month. Tests process and results are given in Figs. 4, 5 and 6.

As indicated by Fig. 5 creep curves at three different loading level all are horizontal lines. There is only instantaneous creep strain occurrence of the GFRP when applied loading. Creep strain is not increasing with time increasing. Creep properties of the GFRP are obviously different from that of conventional geosynthetics. Creep tests have lasted more than four months. Creep strain always has not increased. Then isochronal curves of loading vs strain are repeated a curve. It is given in Fig. 6. The long term creep strain is stationary no matter what the serviceable life is. The more the loading level is, the more creep strain of the GFRP is, which is the same as conventional geosynthetics. As can be seen in Fig. 6, it is conformable using quadratic polynomial to fit isochronal curves. There is no long term creep phenomenon occurrence because of material particularity. Therefore, creep reduction factors of the GFRP can not be calculated by conventional methods. It also can not be gained according to the long term allowable strain value. But creep failure occurs of the GFRP when applied load is 40% of the tensile strength. The creep reduction factor of the GFRP is at least 2.5.

Fig. 4 Creep test of the GFRP anchor

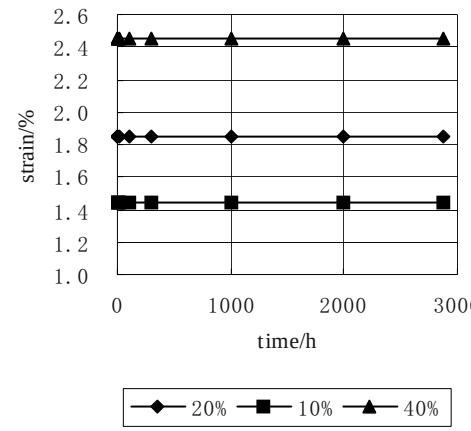

Fig. 5 Strain-time curves of GFRP

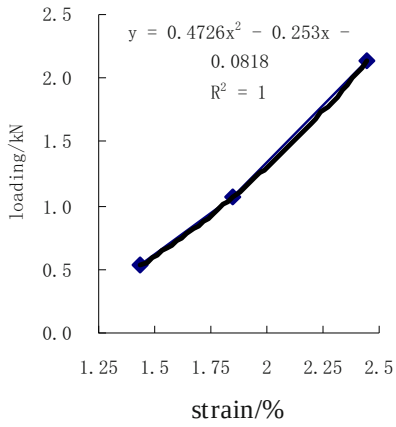

Fig. 6 GFRP isochronal curve of load-strain

CONCLUSIONS

Test results show that as a new type of geosynthetics, creep properties of the GFRP are perfect. There is only instantaneous small strain occurrence when applied load in three groups of tests. There is no creep strain increasing with time increasing. Indoor temperature during tests ranges from winter to spring lasted four months. But creep properties of the GFRP have not been affected by temperature change. It can be concluded that creep phenomenon effect on the GFRP can be ignored when bearing load is smaller than 40% of the tensile strength in application engineering. The creep results of GFRP obtained from this paper conform to the creep research conclusions by other scholars on AFRP and CFRP. Creep reduction factor of GFRP should be considered at least 2.5 when designed because of creep failure occurrence. Creep test results can offer references for development and wide application of GFRP.

REFERENCES

Alsayed SH (2000) Fiber-reinforced polymer repair materials — some facts. Civil Engineering (8): 131-134

Hamid S, Fares ET (1999) Long-term behavior of aramid fiber reinforced plastic (AFRP) tendons. ACI Materials 96(3): 297-305

Karbhri VM (2002) Response of fiber reinforced polymer confined concrete exposed to freeze and freeze-thaw regimes. J. Journal of Composites for Constructure 6(1): 35-40

Karbhari VM, Chin JW (2003) Durability gap analysis for Fiber-Reinforced Polymer Composites in Civil Infrastructure. Journal of Composites for Constructure 7(3): 238-247

Somjai K, Rakesh KG, Hota VS, Ganga R (2002) Effect of aging environment on degradation of glass-reinforced epoxy. Journal of Composites for Constructure 6 (1):61-69

Itaru N, Eishi M (2002) Long-term deterioration of GFRP in water and moist environment. Journal of Composites for Constructure 6(1): 21-27

Zou XW (2003) Long-term properties and transfer length of fiber-reinforced polymers. Journal of Composites for Construction 7(1):10-19

Proceedings of the 4th Asian Regional Conference on Geosynthetics
June 17 - 20, 2008 Shanghai, China

STUDY ON HYSTERESIS PROPERTIES OF PIEZOMETER TUBES USING CIRCULATING WATER MODEL

L.H. Li[1], L. Chen[2], J. Li[3] and Z. Wang[4]

ABSTRACT: Study on hysteresis phenomenon of piezometer tubes through comparing reading of pore water pressure sensors and piezometer tubes has been carried out. Some conclusions have been gained. Hysteresis phenomenon is more obvious with the distance of piezometer tubes to soil bottom increasing. Hysteresis phenomenon of piezometer tubes at soil middle is always obvious until the periodicity reaches 20.8 min. But head loss and hysteresis phenomenon both are small near soil bottom whatever the periodicity is. Hysteresis phenomenon can be ignored when the periodicity reaches 46.5 min. It shows that dry density has some influence on hysteresis phenomenon. Hysteresis phenomenon because of effect of different dry densities becomes small with increasing of the periodicity.

KEYWORDS: hysteresis properties, piezometer tubes, circulating water, woven geotextiles

INTRODUCTION

In many cases of earth and rock-fill dam and reservoir dam, it is convenient and economical to choose piezometer tubes for long term inspection of water level. In the proper position of earth and rock-fill dam，precise and immediate measurement with piezometer tubes could observe seepage of building, which is significant for the security of dams. But in the long term inspection, because of some reasons, data from piezometer tubes could not reflect the water level of dams precisely.

Reading of the water level from piezometer tubes and actual variation in water level is not consistent. Water level of piezometer tubes falls behind than actual water level. It means that there are hysteresis properties. Hysteresis time of every piezometer tube at the same section can be different. Therefore, it is necessary to determine hysteresis time before analysis of data from piezometer tubes to avoid gaining unsafe results. It is common to draw water level of dams and water level from piezometer tubes by hands and observe peak time to get hysteresis time, which is not precise and not easily computerized.

There are quite a few scholars doing researches about hysteresis properties of piezometer tubes, which focus on application in construction projects. For example, the time when water level of tubes gains new balance is calculated by seepage principle of varying head in incompressible soil. Several hysteresis factors of piezometric tubes in soil dams (Shen R G 1990), application of artificial intelligence technology in calculation of piezometer tubes hysteresis time (Si C L 2005).

When geosynthetics are used in filtration, there is also hysteresis phenomenon of piezometer tubes. Study on hysteresis properties of piezometer tubes using circulating water model has been carried out in this paper and some conclusions have been gained.

TEST AND RESULTS

Test Samples

Indexes of samples are given in Table 1. Filter material is woven geotextiles with 0.6 mm of equivalent aperture.

Table 1 Indexes of samples

Sample	c (kPa)	ϕ ($^\circ$)	d_{85} (mm)
Silt	19.2	27.1	0.07

Test Devices

Modification to test model is carried out according to laboratory circulating water model. Pore water pressure sensors are used to measure variation in water level in soil. Test model is given in Fig. 1. Right equipment of the model is a circulating system, which can supply circulating water for soil. Middle part of the model is

[1] Assistant Researcher, State Key Laboratory of Hydroscience and Engineering, Tsinghua University, Beijing 100084, CHINA. Email: lilihua466@163.com
[2] Associate Professor, State Key Laboratory of Hydroscience and Engineering, Tsinghua University, Beijing 100084, CHINA. Email: lunchen@tsinghua.edu.cn
[3] Graduate Student, Master, Department of civil engineering, Wuhan University, Wuhan, CHINA. Email: lijie466@tom.com
[4] Professor, Department of Civil engineering, Wuhan University, Wuhan, CHINA. Email: wazh136@163.com

filter equipment. Soil samples and woven geotextiles are placed in the container. Pore water pressure sensors and piezometer tubes are connected with the container arm at different parts. There are eight piezometer tubes and three pore water pressure sensors used in test. Inner diameter of piezometer tubes is 2.7 mm and the distance between every two piezometer tubes is 25 mm. Reading of three pore water pressure sensors is compared with measured values of piezometer tubes at corresponding position. The periodicities taken in the test are 0.5, 2.5, 9.8, 12.5, 20.8 and 46.5 min.

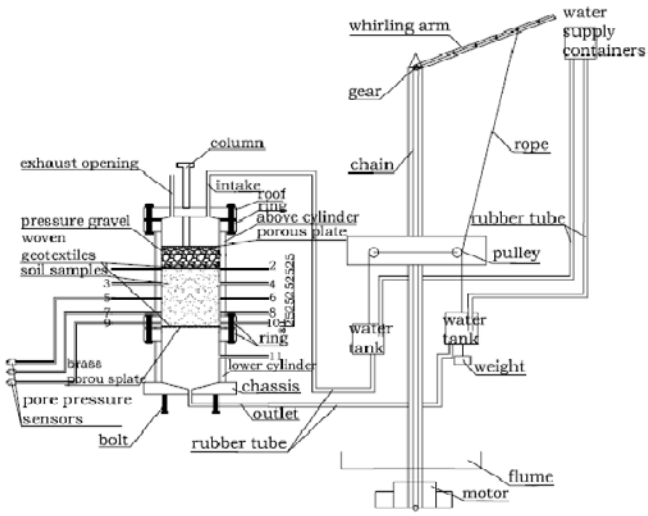

Fig. 1 Test device

Test Methods

Soil samples are placed in the container with 100 mm of the soil height. Soil samples are compacted by four layers. Two different dry densities are adopted in the test. There are 1.5 g/cm^3 and 1.8 g/cm^3. Woven geotextiles are placed at the upper and bottom of the soil respectively. A permeable plate and gravel are placed on surface of the upper woven geotextile, which can guarantee water reaches inner soil. Water is supplied from down to upper and soil samples are kept saturation for 12 hours. In and out water tubes, piezometer tubes and pore water pressure sensors are connected. Air discharge is carried before test beginning. Circulating water are supplied lasted at least 20 periodicities. Stability of filter layer and reading are observed. The direction of supplied water is changed from upper to down after some time. Reading is observed as mentioned above.

Tests Results and Analysis

(1) Comparing results at two different dry densities with T=0.5 min

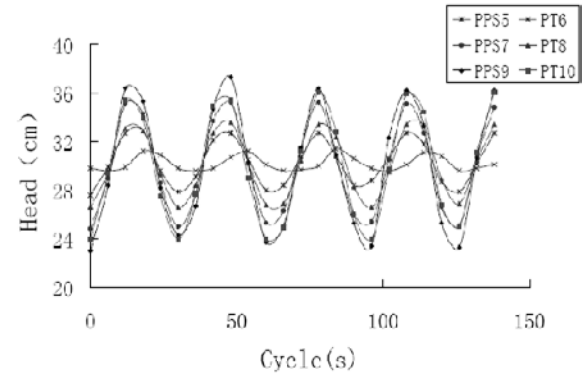

PPS-Pore Water Pressure Sensors
PT-Piezometer Tubes

(a) $\rho = 1.5$g/cm^3, T=0.5 min

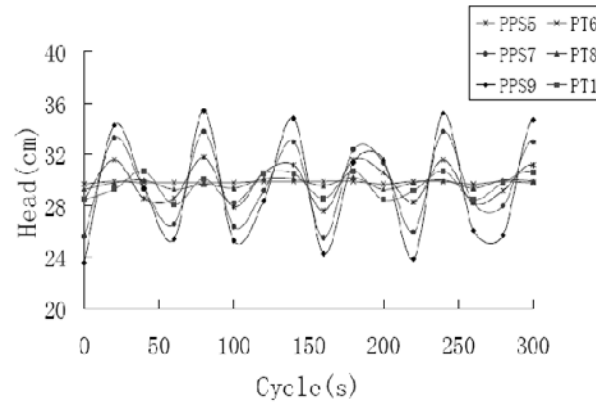

(b) $\rho = 1.8$g/cm^3, T=0.5min

Fig. 2 Comparing results of PPS and PPT

Fig. 2 is comparing results at two different dry densities when periodicity is 0.5 min. As can be seen in Figs. 2a and 2b, there is no hysteresis phenomenon at contacting place between soil and geotextiles with 0 mm of the soil body height at two different dry densities. The head loss mainly results from water-head of piezometer tubes. The head loss is smaller when the dry density is 1.5 g/cm^3 than that the dry density is 1.8 g/cm^3. It can be seen that dry density of soil has influence on variation in water level of piezometer tubes.

Test results show that the measured value difference of piezometer tubes and the pore water pressure sensors at 25 mm of the soil body height results from in and out pressure difference of piezometric tubes, which is as the same as at 0 mm of the soil body height. But at 50 mm, there is energy loss and hysteresis phenomenon at different dry densities and the hysteresis properties are very obvious. The bottom height of the test soil is 0 mm and the middle height of the test soil is 50 mm. It can be concluded that the far the distance from the bottom to the middle is, the more obvious the hysteresis properties are when the periodicity is 0.5 min.

(2) Comparing results at two different dry densities with T=2.5 min

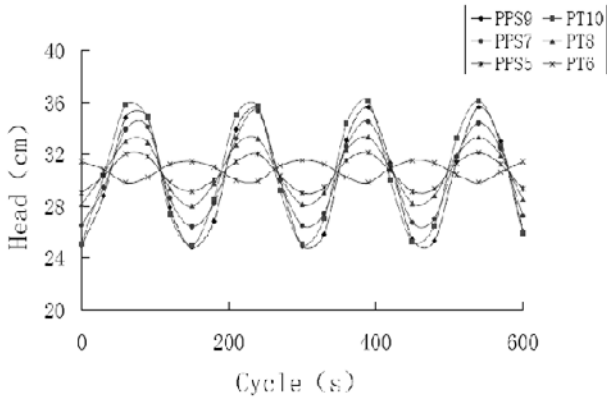

(a) ρ=1.5 g/cm^3, T=2.5 min

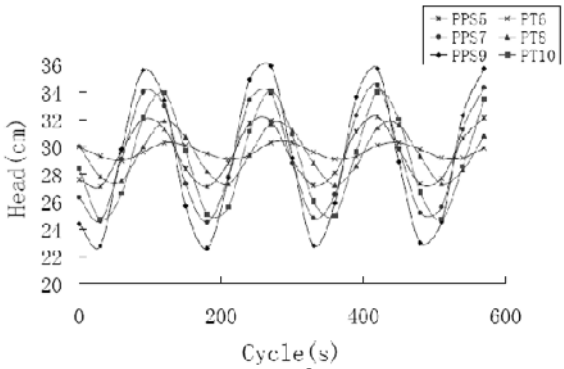

(b) ρ=1.8 g/cm^3, T=2.5min.

Fig. 3 Comparing results of PPS and PPT

Fig. 3 is comparing results at two different dry densities when periodicity is 2.5 min. As can be seen in Figs. 3a and 3b, there is no hysteresis phenomenon at 0 and 25 mm of the soil body height at two different dry densities. Energy loss mainly results from water pressure difference. Energy loss is increasing with the distance from bottom to soil middle increasing. In the middle soil with 50 mm of the height, there is large hysteresis phenomenon. There are obvious hysteresis phenomenon and energy loss at different height in soil when the dry density is 1.8 g/cm^3. It also shows that dry density has influence on hysteresis phenomenon.

(3) Comparing results at two different dry densities with T=20.8 min

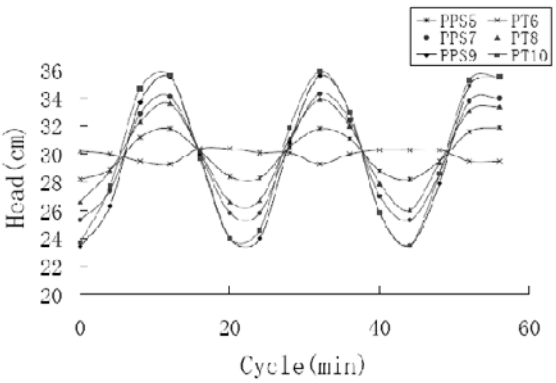

Fig. 4 Comparing results of PPS and PPT
(ρ=1.5 g/cm^3, ρ=1.8 g/cm^3, T=20.8 min)

Test results when periodicity is 20.8 min are given in Fig. 4. As can be seen in Fig. 4, there are no energy loss and hysteresis phenomenon at 0 mm of the height. But there is small energy loss at 25 mm of the height and there are large energy loss and hysteresis phenomenon at 50 mm of the height. It shows that it is difficult to exactly measure head pressure in short time with piezometer tubes at middle soil. Therefore, long term comparing between piezometer tubes and pore water pressure sensors are carried out.

(4) Comparing results at two different dry densities with T=46.5 min

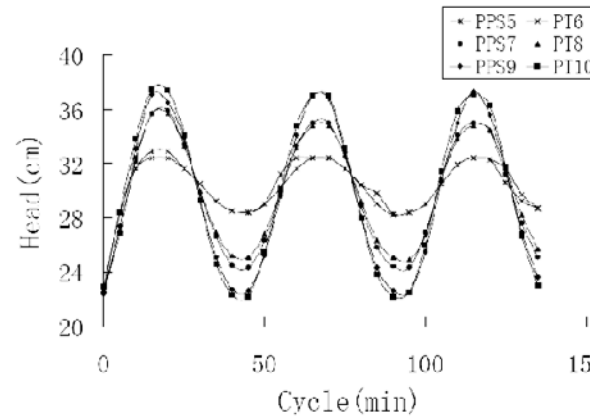

Fig. 5 Comparing results of PPS and PPT
(ρ=1.5 g/cm^3, ρ=1.8 g/cm^3, T=46.5 min)

Comparing results at long term periodicity is given in Fig. 5. As can be seen in Fig. 5, it is different from results mentioned above. Reading of the piezometer tubes and pore water pressure sensors is the same at 46.5 min. of periodicity whatever the position is. It shows that the difference between piezometer tubes and pore water pressure sensors can be ignored with increase of the circulating periodicity.

CONCLUSIONS

Study on hysteresis phenomenon of piezometer tubes through comparing reading of pore water pressure sensors and piezometer tubes is carried out. Some conclusions can be gained.

(1) Test results show that the reading difference of piezometer tubes and pore water pressure sensors mainly results from the resistance of the soil connected with piezometer tubes, which makes it difficult to water level rising in immediate time.

(2) Head loss is large during circulating of reciprocate water at 0.5 min of periodicity. Hysteresis phenomenon is more obvious with the distance of piezometer tubes to soil bottom increasing. Hysteresis phenomenon of piezometer tubes at soil middle is always obvious until the periodicity

reaches 20.8 min. But head loss and hysteresis phenomenon both are small at near soil bottom whatever the periodicity is. Hysteresis phenomenon becomes small with increasing of periodicity. Lastly, hysteresis phenomenon can be ignored when the periodicity reaches 46.5 min.

(3) There are obvious hysteresis phenomenon at different position when the periodicity is 2.5 min and the dry density is 1.8 g/cm^3, which shows that dry densities have some influence on hysteresis phenomenon. Hysteresis phenomenon because of effect of different dry densities becomes small with increasing of the periodicity.

ACKNOWLEDGEMENTS

The supports of National Natural Science Foundation of China (Grant No. 50578086) and National Post Doctoral Science Foundation of China (Grant No. 2005038041) are gratefully acknowledged.

REFERENCES

Chen L, Xu Q, Yi HQ, Zhuang YF (2007) Simulating test study on the seepage stability of the soil-geotextile filtration under cyclic flow. Hydroelectric Journal 26(4): 115-119

Chen L,Yi HQ, Xu Q, Zhuang YF (2006) The study of the structure stability simulated tests in soil-geotextile filtration. Hydroelectric Journal: 117-121

Chew SH, Zhao ZK, Karunaratne GP (2000) Revetment geotextile filter subjected to cyclic wave loading Geotechnical Special Publication 8: 162-175

Shao NC (2001) Some problems about piezometric tube. Dam Observation and Geotechnical Tests 25(5): 6-7

Shen RG (1990) Discussion the hysteresis time piezometric level of several major factors. Zhe Jiang Water Science and Technology (2):26-27

Si CD, Qie ZH, Wu XM, Liu RX, Liu QY (2005) The methoed of calculating hysteresis time of piezometric tube for earth-rock dam. Water Science and Engineering (3):3-6

Wang Z (2002) Research on the applications of geosynthetics in foreign countries. Hongkong: Modern Knowledge Press

Physical Tests and Centrifuge Tests

EVALUATION OF INTERFACE PARAMETERS FROM PULLOUT TEST IN SILTY SAND AND WEATHERED CLAY

D.T. Bergado [1], P.V. Long [2], J. Saowapakpiboon [3] and P. Voottipruex[4]

ABSTRACT: The interface parameters which are needed for both finite element and conventional analyses of geotextile-reinforced earth structures such as the local shear stress/shear displacement, the interface interaction coefficient and the in-soil stress/strain of the reinforcement have been successfully interpreted by the newly proposed method considering the softening behavior and non-uniform distribution of shear stress along the extensible reinforcement. Results from this study indicate that the interpretation of pullout tests using conventional methods underestimated both the shear stiffness and the peak shear strength at the pullout interface of extensible reinforcement.

KEYWORDS: interface parameters, geotextile-reinforced earth structure, pullout test

INTRODUCTION

Geosynthetics can play important and vital roles in the protection, mitigation and rehabilitation efforts in affected coastal areas. Geosynthetics have been used in hydraulic and geotechnical engineering for about the past two or three decades. Their use is well established for the purposes of material separation, filters, and reinforcement. In addition, all kind of bags are made now from synthetic fabric. The use of geosynthetics has advantages such as speed of construction, flexibility and durability, use of local soil materials rather than imported quarry product, and its cost effectiveness. Therefore, it is strongly recommended to use the geosynthetics engineering applications for restoring and rehabilitation of the recent devastations caused by the Tsunami. This paper demonstrates the geosynthetic applications of high-strength geotextile to mitigate tsunami devastations focusing on soil reinforcement application.

The use of geosynthetics has unique advantages over other soil strengthening techniques, due to their low mass per unit area, strength, and stiffness characteristics. However, the use of geosynthetics requires a proper understanding of soil-geosynthetic interaction mechanisms. The pullout behavior of geogrids and geotextiles has been investigated by full-scale tests, laboratory model tests and numerical analyses (Sugimoto and Alagiyawanna 2003). However, most of the previous studies were directed to investigate the interaction parameters (i.e., pullout resistance and shear stress-strain characteristics) between geosynthetics and granular soils. Few researches have been done relevant to the evaluation of the interaction parameters between the cohesive soils and the geosynthetics (Bergado et al. 1991). Utilizing of cohesive soils would involve considerable savings on condition that the intended engineering purpose can be achieved. In this paper, the interactions of high-strength geotextile with silty sand and weathered clay have been compared.

REINFORCED IN PULLOUT TEST

As mentioned earlier, the pullout mechanism of reinforcements from soils has been commonly investigated by pullout tests. However, at present, pullout tests on geotextile reinforcement have not been interpreted satisfactorily. The high elongation, confinement-dependent behavior of geosynthetics, and the slippage at the clamped end during pullout are still the main barriers for obtaining reliable results. The commonly used method (Collios et al. 1980) for interpretation of pullout tests were based on the assumption of uniform distribution of stress, and thus, the pullout shear stress was obtained as follows:

$$\tau = P/2L = \sigma \tan\delta_a + c_a \quad (1)$$

[1] Professor, School of Engineering and Technology, Asian Institute of Technology, THAILAND. Email: bergado@ait.ac.th
[2] President, Vina Mekong Engineering Consultants, VIETNAM. Email: h2pvl@vnn.vn
[3] Doctoral Candidate, School of Engineering and Technology, Asian Institute of Technology, THAILAND. Email: st103619@ait.ac.th
[4] Associate Professor, Department of Teacher Training in Civil Engineering, King Mongkut's Institute of Technology North Bangkok, THAILAND. Email: pnv@kmitnb.ac.th

where:

P=pullout force per unit width of reinforcement

σ=total normal stress at interface

δ_a and c_a=friction angle and cohesion at pullout interface, respectively

L=displaced length of the reinforcement corresponding to pullout force, P.

The values of the displaced length (effective length), L, can be obtained from the measured displacements at various points inside the shear box (Hayashi et al., 1994). However, the assumption of uniform distribution of shear stress along the soil-reinforcement in pullout loading is not reliable for the case of extensible reinforcement (Long et al. 1995). A general distribution of reinforcement displacement, u(x), shear stress distribution at interface, τ(x), and tension force (per unit width), T(x), along the reinforcement can be schematically illustrated in Fig. 1. The relation between shear stress, τ, acting along an infinitesimal interface, dx, and the mobilized tensile force per unit width of the reinforcement, T, is expressed by the following equation:

$$\frac{dT}{dx} = 2\tau \tag{2}$$

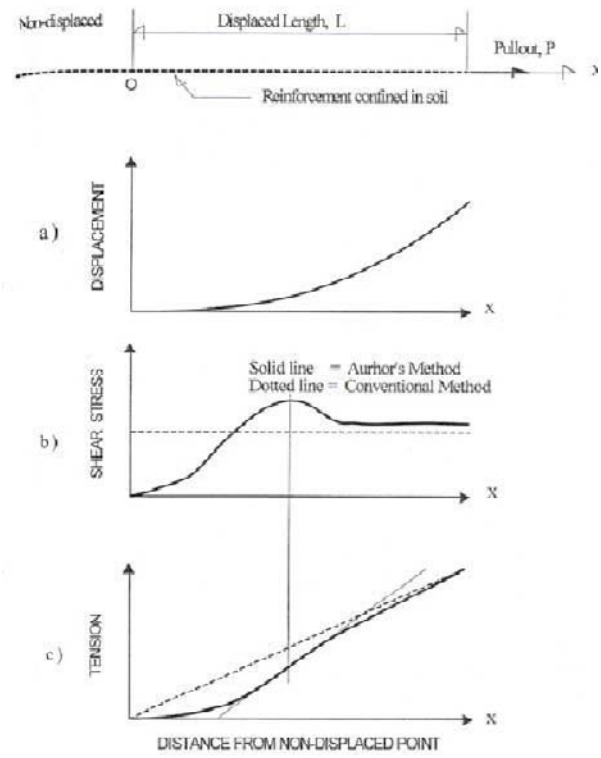

Fig. 1 Schematic diagrams for distribution of displacement, shear stress, and tension along the extensible reinforcement in pullout test

The shear stress given by Eq. 2 is the "local" shear stress at a considered point while the shear stress presented in Eq. 1 is the "global" shear stress along the displaced length. As can be seen in Figs. 1b and 1c, the shear stress interpreted by Eq. 1, referred to as the conventional method, is generally smaller than those calculated from Eq. 2.

METHOD OF INTERPRETATION

The compatibility between displacement, u, and tensile strain, E, of the reinforcement is given as follows.

The tangent stiffness of the in-soil tension-strain of reinforcement, S_t can be expressed as:

$$S_t = \frac{dT}{d\varepsilon} \tag{4}$$

Differentiation of Eq. 3 and substitution for T and E from Eqs. 2 and 4, the governing equation at soil-geotextile interface can be obtained as follows:

$$\frac{d^2u}{dx^2} = \frac{2\tau}{S_t} \tag{5}$$

Under the pullout force per unit width of reinforcement, P, the reinforcement displacements are assumed to decrease gradually from the pullout end to some location having, no displacement (non-displaced point) as given in Fig. 1. Thus, the reinforcement displacement, u = y(x), is an ascending, non-linear function of x as presented in Fig. 2. Practically, the plot of y(x) can be divided into small segments so that in each segment, the function y(x) can be approximated by a parabola, $Y(X) = AX^2$, in local coordinate (X, Y) as illustrated in Fig. 2. Thus, under the pullout P_j, for the segment i from node i to node i+1, the approximated displacement can be written in the following form:

$$u_{i,j} = y_j(x) \approx Y_{i,j}(X) = A_{i,j}X^2 \tag{6}$$

for $X_{i,j} \le X \le X_{i+1,j} = X_{i,j} + \Delta x$

The physical meaning of the curve fitting coefficient, A_{ij} can be obtained from Eqs. 5 and 6 as follows:

$$A_{i,j} = \tau_{i,j}/S_{i,j} \tag{7}$$

Rewriting Eq. 6 for nodes i and i + 1:

$$u_{i,j} = A_{i,j}\ X_{i,j}^2 \tag{8a}$$

$$u_{i+1,j} = A_{i,j}\ X_{i+1,j}^2 \tag{8b}$$

Eqs. 8a and 8b lead to:

$$\sqrt{A_{i,j}} = \frac{\sqrt{u_{i+1,j}} - \sqrt{u_{i,j}}}{\Delta x} \quad (9)$$

where

$$\Delta x = x_{i+1,j} - x_{i,j} = X_{i+1,j} - X_{i,j} \quad (10)$$

Therefore, from the measured values of reinforcement displacement at two adjacent locations i and i + 1 under various values of pullout, P_j, the values of A_{ij} can be computed. Then, from the ($A_{i,j}$ versus $u_{i,j}$) plot, the function A = f (u) can be established for the general relation between the displacement, u, and the corresponding coefficient A.

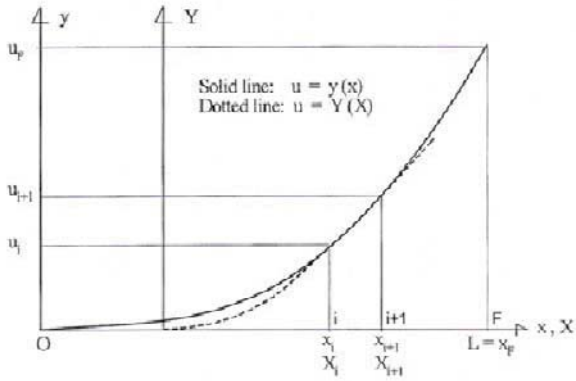

Fig. 2 Approximation for the distribution of reinforcement displacements

PULLOUT DISPLACEMENT

The pullout displacement is usually measured at the pullout head outside the shear box. This displacement includes the unavoidable slippage between the reinforcement and the clamping system as well as the deformation of the connection system from the inner clamps to the measured location. Therefore, the following extrapolation scheme has been derived for obtaining the pullout displacement excluding the aforementioned effects.

Eq. 8b can be written in the other form as:

$$u_{i+1,j} = A_{i,j}(X_{i,j} + \Delta x)^2 = u_{i,j} + A_{i,j}\Delta x^2 + 2A_{i,j}X_i\Delta x \quad (11)$$

From Eqs. 3 and 6, the reinforcement strain, $\varepsilon_{i,j}$, at node i can be expressed by:

$$\varepsilon_{i,j} = du/dX = 2A_{i,j}\,X_i \quad (12)$$

Eqs. 11 and 12 yield:

$$ui+1,j = ui,j + Ai,j\,\Delta x^2\,\varepsilon i,j\,\Delta x \quad (13)$$

For any integer value k, Eq. 13 can be written for the general case of node i + k -1 as follows:

$$ui+k+1,j = ui,j + Ai+k,j\,\Delta x^2 + \varepsilon i+k,j\,\Delta x \quad (14)$$

The strain $\varepsilon_{i+k,j}$ in Eq. 14 can be calculated from the nodal displacements of the segment (i + k + 1) as follows:

$$\varepsilon i+k,j = (ui+k,j - ui+k-1,j) / \Delta x + Ai+k-1,j\,\Delta x \quad (15)$$

Suppose that the reinforcement portion from node i + 1 to the pullout end at node F, is divided into n segments having equal intervals, Δx, the displacement at pullout end, $u_{Fj} = u_{i+1+n,j}$, can be calculated by Eqs. 14 and 15 for k = 1 to n from the known values of $u_{j,j}$ and $u_{j+1,J}$. Then the pullout-displacement relation can be obtained as the plot of Pj versus u_{Fj}.

PULLOUT-DISPLACED LENGTH

The ascending function for displacement, u = y(x), yields the following behavior:

$$ui+1,j = ui,j+1 \;\leftrightarrow\; xi+1,j = xi,j+1 \quad (16)$$

Substitution for $u_{i+1,j}$ and $x_{i+1,j}$ from Eq. 16 into Eqs. 10 and 11, one obtains:

$$\sqrt{A_{i,j}} = \frac{\sqrt{u_{i+1,j}} - \sqrt{u_{i,j}}}{x_{i,j+1} - x_{i,j}} \quad (17)$$

Eq. 17 is also true for any value of j satisfying the increment of $(x_{i,j+1} - x_{i,j}) \le \Delta x$. Rewriting Eq. 17 for node F at the pullout end, the increment of displaced length, $\Delta L_j = x_{Fj+1} - x_{Fj} \le \Delta x$., that was caused by the incremental pullout, $\Delta P_j = P_{j+1} - P_j$ can be obtained in the following form:

$$\Delta L_j = \frac{\sqrt{u_{F,j+1}} - \sqrt{u_{F,j}}}{\sqrt{A_{F,j}}} \quad (18a)$$

Then, the displaced length, Lj+1, corresponding to the pullout force, Pj+1, can be calculated as the sum of

displaced-length increments as follows:

$$L_{j+1} = \sum_{0}^{j} \Delta L_j \qquad (18b)$$

From Eq. 2, it can be derived that the slope of pullout-displaced length curve is twice of the shear stress at interface. Therefore, the shear strength parameters at interface can be determined directly from the (P_j versus L_j) plot in the manner of Fig. 3. The peak shear strength, τ_p, and the critical state strength, τ_r, at pullout interface can be obtained from the slopes of lines BB' and AA', respectively, as seen in Fig. 3.

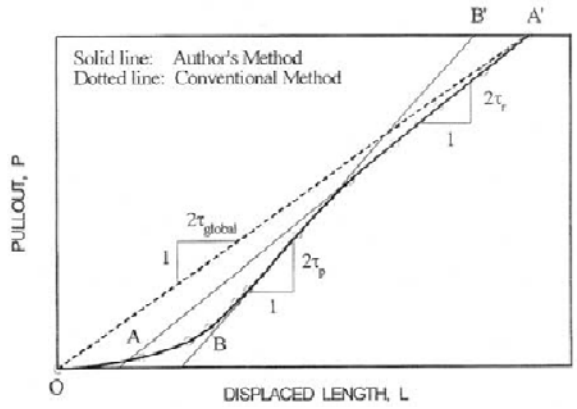

Fig. 3 Interpretation of shear strength at soil-reinforcement interface

SHEAR STRESS-RELATIVE SHEAR DISPLACEMENT AT INTERFACE

From Eq. 2, the shear stress, τ_j, corresponding to the pullout displacement u_{Fj} can be expressed by the following equation:

$$\tau_{Fj} = \frac{T_{F,j+1} - T_{F,j}}{2\Delta L_j} = \frac{P_{j+1} - P_j}{2\Delta L_j} \qquad (19)$$

where $T_{F,j+1}$ and $T_{F,J}$ are tension forces per unit width of the reinforcement at the pullout end that are equal to the pullout P_{j+1} and P_j, respectively.

REINFORCEMENT STRAIN

From Eqs. 15 and 16, the in-soil strain of the reinforcement, $\varepsilon_{F,j+I}$, corresponding to the tension at the pullout end, $T_{F,j+1} = P_{j+I}$, can be derived as follows:

$$\varepsilon_{F,j+I} = (u_{F,j+1} - u_{F,j})/\Delta L_j + A_{F,j}\,\Delta L_j \qquad (20)$$

Thus, the in-soil tension/strain relation can be constructed from the P_j versus $\varepsilon_{F,j}$ plot.

SUMMARY OF INTERPRETATION PROCEDURES

As presented in the previous sections, only two measured locations of reinforcement displacement are needed for interpretation of the behavior at pullout interface including the in soil tensile stress-strain of the reinforcement. Assume that the displacements are measured at points Band C in Fig. 4. To satisfy the assumption of parabolic distribution of displacement within the considered segment, the distance between these measured points should be selected based on the stiffness of the reinforcement. If length FB and BC is not the same, the value of Δx must be taken as the actual interval of the corresponding points. For convenience, the value of i = 1 can be assigned for point C. The procedures of interpretation are summarized in the following steps:

Step 1: Using Eq. 9 and Δx = CB to calculate the coefficient $A_{i,j}$ from the measured displacement at C and B, denoted as u_{1j} and u_{2j}, respectively. Construct the (A_{1j} versus u_{1J} plot and obtain the general relation A = f(u) from this plot, e.g. by curve fitting.

Step 2: Calculate ε_{2j} by Eq. 15 using k = 1 and Δx = BC. Compute A_{2j} = f (u_{2j}) for segment CF, then obtain the displacement at the pullout end, $u_{Fj} = u_{3j}$, using Δx = CF in Eq. 14. The pullout-displacement relation can be plotted from the values of P_j and u_{Fj}.

Step 3: Calculate A_{Fj} from the values of u_{Fj}. Then, the relations of pullout-displaced length, shear stress-shear displacement, and in-soil stress-strain of the reinforcement can be calculated by Eqs. 18b, 19 and 20, respectively. The global strength, τ_{global}, the critical state strength, τ_r, and the peak strength, τ_p, of soil-reinforcement interface can also be determined directly from the pullout-displaced length curves by means of the slopes of the corresponding line OA', AA' and BB', respectively, as illustrated in Fig. 3.

LARGE PULLOUT TESTS

The high-strength, woven-nonwoven polyester geotextile PEC200 with nominal mass of 700 g/m^2 and rupture strength of 200 kN/m, was used as the reinforcement. The investigation involves the use of weathered Bangkok clay. The weathered clay specimen was compacted at 28 % water content at a dry density of 15.1 kN/m^3, corresponding to 95% standard Proctor compaction on the wet side of optimum. Likewise, a water content of 13% and dry density of 17.0% kN/m^3, corresponding to about 95 % standard Proctor compaction, were maintained for the silty sand samples. The pullout box was made of 9.5 mm thick steel plates with inside dimensions of 1270 mm in length by 762 mm in width by 508 mm in height. The normal stress was

applied by a pressurized air bag. The pullout force was applied by a 225 kN capacity electro-hydraulic controlled jack and was measured by an electrical load cell. The clamped end of geotextile was located inside the compacted soil in order to ensure that the geotextile specimen is always confined throughout the pullout test. This way, no coupling of unconfined and confined behavior of geotextile would result during the pullout test which is an important consideration for extensible reinforcements. The pullout end of geotextile specimen is positioned at 0.25 m from the front wall for minimizing the effects of stress concentration resulted from the reaction of the front wall. The layout of geotextile specimen together with the clamping system is presented in Fig. 4. The displacements were measured by LVDTs connected to automatic data acquisition (ADA) system. The locations of displacement measurement are also given in Fig. 4. A total of five LVDTs were used. One was attached directly to the outer clamps (pullout head) for measuring the pullout displacement. The other four were connected to the geotextile reinforcement using wire extensometers. The net dimensions of the geotextile specimen were 500 mm in width by 900 mm in length. The pullout rate of 1 mm/min was used for all tests. Four series of pullout tests at different normal stresses of 25, 75 and 125 kPa were performed. To evaluate the resistance contributed by the inner clamping system, two series of dummy tests were also carried out in the same conditions with the corresponding pullout tests but without reinforcements. The net pullout force was obtained as the difference between the pullout test and the corresponding dummy test. Thus, the term "pullout", P, presented in this study is the net pullout force per unit width of reinforcement.

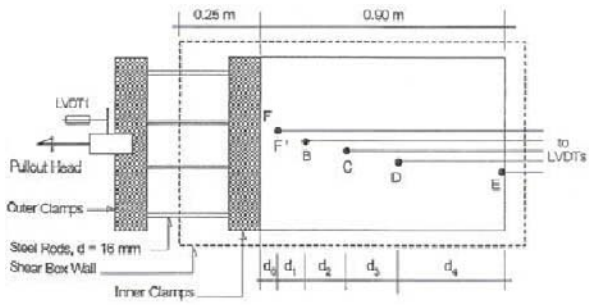

Fig. 4 Clamp system and instrumentation for large pullout test

INTERPRETED RESULTS

Pullout-displacement

The measured pullout-displacements curves at selected points along the reinforcement are plotted in Fig. 8. It can be seen from these figures that the displacement of geotextile reinforcement developed progressively with the increases of pullout force. Using the measured displacements at point B and C (Fig. 5), the curve fitting coefficients, A, were calculated and are presented in Fig. 6 as function of geotextile displacement. u. It is interesting to note that the shear stress-shear displacement relations can be roughly estimated from this plot without using the measured pullout force because the value of A is the ratio of shear stress to the reinforcement stiffness, A= τ/S .The stiffness of geotextile PEC200 is almost constant as seen in later sections. In the other words, the normalized shear stress-shear displacement relation can be approximated in terms of Fig. 6 if the reinforcement stiffness is constant.

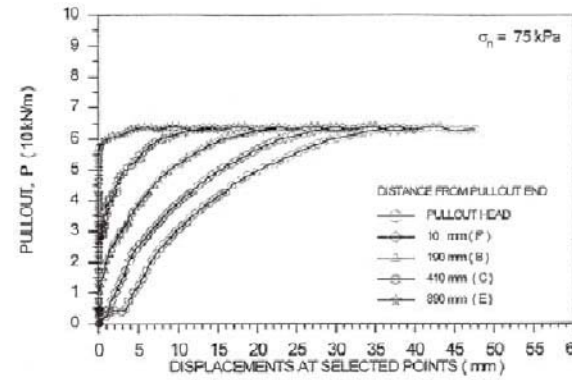

Fig. 5 Pullout-displacement at selected points in pullout test of PEC200/Clay. (normal stress = 7 .5 tsm)

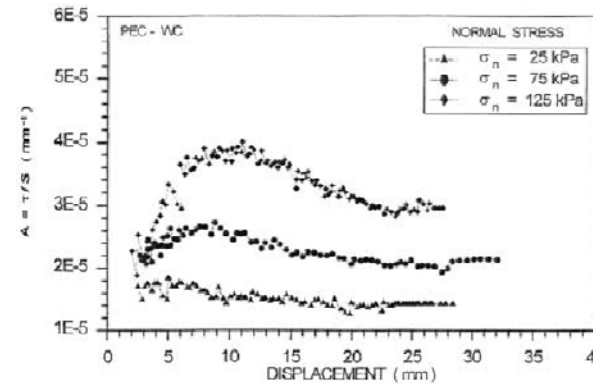

Fig. 6 A versus u relation from pullout tests of PEC200/weathered Clay

Behavior at Soil/Geotextile Interface

The shear stress-relative shear displacement relations interpreted from the proposed method are plotted in Fig. 7 for clay backfill, respectively. The corresponding relationships obtained from the conventional method are also given in these figures as dotted lines for comparison. As mentioned previously, the shear stress interpreted from the proposed method is referred as "local stress", τ =

dT/(2dx), at a considered point while the shear stress calculated from the conventional method is the "global stress", $\tau = T/(2L)$, along the displaced length, L. From now on, the terms "global" and "local" are used to refer the interaction behavior interpreted from the conventional method and the author's method, respectively. The local shear stress-relative displacement curves exhibit the softening behavior with peak strength occurring at small relative displacement of about 3 mm to 6 mm, while, the global shear stress-pullout displacement gave no distinct peak with displacement as large as 20 to 30 mm for fully mobilizing shear strength. This is because the displacement of geotextile reinforcement developed progressively along the specimen and, thus, the peak values of shear stress along the soil-geotextile interface cannot be mobilized at the same time. Consequently, the shear stiffness and peak shear strength obtained from the global shear stress were smaller than that interpreted from the local stress. However, when the whole length of the reinforcement had moved under large pullout displacements, both global and local shear stresses were converted to the critical state strength.

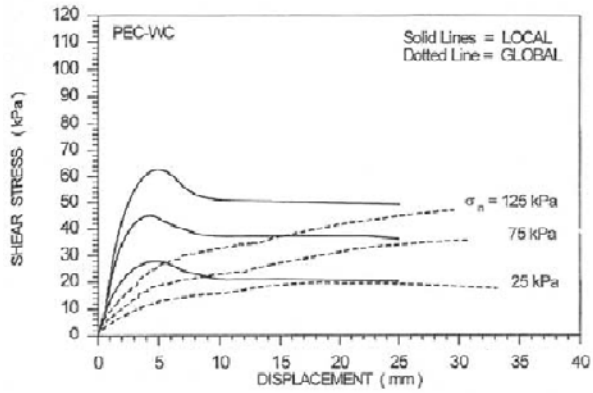

Fig. 7 Shear stress-relative shear displacement curves for pullout interface of PEC200-weathered Clay

The failure envelopes at the soil-geotextile interfaces are plotted in Fig. 8. The corresponding failure envelopes of soil only by large direct shear tests are also given in these figures as dotted lines for comparison. To evaluate the bonding efficiency at interface, the interaction coefficient, R_i, defined as the ratio of pullout interface shear strength to the soil shear strength determined by the corresponding large direct shear test at the same normal stress, is introduced. It should be noted that the interaction coefficient defined herein can be used very conveniently in modeling the stress-strain relation at soil-reinforcement interface for finite element analysis of reinforced earth structure (Vermeer and Brinkgreve, 1995). The values of R_i calculated from global strength (conventional method) and local strength (author's method) are given in Fig. 9 for weathered clay confinements. The results indicated that the interaction coefficient is slightly dependent on the normal stress. When normal stress increased from 25 kPa to 125 kPa, the values of R_i calculated by the local strength at critical state decreased and from 0.81 to 0.72 for clay-geotextile interfaces. The corresponding values computed at peak strength is from 1.07 to 0.92. Moreover, the values of R_i calculated by global strength are almost the same as that computed from local strength at critical state.

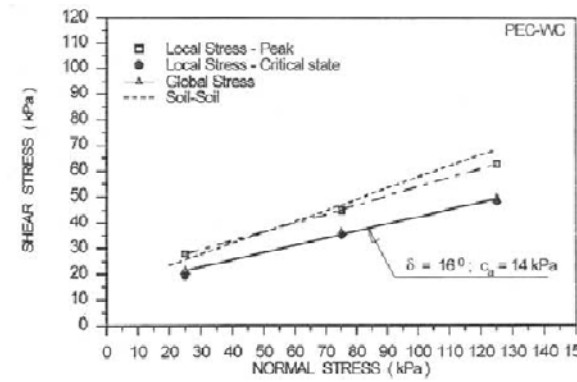

Fig. 8 Failure envelopes for pullout interface of PEC200-weathered Clay.

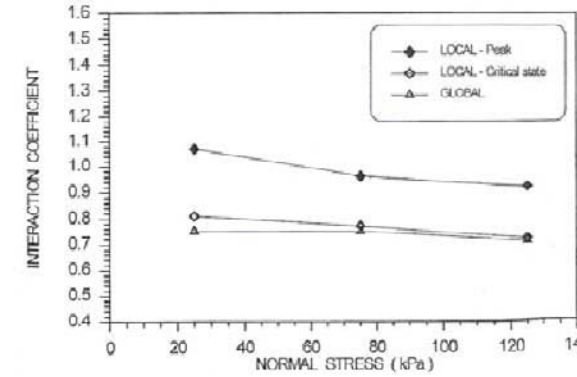

Fig. 9 Interaction coefficients of weathered Clay-PEC200 pullout interfaces

CONCLUSIONS

The pullout behavior of high strength geotextile PEC200 confined in weathered clay has been studied by large pullout tests. The measured displacements along the reinforcement implied that the distribution of shear stress along the interface surface was highly non-uniform. Thus, the conventional method of interpretation, which was based on the assumption of uniform distribution of shear stress, would not yield the proper parameters of soil-geotextile interface. A new method considering the softening behavior and non-uniform distribution of shear stress at interface has been presented. The extrapolation scheme for obtaining the net pullout displacement

excluding slippage at clamped end has also been included. Moreover, the results from this study indicated that the conventional method underestimated both the shear stiffness and the shear strength at the pullout interface.

REFERENCES

Almohd I, Abu-Farsakh M, Khalid F (2006) Geosynthetic Reinforcement-Cohesive Soil Interface during Pullout. Proc. of the 13th Great Lakes Geotechnical and Geoenvironmental Conference, Editor, Hani H. Titi, Milwaukee, Wisconsin, USA: 40-49

Bergado DT, Shivashankar R, Sampaco CL, Alfaro MC (1991) Behavior of a welded wire wall with poor quality, cohesive-friction backfills on soft Bangkok clay: a case study. Canadian Geotechnical Journal 28: 860-880

Collios A, Delmas P, Gourc JP, Giroud JP (1980) Experiments on soil reinforcement with geotextiles. Proc. ASCE Symposium on the Use of Geotextiles for Soil Improvement, Portland: 53

Hayashi S, Makuichi K, Ochiai H (1994) Testing methods for soil-geosynthetic friction behavior — Japanese Standard. Proc. 5th Int. Conf. on Geotextiles, Geomembranes Related Products, Singapore 1: 411-426

Long PV, Bergado DT, Balasubramaniam AS (1995) Interpretation of behavior at pullout interface of soil/geotextile. Proc. 10th Asian Regional Conference on Soil Mechanic and Foundation Engineering, Beijing, China

Sugimoto M, Alagiyawanna AMN (2003) Pullout behavior of geogrid by test and numerical analysis. Journal of Geotechnical and Geoenvironmental Engineering, ASCE 129(4):361-371

Warnitchai P (2005) Lessons learned from the 26 December 2004 Tsunami disaster in Thailand. Proc. of Scientific Forum on Tsunami, its Impact and Recovery, Bangkok, Thailand

Proceedings of the 4th Asian Regional Conference on Geosynthetics
June 17 - 20, 2008 Shanghai, China

PULLOUT BEHAVIOUR OF DIFFERENT GEOSYNTHETICS EMBEDDED IN GRANULAR SOILS

N. Moraci[1] and G. Cardile[2]

ABSTRACT: The paper deals with the results of a large experimental program aimed at the study of the behaviour of different geosynthetics in static pullout conditions. The pullout tests were carried out using a large test apparatus composed by a pullout box, a vertical load application system, a horizontal force application device, a special clamp, and all the required instrumentation. The displacements of the specimen have been measured and recorded through inextensible steel wires connected to the specimen in at least six different points and to RVDTs fixed to the external back side of the box. Tests have been performed on a uniform medium sand compacted at 95 % Proctor. Two different types of geosynthetics have been tested. More than 10 pullout tests have been performed, varying the applied vertical pressures (10, 25, 50 kN/m^2). The horizontal speed has been equal to 1.0 mm/min for all tests. The discussion of the test results allows to evaluate the influence of applied vertical pressures on pullout behaviour.

KEYWORDS: pullout, resistance, interface friction, dilatancy, geogrid

INTRODUCTION

Pullout tests are necessary in order to study the interaction between soil and geosynthetics in the anchorage zone; hence these properties have direct implications in the design of reinforced soil structures.

In fact, in order to analyse the internal stability of reinforced earth structures, it is necessary to evaluate the pullout resistance of reinforcement, mobilized in the anchorage zone.

The pullout resistance can be evaluated by means of the following equation:

$$P_R = 2 \cdot L \cdot \sigma'_V \cdot \mu_{S/GSY} \quad (1)$$

where P_R = Pullout resistance (per unit width); L = reinforcement length in the anchorage zone; σ'_V = effective vertical stress; $\mu_{S/GSY}$ = soil-geosynthetic interface apparent coefficient of friction.

The soil-geosynthetic interface apparent coefficient of friction can be determined by means of large scale pullout tests, using the following expression:

$$\mu_{S/GSY} = \frac{P_R}{2 \cdot L \cdot \sigma'_V} \quad (2)$$

It is important to notice that the determination of $\mu_{S/GSY}$ using Eq. (2) can be performed without any assumption about the values of the soil shear strength angle mobilized at the interface, since all the parameters of the above equation can be easily determined by means of pullout tests. Anyhow, it is important to define the role of all the design (and test) parameters on the mobilization of the interaction mechanisms (frictional and passive) in pullout condition, including geosynthetic length, tensile stiffness, geometry and shape, vertical effective stress and soil shear strength.

This paper deals with some results of an experimental research carried out in order to study the factors affecting the pullout behaviour of different geogrids.

TEST EQUIPMENT, MATERIALS AND PROCEDURE

The test apparatus is composed by a pullout box (1700 × 600 × 680 mm), a vertical load application system, a horizontal force actuator device, a special clamp, and all the required instrumentation (Fig. 1). The pullout box consists of steel plates welded at the edges; the front wall has an opening 45 mm wide. This opening is necessary to allow the insertion of the clamping device and of the sleeves fixed to the front wall. A smaller opening is provided at the back wall of the box in order to allow the connection between the internal displacement measurement systems and the transducers

[1] Associate Professor, Department MECMAT, Mediterranean University of Reggio Calabria, ITALY. Email: nicola.moraci@unirc.it
[2] Ph D. Student, Department MECMAT, Mediterranean University of Reggio Calabria, ITALY. Email: giuseppe.cardile@unirc.it

fixed on the external wall. An air filled cushion applies the vertical load. A steel plate is used to restrain the air cushion. An electric jack applies the pullout force, which is measured using a load cell. The apparatus is capable to keep the geosynthetic specimen always confined into the soil for the test duration. Friction between the soil and the side walls of the box is minimized by the use of smooth Teflon films. The equipment incorporates two sleeves near the slot at the front of the pullout box, in order to avoid front wall effects. The specimen displacements have been measured and recorded using inextensible steel wires connected to at least six different points along the geogrid specimen. The wires have been connected to displacements transducers (RVDT) fixed to the external back side of the box. All the measurements have been digitally recorded.

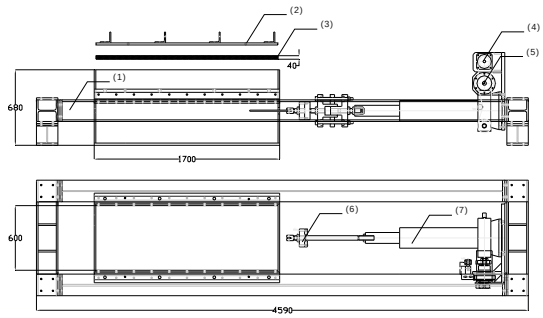

Fig. 1 Scheme of pullout test apparatus: 1) frame; 2) steel plate; 3) air bag; 4) electric engine; 5) reducer; 6) load cell; 7) electric jack (Moraci and Recalcati 2006)

Pullout tests have been performed on two different geogrids (knitted and welded, described respectively as GK and GW).

The mechanical properties of the two different geogrids are reported in Table 1. The tensile strength has been evaluated by wide width tensile tests (EN ISO 10319).

A granular soil has been used in these tests. The soil has been classified as a uniform medium sand with uniformity coefficient $U=d_{60}/d_{10}$ =1.5 and average grain size d_{50}=0.22 mm. Standard Proctor compaction tests gave a maximum dry unit weight γ_{dmax}=16.24 kN/m3 at an optimum water content w_{opt} =13.5%. Direct shear tests, performed at an initial unit weight equal to 95% of γ_{dmax} (obtained at a water content of 9%), yield very high single values of the peak shear strength angle ϕ'_p, in the range 48° (for σ'_v=10 kPa) to 42° (for σ'_v=100 kPa). The shear strength angle at constant volume ϕ'_{cv} was 34°.

The pullout tests were performed at a water content of 9% (dry of optimum) in order to simulate the typical construction conditions of earth reinforced structures.

Table 1 Tensile stiffness and strength of the different geogrids

Geogrid	Polymer	T_F (kN/m)	ε_F (%)	$J_{2\%}$ (kN/m)	$J_{5\%}$ (kN/m)
GK	PET	168.2	12.1	1630.0	1078.0
GW	PET	139.26	12.6	1294.0	711.0

TEST RESULTS

Constant displacement pullout tests have been performed, varying the applied vertical pressures (10, 25 and 50 kPa). The horizontal speed, equal to 1.0 mm/min, and the specimen length, equal to 1.15 m, were the same for all the tests.

Fig. 2 shows, for the two different geogrids, the pattern of the pullout force versus the displacement, measured at the specimen edge attached to the clamp. The different curves on the graphs are referred to the different applied confining pressures.

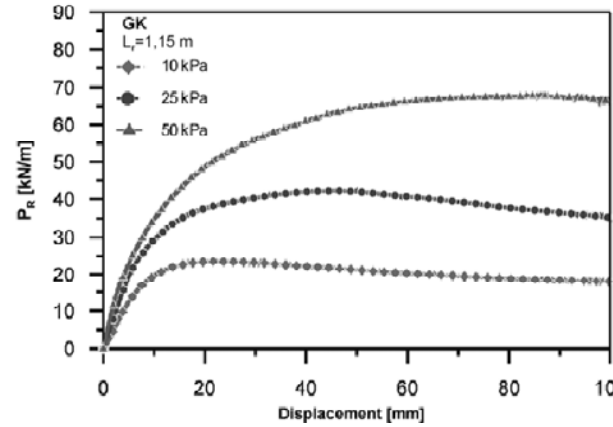

(a)

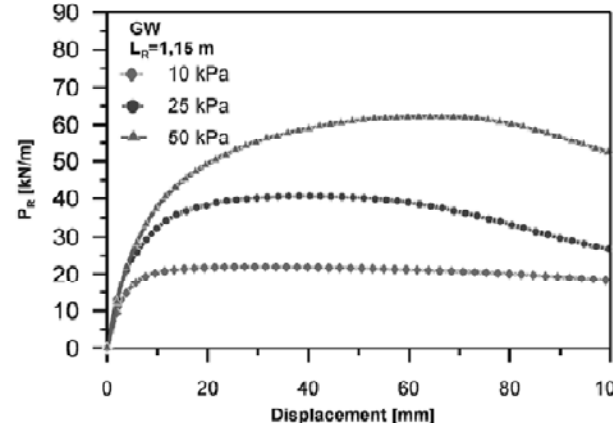

(b)

Fig. 2 Pullout curves: (a) knitted geogrid; (b) welded geogrid

The pullout curves generally show a strain hardening behaviour, with a progressive increase of the pullout resistance with the increase of the displacement.

The values of peak pullout resistance measured in the tests are, for the two different geogrids, quite similar being the differences range from 4% to 13%. The higher values of measure pullout resistance refer to knitted geogrids (Fig. 3).

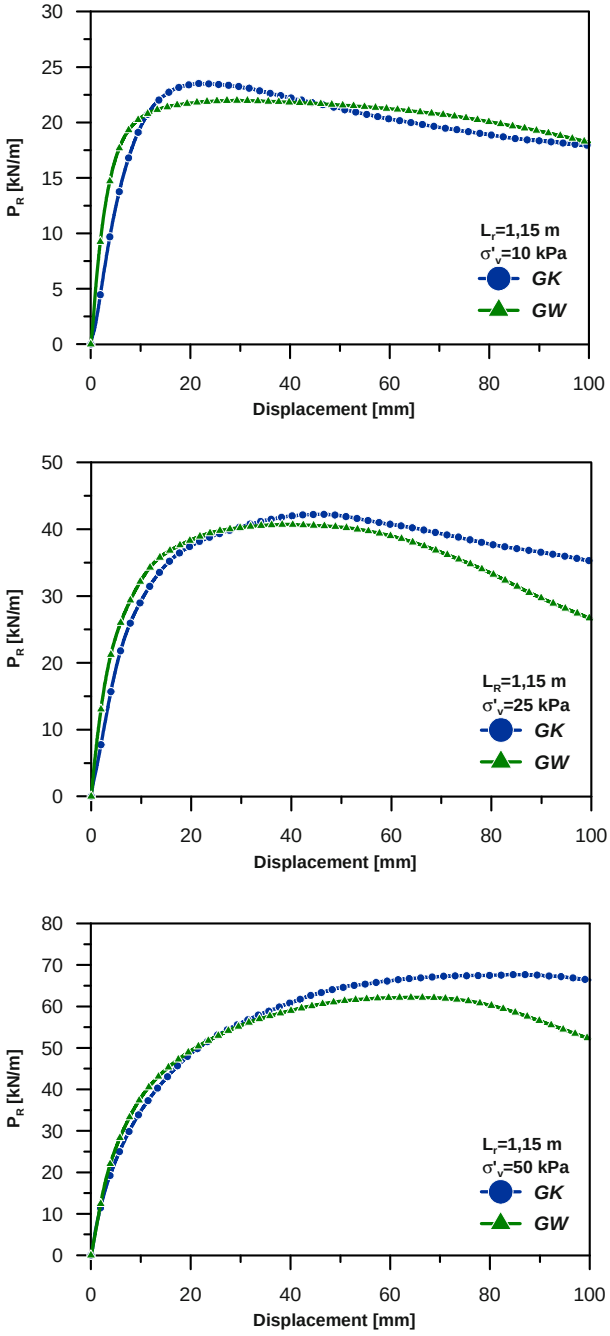

Fig. 3 Comparison of pullout curves for knitted and welded geogrids at the same applied vertical stress

The influence on the peak pullout resistance of the confining stress can be analysed by means of Fig. 4. This graph represents the peak pullout resistance P_R for the different values of the confining stress; it is possible to notice a clear curvature in the curves that fits the experimental data.

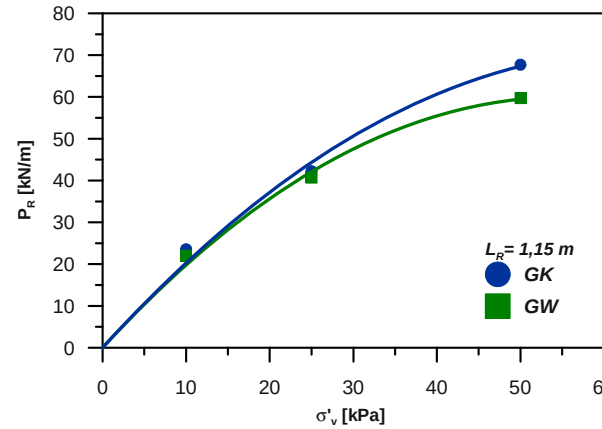

Fig. 4 Peak pullout resistance envelopes for the knitted and welded geogrids

Moreover, the influence of the vertical confining stress on the pullout behaviour can be emphasized normalising the different pullout curves respect to the σ'_V used in the tests (Fig. 5).

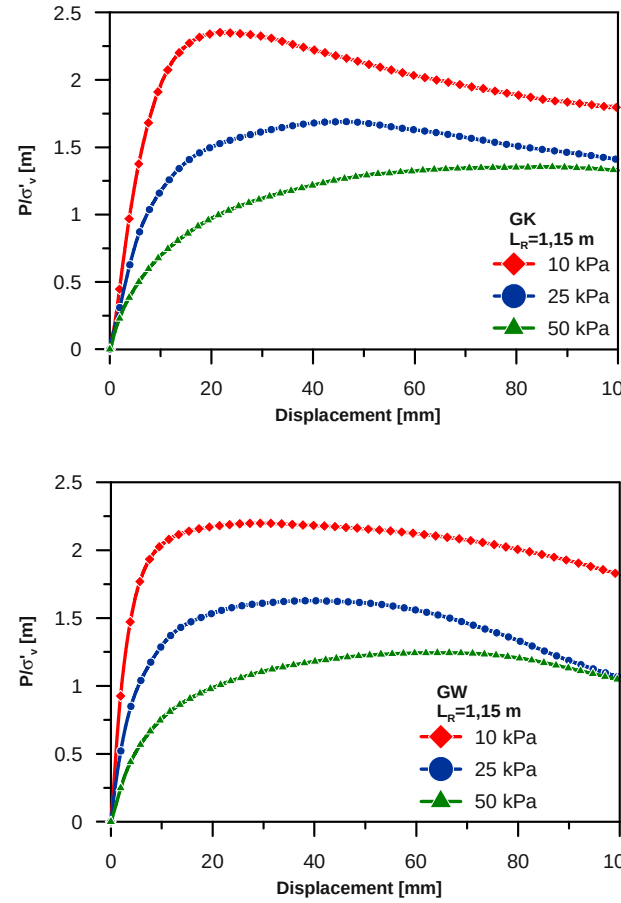

Fig. 5 Normalized pullout curves (P/σ_V') for the knitted (GK) and the welded geogrid (GW)

From these charts it is possible to notice an important reduction in the normalized pullout resistance passing from low to high confinement stress. The experimental results can be explained by means of soil dilatancy

phenomena, due to the different work necessary to expand the dilatancy surface at different vertical effective confining stresses.

Fig. 6 shows the trend of the peak pullout interface apparent coefficient of friction as a function of the applied vertical effective stress for the two different geogrids. It is possible to observe a reduction in the mobilized peak pullout interface apparent coefficient of friction with the increase of the applied vertical effective stress. The analysis of the test results allows to observe that the peak mobilized apparent interface coefficient of friction for low vertical effective confining stress (10 kPa) is higher than the corresponding one measured at higher vertical effective stresses (50 kPa) due to the dilatancy behaviour. In particular, the percentage variations due to dilatancy are up to 81% for the geogrid GK and up to 90% for the geogrid GW.

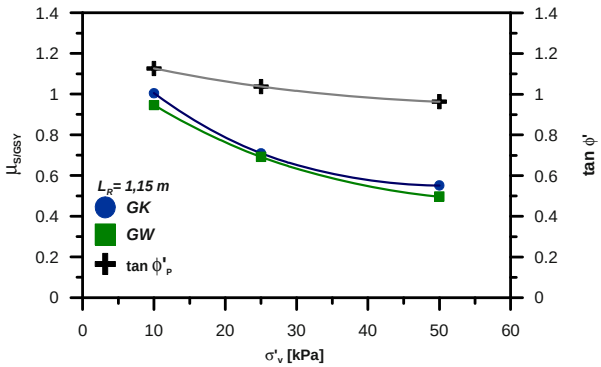

Fig. 6 Peak interface apparent coefficient of friction vs. σ'$_v$ for the two different geogrids

Also in this case the values of mobilized peak pullout interface apparent friction coefficient for the two geogrids are similar, being the differences range from 2.6 % to 10 %, and the higher values refer to the knitted geogrid.

The curves in Fig. 7 represent, for the different applied vertical stresses and geogrids, the distributions of the nodal displacements of the reinforcement specimen for the values of the applied pullout forces that cause the movement of the last bar. This force represents the pullout "trigger force", P_i. During this phase, the portion

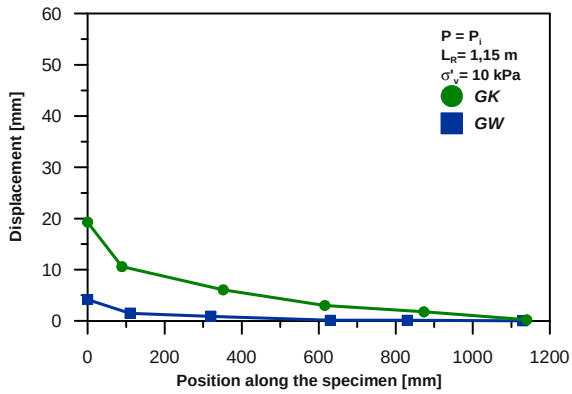

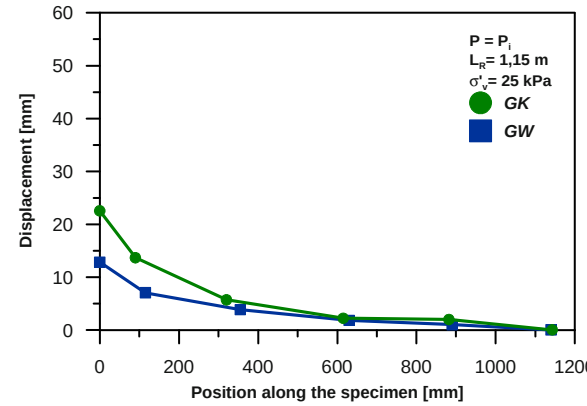

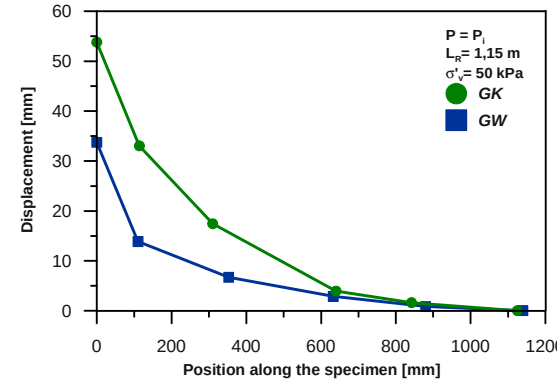

Fig. 7 Displdisplacements measured along the specimens at the pullout trigger force

of the specimen where developing the interaction mechanisms that determines the pullout resistance (active length) increases with the pullout force.

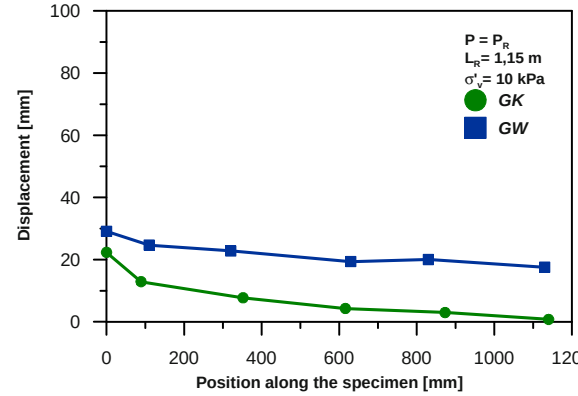

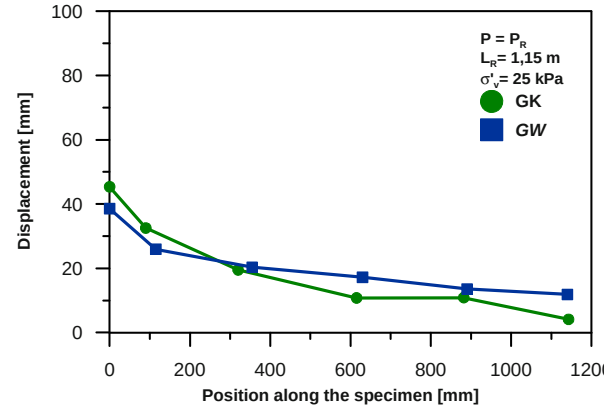

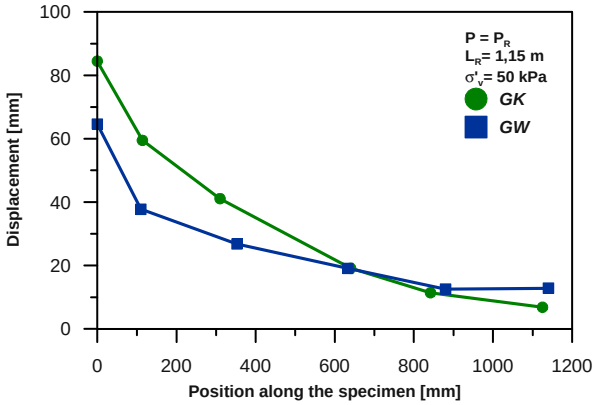

Fig. 8 Displacements measured along the specimens at the peak pullout resistance

Table 2 Pullout force and strain at the trigger phase and at the peak condition

GG	σ'_V (kPa)	P_i (kN/m)	ε_i (%)	P_r (kN/m)	ε_r (%)	P_i/P_r
GK	10	23,4	1,7	23,5	1,9	0,99
GK	25	38,5	2,0	42,2	3,6	0,91
GK	50	65,2	4,8	67,7	6,9	0,96
GW	10	15,4	0,4	22,0	1,0	0,70
GW	25	35,2	1,1	40,7	2,3	0,86
GW	50	54,7	3,0	59,7	4,6	0,92

The nodal displacement distributions confirm the different pullout behaviour of reinforcement with the variation of confinement stress. In fact, for low values of σ_v', it is possible to observe an almost uniform distribution of the displacements; vice versa for high confinement stresses, the curves show a clear non linearity of the displacements distribution. These differences are related to the effects of reinforcement extensibility on the mobilization of the interface mechanisms. In particular, for high values of σ_v', a progressive mobilization of the interface interaction mechanisms develops. Vice versa, for low values of σ_v', the mobilization of the resistance along the reinforcing element is almost uniform.

Moreover, the nodal displacements curves allow to use in a correct way the displacement stability analysis methods because by means of these curves it is possible to obtain, for different anchorage length and confinement stress, the pullout resistance values that are mobilized for a given displacement of the section that represents the boundary limit between the active zone and the anchorage length.

Finally, it is possible to notice that the trigger force represents a percentage of the peak pullout force that is comprised between 91% and 99% for the geogrid GK, and between 70% and 92% for the geogrid GW.

CONCLUSIONS

The test results clearly show the influence of the vertical effective stress on the pullout behaviour of two different geogrids. The main conclusions are:

- the pullout resistance P_R and the interface apparent coefficient of friction $\mu_{S/GSY}$ depend on the dilatancy of the soil at the interface;
- due to dilatancy effects, the interface apparent coefficient of friction mobilized at 10 kPa is higher than ones at 50 kPa. In particular, the percentage variations due to dilatancy are up to 81% for the geogrid GK and up to 90% for the geogrid GW;
- the values of peak pullout resistance measured in the tests are, for the two different geogrids, quite similar being the differences range from 4% to 13%;
- both at the trigger phase and at the peak condition the reinforcement strain increases with the increase of applied vertical stress;
- in the trigger phase the reinforcement medium strains range from 1,7% to 4,8%, for the knitted geogrid, and from 0,4% to 3%, for the welded geogrids;
- at the peak condition the medium strains range from 1,9% to 6,9%, for the knitted geogrid, and from 1% to 4,6%, for the welded geogrids;
- for specimen of length equal to 1.15 m the trigger force represents a percentage of the peak pullout force that is comprised between 91% and 99% for the geogrid GK, and between 70% and 92% for the geogrid GW;
- the node displacements curves obtained by pullout tests may be useful in stability analysis performed by means of displacement methods.

REFERENCES

EN ISO 10319 (1992) Geotextile wide-width tensile test. International Organization for Standardization, ISO, Ginevra.

Moraci N, Recalcati PG (2006) Factors affecting the pullout behaviour of extruded geogrids embedded in compacted granular soil. Geotextiles and Geomembranes (Elsevier) 24: 220-242

PROTECTION EFFICIENCY OF NONWOVEN POLYPROPYLENE GEOTEXTILES AGAINST IMPACT DAMAGE

D.K. Atmatzidis[1] and D.A. Chrysikos[2]

ABSTRACT: European Standard EN ISO 13428:2005 specifies an index test to determine the protection efficiency offered by a geotextile against the impact load of a hemispherical object. Laboratory tests were conducted on 70 nonwoven polypropylene geotextiles (needle-punched, heat-boned, post-treated) made of staple fibers or continuous filament, with mass per unit area 113－2217 g/m^2 and thickness 0.50－1.88 mm. The effect of impact energy and of a deformable pad instead of the rigid support was evaluated. The protection efficiency of the geotextiles, as represented by the percent residual thickness of the lead plates in the impact areas, ranged between 17.3% and 89.2%. An excellent linear correlation (R^2=0.95) was obtained between residual thickness and geotextile mass per unit area. Use of a deformable support improved the measured protection efficiency by 5%－400% depending on geotextile mass. Half of the standard impact energy resulted in protection efficiency improvement by 10%－150% depending on geotextile mass. When the standard impact energy was doubled, geotextiles with mass up to 800 g/m^2 provided no protection.

KEYWORDS: geotextiles, geomembranes, protection efficiency, impact loads

INTRODUCTION

Survivability of geomembranes used as liners in a project or structure requires adequate protection during installation and construction, during load application and during the lifetime of a project. The level of protection provided to a geomembrane by a geotextile has been investigated in the past by testing various geotextile—geomembrane combinations (a) "in-isolation" by conducting tensile strength, puncture resistance or impact resistance tests (i.e. Koerner et al. 1986; Lafleur et al. 1986; Puhringer 1990) and (b) in specially constructed equipment by applying static point loads through natural aggregate or through geometrically specified elements (i.e. Brummermann et al. 1994; Zanzinger 1996; Gallagher et al. 1999). As a result, it is common practice to place a nonwoven needle-punched geotextile in contact with the geomembrane on the side where the mechanical loads are to be applied. Some national standards require the use of geotextiles with a very high mass per unit area of 2000 g/m^2 to 4000 g/m^2 (Heerten 1993, Seeger and Muller 1996) while other standards suggest lower values in the range of 350 g/m^2 to 500 g/m^2 (Corbet and Peters 1998). An empirical relationship (Koerner 2005) is also available in order to determine the mass per unit area of a geotextile for puncture protection of specific geomembranes.

During the installation and construction phases, geomembranes should be protected against the damaging action of impact loads such as rocks, other materials and hand-held equipment falling on them. The worst possible condition is when the geomembrane rests on a hard, unyielding surface. However, there are no guidelines for the selection of geotextile mass per unit area in order to protect a geomembrane against impact damage.

European Standard EN ISO 13428, approved in 2005, describes an index test for the determination of the protection efficiency provided by a geotextile to a geomembrane resting on a hard surface and exposed to the impact load of a hemispherical object. The laboratory investigation reported herein is based on the application of these standard procedures in order to test a large number of nonwoven polypropylene geotextiles. Scope of the investigation is to provide adequate documentation of the relationship between protection efficiency and geotextile physical characteristics.

MATERIALS AND PROCEDURES

According to EN ISO 13428, the index test to quantify the protection efficiency of a geotextile against impact damage is conducted by subjecting a test specimen to an impact load produced by a rigid probe with a hemispherical head (20 mm diameter). The falling height is 1±0.01 m and the mass of the probe is 1000±2 g.

[1] Professor, Department of Civil Engineering, University of Patras, GREECE. Email: dka@upatras.gr
[2] Lecturer, Department of Civil Engineering, University of Patras, GREECE. Email: dac@upatras.gr

The specimen lies on a rigid support consisting of a 40 mm thick steel plate. A lead plate with nominal thickness of 1.8±0.2 mm is placed between the steel plate and the specimen. The residual thickness of the lead plate in the impacted areas, expressed as a percent of the original thickness, is an index of the protection efficiency provided by the geotextile.

Shown in Fig. 1 is the laboratory testing frame used for conducting the tests reported herein. Shown in Figure 2 are the standard and a modified probe with a mass of 1000 g and 2000 g, respectively, which were used in combination with various falling heights in order to conduct tests with impact energy ranging from 5 Nm to 20 Nm (standard impact energy is 10 Nm). To investigate the effect of support rigidity, the standard steel plate was covered by a 25 mm thick rubber pad with characteristics as specified by EN ISO 13719 (long term protection efficiency against static point loads). The rigid and the deformable supports with lead plate and geotextile on top are shown in Fig. 3.

Fig. 1 Laboratory testing frame

For the purposes of the experimental investigation reported herein, geotextile specimens were taken from large size samples obtained from ten different manufacturers. The size of the samples ranged from 4 m^2 to 12 m^2 with a width equal to the standard production roll width of each manufacturer. Some manufacturers provide samples covered two different groups of their products. The number of different geotextiles (number of grades per product series) tested ranged from three to eight, yielding a total of 70 samples from 13 different product series. Only nonwoven, polypropylene geotextiles were tested. The group consisted of needle-punched with staple fiber (53%), needle-punched with continuous filaments (19%), needle-punched with staple fibers and thermally post-treated (14%) and heat-bonded (14%). In order to avoid the use of commercial names, a generic notation is used (i.e. M1) to identify manufacturers and product series. Numbers in parenthesis next to an iden-

Fig. 2 Rigid probes, 1000g and 2000g mass

Fig. 3 Rigid and deformable support configurations

tification code, i.e. M1 (6), indicate the number of different geotextile grades tested in that series. The nominal ranges of physical property values for the geotextiles tested are presented in Table 1.

All geotextiles were tested according to EN ISO 13428 to obtain lead residual thickness values. To obtain base-line values, tests were also conducted without placing a geotextile over the lead plate. An example of impacted lead plate is shown in Fig. 4. Nine geotextiles, representative of the range of physical properties of the whole group, were selected to investigate (a) the effect of impact energy lower or higher than the standard by a factor of two and (b) the effect of varying support rigidity.

Table 1 Physical properties of geotextiles

Geotextile Series	μ_A (g/m^2)	t (mm)
M2 (7)	120-520	1.0 – 4.0
M4 (6)	135-405	1.2 – 3.1
M6 (6)	350 – 2100	3.7 – 9.3
M7 (7)	320 – 1200	3.2 – 8.0
M10 (4)	300 – 2000	4.3 – 9.7
M11 (3)	500 – 1200	4.1 – 10.0
M12 (4)	180 – 370	1.3 – 2.2
M13 (8)	105 – 325	1.0 – 2.9
M14 (5)	600 – 1200	4.5 – 8.3
M15 (6)	136 – 375	0.47 – 0.85
M16 (4)	180 – 335	0.85 – 1.50
M17 (6)	120 – 500	1.0 – 3.3
M18 (4)	500 – 1300	4.7 – 8.5

μ_A: mass per unit area t: thickness

RESULTS AND DISCUSSION

The results obtained for each series of geotextiles tested, were used in order to obtain correlations between the residual thickness, S_r (%), and the physical properties of the geotextiles (mass per unit area, μ_A, and thickness, t). The values used for physical properties are those obtained during each test, as specified by EN ISO 13428 and may differ from the nominal values presented in Table 1. As a first order approximation, a linear relationship was used. Similarly, linear correlations were obtained for the complete set of data as well as for groups of data representing products which are (a) needle-punched with staple fibers, (b) needle-punched with continuous filaments, (c) needle-punched with staple fibers and thermal post-treatment of both surfaces and (d) heat-bonded.

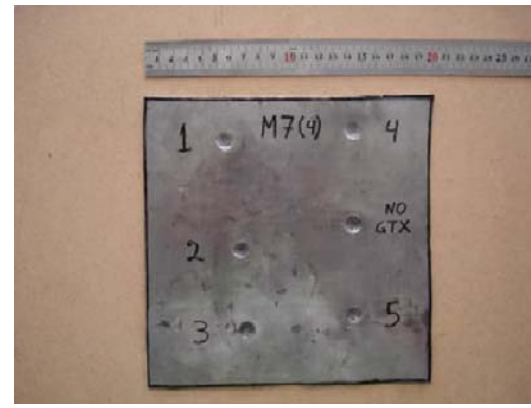

Fig. 4 Typical impacted lead plate

The linear correlation between residual thickness, S_r (%), and geotextile mass per unit area, μ_A, appears to be very good for most of the geotextile series tested. For one series a low value for the correlation coefficient (R^2=0.514) was obtained while for ten out of thirteen series the values were over 0.900 and as high as 0.997. The correlation between residual thickness, S_r (%) and geotextile thickness was not as good. Only six out of thirteen series had correlation coefficient values over 0.900 while for two series the value was below 0.300. Accordingly, only the correlations of residual thickness, S_r (%), with mass per unit area, μ_A, are summarized in Table 2 and typical graphs are presented in Fig. 5.

Table 2 Correlations between residual thickness, S_r(%), and geotextile mass per unit area, μ_A

Geotextile Series	S_r (%)=A·μ_A+B		
	A	B	R^2
M2 (7)	0.0297	17.10	0.840
M4 (6)	0.0442	12.41	0.725
M6 (6)	0.0317	16.46	0.985
M7 (7)	0.0346	17.38	0.947
M10 (4)	0.0310	11.73	0.994
M11 (3)	0.0348	13.80	0.997
M12 (4)	0.0267	15.57	0.987
M13 (8)	0.0348	13.24	0.957
M14 (5)	0.0474	11.22	0.986
M15 (6)	0.0304	15.27	0.898
M16 (4)	0.0258	15.89	0.514
M17 (6)	0.0283	18.49	0.913
M18 (4)	0.0323	18.77	0.989

R^2: correlation coefficient

Presented in Fig. 6 are the correlations of residual thickness, S_r (%), with mass per unit area, μ_A, and thickness, t, for the complete set of data. It is confirmed that correlations with geotextile mass per unit area are

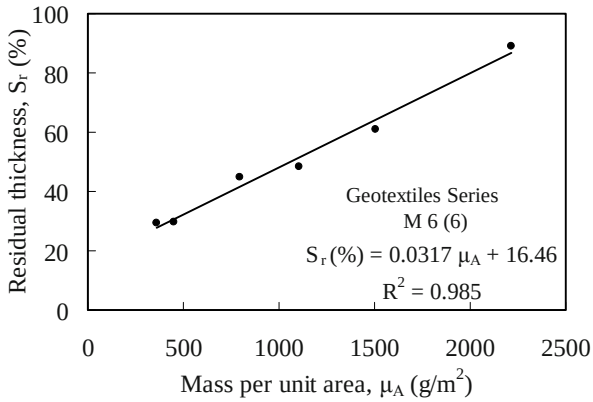

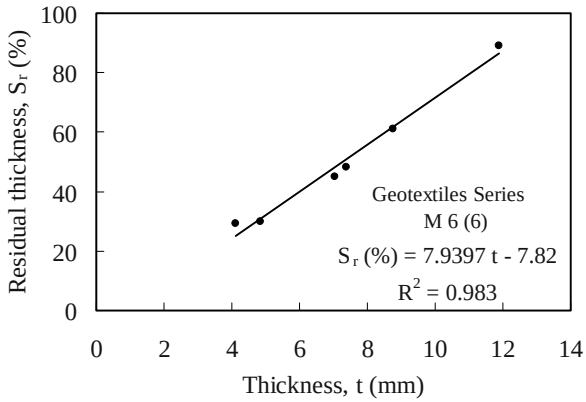

Fig. 5 Typical correlations of residual thickness with geotextile physical properties

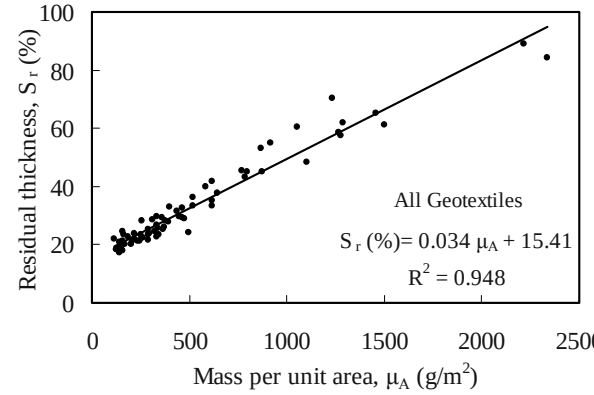

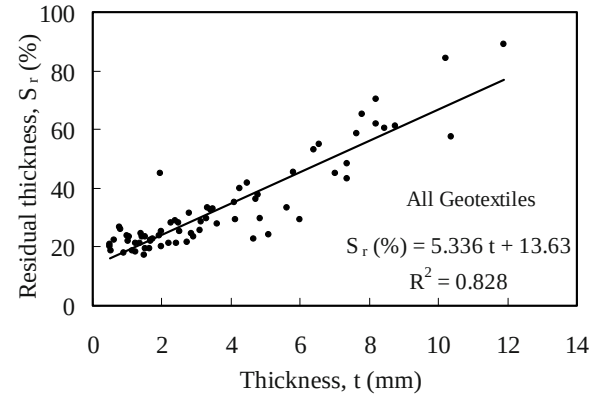

Fig. 6 Overall correlations of residual thickness with geotextile physical properties

qualitatively superior to correlations with geotextile thickness. Using the overall correlation with mass per unit area, the expected residual thickness for each geotextile was computed and the results were compared with the measured value. The resulting error ranged between ± 5%, ± 10% and ±20% for 30%, 72% and 97% of the geotextiles, respectively. Accordingly, the linear relationship obtained has a very good overall predictive capability.

Base-line Value

The remaining (residual) thickness of the lead plate used to conduct tests according to EN ISO 13428 when no geotextile is placed over it, should be considered as the base-line value. During this investigation, an extra drop of the probe was allowed after removal of the geotextile specimen on forty-five different lead plates. The average residual thickness of the lead plate without geotextile was computed to be equal to 15.20%. This value is in very good agreement with the value of 15.41% obtained through the linear correlation shown in Fig. 6. However, the results of correlations per geotextile series, summarized in Table 2, indicate a variation of the base-line value between 11.22% and 18.77%. This fact suggest a difference in behavior between different product series which may be attributed to the effect of differences in raw materials used and manufacturing processes.

Effect of Materials and Processes

In an attempt to evaluate the effect of differences in raw materials used and manufacturing processes employed, the available data were separated in four groups and new correlations were obtained of residual thickness versus mass per unit area. The results presented in Fig. 7 indicate good to excellent correlations for the four groups of products. It can be observed that: (a) heat-bonded products yielded lower residual thickness values (provided the lower protection efficiency) compared to the other three geotextile types, (b) thermal surface post-treatment offers a small advantage over heat-bonded products, but no advantage when compared to the other two types of products, (c) if a geotextile with relatively low mass per unit area (less than 400 g/m^2) is to be used, then needle-punched, staple fiber products should be preferred and (d) if for specific reasons, such as long term protection, a heavy geotextile is to be used, continuous filament products may offer the highest protection against impact damage.

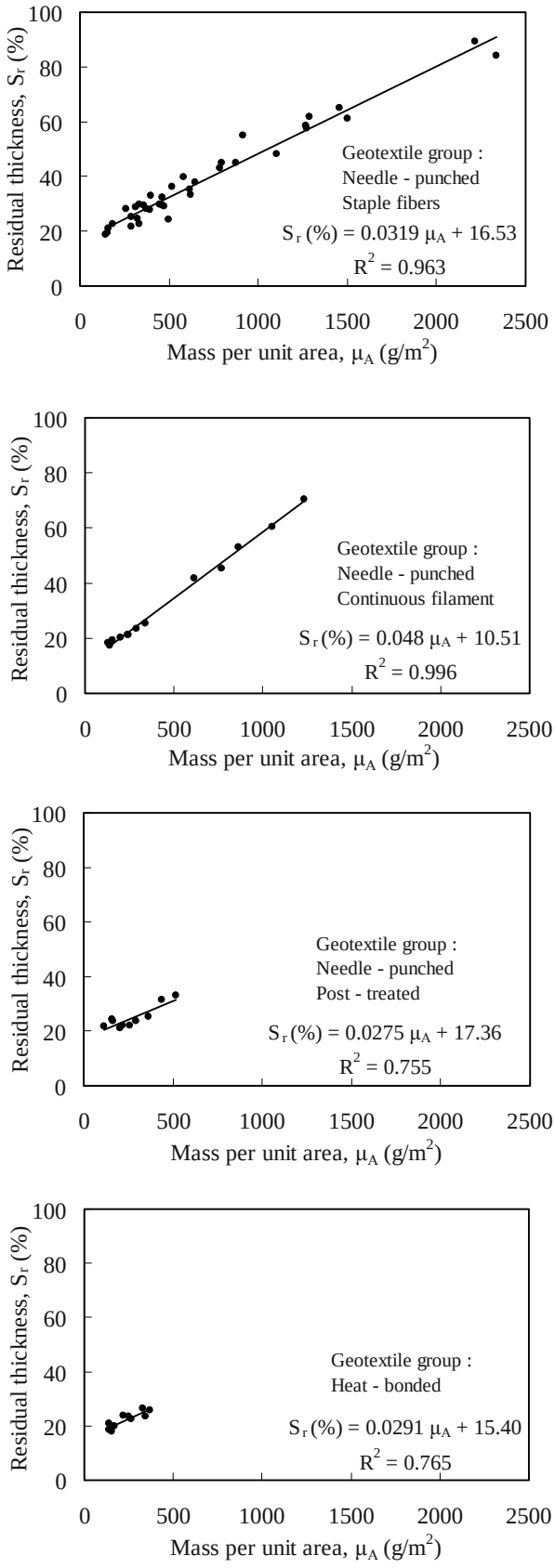

Fig. 7 Correlations of residual thickness with mass per unit area of geotextile groups

Performance Testing

Annex A of Standard EN ISO 13428 describes modifications to the standard procedures which can be used for a performance test. These modifications include increased or decreased impact energy to simulate real conditions and supporting the specimen on a piece of the real support. A limited insight on the effect of impact energy and support rigidity is provided by the information presented next. Tests were conducted on nine geotextiles representing the mass per unit area range of values of the complete group of geotextiles tested.

The effect of impact energy on residual thickness is shown in Fig. 8. It can be observed that increased or decreased impact energy has a significant effect especially for geotextiles in the lower range of mass per unit area values. Using half the standard impact energy (5 Nm) improves the protection efficiency of the geotextiles by 100% to 150% for mass per unit area values up to 500 g/m^2. As the mass per unit area further increases, this effect becomes gradually smaller (10% or less for mass per unit area over 2000 g/m^2). Using double the standard impact energy (20 Nm) protection against impact damage can be provided only by geotextiles with mass per unit area of 800 g/m^2 or higher. A smaller increase of impact energy, such as the 50% increase for which results were obtained, significantly reduces the protection efficiency of geotextiles with rather low values of mass per unit area (up to 500 g/m^2).

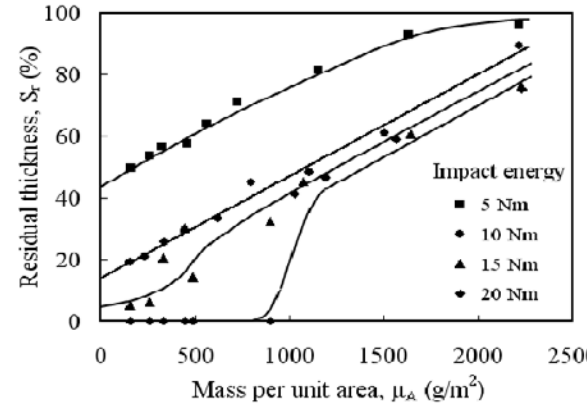

Fig. 8 Effect of impact energy

The rigidity of the support on which the geosynthetics are placed should be expected to have a significant effect on the protection efficiency against impact damage. As the support beneath the geosynthetics deforms, a greater amount of impacting energy can be absorbed and the impact damage will be less severe. For soil supported geotextiles, Koerner (2005) recommends impact energy reduction factors ranging from 30—3 when the CBR value of the supporting soil ranges from 0—20. A validation of this

beneficial effect is provided by the data presented in Fig. 9. A rubber pad used for long-term protection efficiency testing according to EN ISO 13719 was placed over the steel plate which is the standard support for impact damage index testing. The residual thickness values obtained ranged between 79% and 87% indicating that excellent protection can be obtained by using geotextiles in the low range of mass per unit area values if the support of the geosynthetics can assist in the absorption of an amount of the impacting energy.

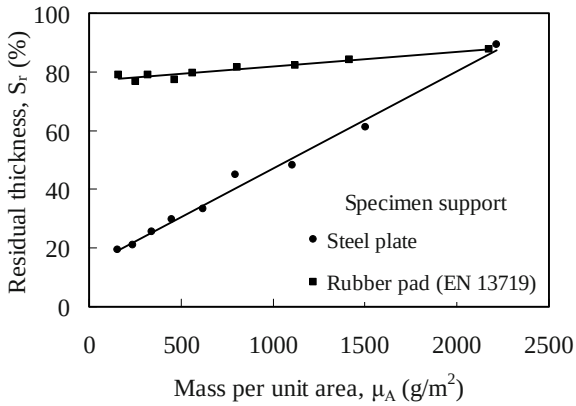

Fig. 9 Effect of support rigidity

CONCLUSIONS

Based on the results obtained and the observations made during the experimental investigation reported herein, the following conclusions may be advanced with respect to the protection efficiency against impact damage provided by nonwoven polypropylene geotextiles:

1. Very good to excellent linear correlations exist between the mass per unit area of geotextiles and the protection they provide to other geosynthetics (i.e., geomembranes) against impact damage, as measured by the residual thickness index of Standard EN ISO 13428.

2. Nonwoven, needle-punched products are to be preferred, with continuous filament products having an advantage over staple fiber products at higher mass per unit area ranges.

3. Impact energy and support rigidity should be evaluated according to site specific conditions since their effect is significant on the protection efficiency provided by geotextiles.

ACKNOWLEDGEMENTS

The contribution of Ms. V. Alexopoulou and Mr. G. Papadimitratos, Civil Engineers, in conducting the tests is acknowledged. The following manufacturers provided large-size geotextile samples: Bondofibra, Bonar, Du Pont, Fibertex, Geofabrics, Naue Fasertechnik, Polyfelt, Synthetic Industries, Terram, TC Mirafi.

REFERENCES

Brummermann K, Blumel W, Stoewahse C (1994) Protection layers for geomembranes: effectiveness and testing procedures. Proc. 5th International Conference on Geotextiles, Geomembranes and Related Products, Singapore 3: 1003-1006

Corbet SP, Peters M (1996) First Germany/USA geo-membrane workshop. Geotextiles and Geomembranes 14(12): 647-726

Heerten G (1994) Geotextile and/or GCL protection systems for geomembranes. Geosynthetic Liner Systems: Innovations, Concerns and Designs, R.M. Koerner and R.F. Wilson-Fahmy, Editors, IFAI, Philadelphia, PA, USA: 115-167

Gallagher EM, Darbyshire W, Warwick RG (1999) Performance testing of landfill geoprotectors: background, critique, development, and current UK practice. Geosynthetics International 6(4): 283-301

Koerner RM (2005) Designing with geosynthetics. Fifth Edition, Pearson Prentice Hall, NJ, USA

Koerner RM, Monteleone MJ, Schmidt JR, Roethe AT (1986) Puncture and impact resistance of geosynthetics. Proc. 3rd International Conference on Geotextiles, Vienna, Austria III: 677-682

Lafleur J, Akber SZ, Hammamji Y (1986) Influence of geotextile on the behavior of geotextile-geomembrane composites. Proc. 3rd International Conference on Geotextiles, Vienna, Austria III: 935-940

Puhringer G (1990) Pyramid puncture test for evaluating the protection function of geotextiles. Geosynthetic Testing for Waste Containment Applications, R.M.Koerner, Editor, STP1081, ASTM, Philadelphia, PA, USA: 185-194

Seeger S, Muller W (1996) Requirements and testing of protective layer systems for geomembranes. Geotextiles and Geomembranes 14(7/8): 365-376

Zanzinger H (1996) Efficiency of geosynthetic protection layers for geomembrane liners: performance in a large-scale model test. Geosynthetics International 6(4): 303-317

STUDY ON DIRECT SHEAR TEST ON INTERFACE PERFORMANCE OF GEOGRID AND CORASE-GRAINED SOIL

W.D. Deng [1], C.Z. Deng [2] and Q.R. Yan[3]

ABSTRACT: In expressway construction for mountain areas, uni-axial and biaxial geogrid are commonly used as reinforcement for subgrade and coarse-grained soil is commonly used for subgrade filling. The paper, based on this fact, mainly talks about such main factors which affect reinforced soil interface like compactness, water content, geogrid pore diameter and coarse-grained soil diameter with large direct shear test method. Following conclusions are thus made: interface friction angle will increase with the increase of filling compactness and will decrease at increasing extent with the increase of water content; interface friction angle is related to geogrid pore diameter and there's an optimum pore diameter; interface friction coefficient ratio will increase with the increase of P_5 content in coarse grain filling.

KEYWORDS: geogrid, shear test, reinforced soil interface

INTRODUCTION

Parameter of interface where reinforcement and filling are reacted to each other is a key factor to engineering design. At present, direct friction test and pullout test are available to determine features of interface between reinforcement and filling. A lot of researches have been made by foreign experts on interface performance. Reinforcement includes geo-textile and uni- axial geogrid, and filling includes sand and clay soil. In recent years, domestic scholars begin to carry out studies on geogrid interface performance and have obtained some achievements. However, there are still lots of factor not studied or studied superficially. For example, the object is mainly focused on fine grain filling and no study involves influence of factor like geogrid pore diameter and filling grain diameter to reinforced soil interface.

In expressway construction for mountain areas, geogrid is always used for subgrade reinforcement and coarse-grained soil mixed with soil and sand are commonly used for subgrade filling. Compactness of subgrade, water content of fillings, geogrid pore diameter and filling grain diameter all impose impact on interface performance of reinforced soil. Therefore, it is necessary to carry out study on it so as to get clear of its features for reference for future engineering design.

TEST METHOD AND CONTENT

Test Instrument and Method

JY50-4G large direct shear and compression apparatus (shown in Fig. 1) in Rock and Soil Laboratory of Chongqing Communications Research and Design Institute is used for the test. Both upper and lower shear box is in dimension of 50×50cm and 20cm high. Direct shear friction test is carried out as per *Test Methods of Geosynthetics for Highway Engineering* (JTG E50–2006). In consideration of large grain diameter of filling, 2cm slot height is reserved for upper and lower shear box. During the test, strain control is applied. Direct shear friction test is conducted for reinforced soil under 4 different pressure of 100 kPa, 200 kPa, 300 kPa and 400 kPa respectively at shear speed of 1.5 mm/min. Corresponding strength value τ will measures. Then τ-p curve is plotted based on test result for further analysis.

Test Materials

Two kinds of geogrid are used for the test: one is TGDG130 uni-axial polypropylene geogrid used in field construction Section 9 for Guangdong-Tianjin-Shanwei Expressway. Physical index is shown in Table 1. The other geogrid is CATT biaxial polyethylene geogrid. Grid pore diameter ranges from 5×5cm, 10×10cm,

[1] Professor, Chongqing Communications Research & Design Institute, CHINA. Email: dengweidong@ccrdi.cmhk.com
[2] Assistant Engineer, Sichuan Chengnan Expressway Co., Ltd, CHINA. Email: dcz1218@sina.com
[3] Assistant Professor, Chongqing Communications Research & Design Institute, CHINA. Email: yanqiurong@ccrdi.cmhk.com

15×15cm to 20×20cm. Geogrid with 4 different pore diameters has the same width and thickness in horizontal and vertical rib. Limit tensile strength for single grid is 7.80 kN and peak strain is 9.28%.

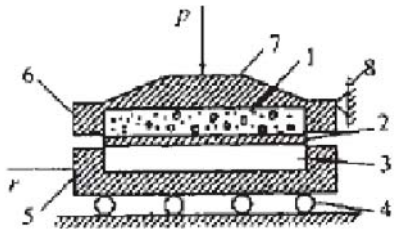

(1) soil sample, (2) reinforcement, (3) wood block, (4) ball, (5) lower shear box, (6) upper shear box, (7) pressuring plate, (8) frame

Fig. 1 Diagram of direct shear test

For study on impact of compactness on reinforced soil interface, filling which is used in field construction Section 9 for Guangdong-Tianjin-Shanwei Expressway is used as filling for this test and TGDG130 uni-axial polypropylene geogrid is used as reinforcement. For study on impact of pore diameter, water content and coarse grain content on reinforced soil interface, filling which is used in K81+370—K81+410 of Section A1 for Zhongxian-Dianjiang Expressway, and CATT geogrid with different pore diameter are used as reinforcement. Curve grain size distribution for fillings is shown in Fig. 2 and its grading components and basic physical index is shown in Tables 2 and 3 respectively. Fillings are in coarse grain.

Table 1 Basic technical parameter of TGDG130 uni-axial geogrid

Tensile yield strength	Limit to anti strain failure	2% strain strength	5% strain strength	Ribs of calculated width
146 kN/m	7.11%	60.83 kN/m	50 kN/m	55 Ribs/m

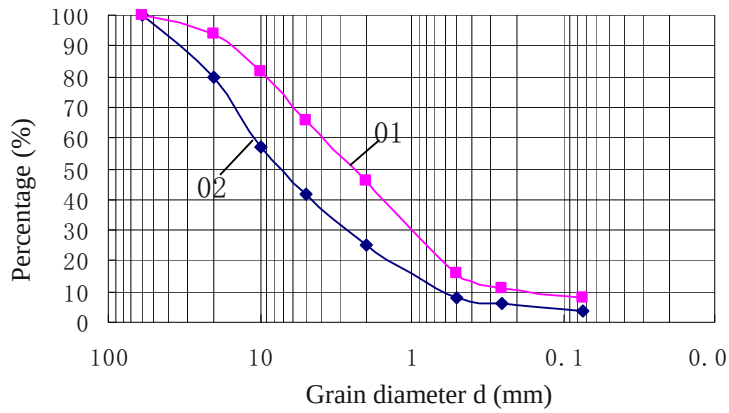

Fig. 2 Curve of grain size distribution for fillings (Curve 01 – filling of Section 9 on Guangdong construction site, Curve 02 – filling of section A1 on Chongqing construction site)

Table 2 Grade components of fillings

	Grain diameter (mm)	20—60	10—20	5—10	2—5	0.5—2	0.25—0.5	0.074—0.25	<0.074
Percentage (%)	Fillings in Guangdong construction site	6.0	12.6	16.0	19.5	29.9	5.2	3.0	7.8
	Fillings in Chongqing construction site	20.5	22.2	15.5	16.5	17.3	2.0	2.6	3.4

Table 3 Basic physical index for fillings

	Coefficient of uniformity (C_u)	Coefficient of curvature (C_c)	maximum dry density	Optimum water content	P_5 content for coarse grain with diameter over 5 mm
Fillings in Guangdong construction site	20	1.25	1.88 g/cm^3	11.5%	34.6%
Fillings in Chongqing construction site	18.33	1.36	2.10 g/cm^3	8.23%	58.2%

TEST RESULT AND ANALYSIS

For purpose of better analysis, friction coefficient ratio K is used as follows:

$$K=\frac{\tan\phi_{sg}}{\tan\phi}=\frac{f_{sg}}{\mu} \quad (1)$$

where, Φ_{sg} —Friction angle of interface between reinforcement and filling;

Φ—Internal friction angle of filling or comprehensive friction angle;

f_{sg}—Friction coefficient of interface between reinforcement and filling;

μ—Friction coefficient of filling.

Impact of Compactness on Interface Performance

Test result shows that compactness greatly influences anti shear strength of plain fill and reinforced soil interface. What we can get it out is from change of cohesion and internal friction angle. Please refer to Table 4 for details. Compactness is increased from 90% to 93%; c、φ value for plain fill without reinforcement is increased by 3.7 kPa and 1.8° respectively; c、φ value for reinforced interface is increased by -6.2 kPa and 3.6° respectively, and friction angle of reinforced soil interface is also significantly increased. In addition, with greater compactness, soil grain and geogrid surface will be in closer contact. Therefore, compactness of soils scattered in geogrid pores is also increased. As a result, friction angle of reinforced soil will increase with the increase of compactness, but it is hard to determine rule of cohesion.

With further analysis we can figure out that, compared with plain fill without reinforcement, total strength of reinforced soil interface τ will decrease by 14.2%, 15.0%, 15.4% and 15.6% respectively under overburden pressure p of 100 kPa, 200 kPa, 300 kPa and 400 kPa at 90% compactness. It will decrease by 18.2%, 15.0%, 13.6% and 12.8% respectively at 93% compactness. So we can conclude that decrease of total strength τ will be smaller at higher compactness and under higher overburden pressure and will be greater at lower compactness and under higher overburden pressure.

Table 4 Parameters of fill and reinforced soil at different compactness

Compactness	Plain fill		Reinforced soil interface		Friction coefficient ratio
	c (kPa)	φ (°)	c (kPa)	φ (°)	K
90%	39.7	34.3	35.6	29.7	0.837
93%	43.4	36.1	29.4	33.3	0.900

Impact of Geogrid Pore Diameter on Interface Performance

During the test, we get interface parameters of geogrid with different pore diameter under optimum water content and at 93% compactness, shown in Table 5. From test result we can see that geogrid pore diameter significantly influences interface performance. Pore diameter seems not so related to cohesion, but is in a certain relation with friction angle, i.e., there's an optimum pore diameter. Within the 4 different geogrid pore diameter, friction angle of reinforced soil interface reaches its maximum value when pore diameter is 15 cm.

From test result shown in Table 5, we can see that, compared with plain fill without reinforcement, total strength of reinforced soil interface τ is decreased by 9.9%, 8.3%, 7.7% and 7.3% respectively under overburden pressure p of 100 kPa, 200 kPa, 300 kPa and 400 kPa when geogrid pore diameter is 15cm. Such total strength τ is decreased at smallest extent for the 4 pore diameters.

During the test, index d_{50} is used for filling, which means grain diameter of filling when pass percentage is 50%. d_{50} for the tested filling taken from Chongqing construction site is 7.5 mm. Fig. 3 is the curve of relation between d_{50}/(geogrid pore diameter) and friction angle of reinforced soil interface. From the curve we can figure out that friction angle is decreasing rapidly when d_{50}/(geogrid pore diameter) value is greater than 0.075. Interface friction angle is larger when such value is between 0.04 and 0.075. Therefore, there should be some geogrid at a proper pore diameter in certain grade of filling, then from which we could get optimum test result. In practical engineering application, attention should be paid to matching between filling grade and geogrid pore diameter. Index d_{50}/(geogrid pore diameter) could be used as one of design control indices. Value of such d_{50} should be taken around 0.05.

Table 5 Interface parameter of geogrid with different pore diameter

Parameter	Plain fill	Geogrid pore diameter (cm)			
		5	10	15	20
Pseudo-cohesion C (kPa)	25	25.4	21.4	19.8	18.1
Internal friction angle φ (°)	35.8	30.6	32.6	34.1	32.7
Friction coefficient ratio (K)		0.817	0.885	0.937	0.888
d_{50} /geogrid pore diameter		0.15	0.075	0.05	0.0375

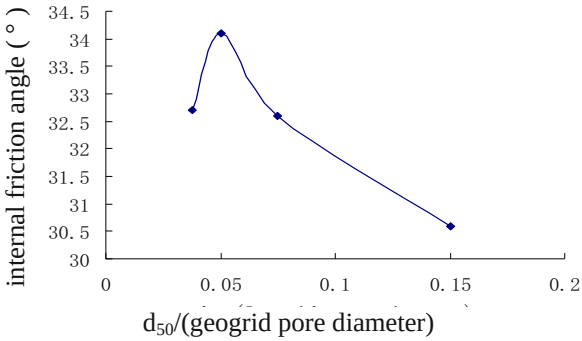

Fig. 3 Curve on relation between d_{50}/(geogrid pore diameter) and internal friction angle

Impact of Water Content on Interface Feature

It is inevitable that reinforced engineering will be affected by water. Lots of engineering practices show that disease of reinforced engineering is in close relation with change of water content in the fill.

We carried out shear test to geogrid of 15 cm pore diameter and at 93% compactness under water content of 8.23%, 10% and 12% respectively and we get that soils with 8.23% water content have the optimum water content.

From the test we can figure out that both internal friction angle of plain fill and interface friction angle of geogrid reinforced soils will decrease with the increase of water content. Friction angle will decrease to a greater extent especially when water content is greater than 10%. Please refer to Table 6 for parameters of fill and reinforced soil interface with different water content. For plain fill, internal friction angle will increase to 35.8 degree when it is with optimum water content (8.23%) and such angle will decrease to 25.9 degree when water content of soils increases to 12%. For reinforced soil interface, internal friction angle will reach 34.1 degree when water content is 8.23% and decrease to 21.9 degree when water content is increased to 12%. Friction angle will decrease sharply when water content exceeds a certain value. For decrease percentage, please refer to Table 7. Therefore, we can conclude that interface friction angle will decrease at increasing extent with the increase of water content for geogrid reinforced soils. As geogrid surface is smooth and do not absorb water, friction angle will decrease due to lubrication of water in geogrid surface when water content is increased. In a word, special attention should be taken in value taking of reinforced soil interface parameters during reinforcement design for immersed embankment.

Table 6 Parameters of fill and reinforced soil interface with different water content (optimum water content: 8.23%)

Parameter		Plain Fill		Grid (Pore diameter =15 cm)		Friction coefficient ratio
		c (kPa)	φ (°)	c (kPa)	φ (°)	(K)
Water Content （%）	8.23	25	35.8	19.8	34.1	0.937
	10	41.7	30.9	46.3	27.4	0.866
	12	26.0	25.9	33.4	21.9	0.827

Table 7 Reduction percentage of friction angle and internal friction angle for the test

	Plain Fill（Different water content %）			Optimum water content + Geogrid with different bore diameter (cm)				Geogrid of 15cm bore diameter, different water contents (%)		
	8.23	10	12	5	10	15	20	8.23	10	12
Internal friction angle	35.8°	30.9°	25.9°	30.6	32.6	34.1	32.7	34.1	27.4	21.9
Reduction percentage of internal friction angle				14.5%	8.9%	4.7%	8.7%	4.7%	11.3%	15.4%

Impact of P_5 Content for Different Coarse Grain on Interface Performance

Interface direct shear test is carried out based on another two kinds of gradation fill by increasing P_5 content of coarse grain (above 5mm) filling taken from in the fill Chongqing construction site referred in Table 2: Gradation 1: P_5 content of coarse grain above 5 mm is 73.2%, coefficient of uniformity (Cu) is 20.5, and coefficient of curvature (Cc) is 2.3. Gradation 2: P_5 content of coarse grain above 5mm is 43.2%, coefficient of uniformity (Cu) is 13.2, and coefficient of curvature (Cc) is 1.1. The test result under optimum water content, 93% compactness, 150 mm (bore diameter) biaxial plastic CATT geogrid is shown in Table 8.

From Table 8, we can see that coefficient ratio of reinforcement interface friction under gradation 1 fill reaches 0.950, while that under gradation 2 fill it is 0.895, which indicates that the more P_5 content of coarse grain in fill, the bigger the interface friction coefficient ratio is.

Table 8 Direct shear test result for 150 mm (bore diameter) CATT biaxial geogrid and fill with different P_5 content

P_5 content of fill	Internal friction angle of plain fill	Friction angle of reinforcement interface	K (friction coefficient ratio)
58.2% (Original gradation)	35.8°	34.1°	0.937
73.2% (Gradation 1)	38.2°	36.8°	0.950
43.2% (Gradation 2)	32.2°	29.4°	0.895

CONCLUSIONS

First, reinforced soil interface strength is affected by such factors as fill compactness, water content, grain coarse content and geogrid bore diameter. The more the fill compacted, the bigger the interface friction angel is. Bigger water content leads to a smaller interface friction angle. The more coarse grain contained, the bigger the friction angle is. There is an optimum ratio between optimum fill gradation and grid bore diameter. The test here shows that the interface friction angle will reach maximum value when the ratio between the fill d_{50} and the geogrid bore diameter is around 0.05.

Second, the reinforcement interface friction angle is normally a little bit smaller than the soil internal friction angle. The friction coefficient ratio is generally between 0.82 and 0.95, which basically align with the results of related tests carried out both in and abroad (reinforcement interface friction coefficient is 0.88~ 0.92 $tg\varphi_s$).

Third, fill water content impose great impact on friction angle of reinforced soil interface. Thus, water drainage of reinforced soil project should be a big concern. In wet and rainy areas, or areas where clay soil with high liquid limit is used as fill, the reinforcement interface parameter should be determined per to reinforcement interface friction test, or a lower interface friction coefficient should be used in such cases.

REFERENCES

Wu JH, Chen H et al. (2001) Study on Geo-synthetics and Soil Interface Performance. Chinese Journal of Geotechnical Engineering 23(1): 89- 93

Shi YZ (2003) Test on Interface Performance of Geogrid , Rock and Soil Mechanics 24(2); 296-299

Zhou ZG, Zheng JL et al. (1998) Study on Netlon Geogrid and Soil Interface Performance, Journal of Changsha Communications University 14(3): 34-39.

Ministry of Communications (1999) Technical Specifications for Application of Geo-synthetics in Highway (JTJ/T 019-98）, China Communications Press

Proceedings of the 4th Asian Regional Conference on Geosynthetics
June 17 - 20, 2008 Shanghai, China

CENTRIFUGAL MODELING OF A GEOGRID-REINFORCED EMBANKMENT ON SOFT SUBSOIL

J.F. Chen[1], S.B. Yu[2], J. Han[3], Z.M. Shi[4] and M.R Shen[5]

ABSTRACT: A centrifugal model test was performed to investigate the behavior of a geogrid-reinforced embankment on soft subsoil. The prototype was a reinforced embankment with four-lane driveways using lime-stabilized soil as backfill, which was 4-meter high, 26-meter wide, and over 20-meter thick soft silty clay. The slope angle of this embankment was 1.5(H):1.0(V). One plastic window screen by removing 2/3 of its strings was used to simulate the prototype geogrid while sand drains with 5-mm diameter were used to simulate prototype prefabricated vertical drains. Displacements, soil pressures, and pore water pressures were measured during the test. Test results showed: (1) the settlement estimated from the markers installed on the front face of the foundation was approximately 90% of that measured by displacement sensors; (2) the elastic displacement of the subsoil was approximately 11% of the total displacement; (3) the total settlement in the prototype embankment was 1.7 m and 300-mm wide cracks occurred at the central portion of the embankment.

KEYWORDS: centrifuge modeling, embankment, geogrid, soft subsoil, prefabricated vertical drains

INTRODUCTION

Centrifugal modeling, because of its capability to simulate *in situ* stress field and gravity dependent processes, is a powerful tool to investigate of geotechnical problems. Many studies have shown that centrifugal modeling is particularly valuable in understanding mechanisms and providing data for validation of numerical analyses. Furthermore, centrifugal modeling offers advantages of repeatability, great control over the entire test, short consolidation time and possibility of testing to failure. In recent years, centrifugal modeling has been increasingly used to study retaining structures, underground excavations, foundations, geoenvironment, and permafrost (Taylor, 1995; Xing, 2005; Bai, 2001).

Geogrid has been widely used to maintain stability of embankments on soft clay during or after construction. A series of centrifugal model tests were conducted by Sharma and Bolton (1996, 2001) to investigate different reinforcement mechanisms of geogrid and geotextile and the role of wick drains in improving the stability of embankments. A technique was successfully used to measure reinforcement force in the study.

Hu and Chen (2003, 2005) investigated the contribution of geotextile to the stability of embankments using centrifuge model tests.

This paper presents a centrifugal study to investigate the behavior of a geogrid-reinforced embankment using lime-stabilized soil as backfill on soft silty clay installed with wick drains.

DESIGN OF MODEL TEST

To simulate the related engineering projects (Zhang, 1997; Luo, 2000) and the specifications of highway design, a four-lane embankment using lime-stabilized soil as backfill was selected for the centrifugal model test. The prototype embankment with 1.5(H):1.0(V) slopes with height of 4m and width of 26 m, and over 20 m thickness soft subsoil.

The centrifugal test was performed using Tongji University's geotechnical centrifuge with capacity of 150g•t and 3 m radius arm as shown in Fig. 1. The container has internal dimensions of 900 mm in length, 700 mm in width, and 700 mm in depth. Based on Yao (2004), the boundary effect of the side friction in centrifuge tests is only limited to the distance of approximately 100mm from

[1] Associate Professor, Department of Geotechnical Engineering and Key Laboratory of Geotechnical & Underground Engineering of Ministry of Education, Tongji University, CHINA. Email: jf_chen@tongji.edu.cn
[2] Ph.D. Student, Department of Geotechnical Engineering, Tongji University, CHINA. Email: yusongbo@gmail.com
[3] Associate Professor, Department of Civil, Environment & Architectural Engineering, the University of Kansas, USA. Email: jiehan@ku.edu
[4] Associate Professor, Department of Geotechnical Engineering, Tongji University, CHINA. Email: zm_shi@tongji.edu.cn
[5] Professor, Department of Geotechnical Engineering, Tongji University, CHINA. Email: shenmingrong@sina.com

the side of the container wall. In the present study, the distance from the toe of the embankment to the boundary of container was more than 200 mm. Fig. 2 shows the cross-section of this centrifugal model.

The embankment on soft clay likely fails due to an increased load and/or reduced soil strength as a result of the generation of excess pore pressures. Therefore, particular attention was paid to the behavior of the reinforced embankment during construction.

Fig. 1 Geotechnical centrifuge machine

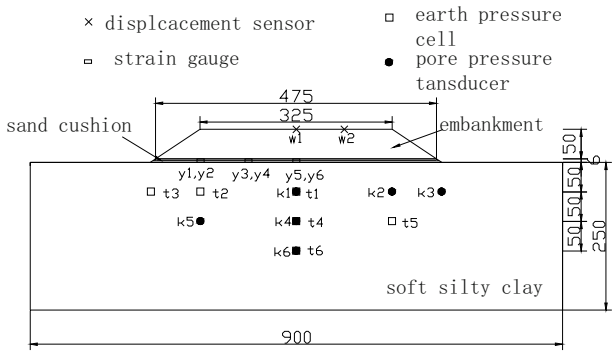

Fig. 2 Instrument layout in the centrifugal model (unit: mm)

MATERIAL MODELLING

Geogrid

Geogrid, as reinforcement, can resist the spreading of the embankment and the lateral displacement of the clay foundation, and thus contributes towards the stability of the embankment. Geogrid mobilizes its tensile resistance mainly by generating passive resistance to the soil particles confined between its apertures (Sharma and Bolton 1996). The use of scaled down geogrid for model reinforcement was well discussed by Viswanadham and Konig (2004). Two scaling relationships were deduced to model geogrid considering two basic requirements: scaling of tensile stiffness and scaling of bonding strength, i.e.,

$$\frac{J_m}{J_p} = \frac{1}{N} \tag{1}$$

$$\frac{f_m}{f_p} = 1\left(\frac{\text{kN}}{\text{m}^2}\right) \tag{2}$$

where J is the secant modulus of geogrid, which is equal to its Young's modulus E_r multiplied by its cross-section area A_r; f is the coefficient of interface friction between soil and geogrid; the subscripts m and p stand for model and prototype, respectively.

A plastic window screen by removing 2/3 of its strings was used to simulate the prototype geogrid in the present study. Fig. 3 shows the tension-strain curves of the model geogrid obtained by testing 50 mm wide strips in a tensile testing machine. The model geogrid has an average secant modulus of 11.4 kN/m and a tensile strength of 1.11 kN/m at 10% axial strain, which are equivalent to a secant modulus of 912 kN/m and a tensile strength of 88.9 kN/m for a prototype geogrid at the same strain at the acceleration of 80 g.

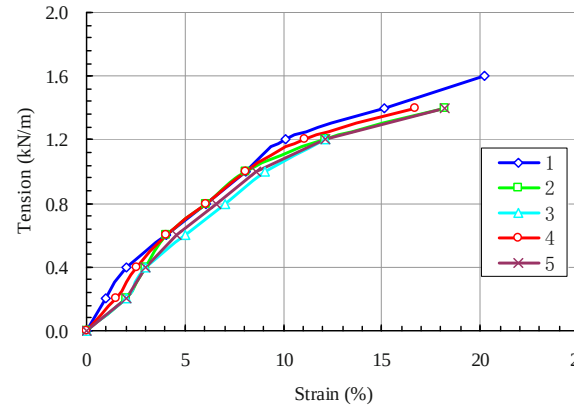

Fig. 3 Tension versus strain for the model geogrid

Prefabricated Vertical Drain

Since typical prototype prefabricated vertical drains (PVDs) are only several millimeters thick, it is hard to scale down its geometrical sizes by a factor of 1:N. However, model drains may be chosen according to the same average degree of consolidation as the prototype ones (Hou, 1995) based on the following equation:

$$d_m = \frac{d_p}{d_{wp}} \times d_{wm} \tag{3}$$

where d is the spacing between drains; d_w is the nominal diameter of a drain; subscripts m and p stand for model and prototype, respectively.

In the this test, sand drains with 5 mm diameter were installed at 140 mm center-to-center spacing in a triangular pattern. At the acceleration of 80 g, the model sand drains were equivalent to prototype PVDs being 100 mm in width, 5 mm in thickness, and 1.5m center-to-center spacing.

Subsoil

The soft silty clay of the third stratum in Shanghai was chosen as the soil for the model foundation and the embankment after mixed with lime. The soil was obtained from the field, air-dried, crushed, and sieved through a sieve size of 2 mm. The properties of the soft silty clay were determined as follows: density=1.73 g/cm^3; insitu water content=44 %; plasticity index =16.1; total strength cohesion 6 kPa; total strength friction angle =23°.

Embankment

Air-dried silty soil was mixed with 8 % lime to shape the embankment. The dry density-water content curve of the lime-stabilized soil was obtained as shown in Fig. 4 through compaction tests. The properties of lime-stabilized soil are: optimum water content=22%, maximum dry density =1.66 g/cm^3, and unconfined compression strength =713 kPa.

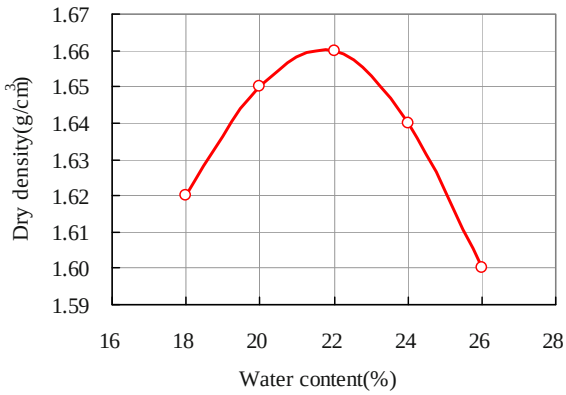

Fig. 4 Curve of compaction test for lime-stabilized soil

Sand Cushion

Medium sand passing a sieve size of 1.25 mm was used as a cushion at the interface between the soft foundation and the embankment. The density of the placed sand cushion was 1.24 g/cm^3.

TEST PROCEDURES

A thin film of silicone grease was smeared onto the inside vertical surfaces of the container to reduce the friction between the container and the soil. Four steel tubes (350 mm in height and 76 mm in diameter) were placed at four corners of the container to collect the water drained from the soil during consolidation. The tubes had cuts at the height of 238 mm so as to maintain a constant groundwater table at the depth of 1.0 m from the ground surface as the prototype. In Shanghai, the typical groundwater table is at between 0.6 to 1.6 m deep from the ground surface.

The subsoil was placed in 10 layers at a lift thickness of 30 mm each. The weighted air-dried soil was uniformly spread into the container, and then water was sprayed onto the soil to saturate it. Seven rows of plastic markers were placed on the front face of the foundation using pins, which would monitor the displacements of the foundation. The locations of the markers were determined using the photographs taken in-flight through the front Plexiglas window. Six earth pressure cells and six pore pressure transducers were installed at various locations in the subsoil to monitor the variations of earth pressures and pore pressures during consolidation and loading. Two displacement sensors were installed during consolidation and the construction of the embankment. The layout of these instruments is shown in Fig. 2.

In order to reach the similar stress level and degree of consolidation in the model foundation as those in the prototype, the model was subjected to an acceleration of 80 g for 4 hours, which is equivalent to the consolidation of the prototype for 3 years according to the centrifugal scaling law.

After consolidation, sand drains were installed using a thin shell steel tube with 5 mm diameter and then 5 mm thick sand cushion was placed. An instrumented model geogrid with strain gauges was placed in the middle of the cushion. The pre-constructed embankment at 93 % compaction level was placed above the sand cushion.

The four-staged construction of the embankment was simulated by increasing the acceleration. In terms of the prototype, there was a month break period between the first 3 stages while a 9-month break existed at the last stage as shown in Fig. 5. The four levels of accelerations at 20 g, 40 g, 60 g, and 80 g are equivalent to the construction heights of 1 m, 2 m, 3 m, and 4 m, respectively.

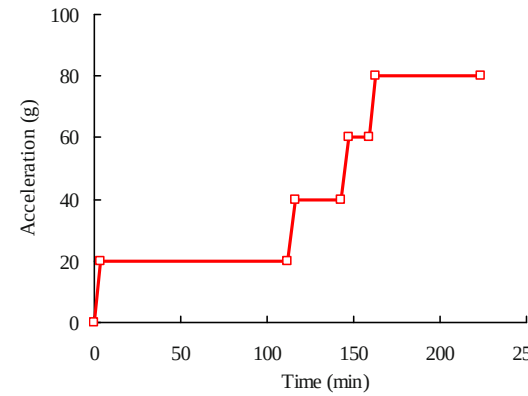

Fig. 5 Acceleration versus time

TEST RESULTS

Consolidation Period

Displacement vectors of the subsoil and the settlement-time curve were obtained by analyzing the locations of the markers on the photographs taken in-flight during the centrifuge test, as shown in Figs. 6 and 7.

The dash lines in Fig. 6 represent the displacement of the subsoil before the acceleration field reached 80g while the continuous lines represent the displacement of the subsoil during 4 hours' consolidation in the centrifugal model test. The displacement vectors show a concave shape with the angles ranging from 16.7° to 47.8° between the dash lines and the vertical lines, which exceed the angles of the locations between the lines connecting the rotation center of the centrifuge to the specific soil masses and the vertical lines. The phenomenon of the inclined soil displacements only occurred when the acceleration was increased to 80 g. However, the angles between the continuous lines and the vertical lines were in the range of 0° to 8.4°, which approximately equal to the angles of the locations of the soil masses. The uppermost row of the markers showed the settlement varied from 42.4 to 51.1 mm with an average of 48.7 mm. The second row close to the uppermost had the settlement ranging from 41.1 to 43.7mm with an average of 42.4mm.

Fig. 7 shows the development of settlement with time during the consolidation. The settlement of the ground was 23.8 mm at the beginning of 80 g acceleration (i.e., the corresponding time was 0). When the centrifugal test was conducted for approximately an hour at 80 g, the displacement sensors ran out the limit at the settlement of 48.3 mm. At the same moment, the corresponding settlement of 43.1 mm was measured from the photographs taken in-flight, which is 10.7% less than the settlement measured by the displacement sensors. Based on this same ratio, the total settlement of the ground at the end of the consolidation was estimated to be 54.5 mm. As a result, the thickness of subsoil was 245.5 mm, which is 4.5 mm less than the designed thickness. When the centrifuge stopped, the thickness of subsoil was 251.7mm, indicating 6.2 mm elastic rebound, which is approximately 11% of the total settlement.

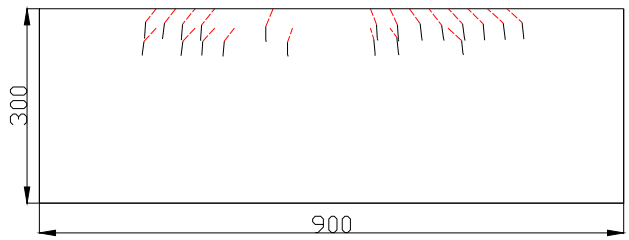

Fig. 6 Displacement vectors during consolidation

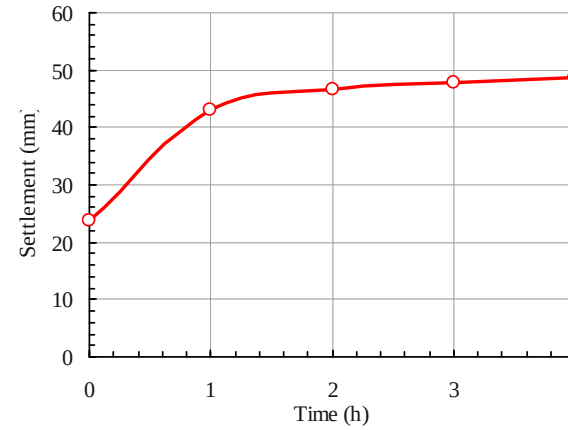

Fig. 7 Settlement versus time during consolidation

Loading Period

The construction of the embankment induced a significant displacement in the subsoil as shown in Fig. 8. The largest settlement developed at the center of the embankment while the ground heave was observed outside of the embankment toes. The distribution of horizontal displacement was more concentrated under the shoulders of the embankment.

At the acceleration of 80 g, the settlement at the central portion of the embankment measured by the displacement sensor was 27.6 mm including 6.2 mm elastic rebound. Therefore, the total settlement induced by the construction of the embankment was 21.4 mm, which is equivalent to 1.7 m settlement of a prototype embankment.

Only half of the earth pressure cells and the pore pressure transducers installed in the subsoil survived during the test, which included t2, t3, and t6 for earth pressure cells and k1, k2, and k3 for pore pressure transducers. The measured earth pressures under the embankment shoulders were higher than those under the embankment toes as shown in Fig. 9. Fig. 10 showed that the pore pressures increased during the construction of the embankment and dissipated during the break. The rate of dissipation was dependent on the drainage path. Since Point k1 was located at 70 mm away from the nearest sand drain, farther than other points, the rate of dissipation at this location was slower.

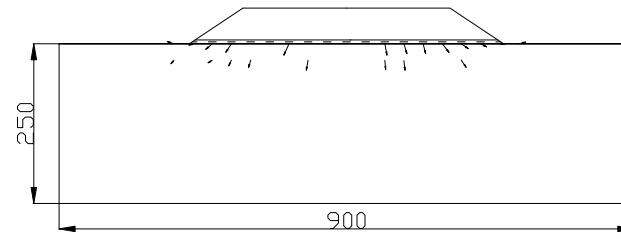

Fig. 8 Displacement vectors during loading

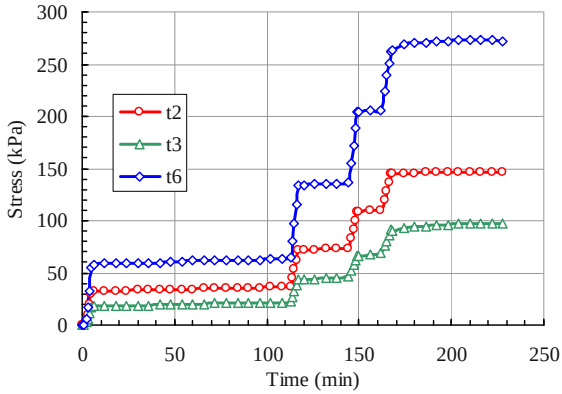

Fig. 9 Earth pressures versus time

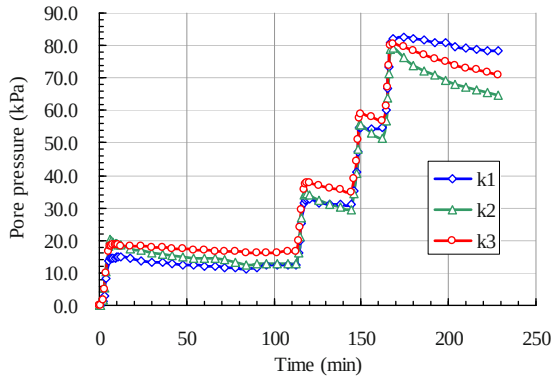

Fig. 10 Pore pressures versus time

The photo in Fig. 11 shows the distinct cracks of approximately 3 to 4 mm wide (equivalent to 300 mm in a prototype embankment) occurred at the center of the model embankment. However, no obvious slip surface in subsoil and the model geogrid was found after the test.

Fig. 11 Cracks on the embankment surface

No tensile stress in the model geogrid was measured because the strain gauges on the geogrid were damaged during the test.

CONCULSIONS

The behavior of geogrid-reinforced embankment on soft clay subsoil was investigated in a centrifugal test. The secant modulus of the plastic window screen after removing 2/3 of its strings was 11.4 kN/m, which was appropriate to simulate the prototype geogrid.

The settlement measured using the markers installed on the front of the foundation was about 90% of that measured using the displacement sensors. The elastic rebound of the subsoil induced by unloading was measured which was approximately 11% of the total displacement during the consolidation.

With the presence of sand drains in clay subsoil, the excess pore pressures dissipated obviously during the break. The total settlement of the subsoil was 1.7 m and 300 mm wide cracks occurred at the embankment surface in the prototype embankment during the construction.

ACKNOWLEDGEMENTS

The financial support from the Natural Science Foundation of China under grant No. 50508030 is gratefully acknowledged. The first author would also like to thank the China Scholarship Council for supporting his visit at the University of Kansas, USA as a visiting scholar.

REFERENCES

Bolton MD, Shama JS (2001) Centrifugal and numerical modelling of reinforced embankments on soft clay installed with wick drains. Geotextiles and Geomembranes 19: 23-44

Chen SL, Zhang BH., Zhang JM (2005) Centrifugal modelling of reinforced embankments on soft clay. Chinese Journal of Rock Mechanics and Engineering 24(15): 2751-2756

Hou YJ (1995) Centrifuge modeling of soft clay installed with plastic drains. Dam Observation and Geo-technical Tests 19(5): 18-20

Hu HL, Chen SL, Shen ZJ (2003) Centrifugal & numerical modeling of geosynthetic reinforced embankments on soft clay. Rock and Soil Mechanics 24(3): 389-394

Luo D, Liao DS, Wang LJ (2000) Application of earthwork grate in treatment of soft road foundation. Metal Mine Design & Construction 32(4): 43-44

Malushitsky YN (1975) The centrifuge model testing of waste-heap embankment. Cambridge University Press:

5-11

Shama JS (1996) Centrifuge modelling of an embankment on soft clay reinforced with a geogrid. Geotextiles and Geomembranes 14: 1-17

Taylor RN (1995) Geotechnical centrifuge technology. Blackie Academic and Professional, London

Viswanadham BVS, Konig D (2004) Studies on scaling and instrumentation of a geogrid. Geotextiles and Geomembranes 22: 307-328

Xing JX, Xing YC, Liang JH (2005) Development and thoughts of geotechnical centrifuge modeling. Journal of Water Resources and Architectural Engineering 3(1): 27- 31

Yao, MY, Zhou SH, Li YC (2004) Boundary effect analysis of centrifuge test. Chinese Quarterly of Mechanics 25(2): 291-296

Zhang CH, Yuan WM, Dai JQ (1997) Soft foundation treatment for expressways. China building and construction press: 96-106 (in Chinese)

Zhou J (2002) The latest application of centrifuge model test. Shanghai Geology (1): 52-56

Proceedings of the 4th Asian Regional Conference on Geosynthetics
June 17 - 20, 2008 Shanghai, China

DETERMINATION OF INTERFACE SHEAR STRENGTH OF GEOSYNTHETICS USING CENTRIFUGE

W. Wu[1], M.S. Acharya[2] and F. Aschauer[3]

ABSTRACT: In the present paper, a tilt table device for testing the interface shear strength in geotechnical centrifuge is presented. By combining the advantages of tilt table and centrifuge, our tests cover a wide range of stresses from 10 kPa to 100 kPa. After a detailed description of the tilt table device, the test process in a centrifuge and its evaluation procedure is presented. The softening behaviour in the post peak regime is investigated by controlling the displacement with a relaxation mechanism. The test results in centrifuge are discussed and compared with 1g-tilt table tests and large box direct shear tests.

KEYWORDS: interface shear strength, geomembrane, tilt table test, centrifuge, large box shear test

INTRODUCTION

Correct estimates of the shear strength of soil-geomembrane interface are crucial for safe and economic design of structures where geosynthetics elements are used. The interface shear strength between soil and geosynthetic material can be determined either by tilt table test or direct shear test, e.g. ASTM 5321. Usually, tilt table tests are carried out at extremely low stress level of less than 10 kPa. Such tests are particularly relevant for the design of surface liners. In principle, the pressure in 1g-tilt table tests can be increased by stacking dead weight. However, towering dead weights often leads to overturning and non-uniform stress distribution. On the other hand, due to mechanical difficulties, direct shear tests at extremely low stress level do not provide reliable results. Moreover, tilt table tests and direct shear tests differ in boundary conditions. Tilt table tests are force-controlled, while direct shear tests are displacement-controlled. Once the shear strength is fully mobilised in a tilt table test, the soil specimen loses its stability and starts an accelerated motion downwards. The tilt table test provides the peak strength but not the residual strength. In a direct shear test, the soil specimen is restrained and remains stable when the peak strength is reached and beyond. Comparisons between both tests indicate that the shear strength determined in direct shear tests is somewhat higher than in tilt table tests (Girard et al. 1990; Koutsourais et al. 1991; Izgin and Wasti 1998; Lalarakotoson et al. 1999). A plausible explanation of this discrepancy is not available. Therefore, it is desirable to have one kind of test covering the entire range of stress level.

In the present paper, a tilt table device for testing the interface shear strength in geotechnical centrifuge is presented. By combining the advantages of tilt table and centrifuge, our tests cover a wide range of stresses from 10 kPa to 100 kPa. After a detailed description of the tilt table device, the test process in a centrifuge and evaluation procedure is presented. The softening behaviour in the post peak regime is investigated by controlling the displacement with a relaxation mechanism. The test results in centrifuge are discussed and compared with tilt table tests and large box direct shear tests in 1-g environment.

The centrifuge tilt table tests provide the complete stress-displacement with both peak strength and residual strength. Some recent publications in the literature suggest that the tilt table test is appropriate for characterising soil-geosynthetics interfaces (Lopes et al. 2001; Ling et al. 2002; Briançon et al. 2002; and Pedersen et al. 2003). The present paper shows that the tilt table test can be improved to explore the behaviour beyond the peak strength.

In view of the above exposition, the main objective of the present paper is twofold. First, the tilt table device is improved to allow for the investigation of the softening behaviour beyond the peak strength. This is made possible by a relaxation mechanism, which first holds back the soil specimen from sliding down and then mobilises the shear strength by translating the soil

[1] Institute of Geotechnical Engineering (IGE), Universität für Bodenkultur (BOKU), Vienna, AUSTRIA, Email:wei.wu@boku.ac.at
[2] IGE/BOKU, AUSTRIA, Email: madhu_sudan.acharya@boku.ac.at
[3] IGE/BOKU, AUSTRIA, Email: Franz.aschauer@boku.ac.at

specimen with prescribed displacement. Second, the tilt table device is integrated into a geotechnical centrifuge to increase the pressure in the tilt table test.

TILT TABLE DEVICE

As shown in Fig. 1, the tilt table device consists of a base platen (1), a trough (2) and a shear box (12). The tilt table device weighs about 37 kg. The shear box is about 193 mm long and 174 mm wide. The shear box is guided by a linear slide on each side and slides along the trough base. The base platen and the trough are hinged at the pivot (3) on the one side. On the other side, the trough is connected to a lead screw of a spindle lift. The spindle lift (4) is hinged to the base platen on the pivot (5).

An important component of the tilt table device is a relaxation mechanism (11), which is introduced to measure the properties in the post peak regime. The relaxation mechanism consists of a stepper motor M1, a worm gear box and linear guides with a holder for load cells W2. The holder for the displacement transducer provides also the guide for a parallel translation of the shear box and the load cells and guarantees that the shear box and the load cells W2 are translated as an entity. The relaxation mechanism is mounted onto the rear bottom of the trough and connected to the load cells trough two openings in the trough bottom. When the critical inclination of the trough is reached, the shear box tends to slide down the trough. The relaxation mechanism will hold back the shear box.

The trough can be raised by the spindle lift, which is driven by a stepper motor M2 and worm gear box, which allows for a precise transformation of the rotary motion into linear motion via a lead screw. Since the tilt table in the centrifuge is not accessible during testing, the stepper motor is connected to the I/O control panel of the centrifuge. From the control panel the tray can be raised or lowered at a given rate, e.g. 1°/min. The tilt table device is designed to accommodate soil specimen in a mould in the trough base. The friction behaviour of geomembrane can be studied on both sides, e.g. a sand specimen in the shear box and a clay specimen in the mould. In the present paper, however, an aluminium plate is put into the mould.

During testing the base platen is mounted to the base of the centrifuge loader by four screws. The geomembrane is held in place by two steel clamps. Each clamp is fixed by five screws to ensure uniform stress within the geomembrane. Two parallel load cells are integrated into the steel clamp to measure the tensile force in the geomembrane (W1 in Fig. 1). The tensile force in the geomembrane provides an excellent indication for the post peak behaviour.

The shear box is placed on the trough base. The displacement of the shear box is measured by a displacement transducer (8), which is mounted on the trough. The traction force exerted by the shear box is measured by two parallel load cells (W2 in Fig. 1).

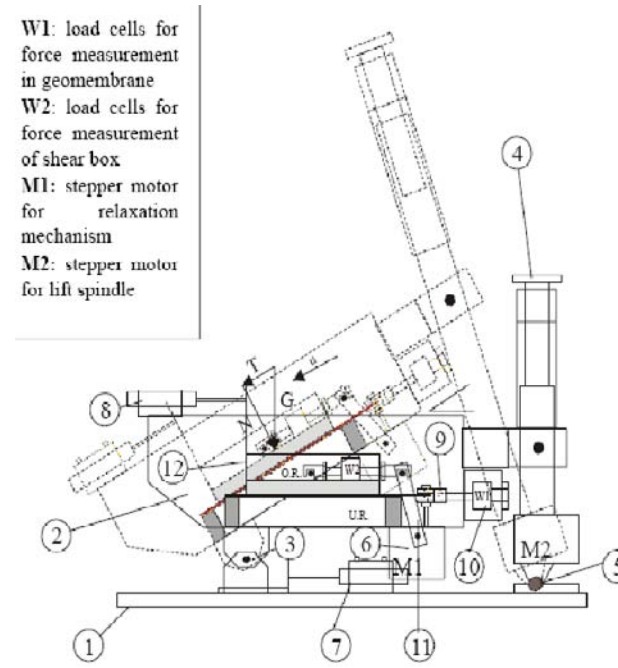

Fig. 1 Components of the tilt table device

After the spindle lift is stopped, the shear box is "relaxed" by prescribing a displacement increment down slope. This is done by switching on the stepper motor M1. To facilitate automatic measurement of the inclination, the rotation around the hinge (3) is converted into a linear displacement via rack and pinion. As the trough is raised via the spindle lift, the pinion rotates on the pivot and transforms the rotation into a linear displacement.

GEOTECHNICAL CENTRIFUGE

Geotechnical centrifuge model testing is widely recognised as an important tool for investigating complex geotechnical problems via small sized models. In order to achieve mechanical similitude in small sized models, it is necessary to replicate the in-situ stress state. In small sized models, the geotechnical centrifuge is used to increase the stress level to reach mechanical similitude. However, in the tilt table test, the specimen size is not reduced and the centrifuge is used only to increase the stress level.

The geotechnical centrifuge at Universität für Bodenkoltur (BOKU) in Vienna was manufactured by Trio-Tech, USA and was put into operation in 1990. The

centrifuge has mainly the following components: swinging basket, balancing counterweight, DC motor and aerodynamic enclosure. The diameter of centrifuge is about 3 m and it can generate an acceleration of 200 g with 400 rpm. It can carry a model with maximum load of 90 kg.

TESTING PROCEDURE

The geomembrane is placed on the trough base and fixed by the two clamps. The geomembrane should be slightly stretched by adjusting the screws of the clamp in order to measure the stress from the beginning of test. After putting the shear box in place, the displacement transducer, the load cell and the relaxation mechanism are connected to the shear box. The shear box should be moved back and forth several times while the readings of displacement transducer and load cell are taken in order to avoid play. Afterwards, depending upon the type of test interface, the shear box is filled with a batch of sand (445 g) or the testing material (geotextile) is placed. The maximum fill height (sand) is about 80 mm. A steel plate of 7648 g is placed on the top of the sand /geotextile surface. The total weight on the geomembrane varies from 7660 g to about 8093 g. By varying the acceleration in the centrifuge, the shear strength of interface can be investigated in a wide range of stress level from 10 to 100 kPa.

After the specimen preparation, the tilt table is placed into the platform of the centrifuge. The base platen is mounted onto the platform by screws. The centrifuge is put into operation and an input of rotation speed is made at the control panel. After the specified rotation speed is reached, the first readings are made, which serve as the reference. By switching on the stepper motor M2 the trough is raised at the speed of about 1°/min. With increasing inclination, the shear strength at the interface is gradually mobilized, which is characterized by an increase in displacement, in force exerted by the shear box and in force in the geomembrane. After the shear stress (the friction angle) reaches a certain level, e.g. 20°, the stepper motor of the spindle lift is stopped and the shear box and the load cell are translated down slope by a displacement increment of 1-2 mm. In general, a displacement increment down the slope will reduce the shear force in W2 to some extent. After the relaxation, the shear box is again held back. The trough is raised by switching on the stepper motor of the spindle lift. The increase in inclination gives rise to further mobilization of the shear force in the regime before peak. In the post peak regime, however, further tilting does not lead to further increase in shear force. A tilt table test in centrifuge consists of a number of sequences of mobilization and relaxation. In this way, the post peak behaviour can be investigated incrementally. To sum up, the following parameters are measured during a tilt table test in centrifuge: the inclination of the trough, the traction force exerted by the shear box, the displacement of the shear box and the traction force in the geomembrane.

PRESENT TESTS

A series of tests were carried out with the tilt table device in the centrifuge. The radial accelerations in these tests were 6 g, 12 g, 18 g, 24 g, 30 g and 36 g. Starting from $\alpha = 0°$, the trough was raised continuously until an inclination of about 22°, where the trough was stopped and the first relaxation was started. Afterwards, the relaxation mechanism was locked and the trough was raised by $\Delta\alpha \approx 1°$. Tests were continued by alternating between relaxation and mobilization and terminated at $\alpha \approx 34°$. The displacement was about 0.3 mm at the first relaxation ($\alpha \approx 22°$) and about 3.2 mm at test end ($\alpha \approx 34°$).

In order to compare the results from the centrifuge with other tests, the same materials were tested in 1-g environment. These tests include tilt table tests in a large tilt table with an area of 50 cm by 50 cm and direct shear tests in a large shear apparatus with an area of 50 cm by 50 cm. As mentioned before, the normal stress in tilt table tests need be corrected, when comparison with direct shear tests is made.

This paper describes the results of series of eleven interface friction tests combinations (Table 1), which were carried out in the tilting table in centrifuge, in the large shear box and in the 1g-tilting table. The interface was either between geomembrane and geotextile or geomembrane and sand. For each of these interfaces, 1-g tilting table and large box shear tests were also carried out. In the present tests, five types of HDPE geomembrane and two types of geotextiles TS800 and TS011 from the manufacturer Polyfelt were used. The HDPE geomembrane with the following surface profile were used.

- smooth surface (denoted by S)
- raised elliptical surface profile (denoted by E)
- rough surface profile (denoted by R)
- web raster (50x50) profile (denoted by RS50)
- web raster (12x12) with spike (denoted by RS12)

Standard coarse sand was used as fill material in these tests. The properties of the sand used in the test are given in Table 2. Sand with similar properties is often used as drainage material in practice. The sand consists mainly of quartz and has sub-rounded grains. As can be

seen from Table 2, the extremely low uniformity coefficient indicates that the sand grains are uniform with small size variations.

Table 1 Summary of test interfaces

Test No.	Description of interface	Notation
1	Smooth surface geomembrane (S) with polyfelt TS800 geotextile	S-TS800
2	Smooth surface geomembrane (S) with Coarse sand	S-Coarse Sand
3	Elliptical surface geomembrane with polyfelt TS800 geotextile	E-TS800
4	Elliptical surface geomembrane with coarse sand	E-Coarse Sand
5	Rough surface geomembrane with polyfelt TS800 geotextile	R-TS800
6	Rough surface geomembrane with coarse sand	R-Coarse Sand
7	Web raster (50x50) surface geomembrane with polyfelt TS800 geotextile	RS50-TS800
8	Web raster (50x50) surface surface geomembrane with coarse sand	RS50-Coarse Sand
9	Web raster (12x12) spike surface geomembrane with polyfelt TS800 geotextile	RS12-TS800
10	Web raster (12x12) spike surface geomembrane with polyfelt TS011	RS12-TS011
11	Web raster (12x12) spike surface geomembrane with coarse sand	RS50-Coarse Sand

Table 2 Properties of test sand

Specific gravity γ_s [g/cm^3]	2.64
Minimum void ratio, e_{min}	0.54
Maximum void ratio e_{max}	0.78
Mean grain diameter d_{50} [mm]	0.95
Maximum grain diameter d_{max} [mm]	2.00
Uniformity coefficient:U= d_{60}/d_{10}	1.4
Curvature coefficient: C= $d^2_{30}/(D_{60}/d_{10})$	1.0

EXPERIMENTAL RESULTS

Typical test results under a radial acceleration of 24 g are given in Fig. 2a and 2b, which show the increase in friction angle with tilting angle α and decrease in normal stress with the inclination.

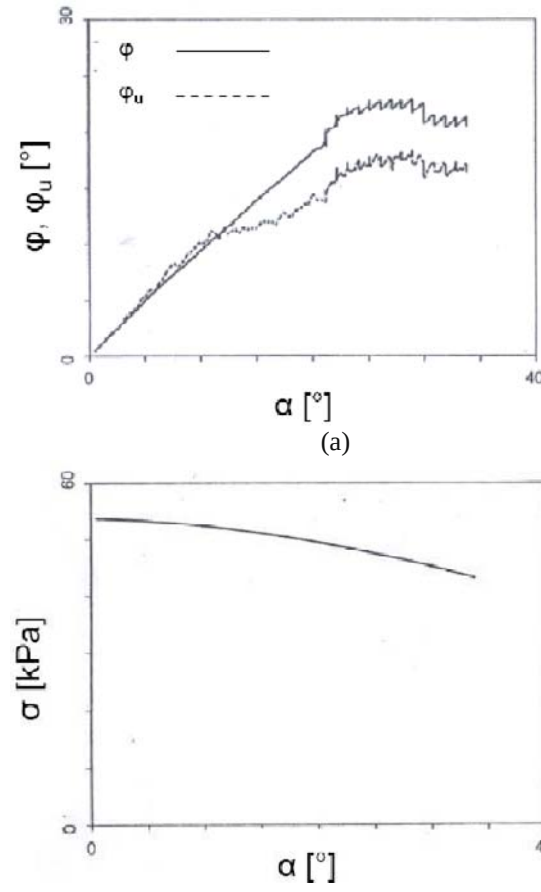

Fig. 2 Typical test results with geomembrane and sand interface in tilt table test at 24 g

For the geomembrane-sand interface, the following observations can be made from Fig. 2a (solid line). Starting from α = 0°, the mobilized friction angle increases approximately linearly with the inclination until the first relaxation at α ≈ 22°. The first five relaxations till α ≈ 25° lead to hardening response, which is characterized by increasing mobilized friction angle with the inclination. From α ≈ 25° to α ≈ 30°, the mobilized friction angle remains nearly unchanged with a peak friction angle of about 22.5°. Beyond α ≈ 30° the interface shows softening response, which is characterized by decreasing mobilized friction angle. The interface shows moderate softening behaviour with a residual friction angle of about 21.9°. Similar observations can also be made for the friction behaviour between the geomembrane and the underlying trough base (dotted line in Fig. 2a). As can be seen in Fig. 2b, with the inclination, the normal stress decreases monotonically, while the shear stress first increases to reach its maximum and then declines to approach the residual shear strength.

The test results of the tilting table test in centrifuge with different interfaces are presented in Fig. 3, which shows the relationship between friction angle and the

normal stress. Similarly, the results from large box shear tests are presented in Fig. 4. As can be seen from the Figs. 3 and 4, with increase in stress level, the friction between smoothed surface geomembrane and geotextile or sand interface remained almost unchanged in case of centrifuge tilting table test whereas it decreased slightly in large box shear test.

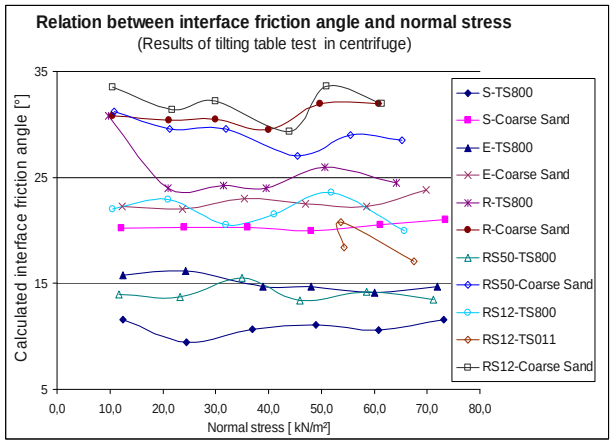

Fig. 3 Test results of tilting table test in centrifuge with different types of geomembrane/geotextile and geomembrane/ sand interface

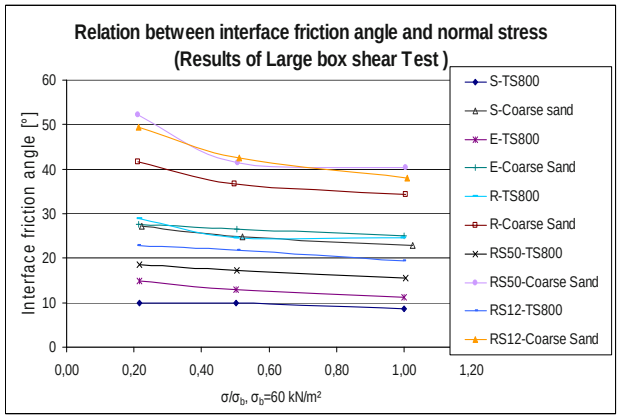

Fig. 4 Large box direct shear test results with different types of geomembrane/geotextile and geomembrane/ sand interface

In general, there is a decreasing tendency in friction angle with the increasing stress level in shear box tests but the results of tilting table test in centrifuge do not show any clear tendency. Fig. 3 shows some fluctuations in friction angle which may be due to relaxations in tilting angle. Fluctuations are more in case of rough interfaces compared to smooth interfaces. As can be observed in Fig. 3, the test results of some rough interfaces shows slightly increasing tendency in interface friction angle with increasing stress level, which is an opposite tendency to that of direct shear test results.

The test results of the tilting table test in centrifuge, 1g-tilting table test and large box shear tests of geomembrane-geotextile interface are presented in Fig. 5. The results show that with increasing roughness of the interface surface, centrifuge tilting table results become inconsistent and seems unrealistic compared to box shear test. In such case, box shear test results seem more appropriate.

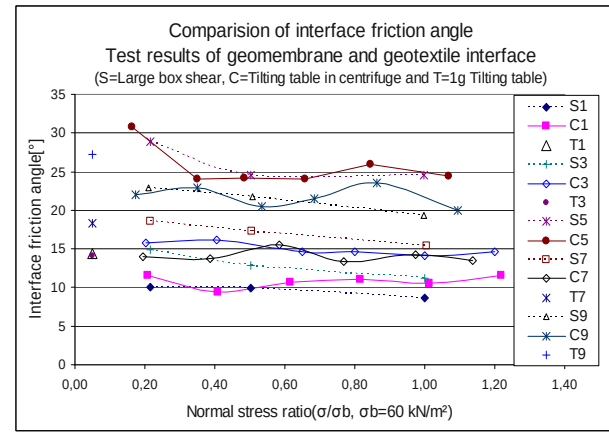

Fig. 5 Test results with various types of geomembrane/geotextile interface

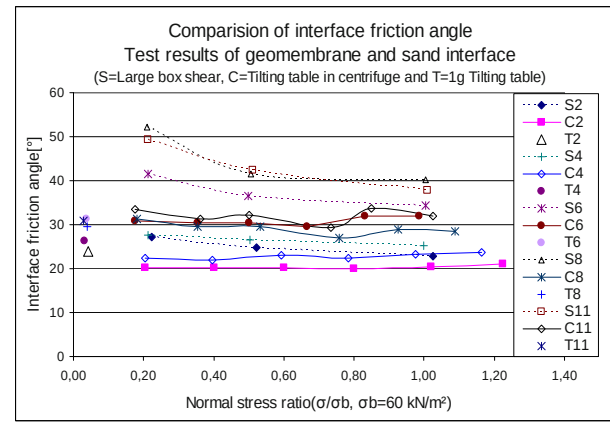

Fig. 6 Test results with various types of geomembrane/coarse sand interface

Similarly, the three different tests results of geomembrane-coarse sand interface are presented in Fig. 6. The results show that with the increase in surface roughness, the difference between the tests (centrifuge tilting table and shear test) results also increases. With increasing stress and roughness of the interface surface, more fluctuations in interface friction angles can be observed. The shear box test results in higher interface friction angle compared to centrifuge tilting table test. As can be seen from Fig. 6, the results from centrifuge tilting table tests remain nearly unchanged throughout all stress level, whereas there is a decreasing tendency in friction angle in case of shear box tests. In this case, the

centrifugal tilting table test results seem to be more appropriate compared to box shear test results. In general, it seems that centrifuge tilting table test is more suitable for testing smooth surface geomembrane and sand interfaces, whereas the shear box test is more appropriate for rough surface interfaces.

CONCLUSIONS

The tilt table device in centrifuge provides an alternative to the direct shear test for a wide range of normal stress. By using radial acceleration up to about 40g we are able to test interface shear strength under a range of normal stress from 10 kPa to 100 kPa. In centrifuge tilting table, the softening behaviour in the post peak regime can be investigated by controlling the displacement of the shear box with a relaxation mechanism.

The frictional angle from the tilt table tests in centrifuge does not show clear dependence on the stress level but it is found to increase with decreasing stress level in case of box shear test. In general, the friction angle from direct shear tests is higher than from the tilt table tests in centrifuge. The present test results show that with increasing roughness of the interface surface, centrifuge tilting table results become inconsistent and seem unrealistic compared to box shear test results.

ACKNOWLEDGEMENTS

The paper is based on several MSc thesises in our institute. We thank our students H. Marent and H. Hartl for their works.

REFERENCES

ASTM D 5321-92(1997), Standard test method for determining the coefficient of soil and geosynthetic and geosynthetic and geosynthetic friction by the direct shear test

Briançon L, Girard H, Poulain D (2002) Slope stability of lining systems—experimental modeling of friction at geosynthetic interfaces, Geotextiles and Geomembranes 20: 147- 172

Girard H, Fisher S, Alonso E (1990) Problem of friction posed by the use of geomembranes on dam slopes—examples and measurements, Geotextiles and Geomembranes 9: 129-143

Izgin M, Wasti Y (1998) Geomembrane-sand interface frictional properties as determined by inclined board and shear box tests, Geotextiles and Geomembranes 16: 207-219

Koutsourais, MM, Sprague CJ, Pucetas RC (1991) Interfacial friction study of cap and liner components for landfill design, Geotextiles and Geomembranes 10: 531-548

Lalarakotoson S, Villard P, Gourc, JP (1999) Shear strength characterization of geosynthetic interface on inclined planes, ASTM, Geotechnical Testing Journal 22(4): 284-291

Ling HI, Burke C, Mohri Y, Matsushima K (2002) Shear strength parameters of soil geosynthetic interfaces under low confining pressure using a tilt table, Geosynthetics International 9 (4) 373-380

Lopes PC, Lopes ML, Lopes MP (2001) Shear behaviour of geosynthetics in the inclined plane test—influence of particle size and geosynthetic structure, Geosynthetics International(8)4: 327-342

Narejo DB (2003) A simple tilt table device to measure index friction angle of geosynthetics, Geotextiles and Geomembranes 21: 49-57

Pedersen RC, Olson RE, Rauch AF (2003) Shear and interface strength of clay at very low effective stress, ASTM, Geotechnical Testing Journal 26(1): 1-8

Proceedings of the 4th Asian Regional Conference on Geosynthetics
June 17 - 20, 2008 Shanghai, China

EXPERIMENTAL INVESTIGATION OF PULL-OUT RESISTANCE OF UNIAXIAL GEOGRIDS

G. Baykal[1] and O. Dadasbilge[2]

ABSTRACT: The pullout performance of a locally manufactured geogrid is investigated by laboratory pullout test, performed with a modified large scale direct shear device which has been designed and constructed at Bogazici University, Due to the lack of a generally accepted standard method, all researchers have developed their own equipment. The differences in the testing procedures and equipment make the comparison of the test results difficult. But mainly the logic and effect of the various parameters on the pull out performance is the same in most of the papers presented so far. The test device presented here is a multi purpose large size direct shear device capable of conducting pull out tests. With 0.3 m×0.3m×0.3m sample box, the testing equipment is very practical. Uniaxial polypropylene geogrid and crushed rock was tested. The effects of displacement rate, confining pressure and specimen width on the pull out response have been investigated. The coefficient of interaction, which is required for the design of reinforced earth structures has been computed under different confining pressures. The results are interpreted and conclusions are presented. Comments for a better test setup are made.

KEYWORDS: Pullout tests, geogrid, interaction coefficient

PULL-OUT RESISTANCE OF GEOGRID REINFORCEMENT

The use of geotextiles and related materials is rapidly increasing in civil engineering applications. A major application area for geotextiles and geogrids is reinforcing of slopes and embankments. In order to make an appropriate material selection, the geogrid/geotextile should be tested as a composite reinforcement-soil system in confined media, through which the following aspects have to be assessed:

a) "stress-strain-strain rate" behavior of the confined reinforcement-soil composite system,

b) pull-out performance and the associated load transfer mechanism.

There are a lot of factors that affect the interface properties of a confined reinforcement and this makes the evaluation of a standard method difficult. Because of the lack of a standard method, no direct comparison can be made between the large number of studies, made with different types of pull-out devices, the associated boundary effects, testing procedures and soil placement and compaction schemes.

Fundamental Aspects of Pull-out Testing

The so-called "interface properties" of a confined reinforcement is the shear stress-displacement relationship which is developed along the soil-reinforcement interface, when a load is acting on it. This relation is tested either in a direct shear or in a pull-out box and test results are reported in terms of a friction ratio, $\tan\varphi/\tan\delta$, in both cases. Here, δ represents the soil-reinforcement interface friction angle and φ is the soil friciton angle. The outcoming value is called also the efficiency factor. According to several tests, values between 0.6 and 1.0 for geotextiles, and larger than 1.0 for geogrids are reported. Researchers gave conflicting results for frictional resistance of geosynthetic reinforcements obtained from direct shear and pull-out tests. But mainly it was reported that pull-out tests gave higher shear strength values for higher normal stresses.

PULL-OUT TESTS

Displacement controlled laboratory pull-out tests have been conducted to investigate the anchorage properties of a locally produced PP geogrid embedded in 15－30 mm crushed stone. The results have been plotted and evaluated. The effect of different testing parameters like applied normal pressure, displacement rate and specimen size has been investigated and conclusions are made.

[1] Professor, Department of Civil Engineering, Bogazici University, TURKEY. Email:baykal@boun.edu.tr
[2] MSc Civil Engineer, TURKEY

Description of the Test Apparatus

A large size direct shear device has been modified for pull-out testing. The inner dimensions of the box are 0.30 m in width, 0.30 m in length and 0.30 m in depth. Compared to the pull-out devices used by other researchers and recommended by ASTM and DIN standards, it is quite small and therefore not ideal for testing reinforcements with large apertures like geogrids. But still, it gives an idea about the effect of various parameters on the pull-out characteristics.

The application of vertical pressure is provided by means of an air-compressor, a pressure regulator and an air bag. Fig. 1 presents a sideview of the testing equipment. The pressure may be raised up to 150 kPa with a sensitivity of 3 %.

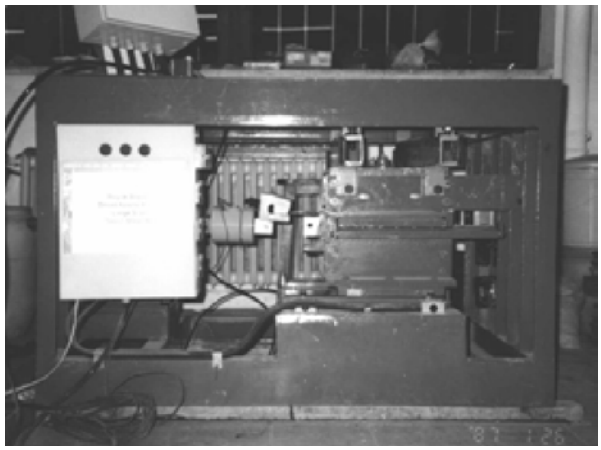

Fig. 1 Side view of the multipurpose direct shear & pull out box

The regulator has counterbalancing property which compensates pressure fluctuations due to volume change of the material being tested. The pull-out force is applied by means of a speed controller unit, motor reduction unit and a continuous shaft connected to the lower box. The speed controller unit has vectorial speed controlling property, which enables the operation speed to be kept constant throughout the experiment by preventing the effects of shear strength variations on rate of displacement at different stages of the experiment. The rate of displacement may be changed between 0.5 to 6.0 mm/min with 0.01 mm/min sensitivity.

The pull-out load is obtained numerically through a digital load indicator in kg. No LVDT's or other electronic devices have been used for measuring the front and back displacements in the geogrids. Instead, tell tales have been extended from the back of the pull-ot box over a milimetric scale and fastened to two different masses of 1 kg each, in order to provide a convenient and correct reading.

The upper side of the box consists of four different steel plates, each of which having a width of 20 mm. A horizontal slot of 10 mm×280 mm has been constructed in the front part in order to allow the geogrid to be extended out of the box in the level of the load cell. The load is transferred to the geogrid through a clamp designed and constructed according to ASTM D 4595 (Reapproved in 1994). The clamp is located outside the box, because of limited place.

Two circular slots are located in the rear wall to permit reinforcement instrumentation. No sleeves could be installed inside the front wall because of limited box dimensions.

Uniaxial polypropylene geogrid reinforcements of 55 kN/m ultimate strength are used in the tests. Crushed stone is poured into the pull-out box in two layers, levels and compacted using standard proctor energy. When the level of the slot in the front wall is reached the geogrid is placed on the bottom layer of the crushed stone. The geogrid specimen is bolted to the clamp and inextensible tell tale wires are connected to the geogrid at two locations. The wires are extended through the back slots over a milimetric scale and connected to two separate countermasses of 1 kg each. The wires are encased in polyethylene tubes placed along the reinforcement in order to prevent them from the normal pressure effect. The top layer of crushed stone is placed in two layers and compacted. The airbag is placed on the upper layer of crushed stone and fixed to the carrying frame. Then the normal pressure is applied to the system through the air compressor (Fig. 2).

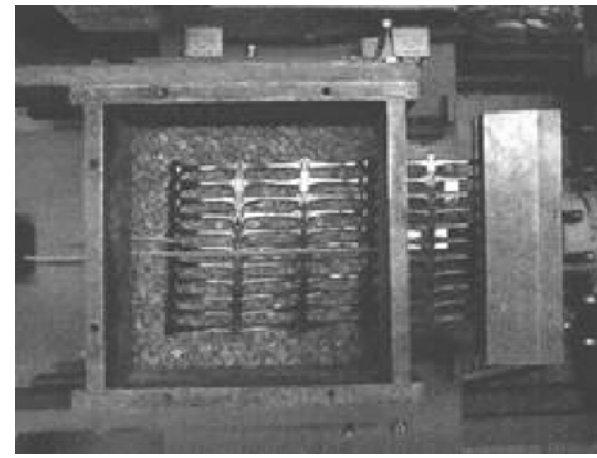

Fig. 2 Placement of the geogrid and ASTM clamp

The tests have been performed under different displacement rates and normal pressures. The pull-out force and displacements in the front and rear nodes are recorded every 15 seconds. The first few readings until the specimen settles are ignored. The test is stopped when pull-out or geogrid failure occurs. Pull-out occurs when the front and rear nodes make equal displacements under constant or decreasing pull-out load.

Pull-out Tests

A series of pull-out tests have been performed on the same geogrid type, in order to eliminate the material property effect on the test results. The main parameters studied in the tests are normal pressure, displacement rate and specimen width. Other parameters like soil thickness, sleeve length and specimen length have been kept beyond the scope of the testing because of the available test setup limitations.

The soil thickness and specimen length have been kept constant for all tests and no sleeve has been used. The coefficient of interaction and interface friction angle between the geogrid and crushed stone has been calculated using the data obtained from the tests.

The tests conducted with different sample widths, normal stress values and pull out rates are presented in Table 1.

TEST RESULTS

Repeatability tests were conducted for each geogrid width and normal stresses. A typical test result for 100 kPa normal stress and 20 cm geogrid width tested at 3 mm/min pullout rate is presented in Fig. 3. The results show that the tests are repeatable. There is slight difference for the tests conducted at 50 kPa of normal stress. At higher normal stresses of 100 kPa and 150 kPa the test results are almost identical. The effect of normal stress on pull out resistance is plotted in Fig. 4. The displacement for mobilization of pullout resistance is larger for lower normal stress.

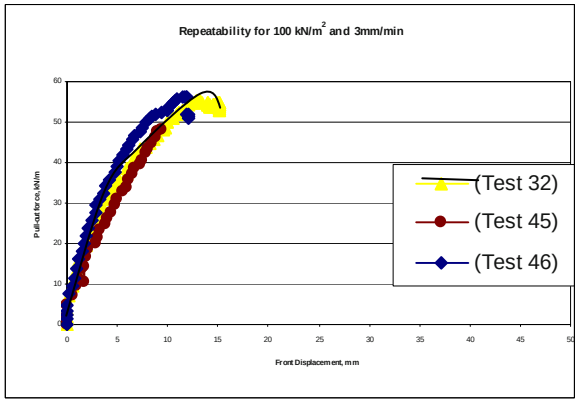

Fig. 3 Repeatability of the tests

The displacement measurements of the front end of the geogrid and corresponding pullout resistance for 20 cm geogrid width is presented in Fig. 5. The measurements are obtained at two locations of the geogrid. One at the front and the other one at the end. Once these two displacement values become equal pull out of the geogrid has occurred. In Fig. 6 the nodal displacements measured at the clamp, at the front part and end part of the geogrid is presented. All presented results show that the test setup works and the results are repeatable.

Table 1 List of pull-out tests performed

Test No	Displacement Rate (mm/min)	Applied Normal Pressure (kN/m2)	Specimen width (mm)
1	3	100	200
2	3	50	200
3	3	50	200
4	3	150	200
5	5	50	200
6	5	100	200
7	5	150	200
8	1	50	200
9	5	100	200
10	5	100	200
11	5	150	200
12	5	150	200
13	5	50	200
15	3	150	200
17	3	100	200
19	3	50	200
28	5	150	100
29	5	100	100
30	5	50	100
31	3	150	100
32	3	100	100
33	3	50	100
37	5	150	100
39	5	100	100
40	5	100	100
41	5	50	100
43	3	150	100
44	3	150	100
45	3	100	100
46	3	100	100
47	3	50	100
55	5	50	100
56	5	100	100

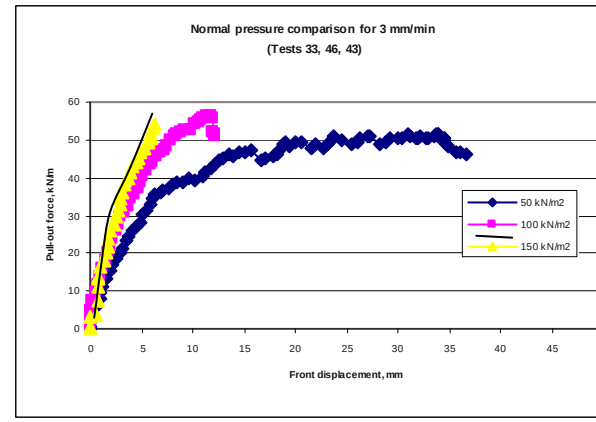

Fig. 4 Effect of normal stress on pullout resistance

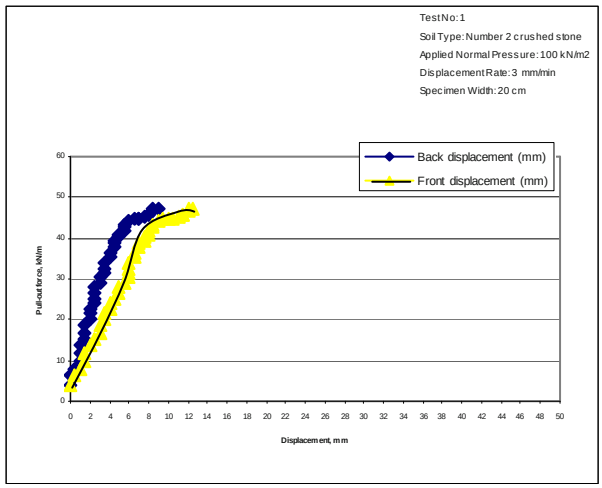

Fig. 5 Pullout resistance for 20 cm width geogrid

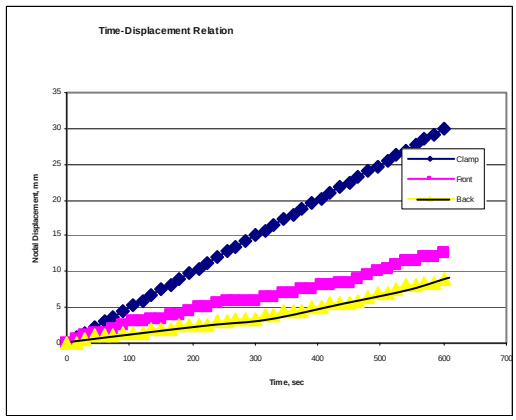

Fig. 6 Nodal displacements for 20 cm geogrid

A typical test result for 20 cm geogrid width (Figs. 5 and 6) and for 10 cm geogrid width (Figs. 7 and 8) are presented. Mobilization of pull out resistance with displacement and displacement of front and rear nodes with time are shown in these figures.

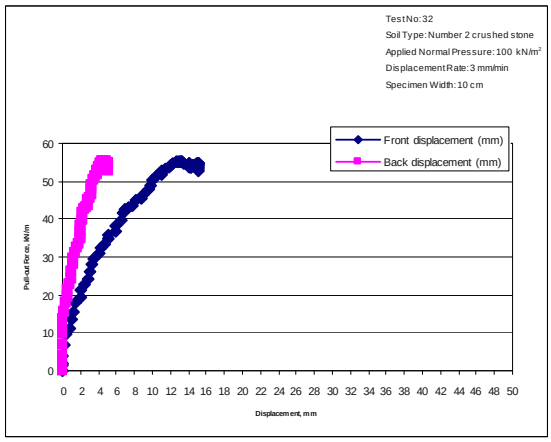

Fig. 7 Pullout resistance for 10 cm width geogrid

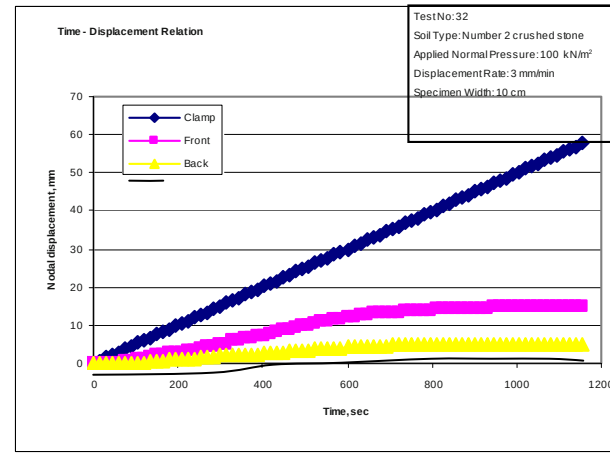

Fig. 8 Nodal displacements of the clamp, front and end part of the geogrid for 10 cm sample width

The displacement measurements for 10 cm sample width. With smaller width the geogrids anchorage has increased when compared to that of 20 cm sample width.

Determination of the Interaction Coefficient at the Geogrid - Soil Interface

The interaction coefficient is determined according to the following relation :

$$COI = F_{pullout} / (2\ B\ L_a\ \sigma_v\ \tan\varphi)$$

where,

COI Coefficient of interaction, or efficiency factor, or bond coefficient; $F_{pullout}$ Pullout force, kN

B Width of geogrid specimen, m

L_a Mobilised anchor length, m

σ_v Normal vertical stress, kN/m^2

φ Soil friction angle

Using the COI the interface friction angle δ between soil and geosynthetics is computed as :

$$COI = \tan\delta / \tan\varphi$$

The summary of calculated interaction angles are presented in Tables 2 and 3 for geogrid widths of 10 and 20 cm respectively.

Table 2 Interface friction angle values for 10 cm geogrid with, 27 cm embedment length and φ=53º

Test No	Displ rate	σ_v	$F_{pullout}$	COI	δ
	mm/min	kN/m^2	kN		º
33	3	50	4,69	1,31	60
46	3	100	5,62	0,78	46
43	3	150	4,94	0,46	31
55	5	50	3,96	1,11	56
29	5	100	5,36	0,75	45
28	5	150	5,51	0,51	34

Table 3 Interface friction angle values for 20 cm geogrid with, 27 cm embedment length and φ=53º

Test No	Displ Rate mm/min	σ_v kN/m^2	$F_{pullout}$ kN	COI	δ º
19	3	50	7,43	1,04	54
17	3	100	9,51	0,66	41
4	3	150	9,89	0,46	31
13	5	50	7,49	1,05	54
10	5	100	10,03	0,70	43
11	5	150	10,37	0,48	33

Sample width of 10 cm resulted in higher interface angle compared to that of 20 cm geogrid width. The longer shape of the geogrid sample (10 cm / 27 cm) helped in mobilization of the interface strength. The order of magnitude of the test results are acceptable demonstrating potential use of smaller size pull out boxes.

CONCLUSIONS

The test results have shown that the equipment used in this study needs certain improvements for a more realistic simulation of the pull-out mechanism, but even in its current condition important facts can be concluded. Following conclusions can be made considering the test results.

The specimen width is effective on the pull-out performance. A certain ratio has to be kept between the geogrid width and pull-out box width in order to minimize the side wall effects (>2). The friction forces occurring on the side walls cause a reduction in the normal stress, resulting in lower peak pull out force. In all tests performed on 20 cm wide geogrids the pull-out force remained under 50 kN/m with one exception, while the test performed on 10 cm wide geogrids values of 55 kN/m or higher have been measured. It is assumed that the latter case is more realistic, as in practice there is adequate clearance between the reinforcement and edge of the confining media. On the other hand a too narrow geogrid would be unable to represent the real case, either as the number of the apertures would decrease. A minimum specimen width, which would represent the natural conditions and a maximum specimen width / pull-out box width ratio, which would minimize the side wall friction effects is required.

Normal pressure is the major and most meaningful parameter in the pullout mechanism. In any kind of geogrid reinforced retaining wall or slope stabilization, different normal pressures act on the geogrid layers, depending their placement depth. Test results showed that less displacement and elongation occur under higher normal pressures. This result is sufficient to make the conclusion that under high normal pressures it is the interface friction force which resists pull-out, while under low normal pressures passive resistance of the transverse ribs assists the friction forces.

During the tests the highest normal stress was 150 kN/m^2 and even under this pressure the whole geogrid length was mobilized. The length of the pull-out box should be increased to find the anchorage length.

The longer pullout boxes suggested by DIN and ASTM may give reliable results however they are rather expensive test equipment to have in many laboratories throughout the world. With larger size the normal pressure system becomes very expensive and the box should be made very rigid to withstand those pressures. However a smaller size pullout box is practical in many ways. Provided that the user understands the drawbacks and deficiencies of the smaller size, for parametric studies related to soil type, compaction, soil geogrid interaction and soil pressure effects can be investigated.

Planned work in our laboratory will introduce recently developed thin pressure sensors to face and side walls and geogrid junctions to obtain more data for use in models.

REFERENCES

ASTM D 6706 (2007) Standard Test Method for Measuring Geosynthetic Pullout Resistance in Soil

DIN EN 13738. Geotextilien und geotextilverwandte Produkte, Bestimmung des Widerstandes gegen Auszug aus dem Boden

Koerner RM (1997) Designing With Geosynthetics, Fourth Edition Prentice Hall, New Jersey

Farrag K, Juran I, Acar, Yalcin (1993) Pull-out Resistance of Geogrid Reinforcements. Geotextiles and Geomembranes 12: 133-159

Hayashi S, Makiuchi K, Ochiai H (1994) Testing Methods For Soil-Geosynthetic Frictional Behaviour —Japanese Standard. Fifth International Conference on Geotextiles, Geomembranes and Related Products, Singapore: 5-9

Cancelli A, Rimoldi P, Togni S. Frictional Characteristics of Geogrids By Means of Direct Shear and Pull-out Tests

Ochiai H, Hayashi S, Otani J, Hirai T (1992) Evaluation of Pull-out Resistance of Geogrid Reinforced Soils. Earth Reinforcement Practice, Rotterdam

Geosynthetic Researche Institute Drexel University "GRI Test Method GG5." January 1991, Philadelphia

DEVELOPMENT AND APPLICATION OF CS-LB01 GEOSYNTHETICS PULLOUT TEST SYSTEM

H.P. Yang[1], M. Guo[2], L. Wan[3] and Y.X. He[4]

ABSTRACT: In order to obtain the interfacial parameters and study the mechanism of the reinforcement in the structure of expansive soils-geogrid, a large-scale pullout test system was developed successfully. Compared with the current apparatus, it has its distinctive advantages: Firstly, it has the large dimension 1.2 m (length)×0.5 m (width)× 0.5 m (height). Secondly, two test control methods including constant force control and constant speed control can be alternated in pullout tests. Thirdly, it is suitable for all kinds of soils and geosynthetics. Fourthly, the loading method becomes more reasonable because air bags were set up on the surface and bottom of the test box combining with the servo control loading system. Fifthly, the influence of friction between test sample and sidewall was reduced. Furthermore, the level of artificial intelligence of the test system is greatly improved by equiping datum acquisition and analysis system with high-precision transducers of force and displacement, and complementing compaction and lifting devices. To validate the practicability and reliability of the system, pullout tests are carried out at the condition of constant force control and constant speed control, respectively. And the tests considering friction effect between sample and sidewall are conducted. In the end, all the results show that the system can simulate the field working condition of expansive soils reinforced with geogrid, obtain the stress, deformation and the soil-geogrid interaction, as a result, it becomes more convenient to study the reinforcing mechanism and acquire test parameters.

KEYWORDS: geosynthetics, expansive soil, loading by air bag, servo control system, pullout test

INTRODUCTION

Just as one of the most effective research methods which is used to study the interfacial friction characteristics between soils and geosynthetics, the advantage of the pullout test lies in its achievement to be able automatically to reflect the dilatancy of soils and compressive effects. The measurement results had proved that the pullout test can simulates the working conditions of reinforcing materials in soil and behavior of reinforced soil well and puts forward a method by which the appropriate interfacial parameters for the present reinforced earth design can be obtained. Therefore, the development of pullout test equipment and related test technology for simulating the interfacial parameters between reinforcing materials and soils has been paid increasing attention all over the world.

F Wilson-Fahmy (1995) in the USA has developed a large size pullout test apparatus, and in the vertical direction single-side air pressure bag was used for loading, and the horizontal loading was provided by the hydraulic jack. M Sugimoto (2001) in the Japan has developed a medium-sized 0.68 m (length) × 0.3 m (width)×0.62 m (height) pullout test apparatus, and in the vertical direction double-faced air pressure bags were used for loading, and it is aimed at interfacial interaction between sand and geogrid. Xu Lin-rong (2003) in the Central South University developed a specialized apparatus that is primarily used to study the interfacial interaction between expansive soil and geogrid. The apparatus was mainly made of steel and wood, and in the vertical direction oil jack loading was applied, and the horizontal loading was provided by the pulley, motor and gearbox. The Xia Men BPR developed a small size pullout test apparatus which are based on direct shear test apparatus, and the horizontal loading was provided by the weights.

However, no matter at home or abroad, there is no a uniform standard and reliable test method. There are a number of shortcomings in the traditional pullout test apparatus: (1) the vertical direction uses oil jack loading or pre-loading, so it is difficult to ensure the uniform distribution of the normal force. Furthermore, it is impossible for the cancellation of the friction resistance between test

[1] Professor, School of Highway Engineering, Changsha University of Science & Technology, CHINA. Email:cscuyang@163.com
[2] Postgraduate, School of Highway Engineering, Changsha University of Science & Technology. CHINA.
[3] Graduate, Jiangsu Traffic and Science Research Institute. CHINA.
[4] Postgraduate, School of Highway Engineering, Changsha University of Science & Technology. CHINA.

sample and sidewall. (2) as the control approach of the pullout is single, the existed apparatus can be adopted by constant force control or constant speed control. (3) there is no special consideration for compaction question in pullout test apparatus general, but test sample by layers is of importance in well simulating the condition. (4) because the dimension of the apparatus is limited and the small interface area, it can only be used in small particles test sample. Aiming at the situation and development at home and abroad, and the existing problems of the pullout tests, basing on the constructive science and technology item of the westward traffic, a large-scale geosynthetics pullout test system named CS-LB01 was independently designed by Changsha University of Science & Technology. This paper briefly presents the pullout test apparatus and its application.

THE COMPOSITION AND FUNCTION OF THE TEST SYSTEM

Fig.1 shows the composition and general layout of The CS-LB01 system. The apparatus is composed of four parts: (1) pullout test apparatus, (2) loading servo control system, (3) test data acquisition system and (4) compaction and lifting auxiliary equipment, thereinto the pullout test apparatus is the kernel parts.

Pullout Test Apparatus

Fig. 2 shows the schematic diagram of a newly developed pullout test apparatus. The pullout test apparatus consists of pullout device, the test box, the fixture and support. The main characters of the pullout test apparatus are shown in Table 1. From this we can have an idea that the apparatus can be referenced for wide contact surface and it can provide vertical loading large enough and enough level relative displacement.

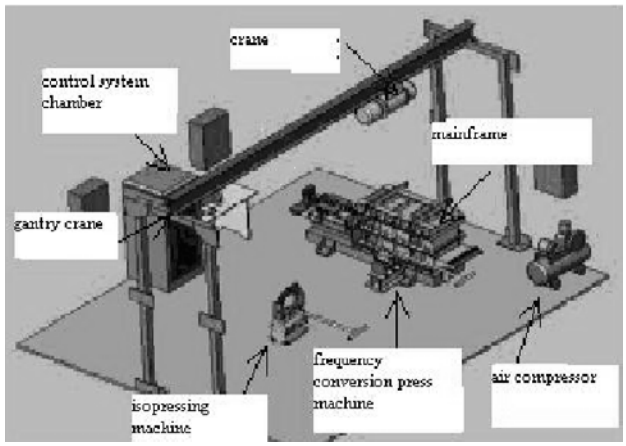

Fig.1 Model of CS-LB01

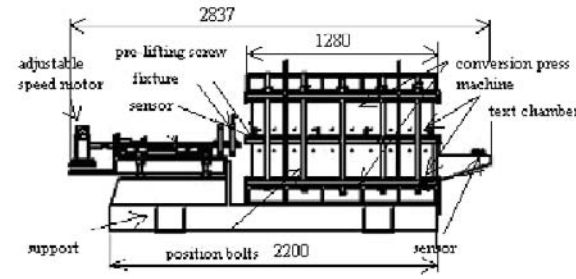

Fig.2 Pullout Test Apparatus

Table 1 Working parameters of the main frame of pullout test system

Length (cm)	120
Width (cm)	50
Height(cm)	50
vertical force (Mpa)	0-1
Horizontal force (kN)	0-30
Maximum displacement (mm)	150
Displacement accuracy (%)	1%
Pullout speed (mm/min)	0-3
Interval of the data collection (s)	5-30

Pullout device

The pullout device consists of Step-Motor, turbine worm transmission, the orbit and the tensile force sensor. In order to obtain stable loading and provide enough horizontal tensile force, straight sliding tracks, ball screws and so on are applied. Accordingly, the pullout test can be realized by constant force control or constant speed control, and the loading process is steadying, the use of the Step-Motor can make the pullout speed change in wide dynamic range.

The test box

The test box is composed of upper and lower parts. The pullout test apparatus was mainly made of steel. The main characteristics are as for: it has the large dimension, for the inside dimensions of the box are 1.2 m (length)× 0.5 m (width)× 0.5 m (height), so that it meets the specified requirements according to depth to diameter ratio for the pullout test and the thickness of packing compaction by layers. It is the biggest pullout test apparatus in china.

The fixture and support

To ensure that the tensile geotextile will not slide in the fixture during the test, and shearing failure by the sidewalls of the box or the cutting edge of the fixture will not be caused , the design of the fixture is adopted by the way of up-down serrated steel plate interlocking. Its width is 0.12 m, and fixed with plate and screw (12

total) in both sides. Hence, the pressure applied in the geotextile has been strengthened and its function can be greatly improved. Similarly, to ensure the process of the test is safe and reliable, the support is made of steel which can endure the large pressure and caused less displacement.

Loading Servo Control System

Taking into consideration of the difficulties in static loading and stress unevenness of pressing which are caused by oil jack loading or water tank loading, two air pressure bags were provided at the top and bottom to maintain similar boundary conditions. The film of air pressure bags was made of high elasticity synthetic rubber, and the pressure can be adjusted continually and arbitrarily in the range of 0－1 MPa. The stabilized pressure system of the CS-LB01 consists of air compressor, gas steel cylinder and pressure valve. The system is very efficient for solving the difficult problem of air pressure bags leakage and air pressure stability. The main working principle is that of automatic regulation function of the pressure valve. Once the air pressure is higher than the setting, it can auto-exhaust, on the contrary, it can auto-inlet. In this way, the air pressure can keep relatively stable in the test and the reservoir would run at a relatively narrow range of air pressure about ±2%. Consequently, not only loading is accurate and convenient, but also it can simulate the field working conditions of high fill sub grade below 50 m. In order to ensure the vertical forces provided by air pressure bags was applied on the interface as much as possible and reduce the loss of vertical forces caused by friction between test sample and sidewall, pre-lift screw is placed on the rolling joint. Then, the test chamber can freely move alone the position bolts, and the pressure produce by air bags act on the interface completely.

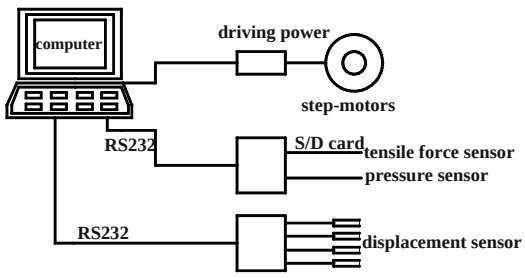

Fig.3 Schematic view of data acquisition System

Test Data Acquisition System

We can acquire not only the force data, but also the deformation and displacement which are achieved by 4 metal detection wires and the displacement sensor through test. All the sensors were connected with the computer, so the data acquisition can be available for automation. Meanwhile, software operation platform is developed on this basis, and data acquisition can be detected in 1－30 s once according to the condition and the requirement of the test. After the test, we can store the data into the database and the relationships between tensile force and displacement, tensile force and pressure are shown in form of the pictograph for researches and analysis. Fig. 3 shows the schematic diagram of data acquisition system.

Compaction and Lifting Auxiliary Equipment

Considering the characteristics of expansive soil, and based on the field construction practice, two equipments for compaction have been developed for CS-LB01 system: one is the light weight frequency conversion press machine and the other is the heavy duty compactor. In this way, the test can simulate the requirements of construction. As a result, the compaction has reached the request. The large-scale geosynthetics pullout test system CS-LB01 are elaborate and self-contained, and has several advantages: the pullout test apparatus is used widely, and this apparatus is easy to operate, and the pullout test can simulate the actual working condition objectively. Moreover, if only we refit the pullout test apparatus, this system can be added other new functions. For instance, fixture is put on the caudal end, which can be used to test the tensile strength of geosynthetics in the working condition of filling or in the air. If an air pressure bag is put on the front sidewall of the test chamber, it can change the boundary condition and experiment research on a flexible boundary condition. Embedding the sensor in the reservation duct of the side-wall within a certain range, we can develop the study on shear band to determine the effect range of geosynthetic reinforced soil.

APPLICATION EFFECT AND ANALYSIS OF THE SYSTEM

To validate the practicability and reliability of the CS-LB01 system and obtain the interface parameters between geogrid and expansive soil in Guangxi, pullout tests are carried out at the condition of constant force control and constant speed control, respectively. And the tests considering friction effect between sample and lateral are conducted. The test results show that the CS-LB01 system can achieves the anticipated goal and the function. Besides, it is convenient and effective for experimental research about the interaction between geogrid and expansive soil.

Testing Materials

The filling are NingMing weathered soil and BaiSe residual soil that are two typical expansive soil in Guangxi. The properties of the soil are shown in Table 2. Geogrid RS35PP was taken as geotechnical reinforcement materials which were produced by Hubei Nete Geosynthetics LTD. Main physical parameters of geogrid RS35PP are shown in Table 3.

Table 2 Ning Ming grey- black shale weathered soil properties

Moisture capacity (%)	25.0
Liquid limit (%)	57.3
Plastic limit (%)	31.0
Dry unit weight (g/cm^3)	1.82
specific surface area (m^2/g)	161.11
fine-grain soil content (<0.074mm) (%)	93.7
free swelling capacity (%)	42.0

Table 3 BaiSe brown eluvia soil properties

Moisture capacity (%)	30.1
Liquid limit (%)	60.58
Plastic limit (%)	21.93
Dry unit weight (g/cm^3)	1.86
specific surface area (m^2/g)	194.33
fine-grain soil content (<0.074mm) (%)	98.61
free swelling capacity (%)	115.0

Table 4 Physical properties of geogrid

Geogrid model	RS35PP
Tensile yield strength (kN)	>35kN
Yield elongation(%)	<10
The tensile strength at yield elongation 2%	>10kN
The tensile strength at yield elongation 5%	>20kN

Constant Force Control Method

To check the function of the apparatus and determine the appropriate control method of the pullout test, in the condition of the overburden pressure of 50 kPa, reinforced soil composed of expansive soil and geogrid (80 cm × 42 cm) was tested in constant force control method. The initial point of the tensile forces has been supposed to be 0.5 kN. When the drawing speed in the test is slower than 0.08 mm/min, one grade of tensile forces is added on. The increment of tensile forces is 0.5 kN per grade. Fig.4 shows the test record. It can be seen that when the tensile forces is small, the displacement of geogrid was nearly unchanged. With the increase of the tensile forces, the displacement increases firstly and then remains a high level. When the tensile forces reaches 4.5 kN and after sustained for a certain time, the mass movement of the geogrid was shown in displacement curve. The displacement curve is straight up.

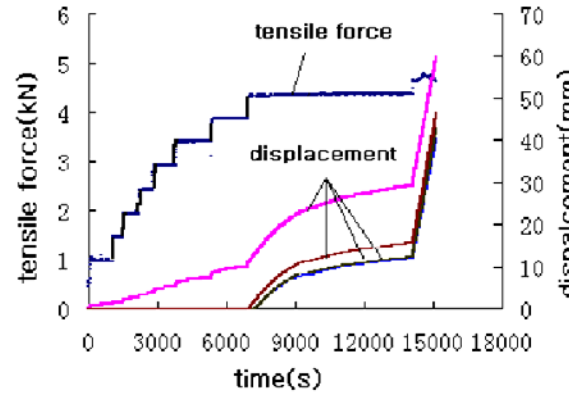

Fig.4 Test results by constant force control

Constant Speed Control Method

The geogrid was pulled out at 1.0 mm/min, and the soil moisture is 25%, the geogrid size is 60 mm × 42 mm, and four kinds of overburden pressure were applied in the test. Fig. 5 shows the result of the test. It can be seen from Fig. 5a that the tensile force increased with increase of overburden pressure, and the maximum tensile forces can achieve 5.9 kN, which was larger than one in constant force control method by 31%. The overburden pressure-shear stress relationship of geogrid as shown in Fig.5b, through regression analysis, c, φ of interaction between soil and geogrids can be obtained. The relationship between the pseudo-friction coefficient and overburden pressure as shown in Fig. 5c. And there is logarithmic relationship between them, and the analysis has shown that the pseudo-friction coefficient decreased with the increase of overburden pressure.

Comparison Tests for Analyzing the Sidewall Friction Effect

The existing methods of cancellation of the friction resistance betweem sidewall and packing are as follows: (1) put the lubrication on the sidewall of the test chamber (2) make the sidewall of the test chamber by the Plexiglas. However, both of these cannot solve the problem of the influence of friction radically especially when the compaction of filler meet the field control standard. As above mentioned, the CS-LB01 system possesses its own special features of cancellation of the frictional resistance. In order to test the possible influence to friction in results, we carried out another experimental research on Base expansive soil. The interfacial area of the reinforcements was 80 cm × 42 cm.

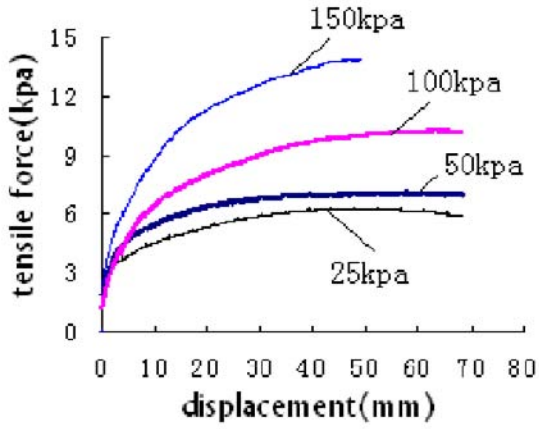

(a) Tensile force-displacement curve

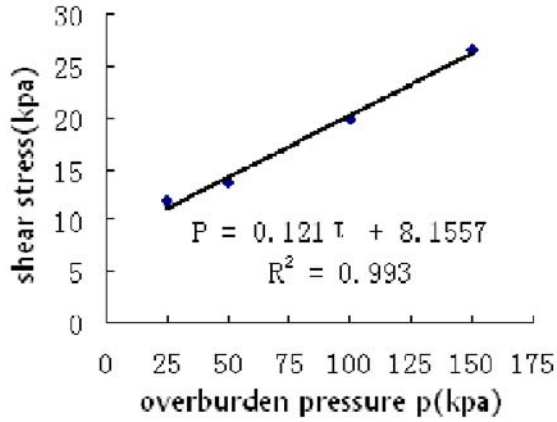

(b) Shear stress-overburden pressure curve

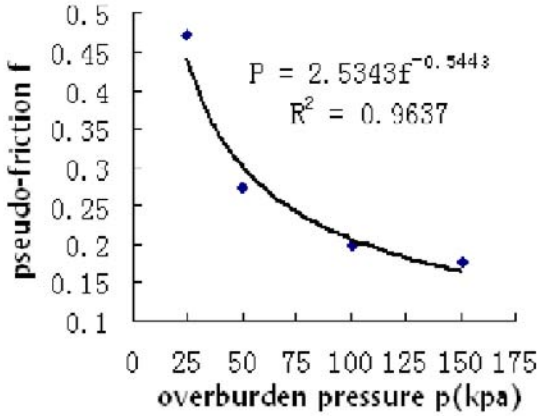

(c) pseudo-friction-overburden pressure curve

Fig. 5 Test results by constant speed control

Adopt the overburden pressure of 50 kPa also, and at the constant speed control of drawing speed of 1.0 mm/min. Fig. 6 shows the test Contrast result. It can be seen that there were many differences in two conditions. The maximum tensile forces can be achieved 57.2 kN, compared to the previous condition, the tensile forces increases by 24.14%. So that it can not be ignored that the great influence of friction resistance between test sample and sidewall.

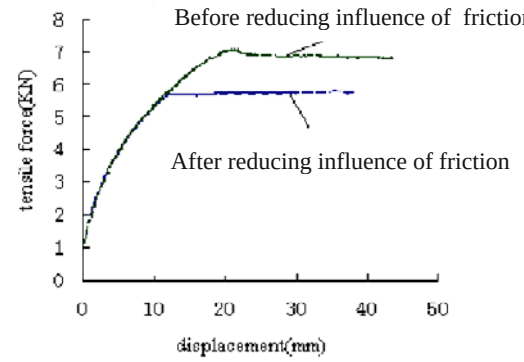

Fig.6 Comparation between the before and after the elimation of friction on both sides

CONCLUSIONS

Along with the widely application of reinforced earth technique in the engineering, people will pay more and more attention to the pullout test that is used to identify the interfacial friction parameters between soils and geosynthetics. Moreover, with the development of a large-scale geosynthetics pullout test system CS-LB01, the testing running in the former stage showed that the CS-LB01 system can solve the weakness of traditional test apparatus well. The CS-LB01 system has the following advantages: (1) It has the large dimension, and it is suitable for kinds of soils and geosynthetics (2) The system has the scientific loading method, and two air pressure bags were provided at the top and bottom to maintain actual boundary. Meanwhile, installation of pressure-static loading servo control system and pre-lifting screw make the test condition coincide with the actual working conditions. (3) This system is successfully used for multiple-spot measurement and data acquisition automation. Accordingly, we can obtain the relationship between displacement and tension force of the geosynthetics exactly. All the results show that the successful development of CS-LB01 provides a platform for the research of the application of geotextile in civil engineering, inquire reinforcing mechanism and the construction of design theory. Simultaneously, the birth of the CS-LB01 system and the improvement indicates the beginning of high-level development of research on reinforcing mechanism in a new round.

REFERENCES

Bao CG (2004) Study on the interaction between of geosynthetics and soil in China. Proc of 3rd Asian Regional Conference on Geosynthetics, Seoul, Korea, 2004: 104-115

Mc Gown A, et al. (1982) Load exlension testing of geotextiles confined in-soil. 2nd Inter Conf on Geotextiles

Schdosser F, Long NT (1974). Recent result in French research on reinforced earth. Journal of the construction Division, ASCE, 100 (3):223-237

Murad Y, Abu-Farsakh, Khalid Farrag,et al. (2004) Evaluation of interaction between geosynthetics and marginal cohesive soils from pullout tests. Geo Jordan: 299-310

Ragui F, Wilson-Fahmy, Robert M Koerner (1994). Experimental behavior of polymeric geogrids in pullout.Journal of Geotechnical Engineering, 120 (4):661-676

Sugimoto M, Alagiyawanna AMN, Kadoguchi K (2003) Influence of rigid and flexible face on geogrid pullout tests. Geotextiles and Geomembranes, 19: 257-277

Xu LR, Ling JM (2004) Experiment on Interface Friction Coefficient Parameters between Geogrids and Expansive Soil. Journal of Tongji University, 32 (2):172-176

Shi YZ (2003) Pulling-experimental study of geotechnical composite material. Geotechnical Engineering World, 6 (10):75-78

Yang HP et al. (2006) Current Situation and Development of Geogrid Pullout test. Journal of Changsha Communications University, 22 (1):36-41

GEOTECHNICAL CENTRIFUGE EXPERIMENT AND FORCE ANALYSIS OF REINFORCED CUSHION WITH PILE CAP NET STRUCTURE EMBANKMENT

B.P. Doanh[1], Q. Luo[2], L. Zhang[3] and Y. Yang[4]

ABSTRACT: Using pile-cap-net structure embankment method in small-scale geotechnical centrifuge experiment to attain higher force capability of reinforced cushion on high strength pile composite foundation is a new and modern technology soil test where study variation rules of reinforced cushion in changes of pile spacing and of pile cap sizes on composite foundation are considered. The method operates on its basic principle once small–scale model establishment placing in the centrifugal acceleration environment reflected real stress level of structure through increasing centrifugal force on experimental materials as well as measuring strain value of reinforced cushion through pile spacing and loading. Then, soft soil foundation was handled with CFG piles under vibrating sinking pipe construction model, pile-cap-net structure embankments in sparse pile design with similar ratios of pile cap, pile cap coverage ratio and pile allocation ratio made the reinforced net receive heavier force than using pile-net structure embankments method. With strain value of reinforced cushion under impact of loading allocation varied in the form of M letter line. The result showed that with strength improvement of reinforced cushion under the pile-cap-net structure embankment, the construction can be successful.

KEYWORDS: centrifuge, cushion, geogrid, reinforcement, pile composite foundation, pile-cap-net structure embankments, pile-net structure embankments

INTRODUCTION

Using technology of centrifugal model test to study variation rules of reinforced cushion in changes of pile spacing and of pile cap sizes on composite foundation was focal handling with improving force capability of reinforced cushion on the high strength pile composite foundation which was a great problem to road and railway construction in China. Meanwhile, there is lack of theory system of design and calculation methods on the high strength pile composite foundation. On the other hand, under loading effect, design of reinforced cushion needed to increase bearing capacity and stability of soil foundation; to limit lateral deformation, settlement and uneven settlement of composite foundation.

Due to complication of force structure and its closed link with soil of piles on reinforced cushion on composite foundation, the number experiment on studying on force capacity and allocation rule on reinforced cushion on composite foundation using high strength pile under effect of embankment flexible load was limited.

Geotechnical centrifuge model test on soil mechanics combined on-site experiments on soft soil foundation on Da-Cheng railway route (with $v > 200$ km/h) and in-house seven experiment groups on centrifugal accelerators simulating cement flyash gravel with space changes between pile space and variation of pile cap size under the allocation rule and force capability of reinforced cushion.

This method enables to clearly reflect operating status of original structure in the real life. Besides, the method also resolved with disadvantages of low stress level of in-house small-scale model test, supplementing to on-site experiment, securing high economic efficiency, easy controllability, maneuverability and repeatability and certain reliability.

In this paper, firstly, the design model and experiment method are demonstrated with experiment and measurement equipment, materials including soft soil foundation, embankment soil, reinforced net materials and CFG piles and test process. Then, experiment result and data analysis followed with impact of coverage of pile cap to force capability of reinforced cushion

[1] Lecturer, Hanoi University of Civil Engineering, Hanoi, VIETNAM; Ph.D Student, Roadbed engineering & Soil technology, Southwest Jiaotong University, Chengdu, CHINA. Email: fuying771020@163.com

[2] Professor, Department of Road&Railway, Southwest Jiaotong University, Chengdu, CHINA. Emal:lqrock@vip.163.com

[3] Ph.D student, Lecturer, Southwest Jiaotong University, Chengdu, CHINA. Email: lzhang2002@sohu.com

[4] Master student at Southwest Jiaotong University, Chengdu, CHINA. Email: yaoyfw@163.com

DESIGN MODEL AND EXPRIMENT METHOD

Experiment and Measurement Equipment

The experiment comprised 7 model tests with different parameters, including 4 tests on changes in pile spacing and 3 tests on changes in pile cap size.

Model sizes were in detailed as follows: 100 mm high foundation, 150 mm thick soft soil foundation, 6.25 mm pile radius, 150 mm long pile and piles were allocated in the form of equilateral triangle.

The geotechnical centrifuge machine named TLJ-2 belonging to the Southwest Jiaotong University was used for the experiment with measurement equipment of 10 strain gauges that were allocated along cross-section of two strips or five gauges for each strip. See more details on the Fig. 1.

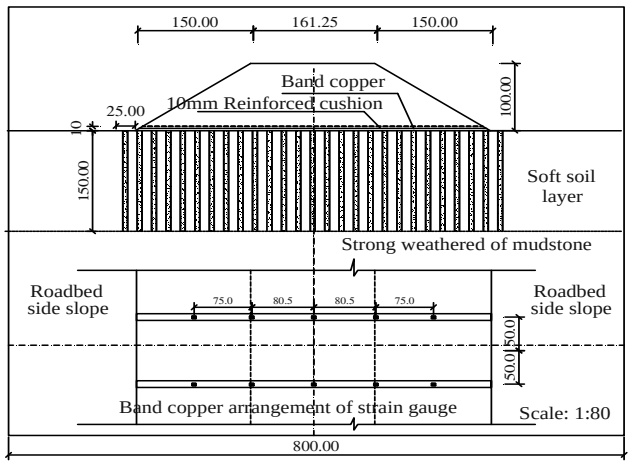

Fig. 1 Measurement equipment allocation

Centrifugal experiment model size was given based on small-scale of model with ratio of N=80.

The main parameters were 3 meters long radius, 2.7 meters real radius (from core of model to centre of main axis). The acceleration scope is within 10-200 g. The biggest load effect was 1000-500 kg (equivalent to 100 －200 kg). The model size was $0.8\times0.6\times0.6$ m^3.

Experiment model simulated real embankments with parameters including: embankment was a high part of soft ground embankment in double-track railway road designing, 12 m thick soft soil, 12.9 m wide embankment, 1:1.5 slope gradient, 8.2 m high embankment.

The bottom on embankment was designed with a 0.5 m thick sand-gravel cushion with a geotechnical grille in the middle bearing bidirectional force at tensile strength 50 kN/m.

Soft soil foundation was handled with CFG piles constructed by the vibrating sinking pipe model passing soft soil layer to the top of silt clay, 0.5 meter pile radius, 12m long piles and 1.3m pile spacing. Pile allocation was in the form of equilateral triangle. See Fig. 2.

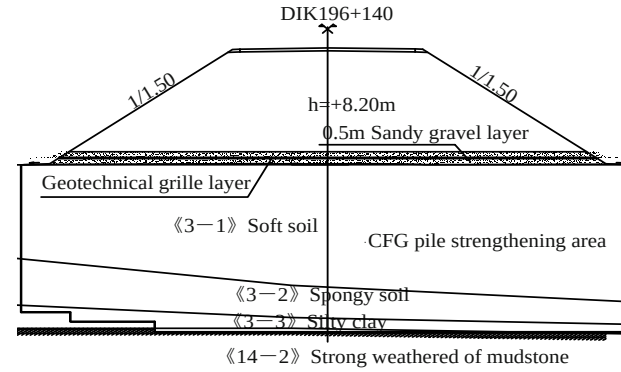

Fig. 2 Design cross-section

Test models from 1 to 4 were conducted with design of pile without cap, pile spacing were 18.75 mm, 25 mm, 31.25 mm, 37.5 mm, respectively; simulating on-site original sizes of 1.5 m, 2 m, 2.5 m, 3 m (equivalent to 3, 4, 5, 6 fold of pile diameters), and pile replacement ratio(Rp) as follows: Rp = 10.06%;5.67%;3.62%;2.52%, respectively. Test models from 5－7 were conducted with design of pile with cap, pile spacing were 37.50 mm (equivalent to 6 fold pile radius), pile cap had sizes of 11, 17, 23 mm, respectively, equivalent to pile cap coverage (Rc,) were: Rc =9.94%; 23.73%; 43.44%)**,** respectively. See Fig. 3.

Force net of reinforced cushion used copper strips for simulation purpose, space between copper strip was allocated based on pile spacing to ensure each copper strip was laid on the top of pile. See Fig. 3.

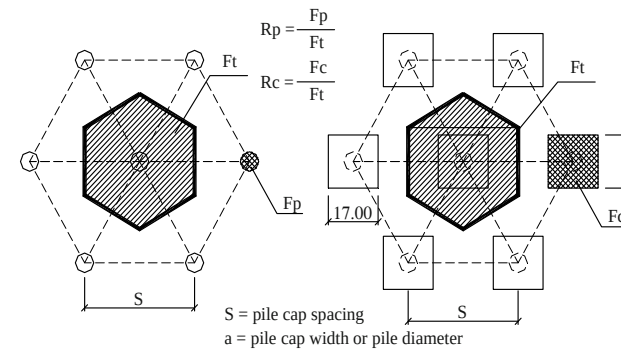

Fig. 3 Pile replacement ratio & pile cap coverage

Materials

As centrifugal experiment model used similarity theory to minimize experiment model scale, materials for experiment and boundary condition must satisfy conditions and principles of similarity theory.

Soft soil foundation

Soft soil used in in-house experiment was taken directly from the site, see Fig. 2 for main physical and mechanical parameters of soft soil layer. Soft soil was extracted from 1m deep from the face of original foundation; due to far distance from the site to the laboratory, dry climate condition and the soil extraction complied with standards, however, timidity lost of soft soil was unavoidable leading strength index to hike.

Statistics demonstrated that at confidence interval with reliability was 0.95, soil strength values were c[13.48kPa，29.94kPa]，ϕ[5.33°, 11.93,° respectively]. The selected ratios were lower confidence limit including c=13.48 kPa, ϕ=5.33° as ratios for controlling soft soil strength.

Table 1 Physical and mechanical parameters of soil layers

Natural water content (%)	Density (kN/m^3)	c (kPa)	ϕ(°)
34.5	18.93	21.71	8.63

Consolidation of soft soil by centrifugal accelerators revealed that once soft soil was laid under preparation with water content of 37% within 3 hours, the result was strength ratios of soft soil met similar conditions of real site, see more on Fig. 3.

Table 2 Physical and mechanical parameters of soil layers after consolidation

Test models	Natural water content (%)	Density (kN/m^3)	c (kPa)	ϕ(°)
1	35.90	18.66	07.25	2.89
2	35.75	18.70	13.13	0.72
3	35.51	18.87	04.00	4.86
4	35.18	18.66	12.13	0.23
5	36.11	18.79	08.25	2.72
6	35.75	19.12	10.38	2.86
7	35.65	18.96	12.50	2.35

Embankment soil

Experimental test used embankment soil which was red-bed mudstone taken from the site. The heavy compaction test revealed ratios including: optimum water content was at 10.8%, maximum dry density at 21.7 kN/m^3. Foundation was embanked at compacted density of K=0.95 and dry density at 20.62 kN/m^3.

Reinforced net materials

On site reinforced net material was geotechnical grille, which may not simulate the reality in small-scale experiment; therefore, the principle of similarity on strength was used alternatively in this case with band copper strips at tensile strength of 375MP and elongation of 8%. All test models had reinforced net strength ratio which was equivalent to 300 kN/m in the real one. Test models from 1 to 4 were described with band copper strips allocation on Fig. 5. Test models from 5 to 7 were reflected band copper strips in the form of a net with 30x30mm and 10mm new wide parameters.

CFG pile materials

On site CFG pile construction had diameter of ϕ50 cm, experiment model test based on strain equivalent principle and density equivalent used galvanized iron with 0.3mm wide, generated CFG pile with ϕ6.25 mm diameter and filling mineral powder inside, see more details on Table 3.

Table 3 Real sizes of piles in the model and on site

Material	E(MPa)	A(mm^2)	EA
CFG	2.3×10^4	3.07×10^{-5}	0.705
Galvanized iron	1.2×10^5	5.60×10^{-6}	0.673

Test Process

Foundation soil passing preparation on centrifugal accelerators with acceleration ratio of n=80g, was under consolidation within 3 hours to ensure similar ratios of soil embankment strength between in-house experiments and on site construction ones. After handling soft soil with CFG pile, small bead sand layer was scattered on the foundation and a reinforced net was installed in the middle of sand layer and finally all were laid over the finished preparation foundation for drawing deformation measurement net on cross-section. After finishing model establishment, experiment proposal on loading test was approved.

The first things preparing for loading test were running preloading within 2 min at acceleration of 16 g to ensure safe for all parts of the model, especially touch of equipment and eliminating negative effect caused by model establishment process to the model. Embankment experiment conducted a unique time of embankment, however, to simulate on site embankment construction, time of embankment was counted equivalently through using centrifugal accelerators based on loading similarity principle and the result was: embankment of the in-house model was 10cm high, dividing into 4 times of embankment, each embankment took 45 days, total construction time was 6 months. The embankment got stabilization within 6 months and simulated the next four year operation, see Table 4.

Table 4 The loading process of centrifugal models

Period	Acceleration loading (g)	Time loading (min)	Side of fill (d)
Embank to 2 m	27.23	87.41	45
Embank to 4 m	49.64	26.30	45
Embank to 6 m	67.23	14.34	45
Embank to 8 m	80	10.13	45
Stabilization	80	41.63	185
First year operation	80	82.125	365
Second year operation	80	82.125	365
Third year operation	80	82.125	365
Forth year operation	80	82.125	365

EXPERIMENTAL RESULT AND DATA ANALYSIS

Impact of Pile Spacing to Force Capability of Reinforced Cushion

The result showed that by increase of pile spacing, strain average value of reinforced cushion under test models from 1 to 4 was allocated in the form of M letter line. At the centre of embankment and two sides of center of side slope, strain average value was small, but large at the two sides of road shoulder. See more on Figs. 4 and 5.

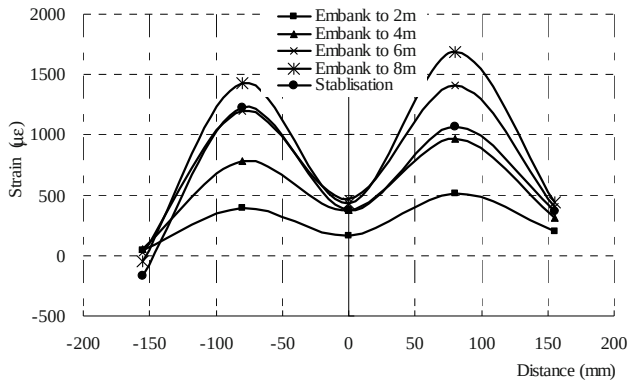

Fig. 4 Curve describing link loading process of centrifugal

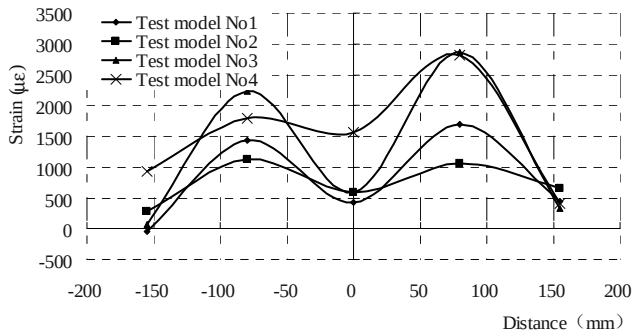

Fig.5 Test model No.1－4. Curve describing strain allocation in reinforcement by time once embankment filling enters the 8 m

Result from the test models from 1 to 4 was once pile spacing and loading increased strain average value of the group also rose, once the embankment process finished (at biggest loading), reinforced cushion reached the highest strain average value which then fell down gradually, see on Fig. 6. Soil embankment of experiment test No. 4 with size (six fold of pile diameter) incurred failure, appearing into deformation with piles piercing into embankment, strain value of reinforced net surpassed optimum value, reinforced net appeared into rupture. See Fig. 7.

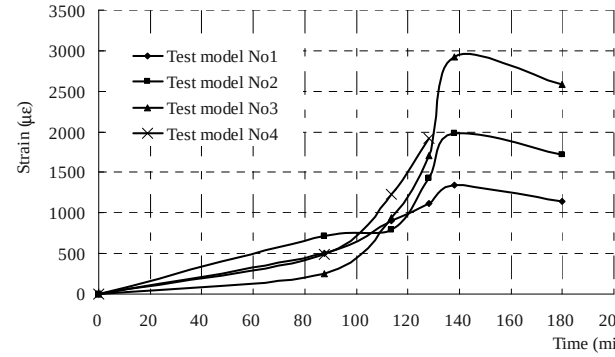

Fig. 6 Curve describing link between strain in reinforcement and loading process

Fig. 7 Test model No. 4 deformation and failure of reinforced cushion

Impact of Coverage of Pile Cap to Force Capability of Reinforced Cushion.

The result showed that strain average value of test models from No.5 (pile cap size of 11×11 mm) to test No. 7 (pile cap size of 23×23 mm) was contradicted to the increase of pile cap size; strain average value was allocated in the form of M letter line. At the centre of embankment and two sides of center of side slope, the value was small but large at the two sides of road shoulder. See Fig. 8.

Once loading was increased by time in design with pile cap construction, strain value of reinforced cushion increased gradually, especially at periods of construction

and after a year stabilization and operation periods, the value increased clearly and kept stable gradually. See Fig. 9.

Besides, experimental result showed that, by increase of pile cap size, strain value of reinforced cushion decreased gradually in line with the decrease of foundation settlement. See Fig. 10.

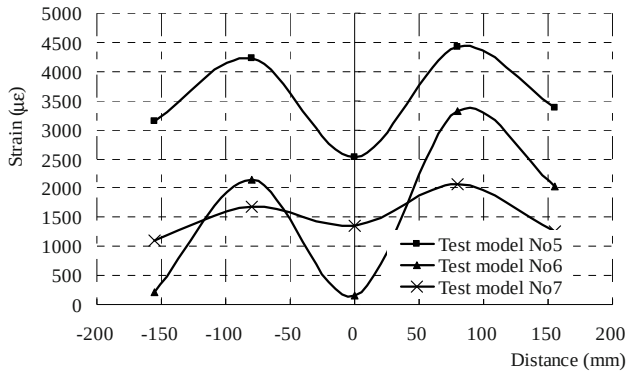

Fig.8 Curve describing strain allocation in reinforcement by time once embankment filling enters the 8 m

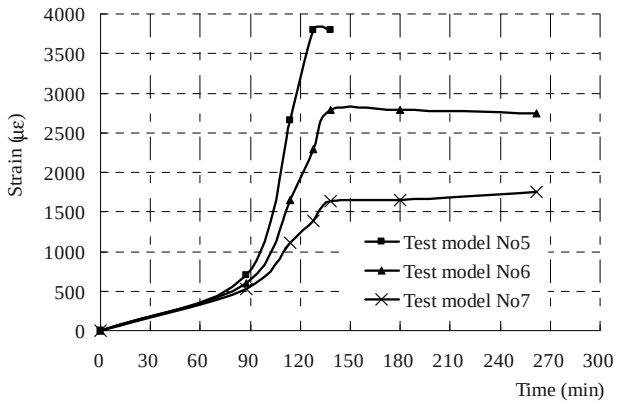

Fig. 9 Test models No.5－7 Curve describing link between strain in reinforcement and loading process

Comparing Impacts of Pile Spacing and Pile Cap Coverage to Force Compatibility of Reinforced Cushion

The result showed that in construction design of pile without cap, strain value of reinforced cushion and pile spacing was on the same card to increase gradually. Meanwhile, in the context that pile spacing was unloaded, strain value and coverage of pile cap were on different cards.

Comparing test models Nos .1 and 5, pile allocation ratio and coverage of pile cap were similar but strain value of two models was greatly different. Of which, strain value of test model No.1 was 2.78 fold higher than strain average value of test model No.5. See Fig. 10.

From above mentioned analysis, the final result was: in the context of construction design of sparse pile with pile cap and coverage ratio of pile cap; and pile allocation ratio of design without pile cap were similar, methods comprising Pile-Cap-Net Structure Embankments), Pile-Net Structure Embankments should be used to deal with soft soil. In the first method, reinforced net received heavier force than that in the second one. In the reality, strength of reinforced net in construction in the first design method should be improved. Comparison experimental data of test models No.1, 2 and 6, 7 showed that strain values were quite similar with each other in line with pile spacing diameters.(Test models No.6－7 used calculation principle on pile cap coverage and pile allocation ratio were similar, converting to variables of pile spacing diameters. The ratio was appropriately 2:1.

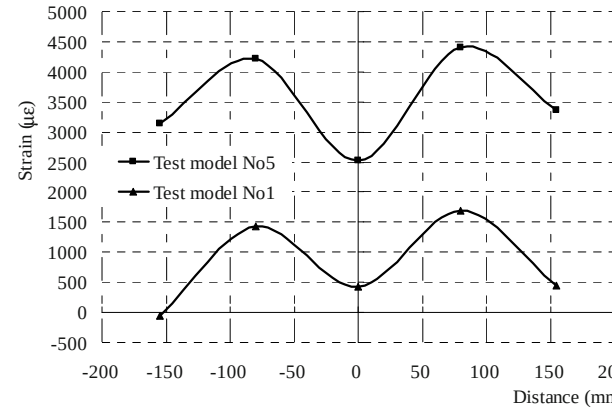

Fig. 10 Comparing strain values of reinforced net of test models

CONCLUSIONS

Centrifuge test model was used for simulating geotechnical experiment, analysing allocation rules of reinforced cushion on composite foundation using high strength piles under impact of embankment loading and the final results as follows:

1) Strain value of reinforced cushion under impact of loading allocation in the form of M letter line, was attained maximum value at the two sides of road shoulder, and was fairy small at center cross-section; allocation rule had a closed relationship with deformation of embankment.

2) Strain value of reinforced cushion under impact of loading increased gradually by increase of pile spacing, and decreased gradually by increase of pile cap size. Once embankment finished (with biggest loading), strain value of reinforced cushion reached the maximum value and then fell down gradually and tended to be stable after that.

3) Once using Pile-Cap-Net Structure Embankments designing method for handling with soft soil**,** coverage of pile cap and pile allocation ratio of design with pile were similar; in the first method, reinforced cushion

suffered heavier force than that of the second method. In contrast, once strain value was similar, the first method with pile spacing (using calculation principles for similar pile cap coverage and pile allocation ratio and converting into ratio of pile diameter spacing) nearly double the pile spacing of the second method. The *in-situ* construction need improve strength of reinforced cushion in the first method.

REFERENCES

Rao WG (2004) Pile — Net Composite Foundation Practice and Principle. China Water resources & Hydropower press

Li SP (2001) Using geotechnical net in strengthening soft soil foundation. Subgrade Engineering 6: 99

Zhang L, Luo Q, Zhou C, Pei FY (2007) Comparative Research on Reinforcement Plans of Thick Soft Clay Ground Based on Centrifugal Model Tests. Chinese Journal of Geotechnical Engineering. 29(3): 982-987

Jian ML, Zhang DG (2006) Technology and Engineering practice of CFG pile composite foundation. China Water resources & Hydropower press

Luo Q, Liu JY, Zhang L (2003) Experimental study on Earthwork synthetic material reinforced sand blankets decrease settlement for soft ground. China Joumal of Geotechnical Engineering. 25(6):710-714

China railway siyuan survey and design group Co., Ltd. (2007) Jing-Hu high-speed railway research comprehensive technology of CFG pile composite foundation

CENTRIFUGE SHAKING TABLE TESTS ON SATURATED REINFORCED SOIL WALLS

J. Izawa[1] and J. Kuwano[2]

ABSTRACT: This paper discusses effects of saturation of backfill on seismic stability of reinforced soil wall by using the centrifuge shaking table tests. Before the shaking table test, static stability of reinforced soil wall with saturated backfill was investigated by raising the water level under the centrifugal gravity. As a result, the wall showed sufficient stability statically. The wall with unsaturated backfill showed higher seismic stability and deformation was not observed in the centrifuge shaking table test. On the other hand, large residual displacement was observed in the case of fully saturated case. The cause of the low seismic stability of the saturated reinforced soil wall was due to the decrease of stiffness of back fill soil following increase of pore water pressure, although no liquefaction occurred. In order to clarify the decrease of stiffness of backfill, relationships between shear stress and shear strain of backfill during earthquake were determined using response acceleration time histories. As a consequence, shear stiffness of backfill wall was about 25% smaller than that of unsaturated one. Additionally, it is considered that the decrease of pullout resistance between soil and reinforcement due to the decrease of effective confining pressure of the reinforcement was also one of reasons too.

KEYWORDS: geogrid reinforced soil wall, centrifuge shaking table test

INTRODUCTION

Many embankments and natural slopes have collapsed in 2004 Niigataken Chuetsu Earthquake because the water content was much higher than usual due to heavy rain a few days before the earthquake. Some reinforced soil walls were also damaged due to high water content in backfill although collapse was not observed. This paper discusses the effects of saturation of backfill on seismic stability of reinforced soil wall by using the centrifuge shaking table tests.

OUTLINE OF TESTS

Model Reinforced Soil Wall

Tests were conducted by using Tokyo Tech Mark 3 Centrifuge and Horizontal & Vertical 2D shaker (Takemura et al. 2002). Fig. 1 shows a schematic view of the model reinforced soil wall used in the tests. The wall was designed based on Japanese standard (PWRC 2003). The model was made with dry Toyoura sand with relative density of 80%. Height of the wall was 200 mm in model scale, which corresponded to 10m in prototype. Poly-Carbonate plate with 0.5 mm thickness and 9 mm width was used for the model reinforcement. As shown in Fig. 1, 6 model reinforcements were attached to each divided facing wall panel, which was made with acrylic plate with 3 mm in width. Table 1 and 2 summarize

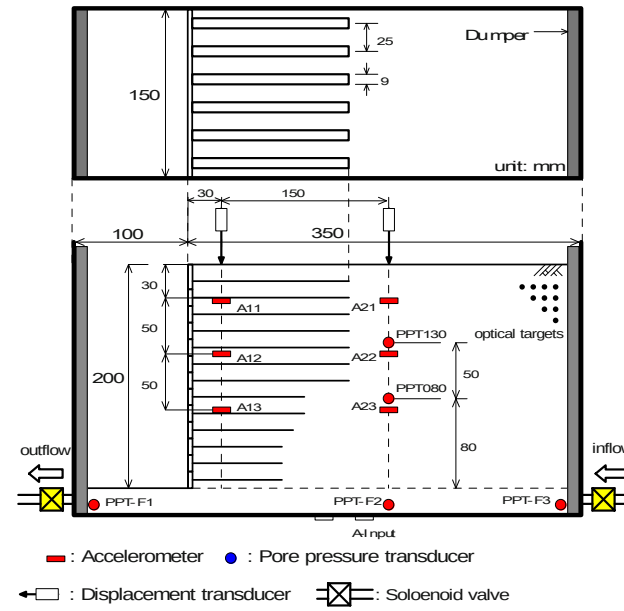

Length of reinforcements (from crest)	1-7 level :	140mm
	8-9 level :	100mm
	10 level :	90mm
	11-13 level :	80mm

Fig. 1 Schematic view of model reinforced soil wall

[1] Assistant Professor, Department of Civil Engineering, Tokyo Institute of Technology, JAPAN. Email: jizawa@cv.titech.ac.jp
[2] Professor, Geosphere Research Institute, Saitama University, JAPAN. Email: jkuwano@mail.saitama-u.ac.jp

Table 1 Properties of Toyoura sand (Dr=80%)

Average particle size	: D_{50}	0.19 (mm)
uniformity coefficient	: Uc	1.56
Permeability	: k	2.0×10^{-4}(m/sec)
Internal frictional angle	: ϕ	43.0(deg.)
Dry density	: γ_d	15.4(kN/m^3)
Saturated density	: γ_{sat}	19.4(kN/m^3)
Submerged density	: γ'	9.59(kN/m^3)

Table 2 Properties of reinforcement

Tensile stiffness		506.8 (kN/m)
Pullout frictional angle	: ϕ_p	12.9 (deg.)

Table 3 Test procedure

1. Increase of centrifugal acceleration up to 50G
2. i) Raising of water → Decrease
   ii) Shaking table test for unsaturated model
3. Decrease of centrifugal acceleration up to 1G

---

4. Saturation of backfill at 1G
5. Increase of centrifugal acceleration up to 50G
6. Shaking table test for saturated model
7. Decrease of centrifugal acceleration up to 1G

properties of Toyoura sand and mode reinforcement respectively. Additionally, some optical targets were set in the front surface of the model in order to observe the deformation of the model in detail. Vectors of displacement, distributions of strain and so on were calculated from displacements of such targets.

Test Cases

As indicated in Table 3, 3 kinds of test, which were Water raising test, shaking table tests for unsaturated model and saturated model, were conducted as follows.

(1) Water raising test

Fig. 2 shows a conceptual diagram of water raising test. The test was conducted to investigate instability of reinforced soil wall due to change of stress condition in the backfill caused by saturation of backfill as indicated in Fig. 3. In the test, water was raised up to 20 mm above the upper surface of the wall through the rotary joint and solenoid valve in the centrifugal acceleration of 50 G. Note that the front side of the wall was also filled by water. Such was not modelled reinforced soil walls filled with water due to rain appropriately. In addition, it is considered that safety of the model reinforced soil wall used in the water raising test was higher than the real

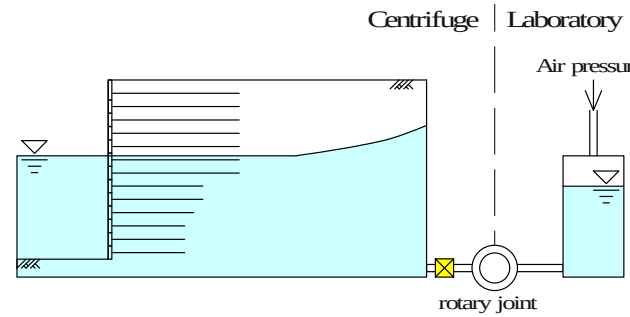

Fig. 2 Configuration of raising water level

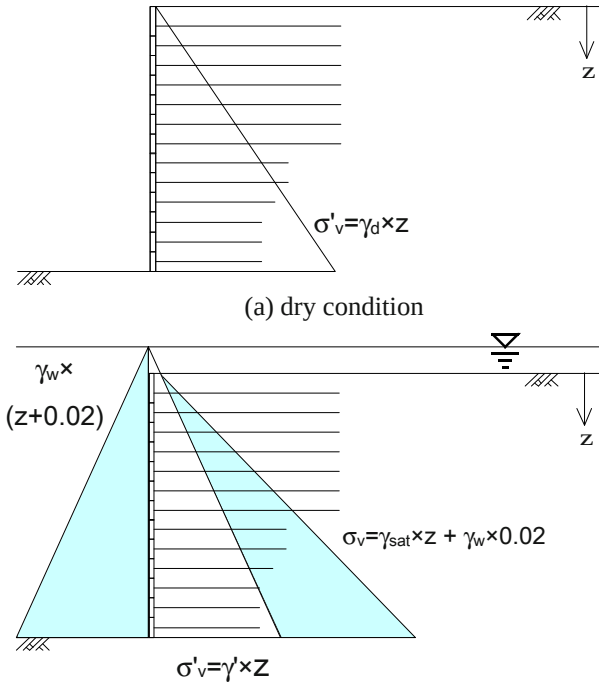

Fig. 3 Distribution of effective vertical pressure

situation because water pressure acting on the wall could play as resistance against the movement of the wall in the active direction. After raising water up to the prescribed level, water was drained away by opening the solenoid valve for outflow.

(2) Shaking table test for unsaturated model

After draining away water from the backfill, sinusoidal waves with frequency of 100 Hz were applied to the model in the centrifugal acceleration of 50 G. In this test, backfill of the model reinforced soil wall was unsaturated condition because water was not completely drained. Additionally, it is considered that shear stiffness and strength of the backfill was higher than those in saturated condition. Fig.3 shows time histories of sinusoidal waves applied in the saturated case. In the unsaturated case, only Step1－3 were applied.

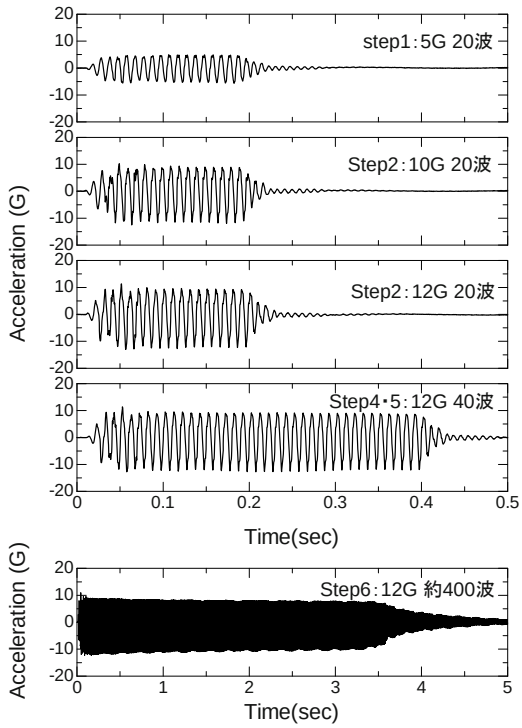

Fig. 4 Time histories of input waves

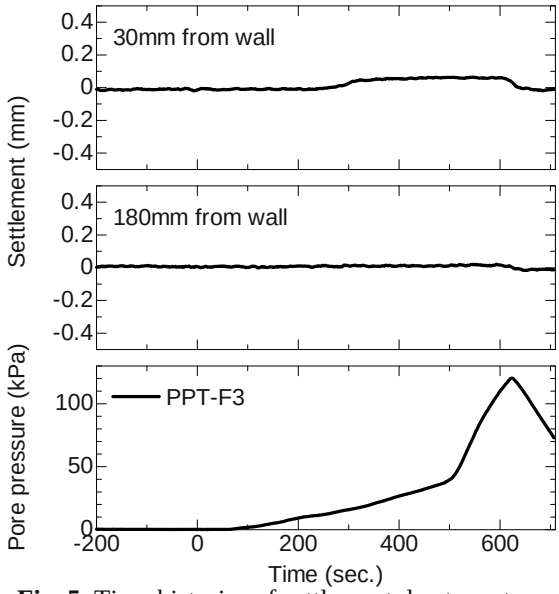

Fig. 5 Time histories of settlement due to water raising

(3) Shaking table test for saturated model

After finishing the shaking table test for unsaturated model, centrifugal acceleration was decreased to 1G once and the model was filled by water in the gravity field. After that, shaking table tests were made in the centrifugal acceleration of 50 G. Applied accelerations were indicated in Fig. 4.

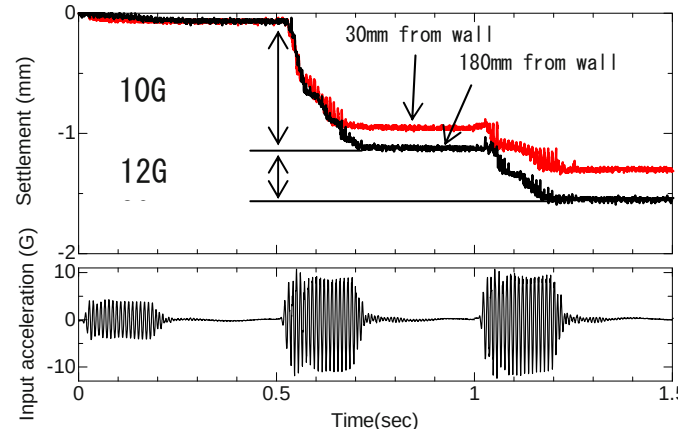

Fig. 6 Time histories of settlements in unsaturated case

RESULTS AND DISCUSSIONS

(1) Water raising test

Fig. 5 shows time histories of settlement of crest together with water pressure at foundation. Along with the water rising, stability of the model wall decreased because pullout resistance also decreased due to decrease of effective stress acting on reinforcements. However, the model wall did not show any displacements due to the raised water as shown in Fig. 5. This means that reinforced soil wall has sufficient stability in static even if the backfill is saturated.

(2) Shaking table test for unsaturated model

Time histories of settlements at crest and input acceleration were indicated in Fig. 6. Although the settlements cumulated with shaking, the wall did not collapse and made a stable state after shaking. In general, stiffness of soil decreases in proportion to increase of strain. However, settlement observed in Step 3 was smaller than that in Step 2 although almost the same input acceleration was applied to the model. The cause of such behaviour is that decrease of stiffness of the backfill could be prevented by tensile stress generated in deformation of the reinforced soil wall.

(3) Shaking table test for saturated model

i) Excess pore water pressure

Time histories of pore water pressure ratio indicated by $\Delta u_{max}/\sigma_v'$, where Δu_{max} and σ_v' indicates maximum excess pore water pressure during shaking and vertical effective stress before shaking respectively, are demonstrated in Fig. 7. In all steps, $\Delta u_{max}/\sigma_v'$ did not reached to 1 and liquefaction did not occurred during shaking. Although settlements increased with shaking, velocity of settlement did not increase due to increase of

pore water pressure. Consequently, it is considered that stability of the reinforced soil wall is not affected largely by excess pore water pressure during shaking.

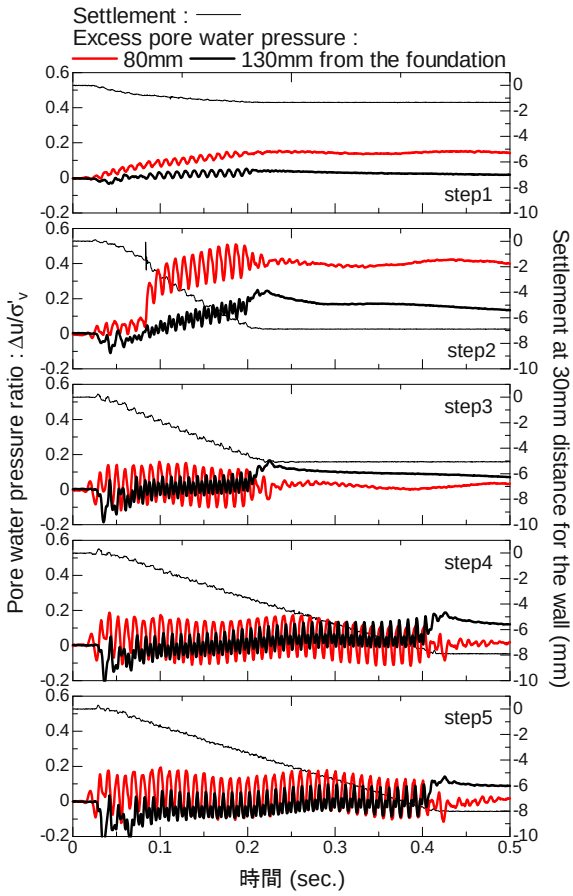

Fig. 7 Time histories of excess pore water pressure and settlement in saturated case

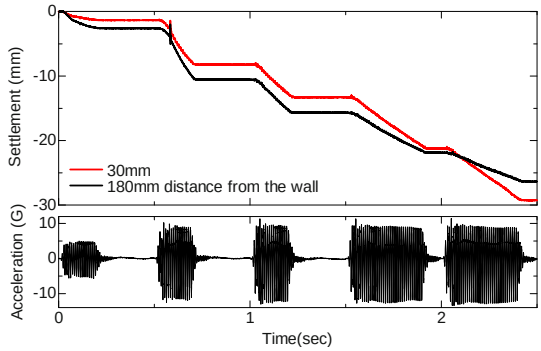

Fig. 8 Time histories of settlements in saturated case

ii) Deformation mode

Fig. 8 shows time histories of settlements together with input acceleration in the shaking table test for saturated reinforced soil wall. Quite large settlements were observed in the saturated case compared with those in the unsaturated case. Vertical distributions of horizontal displacement of the wall, which were obtained from the displacements of optical targets set in the model; are shown in Fig. 9. Horizontal displacement can be divided to three components, which are sliding displacement, shear displacement at upper part and shear displacement at lower part, as indicated in Fig. 9.

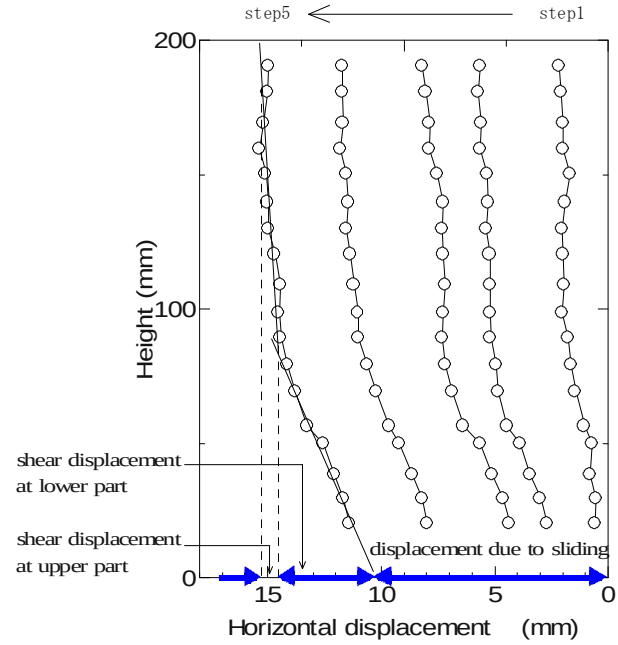

Fig. 9 Vertical distribution of horizontal displacement in saturated case

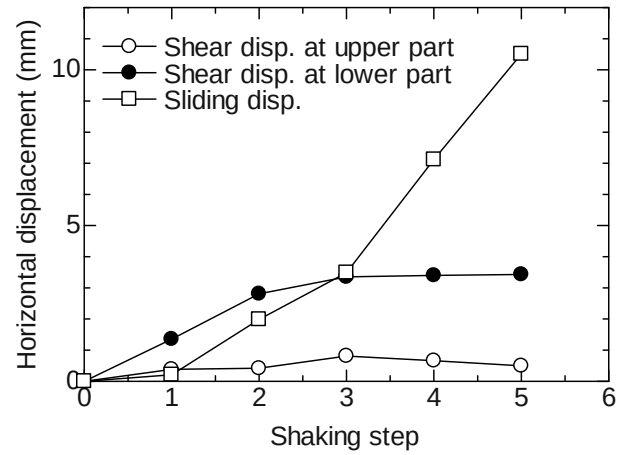

Fig. 10 Components of horizontal displacement

Displacements of each component are plotted against the shaking step in Fig. 10. In all steps, shear displacement at upper part were much smaller than the other components. During early shaking step, in other word, before 3rd shaking step, shear displacement at lower part were the largest. After 3rd Step, horizontal displacements due to sliding were getting remarkable. Fig. 11 shows distributions of maximum shear strain in Steps 3 and 4 calculated from displacements of optical targets. These figures clearly show that clear concentration area was formulated in and behind the reinforced area during 4th shaking Step. In addition, it is considered that sliding surface occurred in such concentration area. Con-

sequently, it is inferred from these results that displacement due to sliding was getting remarkable after formulation of the sliding surface.

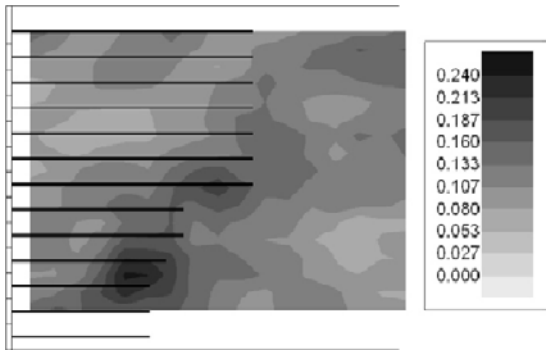

(a) Distribution after Step 3

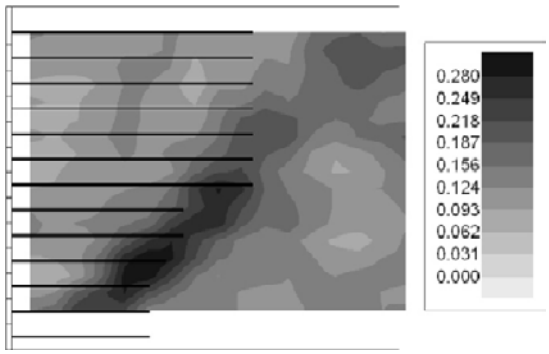

(b) Distribution after Step 4

Fig. 11 Distribution of maximum shear strain γ_{max}

(4) Effect of saturation of backfill

Results of the centrifuge shaking table tests clearly showed that seismic stability of reinforced soil wall decreased due to saturation of the backfill although clear collapse was not observed even in the saturated case. Such degradation of seismic performance seems to be caused by degradation of shear stiffness of backfill material and decrease of pullout resistance as follows.

i) Degradation of shear stiffness of backfill

Generally, shear stiffness of soil depends on effective confining pressure. It is considered that shear stiffness of soil decrease in saturated condition because effective stress decrease. Here, degradation of backfill material is discussed by using acceleration records.

Shear stress and shear strain can be calculated from following equation assuming the shear deformation of the reinforced area as Fig. 12.

Shear stress : $\tau = \rho H_1 A_{11} + \rho \dfrac{H_2}{2} A_{12}$

Shear strain : $\gamma = \left(\iint A_{13} - \iint A_{11} \right) \Big/ H_2$

* ρ : density of backfill material (kN/m^3)
A : Acceleration (m/s^2)

In general, this method can not calculate exact values of shear stiffness and shear strain. However, relative comparison of difference between saturated and unsaturated backfill can be made. Fig. 13 shows the relationships between shear stress and shear strain obtain from

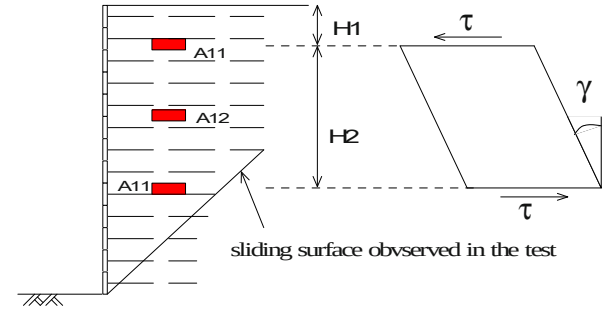

Fig. 12 Assumed shear deformation

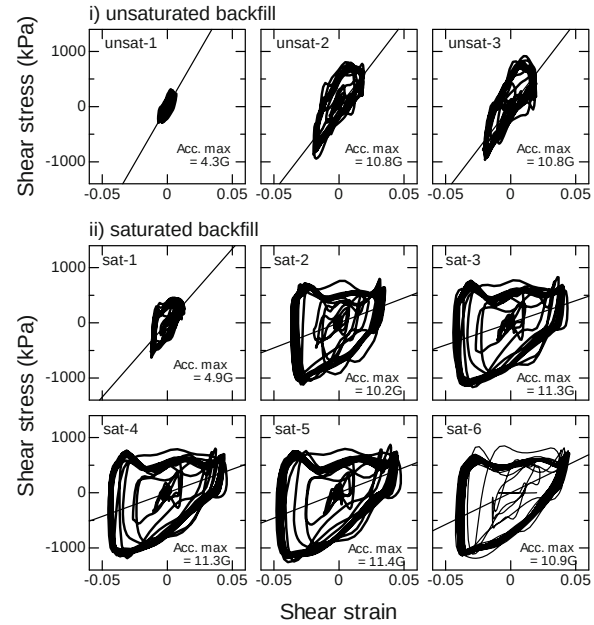

Fig. 13 Shear stress and shear strain relations

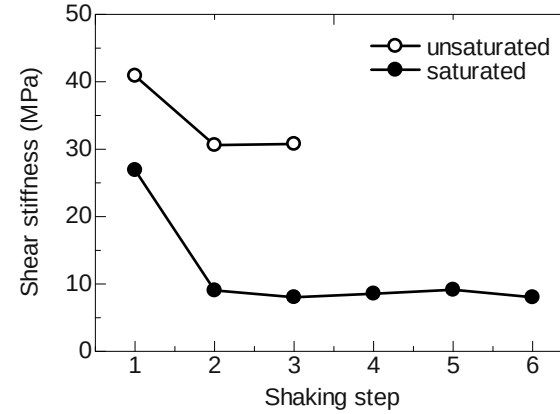

Fig. 14 Degradation of shear stiffness due to shaking

calculation. Shear stiffness obtained from the skeleton line of the shear stress and shear strain relations are plotted against shaking step in Fig. 14. As shown in Fig.

14, shear stiffness of the backfill decreased about 40% due to saturation of backfill. However, no degradation of shear stiffness of the backfill was observed in both cases after shaking Step 2. There are two reasons for such status.

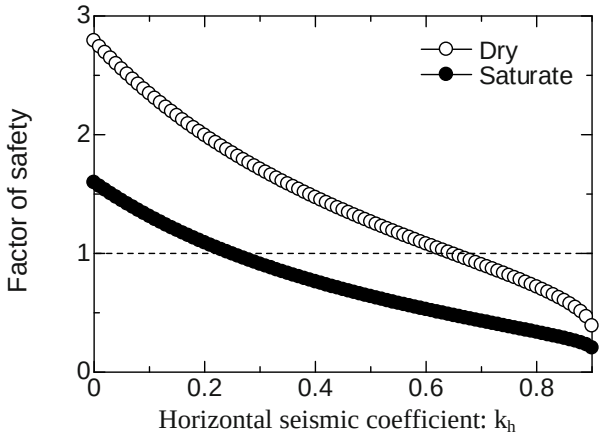

Fig. 15 Factor of safety vs Horizontal seismic coefficient obtained from two wedge analysis

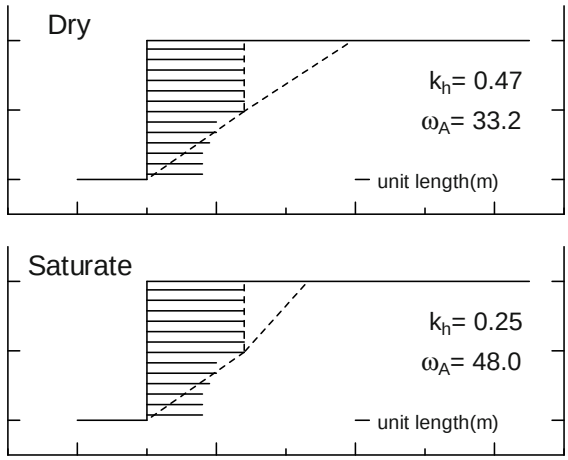

Fig. 16 Failure sections obtained from two wedge analysis

One is the restraining effect to keep shear stiffness from decreasing due to tensile stress of reinforcements caused by shear deformation of the reinforced area. The other is that main component of deformation changed from shear deformation to sliding deformation.

ii) Degradation of pullout resistance

Sliding surface was formulated at shaking Step 4 in saturated case and displacement due to sliding was getting larger in which case the pullout resistance affected to stability of reinforced soil wall. It is considered that internal friction angle of backfill "ϕ" and pullout friction angle "ϕ_p", which decide the pullout resistance, is the same regardless of saturation of backfill material. To the contrary, effective vertical stress acting on reinforcement "σ_v'" decrease due to saturation of backfill and pullout resistance also decrease. Consequently, seismic stability of the reinforced soil wall decreases.

In this tests, effective vertical stress decrease from 15.5 kN/m^3 (ρ_d: dry density) * Hieght to 15.5 kN/m^3 (submerged density) * Hieght due to saturation of backfill. Effect of such degradation of effective stress on the seismic stability of reinforced soil wall was discussed by using Two-Wedge analysis (Izawa et al. 2002). Assuming the ϕ and ϕ_p are not affected by saturation, two cases were made with using dry density and submerged density in the calculation. Fig. 15 shows the relationships between factor of safety due to sliding and horizontal coefficient at failure. Failure sections at Fs=1.0 are also indicated in Fig. 16. This result clearly shows that seismic stability of the reinforced soil wall decreased largely due to saturation of backfill because the pullout resistance decrease by degradation of effective vertical stress acting on reinforcements.

CONCLUSIONS

In this study, effects of saturation of backfill were investigated by using centrifuge model test. In conclusion, I would like to state the following points.

1. Reinforced soil wall showed sufficient stability in static even if the backfill was filled by water.
2. Remarkable degradation of shear stiffness of backfill material due to deformation of reinforced are was not observed in both saturated and unsaturated case. It is considered that that is the reason why tensile stress generated in reinforcement due to deformation can keep the shear stiffness from decreasing.
3. Resistance for sliding decreased due to degradation of pullout resistance. Such degradation of pullout resistance was caused by decrease of effective vertical pressure acting on reinforcements due to saturation of backfill. Consequently, stability of reinforced soil wall decreased.

REFERENCES

Takemura J, Takahashi A, Aoki Y (2002) Development of horizontal-vertical 2D shaker in a centrifuge, Proc. of Physical Modeling in Geotechnics: 163-168

Public works research centre (PWRC) (2003) Manual for design and construction of reinforced soil wall (Terre-Armee) 3rd edition

Takahashi A, Takemura J, Shimodaira T (2001) Seismic performance of reinforced earth wall with geogrid, Proc. of 15th ICSMGE: 1265-1268

Izawa J, Kuwano J, Takahashi A (2002) Behavior of steep geogrid-reinforced embankments in centrifuge tilting tests, Proc. of Physical modeling in geotechnics: 993- 998

CENTRIFUGE MODELING ON FIBER REINFORCED FLY ASH SLOPE

D.K. Bhardwaj [1] and J.N. Mandal [2]

ABSTRACT: Randomly distributed fiber reinforced soils have recently attracted increasing attention in geotechnical engineering. Due to non availability of the land construction of fly ash embankments with steep slopes is very important. For the experimental work natural fiber, coir, at fiber content of 1% (by dry weight) has been used. Direct shear test, unconfined compression test have been performed without and with coir fiber. Centrifuge tests have been performed on fly ash without and with coir fiber reinforcement at slope angle ($\theta = 71.5°$). Centrifuge tests have performed to observe the effect of coir fiber reinforcement in fly ash slope models. All the centrifuge tests were performed at 80 % compaction effort. Coir fiber reinforcement reduces the settlement of the slope and it fails at higher values of 'g', which means that fiber reinforced slopes, can sustain higher loads. Fiber reinforcement changes the brittle behavior of fly ash into ductile behavior. Factor of safety of all slope models have been found out using limit equilibrium method based on software, GEOSLOPE. Experimental results are compared with finite element analysis, using the software PLAXIS Version 8.

KEYWORDS: fly ash, coir fiber, centrifuge, shear strength

INTRODUCTION

High ash content (30%－50%) of Indian coals are contributing 90 million tons of fly ash per year and cover 265 km^2 of area as ash pond by 2015 it would require 1000 km^2 for its disposal. (Das and Yudhbir 2005). An increasing number of experimental and numerical studies on the subject have been conducted by several researchers in the past few decades. (Waldron 1977), and (Wu et al. 1988) reported that plant roots increase the shear strength of the soil and the stability of natural slopes. (Gray and Ohashi 1983) performed the direct shear tests on sand specimens and found that there is increase in shear strength and ductility of the soil, and reduction in post peak strength due to the inclusion of discrete fibers. (Kaniraj and Havanagi 2001) carried out experimental studies on some Indian fly ashes mixed with randomly oriented fibers. (Mandal et al. 2004) carried out centrifuge modeling on polypropylene fiber reinforced fly ash and performed the finite element analysis using software Ansys. Mandal et al. (2005) used the waste rubber tire chips for the reinforcement of soil. In this paper a centrifuge modeling of reinforced soil slope with coir fiber has been addressed.

EXPERIMENTAL INVESTIGATION

Though lots of work has been carried out on various types of soil but much attention has not been given on the use of waste material like fly ash with coir fiber. Therefore, a centrifuge modeling on coir fiber reinforced fly ash slope has been addressed in this paper.

Properties of Fly Ash and Coir Fiber

Physical properties of fly ash and coir fiber are shown in the Tables 1 and 2 respectively. Direct shear test, unconfined compression test have been performed without and with coir fiber. Table 3 shows the angle of friction and adhesion for soil samples without and with coir fibers

Table 1 Physical properties of fly ash

Properties	Value	Unit
Specific Gravity	2.154	-
Moisture Content	0.42	%
Max. Dry Density	12.017	kN/m^3
Optimum Moisture Content	25.50	%
Cohesion	12.0	kN/m^2
Angle of Shearing Resistance	28.34	(◦)
Permeability	5.91 E-03	m/sec

[1] Management Trainee, Garware Wall Ropes Ltd., Pune, INDIA. Email: dkfriend@rediffmail.com
[2] Professor, Department of Civil Engineering, IIT Bombay, INDIA. Email: cejnm@civil.iitb.ac.in

Table 2 Physical properties of coir fiber

Properties	Requirements
Fiber Length	1 inch
Color	Brown
Rope Strength	2000 N/m
Elongation	22 %

Table 3 Values of adhesion and angle of friction

Type of Fiber	c (kPa)	φ (◦)
No Fiber	9.5	18.32
Coir Fiber	11.0	26.03

TESTING PROGRAM

Preparation of the Model

Centrifuge tests were performed on fly ash without and with coir fiber reinforcement at slope angle, θ = 71.5°. Silicon grease was applied in the inner sides of the glass plates to minimize the effect of friction. Figure 1 shows the dimensions of the slope model used in the test for θ = 71.5°. All samples were made at optimum moisture content. All three potentiometers were adjusted in such a manner that their locations are 2.5 cm, 1.5 cm and 1.5 cm respectively from the back face of sample. No surcharge was used in this case; the sample was allowed to fail under self weight, by increasing the RPM.

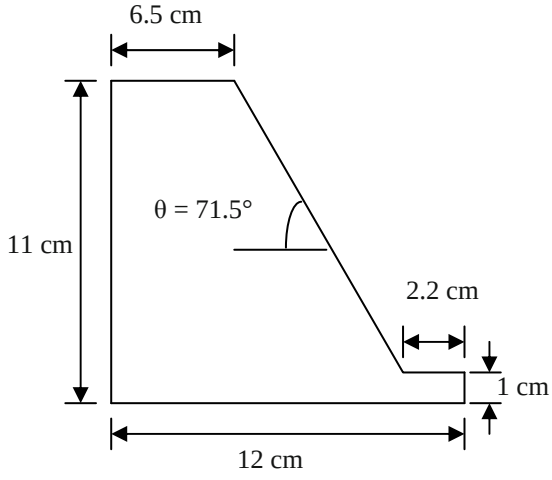

Fig. 1 Dimensions of the slope model used in centrifuge test, for θ = 71.5°

Test Procedure

The fly ash slope model was performed in a centrifuge available at IIT Bombay. Fiber was mixed in the soil 1% by dry weight of the soil and the compaction effort has arrived at 80%. To find out the actual displacements of the slope models, these potentiometers were calibrated.

Centrifuge Modeling

Reinforced Soil

Figures 2 and 3 show the coir fiber fly ash slope model before and after failure (at θ = 71.5°) respectively. Data obtained from the centrifuge test, shows that coir fiber reinforced slope achieves the angular velocity equal to that of unreinforced soil i.e. 510 rpm after 854 seconds from the beginning of the test. And finally coir fiber reinforced slope failed at 550 rpm after 1451 seconds from the beginning of the test. Scale factor of coir fiber reinforced slope at 550 rpm was 78.

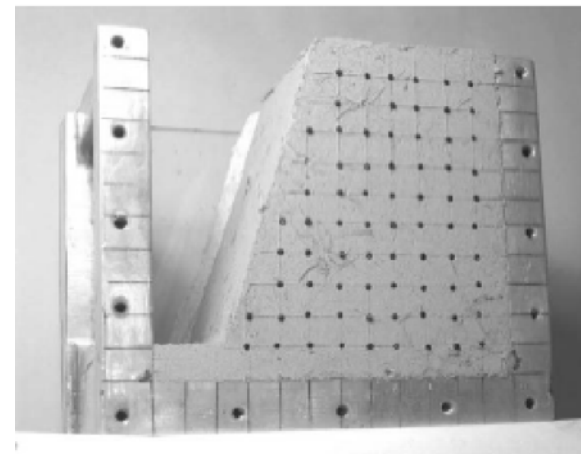

Fig. 2 Slope model for reinforced soil before failure at θ = 71.5°

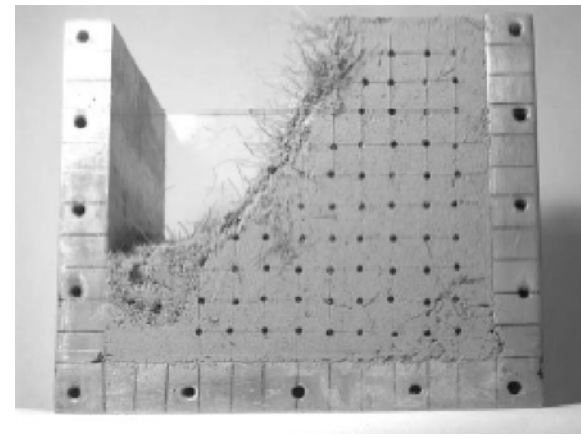

Fig. 3 Slope model for reinforced soil after failure at θ = 71.5°

Figs. 4 and 5 show the variation of potentiometer reading with time without and with reinforcement respectively.

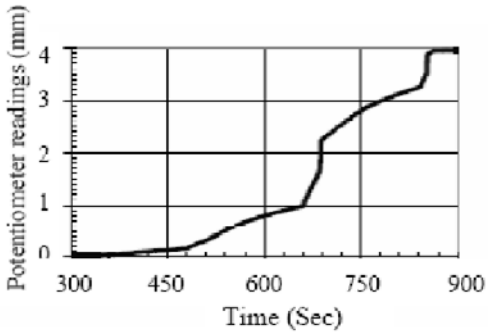

Fig. 4 Variation of potentiometer reading with time for without reinforcement

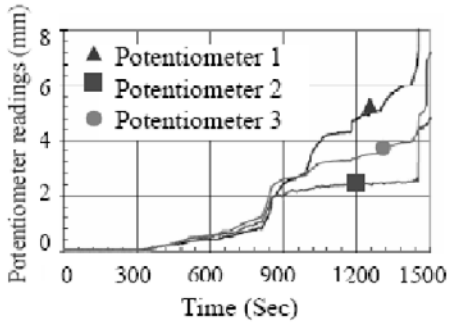

Fig. 5 Variation of potentiometer reading with time for with reinforcement

Results of centrifuge test for unreinforced and reinforced soil are given in Table 4.

Table 4 Centrifuge test results at θ = 71.5°

Type of Fiber	Parameters			
	G (cm/sec^2)	Time	ω (rpm)	N
No Fiber	981	23.07	510	67
Coir	981	23.07	550	78

Factor of Safety

GEOSLOPE software was used to determine the factor of safety for unreinforced and reinforced slope. Values of minimum factor of safety obtained from Bishop's Method are given in Table 5.

Table 5 Factor of safety (FOS) obtained from Bishop's Method

Type of Fiber	FOS (θ = 71.5°)
No Fiber	0.845
Coir Fiber	1.020

FINITE ELEMENT ANALYSIS

The finite element method was carried out for the analysis and to study the behavior of fly ash slope with out and with coir fiber reinforcement. The problem is considered as a plane strain problem. The finite element analysis was done using the software called PLAXIS Version 8.

Unreinforced Soil

Input parameters required for unreinforced soil are given in Table 6.

Table 6 Input parameters for unreinforced soil at θ = 71.5°

Parameters	Value	Unit
Unsaturated unit weight (γ)	12.02	kN/m^3
Saturated unit weight (γ_{sat})	15.08	kN/m^3
Young's modulus (E)	3335	kN/m^2
Cohesion (c)	9.5	kN/m^2
Friction angle (φ)	18.32	(◦)
Poission's ratio (υ)	0.3	-
Dilatancy angle (ψ)	0	(◦)

Prototype dimensions, deformed mesh, vertical displacements and total displacements for unreinforced soil are given in Fig. 6. Results are shown in Table 7.

Table 7 Finite element analysis results for unreinforced soil at θ = 71.5°

Parameters	FEM values
Total displacement (mm)	742.71
Vertical displacement (mm)	441.80
Vertical displacement on top surface (mm)	426.88
Total vertical stress (kN/m^2)	90.07
Shear stress (kN/m^2)	17.67
Shear strain (%)	135.79
Factor of safety	0.833

Results of finite element analysis for unreinforced soil at θ = 71.5° show that extreme vertical displacement is 441.80 mm and the extreme vertical displacements of top surface is 426.88 mm. Extreme total displacement is 742.71 mm. Shadings of total displacements show that maximum displacements occur on top of the slope and these shadings also form slip circles along the direction of failure.

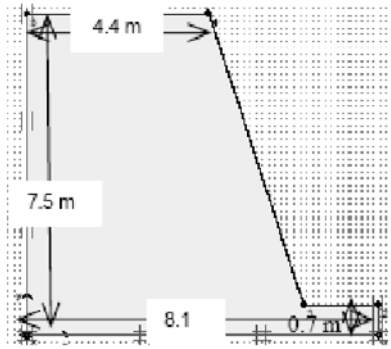

(a) Prototype dimension

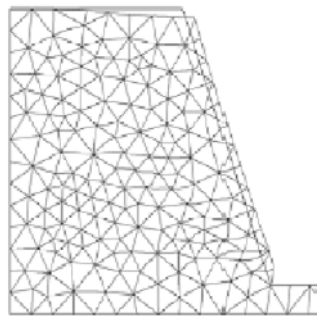

(b) Deformed mesh

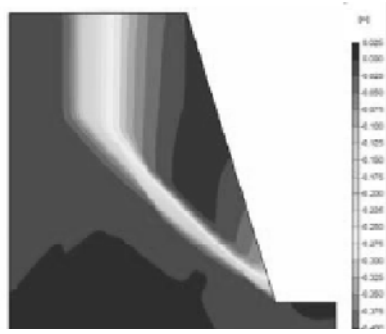

(c) Vertical displacement

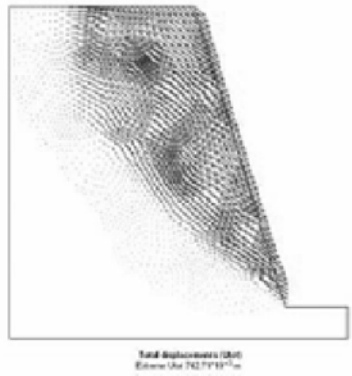

(d) Total displacement

Fig. 6 Prototype dimensions, deformed mesh, vertical displacements and total displacements for unreinforced soil

Reinforced Soil

Input parameters required for coir fiber reinforced soil are given in Table 8.

Table 8 Input parameters for coir fiber reinforced soil at θ = 71.5°

Parameters	Value	Unit
Unsaturated unit weight (γ)	11.84	kN/m^3
Saturated unit weight (γ_{sat})	14.98	kN/m^3
Adhesion (c)	11.0	kN/m^2
Friction angle (φ)	26.03	(◦)
Poission's ratio (υ)	0.3	-
Dilatancy angle (ψ)	0	(◦)

Prototype dimensions, deformed mesh, vertical displacements and total displacements for coir fiber reinforced soil are given in Fig. 7. Results of finite element analysis for coir fiber reinforced soil at θ = 71.5° show that extreme vertical displacement is 201.03 mm and the extreme vertical displacements of top surface is 193.74 mm. Extreme total displacement is 331.64 mm. Shadings of total displacements show that maximum displacements occurs on top of the slope and these shadings also form slip circles along the direction of failure. Extreme vertical total stress is 89.75 kN/m^2, while actual maximum vertical total stress is 87.62 kN/m^2. Extreme shear stress is 17.23 kN/m^2. At some places shear stress is positive and at other places it is negative, which shows tensile and compressive stresses. Value of factor of safety is 1.039. Extreme shear strain is 62.87 %. From shear strain variation, it is clear that shear strain is maximum along slip circle. These results are also compared with unreinforced soil in Table 9.

Table 9 Finite element analysis results for coir fiber reinforced soil at θ = 71.5°

Parameters	FEM (unrein-forced)	FEM (Coir fiber reinforced)
Total displacement (mm)	742.71	331.64
Vertical displacement	441.80	201.03
Vertical displacement on top surface (mm)	426.88	193.74
Total vertical stress (kN/m^2)	90.07	89.75
Shear stress (kN/m^2)	17.67	17.23
Shear strain (%)	135.79	62.87
Factor of safety	0.833	1.039

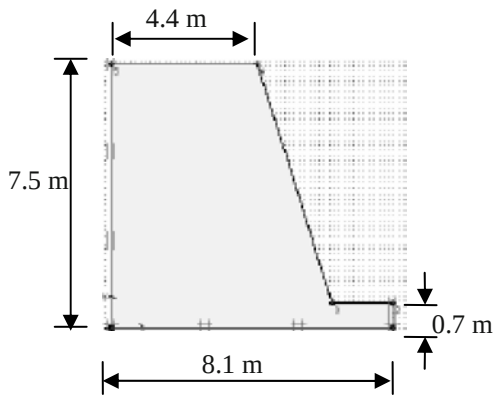

(a) Prototype dimension

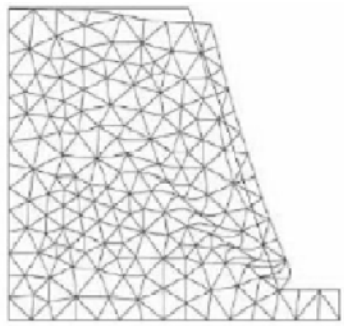

(b) Deformed mesh

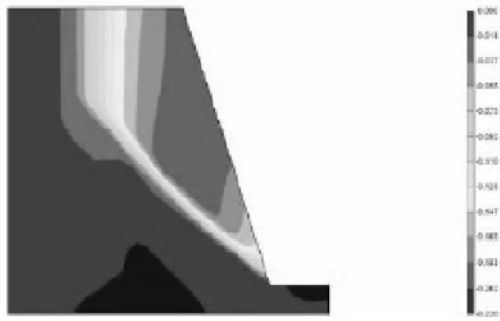

(c) Vertical displacement

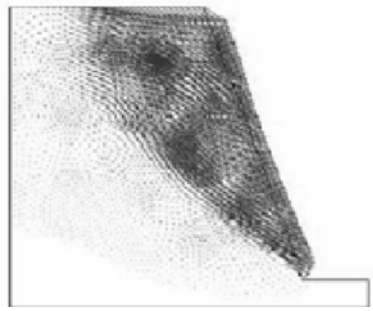

(d) Total displacement

Fig. 7 Prototype dimensions, deformed mesh, vertical displacements and total displacements for coir fiber reinforced soil

Maximum vertical displacements of the top surface and factor safety obtained from finite element analysis are compared with the experimental results. These values are given in Table 10. Comparison between factor of safeties obtained from Bishop's and finite element analysis are given in Table 11.

Table 10 Maximum vertical displacements obtained from experiments and finite element analysis at θ = 75.1°

Type of Fiber	Maximum vertical displacement of top surface (mm) (Experimental) (a)	Maximum vertical displacement of top surface (mm) (FEM) (b)	Percentage error (%) [(a-b) * 100/a]
No Fiber	388.60	426.88	9.85
Coir Fiber	241.20	201.03	16.65

Table 11 Factor of safety (FOS) values obtained from Bishop's method and finite element analysis at θ = 75.1°

Type of Fiber	FOS (Bishop's method)	FOS (FEM)
No Fiber	0.845	0.833
Coir Fiber	10.20	1.039

CONCLUSIONS

Centrifuge tests were performed without and with coir fiber reinforcement. The scale factor of 67, for unreinforced slope was observed increased to 78 for the case of reinforced slope. To verify the experimental results, finite element analysis based on software PLAXIS version 8 was used. The maximum vertical displacement of top surface from experimental study was observed decreasing to 241.2 mm for the coir fiber slope compared to that unreinforced slope with 388.60 mm displacement. The variation between finite element results and experimental results for maximum vertical displacement of the top surface was found less than 17%. In case of reinforced slopes displacements are less as compared to unreinforced slopes. Due to coir fiber reinforcement, the values of factor of safety obtained from finite element analysis show the similar trend of increase as in case of Bishop's method.

REFERENCES

Das SK, Yudhbir (2005) Geotechnical characterization of some Indian fly ash. J. of Materials in Civil Engineering. ASCE. 17(5): 544 –552

Gray DH, Ohashi H (1983) Mechanics of fiber reinforcement in sand. J. of Geotechn. Engrg. ASCE. 109(3): 335-353

Kaniraj SR, Havanagi VG (2001) Behavior of cement-stabilized fiber-reinforced fly ash–soil mixtures. J. of Geotech. and Geoenviroment Engrg. ASCE. 127 (7): 574–584

Mandal JN, Kumar S, Meena CL (2005) Centrifuge modeling of reinforced soil slopes using tire chips. GSP 140. Slopes and retaining structures under seismic & static conditions, Geotechnical Special publication No. 130-142 & GR-18 proceeding of sessions of the Geo-Fabrics 2005 congress. ASCE. January 24-26. 2005, Austin, Texas: 1-8

Mandal JN, Kumar S, Sambasivarao P (2004) Centrifuge modeling and finite element analysis of fiber reinforced fly ash slopes. Proceedings of the third Europen Geosynthetics Conference, Geotechnical Engineering with Geosynthetics, Munich, Germany. 01-03 March, 2004. 1: 165-168

Ranjan G (2000) Basic and applied soil mechanics, New Age International Limited, Publishers, Daryaganj, New Delhi, India

Waldron LJ (1977) Shear resistance of root-permeated homogeneous and stratified soil, Soil Sci. Soc. Am. Proc. 41: 843–849

Wu TH, McOmber RM, Erb RT, Beal PE (1988) Study of soil-root interaction, J. of Geotech. Engrg. ASCE. 114(12): 1351–1375

Reinforcement

IMPORTANCE OF STRONG CONNECTION BETWEEN GEOSYNTHETIC REINFORCEMENT AND FACING FOR GRS INTEGRAL BRIDGE

F. Tatsuoka[1], D. Hirakawa[2], H. Aizawa[3], H. Nishikiori[3], R. Soma[3] and Y. Sonoda[3]

ABSTRACT: A new bridge system, called the GRS integral bridge, is proposed. This consists of an integral bridge, which integrates a pair of RC abutment and a continuous girder without using girder supports, and a pair of geosynthetic-reinforced soil (GRS) retaining walls having full-height rigid (FHR) facings constructed after the completion of reinforced backfill walls. A pair of FHR facing function as the abutments to which a girder is integrated. Results from model tests indicate that, when reinforcement layers are firmly connected to the FHR facing, GRS integral bridges become much more cost-effective in construction, long-term maintenance and stability than conventional type bridges, integral bridges with unreinforced backfill and bridges using GRS retaining walls as abutments.

KEYWORDS: connection strength, geosynthetic reinforced soil, integral bridge, reinforced backfill

INTRODUCTION

Despite its universal use, the conventional type bridge abutments (Fig. 1) have a number of drawbacks: 1) As the abutment is a cantilever structure supporting unreinforced backfill, a pile foundation is usually necessary while the abutment may become very massive. 2) Although the abutment is not allowed to move once constructed, measures should be taken to prevent movements by earth pressure and settlement and lateral flow in the subsoil by backfill construction. 3) The construction and long-term maintenance of girder-supports and connections are costly. 4) A bump may be formed behind the abutment by settlement of the backfill due to its self-weight and traffic loads. 5) The seismic stability of the backfill and the abutment supporting the girder via a fixed-support is relatively low.

As more cost-effective bridge systems alleviating the problems by using girder supports and connections, the integral bridge (Fig. 2a) is now widely used in Europe and North America, while the geosynthetic-reinforced soil (GRS) retaining wall (RW) with full-height rigid (FHR) facing used as the abutments (Fig. 3) has been proposed and used. Fig. 4 shows the GRS integral bridge, which combines these two systems, proposed recently (Tatsuoka et al., 2007, 2008). This paper reports that, when geosynthetic reinforcement layers are firmly connected to the FHR facing, GRS integral bridges become more cost-effective in construction and long-term maintenance and more statically and dynamically stable than the above two bridge two types.

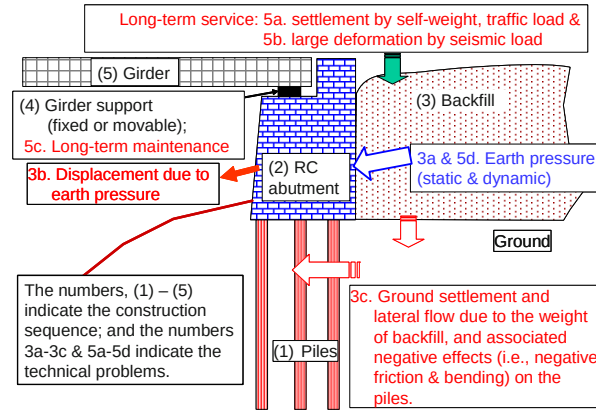

Fig. 1 Conventional type bridge abutments.

INTEGRAL BRIDGE AND GRS-RW BRIDGE

The popularity of the integral bridge (Fig. 2) is due to high cost-performance by low construction and maintenance cost resulting from no use of girder-supports (or bearings) and the use of a continuous girder (or deck). However, the backfill may exhibit excessive settlement by self-weight and traffic load. Furthermore, as the structural part and the backfill are not unified, their seismic stability cannot be very high. Moreover, as a continuous girder is integrated to abutments, seasonal thermal expansion and contraction of the girder results in cyclic lateral displacements of the abutment (Fig. 2b). Then, the earth pressure on the back of the abutment gradually increases, while the settlement in the backfill takes place and increases gradually.

With a GRS RW bridge (Fig. 3), a girder is supported by sill beams via movable and fixed supports placed on a pair of GRS RWs with FHR facing, illustrated in Fig. 4.

[1] Professor, Department of Civil Engineering, Tokyo University of Science, JAPAN. Email: tatstuoka@rs.noda.tus.ac.jp
[2] Assistant Professor, Department of Civil Engineering, Tokyo University of Science, JAPAN
[3] Graduate and undergraduate students, Department of Civil Engineering, Tokyo University of Science, JAPAN

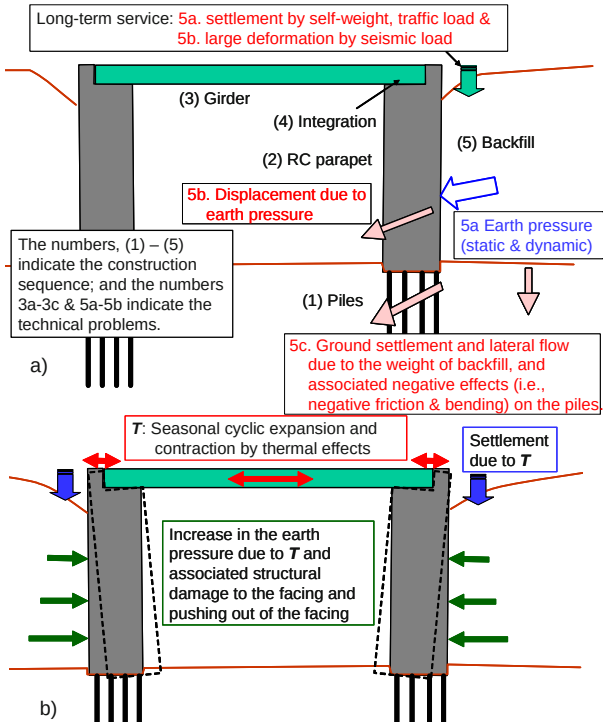

Fig. 2 Integral bridge: a) construction sequence and several unsolved old problems; and b) a new problem by thermal expansion and contraction of the girder

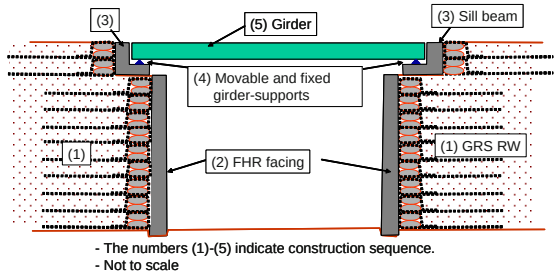

Fig. 3 GRS-RW bridge

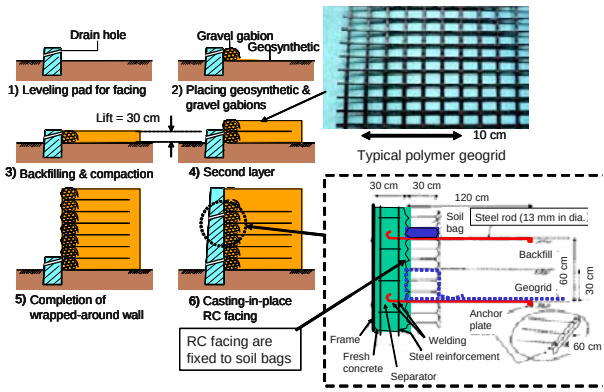

Fig. 4 Staged construction of geosynthetic-reinforced soil (GRS) retaining wall (RW) with a full-height rigid (FHR) facing (Tatsuoka et al. 1997)

This wall system has been standardized in Japan and has been constructed at more than 600 sites with a total wall length more than 95 km as of June 2007. Its main features are as follows: 1) As FHR facing is a continuous beam supported by many geosynthetic reinforcement layers with a small vertical spacing (30 cm), the internal stresses in the facing and the stresses in the subsoil below the facing bottom are much lower than with conventional RWs as cantilever structures. Moreover, high tensile force in the reinforcement results from high connection strength at the back of FHR facing, which results in high confining pressure and therefore high stiffness and shear strength in the backfill. 2) The backfill is constructed to a full wall height with a help of gravel gabions placed at the shoulder of each soil layer. 3) A small vertical spacing, 30 cm, between planar geosynthetic reinforcement layers facilitates high compaction of the backfill. 4) After a full height of reinforced backfill has been completed and then sufficient deformation of the backfill and supporting ground has taken place, a lightly steel-reinforced concrete facing is cast-in-place directly on the wrapped-around wall face ensuring a strong connection to the

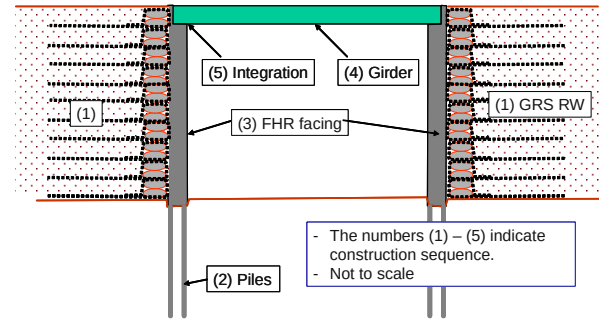

Fig. 5 GRS integral bridge; the reinforcement connected to the facing (not to scale)

Bridge type	Cost & period of construction	Maintenance cost	Seismic stability	Total
Conventional	1 A, B	1 C, D	1 F, G 252 gal*	3
Integral	2 B	1 D, E	2 F 641 gal*	5
GRS RW	3	1 C, D	2 G 589 gal*	6
GRS Integral	3	3	3 1,048 gal*	9

(* Acceleration at failure in model shaking table tests)

Fig. 6 Rating of different bridge types

A= massive & strong parapets necessary because of cantilever structure.
B= piles usually necessary because the parapet is a cantilever structure and the backfill is constructed after construction of piles & parapets.
C= cost for construction and long-term maintenance of girder supports.
D= intolerable backfill settlement by self-weight and traffic loads during long-term service (intolerable settlement of the sill beam with GRS RW bridges).
E= thermal expansion and contraction of the girder, resulting in cyclic lateral displacements of parapets and associated increase in the earth pressure, which may damage the parapets and intolerable backfill settlement.
F= large settlements in the backfill and large dynamic earth pressure by seismic loads
G= low seismic stability due to independent performance of abutments (unstable sill beam in seismic events with GRS RW bridges).

reinforced backfill. By this staged construction, a) negative interactions between the FHR facing and the compression of the backfill during the backfill construction can be avoided; b) large compression of soft subsoil can be accommodated ensuring the stability of wall; c) the backfill near the wall face can be compacted dense with better mobilization of reinforcement tensile force; and d) a good alignment of completed wall face can be easily made.

Although the GRS-RW bridge (Fig. 3) is more cost-effective than the conventional bridge type (Fig. 1), it has the following drawbacks: 1) The girder cannot be very long and heavy due to low stiffness of the backfill supporting the girder. 2) Girder-supports, which are costly in construction and long-term maintenance, are used. 3) Although the dynamic stability of GRS RW with a FHR facing is very high (e.g., Tatsuoka et al. 1998; Koseki et al., 2006), the dynamic stability of the sill beam is relatively low. This is because the mass of the sill beam is much smaller than the girder while the anchorage of the reinforcement layers connected to the back of the sill beam is low due to their shallow depths.

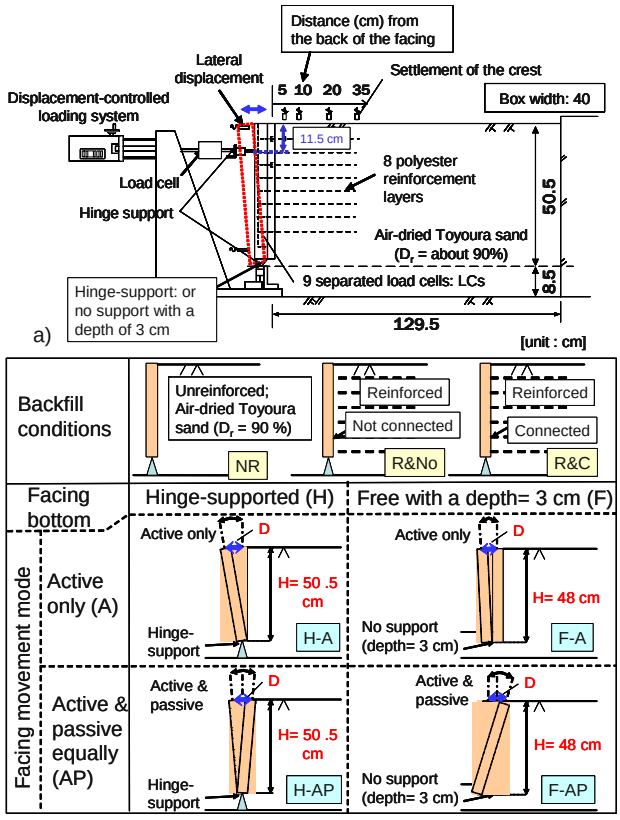

Fig. 7 a) Static model test configurations (this figure represents case *H-A* when the backfill is reinforced with connection to the facing); and b) model test cases

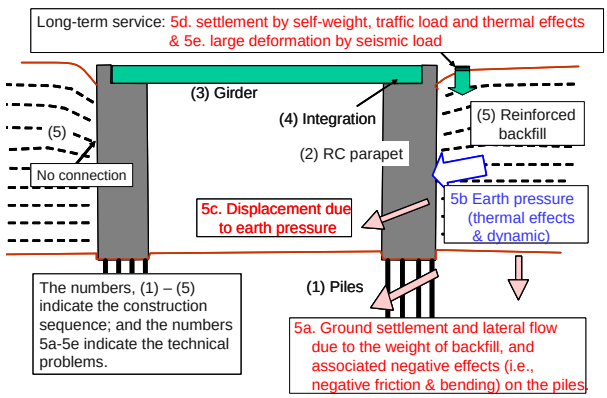

Fig. 8 Integral bridge with reinforced backfill: reinforcement not connected to the facing

GRS INTEGRAL BRIDGE

The GRS integral bridge (Fig. 5) takes advantage of the superior features of the integral bridge (Fig. 2a) and the GRS RW bridge (Fig. 3) while alleviating their drawbacks. In particular, a foundation becomes lighter than the one for an integral bridge due to lower load applied to the foundation, like GRS RW bridges. Furthermore, the GRS integral bridge can alleviate detrimental effects of thermal cyclic contraction and expansion of the girder, as shown below.

In Fig. 6, the conventional type bridge, the integral bridge with unreinforced backfill, the GRS RW bridge and the GRS integral bridge are rated in three items based on their full-scale field performance in the past and results from the static model tests described in this paper and the shaking table tests (Hirakawa et al. 2007; Aizawa et al. 2007; Tatsuoka et al., 2007, 2008). The full point allocated to each item is three, which is reduced one by one when any of the negative factors $A-G$ is relevant. The respective bridge models collapsed at the accelerations shown in the second column from the right in the shaking table tests. A total full point equal to nine is given only to the GRS integral bridge.

MODEL STATIC LOADING TESTS

A series of model tests were performed to evaluate the effects of cyclic lateral displacements of the facing on the performance of the backfill that is reinforced or not (Fig. 7). In case *R&Co*, geosynthetic reinforcement layers are connected to the facing to simulate the GRS integral bridge (Fig. 5). In case *R&No*, the reinforcement is not connected to the facing to simulate a bridge type illustrated in Fig. 8. With this type, after the structural part (Fig. 2) is completed, the backfill is constructed being reinforced with the reinforcement not connected to the facing. As shown below, this bridge type is not recommendable due to low performance. The backfill was air-dried poorly graded sub-angular sand, Toyoura sand, with D_r= 90 %. The unreinforced backfill was produced by air-pluviation. The backfill was compacted by hand-tamping when reinforced. The reinforcement was a Polyester geogrid with a strand width of 1 mm; spacing between the adjacent strands= 18 mm; covering ratio= 9.5 %; and rupture tensile strength at an axial strain rate of 1.0 %/min.= 19.6 kN/m.

The bottom of the model facing was: either a) hinge-supported allowing only rotation about the hinge to simulate a FHR facing supported with a pile foundation; or b) placed in the subsoil with a depth of only 3.0 cm to simulate a FHR facing without any foundation. At a distance 11.5 cm down from the top, the FHR facing was cyclically displaced, at a displacement rate of 0.004 mm/sec. The facing was laterally displaced either between the neutral state (displacement at the facing top d= 0) and an active state at a positive d with a fixed amplitude (D) (case *A*); or between an active state at a d= D/2 and a passive state at d = -D/2 (case *AP*). Cases *A* and *AP* simulate the behaviours of integral bridges completed in summer and fall, respectively.

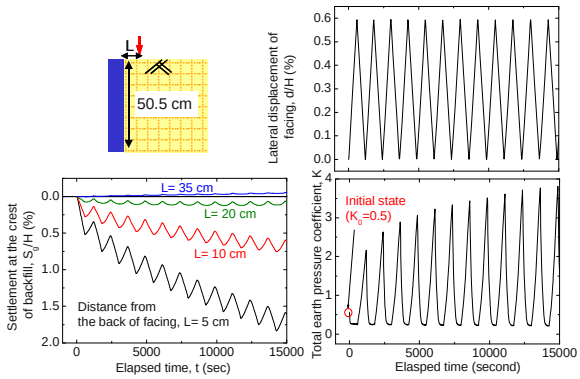

Fig. 9 Typical test result, unreinforced Toyoura sand (case *NR H-A*, D/H= 0.6 %)

Fig. 9 shows the time histories of the lateral displacement at the facing top, d; the total earth pressure coefficient, K= $2Q/H^2\gamma$, and the backfill settlement at different distances L back the facing from a typical test on unreinforced backfill with D/H= 0.6 %. Here, Q is the total earth pressure per width of facing; H is the wall height (50.5 cm for the hinge-support and 48 cm for the free condition at the footing bottom); and γ is the dry unit weight of the backfill (1.60 gf/cm^3).

Fig. 10a shows the K- d/H relations when the backfill is unreinforced (case *NR*). Despite a very small facing displacement, the passive earth pressure increases significantly with cyclic loading. When this takes place with full-scale structures having unreinforced backfill, by this earth pressure increase, the facing structure may be damaged and the facing bottom is strongly pushed outward. When the backfill is reinforced (case *R&C*; Fig. 10b), the earth pressure increase is similarly large. However, as the reinforcement is connected to the facing and the facing performs as a continuous beam supported by a number of reinforcement layers, the facing is not damaged while the facing bottom is not pushed outward. Rather, higher earth pressure results in higher stiffness and strength of the backfill. It may also be seen from Figs. 10a & b that the effects of facing movement mode, active only or active and passive equally, has no significant effects on the development of earth pressure.

Fig. 11a shows the effects of backfill condition and the facing movement mode on the development of the passive earth pressure when D/H= 0.2 %. The earth

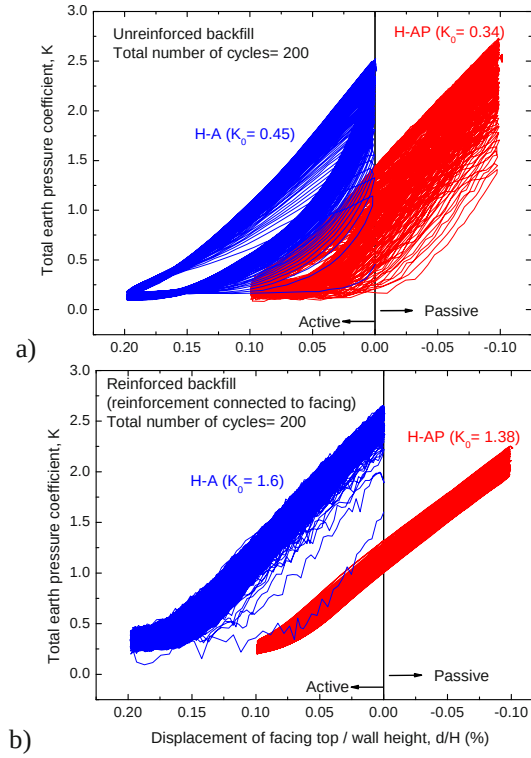

Fig. 10 K - d/H relations when D/H= 0.2 % (cases *H—A* and *H—AP*); a) unreinforced backfill; and b) backfill reinforced without connection to facing

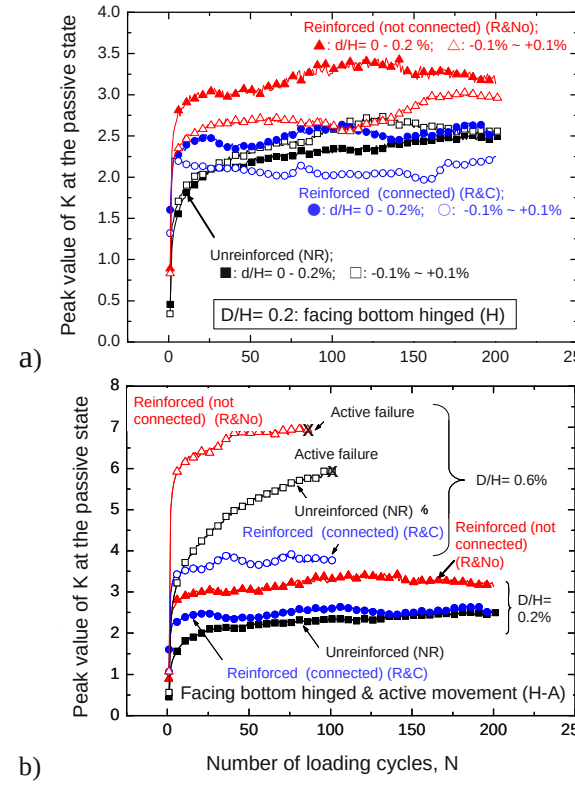

Fig. 11 Increase in passive earth pressure with cyclic loading; a) D/H= 0.2 %; and b) D/H= 0.2 % & 0.6 %

pressure increase is largest when the backfill is reinforced without connection to the facing. This trend becomes stronger with an increase in the facing

displacement (Fig. 11b). These results clearly indicate the importance of connecting reinforcement to the facing.

Fig. 12 shows the relationship between the backfill settlement when d= 0 at L= 5 cm and the number of loading cycles. The backfill settlement increases with an increase in D/H and the settlement is larger when the

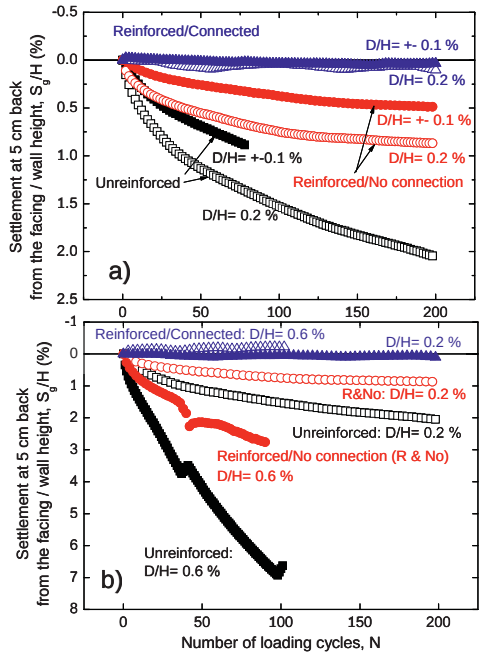

Fig. 12 Increase in backfill settlement with cyclic loading; a) D/H= 0.2 % & ;- 0.1 %; and b) D/H= 0.2 % & 0.6 %

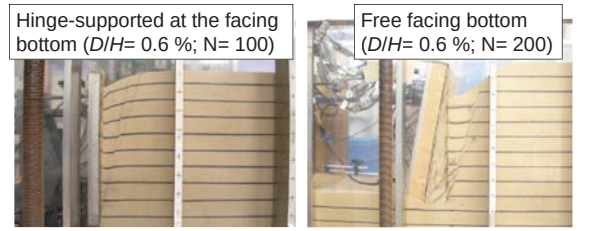

a) Unreinforced backfill

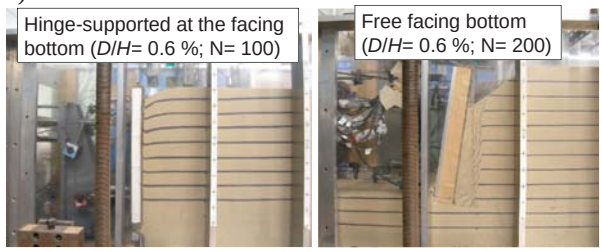

b) Reinforced without connection

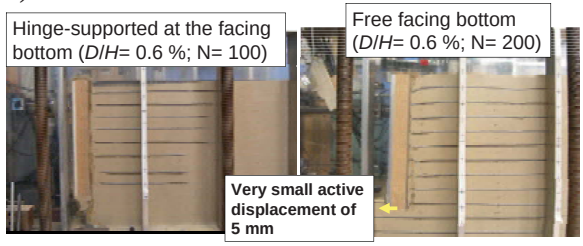

c) Reinforced with connection

Fig. 13 Failure of backfill by cyclic active horizontal displacement of facing

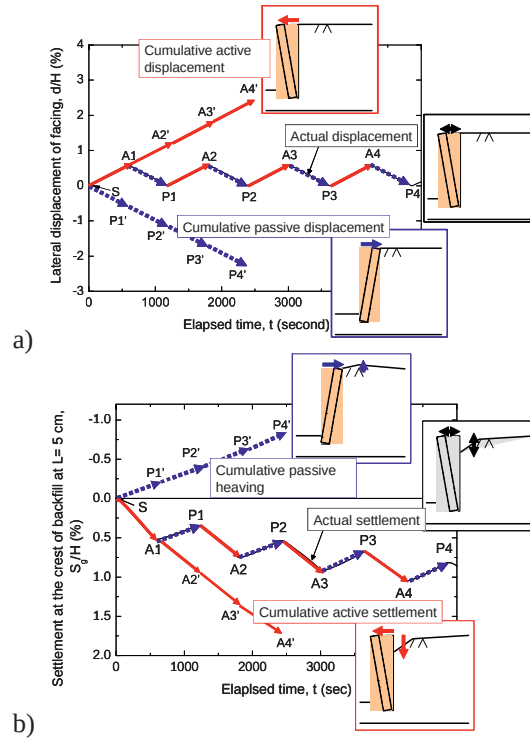

Fig. 15 Dual ratchet mechanism in the unreinforced backfill, case *NR H-A*: a) lateral displacement at the facing top; and b) backfill settlement

facing moves only on the active side. Furthermore, the backfill settlement cannot be effectively restrained by reinforcing the backfill if the reinforcement is not connected to the facing (i.e., case *R&No*). On the other hand, the backfill settlement becomes nearly null when the reinforcement is connected to the facing (i.e., case *R&C*). This result is due to, firstly, that, when the reinforcement is connected to the facing, the confining pressure in the backfill becomes higher, which makes the backfill less deformable and the membrane effect of the reinforcement prevents the formation of an active wedge.

When the facing bottom is rather free without supported by a pile foundation, the active failure takes place much easily in the unreinforced backfill, while the settlement increases and the facing bottom is pushed out (Fig. 13a). It is also the case with the reinforced backfill if the reinforcement is not connected to the facing (Fig. 13b). On the other hand, when the reinforcement is connected to the facing, even when the facing bottom is free, the active failure in the backfill and associated large settlement in the backfill do not take place (Fig. 13c).

DUEL RATCHET MECHANISM

The development of high earth pressure and large settlement in the backfill by a small amplitude of cyclic lateral displacement of facing is due to the dual ratchet mechanism in the backfill explained below. Firstly, by small active displacement of the facing in each cycle, small active sliding develops along the active shear band (e.g., processes S → A1 & P1 → A2 in Figs. 14 and 15).

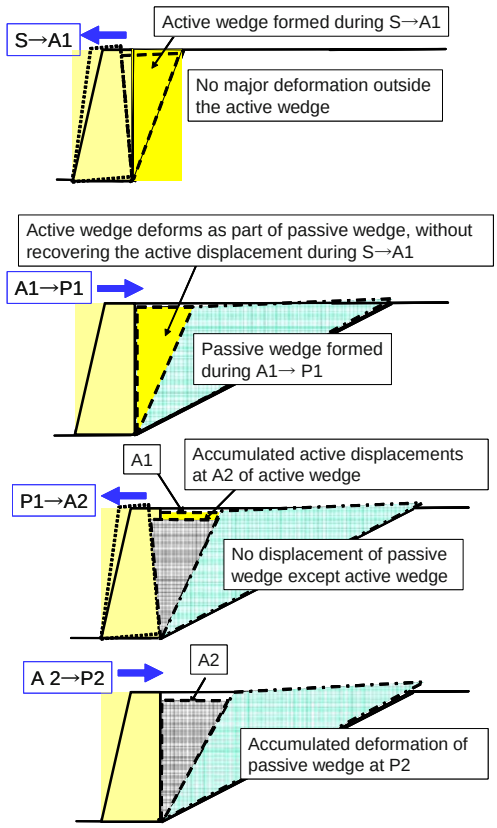

Fig. 14 Dual ratchet mechanism in the backfill

When subsequently subjected to small passive displacement of the facing (e.g., processes A1 → P1 & A2 → P2 in Figs. 14 and 15), the active sliding is not activated, because the passive deformation of the passive wedge zone, which is much larger than the active wedge zone, is easier to take place and the active wedge deforms in the passive mode as part of the passive zone. Although it is small in each cycle, the active sliding in each cycle accumulates with cyclic loading as illustrated in Fig. 15a (i.e., the active ratchet mechanism). The accumulated active sliding eventually reaches the value when the active failure takes place during monotonic active loading. Secondly, the passive sliding is inactive when the facing moves toward the active direction (e.g., processes S → A1 & P1 → A2). Although it is small in each cycle, the passive strain in the passive zone accumulates with cyclic loading (Fig. 15a), which gradually increases the passive earth pressure with cyclic loading (i.e., the passive ratchet mechanism). As the passive displacement of the facing when the passive failure takes place during monotonic passive loading is very large, the active failure takes place far before the passive failure takes place during cyclic loading.

It is to be noted that the dual ratchet mechanism becomes active also when relative lateral displacements take place between the facing and the backfill in seismic events. Therefore, firm connection of the reinforcement to the facing is essential to achieve high seismic stability of GRS integral bridge (Fig. 5).

It is seen from Fig. 11 that the earth pressure increase with cyclic lateral displacement of the facing is largest when the backfill is reinforced but without connection to the facing. This trend can be explained as follows. In this case, significant active failure takes place in the backfill immediately behind the facing (Fig. 13b left). On the other hand, the stiffness of the reinforced backfill is relatively high. Then, the force that is necessary to push inward the facing from an active state becomes large.

CONCLUSIONS

A new bridge system, called the GRS integral bridge, is proposed, which combines an integral bridge and geosynthetic-reinforced backfill. When geosynthetic reinforcement layers are firmly connected to full-height rigid facing, this bridge type becomes very stable and highly cost-effectiveness in construction as well long-term maintenance. This can be attributed to: 1) no use of girder-supports; 2) use of a continuous girder; and 3) reinforcing the backfill with full-height rigid facing constructed after the completion of reinforced backfill.

REFERENCES

Aizawa H, Nojiri M, Hirakawa D, Nishikiori H, Tatsuoka F, Tateyama M, Watanabe K (2007a) Validation of high seismic stability of a new type integral bridge consisting of geosynthetic-reinforced soil walls, Proc. of 5th Int. Sym. on Earth Reinforcement (IS Kyushu 2007)

Hirakawa D, Nojiri M, Aizawa H, Nishikiori H, Tatsuoka F, Tateyama M, Watanabe K (2007b) Effects of the tensile resistance of reinforcement embedded in the backfill on the seismic stability of GRS integral bridge, Proc. of 5th Int. Sym. on Earth Reinforcement (IS Kyushu 2007)

Koseki J, Bathurst RJ, Guler E, Kuwano J, Maugeri M (2006) Seismic stability of Reinforced Soil Walls, Proc. of 8th International Conference on Geosynthetics, Yokohama 1: 51-77

Tatsuoka F, Tateyama M, Uchimura T, Koseki J (1997) Geosynthetic-reinforced soil retaining walls as important permanent structures," Geosynthetic International 4(2): 81-136

Tatsuoka F, Koseki J, Tateyama M, Munaf Y, Horii N (1998) Seismic stability against high seismic loads of geosynthetic-reinforced soil retaining structures," Keynote Lecture, Proc. 6th Int. Conf. on Geosynthetics, Atlanta 1: 103-142

Tatsuoka F, Hirakawa D, Nojiri M, Aizawa H, Tateyama M, Watanabe K (2007a) A new type integral bridge comprising of geosynthetic-reinforced soil walls, Proc. of 5th Int. Sym. on Earth Reinforcement (IS Kyushu 2007)

Tatsuoka F, Hirakawa D, Nojiri M, Aizawa H, Tateyama M, Watanabe K (2008) Integral Bridge with Geosynthetic-Reinforced Backfill, the First Pan American Geosynthetics Conference & Exhibition, Cancun, Mexico

STUDY ON SEISMIC PERFORMANCE OF GEOGRID REINFORCED SOIL RETAINING WALLS AND DEFORMATION CHARACTERISTICS OF BACKFILL SOIL

S. Nakajima[1], K. Hong [2], S. Mulmi [3], J. Koseki [4], K. Watanabe [5] and M. Tateyama [6]

ABSTRACT: Based on results from a series of shaking table model tests on geogrid reinforced soil retaining walls, effects of material properties (i.e. pullout resistances, rupture strength and tensile rigidities) on seismic performance of reinforced soil retaining walls are discussed. Although the material properties of two geogrid models used in this study were largely different, residual displacements of wall facing were almost equal to each other. It is also attempted to obtain deformation characteristics of reinforced backfill soil from its dynamic responses and displacements of wall facing by assuming that the reinforced backfill would behave as one macro element.

KEYWORDS: shaking table model tests, material properties, deformation characteristics of reinforced backfill, geogrid

BACKGROUND

Geogrid reinforced soil retaining walls (RRW) having a full-height rigid wall facing showed higher seismic performance than conventional concrete retaining walls during recent earthquakes (Koseki et al. 2006). Due to ductile seismic performance of the reinforced soil retaining walls, it is requested to shift design procedure to performance-based design from conventional limit-equilibrium methods. In the performance-based design, seismic performance of retaining walls would be typically verified by confirming that the residual displacements do not exceed the allowable ones.

A series of shaking table model tests on the RRW has been conducted so as to investigate into their seismic behaviors (Watanabe et al. 2003). Based on an observation during the previous model tests, a procedure to predict residual displacements of the RRW, which considers shear deformation of the reinforced backfill and subsoil beneath the reinforced backfill, was developed (Koseki et al. 2004). In these model tests, however, a phosphor bronze strip was used as geo-grid model without referring to any similitude. Because use of the phosphor bronze as the reinforcement model made it possible to measure the tensile force during shaking. In addition to this, internal stabilities of the RRW were rather highlighted at the previous series of the model tests.

Based on the above background, effects of material properties of the geogrid models on seismic performance of reinforced soil retaining walls were firstly investigated in this study. Secondly, it is also attempted to introduce the deformation characteristics of the reinforced backfill into the proposed procedure to predict residual displacements of the reinforced soil retaining walls.

GEOGRID MODEL

Two types of geogrid models were used in this study. For the one type of the model, which will be called as PB hereafter, phosphor bronze strips having a width of 3 mm and a thickness of 0.1 mm were prepared in a lattice shape, and their cross points were fixed by soldering as shown in Fig. 1. Sand particles were pasted on the surface of the reinforcement PB so as to mobilize the frictional resistances effectively. For the other type of model as also shown in Fig. 1, a polyester mesh sheet having a thickness of 0.6 mm and a mesh size of 3 mm was used. The latter model will be called as PE hereafter.

MATERIAL PROPERTIES OF GEOGRID MODELS

Pullout tests and direct tension tests were carried out (Nakajima et al. 2007) so as to compare the material properties of the geogrid models. Test apparatuses for

[1] Student, Department of Civil Engineering, University of Tokyo, JAPAN. Email:s-nakaji55@pwri.go.jp
[2] Student, Department of Civil Engineering, University of Tokyo, JAPAN. Email:hkimhor@iis.u-tokyo.ac.jp
[3] Student, Department of Civil Engineering, University of Tokyo, JAPAN. Email:smulmi@iis.u-tokyo.ac.jp
[4] Professor, Institute of Industrial Science, University of Tokyo, JAPAN. Email:koseki@iis.u-tokyo.ac.jp
[5] Assistant Senior Researcher, Foundation and Geotechnical Engineering, Railway Technical Research Institute, JAPAN. Email:nabeken@rtri.or.jp
[6] Head, Foundation and Geotechnical Engineering , Railway Technical Research Institute, JAPAN. Email:tate@rtri.or.jp

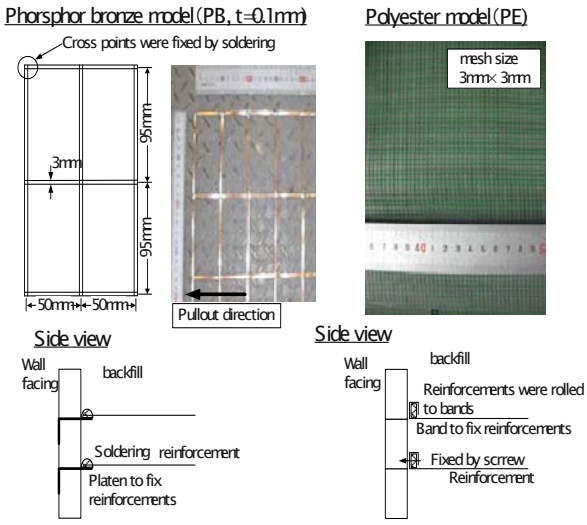

Fig. 1 Geogrid models

pullout tests are shown in Fig. 2. A specimen of the reinforcement model having a width of about 27 cm and a length of 50 cm (the total length including the portions in air was about 90 cm) was placed on a model ground consisting of air dried dense Toyoura sand having a relative density of about 90%. Density of the model ground in pullout tests was set equal to the backfill layers in the shaking table model tests which will be discussed later.

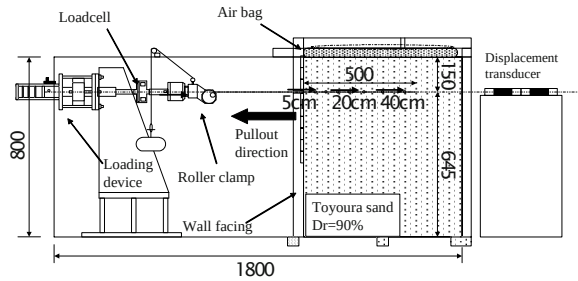

Fig. 2 Apparatuses for pullout test (unit in mm)

So as to simulate the stress state of the backfill layers in shaking table model tests, overburden pressures of the pullout tests were set equal to 5 kPa (middle height of the backfill) and 10 kPa (bottom of the backfill). In Fig. 3, pullout resistances are plotted versus the pullout displacement measured at a distance of 5cm from the wall facing. With increase in the overburden pressure, the peak resistance T_{peak} increased in case of the model PE. Rupture of the phosphor bronze strips occurred at the pullout resistance of about 800 N in case of the model PB (t=0.1 mm). Test result on the model PB (t=0.2 mm) having a different shape and thickness (Nojiri et al. 2007) is also plotted in Fig. 3. The peak pullout resistance of the model PB (t=0.1 mm) was thought to be lower than that of the model PE by referring to the test results on the model PB (t=0.1 mm) although the shapes and the test conditions were slightly different.

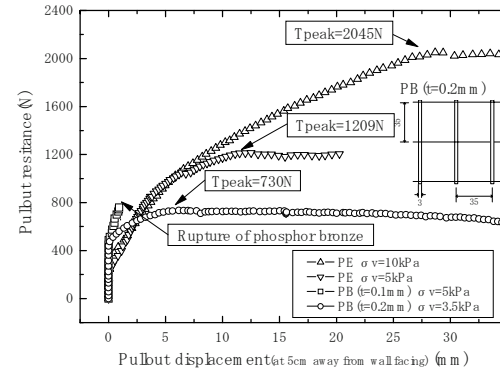

Fig. 3 Comparison of pullout resistances

To evaluate the rupture strength and tensile rigidity of the geogrid models, direct tension tests of the geogrid models were conducted. The width of the geogrid model in the direct tension tests was set equal to 5 cm in case of the model PE, while one strip having a width of 3 mm was tested in case of the model PB for the convenience of the test preparation. Constant strain rate loading of 1%/min was applied in both cases. Tensile loads that are converted to the values per unit width are plotted versus the tensile strain in Fig. 4. Rupture strength Te(peak) are also indicated in Fig. 4. The rupture strength of the model PE was about eight times larger than the ones of the model PB because the number of the strips parallel to the tensile direction of the model PE was much larger than that of the PB.

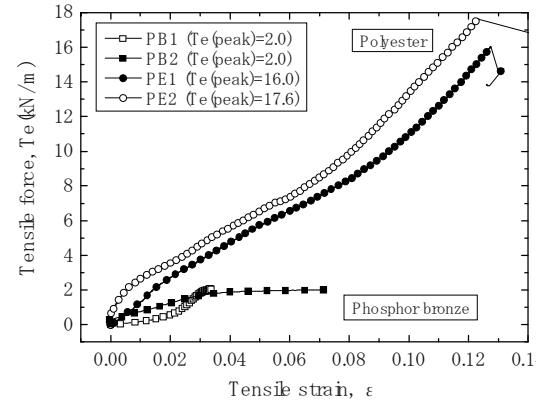

Fig. 4 Results from direct tension tests

Equivalent tensile rigidities per unit width and single strip of the two models, when the Te (peak) values and half of them were mobilized, are summarized in Table 1. The values of tensile rigidity of single strip of the model PB were larger than those of the model PE made of polyester, while the values per unit width of the model PE were larger than those of the model PB due to larger number of the strips of the model PE.

Table 1 Comparison of tensile rigidities

	Te(peak)/2 (kN/m)	Te(peak) (kN/m)	Te(peak)/2 (kN/strip)	Te(peak) (kN/strip)
	Per unit width		Per single strip	
PE1	120.5	143.1	0.36	0.43
PE2	105.1	130.0	0.31	0.39
PB1	65.7	60.5	65.7	5.25
PB2	65.7	29.0	65.7	2.52

MODEL TEST PROCEDURE

As shown in Fig. 5, two models of the geogrid reinforced soil retaining walls PE and PB were tested in this study. They had a height of 500 mm and they were placed on a horizontal subsoil layer having a thickness of 200 mm. During preparation of the backfill layers, the two geogrid models were fixed with the wall facing at a vertical spacing of 50 mm as shown in Fig.1. The cross section of the reinforced soil retaining wall model with different arrangements of reinforcements (R1, Watanabe et al. 2003) is also shown in Fig. 5. Deformation characteristics of the reinforced backfill of the test R1 will be compared with the ones from this study later. Both the subsoil and backfill layers consisting of air dried Toyoura sand having a relative density of about 90% were prepared by air pluviation using a sand hopper.

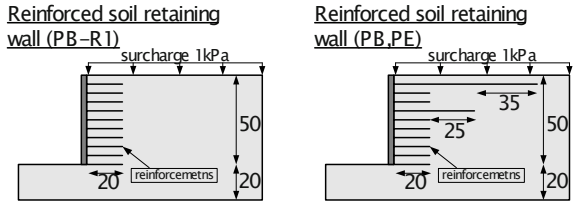

Fig. 5 Cross sections of models (unit in cm)

Seismic loads were applied by shaking the soil container horizontally with irregular waves as typically shown in Fig.6, while the maximum base acceleration was gradually increased from 0.9 G to 1.5 G at an increment of about 0.3 G. The final shaking step having the maximum acceleration of about 1.5 G was applied twice in both tests.

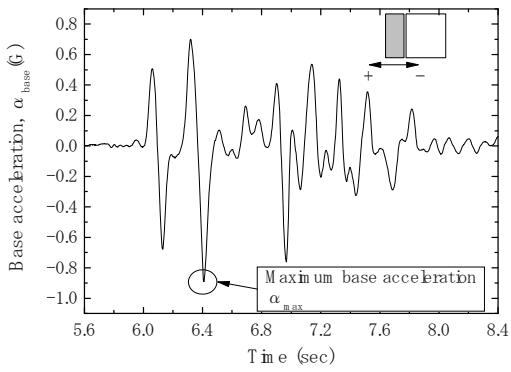

Fig. 6 Typical time history of base acceleration

RELATIONSHIP OF RESIDUAL DISPLACEMENTS AND MATERIAL PROPERTIES

Residual displacements after each shaking step are plotted versus the maximum base acceleration in Fig. 7. Sliding displacement, tilting angle of the wall facing, and settlement of the backfill layers at the horizontal distances of 100 mm from the wall facing are concerned as the representative residual displacements in this study.

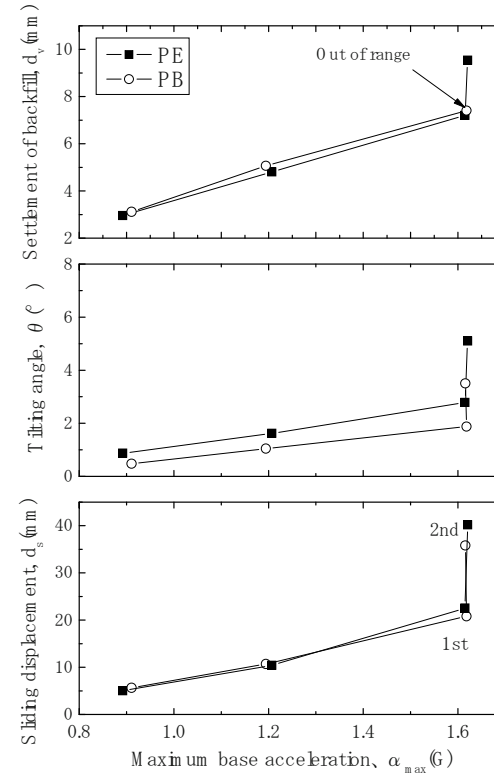

Fig. 7 Comparison of residual displacement

Seismic performances of the two reinforced soil retaining walls were similar to each other even though the material properties like pullout resistances, rupture strength and tensile rigidity were largely different from each other. Tilting angle of the wall facing of the model PB was slightly smaller than that of the model PE, while larger mobilized resistances could be expected with the model PE according to the aforementioned test results from the pullout tests and direct tension tests.

It was observed in previous model tests on reinforced soil retaining walls that the sliding displacement of the wall was induced by the shear deformation of the subsoil beneath the reinforced backfill, and tilting of the wall was induced by the shear deformation of the reinforced backfill. Sliding displacements of the two model tests were almost similar to each other because the subsoil conditions were the same in this study.

On the other hand, tilting angle of the model PB was smaller than that of the model PE. Two factors might

have affected this behavior. Firstly, the shear deformation of the reinforced backfill itself of the model PB was larger than that of the model PE. Possibly because the rigidity of the reinforced backfill of the model PB would be lower than that of the model PE by referring to the tensile rigidity as compared in Table 1. Secondly, tilting of the wall facing due to the shear deformation of the reinforced backfill was restricted by the pullout resistances of the reinforcement having the length of 45 cm and 80 cm. Pullout resistance of the model PB before its rapture was higher than those of the model PE as shown in Fig. 3. Based on the observation that tilting angle of the model PB was lower than that of the model PE, the latter factor seems to overcome the former factor in this study.

DEFROMATION CHARACTERISTICS OF REINFORCED BACKFILL

As discussed above, deformation characteristics of the reinforced backfill are important in evaluating the seismic performance of the reinforced soil retaining walls. Based on the model test results, shear stress-strain responses of the reinforced backfill were computed so as to develop a procedure to evaluate residual displacement of the reinforced soil retaining walls.

Shear deformation of the reinforced backfill considered in this study is schematically illustrated in Fig. 8. Shear forces acting on the reinforced backfill can be computed as a sum of inertia force from dynamic responses of the reinforced backfill measured by accelerometers installed in the backfill layers. Shear stress of the reinforced backfill was computed by normalizing the shear force computed at the bottom of the reinforced backfill with its area of the reinforced backfill as shown in Fig.8. Acceleration records at the middle height of the reinforced backfill were used to evaluate the shear force in this computation. As also illustrated in Fig.8, averaged shear strain of the reinforced backfill can be regarded as the tilting angle of the wall facing by assuming that the reinforced backfill would deform uniformly as one macro element.

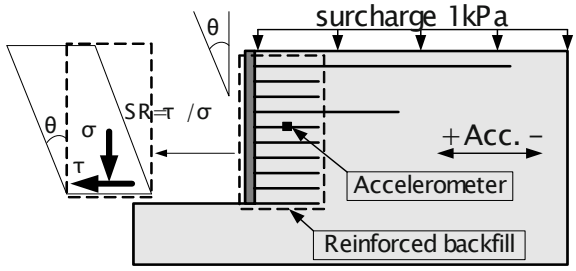

Fig. 8 Schematic diagram of shear deformation of reinforced backfill

Shear stress ratio, which is defined as the shear stress normalized by the overburden pressure at the bottom of the reinforced backfill, is plotted versus the shear strain in Figs. 9 to 11. The overburden pressure was assumed to be constant by neglecting the effect of vertical inertia forces for simplicity in this computation. As shown in Fig. 8, mobilization of the positive shear stress ratio means that the reinforced backfill was subjected to the inertia force to the active direction. Fig. 9 shows stress-strain relationship of the reinforced backfill in case of the test R1 which didn't have extended reinforcements. The cross section of the model ground in the test R1 was the same as those of the tests PB and PE while the shaking by using the

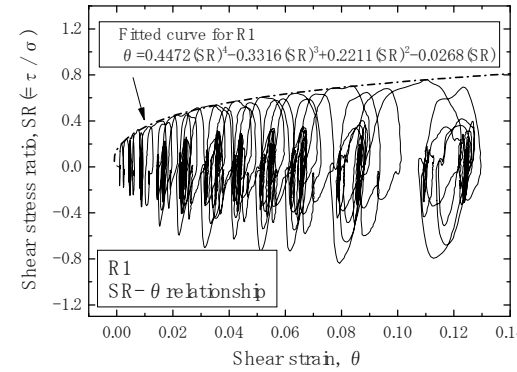

Fig. 9 Stress-strain relationship in test R1

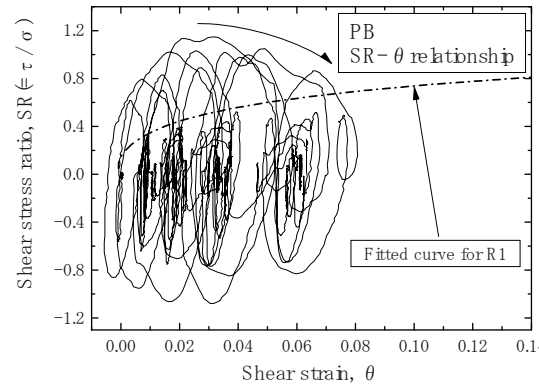

Fig. 10 Stress-strain relation ship in test PB

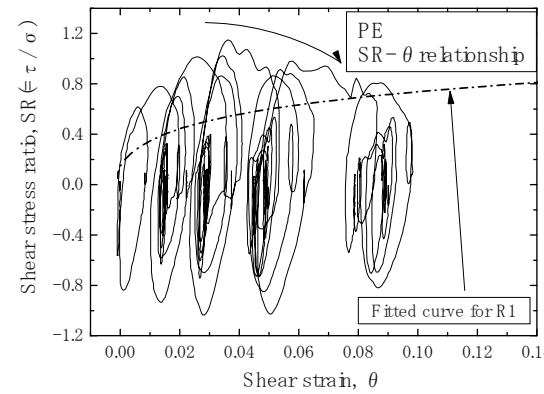

Fig. 11 Stress-strain relation ship in test PE

irregular waves, which are typically shown in Fig. 6, was cyclically applied at the maximum acceleration of about 100 gals to 1100 gals with its increment of about 100 gals. Figs. 10 and 11 show the stress-strain relation ships of the test PB and PE respectively.

It was found from Figs.9 to 11 that the shear strain was accumulated while the positive shear stress ratio (i.e. inertia force toward the active direction applied to the backfill) was mobilized. As also indicated in Figs. 10 and 11, the mobilized values of SR were reduced after the peak value was exhibited in case of the tests PB and PE. Strain softening behavior might have affected these behaviors because shaking in the tests PB and PE was continued even after failure plane formed at just outside of the uppermost reinforcement in un-reinforced backfill as typically shown in Fig. 12. It was also observed in Fig. 12 that the reinforced backfill exhibited the uniform shear deformation as assumed in this computation.

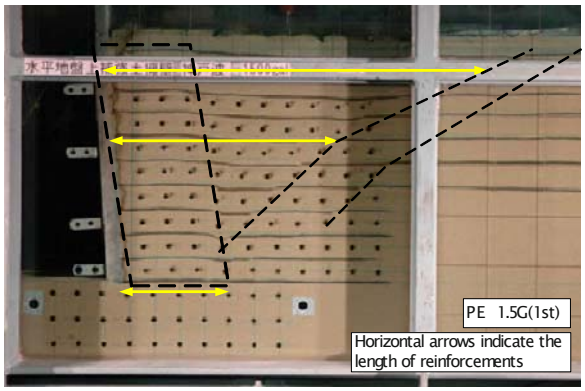

Fig. 12 Photo taken after the shaking at 1.5G(1st) in the test PE

Upper bound of the stress-strain relationship of the test R1 was fitted by using polynomial equation as shown in Fig. 9. This fitted curve of the test R1 is also shown in Figs. 10 and 11. As clearly shown in Fig.10 and 11, mobilized shear stress ratio by the tests PB and PE exceeded the fitted curve of the test R1. Pullout resistances by extended reinforcements were thought to be mobilized due to shear deformation of the backfill in these tests. In further study, the effects of the extended reinforcements should be properly taken into account.

SUMMARY

Results of this study can be summarized as follows:

1) Seismic performance of the reinforced soil retaining walls by using different two geo-grid models was almost equal to each other although the material properties of the geogrid models were largely different.
2) Tilting angle of wall facing in the test PB was smaller than that of the test PE although larger resistances could be expected by the test PE.
3) Larger pullout resistances mobilized by the model PB at relatively small pullout displacements range would work effectively to reduce the tilting angle of wall facing although the peak pullout resistance of the model PB was smaller than that of the model PE.
4) Stress-strain relationships of the reinforced backfill can be computed based on measurements of dynamic response of the reinforced backfill and tilting angle of the wall facing, while effect of the pullout resistances of extended reinforcements should be properly introduced in further study.

REFERENCES

Koseki J, Bathurst RJ, Guler E, Kuwano J, Maugeri M (2006) Seismic stability of reinforced soil walls, Keynote lecture, Proc. of the 8th International Conference of Geosynthethics, Proc. of the 8ICG 1: 51-78

Koseki J, Kato N, Watanabe K, Tateyama M (2004) Evaluation of seismic displacement of Reinforced walls, Proc. of the 3rd Asian Regional Conference on Geosynthetics: 217-224

Nakajima S, Hong K, Mulmi S, Koseki J, Watanabe K, Tateyama M (2007) Model tests on seismic performance of geo-grid soil reinforced soil retaining walls by using different geo-grids, International Workshop on Earthquake Hazards and Mitigations (EHAM2007)

Nojiri M, Aizawa H, Nishikiori D, Sasada Y, Hirakawa D, Tatusoka F (2007) Effects of pullout resistance on performance of geosynthethics reinforced-soil structure (in Japanese), 42nd Japan National Conference on Geotechnical Engineering: 1573-1574

Watanabe K, Munuf Y, Koseki J, Tateyama M, Kojima K (2003) Behaviors of several types of model retaining walls subjected to irregular excitation, Soils and Foundations 43 (5): 13-27

Proceedings of the 4th Asian Regional Conference on Geosynthetics
June 17 - 20, 2008 Shanghai, China

DEVELOPMENT OF REINFORCED EARTH WALL SYSTEM WITH STEEL-FRAMED FACING

S.D. Cho[1], K.W. Lee[2], J.H. Kim[3], C. Choi[4] and C.W. Seo[5]

ABSTRACT: This paper introduces a recently developed reinforced retaining wall system. The new system incorporates a steel-framed facing that might be assembled on-site and steel strip or geogrid type reinforcements for backfill area. In order to enhance scenery view design of earth wall construction, dual-structured facing is proposed in which 135mm room for planting space locates in the front of facing. A reinforced earth walls using the proposed system was constructed to verify constructability of the proposed system and facing movement and tensile characteristics of reinforcement were measured to understand the mechanical behavior. In this paper, details of the proposed system are described and test results for field measurements are discussed.

KEYWORDS: steel-framed facing, steel strip reinforcement, field pilot construction, field measurement, reinforced earth wall

INTRODUCTION

Reinforced-earth system has been popularized since its introduction to Korean civil engineering society in early 1980's (Cho et al. 1985). Among others its cost-saving, scenic-view, and handy-construction are cardinal features in which the system had led its wide applications and construction markets. Since the first pilot construction of the reinforced-earth system using zinc-galvanized steel bar the specific feature of South Korea (nearly 70% of land are mountainous area) brings such a wide use of the system to expand our residential/ industrial area (Cho & Shin 1999).

Nowadays, the increased use of reinforced-earth wall for the purpose of obtaining more land brings several additional demands such as environmental-friendly, better stable and constructible, and economical system. Besides others environmental or better view is the key issues to be considered and resolved.

This paper introduces a recently developed reinforced retaining wall system with consideration of the current demands. The new system incorporates a steel-framed facing that might be assembled on-site and steel strip or geogrid type reinforcements for backfill area. In order to enhance scenery view design of earth wall construction, dual-structured facing is proposed in which 135 mm room for planting space locates in the front of facing. Details on the new system and pilot construction are described in this paper.

A NEW MSEW SYSTEM DESCRIPTION

This section describes a new MSEW system, components, and its assemblage and construction. MSEW system generally consists of facing wall, reinforcement, and backfill. Steel-framed reinforced earth wall, referred to as SFREW hereafter, developed in this work provides a role of facing wall. However, the way of framework for SFREW is a distinguished factor to that of conventional facing wall. SFREW holds high gravity because it is filled with granular soil within frames while the conventional ones such as panel- and block-type facings has less vertical weight due to its light weight. As a consequence SFREW provides higher overturning and shear resistance against active driving force. The new facing system also requires a new method to connect between the facing and reinforcing materials (KICT 2007).

[1] Research Fellow, Geotechnical Engineering Research Dept. Korea Institute of Construction Technology, 2311 Daewha-Dong Ilsan-Gu Goyang-Si Gyeonggi-Do, 411-712, KOREA
[2] Researcher, Geotechnical Engineering Research Dept. Korea Institute of Construction Technology, 2311 Daewha-Dong Ilsan-Gu Goyang-Si Gyeonggi-Do, 411-712, KOREA.
[3] Senior Researcher, Geotechnical Engineering Research Dept. Korea Institute of Construction Technology, 2311 Daewha-Dong Ilsan-Gu Goyang-Si Gyeonggi-Do, 411-712, KOREA.
[4] Senior Researcher, Geotechnical Engineering Research Dept. Korea Institute of Construction Technology, 2311 Daewha-Dong Ilsan-Gu Goyang-Si Gyeonggi-Do, 411-712, KOREA. E. chchoi@kict.re.kr
5 Manager, R&D Section, Dong-A Steel Technology Co., Ltd.

Steel-framed Wall Facing

Fig. 1 presents a schematic of the steel-framed wall facing consisting of front column, connector, back screen, bracing, and back column. All steel components are designed to provide enough structural stability when they are subjected to vertical and horizontal stress after construction. The shape and dimension of the components are shown in the figure. Yield strength and allowable tensile strength of the steel are 2400 kg/cm^2 and 1400 kg/cm^2, respectively, and the thickness is 4.5 mm. F10T M16 steel bolt is used to assemble the system and 550 g/cm^2 of zinc are coated to protect the corrosion of steel. Fig. 2 is a schematic of back view for the facing. Again, the location and spacing of the steel components are designed with the consideration of structural stability during its performance.

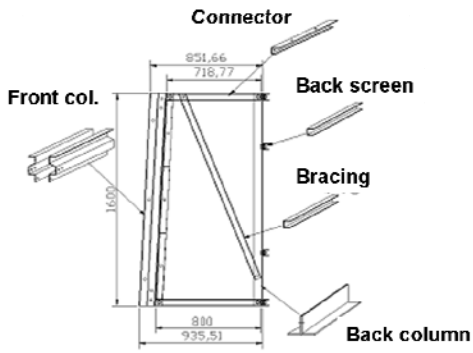

Fig. 1 Steel-framed facing wall components (dimensions in mm)

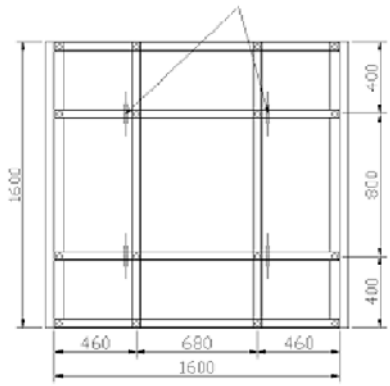

Fig. 2 Schematic back-view of steel-framed facing (dimensions in mm)

Fig. 3 shows a schematic of SFREW system including facing, reinforcement, connection between facing and reinforcement, and backfill. Front of the facing wall inclines three degree and back is vertical. Both of steel strip and geogrid-type reinforcement are attachable to the facing and 0.8 m spacing resides for reinforcement within 1.6 m(height)×1.6 m(width) size unit. The front facing is dual-structured for planting area and it provides a better earth wall system in terms of scenery view design.

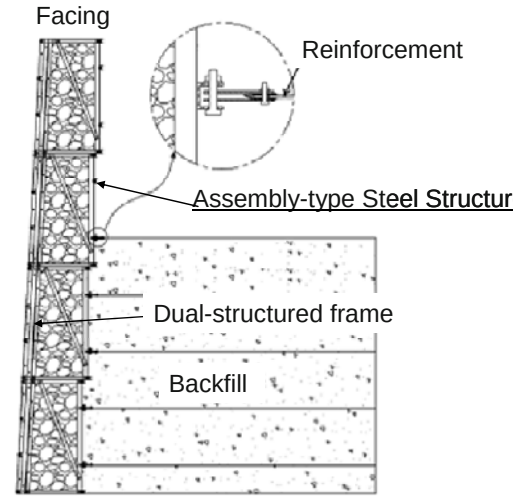

Fig. 3 Construction schematics of SFREW including facing, connection between facing and reinforcement, backfill, and dual-structured facing

Reinforcements

As described before SFREW system can be formed both of steel strip and geogrid reinforcement. However, this section focuses on the developed steel strip in this work.

The steel strip developed here has dimension of 65 mm(width)×4.5 mm(thickness) and punching holes of D=11 mm in every 50 cm spacing. As punching to create hole, approximately 2 mm rising around perimeter of holes is formed. The holes play two roles in that the rising increases frictional resistance between backfill material and strip, and the horizontal steel-bar is laid to improve tensile pullout resistance as shown in Fig. 4. In the meanwhile, the facing wall and steel-strip are connected via mechanical bolting between ㄷ-type back screen and D=11mm punching hole as shown 'Detail A' in Fig. 5. Double-steel strip for the 150 mm area from the back screen are used to improve connection strength. Regarding the horizontal steel-bar, 2－3 bars are recommended to lay out for each reinforcing layer.

In the stability point of view for SFREW the performance of reinforcement in its life span is a key issue. In general long-term design strength T_a is estimated for the design of MSEW system and it is compared to required maximum tensile strength as a reinforcement T_{max} for the evaluation of long-term stability analysis. The long-term design strength T_a of steel strip is obtained using Eq. 1.

$$T_a = 0.55\frac{F_y A_c}{S_h} \quad (1)$$

where F_y, A_c, are S_h yield strength (k/Nm^2), effective area (m^2), and horizontal spacing of reinforcing strip (m), respectively. Table 1 presents properties and long-term tensile strength of zinc-coated steel strip proposed in this study. Zinc-coating has the developed steel-strip to be anti-corrosive and the minimum thickness of coating is to be 86μm for normal condition (140 μm for submerged condition) or 610 g/m^2 in accordance to FHWA(2001) and AASHTO M-111, respectively.

Table 1 Mechanical properties of zinc-coated steel strip

Type	F_{fail} (kN)	T_a (kN/m) 75yr	100yr	Width (mm)	Thick (mm)	Zinc-Coat (μm)
Steel-strip	104	49.00	39.47	65	4.5	86 (normal) 140 (submerged)

Fig. 4 Developed steel-strip with punching holes and horizontal steel bar

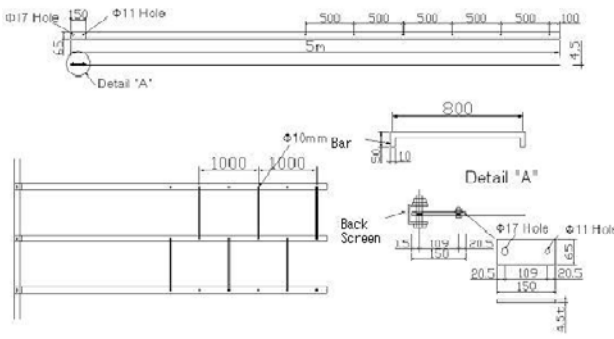

Fig. 5 Schematic of developed steel-strip and its connection to facing (dimension in mm)

Backfill Materials

Type of backfill material corresponds to FHWA (2001) recommendation as given in Table 2. Gradation limits of the table are determined by AASHTO T-27.

Table 2 Backfill material

U.S Sieve Size	Percent Passing
4 in (102 mm)	100
No. 40 (0.425 mm)	0—60
No. 200 (0.075 mm)	0—15
Plasticity Index (PI) < 6	

SFREW PILOT FIELD CONSTRUCTION AND TEST

To verify the field applicability of proposed SFREW system pilot wall with six steps of steel frame (9.6 m in height) together with three meter top-fill was constructed and overall behavior of the wall was evaluated.

Pilot Field Construction

Pilot construction took place at unoccupied land located Whasoongun, Junranamdo. Fig. 6 shows a schematic cross-sectional view of SFREW with geo-logical information. Reinforcing strips were vertically layered with 80 cm spacing. The strip length was designed based on the guidelines given in FHWA (2001) and Korea Geotechnical Society (1998). The 5 m-long strips were installed regardless of the vertical location.

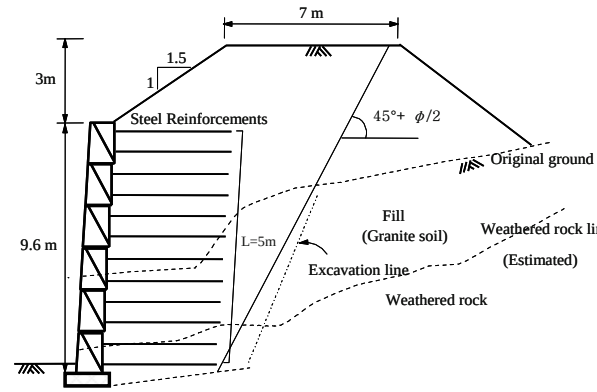

Fig. 6 Cross-sectional view of SFREW pilot field construction.

Field site-exploration indicated that 0.5 m—5 m fill lies on top of the weathered rock layer as shown in Fig. 6. The fill is classified to SP according to USCS and the weathered rock is relative weak in that a bucket of hoe is able to break down the layer. Based on such field exploration results, it is indicated that the unoccupied land was excavated for a certain purpose of land-use. The excavated weathered soils were recycled for backfill material of the wall.

Fig. 7 presents photographs of main construction stage for SFREW and they are: (a) steel-framed facing

wall installation, (b) reinforcing and backfill, (c) compaction of backfill, (d) sensor installation for the evaluation of SFREW behavioral characteristics, (e) placement of reinforcing steel-strip, and (f) front-view of the wall after construction. Facing movement, active earth pressure acting toward facing, and tensile extension of reinforcement were measured along elapsed time during and after construction.

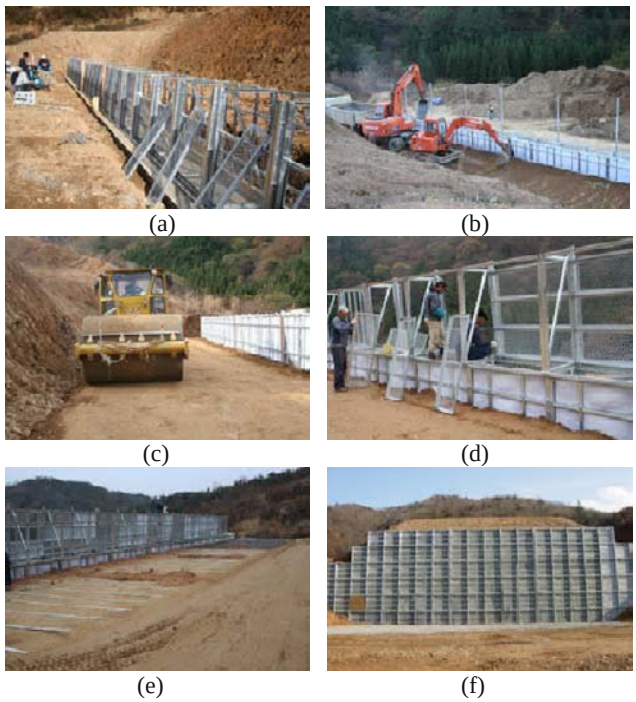

Fig. 7 Photographs of SFREW construction: (a) steel-framed facing installation, (b) reinforcing and backfill, (c) compaction, (d) sensor installation, (e) steel-strip reinforcement, and (f) post-construction view

Field Behavior of SFREW System

A series of field measurement were carried out to understand the stability issue and behavioral characteristics of SFREW. Measured behavioral characteristics include facing movement, active earth pressure acting toward facing, and tensile extension of reinforcement.

Fig. 8 presents the measured facing movements with construction stages and certain time periods when the steel-strip was used for reinforcing backfill area. It is indicated in the figure indicates that the most displacement occurred in the middle of construction in that blue diamond line covers more than 50% of total displacement after 60 days of construction along all vertical section. It is also noted that the displaced shapes of facing for all stages are very similar. It again leads the conclusion that the displacement occurred in the middle of construction dominates the overall behavior of the wall. Maximum displacement of the wall was measured to be 50.8 mm which corresponds to 0.0053 H. In general 0.03 H is an allowable horizontal movement to be safe against overturning. It is concluded that SFREW provide a stable reinforced earth system. Even though details on geogrid reinforcement were not given in this paper, pilot construction and measurements were carried out for SFREW with geogrid reinforcement and facing movement along construction stages are shown in Fig. 9. Maximum movement of geogrid section was measured to be 78.4 mm and 0.0082 H. While SFREW with geogrid reinforcement also provides satisfactory performance comparing to allowable horizontal move-ment 0.03 H, it is noted that SFREW with steel-grid causes less wall movement than that with geogrid.

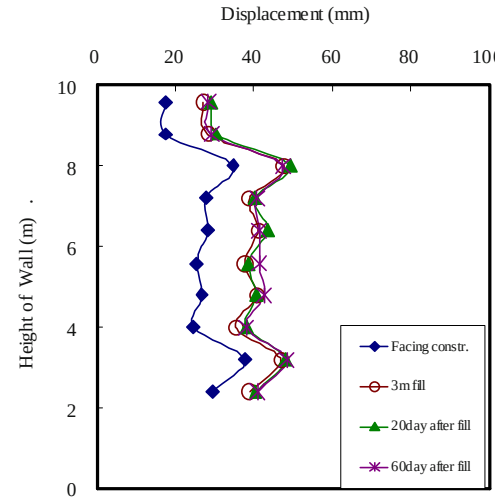

Fig. 8 Facing movement of SFREW with steel-strip reinforcement during and after certain time periods of construction

Even though the measured strain characteristics in steel-strip are not presented in graphical form here, they are measured for each layer at several locations behind the wall. Results showed that maximum induced tensile stresses were less than 16.7 t/m for all locations which corresponds to 34% of long-term strength (75 year) and it was not increased after construction. Based on this observation it is proven that the developed reinforced steel-strip is field applicable and mechanically stable. The fact that induced tensile stresses were not increased after construction may be a coincident phenomenon to the results of facing movement as described before.

In the meantime, MSEW tends to move outward due to active earth pressure, which causes the tensile stress in reinforcement to be induced. From the field observation SFREW system leads relatively small tensile stresses to be induced. It brings us to conclude that the proposed steel-strip develop good reinforcing effect together with backfill soils.

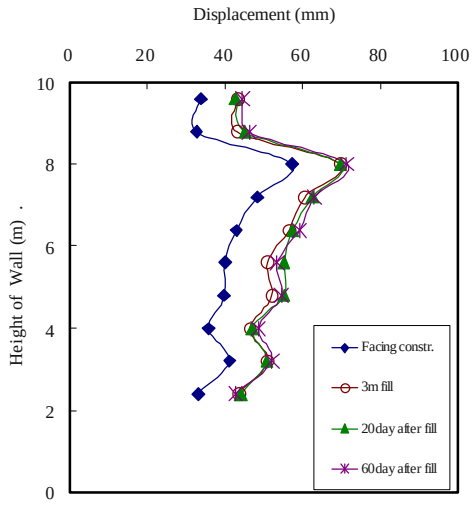

Fig. 9 Facing movement of SFREW with geogrid reinforcement during and after certain time periods of construction

Scenery View of SFREW

As discussed earlier, environmental-friendly or scenery view is another important challenge for the development of new reinforced earth-wall system. It was described in Fig. 3 that SFREW has a capability to provide a room for planting zone via dual-structured facing frame. Rather than lengthy explanation, Fig. 10 shows how the system makes scenery view to be possible. It may adopt wood cover in front or let any kinds of planting to feed because of openings. This feature gives a designer to establish better view or environmental-friendly earth wall system.

Fig. 10 Scenery view of SFREW

CONCLUSIONS

In this paper a recently developed reinforced retaining wall system was discussed. The new system incorporates a steel-framed facing for on-site assemblage and steel-strip reinforcement. In order to enhance scenery view design of earth wall construction, dual-structured facing is designed in which 135 mm room for planting space locates in the front of facing. A reinforced earth wall using the developed system was constructed to verify constructability of the proposed system and facing movement and tensile characteristics of reinforcement were measured to understand the mechanical behavior.

The maximum facing movement and developed tensile stress in steel-strip were 0.0053 H and 34% of ultimate long-term strength (75 year), respectively. Based on these observations, it is concluded that the new system is safe against overturning and the steel-strip is good to develop enough reinforcing effect together with backfill soils. Correspondingly, it is verified that the new facing and steel reinforcing strip provide stable and environmental-friendly reinforced earth wall system. As a cardinal feature, it must be noted that the dual-structured facing gives flexibility for a designer to handle better scenery view.

ACKNOWLEDGEMENTS

This work was supported by Dong-A Steel Technology Co., Ltd. The authors are grateful for the support.

REFERENCES

Cho SD, Cho JG, Hong SW (1985) A Study on Geo-textiles and Reinforced Earth Method, KICT 84-W-1, Korea Institute of Construction Technology

Cho SD, Shin EC (1999) Application of Geosynthetics and Earth Reinforcement Techniques in Korea, Special Volume for the Proceedings of the 11th ARC on Soil Mechanics and Geotechnical Engineering, Earth Reinforcement Technique in Asia, ISSMGE-TC9: 43-50

FHWA (2001) Mechanically Stablized Earth Walls and Reinforced Soil Slopes Design and Construction Guidelines. Publication No. FHWA-SA-96-071

KICT (2007) Enviroment-Friendly Reinforced Soil Wall using Assembly-Type Steel Structure. Research Report. Korea Institute of Construction Technology. KICT2007-010. Written in Korean

KGS (1998) Geosyntethic Design and Construction, Korea Geotechnical Society. Gumiseokwan. Written in Korean

GEOGRID REINFORCED SEGMENTAL RETAINING WALL FOR NH5, DHARMAVARAM TO TUNI, ANDHRA PRADESH, INDIA

T.W. Yee[1] and P. Dutta[2]

ABSTRACT: The NH5 is a 1,000 km long highway passing mostly through Andhra Pradesh, connecting Chennai with Kolkata via short stretches of NH60 and NH6. The Dharmavaram-Tuni Package involves a 47 km long four-lane highway that is part of the Vijayawada to Vishakhapatnam Section of NH5. Construction of the geogrid reinforced segmental retaining wall for this project was carried out at four different locations along the highway. The total constructed wall facing area was approximately 25,000 m^2, with wall heights of up to 13.6 m. The fascia units used were 200 mm high, proprietary, dry cast concrete segmental units with smooth faced finish. A total of 142,000 m^2 of polymer coated high tenacity polyester geogrids were used as soil reinforcement in the construction of the segmental retaining walls.

KEYWORDS: highway, geogrid, reinforced soil, segmental retaining wall

INTRODUCTION

According to an Asian Development Bank (ADB) report in 2002, India has about 3.3 billion km of roads. It is reputed to have the second largest land transportation network in the world. India's road network consists of three categories:

- 58,000 km of national highways;
- 119,000 km of state highways/roads and
- 3,122,000 km of rural roads.

While national highways account for less than 2% of the total network in terms of length, they carry about 40% of the total traffic in India. National highways are managed by two agencies; the National Highways Authority of India (NHAI) and the Ministry of Road Transport and Highways (MORTH). NHAI was established in 1988 and operationalized in 1995 as an operating arm of MORTH. NHAI is responsible for one fourth of the national highways which carry around 25% of the nation's total traffic, while MORTH is responsible for the remaining three fourths of national highways which carry around 15% of India's total traffic.

India's economy has long suffered a chronic capacity shortage of its highway system (ADB 2002). The majority or 59% of the national highway systems is of two-lane standard while 39% is of single-lane standard and 2% is of four-lane or higher standard (ADB 2002). Faced with this inadequate capacity, the Government of India has decided to launch the radical US$13 billion National Highways Development Program of upgrading key national highway corridors, consisting of

- 6,000 km of the golden quadrilateral,
- 4,000 km of the north-south corridor, and
- 3,300 km of the east-west corridor.

The National Highway No. 5 (NH5) is a 1,000 km long highway passing mostly through Andhra Pradesh and links Chennai with Kolkata. Fig. 1 shows road network of National Highways Development Project and layout of NH5 from Chennai with Laxmanath where short stretches of NH60 and NH6 connect the highway with Kolkata.

Fig. 1 Road network of National Highways Development Program and layout of NH5 (NHAI)

[1]Sales and Marketing Manager, Ten Cate Industrial Zhuhai Co. Ltd., HongKong. CHINA. Email: tw.yee@tencate.com
[2]General Manager, Z-Tech India Ptv Ltd, INDIA. Email: pdutta24@hotmail.com

DHARMAVARAM-TUNI PACKAGE

Andhra Pradesh

Andhra Pradesh is a state in India that is situated on the southern portion of the Deccan plateau which is one of the oldest geological formations in India. The Eastern Ghats, a discontinuous mountain range that borders the southeastern edge of the Deccan Plateau, runs parallel to the eastern coastline facing the Bay of Bengal. The coastal plains lie between the Eastern Ghats and the Bay of Bengal. The mighty Godavari and Krishna rivers cut their way through the Deccan Plateau and the Eastern Ghats, forming large deltas before entering the Bay of Bengal. It is the fifth largest state in India in area (276,754 km^2) and population (about 74 million). It has the largest coastline (970 km) in India.

Project Location

The Dharmavaram-Tuni package is located in the district of East Godavari, situated northeast in the state of Andhra Pradesh. The geology of the area is generally Pre-Cambrian while the Godavari River valley area is Recent and Pleistcene. The landform in East Godavari can be broadly classified into three natural divisions; the delta, the upland, and hill tracts. Soils are alluvial in the deltas of the Godavari River. Red loamy soil is found in upland and hill areas. The climate of the area is classified as Tropical wet and dry. The temperature reaches a maximum of 48℃ from April to June and is moderate for the rest of the year. The average annual rainfall of the district is around 1,280mm.

The Dharmavaram-Tuni Package involves 47 km of four-lane highway from 253 km to 300 km of the Vijayawada to Vishakhapatnam Section of the NH5 (Kumar 2004) through upland areas. Fig. 2 shows the layout of the NH5 from Rajahmundry to Tuni which constitute two construction packages i.e. Rajahmundry-Dharmavaram Package and Dharmavaram-Tuni Package. The project area is affected by cyclones from the Bay of Bengal during the months of November and December with maximum wind speeds close to 50 m/s.

Project Brief

The Dharmavaram-Tuni Package was essentially a road upgrading project. The highway was widened to four lanes. Retaining walls up to maximum height of 13.6 m were constructed to allow widening of the embankment approach to the enlarged Tuni Road-Over-Bridge (ROB). Three new Vehicular-Under-Passes (VUP's) were created along the highway package that involved construction of retaining walls; of which two have maximum heights of 7.8 m while the third has a maximum height of 8.4 m.

Fig. 2 Layout of NH5 from Rajahmundry to Tuni

PROPOSED WALL SYSTEM AND DESIGN

The wall system proposed by the contractor for the NH5, Dharmavaram-Tuni Package was a geogrid reinforced segmental retaining wall system, selected for a variety of reasons which included conformance to project definition, economics, aesthetics as well as proven track record in India.

Fascia Unit

The fascia unit used in the construction of the segmental retaining wall for the NH5, Dharmavaram-Tuni Package is a proprietary design. The unit is a dry cast concrete module, smooth beveled face of height 200 mm and width 450 mm. On plan, it looks like the alphabet 'I' with an enlarged top flange, of an alphabet height of 300 mm. The bottom of the fascia unit has an anchor bar to improve inter-unit shear resistance. Each fascia unit weighs approximately 35 kg. The fascia units are stacked to achieve a vertical inclination of 1 in 40.

Geogrid Reinforcement

The reinforcement used in the construction of the segmental retaining wall for the NH5, Dharmavaram-Tuni Package is a polymer coated high tenacity geogrid. Three different grades of tensile strength were used for the design of the retaining walls of this project. Fig. 3 shows the geogrid laid out and sandwiched between courses of fascia units.

Table 1 Allowable long term design strength of geogrids used for NH5, Dharmavaram-Tuni Package

Property of geogrid	Strength of geogrid	Partial factor	Geogrid Type 1	Geogrid Type 2	Geogrid Type 3
Ultimate tensile strength	T_u (kN/m)		60	100	120
Long term creep		f_{mc}	1.67	1.67	1.67
Construction damage		f_{md}	1.13	1.05	1.05
Environment degradation		f_{me}	1.1	1.1	1.1
Allowable long term design strength, $T_a = T_u / (f_{mc} \times f_{md} \times f_{me})$	T_a (kN/m)		28.9	51.8	62.2

Fig. 3 Geogrid reinforcement and fascia units for NH5, Dharmavaram-Tuni Package

Table 1 shows the derived allowable long term design strength of the geogrids used for the design of the segmental retaining walls for the NH5, Dharmavaram-Tuni Package. The FHWA and GRI procedure was used to derive the allowable long term design strength of the geogrids. The design life was 120 years at average ambient soil temperatures of 30℃. A total of 142,000 m^2 of geogrids were used as reinforcement in the construction of the segmental retaining walls for the NH5, Dharmavaram-Tuni Package.

Backfill Soil

The backfill material was obtained from a nearby borrow area (2 km right hand side of 259 km+500 m). Soil tests were done at the Division of Soil Mechanics and Foundation Engineering, College of Engineering, Anna University of Chennai. Table 2 shows the test properties compared against the input design values. The internal friction and cohesion were obtained from direct shear test in the laboratory.

Subsoil Drainage

Clean aggregates of 10 to 20 mm stone size were placed within the cores of the fascia units and to a minimum of 300 mm behind the blocks. This created a drainage column for the wall facing. At the bottom of the drainage column a 150 mm diameter perforated PVC pipe wrapped around with a filter geotextile was used to drain water away (see Fig. 4). The aggregate column, besides functioning as a drainage column, also served to provide a positive interlock between the fascia units thus improving the fascia unit interlayer shear resistance.

Table 2 Properties of backfill soil used for NH5, Dharmavaram-Tuni Package

Property	Tested	Design
Internal friction (deg.)	40	39
Cohesion (kg/cm^2)	0.45	0
Bulk density (kN/m^3)	-	21
Gravel (%)	15	-
Sand (%)	56	-
Silt (%)	10	-
Clay (%)	9	-
Liquid limit (%)	47	-
Plastic limit (%)	24	-
MDD[1] (g/cc)	2.1	-
OMC[2] (%)	10	-

[1]MDD = Maximum dry density (Modified Proctor)
[2]OMC = optimum moisture content (Modified Proctor)

Fig. 4 Geotextile wrapped subsoil and aggregate drainage within and behind fascia units for NH5, Dharmavaram -Tuni Package

Component Interaction Properties

Fig. 5 shows the connection strengths of the geogrids with the fascia units. These were provided by the manufacturer of the geogrids, which were based on tests conducted at TRI Geosynthetic Services. The value of 0.8 was used in design for the coefficient of geogrid pullout from soil, C_{po}, and 0.9 for the coefficient of geogrid direct shear against soil, C_{ds}. These values were in line with the test results reported by Koutsourais et al. (1998).

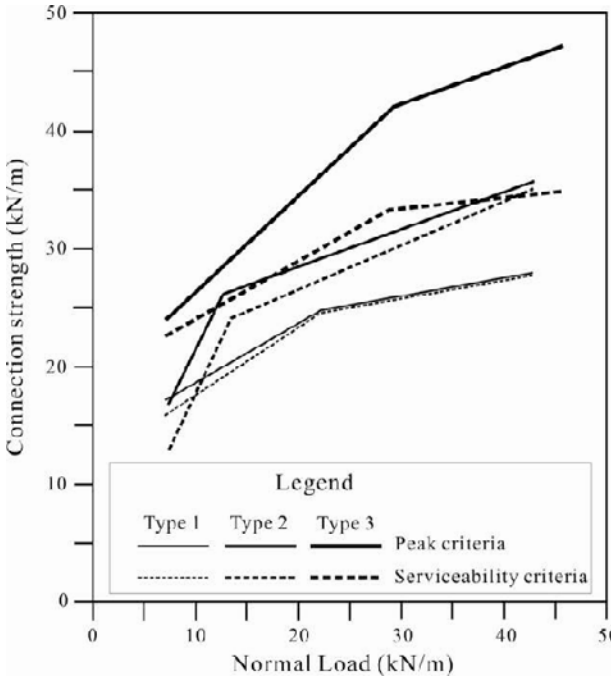

Fig. 5 Connection strength of geogrid reinforcement with fascia units used for NH5, Dharmavaram-Tuni Package

Failure Mechanisms and Minimum Factors of Safety

Earth retaining structures may be classified based on two principal categories of externally or internally stabilized systems (O'Rouke & Jones 1990).

Gravity walls like masonry wall, concrete wall, cantilever wall, counterfort wall, gabion structure, crib wall, bin structure and cellular cofferdam are classified as externally stabilized systems and the design involves provision of adequate safety against modes of soil failure external of the wall structure.

Internal stabilized systems are identified by reinforced soils with predominantly horizontally layered soil reinforcing elements. The key aspect of an internally stabilized system is its incremental form of construction. In effect, the soil mass is partitioned so that each partition receives support from a locally inserted reinforcing element. Reinforced soil structures are designed to ensure that there is adequate safety against modes of soil failure within the reinforced soil zone. This is done in addition to the provision of adequate safety against soil failure external of the reinforced soil zone.

Also, stabilities of the facing elements and the connections of reinforcements to facing elements, which are usually specific to the particular wall system used, have to be ensured in design.

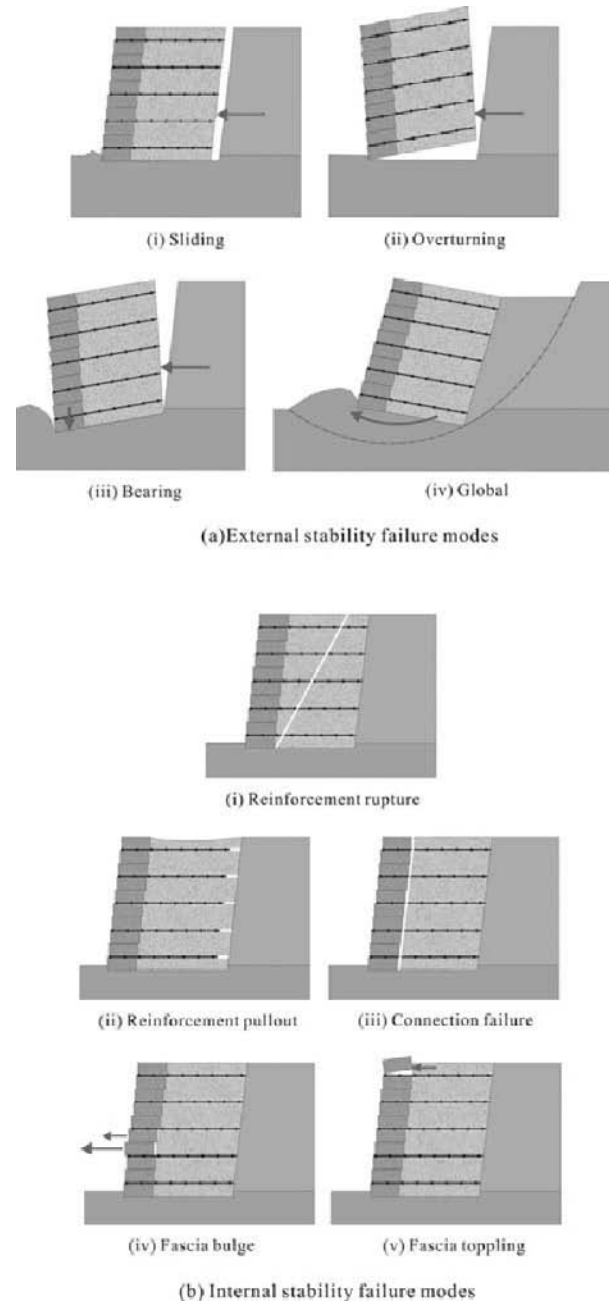

Fig. 6 Possible failure modes evaluated in the design of geogrid reinforced segmental retaining wall

The design of geogrid reinforced segmental retaining wall involves the evaluation of various possible failure

modes and ensuring adequate safety against each mode of failure. The possible failure modes are summarized as follows (see also Fig. 6):

- External stability
  - Sliding failure
  - Overturning failure
  - Bearing capacity failure
  - Global slip failure
- Internal stability
  - Reinforcement rupture
  - Reinforcement pullout
  - Reinforcement to fascia unit connection failure
  - Fascia bulge
  - Toppling of top fascia units

The design follows the National Concrete Masonry Association (NCMA) method. The tensile strength of geogrid is factored by applying a series of partial factors as shown in Table 1 to derive the allowable long term design strength.

Table 3 shows the minimum factors of safety against various possible failure modes (other than tensile failure of the reinforcement) adopted in design in accordance with NCMA (1997).

Table 3 Minimum factors of safety against various possible failures used for NH5, Dharmavaram-Tuni Package

Failure Mode	Minimum factor of safety
External stability	
Sliding failure	1.5
Overturning failure	2.0
Bearing capacity failure	2.0
Global slip failure	1.5
Internal stability	
Reinforcement pullout	1.5
Connection failure	1.5
Fascia bulging	1.5
Fascia toppling	1.5

Design and Detailing

The design analyses were carried out using the commercially available software NCMA SRW version 3.22. The design surcharge loads were 24 kN/m^2 and 12kN/m^2 for live load and dead load respectively. Figure 7 shows the reinforcement details of highest section of the geogrid reinforced segmental retaining walls for the NH5, Dharmavaram-Tuni Package.

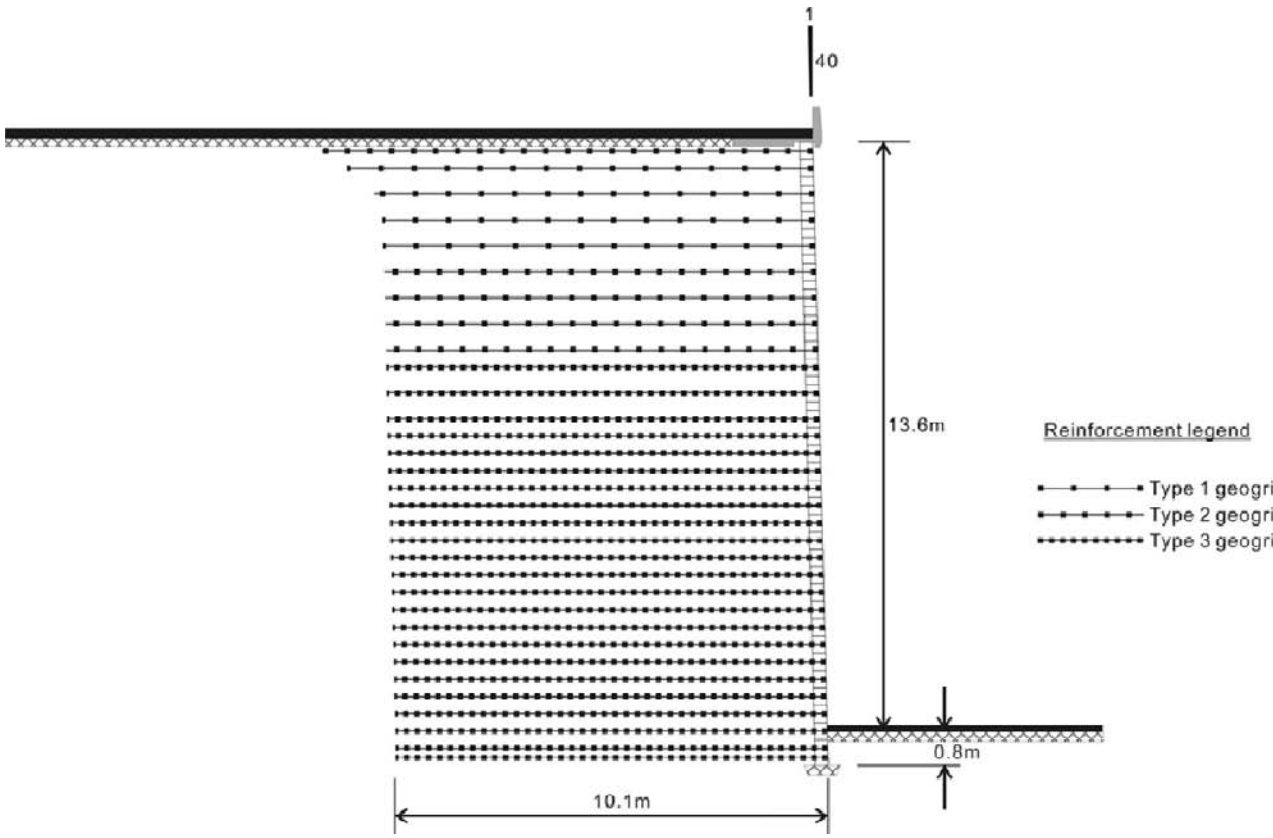

Fig. 7 Reinforcement details of highest section of the geogrid reinforced segmental retaining wall for NH5, Dharmavaram-Tuni Package

CONSTRUCTION

Manufacture of Fascia Units

The fascia units used in the construction of the geogrid reinforced segmental retaining walls for the NH5, Dharmavaram-Tuni Package were manufactured in a factory in Anakapalle of the adjacent district of Vishakhapatnam.

The units were dry cast in steel moulds under compression force of 70 metric tons. They were then placed in a mist curing chamber that could accommodate 1,800 units at any one time. A total of about 280 thousand units were produced for the project. Fig. 8 shows the manufacturing of fascia units for the NH5, Dharmavaram-Tuni Package.

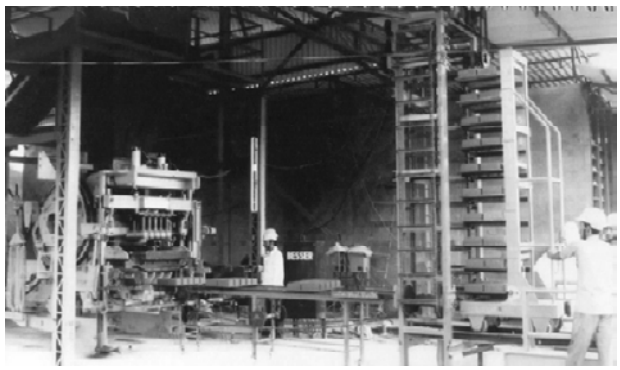

Fig. 8 Manufacturing of fascia units at Anakapalle for NH5, Dharmavaram-Tuni Package

Installation Process

Before the commencement of wall erection, the subgrade condition was checked along the wall alignment. Any soft material encountered was removed and replaced with well compacted granular material. A 600 m wide trench was excavated to receive the base course aggregates. The depth of trench was such that the designed wall embedment will sit on a minimum of 150 mm layer of base course aggregates. The base course aggregates were then placed in the trench and adequately compacted.

The initial layer of fascia units was then placed over the base course aggregates. The initial layer of fascia units was carefully checked for proper leveling. A hand level was used to check each unit, side-to-side, front-to-back and across three full units.

Clean aggregates of 10 to 20 mm stone size were then placed within the cores of the fascia units and to a minimum of 300 mm behind the blocks. Subsequent layers of fascia units were placed in tandem with the sequential backfilling and laying of geogrids. A 150 mm diameter perforated pipe, wrapped over with a non-woven geotextile, was placed behind the fascia unit at the designated level and eventually connected to a discharge point.

Backfilling was carried out in lifts of 200 mm. The backfill soil was compacted to a minimum of 95% of the maximum dry density and plus or minus 2% of the optimum moisture content, according to Standard Proctor.

At the designed level the designated geogrid was laid over the compacted backfill. The geogrid was laid with the machine direction perpendicular to the wall face alignment, from the front of the wall face extending to the back of the reinforced soil zone. The geogrid was laid flat and free of wrinkles.

Fig. 9 View of geogrid reinforced segmental retaining wall under construction at Tuni ROB of NH5, Dharmavaram-Tuni Package

Fig. 10 View of geogrid reinforced segmental retaining wall under construction at km 292+412m VUP of NH5, Dharmavaram-Tuni Package

Fig. 9 shows the view of laid out geogrid for the segmental retaining wall at Tuni ROB. Fig. 10 shows the view of placement of backfill over laid out geogrid for the segmental retaining wall at 292 km+412m VUP.

Fig. 11 View of geogrid reinforced segmental retaining wall under construction at Kathipudi VUP of NH5, Dharmavaram-Tuni Package

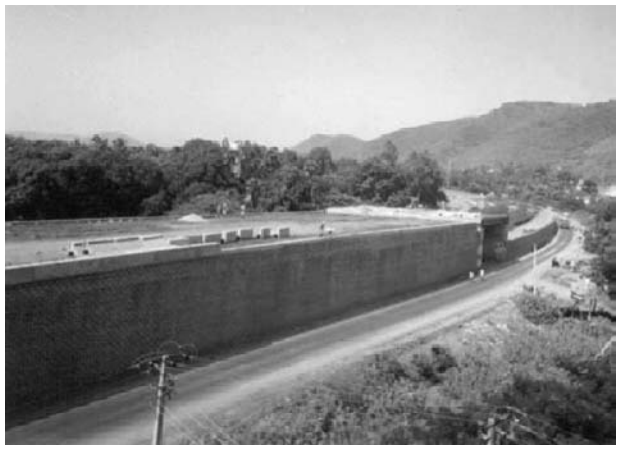

Fig. 12 Aerial view of geogrid reinforced segmental retaining wall under construction at 291 km +550 m VUP of NH5, Dharmavaram-Tuni Package

Fig. 13 Oblique frontal view of geogrid reinforced segmental retaining wall for NH5, Dharmavaram-Tuni Package

Fig. 11 shows the view of geogrid reinforced segmental retaining wall under construction at Kathipudi VUP. Fig.12 shows the aerial view of a substantially completed geogrid reinforced segmental retaining wall at 291 km+550 m VUP.

Fig. 13 shows the oblique frontal view of a substantially completed geogrid reinforced segmental retaining wall for the NH5, Dharmavaram-Tuni Package.

The project which started in October 2003 was completed in February 2005 and has been opened to traffic since. To date all the retaining walls are performing satisfactorily.

Quality Assurance

The three main components of the geogrid reinforced segmental retaining wall system for the NH5, Dharmavaram-Tuni Package are geogrid, fascia unit and compacted backfill.

For each batch of geogrid delivered to site, a conformance certificate is required to ensure the geogrid supplied to site meets the design strength requirements of the project. Fig. 14 shows the typical setup for the testing of tensile strength of geogrid for the assessment of long term design strength.

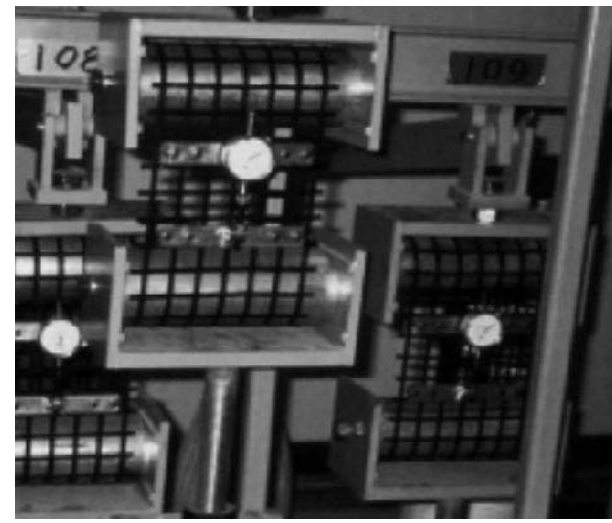

Fig. 14 Typical setup for the testing of tensile strength of geogrid for the assessment of long term design strength

Fig. 15 Core cutting of fascia unit in preparation for concrete compressive strength test for the NH5, Dharmavaram-Tuni Package

Fascia units are tested for concrete compressive strength. Fig. 15 shows the core cutting of a produced fascia unit in preparation for testing of concrete compressive strength.

To ensure that compaction during placement of backfill was adequate, the quality of the compacted backfill was regularly checked using a Nuclear Moisture-Density Apparatus (see Fig. 16).

Fig. 16 In situ determination of soil density of compacted backfill for NH5, Dharmavaram-Tuni Package using Nuclear Moisture-Density Apparatus

This is a nondestructive and relatively quick method for determining density and unit weight of soil in place. This apparatus contains a radioactive source and a radiation detector. It works on the principle that the amount of gamma radiation reaching the detector varies inversely with the soil unit weight and when properly calibrated will quickly determine the density of the soil. This equipment can only be operated by trained personnel thoroughly familiar with safety procedures as the equipment, if not properly used, could be hazardous to the user due to the presence of radioactive matter (Liu & Evett 2003).

Site Issues

The main issue at site concerns working space constraints. Construction had to be carried out while the road is still kept open to traffic flow. The works of the geogrid reinforced segmental retaining wall were done location by location to avoid creating too many choking points along the highway during the construction of highway for the NH5, Dharmavaram-Tuni Package. All construction activities for the geogrid reinforced segmental retaining walls have to be basically kept within the confines of the area behind the wall facings to minimize disturbances to traffic flow.

The construction of the geogrid reinforced segmental retaining walls for the NH5, Dharmavaram-Tuni Package was in an area affected by the monsoon rains and cyclones coming from the Bay of Bengal. Inclement weather was an issue during the monsoon months of 2004 resulting in significant work time loss over many months.

CONCLUSION

Twenty five thousand square meters of geogrid reinforced segmental retaining walls with maximum height of 12.6 m have been designed and successfully completed at four locations along the NH5, Dharmavaram-Tuni Package. The completed walls have been opened to traffic and to date is performing satisfactorily.

REFERENCES

ADB (2002) Technical Assistance to India for Preparing the National Highway (Corridor) Sector Project, Report No. TAR:IND 34420, Asian Development Bank, Manila

Koutsourais M, Sandri D, Swan R (1998) Soil Interaction Characteristics of Geotextiles and Geogrids, Proc.of the 6th International Conference on Geosynthetics, Atlanta 2: 739-744

Kumar S (2004) Geogrid reinforced retaining wall – case histories, Proceedings Conference on Geosynthetics India, New Delhi: 45-53

Liu C, Evett JB (2003) Determining the Density and Unit Weight of Soil in Place by Nuclear Methods, Soil Properties – Testing, Measurement, and Evaluation (5th Edition), Prentice Hall, New Jersey, Chapter 15: 217-232

NCMA (1997) Design manual for segmental retaining walls (2nd Edition), National Concrete Masonry Association, USA

O'Rourke TD, Jones CJFP (1990) An overview of earth retention systems: 1970-1990, Proceedings ASCE Speciality Conference on Earth Retaining Structures, Cornell, June: 22-51

WETTING-INDUCED GEOSYNTHETIC REINFORCED SLOPE FAILURE

J.Y. Wu[1] and A.H. Tang[2]

ABSTRACT: Failures of geosynthetic reinforced soil slope (RSS) initiated by intense rainfall have been often reported recently. These incidents were likely to be the effect of strength reduction upon wetting for unsaturated fill. This paper proposes a practical approach to evaluate the probable erroneous in analysis that responsible for such failures. A case study for a collapsed highway RSS was conducted to verify the developed protocol. The results were consistent with those observed in the field. The rational procedures found in this research offer a quick and simple way to estimate the stability of RSS upon wetting.

KEYWORDS: reinforced soil slope, intense rainfall, failure

INTRODUCTION

Geosynthetic reinforced soil slope (RSS) technology has been widely used in Taiwan for the past decades. However, with its increasing uses, observed failures also have been often reported. Based on a comprehensive forensic survey, most of the RSS failures were initiated by intense rainfall or poor dissipation of seepage (Wu & Tang 2006). It appears to be anomalous as these structures all had shown sufficient safety factor under severe rainstorm conditions based on their safety analyses. Thus, studies of wetting-induced failures and back analyses are essential to substantiate the accuracy of the analysis used in the design.

Conventional safety design of RSS under rainstorm condition is based on the limit equilibrium approach, which generally assumes a condition of rising groundwater level. However, the accuracy of the analysis depends on whether or not the assumed mode of failure adequately represents the conditions actually leading to collapse. Numerous studies for slope stability have indicated that the failure mechanism upon wetting involves moisture infiltration into the slope surface that leads to decreases in matric suction and soil strength (Chen et al. 2004; Collins & Znidarcic 2004; Crosta 2004; Sako et al. 2006). Although many researches have been conducted on the effect of wetting-induced slope instability, standard procedures have not been established to predict the corresponding slope safety. Available researches for RSS also seldom address to the effect of wetting on the stability. The sophisticated failure mechanisms and time-consuming analyses for unsaturated soils also make most engineers difficult to integrate theory into practice.

This study proposes a practical approach to the problem, in which a modified direct simple shear test was derived to observe the strength loss of compacted fill upon wetting. Computer limit equilibrium analyses were then performed using the observed strength parameters for rainstorm conditions. The practicability of the procedures was then verified by using an actual case of failure in which a geosynthetic reinforced slope collapsed after it was attacked by a typhoon.

EXPERIMENTAL PROGRAM

Testing Material and Specimen Preparation

The soil studied was a yellowish sandy material collected at the site where a highway RSS collapsed after it was attacked by a typhoon. The sand can be classified as poorly graded sand with silty clay (SP-SC) according to the Unified Soil Classification System (ASTM D2487). Table 1 presents their detailed physical properties. To observe the effect of infiltration on the stability of RSS with different moisture contents, specimens were compacted to 90% of standard Proctor maximum density with three moisture contents, namely OMC-2%, OMC, and OMC+2%.

Test Procedures

Determining the shear strength parameters of an unsaturated soil involves a sophisticated and time

[1] Associate Professor, Dept. of Civil and Engineering Informatics, Chung Hua University, CHINA. Email:jasonwu@chu.edu.tw
[2] Manager, ACE Geosynthetics Enterprise Co., Ltd., CHINA. Email:amy@goldjoint.com.tw

-consuming testing program (Cabarkapa and Cuccovillo 2005). For most of the geotechnical engineering firms in practice, their testing laboratories usually do not have the capability to measure the shear strength of unsaturated soils. There is a general lack of familiarity as regards equipment, procedures, and results (Abramson et al. 2002).The experiment in this research was therefore designed specifically to develop a simple protocol using current available equipment for the practicing engineers. Considering the influences of cost, times, and simplicity of the test, simple direct shear test (ASTM D 3080) was used to observe the effect of wetting on the variations of shear strength for sandy material compacted with different values of moisture content.

To examine the effect of wetting on the strength reduction of compacted sand, sample was vertically loaded without inundation to simulate the fill construction. Each sample was then soaked for 4, 12, or 24 hours to observe the effect of different time of soaking on the strength variations. Hydrocollapse due to wetting was recorded with time. The sample then was sheared to failure. Test procedures were similar to those described by Melinda et al. (2004) except shearing was not initiated until soaking of the sample was completed for the specified time. This was to simulate a rainfall-induced landslide of a fill slope under its self-weight. The primary object of the test was to observe the reduction of strength upon wetting and also keep simplicity of the testing protocol; suction was therefore not monitored throughout the test. Such arrangements were easy to perform yet able to acquire reasonable test results in relevant to the effect of wetting on unsaturated soils.

Table 1 Physical properties of tested soil

Property	Value
Specific gravity	2.6
Coefficient of curvature, C_c	0.76
Coefficient of uniformity, C_u	9.1
% of fines (%)	8.24
Liquid limit (%)	26
Plastic limit (%)	12
USCS soil classification	SP-SC
Maximum dry density (kN/m^3)	17.6
Optimum moisture content (%)	17

RESULTS AND DISCUSSIONS

Effect of Wetting on the Shearing Behavior

Figs. 1 to 3 illustrate the effect of wetting on the shearing behavior of sandy fill compacted to 90% of standard Proctor maximum density with varying moisture contents and soaking periods. The normal stress applied was 100 kPa. Detailed results of other testing schemes can be found in Tang (2005). It can be seen that the as-compacted moisture content and the soaking periods presented significant effects on the shear strength of compacted sand. Specimen compacted dry-of-optimum (OMC-2%) demonstrated the highest strength and a brittle behavior before wetting. However, its strength reduced to about 40% of its initial value and became the lowest after water was introduced to the specimen. Although the infiltration caused the strength to vary with the time of soaking, the final strength varied little for specimens compacted at higher moisture contents (OMC and OMC+2%).

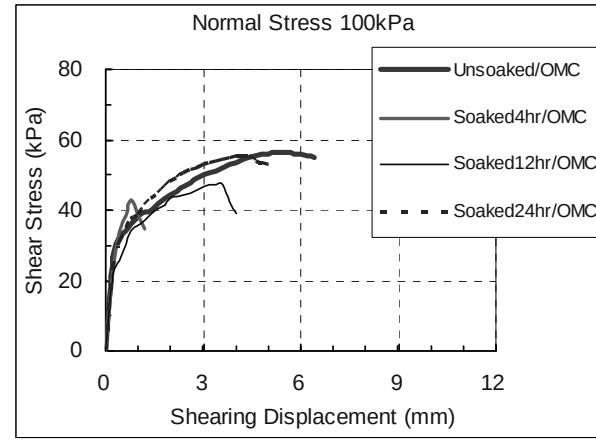

Fig. 1 Effect of wetting on the shearing behavior of a compacted fill (90% compaction, OMC)

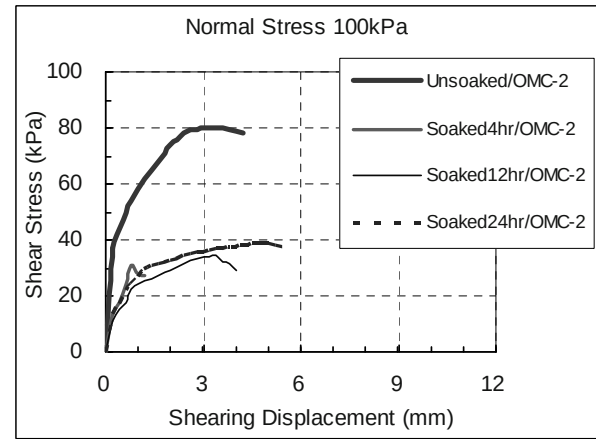

Fig. 2 Effect of wetting on the shearing behavior of a compacted fill (90% compaction, OMC-2)

Strength Parameters

Strength parameters are the crucial input in order to analyze the safety of a slope. The determinations of these parameters in a truly manner corresponding to those conditions at the site are thus vital to an accurate

prediction for the slope safety. Abramson et al. (2002) stated that the shear strength of unsaturated soils can be readily accommodated within conventional slope analyses by using a concept of total cohesion. With this approach a modified value of total cohesion is used to include the effect of matric suction within the slope.

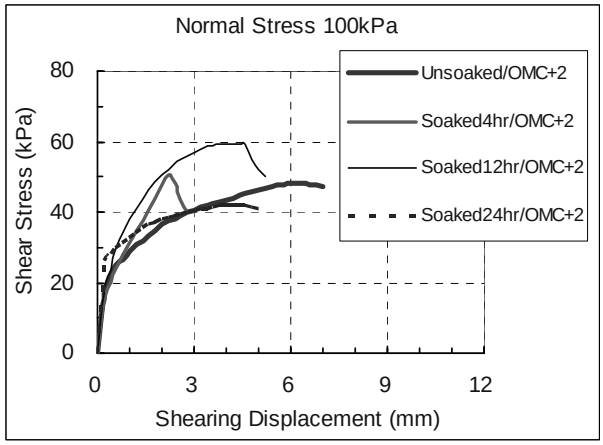

Fig. 3 Effect of wetting on the shearing behavior of a compacted fill (90% compaction, OMC+2)

Fig. 4 summarizes all strength parameters tested for samples compacted to 90% of standard Proctor maximum density with varying moisture contents. In general, the infiltration caused the cohesion to decrease with the increase of soaking times. The cohesion was totally vanished after 24 hours of infiltration for samples compacted with less moisture contents (OMC and OMC-2%). The reduction was up to 100% in comparison with its initial value before wetting.

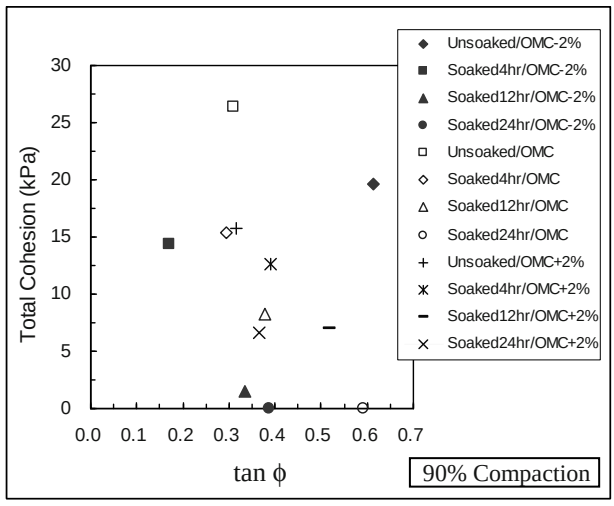

Fig. 4 The effect of wetting on the reduction of strength parameters for soils with varying moisture contents

According to Fredlund and Rahardjo (1993), the decrease of cohesion can be attributed to the loss of matric suction due to infiltration. Conversely, the friction angle increased with the increase of soaking time. It appears to be anomalous as research findings have indicated that friction angle is effectively independent of matric suction (Fredlund and Rahardjo 1993). Such phenomenon should be the effect of further consolidation of soil particles triggered after the hydrocollapse of soil sample. A longer consolidation promotes greater increases in the effective stress. It can be seen that samples compacted with less moisture content (OMC-2%) presented significant strength weakness upon wetting. It is logical to conclude that fill slope compacted dry-of-optimum will be more vulnerable to fail after intense rainfalls. Rehardjo et al. (2003) and Chen et al. (2004) reported many landslides of man-made slopes coincided with such behaviors.

Stability Analysis

Almost all traditional slope stability analyses are conducted using computer programs based on limit equilibrium methods. ReSSA has been the one on the market recently used by practicing engineers. It is relatively easy, simple, and user-friendly. To reduce the annoyance of facing unknown challenges for engineers, this paper proposes that conventional program such as ReSSA still can be used for unsaturated slope stability analyses. However, the reduced strength parameters observed using the above modified simple direct shear test must be used to account for the effect of infiltration on the strength loss. For normal and earthquake conditions, drained or undrained strength parameters applied for stability analyses of fill slope remain unchanged as those would be used in the conventional procedures. For intense rainfall condition, boundary of infiltration should be established first and the strength parameters for soil strata within the range of wetting band should be revised using the reduced values.

High-intensity rainfall induced landslides of fill slope often occurred on relatively shallow slip surfaces. The depth of the wetting front can be approximated based on soil characteristics and rainfall conditions (Abramson et al. 2002) or in terms of pore pressure (Collins & Znidarcic 2004). A more practical alternative would rather assume a reasonable depth of wetting front. The landslides in the unsaturated fill slopes are generally shallow and the failure surfaces are usually parallel to the slope surface. Therefore, for a short-term intense rainfall condition, the depth of wetting front of a sandy fill typically for RSS can be assumed reasonably within a range of 2 to 6 m. For long-term condition, a worst case can be assumed that the phreatic surface rises to coincide with the slope surface and that the slope is completely saturated.

FHWA (2001) indicated that the interaction behavior between soil and geosynthetics in the anchorage zone determines the stability of reinforced earth structures. The pullout resistance of the embedded geosynthetic is a function of soil-geosynthetic interface shear resistance. It can be described by the following equation (Moraci and Recalcati 2006):

$$P_R = 2L\sigma'_v \, f_b \tan\phi' \quad (1)$$

where P_R is the pullout resistance; L is the reinforcement length in the anchorage zone; σ_v' is the effective vertical stress; f_b is the soil-geosynthetic interface apparent coefficient of friction; and ϕ' is the soil shear strength angle. Based on Moraci and Recalcati (2006), the value of f_b are largely influenced by the value of shear strength of the fill material. Therefore, a reduction of soil shear strength certainly causes f_b to decrease as well.

CASE STUDY

To evaluate the usefulness and the practicability of the developed protocols, a case study was performed using site conditions and soil parameters from an actual case of failure. The site consisted of typical cut and fill constructions for a 15-m wide highway winding through a mountainous area. A 19-m high tiered reinforced slope was used to support the widening of the highway. The fill material for the RSS construction was the same as those described earlier.

Pre-construction stability analysis based on the traditional groundwater rising procedures indicated that the slope presented a safety factor of 1.63 for intense rainfall condition. However, the RSS collapsed during an attack of typhoon with an enormous rainfall and caused serious traffic interruption of the highway (Fig. 5).

Fig. 5 RSS collapsed during an attack of typhoon

Forensic field investigation after the failure had observed that the collapsed fill was totally saturated because of the infiltration of rainfall. The saturation also caused the shear strength of the fill material dropped significantly. This happens to be the situation essentially similar to those inundated samples observed in the laboratory as described earlier. The designer ignored the effect of strength reduction upon wetting for unsaturated fill material. Therefore, it has shown reasonable evidence that the collapse was likely because of the erroneous stability analysis.

The safety of the RSS was examined further using the protocols developed in this study. Strength parameters of the fill material were reduced in stages to simulate the effect of infiltration resulting from the downward movement of wetting front. The reductions of pullout resistance of geogrid also can be simulated using reduced values of f_b in ReSSA.

Fig. 6 presents a summarized result showing the variations of the factor of safety (F_s) with the depth of wetting front and the reduction of pullout resistance. The analyses were obtained using strength parameters after 24 hours of infiltration. Detailed results of all analyses can be found in Tang (2005). It can be seen that the values of F_s decreased with the increase of depth of wetting front. The reductions of pullout resistance of the reinforcements also presented significant negative effect on F_s.

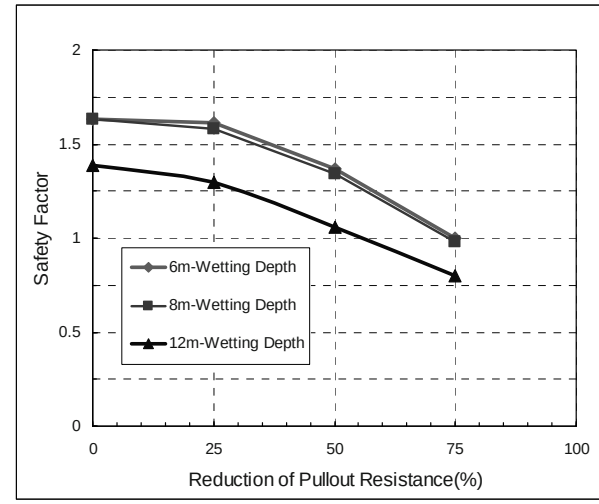

Fig. 6 The variations of factor of safety with the depth of wetting front and the reduction of pullout resistance

Based on the results of the simulations, failure of RSS will be highly likely when the wetting depth increases to 12-m and the pullout resistance drops over 50%. The failure plane essentially passes along the interface of cut and fill. The calculated factor of safety and the predicted mode of failure have shown a good

agreement with what was observed in the field (Fig. 7). The illustrated case study shows that sophisticated infiltration and slope stability analysis may not always necessary for analyzing rainfall induced slope failure. Rational results also can be available using traditional analysis with proper experimental simulations. Further studies are underway to verify the presented method.

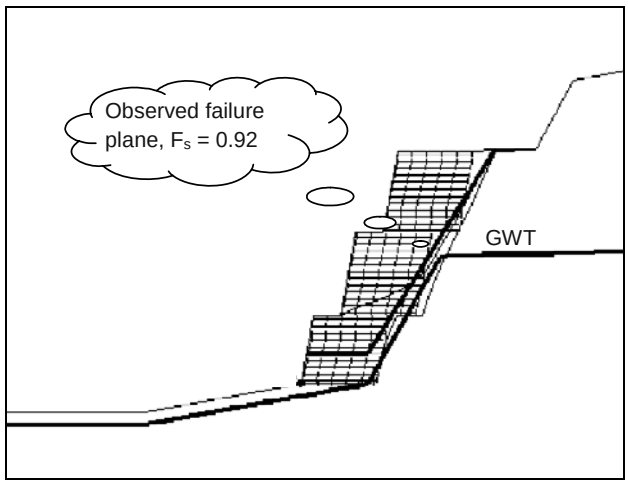

Fig. 7 Result of stability analysis showing a wetting depth of 12-m caused the RSS to collapse

CONCLUSIONS

Based on the study, the following conclusions can be drawn:

- The modified simple direct shear tests developed in this research appropriately simulate the strength reduction upon wetting in the field.
- In general, the infiltration caused the cohesion to decrease with the increase of soaking times. For samples compacted with less moisture contents, the cohesion could be vanished completely after 24 hours of infiltration.
- Samples compacted with less moisture content presented significant strength weakness upon wetting. Common practices for RSS compacted dry-of-optimum thus will be more vulnerable to have failures after intense rainfall.
- The results of a case study demonstrated that the calculated safety factor and the predicted mode of failure agreed reasonably with what was observed in the field.
- The proposed method in this study offers a simple and practical way to evaluate the stability of RSS upon wetting.

REFERENCES

Abramson LW, Lee TS, Sharma S, Boyce GM (2002) Slope Stability and Stabilization Methods. 2nd. ed., John Wiley and Sons, Inc., New York, NY, USA

Cabarkapa Z, Cuccovillo T (2005) Automated triaxial apparatus for testing unsaturated soils. Geotechnical Testing Journal, ASTM 29(1): 1-9

Chen H, Lee CF, Law KT (2004) Causative mechanisms of rainfall-induced fill slope failures. J. of Geotech. and Geoenvironmental Engrg. ASCE 130(6): 593-602

Collins BD, Znidarcic D (2004) Stability analysis of rainfall induced landslides. J. of Geotech. and Geoenvironmental Engrg. ASCE 130(4): 362-372

Crosta GB (2004) Introduction to the special issue on rainfall-triggered landslides and debris flows. Engineering Geology 73(3-4): 191-192

Fredlund DG, Rahardjo H (1993) Soil Mechanics for Unsaturated Soils. John Wiley and Sons, Inc., New York, NY, USA

FHWA (2001) Mechanically Stabilized Earth Walls and Reinforced Soil Slopes, Design and Construction Guidelines, Report No. FHWA-NHI-00-043, FHWA, Washington, D.C. USA

Melinda F, Rahardjo H, Han KK, Leong EC (2004) Shear strength of compacted soil under infiltration condition. J. of Geotech. and Geoenvironmental Engrg. ASCE 103 (8): 807-817

Moraci N, Recalcati P (2006) Factors affecting the pullout behavior of extruded geogrids embedded in a compacted granular soil. Geotextile and Geomembrane 24 (4): 220-242

Sako K, Kitamura R, Fukagawa R (2006) Study of slope failure due to rainfall: a comparison between experiment and simulation. Proc. 4th Int. Conference on Unsaturated Soils, ASCE, Carefree, USA 2: 2324-2335

Tang AH (2005) Forensic case studies of reinforced earth structures failures, Master Thesis, Department of Civil and Engineering Informatics, Chung Hua University, Hsinchu, Taiwan. ROC

Wu JY, Tang AH (2006) Case studies of geosynthetic reinforced earth structure failures. Proc. 8th Int. Conference on Geosynthetics, Yokohama, Japan: 1105-1108

Proceedings of the 4th Asian Regional Conference on Geosynthetics
June 17 - 20, 2008 Shanghai, China

SIMULATING PLANE STRAIN TESTS OF SAND SPECIMEN REINFORCED WITH H-V ORTHOGONAL INCLUSIONS BY PFC

S.L. Zhang[1], M.X. Zhang[2] and A.A. Javadi[3]

ABSTRACT: Soil reinforced with horizontal-vertical (H-V) orthogonal inclusions is a new concept of reinforced soil. In the H-V reinforced soil, besides the traditional horizontal reinforcements, vertical reinforced elements are also placed on the horizontal ones in spacing. When the soil structure reinforced with H-V inclusions is subjected to load, besides the frictional resistances between soil and the horizontal inclusions, passive resistances in the soil enclosed within the H-V reinforcing elements will be provided. Passive resistances and frictional ones not only strengthen the reinforced soil, but also restrict the deformation of the soil, and then increase the strength and stability greatly. The H-V inclusions influenced the movement of the soil particles and changed the shear band of the reinforced soil. A series of plane strain tests of sand specimen reinforced with H-V orthogonal inclusions were carried out. Particle Flow Code (PFC), based on the discrete element theory, was introduced to simulate the plane strain tests of H-V reinforced sand. The macro stress-strain relation of sand was reproduced and verified by PFC model. The occurrence and propagation of shear band was analyzed by the confining pressure-time history, and the displacement and movement of the soil particles of PFC model. The effect of configuration of H-V inclusions, stiffness and position of the reinforcements, particle size on the formation and extension process of the shear band were discussed. The comparison between the results from plane strain tests of sand specimen reinforced with H-V orthogonal inclusions and the ones by PFC shows the PFC model can simulate the propagation of shear band and failure of the sand specimen reinforced with H-V orthogonal inclusions accurately.

KEYWORDS: horizontal-vertical (H-V) orthogonal inclusions, plane strain test, shear band, Particle Flow Code (PFC)

INTRODUCTION

The formation of shear band is a common feature of soil failure therefore the study on shear band is important to the security and stability of earth structures. Many laboratory tests and numerical analysis have been carried out to study the shear band in soil. With the developments in experimental techniques, particularly in imaging and sensing, shear band has been observed to initiate during hardening. The X-ray computed tomography and the technique of digital image correlation (DIC) have been used to study the shear band recently.

Sand consists of discrete particles and associated voids, therefore be inherently anisotropic in its response. The velocity of sand particles was assumed varied linearly across the shear band. Shear band displacement fields also are used as a basis for shear band strain calculations. Displacements of grid points have been used for strain calculations. Mooney inferred shear band strain from movements of individual sand grains, thus accommodating directly the erratic nature of particle movement. Oda used particulate-based numerical approaches to obtain the evolution of grain-scale processes .

In present paper, soil reinforced with H-V orthogonal inclusions is studied. In the H-V reinforced soil, besides the traditional horizontal reinforcements, vertical reinforced elements are also placed on the horizontal ones in spacing. When the soil structure reinforced with H-V inclusions is subjected to load, besides the frictional resistances between soil and the horizontal inclusions, passive resistances in the soil enclosed within the H-V reinforcing elements will be provided. Therefore the deformation of the soil is restricted, the strength and the stability is also increased greatly. A series of plain strain tests were carried out and the PFC^{2D} was used to simulate the onset and development of shear band in sand reinforced with H-V inclusions. From the result of PFC^{2D} simulation, the shear band characteristics of sand specimen were analyzed.

[1] Ph.D Student, Department of Civil Engineering, Shanghai University, CHINA. Email: shilei.zhang@163.com
[2] Professor, Department of Civil Engineering, Shanghai University, CHINA. Email: mxzhang@staff.shu.edu.cn
[3] Professor, School of Engineering and Computer Science, University of Exeter, UK. Email: A.A.Javadi@exeter.ac.uk

EXPERIMENTAL PROGRAM

The proposed H-V reinforcing elements would be placed for in situ applications (Fig. 1a). H-V reinforcement which shown in Fig. 1b was used in plain stress test.

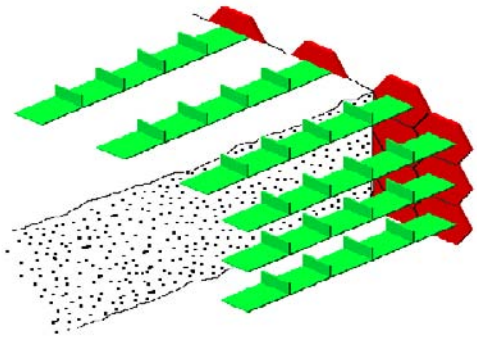

(a)

(b)

Fig. 1 The typical H-V reinforcing elements: (a) soil structure reinforced H-V inclusions. (b) H-V reinforcement used in plain strain tests

A series of plain strain tests were performed to investigate sand reinforced with H-V inclusions. All the specimens were prepared in dry condition with in a split cylinder mould. Uniform, clean, beach sand from shores of Fujian Province in China was used. The particle sizes of sand mainly distributed in 0.25-1 mm. The sand has a relatively uniform grain-size distribution with median grain size D50 of 0.54 mm. The physical properties of the sand are presented in Table 1. The reinforcements used in the tests are galvanized iron sheet with a thickness of 0.10 mm, and high of vertical inclusion is 5, 10, 15, 20 mm.Confining pressure in test was 50, 100, 150, 200 kPa.

Typical stress-strain curves for the sand reinforced with H-V inclusions are presented in Fig. 2. These figures indicate that reinforcing sand with the H-V reinforcement increases the yield stress and shear strength of the soil considerably, compared with horizontally and unreinforced soil. The figures also show that the maximum deviator stress increases with increasing the height of vertical reinforcement.

Table 1 Physical properties of sand

Unit weight γ [kN/ m^3]	Moisture content ω [%]	Specific gravity *Gs*	Void ratio *e*
17.23	0.16	2.643	0.58

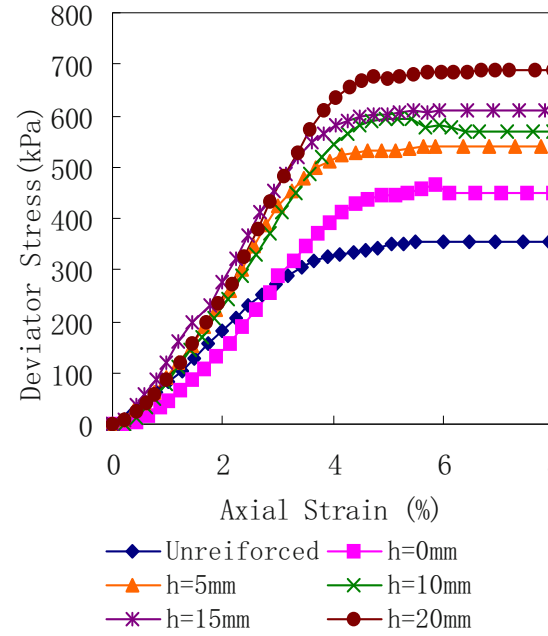

Fig. 2 Deviator stress versus axial strain curves of sand reinforced with different inclusions

PFC^{2D} SIMULATION ANALYSES

PFC^{2D} based on the discrete element theory, was introduced to simulate the plain strain test of H-V reinforced sand. The parameters used in PFC^{2D} model was uniformed with the plain strain test. Firstly, a rectangular specimen consisting of H-V inclusions and arbitrarily placed particles confined by four frictionless walls was generated in PFC^{2D}, and then the particle parameters are set to the assembly. After the specimen was generated, the model was loaded by controlling the velocity of the wall. The procedure is shown in Fig. 3. The comparison of numerical results and the plain strain test results is shown in Fig. 4.

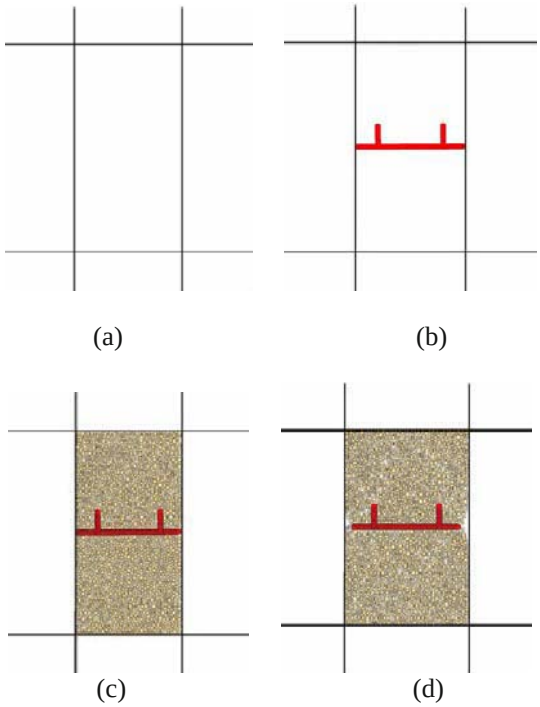

Fig. 3 Simulation of plain strain test of H-V reinforced sand specimens by PFC^{2D}: (a) wall; (b) wall and H-V inclusions; (c) specimen after particle generation; (d) specimen after loading

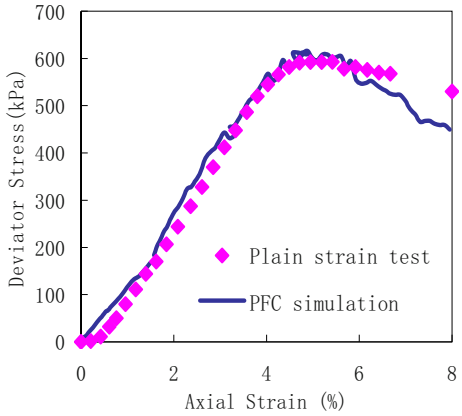

(a) σ=50 kPa

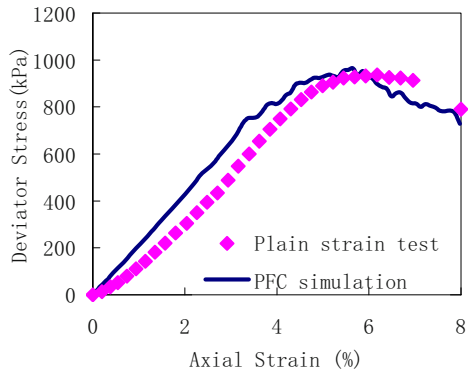

(b)σ=100 kPa

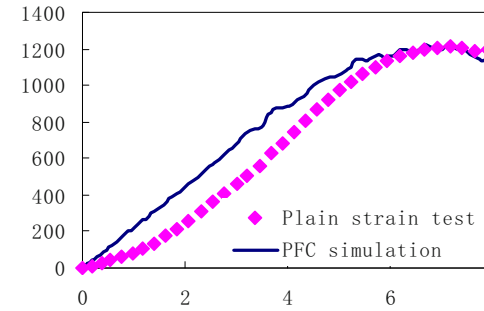

(c) σ=150 kPa

Fig. 4 Comparison between PFC model and lab test result

The displacement fields of sand in different axial strain are shown in Fig. 5. Before peak stress, the particles in specimen moved irregularly. After the peak stress, the particle's movement shows regularly in field. The grains which restricted between the vertical reinforcements almost show no displacements, or only move vertically. But in some areas, the particle's movement trace is deflected. The ordering of grain's movement beget the generation of shear band. Form the Fig. 5b, the shear band in sand specimen reinforced with H-V inclusions can be observed clearly. Due to the vertical reinforcements and the friction between grain-grain and grain-wall, the shear band expands like wedge shape.

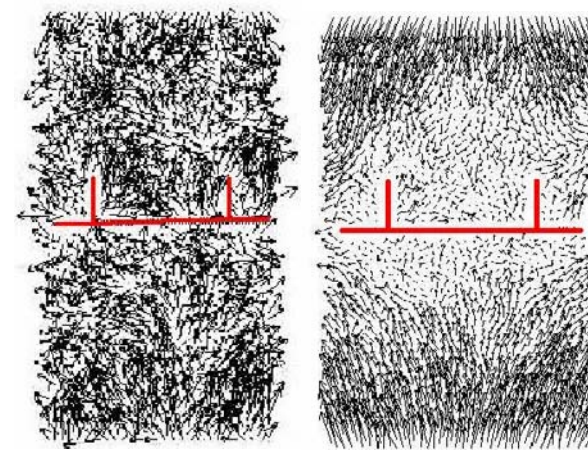

(a) (b)

Fig. 5 Displacement field of sand in different axial strains: (a) initial state; (b) failure state

Fig. 6 shows the rotation of the particles in PFC^{2D} model. The particle is presented by a short line. If the particle is rotated, the line is rotated accordingly. At the initial state of the test, the lines were all horizontally, it shows that the particles were in still state. When specimen was pressed, the displacement of particle varied. The Fig. 6b shows the particles in shear band

were rotated obviously. Direction of the particle rotation paralleled the shear band. The rotation occurred mainly in the shear band, and the thickness of the shear band is approximate to 3—4 grain diameters.

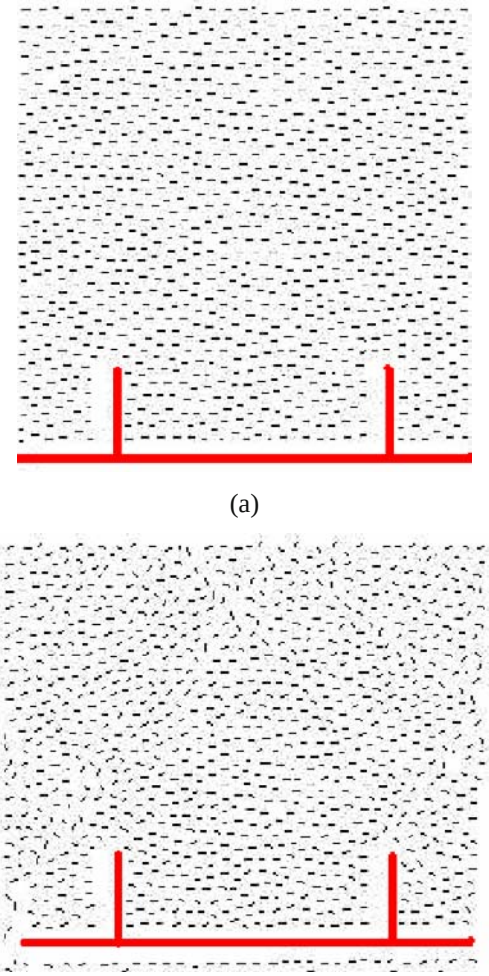

(a)

(b)

Fig. 6 The rotation of particles in PFC^{2D} model: (a) initial state; (b) failure state

CONCLUSIONS

From the reasonable accordance between the simulation and laboratory tests, it is concluded that the PFC^{2D} simulation can provide a useful tool to simulate the behavior of H-V reinforced sand. Based on the simulation, we reached that the shear band in H-V reinforced sand generate after stress peak. The H-V reinforcements not only restrict the deformation of sand effectively, but also affect the generation of the shear band. The particle rotates obviously in the shear band, and the direction of the grain rotation paralleled the shear band.

ACKNOWLEDGEMENTS

The financial assistance from the National Natural Science Foundation of China (NSFC) (grant number: 50678100) is herein much acknowledged.

REFERENCES

Alshibli KA, Sture S, Costes NC, Frank ML, Lankton MR, Batiste SN, Swanson RA (2000) Assessment of localized deformations in sand using X-ray computed tomography. Journal of Geotechnical Testing 23(3): 274-299

Finno RJ, Harris WW, Viggiani G, Mooney MA (1997) Shear bands in plane strain compression of loose sand. Geotechnique 47(1): 149-166

Lade PV, Wang Q (2001) Analysis of shear banding in true triaxial tests on sand. J. Eng. Mech., ASCE 127 (8): 762-768

Mooney MA, Finno RJ, Viggiani G (1998) A unique critical state for sand. Journal of Geotechnical and Geoenvironmental Engineering, ASCE 124(11): 1100-1108

Oda M, Iwashita K (2000) Study on couple stress and shear band development in granular media based on numerical simulation analyses. International Journal of Engineering Science 38(15):1713-1740

Rechenmacher A, Finno RJ (2004) Digital image correlation to evaluate shear banding in dilative sands. Geotechnical. Testing Journal, ASTM, 27(1): 13-22

Saada AS, Liang L, Figueroa JL, Cope CT (1999) Bifurcation and shear band propagation in sands [J]. Geotechnique 49 (3): 367-385

Zhang MX, Javadi AA, Min X (2006) Triaxial tests of sand reinforced with 3D inclusions. Geotextiles and Geomembranes 24(8): 201-209

.

Proceedings of the 4th Asian Regional Conference on Geosynthetics
June 17 - 20, 2008 Shanghai, China

INVESTIGATION ON RESTRAINT EFFECT OF GEOGRIDS ON SHALLOW LAYER FAILURE OF EXPANSIVE SOIL SLOPE

M.Y. Wang [1], J.T. Cai [2], H. Xu [3] and Y.H. Tang [4]

ABSTRACT: In recent years, "expansive soil slope reinforced with geogrid" technology has been successfully applied in some projects in China, but there is lack of study on its engineering behavior and mechanism. Effect of long-term weathering of atmosphere on expansive soil is considered, an ideal elastoplastic model is adopted to simulate the behavior of interface between geogrids and expansive soil, numerical analysis of stress and deformation characteristics of expansive soil slope reinforced with geogrids is carried out, and the strength reduction method based on stress state is utilized to analyze the stability of reinforced slope. Based on the results, the restraint effect of geogrids on shallow failure of expansive soil slope under atmosphere weathering effect is studied. Results show that reinforced geogrid can effectively solve the shallow failure problem of expansive soil slope, and deformation of the slope is restrained to a greater or less extent with different vertical space between geogrids.

KEYWORDS: geogrid, expansive soil slope, shallow layer failure, strength reduction methods, numerical analysis

INTRODUCTION

Expansive soil has a high clay content, and strong hydrophilic minerals rich in bentonites and illites, as well as exchangeable cations, its liquid limit is usually more than 40%, and its plasticity index is generally greater than 20. Expansive soil is a special stiff clay with a high liquid limit and many fissures, and it is characterized by special expansion-shrink characteristics, fissure character and overconsolidation nature. A large number of engineering practice show that because these special character, expansive soil slope usually lose its stability, and the failure mode mainly appears as shallow and progressive failure (Bao 2004; Yin et al. 2004). Though expansive soil slope is of obvious shallow layer nature in failure, it doesn't fails along the slope surface, and position of failure plane is related to the height of slope, both of which have important signification to investigate the failure mechanism. Skempton (1964), Chandler (1972, 1974), Chandler and Skempton (1974) hold that failure of cut slope in overconsolidation stiff clay with multi-fissures during the period of several years to several decades is attribute to the reduction in shear strength parameters of clay due to long term weathering, etc. Chandler (1972) pointed out that long-term radiation and wetting and drying cycle will make clay grains gradually to be sandified, cohesion of clay within atmospheric influence depth will gradually be weakened to approximately zero (1—2 kPa). Shen (2004) systematically summarized the effect of weathering on geotechnical engineering and proposed the design concept of resistance to weathering.

Reinforcement of expansive soil slope with geogrids is a new technique developed recently, and it has been used successfully in some expressways, railways and canals in China, and broken through the relevant provisions of existing specifications. As for the South-To-North Water Transfer Project (Middle Route Scheme) in China under construction, measures like expansive soil reinforced with geogrids will be adopted to strengthen and treat the expansive soil slope. Because of the rare engineering application before, scholars in the world have little studied the interaction characteristic between geogrids and expansive soils and the engineering behavior of expansive soil slope reinforced with geogrids. Only a few researchers conducted model tests on the reinforced expansive soils (Xu et al. 2005; Wu et al. 2004), and tried to carry out some experimental studies on the interface behavior between geogrids and expansive soil (Xu et al. 2004).

In the light of existing specifications, the limit equilibrium method is usually adopted to analyze the

[1] Ph.D Student, Institute of Geotechnical Engineering, ZheJiang University, Hangzhou, CHINA; Senior engineer,Yangze River Scientific Research Institute, Wuhan, CHINA. Email:wmy_90@163.com
[2] Graduate student, Yangze River Scientific Research Institute, Wuhan, CHINA. Email: shuffle11@163.com
[3] Ph.D, Yangze River Scientific Research Institute, Wuhan, CHINA. Email:mechanics007@yahoo.com.cn
[4]Graduate student, Yangze River Scientific Research Institute, Wuhan, CHINA. Email:tyh0529@126.com

stability of reinforced slope, in which only the friction at the interface between geogrid and the fills is considered, and a centralized tension force acting on the soil slice is adopted to model reinforced action, this calculation method cannot evaluate the effect of reinforced geogrids correctly (Wang et al. 2000). Bao (2006) makes a systematic analysis on the current status of reinforced mechanism and develops a new integrated reinforced mechanism, namely directly reinforcement and indirect strengthening actions.

In the paper, taking long term atmosphere weathering action on strength parameters of expansive soil into account, based on test of interaction between geogrids and expensive soils, the stress and deformation of expansive soil slope reinforced with geogrids is analyzed by using nonlinear finite difference method and the strength reduction method based on stress state is adopted to analyze the stability of reinforced slope. The restraint effect of geogrids on shallow layer failure of expansive soil slope under atmosphere weathering effect is studied.

NUMERICAL ANALYSIS METHOD AND MODEL

Simulation of Interaction between Geogrids and Expansive Soils

Geogrid is a typical ductile material with a small flexural rigidity, and under an ordinary operating condition, tension stress of geogrids embedded in soils is smaller than its tensile strength, thus structural behavior of geogrids is modeled as linear elasticity. On the other hand, geogrid produces friction and snap-in force with the fills in tangent plane direction, while it is restricted with the fills in normal plane direction, which meets the contact constraint condition. The interaction is shown in Fig.1, of which σ_m is confining stress, τ is shear stress at the interface, N is resultant force of section stresses produced from geogrids. An ideal elasto-plastic model is adopted to model the behavior of interaction between geogrids and the fills, as shown in Fig. 2. When shear stress at the interface is less than its shear strength, the interface is at elastic and binding state, relationship between shear stress and relative displacement at the interface is linear elasticity, ratio of them is the tangential stiffness κ of the interface. Once shear stress at the interface reaches its shear strength, the interface becomes at friction slip state as shown in Fig. 2a. The linear Mohr-Coulomb strength model is adopted as shear strength of the interface, as shown in Fig. 2b, and described in Eq. (1), where c is the pseudo cohesion, and φ is the pseudo frictional angle at the interface.

$$\tau_{\max} = c + \sigma_m \tan\phi \tag{1}$$

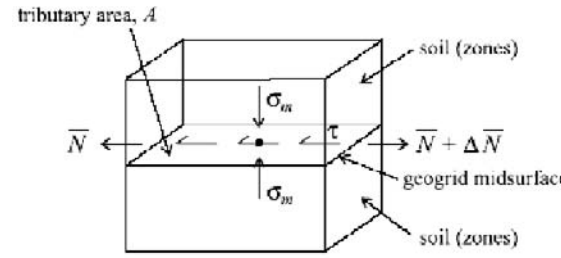

Fig. 1 Mechanical model of geogrid

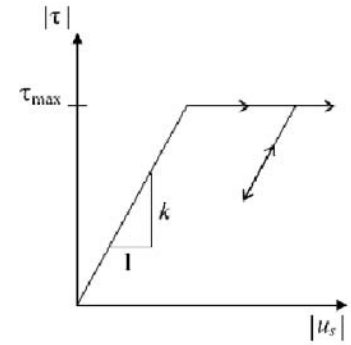

(a) Relationship between shear stress and relative displacement

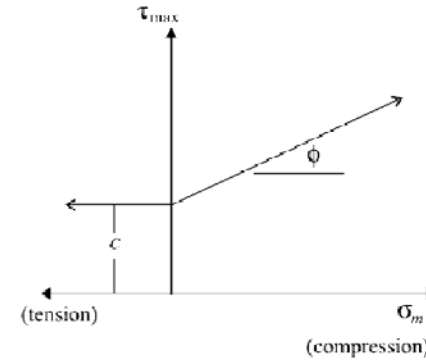

(b) Shear strength criterion

Fig. 2 Interface model between geogrid and the fills

Analysis Method for Stability of Reinforced Slope

The strength reduction method based on stress field is adopted to analyze the stability of slope, and the strength parameter of soils is reduced at the same time, as shown in Eq. (2), where ω is reduction factor, namely safety factor; c', φ' are cohesion and internal friction angle after reduction, respectively.

$$c' = c/w\,,\ \tan\varphi' = \tan\varphi/w \tag{2}$$

In this paper, the equivalent plastic strain transfixion is taken as the criteria of slope instability.

Simulation Method of Deformation due to Moisture Absorption of Unsaturated Expansive Soil

Zhu (2003) states that the change in moisture content field will make the concrete expansion-shrink, lead to the redistribution of structural stress, this problem is similar to the thermal stress, and the same numerical solution method can be adopted.

Strain increment due to moisture absorption of unconstrained isotropic expansive soil can be expressed as Eq. 3, where α is linear expansion coefficient, δ_{ij} is Kronecker symbol, $d\omega$ is moisture content increment, $d\varepsilon_{ij}^{\omega}$ is strain increment due to moisture absorption.

$$d\varepsilon_{ij}^{\omega} = \alpha\delta_{ij}d\varepsilon \tag{3}$$

Based on the generalized Hook law, introducing the rigid side-limit condition, relation between expansion ratio without load and linear expansion coefficient α can be calculated as shown in Eq. 4a, where $\Delta\omega$ is moisture content increment in expansion ratio test without vertical load, δ is expansion ratio without load; when Poisson's ratio υ takes 0.3, it can be simplified as the Eq 4b.

$$\alpha = \frac{\delta\ (1-\upsilon)}{\Delta\omega\ (1+\upsilon)} \tag{4a}$$

$$\alpha = 0.54\frac{\delta}{\Delta\omega} \tag{4b}$$

Stress equilibrium equation considering the expansive action due to moisture absorption of expansive soil can be written as expression (5).

$$\frac{\partial\sigma_{ij}}{\partial x_j} + \rho F_i + \frac{\partial}{\partial x_j}\left(\frac{E\alpha w}{1-\upsilon}\right) = 0 \tag{5}$$

where σ_{ij} is stress tensor, $i, j=1, 2, 3$; x_j is coordinate in the j direction, ρ is the density of soil masses, F_i is body force.

This paper adopts the initial strain method to analyze stress and deformation of reinforced expansive soil slope due to moisture absorption action, and regards the strain caused by change in moisture content as initial strain.

Computation Module and Parameters

Computation module is as shown in Fig. 3. The height of expansive soil slope is 10.0 m with a slope of 1:2 and geogrids are lay down horizontally. High density polyethylene (HDPE) unilateral geogrids and the middling expansive soils from Xinxiang in China are adopted to carry out a pull-out test to investigate the interface characteristic between geogrid and expansive soil. Tensile strength per unit width and elastic modulus of geogrid is 50 kN/m and 1200 Mpa, respectively. Mohr-Columb elasto-plastic constitutive model and the associative flow rule are utilized to simulate expansive soil, consolidation and undrained strength parameters in natural condition are taken. Atmospheric influence zone is set to be as deep as 2.0 m, cohesion of expansive soil under long term weathering action is reduced to 2.0 kPa, but friction angle is constant (Chandler 1972, 1974). Parameters of expansive soils are shown in Table 1.

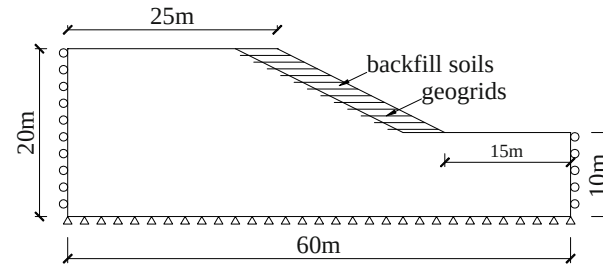

Fig. 3 Section of expansive soils slope reinforced with geogrids

Table 1 Mechanical parameters of expansive soils

Soils	E	c	φ	ρ	μ
	N/ m^2	kPa	degree	kg/m^3	
unweathered	5×10^7	20	17	2000	0.35
weathered	5×10^7	2	17	1850	0.35

RESTRAINT EFFECT OF GEOGRIDS ON SHALLOW LAYER FAILURE

Based on the stress state of expansive soil slope reinforced with geogrids, the strength reduction method is utilized to analyze the stability. Length of geogrids embedded in expansive soils and the vertical space between geogrids are considered. Horizontal length of 4.5 m and 6.7 m of geogrids is corresponding to the depth of 2.0 m and 3.0m vertical to slope surface, respectively. Tangential stiffness of the interface between geogrid and expansive soil is 2.3×10^6 N/m^3, Pseudo cohesion and pseudo frictional angle of the interface is 16 kN/m^2 and 10°, respectively. Computation schemes and results are shown in Table 2.

Table 2 Safety factor and positions of potential slip plane of slope with different vertical space between geogrids

Scheme	Vertical space between geogrids /m	Horizontal length of Geogrids /m	Safety factor	Slip plane position
1	0.4	4.5	1.68	geogrid's end
2	0.6	4.5	1.64	geogrid's end
3	0.8	4.5	1.57	geogrid's end
4	0.4	6.7	1.75	non-weathered soil
5	0.6	6.7	1.74	non-weathered soil
6	0.8	6.7	1.73	non-weathered soil

It can be seen from Table 2 that after geogrids are reinforced, slope's safety factor is more than 1.55, and the closer the geogrids are arranged, the greater the safety factor of slope is; when geogrids' horizontal length is 4.5 m, namely when geogrids penetrate just through the weathered layer, vertical space between geogrids will affect greatly the safety factor of slope. Fig. 4 shows the potential slip plane of non-reinforced expansive soil slope, it is a typical shallow slip plane with a safety factor of 0.94; Fig. 5 gives a potential slip plane of slope reinforced with geogrids (Scheme 5), with the safety factor increasing to 1.74. After geogrids are reinforced, potential slip plane moves toward the deep part of slope, its safety factor is greatly increased, geogrids can effectively restrain the shallow layer failure of expansive soil slope.

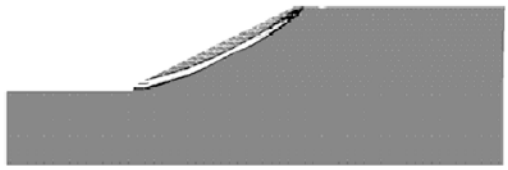

Fig.4 Typical slip plane of slope without geogrids (safety factor = 0.94)

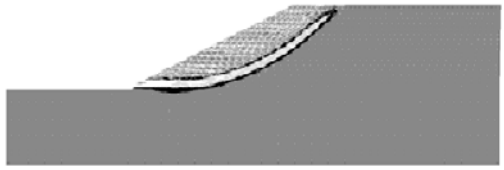

Fig.5 Typical slip plane of slope reinforced with geogrids (Scheme 5, safety factor=1.74)

Calculation schemes and potential slip planes obtained by considering effect of moisture content on the strength parameters of interface between geogrid and expansive soil and the vertical space between geogrids are shown in Table 3.

Table 3 Effect of the strength parameters of interface on the stability of reinforced slope (the horizontal embedded length of geogrid is 6.7 m)

Scheme	Vertical space between geogrids /m	c /kPa	φ /degree	Safety factor	Slip plane position
7	0.6	16	16	1.76	non-weathered soil
8	0.6	1	10	1.72	non-weathered soil
9	0.8	1	10	1.64	weathered soil

It can be seen from Tables 2 ang 3 and Fig. 5 that when vertical space between geogrids is 0.6 m, even if cohesion of the interface is reduced to 1 kPa and friction angle of the interface is 10 degree, it exerts little effect on the safety factor of slope and position of potential slip plane, which shows that shear stress of the interface is less than its shear strength, there is little relationship between stress state of slope and strength of the interface.

In comparison with Schemes 6 and 9, if vertical space between geogrids is 0.8 m, when cohesion of the interface is reduced to 1 kPa, potential slip plane is located in shallow weathered layer; when cohesion of the interface is kept at 16 kPa, potential slip plane moves into non-weathered layer, this shows that when strength of the interface is small, the interface is at plastic yield state, stress state in reinforced zone of slope is redistributed, so safety factor of slope is reduced.

In comparison with Schemes 8 and 9, strength parameters of the interface are the same (cohesion is 1 kPa, friction angle is 10 degree), when vertical space between geogrids is 0.6 m, potential slip plane lies within non-weathered layer; when vertical space between geogrids is 0.8m, potential slip plane is located at shallow weathered layer. Furthermore, it also shows that even if cohesion of the interface between geogrid and expansive soil is reduced to 1 kPa, keeping the interface at plastic yield state, safety factor of slope is still increased from 0.94 before reinforced to 1.64 after reinforced.

In comparison with Schemes 4, 5, 6 and 7, when cohesion of the interface is maintained at 16 kPa, and the horizontal embedded length of geogrid is 6.7m, the vertical space between geogrids exerts little effect on the position of potential slip plane and the safety factor.

As shown above, it follows that reasonable space vertically arranged between geogrids is dependent on strength parameters of the interface between geogrids and the fills. In addition, it is also affected by horizontal embedded length of geogrids etc.

RESTRAINT EFFECT OF GEOGRIDS ON DEFORMATION OF EXPANSIVE SOIL SLOPE

Restraint Effect of Geogrids on Deformation of Expansive Soil Slope without Moisture Increment

The horizontal embedded length of geogrids is set to 6.0m. That is, geogrids penetrate weathered layer into non-weathered soil. The vertical space between geogrids is 0.4 m, 0.8 m, 1.2 m, respectively. Tangential stiffness of the interface between geogrid and expansive soil is 2.3×10^6 N/m^3, Pseudo cohesion and pseudo frictional angle of the interface is 16 kN/m^2 and 10°, respectively.

The horizontal displacements of surface of slope reinforced with geogrids of different vertical space are shown in Fig. 6. It can be seen from Fig. 6 that horizontal displacement of reinforced slope is not uniformly distributed along height; magnitude at the middle is bigger while the magnitude at the top and bottom are smaller. Geogrids can restrain horizontal displacement of expansive soil slope under long-term weathering of atmosphere, the smaller the vertical space between geogrids, the smaller the displacement of slope surface.

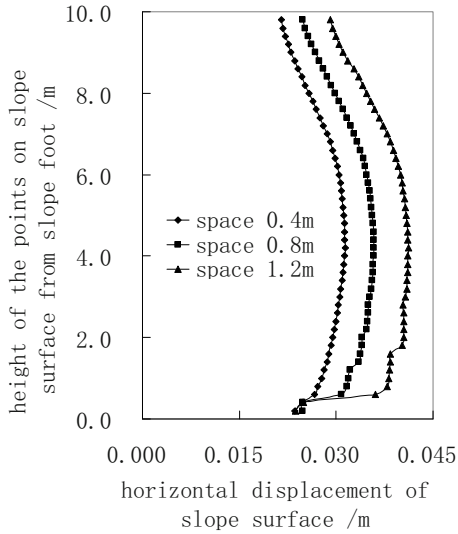

Fig. 6 Horizontal displacement of surface of slope reinforced with geogrids of different vertical space

Restraint Effect of Geogrids on Deformation of Shallow Layer of Slope due to Moisture Absorption of Expansive Soil

Based on observed data (Chen 2001), initial moisture content of compacted expansive soil in reinforced zone is assumed to be 16.3%, which is the optimum moisture content; it reachs 25.8% at the slope surface after it fully rains, which is the saturation moisture content; it is constant when depth under slope surface exceeds 2 m, and moisture content increment in 0 m to 2 m depth under slope surface assume to be linear along the depth. Linear expansion coefficient of expansive soil obtained via expansion ratio test without vertical load is 20.2%. Based on test for interface characteristic between geogrids and expansive soil, pseudo cohesion of interface decreases to 10 kN/m^2 and pseudo friction angle is 10º after moisture increment.

When the vertical space between geogrids is 0.4 m, 0.8 m, 1.2 m, respectively, and the horizontal embedded length of geogrids is 6.0 m, the horizontal displacement of slope surface after moisture absorption is shown in Fig.7.

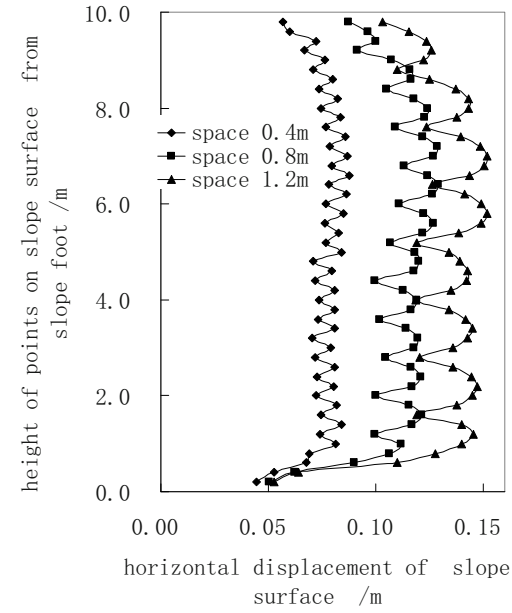

Fig.7 Horizontal displacement of surface of expansive soil slope reinforced with geogrids of different vertical space after moisture increment

It can be seen that the smaller the vertical space between geogrids, the smaller the horizontal displacement, and the greater the restraint effect of geogrids on deformation of slope. It can also be seen from Fig. 7 that horizontal displacement in the position of geogrids is much smaller than other areas, and the discrepancy increases with increase of vertical space between geogrids.

CONCLUSIONS

In this paper, considering long term atmosphere weathering action on strength parameters of expansive soil, the stress and deformation of expansive soil slope reinforced with geogrids are analyzed by using non-linear FDM, and the strength reduction method based on stress state is adopted to analyze the stability of reinforced slope. Restraint effect of geogrids on shallow layer failure of expansive soil slope is investigated. It comes to the following conclusions:

1. Reinforced geogrids can effectively restrain the shallow failure of expansive soil slope under long term atmosphere weathering effect; after reinforced, potential slip plane moves toward the deep zone, and safety factor of slope will be increased greatly.

2. When strength parameters of the interface is lesser due to moisture increment, it may make the interface reach the plastic yield state, redistribute the stress state in reinforced zone of slope; even if cohesion of the interface is reduced to 1kPa, geogrids still can make the slope maintain at steady state.

3. With the different vertical space of geogrids, the deformation of the slope can be restrainted to a different extent.

4. Under condition of moisture absorption of unsaturated expansive soils, there is obvious restraint effect of geogrids on the shallow deformation of slope, the horizontal displacement of slope surface is dependent on vertical space of geogrids. Horizontal displacement in the position of geogrids is much smaller than those in other areas, and the discrepancy increases with increase of vertical space between geogrids.

5. Reasonable vertical space between geogrids is dependent on strength parameters of the interface between geogrid and the fills, and is affected by horizontal embedded length, etc.

REFERENCES

Bao CG (2004) Fissuring property study of expansive soils. Proc. Symposium on Theory and Practice of Expansive Soil Treatment Technology. China Communication Press: 24-35 (in Chinese)

Bao CG (2006) Study on interface behavior of geosynthetics and soil. Rock Mechanics and Engineering 25(9): 1735-1744 (in Chinese)

Chandler RJ (1972) Lias clay:weathering processes and their effect on shear strength. Geotechnique 22(3): 404-431

Chandler RJ, Skempton AW (1974) The design of permanent cutting slopes in stiff fissured clays. Geotechnique 24(3): 457-466

Chandler RJ (1974) Lias clay:the long-term stability of cutting slope. Geotechnique 24(1): 21-38

Chen SX, Chen SY (2001) Analysis of stability of unsaturated soil slope due to permeation of rainwater. Rock and Soil Mechanics 22(4): 447-450 (in Chinese)

Skempton AW (1964) Fourth Rankine Lecture:long-term stability of clay slopes. Geotechnique 14(2): 77-101

Shen ZJ (2004) Weathering resistant design-An important aspect of future development of geotechnical engineering design. Geotechnical Engineering 26(6): 866-869 (in Chinese)

Wang Z, Wang XQ (2000) Some problems on foundations reinforced with geosynthetics. J. Geotechnical Engineering. 22(4):503–505 (in Chinese)

Wu M, Yan Y (2004) Technology of using sealing methods to construct weak expansive soil embankment. Proc. Symposium on Theory and practice of expansive soil treatment technology China Communication Press: 316-324 (in Chinese)

Xu LR, Ling JM, Lui BC (2004) Experiment on interface friction coefficient parameters between geogrids and expansive soils. TongJi University. 32(2): 172-176 (in Chinese)

Xu Y, Yang GL, Wu YZ (2005) Model test on reinforced expansive soils retaining wall. Railway Sience and Engineering 2(4): 11-15 (in Chinese)

Yin ZZ, Lv QF, Yuan JP (2004) Slope stability analysis of expansive soils. Proc. Symposium on Theory and practice of expansive soil treatment technology China Communication Press: 61-69 (in Chinese)

Zhu BF (2003) Thermal stresses and temperature control of mass concrete. China electric power press, China: 153-155 (in Chinese)

DETERMINATION OF CUT SLOPE REINFORCEMENT USING AHP TECHNIQUE

J.G. Han[1], J.Y. Lee[2] and M.H. Lee[3]

ABSTRACT: Analysis was performed using AHP(Analytic Hierarchy Process) technique for the determination of priority on the effect factors and the preferences on cut-slope reinforcing methods. The results of data taken from professional group, researchers, design engineers and construction engineers, shows that stability, durability and environmental condition are most important effect factors. The retaining wall and the cutting methods were predominant for stability, economical efficiency, and maintenance/management in the preferences evaluation interpreted for the increasing method of safety factor on the cut-slope reinforcing methods.

KEYWORDS: AHP, cut-slope, reinforcing method, effect factors

INTRODUCTION

Public constructions have been more gigantic in sizes, and became essential for the working scale such as of filling and cut-slope large. During the cutting and filling processes of slope, many counter measuring methods of stabilization apply. The counter measuring methods are classified as shown in Fig. 1; the increasing stability method or the maintaining stability methods. These methods are usually applied as individual methods or joint methods (Han 1997). Practically, such methods are applied appropriately to construction sites under engineering judgments. For the applying rational engineering methods on slope stability the quantity analysis of effect factor (such as stability and economic analysis, priority investment rating and so on) are needed, especially for slope stability of constructions involving large budgets and many labours. In other words, comments and choices of alternative methods with likeness results are composed with many potential problems. In other to overcome such drawback, the selected methods have to be evaluated based on quantitative values.

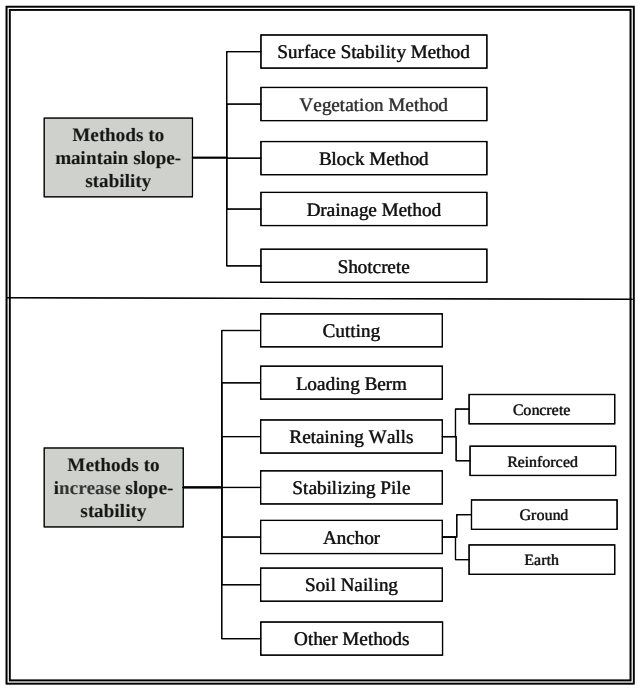

Fig. 1 General stability method for cut-slope

Analysis of such method is one of the multi-attribute decision making method such on Goal Programming, Utility Function, and Analytic Hierarchy Process (AHP).

Recently, “Fuzzy”, “Professional System” and “Genetic algorithm” (Ahn et al. 2001, Lee 2000), AHP method involves decision makings based on collaborations with the professionals of other fields (Cho et al. 2005).

The most characteristic feature of AHP is on sorting out complex problems classify and pinpointing the importance of each contributing factors using pairwise comparison. AHP is recognized for its usefulness; mainly recognized for its human-like problem approaching, analyzing, and understanding frame as well as for gathering numerical values and results through systematic ratio scales of importance or preference using models. Further more, AHP is highly appraised

[1] Associate Professor, Department of Civil & Env. Engineering, Chung-Ang University, KOREA
[2] Ph.D Candidate, Department of Civil Engineering, Chung-Ang University, KOREA, Email : geoljy@wm.cau.ac.kr
[3] BK Research Associate, Department of Civil & Env. Engineering, Han-Yang University, KOREA

theoretically because AHP adopts methods like scale select, weight determination process, sensitivity analysis, which are all officially approved and heavily inspected, despite its concise applying process.

Due to such advantages it can be said that AHP is the most widely used method out of all existing decision making methods. AHP helps to make decisions on complex and different viewpoints in its field of apply such as demand and supply of energy, means of transportation, planning for high school education, establishing environmental regulations, establishing military enforcement and many other problems in public sector. Further more in the field of engineering, this method is applied in studies on priority investment rating results R&D and management, risk management of building construction a landslide prediction, road size decisions, GIS decision making, bridge structure as well as form in especially thin method need for decision makings, closely tied in many other areas with the field of construction.

In this research, it is intended to apply AHP method for total decision making required in choosing for the cut-slope reinforced method which occurs during various civil construction site. The intension is to find out the preference of professionals using AHP to safety increasing method displayed in Fig. 1, which is one of the most commonly used cut-slope reinforced method.

AHP METHODOLOGY

AHP is one of the decision making method created for effective problem dealing solution stating that human interface protects the 3 distinctive principles listed below (Saaty 1995).

Hierarchical structuring principle
Weighting principle
Consistency principle

Underling principles of AHP are directly projected in model's structures and structuring methodology. In fact, the explanation of sequential structure, measuring the importance on evaluating factors of the set up structures, and inspecting of the consistency on such decision completes the structure of the model.

AHP sets its basic assumptions as product compassion, homogeneity, independency, and the basic theory of dependency. (Vargas 1990)

Analyzing process to obtain optimum solution using the AHP method starts with brainstorming process, hierarchical structuring process, weight factor setting, measuring process, and evaluation process.

Fix up, group, and arrange of properties for hierarchical structuring, then line them up based on their levels. The highest level is the level 1; aiming of the principle problems. Level 2 describes the outside effects effecting level 1 in details. By repeating the process the hierarchical structuring properties can be analyzed.

To calculate the weight factors, use the pairwise comparison form of survey to professionals to find out their preference or comparative importance. Describe the decision of the evaluator verbally during the process of pairwise comparison, and give reasonable value for the response. The value gets included to the standard numerical value. Following the Miller's(1956) psychological experiment result, 9 points are given as standard in AHP for comparison using pairwise comparison.

After the relative weight factor computation, combine the result that produce relative weight factor of a suggested, by each evaluation element, alternative to calculate synthetic index to set, by optimizing the alternative that has the largest value, the following Eq 1.

$$R = \sum_{i=1}^{n} W_i Z_i(x) \tag{1}$$

Where, R is synthetic index of an alternative, W_i is the value of each index, Z_i is the weight of each index.

Then, $n, n = \sum \lambda I$ is a root characteristic equation of λ, and w is native vector of matrix A on the native vector λ. If we assume the only characteristic root that is not 0 to be $\lambda_{\max}$ (the maximum characteristic root), it becomes, $\lambda_{\max} = n$, $\lambda_i = 0$.

At this moment, because the maximum characteristic root $\lambda_{\max}$ is bigger or equal to the number (n) of pair wise comparison factor, it can, as long as $\lambda_{\max}$ approaches n, refer to pair wise comparison matrix A has consistency. And we can find $\lambda_{\max}$ through CI (consistency index) and CR(consistency rate).

Consistency index: $(CI) = (\lambda_{\max} - n)/(n-1)$

Consistency rate: $(CR) = (CI / RI) \times 100(\%)$ (2)

In where, RI is Random Index.

Random Index on the n values varies from 1 to 10 is shown in Table 1, and according to experience, if consistency rate calculated from the above equation is within 10%, we regulate those pair wise comparison matrix has a consistency.

Table 1 Random Index (Cho et al. 2005)

n	1	2	3	4	5	6	7	8	9	10
R.I	0	0	0.58	0.90	1.12	1.24	1.32	1.41	1.45	1.49

HIERARCHICAL STRUCTURE AND DATA ANALYSIS FOR THE APPLYING METHODS

On choosing the slope stability methods the chosen method using the increase method on slope stability become priorities, which due to and commonly applied reinforced method. Hierarchical structures based on methods which have applied most commonly in the field are reflected in Fig. 2. In Fig. 2, the first step of hierarchical structure considers economic efficiency, workability, maintenance/management, stability and durability, and environmental condition. The second step applies, among Loading berm, Reinforced concrete wall, Reinforced soil wall, Stabilizing pile, Anchor and Soil nailing. Also, to increase credibility of than study, experienced people in researcher is institutions, constructors and designers became primary subjects. Among participants, those who have experiences of 10 years or more had the highest percentage with 59%. The various industries had different proportions; 44% research institute, 28% constructor, 28% designer and level of education was 22% Ph.D, 39% master's degree, and 22% bachelor degree. Therefore, it is sensitive that proper distribution and credibility of the result were reflected.

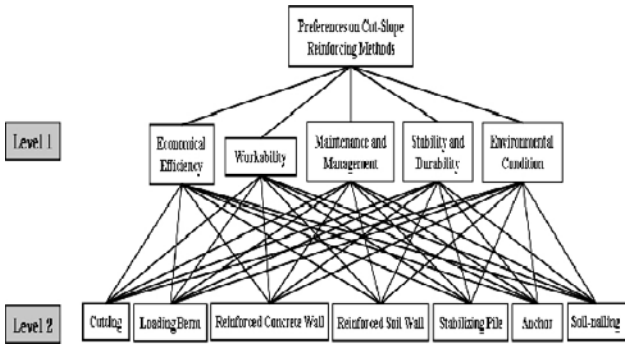

Fig. 2 The hierarchy process of evaluation item

ANALYSIS RESULT

Weight Factor for each evaluation element

Fig. 3 is the result from the analysis, based on each occupation, of weight factor on considerable factor in selecting reinforced method. The consistency rate of all results is 0.01—0.02 (1—2%) and satisfies all restrictions that AHP technique suggested within 10%. Commonly, professionals in all sectors concluded that stability and durability are the most important evaluation element.

Professionals of a researcher is institute granted about similar weight factor to the rest clauses besides stability and durability, and professional constructors, designers evaluate stability and durability and environmental condition to more than 50% of the whole weight factor. Next, it also evaluated maintenance and management; they evaluated workability and economic efficiency as other important clauses, which due to their owns characteristic on the work,

Fig. 4 and Table 2 are analyzed by combining all professionals' opinions, and when combining all the opinions, the weight factors are listed from the highest to lowest in order of stability and durability, environmental condition, maintenance/ management, workability and economical efficiency, respectively.

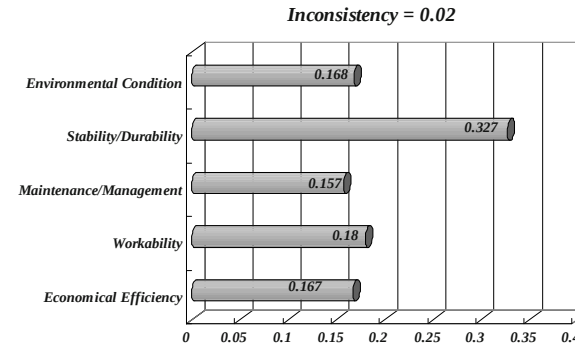

(a) Researchers

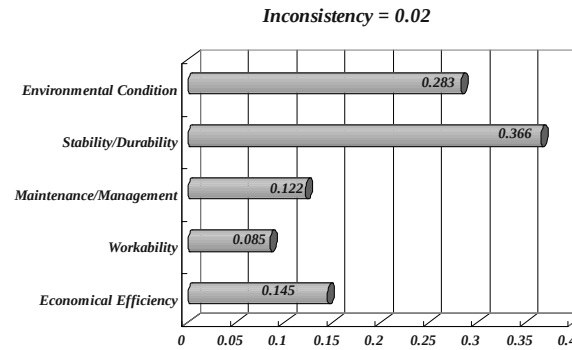

(b) Design Engineers

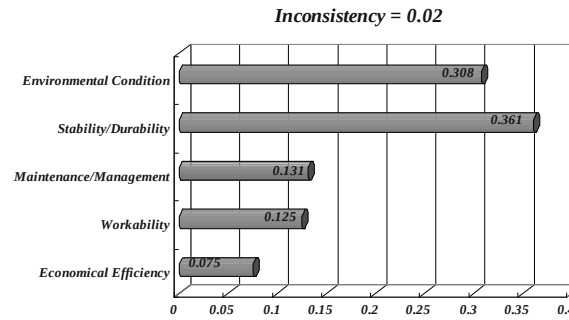

(c) Construction Engineers

Fig. 3 Weight factor of evaluation element (Job)

THE PREFERENCES ON CUT-SLOPE REINFORCED METHOD

Table 3—7 illustrates the analyzed results for professional's preference on the cut slope reinforced

method; the reinforced soil wall method out of 7 methods showed the highest preference. This result is the outcome of outstanding achievements on its durability, stability, and environmental compatibility, which is reflected on the weighted factors evaluation process in Fig. 4. Retaining concrete wall received high relatively appraises in its durability, stability and maintenance simplicity, where as Loading berm, cutting and anchor, were all highly evaluated for economic efficiency and workability. The method preferences for soil nailing, stabilizing pile method was evaluated relatively well for its environmental compatibility, and durability and stability, but these methods show that it is the least preferred method since it received low evaluation for other factors. Figs. 5 and 6 illustrates the preferred methods chart and weighting of factors contributing in choosing methods.

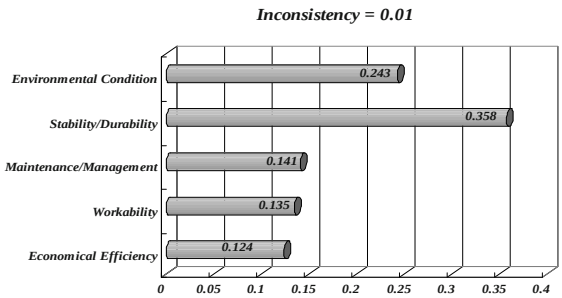

Fig. 4 Weight factor of evaluation elements (Total)

Table 2 Weight factor of evaluation elements (Total)

	A	B	C	D	E	Weight
A	1.0	1/1.1	1/0.74	1/0.4	1/0.5	0.124
B		1.0	1.1	1/0.4	1/0.6	0.135
C			1.0	1/0.4	1/0.6	0.141
D				1.0	1.4	0.358
E					1.0	0.243

A : Economical Efficiency, B : Workability
C : Maintenance/Management, D : Stability/Durability
E : Environmental Condition

Table 3 Weight factor of reinforcing method for economic efficiency

	A	B	C	D	E	F	G	Weight
A	1.0	4.2	4.1	3.9	1.6	2.4	1.9	0.304
B		1.0	1.7	1.7	0.4	1.5	1.1	0.114
C			1.0	0.7	0.3	0.9	0.9	0.072
D				1.0	0.3	0.8	0.7	0.077
E					1.0	1.5	1.3	0.211
F						1.0	0.7	0.099
G							1.0	0.122

A : Cutting, B: Soil-Nailing, C: Anchor
D: Stabilizing Pile, E : Loading Berm
F : Retaining Concrete Wall, G : Reinforced Soil Wall

Table 4 Weight factor of reinforcing method for workability

	A	B	C	D	E	F	G	Weight
A	1.0	2.3	2.8	3.6	1.8	2.9	1.6	0.271
B		1.0	1.9	2.0	0.4	2.0	1.6	0.151
C			1.0	1.6	0.6	0.8	0.6	0.090
D				1.0	0.3	0.5	0.5	0.062
E					1.0	1.0	0.8	0.173
F						1.0	0.8	0.112
G							1.0	0.141

Table 5 Weight factor of reinforcing method for maintenance and management

	A	B	C	D	E	F	G	Weight
A	1.0	1.2	1.1	1.2	0.8	0.6	0.5	0.115
B		1.0	0.9	1.5	0.5	0.5	0.4	0.097
C			1.0	1.6	0.6	0.4	0.4	0.103
D				1.0	0.6	0.4	0.4	0.081
E					1.0	0.5	0.5	0.142
F						1.0	0.8	0.221
G							1.0	0.241

Table 6 Weight factor of reinforcing method for stability and durability

	A	B	C	D	E	F	G	Weight
A	1.0	1.4	1.4	1.2	1.4	0.7	0.7	0.142
B		1.0	0.5	0.6	0.8	0.4	0.4	0.080
C			1.0	1.2	0.8	0.6	0.5	0.116
D				1.0	0.9	0.5	0.5	0.109
E					1.0	0.4	0.4	0.107
F						1.0	1.7	0.238
G							1.0	0.208

Table 7 Weight factor of reinforcing method for environmental condition

	A	B	C	D	E	F	G	Weight
A	1.0	0.4	0.4	0.5	0.7	0.7	0.4	0.073
B		1.0	0.7	1.5	0.8	1.8	0.7	0.159
C			1.0	1.6	0.8	1.6	1.1	0.185
D				1.0	0.9	1.7	0.6	0.133
E					1.0	1.6	1.3	0.172
F						1.0	0.5	0.095
G							1.0	0.184

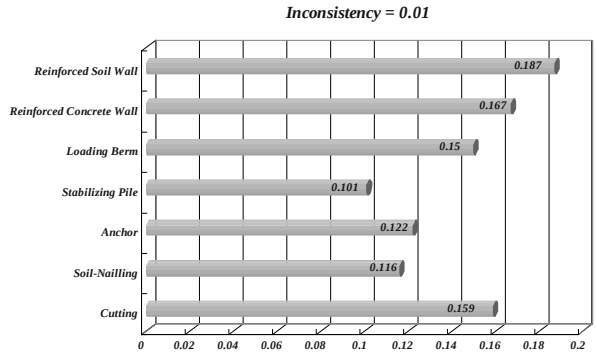

Fig. 5 Weight factor of reinforcing methods (Total)

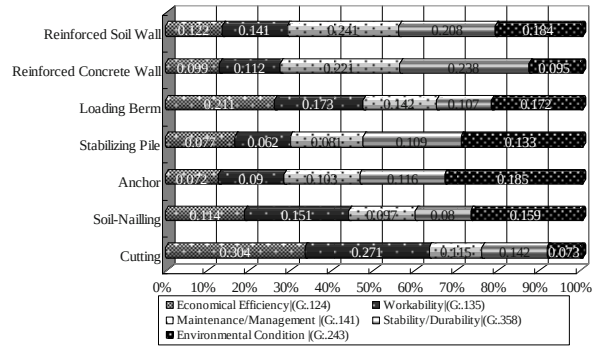

Fig. 6 The importance of evaluation elements for each method

CONCLUSION

Recently, to the application of reasonable counter measuring method on the collapse slope. AHP method was adapted after reviewing of economic analysis, construction, stability, durability analysis, and environmental comparability analysis, which are all contributing factors when choosing methods. We have analyzed the weighting factor of which are consideration factors when choosing methods for cut-slope, and the preference of slope reinforcing method from professionals in various fields. The result of the consistency test was 1%－2%, which concluded to be a creditable result since the allowed restriction of AHP method was within 10%. The summarized researches are as followed.

On choosing the methods, if the most important factor that were analyzed to be the stability and durability. Stability, durability and environmental compatibility took up over 50% of the total contributing factors. Also, the professionals in the field including designer indicated that economic and construction factors were the second most contributing factors, reflected from each other their specialized condition in the field.

The analyzed results for professional's preference on the cut slope reinforced method; the reinforced soil wall method out of 8 methods showed the highest preference. This directly reflects the good research results of stability, durability, maintenance simplicity and economic factors.

The categorized of result weighting evaluation factors showed that environmental compatibility was listed as the second most important factor. In practically, on choosing method, the effect of environmental factor was weak. This reflects that there is a difference between the reality decision making and ideal decision making. Therefore, it is concluded that economic factor, simplicity of maintenance, stability and durability are the main contributors when it comes to choosing a method.

REFERENCES

Lee CK (2000) Optimal Selection of a Maintenance Method for Bridge Structures Using fuzzy and Genetic Algorithms, Ph.D thesis, Chung-Ang University (in Korea)

Ahn JW, Kim YS, Kim SS(2001) A case study on the selection of a bridge superstructure type using AHP technique and LCC concept, KSCE (in Korea) 21 (S-D): 673-681

Han JG (1997) Stability analysis and design of slopes using stabilizing stability, Ph.D thesis, Chung-Ang University (in Korea)

Cho KT, Cho YG, Kang HS (2005) The analistic Hierarchi process, Dong-Hyun Publishing (in Korea)

Miller GA (1956) The Magical Number Seven, Plus or Minus Two: Some Limits on Our Capacity for Processing Information, Psychological Rev 63

Vargas LG (1990) An Overview of the Analytic Hierarchy Process and Its Applications, European Journal of Operational Research 48: 2-8

Saaty TL (1995) Decision Making for Leaders (AHP series), RWS Publications 3

GEOMETRY DESIGN METHOD CONSIDERING SURCHARGE LOAD BEHIND TIERED REINFORCED SOIL WALL

J.G. Han[1], K.K. Hong[2], J.S. Kim[3] and M.H. Lee[4]

ABSTRACT: The construction of reinforced soil wall is a recent trend in construction work due to the economical advantage and construction efficiency. However, there have been increasing numbers of large scale collapse accidents in tiered reinforced soil wall due to inconsistent in a design manual and uncertainty in stability evaluation. The surcharge load behind the wall has effects on the stability of tiered reinforced soil wall as well as the whole ground. Therefore, this study interpreted the method of surcharge load suggested in the typical design methods (i.e., NCMA and FHWA), which are applicable in Korea. The analysis resulted in the reasonable design method and the suggested method was applied in the field case using the numerical analysis. The numerical simulations confirmed that the surcharge load behind the wall should be considered for the slip failure surface to evaluate the tiered reinforced soil wall.

KEYWORDS: surcharge load, tiered reinforced soil wall, geometry design method, numerical analysis

INTRODUCTION

The application of reinforced soil wall has increased because of upgrade feature of the ground strength and stability of the construction as well as good for the economical advantage and construction efficiency. Therefore, the construction of reinforced soil wall is a recent trend in construction work and the scale of reinforced soil in the field wall has been grown up like tiered reinforced soil wall. However, there have been increasing numbers of large scale collapse accidents in tiered reinforced soil wall which due to the uncertainty in surcharge load and stability evaluation. The surcharge load behind the upper wall has effects on the stability of tiered reinforced soil wall as well as the whole ground (Han et al. 2005).

In Korea, most of the design for the reinforced soil wall is following the design manual of NCMA (National Concrete Masonry Association 1996) and FHWA (Federal Highway Administration 2001). The design manual of NCMA and FHWA using limit equilibrium theory propose to satisfy the stabilities of internal, external, local and global in the reinforced soil wall. However, collapse has happened frequently due to inconsistent in a design manual in Korea. Therefore, the understanding of mechanical behavior in the tiered reinforced soil wall is required (Yoo 2002).

This study is to interpret the method of surcharge load suggested in the typical design method. The case study was conducted on the suggested method using numerical analysis, in which the behavior of ground by offset distance of the surcharge load and the tiered reinforced soil wall was analyzed.

PROPOSED OF GEOMETRY DESIGN METHOD

The surcharge load behind the upper wall should be considered in the whole area of the slip failure surface (see Fig.1).

The Design Considering Upper Wall in NCMA and FHWA

In the design by the criterion of NCMA and FHWA, the upper wall (A_1) is applying by converted value (q_1) of distributed surcharge load to evaluate bearing capacity of the tiered reinforced soil wall as shown in Fig. 2a.

The Existing Design Considering the Surcharge Load behind the Wall

[1] Associate Professor, Department of Civil & Env. Engineering, Chung-Ang University, KOREA
[2] Ph.D. Candidate, Department of Civil Engineering, Chung-Ang University, KOREA, Email: kkhong@wm.cau.ac.kr
[3] Formerly Graduate Student, Department of Civil Engineering, Chung-Ang University, KOREA
[4] BK Research Associate, Department of Civil & Env. Engineering, Hanyang University, KOREA

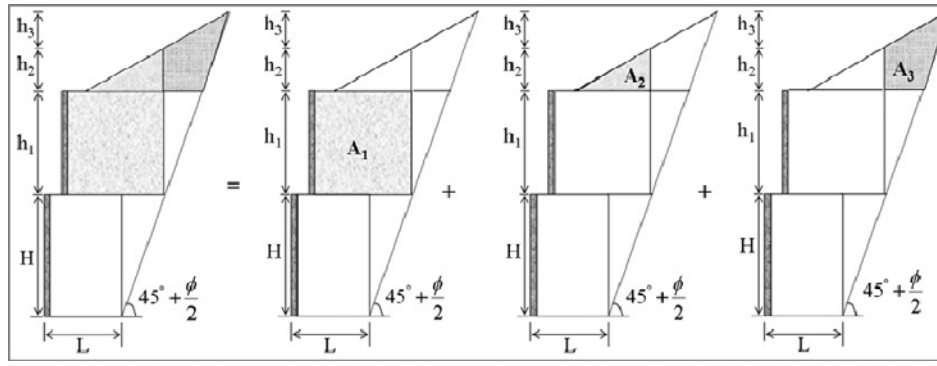

Fig. 1 The geometry design method considering the surcharge load behind the wall

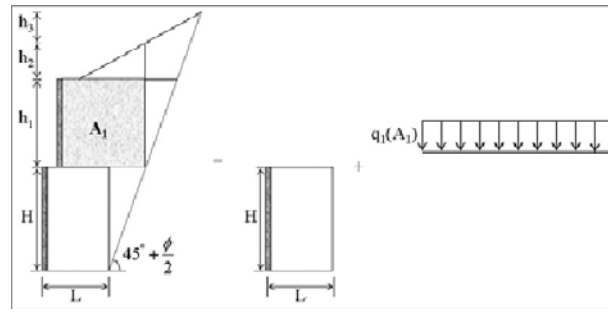

(a) The considering of upper wall in NCMA and FHWA

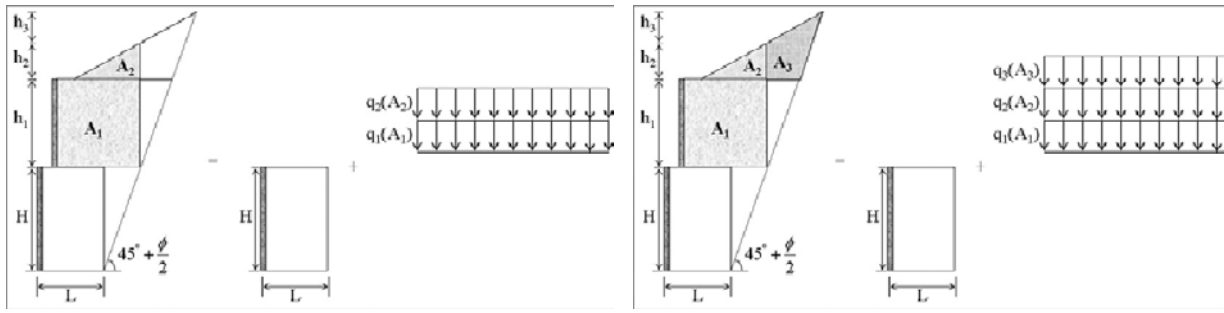

(b) The existing design considering the surcharge load (c) The design considering slip failure surface

Fig. 2 The design method considering the surcharge load in the tiered reinforced soil wall

In Korea, the upper wall (A_1) and the surcharge load (A_2) is applying by converted value (q_1, q_2) of distributed surcharge load (Fig. 2 b). However, this method contains unstable parts such as characteristic of backfill material on the slip failure surface.

The Design Method Considering Slip Failure Surface

If the offset distance of surcharge load is included on the slip failure surface as shown in Fig. 2, the stability of reinforced soil wall would be underestimated because outside load of the slip failure surface of external is unreflected. The wedge failure of reinforced soil wall has slip failure angle($45^\circ + \phi/2$) from bottom of lower wall. Therefore, the stability of tiered reinforced soil wall surcharge as seen in Fig. 2 has been affected on the slip failure surface.

After the extending of the slip failure surface to embanked area behind the wall, the application of the whole embanked load in side slip surface may be considered as a surcharge load of the smallest range. Therefore, the tiered reinforced soil wall has to evaluate the global stability considering surcharge load behind the upper wall when offset distance between the upper and lower wall is considered.

CASE STUDY ON THE SUGGESTED METHOD

Case study on the collapse area is applied the suggested method, to confirm influence of surcharge load behind the tiered reinforced soil wall in stability. The collapse of the structure is often occurring in the tiered reinforced soil wall during construction of embankment and pile driving to foundation of abutment after completing the reinforced soil wall (Han et al. 2005).

The heights of upper and lower wall in the applied as shown in Figs. 3 and 4, respectively and the stability analysis considered the last embankment step after completing of the tiered reinforced soil wall. Table 1 shows design parameters using the analysis. Especially, the internal friction angle of foundation ground applied increased value gradually because the stability of the wall is related with compaction condition of foundation ground in field. The material parameters were applied for the suitable value using the report of soil property.

The conditions of soil, reinforcement and load, as shown in Figs. 3 and 4, were equally applied. The internal friction angle of foundation ground, which based on consider the results of site investigation on the field, is applied from 30° to 35° because the bearing capacity of wall by compaction becomes different. The external stability in this range was evaluated. The external stability was conducted about base sliding (Fs≥ 1.5), overturning (Fs≥ 2.0), bearing capacity (Fs≥ 2.5, Fs≥ 2.5) and the results as presented in Tables 2 and 3.

The analysis result based on the NCMA manual satisfied the requirement. However, the result by FHWA manual was less than the requirement of safety factor partially, in 30°－35° ranges when surcharge load is considered by geometry design method. This means that foundation ground was weakened by bad compacted state or its collapse occurred. The results could be confirmed by the settlement of foundation ground or collapse cases on the tiered reinforced soil wall.

Therefore, the influence area of surcharge load behind wall in design and construction should be considered in extent of slip failure surface. That is, in the field, because the tiered reinforced soil wall using existing design method is expected to be unstable after construction and the application of suggested geometry design method may be more reasonable.

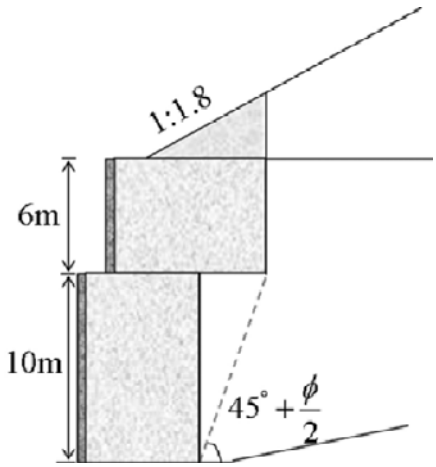

Fig. 3 Analysis section for existing design method

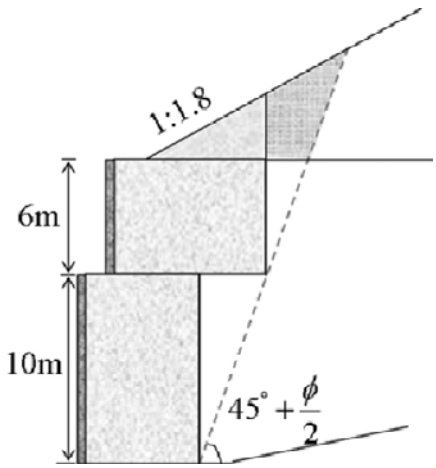

Fig. 4 Analysis section for geometry design method

Table 1 Design parameters using analysis

Items		Values
Backfill	Internal friction angle	30°－35°
	Unit weight	19 kN/m^3
Foundation ground	Internal friction angle	30°. 31°, 32°, 33°, 34°, 35°
	Unit weight	19 kN/m^3
Reinforcement	Allowable tensile strength	80 kN/m
	Length	10.56 m
Angle behind upper wall		29°
Offset distance between the walls		3 m
Height	Lower wall	10 m
	Upper wall	6 m
Surcharge load	q_1	133.0 kN/m^2 133.0 kN/m^2
	q_2	218.4 kN/m^2 185.4 kN/m^2
	q_3	241.2 kN/m^2 251.4 kN/m^2

Table 2 Analysis result by NCMA design manual (Bearing capacity, $F_s \geq 2.0$)

Items	Internal friction angle of original ground and backfill = 30°			Internal friction angle of original ground and backfill = 35°		
Surcharge load / Internal friction angle of foundation ground	q_1=13.3	q_2=21.84	q_3=24.12	q_1=13.3	q_2=18.54	q_3=25.14
30°	3.286 OK	2.492 OK	2.337 OK.	3.803 OK	3.246 OK	2.733 OK
31°	3.796 OK	2.878 OK	2.699 OK	4.394 OK	3.750 OK	2.034 OK
32°	4.394 OK	3.332 OK	3.124 OK	5.089 OK	4.343 OK	3.643 OK
33°	5.096 OK	3.863 OK	3.622 OK	5.903 OK	5.038 OK	4.240 OK
34°	5.923 OK	4.487 OK	4.209 OK	6.863 OK	5.856 OK	4.928 OK
35°	5.902 OK	5.230 OK	4.903 OK	7.999 OK	6.825 OK	5.743 OK

Table 3 Analysis result by FHWA design manual (Bearing capacity, $F_s \geq 2.5$)

Items	Internal friction angle of original ground and backfill = 30°			Internal friction angle of original ground and backfill = 35°		
Surcharge load / Internal friction angle of foundation ground	q_1=13.3	q_2=21.84	q_3=24.12	q_1=13.3	q_2=18.54	q_3=25.14
30˚	2.155 NG	1.508 NG	1.389 NG	2.647 OK	2.171 NG	1.753 NG
31˚	2.500 OK	1.750 NG	1.611 NG	3.072 OK	2.518 OK	2.034 NG
32˚	2.907 OK	2.035 NG	1.874 NG	3.572 OK	2.928 OK	2.365 NG
33˚	3.386 OK	2.370 NG	2.182 NG	4.159 OK	3.410 OK	2.754 OK
34˚	3.950 OK	2.765 OK	2.546OK	4.853 OK	3.979 OK	3.214 OK
35˚	4.621 OK	3.234 OK	2.978OK	5.677 OK	4.654 OK	3.789 OK

CHARACTERISTICS OF GROUND BEHAVIOR BY NUMERICAL ANALYSIS

Condition of Analysis

The maximum displacement distribution of the analysis section was analyzed to confirm the behavior of the whole ground depending on the lower offset distance by the upper wall as well as the upper offset distance by the surcharge load. The analysis section as shown in Table 4 is considered 2 m, 4 m, 10 m and 15 m representatively among offset distance (D_1) between each wall, which is satisfied standard of NCMA and FHWA. The offset distance (D_2) between upper wall and surcharge load, is considered as minimum distance (1m) and maximum distance(6m), respectively (see Table 4).

The analyses were conducted by FEM, PLAXIS 8.0 program. The ground and facing block applied to Mohr-Coulomb model and Linear-Elastic model, respectively.

The parameters of ground were considered on weathered rock and weathered soil, which generally is distributed in Korea. The elastic modulus of reinforcement was considered with 5,000,000 kN/m^2 so that internal stability of reinforced soil mass was assured and the facing block and foundation ground were considered only bearing resistance by friction.

Table 4 Selection of analysis section

Items	Range of offset distance between lower wall and upper wall	Range of offset distance between upper wall and surcharge load	Representation section	
			Offset distance between lower wall and upper wall (D_1)	Offset distance between upper wall and surcharge load (D_2)
Case A	11－15 m	1 ~ 6m	15 m	1, 6 m
Case B	7－10 m		10 m	
Case C	3－6 m		4 m	
Case D	1－2 m		2 m	

Table 5 Summary of material parameters

Items	γ_t (kN/m^3)	c (kN/m^2)	ϕ (deg.)	E (kN/m^2)	ν
Facing block	24	-	45.0	300×E5	0.25
Backfill	19	20	35.0	2×E5	0.3
Embankment soil	19	10	35.0	2×E5	0.3
Foundation ground	22	100	38.0	3×E5	0.2
Reinforcement	-	-	-	50×E5	-

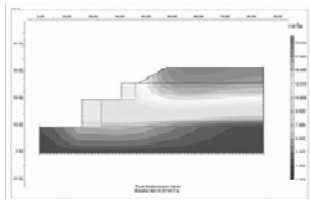

(a) D_1 : 15m, D_2 : 6m (b) D_1 : 15m, D_2 : 1m

Fig. 5 Distribution type of maximum displacement (Case A)

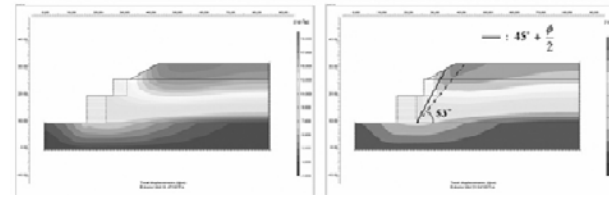

(a) D_1 : 10m, D_2 : 6m (b) D_1 : 10m, D_2 : 1m

Fig. 6 Distribution type of maximum displacement (Case B)

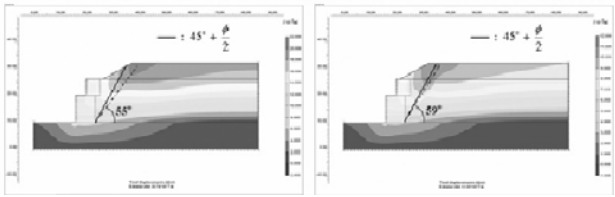

(a) D_1 : 4m, D_2 : 6m (b) D_1 : 4m, D_2 : 1m

Fig. 7 Distribution type of maximum displacement (Case C)

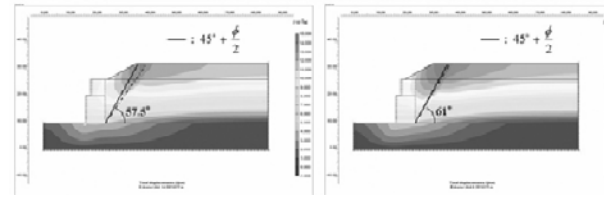

(a) D_1 : 2m, D_2 : 6m (b) D_1 : 2m, D_2 : 1m

Fig. 8 Distribution type of maximum displacement (Case D)

Review of Slip Failure Surface Considering the Behavior of the Whole Ground

The analysis results using FEM are interpreted in the as follows; (1) In case A, the distribution of total displacement is presented the maximum displacement on the ground surface. The displacement is decreased, when the depth of ground is deep the foundation ground as shown in Fig. 5. These results are general displacement type on the ground. (2) In case B, the distribution of

maximum displacement was similar to wedge failure surface in the whole ground according to the offset distance by surcharge load is decreased as shown in Fig. 6. (3) The case C, which is less offset distance between lower and upper wall than case A and B, is presented that the slip failure is smaller than wedge failure angle in the maximum offset distance (6 m) by surcharge load. However, the failure angle was similar to wedge failure angle, when the offset distance (D_2) by surcharge load becomes more close. (4) The stability of the case D is excepted allowable range in the design method of NCMA and FHWA. Therefore, the collapse was occurred irrespective of offset distance (D_2) in all sections. The distribution of maximum displacement was similar to wedge failure surface, when the offset distance (D_2) by surcharge load became more close as shown in Fig. 8.

As a results, the behavior of the whole ground becomes similar to wedge failure surface, when offset distance (D_2) between surcharge load and the walls is long distance. On the other hand, the collapse type was similar to wedge failure from bottom of the lower wall in short distance (D_2). That is, the collapse type of the tiered reinforced soil wall should be classified by surcharge load condition, and the stability of the whole ground including structure has to be evaluated.

CONCLUSION

The behavior of the tiered reinforced soil wall has greatly affected by the considering method of surcharge load behind the wall, the lower offset distance by the upper wall and the upper offset distance by the surcharge load. This study found that the collapse accidents of the tiered reinforced soil wall have been increasing because of inconsistent in a design manual and uncertainty in stability evaluation.

Therefore, this study interpreted the method of surcharge load suggested in the typical design method, NCMA and FHWA, which are applicable in Korea, and the case study was conducted on the suggested method using FEM, in which the behavior of ground by offset distance of the surcharge load and the tiered reinforced soil wall was analyzed. The results confirm that the tiered reinforced soil wall have to evaluate the global stability considering surcharge load behind the upper wall if surcharge load behind the wall exists.

The numerical analysis confirmed that the distribution type of the maximum displacement changed from circular failure to wedge failure, when the offset distance (D_2) by surcharge load becomes more close. This means that the collapse type should be considered by surcharge load condition in stability evaluation of the tiered reinforced soil wall. The result shows that the lower offset distance by the upper wall and the upper offset distance by the surcharge load are important to evaluate the stability of the wall and the whole ground including structure.

REFERENCES

Han JG, Cho SD, Jeong SS, Lee KW, Kim JS (2005) Case Study on the Countermeasure Methods and Collapsed Sources of Segmental Retaining Wall Considering Site Conditions. Korean Geosynthetics Society [J] (in Korean) 4(3): 35-43

Federal Highway Administration (2001) Mechanical stabilized earth wall and reinforced soil slopes design and construction guideline. FHWA Demonstration Project 82 (Elias, V and Cristopher BR). Washington, DC, USA

National Concrete Masonry Association (1996) Segmental retaining wall design manuals. 1st Edition, Virginia, USA

Yoo CS (2002) Design Aspects of Soil-reinforced Segmental Retaining Walls in Tiered Arrangement-Case Study. Korean Geosynthetics Society [J] (in Korean) 1(1): 31-41

STUDY ON THE GEOGRID REINFORCED SOIL RETAINING WALL OF CONCRETE RIGID FACE BY FIELD TEST

G.Q. Yang[1], P. Lv[2], B.J. Zhang[3] and Q.Y. Zhou[4]

ABSTRACT: The field test of moulding concrete rigid panel faced geogrids reinforced soil retaining wall is done in the Gan (Zhou)-Long (Yan) railway main line of China. The basement vertical pressure of reinforced soil retaining wall is non-linear along the reinforcement length, and the maximum value is at the middle of the reinforcement length, moreover the value reduce gradually at former and bottom. The testing lateral pressure of the reinforced soil wall is non-linear along the height and the value is less than the active lateral earth pressure. The distribution of tensile strain along reinforcement at the upper wall is single peak value,but the distribution of tensile strain along reinforcement at the lower wall is twin peak value. The potential fracture plane at upper wall is similar to "*0.3H method*", but the potential fracture plane at lower wall is near to the active Rankine earth pressure theory. The position of the maxmium lateral displacement of the wall face during construction at lower wall, moreover the position of the maxmium lateral displacement of the wall face after construction at top of the wall.

KEYWORDS: geotechnical engineering, concrete rigid panel faced, geogrids, reinforcement soil wall, field test

INTRODUCTION

The geogrid reinforced soil retaining wall is applied widely in the world with advantages of low cost, simple construction and strong ability to adapt for the deformation. With the construction of railway in mountainous region as well new built railways over across existing railways, the height of retaining wall will increase. The study of high railway geogrid reinforced soil retaining wall on failure mode and forcing mechanism is still in the exploratory stage (Xiao et al. 2006; Zhang 2002; Yung and Ying 2002; iang and Jiang 2005; Helwany SM B et al. 1997; Rowe R K et al. 2001; Rajagopol et al. 1995; Bathurst et al. 2001). The *Code for Design on Retaining Structures of Railway Subgrad*e (*TB10025-2006*) in China is limited to design of single-step retaining walls with a height lower than 10 m. And this will constraine the application and development of geogrid reinforced soil structural technology. In this paper, the field test of 12.2-metre-high geogrid reinforced retaining wall with integral cast-in-situ concrete slab is done in Gan (Zhou) -Long (Yan) Railway of China. The test includes the basement stress, lateral soil pressure of the wall back, tensile force of the reinforcement and the horizontal deformation. This paper will analyse the test data from the begin to 1.5a after the completion of the wall.

The integral cast-in-situ concrete slab geogrid reinforced soil retaining wall lies in the segment GDK144+130 — GDK144+165 of Gan-Long railway, south of the Changting County railway station in Fujian province of China,the height of the wall is 12.2 m. The upper of the wall, 0—7.5 m, is filled with rammed clay, reinforcement materials is plastic geogrids EG65R, the vertical spacing is 0.4 m; The lower of the wall is reclaimed gravel soil, reinforcement is used with plastic geogrid EG130R, the vertical spacing is 0.5 m. The crushed stone parcel was used in the slope, steel bolts were embedded in the wall's construction. The crushed stone parcel was laid with geotextile, peripherally set C15 30 cm cast-in-situ reinforced concrete slabs internally attached with reinforcement net, reinforcement net was connected with bolt.

ARRANGEMENT SCHEME OF MEASURING POINTS

The arrangement of measuring points on test section is shown in Fig. 1.

[1] Professor, Department of Civil Engineering, Shijiazhuang Railway Institute, CHINA. Email: gtsyang@163.com
[2] Lecturer, Department of Civil Engineering, Shijiazhuang Railway Institute, CHINA. Email: lvpeng2941@163.com
[3] Associate professor, Department of Civil Engineering, Shijiazhuang Railway Institute, CHINA. Email: zbj1911@163.com
[4] Lecturer, Department of Civil Engineering, Shijiazhuang Railway Institute, CHINA. Email: zhouqy_007@163.com

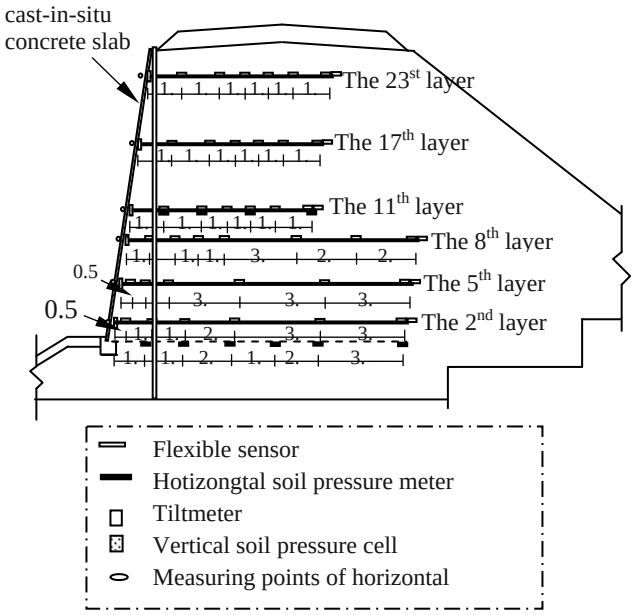

Fig. 1 Arrangement of instrument on the section

The test begin with the construction, in the construction process, laying a geogrid reinforcement each, reading the data of flexible sensor and cell once. A monthly reading is fine after the completion. To measure the level deformation of the wall during construction, observation points for horizontal displacement are arranged in the parcel, the elevation of which is the same as flexible sensor. After the completion, drill at top of the wall, lay tiltmeters, then, observe the horizontal deformation using a vertical tiltmeter.

ANALYSIS OF TEST RESULTS

Characteristics of Basement Vertical Soil Pressure

The distribution curve of basement vertical soil pressure along reinforcement length in the construction period and at different times after the completion is shown in Fig. 2 and Fig. 3. As can be seen from the figures: With the height increasing, basement vertical soil pressure gradually increases. The distribution of vertical soil pressure is not identical with the linear distribution used in current standard. Experimental results show that: its magnitude along the length of geogrid reinforcement is nonlinear distribution, the maximum is near the middle of reinforcement, to the wall face and the end of reinforcement direction, it is gradually decreasing; The maximum number is larger than the theoretical value $\sigma_v = \gamma \cdot h$, stress concentration emerges. Analyzing the reasons: reinforced soil will produce overturning moment under non-reinforced soil lateral soil pressure, which made the distribution of vertical soil pressure nonlinear. Theoretically, there should be larger vertical soil pressure close to the wall, and the minimum vertical soil pressure should be at the end of geogrids. But in practical engineering, the vertical soil pressure close to the wall will decrease, may be due to the lower retaining wall's displacement causes stress release, soil blister caused by wall slab friction, reinforcement and soil interaction and other reasons.

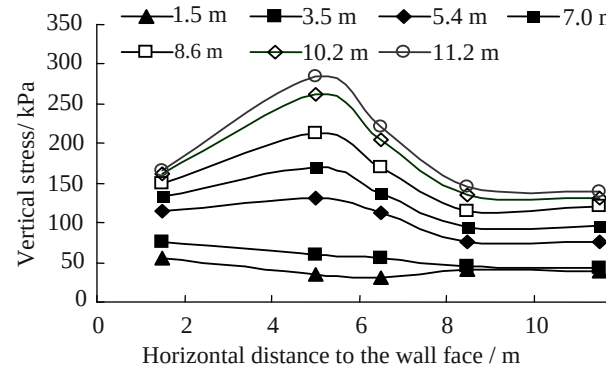

Fig. 2 Distribution of basement pressure during construction

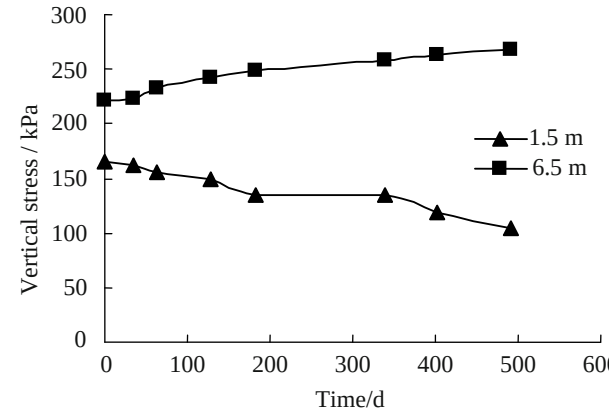

Fig. 3 Distribution of basement pressure after construction

After the completion, the high reinforced soil-retaining wall under larger self-weight load may cause the approved ground to sink and leads to the soil blister effect at the leading end and tail end of the reinforcement, and the overturning moment transmitted by non-reinforced soil's lateral earth pressure may lead to the vertical soil pressure near the wall face decreasing, while increasing near the central part of reinforcement.

Characteristics of Lateral Earth Pressure

Fig. 4 and Fig. 5 show the test results of lateral earth pressure of the retaining wall in the construction period and at different times after the completion. The lateral earth pressure is analyzed as follows.

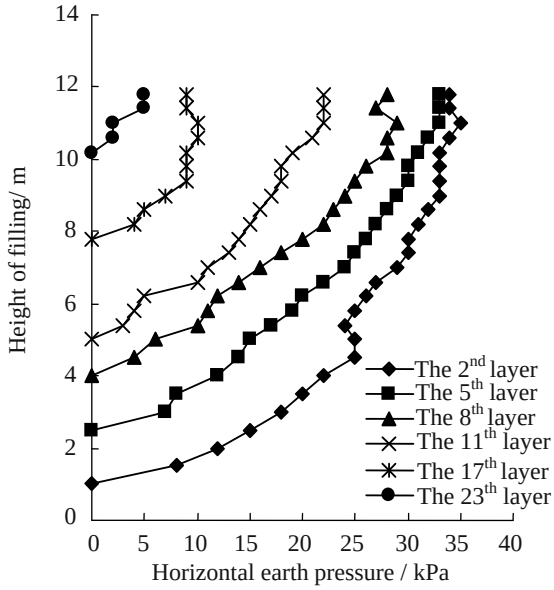

Fig. 4 The lateral earth pressure of different

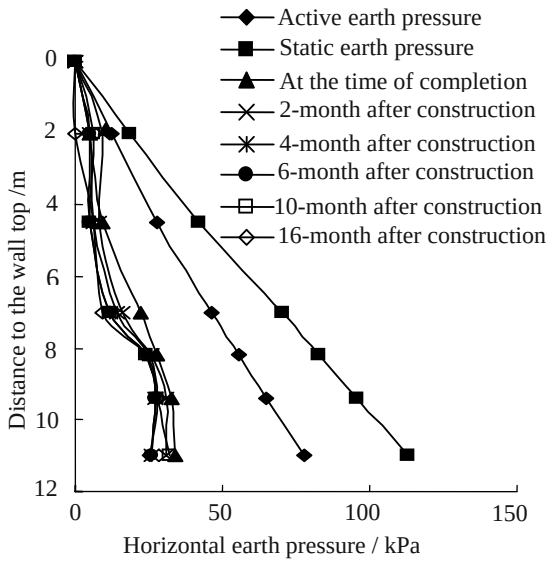

Fig. 5 The lateral earth pressure along wall height

With the increase of wall height, the lateral earth pressure of different layers increases. With the increase of height, the wall face begins to produce horizontal deformation and result in the decrease of lateral soil pressure, which made growth rate of soil pressure decreased and the actual measured lateral soil pressure less than the theoretical value. Only the value above the central part is close to active soil pressure, the value below the central part is less than active earth pressure.

Lateral earth pressure is nonlinear distribution along the height. Below the central part of the wall, lateral earth pressure presents an increasing trend. During construction of the retaining wall, the integral cast-in-situ concrete slab was laid on the strip foundation of the wall basis after the completion, this type of slab plays a restraint role to the wall horizontal deformation, resulting in a greater lateral earth pressure at the bottom, but the value is only about 1/3 of the active soil pressure.

After the completion, the lateral earth pressure is decreasing with time going. That is mainly based on the horizontal deformation gradual increasing, the reduction of vertical stress near the wall which caused by foundation settlement and the friction between parcel and the wall slab, thus, leading to lateral earth pressure gradual decreasing. This is consistent with the conclusion of facing slab horizontal deformation analyzed later.

Characteristics of Geogrid Reinforcement Strain

Fig. 6 is the deformation curve of reinforcement along the length in different locations.

In the testing, a flexible displacement meter was embedded at the end of geogrid reinforcement. From the test results, we can see that the inconsistencies of reinforced soil and non-reinforced soil vertical settlement produces settlement difference in the section, the test results show greater deformation value. This illustrates that reinforced soil has good overall effect which can be considered using bond gravity retaining wall (Yang et al. 2000; Yang et al. 2003).

With the increase of super-stratum thickness, reinforcement strain of each layer increases. The measured strain of short reinforcements in reinforced soil upper clay fillings ranges from 0.1% to 0.97%. In accordance with the actual stretching rate corresponding with construction process, the measured range is equivalent of that geogrid was subjected to a load range of 1.74 kN/m－8.7 kN/m, comparing this value, 69.17 kN/m, with the ultimate tensile strength of geogrid, it is only 2.5%－12.5% of the ultimate tensile strength of geogrid. The measured strain of geogrid reinforcement in gritstone fillings of reinforced soil ranges between 0.16% to 0.88%, according to the actual stretching rate corresponding with construction process, the measured range is equivalent of that geogrid was subjected to a load range of 5.23 kN/m－17.41 kN/m, comparing this value with the geogrid ultimate tensile strength 139.83 kN/m, it is only 3.8% to 12.4% of the ultimate tensile strength. Therefore, the actual forcing of the two models geogrid are far less than the design values, meanwhile, creep deformation produced under this low numerical tension is very small. The conclusion also can be confirmed from the curve of each layer reinforcement stress along with time change after the completion.

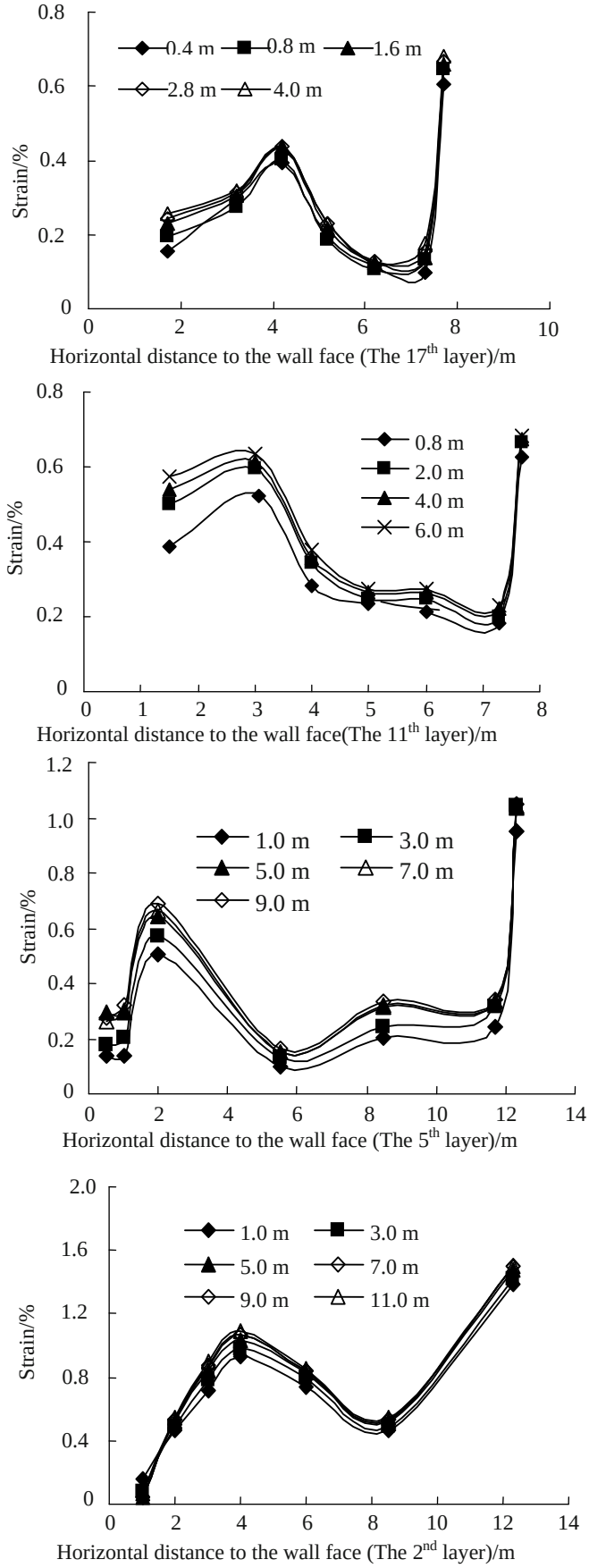

Fig. 6 The strain of reinforcement on different layers

Strain of the reinforcement in upper wall shows a single-humped distribution, the greatest strain is further away from the facing slab at the top of the wall, gradually close to the slab downward; while, strain of the lower part of the reinforcement shows a double-humped distribution, one peak value is near the slab, and the second one is away from the slab. The first strain peak value may be due to wall lateral earth pressure, the second is likely the result of soil self-respect, frictional resistance of filling to reinforcement (Wang et al. 2003), (He et al. 2003; Chen et al. 2000; Chen et al. 1999; He et al. 2000).

After the completion, reinforcement deformation of each layer mainly remains constant as time continues. After the line track-laying, reinforcement deformation of each layer is less affected by external load.

Characteristics of the Potential Slide Surface

Connect the largest tension location of the testing reinforcement of each layer in reinforced soil, analyze the location of the potential slide surface (for the lower part of the wall, choose the strain peak away from facing slab), as shown in Fig. 7.

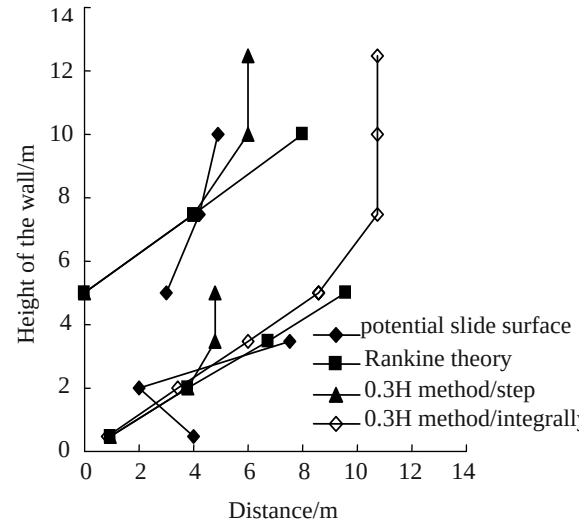

Fig.7 The potential slide surface

As far as the whole wall height is concerned, the measured potential slide surface presents a curve distribution. Shape of the wall's lower part is relatively close to "*0.3H method*", while, the upper part was not so.

If the reinforced earth retaining wall is taken as double-step, the upper step is 7.5 m high, the lower is 4.7 m high, step width of the two walls is zero. Draw the potential slide surface determined by Rankine earth pressure theory and "*0.3H method*", then analyze the wall separately. From the figure, we can see, the shape of the potential slide surface in upper wall approaches "*0.3H method* ", and the lower wall is close to Rankine earth pressure theory.

Characteristics of Horizontal Deformation of the Wall

On the wall face of the 2nd, 5th, 8th, 11th, 17th and 23th reinforcement height, observation points for horizontal deformation were set respectively to observe the horizontal deformation in wall construction and after the completion. After the completion, set vertical tiltmeter 0.5m behind rail cap-stone of the testing section top, to observe horizontal displacement after the completion, the test results is shown in Fig. 8.

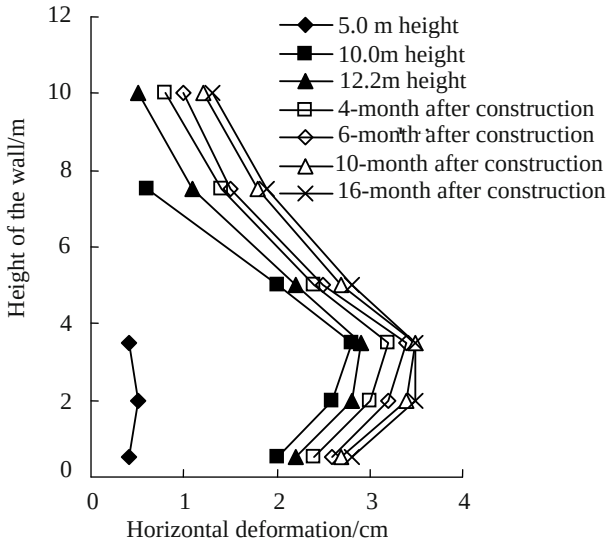

Fig. 8 The horizontal deformation of the wall face

Observations shows that: With the increase of wall height, the horizontal deformation of measuring points with different heights are gradually increasing, the largest horizontal deformation is in lower part of the retaining wall. After the completion, the horizontal deformation presents an increasing trend along with time, but in a very small growth rate. Therefore, when we considering the impact of construction process, the greatest horizontal deformation occurs in the lower part of the wall. While, occurs at the top of the wall after the completion.

When the top was laid ballast, horizontal deformation of the wall's top increases significantly, moreover, the measuring points 2.0 m below the top are less impacted by external load.

CONCLUSIONS

Through the field test of concrete rigid panel faced geogrids reinforced soil retaining wall, a great deal of observational data is achieved, characteristics of the deformation and forcing of the structure are initially grasped.

The vertical soil pressure along reinforcement is nonlinear distribution, the maximum occurs in the vicinity of the reinforcement central part, and gradually decreases to the wall face as well to the end of reinforcement. After the completion of the wall, the vertical stress near the wall is in decline, and rising near the reinforcement central part.

The measured lateral earth pressure are less than active earth pressure numerically, and with a nonlinear distribution along height of the wall. Based on the horizontal deformation gradual increasing, the vertical soil pressure reduction near the wall face that caused by foundation settlement and friction between parcel and the facing slab, the measured lateral earth pressure presents a decreasing trend along with time after the completion.

Strain of the upper reinforcement along length shows a single-humped distribution. The greatest strain is further away from the facing slab on the top of the wall, gradually close to the slab downward. The distribution of the strain of lower reinforcement is double-humped.

The potential slide surface of the geogrid reinforced soil retaining wall is a curve distribution. The shape of the upper wall approaches the *"0.3H method "*, and the lower wall is close to Rankine earth pressure theory.

With the increase of wall height, the horizontal deformation of the wall face is gradually increasing, the largest deformation is in the lower part of the wall. After the completion, the horizontal deformation presents an increasing trend, but in a very small growth rate, the greatest horizontal deformation occurs at the top of the wall.

REFERENCES

Bathurst RJ, Walters DL, Hatami K (2001) Full-scale performance testing and numerical modeling of reinforced soil retaining walls. In Proceedings of International Symposium on Earth Reinforcement. Fukuoka:IS Kyushu 202-231

Chen Q, He CR (1999) The Mechanical Property of Two Type of Tied Reinforcement of Reinforced Retaining Wall,Journal of Sichuan University 3(4): 97-102

Chen Q, He CR (2000) The prototype measurement of retaining wall reinforced by a new type of wedgy tied reinforcement, China Journal of Geotechnical Engineering 22(3): 289-293

He CR, Chen Q, Fu HY (2000) Measurement and computation of earth pressures on two retaining structures, China Journal of Geotechnical Engineering 21(1): 55-60

He TQ, He CR, Yu JH (2003) The prototype measurement of single-step compound reinforced retaining

wall with super height, Building Science Research of Sichuan 29(2): 74-78

Helanys SMB, Reardon G, Wu JT (1997) Effects of backfill on the performance of GRS retaining walls. Geotextiles and Geomembranes 17(2): 1-16

Jiang ZX, Jiang LW (2005) Distribution map forms of active earth pressure on retaining structures in Nanning—Kunming Railway. Chinese Journal of Rock Mechanics and Engineering 24(5):1035-1040

Rajagopol K, Richard JB (1995) Behaviour of geosynthetic reinforced soil retaining walls using the finite element analysis. Computers and Geotechnics 17(4): 279-299

Rowe RK, Skinner GD (2001) Numerical analysis of geosynthetic reinforced retaining wall constructed on a layered soil foundation. Geotextiles and Geomembranes 19(7): 387-412

The Professional Standards of People's Republic of China (2006) Code for design on Retaining engineering structures of railway subgrade (TB10025-2006). Beijing: China Railway PublishingHouse

Wang XX, Lian R (2003) Test and analysis of two-step retaining wall reinforced by geogrid, Chinese Jounal of Geotechnical Engineering 25(2): 220-224

Xiao CZ, Luan MT, Yang Q, Li F (2006) Numerical analysis of performance of geogrids-reinforced retaining walls by nonlinear FEM. Chinese Journal of Rock Mechanics and Engineering 25(10): 1990-1996

Yang GQ, Cai Y (2000) Study on the multi-steps reinforced earth retaining wall, China Journal of Geotechnical Engineering 22(2): 254-257

Yang GQ, Cai Y, Su Q (2003) Testing study on deformation and stress of reinforced earth retaining wall for high embankment, Chinese Journal of Rock Mechanics and Engineering 22(2): 321-326

Yung SF, Ying CH (2002) Passive earth pressure with critical state concept, Journal of Geotechnical and Geoenvironmental Engineering 128(8): 651-656

Zhang XH (2002) Relations between soil nailing and bolting. Chinese Journal of Rock Mechanics and Engineering 21(2): 69-71

EFFECT OF REINFORCED SAND CUSHION ON THE LIMIT FILL HEIGHT OF EMBANKMENT ON SOFT CLAY FOUNDATION

L.M. Wei[1], J.D. Niu[2] and H.J. Huo[3]

ABSTRACT: The method combining the large scale model test, the in situ test and the finite element simulation was used to analysis the effects of reinforced sand cushion on the bearing capacity and settlement of soft clay foundation. The in situ test embankment which loaded to fail was performed to verify the reasonableness of the finite model in this paper. The development trend of reinforcement tension was discussed too. The results indicate that the limit fill height of embankment on soft clay foundation can be significantly improved by using the reinforced sand cushion, but its contribution to reduce the settlement is not very obvious. In addition, the tensions of reinforcements in different layers increase with heightening of the filling height, and the maximum tensions of reinforcements of different layers are not obviously different to each other under the same fill height.

KEYWORDS: reinforced sand cushion, soft clay foundation, reinforcement tension, limit fill height, settlement

INTRODUCTION

Since laboratory tests and theory analysis on the bearing capacity of reinforced earth slabs were carried out by Binquet and Lee (1975 a, b), the application and research of reinforced earth foundation have been studying by geotechnical engineers. Recently, with more and more new geosynthetics can be utilized in civil engineering, many kinds of geosynthetics were used as reinforcements to improve the soft clay foundation, so analyzing correctly the contribution of reinforced sand cushion to the bearing capacity and settlement of soft clay foundation and the development trend of tension force in reinforcements become the key technical issues. In this paper, the method combining the large scale model test, the in-situ test and the finite element method was performed to analysis the effect of reinforced sand cushion on limit fill height of embankment on soft clay foundation.

LARGE SCALE MODEL TEST AND FINITE ELEMENT NUMERICAL SIMULATION

Instruments of Large Scale Model Test

The large scale model test was performed in a sand well (3 m×3 m×5 m). The structure that bearing the reaction force during loading was composed of two I type iron beams and two railway rails, which fixed on the top of the sand well and connected to loaded member. A reinforced concrete structure (1.8 m×0.25 m×0.5 m) was used to simulate the rigid shallow strip foundation, with embedded depth of 24cm. The sand used in this test was poorly graded sand, with maximum void ratio e_{max} =1.013, minimum void ratio e_{min} = 0.580, specific gravity G = 2.65, water content w =3.3%. The compaction was accomplished by using vertical vibration equipment layer by layer and the relative density D_r of sand was controlled according to D_r= 0.6. The polypropylene reinforcements were adopted, their width b was 1.5 cm, thickness was 0.1 cm, single length l was 290 cm. The distance U from the bottom of the foundation to the top of the uppermost reinforcement layer was 0.12 m.The vertical spacing of reinforcement was 0.12 m, and the linear density of reinforcement LDR= 15%.

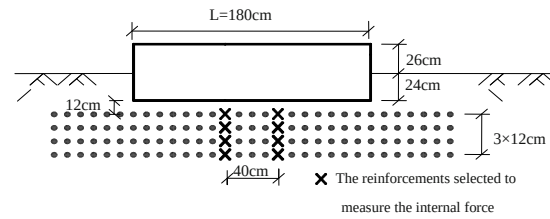

Fig. 1 Layout of tested reinforcements

[1] Associate Professor, School of Civil Engineering and Architecture, Central South University, CHINA. Email:lmwei@mail.csu.edu.cn
[2] Lecturer, School of Civil Engineering and Architecture, Central South University, CHINA. Email: niudong@mail.csu.edu.cn
[3] Master, School of Civil Engineering and Architecture, Central South University, CHINA. Email:hunavy@163.com

At each layer, two reinforcements that near the middle position of the foundation were selected to measure their internal force, whose state of stress are close to plane strain state. The selected reinforcements in this test are shown in the Fig. 1.

As shown in Fig. 2, seven internal force sensors were arranged at every tested reinforcements [J].

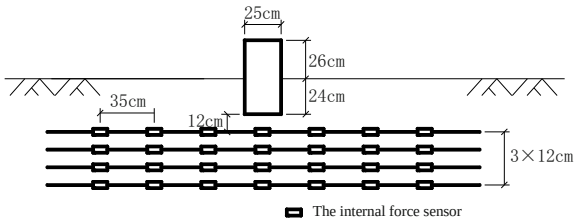

Fig. 2 Layout of internal force sensors in tested reinforcements

Results of Large Scale Model Test

The distribution of maximum internal force of reinforcements is shown in Fig. 3.

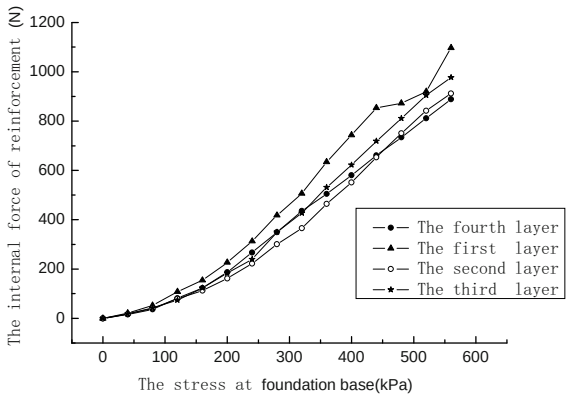

Fig. 3 The measured maximum internal force of reinforcements

It can be seen that the tensions of reinforcements in different layers increase with the increase of contact pressure. The maximum internal force of reinforcements was 1097.12 N, which appeared in the first layer. The maximum tensions of reinforcements in four layers are not obviously different to each other under the same fill height, and the ratio of the biggest of four maximum to the smallest one is between 1.0 and 1.23.

IN SITU TEST AND NUMERICAL SIMULATION OF EMBANKMENT ON SOFT CLAY FOUNDATION

The In-situ test of Embankment on Soft Clay Foundation

A certain railway test embankment was built on soft clay foundation. The groundwater level was near to ground surface. The bottom width of the embankment was 21.6 m and slope ratio was 1:1.5. The embankment geometry is shown in Fig. 4. The unit weight of soft clay was 17.6 kN/m^3. The consolidated-undrained strength was tested: the cohesion c=8 kPa and the angle of internal friction=13.5°. The unit weight of the embankment filling was 17.5 kN/m^3.When the embankment was built at the height of about 3.5 m to 4.0 m, the embankment collapsed.

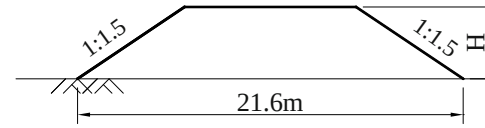

Fig. 4 The in situ test embankment

Numerical Simulation of In-situ Test

According to the soil stratum condition and the geometry of the in situ test embankment, the model of finite element analysis was founded as shown in Fig. 5. The calculated area of foundation was 50 m in length and 15 m in depth.

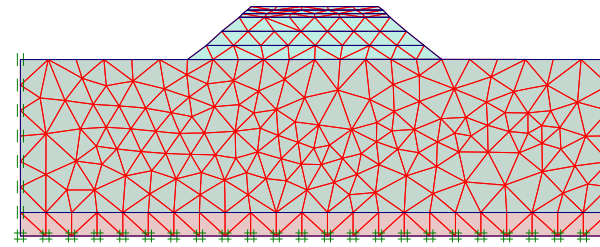

Fig. 5 The schematic diagram of the finite element model and the meshing

The finite element analysis that simulating the in situ test embankment was carried out by using the afore-mentioned model and calculation parameters. In the process of numerical simulation, Firstly, the embankment was filled according to 1.2 m every layer, when the height of embankment reached 3.6 m, the thickness of filling every layer was reduced to 0.3 m. The results of numerical simulation indicate that the embankment fails when the height of embankment reaches 3.9 m, and the plastic points at this stage in the subgrade are shown in Fig. 6.

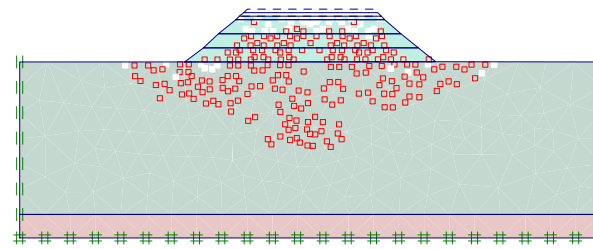

Fig. 6 Plastic points in subgrade for natural foundation

By all these above- mentioned, the conclusion that the limit fill height of this test embankment is 3.6 m can be deduced. The result from finite element simulation coincides with that from in situ test, which validates the reasonableness of finite element model and the calculation parameter.

NUMERICAL SIMULATION OF SUBGRADE ON SOFT CLAY FOUNDATION WITH REINFORCED SAND CUSHION

Design of Reinforced Sand Cushion

In order to analysis the effect of reinforced sand cushion on limit fill height, the reinforced sand cushion was planned in the in situ test embankment, with 1.8 m in thickness and four layers reinforcement. The distance U from the ground surface to the top of the uppermost reinforcement layer was 0.35 m.The vertical spacing of every layer of reinforcement was 0.30 m. The reinforcement made of polypropylene, with a width b of 2.2 cm, thickness δ of 0.15 cm, and single length l of 31.6m. The tensile strength was more than 8000 N/per strip, breaking strain was less than 10%, the elongation at working load (1140 N/per strip) ε_w was 2%. The friction coefficient between the reinforcement and soil was 0.38.

The Numerical Simulation of Subgrade with Reinforced Sand Cushion

Limit fill height of embankment

According to the soil stratum condition and the geometry size of the in situ test, the finite element model was established as shown in Fig. 7.

The Mohr-Coulomb elasto-plastic constitutive relationship was used to describe the soil behavior, and the geotextile structural element was used for representing the behavior of reinforcements. The related calculation parameters are listed in Table 1.

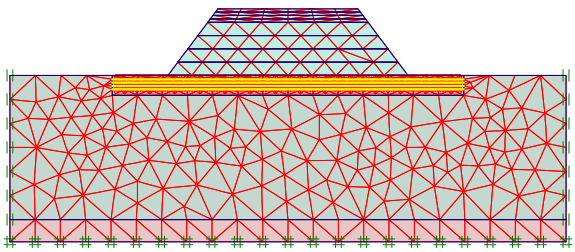

Fig. 7 The finite element model of embankment on soft clay foundation with reinforced sand cushion

Table 1 Calculation parameters used in FEM analysis for in-situ test

Items	Filling	Soft clay	sand cushion	subsoil
Unit weight γ /kN/m^3	17.5	17.6	20	19
Cohesion *c*/kPa	1	8	1	23.97
Internal friction angle/°	30	13.5	40	24.08
Young's modulus E /kPa	30000	2200	13000	3098
Poisson ratio	0.31	0.33	0.31	0.32

Similar to the FEM analysis for natural foundation, the thickness of filling was adopted as 1.2 m every layer at first. When the height of embankment was added to 4.8 m, the thickness of layer was reduced to 0.3 m.The results of numerical analysis indicate that when the height of embankment access to 5.7 m, the embankment failed, and the plastic points at this stage in the subgrade are shown in Fig. 8. It is concluded that the limit fill height of embankment built on the reinforced sand cushion foundation is 5.4 m.

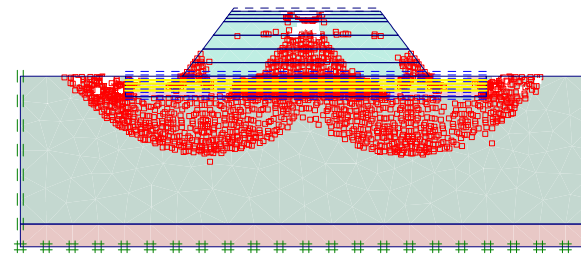

Fig. 8 Plastic points in subgrade for reinforced soil foundation

The internal force in reinforcements

The development of maximum internal force of every layer reinforcements during construction of embankment is shown in Fig .9. It shows that the maximum internal force of every layer reinforcement increase with the increase of fill height according to non-linear trend. The maximum tensions of reinforcements in four layers are not obviously different to each other at under the same fill height, and the ratio of the maximum tension for four layer reinforcement is between 1.0 and 1.4. The result coincides with that from the large scale model test. All these above express the internal force of reinforcements in different layers are approximate to equal, which agree with the basic failure hypothesis supposed by Binquet and Lee (1975b).

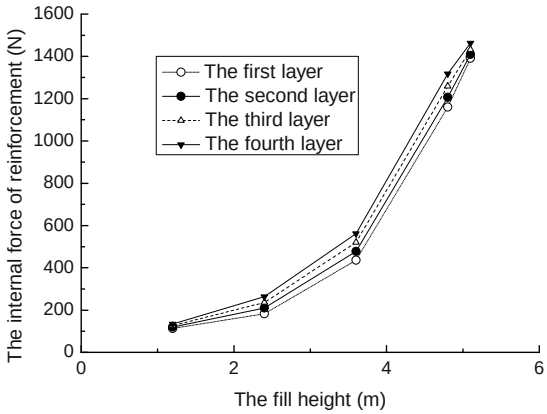

Fig. 9 The development of maximum internal force of every layer reinforcements

EFFECT OF REINFORED SAND CUSHION

Effect of Reinforced Sand Cushion on Limit Fill Height of Embankment

Based on the analysis results above, the limit fill height of embankment for natural foundation and reinforced soil foundation in the same soil stratum and embankment condition can be deduced, namely, 3.6 m for natural foundation and 5.4 m for reinforced soil foundation. It indicates that the limit fill height of embankment can increase 1.8 m by using reinforced sand cushion, the so the improved ratio of limit fill height for reinforced soil foundation to natural foundation is 1.5.

Effect of Reinforced Sand Cushion on Foundation Settlement

The comparison of settlement of nature foundation with that of reinforced soil foundation is shown in Fig. 10.

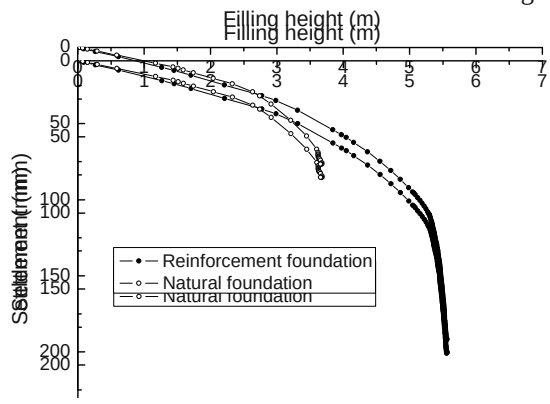

Fig. 10 Comparison of settlement for natural foundation and reinforced earth foundation

It can be seen that reinforced sand cushion can improve the limit fill height of embankment on soft clay foundation significantly. But when the fill height is less than the 60% of limit fill height that on natural foundation, the effect of reinforced sand cushion on reducing the settlement of foundation is not very obvious. With the fill height increase, the contribution of reinforced sand cushion to reduce the settlement of foundation is mobilized gradually. Under the same contact pressure, the settlement of reinforced soil foundation is 70%－90% of that of natural foundation.

CONCLUSIONS

The reinforced sand cushion can heighten the limit fill height of embankment on soft clay foundation significantly. For the in situ test embankment mentioned in this paper, the limit fill height of embankment can be improved from 3.6m to 5.4m by it, the improving ratio is 1.5.

The contribution of reinforced sand cushion to reduce the settlement of foundation is not very obvious. Under the same filling height, the settlement of reinforced soil foundation is 70% － 101% of the settlement of natural foundation.

The results both from the large scale model test and finite element numerical simulation indicate that the tensions of reinforcements in different layers increase with the filling height of embankment, and the maximum tensions of reinforcements in the four layers are not obviously different to each other under the same fill height, which agree with the basic failure hypothesis supposed by Binquet and Lee (1975b).

REFERENCES

Binquet J, Lee KL (1975a) Bearing capacity tests on reinforced earth slabs. Geotech. Engrg [J] ASCE 101(12): 1241-1255

Binquet J, Lee KL (1975b) Bearing capacity analysis of reinforced earth slabs. Geotech. Engrg [J] ASCE 101(12): 1257-1276

Brown BS, Poulos HG (1977) Analysis of foundation on reinforced soil, Proc. 9th International Conference on Soil Mechanics and Foundation Engineering 3: 595-598

Bassett RH, Last NC (1978) Reinforcing earth below footings and embankments. Proc. Symposium on earth reinforcement, ASCE Annual Conference, Pittsburgh, Pa: 202-231

Fragaszy RJ, Lawton E (1984) Bearing capacity of reinforced sand subgrades. Geotech. Engrg [J] ASCE 110(10): 1500-1507

Marei NE (2002) Influence of grain size of granular

cushions on performance of double footings overlying soft clay. Journal of Engineering and Applied Science 49(2): 241-257

Milovic D (1977). Bearing capacity tests on reinforced sand. Proc. 9th International Conference on Soil Mechanics and Foundation Engineering 1: 651-654

Ministry of Railways capital construction bureau engineering department. The experience of constructing embankment on soft clay zone (1959) China Civil Engineering Journal 6 (10)

Tatsuoka F, Miki G (1983) Bearing capacity of reinforced model sand ground. Symposium on Recent Development in Ground Improvement Techniques/Bangkok/ 29(3): 153-160

Verma BP, Char AN (1986) Bearing capacity tests on reinforced sand subgrade Geotech [J] Engrg. ASCE 112 (7): 701-706

Wei LM, Hua ZK (1977) Measurement and analysis of reinforcement tension for reinforced earth foundation. Chinese Journal of Geotechnical Engineering 19 (1): 15-21

APPLICATION OF THE GEOGRID REINFORCED SOIL RETAINING WALLS FOR A HIGH SLOPE SUPPORTING PROJECT

H. Zhu [1], Y. Ma [2], Y.X. Liu [2] and J. Wang [1]

ABSTRACT: T his paper introduces a supporting project of 35 metres high slope in the first middle school sports ground of ZiGui county. By designing the high-steep reinforced soil retaining walls with single 17 metres and slope ratio 1:0.3, this system effectively solved the technical problem of foundation load deficiency and terrain restrictions. Moreover, this paper illustrates the characteristic of the geogrid reinforced soil retaining walls, and discusses the noticeable problems in design and construction, so it has relevance to similar design and construction of geogrid reinforced soil retaining walls projects.

KEYWORDS: geogrid, reinforced soil retaining walls, design, construction, effect

INTRODUCTION

The high slope supporting project of the first middle school sports ground in ZiGui County is located in MaoPing town. ZiGui County located in the Three Gorges Warehouse district. The project is located at the right bank of Three Gorges Dam upper reaches and the retaining of the natural environment was seen as very advantageous. With the establishment of a civilized school in the province, the establishment of the school was seen to improve the step by step teaching facilities and the hardware environment. The student sports ground especially needed to be improved because it has a high slope and near Three Gorges reservoir. The sports ground failed to reach required standard of a 400 metres oval running track and a 110 metres straight line running track for the exercise of students. Because of the restricted terrain and the influence of elevation, the sub grade foundation loads of the sports ground was difficult to be achieved if only traditional masonry gravity retaining wall structure was adopted. Therefore it was necessary to expand foundation or the pile foundation, which would increase investment. It also would increase the construction difficulty because of the difficulty to guarantee the safety of masonry gravity retaining walls (Fig. 1). Therefore, it was very important to investigate the use of other types of retaining walls construction to resolve these problems.

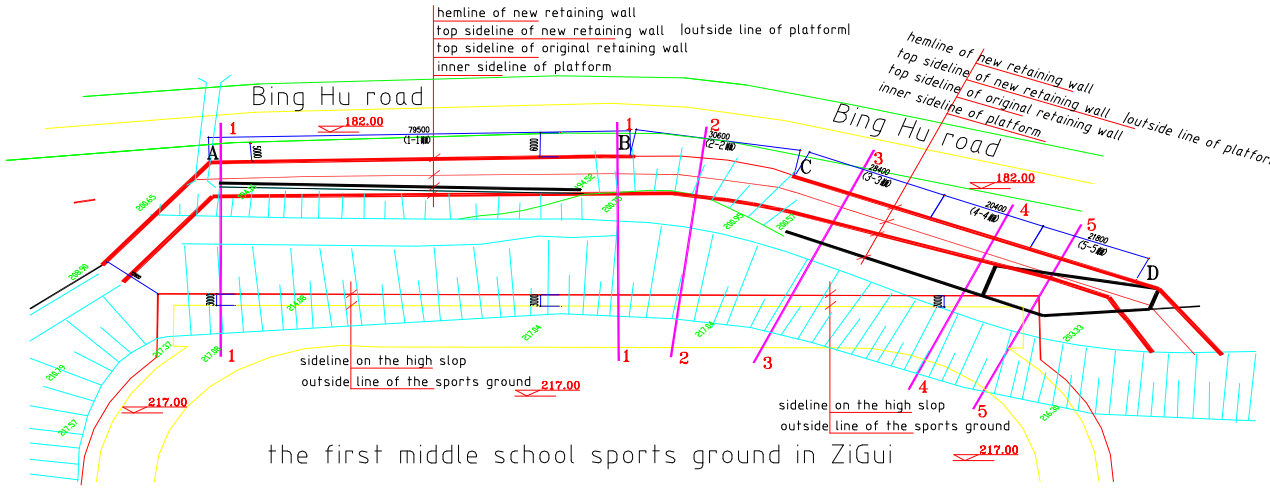

Fig. 1 The plan of the high slop supporting project of the first middle school sports ground in ZiGui County

[1] Hubei Nete Geosynthetics Ltd, Yichang, Hubei 443000, CHINA. Email:nete@263.net
[2] Central Southern Geotechnical Design Institute, Wuhan, Hubei 430071, CHINA

PROJECT DESIGN

The high slope supporting project of the first middle school sports ground in ZiGui County is designed by Central Southern Geotechnical Design Institute in Wuhan.

Design Basis

1) The first middle school sports ground of ZiGui county slope geotechnical engineering surveys report Hubei province geological surveys project company;

2) Construction Unit provides original rubble stone retaining walls relevant design date;

3) Construction slope project technical norm GB50330-2002;

4) Construction foundation technical norm DB42/242-2003;

5) Road reinforced project technical norm JTJ015-91;

6) Concrete structure technical norm GB50010-2002;

7) Geotechnical engineering governance handbook.

Level High Slope

The design of high slope supporting project of the first middle school sports ground of ZiGui county mainly had four difficulties: Firstly, the project is restricted by terrain. It is an important passage to get in and out of the Three Gorges—Binhe Road. Beside the red line at the bottom of slope, so the slope cannot be put. However, the width of sports ground at the top of slope must reach the required standard so retaining walls can only make cliffy. Secondly, could the foundation load of the gravity retaining wall with 35 meters height be satisfied? Thirdly, is this cliffy retaining wall economical and safe? Fourthly, the original rubble retaining wall with 18 metres height could not be dismantled. Therefore another issue was how to integrate the original rubble retaining wall with the new retaining wall? After consideration of many designs, the gravity rubble stone retaining wall was integrated with a geogrid reinforced soil retaining wall was adopted.

The project was divided into four sections:

1) The lattice form rubble stone retaining wall was adopted at the under parts of the AB section. The filling at the upside of AB section was protected by the rubble masonry lattice form skeleton, and grass was grown in lattice form to prevent soil erosion;

2) The under part of the BC section was a rock slope, so its natural slope shape was maintained. The upside of BC section was treated same as AB section;

3) Lattice form rubble stone retaining wall was adopted at the under part of CD section and geogrid reinforced soil retaining wall was adopted at its upside. The reinforced soil retaining wall has support as well as virescence function and prevents soil erosion;

4) The platform with 1.0－5.0 m width was set up at the up and down grade joint (elevation 200.00 m).

This paper mainly introduces the geogrid reinforced soil retaining wall (upside of the CD section). The geogrid reinforcing soil slope was adopted.

Reinforced Soil Retaining Walls Design

This design adopted USA TET Co. geogrid reinforced soil retaining walls design software to design and calculate the full considered inner and exterior stability as well as the overall stability of the structure.

1) The geogrid reinforcing soil slope is also called wraparound or packaged reinforced soil retaining wall. It is a flexible structure with the wall surface wrapped by the mesh bag fill and geogrid. Each geogrid was connected from slope bottom to top by a special-purpose connection stick and formed a hole which ensured integrity and stability of the retaining wall; The earth fill in mesh bag had been mixed with grass seed, bush seed and flower seed which were suitable for local growth and grew after several months to form the green ecology wall surface. It provided geogrid security and also beautified the environment of the overall project.

2) The geogrids smallest reinforced length was not shorter than 0.7 H (H was wall height). This design adopted the reinforced method that the length was not equal and the layer distance was 500 mm. The lapping width of neighboring geogrid on the same layer was 10 mm (Fig. 2).

3) Reinforced soil filling materials were rolled on layers and the compacted thickness with 300－500 mm was chosen according to compacted property. The mixture of good quality granular arenosol and gravel ($\leqslant$ 200 mm) was chosen as filling. The percentage content of gravel was not higher than 30% and the compacted coefficient was not lower than 0.95. Direct contact of the edges and corners stones with the geogrid was avoided when the filling was paved. The distance of compacted machine and wall surface was not less than 1.5m. Small equipment or manpower was used to tamp filling in the range.

4) A drainage layer with 300－500 mm thickness was set up in the reinforced soil retaining wall at intervals of 4.0－5.0 m heights. Coarse aggregate (middle rude sand bearing macadam) with good water permeability was used in the drainage layers.

5) The perfect drainage and waterproof measure was adopted to ensure the free drainage of rainwater and surface water.

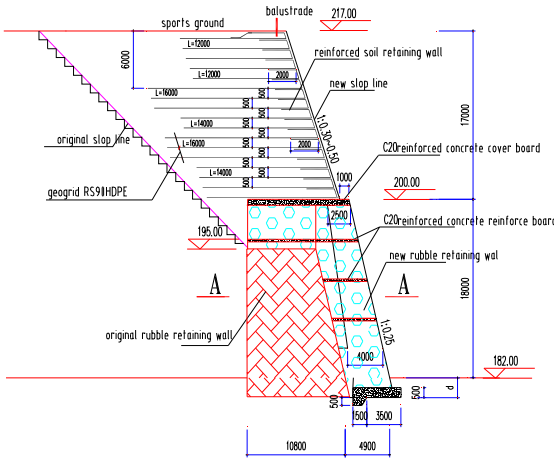

Fig. 2 The supporting section plan of the sports ground high slop

CHARACTERISTICS OF REINFORCED SOIL RETAINING WALL

Compared with the traditional concrete retaining wall and gravity style retaining wall, the geogrid reinforced soil retaining wall has the following characteristics:

1) The geogrid reinforced soil retaining wall is a flexible structure and can adapt to foundation deformation better than the traditional stiff structure retaining wall. Its structural advantage can be better showed when it is used in the place of bad foundation. Moreover, according to correlative report, reinforced soil retaining wall has a better anti-earthquake ability than a rigid structure retaining wall.

2) Geogrid reinforced soil retaining wall can economize project investment. The retaining wall can be made high and steep as well as reducing effective land filling materials. Therefore it has an economic cost advantage.

3) The slope surface of non-board geogrid reinforced soil retaining wall has the afforested protection, which can green and beautify the environment and restore natural ecology. So it has better environmental benefits.

4) The geogrid reinforced soil retaining wall was constructed rapidly and conveniently, effectively reduces the construction time and guaranteeing construction quality.

5) The design and construction of geogrid reinforced soil retaining walls have gradually matured. With the development in recent years, the reinforced soil technology has been widely used in projects such as highways, railways, airports, harbors and ports, dams, city planning and environmental protection projects.

The geogrid reinforced soil retaining wall adopted in the high slope supporting project of the first middle school sports ground in ZiGui County has taken full advantage of the above characteristics. The reinforced soil retaining wall has achieved remarkable economic and social benefit in many aspects such as technology, quality, security, economy and environment. A single 17 meters high green geogrid reinforced soil retaining wall is located in the new county town of ZiGui, Three Gorges storehouse district (Figs. 3 and 4) and has become a reference case for geogrid reinforced soil retaining walls.

Fig. 3 The construction finished of geogrid reinforced soil retaining wall

Fig. 4 Completed geogrid reinforced soilretaining wall

POTENTIAL PROBLEMS IN DESIGN AND CONSTRUCTION

Although over 60 projects have achieved good economic and social benefits, some technical problems were found in the design and construction of geogrid reinforced soil retaining wall projects. In order to make this new style supporting structural system of geogrid reinforced soil retaining walls develop healthily and smoothly some related issues are discussed below for reference.

Choice of Plans for Reinforced Soil Retaining Walls

The plans of geogrid reinforced soil retaining walls must be chosen while considering the project's landform and geological conditions. Sufficient spaces are needed behind the retaining walls to obtain enough reinforced area to guarantee the inside and outside stabilization of the retaining walls. In other words, a geogrid reinforced soil retaining wall is fit for a filling project and particularly a project of a side-hill fill or filling joint in mountain and hilly terrain where it can display its unique function.

Geogrid Long-term Design Strength Determination

When the geogrid long term design strength is determined, it should be firstly considered that the grid will bring creep under long-term stress. Creep strength is obtained through the creep test and is indicated with the creep coefficient (f_c). Moreover, we should consider the material reduction factor (fm); different packing material reduction factor (f_d); environment and soil body influence reduction factor (f_c); bar joint strength reduction factor (f_j). The final long-term design strength (T_d) is:

$$T_d = \frac{T_{ult}}{f_c \times f_m \times f_d \times f_e \times f_j} \tag{1}$$

T_{ult} indicates quality tensile strength

Different Material Choice of Geogrid

When designing reinforced soil retaining walls using geogrid, the choice of different material geogrid must be paid attention to. The production of uni-axial geogrid uses HDPE or PP as the raw material. Though two kind of different material grid such as RS50 HDPE and RS50 PP. They have the same quality tensile strength but their creep strength is very different. Only one international company has done a creep test. The experimental result is as follows: The creep strength of PP grid under long-term load press will be 12% of the limit tensile strength after 120 years. The creep strength of HDPE grid under long term load press will be 40% of the limit tensile strength after 120 years. HDPE creep strength is 3 times more than the PP creep strength.

Geogrid Paving

Geogrid must be paved flatly and keep uprightness with wall surface, which can't be folded. One end of grid is fixed and the other end is tightened and fixed with the piece. Only then can the grid play the greatest role in the soil. In the curve and corner district (Fig. 5) when the gird is paved with excurvature, crevices will appear on the corner. In order to ensure continuity of the reinforced soil, the same model grid crumb is paved in the crevice part, overlaying all the reinforced districts. When the gird is paved with introflexion, the parts of grids will overlap on the corner, and the friction coefficient in the places of grid overlapped will decrease. As a result, a coarse sand layer with 100—200 mm thickness must be paved between the two layers of grids to ensure the function of friction drag.

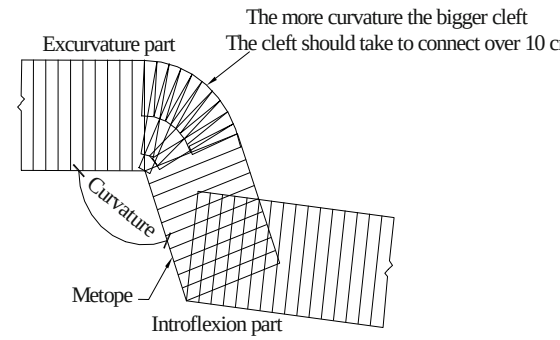

Fig. 5 Paving geogrid in the curve and corner districts

Reinforced Soil Filling and Rolling

The filling quality, paving thickness and rolling are closely related with the project quality of geogrid reinforced soil retaining walls. The filling quality should strictly satisfy the design request. The paving thickness should be decided by on-site tests, and then filling should be compacted with different layers. When the vibratory roller compaction is adopted, small roller compaction equipment (such as manpower dynamoelectric tamper) should be used near the wall surface at 1.5 m. The movement direction of roller compaction equipment should be parallel to the level trend of retaining walls. The number of times of roller compaction should be decided by experiments combined with concrete roller compaction equipment and filling properties. The next

round vestige of roller compaction should overlap 1/3rd of the width of round vestige with previous round vestige. The first static pressure is non-vibratory, and the roller compaction goes along gradually from central section of grid to the rear part, then changes direction to the wall surface of the retaining walls (Fig. 6).

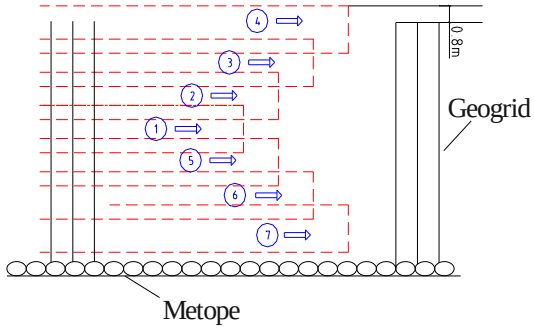

Fig. 6 Rolling equipment movement Schematic drawing

FURTHER ADVICE

1) In order to fully develop the structural advantage as well as the economic and social benefit of reinforced soil retaining walls, appropriate reinforced soil retaining walls are chosen according to the character of geogrid reinforced soil retaining walls combined with the actual project and the concrete circumstance of design and construction.

2) Confirming correctly and reasonably the geogrid long-term design strength is one of the most important design factors to ensure the safe usage of reinforced soil retaining walls in the limit time of design. The designer should distinguish clearly what is geogrid long-term design strength, the quality strength and the creep strength, determining their correlation and different functions. Only then can the geogrid long-term design strength be confirmed correctly and reasonably to make the design of geogrid reinforced soil retaining walls safety and credibility.

3) The correct and reasonable use of different material geogrid is another important factor to ensure the safe usage of reinforced soil retaining walls in the limit time of design. The authors suggest designers clearly mark HDPE in their design document when designing geogrid reinforced soil retaining walls in order that construction companies can correctly purchase the materials required for the project. If related technique parameters of HDPE grid are adopted in the design document but PP grids are used in construction, geogrid reinforced soil retaining walls will have the hidden danger when constructed and in use. This is worthy of the high attention of all parties involved in the project.

4) The paving method of geogrid is very simple. However it must be performed strictly in accordance with the design documents. It should be noted that adjacent geogrids will have crevices or overlap each other when geogrids are paved in the curve and corner districts. Only like this can frictional resistance play an important role and the project quality of the geogrid reinforced soil retaining walls can be guaranteed.

5) The technical parameters of filling must satisfy the design request strictly. The filling paving thickness and rolling times should be decided through on-site tests. Only under the conditions of adopting filling that satisfies the design request and the best water content. The scientific construction is carried out according to the paving thickness and rolling times decided by experiments, then the compaction can attain 95% of the design request. Then the project quality of the geogrid reinforced soil retaining walls can be guaranteed.

CONCLUSIONS

1) The high slope supporting project of the first middle school sports ground in ZiGui County was finished in December 2005. Thorough monitoring has taken place from December 2005 to July 2007. The largest sedimentation of the slope top was 4.2cm, and the largest displacement was 3.4 cm, hence the geogrid reinforced soil retaining wall is stable.

2) The project has become a scenic feature of the Three Gorges Storehouse district front door because of the design and construction success of the retaining wall.

3) Only are above problems highly noticeable in each link of the projects design and construction. This geogrid reinforced soil retaining wall structure with its new technique, new technology and new materials can be of better service for project and shows the special features.

REFERENCES

Xu GL, Liu FS, Guang HM (2004) The Modern Reinforced Soil Technique and Engineering Application. Wuhan, China University of Geo-sciences Press

Dobie M (2001) Used for Reinforced Soil Structure in High Density Polyethylene and Polypropylene Geogrid Specification and Examination. The first national geosynthetic test technique seminar collection

USING FLAC^{3D} NUMERICAL SIMULATION METHOD TO CHOOSE THE REINFORCED LENGTH OF THE SOIL RETAINING WALL

J.W. Su[1] and Y.M. Shu[2]

ABSTRACT: A finite difference software (FLAC ^{3D}) was used to carry on numerical simulation of reinforced soil retaining wall which had observed engineering data. Then the results were compared with those which were derived from limited balance method. The results showed that the finite difference software FLAC ^{3D} could simulated very well. In this paper, a reinforced soil retaining wall which was 60 meters high was set up to study the effect the reinforced length had on soil retaining wall. The simulation and analysis showed that with the increase of reinforced length, the side displacements of the panel and the pulling stress in reinforced layers decreased gradually. The maximum pulling stress focused on the lower half of the reinforced soil retaining wall. With the increase of the reinforced length, the probable destroyed cross because of the shearing moved away from the panel. Taking the allowing anti-pulling intensity as the main condition, we chose the optimal reinforced length.

KEYWORDS: reinforced soil retaining wall, working behavior, reinforced length, FLAC ^{3D} numerical simulation

INTRODUCTION

Because of its economy and safe and the convenience in construction, the reinforced geogrid retaining wall was widely used in reinforced soil engineering such as super highway, railway engineering and slope treatment in urban areas. Many researchers tried to study the working behavior and mechanism of the reinforced soil retaining wall using numerical analysis methods such as finite element. Karpurapu and Bathurst carried on the finite element analysis for soil retaining wall which had rigid foundation under it. For PWRI experimental wall in Japan, Huabei Liu studied the effect that various parameters had on the working behavior of the reinforced geogrid retaining wall through the use of finite element analysis of elasticity and plasticity. The results showed comparatively good similarity with the experimental results. However, finite element method had some deficiencies in the calculation of reinforced soil retaining wall. For example, several stress and strain relationships of soil body, reinforced body, the interaction between them and the corresponding parameters couldn't be fixed precisely. For the deficiencies in finite element method, Qianqian Chang carried on the numerical simulation of a reinforced soil retaining wall which had the observed data using the FLAC ^{3D} finite difference software. This testified that the utilization of FLAC ^{3D} in simulation could reflect the working mechanism of the soil retaining wall more effectively. Then she studied the effect that the space between reinforced steels had on the working behavior of the soil retaining wall. This paper simulated the side displacements of the panel and pulling stress in the reinforced layers under four different conditions (The reinforced length are 2.0 m, 2.5 m, 3.0 m and 4.0 m, separately.) through the utilization of numerical simulation method of FLAC^{3D}. Then the effects of them on the working behavior of the soil retaining wall were analyzed. Through the study of the laws above, the appropriate reinforced length was fixed and this will give guidance to the design of the engineering construction.

NUMERICAL SIMULATION ANALYSIS USING FLAC^{3D}

The model used in simulation analysis was the separated calculation model which took consideration of the interaction between geogrid and soil body. It was constituted by soil body element, geogrid element, panel element and interface element. In the process of calculation, "life and death" element was used to take consideration of the gradual filling of soil body and gradual infliction of load. Geogrid element was embedded inside the FLAC ^{3D} finite difference software, so great glide of strains could be simulated through the movement of the differencing point in the grid. There are

[1] Graduated Student, Dongfang Electric Coporation, CHINA.Email:snmsnmmaster@sina.com
[2] Professor, College of Hydroelectric Engineering, Hohai University, CHINA. Email: yimingshu2004@yahoo.com.cn

nine parameters in the geogrid element to change its characteristics in material and mechanics.

Numerical Simulation of RMC Reinforced Soil Retaining Wall

In order to test the rationality and validity of the calculating model, a testing wall (short for "RMC reinforced soil retaining wall") which was filled by Royal Military College of Canada was first simulated. The wall was 6 m in length, 2.4 m in width and 3.0 m in height. The panel of the wall was composed of four layers of concrete clods which was 0.75 m high and the bottom of the panel was connected to the base under it. The bidirectional geogrid which made of macro-molecular polymer were used for reinforcement. There are four layers of geogrid, the space between layers was 0.75m and the reinforced length in every layer was 3 m. The filling materials were close-grained grit soil. Besides, about 300 electrical elements such as devices for measuring displacement, sedimentation, strains, soil pressure were buried inside the soil retaining wall to observe its working behavior.

Side displacements of the panel

The side displacements of the panel calculated in this paper were those which occurred after the construction of the soil retaining wall, but the observed ones were those which occurred before the obvious deformation of the soil retaining wall. The calculated and observed side displacements of the whole panel were shown in Fig. 1. From the figure, we can concluded that the calculated tendency of the side deformation of the panel were comparatively consistent with the observed ones.

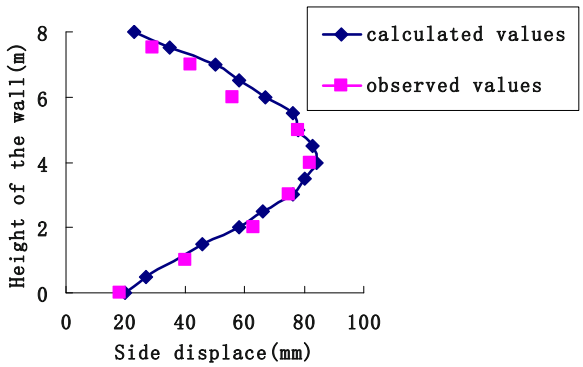

Fig. 1 The calculated and observed side displacements of the whole panel along the height of the wall

The distribution of the pulling strains in reinforced layers

The amount of reinforced layers of the soil retaining wall was very big, so we only chose five layers to calculate and then compared with the observed pulling strains. The five representative reinforced layers were 0.65 m, 1.65 m, 3.65 m, 5.65 m, 7.65 m high, separately. The calculated and observed pulling strains were shown in Fig. 2. From the figure, we can concluded that the calculated tendency of pulling strains were basically consistent with the observed ones. Both of them showed the same distributed tendency of the pulling strain in reinforced layers: the pulling strain increased gradually towards the direction of the panel, and then smoothly transited to the location of the panel. This distributed tendency was basically consistent with those in the assumed active and passive areas in limited balance analysis. Moreover, the differences between the calculated and observed maximum pulling strain in every layer were not so big.

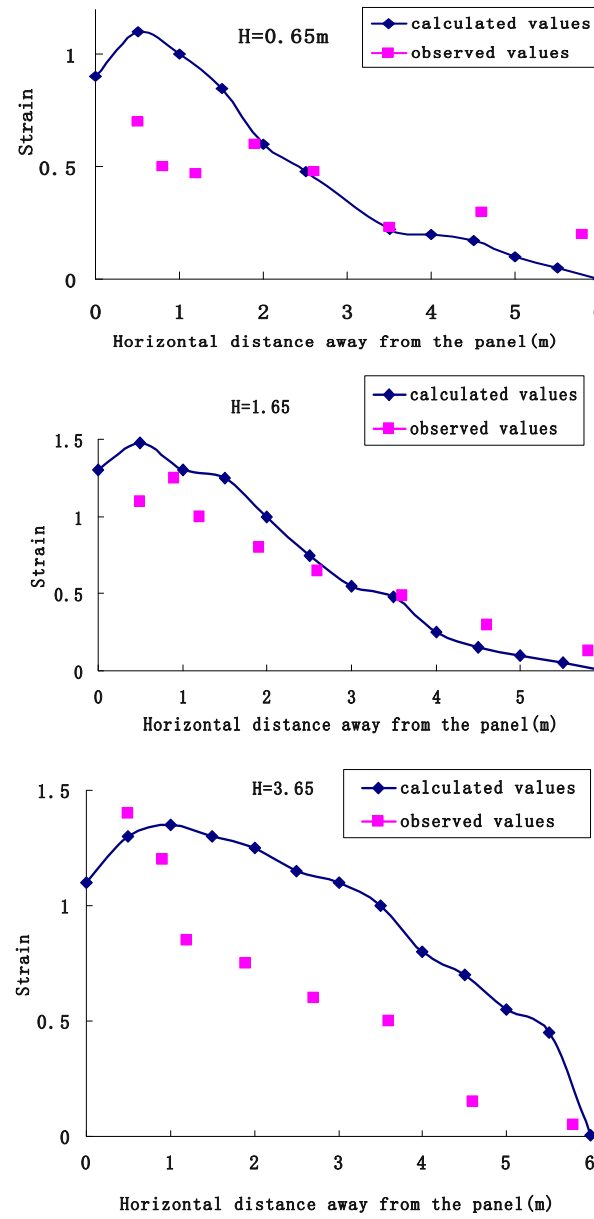

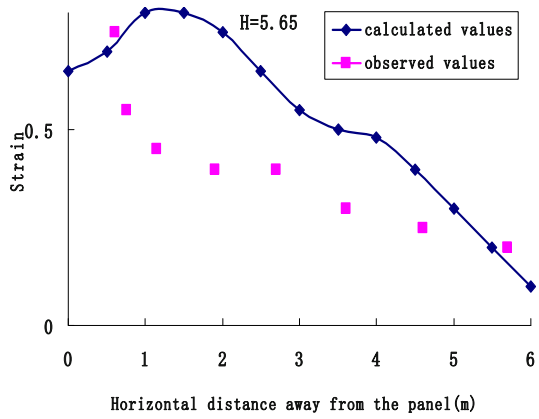

Fig. 2 Copmarison of the calculated and observed pulling strains in the reinforced layers

Analysis Model and Its Parameter Choosing

Based on the numerical simulation above, we set up a reinforced soil retaining wall which was 6.0 m in height. Its panel was composed of tow concrete block which was 0.25 m high and eleven concrete blocks which was 0.5 m high, with uniform grit filled in it. The geogrid was unilateral and made of fifteen layers of macromolecular polymer which was 5mm thick. Its yield tension was greater than 80 kN/m and yield extending rate was less than 10%. The foundation was made of uniform close-grained soil. Fig. 3 showed the model of the reinforced soil retaining wall. Four different conditions were chosen (The reinforced length are 2.0 m,2.5 m,3.0 m and 4.0 m, separately.) to carry on numerical simulation. The parameters were analyzed and settled following the references, and were shown in Table 1.

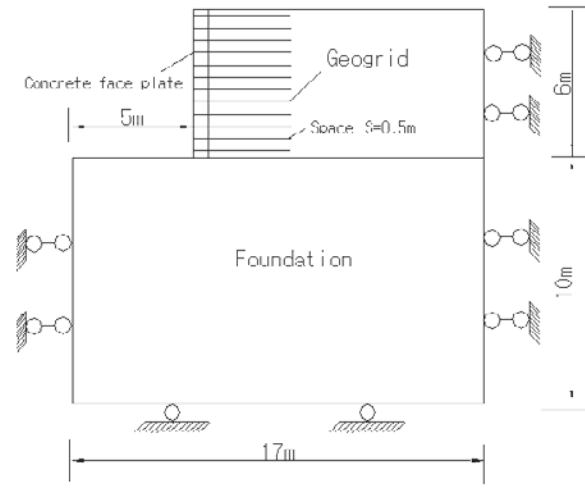

Fig. 3 Sketch map of the reinforced retaining wall model

Table 1 List of parameters of groundsill and filling element

parameters		Elastic moduli (MPa)	Poisson ratio	Interior frictional angle(°)	Dilstion angle (°)	Cohesion（KPa）	Bulk moduli (MPa)	Shear moduli (MPa)	Density（kg/m^3）
Foundation	Sand	25.01	0.3	30	0				1800
Filling materials	Uniform grit	50.3	0.3	35	7	0			1900

Table 2 List of parameters of other elements

Element type		Elastic moduli (MPa)	Poisson ratio	Interior frictional angle(°)	Dilstion angle (°)	Tang-ential rigidity (kPa/m)	Normal rigidity (kPa/m)	Cohesion (kPa/m)	Density（kg/m^3）
Geogrid		200	0.4	30		2×10^3		0	
Inter face	A			20	0	2×10^3	220×10^6	0	
	B			30	0	2×10^3	1.12×10^6	0	
Panel		25.25×10^3	0.17	45	0				2000

A-Interface of the panel and the filling materials
B-Interface of the filling materials and the foundation

RESULT ANALYSIS

Effect of Reinforced Length on Side Displacements of the Panel

The simulated tendency of ratio of side displacements and height along height of the wall was shown in Fg. 4. From the figure, we can see: First, the location of maximum side displacements of the panel was in the sub-central part, about in 2.4 m from the bottom of the wall. The side displacements in the bottom and top of the panel were a little small. This phenomenon due to the comparatively great active soil pressure focused near the central of the wall. And this could lead to the comparatively great displacements outward the panel to balance the moment produced by soil pressure. This conclusion was consistent with those derived from Xiwu Yang who carried on acentric modeling test and concluded that reinforcing steel bar between H/3 and H/2 in the sub-central of the side slope was the most economical and reasonable scheme. Moreover, in the practical engineering, the phenomenon of tympanites tends to occur near the central of the wall. The conclusion was also consistent with this. Second, the side displacements decreased with the increase of the reinforced length. The reason was that lateral restriction imposed on the soil body decreased because of the decrease of reinforced length. This led to the occurrence of outward displacements of soil body in the function of active soil pressure.

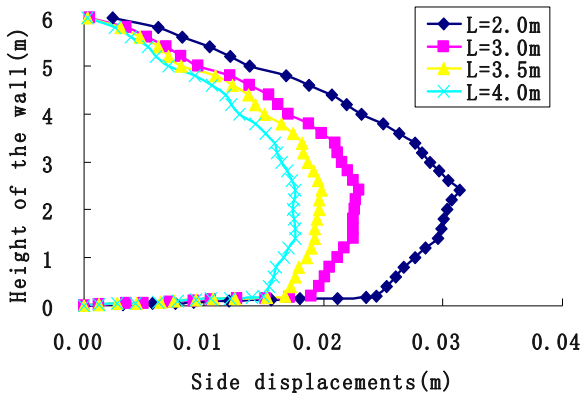

Fig. 4 The calculated and observed side displacements of the whole panel along the height of the wall

Effect of Reinforced Length on Pulling Stress in the Reinforced Layers

The maximum pulling stresses in every reinforced layer of reinforced soil retaining wall were shown in Fig. 5 (Note: The number N from the bottom to the top of the wall was 1, 2, …, to 12 in turn). From the figure, it can be seen that maximum pulling stresses in every reinforced layer were all occurred in the first layer of the nether part of the wall. Moreover, the maximum pulling stress of the soil retaining wall decreased from 2.36 MPa to 1.78 MPa with the increase of reinforced length and the difference of stress between layers also decreased gradually inside the soil retaining wall. Thus, we can conclude that the change of reinforced length changed the distribution of stress of the soil body and steel bar. From the results derived from experiment using four reinforced length, it can be seen that the bigger the reinforced length, the more favorable the retaining wall. However, the longer the steel bar, the smaller the maximum pulling stress of the steel bar. The intensity of the steel bar can't be sufficiently exerted. So there are must be a optimal length.

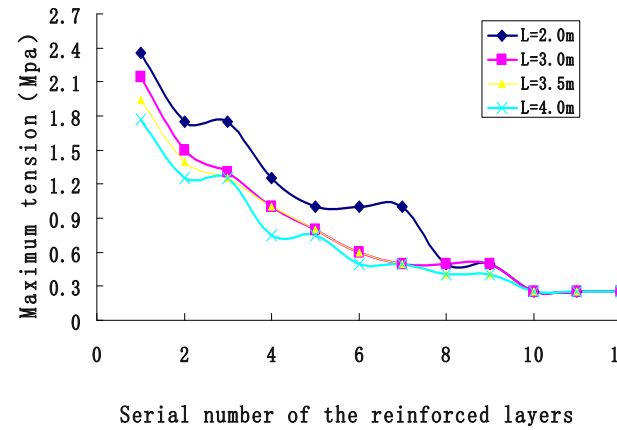

Fig. 5 The maximum pulling stresses in every reinforced layer of reinforced soil retaining wall

Map of Plastic State

Fig. 6 is the map of plastic state. From Figs. 6a—d, plastic area moves away the panel with the increase of reinforced length on the whole. The reason was that reinforced area could be seen as a whole after the reinforcement. That is to say, this area couldn't be destroyed so long as the anti-pulling intensity of the steel bar didn't be reached. If destroyed, it will only occur outside the reinforced area, so plastic area moved away the panel. However, this tendency wasn't obvious when reinforced length exceeded 3 m. This phenomenon reflected two aspects: First, the characteristic of soil body as a whole would be enhanced by reinforcement. The increase of reinforced length extended the reinforced area in the wall, so most reinforced area was ensured in the stable state. From the limited balance theory, the anti-sliding stability, anti-overturning stability, anti-sliding of the whole in the deep layer and bearing

capacity of the foundation would be enhanced with the increase of the reinforced length. Thus, reinforcement could change the distribution of the stress of the soil body and improve the stability of the reinforced body. Second, it also illuminated that the maximum reinforced length was not the better for soil retaining wall. The intensity of the steel bar couldn't be sufficiently exerted when exceeding certain length and the effect on the soil retaining wall was not obvious, too.

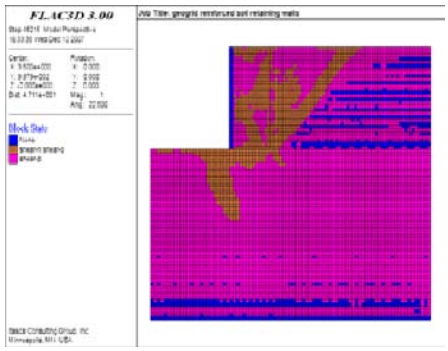

(a)

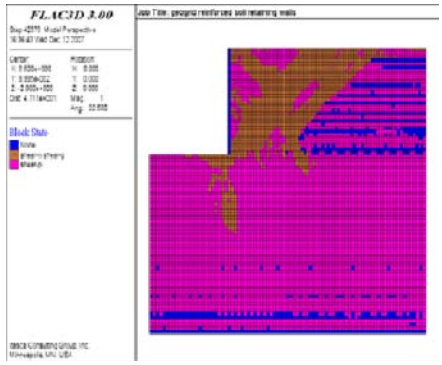

(b)

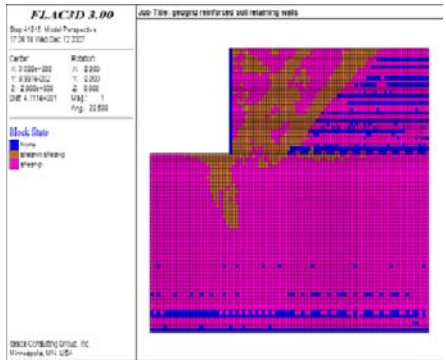

(c)

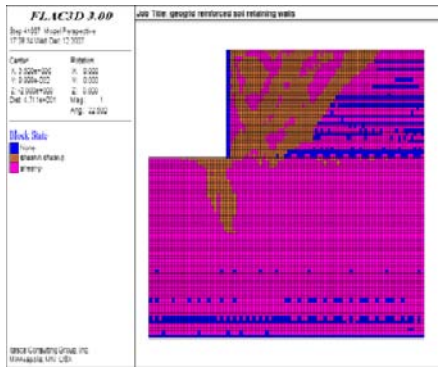

(d)

Fig. 6 Map of plastic state

CHOOEING THE REINFORCED LENGTH

Fixing the Optimal Reinforced Length Primarily

The equation to fix the allowing anti-pulling intensity of the geogrid could be gained according to the references. That was

$$Ta = Tu\left(\frac{1}{Fld \times Fcr \times Fcd \times Fbd}\right) \tag{1}$$

In the Eq. (1) above, the yield tension *Tu* was great than 80 kN/m in this paper. The mechanical destroy factor *Fld*, the peristaltic change factor *Fcr*, the chemical destroy factor *Fcd* and the biological destroy factor *Fbd* were all considered, in the end we could educe that the allowing anti-pulling intensity of the geogrid *Ta* equaled to 12.9 kN/m. From four conditions above, it can be seen that the anti-pulling intensity of the geogrid was 2.36 MPa when the reinforced length was 2.0 m. That was 11.8 kN/m after conversion and this value accorded with the intensity need of geogrid. So the optimal reinforced length was chosen to be 2.0 m in this paper.

Judgment of the Relative State between the Geogrid and Soil

Using the optimal reinforced length chosen above, we simulated the relative state between the geogrid and soil to test its rationality.

The law of shear intensity in the interface used Coulomb Law in FLAC^{3D} and the equation was as follows:

$$\tau_{\max} = c + \sigma_n \tan\phi \tag{2}$$

In the Eq. 2 above, τ_{max} stands for the maximum shearing strength, c stands for the cohesion, σ_n stands for the normal strength and φ stands for the fricative angle.

When shearing strength in the interface was less than the shearing intensity, the condition in the interface was elastic cohesion. Once exceed the shearing intensity, the condition was sliding in rigid frication, that was to say, the shearing destroy was the ideal elastic and plastic ones. In FLAC^{3D}, the coupled stress of the geogrid indirectly reflected the relative displacements between the geogrid and soil. The larger the coupled stress, the larger the displacements between them.

The coupled stresses of the geogrid were shown in Fig. 7 when the reinforced length was 2.0 m. From the figure, it can be seen that the maximum coupled stress was 0.1456 MPa. It was 0.728 kN/m after transition and less than the shearing intensity in the interface (1.35096 kN/m). This phenomenon illustrated that there were not relative frication slide between the geogrid and soil and they were all in the condition of elastic cohesion, that was to say, the steel bar were not be pulled out. So the optimal reinforced length chosen above satisfied the need of anti-pulling out and 2.0 m was the rational value.

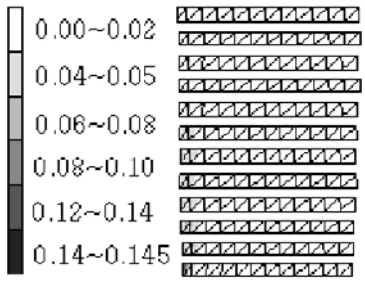

Fig. 7 Coupled stresses of the geogrid (Mpa)

CONCLUSIONS AND EXPECTATIONS

(1) The reinforced length of the reinforced soil retaining wall had comparatively great effect on the side displacements of the panel. The side displacements decreased gradually with the increase of the reinforced length.

(2) The maximum pulling stresses focused on the lower half of the reinforced soil retaining wall and decreased with the increase of the reinforced length.

(3) Reinforcing the soil retaining wall with steel bar could change the distribution of stress. The plastic area of the soil retaining wall moved away the panel with the increase of the reinforced length. This tendency was obvious when the reinforced length was less than 3 m, but the tendency was very small when the reinforced length was great than 3 m.

(4) The optimal reinforced length was fixed according to the allowing anti-pulling intensity of the geogrid. This value will give reference to the practical engineering.

(5) Multiple conditions should be studied in the future to enrich the design thoughts of the soil retaining wall and give more reference to the design and construction of the soil retaining wall.

REFERENCES

Bathurst RJ, Hatami K (1998) Seismic Response Analysis of a Geosynthetic-Reinforced Soil Retaining Wall. Geo-synthetic International 5(1–2): 127-166

Bathurst RJ, Hatami K (1999) Earthquake Response Analysis of Reinforced-Soil Walls Using FLAC, FLAC and Numerical Modeling in Geomechanics, Detournay, C. and HartR, Eds., Proceedings of the International FLAC Symposium on Numerical Modeling in Geomechanics. Minneapolis, MN

Chang QQ, Shu YM, Huang S (2007) Effect of bar spacing on performance of reinforced soil retaining walls. Journal of Hohai University (Natural Sciences) 35(5):557-562

Complied committee of Engineering applied handbook of geosynthesized metrical (2000) Engineering applied handbook of geosynthesized metrical. Chinese Architecture Press, Beijing

Liu HB, Ling HI (2004) Elasto-plastic finite element study for parameters of geogrid-reinforced soil retaining wall. Chinese Journal of Geotechnical Engineering 26(5): 668-673

Itasca Consulting Group Inc. (2002) Fast Lagrangian Analysis of Continua in 3 Dimensions User's Guide. Version 2.1. Itasca Consulting Group Inc., USA

Karpurpu R, Bathurst RJ (1995) Behaviour of geosynthetic reinforced soil retaining walls using the finite element method. Computers and Geotechnics 17: 279－299

Qian JH, Yin ZZ (1996) Theory and calculation of geoengineering. Chinese Hydroelectrical Press, Beijing: 401-451

Rowe RK, Skinner GD (2001) Numerical Analysis of Geosynthetic Reinforced Retaining Wall Constructed on a Layered Soil Foundation. Geotextiles and Geomembranes 19: 387-412

Yang X, Yi ZJ (2002) Study on reasonable distribution of reinforcement for reinforced slope. China Civil Engineering Journal 35(4): 60-64

UPPER-BOUND LIMIT ANALYSIS OF REINFORCED SLOPES FOR CLAY SOIL

X.J. Feng [1], Q. Yang [2] and C.Z. Xiao [3]

ABSTRACT: An upper-bound limit analysis approach is applied to determine the limit height of reinforced slopes for clay soil. The reinforcement is uniformly distributed over the height of the slope, and tensile failure is occurred in each layer. A rigorous upper bound to the slope height is calculated. Two methods were described to considering the influence on the limit height from pore-water and the sensibility of influence on stability of slopes from pore water and cohesion of soil is discussed.

KEYWORDS: reinforced slope, upper-bound limit analysis, pore-water

INTRODUCTION

Reinforced soil retaining structures have been widely used because they offer economic benefits compared to conventional retaining systems (Desai et al. 2005). Because of this practical importance, the analysis of slope stability has received wide attention in the literature. Limit equilibrium analysis has been the most popular method for slope stability calculations for its simplicity, especially for Bishop's simplified method (Yu et al. 1998). As neither the static admissibility of the stress field nor the kinematics admissibility of the collapse mechanism can be proved for any of the limit equilibrium slice method, the hypothesis that the methods satisfying three equations of global equilibrium is rather arbitrary. The upper bound technique of limit analysis is used in this paper. This technique was used earlier in the two-dimensional analysis of rotational collapse of slopes(Chen, Giber & Fang 1969), and it was suggested that it be used with translational mechanisms (Karal 1977; Izbicki 1981). A limit analysis solution to the total amount of uniformly distributed reinforcement in slopes (amount necessary to prevent collapse) is presented by Michalowski in 1997. The technique additionally included the effect of pore-water pressure. As a result, a set of comprehensive design charts for reinforced slopes was presented. Most of studies about reinforced soil have done by researchers were focused on the sandy soil both in numerical and experimental way. Although all of the advices were approved to using the reinforced soil structures in sandy soil for it can supply more bearing capacity and have good drainability, the studies to promote the reinforced technique to the clay soil is also important. It is well known that the cohesive of the clay soil significantly influences the stability of slopes. Meanwhile, a survey report indicated that the rain is the most critical cause to the collapse of reinforced slopes in Taiwan. It is particularly necessary to pay more attention to the negative influence from pore-water. In this paper, the limit analysis technique was used for clay soil, and some design charts and comparisons were supplied.

UPPER-BOUND LIMIT ANALYSIS

The upper-bound limit analysis for slopes can be described as: for a rigid plasticity soil slope, the rate of work done by external loads is equal to the energy dissipation rate in any kinematically admissible failure mechanism, and the relative slope height will be the upper-bound limit height.

$$\int_V \sigma_{ij}^* \varepsilon_{ij}^* \,\mathrm{d}V \geq \int_s T_i v_i \,\mathrm{d}s + \int_V \gamma_i v_i^* \,\mathrm{d}V - \int_V u \varepsilon_{ii}^* \,\mathrm{d}V \qquad (i, j = 1, 2, 3) \qquad (1)$$

Where ε_{ij}^* is the strain rate in a kinematically admissible velocity field; σ_{ij}^* is stress tensor associated with ε_{ij}^*; velocity v_i^* is v_i on boundary S; γ_i is the vector of body forces; S and V are loaded boundary and volume, respectively, and u and ε_{ii}^* are the pore pressure and volumetric deformation rate of the skeleton structure.

[1] Ph.D Student, Department of Civil Engineering,Dalian University of Technology, CHINA. Email: fxjdl@163.com
[2] Professor, Department of Civil Engineering,Dalian University of Technology, CHINA. Email:qyang@dlut.edu.cn
[3] Associate Professor, School of Civil Engineering, Hebei University of Technology,CHINA. Email: xiaochengzhi2@sina.com

The rotational collapse mechanism can lead to the least upper bounds to critical heights of unreinforced slopes with a log-spiral failure surface (Chen 1975). The slip surface in this paper is supposed to follow this logarithmic spiral equation:

$$R = R_0 \exp\left[\left(\theta - \theta_0\right)\tan\varphi\right] \tag{2}$$

Where φ is internal friction angle of soil; and R_0 is the radius of log-spiral related to angle θ_0 (Fig. 1). The admissibility of rotational failure requires that the velocity jump vector be inclined at angle φ to the failure surface, and its magnitude propagates according to

$$v = R\dot{\omega} \tag{3}$$

where $\dot{\omega}$ is the rate of rotation of the moving mass.

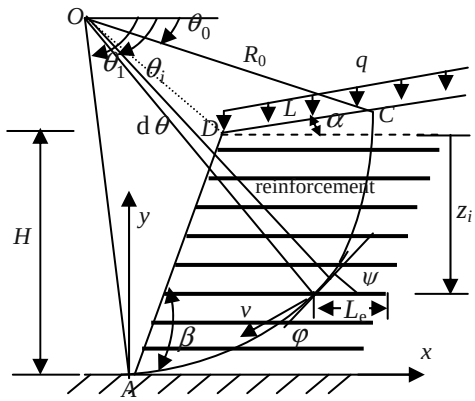

Fig. 1 Failure mechanism of the reinforced slope

The contribution to energy dissipation on the left-hand side of Eq. 1 is composed of two parts, one part is from the cohesion along the failure surface AC, and the other one is from reinforcement. For terms on the right-hand side of Eq. 1 are those due to the soil weight and pore-water pressure. Then Eq. (1) can be expressed as:

$$\dot{W}_s + \dot{W}_r = \dot{W}_g + \dot{W}_p \tag{4}$$

where $\dot{W}_s$ and $\dot{W}_r$ are the energy dissipation of soil cohesion and reinforcement; $\dot{W}_g$ and $\dot{W}_p$ are the work rate done by soil weight and pore pressure respectively. $\dot{W}_g$ and $\dot{W}_s$ have been given by Chen in (1975)

$$\dot{W}_g = \gamma R_0^3 \dot{\omega}\left(f_1 - f_2 - f_3\right) \tag{5}$$

$$\dot{W}_s = \frac{c\dot{\omega}R_0^2}{2\tan\varphi} f_s\left(\theta_1, \theta_0\right) \tag{6}$$

where the function f_1, f_2, f_3 and f_s are given in Appendix.

The energy dissipation of reinforcement is given

$$\mathrm{d}\dot{W}_r = k_t\left[v\cos\left(\psi - \varphi\right)\right]\mathrm{d}l\sin\psi \tag{7}$$

$$\dot{W}_r = = \frac{1}{2} k_t R_0^2 \omega f_r\left(\theta_1, \theta_0\right) \tag{8}$$

where k_t is the average tensile strength which defined as:

$$k_t = T_t / S_v \tag{9}$$

The function f_r is showed in Appendix.

Consideration of the influence of the pore water included in the last term of Eq. 1 references the research of Michalowski (1995):

$$\dot{W}_p = \gamma R_0^3 \dot{\omega} r_u f_5 \tag{10}$$

where r_u is the pore pressure coefficient as defined by Bishop and Mogenstern (1960); f_5 is also given in Appendix, and the further details is described in the paper by Michalowski (1995).

Substituting Eqs. 5, 6, 8 and 10 to Eq. 4 leads to the expression of limit height of the reinforced slopes:

$$H = \frac{c}{\gamma} \cdot \frac{f_4 \sin\beta\left(f_s / \tan\phi + k_t / c\, f_r\right)}{2\sin\left(\beta - \alpha\right)\left(f_1 - f_2 - f_3 + r_u f_5\right)} \tag{11}$$

Where γ and c is the unit weight and cohesive. The function f is given in Appendix. Chen called f as stability number. Here the object is not the dimensionless required strength of reinforcement $k_t / \gamma H$, for that the existence of cohesion make the value of $k_t / \gamma H$ dependent on k_t. The right-hand side of Eq. 11 is a function of θ_0 and θ_1. The codes were written to search the upper bound to H in Eq. 11 through varying θ_0 and θ_1.

MOISTURE CONTENT

The above method about considering of pore-water pressure was defined by Bishop and Morgenstern in limiting equilibrium analysis, and it is mainly applied to the saturated soil. However, the states of most reinforced soil structures were unsaturated, another technique is necessary to put forward to solve the influence of pore-water in unsaturated soil. Many researches found that the shear strength of clay soil is significantly dependent on the moisture content of soil, especially for the cohesion. With the ascending of the water content in soil, the cohesion increases first and then decrease. The turning point is called bound moisture content which is less than plastic limit and the true point needs test. Under natural conditions, most of the soil state in the descending branch. The relationships between cohesion and moisture content are different, some meet the exponential decrease, some meet parabolic relation, or even more complex ones. The data from references showed that the errors between different relationships are slightly. From a recent direct shear test for red clay, a parabolic relationship was obtained:

$$c = 181.1 - 7.56\omega + 0.08\omega^2 \quad (12)$$

where c is the cohesion and ω is the moisture content. Take this test for example, the variable of limit height of reinforced slopes with the change of moisture content is calculated.

It should pointed out that, the moisture can also influence the interaction between reinforcement and soil, in fact, it has been confirmed through tests. However, the resistance in clay soil is always small, even in the lower moisture content, for that clay soil can only supply limited bearing resistance. So reinforced soil structures are unfitted for the clay soil unless some effective measures are taken to increase the interface friction in order to make the reinforcement being made full use of. And it is likely to come truth in future. Considering of this, take the equation (12) as an example, assuming all reinforced layers occur tensile failure, and the reinforcement is uniformly distributed., the limit height of reinforced slopes are calculated in the following section.

COMPUTATIONAL RESULTS

The expression in Eq. 11 was used to calculate the limit height of reinforced slopes *H*, as a function of slope inclination angle β and the internal friction angle of the slope fill. The results of calculations are shown in diagrams (Fig. 2a—Fig. c) for pore-pressure coefficient r_u equal to 0, 0.25, and 0.5, respectively, for slope inclination angles in the range of 30—90°, the internal friction angle of 20—40°, and cohesion equal to 0 and 10 kpa, for average tensile strength k_t equal to 10 kpa. That cohesion=10 kpa is selected for comparing analysis, whereas, clay soil is no less than this level. Another kind of calculations of H with the consideration of the decrease of the cohesion are shown in diagram (Fig. 4) for the internal friction angle equal to 5° as the clay soil usually owns a lower internal friction angle, for slope inclination angles and average tensile strength of reinforcement in the same range as the former analysis. The code was used in which angles θ_0 and θ_1 were varied and the minimum of H was sought.

The studies of the sensibility of influence factors on the stability of reinforced slopes by Qing yang and other researchers showed that the cohesion and internal friction angle of the fill are the most sensible factors. Fig. 2 highlights this conclusion. The limit height of reinforced slopes for zero cohesion is less than half of that for cohesion=10 kpa for any pore-pressure. It decreases with the increasing of r_u which can see from Fig. 3 clearer.

The studies of the sensibility of influence factors on the stability of reinforced slopes by Qing yang and other researchers showed that the cohesion and internal friction angle of the fill are the most sensible factors. Fig. 2 highlights this conclusion. The limit height of reinforced slopes for zero cohesion is less than half of that for cohesion=10 kpa for any pore-pressure. It decreases with the increasing of r_u which can see from Fig. 3 clearer.

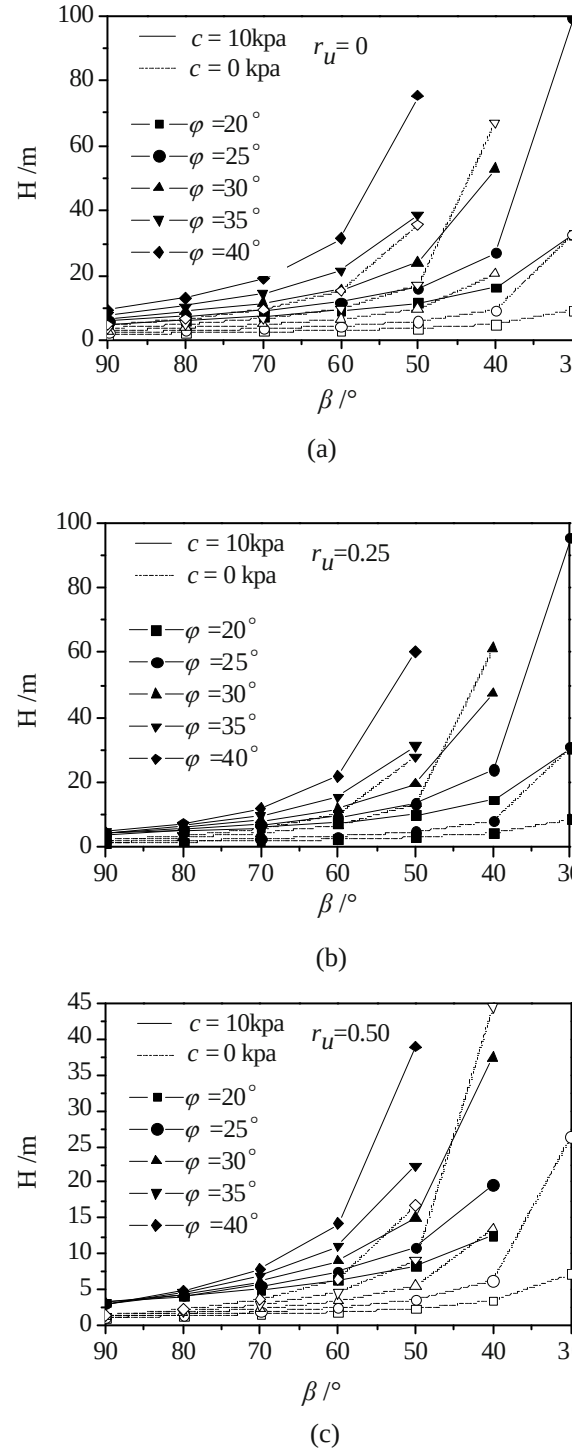

Fig. 2 Limit heights of uniformly reiforced slopes; (a) r_u=0; (b) r_u=0.25; (c) r_u=0.50

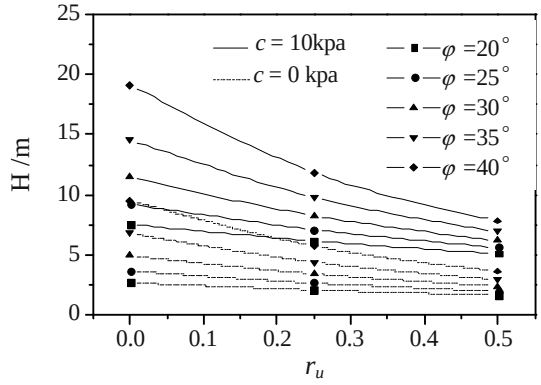

Fig. 3 Limit heights of uniformly distributed reinforcement in slopes (β=70°)

Charts for limit heights of reinforced slopes with considering the influence on the cohesion from moisture content are given in Fig. 4. Calculations were performed assuming the moisture content changing from 10% to 50%.With the increasing of moisture content ω, the limit heights for any inclined slope angles will decrease. Rain infiltration will increase the moisture content of the slopes, which may bring about a collapse. And the steep slopes will be more danger in this circumstance.

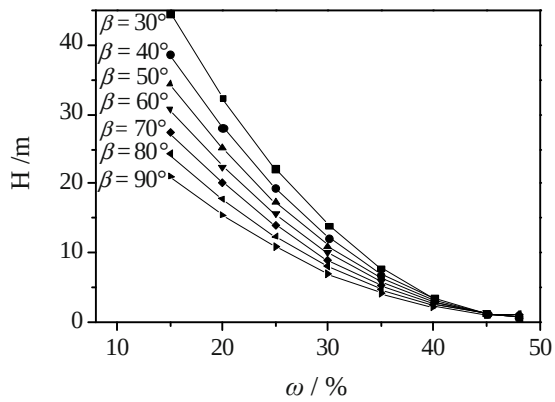

Fig. 4 Limit heights of reinforced slopes for different moisture content

CONCLUSIONS

Two techniques were described for considering the influence from pore-water in calculating the limit height of reinforced slopes. The former is fitted for the satured sandy soil, while the latter is suitable for the clay soil. The results indicated that the limit height of reinforced slope is more susceptible to the cohesion than pore-water with the assumption that cohesion is a constant for any moisture content.

Based on the rainfall intensity, rainfall duration and seepage properties, the distributed of the moisture content of different district of slope may be obtained, and then we can predicted the limit height.

REFERENCES

Bishop AW, Morgenstern NR (1960) Stability coefficients for earth slopes. Geotechnique, London, England, 10(4): 129-150

Chen WF (1975) Limit Analysis and Soil Plasticity[M]. New York: Elsevier Scientific Publishing Company

Michalowski RL (1995) Slope stability analysis: a kinematical approach. Geotechnique, London, England 45(2): 283-293

Michalowski RL (1997) Stability of uniformly reinforced slopes. Journal of Geotechnical and Geoenvironmental Engineering. ASCE 123(6): 546-556

Desai CS, Ei-hoseiny KE (2005) Prediction of field behavior of reinforced soil wall using advanced constitutive model. Journal of Geotechnical and Geoenvironmental Engineering. ASCE 131(6):729-739

Yu HS, Salgado R, Sloan SW (1998) Limit analysis versus limit equilibrium for slope statility. J. Geotechnical and Geoenvironmental Engineering 124(1): 1-11

Qian JH, Yin ZZ (1996) Soil Engineering Principle and Calculation. China Water Power Press, Beijing

Xiao CZ (2005) A study on rheologic properties of geogrids and long-term performance of reinforced earth walls. Ph.D.Dissertation. Dalian University of Technology.

APPENDIX

$$f_1=\frac{1}{[3(1+9\tan^2\varphi)]}\cdot\{(3\tan\varphi\cos\theta_1+\sin\theta_1)\cdot \exp[3(\theta_1-\theta_0)\tan\varphi]-(3\tan\varphi\cos\theta_0+\sin\theta_0)\}$$

$$f_2=\frac{1}{6}\frac{L}{R_0}\left(2\cos\theta_0-\frac{L}{R_0}\cos\alpha\right)\sin(\theta_0+\alpha)$$

$$f_3=\frac{1}{6}\exp\left[(\theta_1-\theta_0)\tan\varphi\right]\left[\sin(\theta_1-\theta_0)-\frac{L}{R_0}\sin(\theta_1+\alpha)\right]\left\{\cos\theta_0-\frac{L}{R_0}\cos\alpha+\cos\theta_1\exp[(\theta_1-\theta_0)\tan\varphi]\right\}$$

$$f_4=\sin(\theta_1+\alpha)\exp[(\theta_1-\theta_0)\tan\varphi]-\sin(\theta_0+\alpha)$$

$$f_s=\exp[2(\theta_1-\theta_0)\tan\varphi]-1$$

$$f_r=\sin^2\theta_1\exp[2(\theta_1-\theta_0)\tan\varphi]-\sin^2\theta_0$$

$$\frac{H}{R_0}=\frac{\sin\beta}{\sin(\beta-\alpha)}f_4(\theta_1,\theta_0)$$

$$\frac{L}{R_0}=\frac{\sin(\theta_1-\theta_0)}{\sin\theta_1}-\frac{\sin(\theta_1+\beta)}{\sin\theta_1\sin\beta}f_4(\theta_1,\theta_0)$$

AN EXPERIMENTAL STUDY ON THE EFFECT OF REINFORCING MATERIALS FOR THE STABILIZATION OF SOFT GROUND

S.D. Cho[1], T.G. Ham[2], K.S. Yang[3] and S.K. You[4]

ABSTRACT: The improvement of a bearing capacity with Geotextile, Geogrid, Bamboo-net is a common practice to obtain a trafficability of construction vehicles for the soft ground in KOREA. Nevertheless, the geotechnical behaviour, design method, and codes for surface remediation have not been well researched. In order to understand the behavioral characteristics of reinforced geosynthetics, Past examples for surface remediation were investigated and bearing capacity tests have been performed on soft-modeled ground with geosynthetic system. From the past examples for the remediation, it was found that Bamboon-net was commonly used for reinforced material where $\tau < 0.1$ tf/m^2 due to its flexural stiffness. For the bearing capacity tests, two types of clayey samples were used in this study, one obtained from Kwangyang and the other from Yonjongdo. Test results indicated that the bearing capacity of reinforced Kwangyang clay (c=0.1 tf/m^2) was approximately 125% higher than that of reinforced Yongjondo clay(c=0.17 tf/m^2). Correspondingly, it is concluded that the bearing capacity of reinforced ground is related to the shear strength property of ground without reinforcement.

KEYWORDS: surface stabilization, reclamation, soft ground, settlement, geotextile

INTRODUCTION

Soft ground surface stabilization method has been actively studied in the advanced countries such as Japan, Europe, etc. since 1960 and a number of associated new technologies and engineering methods were suggested. In general, soft ground surface stabilization method contains ground reinforcing method, ground drain/drying method, replacement method, ground mixing method, vacuum consolidation method, and etc. depending on its principle of improvement and method. Domestically ground reinforcing method is widely used, where geosynthetic or bamboo is used as the reinforcing material. Nevertheless, engineering behavior, design method, specification standard, and etc. of the reinforced soft ground have not been proposed reasonably yet.

In this study, construction site concerned, technical data, thesis, and etc. were collected and analyzed to evaluate the status of applying domestic ground stabilization method. Furthermore, deformation behavior of soft ground reinforced with geotextile through the model test to evaluate the bearing capacity enhancing the effect of the bearing capacity of the reinforcing material was evaluated. Also on-site load test for the bamboo net reinforced system produced by a variety of binding methods was conducted to evaluate the engineering characteristic and optimal binding method of bamboo net.

CONTENTS OF RESEARCH

Analysis of Example of Reinforcement Applied Site

Considering the nature of surface stabilization method implemented for securing the trafficability prior to applying the surface reinforcement method, the example of design and test construction for the nation-wide large scaled ports (28 trade ports, 24 coastal ports, 8 new harbors) was inspected. As the result of the survey, it was found that ground stabilization method had been applied mainly in the areas such as Pyeongtaek, Yeosoo, Kwangyang, Jinhae, Busan, and etc. of ground stabilization method depending on the strength of soil as shown in Table 1.

The thickness of soil covering was measured to be 1.0－2.5 m in general. In case the strength of soil was less than 0.1 tf/m^2, bamboo net was mainly used, while geosynthetic was used in case it exceeded the value

[1] Senior Researcher in Chief, Geotechnical Engineering Division, Korea Institute of Construction Technology, KOREA. Email: sdcho@kict.re.kr
[2] Senior Researcher, Geotechnical Engineering Division, Korea Institute of Construction Technology, KOREA. Email:hamtg@kict.re.kr
[3] Chief Researcher, Korea Port Engineering Corp. KOREA. Email:fdnstone@dreamwiz.com
[4] Assistant Professor, Dept. of Civil Engineering, Myongji College, KOREA. Email:yousk@mic.ac.kr

mentioned above. Furthermore, although it varied depending on the condition applied in, when the strength of the soil in 0.1－0.133 tf/m^2 was reviewed, the effect of reducing the thickness of soil covering by approx. 0.5－1.0 m was seen in case of using the rigid material (bamboo net).

From the afore-mentioned results, it was judged that the bamboo with high flexural rigidity net was used in the consideration of the rigidity effect, as there might cause some problems in access of the equipment when using the geosynthetic that was low in shear strength (less than 0.1 tf/m^2).

At present, in the formula to calculate bearing capacity used domestically, neither design variable nor its estimation method for the influence of reinforcing material flexural rigidity on the bearing capacity improvement is suggested. Therefore, dynamic integer based on the mutual interaction between the reinforcing material flexural rigidity and the ground needs to be added.

Table 1 Surface reinforcement method applied depending on cohesion of soils

cohesion (tf/m^2)	Surface Reinforcing Method	Soil covering thickness (m)	Site applied
0.050	bamboo net(0.4m interval)		Busan 00
0.054	bamboo net(0.7m interval)	2.5	Pyeongtaek 00
0.069	bamboo net(0.5m interval)	1.5	Shinseondae 00
0.100	geosynthetic(15t/m)	1.0	Pyeongtaek 00
0.100	geosynthetic(15t/m)	2.5	Kwangyang 00
0.100	bamboo net(1.0m interval)	2.0	Kwangyang 00
0.100	geosynthetic(15t/m, 2sheet)	2.0	Jinhae 00
0.130	bamboo net(0.5m interval)	1.2	Shinseondae 00
0.133	bamboo net(0.5minterval)		Kwangyang 00
0.190	geosynthetic(20t/m)	1.2	Kwangyang 00
0.250	geosynthetic(15t/m)	1.0	Kwangyang 00
0.400	geosynthetic (15t/m+10t/m)	2.5	Busan 00
0.510	geosynthetic (20t/m)	1.2	Kwangyang 00

Present Status of Surface Reinforcement Design Method and Analysis of Problems

Ground stabilization method is basically a method to maintain the balance of the bearing capacity of ground and the surface load such as the small construction-use machines and soil covering on the reinforcing material laid. Accordingly, the design requires the proper evaluation of the bearing capacity of reclaimed ground in advance.

For the design of ground stabilization method, some methods have been suggested to adopt the theory of elasticity based on the formula of the bearing capacity of Terzaghi with some variations applied. Nevertheless, the deformation in case of ultra-soft ground occurs in serious condition beyond the range of elastic deformation that causes a lot of problems, for example, the change in the unknown parameters included in the formula such as tension acted on the ground condition and the reinforcing material during the construction. Therefore it is a recent tendency that empirical design based on the construction performance is carried out.

In this study, the evaluation was carried out for the bearing capacity of soft ground considering the reinforcing effect of the reinforcing material using the formula suggested by Yamanouchi. (See the Fig. 1)

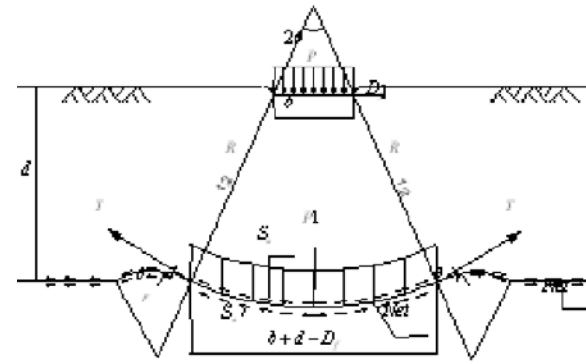

Fig. 1 Model of the bearing capacity in case loading the construction equipment is considered

$$q_a = \frac{1}{F}\left(1+\frac{d-D_f}{b}\right)\cdot\left[\left\{5.3\cdot c+T_{all}\cdot\left(\frac{2\cdot\sin\theta}{b}+\frac{1}{r}\right)+\frac{4\cdot S_a\cdot R(1-\cos\theta)}{b+d-D_f}\right\}+r\cdot D_f\right] \quad (1)$$

In the Eq. 1, tensile strength (T) was used for that of the reinforcing material, but r, θ, D_f in relation with deformation are still remained with the unknown values. There are two methods to presume these variables ①Analogical method from the example of on-site test measurement ②Model test.

With reference to the measurement of ①, Watari et al. (1986), Matsui et al. (1976), Nishibayashi et al. (1984), have been suggested. According to Nishibayashi et al. (1980, 1984), the deformation of ground at the stable condition is defined as shown in the Fig. 2 in consideration of the cor-relationship with the adhesive strength of ground.

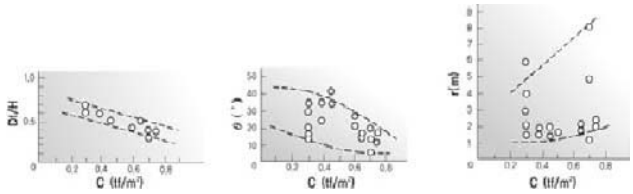

Fig. 2 Feature of deformation in case of the ground in stable condition (Nishibayashi et al, 1984)

As for ②, Yazima et al. (1988) suggested with the relationship of loading plate, the amount of settlement and deflection angle (θ) applying adhesive strength as its parameter based on several indoor testing data. Meantime, they described the method to decide r assuming the undrained deflection mode of soft ground.

Nevertheless, these values vary in complexity depending on the condition applied in at the time of soil covering installation and ground condition, and therefore the estimation of parameter accompanied by deformation is very difficult. In reality, empirical design is carried out as shown in the Table 2 based on the past construction performance. Furthermore, the bearing capacity formula is used in the same way regardless of the material characteristic of rigid material (bamboo net) and non-rigid material (Geotextile, Geogrid) is used for the current surface reinforcing material. Consequently, as afore-mentioned, it is believed that the bearing capacity of calculating formula requires dynamic integer based on the mutual interaction between the reinforcing material and ground depending on the type of the reinforcing material in addition.

In this study, model test was carried out for the purpose of assuming the parameters accompanied by the deformation suitable for the domestic soft ground with the afore-mentioned background.

Table 2 Application of Design Integer

Division	Application of Design Integer
D_f/H	·In case the strength of soil is extremely low, the deformation mode is enlarged, and then maximum tension is assumed to occur to the sheet before the effect of D_f is exerted. Accordingly as it become the unsafe design in view of D_f effect, normally it is set up as D_f=0.
θ	·In case of measurement, θ is within the range of 10° ～40° having the higher dispensability. Its average value is approx. 20°.
r	·In case of measurement, r is measured to be 2m～8m having higher dispensability too. The average value is approx. 3m.

TESTS

Laboratory Model Test

Laboratory model test was carried out in order to evaluate the bearing capacity enhancing the effect of the reinforcing material depending on the degree of softness of soft ground by analyzing the deformation behavior of soft ground reinforced with Geotextile.

In this research, the size of soil container for the model tester was 100cm high, 80cm wide and 15 long. Boundary condition through the numerical analysis was investigated to evaluate whether it required ground stabilization method model test or not. For the numerical analysis, the program of general Finite Element Analysis in the name of Plaxis 8.2 was used, where the total 10 cases were conducted adjusting whether to be reinforced or not, loading condition and size of mode. Under the condition of secondary 2-dimension plane strain, physical properties of clay ground used for the numerical analysis were as shown in the Table 3.

In this model test, the width of load applied to the soft ground was 10 cm, on which Geotextile was installed. Physical properties of clay used for model test is as shown in the Table 4. Furthermore, total 6 LVDT was used to measure the amount of heaving of the surrounded ground and the center of loading plate. In order to imitate the rapid installation (undrained condition) on the actual site, Gradual loading work was carried out at the center of clay ground after increasing the load by approx. p=0.14 tf/m^2 (1.4 kPa) from the static load with the lapse of 15 minutes based on the rapid loading. Tree diagram of model test device used for the test is as shown in the Fig. 3.

Table 3 physical properties of clay used for numerical analysis

Clay	Unit Weight (kN/m^3)	Coheshon (kN/m^2)	Poisson's ratio	Elastic modulus
Kwangyang	17	1.5	0.45	15.0

Table 4 Physical property of clay used for Model Test

Specimen	Gs	LL (%)	PI (%)	Cohesion (kN/m^2)	Water content (%)
Kwangyang	2.65	45.9	21.7	1.0	110
Youngjongdo	2.69	29.4	8.03	1.7	63

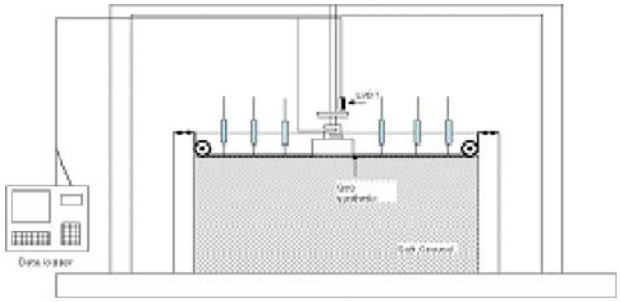

Fig. 3 Tree diagram of Model Testing Device

Evaluation of Engineering Characteristic of Bamboo Net

On-site load test was carried out against the bamboo net with every different binding material and interval of bamboo net to evaluate the stress per condition-deformation behavior. Conceptual diagram of load test device used for the test is as shown in the Fig. 4.

In order to determine the dynamic characteristic of bamboo net, depending on the site situation, the location of lap joint was divided into two cases of center and edge as shown in the Table 5. Then the test was conducted for three materials such as steel wire, PP band and tie cable.

Table 5 Testing Condition of bamboo net

Case	Bamboo net interval	Binding material	Remark
1	0.4 m×0.4 m	Steel wire	Center of lap joint
2	0.5 m×0.5 m		
3	0.7 m×0.7 m		
4	1.0 m×1.0 m	Tie Cable	
5	0.5 m×0.5 m		
6	1.0 m×1.0 m	PP band	
7	1.0m×1.0 m		
8	0.4m×0.4 m	Steel wire	Edge of lap joint
9	0.5 m×0.5 m		
10	0.7 m×0.7 m		
11	1.0 m×1.0 m		

RESULTS OF STUDY

Evaluation of Buckling Effect

The result of numerical analysis is as shown in the Fig. 5. In the Figure, horizontal displacement was measured to be its highest in amount of heaving at around 40 cm from the center, but little at around 80 cm. Furthermore, vertical displacement was little at the depth of 40 cm or more.

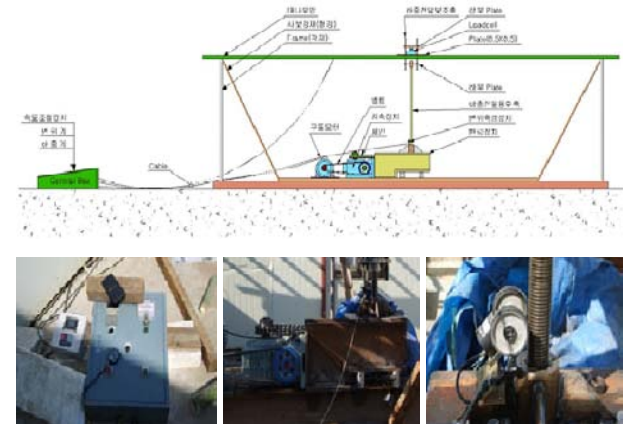

(a) control box (b) load delivery system (c) displacement measuring gauge

Fig. 4 Conceptual Diagram of load test device

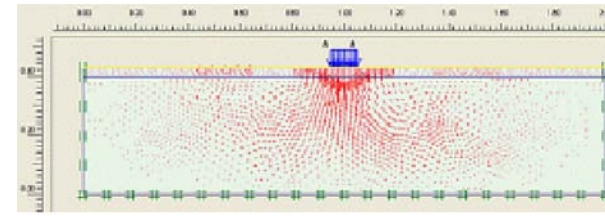

Fig. 5 Displacement of Ground after Reinforcement

Result of Model Test

Fig. 6 shows the relationship between loaded stress and the amount of settlement to survey the degree of disparity in the bearing capacity depending on the ground surface. In the figure, the allowed indicates yield stress p_{yn} at each clay ground. As result of calculating the maximum bearing capacity from the relationship between load and the amount of settlement, the maximum bearing capacity p_{yn} was 0.56 tf/m^2 at Youngjongdo and 0.42 tf/m^2 at Kwangyang.

In order to evaluate the bearing capacity-enhancing effect by the reinforcing material, the Bearing Capacity Ratio (BCR) that is defined as the ratio of the allowable bearing capacity (q_a) of pre-reinforcement clay ground and the allowable bearing capacity (q_{ap}) obtained from the model test after reinforcement was calculated. As the model test was not available in case of the allowable bearing capacity (q_a) for pre-reinforcement clay ground, the case of no reinforcement (T=0) in Eq. (1) was evaluated. As result of calculating the bearing capacity, BCR showed 1.55 (0.42/0.27) and 1.24 (0.56/0.45) for Kwangyang clay and Youngjongdo clay respectively. Subsequently, in case of the bearing capacity enhancing effect when the same reinforcing material were used, Kwangyang clay with the adhesive strength in 0.1 tf/m^2 was approximately 125% higher than that of reinforced Yongjondo clay (c=0.17 tf/m^2).

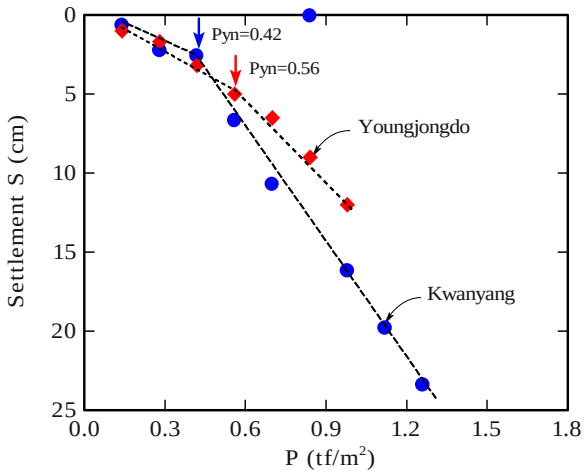

Fig. 6 Degree of the bearing capacity variation depending on the type of ground surface

Engineering Characteristic and Optimal Binding Method of Bamboo Net

Maximum load of bamboo net was measured to be in the range of 2.10 kN — 11.02 kN depending on its interval, depending on its interval, showing bigger maximum load at shorter interval—the typical tendency, when the displacement was in the range of 181 mm—604 mm.

In the test under the same interval of bamboo net (1.0×1.0 m) but with different binding material used for the joint, it was measured to be 3.66 kN, 2.68 kN and 2.10 kN in case of steel wire, Tie cable and PP band respectively where the steel wire showed the highest binding force. Of course the member of bamboo net used may not be completely same, but the influence thereon could be neglected. In that case, steel wire showed the highest binding force to the bamboo joint, while tie cable and PP band showing less binding force, resulted from the area jointed with bamboo member getting loose at the time of loading, where the role of load distribution to the overall bamboo net system was insufficient.

CONCLUSIONS

The results derived from this research can be summarized as follow.

1. As result of investigating the example where the ground stabilization method was applied by regions/ strength of soils, in case of the soft ground where the shear strength is low (less than 0.1 tf/m^2), normally the rigid reinforcing material such as bamboo net was used in consideration of the effect of rigidity of reinforcing material.
2. After result of calculating the bearing capacity ratio that is defined with the bearing capacity before reinforcement (q_a) and the allowable bearing capacity after reinforcement (q_{ap}), in case of the bearing capacity effect—enhancing effect where the same reinforcing material was used, it was revealed that Kwangyang clay (c=0.1 tf/m^2) was approximately 125% higher than that of reinforced Yongjondo clay(c=0.17 tf/m^2).
3. Maximum load of bamboo net was measured to be in the range of 2.10kN—11.02 kN depending on its interval, showing bigger Maximum load at shorter interval—the typical tendency, when the displacement was in the range of 181 mm — 604 mm. Furthermore, as for the steel wire binding, binding force for the bamboo joint was most excellent of all, while tie cable and PP band showed less binding force for the joint, resulted from the area jointed with bamboo member getting loose at the time of loading.

ACKNOWLEDGEMENTS

This study was supported by grant R&D/06-Techinical of Construction-C16 from the Ministry of Construction and Transportation in Korea. This support is gratefully acknowledged.

REFERENCES

Watari Y, Higuchi Y, Aboshi H (1986) Field studies of the behavior of geogrids and very soft ground. 3rd International Conference on Geotexties, 2A/3, Vienna Austria:187-191

Matsunaga S, Watari, Isayama S (1988) Reinforcement of very soft ground using bamboo cross beam with polymer. Proc. Intn'l Symp. on Theory and Practice of Earth Reinforcement (IS Kyushu ’88): 425-430

Nishibayashi K (1980) Surface reinforcement (sheet). Doboku-Seko 21(13): 48-56 (in Japanese)

Nishibayashi K (1980) Surface treatment of soft ground with sheet. Kazima Publisher (in Japanese)

Proceedings of the 4th Asian Regional Conference on Geosynthetics
June 17 - 20, 2008 Shanghai, China

NUMERICAL SIMULATION OF GEOGRID REINFORCED LIGHTWEIGHT GEOMATERIALS ON SOFT GROUND AREA

T. Tanchaisawat[1], D.T. Bergado[2], Y.P. Lai[3], S. Piyaboon[4] and P. Anujorn[4]

ABSTRACT: A full scale test embankment was constructed on soft Bangkok clay using rubber tire chip-sand mixtures as lightweight geomaterials reinforced with geogrid under working stress conditions. The wall/embankment was constructed with solid modular concrete facing units and rock filled gabion boxes on both sloping sides of the embankment. This paper attempts to simulate the behavior of the full scale test embankment using PLAXIS finite element 2D program. The important considerations for simulation and sensitivity analyses of the behavior of reinforced wall/embankment were the method of applying the embankment loading during the construction process, the assumed soil permeability values during the consolidation process, and the selection of the appropriate models and properties at the interface between the soil and the reinforcement. The effect of settlement predictions are weathered crust thickness and over-consolidation ratio of soft clay because the lightweight backfill loading is much lower compared to conventional backfill. The computed excess pore water pressure is more accurate in shallow depth than deeper depth. The predicted lateral wall movement agreed well with observed field data.

KEYWORDS: numerical, geogrid, lightweight geomaterials, Bangkok clay

INTRODUCTION

Geosynthetic-reinforced segmental retaining wall or embankment has been well accepted in practice as alternatives to conventional retaining structures; their benefits include sound performance, aesthetics, cost and expediency of construction. This is especially true in soft ground area such as Bangkok, Thailand. Although many geosynthetic-reinforced soil walls have been safely constructed and are still performing well, there are many areas such as alluvial clay or soft clay area that needs in-depth studies in order to better understand the mechanical behavior of this system under more aggressive and harsh environments (Yoo and Song 2006). Issues related to the design and factors affecting the performance of reinforced soil have been addressed by many researches in recent times (e.g. Bathurst et al. 2005; Park and Tan 2005; Skinner and Rowe 2005; Al Hattamleh and Muhunthan 2006; Hufenus et al. 2006). Also, the behavior of reinforced earth structures has been comprehensively studies through field observation of full scale physical model, laboratory model testing, and numerical simulation (Youwai and Bergdo 2004; Bergado and Teerawattanasuk, 2007). An alternative method such as a numerical or simulation by means of appropriate methods such as finite-element (FE) or finite-difference (FD) techniques (e.g. Ho and Rowe, 1994) is essentially required. Most researches assumed plane strain condition for numerical simulations of reinforced earth structures. Hatami and Bathurst (2005) reported a survey of published work on numerical simulation of reinforced soil walls and categorized this work according to: (1) whether numerical models were verified against experimental/field evidence or were simply idealized model; (2) size of experimental models use for verification of numerical models; (3) quality and extent of measured data reported for each experimental/field case; (4) assessment of the accuracy of the physical data; (5) simulation of construction sequence and compaction effects; (6) constitutive models for soil backfill and the availability of laboratory data from which model parameters can be selected; and (7) consideration of load-strain-time effects on mechanical behavior of polymeric reinforcement layers.

The focus of this paper is on the numerical modeling using measurements from a series of systematically instrumented full scale test embankment constructed and monitored in plane strain test facility. Finite element program Plaxis 2D Ver. 8.2 was used to

[1] Lecturer, Department of Civil and Env. Eng'g, Kasetsart University CSC Campus, Sakolnakorn, THAILAND. Email: tawatchai.t@ku.ac.th
[2] Professor, GTE Program, School of Engineering and Technology, AIT, Bangkok, THAILAND. Email: bergado@ait.ac.th
[3] Doctoral Candidate, GTE Program, School of Engineering and Technology, AIT, Bangkok, THAILAND. Email: achorsol@gmail.com
[4] TenCate Geosynthetics (Thailand) Ltd., Bangkok, THAILAND. Email: somsak@polyfelt.co.th

predict the performance of the test embankment during and post construction phases.

FULL SCALE TEST EMBANKMENT

Subsoil Investigation

The test embankment was constructed in the campus of Asian Institute of Technology (AIT). The general soil profile consists of weathered crust layer of heavily overconsolidated reddish brown clay over the top 2.5 m. This layer is underlain by soft grayish clay down to about 8.0 in depth. The medium stiff clay with silt seams and fine sand lenses was found at the depth of 8.0—10.5 m depth. Below this layer is the stiff clay layer. Fig. 1 summarizes the subsoil profile and relevant parameters.

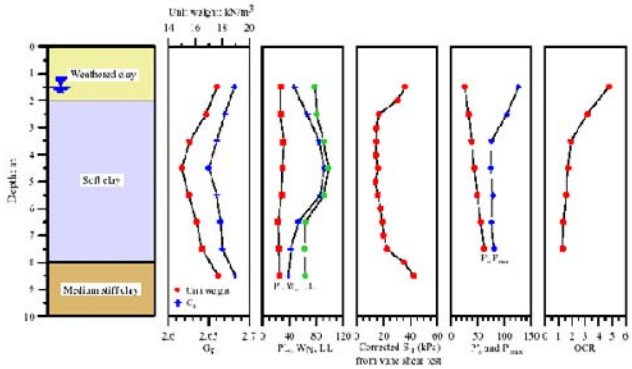

Fig. 1 Subsoil profile and relevant parameters

Embankment Construction

Lightweight geomaterials which made of rubber tire chip-sand mixtures was used as backfill materials. The soil reinforcement was comprised of polyester (PET) geogrid reinforcement material. The facing components were made of segmental concrete block which 0.30×0.30×1.00 m in dimension. The rubber tire chips were mixed with sand in the ratio of 30：70 by weight. The vertical spacing of the geogrid reinforcement was 0.60 m. The backfill was compacted in layers of 0.15 m thickness to density of about 95% of standard proctor. The sand backfill was used as the surface cover for the rubber tire chips-sand. The thickness of the cover was 0.6 m and a non-woven geotextiles was used as the erosion protection on side slope. Hexagonal wire gabions were used on both side of the concrete facing at the front side slopes (Tanchaisawat et al. 2007).

Instrumentation Program

The geogrid reinforcement embankment/wall system was extensively instrumented both in the subsoil and within the embankment itself. Since the embankment was founded on a highly compressible and thick layer of soft clay which dictates the behavior of the embankment to a great extent, several field instruments were installed in the subsurface soils. The instrumentation in the subsoil were installed prior to the construction of the geogrid reinforcement wall and consisted of the surface settlement plates, subsurface settlement gauges, temporary bench marks, open standpipe, groundwater table observation wells, inclinometers, dummy open standpipe, dummy surface settlement plates and dummy subsurface settlement gauges (Figs. 2 and 3).

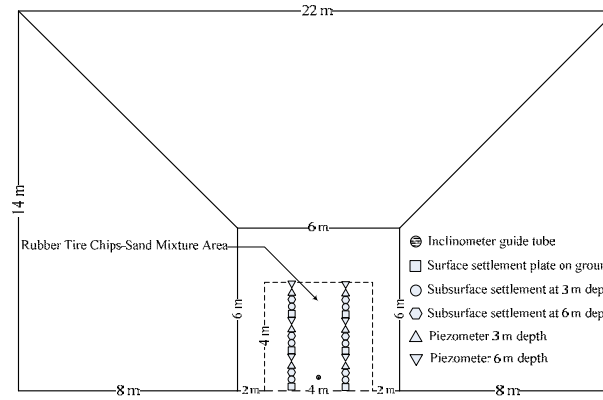

Fig. 2 Plan view of full scale test embankment with instrumentation

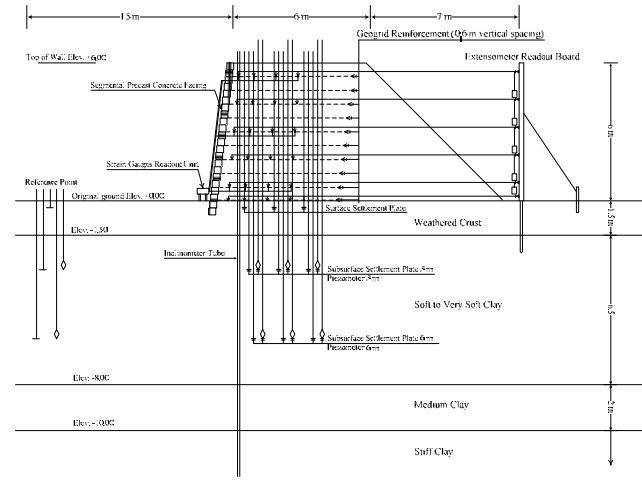

Fig. 3 Section view of full scale test embankment with instrumentation

NUMERICAL APPROACH

The finite element analysis were conducted using a finite element software, PLAXIS 2D version 8.2

developed by PLAXIS B. V. (2004). The program allows a realistic simulation of construction sequences, and the inclusion of reinforcement and interface elements at any stage of the analysis without any significant changes in the input data and finite element mesh. The FE model of reinforced embankment consisted of geogrid reinforcement, soil-to-reinforcement interaction and concrete facing elements and their connections. The six-node triangular element was used in model simulation (Fig. 4). The soft soil model (SSM), which is similar to the cam clay model, was used to model the behavior of a soft clay foundation. The linear elastic material model was used to model as medium clay layer, concrete block facing, and geogrid reinforcement. The elastic perfectly plastic with Mohr-Coulomb failure criteria was used to model the behavior of weathered crust and backfill material.

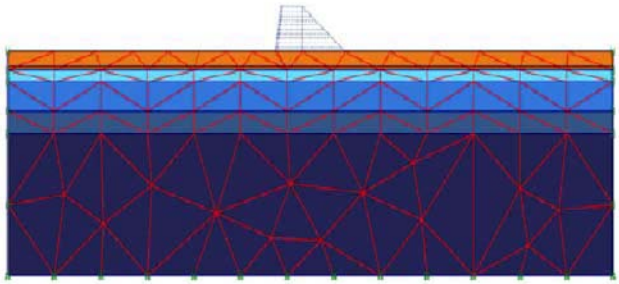

Fig. 6 Finite element model of full scale test embankment

Model Parameters

The backfill soil material used in the embankment is silty sand and rubber tire chip-sand mixtures. The elastic, perfectly plastic Mohr-Coulomb model can be used to represent the backfill material. At the construction site, the upper layer 1.5—2.5 m depth consists of the weathered crust, which is heavily overconsolidated. Elastic, perfectly plastic model with constant value of Poisson's ratio has been used for this soil. The Cam Clay model has been widely used for representing stress-strain relationship of the soft Bangkok clay, which is normally consolidated and lightly overconsolidated. In PLAXIS software, Cam Clay type model which is modified Cam Clay Model and Soft Soil model are available. The linear elastic model is used for predicting the behavior of the medium stiff clay layer. The geogrid reinforcements are flexible materials capable only of resisting tensile stresses, and in PLAXIS software this type of material is modeled as "geotextile". The elastic perfectly-plastic model was used to simulate the constitutive relations of soil-geogrid interface. The segmental precast concrete was used as embankment facing the size of block is 0.3 $\times$0.3$\times$1.0 m. In this study, the precast concrete facing was modeled as elastic beam. The input data for FEM simulations are tabulated in Table 1.

The in-situ stress was introduced in the foundation soil by adopting K_o procedure. Then, the backfill was constructed into 10 layers, as was done in the field. The compacted backfill was included in each layer, and the reinforcement was placed on a layer before the next layer was installed. The compacted backfill in a given layer was assigned with the material parameters according to the stress state induced after installing the layer.

RESULTS AND DISCUSSIONS

Surface Settlements

The observed and predicted surface settlements of the test embankment are plotted together in Fig. 7. As expected the predictions from Asaoka (1978) closely followed the observed data while the predictions from one-dimensional method overpredicted. The predicted surface settlements from FEM analysis agreed well with observed data. The computed surface settlement at the beginning of construction is greater than that measured values due to the partially drained behavior effect on the soft clay foundation at the early stages of the construction which can be related to the method of applying the embankment loading on the construction process or stress level. However, the computed settlements after 90 days agreed well with those measured values in the field when the drained behavior is consistent with the actual permeability values.

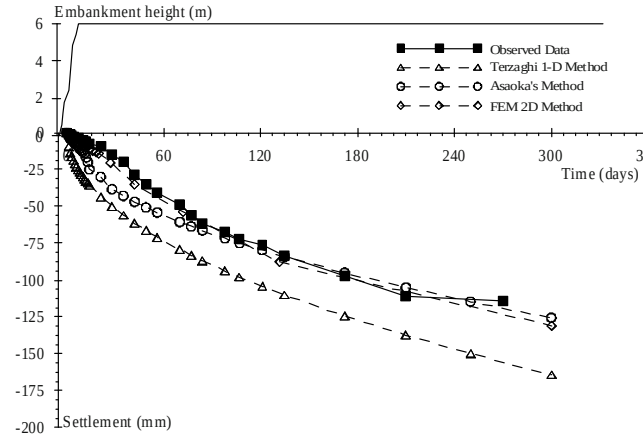

Fig. 7 Observed and predicted surface settlements

Table 1 Selected Parameters for Finite Element Modeling

Material	Depth m	Model	Type	γ_{unsat} kN/m^3	γ_{sat} kN/m^3	k_x m/d	k_y m/d	λ^*	κ^*	OCR	c' kN/m^2	ϕ' deg	E kN/m^2	υ'
Foundation Soil														
Weathered Crust	0.00 - 2.50	EP(MC)	U	16.0	18.0	2.0E-03	1.0E-03				50.0	24.0	5000	0.25
Soft Clay 1	2.50 - 4.00	SSM	U	13.0	15.0	8.0E-04	4.0E-04	0.130	0.026	1.2	10.0	23.0		0.33
Soft Clay 2	4.00 - 8.00	SSM	U	13.0	15.0	1.0E-04	5.0E-05	0.120	0.024	1.15	10.0	23.0		0.33
Soft Clay 3	8.00 - 11.00	SSM	U	13.0	15.0	4.0E-04	2.0E-04	0.110	0.022	1.0	15.0	23.0		0.25
Midium Clay	11.00 - 30.00	Elastic	U	13.0	15.0	4.0E-03	2.0E-03						7000	0.25
Backfill Soil														
Sand	-	EP(MC)	U	18.0	20.0	1.6E+00	8.0E-01				10.0	25.0	6000	0.33
Tire Chip-Sand Mixtures	-	EP(MC)	U	13.6	13.6	1.6E+00	8.0E-01				14.2	25.0	780(G)	0.33
Reinforcement														
Geogrid GX100/30	-	Elastic	-	EA = 50 kN/m (Tension Mode)				Interaction Parameter = 0.95						
Facing														
Modular Concrete Block	-	Elastic	-	EA = 1.05 E+10 kN/m			EI = 8.75E+8 kNm^2/m		w = 7.2 kN/m/m					0.15

Note :

EP(MC)	Elastic Perfectly Plastic (Mohr-Coulomb)	EA	Axial Stiffness
SSM	Soft Soil Model	EI	Bending Stiffness
Elastic	Linear Elastic	w	Unit Weight (concrete)
U	Undrained Condition		
(G)	Shear Modulus		

Excess Pore Water Pressure

The excess pore water pressure below the lightweight embankment was obtained from open stand pipe piezometer. Fig. 8 shows the measured and after construction at 3 m depth. The maximum pore water pressure of 57 kN/m^3 occurred at 15 days after end of embankment construction. The trend of excess pore water pressure dissipation is an indication of consolidation of soft foundation subsoil in the overconsolidation range when the load is below the maximum past pressure. After 50 days, the excess pore water pressure dissipated very fast with time. The excess pore water pressure decreased to 18 kN/m^2 and 25 kN/m^2 at 3 m and 6 m depths, respectively. The excess pore water pressure becomes constant with time after 120 days from the end of construction. The 1-D method overpredicted the excess pore water pressures than the predictions from the Skempton and Bjerrum (1957). The computed excess pore water pressures from FEM 2D method reasonably agree well with observed data.

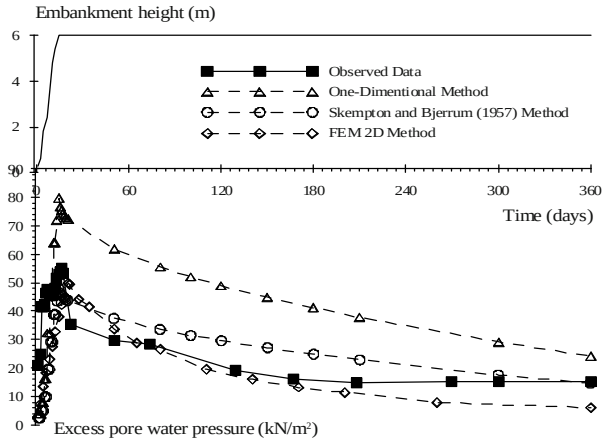

Fig. 8 Observed and predicted excess pore water pressures at 3 m depth

Lateral Wall Movements

The comparison between the FEM results and observed field lateral wall movement is shown in Fig. 9 for end of construction and after 13 months of construction. The computed lateral displacements of the wall face generally agreed with the observed field data. In the weakest zone of soft clay at depths of 3—4 m below the ground surface, the computed subsoil lateral displacements overpredicted the observed data. Since the lateral wall movement coincides with the results of vertical settlements, the partially drained consolidation process at very early stages of construction is not modeled well by the undrained finite element analysis (Schaefer and Duncan 1988; Chai and Bergado 1993).

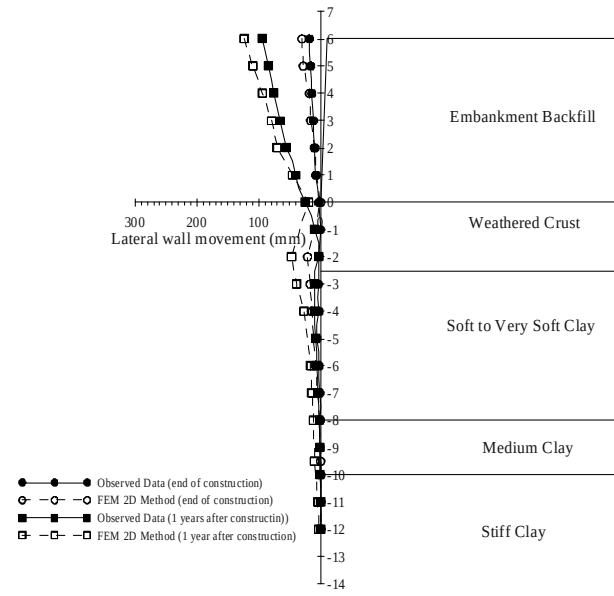

Fig. 9 Observed and predicted lateral wall movements

CONCLUSIONS

The numerical simulation based on finite element analyses under plane strain condition using PLAXIS computer software were carried out to study the behavior of a lightweight embankment reinforced with geogrid on soft ground foundation. The numerical simulation techniques adopted in this paper captured the overall behavior of the reinforced soil wall/embankment system on a soft foundation through good agreement between the field observations and the simulated values. The important simulation considerations in the FEM analysis consisted of the method of applying the embankment loading during construction process, the selection of an appropriate soil and reinforcement models, the estimation of soil permeabilities soft foundation, and the selection of appropriate parameters at the interface between the lightweight tire chips-sand backfill soil and geogrid reinforcement corresponding to the interaction mechanism. The predicted results were shown to be generally in good agreement with measured settlements, excess pore water pressures and lateral wall movements.

ACKNOWLEDGEMENTS

Sincere thanks and appreciation go to Assoc. Prof., Dr. Panich Voottipruex from King Mongkut`s Institute of Technology North Bangkok for his kind assistance and usefull discussion. This work was derived mainly from a research project funded by the Royal Thai Government conducted at the Asian Institute of Technology. The facilities provided by the research project are gratefully acknowledged.

REFERENCES

Al Hattamleh O, Muhunthan B (2006) Numerical procedures for deformation calculations in the reinforced soil walls. Geotextiles and Geomembranes 24(1): 52-57

Asaoka A (1978) Observation procedure of settlement prediction. Soils and Foundations 18(4): 87-101

Bathurst RJ, Allen TM, Walters DL (2005) Reinforcement loads in geosynthetic walls and the case for a new working stress design method (Mercer Lecture). Geotextiles and Geomembranes 23(4): 287-232

Bergado DT, Teerawattanasuk C (2007) 2D and 3D numerical simuations of reinforced embankments on soft ground. Geotextiles and Geomembranes, (in press)

Chai JC, Bergado DT (1993) Some techniques for FE analysis of embankment on soft ground. Canadian Geotechnical Journal 30: 710-719

Hatami K, Bathurst RJ (2005) Development and verification of a numerical model for the analysis of geosynthetic-reinforced soil segmental walls under working stress conditions. Canadian Geotechnical Journal 42: 1066-1085.

Ho SK, Rowe RK (1994) Prediction behavior of two centrifugal model soil walls. Journal of Geotechnical Engineering ASCE 120(10):1845-1873

Hufenus R, Rueegger R, Banjac R, Mayor P, Springman SM, Bronnimann R (2006) Full-scale field tests on geosynthetic reinforced unpaved roads on soft subgrade. Geotextiles and Geomembrane 24(1): 21-37

Park T, Tan SA (2005) Enhanced performance of reinforced soil walls by the inclusion of short fiber. Geotextiles and Geomembranes 23(4): 348-361

PLAXIS BV (2004) PLAXIS 2D Version 8.2, Finite Element Code for Soil and Rock Analysis, AA Balkema, Delft, Netherlands

Schaefer UR, Duncan JM (1988) Finite element analysis of the St. Alban test embankments. ASCE Geotechnical Special Publication 18: 158-177

Skempton AW, Bjerrum L (1957) A contribution to the settlement analysis of foundations on clay. Geotechnique 7: 168-178

Skinner GD, Rowe RK (2005) A novel approach to estimating the bearing capacity stability of geosynthetic reinforced retaining walls constructed on yielding foundations. Canadian Geotechnical Journal 42: 763-779

Tanchaisawat T, Bergado DT, Kanjananak T (2007) Lightweight geomaterials for bridge approach utilization, Proceedings 16th Southeast Asian Geotechnical Conference 2007, 8-11 May 2007, Subang Jaya, Malaysia

Yoo S, Song AR (2006) Effect of foundation yielding on performance of two-tier geosynthetic-reinforced segmental retaining walls: a numerical investigation. Geosynthetics International 13(5): 181-194

Youwai S, Bergado DT (2004) Numerical analysis of reinforced wall using rubber tire chips-sand mixtures as backfill material. Computers and Geotechnics 31(2): 103-114

A STUDY ON THE DEFORMATION BEHAVIOR OF LABORATORY GEOSYNTHETICS REINFORCED SOIL WALLS

M.S. Won[1], Y.S. Kim[2] and K.J. Lee[3]

ABSTRACT: Direct shear tests, wide-width tensile tests, and laboratory geosynthetics reinforced soil (GRS) wall tests were performed to examine and understand the external deformation behavior characteristics of GRS walls respectively constructed with non-woven geotextile (NWGT) and geogrid as reinforcement material. The result of laboratory GRS walls tests showed that the external displacement of the wall with geogrid, which had more stiffness than NWGT, appeared to be smaller than the wall with NWGT during both under construction and in the beginning of the loading, but the wall with geogrid showed larger displacements than the wall with NWGT as the load is increasing. The interface shear stress at the initial shear strain appeared to be higher at the soil-geogrid interface than at the soil-NWGT interface, but quite different phenomena in interface shear stress with increasing shear strain. It could be concluded that the NWGT would be a reasonable reinforcement of the wall under limited allowable deformations.

KEYWORDS: GRS walls, soil-geosynthetics interface, direct shear test, geogrid, non-woven geotextile

INTRODUCTION

Tensile force of reinforcement in reinforced soil is caused by shear stain in the soil which is connected or closed to the reinforcement, and provides resistance to tensile strain in the soil which is weak in tension. Shear characteristics at soil-geosynthetic interface are very important to examine the deformation behavior and failure mechanism of reinforced soil. The scale of direct shear tests is relatively smaller than pullout tests, and it is easy to analyze the shear strength of the reinforcement-soil interface. Direct shear test is useful to examine the shear behavior characteristic of reinforcement-soil interface (Bauer and Zhao 1993; Jewell and Worth 1987; Palmeira and Milligan 1989; Shewbridge and Sitar, 1989).

This study is performed to examine the relationship between shear strain-stress characteristics at soil-geosynthetic interface and external deformation behaviors of GRS walls carried out on laboratory GRS walls and direct shear tests with NWGT and geogrid.

SHEAR STRENGTH CHARACTERISTICS OF SOIL-GEOSYNTHETIC INTERFACE

The soil used in this study is classified as low plastic clayey soil (CL) by the Unified Soil Classification System. Table 1 and Fig. 1 respectively show the particle size distribution and soil properties used. NWGT and geogrid are used as reinforcement materials, and their properties and load-elongation properties are shown in Table 2 and Fig. 2.

Table 1 Soil properties used

γ_{dmax} (kN/m³)	w_{opt} (%)	C (kPa)	Φ (°)	LL (%)	PL (%)	Gs	USCS
18.39	15.8	54.8	29.1	30	22	2.67	CL

Table 2 Geosynthetic reinforcement properties used

Material	Description	Wide-width tensile test ASTM D 4595	
		Stiffness (kN/m)	Strength (kN/m)
Polyester	NWGT needle-punched	38	35
Polyester	Geogrid coated with PVC resin	267	43

Fig. 3 shows a large direct shear test apparatus used in this study. The inside dimension of the shear box is 30 cm by 30 cm in plane and 15cm in height (Volume= 13,5000 cm^2). As shown in Fig. 3, the soil and a wooden block (29.8 cm×29.6 cm×5.6 cm) which had been wrapped with NWGT or geogrid, were respectively put on the upper and lower part of the shear box. Soil

[1] Visiting Professor, Dept. of Civil Engineering, Kunsan National University, Republic of Korea Email: wondain@kunsan.ac.kr
[2] Professor, Department of Civil Engineering, Chonbuk National University, Republic of Korea Email: yusung@chonbuk.ac.kr
[3] Assistant Professor, Department of Civil Engineering, Seonam University, Republic of Korea Email: kingjoon@hanmail.net

compaction on the upper part of the box was conducted at the condition of the optimum moisture content with a rammer which has 4.5 kg in weight and 45cm in falling height. Total number of compaction layers was 2, with each layer being compacted 95 times with the rammer, and its compaction degree was at least 93%. Over 12 hours consolidation, direct shear test was performed with 0.5 mm/min in shear strain rate and consolidation and un-consolidation, CU condition. During the test, shear stress, shear stain and vertical displacement were automatically measured every 30 second with a data logger.

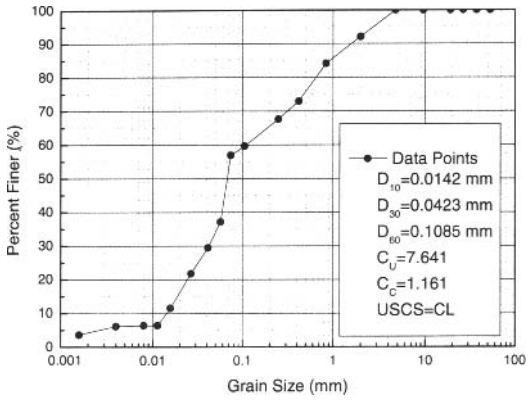

Fig. 1 Particle size distribution curve

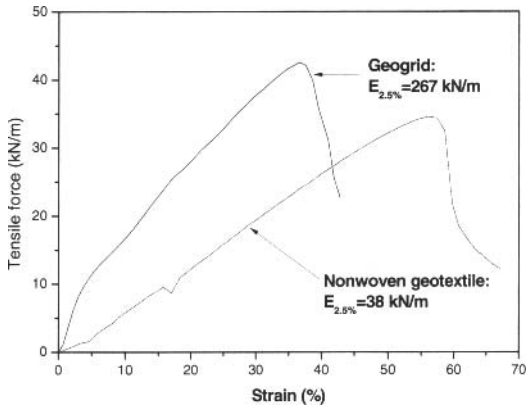

Fig. 2 Tensile strength-elongation properties of the reinforcement

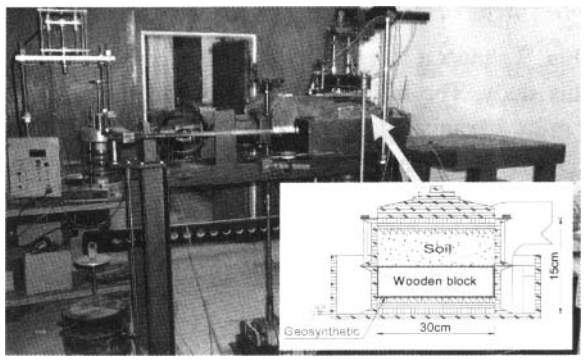

Fig. 3 A large direct shear test apparatus used

Normal stress condition during the test was in 4 phases at 50, 100, 200, 300 kPa, and all tests had finished when shear strain had reached at 16.7% (=50 mm in shear displacement). Fig. 4 indicates shear stress-displacement at soil-soil and soil-geosynthetics reinforcement interfaces under 200 and 300 kPa in normal stress.

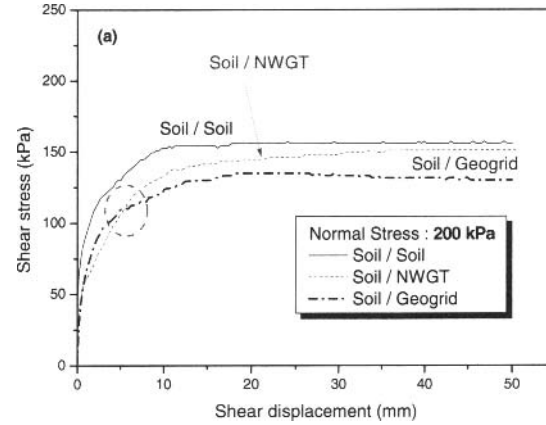

(a) Normal stress: 200 kPa

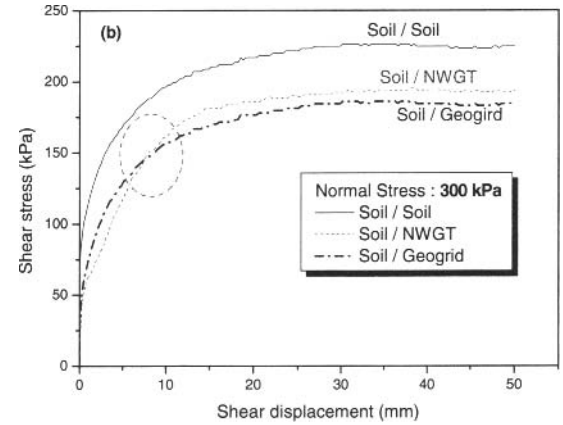

(b) Normal stress: 300 kPa

Fig. 4 Direct shear test results: shear stress-displacement relationships

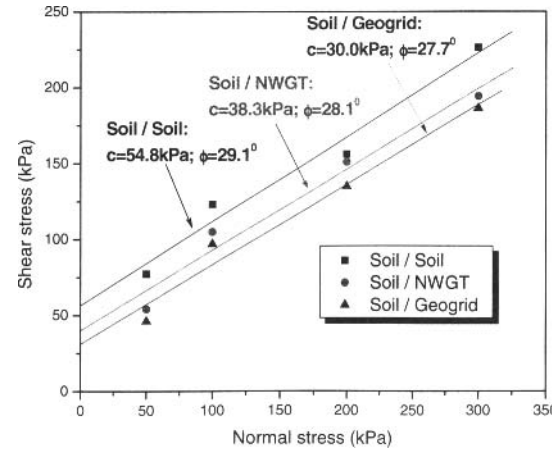

Fig. 5 Direct shear test results-failure envelope

Shear stress increases with increasing normal stress, as well as increasing shear displacement, and most shear stress-displacement curves show a similar trend with increasing normal stress. As shown in Figs. 4 and 5, shear strength increases in proportion to normal stress at soil-soil, soil-NWGT, and soil-geogrid interface. Shear stress at soil-geogrid interface in the beginning of shear displacement was pretty larger than soil-NWGT's, but shear stress at soil-NWGT interface over approximately 5.7 mm(=2.5% in shear strain) shear displacement was larger than soil-geogrid's. This phenomenon might be caused by the difference in structure between NWGT and geogrid, where NWGT in general has a small stiffness and rough surface sheet; whereas most geogrids are stiffer than NWGT and have apertures.

LABORATORY GRS WALLS TESTS AND RESULTS

Laboratory GRS wall tests were used with low plastic clayey soil, CL, as backfill material, and NWGT and geogrid as reinforcement (see Table 1 and 2). Fig. 6 and 7 show the schematic and sectional view of laboratory GRS wall tests. In Fig. 7, Case 1 is unreinforced soil wall. Case 2 and Case 3 are respectively reinforced with NWGT and geogrid as reinforcement. Unreinforced soil wall, in Case 1, was constructed with wooden blocks which were put in front of the facing of the wall to compact backfill and to build the wall. After construction of the wall, the wooden blocks were taken out from the facing.

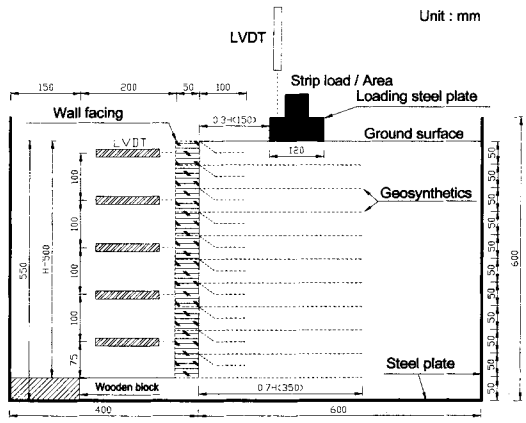

Fig. 6 Schematic of laboratory GRS walls setup

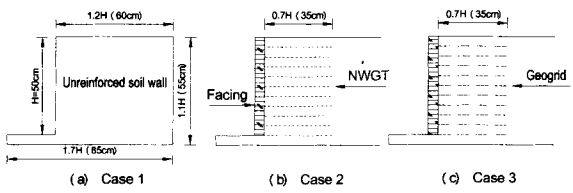

Fig. 7 Sectional view of laboratory GRS walls tests

The facing of the GRS walls was constructed by wrapping rectangular steel pipes with NWGT or geogrid as shown in Fig. 6. The deformation of the facing under construction of the GRS walls was allowed to develop by the friction between reinforcement and soil interface. Backfill material was compacted with a small rammer, which had 45cm in falling height and 4.5 kg in weight. Its compaction degree was more than 95%, and its moisture content was approximately 16%. Laboratory unreinforced soil and GRS walls, which have dimensions of 60 cm long, 50 cm wide, and 50cm high, as shown in Fig. 6 and 7, were constructed in a steel box, with an internal dimension of 50 cm by 100 cm in plane and 60 cm in height. Length of reinforcement is 70% of the wall height (H), 0.7 H(=35 cm), its vertical spacing is 0.1 H(= 5 cm), and a strip loading put at 0.3 H distance based from wall facing and its loading rate was 1 mm/min.

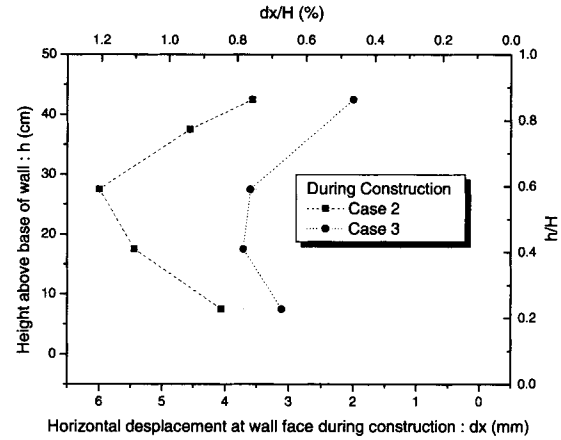

Fig. 8 Horizontal displacement at the facing during the construction

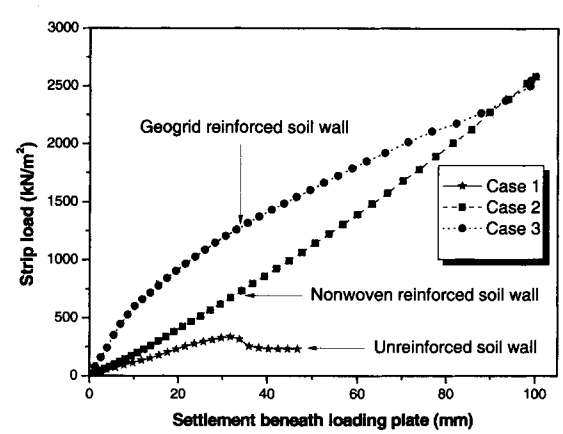

Fig. 9 . Loading and settlement relation curves

Fig. 8 shows horizontal displacement at the facing during the construction of the wall. Maximum horizontal displacement at Cases 2 and 3 during the construction was respectively 1.2% and 0.8% of the wall height. Horizontal deformation at Case 3 reinforced with stiffer

geogrid than NWGT was smaller than Case 2 with NWGT. Figs. 9 and 10 show settlement and horizontal displacement that occurred during the loading. They show that there is a lot of reinforcement effect to restrain the external deformation. Settlement from the beginning of the loading to 2,000 kPa was significantly smaller at Case 3 than Case 2. However, this trend was significantly decreased near 2,000 kPa, and settlement at Case 2 at the loading of 2,500 kPa was smaller than Case 3. Horizontal displacement at the facing showed a similar trend to settlement behavior. This means the external deformation behavior of GRS walls behaves in the same manner as the deformation behavior of shear stress-strain at the interface between reinforcement and soil, and NWGT as reinforcement is also useful in the case of the limited allowable deformation of GRS walls.

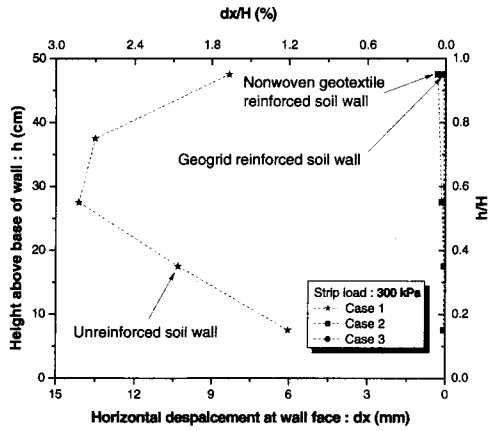

(a) Strip load: 300 kPa

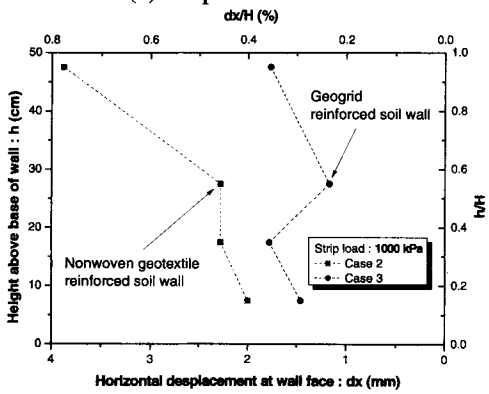

(b) Strip load: 1,000 kPa

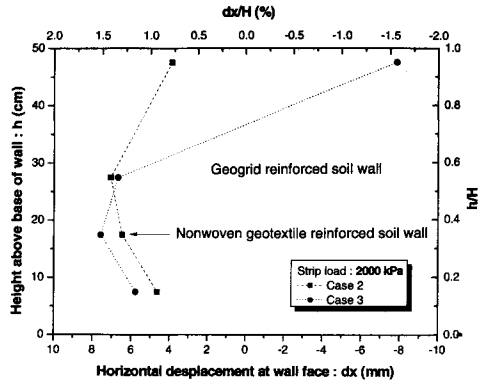

(c) Strip load: 2,000 kPa

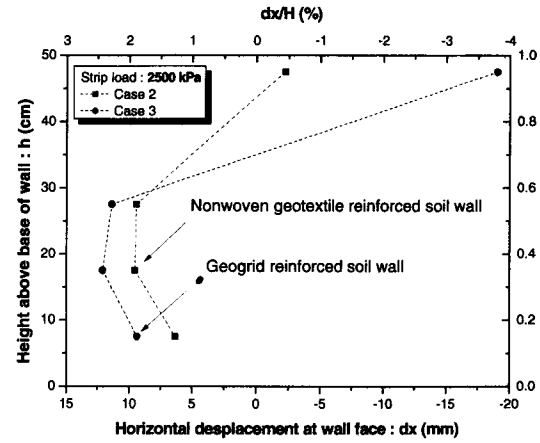

(d) Strip load: 2,500 kPa

Fig. 10 Horizontal displacement at the facing during the loading

CONCLUSION

Shear stress of soil-geogrid interface from the beginning of shear strain to approximately 2.5% was larger than shear stress of soil-NWGT interface. However, shear stress of soil-NWGT interface over 2.5% of shear strain was larger than the shear stress of soil-geogrid interface. Therefore, shear strength of soil-NWGT was larger than the shear strength of soil-geogrid. The external deformation behavior of laboratory GRW walls constructed with NGWT and geogrid as reinforcement respectively was pretty similar to shear behavior characteristics of reinforcement-soil interface. Therefore, NWGT is useful and reasonable when GRS walls are allowed to deform within the limited deformation.

REFERENCES

Jewell, RA, Worth CP (1987) Direct shear tests on reinforced sand, . Géotechnique, 37 (1): 53-68.

Palmeira EM, Milligan GWE (1989) Large scale direct shear tests on reinforced soil. Soils and Foundations, 29 (1): 18-19.

Qiu JY, Tatsuoka F, Uchimura T (2000) Constant pressure and constant volume direct shear tests on reinforced sand. Soils and Foundations, 40 (4): 1-17.

Shewbridge SE, Sitar N (1989) Deformation characteristics of reinforced sand in direct shear. J. of Geotech. Engrg., ASCE 115 (8): 1134-1147.

REDUCED SCALE SHAKING TABLE TESTS ON GEOSYNTHETIC REINFORCED SOIL RETAINING WALLS

E. Guler[1] and O. Selek[2]

ABSTRACT: Geosynthetic Reinforced Soil Retaining Walls offer cost-efficiency, higher performance, aesthetic appearance and much more durability. To help improve the inadequacies of the current seismic design methods and to gain a better insight into dynamic behavior of Geosynthetic-Reinforced Soil Retaining walls under earthquake loads, additional numerical and experimental tests must be adopted. In order to gain a better insight into dynamic behavior of Geosynthetic-Reinforced Soil Retaining walls, a series of reduced-scale (½ and ¼) Geotextile Reinforced Soil Retaining Wall models were tested using the shaking table facility at the Kandilli Observatory and Earthquake Research Institute (KOERI) of Bogazici University, Turkey. Linear displacement transducers were used to measure the strains of the geotextile reinforcements and laser displacement sensors were used to measure the displacements of the facing blocks which constitute the front wall of the retaining structure. Accelerometers were placed onto several locations of the soil structure to evaluate the acceleration amplifications that occurred. Preliminary results obtained from these tests show that the walls survived the El-Centro earthquake record with nearly no permanent displacements. The findings from the two models were observed to be consistent.

KEYWORDS: geosynthetics, reinforced soil, shaking table

INTRODUCTION

With the increasing use of geosynthetic-reinforced soil walls (GRS walls), their performance during earthquakes has started to be documented extensively. The amount of GRS wall construction is increasing worldwide due to the cost savings compared to conventional retaining structures, and their good performance observed during earthquakes is boosting the construction rate. For example, in Japan, the good seismic performance of GRS walls observed during the 1995 Hyogoken-Nanbu (Kobe) earthquake resulted in a sharp increase in the construction rate of these structures (Tamura 2006).

In the design of GRS walls, a limit equilibrium approach is commonly adopted to consider the seismic stability. The effect of the earthquake is taken as a destabilizing pseudo-static force and the wall is designed to satisfy the required factor of safety under the considered forces. However, the nature of these structures enables large amounts of displacement before failure, so catching up with the global trends toward limit states (performance-based) designs is a primary requirement (Koseki et al. 2006).

Variations of the classical Newmark sliding block method have been suggested to estimate the earthquake-induced displacements in GRS walls. Application of this method may give satisfactory results when the earthquake loads are large so that the threshold acceleration is exceeded and a failure plane is formed in the unreinforced backfill. However, investigations have shown that before the formation of failure planes, shear deformations of the foundation and the reinforced backfill will control the seismic response (Koseki et al. 2006).

The most straightforward method to predict the seismic behavior of GRS walls is to test using shaking tables. Even though it is hard to define and fulfill scaling laws for these structures, reduced-scale modeling is the most feasible testing alternative. These tests provide qualitative insights, and the results can be used to develop and validate numerical codes that will be used to predict the seismic response of the prototype (Koseki et al. 2006).

This study presents preliminary results from a series of reduced-scale shaking table tests that were conducted using the shaking table facility at the Kandilli Observatory and Earthquake Research Institute (KOERI) of Bogazici University.

The preferred type of GRS walls differs in every country due to local requirements and conditions. In Turkey, the facing is constructed using concrete blocks,

[1] Professor, Department of Civil Engineering, Boğaziçi University, TURKEY. Email: eguler@boun.edu.tr
[2] PhD Student, Department of Civil Engineering, Boğaziçi University, TURKEY. Email: oznur.selek@boun.edu.tr

which have no shear connections but rely on the interface friction with the geosynthetic. This study is one of the initial studies to test the seismic performance of this GRS wall specific to Turkey.

BACKGROUND

Shaking table tests reported in the literature prior to 2002 are summarized by Bathurst et al. (2002). None of these tests involved GRS walls with segmental (modular block) facing.

Shaking table tests on GRS walls with full-height rigid facings were performed by Watanabe et al. (2003) and El-Emam and Bathurst (2004, 2005) after 2002.

Bathurst et al. (2002) reported the results of shaking table tests in which 1 m high model GRS walls with vertical and inclined facings constructed with segmental blocks, vertical incremental panel and rigid full-height panels were tested. The vertical wall with no shear connections between the blocks showed the worst seismic performance, but having an inclined surface greatly improved the performance.

Shaking table tests on 2.8 m high (full-scale model) GRS segmental walls carried out using the vertical and horizontal components of the Kobe earthquake accelerogram showed that reducing the reinforcement spacing and increasing the length of the top reinforcement improved the seismic performance (Ling et al. 2005). The maximum deformation with a peak ground acceleration scaled to 0.86 g was less than 100 mm.

TESTING

In the study introduced in this paper, several ½ and ¼ scale models were tested on the whole. Tests on one ½ scale model and one ¼ scale model of the same prototype wall will be presented here.

The acceleration record of the El Centro earthquake was simulated on the shaking table. For the two models mentioned, the original acceleration record was magnified by two and testing began with the new record scaled-down to 10% and increased with 10% increments. The results presented in this paper are from 50% and 100% tests.

The duration of the earthquake applied to the model was scaled down by the square root of the scale of length in accordance with the established scaling rules (Iai 1989).

Setup for ½ Scale Model Testing

A steel box of 215 cm high and 278 cm deep was used to contain the reinforced soil. A woven geotextile was used as the reinforcing material and the backfill was moist sand of water content about 5%. The geotextile length was 85 cm in all layers. The geotextile reinforcement was placed at 20 cm intervals.

The inner sides of the steel box were covered with floating polyethylene sheets during construction to minimize friction. Three blocks (20 cm×10 cm×10 cm each) that were ½ scale models of the blocks used in the prototype wall were placed on the face. No shear connection between facing blocks was used except for the top 2 rows. Each layer of sand was compacted using a vibratory compactor before the placement of geotextile. The back 10 cm were filled with rubber chips to minimize the reflection of seismic waves from the back of the steel box. The walls were 2 m tall, making them one of the tallest reduced-scale walls of its kind.

Eight laser displacement sensors placed on a post were used to measure the displacement of the wall face. Five of these sensors were placed at 19cm, 59 cm, 99 cm, 139 cm, and 179 cm heights. The last three were placed at 197 cm.

Eight LVDTs in two rows were placed on a pole. Each row of LVDTs was used to measure the displacements of a specific geotextile layer (layers at 40 cm and 160 cm heights). The displacement in the horizontal direction was transferred into a vertical displacement using fishing lines and pulleys. The difference in displacements measured at different depths from the wall face was used to calculate the strains in the geotextile.

In addition to these measuring devices, five accelerometers were placed on the face of the wall and five were buried in the top layer of soil. One LVDT and one accelerometer were used to measure the displacement and acceleration of the shaking table, respectively.

Setup for ¼ Scale Model Testing

The setup was similar to the ½ scale model. This time, the facing blocks used were 10 cm×5 cm×5 cm. The geotextile length was 42.5 cm and the geotextile reinforcement was placed at 10 cm intervals. The total wall height was 1 m. No shear connection between facing blocks was used.

Five laser displacement sensors were used to measure facing displacements. One row of 4 LVDTs was used to measure the displacements of the geotextile layer at 40 cm height. Three accelerometers were placed on the face of the wall and five were buried in the top layer of soil.

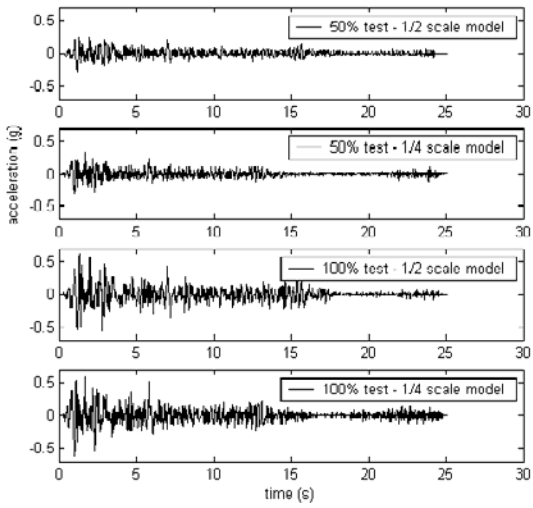

Fig. 1 Shaking table accelerations

The displacement and acceleration of the shaking table itself were measured as previously mentioned.

RESULTS

The table acceleration records for the tests considered in this paper are given in Fig. 1. The maximum accelerations recorded were 0.276 g, 0.348 g, 0.622 g, and 0.626 g for ½ scale model in 50% test, ¼ scale model in 50% test, ½ scale model in 100% test, and ¼ scale model in 100% test, respectively.

Results of 50% test on ½ Scale Model

The maximum permanent displacement observed on the wall face was 1.47 mm at 179 cm height. Wall face displacement at 179 cm height relative to the shaking table displacement is plotted in Fig. 2.

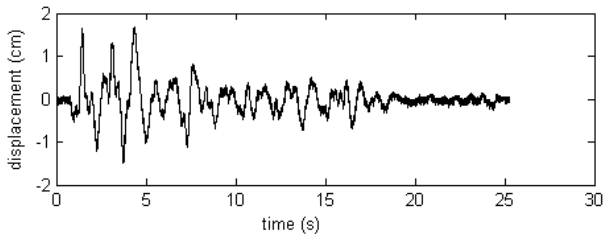

Fig. 2 Wall face displacement at 179 cm height relative to the shaking table displacement for 50% test on ½ scale model

The maximum strains observed in the geotextile during testing were 1.17% and 0.296% for the geotextile layers at 40 cm and 160 cm heights, respectively.

Results of 50% Test on ¼ Scale Model

The maximum permanent displacement observed on the wall face was 1.18 mm at 59 cm height. Wall face displacement at 59 cm height relative to the shaking table displacement is plotted in Fig.3. The maximum strain observed in the geotextile layer at 40 cm height was 0.408% during testing. The location of geotextile layer for which the strain measurements were taken was dependent on the setup of the LVDTs, which was fixed. This height of 40 cm corresponds to a height of 80 cm in the ½ scale model. Therefore, the strain measured is consistent with the strains measured in the previous test.

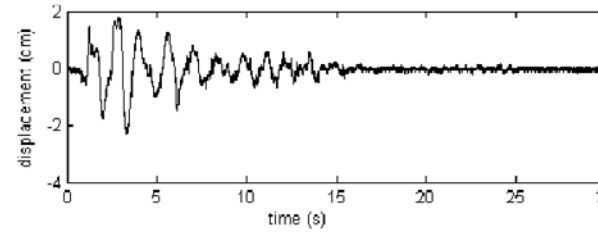

Fig. 3 Wall face displacement at 59 cm height relative to the shaking table displacement for 50% test on ¼ scale model

Results of 100% Test on ½ Scale Model

The maximum permanent displacement observed on the wall face was 1.23 mm at 179 cm height. This is not significantly different from the permanent displacement observed in the test with 50% lower peak acceleration. Wall face displacement at 179 cm height relative to the shaking table displacement is plotted in Fig. 4.

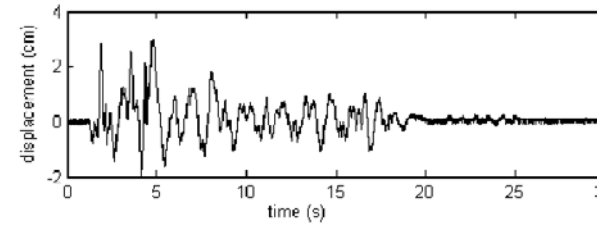

Fig. 4 Wall face displacement at 179 cm height relative to the shaking table displacement for 100% test on ½ scale model

The maximum strains observed in the geotextile during testing were 2.37% and 0.442% for the geotextile layers at 40 cm and 160 cm heights, respectively.

Results of 100% Test on ¼ Scale Model

The maximum permanent displacement observed on the wall face was 1.34 mm at 19 cm height. Wall face

displacement at 19 cm height relative to the shaking table displacement is plotted in Fig. 5. The permanent displacement observed at 59 cm height was 1.04 mm. Again, the permanent displacements are not significantly different from the test with 50% lower peak acceleration for the same model.

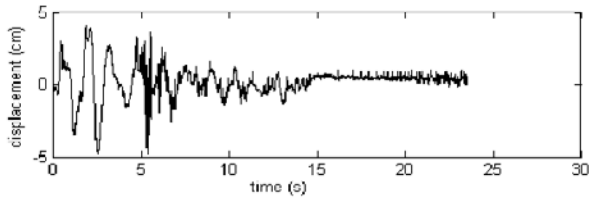

Fig. 5 Wall face displacement at 19 cm height relative to the shaking table displacement for 100% test on ¼ scale model

The maximum strain observed in the geotextile layer at 40 cm height was 1.61% during testing.

CONCLUSIONS

The test results and the corresponding values in the prototype wall of 4 m height are summarized in Table 1. The fact that the difference in the displacements of the two models is small is a proof that the boundary effect is really minimized. This minimized difference is probably due to the fact that the difference of the boundary friction effect is more dominant in the ½ scale model, since the prototype width is half the prototype width in the ¼ model.

The shaking table functioned by inputting the desired acceleration record and trying to attain the closest possible output acceleration. The difference between input and output accelerations was kept at minimum by continuous checking and correcting, but small variations were unavoidable (as seen in Fig. 1). This may be regarded as another reason for the small difference between the permanent displacements measured in the two models.

Considering the maximum geotextile strains, all measurements are seen to be consistent. In the ½ scale model tests, the maximum strain, therefore the maximum tensile stress in the geotextile at 40 cm height was significantly higher than that in the geotextile at 160 cm. Since the region of higher tensile stresses in the reinforced soil is further back at the higher level, it may be assumed that the instrumented area of geotextile was not in this critical region for the upper layer.

Taking the preliminary test results presented in this paper into consideration, it may be concluded that the strains therefore the tensile stresses in the geotextile layers remained much lower than that can be accommodated. In addition, there were nearly no permanent face displacements. Hence, considering both the failure resistance and the serviceability, the use of geosynthetic reinforced soil retaining walls in seismically active areas can be regarded as an intelligent choice.

Table 1 Displacement and strain measurements on model walls and their corresponding values on the prototype wall

		½ Scale Model	Prototype Wall	¼ Scale Model	Prototype Wall
50 % Test	Maximum permanent face displacement	1.47 mm @ 179 cm height	2.94 mm @ 358 cm height	1.18 mm @ 59 cm height	4.72 mm @ 236 mm height
	Maximum strain in geotextile	1.17% @ 40 cm height 0.296% @ 160 cm height	1.17% @ 80 cm height 0.296% @ 320 cm height	0.408% @ 40 cm height	0.408% @ 160 cm height
100 % Test	Maximum permanent face displacement	1.23 mm @ 179 cm height	2.46 mm @ 358 cm height	1.34 mm @ 19 cm height	5.36 mm @ 76 mm height
	Maximum strain in geotextile	2.37% @ 40 cm height 0.442% @ 160 cm height	2.37% @ 80 cm height 0.442% @ 320 cm height	1.61% @ 40 cm height	1.61% @ 160 cm height

REFERENCES

Bathurst RJ, Hatami K, Alfaro MC (2002) Geosynthetic reinforced soil walls and slopes: seismic aspects, Geosynthetics and Their Applications (S.K. Shukla Ed.), Thomas Telford: 327-392

El-Emam M, Bathurst RJ (2004) Experimental design, instrumentation and interpretation of reinforced soil wall response using a shaking table, International Journal of Physical Modelling in Geotechnics, 4(4): 13-32

El-Emam M, Bathurst RJ (2005) Facing contribution to seismic response of reduced-scale reinforced soil walls, Geosynthetics International, 12(5): 215- 238

Iai S (1989) Similitude for shaking tests on soil-structure-fluid models in 1g gravitational fields, Soils and Foundations, 29(1): 105-118

Koseki J, Bathurst RJ, Güler E, Kuwano J, Maugeri M (2006) Seismic stability of reinforced soil walls, 8th International Conference on Geosynthetics, 18-22 September 2006, Yokohama, Japa

Ling HI, Mohri Y, Leshchinsky D, Burke C, Matsushima, K. and, Liu, H. (2005). Large-scale shaking table tests on modular-block reinforced soil retaining walls, Journal of Geotechnical and Geoenvironmental Engineering, ASCE 131(4): 465-476

Tamura Y (2006) Lessons learnt from the construction of geosynthetic-reinforced soil retaining walls with full-height rigid facing for the last 10 years, 8th International Conference on Geosynthetics, 18-22 September 2006, Yokohama, Japan

Watanabe K, Munaf Y, Koseki J, Tateyama M, Kojima K (2003) Behaviors of several types of model retaining walls subjected to irregular excitation, Soils and Foundations 43(5): 13-27

A NUMERICAL MODEL FOR EPS GEOFOAM SEISMIC BUFFERS

Y.M. Wang [1], and R.J. Bathurst [2]

ABSTRACT: Based on an explicit time-marching finite difference approach, a multiple horizontal layer model is proposed to compute the compression–load–time response of EPS geofoam seismic buffers placed against rigid walls to attenuate earthquake-induced dynamic loads. The seismic buffer is modeled as a linear elastic material. The soil wedge is divided into a number of horizontal slices. The boundaries of each horizontal slice are connected by a series of stress-dependent linear springs. The distribution and magnitude of compressive displacement and load on the EPS geofoam buffer are computed numerically. A physical test carried out at the Royal Military College of Canada, is used to investigate the accuracy of the model. The numerical results and physical test results for displacement and load on EPS geofoam buffers are compared and analyzed. The model is shown to capture the trends observed in the physical reduced-scale model shaking table test up to a base excitation level of about 0.g. Quantitative predictions are shown to be in reasonable agreement with physical test results. The model provides a possible method to analyze and predict the force and deformation distribution of an EPS geofoam seismic buffer placed against a rigid retaining wall.

KEY WORDS: seismic load, EPS geofoam, retaining wall, horizontal slice method, numerical model

INTRODUCTION

Expanded polystyrene (EPS), which is classified as a "geofoam" material in geosynthetics terminology, has been proposed to reduce earthquake-induced dynamic loads between rigid retaining walls and the retained soil backfill. Inglis et al. (1996) reported the first installation of panels of EPS from 450 to 610 mm thick placed against a series of rigid basement walls to attenuate seismic-induced lateral earth forces at a site in Vancouver, Canada. Hazarika et al. (2003), Bathurst et al. (2007a) Zarnani and Bathurst (2007) performed shaking table tests on the seismic response of reduced-scale model retaining walls to demonstrate that compressible EPS geofoam seismic buffers can significantly reduce the dynamic loads against rigid retaining wall structures. A simple displacement model for response analysis of EPS geofoam seismic buffers was proposed by Bathurst et al. (2007b). Nevertheless, a numerical model that can accommodate more complex structures and a wider range of geometry is lacking. This paper describes a multiple layer displacement model for force and displacement analysis of EPS geofoam seismic buffers placed against rigid retaining walls. The method can be used to analyze and predict the magnitude and distribution of the force and deformation of the EPS geofoam seismic buffers by modeling the retained soil using multiple horizontal layers.

PHYSICAL AND NUMERICAL MODELS

Physical Model

The physical shaking table test and experimental arrangement used at the Royal Military College of Canada (RMC) to investigate the behavior of geofoam seismic buffers is shown as Fig. 1.

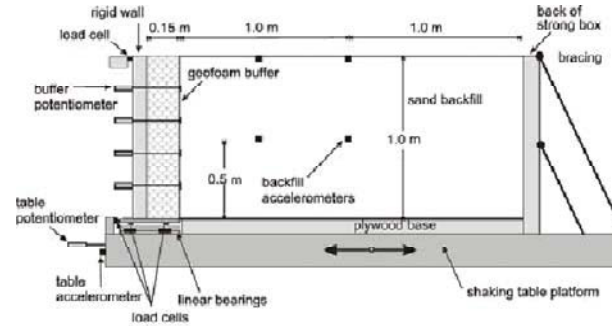

Fig. 1 . General arrangement of shaking table test configuration and instrumentation (after Bathurst et al. 2007a)

The experiment wall has a height of 1m and a width of 1.4 m. The size of the shaking table is 2.7 m×2.7 m. The geofoam buffer was 15cm thick and was placed between the rigid wall and the sand backfill. The shaking table was accelerated using a stepped sinusoidal base excitation record applied in the horizontal direction only**.** The potentiometers and load cells were installed in order

[1] Professor, College of Traffic and Communications, South China University of Technology, CHINA. Email: ctymwang@scut.edu.cn
[2] Professor, Department of Civil Engineering, Royal Military College of Canada, CANADA. Email: Bathurst-r@rmc.ca

to record the displacement and force against the seismic buffer retaining wall (Bathurst et al. 2007a; Zarnani and Bathurst 2007).

The backfill soil was artificial sintered silica-free olivine sand. The soil properties are given in Table 1. According to the ASTM (2006) classification system, the EPS geofoam buffer is Type 1 with the properties shown in Table 2.

Table 1 Backfill soil properties

Parameter	Value
Soil density	1600 kg/m^3
Peak friction angle	51^o
Residual friction angle	46^o
Soil-buffer interface friction angle	15^o
Cohesion	0
Soil elastic modulus, E_s	15.2 MPa
Soil shear stiffness, k_{soil}	(varies)
Soil stress factor, χ	500 ~ 2000

Table 2 EPS geofoam buffer properties

Wall [a]	Geofoam		
	Type [b]	Density [b], (kg/m^3)	Dynamic elastic modulus [c], E_b (MN/m^3)
2	I	16	4.1

Notes:
[a] numbering scheme from Bathurst et al. (2007a)
[b] from ASTM (2006) classification system
[c] from Bathurst et al. (2007a)

Numerical Multiple Layer Model

A multiple horizontal layer model is proposed to model the response of seismic buffer retaining walls. Fig. 2 shows the general arrangement of the retaining wall. The compressible geofoam buffer with a thickness of *b* is located between the rigid wall of height *H*, and the retained soil. It is assumed that the backfill soil will fail along a linear surface with an obliquity of α from the heel of the buffer to the horizontal backfill surface under limit equilibrium conditions. The thickness of each horizontal soil slice is *dh.*

The forces acting on the horizontal soil slice i are shown in Fig. 3. Here, m_i is the mass of layer *i* and $\ddot{u}_g$ and *g* are the accelerations in horizontal and vertical directions, respectively. Horizontal acceleration is imposed to simulate horizontal seismic motions only. The forces acting at each boundary of layer i include normal force $N_{j,i}$ and shear force $S_{j,i}$. Here, $N_{1,i}$ and $S_{1,i}$ are the normal force and shear force at the boundary between the soil and geofoam buffer, respectively. $N_{3,i}$ and $S_{3,i}$ are the normal force and shear force acting on the failure surface in the retained soil. $N_{2,i}$ and $S_{2,i}$, and $N_{4,i}$ and $S_{4,i}$ represent, respectively, the normal force and shear force acting on the bottom and the top of layer i.

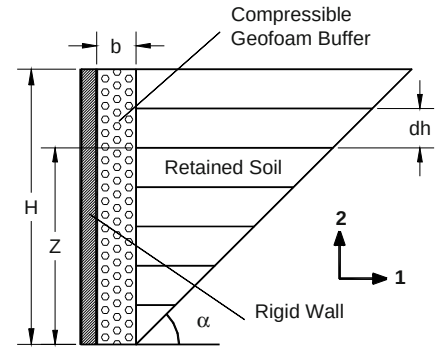

Fig. 2 General arrangement for geofoam buffer wall and retained horizontal soil layers

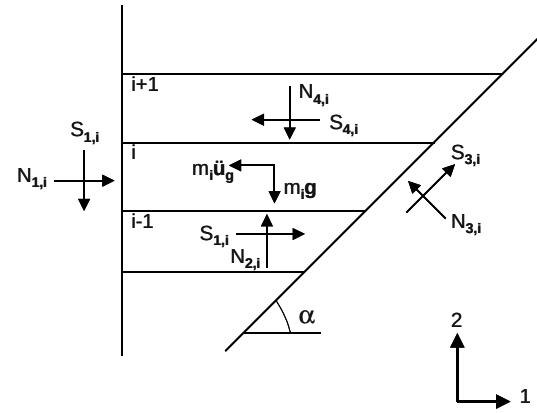

Fig. 3 Forces acting on horizontal soil slice *i*

The forces on the slice boundaries are computed using linear spring models. The normal spring used to calculate the normal force on the boundary between the soil and geofoam is compression-only. Similarly, the normal springs at the other three boundaries of the soil layer permit compression only. All shear interfaces are modeled with stress-dependent linear elastic spring-slip elements to permit plastic sliding.

The equations of motion and force for each horizontal soil layer are solved using an explicit time-marching finite difference approach as described below.

Numerical Solution

Equations of motion

Based on Newton's second law, the equations of motion for soil layer i can be described as:

$$\ddot{x}_{j,i} = \frac{\mathrm{d}\dot{x}_{j,i}}{\mathrm{d}t} = \frac{F_{j,i}}{m_i} \tag{1}$$

In the horizontal and vertical directions, the equations of

motion for soil layer i can be expressed, respectively, as:

$$\ddot{x}_{1,i} = \frac{\mathrm{d}\dot{x}_{1,i}}{\mathrm{d}t} = \frac{F_{1,i}}{m_i} \tag{2}$$

$$\ddot{x}_{2,i} = \frac{\mathrm{d}\dot{x}_{2,i}}{\mathrm{d}t} = \frac{F_{2,i}}{m_i} \tag{3}$$

Here, $\ddot{x}_{j,i}$ and $\dot{x}_{j,i}$ are the acceleration and velocity of soil layer i, $F_{j,i}$ and m_i are the force acting on the layer and its mass, t is time, j =1 is the index for horizontal direction and j = 2 is the index for vertical direction.

Using a difference approximation with time step Δt in Eq. 1 leads to:

$$\frac{\mathrm{d}\dot{x}_{j,i}}{\mathrm{d}t} = \frac{(\dot{x}_{j,i})_{t+\Delta t/2} - (\dot{x}_{j,i})_{t-\Delta t/2}}{\Delta t} \tag{4}$$

Substituting Eq. 4 into Eq. 1 gives:

$$(\dot{x}_{j,i})_{t+\Delta t/2} = (\dot{x}_{j,i})_{t-\Delta t/2} + \left(\frac{F_{j,i}}{m_i}\right)_t \Delta t \tag{5}$$

Hence, the displacement at the end of each time step can be calculated by rewriting Eq. 5 as:

$$(x_{j,i})_{t+\Delta t} = (x_{j,i})_t + \Delta t\left[(\dot{x}_{j,i})_t + \left(\frac{F_{j,i}}{m_i}\right)_t \Delta t\right] \tag{6}$$

Equations of force

The normal force $N_{j,i}$ and shear force $S_{j,i}$ on each boundary of soil layer i can be calculated using the equations shown in Table 3.

For the compression-only forces described earlier, values of $N_{j,i}$ that become positive are set to zero at each time step.

Table 3 Force, displacement and stiffness equations

Boundary of the soil layer i	Force-Displacement Equation	Incremental Normal Displacement Δn_i and Incremental Shear Displacement Δs_i	Stiffness of Normal Spring $k_{N_{j,i}}$ and Stiffness of Shear Spring $k_{S_{j,i}}$
Geofoam -Soil	$(N_{1,i})_{t+\Delta t} = (N_{1,i})_t - (\Delta n_i)_{t+\Delta t} k_{N_{1,i}}$ $(S_{1,i}) = \min(\mu N_{1,i}, \lvert S_{1,i}\rvert) sign(S_{1,i})$ $(S_{1,i}) = \min(\mu N_{1,i}, \lvert S_{1,i}\rvert) sign(S_{1,i})$	$(\Delta n_i)_{t+\Delta t/2} = (\dot{x}_{1,i})_{t+\Delta t/2}\Delta t$ $(\Delta s_i)_{t+\Delta t/2} = (\dot{x}_{2,i})_{t+\Delta t/2}\Delta t$	$k_{N_{1,i}} = E_b \frac{dh \times w}{b}$ $k_{S_{1,i}} = 0$
Failure Surface	$(N_{3,i})_{t+\Delta t} = (N_{3,i})_t - (\Delta n_i)_{t+\Delta t} k_{N_{3,i}}$ $(S_{3,i})_{t+\Delta t} = (S_{3,i})_t - (\Delta s_i)_{t+\Delta t} k_{S_{3,i}}$ $(S_{3,i}) = \min(\mu N_{3,i}, \lvert S_{3,i}\rvert) sign(S_{3,i})$	$(\Delta n_i)_{t+\Delta t/2} = [(\dot{x}_{1,i})_{t+\Delta t/2} \sin\alpha - (\dot{x}_{2,i})_{t+\Delta t/2} \cos\alpha]\Delta t$ $(\Delta s_i)_{t+\Delta t/2} = [(\dot{x}_{1,i})_{t+\Delta t/2} \cos\alpha + (\dot{x}_{2,i})_{t+\Delta t/2} \sin\alpha]\Delta t$	$k_{N_{3,i}} = E_s \frac{dh \times w}{(H - z - dh/2)\sin\alpha}$ $k_{S_{3,i}} = \chi\sigma_n w = \chi N_{3,i} \frac{\sin\alpha}{dh}$
Bottom	$(N_{2,i})_{t+\Delta t} = (N_{2,i})_t - (\Delta n_i)_{t+\Delta t} k_{N_{2,i}}$ $(S_{2,i})_{t+\Delta t} = (S_{2,i})_t - (\Delta s_i)_{t+\Delta t} k_{S_{2,i}}$ $(S_{2,i}) = \min(\mu N_{2,i}, \lvert S_{2,i}\rvert) sign(S_{2,i})$	$(\Delta n_i)_{t+\Delta t/2} = [(\dot{x}_{2,i})_{t+\Delta t/2} - (\dot{x}_{2,i-1})_{t+\Delta t/2}]\Delta t$ $(\Delta s_i)_{t+\Delta t/2} = [(\dot{x}_{1,i})_{t+\Delta t/2} - (\dot{x}_{1,i-1})_{t+\Delta t/2}]\Delta t$	$k_{N_{2,i}} = E_s \frac{z \times w}{(H - z)\tan\alpha}$ $k_{S_{2,i}} = \chi\sigma_n w = \chi N_{2,i} \frac{\tan\alpha}{z}$
Top	$(N_{4,i})_{t+\Delta t} = (N_{4,i})_t - (\Delta n_i)_{t+\Delta t} k_{N_{4,i}}$ $(S_{4,i})_{t+\Delta t} = (S_{4,i})_t - (\Delta s_i)_{t+\Delta t} k_{S_{4,i}}$ $(S_{4,i}) = \min(\mu N_{4,i}, \lvert S_{4,i}\rvert) sign(S_{4,i})$	$(\Delta n_i)_{t+\Delta t/2} = [(\dot{x}_{2,i})_{t+\Delta t/2} - (\dot{x}_{2,i+1})_{t+\Delta t/2}]\Delta t$ $(\Delta s_i)_{t+\Delta t/2} = [(\dot{x}_{1,i})_{t+\Delta t/2} - (\dot{x}_{1,i+1})_{t+\Delta t/2}]\Delta t$	$k_{N_{4,i}} = E_s \frac{(z + dh) \times w}{(H - z - dh)\tan\alpha}$ $k_{S_{4,i}} = \chi\sigma_n w = \chi N_{4,i} \frac{\tan\alpha}{z + dh}$

Updated horizontal and vertical total forces acting on a soil slice are calculated as follows:

$$(F_{1,i})_{t+\Delta t} = (N_{1,i} - m_i \ddot{u}_g(t) + N_{3,i}\sin\alpha + S_{2,i} + S_{3,i}\cos\alpha + S_{4,i} - \beta m_i \dot{x}_{1,i})_{t+\Delta t} \quad (7)$$

$$(F_{2,i})_{t+\Delta t} = (S_{1,i} + N_{2,i} - m_i g - N_{3,i}\cos\alpha + S_{3,i}\sin\alpha + N_{4,i} - \beta m_i \dot{x}_{2,i})_{t+\Delta t} \quad (8)$$

Included in the formulation above is the provision for mass damping using β as the mass damping factor. Parameter χ is a dimensionless stress factor that is used to adjust the interface shear stiffness in proportion to normal stress level.

The angle of the soil wedge from the horizontal (α) in this approach is assumed to decrease with increasing horizontal acceleration ($\ddot{u}_g$) using a closed-form solution from classical pseudo-static wedge theory (Bathurst et al. 2007b).

EVALUATION OF NUMERICAL MODEL

Influence of Number of Slices

A computer code in Visual Basic was written to carry out numerical calculations. The influence of number of slices (n) was investigated for five different cases. Fig. 4 shows the peak dynamic seismic force versus time for the same model and excitation record using n = 10, 20, 30, 40. A value of n = 20 was selected as the minimum number of slices to give consistent and stable numerical results.

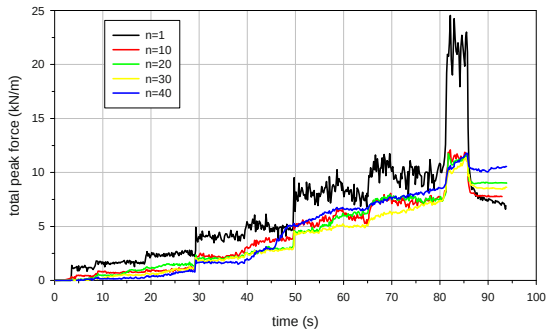

Fig. 4 Influence of number of slices on computed peak dynamic buffer forces

Peak Displacement of EPS Geofoam

Fig. 5 shows the acceleration-time record applied to the model and the peak (dynamic) compression-time response of the seismic buffer for the wall taken from the RMC shaking table tests. The measured compression values (Fig. 5b) include the average of peak values recorded from the four displacement potentiometers installed along the height of the wall and the maximum and minimum peak values. Generally, there is a good agreement between the computed and measured results. The plots show that peak compression increases with increasing peak input acceleration.

After the acceleration reached a peak of 0.9 g, the shaking table test was stopped. The measured data show that the peak (elastic) compression of the geofoam returned to almost zero at this time. However, the computed value is higher showing that the model is not able to capture load relaxation of the soil-EPS system.

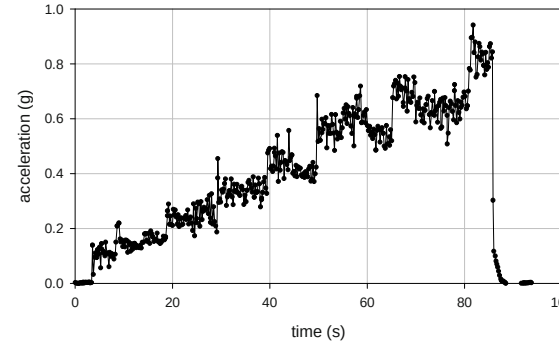

(a) acceleration-time history

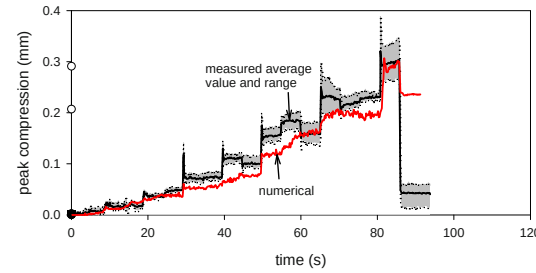

(b) Peak compression-time response

Fig. 5 Acceleration-time record applied to model and peak seismic buffer compression-time response

Vertical Distribution of Buffer Compression

The distribution of peak compressive deformation along the height of the retaining wall at selected times is shown in Fig. 6.

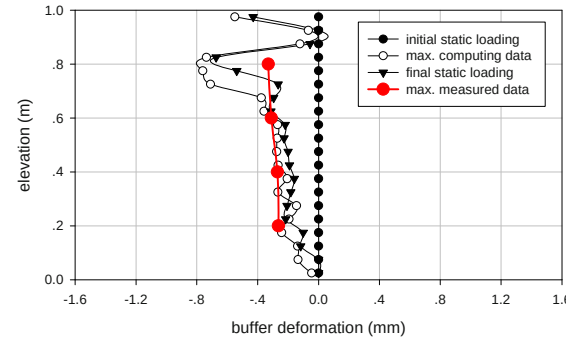

Fig. 6 Compression distribution

The datum in the figure is the end of construction prior to excitation. At the end of shaking when the models have returned to a static load condition and at the final static loading moment, there is permanent compression as noted earlier. However, there is very good agreement between the maximum computed compression and the maximum measured data up to an elevation of about 0.6 m.

Peak Force against EPS Geofoam

The numerical peak forces shown in Fig. 7 were computed from the sum of horizontal forces acting on each slice. Measured values are from horizontal load cells installed against the back of the wall. In both cases these are dynamic loads only. Generally, the computed results capture the trend in the measured data but there is a quantitative under-prediction of the physical test results.

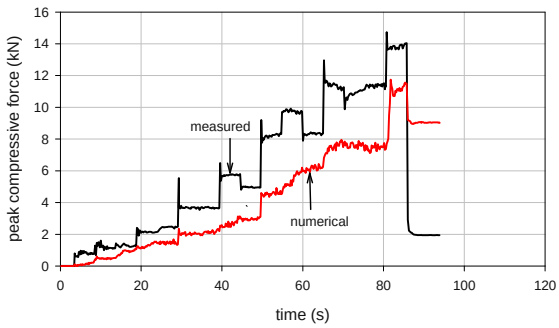

Fig. 7 Peak dynamic force-time response

CONCLUSIONS

(1) The multiple-slice model used here divides the backfill soil wedge acting against the retaining wall into horizontal slices with the height of each slice equal to about 5% to 10% of the height of the retaining wall. The force and displacement at the slice boundaries are computed using linear spring models. The equations of motion and force of each slice are solved using an explicit time-marching finite difference approach. This allows the distribution and magnitude of compressive displacement and load on the EPS geofoam buffer to be computed numerically.

(2) A physical test carried out at the Royal Military College of Canada, is used to investigate the accuracy of the model. The numerical results and physical test results for displacement and load on EPS geofoam buffers are compared and analyzed. The model is shown to capture the trends observed in the physical reduced-scale model shaking table test up to a base excitation level of about 0.9 g. Given the complexity of the system, the quantitative predictions are judged to be in reasonable agreement with physical test results.

(3) The model provides a possible method to analyze and predict the force and deformation distribution of EPS geofoam seismic buffers placed against a rigid retaining wall for a specified ground acceleration record.

ACKNOWLEGEMENTS

The first author would like to acknowledge the financial support provided by the China Scholarship Council, for a Visiting Postdoctoral Fellowship held at the Geo-Engineering Centre at Queen's-RMC at the Royal Military College of Canada (RMC). The work reported in this paper was also supported by grants from the Natural Sciences and Engineering Research Council of Canada (NSERC) awarded to the second author.

REFERENCES

ASTM 6817-06 (2006) Standard Specification for Rigid Cellular Polystyrene Geofoam. American Society for Testing and Materials, West Conshohocken, Pennsylvania, USA

Bathurst RJ, Zarnani S, Gaskin A (2007a). Shaking table testing of geofoam seismic buffers. Soil Dynamics and Earthquake Engineering. 27 (4,): 324-332

Bathurst RJ, Keshavarz A, Zarnani S Take A (2007b) A simple displacement model for response analysis of EPS geofoam seismic buffers. Soil Dynamics and Earthquake Engineering, 274): 344-353

Hazarika H, Okuzono S, Matsuo Y (2003) Seismic stability enhancement of rigid nonyielding structures. In Proceedings of the Thirteenth International Offshore and Polar Engineering Conference, 25-30 May 2003, Honolulu, HI, USA: 1244-1249

Inglis D, Macleod G, Naesgaard E, Zergoun M (1996). Basement wall with seismic earth pressures and novel expanded polystyrene foam buffer layer. Tenth Annual Symposium of the Vancouver Geotechnical Society, Vancouver, BC, Canada: 18

Zarnani S, Bathurst RJ (2007) Experimental investigation of EPS geofoam seismic buffers using shaking table tests. Geosynthetics International, 14 (3): 165-177.

ELASTO-VISCOPLASTIC SIMULATION OF BEARING CAPACITY CHARACTERISTICS OF STRIP FOOTING ON REINFORCED SAND

F.L. Peng[1], M.S.A. Siddiquee[2] and F. Tatsuoka[3]

ABSTRACT: A nonlinear FEM analysis incorporating an elasto-viscoplastic constitutive model for sand that has been developed based on results from comprehensive laboratory stress-strain tests including plane strain compression tests is described. A series of plane strain laboratory model tests on the bearing capacity on a model strip footing (10 cm –wide) performed on unreinforced and reinforced level sand grounds were simulated by the FEM. The simulated footing load and settlement relation and failure mechanism in the unreinforced and reinforced sand grounds were compared with the measured ones. It is reported that the proposed FEM analysis method can simulate very well the test results, including the effects of reinforcing. It is one of the characteristic features of the proposed numerical analysis method that the footing and settlement behaviour around the peak footing load state and the one in the post-peak regime can be simulated in a very stable manner. It is shown that this is due largely to that the realistic viscous properties of sand that are properly modeled are incorporated in the FEM analysis.

KEYWORDS: reinforced sand, bearing capacity, FEM, elasto-viscoplastic model, load-settlement relation

INTRODUCTION

Siddique et al. (1999) and Kotake et al. (2001) examined the effects of different assumptions for constitutive relations on the simulated bearing capacity of footing on sand by the FEM analysis considering strain localization based on the strain-hardening model. However, the simulations by these previous FEM analyses using a plastic strain-hardening constitutive model exhibited higher pre-peak stiffness in the footing load-settlement relation and smaller footing displacements than those in the bearing capacity model tests. On the other hand, the results from recent plane strain compression tests on sand performed along a wide variety of stress paths indicate that this discrepancy is due mainly to that the effects of intermediate stress paths on the strains of soil were not taken into account in the previous FEM analyses (Yasin & Tatsuoka 2000). That is, the shear strain increment that takes place by anisotropic compression at a constant high stress ratio between two stress states is considerably larger than the one that takes place by isotropic compression and shearing at constant confining pressure applied between these two stress states.

Recently, a new class energy-based elasto-viscoplastic model for sand was developed based on a unique stress history-independent energy-based hardening function (Peng et al. 2001; Tatsuoka et al. 2002). The proposed function represents a unique relationship between the modified irreversible strain energy and the instantaneous stress state, which is independent of stress history and stress path. The model was developed based on the results from a series of recent drained plane strain compression tests on saturated dense Toyoura sand with precise stress and strain measurements, performed along a wide variety of stress path.

The objective of this study is therefore to simulate the results obtained from a series of laboratory model test on the bearing capacity of a strip footing on reinforced soil conducted by Huang and Tatsuoka (1990) by the above-proposed energy-based FEM model. In particular, it was examined whether the proposed FEM model can predict properly the different effects of reinforcing by different arrangements of reinforcement layers.

MODEL TESTS AND FEM DETAILS

Laboratory Model Tests

Fig. 1 shows the setup of laboratory model test on the bearing capacity of a strip footing on unreinforced and reinforced sand under plane strain conditions (Huang

[1] Professor, Department of Civil Engineering, Tongji University, CHINA. Email:pengfangle@mail.tongji.edu.cn
[2] Professor, Department of Civil Engineering, King Saud University, Kingdom of Saudi Arabia. Email:sid@ksa.edu.sa
[3] Professor, Department of Civil Engineering, Tokyo University of Science, JAPAN. Email:tatsuoka@rs.noda.yus.ac.jp

and Tatsuoka, 1990). The model ground had dimensions of 183 cm in width, 40cm in length and 74 cm in depth. The model ground was produced by pluviating air-dried Toyoura sand from a silt of a hopper at a controlled fall height into a sandbox. By this method, homogeneous, dense model grounds having very similar relative density values in a range of D_r= 80%~86% were obtained. Different arrangements of strip reinforcement with different lengths, layer numbers, horizontal spacings and stiffness values and rupture strengths of reinforcement were employed. The reinforcing strips had a thickness of 0.5 mm and a width of 3 mm, made of phosphor bronze. Their surfaces were made rough by gluing sand particles. The three groups of laboratory model tests presented in Fig. 2 were analyzed in the present study, where ***L*** is the reinforcement length, ***B*** is the footing width and ***n*** is the number of reinforcement layers.A rigid footing, 10 cm wide and 39.8 cm long, with a rough base, guided against tilting and translation, was used. The footing was loaded at a controlled vertical displacement rate between 0.1 and 0.2 mm/min. The normal and shear stresses at the central third of the footing were measured by means of 5 load cells, each of which could measure the normal and shear forces separately.

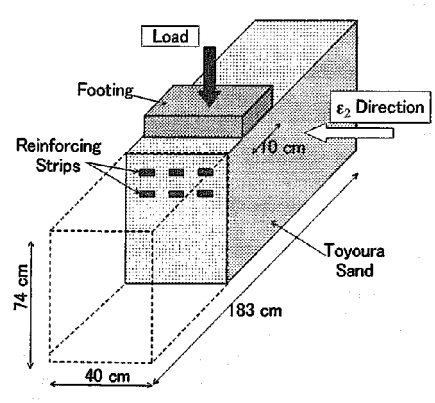

Fig. 1 Laboratory model test (Huang & Tatsuoka 1990)

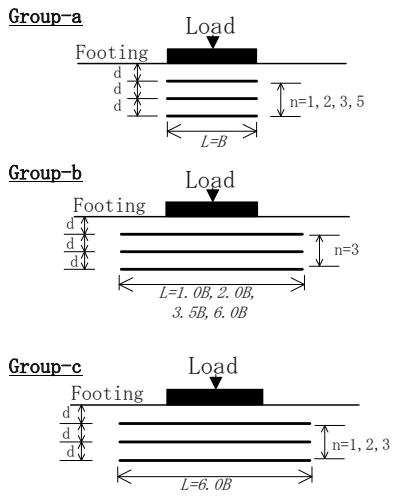

Fig. 2 Three model test groups (Huang & Tatsuoka 1990)

Energy-based Elasto-viscoplastic Constitutive Model for Sand

Fig. 3 shows the non-linear three-component model framework, within which sand was modeled as an elasto-viscoplastic material. Here, ***E*** is the hypo-elastic component; ***P*** is the non-linear plastic component; and ***V*** is the nonlinear viscous component. In the constitutive modeling, a number of factors that affect the strength and deformation characteristics of sand are taken into account, including: (1) pre-peak highly non-linear stress-strain relation described in an energy-based strain-hardening function; (2) non-associated flow; (3) inherent anisotropy in the strength and deformation characteristics; (4) the dependency on pressure level of the strength and deformation characteristics; (5) post-peak strain-softening; (6) shear banding with a characteristics shear band width (i.e., particle size effect); and (7) rate-dependent deformation properties. The details of the sand constitutive model have been report in several previous papers by the authors (e.g., Peng et al. 2001; Tatsuoka et al. 2002).

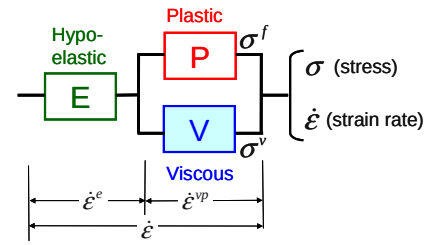

Fig. 3 Non-linear three-component model for elasto-viscoplastic materials (after Tatsuoka et al. 2002)

FEM Model for Sandy Ground

Fig. 4 shows the FEM mesh for the bearing capacity problem, in which only a half domain of the model ground is discretized into four-noded quadrilateral plane elements. The total number of the plane elements and the nodal points are 540 and 581, respectively. The vicinity of the footing is discretized into 1.0 cm×1.0 cm square elements to capture the localized deformation and failure mode observed in the physical experiment. With respect to the boundaries of the model ground, vertical rollers were placed along the footing centerline: i.e., the axis of symmetry. Horizontal and vertical rollers were placed along the bottom and the other lateral boundaries of the analysis domain, respectively, despite that those model ground boundaries were not lubricated. This was because the footing load was found to be overestimated when these model boundaries were modeled as fixed boundaries.

In these FEM analyses, a unit weight of sand γ_d of 15.58 kN/m^3 and an initial void ratio e_o of 0.66 were used as representative values. The actual values of γ_d scattered between 15.40 and 15.65 kN/m^3. The initial stress state of the homogeneous level ground was assumed to be under the K_o-stress condition with K_o = 0.34.

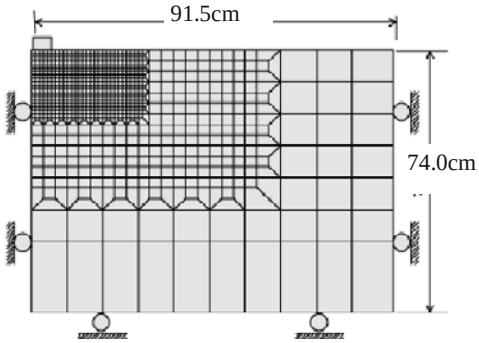

Fig. 4 Finite element mesh used in the present study

Modeling of Reinforcement

Layers of reinforcing strips were modeled by beam elements. That is, each layer consisting of strips was replaced with a platen extending in the lateral and longitudinal directions of the footing. It was assumed that the axial and bending stiffness values of the platen are equal to the respective average values of the strips in each layer. The area and moment of inertia of the beam element per unit length in the ε_2 direction for each layer was calculated based on the total number of strips placed in each layer divided by the width (40 cm) of the sand box. The respective reinforcement layers consisting of 24 strips, with a covering ratio *CR*=18%, have and *I*= 1.875×10^{-6} cm^4 per unit length in the ε_2 direction, respectively. The reinforcing strips were assumed to be linear elastic based on their stress-strain relationships measured by experiments. The Young's modulus, E, of the reinforcement material (i.e., phosphor bronze) was equal to 1.22×10^8 kN/m^2. No interface elements were used, because either pronounced slippage between sand and reinforcement or pull-out failure of reinforcement was not observed in the physical experiments.

Non-linear Solution Techniques and Loading on Footing

A set of non-linear equations was solved by the dynamic relaxation (DR) technique (Tanaka and Kawamoto 1988), which has a reputation in solving highly non-linear equations, especially for high friction angle materials as dense Toyoura sand in the present case. The integration of the elasto-viscoplastic equation was done by the return mapping scheme, which is a first order approximated Euler backward integration. A FEM code with an optimized DR solver developed by Tanaka and Kawamoto (1988) was used. Four-node quadrilateral elements along with reduced integration were used to improve the bounds of solution in the pseudo-equilibrium for sand as a highly non-linear material. To prevent any probable hourglass mode, an anti-hourglass scheme was adopted: i.e., following an elastic stiffness approach of the scheme, a very small elastic stiffness of the actual material elastic stiffness at the start of loading was added to the non-linear system as hour-glass resisting nodal forces whenever any soil element starts to form a hour-glass mode. Convergence was confirmed by checking the global residual force norm and the differential residual force norm between two successive iteration steps.

The central and vertical loading of a rigid footing with rough base in the physical experiment was simulated under displacement control. Uniform vertical displacements were prescribed to the nodal points in contact with the footing base while lateral movements of those nodal points were fixed to simulate the perfectly rough base. Displacement control analyses were conducted at a constant displacement rate of 0.15mm/min. A force norm and an energy norm were specified for an equilibrium iteration tolerance in the calculation of dynamic relaxation scheme. In this present study, the tolerance of both the force norm and the energy norm is of 10^{-6}. All the analyses were carried out until the normalized settlement S/B becomes 0.15 to simulate the behaviour until the post-peak regime.

RESULTS AND DISCUSSIONS

Effects of Number of Short Reinforcement Layers (Group-a)

Fig. 5 compares the normalized load-settlement relationships from the physical tests and the FEM analysis for Group-a. Figs. 6a and b summarise the effects of the ratio of the depth of reinforced zone to the footing width (*B* 10 cm); D_R/B, on the bearing capacity ratio, *BCR* and the ratio of the footing settlement at peak load to *B*, S_f/B. Here, D_R/B is proportional to the number of reinforcement layer (*n*); *BCR* is defined as the ratio of the peak footing load when the ground is reinforced and the one when the ground is unreinforced. The following trends of behaviour may be seen:

(1) The overall load-settlement relations observed in the physical tests are very well simulated for both unreinforced and reinforced grounds (Fig. 5). In particular, the effects of the depth of reinforced zone (i.e., the number of reinforcement layers) on the peak footing load

and the footing settlement at the peak footing load are simulated very well. Despite the above, the FEM analysis predicts generally slightly larger peak footing load than the physical tests. This could not be attributed partly to that the reinforcing strips were modelled as a two-dimensional planar reinforcement and no specific interaction effects at the interface between the soil and the reinforcement were considered. This is because a similar overestimation of peak footing load is observed with both unreinforced and reinforced model grounds.

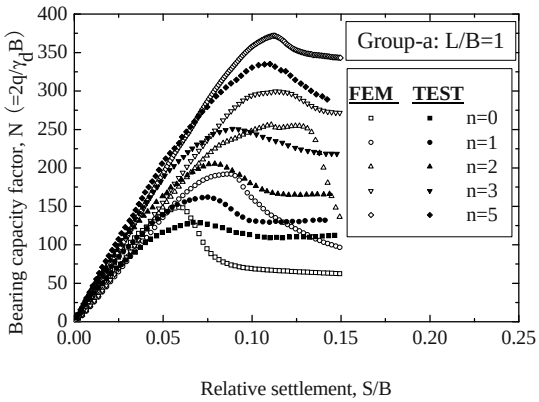

Fig. 5 Normalized load-settlement relations for Group-a obtained from the experiment and the FEM analysis

(2) As seen in Figs. 5 and 6a the initial stiffness and the peak footing load of reinforced ground increase significantly with the increase in the number of reinforcement layers (i.e., the deep-footing mechanism), despite the fact that the so-called anchoring mechanism by a part of the reinforcement layers extending outside the potential failure zone, advocated by Binquent and Lee (1975), is not the unique reinforcing mechanism that increases the bearing capacity of level subjected to a footing load;

(3) As seen in Fig. 6b, the effects of the number of reinforcement layers on the bearing capacity characteristics are significant, at least until the depth of the reinforced zone becomes 1.5 times as large as the footing width, B; As seen in Fig. 6, the settlement at peak footing load increases with the increase in the bearing capacity of ground subjected to a footing load.

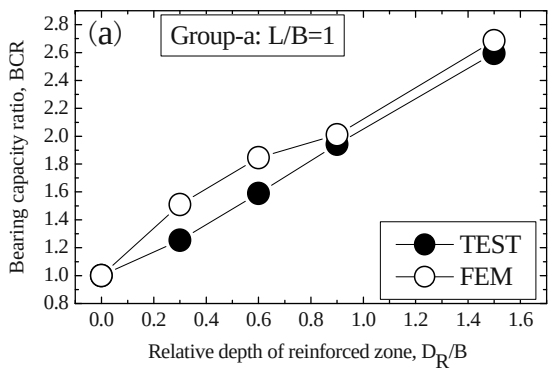

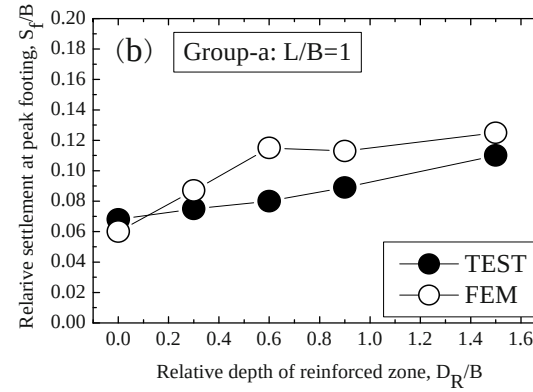

Fig. 6 Comparison between experimental results and FEM analysis for Group-a: effect of number of short reinforcement layers on a) *BCR*; and b) S_f/B

Effects of Reinforcement Length (Group-b)

Fig. 7 compares the normalized load-settlement relationships obtained from the physical tests and the FEM analysis for Group-b. Figs. 8a and b summarise the effects of the ratio of the reinforcement length (L) to B, L/B, on *BCR* and S_f/B. When L/B is larger than unity, the reinforcement layers are extended laterally beyond the footing width. The following trends of behaviour may be noted:

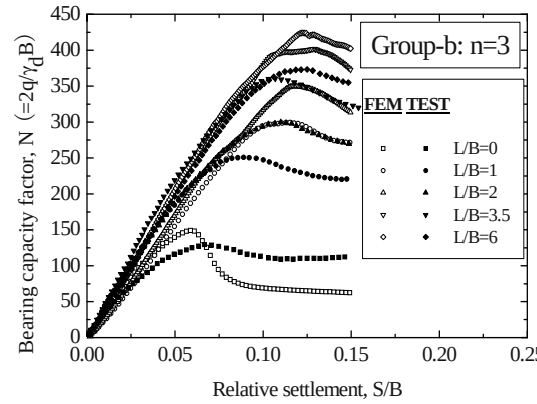

Fig. 7 Normalized load-settlement relationships for Group-b from the experiment and the FEM analysis

(1) As with the case of Group-a, the overall footing load-settlement relation observed in the physical tests is very well simulated for both unreinforced and reinforced grounds. In the physical tests, the effects of reinforcement length L increase at a decreasing rate with L/B for L/B larger than unity. In particular, the increase in *BCR* when L/B increases about 3.5 is essentially zero. Correspondingly, the settlement of footing at the peak footing load does not increase noticeably when L/B exceeds unity. The FEM analysis simulates very well these trends of behaviour. However, the FEM analysis exhibits peak footing load that is slightly larger than

those in the physical tests.

(2) The so-called anchoring effect by the part of the reinforcement layer extending outside the potential failure zone (Binquent & Lee 1975) is not relevant to the present case.

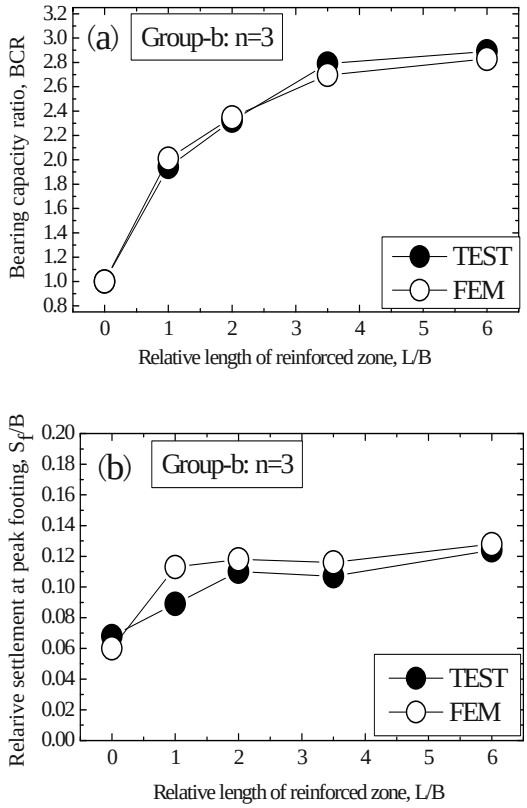

Fig. 8 Comparison between experimental results and FEM analysis for Group-b: effect of reinforcement length on: a) *BCR*; and b) S_f/B

Effects of the Number of Long Reinforcement Layers (Group-c)

Fig. 9 compares the normalized load-settlement relations from the physical tests and the FEM analysis for Group-*c*, while Figs. 10a and b summarise the effects of the number of longer reinforcement layer (*n*) (i.e., the effects of D_R/B) on *BCR*; and S_f/B. Fig. 11 compares between the *BCR* and D_R/B relations in Group-*a* and Group-*c*. The following trends of behaviour may be seen from these figures:

(1) The bearing capacity largely increases with an increase in the number of reinforcement layer (*n*) in a manner similar to that seen observed when *L*/*B*=1 in Group-a (Figs. 5 and 6). This trend is well simulated.

(2) The increase in the bearing capacity with an increase in the number of short reinforcement layers seen in Group-a (*L*/*B*= 1) is due mostly to the "deep-footing" effects. Yet, the "deep-footing effect" is rather dominant also in Group-*c* (*L*/*B* = 6). Such trends as above can also be seen in the results from the FEM analysis.

(3) The difference between Groups *a* and *c* can be attributed to the "wide-slab" effects by longer reinforcement (*L*/*B* = 6) in Group-*c*. The wide slab effects are over-estimated in the FEM simulation. It is likely that the present FEM simulation overestimates the peak footing load when the shear band crosses the reinforcement layers longer than *B*.

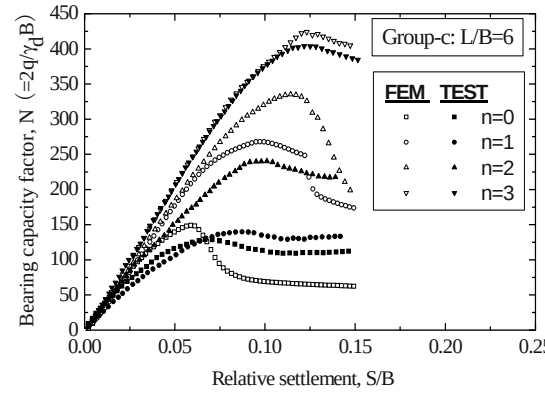

Fig. 9 Normalized load-settlement relationships for Group-c from the experiment and the FEM analysis

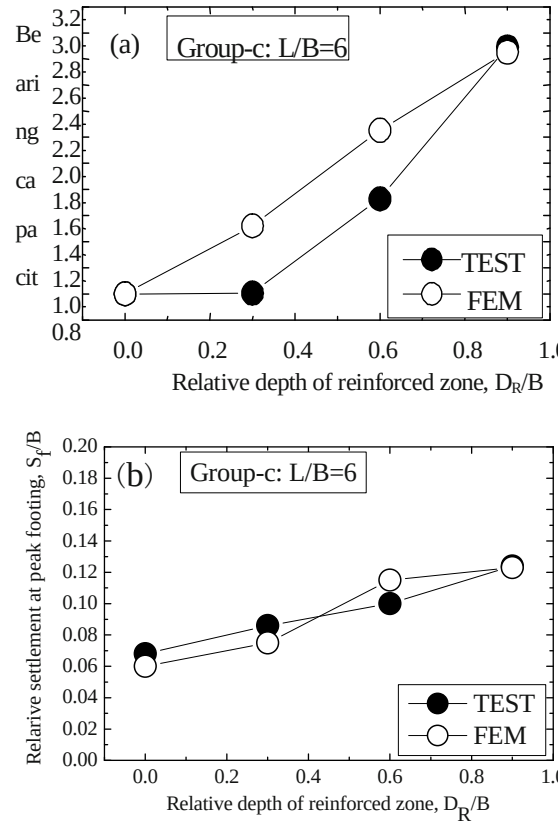

Fig. 10 Comparison between experimental results and FEM analysis for Group-c: effect of number of long reinforcement layers on a) *BCR*; and b) S_f/B

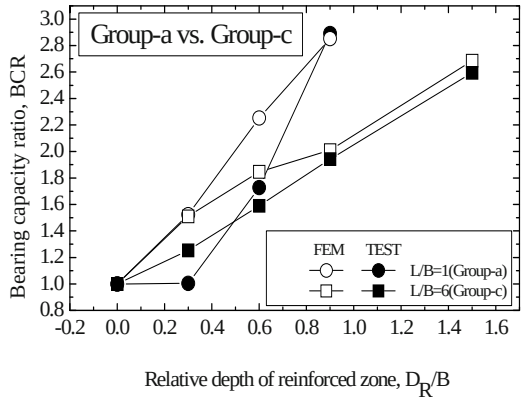

Fig. 11 Comparison between *BCR* and D_R/B relations in Group-*a* and Group-*c*

CONCLUSIONS

(1) The results from FEM simulations of the bearing capacity of a strip footing on unreinforced and reinforced ground were in good agreement with the physical test results with respect to the footing load-settlement relation. In particular, the effects of the number and length of reinforcement layer on the bearing capacity and footing settlements at the peak footing load observed in the physical tests are well simulated.

(2) The FEM code incorporating the newly irreversible strain energy-based hardening model for sand can predict more accurately the peak footing load and settlement than the previous analysis incorporating the irreversible shear strain-based hardening model. This is due mainly to the fact that the newly energy-based hardening model can better simulate the stress-strain behaviour when loaded along stress paths that are prevailing in the ground supporting the footing load.

(3) The proposed numerical analysis incorporating the visco-plastic effects can simulate the footing load-settlement behaviour not only around the peak footing load state but also in the post-peak regime in a very stable manner. It is shown that this stable analysis is due largely to that the realistic viscous properties of sand are properly modeled.

ACKNOWLEDGEMENTS

The first author acknowledges gratefully the support provided by the Ministry of Education, Government, Science and Culture of Japan, SRF for ROCS(SEM), Shuguang Project (No.05SG25), NSFC (No.50679056) and NCET(06-0378).

REFERENCES

Binquent JO, Lee KL (1975) Bearing capacity of loaded footing on reinforced soil. Journal of Geotechnical Engineering 107(6): 819-827

Di Benedetto H, Tatsuoka F, Ishihara M (2002) Time-dependent shear deformation characteristics of sand and their constitutive modeling. *Soil and Foundations* 42(2): 1-22

Huang CC, Tatsuoka F (1990) Bearing capacity of reinforced horizontal sandy ground. Geotextiles and Geomembranes 9(51-82): 236-267

Kotake N, Tatsuoka F, Tanaka T, Siddiquee MSA, Huang CC (2001) FEM simulation of the bearing capacity of level reinforced sand ground subjected to footing load. Geosynthetics International 8(6): 501-549

Peng FL, Tatsuoka F, Siddiquee MSA, Yasin SJM (2001) A new plastic model for granular materials. Proc. of the 10th International Conference on Computer Methods and Advances in Geomechanics (Desai et al. eds), Arizona 1: 383-388

Siddiquee MSA, Tanaka T, Tatsuoka F, Tani K, Morimoto T (1999) FEM simulation of scale effects in bearing capacity of strip footing on sand. Soils and Foundations 39(4): 91-109

Tanaka T, Kawamoto O (1988) Three dimensional finite element collapse analysis for foundations and slopes using dynamic relaxation. Proceedings of Numerical Methods in Geomechanics, Insbruch: 1213-1218

Tatsuoka F, Ishihara M, Di Benedetto H, Kuwano R (2002) Time-dependent shear deformation characteristics of geo-materials and their simulation. Soils and Foundations 42(2): 103-129

Yasin SJM, Tatsuoka F (2000) Stress history-dependent deformation characteristics of dense sand in plane strain. Soils and Foundations 40(2): 77-98

INFLUENCE OF INTERFERENCE ON FAILURE MECHANISM OF CLOSELY CONSTRUCTED CIRCULAR FOOTINGS ON REINFORCED SAND

A. Alimardani Lavasan[1] and M. Ghazavi[2]

ABSTRACT: The influence of reinforcement on the failure mechanism and displacement fields of soil of spread and interfering circular footing on cohessionless granular soil has been studied in this paper. The analyses pursued using finite difference method based on commercially available code, *FLAC*^{3D} (Fast Lagrangian Analysis of continua). The behavior of soil is assumed to be based on Mohr-coulomb criterion with non-associated flow rule by assuming $0 \leq \psi \leq \phi$. To ensure the reliability of numerical method to predict accurately results, numerical results of spread circular footing were compared with the available data from other experimental research. This comparison shows satisfactory agreement. Parametric studies were performed subsequently. The results indicate that the footing interference causes some directional difference in the soil displacement field and failure mechanism of closely spaced footings subjected to vertical loads without eccentricity with respect to spacing between two neighboring footings. In addition, the results show that there exists a significant improvement in the behavior of interfering footings reinforced with reinforcement layers.

KEYWORDS: finite difference method, failure mechanism, displacement field, interfering circular footing

INTRODUCTION

The behavior of two neighboring identical footings is strongly affected by the distance between each other in comparison with the case where the same isolated footing is constructed. In closely spaced footings, both settlement and bearing capacity patterns and failure mechanism would be varied due to interference effects.

The bearing capacity of interfering footings on unreinforced soil was investigated repetitiously. For example, Stuart (1962), Das and Larbi-Cherif (1983 a, b), Graham et al. (1984), Wang and Jao (2002), and Hazel (2004) studied the interference effects on closely spaced footings but the shape of footings in all these studies were considered to be strip on unreinforced soil. Kumar and Saran (2003) studied interfering square footings. Almost all these studies have shown an increase in the bearing capacity of interfering footings that depends on distance between two close footings.

In recent years, the soil improvement has been developed significantly by the use of different kind of reinforcing elements. Much research works have been reported in the literature on isolated footings reinforced with various forms of reinforcements. All these studies have shown that the use of reinforcements in granular soils has led to increase in the footing bearing capacity and significant decrease in settlement in same loading condition. A dimensionless parameter that named BCR has been issued to identify the effect of soil reinforcement on the bearing capacity of an isolated foundation. This is defined as:

$$BCR = q_{u(reinforced)} / q_{u(unreinforced)} \quad (1)$$

where $q_{u(reinforced)}$ and $q_{u(unreinforced)}$ state the ultimate bearing capacity of reinforced and unreinforced footings, respectively.

Influence of interference on bearing capacity of two closely spaced footing on unreinforced soil was considered for first time by Stuart (1962). Results of this study showed increase in interference coefficient of bearing capacity factors at low spacing. The values of these coefficients decrease by increasing distance between two neighboring footings. Finally, by expanding the value of spacing to a limitation, coefficients approached to 1.0 and effect of interference on bearing capacity would be vanished. Thereafter, Das and Larbi-Cherif (1983 a, b), Hezel (2004), Kumar and Ghosh (2007) presented same results.

[1] Ph.D. Student, Department of Civil Engineering K.N.Toosi University, Tehran, IRAN. Email: a_alimardani@alborz.kntu.ac.ir
[2] Associated Professor, Department of Civil Engineering, K.N.Toosi University, Tehran, IRAN. Email: Ghazavi_ma@kntu.ac.ir

Khing et al. (1992), Kumar and Saran (2003), Alimardani Lavasan (2005), Ghazavi and Alimardani Lavasan (2007) performed studies on interfering strip and square footings on reinforced sand. These studies indicated that reinforcing soil causes a significant increase in the bearing capacity of interfering footings. They identified a dimensionless coefficient that called I_f as below:

$$I_f=q_{u(reinforced\text{-}interfering)}/q_{u(unreinforced\text{-}single)} \quad (2)$$

where $q_{u(reinforced\text{-}interfering)}$ and $q_{u(unreinforced\text{-}single)}$ describe ultimate bearing capacity of interfering reinforced footing and single unreinforced footing, respectively. Fig. 1 shows the two interfering shallow circular foundations of diameter D supported by a soil reinforced with layers of geogrid. Character N represents the number of geogrid layers. The diameter of each geogrid layer is denoted by d. Parameter u depicts the depth of the closest geogrid layer from footing. The vertical distance between consecutive layers of geogrid is shown by h. Center to center spacing between two interfering footings is illustrated with Δ.

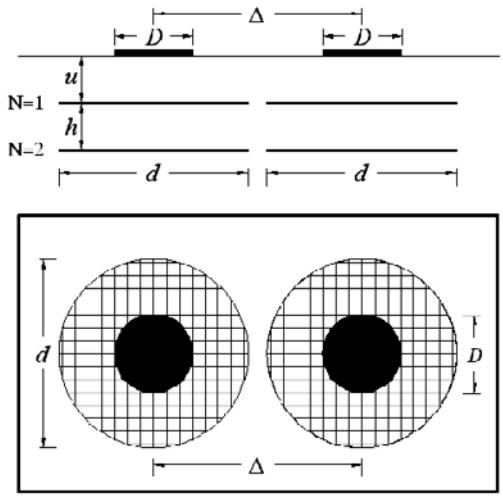

Fig. 1 Geometry of two interfering circular footings supported by geogrid-reinforced soils

The study of interference of circular footing on both unreinforced and reinforced soils appears have apparently received no attention. This study attempts to investigate the variations of soil displacement fields and failure mechanism for interfering circular footings on reinforced and unreinforced conditions.

NUMERICAL ANALYSIS PREOCEDURE

In the present numerical study, finite difference program *FLAC*^{3D} (Itasca Group 2001) was used in model circular interfering footings constructed on unreinforced and reinforced sand. It uses an explicit, time marching method to solve the governing field equations. The Mohr-Coulomb failure criterion was used for prediction of soil behavior. Due to the symmetry of the soil-footing system and to decrease the required time for each analysis, only a quarter part of the system was simulated. Rigid rough-base footings were assumed in numerical studies. It is assumed that the circular footing has a diameter of 15 cm. To ensure the independency between bearing capacity and both boundary conditions and model dimension, the width and depth of soil-footing system was assumed to be about 7D in both lateral and vertical directions, where D is the footing diameter. A maximum settlement of s=20%D was applied to all models with a constant velocity of 5×10^{-6} m/step. Previous numerical studies on bearing capacity of footing showed that the nodes should be more aggregated around footing edges. Typical mesh shape of interfering model is shown in Fig. 2.

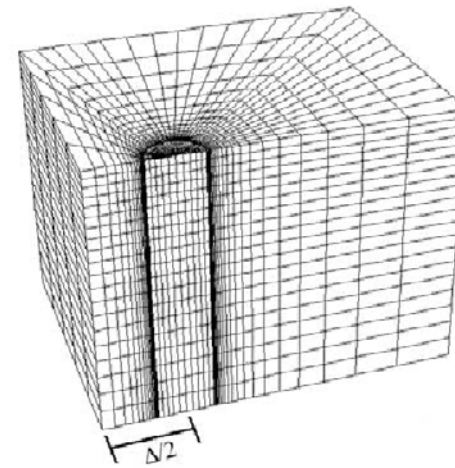

Fig. 2 Mesh shape used in numerical *FLAC* model of interfering circular footing

Soil Properties

Soil mechanical parameters which were used in numerical modeling are presented in Table 1. An elastic-plastic model with the Mohr-Coulomb failure criterion is used in the finite-difference modeling. The difference between ϕ and ψ represents a non-associated plastic flow rule which means the plastic potential surface is not identical to the yield surface. Yin et al. (2001), Erickson & Drescher (2002), Frydman & Burd (1997) and De Borst & Vermeer (1984) found that the dilation angle has a significant influence on the numerical estimation of the footing bearing capacity. This dependence is more significant for higher values of the friction angle. According to previous study on determination of bearing capacity with *FLAC*, more accurate results can be

obtained by considering dilation angle of soil about 2/3 friction angle. By using less dilation angle, local shear failure appears and by increasing dilation angle it tends to change to general shear failure. The difference between φ and ψ dictates the use of non-associated flow rule. Mechanical properties of soil are shown in Table 1.

Table 1. Reinforcement and Mechanical properties of soil

Soil parameters		Geogrid parameters	
Bulk modulus	8×10^3 kPa	Elasticity modulus	6.2×10^6 kPa
Shear modulus	4×10^3 kPa	Poisson ratio	0.33
cohesion	0.1 kPa	Interface parameters	
Density	1.7 kN/m^3	Stiffness per unit area	2.3×10^6 kN/m^3
friction	38°	Cohesion	0
Dilation	20°	friction	28°

Geogrid Properties

The reinforcement layers were modeled according to in-built structural element "geogrid" which is used in *FLAC*^{3D}. Geogrid element is three-noded, flat finite elements that are assigned a finite-element type that embedded interior of soil medium. The geogrid behaves as an isotropic linear elastic material with no failure limit. A shear directed (in the tangent plane to the geogrid surface) frictional interaction occurs between the geogrid and the soil grids, and the geogrid is slaved to the grid motion in the normal direction.

Because the settlement ratios were also small at failure for both unreinforced and reinforced sand in the analysis (i.e., s/D<5% at failure), the strains developed in the geogrid reinforcement were likely to be very small, too. Therefore, a constant modulus of elasticity of E = 6.2×10^6 kPa was used for numerical analyses. To permit sliding between soil and geogrid, an interface element was used on both sides of reinforcement layers. The shear behavior of the geogrid-soil interface is cohesive and frictional in nature and is controlled by the coupling spring properties of: (1) stiffness per unit area; (2) cohesive strength; and (3) friction angle. The total shear stress that develops on geogrid was calculated by balancing the effective confining stress "σ_m" that acts equally on both sides of geogrid surfaces (Itasca 2001). Thus, at first step of all analyses, a gravity calculation was performed to determine the vertical and horizontal stresses that acting at each level due to weight of system.

Mechanical properties of geogrid and soil-geogrid interface are shown in Table 1.

VERIFICATION OF NUMERICAL MODELING

To ensure the accuracy of the numerical modeling, validity of some assumed conditions such as mesh shape, soil and reinforcement mechanical parameters and boundary conditions, and the ultimate bearing capacity and behavior of circular footing on unreinforced and reinforced sandy soil have been determined numerically and compared with data obtained from experiments. Boushehrian and Hataf (2003) conducted laboratory tests on circular and ring footings constructed on unreinforced and reinforced sand. They used a cylindrical steel tank with 1 m diameter and 1 m depth. The rigid circular footing with 15 cm diameter and 7 cm thickness was made from metal and rigid plastic was used to apply loads on the soil surface. A sand which classified as SW in the Unified Soil Classification System with the relative density of about 50% was used in these tests. A comparison of the numerical and experimental load-displacement curves for unreinforced soil (N=0) and reinforced soil with maximum 2 layers of geogrid (N=1 and 2) is illustrated in Fig. 3. As seen, a good agreement between numerical and experimental results exists and this indicates the capability of numerical modeling to predict the behavior of reinforced soil.

ANALYSIS RESULTS AND DISCUSSIONS

Interfering Circular Footing on Unreinforced sand

The first group of numerical analysis was conducted on unreinforced sand. Variations of displacement mechanism at different spacing for half of model were shown in Fig. 4.

As shown in Fig. 4, when two neighboring footing are fully attached together, the contours of displacement tend to spread in the vertical direction around the interference axis. In this case, both footings act as a single semi rectangular footing and the longitudinal direction of interference will be stronger than perpendicular one. Therefore, shear failure zones and shear bands are formed in perpendicular direction of interference axis like two ellipsoids. In Fig. 4, displacement contours of soil surface around the footing symmetries by increasing the space between two footings and the ellipsoid shape of displacement field alters to a circular shape. The mid-part between two neighboring footings shows less displacement than external sides on interference axis. This is due to soil density and strength increasing in this direction. When

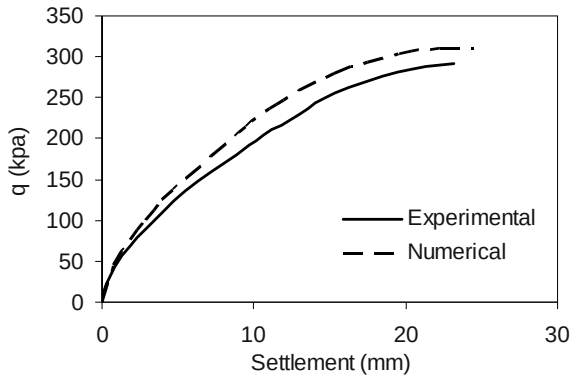

(a) N=0

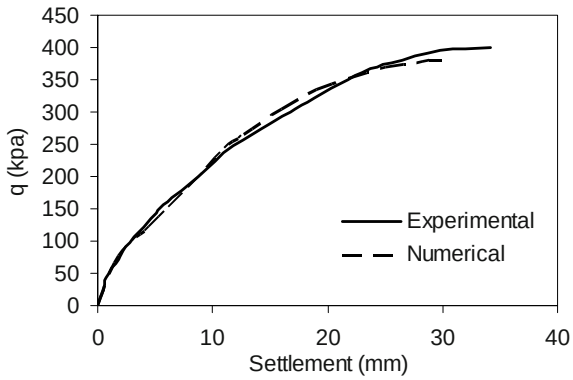

(b) N=1, d/D=2, u/D=0.3

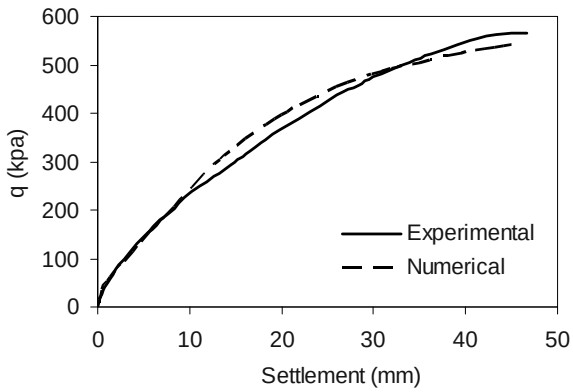

(c) N=2, d/D=2, u/D=0.3, h/D=0.2

Fig 3 Results comparison of numerical and experiment-al methods.

two adjacent footings are distant from each other, the displacement fields would be fully symmetric around each footing as a circular isolated footing. Thus, at this spacing, the influence of interference on the bearing capacity and settlement completely disappears. Variations of interference factor at different spacing are presented in Fig. 5. As seen, when two close footings were fully attached together, the ultimate bearing capacity was maximized. As mentioned before, when two closely spaced footings hang together, the system of

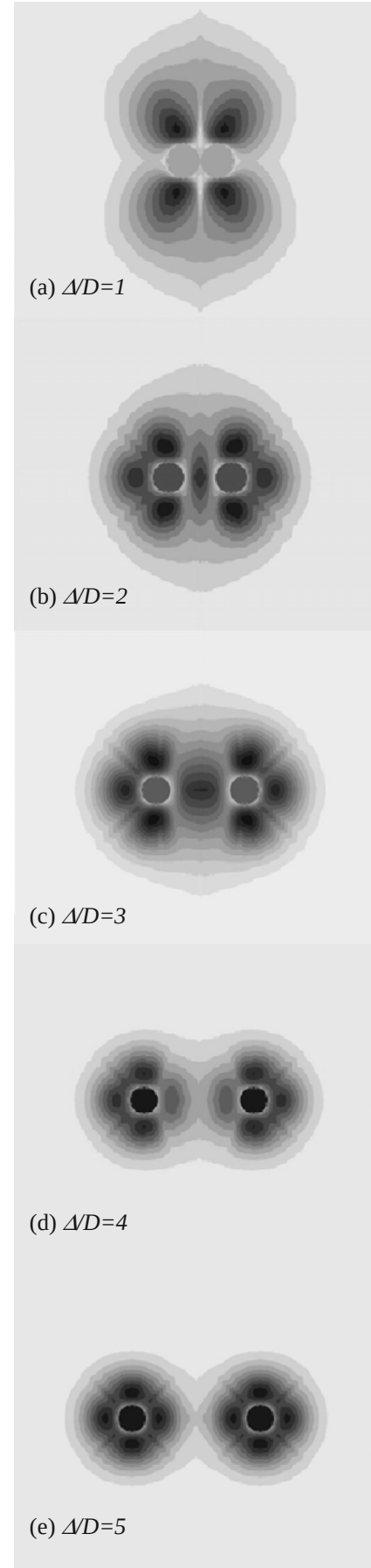

(a) *Δ/D=1*

(b) *Δ/D=2*

(c) *Δ/D=3*

(d) *Δ/D=4*

(e) *Δ/D=5*

Fig 4 Displacement field of soil surface at various spacing for unreinforced sand (N=0).

two-neighbors-footing acts as a single unite with larger dimension and this cause increase in bearing capacity about 47%. By increasing the spacing between two neighboring footing than about 5*D*, influence of interference on bearing capacity disappears.

Interfering Circular Footing on Reinforced Sand

Reinforced sand with 1 geogrid layer (N=1)

The second group of study was conducted on closely constructed circular footing on reinforced sand with one layer of geogrid. Variations of interference factor at different spacing for circular interfering footing on reinforced sand with 1 layer of geogrid are presented in Fig. 6. As shown, interference factor increases about 40% by the use of one geogrid layer in comparison with same interfering footing on unreinforced soil. Variations of interference factor of reinforced and unreinforced sand are the same.

Reinforced sand with 2 geogrid layer (N=2)

The third group of numerical analysis revealed the behavior of interfering circular footings on reinforced sand with 2 layers of geogrid. Variations of If at different spacing (Δ/D) are showed in Fig. 6. As seen, reinforcing soil with 2 layers of geogrid causes a significant increase in ultimate bearing capacity. This

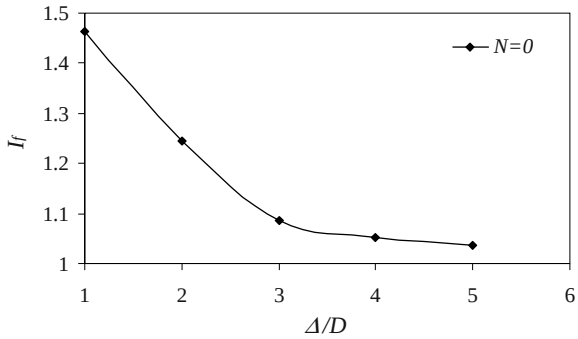

Fig 5 Variation of interference factor at different spacing on unreinforced sand.

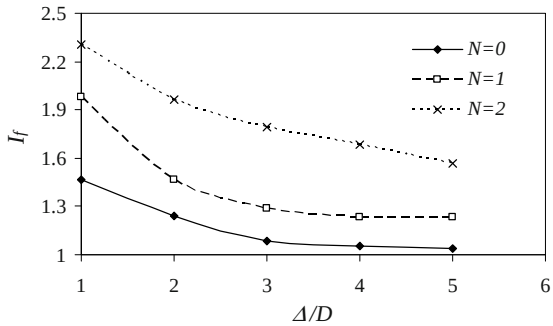

Fig 6 Variation of interference factor at different spacing on reinforced sand (*d*/*D*=2, *u*/*D*=0.3, *h*/*D*=0.2)

Increase percentage is about 65% more than unreinforced at the same spacing ratio. According to Fig. 6, the ultimate bearing capacity decreases by increasing distance between two closely spaced footings for both unreinforced and reinforced sand.

Displacement Field and Failure Mechanism

Single footing on unreinforced sand

Displacement contours at soil surface and beneath the footing for single circular footing on unreinforced sand is presented in Fig. 7. As seen, the propagation of displacement field is fully symmetric around the footing. The shape of displacement beneath the footing shows that a general shear failure has occurred.

Interference between footings on reinforced sand

The variation of unreinforced and reinforced soil displacements beneath the footing in the longitudinal interference axis direction for two closest circular footings Δ/D=1 and 2 are shown in Figs. 8 and 9, respectively.

As shown in Fig. 8, when two adjacent footings are fully attached, the mode of failure in the longitudinal direction of interference axis is not received to failure. This happens because the other side of the footing (lateral direction) fails first. But the mechanism of the failure varies to general shear failure by the use of reinforcement. This phenomenon causes a significant

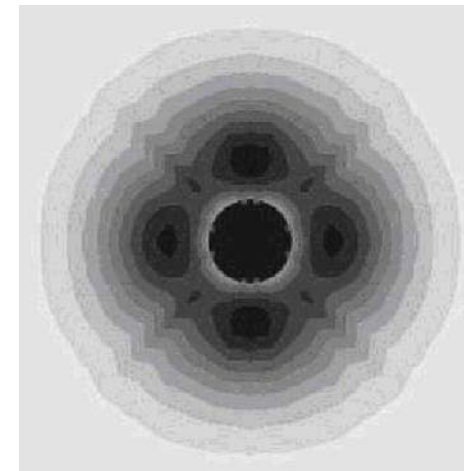

(a) top view of soil surface displacement

(b) view of displacement field beneath the footing

Fig 7 Displacement field of single circular footing on unreinforced sand (*N*=0)

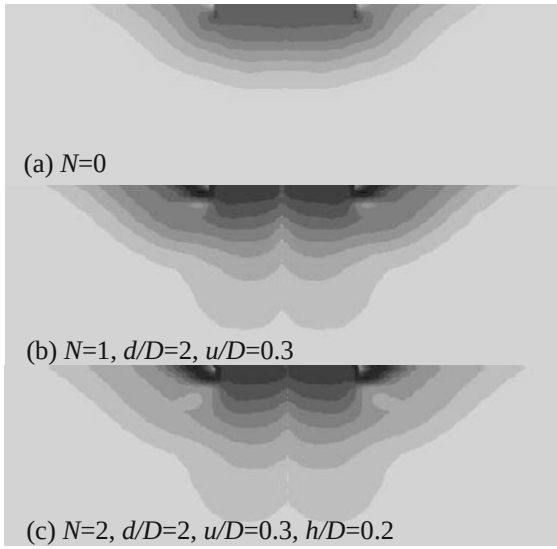

Fig 8 Contours of displacements in longitudinal direction of interference axis (Δ/D=1)

increase in the ultimate bearing capacity. Also, by an increase in the number of reinforcement layers, the influenced depth of footing would increase.

It should be noted that, in the analysis, the ultimate bearing capacity defined as the constant value in the plot of load-settlement.

According to Fig. 9, when no reinforcement is used, the soil surrounding the footing was dilated in an expanded zone. But the dimension of this zone decreases by the use of reinforcement. Therefore, reinforcing the soil would regulate the value of the displacement. It means the footing reinforcement causes to avoid the concentration of displacement or stress at a specific zone around or beneath the footing. In Fig. 9, by increasing the number of reinforcement, the area of zones with maximum value of displacement (zones with darker contours) shrinks by the use of reinforcement. It causes uniformity in the behavior of the soil beneath the footing. As mentioned before, reinforcing the footing soil causes an increase in the capability of the soil to suffer more displacement and load due to footing.

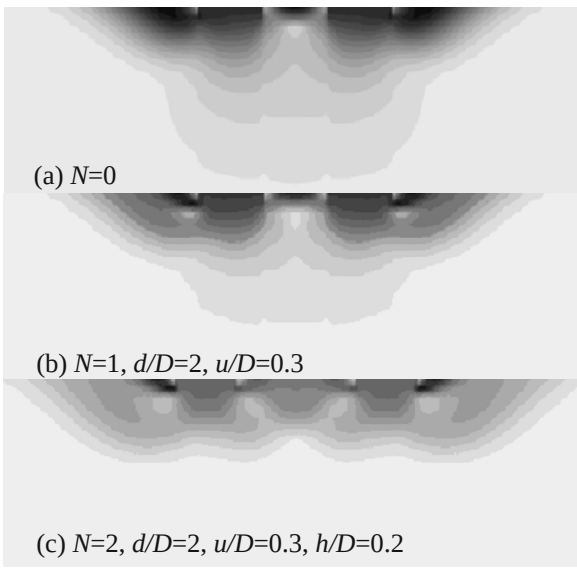

Fig 9 Contours of displacements in longitudinal direction of interference axis (Δ/D=2)

CONCLUSIONS

The results of some numerical analysis on the behavior of two closely constructed rigid rough circular footings on reinforced and unreinforced sand were presented. Based on these analyses, the following general conclusions can be pointed out:

1. When two neighboring circular footings affected on each other, displacement field at soil surface would change to asymmetric.

2. At low spacing ratios, the mode of failure on the longitudinal interference axis and lateral perpendicular axis is different and the former is weaker than the other and failure occurs on this axis first.

3. By the use of reinforcement, the contribution of the soil displacement around and beneath the footing would be more uniform than unreinforced sand.

4. Reinforcing soil causes that difference between weak and strong axes disappears and failure occurs on both at the same time.

REFERENCES

Alimardani Lavasan (2005) Bearing Capacity of Interfering Shallow Footings on Reinforced Sand. MS Thesis, KNToosi University of Technology, Tehran, Iran

Boushehrian JH, Hataf, N (2003) Experimental and Numerical Investigation of the Bearing Capacity of Model Circular and Ring Footings on Reinforced Sand. Geotextiles and Geomembranes 23(2): 144-173

Das BM, Larbi-Cherif S (1983a) Bearing Capacity of Two Closely Spaced Shallow Foundations on Sand. Soils and Foundations 23(1): 1-7

Das BM Larbi-Cherif S (1983b) Ultimate Bearing Capacity of Closely Spaced Strip Foundations. TRB, Transportation Research Record 945:37-39

De Borst R, Vermeer PA (1984) Possibilities and Limitations of Finite Elements for Limit Analysis. Geotechnique 34(2) :199-210

Erickson HL, Drescher A (2002) Bearing Capacity of Circular Footings. J. of Geotech. Engrg. ASCE 128(1): 38-43

FLAC-Fast Lagrangian Analysis of Continua, Version 2.1 (2001) ITASCA Consulting Group, Inc., Minneapolis

Frydman S, Burd HJ (1997) Numerical Studies of Bearing Capacity Factor Nγ. J. Geotech. Engrg. ASCE 123(1): 20-29

Ghazavi M, Alimardani Lavasan A (2007) Influence of Interference on Bearing Capacity of Strip Footing on Reinforced Sand. 5th International Symposium on Earth Reinforcement, Fukuoka, Japan

Graham J, Raymond GP, Suppiah A (1984) Bearing Capacity of Three Closely Spaced Footings on Sand. Geotechnique 34(2): 173-182

Hazel E (2004) Interaction of Closely Spaced Strip Footings. MS. Thesis, University of Oxford, UK

Khing KH, Das BM, Puri VK, Cook ED, Yen SC (1992) Bearing Capacity of Two Closely-Spaced Strip Foundation on Geogrid-Reinforced Sand. Proceedings, International Symposium on Earth Reinforcement Practice, Fukuoka, Japan 1: 619-624

Kumar A, Saran S (2003) Closely Spaced Footings on Geogrid-Reinforced Sand. J. Geotech. Engrg. ASCE 129(7): 660-664

Kumar J, Ghosh P (2007) Ultimate Bearing Capacity of Two Interfering Rough Strip Footings. Int. J. Geomech. ASCE 7(1):53-62

Stuart J G (1962) Interference between Foundations with Special Reference to Surface Footings in Sand. Geotechnique 12(1):15-23

Wang MC, Jao M (2002) Behavior of Interacting Parallel Strip Footing.lectronic Journal of Geo-echnical Engineering, Vol. 7, part A

Yin JH, Wang YJ, Selvadurai APS (2001) Influence of Nonassociativity on the Bearing Capacity of a Strip Footing. J. Geotech. Engrg, ASCE 127(11): 985-989

Proceedings of the 4th Asian Regional Conference on Geosynthetics
June 17 - 20, 2008 Shanghai, China

ANALYTICAL STUDY ON GEOTEXTILE-REINFORCED SOIL RETAINING WALLS DAMAGED DURING THE 2004 MID NIIGATA PREFECTURE JAPAN EARTHQUAKE

M. Mizuhashi[1], H. Sugita[2] and T. Sasaki[3]

ABSTRACT: This paper reviews in brief case histories on the seismic performance of geotextile-reinforced soil retaining walls during the 2004 Mid Niigata Prefecture Earthquake. In addition, by comparing the results of calculations of suitability of these walls based on current design methods with seismic performance of each of structures during the 2004 Mid Niigata Prefecture Earthquake, the applicability of current seismic design to performance-based design is also shown.

KEYWORDS: reinforced soil retaining wall, 2004 Mid Niigata Prefecture Earthquake, performance-based design

INTRODUCTION

It is presumed that geotextile-reinforced soil retaining walls that have had their seismic stability assessed by means of safety factors contained in current seismic design methods have a high seismic performance. However, it would be more rational and economical if their seismic stability was assessed based on the seismic performance required to withstand a strong earthquake. In order to enable the rational design of these walls, it is first necessary to thoroughly understand the problems in the current seismic design methods.

In this paper, case histories on the seismic performance of geotextile-reinforced soil retaining walls during the 2004 Mid Niigata Prefecture Earthquake are reviewed in brief. In addition, by comparing the safety factor of geotextile-reinforced soil retaining walls damaged by the 2004 Mid Niigata Prefecture Earthquake, calculated based on current seismic design methods, with seismic performance of each of the structures studied in this paper, the applicability of current seismic design to performance-based design is investigated.

REVIEW OF CASE HISTORIES

Geotextile-reinforced soil retaining walls, which are the objects of this study, are located in 25 locations within 30 kilometer of the epicenter of the 2004 Mid Niigata Prefecture Earthquake, as shown in Fig. 1. Although five of the reinforced soil retaining walls (plotted in black in Fig. 1) at these 25 locations suffered damage severe enough to influence the road traffic function, serious damage—such as a reinforced soil retaining wall losing its integrity and collapsing—did not occur. Simplified plans of three reinforced soil retaining walls labeled (a), (b) and (c) in Fig. 1, which suffered damage that influenced road traffic functions, are shown in Fig. 2 as (a), (b) and (c), respectively.

Reinforced soil retaining wall (a) suffered the most damage of any of the walls in this study. Its crest settled along the boundary between the original slope and the embankment. Although reinforced soil retaining wall (b) itself was not seriously deformed, its raising embankment deformed, crack could be seen at its crest, and liquefaction occurred in its foundation ground. Damage to reinforced soil retaining wall (c) was very slight—a crack occurred between the original slope and the embankment—and no deformation could be seen in the wall itself. Damage to the fourth and fifth reinforced soil retaining walls was also very slight, limited to small cracks or settlement occurring at their crests, and no large-scale deformation of the walls themselves could be seen.

METHODOLOGY OF CASE ANALYSIS

In this study, the estimated maximum acceleration that affected each reinforced soil retaining wall during an earthquake, the critical design seismic coefficient, and the design safety factor were all compared with the level of earthquake-induced damage in each structure.

[1] Researcher, Earthquake Disaster Prevention Research Group, Public Works Research Institute, JAPAN. Email: mizuhasi@pwri.go.jp
[2] Ph.D, Team Leader,ditto. Email: sugita@pwri.go.jp
[3] Senior Researcher,ditto. Email: t-sasaki@pwri.go.jp

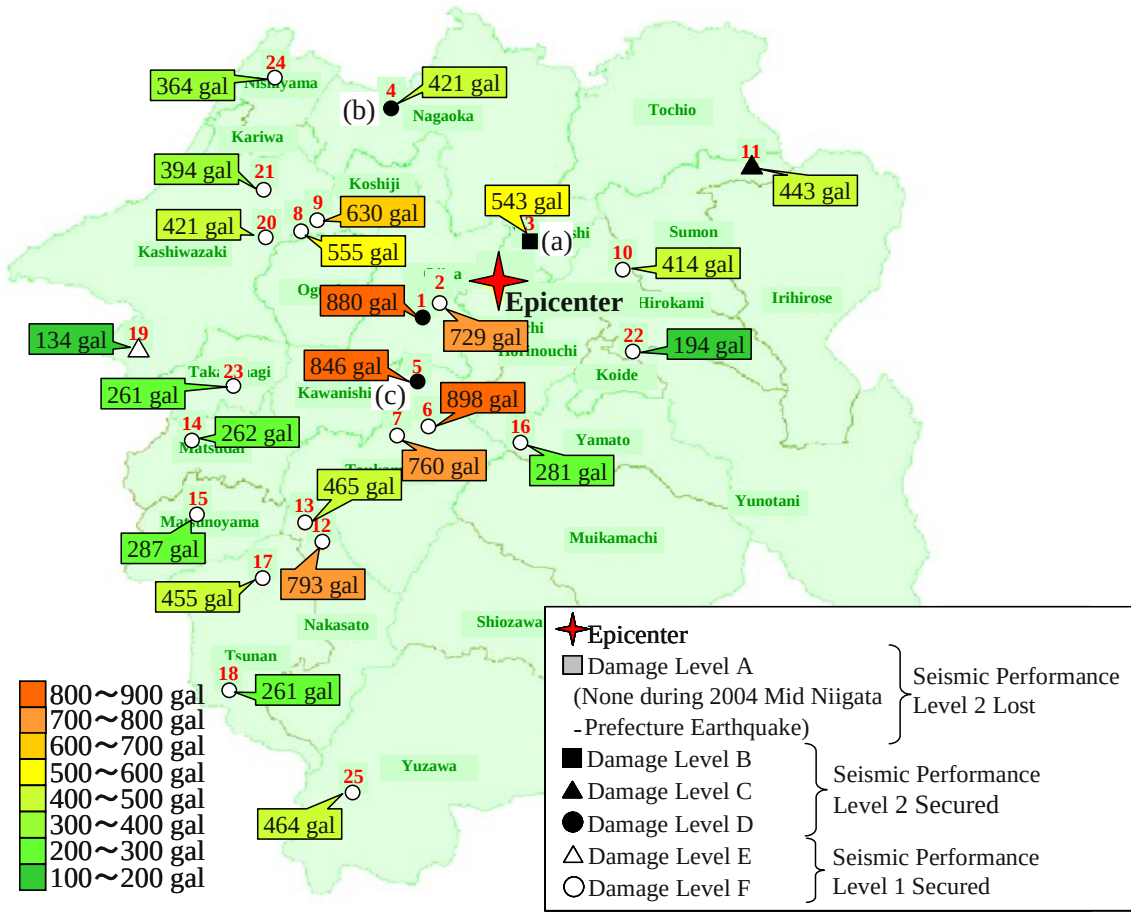

Fig. 1 Outline of cases that are objects in this study

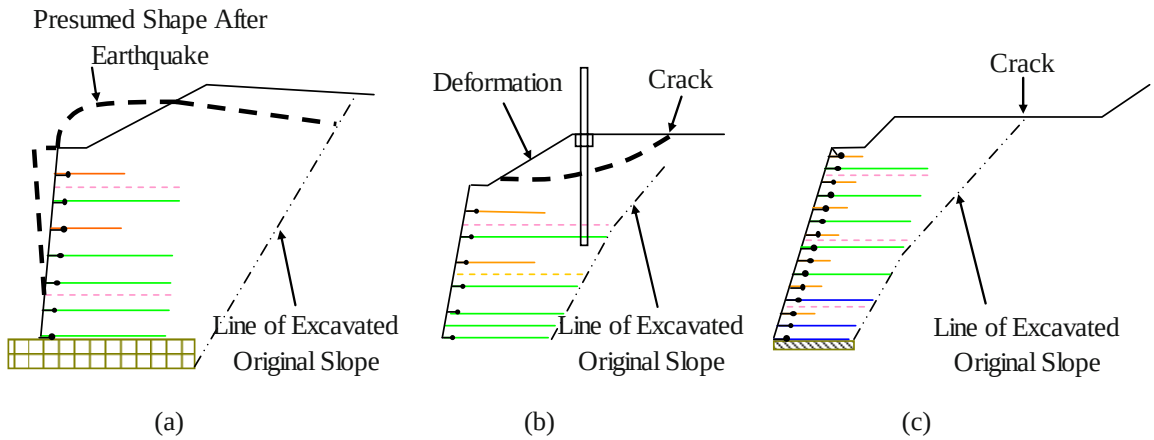

Fig. 2 Simplified plans of geotextile reinforced soil retaining walls

The estimated maximum acceleration and the level of earthquake-induced damage for each structure are also shown in Fig. 1. Estimated maximum acceleration was determined based on results of Suetomi et al. (2002). Earthquake-induced damage level was classified into six categories, as shown in Table 1, based on the influence the structure had on the road traffic function following damage sustained during an earthquake, as shown by Onodera et al. (2005, 2006). For example, the damage level of reinforced soil retaining wall (a) shown in Figs. 1 and 2 was determined as Damage Level B, because although earthquake-induced damage to the wall impeded the road traffic function, it was possible to restore it in a short period of time. As for defining the seismic performance of reinforced soil walls as shown in Table 2, this means that Damage Levels B, C and D secure the Seismic Performance Level 2, and Damage Levels E and F secure the Seismic Performance Level 1.

Table 1 Definition of Damage Level (Onodera et al.)

A: Road traffic function is lost, and a long time is required to restore it.
B: Road traffic function is lost, but it can be restored in a short time.
C: Emergency vehicles can use road, and it can be restored in a short time.
D: General vehicles can use road, and it can be restored in a short time.
E: Usual traffic function can be secured, and road can be restored by ordinary maintainance and repair.
F: No influence.

Table 2 Definition of Seismic Performance

Seismic Performance	Seismic Seviceability Design	Seismic Emargency Repairability Design
Seismic Performance Level 1: Keeping the sound functions	To ensure the normal functions	No repair work is needed to recover the functions
Seismic Performance Level 2: Limited damages and recovery	Tcapable of functions within a short period after the event	Capable of recovering functions by emergency repair works
Seismic Performance Level 3: No critical damages	-	-

The critical design seismic coefficient and the design safety factor were calculated based on the circular arc method in the investigation of general stability shown in the current manual of design—although the mode of deformation in actual phenomena does not always coincide with that supposed in the circular arc method. Critical design seismic coefficient calculated is a design seismic coefficient that makes a minimum safety factor of 1.0. The design safety factor was calculated using design seismic coefficient k_h=0.13 (Zone B, Ground Type I, Large Earthquake Ground Motion) as a safety factor during earthquakes. The soil and ground parameters used were, in principle, those that had been used in design or determined by considering the property of the soil and ground based on the current manual of design. However, there are several reinforced soil retaining walls that have, as a result of calculation, a safety factor, even in ordinary conditions, of less than 1.0. In making calculations for these walls, cohesion was considered as making the safety factor 1.2 under ordinary conditions.

RESULTS OF CASE ANALYSIS

Fig. 3 shows the relationship between damage level and design safety factor against an earthquake ground motion (k_h=0.13). There are several reinforced retaining walls that have a design safety factor against earthquake ground motion of less than 1.0. However, all the reinforced soil retaining walls that are the objects of this study could secure a seismic performance of 2, although some of them could not secure the Seismic Performance Level 1. In addition, the correlation between damage level and safety factor cannot be seen clearly in the causes of the differences in seismic ground motion having affected said structures and other objects. Therefore, below looking into the relationship among estimated maximum acceleration affecting reinforced soil walls, critical design seismic coefficient and seismic performance level, seismic coefficients that should be considered in performance-based design is investigated.

Fig. 4 shows the relationship between estimated maximum acceleration a_{max}[gal] and the critical design seismic coefficient calculated based on the current design method. This means that plots under the broken line in Fig. 4 were affected by stronger seismic ground acceleration than that converted from the critical design seismic coefficient. The minimum critical design seismic coefficient of reinforced soil retaining walls affected by seismic ground motion with a maximum acceleration of approximately 200 gal is approximately 0.095, and the minimum critical design seismic coefficient of reinforced soil retaining walls affected by seismic ground motion with a maximum acceleration of approximately 800 gal is approximately 0.109. Because all the walls in this study secured the Seismic Performance Level 1 or 2, it can be said that the design seismic coefficient of 0.12—0.16 considered in the current design method for reinforced soil retaining walls (and which is the same value as that for concrete retaining walls) is a safer value for a seismic coefficient used for the assessment of the Seismic Performance Level 2 for reinforced soil retaining walls, with regard to the cases in this study. Next, the seismic coefficient used for the assessment of the Seismic Performance Level 1 was investigated. Reinforced soil retaining walls that lost the Seismic Performance Level 1 are distributed approximately under the line of k_h=0.5a_{max}/g (black plots in Fig. 4, g stands for gravitational acceleration). Therefore, it can be said that an acceleration that is approximately 0.5 times supposed maximum acceleration should be considered as the design seismic coefficient used for the assessment of the Seismic Performance Level 1, with

regard to the cases in this study. In short, a design seismic coefficient of approximate 0.1 should be considered for use for the assessment of the Seismic Performance Level 1 against medium-strength earthquake ground motion having a maximum acceleration of approximately 200 gal, and a design seismic coefficient approximate 0.4 should be considered for use for the assessment of the Seismic Performance Level 1 against large earthquake ground motion having a maximum acceleration of approximately 800 gal. However, as previously mentioned, the mode of deformation in actual phenomena does not always coincide with that in a design calculation, and it will be necessary to investigate this point in the future.

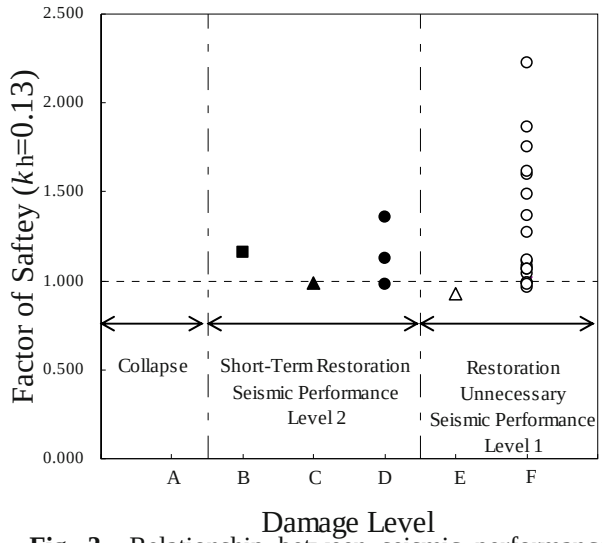

Fig. 3 Relationship between seismic performance level and safety factor

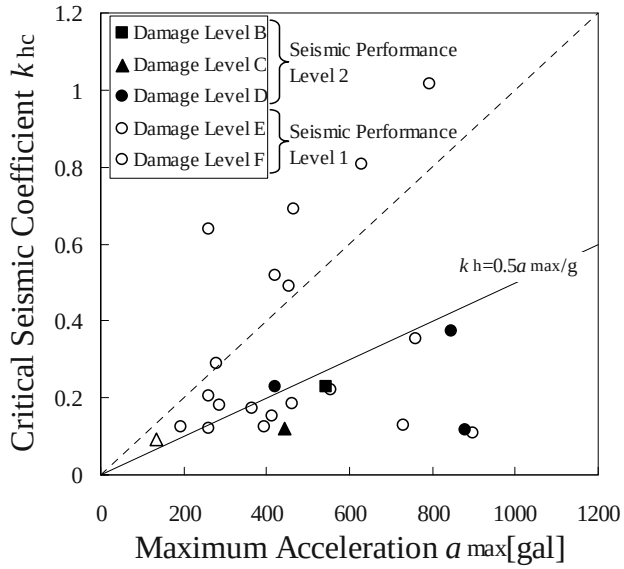

Fig. 4 Relationship between presumed maximum acceleration and critical design seismic coefficient

SUMMARY AND ACKNOWLEDGMENT

Comparing the results of calculations of suitability based on current design methods for reinforced soil retaining walls with the seismic performance level they sustained during the 2004 Mid Niigata Prefecture Earthquake, it is shown that there is a possibility of applying the current design method to performance-based design. Cases in this study were offered by the Reinforced Soil Diffusion Committee, for which we are most grateful.

REFERENCES

Public Works Research Center (2000) Manual of design and construction for geotextile-reinforced Soil

Suetomi I, Ishida E, Fukushima Y, Isoyama R, Sawada S (2006) Evaluation of distribution of horizontal maximum ground motion during the 2004 Niigata-Chuetsu Earthquake. Project with the budget of the promotion of science and technology. Japan Society of Civil Engineering.

Onodera S (2005) Reinforced soil strong against disasters [Topics on road]. DS-9 Recent development and application of ground reinforcement technique I. 40th Japanese Geotechnical Society conference. Japanese Geotechnical Society

National Institute for Land Infrastructure Management. and Public Works Research Institute (2006) Report on Damage to Infrastructures by the 2004 Mid Niigata Prefecture Earthquake. Research report of National Institute for Land Infrastructure Management No.27 and Research report of Public Works Research Institute 203: 204-214.

Proceedings of the 4th Asian Regional Conference on Geosynthetics
June 17 - 20, 2008 Shanghai, China

INTERNAL STABILITY ANALYSIS OF SEGMENTAL GEOGRID-REINFORCED SOIL RETAINING WALLS

H.B. Liu[1]

ABSTRACT: Segmental geogrid-reinforced soil retaining wall is gaining increasing popularity due to its cost effectiveness and ease in construction. Internal stability analysis is a critical step in designing such structures, which to a great extent determines the layout and density of reinforcements. Maximum load in each reinforcement layer and the potential failure surface are two critical parameters in internal stability analysis. Nonlinear Finite Element method was used to investigate the maximum load in each reinforcement layer and its lateral location with different reinforcement densities and different backfilled soils. The effects of reinforcement creep on the two parameters were also analyzed. The results were then compared to those obtained using the suggested internal stability analysis method by FHWA. It was found that with regular reinforcement the locations of maximum reinforcement loads from the FE analysis were closer to the facing than those using the suggested method; it was also found that the maximum reinforcement load was smaller. The results agree with the findings from field and laboratory experiments by other investigators.

KEYWORDS: segmental geogrid-reinforced soil retaining wall, Finite Element method, internal stability, reinforcement load; potential failure surface

INTRODUCTION

Geosynthetic-Reinforced Soil (GRS) retaining wall provides a very attractive alternative for traditional earth retaining structures due to its proved performance and cost-effectiveness in relation to traditional retaining walls. Different facings can be used in GRS walls, but segmental GRS wall with modular-block facing is popular because of its aesthetic appearance and ease in construction. The check of internal stability is a critical step in the design of GRS walls, which determines the length and spacing of reinforcement layers. Many design codes, such as the FHWA design guidelines (Elias et al. 2002), suggest that the maximum reinforcement load be calculated using the active earth pressure coefficient K_a. For vertical wall, the Rankine equation is used:

$$K_a = \tan(45° - \varphi/2) \tag{1}$$

in which φ is the angle of internal friction. If no surcharge exists, the maximum load in each reinforcement layer is then calculated as:

$$T_{\max}^i = \gamma h_i K_a S_v^i \tag{2}$$

in which γ is the unit weight of the backfill soil, h_i is the depth of the reinforcement layer, and S_v^i is the reinforcement spacing. The potential failure surface, which is the surface where maximum reinforcement load locates, is assumed to coincide with the Rankine failure surface if the wall is vertical.

The validity of these assumptions for segmental GRS retaining wall was investigated using nonlinear Finite Element method. Geogrid reinforcement and granular backfill, which are common to segmental GRS walls, were assumed in the analyses. The wall was assumed to be vertical. The results from the Finite Element analyses were discussed together with available field and laboratory experimental results.

FINITE ELEMENT MODEL

The Finite Element model was a GRS wall at a height of 6 m. The modular block facing consists of 30 blocks with a height of 20 cm and a width of 30 cm each, based on the dimension of a real block. The backfill soil was a real sand with an angle of internal friction φ=39°. In order to investigate the effect of backfill soil, a weaker soil with an angle of internal friction φ=33° was also analyzed. The unit weight of the soil was 16 kN/m^3. The backfill soil was assumed to be time-independent and was modeled using the Modified Pastor-Zienkiewicz model for sand (Ling and Liu 2003), which requires 11 model parameters for static analysis. The geogrid

[1] Assistant Professor, Department of Civil Engineering, City University of New York, USA. Email:hbliu@ce.ccny.cuny.edu

reinforcement was an HDPE geogrid with a rupture strength of 54.6 kN/m according to standard ASTM tests, which was modeled using the bounding surface model proposed in Liu and Ling (2007). Both the time-independent and the time-dependent versions of the model were used in the analyses, which require 4 and 9 model parameters, respectively. The interfaces between the soil and the facing blocks as well as those between the blocks were simulated using a thin-layer element capable of reproducing the slip of interfaces. The interfaces between the soil and the geogrid were assumed to be perfectly bounded due to the fact that the simulated geogrid had a large aperture size of 14.5×1.7 cm. The facing blocks were assumed to be linear elastic. The details of the soil model and its parameters, the geosynthetic model and its parameters, as well as the interface element can be found in Ling and Liu (2003), Ling et al. (2005) and Liu and Ling (2007).

The Finite Element analyses were conducted using a modified version of the DYNA-SWANDAYNE-II code (Chan 1993; Liu 2002). The construction sequences of the GRS wall were simulated. In order to eliminate the boundary effects, the backfill soil was extended to a depth of 20 m from the back of facing. A foundation of 3 m was also considered in the analysis, assuming the same soil properties as those of backfill's. The major portion of the Finite Element mesh was shown in Fig. 1.

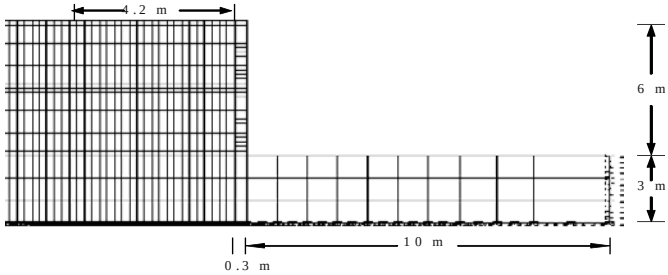

Fig. 1 Part of Finite Element Mesh

The length and the spacing of the geogrid reinforcements were varied in the analyses to investigate their influences on the maximum reinforcement load and the potential failure surface. The effects of the soil strength were also studied. The analyses were firstly conducted without considering the time-dependent properties of the reinforcements, the results of which could be considered to represent the end-of-construction behavior of GRS walls with non-viscous backfills as discussed in Liu and Ling (2007). The creep behavior was then taken into account and a creep analysis for 3 years after the end of construction was conducted to investigate the changes in the reinforcement loads. The summary of the analyses is shown in Table 1.

Table 1 Summary of FE analyses

	soils	Geogrid length L	Geogrid spacing D	Series
Time independent	φ=39°	3.0 m, 4.2 m, 4.8 m	0.6 m	I
		4.2 m	0.4 m,1.0 m	II
	φ=33°	4.2 m	0.6 m	III
Time dependent	φ=39°	2.2 m, 4.2 m	0.6 m	IV
		4.2 m	1.0 m	

MAXIMUM REINFORCEMENT LOADS

The reinforcement loads of the walls with different reinforcement lengths L (Series I) are shown in Fig. 2, together with the loads calculated using Eq. 2. It can be seen that the maximum reinforcement load increased slightly with a decrease in the reinforcement length L in the range investigated, but apart from the reinforcements in the upper portion of the wall, the reinforcement loads were smaller than those calculated using Eq. 2. The maximum reinforcement load in all layers T_{mxmx} occurred at the 2nd or the 3rd layer instead of the bottom layer predicted by the Rankine earth pressure theory. This result indicates that the FHWA method is conservative in calculating the maximum reinforcement load in GRS retaining walls, which is also reported in Allen and Bathurst (2002) from extensive case histories.

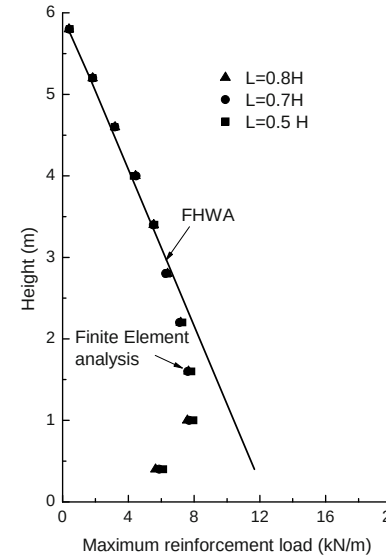

Fig. 2 Reinforcement loads with different lengths of reinforcement

The results of series II are shown in Fig. 3. As expected, larger reinforcement spacing led to much larger

reinforcement load, but the T_{mxmx} 's in the two cases were both smaller than the ones calculated using Eq. 2. The difference was larger with larger reinforce-ment spacing. Besides, it is also interesting to note that, with smaller reinforcement spacing, the reinforcement loads in the upper portion of the wall were larger than the ones calculated using Eq. 2.

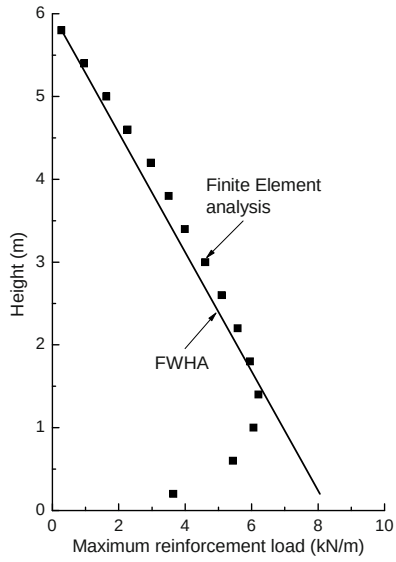

(a) D = 0.4 m

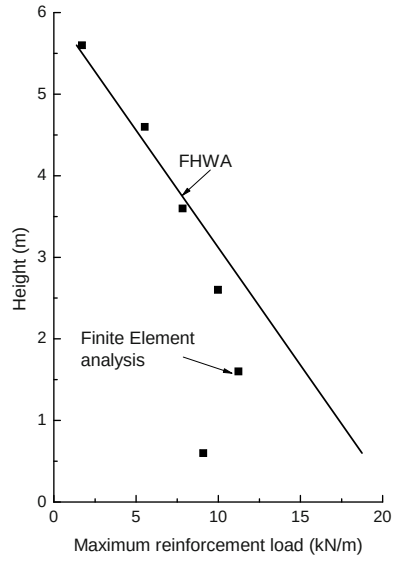

(b) D = 1.0 m

Fig. 3 Reinforcement loads with different reinforcement spacings

Weaker backfill soil did not change the conclusion regarding the maximum reinforcement load, as shown in Fig. 4. As a matter of fact, by comparing with results in Fig. 3, in which backfill soil with larger strength was used, the difference between the results from Finite Element analysis and the one calculated by Eq. 2 was larger with weaker backfill soil.

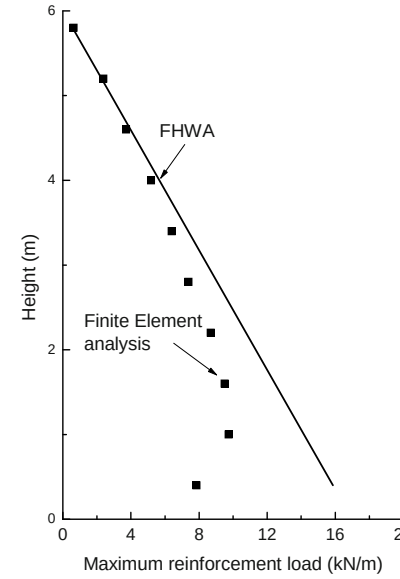

Fig. 4 Results with weaker backfill soil (φ=33°)

The effects of the time-dependent properties of the geogrid reinforcements on the reinforcement loads after 3 years of creep are shown in Fig. 5. By comparing with results in series I and II, it could be seen that the time-dependent properties of the reinforcement led to load redistribution among the reinforcement layers. The maximum loads in the reinforcement layers in the upper portion of the wall increased while the maximum reinforcement loads in all the layers T_{mxmx} decreased. The difference between the results from the Finite Element analyses and those by Eq. 2 were larger after 3 years of creep for this specific HDPE geogrid (Leshchinsky et al. 1997).

POTENTIAL FAILURE SURFACE

The potential failure surface of GRS wall is normally assumed to coincide with the lateral location of maximum load in each reinforcement layer (Ellias et al. 2002). The comparison between the potential failure surface obtained from Finite Element Analysis with L= 0.7 H and D = 0.6 m, and the Rankine failure surface suggested in FHWA guideline, is shown in Fig. 6. The distribution of reinforcement load along each reinforcement layer is also shown in Fig. 6. Clearly, the result from the Finite Element analysis was closer to the facing than the suggested surface. This trend was also reported in Christopher (1993) and Farrag et al. (2004) from their laboratory and field experiments.

The Finite Element analysis results with different reinforcement lengths and spacings are shown in Fig. 7 together with the Rankine failure surface. Generally, the potential failure surfaces from the Finite Element analyses

were all closer to the facing than the Rankine failure surface, however, the one with L=0.7 H and D= 1.0 m was close to the Rankine failure surface. The results in Fig. 7 indicate that, with different reinforcement lengths and spacing, the potential failure surfaces were not the same.

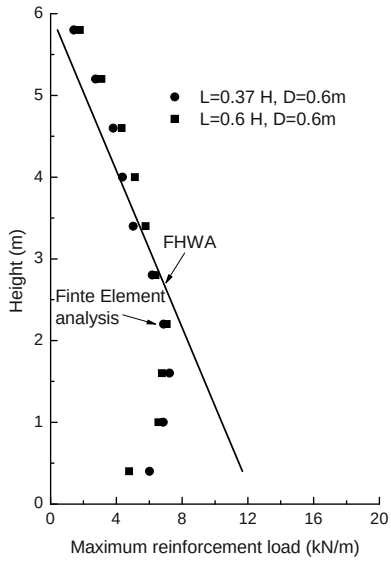

(a) Different reinforcement lengths

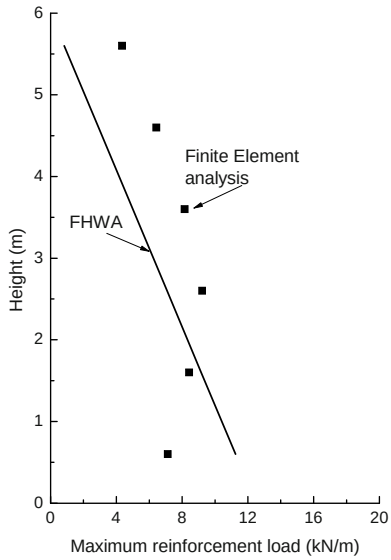

(b) L = 0.7 H, D = 10 m

Fig. 5 Reinforcement loads after 3 years of creep

Reducing the strength of the backfill soil to φ=33°, the potential failure surface from the Finite Element analysis was still closer to the facing than the Rankine failure surface, as shown in Fig. 8. However, it is difficult to make conclusion at this moment since no backfill with even smaller strength was analyzed. The influence of backfill strength on the location of the potential surface deserves further investigation.

The potential surface of the GRS retaining wall after 3 years of creep was also investigated, the results of which are shown in Fig. 9. It can be seen that the potential failure surfaces for the cases with D = 0.6 m and D = 1.0 m were also different. And with regular reinforcement length and spacing (L = 0.7 H, D = 0.6 m), the potential failure surface was also closer to the facing than the surface suggested by FHWA.

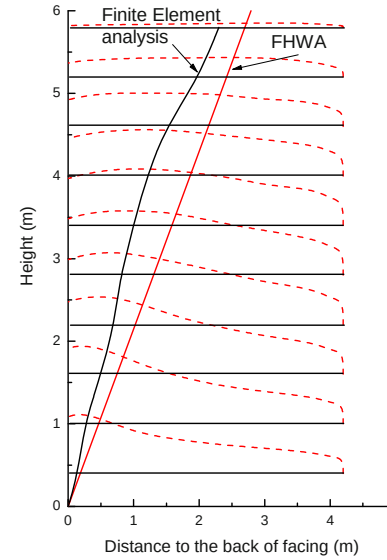

Fig. 6 Potential failure surface (Reinforcement: L =0.7 H, D=0.6 m)

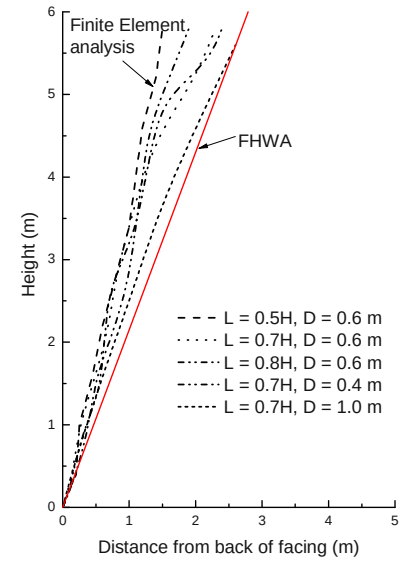

Fig. 7 Comparison of potential failure surfaces with different reinforcement length or spacing

DISCUSSIONS

The maximum reinforcement load obtained from Finite Element analysis for a 6-meter high segmental GRS retaining wall at working stress condition was

smaller than the one calculated using Eq. 2 suggested in the FHWA guideline (Ellias et al. 2002). Similar conclusions regarding the reinforcement load was also reported in Allen et al. (2002) from extensive field and laboratory experiments.

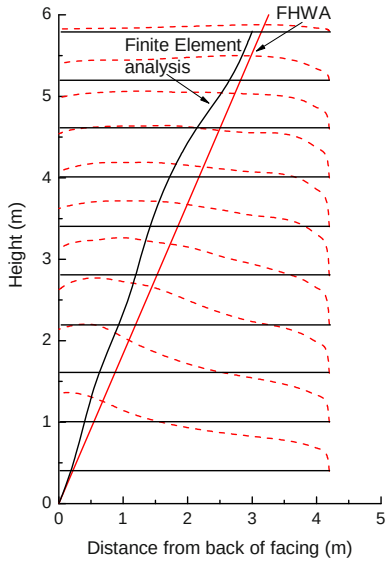

Fig. 8 Potential failure surface with weaker backfill soil

The Finite Element analysis also found that the location of the potential failure surface was closer to the facing than the Rankine failure surface. It also found that with different reinforcement spacing and length, the locations of the potential failure surfaces were different, but generally were all closer to the modular block facing than the Rankine failure surface. These results agreed with the experimental results reported in Christopher (1993). In this PhD thesis, it was reported that that the initial failure surfaces of a series of GRS retaining walls in centrifuge tests were generally steeper than the Rankine failure surface. And with an increase in the centrifugal force, the location of the failure surface could change, indicating that the failure surfaces varied with different reinforcement spacings. Similar trend was also reported in Farrag et al. (2004).

The results of the Finite Element investigation confirm that the current practice of internal stability check for segmental GRS retaining walls may be conservative (Allen and Bathurst 2002). The conservativeness comes from both the maximum reinforcement load and the location of the potential failure surface.

The results in this study were based on the analyses of GRS retaining walls with granular backfills and an HDPE gegrid reinforcement. The effects of the creep of the backfill soil, the stiffness of the geosynthetic reinforcements and different time-dependent properties of reinforcements should be further investigated.

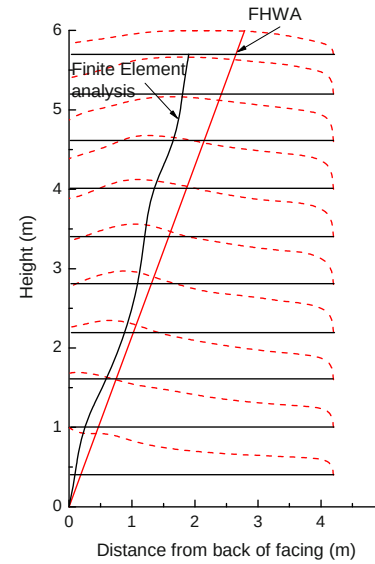

(a) D = 0.6 m, L = 0.7 H

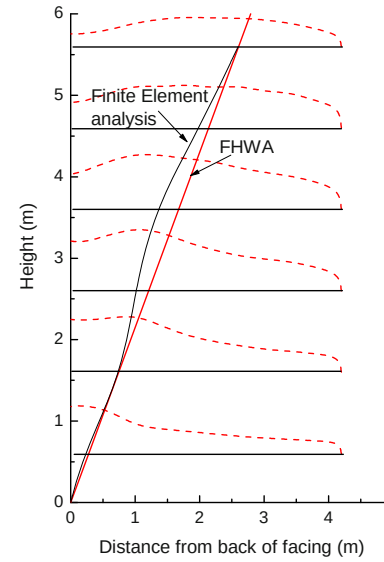

(b) D = 1.0 m, L = 0.7 H

Fig. 9 Potential failure surfaces after 3 years of creep

CONCLUSIONS

A series of Finite Element analyses were carried out in order to investigate the maximum reinforcement load and its lateral location in a segmental GRS retaining wall under working stress condition. Granular backfill and gegrid reinforcement were assumed in the study, which is commonly used in permanent GRS retaining walls. It is found that the method suggested by the FHWA guideline (Ellias et al. 2002) may be conservative in two aspects: firstly, it over-predicts the maximum reinforcement load; secondly, the suggested Rankine failure surface leads to shorter length of reinforcement in the resistant zone. The Finite Element analyses also found

that the locations of the potential failure surface were different with different reinforcement spacings. The results of the Finite Element analyses agreed with the findings from field and laboratory experiments reported by other investigators (Christopher 1993; Allen and Bathurst 2002).

ACKNOWLEDGEMENTS

This work was supported by the National Natural Science of Foundation (No. 50408002) granted to the first author when he was working at Tsinghua University in China. The support is gratefully acknowledged.

REFERENCES

Allen TM, Bathurst RJ (2002) Soil reinforcement loads in geosynthetic walls at working stress conditions. Geosynthetics International 9(5-6): 525-566

Chan AHC (1993) User Manual for DYNA Swandye-II. Department of Civil Engineering, Glasgow University, Glasgow, UK

Christopher BR (1993) Deformation response and wall stiffness in relation to reinforced soil wall design. Ph.D. thesis. Purdue University, West Lafayette, Indiana, USA

Elias V, Christopher BR, Berg RR (2001) Mechanically stabilized earth walls and reinforced soil slopes — design and construction guidelines. Report FHWA-NHI-00-043, Federal Highway Administration (FHWA), Washington, DC

Leshchinsky D, Dechasakulsom M, Kaliakin V, Ling H (1997) Creep and stress relaxation of geogrids. Geosynthetics International 4(5): 463-479

Ling HI, Liu H (2003) Finite element studies of asphalt concrete pavement reinforced with geogrid. Journal of Engineering Mechanics, ASCE 129(7): 801-811

Ling HI, Liu H, Mohri Y (2005) Parametric studies on the behavior of reinforced soil retaining walls under earthquake loading. Journal of Engineering Mechanics, ASCE 131(10): 1056-1065

Liu H (2002) Finite Element Simulation of the Response of Geosynthetic-Reinforced Soil Retaining Walls. PhD Thesis. Department of Civil Engineering and Engineering Mechanics, Columbia University, New York

Liu H, Ling HI (2007) A unified elastoplastic—viscoplastic bounding surface model of Geosynthetics and its applications to GRS-RW analysis. Journal of Engineering Mechanics, ASCE 133(7):801-815

Proceedings of the 4th Asian Regional Conference on Geosynthetics
June 17 - 20, 2008 Shanghai, China

BEARING CAPACITY OF RING FOOTINGS ON REINFORCED CLAY

A. H. Boushehrian[1] and N. Hataf[2]

ABSTRACT: One of the common methods for soil improvement in order to increase the bearing capacity of shallow foundations is reinforcing the soil using geosynthetics. In this paper, the bearing capacity of ring footings on clay reinforced with geogrid has been studied. Laboratory and numerical investigation using the finite element computer code, Plaxis have been performed. The effects of different factors such as the distance to the first layer of reinforcement, vertical distances between layers, and the number of reinforcing layers, the optimum depth of the reinforcement and the stiffness of the reinforcements on the increase of the bearing capacity ratio, of circular and ring foundation have been examined.

KEYWORDS: bearing capacity, reinforced soil, ring footing

INTRODUCTION

One of the appropriate methods to prevent soft soil failure or excessive settlements under loads, is reinforcing the soil with polymeric reinforcements such as geogrids, geotextiles, geonets, etc. The bearing capacity of shallow foundations besides the parameters and conditions of the soil below the foundation depends on the shape of the foundation. Ring footings are usually used for symmetrical buildings like silos, chimneys, and oil storages upon which much study has been done. This study presents a series of laboratory and numerical studies results on the behavior of ring and circular footings placed on the clay reinforced with geogrids.

BEHAVIOUR OF FOOTINGS ON THE REINFORCED SOIL

The bearing capacity ratio of the reinforced soil to non-reinforced soil (BCR) is defined to assess the increase of the bearing capacity. If the reinforcements are placed in suitable distance from the foundation bottom, the BCR will be more than 1.0. Binquet and Lee (1975) used a box with the dimensions of 1.5 m (length) × 0.53 m (width) × 0.33 m(depth), and a strip footing with the width of 7.5 cm in his experiments. Aluminum strips were used in these experiments as reinforcement elements. Akinmusuru and Akinboladeh (1981) experimented on square footings with the width of 10 cm, and woven strip reinforcements. They observed an increase in the BCR between 1 and 0.5, for the ratios of u to B. The optimum number of the reinforcements was 3.

Hataf and Bazyar (2000) observed noticeable increases in the bearing capacities of the reinforced soils, using square footings with the width of 14 cm and tire shred as the reinforcement. They reported the critical rates of z/B and u/B , 0.46 and 0.315. Hataf and Boushehrian (2003) did study the optimum amounts of the depth of one layer of reinforcement and the distances between the multi layers reinforcements in the sandy soil beneath the ring and circular footings experimentally and numerically.

Improving the bearing capacity and the features related to the settlement of clay using horizontal reinforcements has also been studied by Ingoled and Miller (1982), Das (1987), Mandal and Sah (1992).

As mentioned above, several parametric studies have been done on reinforced soils so far, though not much information of the studies on ring footings or on reinforced soils has been reported.

MATERIAL PROPERTIES

The grain-size distribution curve of the tested clay soil is presented in Fig. 1. The soil was classified as clay with low plasticity (CL) using the unified soil classification system. Other features of the soil are shown in Table 1. The internal friction angle and the soil cohesion were obtained from the undrained triaxial test with no saturation of the sample. The used reinforcement

[1]Graduate Student, Civil Engineering Dept., Shiraz University, Shiraz, IRAN. Email:hajianib@shirazu.ac.ir
[2] Professor, Civil Engineering Dept., Shiraz University, Shiraz, IRAN. Email:nhataf@shirazu.ac.ir

was the uniaxial polyethylene geogrid. The tensile strength of the geogrid was 8 kN/m. The size of the openings of the geogrid was 2.7 mm × 2.7 mm, and its thickness was 5 mm.

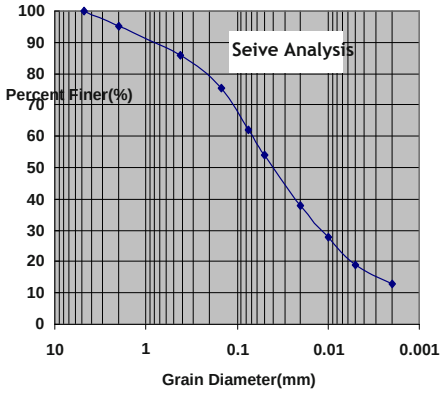

Fig. 1 The grain-size distribution curve of the tested clay

Table 1 Engineering properties of clays used in model tests

Parameter	Clay
Maximum density kN/m^3	16 kN/m^3
Undrained cohesion kN/m^2	4.5(kN/m^2)
Internal friction angle	26^o

LABORATORY TESTS

The cylindrical tank of the tests was made of steel with the diameter/ height of 1 meter and thickness of 4 mm. The load was applied to the foundations using the system of a simple lever. The foundations were also metal and steel with the thickness of 70 mm, the internal diameter of 60 mm, and the external diameter of 150 mm. The numerical results showed the highest quantity of BCR with the ratio of the internal diameter to the external diameter equaling to 0.4.

TEST PROCEDURE

For each test, first the tank was filled with 50-millimeter layers of soil. In order to gain a uniform compaction for each layer, a wooden plate was thrown down on the surface of the soil 15 times from the height of 200 mm, this contributed to a relative density between 1.55 and 1.6 gr/cm3 in the soil. A gauge was used to measure the caused displacement in different spots of the foundation.

EXPERIMENTATION PROGRAM

Tables 2 and 3 indicate the program of the research experiments. In this table, Rl indicates the ring footing on the non-reinforced soil. Rl_x_y indicates the ring footing on the clay with x reinforcement layers in test number y. Cl indicates the circular footing on the non-reinforced soil. Rl_x_y indicates the circular footing on the clay with x reinforcement layers in test number y.

Table 2 Conditions tested in laboratory model tests (Ring footing)

Test No.	U(cm)	Z(cm)
Rl	----	----
Rl-1-1	3.5	----
Rl-1-2	5	----
Rl-1-3	10	----
Rl-1-4	30	----
Rl-2-1	3.5	4
Rl-2-2	3.5	5
Rl-3-1	3.5	4
Rl-3-2	3.5	5
Rl-4-1	3.5	4
Rl-4-2	3.5	5

Table 3 Conditions tested in laboratory model tests (Circular footing)

Test No.	U(cm)	Z(cm)
Cl	----	----
Cl-1-1	3.5	----
Cl-1-2	5	----
Cl-1-3	10	----
Cl-1-4	30	----
Cl-2-1	3.5	3
Cl-2-2	3.5	4.5
Cl-3-1	3.5	3
Cl-3-2	3.5	4.5
Cl-4-1	3.5	3
Cl-4-2	3.5	4.5

LABORATORY RESULTS

Load-deformation curves were drawn upon each loading. The bearing capacity, considering the nature of the failure, was defined using the tangent method by drawing two tangents (one on the first part and the other

on the second part of the curve). The convergence spot of these two tangents defines the bearing capacity.

MULTI-LAYERS OF REINFORCEMENT

The results of the tests performed on circular and ring footings placed on multi-layers of reinforcement layers are presented in Figs. 2 and 3. As specified in the figures, the bearing capacity and the initial module of elasticity the soil increase upon an increase in the number of the reinforcement layers. Of course, this increase in the bearing capacity was observed when there are more than 4 reinforcement layers. BCR are not much different for 3 and 4 reinforcement layers and the reason can be that the reinforcement layers are out of the effective zone of the foundation.

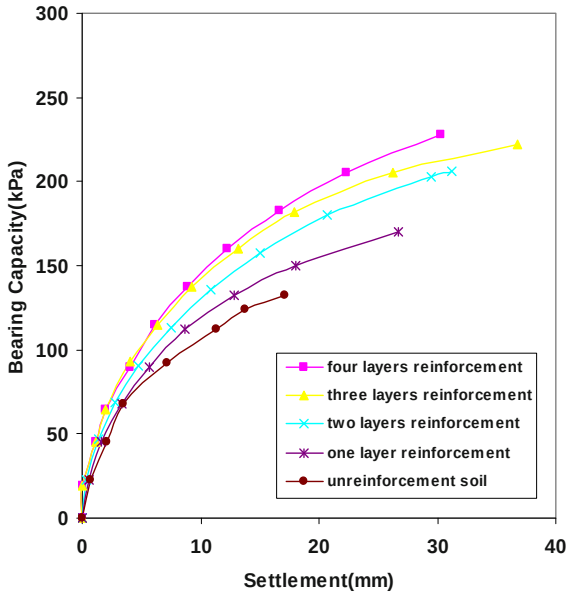

Fig. 2 Test results for a circular footing on multi-layer reinforcement

NUMERICAL ANALYSIS

The final goal was an exact multilateral study of the behavior of the ring footing on the reinforced clay. Since this behavior is different as regards the number of various reinforcement layers, the distance change between them, and the distance between the first reinforcement layer and the surface beneath the foundation, and also conducting experiments for each change in any of these parameters seemed so lengthy in time and even impossible–considering the current loading system, only the results of the finite element program, Plaxis, were used for the layers more than one, and for any change of these parameters.

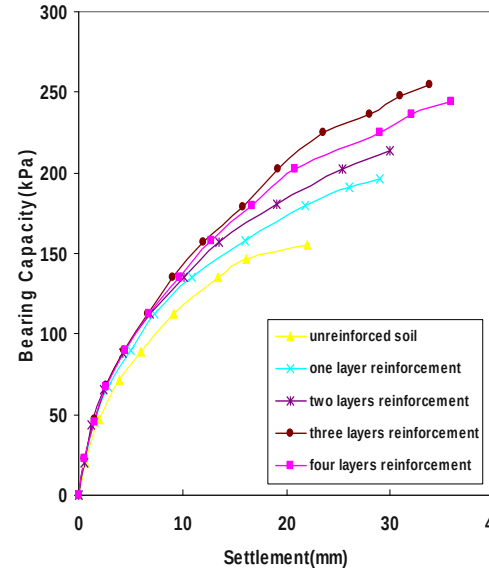

Fig. 3 Test results for a ring footing on multi-layer reinforcement

The method was to make calculations for the implementation program and the ultimate bearing capacity for different distances from one reinforcement layer to the bottom of the foundation. Then, the optimum distance of the first reinforcement to the section beneath the surface of the foundation was defined for the highest amount of the bearing capacity. Meanwhile, all these stages were studied and done in the laboratory simultaneously. We considered this distance fixed for further examinations and for cases with 2, 3 and 4 layers, and changed the distance between the reinforcements for the next stage, and finally considered the figures we came to as the basis for placing the reinforcement layers in the laboratory.

The finite element program, Plaxis, is one of the most powerful numerical programs for analyzing the behavior, deformation, and stability studies in geotechnical engineering projects. Upon running the program for different cases, the ratio of the internal diameter to the external diameter kept being equal to 0.4. A ring footing with the internal diameter of 60 mm and the external diameter of 150 mm, and a circular footing with the diameter of 150 mm, were used in the laboratory. In order to gain the maximum ultimate bearing capacity of the foundation we specified the optimum distance from the first reinforcement to the part beneath the surface of the foundation when using one layer of the reinforcement. Then by considering this distance to be fixed for the cases with two layers and multi layers, we gained the maximum bearing capacity for these cases upon changing the distance between the layers to reach the optimum distance. Final results are presented in Tables 4 and 5.

After drawing the curves, we specified the point which was the maximum bearing capacity for each case (two, three, and four layers) and did make these distances the basis in our tests, and assessed the correctness of these options. The used specifications in the numerical analysis have been presented in Table 6.

Table 4 Variation of bearing capacity, u and z for circular footing

Number of layers	Bearing capacity (kPa)	$\frac{u}{D_0}$	$\frac{z}{D_0}$
2	232	0.2	0.18
3	234	0.2	0.18
4	234	0.2	0.16

Table 5 Variation of bearing capacity, u and z for ring footing

Number of layers	Bearing capacity (kPa)	$\frac{u}{D_0}$	$\frac{z}{D_0}$
2	234	0.55	0.44
3	233	0.55	0.44
4	243	0.55	0.42

Table 6 Parameters used in numerical analysis

Parameter	Value
Undrained internal friction angle (degree)	26
Undrained cohesion (kPa)	4.5
Modulus of elasticity (kPa)	70000
Poison ratio	0.25
Density (kN/m^3)	16
Stiffness of reinforcement (kN/m)	8

CONCLUSION

Laboratory results and the numerical model do indicate the effect of the number of the reinforcement layers, the distance from the first layer to the bottom of the foundation, and the distance between the reinforcements on the bearing capacity of circular and ring footings. Using the reinforcements with more tensile stiffness does not always result in an increase in the bearing capacity ratio. The bearing capacity does increase upon increasing the reinforcement layers so long as these layers are in the effective zone of the foundation. The effect of the reinforcement on the bearing capacity of a circular footing is more than that of a ring footing. Test results do show a good agreement with the numerical results, considering the behavior. More increase is observed in the bearing capacity ratio of sandy soils in comparison with fine-grained soils due to more interlocking between soil particles and the reinforcements.

REFERENCES

Binquet J, Lee KL (1975) Bearing capacity tests on reinforced earthslabs. Journal of Geotechnical Engineering ASCE 101 (12): 1241–1255.

Akinmusuru JO, Akinboladeh JA (1981) Stability of loaded footings on reinforced soil. Journal of Geotechnical Engineering ASCE 107 (6): 819-827

Hataf N, Bazyar MH (2000) Use of Tire shreds for bearing capacity improvement of shallow footings on sands The 3rd International Conference on Ground Improvement Techniques, September 25-26, Singapore, Singapore

Hataf N, Boushehrian JH (2003) Experimental and numerical investigation of the bearing capacity of model circular and ring footings on reinforced sand. Journal of Geotextiles and Geomembranes (21): 241-256

Ingold TS, Miller KS (1982) Analytical and laboratory investigations of reinfored clay second international conference on geotextiles, Las Vegas, USA: 587-592

Das BM (1987) Shallow Foundation in Clay with Geotextile Layers. Proceedings of the 8th Pan American Conference on Soil Mechanics and Foundation Engineering 2: 497-506

Mandal JN, Sah HS (1992) Bearing Capacity Tests on Geogrid-Reinforced Clay. Journal of Geotextiles and Geomembranes (11): 327-333

THE HORIZONTAL DEFORMATION STUDY ON THE GEOGRID REINFORCED EARTH RETIANING WALL

Y. Zhao [1], G.Q. Yang [2], B.J. Zhang [3] and P. Lv [4]

ABSTRUCT: The geogrid's horizontal deformation of geogrid reinforced earth retaining wall was observed by installing the gentle displacement gauge on the geogrids. And the strain rule which increase along with the tensile speed and the strength increasing were concluded from geogrid indoor test at the same time. The geogrid's horizontal deformation rule of geogrid reinforced earth retaining wall was concluded by observing and analyzing the indoor and spot test result and the master of horizontal deformation controlling was confirmed.

KEYWORDS: geogrid, reinforced earth retaining wall, horizontal deformation, test

INTRODUCTION

The geogrid as a kind of Geosynthetics, has the unique performance and efficacy compared with others Geosynthetics. For cost low and constructing convenient and beautiful, the geogrid reinforced earth retaining wall was applied to kinds of civil engineering at large.

When the geogrid is used to the reinforced structure as a kind of material, the geogrid bearing the transferred earth load by the tensile strength mostly and the engineering function acted. The interface character between geogrid and earth performance affect directly the safety and stability of geogrid reinforced earth retaining wall. But the factors which affect the tensile property of geogrid in the earth include tensile speed and ambient pressure. In order to analyze the stress-strain distribution of geogride reinforced structure precisely, the low tensile speed and difference ambient pressure at constructing in the soil should be taken into account which affect the tensile speed and the strength.

In order to study the the master of horizontal deformation controlling of reinforced earth retaining wall, a serial tests have been done.

TEST PROJECT

The test project at the geogrid reinforced earth retaining wall which locate at a free way of Hebei Province, and K56+835, K56+865, K56+935 and K56+965 four sections are selected to do the test. The wall is 5 m high and the is 50×20×15 cm channeled plate which preformed in situ with reinforced concrete and geogrid is pre-buried into the wall shingle and the length of geogrid is 5 m. The same filling is adopted in the reinforced earth body as behind the body.

The single direction geogrid is selected. Main index of the geogrids is shown in the Table 1. The Arrangement of instruments is shown in Fig 1.

Table 1 Main index of the geogrids in test

item	unit	parameter
long tensile strength	kN/m	≥90.0
tensile pull at 2% extensibility	kN/m	≥23.7
tensile pull at 5% extensibility	kN/m	≥45.2
peak strain	%	≤11.5

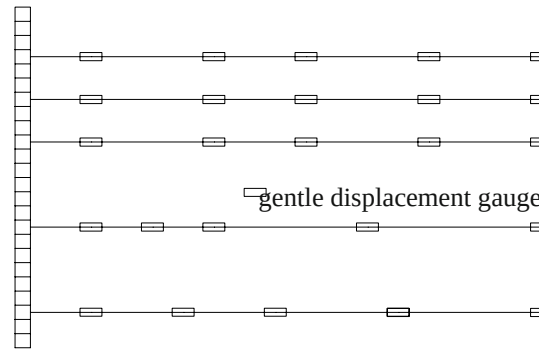

Fig.1 Arrangement of instruments

[1] Lecturer, Department of Civil Engineering, Shijiazhuang Railway Institute, CHINA, Email: zhaoyu790113@163.com
[2] Professor, Department of Civil Engineering, Shijiazhuang Railway Institute, CHINA
[3] Associate professor, Department of Civil Engineering, Shijiazhuang Railway Institute, CHINA
[4] Lecturer, Department of Civil Engineering, Shijiazhuang Railway Institute, CHINA

The inductant and frequency modulation and intelligent gentle displacement gauge is adopted to gauge the geogrid's horizontal deformation. The gentle displacement gauge are install on third layer geogrid at 0.6 m, 1.5 m, 2.4 m, 3.6 m, 5 m from the wall shingle respectively and 0.6 m, 1.2 m, 1.8 m, 3.3 m, 5.0 m on ninth layer and 0.6 m, 1.8 m, 2.7 m, 3.9 m, 5.0 m on fifteenth, eighteenth and twenty-first respectively. These are shown in Fig. 1.

GEOGRID TENSILITY TEST

The geogrid tensility test is assigned to Tinghua University. In order to study the effect between tensile rate and tensility, different tensile speed is used. The speed is 50 mm/min, 10 mm/min, 1 mm/min, 0.1 mm/min, 0.05 mm/min respectively. The test results at different speed are shown in the Table 2. Tensile test curve of geogrids between tensile strength and strain at different tensile speed is shown in Fig. 2.

Table 2 Tensile test result of geogrids

Tensile speed/ mm/min		50	10	1	0.1	0.05
Tensile strength /tensile moudle kN/m	2% extensibility	27.37	23.85	21.22	20.18	18.67
		1368.5	1192.5	1061	1009	933.5
	5% extensibility	51.33	50.04	41.92	39.85	37.68
		1026.6	1000.8	838.4	797.0	753.6
	10% extensibility	87.25	81.48	72.84	71.62	67.51
		872.5	814.8	728.4	716.2	675.1
	peak strain	94.17	89.52	79.18	78.26	76.35
		923.21	848.51	698.21	659.31	619.71
peak strain /%		10.02	10.2	10.55	11.34	11.87

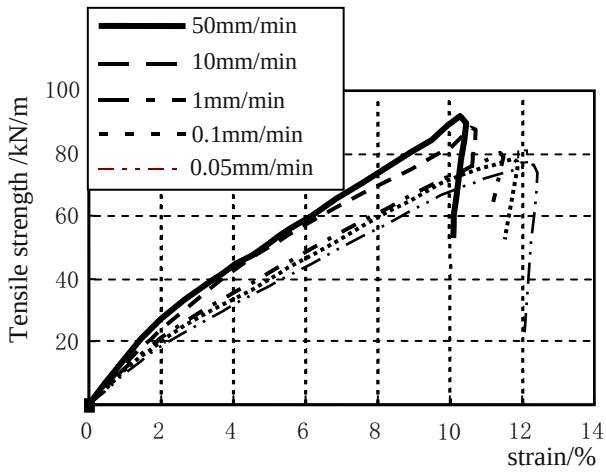

Fig. 2 Tensile test result of geogrids

From the test result, we can concluded that the peak strain increase 20.78% when the tensile speed decrease from 50 mm/min to 0.05 mm/min. for the same geogrid, the tensile strength is higher and the degree affected by the tensile speed is smaller. From Fig. 3, we can conclude that the peak strain decrease with the tensile speed increasing and the tensile strength decreasing scope become smaller with it becomes higher. At the same speed, the peak strain will be higher with the geogrid tensile strength becomes lower.

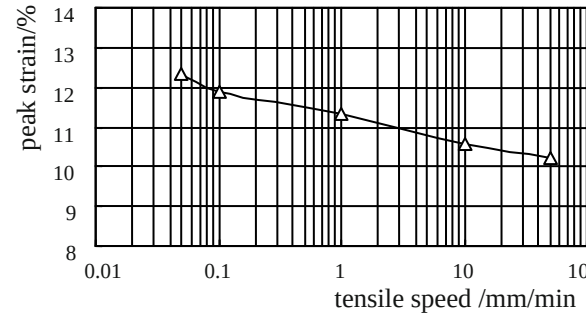

Fig. 3 The curve of peak strain and tensile speed

HORIZONTAL DEFORMATION OF GEOGRID REINFORCED RETAINING WALL

The geogrid deformation different at different layer for the wall shingle stress is different. The geogrid stress is also different at the same layer for the length to the wall shingle different. For the complexity of reinforced mechanism of reinforced earth retaining wall, even under the same load, the earth pressure of wall-rear is different, too. So the deformation is different with the layer different and even at the same layer is different with the length to wall shingle different. The deformation of the geogrid is shown in Fig. 4.

From Fig.4, we can conclude that the maximum measured strain of geogrid is not excess 0.50% at construction period. The geogrid strain is become larger with the depth of filling earth increase, and the strain at the same geogrid is not linear distribution with the length from the wall shingle change. The mostly strain curve have two peak and individual strain only have one peak. The peak close to the wall shingle is the location where latent fracture surface in the reinforced earth body locates. The further peak arises for the reinforced body as a whole bears the stress. The further peak dose not arise at the end of geogrid and location changed with layer change. All the characters show that the length of geogrid should change with layer change for the anchoring action and the character of reinforced earth body filling dose not same to behind it. So the filling characters change gradually from reinforced body to ordinary filling and the anchoring action is little at the end of geogrid.

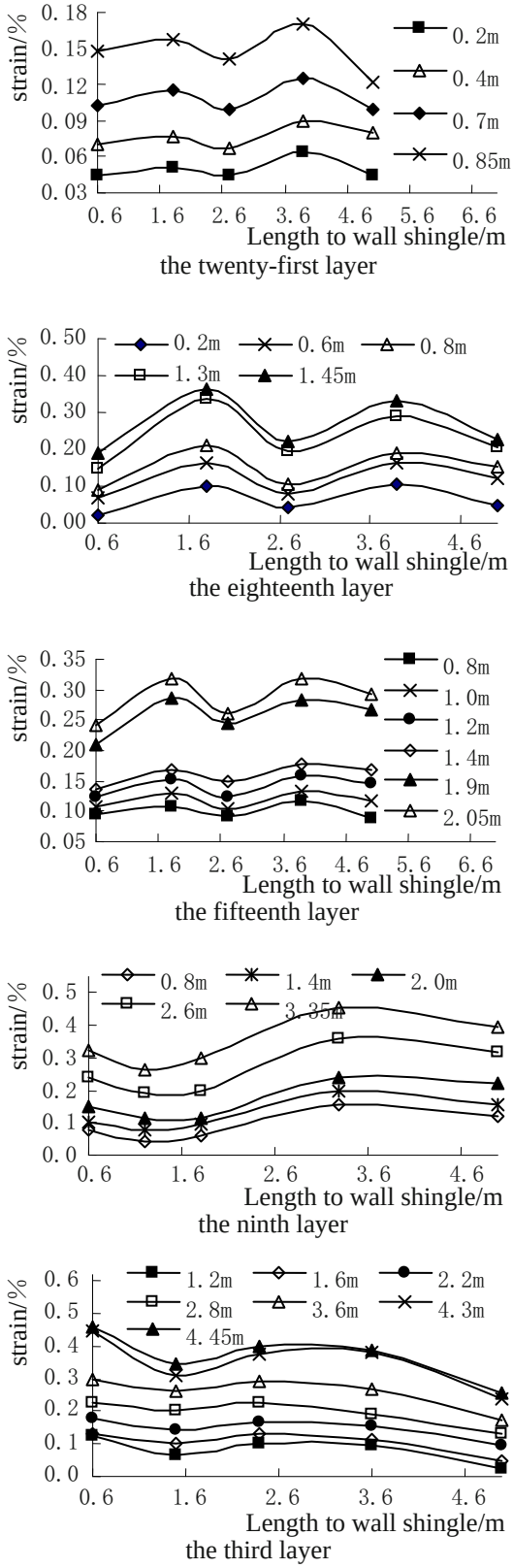

Fig.4 Variation of geogrid's strain with height of wall

The geogrid strain change curve at K36+835 section with time increasing after completed is shown in Fig. 5. We can learn that the geogrid strain increase to peak volume and then decrease from peak to steady situation when the wall completed. All strain volume dose not excess 0.50%.

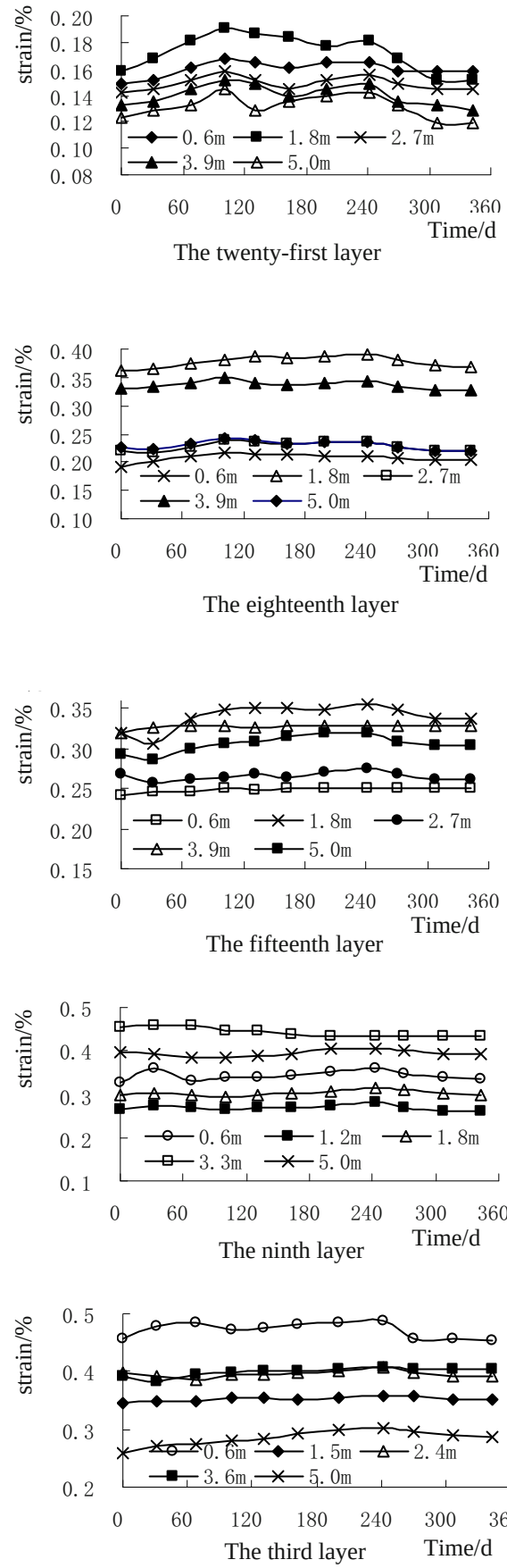

Fig. 5 Variation of geogrid's strain with time

By analyzing the Figs. 4 and 5, we can conclude that the geogrid strain occurs and complete during constructing. The geogrid strain is very small after the wall completed. These meet that the earth pressure is larger at constructing, so the master of horizontal deformation controlling is constructing controlled.

CONCLUSIONS

(1) From the indoor test result, we can find that the strain of geogrid increase with load increase, and is affected by tensile speed directly. The peak strain becomes smaller with tensile speed larger. This reflected in constructing is the strain of geogrid increase with depth of filling larger and also controlled by construct rate. This is confirmed from the result of test in site.

(2) After analyzing the result of test in site, we can conclude that the horizon deformation of geogrid reinforced retaining wall is larger, and dose not change after the wall completed. This shows that the deformation is controlled mainly by loading. For many construction machines are used, which make loading become not less than the loading after completed, the horizon deformation of geogrid reinforced retaining wall is larger at constructing, and dose not change after completed.

(3) The master of geogrid horizontal deformation controlling is constructing controlled during constructing period, and controlling the construct rate above all. This show that the geogrid reinforced retaining wall construction control, above all the constructing rate control, is the master of geogrid horizontal deformation controlling.

REFERENCES

Yang GQ, Cai Y, and Su Q (2003) Deformation and bearing study of reinforced earth retaining wall at high embankment. Rock Mechanics and Engineering Journal 22(2): 321-326.

Yang GQ, Cai Y (2000) Multilevel steps reinforced earth retaining wall test study. Geotechnics and Engineering Journal 22(2): 254-257

Wang X, Zhou SH, Gu XS (2005) Test study reinforced earth retaining embankment wall. Civil Engineering Journal 38(10): 119-124

COMPARE ANALYSIS OF INFLUENCE OF SOIL PROPERTY UPON GEOSYNTHETICS REINFORCEMENT EMBANKMENT

C. Yan[1], S. Li[2] and J.P. Zhou[3]

ABSTRACT: The reinforcement effects of geosythetics in soft subsoil case are studied in this paper, and a Duncan-Chang nonlinear numerical model based on the finite element method (FEM) is developed. The influence of the parameters of soil properties upon the effect of reinforcement is discussed in this paper. And the influence of the parameters of soft soil properties, such as c, φ and γ upon the displacements in toe and middle of the reinforced embankment is also analyzed in this paper. Reinforcement mechanism of geosynthetics is also discussed in this paper and several conclusions are reached.

KEYWORDS: geosynthetics, reinforcement mechanism, embankment, FEM, parameters of soil properties

INTRODUCTION

With the development of geotechnical engineering techonology, geosynthetic reinforcement has been widely used. It can improve stability,decrease lateral and vertical soil deformation (Shen 1998; Jayantha 2000).

The finite element method has been widely used to analyzed geosythetic-reinforced structures (Hinchbergen and Rowe 2003; Qin 2000). The FEM analysis allows the study of the extension of plastic zones and the stress field in the foundation soil (Tandjiria and Low 2002; Zhou 2000).

In this paper the influence of the parameters of soft soil properties upon the effect of reinforcement is analyzed. A numerical method based on the finite element method is used. The geosynthetics is modeled with isoparametric bar element. Soil continuum is modeled by four nodes isoparamrtric elements. To model the soil-geosynthetics interaction, Goodman elements are used at the interface. And a program has been developed. Some test results have been compared with the results calculated by this program, and they were in good agreement.

The finite element meshes and the foundation situations are shown in Fig. 1. The studies involve the numerical results of an embankment built on different foundation situations. The embankment is 8 m height, symmetric, with a final platform of 24 m width and slope inclined *V*/*H*=2/3.

Analyses A and B are similar except in the fact that the first one has reinforcement in the embankment base and the second one dose not. The reinforcement is placed in the embankment base.

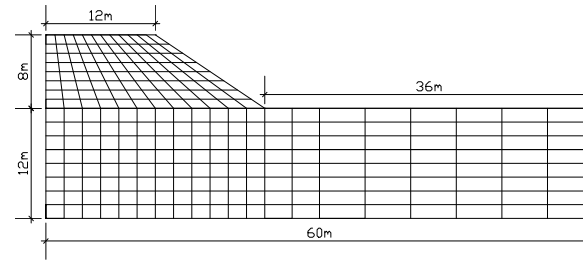

Case A Unreinforcement; Case B Reinforcement

Fig. 1 Finite element mesh and foundation situation

Due to not getting stability factor directly from the results calculated by FEM, the area ratio of plastic region is used to analyze the effect of reinforcement in this paper. The value of area ratio of plastic region is indicated by the number of meshes in plastic region / the total number of meshes in foundation.

Table 1 shows the main parameters of the soil-geosynthetic interfaces and geotechnical properties of soils. The elastic modulus of reinforcement is 1,250 kN/m.

[1] Professor, Department of Civil Engineering, Tianjin University, CHINA. Email:cytj@tju.edu.cn
[2]Associate Professor, Department of Civil Engineering, Tianjin University, CHINA. Email:lisa@tju.edu.cn
[3] Associate Professor, Urban Oil and Gas Distribution Technology, China University of Petroleum, CHINA. Email: ZJP1107@eyou.com

RELATIONSHIP BETWEEN PARAMETERS OF SOIL PROPERTIES OF SUBSOIL AND AREAS OF PLASTIC REGION

Parameters of soil properties of subsoil involve mainly: cohesion, inter friction angle, module coefficient, volume module index, unit weight, failure ratio, module index and volume module coefficient. As follows, the relationship between these parameters and plastic region will be analyzed. in analyzing, at a time only one parameter will be changed and others will be unchanged.

In Table. 1, the cohesion, inter friction angel and module coefficient of subsoil have low initial values.

Table 1 Parameters of soil-geosynthetic interfaces and soil properties

Items	Unit Weight γ (kN/m^3)	Module Coefficient K	Module index n	Failure Ratio R_f	Volume Module Coefficient K_t	Volume Module Index m	Cohesion c (kPa)	Inter Friction Angle φ	$\Delta\varphi$
Embankmant	19.0	200	0.6	0.9	100	0.4	17	16.4°	—
Foundation	17.0	50	0.4	0.7	20	0.7	1.2	14°	—
Sand Layer	17.5	680	0.446	0.96	230	0.34	0	32°	5°
Reinforce-mant-sand Layer	—	500	1.38	0.96	—	—	—	30.2°	—

In this case, the areas of plastic region in foundation are very large. When the embankment is unreinforced, the number of element meshes in plastic region is 107. It is 66.9% of total number of element meshes in foundation (The number of element meshes in foundation is 160.). In this analysis, the change of the areas of plastic region will be researched while one certain parameter is increased gradually and others keep unchanged.

Fig. 2 shows the relationship between the area ratio of plastic region and the cohesion of the soil in foundation. Fig. 3 shows the relationship between the area ratio of plastic region and the inter friction angel of the soil in foundation.

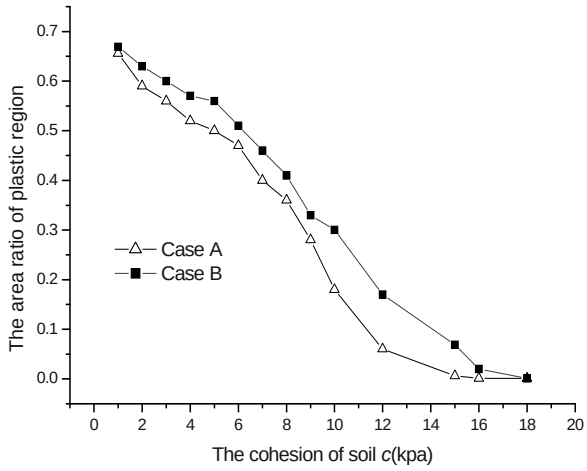

Fig. 2 Area ratio of plastic region vs the cohesion of soil

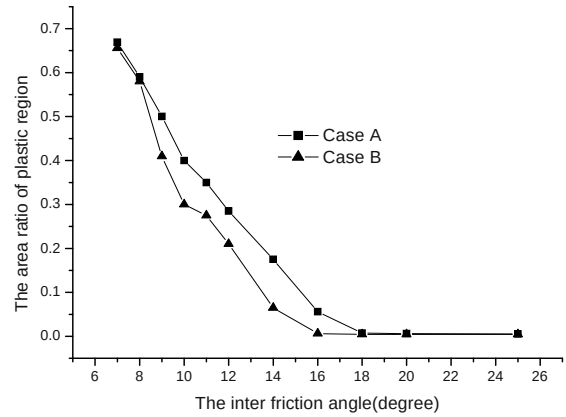

Fig. 3 Area ratio of plastic region vs the inter friction angle of soil

When cohesion of the soil increases from 2 kPa to 15 kPa, the area ratio of plastic region reduces from 0.699 to 0.068 in unreinforced embankment and from 0.656 to 0.0063 in reinforced embankment, respectively. When the inter friction angel of soil in foundation increases from 7° to 16°, the area ratio of plastic region reduces from 0.669 to 0.056 in unreinforced embankment and from 0.656 to 0.0063. But when the cohesion or inter friction angel of soil in foundation keep on increasing, the area ratio of plastic region will not reduce any longer. In this case, reinforcement has little effect to reduce the area of plastic region. The effect of the reinforcement is better when the cohesion of soil in foundation is between 4 kPa to 14 kPa, or the inter friction angel of soil in foundation is between 8°to 16°.

Fig. 4 shows the relationship between the area ratio of plastic region and the module coefficient of the soil in foundation.

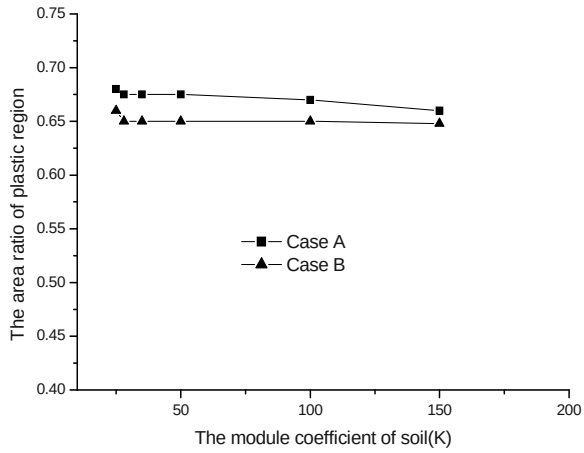

Fig. 4 Area ratio of plastic region *vs* the module coefficient of soil

Fig. 5 shows the relationship between the area ratio of plastic region and the volume module coefficient of the soil in foundation. It is obviously that the module coefficient and the volume module coefficient of the soil in foundation have little effect to the area of plastic region. Its influence can be ignored.

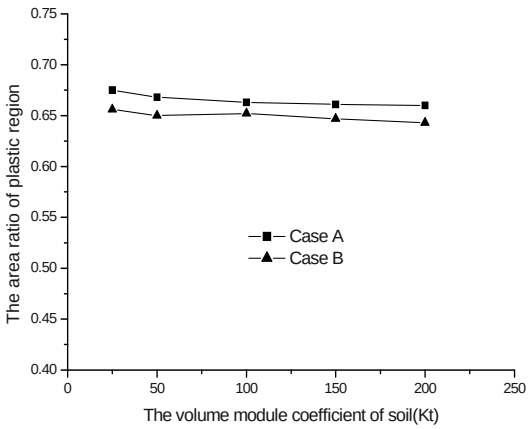

Fig. 5 Area ratio of plastic region vs the volume module coefficient of soil

Fig. 6 shows the relationship between the area ratio of plastic region and the unit weight of the soil in foundation.

Fig. 7 shows the relationship between the area ratio of plastic region and the failure ratio of the soil in foundation. One can see that: unit weight of the soil in foundation has some influence to the area of plastic region. When the unit weight of the soil in foundation increases from 1.4 T/m^3 to 2.0 T/m^3, the area ratio of plastic region reduces from 0.725 to 0.595. And while the unit weight of the soil in foundation is more than 1.5 T/m^3, the effect of the reinforcement is better. The failure ratio has little influence to the area of plastic region and to the effect of the reinforcement.

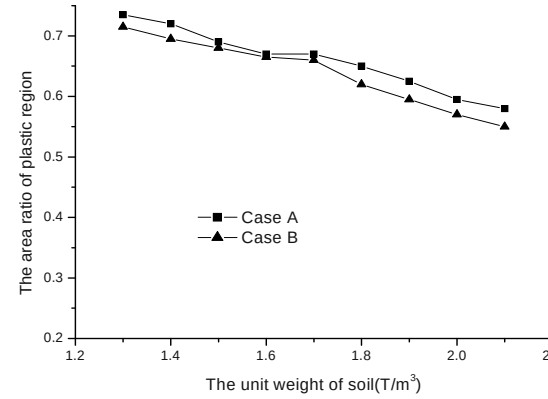

Fig. 6 Area ratio of plastic region vs the unit weight of soil

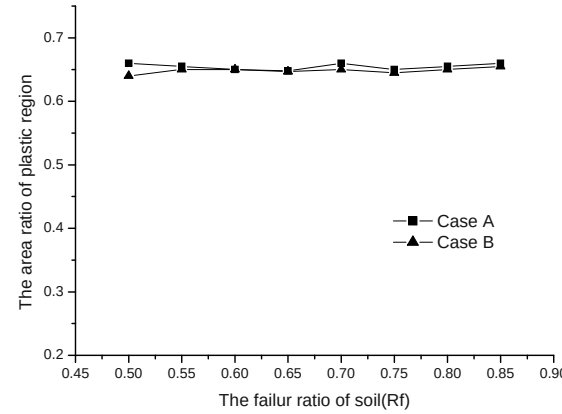

Fig. 7 Area ratio of plastic region vs the failure ratio of soil

RELATIONSHIP BETWEEN THE PARAMETER OF SOIL PROPERTIES OF SUBSOIL AND THE DISPLACEMENT OF FOUNDATION

At follows, the effect of the parameters of soil properties of subsoil upon the displacement in toe and middle of the embankment will be discussed. Calculating the embankment by using the parameters of soil properties of subsoil as indicated in Table 1, by FEM, it can get the following results. In case of unreinforcement, the horizontal displacement in toe of the embankment is 1.01 m and the vertical displacement in center spot on the base of the embankment is 0.791 m. But in case of reinforcement, the horizontal displacement in toe of the embankment is 0.887 m and the vertical displacement in center spot on the base of embankment is 0.732 m. The

same analysis method like above is used to analyze the change of the horizontal displacement in toe of the embankment and the vertical displacement in center spot on the base of the embankment, and the deformation curve is drawn.

Figs. 8 and 9 show the relation curves between the horizontal displacement in toe of the embankment and the vertical displacement in center spot on the base of the embankment and the cohesion and the inter friction angle in foundation, respectively. One can that with the increasing of the cohesion in foundation, the horizontal displacement in toe of the embankment and the vertical displacement in center spot on the base of the embankment have the trend of descend and when the cohesion in foundation is more than 6 kPa, the trend of descend of displacement is more obviously. Reinforcement has more effect to reduce the horizontal displacement, but has little effect to the vertical displacement.

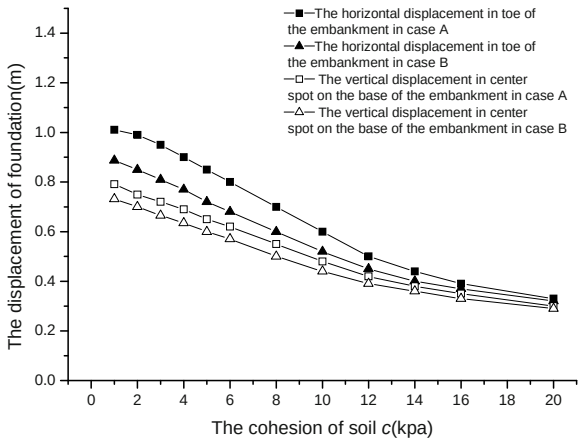

Fig. 8 Displacement of foundation vs the cohesion of soil

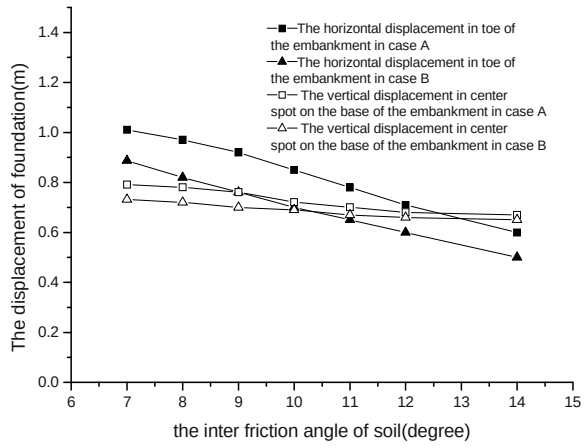

Fig. 9 Displacement of foundation vs inter friction angle of soil

Fig. 9 shows, with the increasing of the inter friction angle in foundation, the horizontal displacement in toe of the embankment and the vertical displacement in center spot on the base of the embankment have the trend of descend. When the inter friction angle is between 7°and 12°, the reduce of the displacement is more obviously. However when the inter friction angle is more than 14°, the decrement of the vertical displacement is little. Maybe the reason is that the inter friction angle is not match for other parameters of soil in foundation. While other parameters are still little, only increasing inter friction angle has not any effect to reduce the displacement of embankment. From the curve in Figs. 8 and 9, one can see that the effect of reinforcement is reducing the lateral displacement of the embankment.

Figs. 10 and 11 show the relation curves between the horizontal displacement in toe of the embankment and the vertical displacement in center spot on the base of the embankment and the module coefficient and the volume module coefficient of soil in foundation, respectively. Fig. 10 indicates that when the module coefficient of soil in foundation increases from 50 to 150, the horizontal displacement in toe of the embankment reduces from 1.01 m to 0.366 m and the vertical displacement in center spot on the base of the embankment reduces from 0.887 m to 0.351 m in case of reinforcement; the horizontal displacement in toe of the embankment reduces from 0.791 m to 0.278 m and the vertical displacement in center spot on the base of the embankment reduces from 0.732 m to 0.275 m in case of unreinforcement. The module coefficient of soil in foundation has more significant effect to the displacement of foundation than the coefficient and the inter friction angle. It is a sensitive parameter.

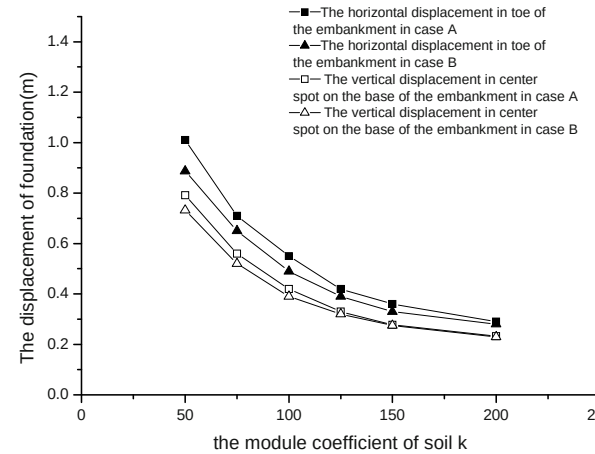

Fig. 10 Displacement of foundation vs the module coefficient of soil

However, the volume module coefficient of soil has little effect on the displacement in foundation. The increasing of the volume module coefficient of soil

makes a little decrement of the vertical displacement in center spot on the base of the embankment, but the change of the horizontal displacement in toe of the embankment can be ignored. When the value of the volume module coefficient is between 20 and 50, the trend of displacement curve in Fig. 11 is sharper, but with the increasing of the value of the volume module coefficient the change of displacement curve can be ignored. The reason is that in the case, the volume module coefficient is not match for other parameters any longer.

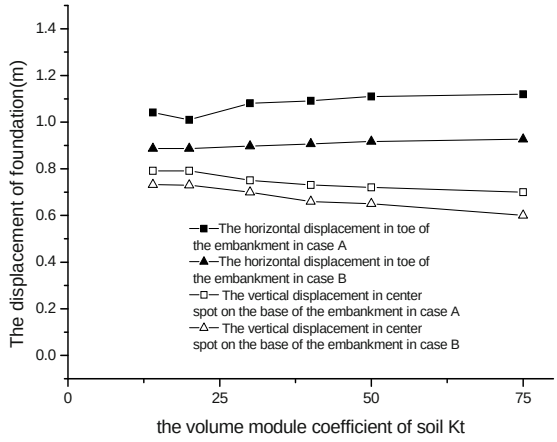

Fig. 11 Displacement of foundation vs the volume module coefficient of soil

While the value of the module coefficient of soil is between 20 and 100, the reinforcement has significant effect. Like above, the reinforcement has more effect of reducing the horizontal displacement than the vertical displacement.

Figs.12 and 13 show the relation curves between the horizontal displacement in toe of the embankment and the vertical displacement in center spot on the base of the embankment and the unit weight and the failure ratio of soil in foundation, respectively. From Fig.12, one can see that the unit weight of soil in foundation has little influence to the displacement in foundation and the curve in Fig.11 is gentle. But with the increasing of the value of the unit weight of soil in foundation, the horizontal displacement in toe of the embankment and the vertical displacement in center spot on the base of the embankment have a little decrement.

The influence of the failure ratio upon the displacement in foundation is very significant. With the increasing of the Rf, the increasing of the displacement is obvious. When Rf is increased from 0.4 to 0.7, the horizontal displacement in toe of the embankment reduces from 0.340 m to 1.01 m and the vertical displacement in center spot on the base of the embankment reduces from 0.267 m to 0.791m in case of unreinforcement; the horizontal displacement in toe of the embankment reduces from 0.328 m to 0.887 m and the vertical displacement in center spot on the base of the embankment reduces from 0.261 m to 0.732 m in case of reinforcement. Hereby, the Rf of soil has significant influence to the displacement in foundation, such as the module coefficient of soil. So, the Rf of soil is also a sensitive parameter. Fig. 13 also indicates that with the increasing of Rf, the effect of Rf upon the displacement in foundation is more obvious. So the value of Rf is very important. From the figures, one can see that reinforcement has more influence on reducing the horizontal displacement than the vertical displacement. As same time, when the value of Rf is more than 0.6, reinforcement can get better efficiency.

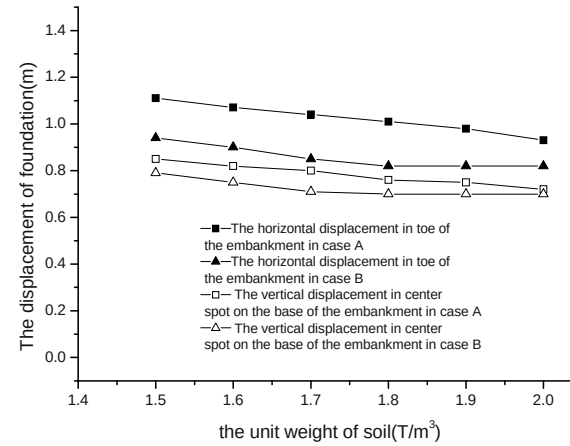

Fig. 12 Displacement of foundation vs the unit weight of soil

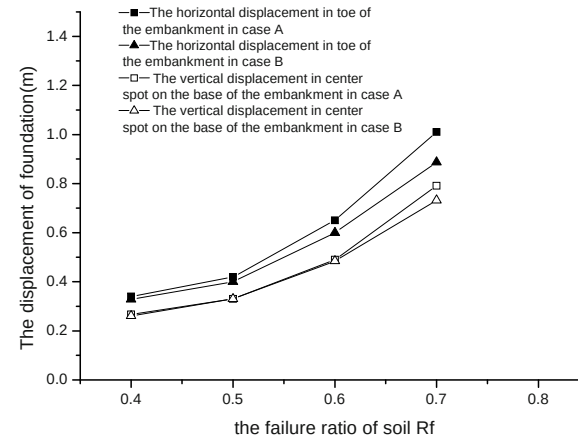

Fig. 13 Displacement of foundation vs the failure ratio of soil

CONCLUSIONS

From the study, the following conclusions can be drawn:

(1) For the area of plastic region, the parameters of soil properties which have significant influence on it are the inter friction angle, the cohesion and the unit weight of soil. In these parameters, the most important one is the inter friction angle of soil. For the displacement of foundation, the parameters of soil which have significant influence on it are the module coefficient, the failure ratio, the cohesion, the inter friction angle and the unit weight of soil. The module coefficient and the failure ratio of the soil in foundation are the sensitive parameters.

(2) When the area ratio of plastic region is between 12.5% and 43.8%, reinforcement has better effect on reducing the area of plastic region. But when the foundation soil is too soft, only reinforcement has little effect on reducing the area of plastic region.

(3) Though the module coefficient, the volume module coefficient and the failure ratio of soil have little effect on reducing the area of plastic region, their values of these parameters have significant influence on the displacement of foundation. So selecting the suitable values of these parameters is very important in calculating displacement by FEM.

(4) Reinforcement has great effect on reducing the horizontal displacement in foundation, but has little effect on reducing the vertical displacement. When the soft subsoil is thin, reinforcement has great effect on reducing the horizontal displacement in foundation and has a little effect on reducing the vertical displacement.

(5) The module coefficient, the volume module coefficient, the volume module index and the module index of soil reflect the module of soil. The cohesion and the inter friction angle of soil reflect the intension of soil. The results calculating by FEM indicate that only considers the intension is not perfectly, the influence of the module of the material can't be ignored. The classic method of limit equilibrium that only considers the intension and ignores the module is not suitable. FEM can model the working states of embankment and it is a good method to fix the classic method of limit equilibrium.

(6) From the displacement embankment, it can reflect the effect of the geosynthetics upon the stability of embankment. In some cases, the intension of geosynthetics is not enough to reduce the area of the plastic region, but it can reduce the horizontal displacement in toe of the embankment and restrict the vertical displacement. Hereby, it can confine the rupture of embankment and the shear failure of subsoil and increase the stability of embankment. However, since the classic method of limit equilibrium not considers this case, so it could not get the correct calculating results accorded with the test results.

REFERENCES

Hinchbergen SD, Rowe RK (2003) Geosythetic reinforced embankments on soft clay foundations: Predicting reinforcement strains at failures. Geotextiles and Geomembrance 21(1):151-175

Jayantha Kodikara (2000) Analysis of Tension Development in Geomembrances Placed on Landfill Slopes. Geotextiles and Geomembrances 18(1): 47-61

Qing F (2000) Analysis of the Reinforcement Embankment on Soft Soil by Geosynthetics with the Finite Element. Master Thesis, Tianjin Univercity, China

Shen ZJ (1998) Limit Analysis of Soft Ground Reinforced by Geosynthetic. Chinese Journal of Geotechnical Engineering 20(4):82-86

Tandjiria V, Low BK (2002) Effect of reinforcement force distribution on Stability of Embankments. Geotextiles and Geomembrance 20(3): 423-443

Zhou JP (2000) Applied Research of Geo-sythetics in Reiforced Embankments. Master Thesis, Tianjin Univercity, China

Proceedings of the 4th Asian Regional Conference on Geosynthetics
June 17 - 20, 2008 Shanghai, China

DESIGN AND CONSTRUCTION OF A 20-METER HIGH REINFORCED SOIL RETAINING WALL

S.Q. Gui[1], Z. B. Zhu[2], Q. Li[3] and P. Luo[4]

ABSTRACT: The project is located in Fengjie County of Chongqing City, China. The retaining wall belongs to a road embankment, which passes through a gully. There are two main concerns about the project, i.e., the stability of the 20-meter high embankment itself and the possible instability of the embankment together with the deposits in the gully along the interface between the deposits and the rock mass. To solve the former problem, a reinforced soil retaining wall with wrap-around geogrids inside and near-vertical reinforced concrete rigid panel outside was employed. For the latter problem, stabilized piles with pre-stressed anchors were used below the reinforced soil retaining structure. The paper discussed the process of the design and construction of the project. At present, the project is still under construction.

KEYWORDS: reinforced soil wall, reinforced concrete rigid panel, design, construction

INTRODUCTION

The project discussed in this paper is located in Fengjie County of Chongqing City, China. Originally, there is a tight turn of a local city road which is along an alluvium valley (see Fig. 1). In order to make better of the transportation conditions there and increase useful land resources, the local government decided to make the road to be straight by cutting the tight turn into a slight turn (Gui 2007).

Fig. 1 The photo of the site (the red line shows the new road and the old one was just behind the line)

The new useful land through the dismantlement of the old road will be used for real estates development of building two 33-story high apartments.

The 20-meter high embankment of the new road will be founded on the deposits in the gully. Therefore, there are two main concerns about the project, i.e. the stability of the 20-meter high embankment itself and the possible instability of the embankment together with the deposits in the gully along the interface between the deposits and the rock masses beneath.

The paper discussed the solutions for the problem through combination of reinforced soil retaining wall with stabilized piles.

GEOLOGICAL CONDITIONS

The site is belonging to hill slopes with gradient of 30－40 degree from the view of physiognomy.

The top cover is composite of artificial fills and alluvium deposits with the maximum thickness of 26 meters. The bed rock is the clayed limestone with the highly weathered rock layer of 1.09－7.61m. No big faults come along the site.

STABILITY ANYLYSES

There are three stability problems of the projects, i.e. overall stability of the deposits together with the embankment, overall and local stability the reinforced soil retaining wall respectively. The first stability

[1] Director, Department of Geotechnical Engineering Design, Three Gorges Geotechnical Consultants Co., Ltd. (Wuhan), CHINA. Email: guishuqiang@vip.sohu.com
[2] Engineer, Three Gorges Geotechnical Consultants Co., Ltd., CHINA. Email: zhuzhengbiao8338@sina.com
[3] Engineer, Three Gorges Geotechnical Consultants Co., Ltd., CHINA. Email: lq_86583606@163.com
[4] Master student, China University of Geosciences, CHINA. Email: luopinghc@126.com

analysis was conducted with limit equilibrium method. The longitudinal profile was divided into 27 blocks (see Fig. 2), and under the minimum safety of factor of 1.3, the residual push forces were calculated, which is the most important parameters for the design of the stabilizing piles. Considering of the reasonable pile length (i.e., minimum length), the piles are placed in block No. 19. Under the saturated conditions and with shearing strength of soil (i.e., c=20.5 kpa and φ=17.5 degree) between cover fills and bedrock, the calculated residual push forces at No. 19 block on piles is 2800 kN/m (Gui 2003).

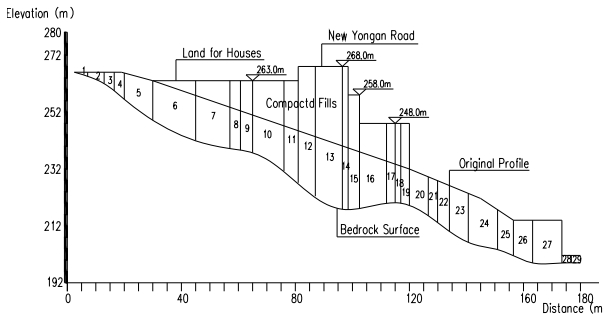

Fig. 2 The main longitudinal profile of the site for overall stability analysis purpose

The stability analyses (overall and local one) of the reinforced soil retaining wall were conducted by the software of ReSSA (2.0), which can consider circular slip surfaces (Bishop Method) and 2- or 3-part wedge slip surfaces (Spencer Method) stability analyses (Leshchinsky 2005). For this project, the factors of safety of overall and local one are controlled to be larger than 1.25 and 1.10 respectively according to Chinese design code.

SOLUTIONS

The reinforced soil retaining wall together with traditional masonry and pile wall are employed for the new road embankment. The total height of the reinforced soil wall is 20 meters, which includes two 10-meter high walls with a 3-meter bench. Total 58 layers' HDPE geogrids with controlled tensile strength of 110 kN/m^2 and 90 KN/m^2 are used. The uppermost 5-meter wall is double reinforced with two concrete panels oppositely. The geogrids are wrapped around at the outer end with a vertical face. The reinforced concrete panels are installed later by the junction of steel bar with geogrids reinforced soil wall (see Fig. 4).

Stabilizing piles are employed in the front of and below the reinforced soil structures. Considering the push forces on the piles were so big, stabilizing piles were combined with pre-stressed anchors (Gui 2007).

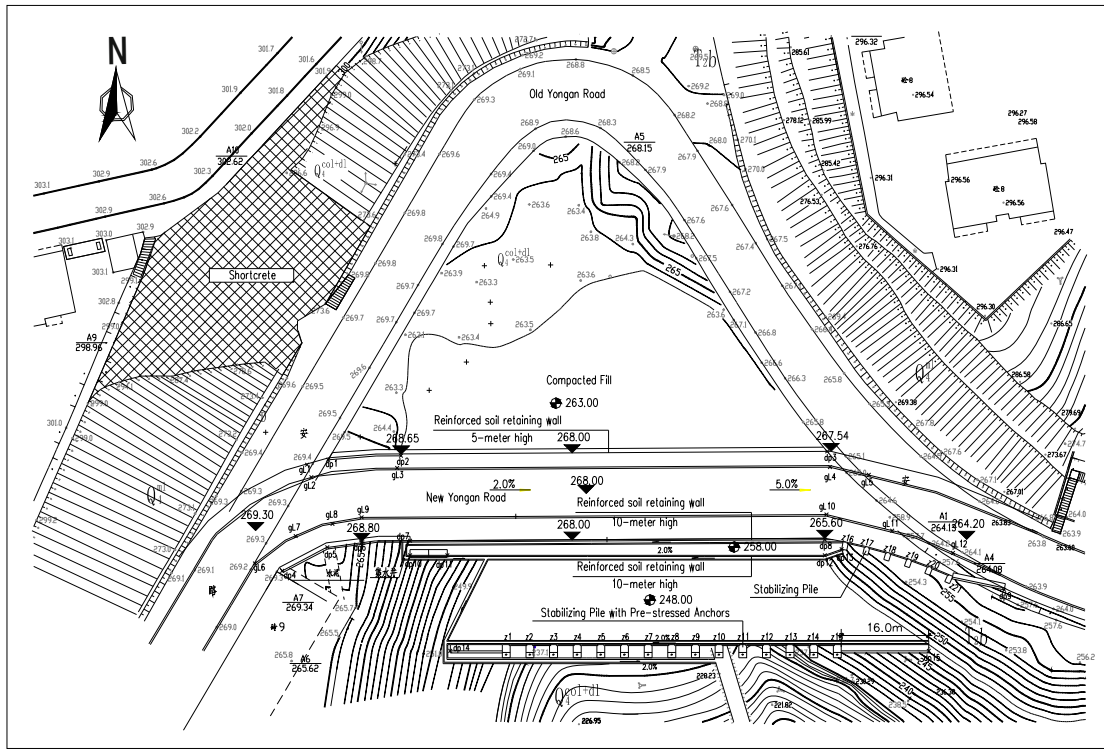

Fig. 3 Layout of the Project

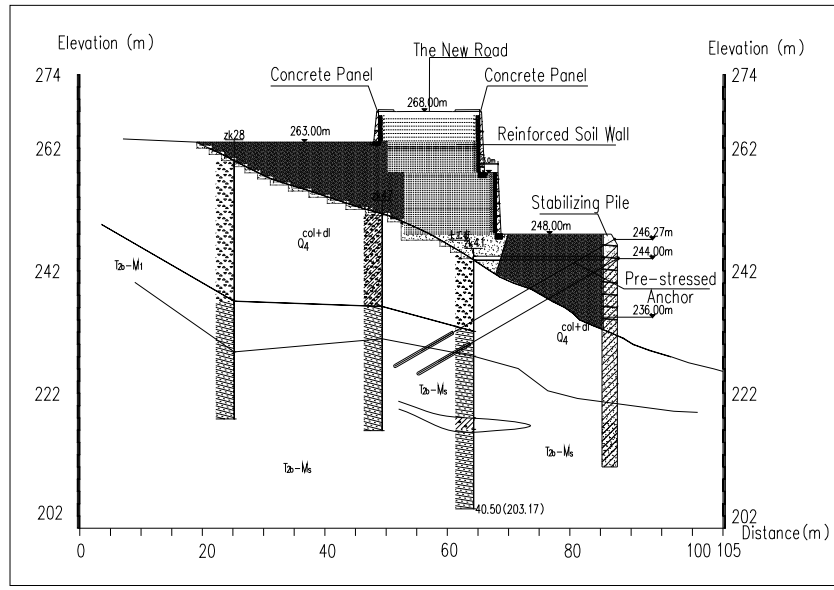

Fig. 4 Cross Section of the Project

Fig. 5 Construction Site Photos Taken in March 5, 2008 (by the courtesy of Mr. Du Jingyan)

CONCLUSIONS

Reinforced soil retaining wall is one of the good retaining structures. However, considering that its retaining efforts are limit, in many cases, the structures shall be combined with some other stronger retaining structures to solve the overall instability problems.

The paper chooses one case history of a road rehabilitation project in China to expatiate on the subject. A reinforced soil retaining wall with wrap-around geogrids inside and near-vertical reinforced concrete rigid panel outside was employed in the project, and stabilized piles with pre-stressed anchors were used below the reinforced soil retaining structure as well. Despite the project is still under construction, we believe that it is a good attempt and hope it will come into success.

ACKNOWLEDGEMENTS

Great appreciation shall be given to Mr. Biquan Yang, Mr. Changwu Zhu, Mr. Zheming Chen, Mr. Liang Fu and Miss Fenny Huang for their kind helps for the paper.

REFERENCES

Gui SG, Li Q, Wu QJ (2007) Design Report of the Quimen Town Project, Three Gorges Geotechnical Consultants Co., Ltd

Gui SQ (2003) Calculating and Design Methods and Their Applications of Stabilizing Piles with Pre-stressed Anchor Cables in Landslides Remediation Works. China University of Geosciences

J David Rogers (1992) Recent Development in Landslide Mitigation Techniques. Reviews in Engineering Geology, IX: 95-11p, Geological Society of America

Leshchinsky D (2005) Design Concepts of Reinforced Walls and Slopes: Review of Basics. Materials of One-Day Workshop on Geosynthetics Reinforced Structures. Bangkok, Thailand, 2005

Leshchinsky D, Hu Y, Han J (2004) Limited Reinforced Space in Segmental Retaining Walls. Geotextiles and Geomembranes 22: 543-553

Gui SQ, et al. Enhancing Internal Stability of Reinforced Soil Slopes with Anchors. Proceedings of the 8th International Conference on Geosynthetics

GEO (2002) Guide to Reinforced Fill Structure and Slope Design. Geotechnical Engineering Office, Hong Kong

Zornberg JG, Leshchinsky D (2003) Comparison of International Design Criteria for Geosynthetics-Reinforced Soil Structures. Proceedings of the International Symposium on Earth Reinforcement-Landmarks in Earth Reinforcement, Ochiai, et al (eds), A.A. Balkema 2: 1095-1106

Reinforced Slope Stability analysis: Program ReSSA (2.0). ADAMA Engineering, Inc

Soil Improvement and Ground Improvement

GEOSYNTHETIC REINFORCED POND ASH SUBGRADE FOR RURAL ROADS

G. Venkatappa Rao[1] and Goutam K. Pothal[2]

ABSTRACT: Pulverised fuel ash, produced in huge quantities by thermal power plants of India, require large land area for disposal and causes environmental hazards. The bearing capacity of a weak pond ash subgrade can be increased by placing a granular course of required thickness on top of the pond ash fill. The load bearing capacity can be increased further and the thickness of the granular course can be reduced by providing a layer of geosynthetics at the interface of the two layers. In the present study, the bearing capacity behaviour of a rectangular load under static compression on the surface of the granular wet mix macadam (WMM) layer underlain by pond ash with a layer of geosynthetic at the interface are presented. Two types of pond ashes and different types of both polymeric geogrids and coir woven geotextiles have been used the study. The results obtained from the load tests at different thicknesses of the WMM layer with and without different types of geosynthetic reinforcement have been presented. The results show that lower thickness of WMM layer with geosynthetics at the interface perform better than that with thicker WMM layer without reinforcement. The effectiveness of coir woven geotextiles for rural road use is highlighted.

KEYWORDS: bearing capacity, pond ash, WMM, geosynthetic, geogrids, geotextiles and coir

INTRODUCTION

Pulverised fuel ash, the by-product of thermal power plants is considered as solid waste and its disposal is a major problem from environment point of view and also it requires lot of disposal areas. Utilization of pond ash to the maximum possible extent is a worldwide problem. To solve the problem, pond ash can be used as a subgrade material for road construction. There are two types of ash produced by thermal power plants, viz., fly ash and bottom ash. These two ash mixed together are transported to the ash pond and this deposit is called pond ash. The decreasing availability of good quality soil for subgrade has led to the increased use of pond ash, whose bearing capacity is relatively low. The bearing capacity of a weak pond ash subgrade can be increased by placing a granular course of required thickness on top of the compacted pond ash subgrade. The load bearing capacity can be increased further by providing a layer of geosynthetics at the interface of the two soil layers. The thickness of the top granular course can be further reduced by intrusion of geosynthetic layer at the interface.

Numerous studies on the bearing capacity of double layered soil systems have been reported by different researchers by taking different types of subgrade and base course material and reinforcements. Meyerhof (1974) has proposed a theory for the ultimate bearing capacity of sand layer overlying a clay layer in an undrained condition. Brown et al (1985) conducted a series of tests to study the effectiveness of a poly-propylene geogrid in improving the performance of pavement, such as resistance to rutting, reflective cracking and fatigue cracking. They also reported that the geosynthetic reduced the rut depth by 20 % to 58 %. Sheo Gopal (1993) conducted the static loading tests in a model with Delhi silt as subgrade (270 mm) and different thicknesses of WBM with non-woven geotextiles and geogrid at the interface. Dixit (1994) conducted the static loading tests on a model by varying the base course, subgrade material reinforced with and without a non-woven geotextile, a woven geotextile and a geogrid at the interface with WBM as base course (100 mm thick) and kaolinite as subgrade (270 mm thick). Khing et al. (1994) also conducted tests for the ultimate bearing capacity of a surface strip foundation supported by strong sand of limited thickness underlain by weak clay with a layer of geogrid at the sand-clay interface. Dutta (2002) and Venkatappa Rao, G. and Dutta, R. K. (2002) conducted static loading tests on a model by using kaolinite clay subgrade (270 mm thick) and sand layer (75 mm thick) as base course. He used 4

[1] Honorary Professor, Department of Civil Engineering, University College of Engineering, Osmania University, Hyderabad, INDIA. Email: gvrao.19@gmail.com
[2] Former Ph. D Student, Department of Civil Engineering, INDIAN Institute of Technology Delhi, New Delhi, INDIA. Email: gkpothal@gmail.com

types of coir woven geotextiles at the interface of the base course and the subgrade. The results of this study show that, a) the reinforcing effect of geosynthetic with small base course thickness is relatively better compared with that of the model with a higher thickness at higher deformation levels b) the behaviour of the models with geosynthetics, having 40% smaller thickness of base course is better than that of an unreinforced model, c) significant improvement occurs in the bearing pressure at a given vertical deformation with geosynthetic.

In the present study, the bearing capacity behaviour of a rectangular load under static compression on the surface of the granular wet mix macadam (WMM) layer underlain by pond ash with a layer of geosynthetic at the interface are presented. Two types of pond ashes and five different types of geosynthetics (2 types of polymeric geogrids and 3 types of coir woven geotextiles) have been used the study. The results obtained from the load tests at different thicknesses of the WMM layer with and without different types of geosynthetic reinforcement have been presented. In the present study the effects of the above parameters on both bearing capacity of rectangular load at specified settlement and ultimate bearing capacity have been made. Bearing capacity ratio is used to compare the performance of reinforced and un-reinforced pond ash.

The results show that lower thickness of WMM layer with geosynthetics at the interface perform better than that with thicker WMM layer without reinforcement. The effectiveness of coir woven geotextiles for rural road use is highlighted.

GEOMETRIC PARAMETERS

A rectangular load of width 'B' being supported on WMM layer of variable thickness overlain on compacted pond ash with and without geosynthetics reinforcement layers as shown in Fig. 1.

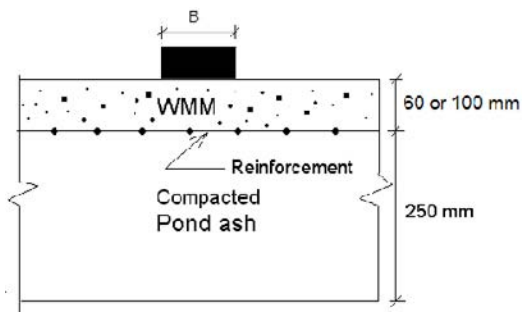

Fig. 1 Typical arrangement for test series with WMM and pond ash with reinforcement at the interface

For the present study, pond ash was selected as the subgrade medium and WMM as granular medium along with different types of geosynthetics (both polymeric geogrids and coir woven geotextiles) as the reinforcement material. Pond ash was procured from the ash pond of the Captive Power Plant (CPP) of National Aluminum Company Ltd. (NALCO), Angul, Orissa, India. From the ash pond two samples of pond ashes were collected. First one from near the slurry disposal point which is coarser in nature and second one far away from the slurry disposal point which is finer in nature. The detail properties are shown in Table 1. These two samples of pond ash are code named as "NC" and "NF" for our study.

The wet mix macadam (WMM) used in this study is prepared in the laboratory as per the norms of MORT&H (2001). Calculated amounts of aggregates were taken according to these specifications and maximum dry density and optimum moisture quantity were determined which are given in Table 2.

Table 1 Properties of pond ash

Physical properties		NF	NC
Grain Size	Gravel (> 4.75mm)	0	0
	C.Sand (4.75-0.475mm)	2	4
	F.Sand (0.475-0.075mm)	40	76
	Silt (0.075-0.002mm)	56	19
	Clay (< 0.002mm)	2	1
Specific gravity		2.02	2.48
Liquid limit (%)		48	33
Plastic limit (%)		Non-plastic	Non-plastic
Maximum dry density (kN/m^3)		10.7	13.6
Optimum moisture content (%)		34.5	25.2
Angle of internal friction (Deg.) at MDD		31	36

Table 2 Properties of WMM

Physical properties		Values
Particle size	> 53 mm	0
	< 53 mm & > 45 mm	1
	< 45 mm & > 22.4 mm	25
	< 22.4 mm & > 11.2 mm	25
	< 11.2 mm & > 4.75 mm	17
	< 4.74 mm & > 2.36 mm	10
	< 2.36 mm & > 0.6 mm	10
	< 0.075 mm	9
Maximum dry density (kN/m^3)		20.4
Optimum moisture content (%)		4.5

The geosynthetic reinforcements used for the study are of polymeric and natural fibre coir. The two types of polymeric biaxial geogrids used are of rigid and flexible types respectively as shown in Fig. 2. These geogrids were code named 'GGR' and 'GGF' respectively. The detailed dimensions and mechanical properties of the geogrids are given in Table 3. The three types of coir woven geotextile used for the study are shown in Fig. 3. These coir geotextiles were code named 'CWA', 'CWB' and 'CWC' respectively. The detailed dimensions and mechanical properties of these coir geotextiles are given in Table 4.

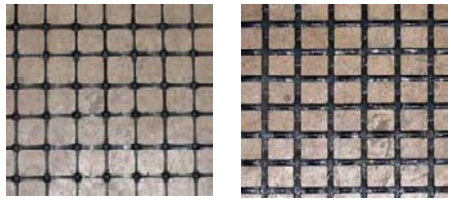

(a) Type GGR (b) Type GGF

Fig. 2 Geogrid Types

(a) Type CWA (b) Type CWB (c) Type CWC

Fig. 3 Coir Geotextile Types

EXPERIMENTAL ARRANGEMENT

The bearing capacity tests were conducted in a rectangular box measuring 750 mm (length) × 300 mm (width) × 400 mm (depth). The tank was made up of 12 mm perspex sheet. The tank was reinforced with a frame made up of mild steel angles so that there will be no lateral yielding of the box during compaction and loading. The inside walls of the box were polished and a thin coating of grease were applied to minimize friction as much as possible. The rectangular load used for the study was made of wood of size 75 mm (width) ×296 mm (length) × 50 mm (height). On the top of the wooden block a ribbed steel plate was placed during loading such that there is no bending of the footing during the loading process.

The pond ash and WMM were pulverized in the laboratory and mixed with predetermined amount of water. For uniform moisture distribution the moist pond ash was placed in several plastic bags and put in airtight containers during the test periods. The moisture content was checked in regular intervals and the corrections were made if found required.

Table 3 Properties of geogrids

Properties	Rigid Geogrid (GGR)	Flexible Geogrid (GGF)
Polymer	Polypropylene	Polyester with epoxy coating
Mass per unit area (gsm)	520	550
Peak tensile strength (kN/m)	50	80
Strain at break (%)	18	19
Aperture size (mm ×mm)	32 × 32	24 × 28

Table 4 Properties of coir geotextiles

Properties	Coir geotextile type		
	CWA	CWB	CWC
Aperture size (mm × mm)	25 × 25	10.0 × 12.5	7 × 4
Thickness (mm)	6.7	8.1	9.6
Mass per unit area (gsm)	360	610	1335
Peak tensile strength (kN/m)	10	19	38
Strain at break (%)	21	22	37

Before the actual loading test, trial compactions were carried out in layers of 50 mm and densities were found out by core cutter method at different depths of the tank. The compaction of different layers was done by using a heavy proctor hammer. A wooden plank of the size of the tank was used above the fill and the hammer was dropped on it for predetermined number of blows for a specific layer. A plastic sheet was placed between the soil and the wooden plank so that it will act as a moisture barrier, to prevent the moisture from the soil to get absorbed by the wooden plank while compaction. The number of blows was changed for different layers. It was decided to start the bottom most layers with 60 numbers of blows distributed over the whole area of the tank and the number of blows increased to 80 numbers as the top most layers is placed. After the trial tests it was found that the pond ash 'NC' was compacted to a dry density of 12.7 kN/m^3 i.e., 93.5 % of MDD. Similarly for "NF" the dry density achieved was 9.6 kN/m^3 i.e., 89.7% of MDD.

After 5 layers of the pond ash layers were compacted, it was overlain by a WMM layer with a layer of reinforcement at the interface. The depth of pond ash in the model tank was kept as 250 mm and the overlying

WMM layer was kept as 100 mm or 60 mm for the un-reinforced condition and 60 mm for the reinforced condition. The details are summarized in Table 5. At the first stage the pond ash was compacted to a depth of 250 mm in 5 layers of 50 mm each. After the preparation of the pond ash layer, a geosynthetic reinforcement of size 745 mm × 295 mm was laid over this. A WMM course of 100 mm or 60 mm for un-reinforced and reinforced case respectively was laid over the reinforcement layer. The 100 mm WMM layer was laid in 3 layers, 40 mm each for the first two layers and 30 mm for the final layer, were compacted as the same method that is adopted for the pond ash but the number of blows were increased to 100 blows per layer. The 60 mm WMM layer was compacted in 2 layers of 30 mm each with the number blows remaining same at 100 per layer. All the layers were compacted by the plate tamping technique using a wooden plate of 745 mm × 295 mm and the modified proctor hammer. The WMM was compacted to a dry density of 19.5 kN/m^3 i.e., 95.6 % of MDD.

Table 5 Plan for model test

Pond Ash	WMM Layer Thickness	Reinforcement Details			No. of Tests
NC NF	0	Unreinforced			2
	100 mm 60 mm	Unreinforced			2 × 2 = 4
	60 mm	Reinforced	Polymeric GGR GGF	Coir CWA CWB CWC	2 × 1 × 5 = 10
				Total =	16

For loading, an automatic Universal Testing Machine (UTM) used. The UTM was a constant strain rate machine and was capable of constant strain rates in the range of 0.01 mm/min to 500 mm/min and a 50 kN load cell. The machine was connected to a computer where the load and settlement was recorded. The load applied to the footing at a constant strain rate of 1.0 mm/min and the settlement and corresponding increase in load was recorded at a settlement interval of 0.5 mm. The setup is shown in Fig. 4.

The load bearing tests were repeated at random and the results obtained were found to be varying between 5 %.

MODEL TEST RESULTS

Bearing Capacity of Unreinforced Pond Ash

The ultimate bearing capacities have been calculated as per Vesic (1963). The ultimate bearing capacity (q_u) of unreinforced pond ash type NC was found to be 283.6 kPa at a settlement (s_u) of 6.7 mm where as the ultimate bearing capacity (q_u) of unreinforced pond ash type NF was found to be 247.1 kPa at a settlement (s_u) of 6.1 mm.

Fig. 4 The load test on progress

Bearing Capacity of Unreinforced Pond Ash Subgrade with WMM

It is observed that the q_u of unreinforced model increased from 422.2 kPa to 504 kPa with an increase of WMM thickness from 60 mm to 100 mm. Similarly, the q_u values for pond ash type NF changed from 428.7 kPa to 525.3 kPa.

Bearing Capacity of Pond Ash Subgrade with WMM Reinforced at the Interface

With intrusion of different types of geosynthetics at the interface of pond ash and WMM, the values of q_u and s_u increased, for both NC and NF type of pond ashes as presented in Tables 6 and 7. The value of q_u for pond ash type NC with reinforcement type GGR was 660.4 kPa, whereas it was 648.9 kPa with GGF type reinforcements.

Table 6 Comparision between ultimate bearing capacity (q_u) of pond ash type NC with different thickness of WMM and reinforcements at interface

Thickness of WMM (mm)	Reinforcement type		q_u (kPa)	Settlement (s_u)	BCR_u
100	Unreinforced		504.0	12.1	1.19
60	Unreinforced		422.2	9.3	-
	Reinforced	GGR	660.4	12.4	1.56
		GGF	648.9	11.2	1.54
		CWA	532.4	12.6	1.26
		CWB	575.1	13.3	1.36
		CWC	620.4	14.5	1.47

Similarly, with coir geotextiles type CWA, CWB and CWC, the q_u increased to 532.4kPa, 575.1kPa and 620.4 kPa at s_u values of 12.6 mm, 13.3 mm and 14.5 mm respectively. Similar observations for pond ash type NF, both for unreinforced condition with different thicknesses of WMM layer i.e., 100 mm and 60 mm and reinforced condition with different types of geosynthetics with constant thickness of WMM layer i.e., 60 mm, have been presented in Table 7.

Table 7 Comparision between ultimate bearing capacity (q_u) of pond ash type NF with different thickness of WMM and reinforcements at interface

Thickness of WMM (mm)	Reinforcement type		q_u (kPa)	Settlement (s_u)	BCR_u
100	Unreinforced		525.3	11.2	1.23
60	Unreinforced		428.7	9.8	-
	Reinforced	GGR	608.0	11.2	1.42
		GGF	587.5	10.7	1.37
		CWA	521.3	12.1	1.22
		CWB	569.3	13.3	1.33
		CWC	588.4	13.7	1.37

From the last column of Table 6, it is observed that the ultimate bearing capacity ratio (BCR_u) was only 1.19 with an increase in the thickness of WMM layer from 60 mm to 100 mm on NC type of pond ash as subgrade. But keeping the thickness of the WMM layer same at 60 mm and providing a layer of geosynthetics at the WMM-pond ash interface, the BCR_u value increased to 1.56 and 1.54 respectively for GGR and GGF types of polymeric reinforcements. With the coir geotextile types CWA, CWB and CWC, the BCR_u values obtained were 1.26, 1.36 and 1.47 respectively. The behaviour is similar in respect of pond ash type NF as evident from the last column of Table 7.

To facilitate a comparision, bearing capacity ratios (BCR) at different deformations have been presented in Fig. 5 for pond ash type NC and in Fig. 6 for pond ash type NF respectively. It is evident that for all the types of geosynthetics there is an increasing trend with deformation. The BCR value raised sharply to about 1.5 at a settlement of about 12 mm for pond ash type NC with both the types of polymeric geogrids after which the slope became flatter reaching a value of 1.6 at a settlement of 20 mm. Whereas the value of BCR with the coir geotextiles remained about the same at 1.1 up to a settlement of 9 mm after which the coir geotextiles type CWC took the steepest slope reaching a value of 1.54 at a settlement of 20 mm, followed by CWB at 1.42 and CWC at 1.27. Similar observations could be made in respect of pond ash type NF.

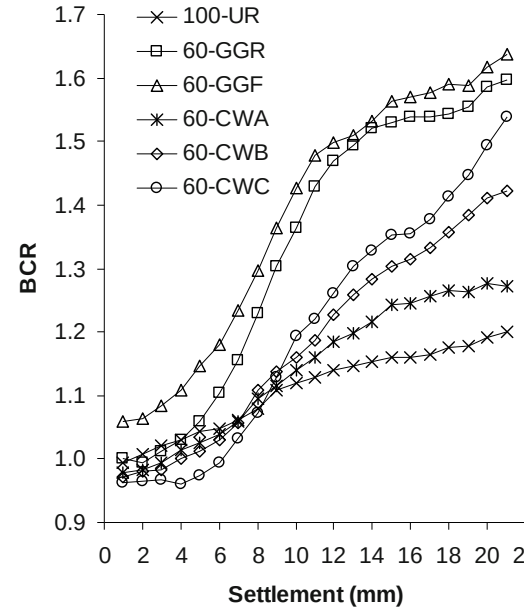

Fig. 5 Bearing capacity ratio vs. settlement of pond ash type NC with and without reinforcements

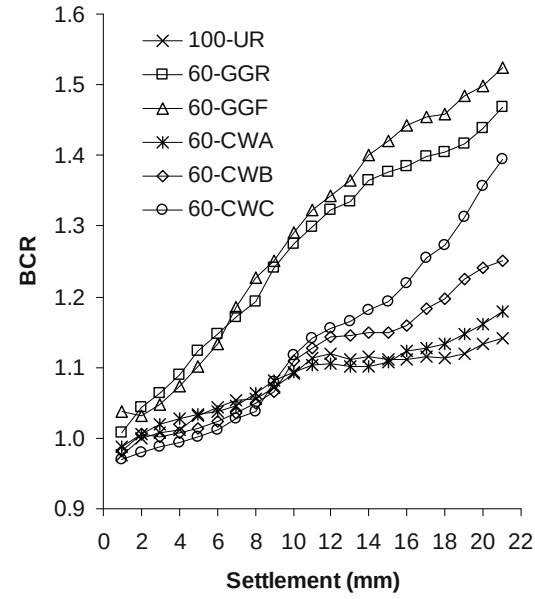

Fig. 6 Bearing capacity ratio vs. settlement of pond ash type NF with and without reinforcements

Biodegradability

Previous studies at IIT Delhi (Singh et al. 2006) clearly indicated that the coir hardly degrades in one year and the life expectancy can be upto a decade. Hence, the potential of coir geotextile, if not same, is comparable to the polymeric materials.

CONCLUSIONS

Based on the test results presented in this chapter, the following conclusions may be drawn.

1. The performance of double layer model with WMM base course and compacted pond ash subgrade is better than the single layer model of pond ash only. The ultimate bearing capacity of the former is greater.

2. The ultimate bearing capacity of the unreinforced double layer model depends on the thickness of WMM base layer.

3. The ultimate bearing capacity of the reinforced double layer model increased significantly with inclusion of both polymeric geogrids and coir woven geotextiles at the interface of both the WMM course and pond ash subgrade.

4. The performance of the coir woven geotextiles is quite different from that with polymeric geogrids.

5. The performance of with the coir woven geotextiles with both the types of pond ash subgrades, clearly depended on their respective physical and mechanical properties. The coir woven geotextile type CWC exhibited the best improvement followed by that with type CWB and CWA.

6. For WMM base course and pond ash subgrade the improvement with polymeric geogrids is exhibited even at very low settlements whereas that with coir woven geotextiles occurred only after a settlement of about 8 mm. This could be attributed to the higher strength at lower strains of the former.

7. The coir geotextile reinforced double layer model of sand and pond ash did not exhibit any improvement upto a settlement of 8 mm. but after a settlement of 8 mm the improvement with the coir woven geotextiles for both types of pond ash types are quite significant. At a settlement of 14 mm and beyond, the double layer model with coir woven geotextile type CWC out performed the polymeric geogrids.

The results with double layer models with coir geotextiles are encouraging for their potential use in rural roads which can tolerate larger settlements (or rutting in repeated loading).

ACKNOWLEDGEMENTS

The authors are very greatful to The General Manager, Captive Power Plant, National Aluminium Company Limited (NALCO), Angul, Orissa, India for his help during the collection of the pond ash samples from the ash ponds of NALCO. Thanks are also due to the Coir Board and the Kerala State Coir Corporation Ltd. Alappuzha, Kerala, India for providing the coir geo-textile samples.

REFERENCES

Brown SF, brunton JM, Hughis DAB, Brodrick BV (1985) Polymer Grid Reinforcement of Asphalt, Proc. Asia of Asphalt Technology 54: 18-41

Dixit A (1994) Behaviour of Model Pavements with Geosynthetics, Unpublished Ph.D Thesis submitted to Indian Institute of Technology Delhi, India

Dutta RK (2002) Alternate Low Cost Material in Ground Improvement, Unpublished Ph.D Thesis submitted to Indian Institute of Technology Delhi, India

Khing KH, Das BM, Puri VK, Yen SC, Cook EE (1994) Foundation in Strong Sand Underlain by Weak Clay with Geogrid at the Interface, Geotextiles and Geomembranes 13: 199-206

Meyerhof GG (1974) Ultimate Bearing Capacity of Footings on Sand Layer Overlying Clay, Canadian Geotechnical Journal 11(2): 223-229

Sheo Gopal (1993) Behaviour of Model Pavements with Geosynthetics under Repetitive Loading, Unpublished Ph.D Thesis submitted to Indian Institute of Technology Delhi, India

Singh RM, Venkatappa Rao G (2006) Sustainable development: Durability of natural geotextiles as erosion control product, 5th ICEG Environmental Geotechnics, Thomas Telford, London: 1060-1067

Venkatappa Rao G, Dutta RK (2002) “Testing and Application of coir based Geotextiles” Published in the Seventh International Conference on Geosynthetics 22-27 Sept, France: 955-958

A STUDY ON SHEAR STRENGTH AND DEFORMATION OF SANDY SOIL REINFORCED WITH TIRE CORD WASTES

M. Esna-ashari [1] and M. Asadi [2]

ABSTRACT: A series of laboratory tests has been carried out on sandy soil specimens reinforced with randomly distributed fiber to investigate the using of tire cord wastes as reinforcement. The strength and deformation characteristics of reinforced specimens were examined in unconfined compression and direct shear tests. These laboratory tests were performed on the specimens with 0% up to 1% fiber content and 10, 20 and 30 mm in length. The influence of fiber content and length of fiber on the reinforced sandy soil properties were studied. The results of tests indicated that the inclusion of tire cord fiber increases the unconfined compressive strength of the specimens and can change the brittle behavior of the sandy soil to more ductile one significantly. Also, it was observed that fiber reinforcement increases the peak shear strength and internal friction angle value of the soil samples in direct shear tests. However, the peak shear strength of specimens is insignificantly affected by the fiber length. Furthermore, initial stiffness for reinforced sandy soil decreases with increase in the length of fibers in some cases.

KEYWORDS: soil reinforcement, shear strength, tire cord fiber

INTRODUCTION

In recent years, the use of fiber reinforcement has been suggested for various geotechnical applications. The concept of reinforcing soil originated in ancient times, when materials such as tree trunks, small bushes and heavy cotton fabrics were used to reinforce soil. The first type of reinforcement used in modern soil reinforcement was developed by Vidal (Schlosser, 1974) using long steel strips. Presently, variety of materials with different shapes and techniques are used in civil engineering applications. Reinforced soils can be obtained by either incorporating continuous reinforcement inclusions such as, sheet, strip or bar within a soil mass in a defined pattern that named systematically reinforced soil, or mixing discrete fibers randomly with a soil fill named randomly reinforced soils.

Soil reinforced with randomly-distributed inclusions have attracted considerable attention over past years, such as concrete technology and more recently in soils (Hataf and Rahimi 2005); (Yetimoglu and Salbas 2003). In this type of soil reinforcement, soil is mixed randomly with discrete small inclusions such as fibers and small meshes until it becomes like a homogeneous material. Material used to more fibers for reinforcement, may be derived from paper, metal, nylon, polyester and other materials having widely varied physical properties.

In comparison with systematically reinforced soil, randomly distributed fiber reinforced soils exhibit some advantages. Preparation of randomly distributed fiber reinforced soils mimics soil stabilization by admixture. Discrete fibers are simply added and mixed with the soil, much like cement, lime, or other additives. Randomly distributed fibers offer strength isotropy and limit potential planes of weakness that can develop parallel to oriented reinforcement (Yetimoglu and Salbas 2003).

Research of different types of reinforcement and materials has been conducted by several investigators. However, an increasing number of studies on the subject have been conducted by several researches in the past few decades. The available research results vary depending on the type of soil, fiber and test performed. The results of pervious studies indicate that stress-strain and strength properties of randomly distributed fiber-reinforced soils are affected by the fiber content, length of fibers and other strength characteristics of soil and fiber. (Gray and Ohashi 1983; Gray and Al-Refeai 1986; Maher and Gray 1990; Micholowski and Zhao 1996; Morel and Gourc 1997; Kaniraj and Havanagi 2001; Hataf and Rahimi 2005). Most of previous researches have shown that the addition of fiber-reinforcement caused significant improvement in the strength and decreased the stiffness of the soil (Tang et al. 2006). In this study, the feasibility of using tire cord waste as reinforcement of a sandy soil is investigated.

[1] Assistant professor, Department of Civil Engineering, Bu-Ali Sina University, IRAN. Email: Esna_ashari@basu.ac.ir
[2] M.Sc., Student, Bu-Ali Sina University, IRAN. Email: Mohammadasadi_1360@yahoo.com

A series of direct shear tests and unconfined compression tests have been carried out on sandy soil reinforced with randomly tire cord with different percentages of fiber, to determine the effects of fiber content and stress-strain properties of reinforced soil. The results obtained from the tests are presented and discussed.

EXPERIMENTAL PROGRAM

The main objectives of this research were to study the effects of adding tire cord fibers on the strength and deformation characteristics of sandy soil reinforced with randomly distributed fibers.

To accomplish the objectives of this investigation, a series of laboratory tests including unconfined compression and direct shear tests were carried out on the sandy soil samples. These laboratory tests were performed on the specimens with 0% up to 1% fiber contents and 10, 20 and 30 mm in length. Also, in order to obtain the maximum dry unit weight and optimum moisture content of specimens at each fiber content, some compaction tests were performed, and $\gamma_{d(max)}$ and w_{opt} were determined for each specimen.

Materials

The soil used in this study was obtained from a site in the north of Zanjan city of IRAN. The soil is classified as sandy silt (SM) and the specific gravity of the solids is 2.67. The index properties of the soil used in this investigation are summarized in Table 1.

Table 1 properties of soil used in experiments

Property	Value
Specific gravity ,Gs	2.67
Coefficient of uniformity, C_U	16.91
Coefficient of curvature, C_C	2.01
Effective grain size, D_{10} (mm)	0.023
Maximum dry unit weight, (KN/m^3)	18.48
liquid limit, LL	23.34
Plastic limit, PL	0
Plastic index, PI	NP

Tire cored wastes were used throughout this study to reinforce the soil. These fibers are nylon fiber which is produced by tire cord manufactories. Some of its index and strength properties are the following:
Diameter=0.015 mm, Colour=White, modulus of elasticity =1500 MPa, Tensile strength=150－200Mpa, Density= 1.12－1.15 gr/cm^3

Testing Procedures

Unconfined compression tests

A series of unconfined compression tests were conducted on the soil specimens with 0% up to 1% tire cord fibers. Tests were performed on soil samples prepared at the maximum dry unit weight and optimum moisture content which determined using the standard proctor test. The specimens tested were 50 mm diameter and 100 mm high. The effects of fiber content and length of fiber on the stress-strain relationships of reinforced samples were considered.

Direct shear tests

In order to define the shear strength parameters for unreinforced and reinforced sandy soil, and to determine the contribution of fiber reinforcement to the shear strength of soil, a series of direct shear tests were performed. The tests were conducted inside a shear box of 100 mm x 100 mm in plane. The tests were carried out at the vertical normal stresses of 50, 100, 200 KPa. The specimens were prepared at the same dry density and fiber content as that of unconfined test samples.

RESULT AND DISCUSSION

As stated before, to determine the compaction characteristics (optimum moisture content and maximum dry density) of soil specimens, some proctor compaction tests were performed. Typical results are shown in Fig 1.

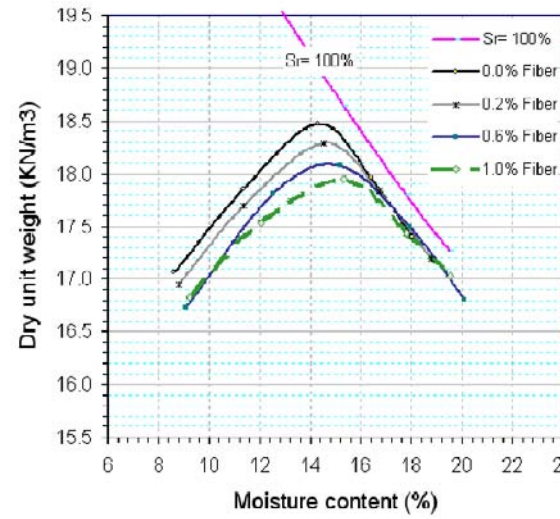

Fig. 1 Compaction test results for reinforced and unreinforced specimens

As can be seen from Fig. 1, the curves show that optimum moisture content increases and maximum dry density decreases with increasing in fiber content.

The fact that the fibers have a lower specific gravity and the reduction in the unit weight of the reinforced soil due to the compaction resistance of the fibers, there is a reduction in the unit weight of the reinforced samples. On the other hand, the interaction between the soil and the fiber reinforcement controls the response of the reinforced soil to compaction. Also, increasing in optimum moisture content is due to water absorption by fibers.

Unconfined Compression Tests

Unconfined compression tests were performed to study the strength of reinforced soil samples with tire cord fibers. The experiments were conducted on the soil specimens with 0% up to 1% tire cord fibers. These tests were performed to establish base strength of soil so that change in strength due to addition of tire cord fibers could be estimated. The stress-displacement curves obtained from the tests for reinforced samples with the fiber content of 0% up to 1% and length of 10, 20 and 30 mm are shown in Fig. 2.

It can be seen that the compressive strength of the reinforced soil specimens increases with increasing fiber content and length. Also, it is observed that the initial tangent modulus decreases with increase in the length of fibers and at the same length of fibers remains practically the same. It means that, the initial stiffness of soil appears not to be affected by the addition of fiber. The percentage of increase in unconfined compression strength of specimens at the same displacement is shown in Table 2.

Table 2 Percentage increase in unconfined compression strength of specimens (L=30 mm)

Fiber (%)	Unconfined Compressive Strength	Stress Ratio
0	138.05	1
0.2	156.88	1.14
0.4	163.15	1.18
0.6	172.56	1.25
0.8	194.53	1.41
1	203.94	1.52

Furthermore, the curves show that the axial stresses and strains increase with increase in fiber content and length of fibers. On the other hand, fiber-reinforced soil specimens exhibit more ductile behavior and smaller loss of post-peak strength than unreinforced soil. The reduction in the loss of post-peak stress is more pronounced for higher fiber content. So, it can be concluded that with adding more than 0.8% fiber content, the ductility of soil specimens increases significantly and as a result, the samples don't fail at a spatial surface failure. The failure pattern of specimens after testing confirms this result.

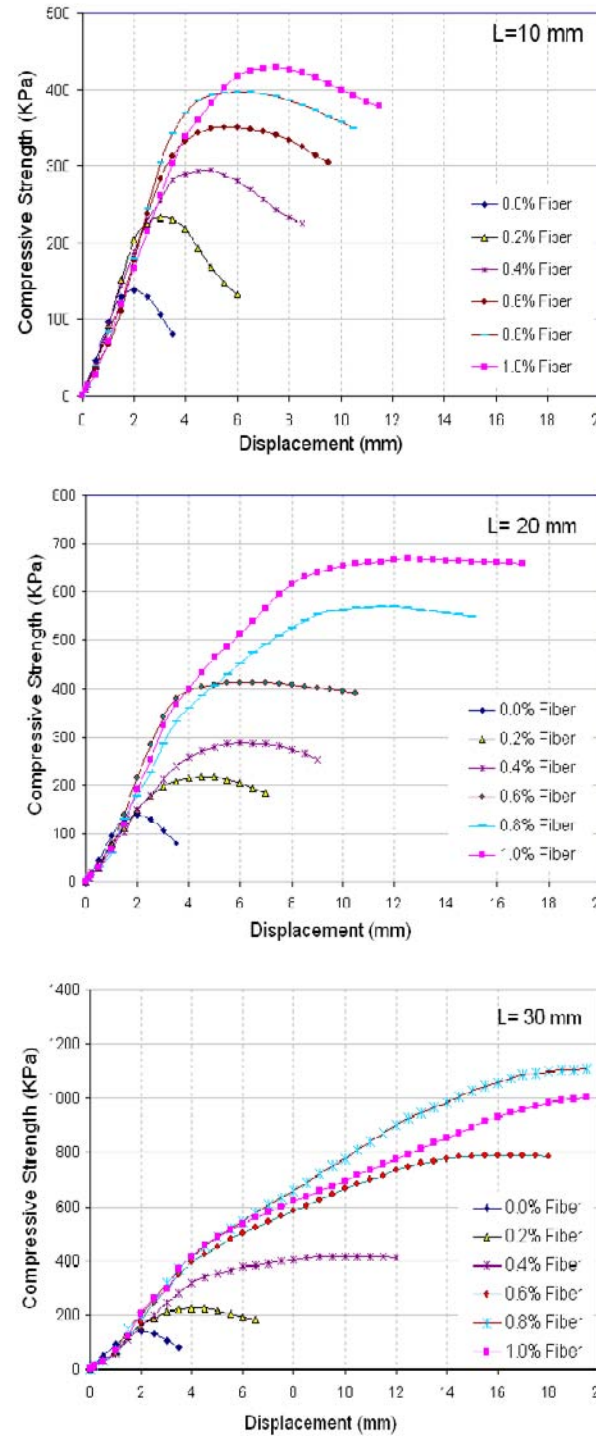

Fig. 2 Unconfined compressive strength-displacement response for reinforced and unreinforced samples

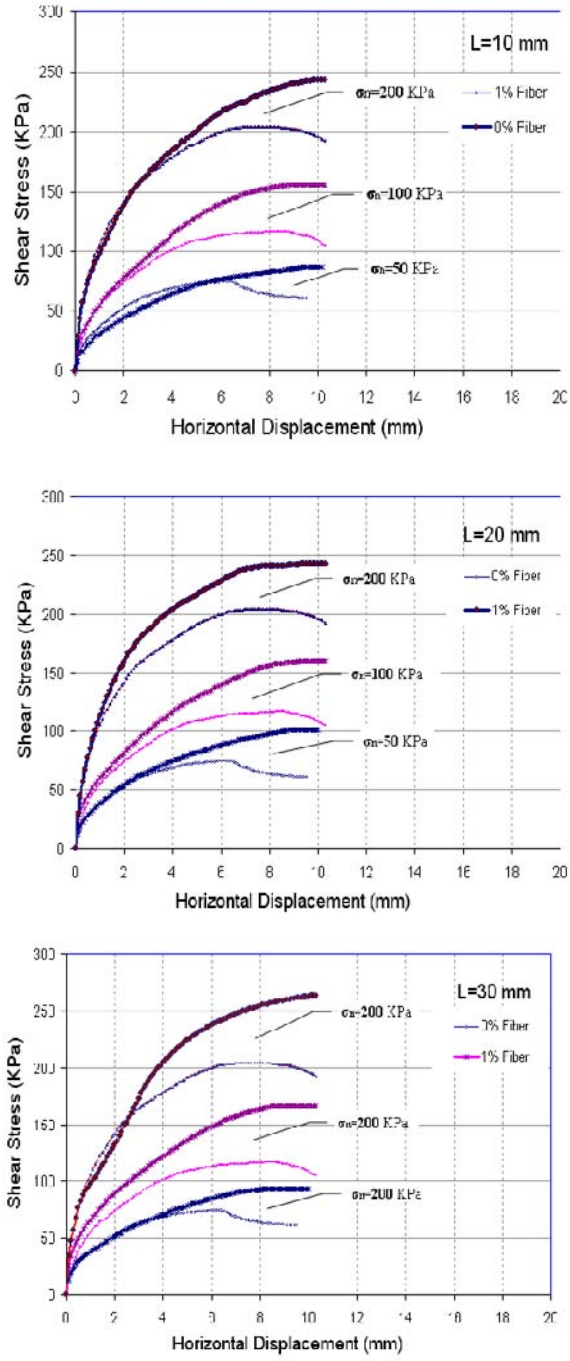

Fig. 3 Hear stress-horizontal displacement response for reinforced and unreinforced specimens

Direct Shear Tests

Soil specimens with and without reinforcement were tested inside a shear box of 100 mm×100 mm in plane and 25 mm in depth. A typical shear stress-horizontal displacement curve with the fiber content of 0% and 1% for 10, 20, 30 mm length of fiber at the normal stress of 50, 100, 200 KPa is showed in Fig. 3. As can be seen, fiber reinforcement increases the peak shear strength of the soil samples.

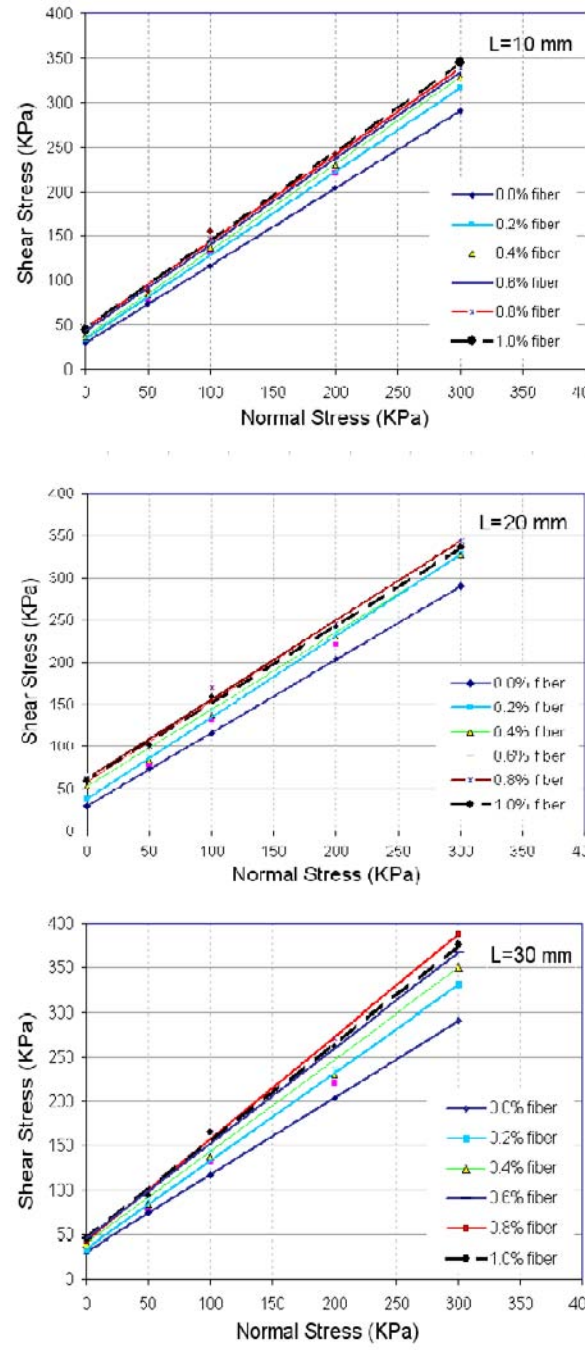

Fig. 4 Mohr-coulomb failure envelopes for reinforced and unreinforced specimens

This increasing in shear strength is observed in all specimens which were reinforced with deferent length of fiber. Also, comparison of obtained results shows that the peak shear strength of specimens is insignificantly affected by fiber length. Furthermore, it can be observed that initial slope of the shear stress-horizontal displacement curves (initial stiffness) for reinforced samples are

the same. Fig. 4 illustrates the mohr-coulomb failure envelopes for reinforced and unreinforced specimens.

Based on results of direct shear tests shown in Fig. 4, it can be concluded that an increase in the fiber content increases the internal friction angle values of the reinforced soil specimens. Also, from the curves it can be seen that the cohesion value is insignificantly affected by fiber content and length. Furthermore, it can be inferred from Fig. 4 that the cohesion and the friction angle values are not affected by change in the length of fibers.

CONCLUSIONS

This study was conducted to investigate the effect of fiber content and length of fibers on the shear strength and deformation of a sandy soil reinforced by randomly distributed fiber. A series of laboratory test including unconfined compression and direct shear tests were performed. Tire cord fibers were used as reinforcement. The following conclusions can be drawn from the study:

Based on results of compaction tests, with increasing in fiber content, maximum dry density decreases and moisture content increases in the reinforced soil specimens. The results of the unconfined compression test indicated that the inclusion of tire cord fiber, improved the unconfined compressive strength of the specimens. Initial stiffness (initial tangent modulus) decreases with increase in the length of fibers and at the same length of fibers remains the same. The results of testing suggest that the fiber reinforcements can change brittle behavior of the sandy soil to more ductile one significantly. Fiber reinforcement increased the peak shear strength of the soil samples in direct shear tests. Comparison of obtained results indicates that the peak strength of specimens is insignificantly affected by fiber length. Based on results of direct shear tests, an increasing in the fiber content leads to increasing in the friction angle values of reinforced soil specimens. However, the cohesion value is insignificantly affected by fiber content and length of fiber.

REFERENCES

Gray DH, Al-Refeai T (1986) Behavior of fabric-versus fiber reinforced sand. J. Geotech. Engrg. ASCE 112 (8): 804–820

Gray DH, Ohashi H (1983) Mechanics of fiber-reinforcement in sand. J. Geotech. Engrg. ASCE. 109 (3): 335-353

Hataf N, Rahimi MM (2005) Experimental investigation of bearing capacity of sand reinforced with randomly distributed tire shreds. J. Construction and building materials. 20 (2006): 910-916

Kaniraj SR, Havanagi VG (2001) Behavior of cement-stabilized fiber reinforced fly ash-soil Mixtures. J. Geotech and Geoin. Engrg. ASCE 127 (7): 574-584

Maher MH, Gray DH (1990) Static response of sands reinforced with randomly distributed fibers. J. Geotech. Engrg. ASCE 116 (11): 1661-1677

Michalowski RL, Zhao AG (1996) Failure of fiber-reinforced granular soils. J. Geotech. Engrg. ASCE 122(3): 226-234

Morel JC, Gourc JP (1997) Mechanical behavior of sand reinforced with mesh elements. Geosynthetics Int. J. 4(5): 481-508

Schlosser F, Long NT (1974) Recent results in French research on reinforced earth. J. Const Div. ASCE 100(3): 223–37

Tang C, Shi b., Gao W, Chen F, Cai Y. (2006). Strength and mechanical behavior of short polypropylene fiber reinforced and cement stabilized clayey soil. J. Geotex and Geomem 25(2007): 194-202

Yetimoglu T, Salbas O (2002) A study on shear strength of sands reinforced with randomly distributed discrete fibers. J. Geotex and Geomem 21 (2003): 103-110

Proceedings of the 4th Asian Regional Conference on Geosynthetics
June 17 - 20, 2008 Shanghai, China

THE USE OF GEOTEXTILE TO COUNTER HEAVE PROBLEM IN SPREAD FOOTING IN JORDANIAN EXPANSIVE SOIL

Omar H. Al-Hattamleh [1]

ABSTRACT: Spread footing as a foundation system is widely used here in Jordan. Cheap cost compare with other foundation types and accumulative practice make them preferable in the construction industry. Overdesign of such footing and the lack of effective heave prediction lead to an unexpected outcome. Several residences building in Irbid province, Jordan, were suffered from severe crack. Subsequently, owners of these houses are enforced to leave their homes. In this paper, a numerical simulation was conducted to simulate the effectiveness of using a geotextile layer beneath the spread footing to counterpart the unexpected heave.

KEYWORDS: analytical analysis, geosynthetic, numerical analysis, soil

INTRODUCTION

The detrimental heave of expansive soils represents an important scientific and technical problem to geotechnical engineers. Lightly loaded structures constructed on expansive soils are often subjected to severe distress subsequent to construction as a result of changes in the pore-water pressures in the soil due to the seasonal water content changes. The structures most commonly damaged are roadways, airport runways, small buildings, irrigation canals, and all near ground surface structures associated with infrastructure development. Changes in the pore-water pressure occur as a result of variations in climate, variations in water table due to pumping, water uptake by vegetation, and removal of vegetation. In this paper, we utilize the membrane action of geotextile to eliminate the heave of expansive soil beneath the spread footing.

DEFORMATION OF THE FABRIC BASED ON MEMBRANE ANALYSIS

The flexibility of the fabric along with the conditions of the load and support leads to the development of a membrane type behavior. This had prompted a number of researchers to apply the membrane analogy to study the deflection of reinforced soil with fabric (Love et al. 1987; Jewell 1988 a & b; Bourdeau 1989; Espinoza 1994, Shukla and Chandra 1994 &1995; Yin 1997 a & b; Deb et al. 2007). Recently, Hattamleh and Muhunthan (2006) apply membrane analogy to investigate the deformation behind reinforced retaining wall. In this paper, membrane analogy is applied to investigate the heave action beneath spread footing laid on expansive soil. Figure 1 shows the problem under consideration on this paper.

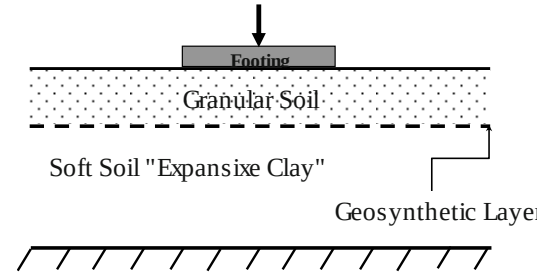

Fig. 1 Problem depiction

Fig. 2 shows static equilibrium for a strip footing of an elastic membrane. Using the stochastic stress diffusion theory (Sergeev 1969; Harr 1977) for two dimensional plane strain conditions, the expected vertical stress at a point (defined by the coordinate x and z) given as (Bourdeau 1989, Hattamleh and Muhunthan 2006):

$$\frac{\partial \sigma_z}{\partial z} = D \frac{\partial^2 \sigma_z}{\partial x^2} \tag{1}$$

where D is the coefficient of diffusion, which governs the rate at which the upper soil layer spreads the applied surface load. The coefficient of diffusion, D, is related to the coefficient of earth pressure at rest, K_o, and the depth as (Bourdeau 1989):

$$D = K_o z \tag{2}$$

[1] Civil Engineering Department, The Hashemite University, P.O. Box 150459, Zarqa 13115, Tel. +962 (5) 3903333 Ext. 5004, JORDAN,E-mail: hattam@hu.edu.jo

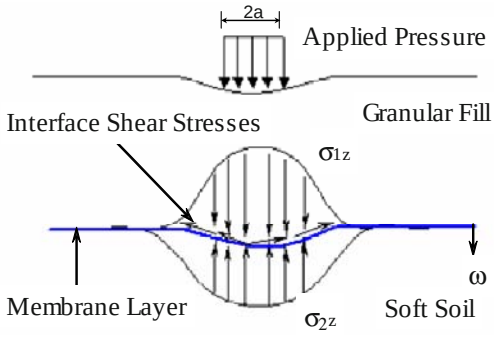

Fig. 2 Static equilibrium of an elastic membrane under Plane strain model

Using the Gaussian distribution (Harr 1977) the expected vertical stress under an applied pressure, q uniformly distributed over a strip of width 2a, is evaluated as:

$$\frac{\sigma_z}{q} = \psi\left(\frac{x+a}{z\sqrt{K_o}}\right) - \psi\left(\frac{x-a}{z\sqrt{K_o}}\right) \tag{3}$$

where ψ is the cumulative Gaussian distribution function:

$$\psi(x) = \int_0^x e^{\frac{-t^2}{2}}\,\mathrm{d}t \tag{4}$$

The compressible soil is assumed to offer a reaction to the loading pressure proportional to its deflection as in Winkler model as:

$$\sigma_{z2} = k_s \omega(x) \tag{5}$$

where σ_{z2} is the vertical, stress at the fabric-lower soil layer interface, $\omega(x)$ the membrane deflection, and k_s the coefficient of subgrade reaction.

The interface frictional stress at the soil fabric interface is given by the Mohr-Coulomb as:

$$\tau(x) = c_a + \mu \cdot (\sigma_z(x) + \gamma H_1) \tag{6}$$

where $\sigma_z(x)$ is the net vertical stress at the backfill underneath fabric interface, γ the unit weight of the backfill upper layer, H_1 the thickness of the soil column above the fabric, ca adhesion between the soil and the fabric, and μ the interface friction coefficient.

The force acting on the deflected membrane is as shown in Fig. 3. The equilibrium of forces in the horizontal direction results in (Fig. 3):

$$T_H(x) + \int_0^x \tau_H(x)dx = T_o \tag{7}$$

where $\tau_H(x)$ is the horizontal component of the friction stress at the interface, $T_H(x)$ the horizontal component of the tensile force in the membrane, and T_o the horizontal tensile force, at the origin of coordinate (i.e., center of geosynthetic layer under the applied pressure).

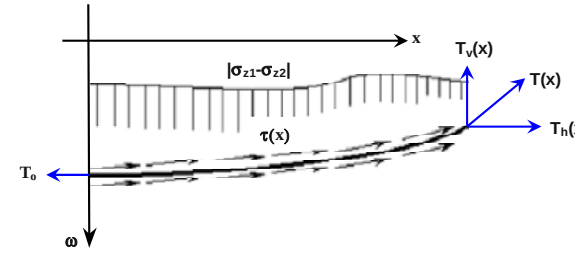

Fig. 3 Forces acting on the deflected membrane

Equilibrium in vertical direction is written as:

$$T_V(x) - \int_0^x (\sigma_{z1} - \sigma_{z2})\mathrm{d}x + \int_0^x \tau_V(x)\mathrm{d}x = 0 \tag{8}$$

where τ_V is the vertical component of the frictional stress.

Taking the derivative of Eq. 8 and using Eq. 5 results in:

$$\frac{\mathrm{d}T_V}{\mathrm{d}x} + \tau_V(x) + k_s\omega(x) = \sigma_{z1} \tag{9}$$

From the geometry of forces and deflection in (Fig.2):

$$\frac{T_V}{T_H} = \frac{\mathrm{d}\omega}{\mathrm{d}x} \tag{10}$$

Rewriting Eq. 10 and taking the implicit derivative with respect to *x*:

$$\frac{\mathrm{d}T_V}{\mathrm{d}x} = \frac{\mathrm{d}(T_H\mathrm{d}\omega)}{\mathrm{d}x} = \frac{\mathrm{d}T_H}{\mathrm{d}x}\frac{\mathrm{d}\omega}{\mathrm{d}x} + T_H\frac{\mathrm{d}^2\omega}{\mathrm{d}x^2} \tag{11}$$

Substituting of Eq. 11 into Eq. 9 results in:

$$\frac{\mathrm{d}T_H}{\mathrm{d}x}\frac{\mathrm{d}\omega}{\mathrm{d}x} + T_H\frac{\mathrm{d}^2\omega}{\mathrm{d}x^2} + \tau_H\frac{\mathrm{d}\omega}{\mathrm{d}x} + k_s\omega = \sigma_{z1} \tag{12}$$

Finally, substitution of the derivative of Eq. 7 into Eq. 12 results in:

$$T_H(x)\frac{\mathrm{d}^2\omega(x)}{\mathrm{d}x^2} + k_s\omega(x) = \sigma_{z1}(x) \tag{13}$$

The boundary conditions are:

$$\frac{\mathrm{d}\omega}{\mathrm{d}x} = 0 \text{ (at x=0)}; \quad T_H = 0 \text{ (at x=L)} \tag{15a}$$

$$T_H = 0 \text{ (at x=L)} \tag{15b}$$

The membrane equation (Eq. 13) can be solved using a finite difference schemes. Assuming that the reinforcement is discretized in intervals of length Δx, Eq. 13 becomes:

$$T_{H,i}\omega_{i-1} + 2(\Delta x^2 k_s - T_{H,i})\omega_i + T_{H,i}\omega_{i+1} = 2\Delta x^2\sigma_{z1} \tag{16}$$

where the subscript i denotes the node number ranging from 1 to *N*.

The above equation can be written in a matrix form as:

$$[B]\cdot(\omega)=(T) \tag{17}$$

where [*B*] is a tridiagonal matrix, and (ω) and (*T*) are the nodal vectors of displacement and tension, respectively. This finite difference scheme can be solved subject to the constraints imposed by Eq. 7 and Eq. 12 and the boundary conditions (Eq.15a and 15b). The solution was obtained with convergence criteria as:

$$\left|\frac{\omega_i^j-\omega_i^{j-1}}{\omega_i^j}\right|\le 10^{-5} \quad \text{and} \quad \left|\frac{T_i^j-T_i^{j-1}}{T_i^j}\right|\le 10^{-5} \tag{18a}$$

And

$$\left|\frac{T_i^j-T_i^{j-1}}{T_i^j}\right|\le 10^{-5} \tag{18b}$$

where *j* and *j*-1 are the current and previous iteration values.

It is worthy to note that: the minimum number of node, *i*, was 40 along the geosynthetic grid. Refining beyond this discretization values gave the same result.

SOIL PROFILE AND CHARACTERISTICS

The proposed model was used to simulate the condition of strip footing placed on Irbid expansive soil in Jordan. Soil profile in the Irbid District in Jordan consists of a clay layer of varying thickness from 1.5 to more than 6 m underlined by weathered materials, regolith, followed by basaltic bedrock. Irbid clays are light to dark brown in color. Grain size distribution of Irbid soil indicates that it contains 5%, 30%, and 65% of sand, silts, and clay fraction respectively. Plasticity characteristics are consistent with depth having Plastic limit of 35%±3 and liquid limit of 75%±3. Therefore, Irbid soil is classified according to the Unified Soil Classification System (USCS) as CH-MH soil, and it has a high swelling potential according to U.S. Bureau of Reclamation (USBR). The ground water table in the city is very deep. Jordan weather is semiarid with a wet season from November to May and the rest of the year is a hot dry season. The total annual precipitation in the region, including sporadic snow, varied from 300 to 850 mm with an average of 550 mm. Soil moisture content increases in the wet season and potentially decreased in the long summer season. Water content varied from 40 % near the surface and stabilized to 32% at depth of 2.5 m. Moreover, in Summer it varied from 25% in the surface and stabilized at depth of 2.5 m to 32%. Dry unit weight of the soil was found to be in the range of 13 to 15 kN/m^3. Nusier and Alwaneh (2002) reported results of odometer swelling pressure tests on remolded samples taken from nearby site, Irbid city, of the similar soil deposits and condition. The test results reported at dry unit weight of 14 kN/m^3 and water content range assembled the seasonal variation of water content as shown in Fig. 4. It's clearly shown that the lower the initial moisture content, the higher will be the swelling pressure and the amount of swell. For initial moisture contents below 24%, the swelling pressure and the amount of swell increases significantly. The swelling pressure of the tested samples varies between 2.5 kPa and 110 kPa. The maximum value of 110kPa is certainly well above the average contact pressure of some light loaded spread footing in the region. Moreover, the amount of swell percentage corresponding to in-situ

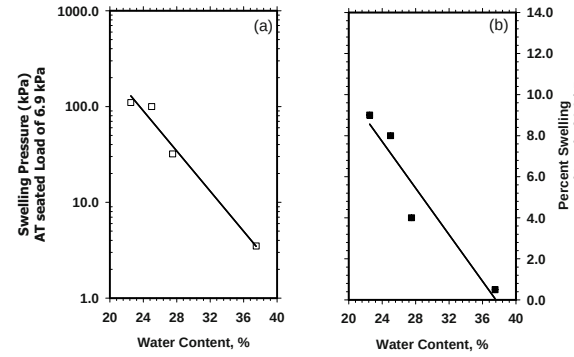

Fig. 4 Moisture content versus (a) swell pressure (b) percent swell as obtained from odometer test

moisture content varies between 0.4% at moisture content of 38% to 4.8% at moisture content of 24%. Under drier initial conditions, values greater than 4.8% would be expected upon wetting of clay.

MODEL PARAMETERS

The model parameters required for the simulation are deduced from measured soil properties. The undrained shear strength of the soil was found to be 80 kPa. The subgrade reaction modulus is given by Bowels (1993) as:

$$ks = 40 q_{ult} \tag{19}$$

where q_{ult} is the ultimate bearing pressure of the footing. Therefore, *ks* will be 16.0 MN/m^3. The interface friction angle between the geosynthetic layer and the granular fill was taken to be 30^o. The reported results later will be for geosynthetic grid materials of a young modulus and allowable tension strength of 500.0 kN/m and 30.0 kN/m respectively. A footing width of 1m was used in this study.

RESULTS AND DISCUSSION

Based on the described finite difference scheme and soil properties mentioned above, the amount of settlement and required geosynthetic length were investigated. Parametric studies were carried out to show the effect of variation of swelling pressure, q_s, on the settlement response. The young modulus of geosynthetic layer as well as andthe thickness of the granular fill layer is are taken as constant throughout the study. Thickness of the granular fill layer is assumed to be as 0.5 m. The chosen thickness is based on the current practice on the region to place a granular fill of 0.5 m underneath the level of footing with out installation of geosynthetic layer. Fig. 5a shows the development of settlement on the surface of the membrane with increasing the loading intensity, while Fig. 5b shows the variation of settlement /upward nonevent with the variation of swelling pressure. From Figure.5a Iit is shown in Fig. 5a that, the width of membrane beneath the footing should at least three times of the width of the footing to mobilize the full membrane action. Moreover Fig. 5b indicates an upward movement of the membrane occurred beyond x/B=1.7. Therefore, the geosynthetic layer primarily diverts the swelling pressure away from acting on footing.

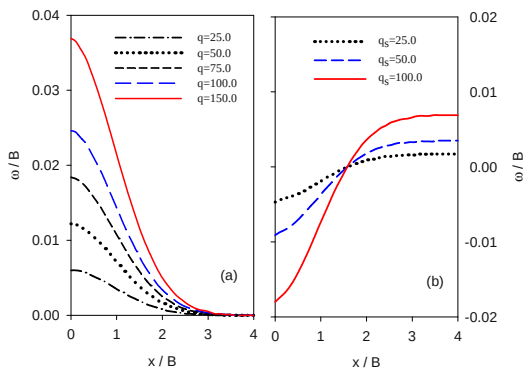

Fig. 5 Normalized settlement profile of reinforced soil, q_s=0 kPa (a) for different applying intensity (b) for variation of swelling pressure at q=25.0 kPa

CONCLUSION

The deflection of strip footing resting on improved soft soil using geosynthetic reinfrorcment placed at the boundary between two different layers was predicted using a finite difference scheme adopt a membrane analogy. The calculated deformations are used to find the required geosynthetic layer length below the footing. Upward movement of the membrane was also investigated. The results show that the minimum geosynthetic of three times width of footing is required to have a membrane-reinforced action, and this length will be able to divert some amount of swelling pressure away from the footing. However, the reported results is roughly and the model still on the stage of development, pear on mind a little known for the effect of cyclic swelling pressure in such scheme.

REFERENCES

Bourdeau PL (1989) Modelling of membrane action in a two-layer reinforced soil system. Computers and geotechnics, 7 (1-2): 19-36

Bowles JE (1997) Foundation Analysis and Design, International Edition, McGraw-Hill Book Co–Singapore

Deb KS, Chandra Basudhar PK (2007) Nonlinear analysis of multilayer extensible geosynthetic-reinforced granular bed on soft soil, Geotech Geol Eng 25: 11–23

Espinoza RD (1994) Soil-geotextile interaction: Evaluation of membrane support. Geotextiles and Geomembranes 13(5): 281-293

Al-Hattamleh O, Muhunthan B (2006) Numerical procedures for deformation calculations in the reinforced soil walls, Geotextiles and Geomembranes 24: 52–57

Harr ME (1977) Mechanics of particulate media: A Probabilistic Approach, McGraw-Hill, New York

Jewell R.A (1988a). Compatibility, serviceability and design factors for reinforced soil walls. Proceedings of the International Geotechnical Symposium on Theory and Practice of Earth Reinforcement, p: 611

Jewell RA (1988b) Mechanics of reinforced embankments on soft soils. Geotextiles and Geomembranes 7 (4): 237-273

Love JP, Burd H J, Milligan, GWE, Houlsby GT (1987) Analytical and Model Studies Of Reinforcement Of A Layer Of Granular Fill On A Soft Clay Subgrade. Canadian Geotechnical Journal 24 (4): 611-622

Nusier OK, Alawneh AS (2002) Damage of Reinforced Concrete Structure due to Severe Soil Expansion, Journal of Performance of Constructed Facilities 16 (1): 33-41

Sergeev IJ (1969) The application of probability — process equations to the theory of stress distribution in non-cohesive soil foundation beds. Soil Mech. and Fdn Engng. 2: 84-88

Shukla SK, Chandra S (1994) A generalized mechanical model for geosynthetic-reinforced found-ation soil. Geotextiles and Geomembranes 13(12): 813-825

Shukla SK Chandra S (1995) Modelling of geosynthetic-reinforced engineered granular fill on soft soil. Gepsynthetics International 2(3), 603-618

Yin JH (1997) A nonlinear model of geosynthetic reinforced Granular Fill over soft Soil. Geosynthetics International 4(5): 523-537

Yin JH (1997) Modeling of geosynthetic reinforced Granular Fill over soft Soil. Geosynthetics International 4(2): 165-185

Proceedings of the 4th Asian Regional Conference on Geosynthetics
June 17 - 20, 2008 Shanghai, China

TREAT CUT SLOPES WITH EXPANSIVE SOILS ADOPTING GEOGRID-REINFORCED TECHNIQUE

H.P. Yang[1], S. Wang[2] and Y.X. He[3]

ABSTRACT: Treating landslides of cut slopes in expansive soils areas is a difficult problem in technique, which has troubled civil engineers for a long time to obtain a safe, economic and environment-protecting treatment measure. A research project of treating highway subgrade in expansive soils areas was sponsored by China Ministry of Communications and a research group was founded and mainly consisted of experts from Changsha University of Science and Technology. The group investigated and analyzed the rules and features of Ningming expansive soil slope failures during the construction of Nanyou expressway in the Chinese Autonomous Region of Guangxi Zhuangzu, put forward and implemented a flexible supporting method, which adopts geogrid-reinforced technique and make use of excavated expansive soils to directly build reinforcement body, to treat landslides of cut slopes. The new technique has brought great benefits in engineering and environmental protection, therefore, a new way for treating landslides effectively of expansive soils cut slopes has been developed and the application of geosynthetics in civil engineering has been broadened. The basic principle, design and construction methods of the geogrid-reinforced technique, the current situation in application, and prospect of the new technology are introduced. In addition, the economic benefit of the technique is also analyzed comprehensively in this paper.

KEYWORDS: expansive soils, landslide of cut slopes, geogrid reinforced, flexible support, treatment technique

INTRODUCTION

Expansive soil mainly consists of montmorillonite and illite, which are all clay minerals with strong hydrophilicity, so it is a kind of clay with high plasticity, and has characteristics of high swelling or shrinking deformation, crack and over-consolidation (Liao SW 1984). The special engineering properties of expansive soil often leads to several disaster of cut slope, such as spalling, erosion, failure of structure, collapse, landslide and so on, which may cause enormous economic losses in the construction of highway. Therefore, the problem of the treatment of cut slope with expansive soil has increasingly been paid attention to.

At present there was not a safe and economic measure for the treatment of cut slope with expansive soil, because the landslide of cut slope with expansive soil is not only related to the property of soil but also closely related to geological structure, climate environment and groundwater (Li SL 1992). It makes the study for landslide more complex and we must consider more actors in treatment plan. Economy and environmental protection requirements also should be taken into account. Combined with the conduct of expansive soils research project sponsored by the West Project Construction Office of Ministry of Communications of China, the expansive soil research group of Changsha University of Science and Technology investigated and analyzed the engineering properties of Ningming expansive soil and the features of landslide of cut slope, put forward and implemented a flexible supporting method for the first time, which adopts geogrid-reinforced technique. The new technique solved the problem of landslide of cut slope with Ningming expansive soil successfully. Accordingly it brought great benefits in engineering, economy and environmental protection.

THE PROPOSING OF FLEXIBLE TREATMENT WITH GEOGRID-REINFORCE TECHNIQUE

Presently, there are many engineering measures adopted in the treatment of slope landslide with expansive soil. They are divided into flexible support and rigid support. For finding out the laws and characters of cut slope's damage of Ningming expansive soil, and proposing effective treatment measures, we investigated and analyzed sliding slopes in Nanyou expressway.

[1] Professor, School of Highway Engineering, Changsha University of Science & Technology, CHINA. Email: cscuyang@163.com
[2] Postgraduate, School of Highway Engineering, Changsha University of Science &Technology, CHINA.
[3] Postgraduate, School of Highway Engineering, Changsha University of Science & Technology, CHINA.

Ningming expansive soils typically exhibited several characteristics (Yang HP et al. 2005):

(1) Landslides mainly involved a cut slope's shallow layer. Sixty-nine percent of the landslides were small, occurring in the layer of light gray expansive clay. Of the large-scale failures, 78 percent occurred along the interface between soil and shale or in the strongly weathered shale. Because the interface was mainly distributed at a depth of 3 to 5.5 m, the depth of the sliding surface rarely exceeded 6 m.

(2) Landslides followed the direction of the underlying strata. The small-scale slides all occurred in parallel to the direction of the stratum and slope. Similarly, most large-scale landslides paralleled the stratum's direction. Therefore, the stratified face of shale and eluvial expansive soil was the preeminent factor in slope failure.

(3) The obliquity of most sliding surface was gentle, the dip of the mud shale stratum ranged from 135 to 158 degrees, and the obliquity of the mud shale stratum ranged from 2 to 16 degrees. Although most of the sliding surfaces ranged from only 2 to 5 degrees, the slope angles ranged from 21.8 to 18.4 degrees.

(4) Landslides occurred seasonally, generally late in the rainy season or following a heavy rain.

(5) Most sliding surfaces were Z shaped rather than circular because of the bedding of soil and rock and because of fissures and cracks, joints in the rock, and the soft interlayer between soil and rock.

Strength degradation of soil is the main reason for cut slope's landslide, and it's controlled by soil structure and water content. In the period of expansive soil road cuts' excavation, slopes' topsoil swells as result of unloading and groundwater's infiltration, and the change of climate, geological environment, engineering activities and fast moving of water change the stress distribution in slopes, as result slopes lose their stability at last (Yang HP et al. 2004).

According to these damage characters and reasons for Ningming expansive soil, the research group adopted a method of flexible support to prevent landslides along the Nanyou expressway's cut slopes. To that end, the researchers examined the following steps: placing and anchoring geogrids in separated layers within the fill material, backfilling and compacting nonexpansive or expansive soil to form a reinforced body with sufficient thickness, enveloping the tops of the slopes, and installing a drainage system in the subbase and on the back of the reinforced structure. This approach was designed to account for the following factors:

(1) Friction and interlock between the geogrid and the fill material, along with the layered geogrid's connection to the outer covering, can provide shear strength sufficient to enable the reinforced structure as a whole to resist landslides.

(2) The flexible reinforced structure permits a slope to deform adequately to release the stress and pressure caused by swelling.

(3) The flexible reinforced structure has a slope gradient of 1:1.5. Being more than 3.5 m thick and more than two-thirds the height of the cut slope, the structure can cover the main surface of a freshly cut slope and provide sufficient weight to resist soil pressure.

(4) Because of its thickness, a reinforced structure can insulate a slope's expansive soil and protect it against fissures and other effects of weathering.

DESIGN SCHEMES FOR FLEXIBLE TREATMENT

According to the failure character of cut slope with Ningming expansive soil and considering the weathering depth, soil property, hydrogeological features and the feasibility of construction, the design schemes of flexible support with geogrid-reinforced were put forward (Fig. 1).

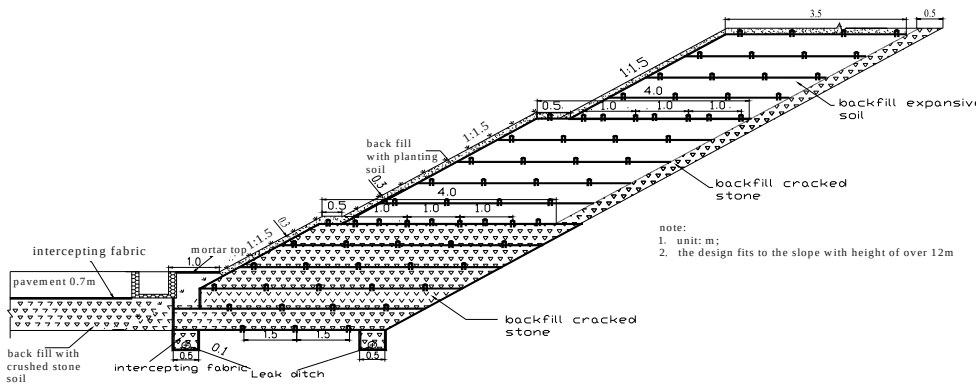

Fig. 1 Slopes treated with flexible support

The following is the explanation:

(1) The width of reinforced body is larger than 3.5 m to satisfy the requirement of mechanical construction, prevent the influence of atmosphere to slopes' soil, and exert the effect of wrapping and support.

(2) In order to reduce soil pressure and ensure the stability of reinforced soil body and the counterpressure effect to slopes' soil, the slope rate of 1:1.5 is adopted in reinforcing slopes.

(3) Referring to relating experience and calculating preliminarily, select the geogrid (its design tensile strength is 35 kN/m) as reinforcing material, and pave a layer of geogrid per two layers of filling soil (the effective length of reinforcing geogrid is 3.5 m, the geogrid is fixing to fill using U-shape nail per 1.2 m, and counter-wrapping underlayer geogrid is obligated to connect with superstratum geogrid with linking sticks, which makes reinforcing body form a integer to resist all kinds of effects).

(4) The bottom 1－3 layers of reinforced body are filled with cracked stone, whose strength and drainage requirement are satisfied; the layers upper 4 layer are filled with excavated expansive soil directly.

(5) The drainage layer of 50 cm cracked stone is designed between reinforcing body and excavated slope's surface, to lead and desiccate the cranny water in slopes. At the bottom of reinforced body, two longitudinal underdrain are set to reduce groundwater level in road bed and at the back of slopes to implement the aim of drainage and diffluence.

(6) The top and surface of slopes is covered with 30cm plowing soil and planting virescence is done to prevent from the washing of rain.

Fig. 2 shows the lattice structure of unidirectional geogrid (TD represents transverse, and MD represents vertical). The geogrids adopted in the design scheme of flexible treatment is respectively called RS35PP and RS50PP which are produced by Hubei Lite Civil Engineering Material Co.Ltd and TGDG35 which is produced by Shaoxing Naite Plastics Co.Ltd. Its physical property parameters presents as Table 1.

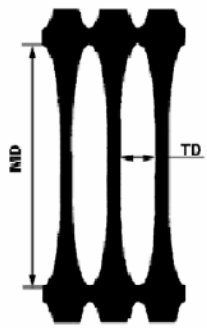

Fig. 2 Lattice structure of unidirectional geogrid

Table 1 Basic technical indexes of geogrid

type of geogrid	size （cm）		thickness （cm）		tensile module
	MD	TD	rib	node	
TGDG35	15.218	1.102	0.060	0.138	35kPa
RS35PP	22.231	1.776	0.050	0.168	35kPa
RS50PP	27.142	1.884	0.080	0.220	50kPa

CONSTRUCTION FOR FLEXIBLE SUPPORT

As we adopted conventional road machines, and there is no special technical requirement, construction is convenient. Basic processes are: (1) according to the design, excavate slopes to form working plane; (2) layer the slopes from down to up, fill drainage layer (the thickness is 50cm) with cracked stone in front of the excavated slopes' plane, and then pave geogrid on which soil is filled and compressed; (3) the obligated geogrid is counter-wrapped and connected with upper geogrid by linking bars to form slope plane. Here, the cracked stone drainage layer behind reinforced body is penetrated from bottom to top, therefore, fissure water in slopes can be drained out. The points in detail are:

(1) The treatment of basement (Photo 1): Clean out loose soil from base, excavate blind drain according to the design，bury PVC pipes and then cover the blind drain with cracked stone. Then roll basement. If base is wet and soft in some part, the ash mixture treatment is available and then use cracked stone wrapped by geogrid for backfill.

Photo 1 Treatment of basement

(2) The paving and the connection of geogrid: firstly, pave the geogrid cut beforehand in the vertical direction of road center line (Photo 2). The connecting width of every two pieces of geogrid (the width of geogrid is 1.3 m) is not less than 5 cm (Photo 3) and the geogrid is fixed with U-shape nails. Upper and below geogrid is connected with linking bars and the connecting length is not less than 30 cm. The geogrid must be stretched to be tight enough and linking bars should be clamped closely

to ensure the integer and effectivity of reinforced soil body.

Photo 2 Counter-wrap and pave geogrid

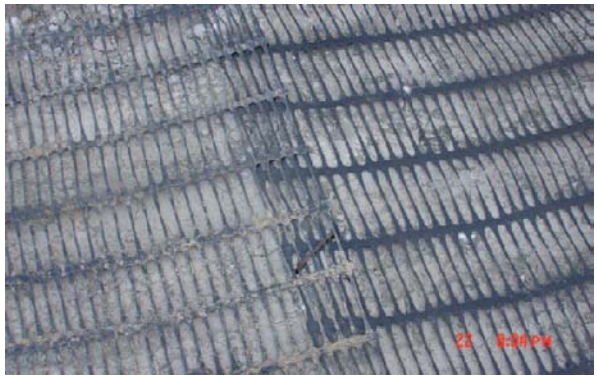

Photo 3 Connection of Geogrid

(3) Compaction of fill: Pave and fill soil according to virtual thickness, and adopt the times of rolling to control the compaction degree, to assure above 80%. And the drainage layer behind walls is forbidden to be compressed (Photo 4).

Photo 4 Compaction of fill

(4) Treatment for the top of reinforced body: At the top, pave 'two fabric and one membrane' till the place of catchwater and then fill good soil with the thickness of 50 cm to avoid the penetration of rain water.

THE EVALUATION OF TREATMENT EFFECTS

Four experimental slopes researched by project team were finished on Nov. 2004. As the successional landslides of other treated slopes in the distributing areas of expansive soil during construction, owners required construction units to adopt the flexible treating technique to deal with landslides problems. Therefore, until September this year, there were fourteen expansive soil cut slopes in Nanyou expressway, adopting such a technique in the total length of 4.8 km. Going through the proof of two dry and rainy seasons, especially the raid of several big typhoons and rainstorms, flexible treating slopes all worked well, and the plants on slopes grew well. At the bottom of reinforced body, underdrains are expedite , there are groundwater flowing, the effect of drainage is good, in rainy season underdrains and blindguts can drain quickly, which can decrease static water pressure of cranny water effectively, and fast drainage can slow down swelling pressure as the groundwater is resorted in slopes. It showed clearly about the treating effects (Photo 5—8).

Photo 5 Comparison of untreated treated cut slope from K138+420 to K138+820

Photo 6 Comparison of untreated treated cut slope from K136+040 to K136+450

Photo 7 Comparison of untreated treated cut slope from K133+804 to K134+100

Photo 8 Effect photo of cut slope's landslide treated by three-step flexible support in a ramp of Ningming

Compared with the rigid retaining wall, a structure providing flexible support is easier and less expensive to construct since it involves a simpler technique. For example, a 7 m high structure providing flexible support was constructed to stabilize a 10 m high, 300 m long cut slope along the Nanyou expressway. Construction was completed in just 20 days at a cost of less than US$ 120,000. However, had a rigid retaining wall been constructed and the slope covered with masonry pitching, the project would probably have cost more than US$147,000 and taken more than a month. Of greater importance, the retaining wall would have had a harder time maintaining slope stability.

Because of the benefits conferred by this technique, the Nanyou expressway's contractor adopted this scheme to address 10 other landslides after the four trial slopes had been constructed. These experiences have demonstrated that the scheme providing flexible support works well in treating cut slopes with expansive soils.

CONCLUSION

According to National planning of road nets, highway of 85,000 km in total will be built in our state. At present, a new high tide of construction is beginning with the development of West China. According to the analysis and prediction of geological condition along major artery and 8 provincial roads that will be constructed in plan , it can be preliminarily confirmed that there will be near 3,300 km roads traversing expansive soil areas in the total 21,000 km length roads are planning to be constructed in West China. The successful experience of treatment technique for subgrade of Ningming expansive soil provides packaged technology for improving the quality of road construction in expansive soil area, assuring the great road performance and prolonging the service life of road. The road construction problem of expansive soil in West China will be solved completely.

Flexible supporting with geogrid is such a comprehensive treatment technique for cut slope of expansive soil that technique reliability, economy and reasonability, environment protection and construction convenience are combined as a whole. Thereinto, using expansive soil directly as fill of reinforcing body is its distinctive character. The successful application of such a technique, of treating Ningming expansive soil cut slopes' landslides in Nanyou expressway, has brought great economic and environment-protection benefits. It can be believed that, for other engineering constructions in expansive soil districts, there are also wonderful application foregrounds for such a new technique.

REFERENCES

Liao SW (1984) Expansive Soil and Railway Engineering. Beijing: China Railway Press

Li SL (1992) The Engineering Geological Research of Expansive Soil in China. Nanking: Jiangsu Science & Technology Press

Yang HP, Zheng JL, Wu XH, Lian XD (2005) The Engineering Treating Technique of Expansive Soil Embankments in Nanyou Expressway in Guangxi Province. The Annual Academy Proceedings of China Road Association in 2005

Yang HP, Zheng P (2004) Geological Investigation and Consideration of Expansive Soil Cut Slopes' landslides in Nanyou Expressway. The Journal of Changsha University of Science & Technology 1(1): 14-19

Yang HP, Qu YX, Zheng JL (2005) New Advances in the Research of Ningming Expansive Soil. Geotechnical Engineering Journal 21(9): 981-987

Feng YY, Zhang YS, Qu YX (2001) The Mechanism Research of Expansive Soil Embankments' Diseases in Nankun Railway in Baise Basin. Geotechnical Engineering Journal 23(1): 463-467

EXPERIMENTAL STUDY ON THE STRENGTH CHARACTERISTICS OF EXPANSIVE SOIL REINFORCED WITH SYNTHETIC FIBERS

Y.H. Tang[1], C.G. Bao[2], M.Y. Wang[3] and J.H. Ding[4]

ABSTRACT: Expansive soil reinforced with synthetic fibers is a modified method developed in recent years, but experimental study results on its engineering behavior are rare at present. Polypropylence monofilament fibers are adopted to reinforce the expansive soil in Xinxiang, China, and the effect of moisture content, compaction degree, fiber content and sample size on the undrained strength behaviour of expansive soil reinforced with synthetic fibers are studied through unconfined compression strength test, and failure model of expansive soil reinforced with synthetic fibers is analyzed. Test results showed that unconfined strength of expansive soil modified with fibers is increased with a rise in compaction degree and fiber content, reduced with the increase of moisture content; under the same condition, strength resulting from small size sample is larger than that of large size sample; non-reinforced expansive soil assumes a brittle failure with an obvious shear failure plane; expansive soil reinforced with synthetic fibers shows a plastic failure with no obvious shear failure planes.

KEYWORDS: synthetic fiber, expansive soil, unconfined compressive strength, undrained intensity index, failure mode

INTRODUCTION

Expansive soils are widely distributed worldwide, and so far they have been found in over 40 countries. Geo-hazards caused by expansive soil occur frequently worldwide and the damageresulting of disasters isare huge. Expansive soil has a high clay content and is rich in bentonites, illites and exchangeable cations with strong hydrophilic property, and its liquid limit is usually more than 40%, and plasticity index is generally higher than 20, both of them are more than those of ordinary clays. It is a special clay with a high liquid limit and too much fissure, characterized by special expansion and contraction feature, over-consolidation nature and fissure character (Liu 1997). Loosely-bound water film around hydrophilic clay grains in expansive soil becausedue to electric double layer is thick, lattice of montmorillonites, illites and mixed-layer minerals can be expanded due to water absorption that makes volume of expansive soil expand, and reduce the suction force, decrease strength parameter; and dehumidifying makes expansive soil contract and crack.

Failure mechanism and treatment measures of expansive soil's levee slope are always the hotspot and difficult problems that scholars have studied. Modified treatment of expansive soil is an effective treatment measures, because it can reduce or clear up its expansion and contraction, improve its shear strength index. Commonly-used modified measures include adding sandy soil (Liang 2006), lime (Cui 2003) , cement (Li 2002), ash fly (Zhang 2002) or organic curing agent (Lei 2004), and expansive soil reinforced with synthetic fibers (Zhang 2005) is a modified method developed in recent years.

Adding fibers into soil mass can enhance the integrity of soil mass and reach the purpose of improving soil mass's strength through the strength of fiber itself and the complicated three-dimensional action between fiber and soil mass (Editorial Board of A Handbook of Engineering Application of Geosynthetic Material (Second Edition) 2000). Soil reinforced with fibers has good environmental protection effect, it is easy to be constructed, and facilitates to take borrow materials in-place with an economic construction cost. Sandy soil reinforced with fibers have been extensively applied in engineering (Mohamad 1990), reinforced fibers general-ly exerts better effect on clay soil (Li 1995). In literature (Ding 2002),

[1] Graduate Student.Yangze River Scientific Research Institute and Civil Engineering Department, College of Architecture and Civil Engineering, South China University of Technology, CHINA. Email: tyh0529@126.com
[2] Professor.Yangze River Scientific Research Institute,Key Laboratory of Geotechnical Mechanics and Engineering of the Chinese Ministry of Water Resources, CHINA. Email: bcgang@public.wh.hb.cn
[3] Senior Eengineer.Yangze River Scientific Research Institute,Key Laboratory of Geotechnical Mechanics and Engineering of the Chinese Ministry of Water Resources, CHINA. Email: wmy_90@163.com
[4] Senior Eengineer.Yangze River Scientific Research Institute,Key Laboratory of Geotechnical Mechanics and Engineering of the Chinese Ministry of Water Resources, CHINA

experimental study on the expansion ratio index of expansive soil reinforced with synthetic fibers has been carried out, but the strength behavior of expansive soil reinforced with synthetic fibers is not considered.

Modified polypropylence monofilament fibers are adopted to reinforce the expansive soil in Xinxiang, China; the effect of moisture content, dry density, fiber content and sample size on the undrained strength behaviour of expansive soil reinforced with synthetic fibers are studied through unconfined compression strength test, and failure model of expansive soil reinforced with synthetic fibers is analyzed.

TEST SCHEMES

Main parameters of modified polypropylence mono-filament fiber selected are shown in Table 1.

Table 1 Parameters of fiber selected

Parameter	Unit	Magnitude
Length	mm	20
Tensile strength	Mpa	≥350
Elongation rate of fracture	%	8-30
Elastic modulus	Mpa	≥3500

Soils used for the test areadopts expansive soils with limestone and iron concretion taken from Xinxiang, China. Colour of soil sample is changed greatly with water content; when water content is low, it shows a greyish white, when water content is high, it shows a greyish green. Grain composition of soil sample has high content of clay grains as high as 31.0%－52.1%; free expansion ratio is 41%－62%, it is weak and neutral expansive soil. Basic physical and mechanical indices of expansive soil samples are as shown in Table 2.

Table 2 Physical and mechanical indices of soil sample

Index Name		Unit	Magnitude
Natural Water Content		%	14.2
Dry Density		g/cm^3	1.85
Specific Gravity			2.72
Liquid Limit		%	38.9
Plastic Limit		%	18.5
Plastic Index		%	20.3
Optimum Water Content		%	18.3
Maximum Dry Density		g/cm^3	1.73
Natura Quick Shear	Cohesion	kPa	90.8
	Frictional Angle	^{0}	39.9

During this test, unconsolidated undrained shear is adopted to keep confining pressure at 0, shear rate at 1mm/min.

The effect of moisture content, compaction degree of compacted soil, fiber content and sample size on the undrained strength property of expansive soil reinforced with synthetic fibers are compared mainly. Test factors are as showedn in Table 3, of which fiber content is the ratio of fiber mass to arid soil mass.

Table 3 Test factors of expansive soil reinforced with fibers

Factor Level	1	2	3	4
Fiber Content/%	0	0.2	0.5	1
Sample Size /Diameter ×Height	101×200	39.1×80	-	-
Compaction Degree /%	98	95	-	-
Water Content /%	14.2	18.3	-	-

STRENGTH PROPERTY AND INFLUENCING FACTORS OF EXPANSIVE SOIL REINFORCED WITH FIBERS

Effect of Fiber Content on the Undrained Strength

When water content of soil sample is 14.2%, compaction degree is 98%, sample size (diameter×height) is 101mm×200mm, stress-strain curves at different fiber contents (i.e., 0, 0.2%, 0.5%, 1%) obtained by the test are shown in Fig. 1.

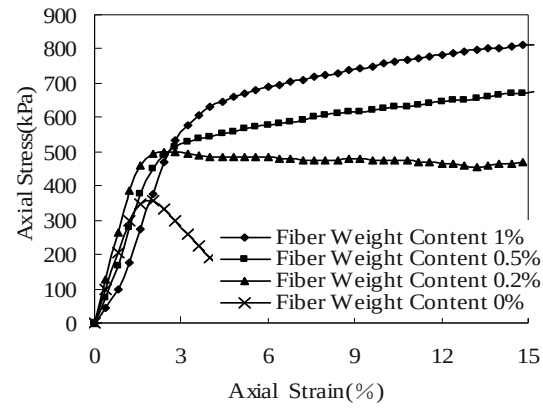

Fig. 1 Stress-strain curves at different fiber content when water content is 14.2%

It can be seen from Fig.1 that the effect of fiber content on the strength is marked, the higher the fiber content, the greater the strength. It may also be seen from the stress-strain curves of non-reinforced soil and reinforced soil with a fiber content of 0.2%, i.e. even if small amount of fibers is added into soils, strength property of soil sample is modified obviously. When strain is 2%, the peak strength of non-reinforced soil is

355 kPa, thereafter axial stress sharply declines. It is also observed during the test process that failure plane that cuts through the entire sample appears, soil mass is obvious brittle shear failure. However the peak strength is 500 kPa, 41% higher than that of non-reinforced soil. After reaching peak strength, axial stress is decreases d slightly with a rise in strain; when strain reaches 15%, axial stress is decreases d only by 5.9% in comparison with peak strength. So softening degree of reinforced soil with a fiber content of 0.2% is slowed up obviously as compared with that of non-reinforced soil.

With the increase in fiber content, stress-strain curve is gradually changed from strain-softening type into a strain-hardening type; the greater the fiber content, the more obvious the strain-hardening phenomenon. Stress-strain curve of non-reinforced soil shows an obvious strain-softening type; after small amount of 0.2% fiber is added, stress-strain curve becomes slightly-softening type; when fiber content is increased to 0.5%, stress-strain curves appear as strain-hardening type. Fiber content that corresponds to critical stress-strain curve of soil reinforced with fibers between softening type and hardening type under certain water content is defined as the critical fiber content under this water content. As shown in Fig. 1, the critical fiber content of soil masses reinforced with fibers under a water content of 14.2% ranges from 0.2% to 0.5%. Critical fiber content at different water contents can be obtained through test.

It can be seen from Fig. 1 that action of fiber is dependent greatly on the strain. When strain reaches to a given degree, then advantage of reinforced soil can only be brought into play more fully performance. When strain is smaller than 2%, stress-strain curves of non-reinforced soil and sample with different fiber contents are almost coincided; but when strain is higher than 2%, axial stress of reinforced soil sample is obviously higher than that of non-reinforced soil sample. This is because during small strain period, fiber is at compressed stage, and action mechanism of fibrous soil has not brought into play; during large strain period, fiber is at tension state, there occurs ccomplicated interaction occurs between fiber and soil, strengthening action of fiber on soil mass is brought into full play.

Rule obtained from test carried out when water content is 18.3% with a big amount of high fiber content is consistent with that when water content is 14.2% with a small amount of fiber content. Stress-strain curves at different fiber contents when water content is 18.3% are as shown in Fig. 2. Fiber contents in Fig. 2 are 0%, 1% and 3%, respectively when water content of sample is 18.3%, compaction degree is 98%, sample size (diameter ×height) is 101mm×200mm.

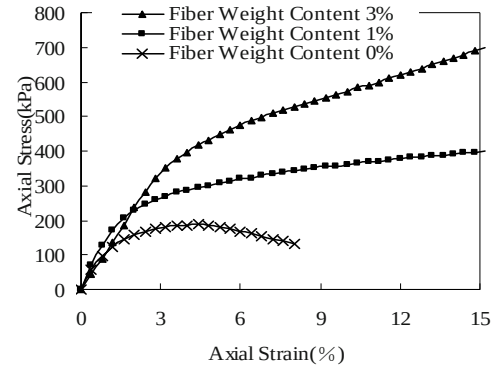

Fig.2 Stress-strain curves at different fiber contents when water content is 18.3%

Effect of Water Content on Undrained Strength

When water contents of soil sample are 18.3% and 14.2%, respectively, compaction degree is 98%, sample size (diameter×height) is 101mm×200mm, stress-strain curves with the fiber content of 1% obtained by the test aare shown in Fig.3.

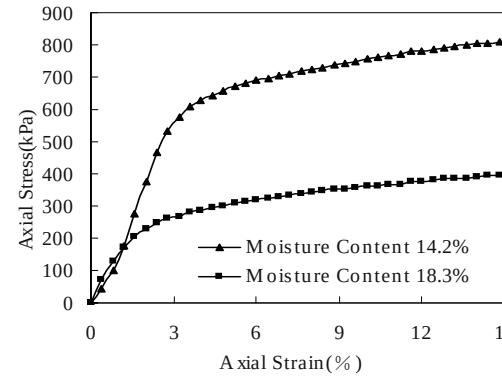

Fig. 3 Stress-strain curves at different water contents

A series of experimental studies on the strength of non-reinforced expansive soil have already done before, those studies showed that strength of non-reinforced expansive soil is very sensitive to the variance in water content; when water content is reduced from 18.3% to 14.2%, its strength is increased from 187 kPa to 355 kPa. It can be seen from Fig. 3 that strength of soil reinforced with fibers is still sensitive to the change in water content. It showed that adding fiber is difficult to change the high sensitivity of expansive soil's strength to water. Wwhen water content is reduced from 18.3% to 14.2%, strength is increasesed from 398 kPa to 814 kPa, rising by 105%. It showed that adding fiber is difficult to change the high sensitivity of expansive soil's strength to water.

Effect of Compaction Degree on Undrained Strength

When water contents of soil sample is 18.3%, compaction degrees are 95% and 98%, sample size (diameter ×height) is 101 mm×200 mm, stress-strain curves with

the fiber content of 1% obtained by the test are shown in Fig. 4.

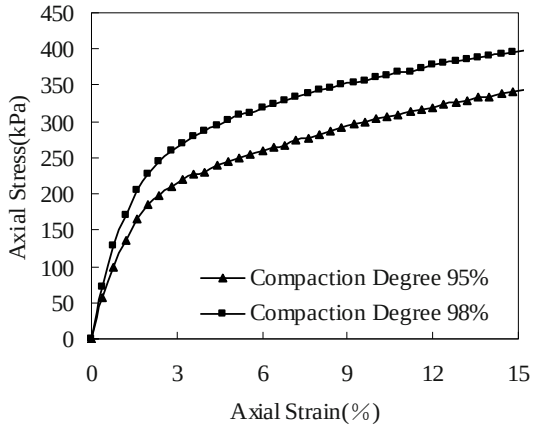

Fig. 4 Stress-strain curve at different compaction degrees

It can be seen from Fig. 4 that stress-strain curve of soil reinforced with fibers at two compaction degrees are strain-hardening type. When compaction degree is increased from 95% to 98%, strength of reinforced soil is increased by 16%, so enhancing compaction degree properly can improve the undrained strength of expansive soil masses reinforced with fibers.

Effect of Sample Size on Undrained Strength

When fiber contents of two samples are 1%, water content is 18.2%, compaction degree is 98%, sample sizes are 101 mm×200 mm and 39.1 mm×80 mm respectively, stress-strain curves for soil samples with two sizes are as shown in Fig. 5.

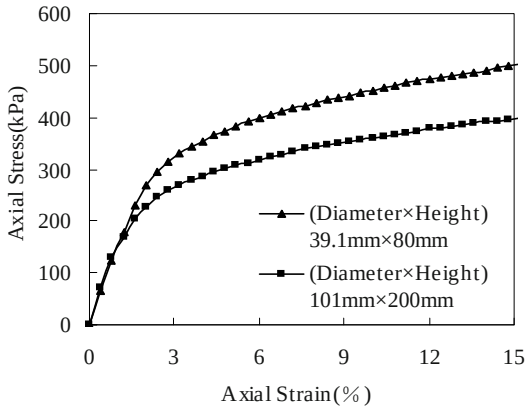

Fig. 5 Stress-strain curve of samples with two sizes

It can be observed that strength of small sample is higher than that of large sample. Strength of soil reinforced with fibers is affected by sample size, and sample's strength is reduced with the increase of sample size.

Stress-strain curves of large and small samples before yield strain are coincident. If nonlinear deformation of sample during initial period of loading is not considered, sample size does not exert a significant effect on the deformation characteristics before yielding, this shows that elastic modulus and yield strain are little affected by sample size.

FAILURE MODEL OF EXPANSIVE SOIL REINFORCED WITH FIBERS

Frequently, non-reinforced soil sample fails suddenly, obvious shear planes are suddenly formed without any clear warnings in advance, which is typical brittle failure as shown in Figs. 6aand 6b. But failure of reinforced soil sample is progressive, which shows a plastic failure as shown in Fig. 6c. Observation on the whole test process of many reinforced soils shows that when strain is quite small, there appear no fissures in sample; when strain is 6%—8.5%, tiny fissures begin to occur in sample; with the increase of strain, tiny fissures appear in many positions of sample; at the same time, bulging deformation appears in samples, when strain is 15%, no obvious shear failure planes appear. If axial strain is increased continually, main fissures don't continue to be developed, but a great deal of tiny cracks is generated around main fissures to form a shear zone with a large scope as shown in Fig. 6c. Deformation of reinforced soil before failure is far larger than that of non-reinforced soil, its ductility and strength are improved greatly in comparison with non-reinforced soil. This shows that adding fiber enhances the global stability of soil masses, reticulate fibrous structure zigzag connected between fibers and soil masses can exert effective space restraint effect on soil mass. Such effect causes the stress of soil mass to be redistributed, prompts the stress to transfer from high-stress area to small stress zone, effectively inhibits the development of main fissures in soil mass, changes the failure mode of soil sample.

(a) (b) (c)

Fig. 6 The failure mode of soil sample under different reinforced condition
(a) Non-reinforced compacted soil
(b) Non-reinforced undisturbed soil
(c) Reinforced compacted soil

CONCLUSIONS AND DISSCUSIONS

In this paper, the following conclusions can be obtained through unconfined compression strength test of expansive soil reinforced with fibers.

(1) Reinforced soil's strength is obvious higher than that of non-reinforced soil, and the more the fiber content, the greater the soil mass's strength is improved.

(2) With the increase of fiber content, stress-strain curve is changesd from strain-softening type to strain-hardening type. When water content is 14.2%, critical fiber content ranges from 0.2% to 0.5%.

(3) Whether fibers bring into play or not is greatly relevant to the strain. When strain reaches to a given degree, advantage of reinforced soil can be brought into full play.

(4) Reinforced fiber is difficult to improve the high sensitivity of expansive soil's undrained strength to water. Unconfined compressive strength of soil reinfor- ced with fibers is very sensitive to the change in water content; when water content is reduced from 18.3% to 14.2%, strength is increased by 105%.

(5) Compaction degree is one of factors affecting the undrained strength of soil reinforced with fibers as well. When compaction degree is increased from 95% to 98%, strength of expansive soil reinforced with fibers is increased by 16%.

(6) Sample's strength is reduced with the increase of sample size; elastic modulus, yield point strain and axial stress before yield are little affected by sample size.

(7) Adding fiber can effectively inhibit the development of fissures in soil mass and change the failure mode of compacted expansive soil. No obvious shear planes appear during the failure process of soil masses reinforced with fibers. Ssample is deformed greatly, its strength and ductility are improved greatly in comparison with non-reinforced soil.

REFERENCES

Cui W, Li HL, Mu NM (2003) Experimental research on engineering character of improved expansive soil with lime. Journal of Soil and Rock Mechanics 24(4): 606-609

Ding WT (2002) Research on the Strength Property of Reinforced Expansive Soil. Master. Thesis, Chang'an University. Xi'an, Chinese

Editorial Board of A Handbook of Engineering Application of Geosynthetic Material (Second Edition) (2000) Reinforced Soil Engineering (Chapter 5). Beijing: China Building Press: 179-189

Li GX, Chen L, Zhang JQ, Jie YX (1995) Experimental Study on Fiber-Reinforced Cohesive Soil; . Journal of Hydraulic Engineering (8): 31-36

Liu TH (1997) The Basic Engineering properties of expansive soil (Chapter 2). Expansive Soil Problem in Engineering Construction. Beijing, China Building Industry Press: 15-28

Li ZP (2002) The Test and Study of the Behavior for Cement-Stabilized Expansive Soil. Journal of Geotechnical Engineer 14(1): 13-16

Lei SY, Hui HQ (2004) Experimental investigation on the properties of expansive soil improved by chemical liquid; . Chinese Journal of Geotechnical Engineering, 26(5): 612-615

Liang XL, Guo DH (2006) Experimental Study on the Weak Expansive Soil Treated with Sand in Roadbed Construction. Journal of Guangdong Civil Engineering and Building (8): 26-28

Mohamad H. Maher and, Donald H. Gray (1990). Static Response of Sand Reinforced with Randomly Distributed Fibers Journal of Geotechnical Engineering, 116 (11): 1661-1677

Zhang JR, Xu SX (2002) Compaction Behaviour on Subgrade Filler of Stabilizing Expansive Soil Mixed with Lime and Fly Ash. Journal of Wuhan University of Technology 24(9): 27-29

Zhang YM, Zhang XD, Zhang HR (2005) Test research of geotechnique textile soil reinforcement mechanism and engineering application. Journal of Soil and Rock Mechanics 26(8): 1323-1326

CHANGE OF FAILURE MECHANISM OF CEMENT TREATED CLAY BY ADDING TIRE CHIPS

Y. Kikuchi[1], T. Sato[2], T. Nagatome[3], Y. Mitarai[4] and Y. Morikawa[5]

ABSTRACT: It is generally known that cement treated clay (CTC) shows improved shear strength in comparison with clay but becomes ductile during shear. Recent research has demonstrated that the toughness of CTC is improved by adding shredded tire chips (cement treated clay with tire chips: CTCT). In the present research, several types of shear tests were conducted on CTCT, including the unconfined compression test, beam bending test, and punching shear test. This paper discusses the relationship between shear modes and the effect on the failure mechanism when tire chips are added to CTC. The test results showed that addition of tire chips improves the toughness of CTC in the unconfined compression shear mode and punching shear mode, but less improvement was seen in the bending shear mode, in which extensive cracks were observed. The difference in these results means that compressive deformation of tire chips is responsible for improvement in the toughness of CTC.

KEYWORDS: cement treated clay, tire chips, stress-strain, X-ray CT, crack propagation

INTRODUCTION

It is generally known that cement treated clay (CTC) shows improved shear strength in comparison with clay but becomes ductile during shear. Recent research has demonstrated that the toughness of CTC is improved by adding shredded tire chips (Yasuhara et al. 2004a). If cement treated clay with tire chips (CTCT) possesses both high shear strength and toughness, it can be used as a barrier material for revetments in controlled waste disposal facilities constructed offshore (Yasuhara et al. 2004b).

Research on used tire chips as geo-materials has been conducted since the early 1990s, mainly in the US and Canada. In Japan, research on tire chips as geo-materials started around 2000 (Ashoka et al. 2002), and was followed by research on composite geo-materials comprising a mixture of existing geo-materials and tire chips.

Yasuhara et al. (2004a) reported that the toughness of CTC is improved by adding tire chips. Fig. 1 shows the stress-strain relationship in unconfined compression tests. The fraction of tire chips to CTC was varied from 0% to 23%. As shown in Fig. 1, shear strength was not changed by adding tire chips, but failure strain was increased by increasing the fraction of tire chips.

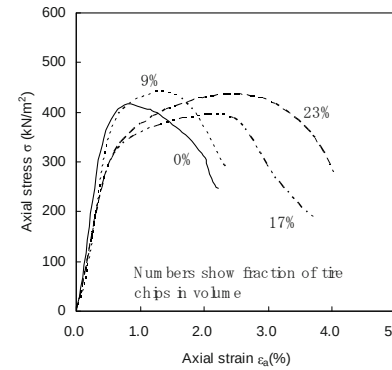

Fig. 1 Effect of tire chips in cement treated clay on stress-strain relationship in unconfined compression test

Use of CTCT as an impervious material has also been investigated. This research mainly focuses on mechanical behavior and mixing conditions. A small number of studies have investigated the failure mechanism of CTCT (Kikuchi et al. 2006; Nagatome et al. 2006).

At the present research, three types of shear tests were conducted on CTCT, these being the unconfined compression test, beam bending test, and punching shear

[1] Head, Foundations Division, Port & Airport Research Institute, JAPAN. Email: kikuchi@pari.go.jp
[2] Research Engineer, Toa Corporation, JAPAN. Email: satoh-ta@pari.go.jp
[3] Research Engineer, Toa Corporation, JAPAN. Email: nagatome@toa-corporation.co.jp
[4] Senior Researcher, Toa Corporation, JAPAN. Email: mitarai@toa-corporation.co.jp
[5] Senior Researcher, Geotechnical & Structural Engineering Department, Port & Airport Research Institute, JAPAN. Email: morikawa@pari.go.jp

test. This paper discusses the relationship between shear modes and the effect of adding tire chips to CTC on the failure mechanism.

MATERIAL

The materials studied in this research were CTC and CTC containing 16.7% by volume of melded tire chips. Dredged slurry, cement, and tire chips were used to prepare the CTC. The dredged slurry was Tokyo Bay clay (ρ_s=2.716 g/cm^3, w_L=100%, w_P=44%), with the water content controlled to 2.8 w_L by adding seawater. The cement was normal Portland cement, the particle density of which was 3.16 g/cm^3. The tire chips were cut from used automobile tires to a size of approximately 2 mm, as shown in Fig. 2. The particle density of these chips was 1.15g/cm^3. The properties of the rubber used in the automobile tires were extension strength: 15－35 MN/m^2, elastic modulus: 1－5 MN/m^2, Poisson's ratio: 0.5, and elongation capacity: 300 － 600% (Komatsu 1993).

Fig. 2 Tire chips (Average diameter is 2 mm)

The CTC was prepared by mixing the three materials under designated mixing condition, as shown in Table 1. The target of unconfined compressive strength of the CTC at 28 days of curing time was 500 kN/m^2.

Table 1 Mixing condition

	CTC (Tire chips: 0%)		CTCT (Tire chips: 16.7%)	
	Mass (kg)	Volume (L)	Mass (kg)	Volume (L)
Saturated clay	1199.0	974.8	999.2	812.3
Cement	79.6	25.2	66.4	21.0
Tire chips	-	-	191.7	166.7
Total	1278.6	1000.0	1257.3	1000.0

The mixture was filled in specified molds, which were covered with wrapping to prevent drying of the specimen. The molds were placed in a high moisture closed box (relative humidity: >95%) under a constant temperature condition (20℃).

UNCONFINED COMPRESSION TEST

Experimental Procedure

Both the compression test and permeability test were conducted using a triaxial compression apparatus designed for the X-ray CT scanner. This apparatus was designed in such a way that the triaxial tests could be performed in the X-ray shield box. Specimens (50mm × 100 mm) were sealed with a membrane and set in the triaxial compression apparatus. The compression test was conducted with no confining pressure, and the permeability test was conduced with applied cell pressure in order to apply a hydraulic gradient. X-ray CT scanning was conducted to determine the initial state of the specimen set in the apparatus. Pressure (40 kPa) was applied to the triaxial cell, and the specimen was consolidated under this condition. Pressure (20 kPa) was applied to the bottom of the specimen to apply a hydraulic gradient, and the permeability test was conducted. After the permeability test, the pressure applied to the bottom of the specimen and triaxial cell was released, and compression was conducted to the prescribed strain.

As described above, X-ray CT scanning, the permeability test, and the compression test were repeated several times until axial strain reached 15%. When conducting X-ray CT scanning and permeability tests, the specimen was fixed to prevent deformation.

Results

Fig. 3 shows the relationship between stress and axial strain with CTC and CTCT. The ◆ marks in the figure show points where CT scanning and permeability tests were performed. As mentioned above, compression was interrupted when each CT scanning and permeability test was conducted. Compressive stress shows a clear drop in each scanning and permeability test due to the relaxation of the specimen at this time.

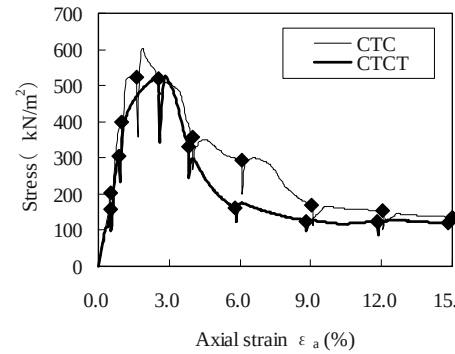

Fig. 3 Stress strain curve

Although the results show that the axial strain at peak strength increases when tire chips are added, there was a small difference in the stress strain relationship with CTC and CTCT due to the numerous types of experiments conducted.

Fig. 4 shows cross-sectional images of each specimen in the initial condition, stress peak condition, and at axial strain of approximately 15.0%. These images were chosen at the middle height of each specimen. The CT images were drawn darker for lower densities and lighter for higher densities. The parts shown in black are air voids which formed in the material during specimen preparation. Pure white indicates the presence of a cement lump or piece of shell, and gray parts approximately 1−3 mm in size are tire chips. The CTC specimen displays no large change from the initial condition to the stress peak condition. However, cracks occurred in the specimen after the peak condition. The cracks in the CTC were basically straight and wide. On the other hand, the CTCT specimen exhibits thin cracks in the specimen at the stress peak. These cracks in the CTCT developed successively in a reticulated pattern as axial strain increased. As mentioned, both the appearance and growth of the cracks in the respective cross sections were different in CTCT in comparison with CTC.

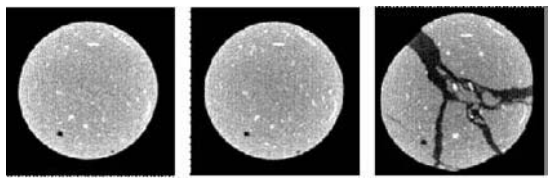

ε_a=0% ε_a=1.6% (peak) ε_a=15.1%

(a) CTC

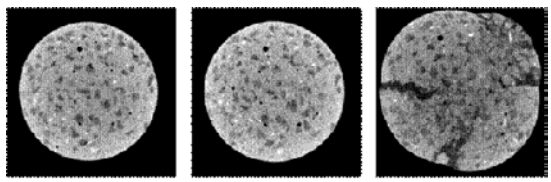

ε_a=0% ε_a=2.6% (peak) ε_a=14.9%

(b) CTCT

Fig. 4 X-ray CT image during unconfined compression test

Fig. 5 shows high magnification images of the cross section of each specimen under unconfined compression around the middle height. The images of CTCT show that cracks appeared around tire chips after reaching the stress peak. This is attributed to the fact that the Poisson's ratios of the tire chips and CTC are different. These thin cracks developed successively around the tire chips, preventing growth into wide cracks.

Fig. 6 shows the relationship between the coefficient of permeability and axial strain for CTC and CTCT. With CTC, the coefficient of permeability increased immediately after crack initiation. In contrast, with CTCT, the coefficient of permeability is about one order smaller than that of CTC at this time. It is considered that the large cracks which formed in the CTC created large water-bleeding channels and thus increased the coefficient of permeability. On the other hand, the cracks in the CTCT were thin and did not create water-bleeding channels until large axial strain of 15%. In this case, a low coefficient of permeability was maintained.

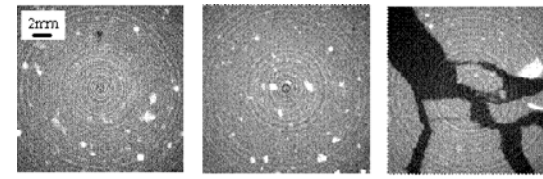

ε_a=0% ε_a=1.6% (peak) ε_a=15.1%

(a) CTC

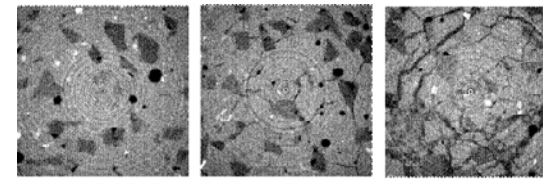

ε_a=0% ε_a=2.6% (peak) ε_a=14.9%

(b) CTCT

Fig. 5 Close up X-ray CT image during unconfined compression test

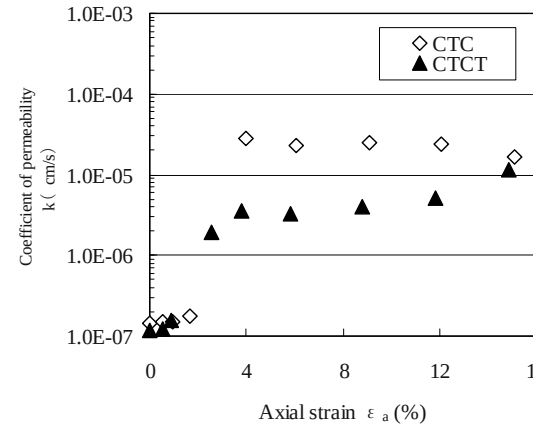

Fig. 6 Relationship between axial strain and coefficient of permeability

BEAM BENDING TEST

Experimental Procedure

The specimens were quadrangular prisms (W 50 mm× H 50 mm×L 200 mm) cured 28 days in a sealed wet condition. These specimens were set in the test apparatus vertically, as shown in Fig. 7. The specimens were placed in contact with the test apparatus at the top and bottom ends on the left side for a length of 20 mm and fixed

from the right with a plate, which was round on its left side. The plate was fixed with screws at the top and bottom ends. The plate was moved right or left by turning the screws. The displacement of the plate was measured by dial gauges. The specimen was bent by moving the plate to the left. The soft cushion to the left of the specimen appears in Fig. 7 as a black material. The cushion did not restrict the deformation of the specimen.

In this experiment, the displacements of the plate at

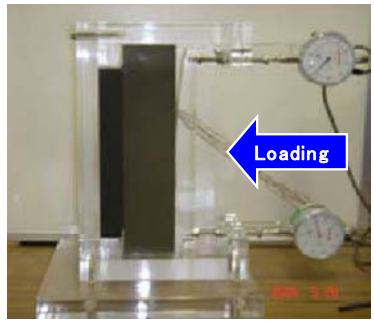

Fig. 7 Image of beam bending test

the top and bottom ends were measured. Internal crack propagation in the specimen was observed with an X-ray CT scanner at prescribed plate displacements, and surface crack propagation was observed visually.

Results

Fig. 8 shows the condition of crack propagation in the specimen as a whole at 8 mm plate displacement. The results for CTC and CTCT are shown in (a) and (b), respectively. Cracks were observed on the extension side in both cases. In the case of CTC, cracks were also observed near the supporting points, and the cracks at the middle height of the specimen were larger than in the CTCT specimen. In the case of CTCT, no cracks were observed at the supporting points.

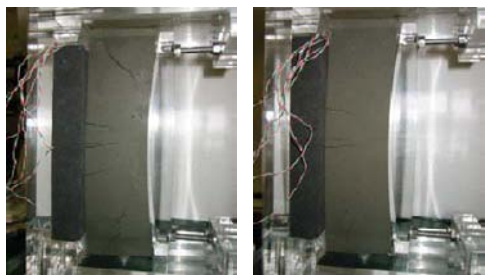

(a) CTC (b) CTCT

Fig. 8 Extension cracks at 8mm of loading plate displacement

Fig. 9 shows the cracks propagating inside the specimen at the middle height of the specimen as observed using the X-ray CT scanner. In this figure, the right and left sides are inverted from Fig. 8. The results for CTC and CTCT are shown in (a) and (b), respectively. Plate displacement is shown in the figure. The cracks that propagated in CTC were straight, whereas those in CTCT were jagged. The presence of tire chips affects this difference. The crack propagation depths in CTCT were shallower than those in CTC, but the difference in the depth was insignificant. The number of the crack was also less significant.

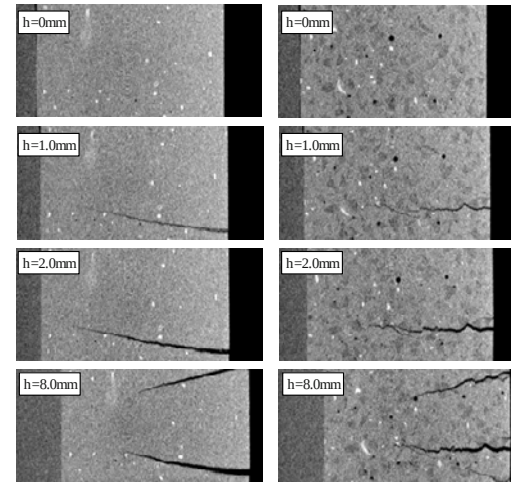

(a) CTC (b) CTCT

Fig. 9 X-ray CT image of cracks propagating inside the specimen at the center of beam height at several plate displacements. The numbers in the figures are the displacement of the plate.

PUNCHING SHEAR TEST

Experimental Procedure

Mixtures of CTC and CTCT were filled to a height of 20 mm in ring-shaped PVC molds (outer diameter: 89 mm, inner diameter: 78 mm, height: 40 mm) (Fig. 10). The bottom end of the PVC ring was closed with an acrylic resin plate. The specimens were sealed and cured in a wet condition for 7 and 14 days.

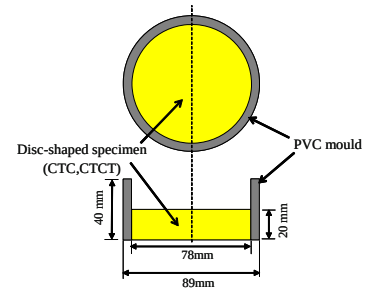

Fig. 10 Specimen used for punching shear test

Fig. 11 shows the outline of the test apparatus. In this test, a model pile was driven into the specimen to simulate the punching shear deformation mode. The sand box of the apparatus was an acrylic resin mold 100 mm

in inner diameter and 440 mm in height. The model pile was made of aluminum and was 15 mm in diameter. The loading devices and pile were attached to the acrylic mold in this apparatus. This apparatus was designed to control the loading tests and to measure the pile resistance and pile displacement while the apparatus was in the sealed X-ray CT box.

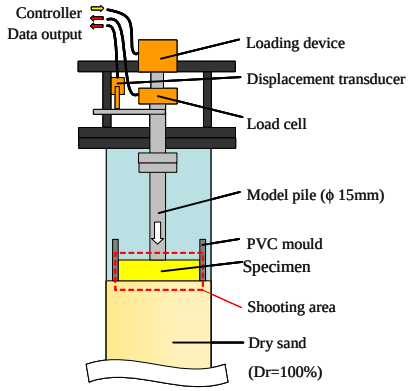

Fig. 11 Apparatus set up for punching shear test

First, a high relative density (Dr=100%) dry sand layer 250 mm in thickness was made with Toyoura sand by the tamping method. The plate-shaped specimens with the acrylic resin plate removed were placed horizontally on the surface of the sand layer. The ring-shaped PVC mold was not removed from the specimen. The loading was strain controlled, and the penetration rate was set at 1 mm/min. Penetration of the model pile was stopped and an X-ray CT scan was conducted at prescribed points.

For reference purposes, a loading test using an acrylic resin plate 89 mm in diameter on the surface of the ground and a pile penetration test were conducted.

Results

Fig. 12 shows the relationship between penetration resistance and pile settlement. The penetration resistances of the acrylic resin plate and pile are also shown in the figure. In the beginning of penetration until 0.5 mm of settlement, the resistance of CTC and CTCT and the 89 mm acrylic resin plate were almost the same. This is because the CTC and CTCT specimens work as a rigid plate at this level. Subsequently, however, the CTC and CTCT specimens deformed with increasing pile penetration. The penetration resistance of the CTC and CTCT specimens increased continuously with increasing penetration depth, even though the settlement of the pile was larger than in the case of penetration of the acrylic resin plate. In the case of CTC and CTCT, penetration resistance decreased rapidly after peak resistance.

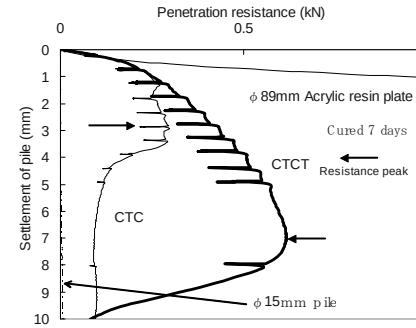

Fig. 12 Relationship of penetration resistance and pile settlement

Settlement of the pile at peak resistance was 2.3 times larger with CTCT than with CTC, and peak resistance was 2 times larger with CTCT than with CTC. As shown by these results, the toughness of CTCT is higher than that of CTC, and an apparent increment of penetration resistance was observed in the case of CTCT.

Fig. 13 shows an X-ray CT image of the vertical cross section through the pile center at prescribed settlement of the pile. The numbers in the figure are settlement of the pile. The white line in each figure shows the boundary of the specimen and the sand ground.

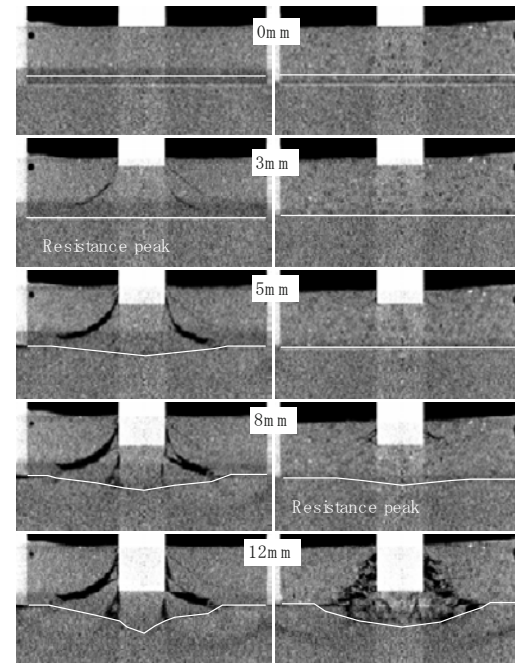

(a) CTC (b) CTCT

Fig. 13 X-ray CT image of vertical cross section around pile toe

In the case of CTC, the cracks which had propagated in the specimen reached the bottom end of the specimen at 3 mm settlement of the pile. At 5 mm pile settlement, cracks separated the part beneath the pile and other part. In the case of CTCT, cracks were not observed at 3 mm pile settlement. Small cracks were observed only around the pile tip at 5 mm pile settlement. The cracks around

the pile widened at 8 mm pile settlement, but these cracks were limited to the area around the pile toe.

Figs. 14 and 15 show enlarged images of CTC and CTCT after peak resistance. Pile penetration was stopped at 5 mm in the case of CTC and at 8 mm in the case of CTCT. Fig. 14 is a horizontal cross section of the specimen below the pile toe. The white dotted circles show the placement of the piles. Fig. 14a is an image from 10 mm below the pile toe in the case of CTC. Fig. 14b is an image from 7 mm below the pile toe in the CTCT. Fig. 15 is a vertical cross section at the central line of the pile. CTC is shown in Fig.15a, and CTCT in Fig.15b. Fig. 14 was scanned during loading, and Fig. 15 was scanned after unloading.

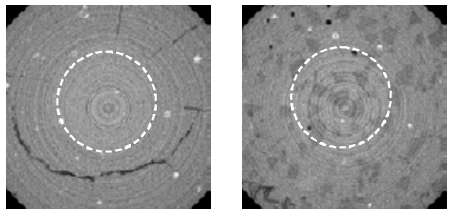

(a) CTC (b) CTCT

Fig. 14 Horizontal cross sectional X-ray CT image of specimen at around peak resistance. (a) was at 10mm lower than pile toe, (b) was at 7mm lower than pile toe

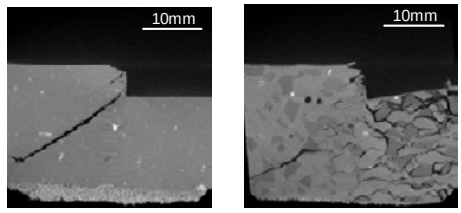

(a) CTC (b) CTCT

Fig. 15 Vertical cross sectional X-ray CT image of specimen after unloading. These figures were at the central line of the pile

An arcuate defect and several radial cracks were observed in the CTC in Fig. 14a. Reticulated cracks were observed in the CTCT in Fig. 14b. This kind of difference was quite similar to the crack propagation observed in the unconfined compression test.

Numerous cracks were observed below the pile toe in the CTCT in Fig. 15b. As mentioned above, this figure was taken after unloading. The avulsed cracks observed below the pile were caused by expansion of the CTCT. This means that the tire chips were deformed during loading and elastically reformed by unloading. The elastic behavior of tire chips prevents formation of the straight, wide cracks shown in Fig. 15(a), and thereby improves the toughness of CTC and its bearing capacity.

CONCLUSION

The effect of tire chips in improving the toughness of cement treated clay (CTC) was investigated by conducting tests on cement treated clay with tire chips (CTCT) in three shear modes, namely, the unconfined compression test, beam bending test, and punching shear test. From the test results, the toughness of CTC was improved in the unconfined compression shear mode and the punching shear mode by adding tire chips. The toughness of CTC showed less improvement in the bending shear mode, and extensive cracks were observed in this mode. The difference in these results means that compressive deformation of tire chips is responsible for the observed improvement in the toughness of CTC.

REFERENCES

Ashoka KK, Takeichi H, Yasuhara K (2002) Triaxial compression test on granulated scrap tire rubber for their use as lightweight geomaterials. Proc. of the International Workshop on Lightweight Geo-Materials: 127-134

Kikuchi Y, Nagatome T, Mitarai Y, Otani J (2006) Engineering property evaluation of cement treated soil with tire chips using X-ray CT scanner. Proc. of 5th ICEG: 1423-1430

Komatsu K (1993) Story of Rubber. JISC:53

Nagatome T, Kikuchi Y, Mitarai Y, Otani J (2006) Engineering properties of cement treated clay with tire chips. Advances in X-ray Tomography for Geomaterials: 373-380

Yasuhara K, Kikuchi Y, Mitarai Y, Kawai H, Ashoka KK (2004a) Improvement effect on deformation and barrier performance of cement-treated soils by mixing tire-chips－Improvement of toughness. Proc. 39th JNCGE: 2323-2324 (in Japanese)

Yasuhara K, Kishida T, Mitarai Y, Kawai H, Ashoka KK (2004b) Utilization of tire chips to port construction. The Foundation Engineering and Equipment 32(7): 79-83 (in Japanese)

Proceedings of the 4th Asian Regional Conference on Geosynthetics
June 17 - 20, 2008 Shanghai, China

APPLICATION OF CEMENT-MIXED GRAVEL REINFORCED BY GEOGRID FOR SOFT GROUND IMPROVEMENT

T. Matsumaru[1], K. Watanabe[2], J. Isono[3], M. Tateyama[4] and T. Uchimura[5]

ABSTRACT: The strength of gravel increased dramatically by adding a little amount of cement and equivalent to that of concrete materials. So, the cement-mixed gravel is expected to be effective to be used as bending member. In this paper, we have described the bending member tests as conducted to investigate the bending deformation characteristics and evaluate the reinforcement by geogrid. It revealed that the peak strength of the cement-mixed gravel did not decrease when the specimen reinforced by geogrid. We proposed slab for ground improvement on soft ground additionally, as the application of bending members. Usually, on soft ground, ground-improvement piles used for the support of embankment is often excessive because of the limitation of the deformation between the piles. Therefore, the ratio of the improvement piles could be reduced by using the slab between soil structure and piles. The efficiency was evaluated by conducting shaking table tests of liquefiable soft ground. In the case of using this slab, the deformation of soft ground and embankment was less, so the efficiency of this method was satisfactorily proven.

KEYWORDS: cement-mixed gravel, geogrid, soft ground, laboratory test, shaking table test

INTRODUCTION

In recent years, cement-mixed gravel, crushed stone for mechanical stabilization with a little volume of cement, are frequently applicable to soil structures allowing a limited degree of deformation. In Japanese railway field, such materials are a standardized type applicable to approach blocks of bridge abutments of a new Shinkansen line (Aoki et al. 2005). From laboratory tests or on-site tests, it has revealed that such materials indicated sufficient strength and deformation characteristics equivalent to concrete (Watanabe et al. 2003, Watanabe et al. 2005). Therefore, cement-mixed gravel where geogrid arranged for the tensile material is likely applicable as bending member, for examples, slab with ground-improvement piles as a new-type countermeasure method for soft ground. As the ratio of piles normally determined by the settlement of ground between piles, arranging the slab between soil structure and piles could reduce the ratio.

The purpose of this paper is to conduct various experiments in order to realize the new countermeasure method. Firstly, we conducted triaxial tests of cement-mixed gravel to evaluate the increase of strength and deformation characteristics by cement-mixture. Then, bending tests succeeded to evaluate bending characteristics with geogrid. Furthermore, we conducted shaking table tests to evaluate the applicability of this material to the slab, which bears embankment on soft ground.

EVALUATION OF COMPRESSION STRENGTH OF CEMENT-MIXED GRAVEL

Experimental Conditions

We used two kinds of gravels (Gravel A and Gravel B) for triaxial tests. Fig.1 shows the compaction curves of the gravels. Even in the case of the compaction by the same energy, the dry densities of two gravels were significantly different. This was because specific gravity (Gs) and uniformity coefficient (Uc) were different as shown in Table 1. The amount of added cement was 2.5% for weight ratio ($=W_{cement}/W_{gravel}$). We conducted experiments after 7-day curing period. Furthermore, we conducted the triaxial tests for gravels without cement for a comparative purpose. In the triaxial tests, we measured triaxial displacement with a LDT (Local

[1] Researcher, Railway Technical Research Institute, JAPAN. Email:matumaru@rtri.or.jp
[2] Assistant Senior Researcher, Railway Technical Research Institute, JAPAN. Email:nabeken@rtri.or.jp
[3] Researcher, Railway Technical Research Institute, JAPAN. Email:junji@rtri.or.jp
[4] Senior Researcher, Laboratory Head, Railway Technical Research Institute, JAPAN. Email:tate@rtri.or.jp
[5] Assistant Professor, Department of Civil Engineering, University of Tokyo, JAPAN. Email:uchimura@civil.t.u-tokyo.ac.jp

Table 1 Conditions of specimens

	Kind of rock	G_s	U_c	Cement mixture	Dry density (g/cm^3)	Confining pressure (kPa)	Water content (%)	Amount of cement		Size of sepcimen (mm)
								W_{cement}/W_{gravel} (%)	W_{cement}/V_{gravel} (g/cm^3)	
Gravel A	Sandstone	2.71	12.1	Yes	1.8, 2.0, 2.2	0, 20, 50	5.0, 8.7	2.50	6.78	φ200*H400
	Sandstone	2.71	12.1	No	1.8, 2.0, 2.2	0, 20, 80	4.0	-	-	φ300*H600
Gravel B	Gabbro	3.03	32.3	Yes	2.41, 2.56, 2.64	0, 20, 50	4.35	2.50	7.58	φ150*H300
	Gabbro	3.03	32.3	No	2.41, 2.56, 2.64	0, 20, 50	4.35	-	-	φ200*H400

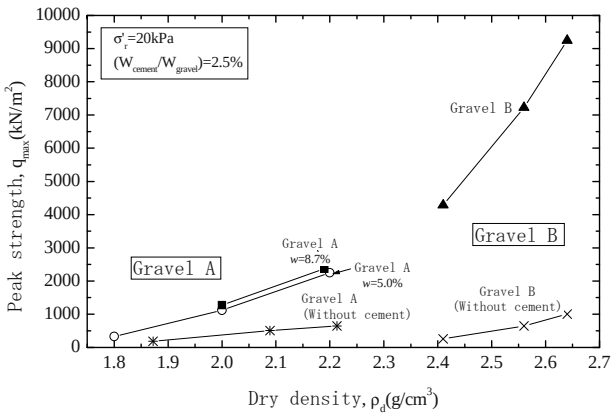

Fig. 2 Relationship between dry density and peak strength

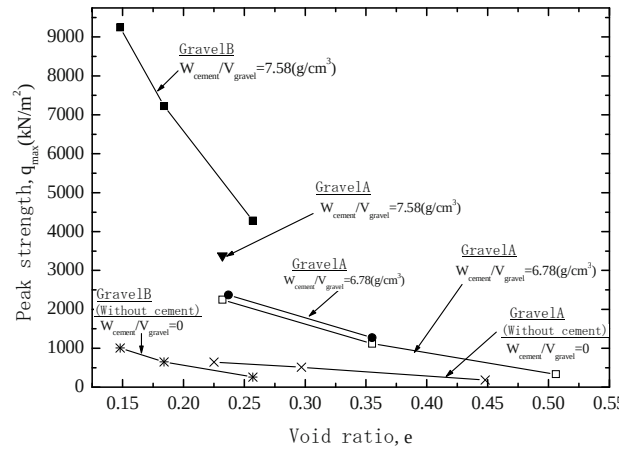

Fig. 3 Relationship between void ratio and peak strength

Deformation Transducer). We also performed loading at the strain rate of 0.01%/min until 15 % axial strain.

Test Results

Fig. 2 shows the relationship between peak strength and dry density. Especially for the specimens of cement mixture, the peak strength was raised by increase of dry density caused by sufficient compaction. Comparing two gravels, the peak strength of cement-mixed Gravel B was larger than that of Gravel A. The reason of this difference was the amount of added cement. The specimens were compacted based on the condition that the weight ratio ($=W_{cement}/W_{gravel}$) was 2.5 %. The ratio of cement weight to gravel volume ($=W_{cement}/V_{gravel}$) is proportional to dry density of gravel under fixed W_{cement}/W_{gravel}. So, the amount of W_{cement}/V_{gravel} of Gravel B was larger than that of Gravel A, as shown in Table 1. For this reason, the peak strength of Gravel B was seemed to be larger.

Fig. 3 shows the relationship between peak strength and void ratio. In order to eliminate the difference of specific gravity between Gravel A and Gravel B, the void ratio was adopted for horizontal axis. Compared with Fig.2, the peak strength had a higher correlation with void ratio than with dry density, as shown in Fig. 3. Furthermore, for the comparison of different gravels with cement mixture, the ratio of cement weight to gravel volume ($=W_{cement}/V_{gravel}$) is more suitable than the weight ratio of cement to gravel ($=W_{cement}/W_{gravel}$). This was likely because the strength of cement-mixed gravel was affected by the void ratio and the ratio of cement weight to the void volume.

ESTIMATION OF BENDING DEFORMATION CHARACTERISTICS OF CEMENT-MIXED GRAVEL

In this chapter, we describe bending member tests of the cement-mixed gravels for the evaluation of bending deformation characteristics of cement-mixed gravel and the effect of the geogrid for bending deformation.

Bending Member Test

We conducted experiments in two cases using two specimens; one of them reinforced by geogrid (Specimen-1) and the other was without geogrid (Specimen-2). We used Gravel A in the triaxial test as described in the preceding chapter, and the geogrid whose assured strength was 30 kN/m and set eyes were 20mm in both directions. The specimens were 200 mm in height, 200 mm in length, and 700 mm in width as

shown in Fig. 4. The specimen was cast in the mold after the sufficient mixture of gravel and cement. After curing for seven days, we conducted the loading in the displacement-control condition (0.3 mm/min). For the Specimen-1, we arranged the geogrid at 50 mm in height from the bottom and measured the strain of the geogrid with a strain gauge arranged at the center of nine strands. Furthermore, we measured the crack of the specimen at the bottom and 50 cm in height from the bottom with a LDT (Local Deformation Transducer).

Fig. 4 shows the load, strain of geogrid and crack width of each specimen. From these figures, it was apparent that the peak strength had occurred when the crack appeared at the bottom of the specimen. Furthermore, the crack width was about 0.13 mm for both specimens at this time. However, the strength of the Specimen-2 without geogrid decreased rapidly after the strength reached its peak, the strength of Specimen-1 reinforced by geogrid maintained. As shown in the figure of strain of geogrid, the tensile force appeared just before the peak strength occurred, and maintained after the peak state. This indicated that the ductility of cement-mixed gravel increased by reinforcement of geogrid.

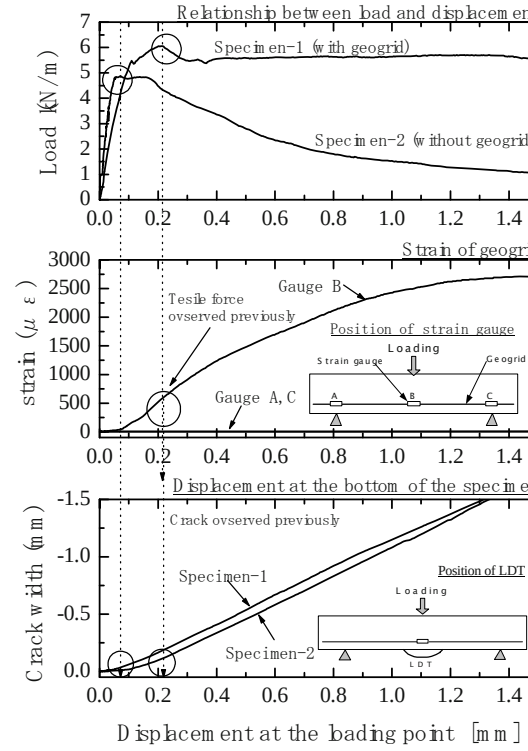

Fig. 4 Results of bending member tests

Convenient Modeling of Bending Deformation Characteristics

According to convenient modeling based on the bending deformation theory of elastic beam, we discussed the effect of geogrid for bending deformation based on the test results of the strain and the deformation.

As shown in the displacement measured with the LDT of Fig. 5, the crack appeared at the center of the bottom and advanced toward the upper with loading. In accordance with the progress of the crack, the sectional force of cement-mixed gravel decreases. Considering these, we discuss the convenient modeling of bending-deformation characteristics using three steps according to the progress of the deformation. Fig. 5 shows the steps.

First step: Peak state (All parts of the cross section is effective)

Second step: Clack length is 50 mm

Third step: Clack length is more than 50 mm

Fig. 7 shows the experimental relationships between the load and displacement, and bending strength calculated by the proposed model. For the calculation of the bending strength, tensile strength of cement-mixed gravel was assumed equal for the Specimen-1 and the Specimen-2. The calculated results were less than those of the experimental were. Such a tendency increased in the second step and the third step. The tensile force was 0.74 kN/m in the first step and 1.3 kN/m in the second

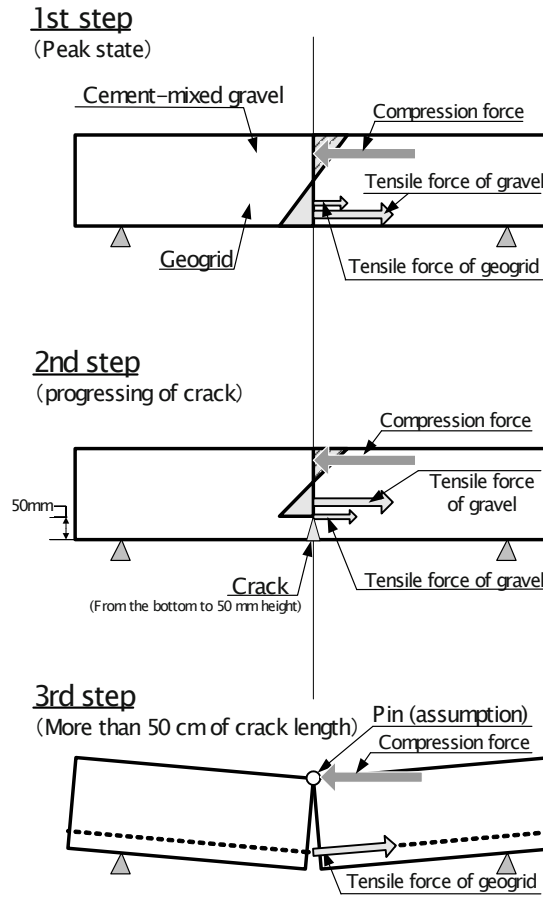

Fig. 5 Proposed model for describing bending deformation

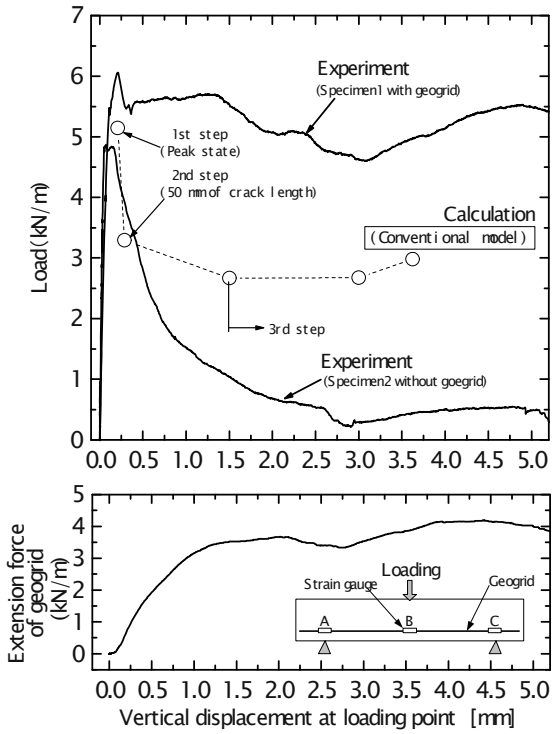

Fig. 6 Evaluation of bending strength by proposed model

step. The bending strength was small in the region where the peak strength transformed from the peak state to the residual state. In the third step, the tensile strength of geogrid showed 3 or 4 kN/m, larger than the values in the first and second step. It was evident that the tensile force of geogrid performed the ductility of the Specimen-1 because the calculated bending strength increased according to the increasing tensile force of the geogrid.

SHAKING TABLE TESTS OF PROPOSED COUNTERMEASURE METHOD FOR SOFT GROUND

From the bending member tests, it was evident that cement-mixed gravel reinforced by geogrid shows high bending deformation characteristics. For this reason, cement-mixed gravel would be suitable for not only mass structures typified by bridge abutment, but also members under bending stress. For example, ground-improvement piles for soft ground should be designed, as the ratio of piles is more than 25 % in order to avoid punching failure of embankment. However, arranging the slab of cement-mixed gravel under embankment may enable to reduce the ratio because the slab supports dead load of embankment and live load. In this chapter, we conducted shaking table tests with the existing method and proposed method in order to ensure this effect.

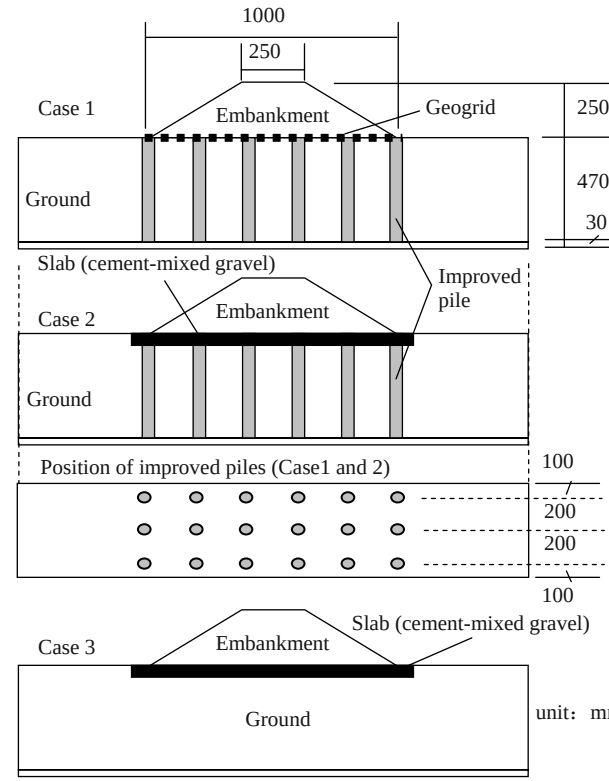

Fig. 7 Cases of shaking table tests

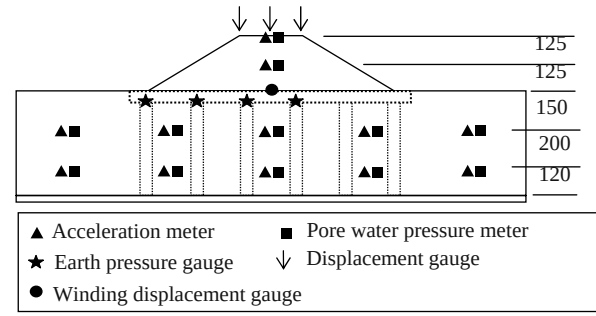

Fig. 8 Arrangement of measurements

Test Conditions

Shaking table tests were conducted as indicated below.

Case 1: Existing countermeasure method (Column-net method)

Case 2: Countermeasure method using slab with improved piles whose ratio is 5 %

Case 3: Countermeasure method using only slab

Fig. 7 shows the experimental models of each case. The case without countermeasure had been already conducted and the details of results were written in Tateyama et al. (2000). The soft ground was produced by liquefaction. The ground and the embankment were prepared by aerial dropping method, whose relative densities were 60 % and 80 %.

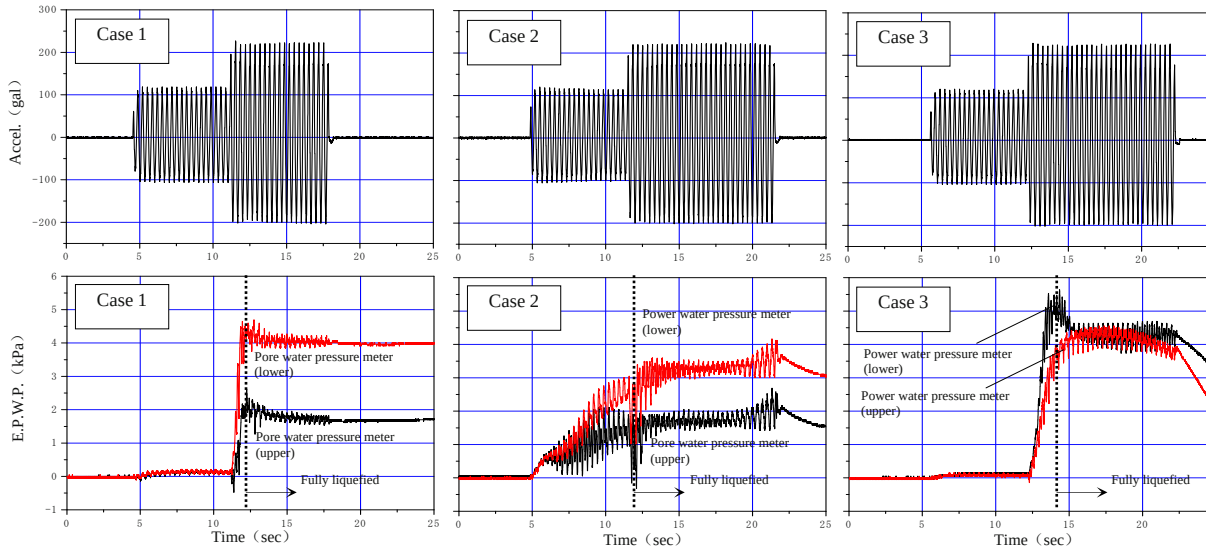

Fig. 9 Time histories of acceleration and E.P.W.P.

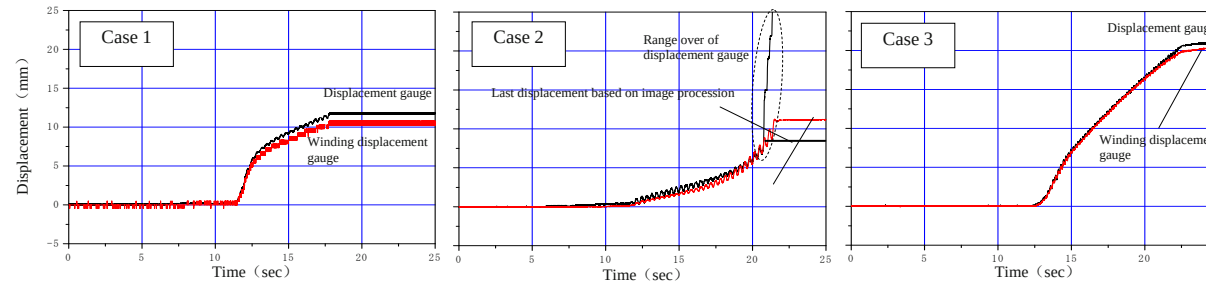

Fig. 10 Time histories of displacement

The slab was made from cement-mixed gravel (Gravel A with 4% cement) and the geogrid was modeled by mesh sheet made from polyester with due consideration of similarity law. The thickness of slab was determined as 4 cm to satisfy the condition that the simple member of slab between piles could support the weight of embankment. The position of the mesh sheet from the bottom of slab was decided as 1 cm. The improved piles used in the Case s1 and 2, whose diameters were 50 mm, were made from loam with cement. The amount of cement was determined, as the unconfined compression strength of specimen was larger than 200 kPa. For input acceleration, the sinusoidal wave of 3 Hz was used, whose amplitude was 100 gal for initial 10 waves and 200 gal for next 20 waves in the Cases 1 and 30 waves in the Cases 2 and 3. The measurements contained acceleration, pore water pressure and displacement of the embankment and the ground, as shown in Fig. 8. Especially, the displacement of the ground was measured not only by winding displacement gauge but also by image procession of reference points arranged in the ground.

Results of Shaking Table Tests

Fig. 9 shows the time histories of the acceleration of inputted motion and excess pore water pressure (E.P.W.P.) in each case. From Fig. 10, it revealed that the E.P.W.P. of the Case 2 had increased at the stage where the inputted motion was 100 gal. In the Case 2, the slab and the improved piles supported the embankment, so the confining pressure might have been smaller than those in the other cases. For this reason, the liquefaction would have occurred when the acceleration of the motion was 100 gal.

It is important for the evaluation of the differences among three cases to compare the results when the degrees of the liquefaction were in the same states. Therefore, we compared the results at the times on the entire liquefaction and after 10 waves from this time. As it was difficult to determine the entirely liquefied time, we defined the time as when the E.P.W.P. reached the effective overburden load. According to this definition, the fully liquefied time was 24th wave in the Case 1, 21st wave in the Case 2, and 27th wave in the Case 3.

Fig. 10 shows the time histories of settlement at the top of the embankment and the ground. The compression settlement of embankment was very small in every case because the settlement of the embankment at the top and the settlement of the ground showed a similar behavior. The settlement at the top of embankment was 40 mm in the case without countermeasure, but 10 mm in the Case

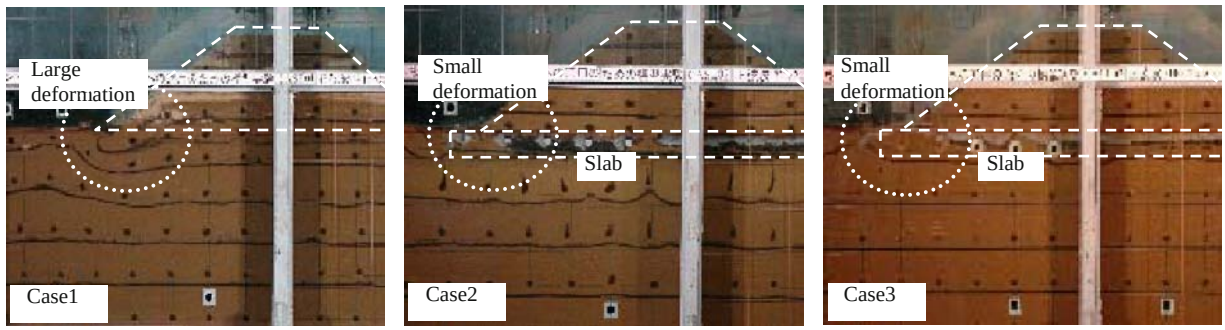

Fig. 11 Photographs after shaking

1, 6 mm in the Case 2, and 15mm in the Case 3. This indicated that the countermeasure methods used in all cases were effective. Comparing the settlement of the embankment in the Case 1 and the Case 2, the settlement of the embankment in the Case 1 was larger than that in the Case 2. The ground between piles might have been settled according to the deformation of geogrid in the Case 1; however, the settlement in the Case 2 would have decreased because the slab supported the weight of the embankment.

Fig. 11 shows the photographs after the experiments in each case. In the Case 1, the embankment and the ground deformed largely around the toe of embankment but were deformed lesser in the Case 2. In the Case 3, the settlement of embankment was slightly larger to compare with those in other cases due to unimproved piles, but a large deformation did not occur as in the Case 2. However, it was predictable that the improved piles would have reached shear failure due to an excessively small ratio of piles, a few piles damaged in the Case 2. Furthermore, from the results obtained in the Case 3, it was apparent that using only slab was effective for the countermeasure of embankment.

CONCLUSIONS

The purpose of this paper was to propose the new type method using the slab of the cement-mixed gravel and the ground improved piles as a countermeasure method on soft ground. Firstly, we conducted laboratory tests aimed to evaluate the compression and the bending strength of the cement-mixed gravel. Then, we performed the shaking table tests to investigate the applicability of the proposed method. As the results, we achieved the following conclusions:

(1) From the triaxial compression tests, we evaluated the strength and deformation characteristics of the cement-mixed gravel. It revealed that the strength of gravel increased by adding the cement. Especially, it was evident that such an effect drastically increased by compaction.

(2) We conducted the bending member tests. In the test, the cement-mixed gravel and the geogrid were likely to role the compressive and tensile member. The bending ductility increased by the tensile force of geogrid. Furthermore, proposed conventional model could describe the bending deformation characteristics.

(3) In order to reduce the ratio of improvement on soft ground, we proposed the method to adopt the slab of cement-mixed gravel reinforced by geogrid to the bottom of embankment. We could prove the effect by shaking table tests of soft ground.

REFERENCES

Aoki H, Yonezawa T, Tateyama M, Shinoda M, Watanabe K (2005) Development of high Seismic performance abutment with geogrid-reinforced cement treated backfill. Proceedings of the 16th International Conference on Soil Mechanics and Geotechnical Engineering, Osaka: 1315-1318

Tateyama M, Kojima K, Sawada R, Yamada T, Jiang G (1970) Shaking table tests of embankment on liquefied ground. Proceedings of annual conference of Japan Society of Civil Engineering: 408-409

Watanabe K, Tateyama M, Jiang GL, Lohani TN, Tatsuoka F (2003) Strength characteristics of cement-mixed gravel evaluated by large triaxial compression tests, Proceedings of the 3rd International Symposium on Deformation Characteristics of Geomaterials, Balkema: 683-693

Watanabe K, Tateyama M, Yonezawa T, Aoki H (2005) Strength characteristics and construction management of cement-mixed gravel. Proceedings of the 16th International Conference on Soil Mechanics and Geotechnical Engineering, Osaka: 619-622

EFFECT OF POLYPROPYLENE FIBERS ON THE STRENGTH AND ELASTIC MODULUS OF SOIL-CEMENT

L. Zhang[1], X.X. Wang[2] and G. Zheng[3]

ABSTRACT: The effect of the content and types of polypropylene fibers which are mixed into the soil-cement mixtures on the strength and elastic modulus of soil-cement isare studied. The test result shows that the unconfined compressive strength of soil-cement, if within a certain range increased with the increasecontent of polypropylene fiber content. Otherwise, the strength falls off consequently when the fibers proportion increased over this range. The elastic modulus of soil-cement decreased along with the increase of fibers. Moreover, both the strength and elastic modulus of soil-cement increased with the content of cement.

KEY WORDS: polypropylene fiber, soil-cement, unconfined compressive strength, elastic modulus

INTRODUCTION

Geosynthetics Aas one of new construction materials, Geosynthetics have been widely used in geotechnical engineering. Compounding with plastic, chemical fibers, synthetic or rubber etc they can be categorized by their ingredients. They help to strengthen and protect soil when they are fixed inside, outside or between the layers of the soil. The advancement achieved in both model design methodologies and experiments since 1990s brings aboutmake the possibility of practical use in engineering.

As a remarkable type of geosynthetics, the advantages of geotextile (or geofabrics) are featured with are significant advantages such as , namely, light weight, excellent the overall continuity (its length can get between hundreds and thousands meters), efficiencytly and conveniencetly to construct, high tensile strength, resistance to corrosion and erosion and good anti-microbial. In particular, the machine–weaved geotextile shows the high permeability and tight combination capability with soil owing to those fine pores inside. However, its disadvantages should not be ignored: it hasthe low Anti-UV (ultraviolet light) capability without special treatment, and it gets aging easily when exposed directly tounder the sunlight, or else it shows some endurance. As Iit pointed out that the capabilities of geotextile are partly dependent on manufacturing factors, such as the materials of polymers, types and the manufacturing procedure.

Generally, there are two technical methods that polypropylene fibers are involved to improve the soil-cement strength at present. First, the long fibers method: long fibers are mixed to strengthen the non-viscous granular soil, that is commixing the long fibers with fine gravels and water in site by jet mixing equipment. Second and newly developed one is the short fibers method, which is marked by its good impact of improving the engineering characteristics of the soil, particularly, strengthening the Anti-viscous granular soil. Such fibers mixed methods can help to reduce the side pressure of the riverbank and the back fill thanks to the perfect tenacity and plasticity.

It is the short-type polypropylene fibers that were used in the test mentioned in this paper.

APPLICATIONS AND BRIEF FUNCTIONS INSTRUCTION OF THE POLYPROPYLENE FIBERS

The Applications of the Polypropylene Fibers in Civil Engineering

The polypropylene fibers have been widely used in many civil engineering areas as following:

(1) *Reinforced Earth*

The soil mixed with fibers (about 25mm long) will form the shapes of meshwork, bar and fascicule .The strength of the earth body hence reinforce because that

[1] Associate Professor, Key Laboratory of Geotechnical and Underground Engineering of Ministry of Education, Department of Geotechnical Engineering, Tongji University, CHINA. Email: tjugege@mail.tongji.edu.cn
[2] Master student, Department of Geotechnical Engineering, Tongji University, CHINA. Email: snoweywang@163.com
[3] Engineer, Shanghai Tongji Project Management &consulting Co.,Ltd, CHINA. Email: billzhenggang@126.com

shearing strength may increase by 20～50%. Moreover, such mixed reinforce earth will not do harm to human and animals or plants.

(2) *The road construction and rebuilding*

Given the common disadvantaged factors in road construction, such like soft foundation, unsuitable cushions and project budget, in-situ foundation treatment is considerable and is regarded to be more economical. Differing from the principle of decreasing soil stress by inserting the geotextiles into the earth, fibers help to improve the engineering characteristics of the foundation soil. Fibers also form grids to stabilize the foundation and improve flexible capability by combining with chemic curing agents as well.

(3) *The earth slope construction*

Mixing the fibers grids into the earth slope which consistsed of cohesive soil can increase the shearing strength of the mass body. That means the gradient of earth slope can be steeper without further protection measures (e.g. retaining wall) which always rises make the cost rising.

(4) *Protection measures of the dike or back fill*

Fibers grids also can be mixed into reinforced earth to retain the comparatively high shearing strength even if the water level decreases suddenly, which is a very common phenomenon in saturated filling filled in dike.

The Common Explanation for Functions of the Polypropylene Fibers

The weaknesses of the concrete such as low tensile strength, cracks, low ductility etc. have limited some applications in civil engineering. Much attention is drawn on how to increase the tenacity and anti-cracking capability. Generally, the primary reasons resulted in cracks are first of all, the principal stress caused directly by external load and secondly, secondary stress and distortion caused by temperature change, by contracting, expanding, uneven settlement. Usually, the cracks may be caused by more than one reason mentioned above. And the distortion is always the major reason contributinge to more than eighty percent of all possibility. Even though increasing the percentage of steel can decrease cracks caused by external loads somewhat, it hardly resists the distortion, especially the plastic shrinkage cracking because the steels can't distribute close. By contrast, polypropylene fibers can create strong binding force by reacting with cement molecules so it can be mixed with concrete easily and distributed homogeneously and densely in concrete that can prevent cracking creating.

THE TEST MATERIALS AND TEST METHOD

The Materials

(1) *Cement*

Considering that the 325# slag cement has been extensively used in engineering so they were selected in this test. Its tensile strength was 6.8 MP and compressive strength was 36.3 MP with 28 days' conservation.

(2) *Soil*

The forth layer clay of Shanghai was selected and its water content is 50%.

(3) *Polypropylene fibers*

The chemical structure of polypropylene fibers, a kind of geotextile involved in this test is:

$$\left[\mathrm{CH}\ -\ \mathrm{CH_2}\right]_n$$
$$\quad\ |$$
$$\quad\ \mathrm{CH_3}$$

With aThe relative density ofis 0.91, it is regarded as one of the lightest synthetic fibers at present. The rupture strength is 210－640 Mpa. The resurgence rate is 0, in other words it hardly absorbs water in the standard condition, and thus its strength is regarded to be unchangeable no matter in wet or dry condition. With regard toCome to elasticity capability, it can get back 96%－100% of original form when the elongation rate is 3%, which is similar with polyamide fiber, terylene. The average length of fibers is about 15 mm with diameter of 26 um. The tensile strength is 520 MPa, and the elastic modulus 3.5 GPa. The rupture prolongation is 15%. Its corrosion proof is favorable. The more detailed information about its physical property ishas showngiven in Table 1.

(4) *The content of the cement and fibers of the specimens:*

Let's refer to Table 2.

The Test Method and Procedure

(1) *Step 1*

Put the test models on the common clay brick whoseich water absorption capability is good (water absorption ratio should be more than 10% and water content less than 20%). And the test models were brushed a thin lay of machine oil or mould releasing agent beforehand.

Table 1 The physical and chemical properties of the polypropylene fibers

Capability \ Material			Polypropylene		
			Short fibers	Long fibers	
				General fibers	Strong fibers
1.	Tensile strength (0.01N/d)	Dry	4.5—7.5	4.5—7.5	
2.		Wet	4.5—7.5	4.5—7.5	
3. The weight ratio of dry to wet (%)			100	100	
4. Collusions strength (0.01 N/d)			8.0—14.0	8.0—12.0	
5. Nodes strength (0.01 N/d)			4.0—6.5	4.0—5.5	
6.	Prolongation rate (%)	Dry	30—60	30—60	
7.		Wet	25—60	25—60	
8. Elastic extension rate (%)			90—100 (when is extended by 3%)		
9. Youngs modulus (N/d)			0.20—0.55	0.40—1.20	
10. Apparent Youngs rate (kN/cm^2)			160—450	330—1000	
11. Specific gravity			0.91		
12.	Water containing rate (%)	Acknowledged value	0		
13.		Under Standard Condition 20℃	0		
14. Behaviors when heat and burnt			Intenerate point:140—160℃, Melting point:165—173℃, (almost no ashes left)		
15. The capability of endurance to the temperature change (exposed outside)			The Strength remained almost constantly		
16. Response to acids			The Strength remained almost constantly (strong hydrochloric acid, oil of vitriol, strong nitric acid)		
17. Response to alkali			The Strength remained almost constantly (in the liquor of 50% concentration of sodium hydroxide or 28% ammonia)		
18. Response to other chemical medicine			Scarcely appeared any significant changes		
19. Responses to the menstruum (alcohol, aether, benzene, acetone, gasoline etc.)			Hardly dissolve in the liquor of alcohol, aether, benzene, or acetone; Imbibe and expand in benzene under the high temperature; would dissolve slowly in the tetrachloroethylene, tetrachloroethane, carbon tetrachloride, chclohexanone, chlorobenzene, tetraline, xylem, toluene under the high temperature.		
20. Coloration			Can be dyed by the paints and dyestuffs; Can be dyed by the acid color with special treatment.		
21. Resistance to the moth and mildew			Can resist		

Table 2 The content of the cement and fibers of the specimens

Forming technology	Length (mm)	Fibers content percentage (%)	Cement content Percentage (%)	Soil content Percentage (%)	Density (×10^3 kg/m^3)
Mixing (Average density: 1.87×10^3 kg/m^3)	15	0.5	13	86.5	1.83
	15	0.5	15	84.5	1.88
	15	0.5	17	82.5	1.86
	15	1.0	13	86.0	1.83
	15	1.0	15	84.0	1.90
	15	1.0	17	82.0	1.87
	15	1.5	13	85.5	1.86
	15	1.5	15	83.5	1.92
	15	1.5	17	81.5	1.91

(2) *Step 2*

The newsprint or other clean papers were required. The size of the paper should cover the four sides of the brick whose surfaces should smooth. Any one of four vertical brick sides which had been touched with cement or other cementation materials should be expired.

(3) *Step 3*

The soil-cement mixtures should be added into the test models only once. Pound and pug with tamper following spiral direction from outside to inside (about 25 circle). To avoid that it would have left holes later, it was doable that inserting the putty knife into the mixtures several times. The mixtures were expected 6—8 mm higher than the coping of the model after pugging. When the patches appearing on the surface after 15 to 30 minutes, scrape and smooth the mixtures which were higher than model, hence the test models were completed.

(4) *Step 4*

Stay models for 24±2 hours on the 20±5℃. The process could prolong but up to two days if temperature was low. Then, the models were compiled numbers. The models had been tested after 28 days' conservation on the standard condition (20±3 degree centigrade; relative humidity was 60%—80%).

(5) *Step 5*

The normal compression strength test apparatus were used in the compression strength tests. The results were recorded and studied to find the relationships between the compressive strength and the distortion of the soil-cement mixtures. In this test, the displacement of distortion had been up to 10 mm and distortion rate reached 0.30 mm/mm.

TEST RESULT ANALYSIS

The Effect on the Unconfined Compressive Strength of the Soil-cement Mixtures by Mixing Polypropylene Fibers

The effect of the content of the polypropylene fibers (W) on the unconfined compressive strength of the soil-cement mixtures were showed in the Fig. 1. Within a certain cement proportion (15% or above), the compressive strength increased with the content of the fibers. As it can be seen from the graph, the strength increased with the rising of W when it was between the 0—1.0% and fell off afterwards.

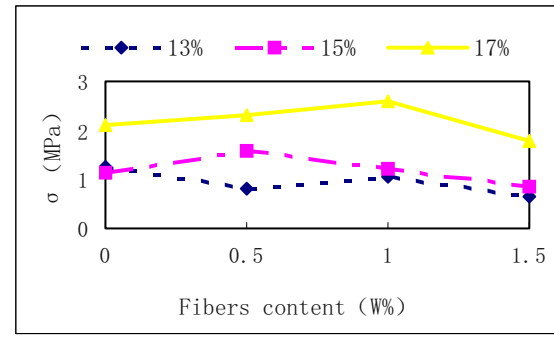

Fig. 1 The effect of fibers content (W) on σ

The Effect of the Polypropylene Fibers on the Elastic Modulus of the Soil-cement Mixtures

Fig. 2 shows the effect of the polypropylene fibers (W) content on the elastic modulus of the soil-cement mixtures (E). Overall, the elastic modulus decreased with the W. It is noticed that E decreased with W in the first 0.5% stage, and the tendency was slightly slowly from the points onwards (between 0.5% and 1.5%).

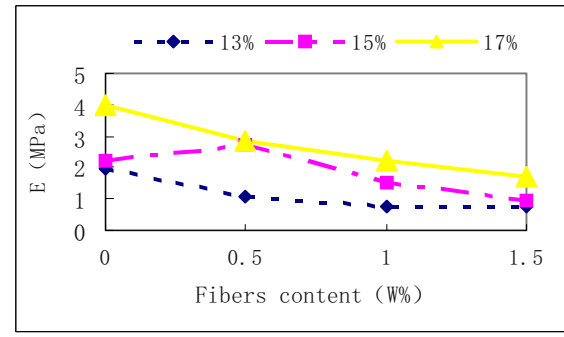

Fig. 2 The effect of fibers content (W) on E

The Effect of the Cement Content on the Strength of the Soil-cement Mixtures

Fig. 3 shows the effect of the cement content on the strength of the soil-cement mixtures. According to the chart, the strength increased steadily with the content of the cement, content of fibers. Similar tends were illustrated in all of three different cement content.

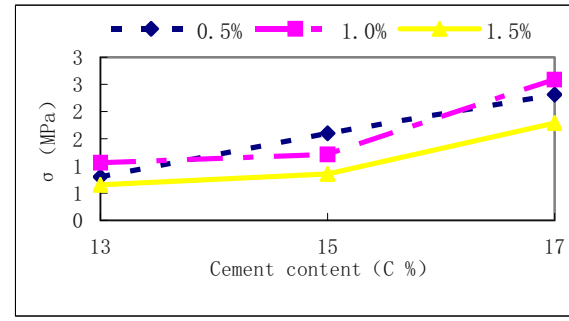

Fig. 3 The relationship of the C and σ

The Effect of the Cement Content on the Elastic Modulus of the Soil-cement Mixtures

Fig. 4 reveals that how differenlyt cement content affectseffect on the elastic modulus of the soil-cement mixtures. In general, E increased with the C smoothly when fibers proportions were more than 1.0%. For the lower fibers content (0.5%), E increased sharply when cement constituted a less proportion but remained constant afterward.

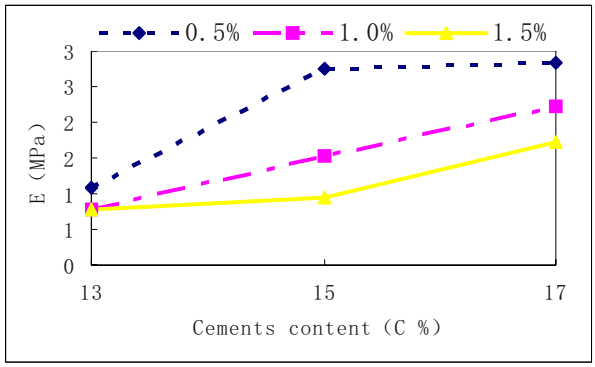

Fig. 4 The relationship between C and E

The Cause and Effect Analysis for the Influence of Polypropylene Fibers to the Unconfined Compressive Strength (σ) and Elastic Modulus (*E*)

When the proportion of mixed polypropylene fibers are restricted within a certain value, the strength of soil-cement mixtures is likely to increase owing to the existence of adhesive property. Having examined those broken specimens, it is marked that the fibers were pulled out or snapped when the breakages happened. The phenomena differed from the broken mechanism of soil-cement mixtures without fibers. As the first crack of specimens comes into being, the fibers close-by would have to bear all the loads if such collapsing force is less than adhesive property, hence the residual stresses are transferred to soil-cement mixtures through the adhesive property between fibers. Moreover, with more and more cracks created, the load beard by soil-cement mixtures increases. With such process repeating, those cracks have been createding in succession until the fibers ishaving been pulled out or snapped. Hence, mixing the polypropylene fibers within a certain value could increase the strength and improve the crack resistance of the soil-cement mixtures, therefore retard cracks expansion.

In addition, the degree of soil-cement mixtures' distortion with fibers could be extended compare with ones without fibers under the equivalence collapsing force, which meant the broken mechanism of the soil-cement mixtures becomes the supple failure mechanism instead of supple failure mechanism and the physical property of the soil-cement mixtures change from rigid to flexible material.

On the other side, for the four compositions of the soil-cement mixtures, namely, cement, soil, water and polypropylene fibers, the chemical reaction between cement and soil could create adhesive force which is regarded as the source of strength of the soil-cement mixtures, by contrast, the polypropylene fibers couldn't create such force.

CONCLUSIONS

The Effect of the Length, Content of Fibers and Cement Content on the Compressive Strength of the Soil-cement Mixtures

(1) The strength of soil-cement mixtures improve with the increase of fibers content when it is within a certain value, otherwise, the strength might decrease. The fibers content should not excess 1.0%. As far as the engineering projects are concerned, the shorter the fibers were the better, so the 1% percentage of 15mm long fibers might be a good ration. And according to this test, the strength could increase by nearly 20% greater than those without fibers.

(2) The compressive strength of soil-cement mixtures increased with the cement.

(3) The strength of the soil-cement increases in the first stage and then, decreases if more fibers areis mixed, and it is suggeststing that the length of fibers should not exceedover 20mm long.

The Effect of the Length, Content of Fibers and Cement Content on the Elastic MODULUS of the Soil-cement Mixtures

(1) The elastic modulus increasesd with the fibers content except for the 25mm long fibers.

(2) When the fibers content preponderatesd over 1.0%, the elastic modulus might decrease with the fibers.

(3) The cement content also could contribute to the elastic modulus.

(4) The increase rate of elastic modulus might slow down when cement content is over 15%.

(5) This test showed that elastic modulus increased firstly and decreased consequently with the increase ofsing the length of the the fiber length.

REFERENCES

China Building Industry Press. Tthe Handbook of the Geosynthetics Applications in Engineering

Nanjing Hydraulic Research Institute. Tthe Handbook of the Geosynthetics Testing

Zhou DG, etc. the Manufacture Technique and the Capability of the Geosynthetics

Xiao L, etc. Construction Material: Soil-Cement Mixtures

Composite Material: Glass Fibers Reinforced Plastic (2002) No.5

Gong XNiaonan, Li MF (2002) the New Development and Expectation of the Geosynthetics, Foundation Treatment (2002) No. 46

Ye SL, Ye GB. Foundation Treatment. China Building Industry Press

Proceedings of the 4th Asian Regional Conference on Geosynthetics
June 17 - 20, 2008 Shanghai, China

EXPERIMENTAL INVESTIGATION ON STRENGTH AND MECHANICAL BEHAVIOR OF COMPACTED SOIL-FIBER MIXTURES

T. Harianto[1], S. Hayashi[2], Y.J. Du[3] and D. Suetsugu[4]

ABSTRACT: A series of laboratory tests has been carried out to investigate the using of C_3H_6 (polypropylene) fiber as an additive to increase the strength of the compacted Akaboku soil. Fiber contents of 0.2%, 0.4%, 0.6%, 0.8%, 1.0%, and 1.2% by weight were selected. The compaction test, unconfined compression test and tensile test were conducted in this study. In this study, fiber content was found as the main factor that affects the strength of the soil specimens. The results indicate that initially dry density increased with increased in fiber content up to 1.0% of fiber content and slightly decreased for fiber content of 1.2%. The similar trend also found in the compressive strength, tensile strength and also ductility of the soil specimens. The strength and ductility significantly increased with increasing the fiber content.

KEYWORDS: Akaboku soil, compaction, ductility, fiber additives, strength

INTRODUCTION

The compacted fine grained soils have been widely used as a landfill barrier material for many years. The construction of barrier layer using suitable materials that maintain the performance of the landfill cover barrier system is very important. When soils are applied to the barrier layer, the soil materials should sufficiently perform in term of design aspects such the hydraulic performance, compressibility, and slope stability. Therefore, to satisfy the functional requirements, analysis and design methods have been developed by some researcher to evaluate the performance of the material used alone or in combination of soil mixtures.

The interest of using fibers has arisen to improve soil performance on the engineering properties of soil mixtures. Some researchers were conducted research by use randomly oriented discrete geosynthetic fiber to reinforced sand, such as Gray and Ohashi (1983), Park and Tan (2005). Nataraj and McManis (1997) studied the strength and deformation characteristics of soil reinforced with randomly distributed fibers compared to natural soil. Tang et al. (2007) concluded that using fiber as reinforcement is advantageous because the strength increase, decreased the stiffness and changed the cemented soils to more ductile. The unconfined compressive strength of silty soil has been found to increase due to the addition of nylon fibers (Kumar and Tabor 2003). Ziegler et al. (1998) found that with an inclusion of discrete polypropylene fibers, the tensile strength of clays tend to increase and induce more ductile failures. The compaction path also significantly effected to the tensile strength (Ibarra et al. 2005).

The increase in strength was accompanied by an increase in the strain to failure. With inclusion of discrete fiber, the toughness significantly increased and led to improvement of the strength behavior of cement (Kaufman et al. 2004). The test by Cai et al. (2006) reported that there is a significant improvement on the engineering properties of the fiber-lime treated soil. Other study used compacted rubber fiber-clay to observe the strength behavior of the composite in drained and undrained loading condition (Ozkul and Baykal 2007). Recently, several researches have been undertaken in order to study potential use of tire-chip mixed with clayey soil as a fill material (Cetin et al. 2006).

The purpose of this study is to evaluate the possibility of using the Akaboku soil (local soil) as an alternative material for landfill barrier. The engineering properties such as compaction characteristic, unconfined compressive strength, and tensile strength were investigated in this study. Furthermore, the relationship between the parameters also evaluated. The authors propose that by combining Akaboku soil with fiber admixture, the engineering properties (i.e., strength) of soil-fiber mixture will develop.

[1]Ph.D student, Institute of Lowland Technology, Saga University, JAPAN. Email: tri@ilt.saga-u.ac.jp
[2]Professor, ditto, JAPAN.Email: hayashi@ilt.saga-u.ac.jp
[3]Assoc.Professor, ditt,. JAPAN. Email: du@ilt.saga-u.ac.jp
[4]Dr., ditto, JAPAN. Email: suetsugu@ilt.saga-u.ac.jp

MATERIALS AND METHODS

The soil specimen used in this study was locally obtained from Kumamoto Prefecture. The tests were carried out for index properties, standard proctor compaction, unconfined compression test, and tensile test. The soil specimen was kept in box under room conditions (25 ±2℃, 50 ± 1 % relative humidity) prior to testing. The basic properties of soil such as grain size analysis, specific gravity of soil solids and Atterberg limits (liquid limit, plastic limit and shrinkage limit) were determined according to standard practice the American Society of Testing Materials (ASTM) D422-63, D854-58, D4318-00, and D427-61. Table 1 summarizes the basic properties of the soil which is used in this study.

Table 1 Basic properties of Akaboku soil

Properties	Values
Specific gravity, Gs	2.59
Consistency limit :	
Liquid limit, w_L (%)	162.0
Plastic limit, w_P (%)	81.7
Shrinkage limit, w_S (%)	48.9
Plasticity index, PI (%)	80.3
Grain size analysis :	
Sand (%)	35
Silt (%)	52
Clay (%)	13

Table 2 Properties of Polypropylene fiber

Properties	Value
Specific gravity	0.91
Fineness (dtex)[1]	15-19
Tensile strength (MPa)	2.0 - 6.0
Elongation at break (%)	70 - 150
Melt point (^{o}C)	160

[1]dtex = 10μg/cm

Polypropylene fiber is the most common synthetic material used to reinforce soil and concrete (Maher and Ho 1994). The primary attraction is that of low cost. It is easy to mix with soil and has relatively high melting point which makes it possible to place the soil-fiber mixture in the oven and conduct the moisture tests. Also, polypropylene is a hydrophobic and chemically inert material which does not absorb or react with the soil moisture or leachate. Type of polypropylene fiber used is RCP17T with 10 mm in length and 50 μm in diameter. The summary of the properties of polypropylene fiber are presented in Table 2.

The mixing procedure in the making of sample was as follows. The soil was slight air dried to bring water content below the measured optimum moisture content (OMC). The soil retrieved in its in-situ state was above its OMC, therefore it was necessary to dry the soil first. The dry soil grinded and run the sample through a No. 10 sieves. The weight of fibers calculated based on dry weight to be added to the soil sample, and bring dry soil sample to desired percentage of OMC. The soil and fibers were then placed in the bowl in alternating rows with five rows of soil and four rows of fibers. The bowl was placed in the mixer using a solid flat paddle. The soil-fiber mixture was mixed for 5 minutes with low speed (1430 rpm) and additional 2.5 minutes with high speed (1720 rpm). The specimens were prepared by mixing the soil with various percentages of fiber content (FC) and the percentages of mixtures (by weight) are shown in Table 3.

Table 3 Composition of mixtures

Serial No.	By weight (%)
1	Natural soil (0.0% Fiber)
2	0.2 % Fiber
3	0.4 % Fiber
4	0.6 % Fiber
5	0.8 % Fiber
6	1.0 % Fiber
7	1.2 % Fiber

Laboratory compaction methods can simulate field compaction reasonably well. Following ASTM D698-70, the standard proctor compaction test was conducted to determine initial compaction characteristics of the soil specimen alone. Compaction energy was equal to the compaction energy used in standard Proctor compaction tests, 593 kJm^{-3}. The compaction results provide information on the OMC at which the maximum dry unit weight or densities (γ_{dmax}) for each soil-fiber mixtures investigated.

The unconfined compression test was used for a quick of obtaining the approximate strength of the soil samples and this testing according to ASTM D2166-66. The soil samples were compacted at OMC with density control method of each specimen, to achieve the same level of dry density as that obtained previously by standard compaction curve of each fiber content (FC). The loading rate of 2.0 mm/min was subjected to the specimens until specimens failed in the test. The strength

and deformation characteristics of soil-fiber mixture with various percentages of fibers (0.2 to 1.2% of FC) compared to natural soil were evaluated. The unconfined compressive strength (UCS) was taken as the peak stress with the corresponding axial strain at failure (ε_f) in the stress-strain curve. The energy absorption capacity (toughness index) was determined in this study. The toughness index (I) can be expressed as the area under the stress-strain curve from an initial state to a post-peak state in a specific stress level.

In order to observe the behavior of soil-fiber mixtures on the tensile force due to desiccation in drying stage, the tensile test was performed. The specimens were prepared cylindrical with 12.47 cm in height and 10 cm in diameter. The compaction procedure is the same as that conducted for the unconfined compression test mentioned above. Also, the FC is the same as the tests mentioned in the previous section. The design of the apparatus for measuring soil tensile strength followed a principle similar to the device used for Brazilian test. The indirect tensile strength (ITS) measured from a compression test machine. The loading rate of 1 mm min^{-1} was subjected to the specimens until specimens failed in this test. The ITS test was conducted by applying load along the cores in between two flat parallel plates according to the indirect Brazilian test described by Dexter and Kroesbergen (1985). The ITS value determined by using a modified equation proposed by Frydman (1964).

$$ITS = \frac{2F\ g(x)}{\pi\ d\ l} \tag{1}$$

where F is the applied force, d and l represent specimen diameter and length. Frydman (1964) suggested a flattening coefficient $g(x)$ by the following equation:

$$g(x) = \left(-\frac{d}{2a}\right)\left\{2x - \sin\ 2x - \left(\frac{2y}{d}\right)\ln\left(\frac{\pi}{4} + \frac{x}{2}\right)\right\} \tag{2}$$

where x is the flattening ratio such that $x = a / y$, and a the width of flattened portion and y the distance between the flattened portion at failure. The Eq. (2) may be applied if the value of $g(x)$ greater than 0.9.

RESULTS AND DISCUSSION

The standard proctor compaction test was conducted to determine the compaction characteristic of natural soil and the soil-fiber mixtures, such as γ_{dmax} and OMC. The summary of the compaction test results are presented in Table 4. The results of the compaction curve with various FC are shown in Fig. 1. The addition of fiber affected both the γ_{dmax} and OMC. The γ_{dmax} reached a peak at FC of 1.0 %. At FC = 1.0%, the γ_{dmax} increased about 11% higher than that of the soil without fiber additives. Moreover, the value of OMC varied within approximately 13% lower than that of the soil without fiber additives. The change is mainly due to the displacement and rearrangement of soil particles induced by inclusion of fiber. With higher FC, more fibers filled the soil voids and therefore the soil specimen density became higher. Except for FC = 1.2%, with the increase in FC, γ_{dmax} increased while OMC decreased. However, for FC = 1.2 %, decreasing in γ_{dmax} indicate that there is an optimum value of FC. The decrease in γ_{dmax} was due to the lower specific gravity of fiber than that of the soil particle. When FC exceeds optimum value, greater amount of fibers with lower specific gravity replaced the soil particles which have higher specific gravity. As a result, the composite specific gravity would be less. Therefore, γ_{dmax} of the soil-fiber mixture decreased with fill more fibers beyond the optimum value of fiber content.

Table 4 Obtained maximum dry unit weight and optimum moisture content at various fiber contents

Fiber Content (%)	Optimum Moisture Content (%)	Max. Dry Unit Weight (kN/m^3)
0.0	78.0	8.13
0.2	74.0	8.19
0.4	73.0	8.27
0.6	69.3	8.58
0.8	68.2	8.73
1.0	65.0	9.03
1.2	70.8	8.42

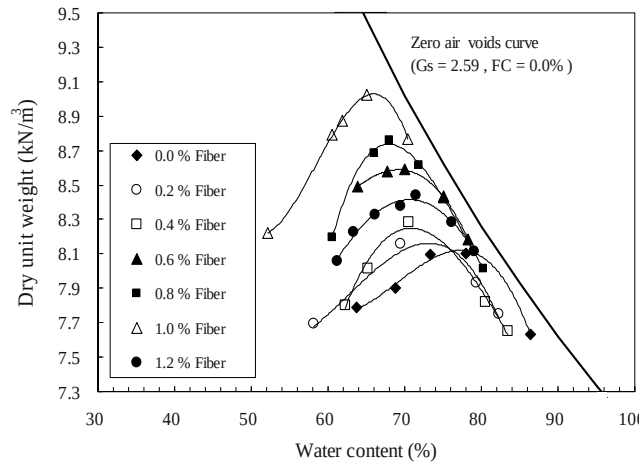

Fig. 1 Compaction curves for the Akaboku soil with various fiber contents

The UCS results showed that the fiber additives have a significant effect on the stress-strain behavior of the

soil-fiber mixture. The stress-strain curves obtained from unconfined compression tests are showed in Fig. 2.

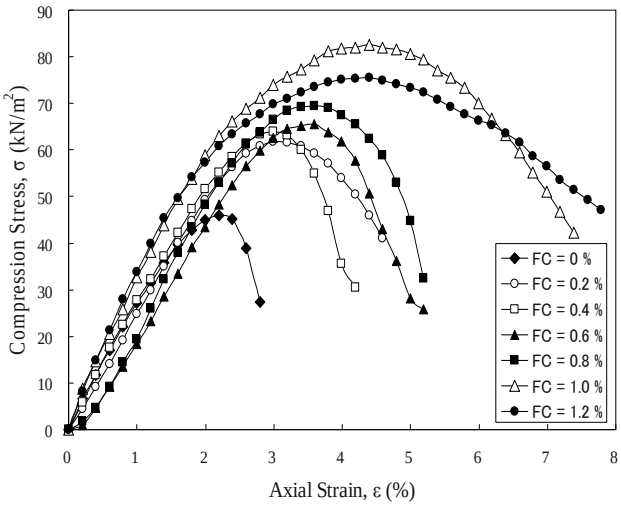

Fig. 2 Stress-strain curves of Akaboku soil with various fiber contents

The values of UCS and ε_f of the soil specimens are given in Table 5. For any FC studied, the UCS initially increased and reach the peak value at FC=1.0%, and then decreased at FC=1.2 % as shown in Fig. 3. The maximum value of UCS (FC=1.0%) increased about 80% as compared with UCS value of FC=0%. It is indicated that an increasing in FC induced an improvement in the strength behavior of the soil-fiber mixtures. The mechanism could be explained as follow, the development of interfacial force and interlock between soil particles and fibers in the compacted soil specimens would give an improvement in the friction resistance. This mainly due to the total contact area between soil particles and fibers increases while increasing the FC which contributes to the increase in resistance to forces applied and consequently the strength of the soil-fiber mixtures increase. Furthermore, the soil-fiber mixtures exhibited a highly ductile behavior as shown in Fig. 3. The similar trend with the UCS is shown for the ε_f at various FC. With increase in FC, the ε_f initially increased up to FC=1.0% and slightly decreased with FC=1.2%. The strain behavior showed that the larger strain in the soil specimens with fiber additives due to the improvement in the stretching resistance. When the soil specimens subjected with load, the interaction between soil particles and the fiber additives improved, which provide the linkage effect in the soil-fiber mixtures. Therefore, the soil-fiber mixtures showed more ductile behavior. As a result, the soil-fiber mixtures are able to hold more deformation and higher strain at rupture. This improvement of soil behavior due to fiber addition suggests the potential application of fiber in engineering practice.

Fig. 4 showed the toughness index of the Akaboku soil with various FC obtained from the unconfined compression test. Initially, a slightly increase of the toughness index occurred up to FC=0.8% and signifi-

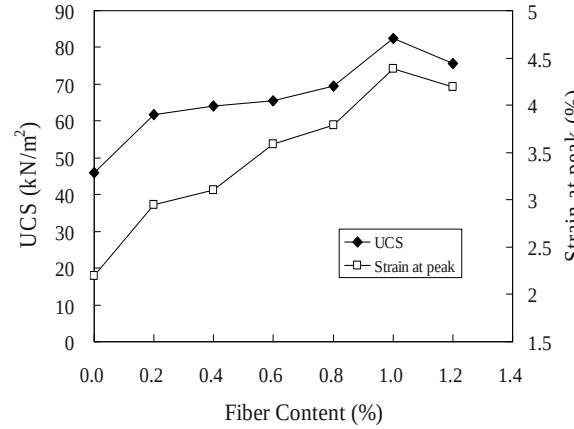

Fig. 3 Variation of stress-strain with various fiber contents

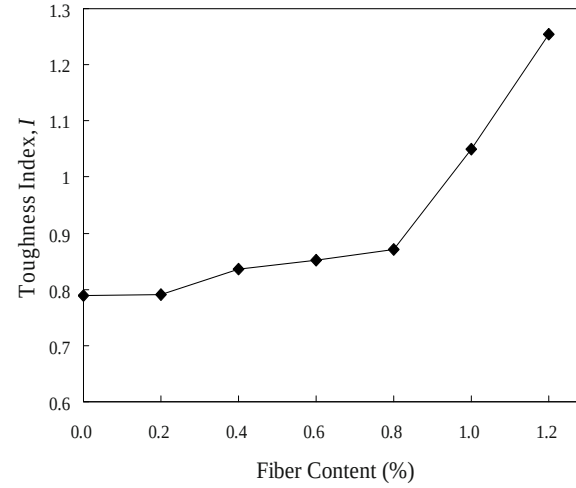

Fig. 4 Toughness index with various fiber contents

Table 5 Value of UCS and ε_f for various fiber contents

Fiber content (%)	Compression test		ITS (kN/m²)
	UCS (kN/m²)	ε_f (%)	
0.0	46.02	2.2	9.53
0.2	61.82	3	13.55
0.4	63.98	3.2	16.73
0.6	65.61	3.6	22.23
0.8	69.48	3.8	26.68
1.0	82.54	4.4	27.53
1.2	75.52	4.2	26.47

cantly increased for the FC higher than 0.8%. The toughness index value greater than unity (i.e. FC=1.0% and 1.2%) indicates an overall increase in energy absorbing capacity, with resulting higher ductility in the post-peak region.

The results of the tensile test are summarized in Table 5. It can be seen in Fig. 5 that the inclusion of fibers increased the tensile strength of the soil. Same behavior with the previous results obtained that initially tensile strength increased up to FC = 1.0% (increased by approximately 190% from the soil of FC=0.0%) and slightly decreased with FC = 1.2% which is beyond the optimum value of FC. The effectiveness of fibers additives depends on the interaction between the fibers and soil. In the tensile test, the mechanism of the fibers interacts to the soil with low normal stress mainly controlled by adhesion. The amount of the adhesion force developed related to the surface contact area of the fibers in the soil (Ziegler et al. 1998). It can be explained that the adhesion force increased by increasing the surface contact area between the soil and fibers. This can be achieved by increase the FC in the soil specimens.

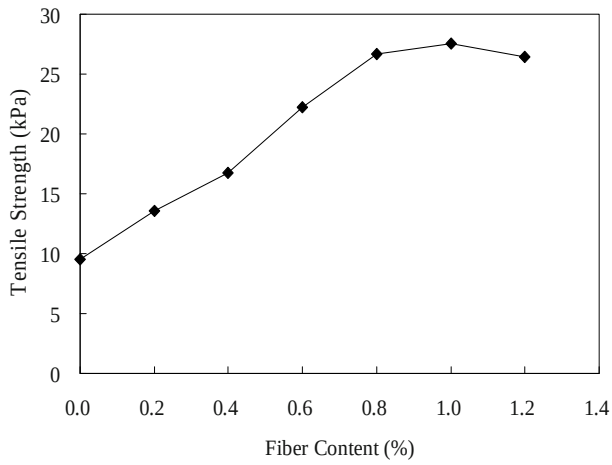

Fig. 5 Tensile strength of Akaboku soil with various fiber contents

Furthermore, studying the relationship between soil mechanics properties is useful in estimating the appropriate property that can be used in specific conditions. Therefore, the relationship between the soil parameters such as γ_{dmax}, UCS and ITS with various of FC were evaluated in this study. From Fig. 6, it can be seen that the UCS increased with increasing in γ_{dmax}. A linear line regression with R^2=0.792 was used for analyze the relationship of the parameters. The UCS increased from 46.02 kN/m^2 at a γ_{dmax} of 8.13 kN/m^3 to 82.54 kN/m^2 at a γ_{dmax} of 9.03 kN/m^3. The results showed that the relationship indicate a good correlation. According to the relationship between ITS and γ_{dmax}, a high correlation was obtained using a linear line regression with R^2=0.915 as we can see in Fig. 7. The results showed that the ITS strongly depends on the density of the soil specimens. The ITS increased from 9.53 kN/m^2 at a γ_{dmax} of 8.13 kN/m^3 to 27.53 kN/m^2 at a γ_{dmax} of 9.03 kN/m^3. The ITS generally increased with increasing γ_{dmax}. The results indicated that there is a good correlation between γ_{dmax} and both UCS and ITS. This behavior can be explained as the higher γ_{dmax}, a more dense packing and rearrangement of the particles occurs, resulting in higher UCS and ITS value.

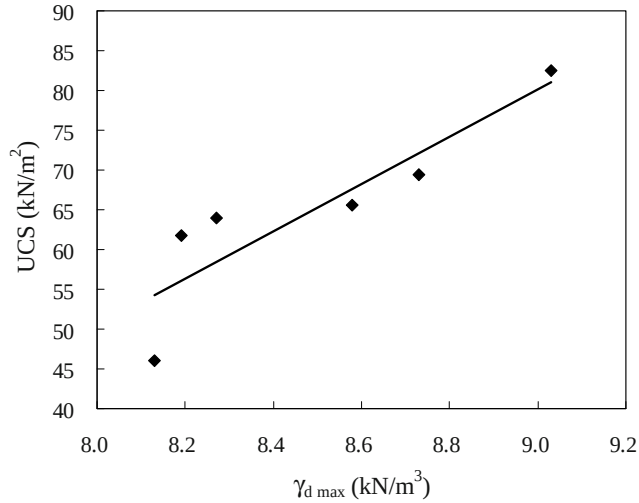

Fig. 6 Relation between γ_{dmax} and UCS

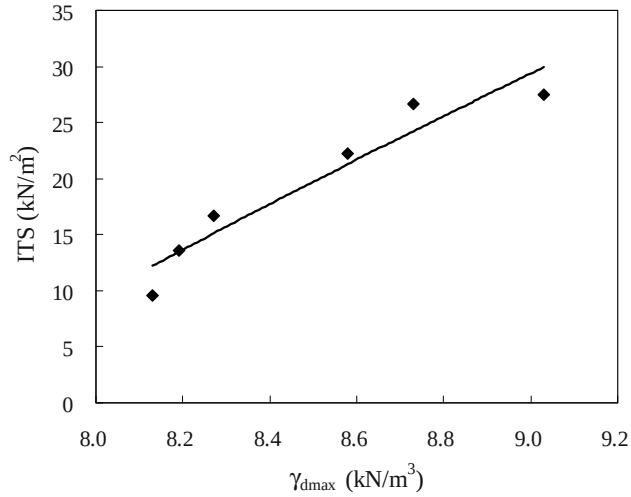

Fig. 7 Relation between γ_{dmax} and ITS

The relationship between UCS and ITS was also observed in this study as shown in Fig. 8. The derived equation obtained from this interrelationship can be used interchangeably to predict the required values of UCS and ITS.

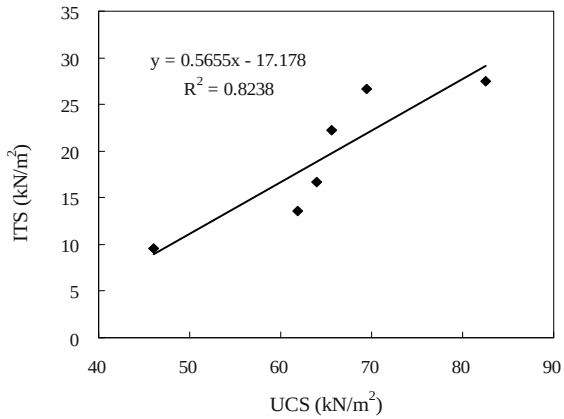

Fig. 8 Relation between UCS and ITS

CONCLUSION

The conclusions from this study can be summarized as follows:

1. The contribution of fiber to the compaction characteristics (i.e. maximum dry density) increases with increasing fiber contents. A slightly decrease of γ_{dmax} was found for fiber content of 1.2%, which indicate that there is an optimum value of fiber content..
2. The effects of fiber inclusion indicate that the UCS and the axial strain at failure of the soil-fiber mixtures increase, decrease the loss of post-peak strength. Furthermore, with the inclusion of fibers, the toughness index of the soil-fiber mixtures increase which indicates that the energy absorbing capacity increase which resulting higher ductility in the post-peak region.
3. The inclusion of fibers also increases the tensile strength of the soil-fiber mixtures. The highest soil tensile strength occurred at the highest dry density of the soil specimen.
4. Significant improvement in the mechanical behavior of the soil-fiber mixtures indicate that there is some potential for the use of fibers mixed with the Akaboku soil in engineering practice (i.e. landfill barrier material). In this study showed that the usefulness of the fibers would improve the strength of the soil.

ACKNOWLEDGEMENTS

The authors would like to acknowledge financial support for this study provided by the Kajima's Foundation Research Grant (2006-2007) (representative person, Dr. Du YJ).

REFERENCES

Cai Y, Shi B, Ng CWW, Tang C (2006) Effect of polypropylene fibre and lime admixture on engineering properties of clayey soil. Engineering Geology 87: 230-240

Cetin H, Fener M, Gunaydin O (2006) Geotechnical properties of tire-cohesive clayey soil mixtures as a fill material. Engineering Geology 88: 110-120

Dexter AR, Kroesbergen B (1985) Methodology for determination of the tensile strength of soil aggregates. Journal of Agricultural Engineering Res 31: 139-147

Frydman S (1964) The applicability of the Brazilian (indirect tension) test to soils. Journal of Applied Science 15: 335-343

Gray DH, Ohashi H (1983) Mechanics of fiber reinforcement in sand. Journal of Geotechnical Engineering 109(3): 335-353

Ibarra SY, McKyes E, Broughton RS (2005) Measurement of tensile strength of unsaturated sandy loam soil. Soil and Tillage Research 81: 15-23

Kaufmann J, Winnefeld F, Hesselbarth D (2004) Effect of the addition of ultrafine cement and short fiber reinforcement on shrinkage, rheological and mechanical properties of portland cement pastes. Cement and Concrete Composites 26: 541-549

Kumar S, Tabor E (1998) Strength characteristics of silty clay reinforced with randomly oriented nylon fibers. The Electronic J. Geotech. Eng. (8)-Bundle B

Maher MH, Ho YC (1994) Mechanical properties of kaolinite fiber soil composite. Journal of Geotechnical Engineering 120(8): 1381-1393

Nataraj MS, McManis KL (1997) Strength and deformation properties of soil reinforced with fibrillated fibers. Geosynthetics Intl 4 (1): 65-79

Ozkul ZH, Baykal G (2007) Shear behavior of compacted rubber fiber-clay composite in drained and undrained loading. Journal of Geotechnical and Geoenvironmental Engineering ASCE 7: 767-781

Park T, Tan SA (2005) Enhanced performance of reinforced soil walls by the inclusion of short fiber. Geotextiles and Geomembrane 23 (4): 348-361

Tang C, Shi B, Gao W, Chen F, Cai Y (2007) Strength and mechanical behaviour of short polypropylene fiber and cement stabilized clayey soil. Geotextiles and Geomembrane 25: 194-202

Ziegler S, Leshchinsky D, Ling HI, Perry ED (1998) Effect of short polymeric fibers on crack development in clays. Soils and Foundations 38(1): 247-253

Proceedings of the 4th Asian Regional Conference on Geosynthetics
June 17 - 20, 2008 Shanghai, China

INFLUENCE OF SO_3 CONTENT ON THE STRENGTH OF CEMENT-FLY ASH STABILIZED CRUSHED-STONES

X. Chen[1], M.K. Zhou[2], P.L. Cong[3] and X. Li[4]

ABSTRACT: The effect of SO_3 contents on strength of cement-fly ash stabilized crushed-stones is investigated. The scanning electron microscope (SEM) and MIP were employed to study the influences of SO_3 in cement. The experimental results showed that the SO_3 contents can affect the strength of cement –fly ash stabilized crushed-stones, and 5% of SO_3 is maximum limited contents for materials performances deteriorated and structure destroyed.

KEYWORDS: cement, fly ash, SO_3, strength

INTRODUCTION

In the cement-based stabilized materials, the quality of cement plays an important role in performance of materials. The cracking of cement stabilized crushed-stone is bad and the forming retard time is shortened due to the execution of new cement standard in China. The shrinkage of cement material could be compensated and cracking could be controlled by using the expansive cement. Some researches have implied that increasing SO_3 can enhance the expansive performance of cement materials and prolong the setting time of cement. But the 28d strength will fall down rapid in Portland cement when the content of SO_3 is more than 3.5% and in Slag Portland cement, this content is 4.0%. Therefore, the norm regulates that the allowable contents of SO_3 are different because different cements have different compositions.

The reason that the largest allowable contents of SO_3 differ in different cement is that kind and content of composite materials can change systems and environments of materials. Cement-fly ash stabilized crushed stones is a new type of cement-based material with high qualities. In this material, the proportion between cement and fly ash is always about 4:10. Because of a large number of fly ash in it, the content of SO_3 can be increased properly to prolong the forming retard time and to control the cracking. At the same time, the structure and performance of material can not be destroyed.

The influence of SO_3 contents in cement on strength of cement-fly ash stabilized crushed stones is tested and its mechanics is analyzed in paper. The maximum SO_3 content in cement was investigated in order to ensure the performances of cement fly-ash stabilized materials.

MATERIALS AND EXPERIMENTAL METHOD

Materials

(1) Cement: Portland cement 32.5.

(2) Fly ash: The fineness of fly ash is shown in Table 1 and the fineness of fly ash accords with the specification of Standard JTJ034-2000

Table 1 Grading analysis of fly ash

Screen size /mm	1.18	0.6	0.3	0.15	0.075
Passage rate/%	100	99.8	97.2	85.2	78.1

(3) Phosphogypsum.: The chemical composition of the phosphogypsum is showed in table 2.

(4) Aggregate: The gradation of the aggregate used is showed in Table 3. It accords with the specification of Standard JTJ034-2000

[1] Ph.D Student, Key Laboratory for Silicate Materials Science and Engineering and Ministry of Education, Wuhan University of Technology, CHINA. Email: chenxiao1981@tom.com

[2] Professor, Key Laboratory for Silicate Materials Science and Engineering and Ministry of Education, Wuhan University of Technology, CHINA. Email: zhoumingkai@163.com

[3] Ph.D Student, Key Laboratory for Silicate Materials Science and Engineering and Ministry of Education, Wuhan University of Technology, CHINA. Email: Congpl@whut.edu.cn

[4] Ph.D Student, Department of Civil Engineering, Tsinghua University, Beijing, CHINA. Email: l-x07@mails. tsinghua.edu.cn

Table 2 The chemical composition of the phosphogypsum

Material	Chemical Composition							
	LOI	CaO	SiO_2	Al_2O_3	Fe_2O_3	MgO	P_2O_5	SO_3
Phosphogypsum	20.5	31.57	2.23	0.85	0.74	0.19	0.71	43.80

Table 3 The gradation of the aggregate

	Screen size (mm) / Passage rate (%)							
	31.5	26.5	19	9.5	4.75	2.36	0.6	0.075
Upper limit	100	97.87	66.10	7.73	1.36	0.89	-	-
Low limit	100	100	100	81.77	16.57	2.13	-	-
Median	100	100	100	100	99.50	76.40	37.50	6.10
Gradation of aggregate	100	99.04	84.75	54.47	37.09	26.10	12.38	2.01

Strength Specimen Preparation

The contents of SO_3 in cement are increased by adding the phosphogypsum and mortar strengths of cements with different contents of SO_3 are tested.

The strength test binder cylinders were compacted to a compacting degree of 95% while the binder stabilized crushed stones was compacted to a compacting degree of 98%. The compacting degree is a ratio of the test specimen's dry density to its maximal dry density; the maximal dry density and the optimum water content of cement-fly ash binder were gained with a tamping test. Tamping tests were conformed to test method JTJ57-94 specifications of ministry communication of China. Cement-fly ash binders was formed with $\Phi 50 \times 50$ mm^3 molds, the cement-fly ash stabilized crushed stones was formed with $\Phi 150 \times 150$ mm^3.

Strength Measure

The unconfirmed compressive strength tests are conformed to test method JTJ57-94. The cylinders were cured in the airproof plastic bags at 25 ± 2℃ till 24 h before the design ages, then the cylinders were steeped into water for 24 h before testing, six cylinders were tested for each data point.

Microscopic Observation

The microscopic observation samples were collected in the middle sections of the compressive strength specimens of 7 day binders, dried with vacuum and covered by a gold layer. The microstructures of the binder samples were studied with the SX-40 scanning electron microscope.

Porosity Measurement

The porosity measurement sample were collected in the middle part of the compressive strength specimen of 7 day binders, the samples were broken into a particle no lager than 3 mm by hand and dried with vacuum too. The pore structures of the binders are studied with Poremaster 33-6 mercury intrusion pressure instrument.

DISCUSSIONS

The Influence of the Contents of SO_3 on Mortar Strength

The mortar samples (4×4×16 mm) are prepared with different cements of SO_3 contents and their strength are tested after 3d, 7d and 28d. The results are listed in Table 4.

Table 4 indicates that the strength of cement is sensitive to the SO_3 contents. Compared with mortar strength of 1.8% SO_3 contents, the SO_3 content increases 4% points, the 3 d mortar strength reduces 60% and strengths of the 7 d and 28 d can not achieve 50%.

The early mortar strength decrease may be the SO_3 increasing the gelatinization time of cement. During the strength forming, SO_3 will react with C-A-H to form AFt and expansive action exhibit. But the structure of mortar is compact and little void can not absorb adequately the expansion of AFt. The structure of mortar will be destroyed and strength decreased. So the SO_3 contents should be limited, too much SO_3 contents can decrease the strength of cement mortar.

Table 4 Effects of SO_3 contents on mortar strength

Content /%	Strength/Mpa					
	3 d		7 d		28 d	
	Flexural	Compressive	Flexural	Compressive	Flexural	Compressive
1.8	6.27	28.7	7.37	34.3	9.74	48.2
2.6	5.33	25.9	6.47	31.1	9.42	46.8
3.4	3.50	16.6	5.26	23.7	8.24	39.8
4.2	3.38	16.5	4.44	20.6	8.54	40.9
5.0	2.93	11.6	3.49	13.6	4.95	23.9
5.8	2.46	11.4	2.63	14.2	4.2	21.8
8.8	2.88	14.3	3.13	18.1	4.77	26.4

The early mortar strength decrease may be the SO_3 increasing the gelatinization time of cement. During the strength forming, SO_3 will react with C-A-H to form AFt and expansive action exhibit. But the structure of mortar is compact and little void can not absorb adequately the expansion of AFt. The structure of mortar will be destroyed and strength decreased. So the SO_3 contents should be limited, too much SO_3 contents can decrease the strength of cement mortar.

Influence of SO_3 Content on Strength of Cement-Fly ash Binder

The samples (Φ50×50mm) are prepared with cements of different contents of SO_3 and fly ash (cement: fly ash=2∶:5).Then unconfined compressive strengths are tested after 3 d, 7d and 28 d. The results are listed in Fig. 1.

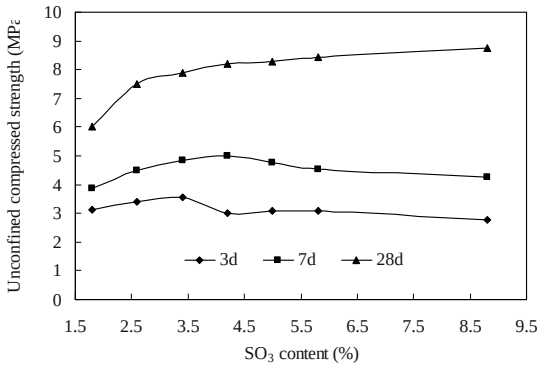

Fig. 1 Influence of SO_3 content on Strength of cement-fly ash binder

Fig. 1 shows that the relation between strength of cement-fly ash binder and SO_3 content is quite different from that between cement mortar and SO_3 content. It is clear that the binder has the highest three day strength when the content of SO_3 in cement is 3.4%. When the content of SO_3 is 4.2%, the highest 7 day strength is gained. With the increase of SO_3 content in cement, the 28 day strength is growing consistently.

It is because that more expansive source unit (AFt) is generated with the increase of SO_3 content. Compared with cement mortar, the structure of cement-fly ash binder is not very compact and there are more void which can absorb more expansion. Therefore, appropriate expansion of AFt will not destroy the structure of cement-fly ash binder, and in stead, it will fill the voids of materiel to improve the strength. However, with further increase of SO_3 content, the expansive source units become more and more and the expansive volume become larger and larger so the allowed space is overstepped. Then the structure of material is destroyed and the strength drops obviously. Besides, some researcher thinks that AFt will develop into a thin rod/needle like crystals which can grow and fill along the void of material in a weakly alkaline system while in a strongly alkaline system it could develop into a bigger rob like crystals which would create a reverse crushing stress in compact system. Then the structure of material would be destroyed and performance would worsen. In cement-fly ash system, the alkalinity is reduced greatly because of adding mass fly ash.

On the other hand, SO_3 can stimulate the pozzolanic activity of fly ash availably and can accelerate the pozzolanic reaction between fly ash and Ca $(OH)_2$ produced by cement hydration to improve the strength.

Influence of SO_3 Content on Strength of Cement-Fly ash Stabilized Crushed Stones

The samples (Φ150×150 mm) are prepared with cements of different contents of SO_3 and fly ash and aggregate (cement: fly ash: crushed stones=4∶10∶90). Then the 7 d and 28 d unconfined compressive strengths are tested. The results are listed in Fig. 2.

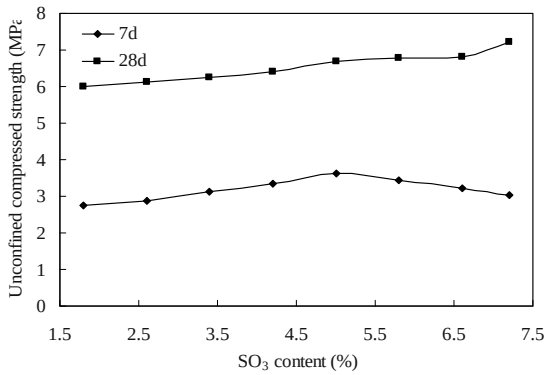

Fig. 2 Influence of SO_3 content on Strength of cement-fly ash stabilized

Fig. 2 shows that the 7 d strength of cement-fly ash stabilized crushed stones reach the maximum when SO_3 content in cement is 5.0%. With the increase of the SO_3 content in cement, the 28d strength tends to increase continually. When SO_3 content increases to 7.2%, the 28d strength is 7.22 MPa which is 120% of that when SO_3 content is 1.8%. Therefore, the SO_3 content is very important for materiel strength.

The pore ratio of cement-fly ash stabilized crushed stones is larger than it of cement-fly ash binder. Therefore, the volume for absorbing expansion is also larger. Compared with the SO_3 content in cement-fly ash binder, the appropriate content of SO_3 in cement-fly ash stabilized crushed stones can increase by about 1%.

MECHANISM OF ACTION

Intensifying Cementing Performance of Materials

With the increase of SO_3 content in cement, it is accelerated that the pozzolanic reaction between the active substances in fly ash (including SiO_2, Al_2O_3) and $Ca(OH)_2$ produced by cement hydration. The AFt crystals (thin rod/needle like) form at the same time (showed in Fig.3), which can grow and fill along the void of materials. They can enhance the conjunctures of the different solid particles in the binder. So the cementing action is improved. Because of absorbing a large amount of water (the percent of structural water volume is 81.2% of AFt Volume in AFt crystal), the AFt can make obvious expansion to improve the early strength of materials.

Improving Pore Structure

Cement-fly ash stabilized material is a kind of porous material. The ratio, size and distribution of pore have important effect on the performance of material. The hydration products make the particles integrate with each other, the formation of AFt always follows a slight expansivity, and it can fill the small pores in the binder, so the strength is improving with the increase of SO_3 content in cement.

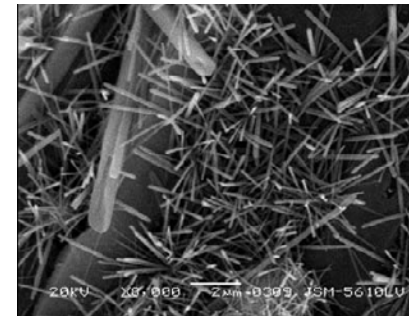

Pattern of AFt

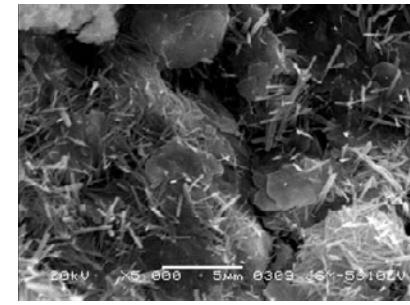

Distribution of AFt

Fig. 3 Pattern and distribution of AFt in cement-fly ash

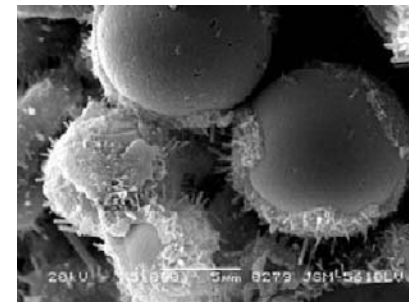

Surface of fly ash after 7d, SO_3 content 1.8%

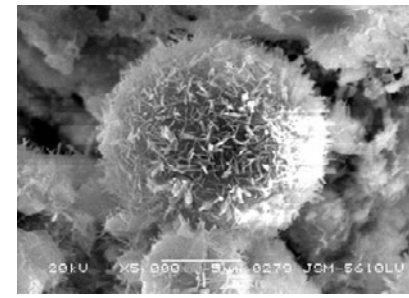

Surface of fly ash after 7 d, SO_3 content 4.2%

Fig. 4 Surface of fly ash in cement-fly ash after 7d

Fig. 5 shows the pore distribution in cement-fly ash (cement: fly ash=2 : 5) prepared with cements containing different contents of SO_3 after 7 d.

In Fig. 5, it is clear that the quantity of large size proes is decreased obviously and the quantity of small size pores is increased. The harmful pore (size<100 nm) changed into the no-harmful pore（size>100nm）. It is because the reaction between fly ash and $Ca(OH)_2$ is accelerated and more hydrating products are formed after SO_3 content in cement increased. Furthermore, because of the formation of AFt, the expansivity is generated and structure of material is compacted.

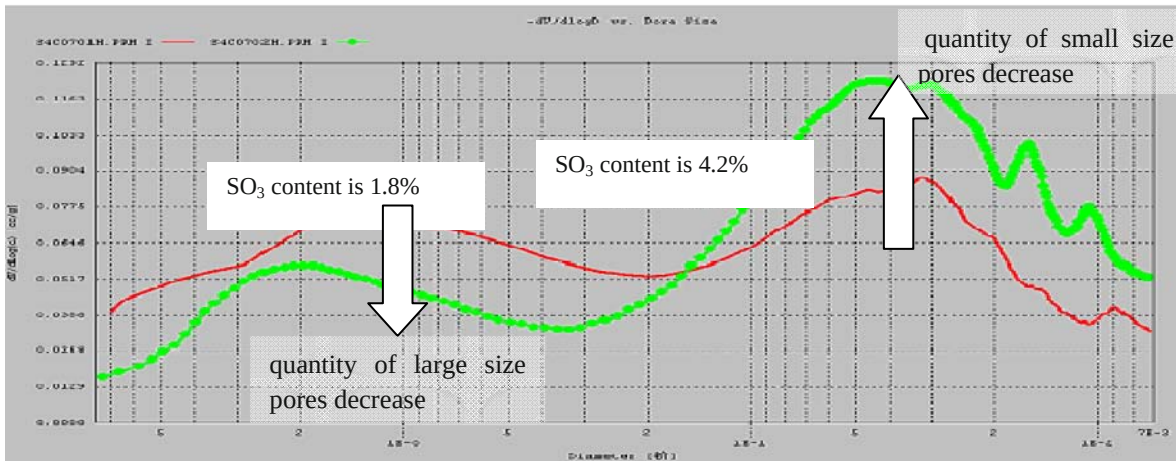

Fig. 5 the pore distribution in cement-fly ash prepared with cements containing different contents of SO_3 after hydrating 7d

CONCLUSIONS

From the above results and discussion the following conclusions can be summarized:

1. The maximum SO_3 contents are different for different cement materials. And 3.0%, 4.2% and 5% is the maximum permitted contents for cement mortar, cement-fly ash and cement-fly ash stabilized stones, respectively.

2. In cement-fly ash stabilized stones, the change SO_3 contents can adjust the setting time of cement and prevent cracking.

3. The increase of SO_3 contents can activate pozzolanic reaction between $Ca(OH)_2$ which is the hydrating product of cement and fly-ash to intensify the cementitious performance. It can also generate a large number of AFt to fill into pores of material and to improve the pore structure. So the performance of material is improved.

ACKNOWLEDGEMENT

We acknowledge the financial support provided by the constructive science and technology item of the westward traffic in China (Project200631800042).

REFERENCES

Sha QL (1998) Semi-rigid based asphalt pavement of expressway. People communication press.

Recension of the Cement Standard (1979.7) China Architecture Industry Press

JTG E30-2005 (2005) The testing regulations of cement and concrete in highway engineering

JTJ 057-94 (1994) The testing regulations of inorganic binder stabilized material in highway engineering

DFP (1993) Thermodynamic Investigation of the CaO-Al_2O_3-$CaSO_4$·$2H_2O$ System at 25℃ and the Influence of Na_2O. Cement and Concrete Research 23(1): 221-232

Ma WP, Brown PW, etc (1997) Hydrothermal Reactions of fly ash with $Ca(OH)_2$ and $CaSO_4$·$2H_2O$. Cement and Concrete Research 27(8): 1237-1248

Wu ZW, Lian HZ (1999) High performance concrete. China railway press

Filter and Drainage Characteristics

DRAINAGE CHARACTERISTICS OF REINFORCED DRAINAGE GEOTEXTILE FOR LANDFILL COLLECTION SYSTEM

J.Y. Lee[1], J.H. Jeong[2] and M.H. Lee[3]

ABSTRACT: The damage of wellpoint and/or clogging of geotextile occurring during the period of landfill construction and its management may cause poor performance of landfill leachate collection system. This paper describes the permittivity characteristics of newly designed geotextile and its application to the landfill leachate collection system, which is to minimize the damage of drainage system caused by the settlement due to landfill construction. The actual landfill leachate collected from in-situ was used for leaching tests. Test results show that the permeability values of reinforced geotextile are in the range between 1×10^{-1} and 1×10^{-4}.

KEYWORDS: clogging, landfill leachate, non-woven fabrics, permittivity, reinforced drainage geotextile (RDG)

INTRODUCTION

In general, the expected life span of a landfill is approximately 30 years and the leachate drainage & collection is important during the period of landfilling as well as the management of landfill leachate collection system after completion of the landfilling. Geotextile is generally used as a protecting material for geomembrane. The geotextile is also used as a filtering material for the prevention of clogging in the landfill drainage system. Polymer is used as a raw material for geotextile (e.g. cloth and non-woven fabrics), which is chemically and biologically stable and therefore nowadays increasingly used in landfill leachate collection system. Moreover, high density geotextiles (≥ 1000 g/m^2) are currently produced and available due to the development of geotextile weaving technology (Brand & Pang 1991; Calhoun 1972; Schneider & Groh 1987).

The hydraulic conductivity of leachate drainage system is known to be reduced by clogging, which results in the increase of leachate level within the landfill area. Consequently, the overall control ability of landfill system will be reduced. The settlement occurring during landfill construction often causes a damage of drainage system. The main purpose of this project is to investigate the applicability of a reinforced drainage geotextile (RDG) using non-woven fabrics for minimizing the destruction of drainage layer in the landfill collection system. Thus, the permittivity changes of RDG were observed and the drainage system using RDG was evaluated.

BACKGROUND

Permittivity of Geotextile

The permittivity of geotextile was evaluated in Delft Hydraulic laboratory using the modified Darcy's law as follows:

$$\left(\frac{\partial Q}{\partial t}\right)^n = K_f A \frac{\partial h}{\partial x} \tag{1}$$

where,

Q : Volume of water collected (mm^3)
t : Duration (s)
n : Values given by turbulent flow (1.0—2.0)
K_f : Permittivity considering turbulent flow
A : Cross-sectional area of specimen (mm^2)
h : Head of water (mm)
x : Distance (mm)

The permittivity of fluid can be expressed as follows (Koerner 1994)

$$\psi_f = \psi_w \frac{\rho_f}{\rho_w}\frac{\mu_w}{\mu_f} \tag{2}$$

where,

ψ_f, ψ_w : Permittivity of fluid, water (s^{-1})
ρ_f, ρ_w : Density of fluid, water (g/cm^3)
μ_f, μ_w : Viscosity of fluid, water (cps)

[1] Professor, Department of Environmental Engineering, The University of Seoul, KOREA
[2] Graduate Student, Department of Environmental Engineering, The University of Seoul, KOREA
[3] BK Research Associate, Department of Civil & Environmental Engineering, Hanyang University, KOREA. Email: mhleecok@hanyang.ac.kr

Clogging Phenomenon of Geotextiles

Clogging is a very slow and continuous phenomenon that can be explained by three different processes: physical, biological, and chemical processes. The conceptual tendency of clogging phenomenon is presented in Fig. 1.

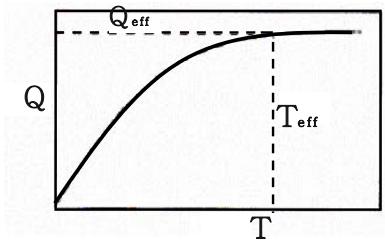

Fig. 1 Conceptual trend of cumulative flow vs time for gradual clogging

EXPERIMENTAL PROGRAMME

Permittivity Testing

Testing apparatus

Fig. 2 shows an experimental setup for permittivity test. A testing column was designed and constructed with clear acrylic tube (200 mm o.d×0 mm thickness x 600 mm length) in order to measure the permittivity of RDG. The lower part of column was fixed and connected to an extension column (200 mm o.d. ×0 mm thickness× 200 mm length) for the installation of natural drainage material. The leachate collected from **S** landfill site was introduced from the top of the column, and the hydraulic head was maintained constant during test.

Testing Procedure

Permittivity testing using clean water

A series of tests, using both the constant head method and the falling head method, were carried out using clean water for the measurement of permittivity of RDG. The flow rate passing through the RDG for 1 minute under constant head was measured and recorded.

Permittivity testing using landfill leachate

A number of constant head tests were conducted using leachate collected from the **S** landfill site in order to measure the permittivity ability in the leachate drainage system. The density and viscosity of leachate were measured, and the permittivity values were corrected using Eq. (2).

(1) Constant Head Test (EPA 1988)

$$\psi = \frac{QR_t}{Aht} \tag{3}$$

where,

ψ : Permittivity (s^{-1})
Q : Volume of water collected (mm^3)
A : Cross-sectional area of specimen (mm^2)
t : Duration (s)
h : Head of water (mm)
R_t : Temperature correction factor

$$R_t = \frac{\mu_t}{\mu_{20°C}} \tag{4}$$

where,

μ_t : Viscosity at room temperature
$\mu_{20℃}$: Viscosity at 20℃

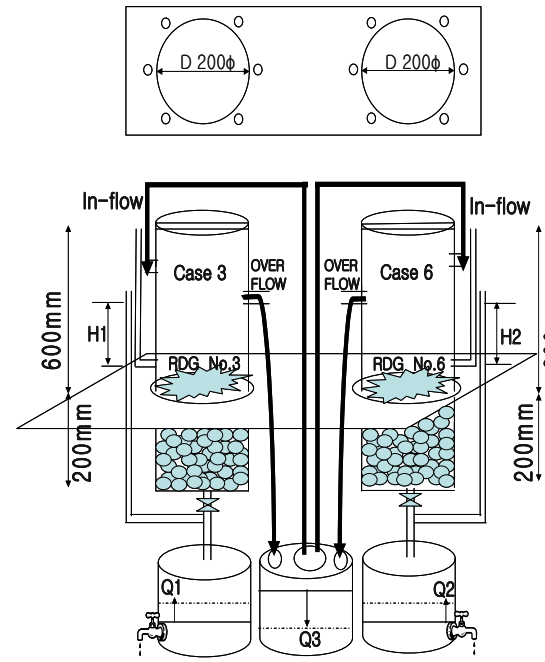

(a)

(b)

Fig. 2 Experimental setup for permittivity test
(a) Schematics of permeameter; (b) Permeameter in use

(2) Falling Head Test (EPA 1988)

$$\psi = \frac{a}{At}\log_e \frac{h_i}{h_f} R_t \quad (5)$$

where,

A : Cross-sectional area of specimen (mm^2)
a : Cross-sectional area of standpipe (mm^2)
Q : Volume of water collected (mm^3)
t : Duration (s)
h_i : Initial head of water (mm)
h_f : Final head of water (mm)

RESULTS AND DISCUSSION

Permittivity of Reinforced Drainage Geotextiles

Table 1 presents the permittivity values of RDG obtained from the constant head tests. From the laboratory investigations, the average permittivity values for case 3 and case 6 were found to be 0.0582 s^{-1} and 0.0608 s^{-1}, respectively. The material properties of non-woven fabrics used for case 3 and case 6 were the same, and the permittivity value of case 6 was found to be slightly higher than that of case 3. The only difference between case 3 and case 6 was the geogrid interval which stuck to the back of fabrics for reinforcing strength. Thus, the different permittivity values were suggested to be caused by the effects of geogrid intervals.

(a) (b)

Fig. 3 Non-woven geotextile for case 3: (a) front; (b) rear

(a) (b)

Fig. 4 Non-woven geotextile for case 6: (a) front; (b) rear

Variation of Permittivity by Landfill Leachate

Two different leachates collected from the **S** landfill site were used in the laboratory experiments, and their qualities were quite different and the amount of leachate also varied according to each month and season (KOSEF 1988). Typical properties of landfill leachate are given in Table 2.

Table 3 Accumulated SS before and after leaching test

		Landfill Site			
		Site No. 1		Site No. 2	
		Before	After	Before	After
SS (mg/L)	No. 3	60	56	382	292
	No. 6		58		266

The suspended solid (SS) can give a significant influence on leaching tests, even in a short period, thus the amount of accumulated SS onto non-woven fabrics was measured and evaluated before and after the leachate penetration. As shown in Table 3, the SS values of Site No. 2 are much higher than those of Site No. 1 since the Site No. 1 is the area where the landfilling was already completed. The removal rate of SS by the RDG was insignificant, but the filtering and isolation ability of RDG were good enough.

CONCLUSIONS

From the laboratory investigation, the following conclusions were made:

(1) The permittivity values of RDG were different under different geogrid distance: 0.0582 s^{-1} for case 3 and 0.0608 s^{-1} for case 6. Nonetheless, the permittivities of RDG were similar to those of ordinary geotextiles.
(2) The SS values for Site No.2 were much higher than those for Site No. 1. The reduction of permittivity appears to be affected by the SS concentration of landfill leachate.
(3) The permittivity values of RDG were in the range between 1×10^{-1} and 1×10^{-4} cm/s, which is better than the values after completion of landfilling, so that the RDG could be used as a filter in the drainage layer.

REFERENCES

Brand EW, Pang PLR (1991) Durability of Geotextiles to Outdoor Exposure in Hong Kong, J. of Geotechnical Engineering 117(7): 979-1000

Calhoun CC (1972) Development of Design Criteria and Acceptance Specifications for Plastic Filter Cloth, Technical Report No. S-72-7, U. S. Army Waterways Experiment Station. Vicksburg, Miss

EPA (1988) Guide to Technical Resources for the Design of Land Disposal Facilities

Koerner RM (1994) Designing with Geosynthetics, 3rd Edition, Prentice Hall Publ. Co., Engewood Cliffs, NJ: 95

KOSEF (1988) A Study on the Design of Geosynthetics as Filter Materials 871-1501-051-1: 16-17

Schneider H, Groh M (1987) An Analysis of the Durability Problems of Geotextiles, Geosynthetics ’87 Conference, New Orleans, USA: 434-440

PILOT SCALE FIELD TEST FOR NATURAL FIBER DRAIN

J. H. Kim[1] and S. D. Cho[2]

ABSTRACT: A pilot test using natural fiber drains was conducted to prove their effective discharge capacity in the field. The pilot test site was divided into 5 different areas, with various combinations of vertical and horizontal drains installed for evaluation. Conventional PDB and FDB, as well as the newly developed SDB, were used as vertical drains, while sand and fiber mats were used as horizontal drains. Based on the monitoring data obtained at the test site, the surface settlements which occurred at PDB, FDB and SDB installation fields were almost identical as well as laboratory model test results. The excess pore pressure measured in SDB was greater than that in PDB and FDB, while the dissipation rate of excess pore pressure in SDB was slower than that in PDB and FDB. The generation and dissipation rates of excess pore pressure measured in the ground from the installation of PDB, FDB and SDB were almost identical to the same extent as the surface settlements measured at the pilot test field. Based on the existing data, natural fiber drains represent a promising alternative material for the improvement of soft clay.

KEYWORDS: fiber drain board (FDB), straw drain board (SDB), plastic drain board (PDB), soil improvements

INTRODUCTION

An increasing number of huge construction projects, promoting national key industries, such as airports, expressways and ports etc., have been constructed on sites underlain by thick soft clay deposits over the past few decades. Vertical drain methods such as sand drains and plastic drain boards (PDB) have been widely used to accelerate consolidation of soft clay deposits. However, these technologies have faced difficulties in their application, such as high construction costs for sand drain due to the limited supply of sand, and long-term environmental disruption from PDB installation as a result of the nonperishable characteristics of plastic materials. Geotechnical researchers have performed numerous experiments to substitute eco-materials for geotextiles used in construction fields, made with various chemical materials such as plastics made with polypropylene or polyethylene. Because the amount of construction materials used for ground improvements or reinforcements is usually tremendous at construction field, construction cost is of great concern in addition to the quality of the materials. Therefore, many researchers are trying to use one of the most abundant and cheap eco-sources, natural fiber from plants, as construction materials. Eco-sound vertical and horizontal drains, made with coconut coir and jute filter, already have been used for eco-sound soft ground improvement in Japan and Southeastern countries. In addition, new types of environmentally friendly vertical drain, made with straw strands and jute filter, called straw drain board (SDB), have been recently developed in Korea. In this paper, results from a field pilot test as well as several laboratory tests for these natural fiber drains are discussed.

TYPES OF VERTICAL DRAINS

The main function of vertical drains is to accelerate the consolidation process by fast dissipation of the excess pore pressure induced by embankment load which usually lasts for 2 to 3 years. However, plastic drain board (PDB) which is nonperishable materials may become a source of pollutant after the completion of consolidation settlement. The idea of natural fiber drain board called fiber drain board (FDB) made with jute filter and coconut coir, which naturally decomposes with time, was first proposed by Professor Lee et al. (1987) of Singapore National University as an alternative method to replace nonperishable plastic drain board. In order to take advantage of agricultural residue, rice straw, which is abundantly produced in Korea, another natural fiber drain board called straw drain board (SDB) was also recently developed in Korea. The width and thickness of

[1] Senior Researcher, Geotechnical Engineering Research Dept. Korea Institute of Construction Technology, 2311 Daewha-Dong Ilsan-Gu Goyang-Si Gyeonggi-Do, 411-712, KOREA
[2] Research Fellow, Geotechnical Engineering Research Dept. Korea Institute of Construction Technology, 2311 Daewha-Dong Ilsan-Gu Goyang-Si Gyeonggi-Do, 411-712, KOREA

both drains were approximately 85—95 mm and 5—10 mm, respectively. The diameters of the coir of FDB and the straw strands of SDB were 5 and 8 mm respectively, with each strand enveloped by two layers of jute burlap. The jute burlap was manufactured from jute fibers, which are available in many parts of Southeast Asia. Three longitudinal stitches hold the coir or strands in separate flow channels within the jute burlap. Fig. 1a shows a fiber drain board (FDB) made with coconut coir and jute filter, while Fig. 1b shows a straw drain board (SDB) made with straw strands and jute filter. The plastic drain board (PDB) shown in Fig. 1c, which was also tested in this study to compare to natural fiber drains, was 10 cm-wide and 5 mm-thick.

(a) FDB (b) SDB (c) PDB

Fig. 1 Prefabricated vertical drains

TENSILE STRENGTH OF VERTICAL DRAINS

Tensile strength of plastic drain board (PDB) and natural fiber drain boards such as FDB and SDB are quite different. The strain on the PDB increased continuously after passing the point of inflection, with/without addition of small tensile force. However, the maximum tensile strength of the FDB and SDB deceased notably after reaching a maximum value, at approximately 10% strain. Despite such differences in strength behavior, the maximum tensile strengths of the FDB and SDB were 1 to 3 kN/width greater than that of the PDB, which proved to be acceptable for field installation.

DISCHARGE CAPACITY OF VERTICAL DRAINS

Fig. 2 shows the discharge capacity obtained from a model test called composite discharge capacity (CDC) test for the PDB, FDB and SDB. CDC apparatus is made with thin cylindrical steel which is 50 cm in diameter and 100 cm in height. With the CDC apparatus, a 65 cm-long drain is directly installed into the soft clay lump and confined by the surcharge load. The CDC test is more advantageous than the triaxial type apparatus in that the discharge capacity of the drain and the consolidation settlement can be monitored simultaneously. The initial discharge capacities of FDB and SDB by CDC test were relatively lower than that of PDB as shown in Fig. 2. The final discharge capacity of the SDB by CDC test was evaluated as 0.77 cm^3/sec under 250 kPa pressure, which was still lower than the 5.0 cm^3/sec of the PDB and 4.6 cm^3/sec of the FDB under the same condition. Moreover, the trend for a decreasing discharge capacity with time of the SDB was also more significant than those of the PDB and FDB. Despite its low discharge capacity, the final settlement from the installation of the SDB was identical to those from PDB and FDB as shown in Fig. 3. Such results of surface settlement from the installation of the SDB is significant, in that SDB has the potential to have the minimum discharge capacity required as a vertical drain.

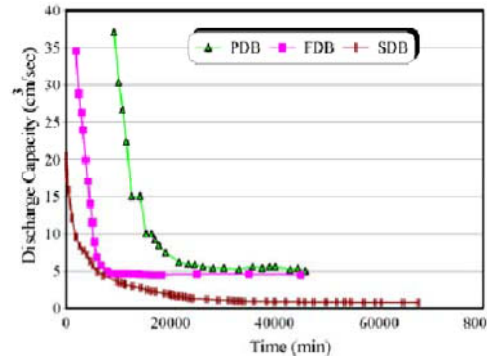

Fig. 2 Discharge capacity results by CDC test

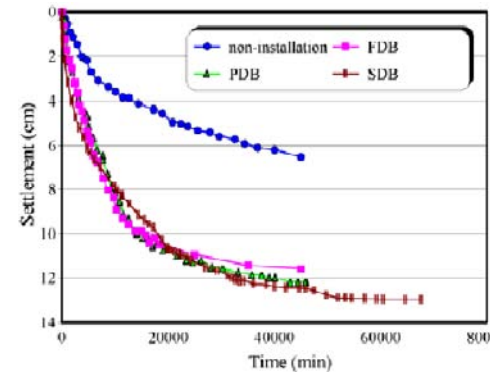

Fig. 3 Settlement curves by CDC test

Different deformation of vertical drain boards are partly explained why the discharge capacity of the PDB decreases drastically, while the settlement curves for the PDB, FDB and SDB are similar. The flexible PDB has a greater potential for reducing the discharge capacity factors, such as kinking or bending, than either the FDB or SDB. Therefore, PDB was found to be relatively more bent and kinked than either the FDB or SDB after the CDC test. These trends are expected to occur similarly or more significantly in the field.

DECOMPOSITION

FDB and SDB samples were embedded in distilled water, sea water and the Kwangyang clayey soil which

was classified as typical low plasticity clay to evaluate decomposition of natural fiber drains as time goes on. Decomposition of FDB and SDB was evaluated by tensile strength test specified in ASTM D5035. Fig. 4 shows variation of tensile strength of FDB and SDB with embedded time. In the first 3 months, notable change in tensile strength of FDB was not identified. However, tensile strengths of FDB decreased drastically after 9 months of embedding in sea water and clayey soil. A similar trend of decrease in tensile strengths of FDB followed in the next 21 months; a period of small decrease after 18 months followed by a period of sharp decrease after 30 months of embedding in clayey soil. This decreasing trend of tensile strength of FDB can be partly explained by changes in temperature from seasonal variation. It was beginning of winter season when FDB samples were embedded in distilled water, sea water and clayey soil. Tensile strength of FDB decreased sharply after every summer season. It is assumed that bacteria multiplies in warm temperatures and accelerates the decomposition of textile structure. However, the tensile strength of FDB after 30 months of embedding in clayey soil is still above the required minimum tensile strength of PDB, which is 1-2kN/width. It is interesting that the tensile strength of SDB after 15 months of embedding in clayey soil decreased almost same amount compared to that of FDB. The study on decomposition of natural fiber materials will be performed continuously.

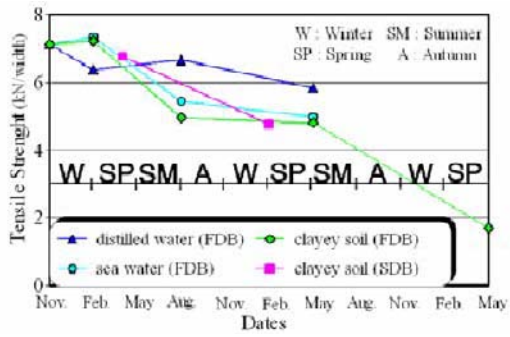

Fig. 4 Variation of tensile strength with time

PILOT SCALE FIELD TEST

Site Investigation

The overall purpose of this pilot scale field test is to evaluate field performance of each vertical drain which has already been verified by laboratory tests. The pilot test is conducted at a 4-lane road construction site connecting two main highways located in Mokpo of the southern coast of Korea. Mokpo is not far from Kwangyang area where the clay sample for CDC tests was collected. Cone penetration test (CPT), standard penetration test (SPT) and thin wall piston sampling in boreholes were carried out to evaluate the soil properties and geological profiles of the pilot test site. Fig. 5 shows the recorded N-values from SPT, cone resistance, q_c, from CPT, natural water content (w_n), liquid limit (LL), plastic limit (PL), compression index (Cc), coefficient of consolidation, (c_v) from oedometer tests and typical soil profile. Based on the results of site investigation, original strata can be classified into 5 soil layers. Two marine clay layers, Clay A and Clay C, were found to be separated by Clay B, which is a stiff clay layer with 3 m in thickness. The Clay A layer was expected to be very soft, for it had high natural water content ranging in between 60%－72%, which is greater than its liquid limit. Low N-value from SPT and low cone resistance from CPTU confirmed that the Clay A layer consists of very soft clayey soils. The liquid limit of relatively stiff Clay B layer is 33%－56%, which is greater than its natural water content ranging from 24% － 42%. Similarly, the liquid limit of Clay C layer is 34%－48%, which is greater than its natural water content ranging in between 33%－43%. The plastic limits of three clay layers are similar and found to be in the range of 21%－29%. Clay A is relatively high-plastic, whereas Clay B and Clay C are low-to-medium plastic based on plasticity chart. The compression index, Cc, of Clay A-layer from oedometer tests ranges in between 0.59 to 0.79 which is relatively greater than that of Clay C in the range of 0.2 to 0.52. The compression index of the intermediate Clay B could not be obtained because undisturbed samples contained small gravels which had made trimming of test sample difficult. Sudden increase in cone resistance at depth of between 6 m and 7 m of field ⑤ was also due to these small gravels contained in Clay B. The coefficient of consolidation of Clay A ranges from 1.7×10^{-4} cm^2/sec to 34.3×10^{-4} cm^2/sec which is greater than that of Clay C ranging from 2.5×10^{-4} cm^2/sec to 54.5×10^{-4} cm^2/sec.

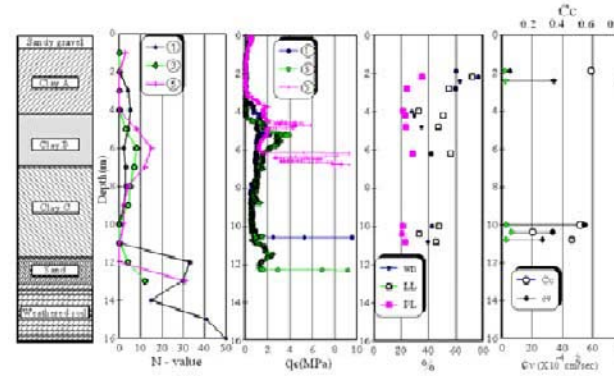

Fig. 5 Soil properties and geological profile of pilot test site

Geotechnical characteristics of the soil profile at the pilot test site can also be explained in terms of geology. Generally, the strata of the pilot test site, which are similar to those typically obtained in western coast of Korea, can be classified into four units. The four units consist of middle to late Holocene tidal deposit (Clay A), early Holocene siderite-containing stiff mud deposit (Clay B), late Pleistocene tidal deposits (Clay C) and late basal gravelly sand deposit (Sand and Weathered soils). Especially, stiffness of Clay B-layer, which is relatively much harder than the other clay strata can be explained in that Clay B-layer is paleosol formed by pedogenesis which had been exposed during the recent glacial age (Choi and Kim 2005,2006).

Test Plan and Present Field Condition

Three types of vertical drain, namely PDB, FDB and SDB, and two types of horizontal drain, sand mat and fiber mat, were installed at the pilot test site. The 170 m long and 50 m wide pilot test site was formerly a rice field. Originally, soil improvement methods involving sand drains and sand compaction piles as vertical drains and sand mat as horizontal drain were planned prior to road construction. However, PDB, FDB and SDB were installed as alternates of sand drain and sand compaction pile for this test. Both fiber mat and sand mat were also installed to compare their effectiveness in addition to their comparison with 3 types of vertical drains. Details of the combination of drain installation at the pilot test site are shown in Fig. 6. As shown in Fig. 6, the test site consists of 5 fields. Fields ① and ② have PDB installed

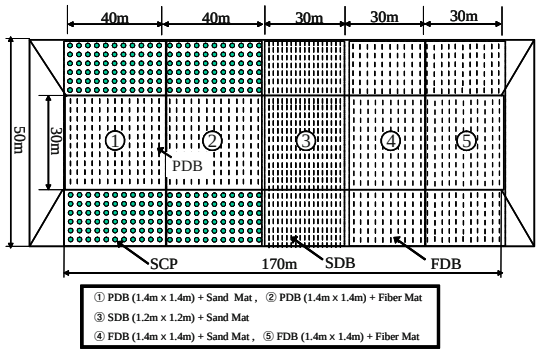

Fig. 6 Plane figure of the pilot test site (not scaled)

as vertical drain in 1.4 m spacing, with sand mat and fiber mat as horizontal drain, respectively. In order to reinforce the high embankment slopes of field ① and ② from shear failure, 70 cm-diameter sand compaction piles were installed in 1.6 m spacing. For comparative study of PDB, field ④ and ⑤ had FDB as vertical drain in 1.4 m spacing, with sand mat and fiber mat as horizontal drain, respectively. New developed proto type SDB was installed at field ③ with 1.2 m spacing with sand mat.

Several instruments such as settlement plate, vibrating wire type piezometers and inclinometers were installed to monitor the soil behavior during ground improvement. Particularly, two types of piezometer were installed; one which measures the variation of pore pressure in soft clay, and another which measures the variation of pore pressure in vertical drains. Most of the instruments were installed immediately after installation of the vertical drains.

Surface Settlements

Fig. 7 shows the surface settlements results from 19 months of monitoring from September, 2005 to April, 2007. Although the embankment height of the PDB installation field was relatively higher than those of the SDB and FDB, the amounts and rates of settlement of the PDB (P-2), SDB (S-3) and FDB (F4, F-5) installation sites were similar.

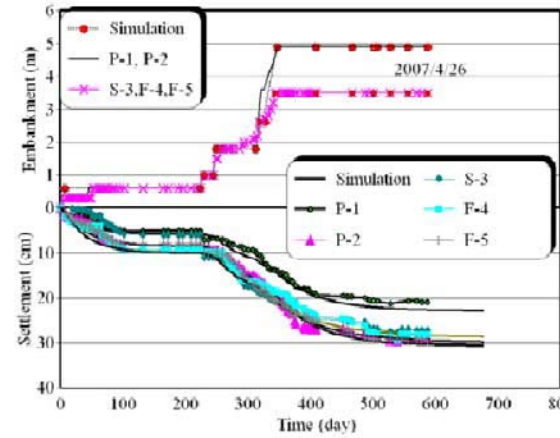

Fig. 7 Surface settlements measured at pilot test site

To more specifically analyze the soil improvement characteristics of the three types of vertical drain, the final settlement was predicted using a simulation method, based on conventional Terzaghi-Barron's consolidation theories, along with the ground investigation results, construction histories and monitored surface settlements. With the simulation method the monitored time-settlement curves were initially plotted, with the predicted time-settlement curves then superposed by applying proper soil properties via trial and error. This method was based on many assumptions and; therefore, a little complicated, but has been verified as very useful with respect to practical problems (Cho 1998). The monitored time-settlement curves obtained from the pilot test, as well as those predicted by the simulation method are shown in Fig. 7. The settlement rates, which is the percentage ratio of the monitored (A) to predicted (B) final settlement, for each test site are also shown in

Table 1. The settlement rates for sites P-1 and P-2, where PDBs were installed, were 91% and 94%, respectively, that for site S-3, where SDBs were installed, was 96% and those for sites F-4 and F-5, where FDBs were installed, were 96%－98%, respectively. Based on the results of the surface settlement, the consolidation processes at the pilot test sites were all similar, regardless the types of vertical drain.

Table 1 Settlement rates

Location	Monitored settlements (A) (cm)	Predicted final settlements(B) (cm)	Settlement rate (A/B) (%)
P-1	20.9	22.9	91
P-2	28.8	30.7	94
S-3	34.1	35.5	96
F-4	28.2	29.2	96
F-5	29.5	30.3	98

Pore Pressures

Generally, a pore pressure analysis is more difficult than that for settlement, in that there are many factors that influence the generation and dissipation of the pore pressure process, such as permeability, degree of saturation and stress history, and so on. In addition, with the exception of the quality of the piezometer itself, time lag, air bubble, clogging and variation measuring points due to settlement, temperature and atmospheric pressure, etc. also influence the observed pore pressure. Therefore, doubt still exists with regard to pore pressure analysis, even though many numerical and monitoring research trials have been performed. This is why a settlement analysis for the evaluation of a consolidation process is clearer than a pore pressure analysis in the field.

Figs. 8 and 9 show the excess pore pressures measured in the ground and vertical drains, respectively. Initially, the embankment construction was stopped after 50 days, but the excess pore pressure measured in the ground and vertical drains increased until 100 days. Therefore, it was found that the time lag phenomena occurred in the field. An additional embankment construction began in May 2006, where the excess pore pressure in the ground and vertical drains was found to gradually increase. The excess pore pressures measured in the vertical drains were relatively greater than those in the ground. This difference in the excess pore pressure between the ground and vertical drains was able to be partly explained by the different installation conditions. Piezometers for measurement of the pore pressure in the ground were installed by filling with sand around the piezometers, but those for measurement of the pore pressure inside the vertical drains were installed inside the thin filter of the vertical drains. Therefore, it was estimated that the piezometers for vertical drains were exposed to a greater clogging effects than those for ground.

In addition, the excess pore pressure measured inside the proto-type SDB and the ground was greater than that in the FDB and PDB, while the dissipation rate of the excess pore pressure in the SDB was slower than those in the PDB and FDB. These results related well with those from the Composite Discharge Capacity (CDC) test, as previously described. However, since the results of the excess pore pressure were quite different from those for the surface settlements, long term monitoring will be necessary.

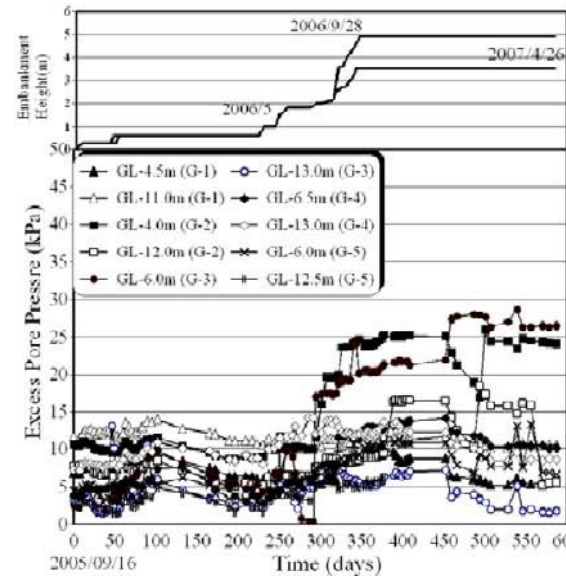

Fig. 8 Excess pore pressure measured in the ground

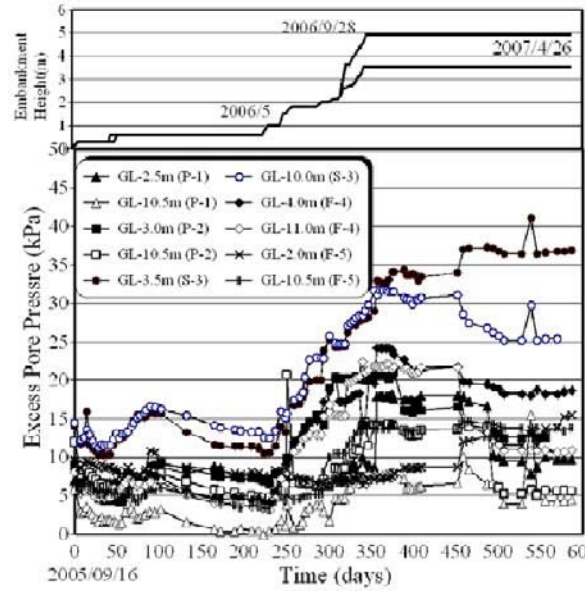

Fig. 9 Excess pore pressure measured in the vertical drain boards

CONCLUSION

In this study, a pilot scale field test for FDB, PDB and proto-type SDB were carried out to evaluate their practical applicability. Based on the monitoring data obtained at the pilot test site, the surface settlements which occurred at PDB, FDB and SDB installation fields were almost identical. The excess pore pressure measured in SDB was greater than that in PDB and FDB, while the dissipation rate of excess pore pressure in SDB was slower than that in PDB and FDB. The generation and dissipation rates of excess pore pressure measured in the ground from the installation of PDB, FDB and SDB were almost identical to the same extent as the surface settlements measured at the pilot test field. Based on the existing data, natural fiber drains represent a promising alternative material for the improvement of soft clay.

ACKNOWLEDGEMENTS

This study was supported by grant R&D/03-kibankisul-A15 from the Ministry of Construction and Transportation in Korea. This support is gratefully acknowledged.

REFERENCES

ASTM D5035. Standard Test Method for Breaking Force and Elongation of Textile Fabrics (Strip Method)

Choi KS, Kim JH (2006) Identifying late Quaternary coastal deposits in Kyonggi Bay, Korea, by their geotechnical properties, Geo Marin-letters, Springer-Verlag, 26: 77-89

Cho, SM (1998) Deformation Characteristics of Soft Clayey Deposits under the Embankment Loading in Korea, Ph.D Thesis, Seoul National University

Lee S L et al. (1987) Fibredrain for Consolidation of Soft Soils, Post-Vienna Conf. on Geotextiles, Singapore: 238-258

Korea Institute of Construction Technology (2006) Soft Ground Improvement Method for Road Construction using Environmentally Friendly Drains, Report of Construction Infra-structure Technology Research & Development Project. Ministry of Construction and Transportation: 399

FILTRATION PERFORMANCE OF A SILT/GEOTEXTILE SYSTEM WITHIN A TRIAXIAL PERMEAMETER

A.A. Aziz [1], T.A. Mohammed[2] and H. Omar[3]

ABSTRACT: This paper describes the performance of a long-term filtration test of a silt with a series of thin melt-bonded nonwoven and a woven monofilament geotextile in a triaxial permeameter. The triaxial permeameter was developed to account for the disadvantages found in earlier hard-walled permeameters used. Procedures to completion of the long-term filtration test within the permeameter including the application of combined vertical and radial flow within the same silt sample and hydraulic conditions are described. System permeabilities for combined vertical and radial flow into a geotextile insert are found to be at least one order of magnitude higher than vertical flow into the same type of nonwoven geotextile. Specimens for scanning electron microscopy (SEM) analysis to investigate filtration mechanisms upstream of and within the geotextile showed clogging sites within the nonwoven geotextile. The system permeabilities obtained for the woven monofilament fabric do not indicate any influence in combined flow and/or direction of flow. For the duration of the filtration tests, the equilibrium system permeabilities are all observed to fall below the permeability of the silt except for the combined radial and vertical system permeability of a smaller opening size of a nonwoven geotextile tested. The results are currently true for one type of soil against thin geotextiles and the applicability of the methodology to other soils and thick geotextiles should be further investigated.

KEYWORDS: silt, geotextile, triaxial permeameter, filtration

INTRODUCTION

Correctly designed and installed, geotextiles have the ability to separate, reinforce, drain and filter soil. In a given application, the overall function is a combination of all the previously stated functions to various degrees. However, in the literature, the emphasis is on the dominant or controlling function of a geotextile in a particular application. In filtration, the geotextile acts similar to a granular filter, effectively retaining particles while allowing primarily cross-plane fabric flow of water with little or no buildup in pore pressure to the surrounding soil.

When the need arises, two methods have been considered to assess the adequacy of a soil/geotextile system to perform filtration and/or drainage functions. These two methods are: (1) methods based on empirical and/or theoretical criteria i.e., in isolation criteria; and (2) methods based on laboratory performance of the soil/geotextile system i.e., in soil compatibility testing. Methods in item (1) are based on expressing the geotextile filter requirements in the form of simple criteria to be met by the geotextile filter. Methods in item (2) consist of conducting laboratory tests that simulate field (i.e., soil) conditions to evaluate the performance of the candidate filters. Proponents of methods in item (1) point to the long testing time, lack of standardized test methods, and the cost of testing involved in performing methods in item (2).

It has previously been proposed that geocomposite vertical drains be utilised as a means of reducing the effects of frost heave damage to existing flexible pavements (D'Andrea and Sage 1989). They investigated the performance of a non-woven geotextile wrapped vertical drain within frost susceptible soils. The results of their tests indicate that the drains accelerated the dissipation of pore pressure in a non-plastic frost susceptible silt but failed to perform up to expectations in a plastic broadly graded glacial till. The soil/geotextile systems were tested within a hard-wall consolidation apparatus. Later, Johnson (1990) instituted a series of filtration tests on the till. The filtration tests were performed within a hard-wall permeameter and where flow through the till/geotextile systems is subjected either (1) vertical downward or (2) combined vertical and radial but upwards. Johnson (1990) found that the non-woven geotextile wrapped vertical drains performed adequately under vertical flow conditions but failed

[1] Senior Lecturer, Department of Civil Engineering, University Putra, Serdang, MALAYSIA. Email: azlan@eng.upm.edu.my
[2] Associate Professor, Department of Civil Engineering, University Putra, Serdang, MALAYSIA.Email: thamer@eng.upm.edu.my
[3] Associate Professor, Department of Civil Engineering, University Putra, Serdang, MALAYSIA Email: husaini@eng.upm.edu.my

when subjected to combined flow testing. In addition, using several filtration criteria, Johnson (1990) found that predictions made on the success or failure of the non-woven geotextiles gave contradicting values. Some criteria would predict the successful use of a geotextile in the till while others would predict its failure. The same finding for the silt is also shown by Aziz (2002). Other times, many instances where the successful use of geotextiles outside the range given by a particular criterion have also been reported (Wood 1982).

Although rigid wall tests have shown their utility, they are not without their share of limitations and complications. In particular, the problems of sidewall leakage and inadequate saturation within the soil, geotextile and testing systems have been cited (Koerner 2005). Furthermore, slight modifications in procedures from a test method can lead to significant changes in test results (Kossendey 1999). A filtration test system that includes a triaxial cell component over the more conventional hard wall permeameter in a test programme appears to offer several advantages. In light of the results obtained by D'Andrea and Sage (1989), the filtration performance of the silt in such a triaxial permeameter warrants investigation and is described in the subsequent sections of this paper.

MATERIALS AND METHODS

Materials Used

Table 1 provides a summary of the engineering properties of the silt used. The index and compaction tests were performed in accordance with methods specified in the Annual Book of ASTM Standards (2000) to characterise the soil used. The silt is uniformly graded, the coefficient of uniformity and coefficient of curvature being 5.3 and 1.7 respectively. Using coefficients of uniformity and curvature criteria as per Luettich et al. (1992), the silt can be classified as internally stable. However, Lawson (1990) and Kossendey (1999) cite German Standards for which the silt falls into the category of problematic soils wherein the soil has a high tendency for internal erosion (i.e., internally unstable). Koerner (2005) and the Swiss Standard SN 670125a (VSS 1983) also do not recommend the use of geotextile filters for the silt.

The coefficient of permeability as shown in Table 1 was obtained via the triaxial test set-up as described below.

Table 1 Properties of silt

Properties	Values
Specific gravity	2.72
Liquid limit/Plastic limit	Non-plastic
Max. dry density	1.61
Optimum water content	21.2
Coefficient of permeability (cm/s)	1.50×10^{-6}
Particle size: % finer than	
No. 100 (0.149 mm)	100
No. 200 (0.074 mm)	98.6
0.02 mm	73
0.05 mm	15
0.01mm	3.9

Table 2 Properties of geotextiles

Items	T3401	T3601	Tetko
Apparent opening size, O_{95} (mm)	0.17	0.08	0.025
Coefficient of permeability ($\times10^{-2}$ cm/s)	3.1	1.8	N/A
Thickness (mm)	0.39	0.60	N/A
Porosity or Percent open area, POA (%)	60.0	50.0	16

Apparatus and Test Procedure

The general layout of the apparatus and ancillary equipment developed for the permeability and compatibility filtration tests in a modified triaxial cell has been described in detail elsewhere by Aziz (2002). The triaxial cell is shown in Fig. 1.

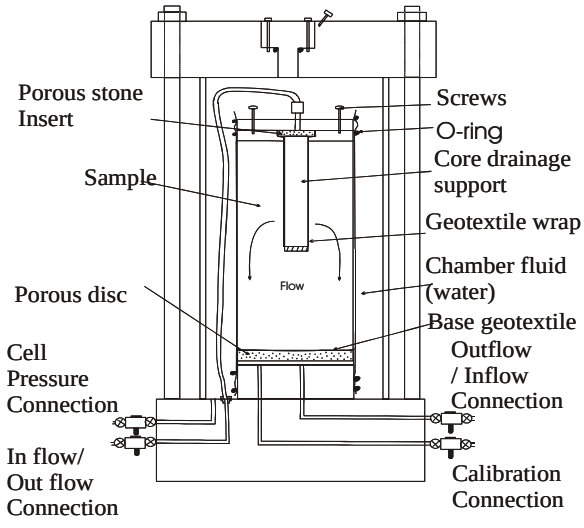

Fig. 1 Modified triaxial cell for filtration test

The system was developed to permit automated as well as manual measurement of variables monitored during all phases of a test. The main features of the system consist of the following:

(1) Constant pressure and monitoring system,

(2) De-aired water system, and

(3) Flow measurement system.

The constant pressure system using compressed air is maintained at the required value on adjustments of the pressure reducing regulator valves located on the air pressure panel. Air at the controlled pressure is then admitted to the bladder in the air/water bladder cell thus pressuring the water without direct contact between air and water. The pressurised water is then led to the triaxial cell respective inlets/outlets. All pressures are monitored and recorded by a Wykeham Farrance Data Acquisition System. In addition, at any time the readout unit of the system allows digital display of the pressurised water sensed by a pressure transducer in a line. Pressure transducers are respectively connected on the cell pressure, back pressure and pore pressure lines. The transducers on the back pressure and pore pressure lines also monitor the outflow or inflow pressure associated with a flow test. Deaired distilled water is supplied to the system by using the Nold vacuum de-aerator and transferred to a reservoir to be stored until required.

The flow measuring system consists of volume change gauges and the triaxial cell. The gauges are manually operated to determine the rates of flow of water through a soil sample confined in a triaxial cell. The inflow and outflow lines are each equipped with volume change gauges to detect any leakage that may occur during a test. The triaxial cell and its essential accessories adopted for permeability tests of a soil and/or filtration tests of a soil/geotextile system are shown in cross-section in Fig. 1. The features of the triaxial cell as shown are used to test the filtration capabilities of a geotextile in both vertical and combined vertical and radial flow directions. The ability to perform permeability tests within the same triaxial cell for a particular soil sample provides data for comparative purposes only. The soil sample (6 inches high and 3 inches diameter) is set up between the top and bottom caps. In the permeability test, porous discs interface between the soil sample and top cap or base pedestal. In the filtration test, the base porous disc is of the same diameter as the soil sample but a smaller diameter porous stone is inserted within the top cap. The base geotextile layer is trimmed to a diameter 0.25 inch greater than the diameter of the soil sample. The edges of the geotextile are flipped over the base of the soil sample. In addition, the upper half of the soil sample contained a central drainage core wrapped with a layer of geotextile. The surface area of the wrapped geotextile is the same as that of the base geotextile. The rigid drainage core provides support for the geotextile wrap and permits the flow of water. Two cylindrical latex membranes, separated by a layer of silicone grease, are placed around the sample to isolate it from the chamber fluid. The membrane is sealed to the top and bottom caps via O-rings. A Perspex cylinder is placed around the sample between the cell top and base. The loading piston normally found penetrating the triaxial cell top has been removed and was replaced with an aluminium plug.

In general, performing the filtration test in the device described above consisted of the following sequential procedures:

(1) Preparation of the soil sample and insertion of the geotextile wrapped internal core at the required height. The silt was lightly tamped with a rod under water on the base pedestal of the triaxial cell to the required density. After insertion of the core, the silt is tamped around it. A split mould is used and suction was applied to the sample on removal of the mould.

(2) After setting up the system, elimination of air bubbles within the voids of the soil sample and saturation through the application of back pressure methods are performed. The application of back pressure is performed to the top end until the value of pore pressure coefficient B of near unity is obtained. Other routine methods to ensure saturation of the system are also adhered to (Head 1986).

(3) Initial consolidation to the required effective stress and to ensure that flow test occurs under no volume change conditions.

(4) Application of the pressure difference to initiate flow under steady state conditions. The flow directions for vertical filtration test as shown in Fig. 1 are from the top of the sample to the bottom of the sample. Following flowrate measurements of the sample associated with vertical filtration test, the triaxial cell is physically inverted into a wood block seating that maintains the stability of the cell. This arrangement allows for the performance of a combined vertical and radial flow test of the silt/geotextile composite. The water then flows from the base pedestal through the geotextile wrapped core and out of the top cap at the same pressure difference. In all the tests performed, the flow direction is therefore always downward i.e., the flow of water is not resisting gravity. It should also be noted that the pressure differentials applied for all tests of the same sample are identical.

(5) At the completion of the tests, after dismantling, the height, diameter and water content of the silt sample are obtained. If required, specimens for scanning electron micrograph (SEM) analysis to investigate filtration mechanisms upstream of and within the

geotextiles can be obtained. It should be noted that a vertical filtration test followed by a combined vertical and radial filtration test allows only specimens along the geotextile wrapped core to be investigated. The mechanisms upstream of the "base" geotextile would have been destroyed. For SEM, the pore water within the specimens was replaced by an ultra-low viscosity embedding resin known as "LR White" (Stutzmann and Clifton 1992). After the resin is cold cured with the aid of an accelerator, the potted specimen is polished and carbon coated for SEM.

RESULTS AND DISCUSSION

Fig. 2 shows the results obtained for the consecutive vertical, combined vertical and radial, and again the vertical filtration tests (V1R2V3) for the nonwoven geotextile T3401. In this sequence, the last vertical filtration test (V3) is repeated for comparative purposes. The test however had to be terminated at 150 hours as there was a power breakdown. As seen, following an initial period of instability, the system flowrates (or permeabilities) remain relatively constant.

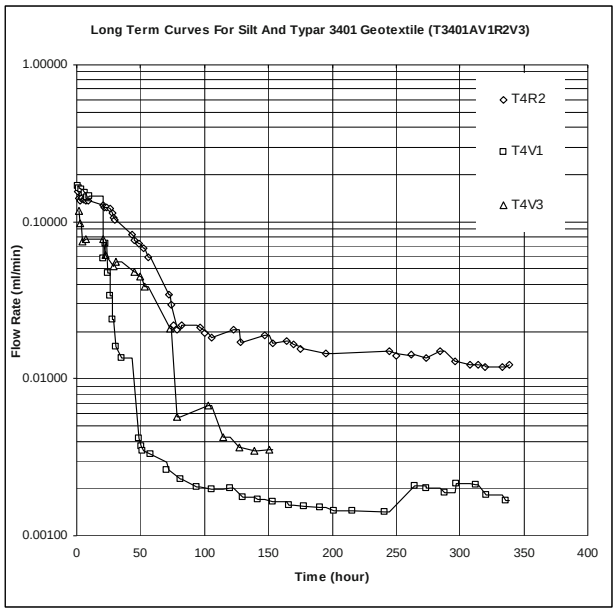

Fig. 2 Long-term flow curves for T3401 V1R2V3

With respect to each of the sequential tests, the system permeabilities obtained under equilibrium conditions are 4.0×10^{-8}, $4.7\text{x}10^{-7}$ and 8.5×10^{-8} cm/s. These values have been obtained by utilising a finite element software product, SEEP/W. To assess whether the sequencing of tests performed had any influence on the results, another sample is replicated and tested. The sequence of filtration test this time is combined vertical and radial followed with the vertical test (R1V2). The system permeabilities obtained under equilibrium conditions are 4.1×10^{-7} and 1.5×10^{-8} cm/s with respect to the second series of tests. In both samples, procedural step 2 described in the preceding section confirmed that, B values obtained are above 0.94 and using initial and final water content values, the degree of saturation is found to be 100%. For the duration of the filtration tests, the equilibrium system permeabilities are observed to fall below the permeability of the silt. However, one order of magnitude higher in the system permeability is obtained with reference to the combined vertical and radial test versus the vertical test. This appears to indicate that combined flow and direction have an influence on the filtration aspects of the silt/geotextile system.

Preliminary investigations on the microphotographs obtained for the T3401 R1V2 tests showed clogging sites within the non-woven geotextile. This is shown in Fig. 3 for the vertical filtration test base specimens. No other favourable or non-favourable mechanisms as reported by Rollin and Lombard (1988) could be identified.

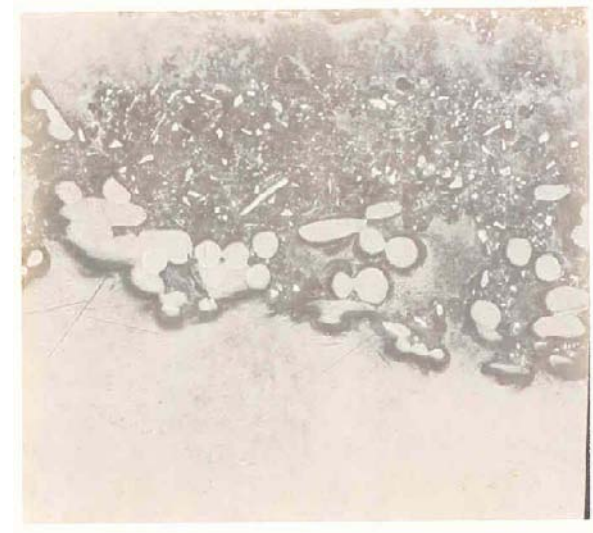

Fig. 3 Microphotographs of clogged sites for T3401 R1V2 base specimens

Table 3 summarises all equilibrium system permeability results of filtration tests performed. Further filtration tests (T3601 V1R2) utilising smaller geotextile opening size in the series of the thin nonwoven thermo-bonded geotextile exhibited two orders of magnitude higher in the equilibrium system permeability for the combined radial and vertical flow against the vertical only flow test. In addition, the combined radial and vertical system permeability is found to be slightly higher than the permeability of the soil. The system permeabilities obtained for the woven monofilament fabric (Tetko R1V2) do not indicate any influence from combined and/or direction of flow. The system permeabilities have

an order of magnitude the same as those obtained for the combined radial and vertical values of T3401 even though the Tetko have smaller O_{95} and POA.

Table 3 Equilibrium system permeabilities of all filtration tests

Geotextile	Test sequence	System Permeability (cm/s)	
		Vertical	Radial
T3401	V1R2V3	4.0×10^{-8}	4.7×10^{-7}
	R1V2	1.5×10^{-8}	4.1×10^{-7}
T3601	V1R2	8.5×10^{-8}	3.2×10^{-6}
Tetko	R1V2	2.2×10^{-7}	1.9×10^{-7}

CONCLUSION

The following conclusions are made based on the filtration test programme:

- the triaxial permeameter developed can be used for a filtration test of a soil/geotextile system;
- stable flow conditions were achieved in all filtration tests;
- combined vertical and radial filtration test exhibited at least one order of magnitude higher in the system permeability than cross plane filtration for the 'problematic' silt and thin nonwoven thermo-bonded geotextile;
- clogging sites are identified from the vertical filtration tests SEM microphotographs;
- system permeabilities obtained for the woven monofilament fabric do not indicate any influence from combined flow and/or direction of flow;
- the equilibrium system permeabilities are all observed to fall below the permeability of the silt except for the combined radial and vertical system permeability of a smaller opening size of a nonwoven geotextile tested.

REFERENCES

ASTM (2000) Annual book of standards. Philadelphia: American Society for Testing and Materials (ASTM)

Aziz AA (2002) A prototype triaxial permeameter for the filtration of a soil/geotextile system. Geotechnical and geoenvironmental engineering in arid lands; Procs. Of the 2nd intern. conf., Riyadh, Saudi Arabia, 6-9 October 2002. Lisse, Swets & Zeitlinger: 101-108

D'Andrea RA, Sage JD (1989) The use of drainage wicks for the mitigation of frost effects on existing roadways. Geosynthetics '89 Conf. Procs. Vol 2, San Diego, CA. St. Paul: Industrial Fabrics Association International (IFAI): 305-315

Head KH (1986) Manual of soil laboratory testing. Vol. 3 Effective stress tests. London: Pentech Press Limited

Johnson BB (1990) The effect of density, hydraulic gradient and flow direction on the clogging potential of non-woven geotextiles in glacial till. M. S. Thesis, Worcester Polytechnic Institute, Worcester, MA May 1990:164

Koerner RM (2005) Designing with geosynthetics. New Jersey: Prentice-Hall

Kossendey T (1999) Long-term performance assessed from compatibility tests. Geotextiles and geomembranes 17: 281-298

Lawson CR (1990) Geotextile filter performance with fine grained soils. Geotextiles, geomembranes and related products; Proc. 4th Intern. Conf., The Hague

Luettich SM, Giroud SP, Bachus RC (1992) Geotextile filter design guide. Geotextiles and geomembranes 11: 335-370

Rollin AL, Lombard G (1988) Mechanisms affecting long-term filtration behavior of geotextiles. Geotextiles and geomembranes 7(1): 119-145

Stutzmann PE, Clifton JR (1992) Microstructural features of some low water/solids, silica fume mortars cured at different temperatures. NISTIR 4790. U.S. Dept. of Commerce, National Institute of Standards and Technology, Gaithersburg, MD 20899

VSS (1983) Schweizer Norm SN 670125a: Filtermaterialien. Zurich: Vereinigung Schwei-zerischer Strassenfachleute (VSS)

Wood I (1982) Vertical drains. Thomas Telford

Proceedings of the 4th Asian Regional Conference on Geosynthetics
June 17 - 20, 2008 Shanghai, China

EVALUATION OF DISCHARGE CAPACITY WITH VARIOUS VERTICAL DRAIN CORE TYPES

E.C. Shin[1], Zhanara Nazarova[2], K.Y. Cho[3], S.H. Kim and J.K. Kang[4]

ABSTRACT: Recently, the demand of suitable land for industrial complex and residential area is being increased with the economic growth, but it is difficult to acquire the areas for development with good ground condition. For efficient and balanced development of land, new development projects are being carried out not only the areas with inland but also those with the soft ground as well. Perfabricated vertical drain technology is widely used to accelerate the consolidation of soft clay deposits and dredged soil incorporated with pre-loading. Several types of prefabricated vertical drains (PVDs) are used in the field. The discharge capacity is the most important factors of PVDs and affect to the consolidation behavior. However, under the field conditions, discharge capacity is changed with various reasons, such as soil condition, confinement pressure, long-term clogging, folding of vertical drains, and so on. Therefore, many researchers and engineers recommend the use of required discharge capacity. In this paper, the experimental study was carried out to obtain the discharge capacity of six different types of PVDs by utilizing the large-scale laboratory apparatus and the required discharge capacity was calculated by several different theoretical methods.

KEYWORDS: prefabricated vertical drain, required discharge capacity, core type, soft marine clay

INTRODUCTION

Recently, many countries in the world have made a reclaimed land from the sea to construct the industrial complex, harbor facility, and residential area. However, the land site which gets by reclamation is mostly saturated soft clay. The permeability of this site contains relatively low so that it not only takes long period of time to be consolidated completely, but also construction period takes so long time. Therefore, soil improvement methods for consolidation are demanded for soft soil like clay, silt, and loose sandy soil. Vertical drain method is one of the consolidation methods for squeezing water out of soft soil. It reduces drainage path of drain as installing vertical drain into ground. This vertical drain method plays a great role to dissipate the excess pore water pressure which built up in saturated soft soil. The types of vertical drain methods are classified by material used in the field. Three types of vertical drains are commonly available such as Sand Drain method (SD), Sand Compaction Pile method (SCP), Packed Drain method (PD), which is method of filling the sand into the geotextile pack, and PVDs(Prefabricated Vertical Drains) method which uses artificial polymer drain. Natural drain method, which disappears naturally in the ground after their drainage functions completed, was developed recently. After 1980s, PVD method has been developed with utilizing polymer artificial drain. Polymer artificial drain is utilized economically and as a construction method, which is being used widely in the world. Polymer artificial drain also can be used in marine construction area because the construction equipments and technology have rapidly developed by now. The installing depth of PVD has increased gradually at the construction site. Now, many construction sites exist where the prefabricated vertical drain was installed successfully up to more than the maximum depth of 50m. After 2000s, various artificial drains have been developed due to its extensive use and technology development by polymer manufacturer. More than 50 types of PVDs are being used in the world. In order to speed up consolidation of clay with using the vertical polymer drain, the discharge capacity is an important influence factor. Now, the discharge capacity test which has been simplified in the laboratory. The confining pressure can be applied to the PVD specimen by rubber membrane with utilizing air pressure or water pressure. This method does not reflect many influence factors which make discharge capacity decrease. Therefore, recently, the design of prefabricated drain has been

[1]Prof. Dept. of Civil & Environmental System Engrg., University of Incheon, KOREA. Email:ecshin@inaheon.ac.kr
[2] Ph. D Student, Geotechnical Institute, Eurasian National University, KAZAKHSTAN
[3]President, DAEHAN *i.m.* Co., Ltd., Seoul, KOREA. Email:bobcho@geosko.com
[4] Ph. D Student of Civil & Environmental System Engrg., University of Incheon, KOREA. Email:jeong99k@inaheon.ac.kr

accomplished with considering discharge capacity in the field condition. Several factors are influenced on the discharge capacity of PVD such as creep effect, smear effect, well resistance, and soil particle clogging. The creep plays a role that it makes area of vertical drain section decrease due to its rolled filter by lateral pressure. The smear effect occurs with the disturbance of soil structure by mandrel during the process of vertical drain installation. The water flow through the space of drain can be retarded by the influence of well resistance. The filter clogging by fine grained soil or organic matter in the field is also a factor to decrease the discharge capacity with the elapsed time after PVD installation. There are also various other influence factors like deformation of vertical drain due to ground settlement (Fig.1), soil depletion of drain which is occurred by physical and chemical phenomenon for a long period of time, and accumulated air inside the vertical drain. So, the discharge capacity could be decreased gradually because of these factors.

In case of prefabricated vertical drain, many researchers like Holtz (1991), Ali (1991), Broms (1994), Bergado (1996), Hansbo (1997) and others have studied the discharge capacity. Roughly to look into research result studied by now, discharge capacity of vertical drains are decreased as time goes by due to vertical deformation, decrease of vertical drain section area by surface load, or deformation by consolidation. However, if the discharge capacity of vertical drain is more than water in void of soil, the phenomenon of consolidation delay will not generated by vertical drain in the ground. In the actual design of vertical drain, the numbers of vertical drain to be installed in the ground are normally more than enough to satisfy the required discharge capacity. Specially, Bergado (1996) reported the summary of previous studies in Table 1 which related to the required discharge capacity. It is known that the different points of discharge capacity suggested by many researchers are overburden pressure by soil layer, hydraulic gradient, material property of prefabricated vertical drains, and condition when it is installed.

With consideration above statements, 6 different types of vertical drains which are named as A, B, C, D, E, and F were used in this study. All of these prefabricated vertical drains are made of geosynthetics and manufactured in Korea. The PVDs specimens with 6 different types of core shape were used in this study. Details of this is described in the later part of paper. The experimental test was conducted to determine the discharge capacity for 6 different types of vertical drains with using a large-scale device in the laboratory. The discharge capacity was evaluated with respect to the ground condition, hydraulic gradient, and overburden pressure. The required discharge capacity was also analyzed by using the method that considered with the degree of consolidation, delay time of 90% consolidation. Finally, the results of discharge capacity and required discharge capacity for 6 different types of PVDs are compared and analyzed with its retail price in the construction industry. It is suggested the economic efficiency of PVDs through this study.

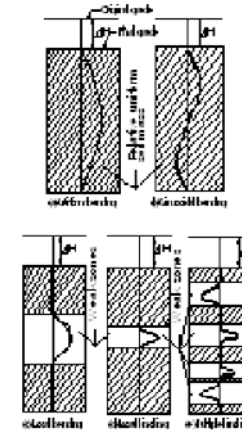

Fig. 1 Deformation of PVD

Table 1 Required discharge capacity of PVDs (Bergado, 1996)

Researcher	Discharge capacity, (cm^3/sec)	Vertidcal stress, (kPa)	Hydraulic gradient
den Hoedt (1981)	2.8	30－50	0.33
Kremer (1983)	25	15	1.0
Jamiolkowski (1983)	0.3－0.5	300－500	-
Rixner (1986)	3.2	In-situ	-
Hansbo(1986)	1.6－3.2	In-situ	-
Holtz & Christopher (1986)	15.8	In-situ	1.0
Voldhuijzen (1986)	25－50	150－350	-
Holtz et al. (1987)	3.2－4.8	300－500	-
Lawrence & Koerner (1988)	4.8	In-situ	-
Koda et al. (1989)	3.2	50	-
de Jager & Oostveen (1990)	10－50	150－300	-

Methods of Consolidation Analysis with Well Resistance

Hansbo's method

Hansbo (1979) derived an approximate solution for vertical drain based on the "equal strain hypothesis" to take both a zone of smear with a reduced permeability and well resistance into consideration.

$$U_{uz} = 1 - \exp\left(-\frac{8T}{\mu}\right) \tag{1}$$

$$\mu = \left[\ln\left(\frac{d_e}{d_w}\right) - 0.75\right] + \left[\left(\frac{k_h}{k_s} - 1\right)\ln\left(\frac{d_e}{d_w}\right)\right] + \left[\pi z(2L - z)\frac{k_h}{q_w}\right] \tag{2}$$

$$T_h = \frac{C_h t}{d_e^2} \quad (3)$$

where, U_{hz} is an average degree of consolidation in depth and C_h is a horizontal consolidation coefficient. The influence diameter is expressed as d_e, it is about 1.13S for rectangular cross section and 1.05S for triangle cross section where S is the center to center spacing between PVD installations. d_w and d_s are the drain spacing and diameter of smear zone, respectively. d_w is a conversion diameter of drain and L is the length of PVD. The horizontal permeability and permeability of smear zone are termed as k_h and k_s. q_w is a discharge capacity of drain.

Onoue's method

Onoue(1988) suggested a simplified formula given below for the average degree of consolidation with respect to radial flow U_r.

$$U_k = 1 - \exp[-8T_h/(F(n')+0.8L)] \quad (3)$$

$$F(n') = \frac{(n')^2}{(n')^2 - 1}\ln(n') - \frac{3(n')^2 - 1}{4(n')^2} \quad (4)$$

where, $n' = nS^{n-1}, L = \frac{32}{\pi^2}\frac{k_h}{k_w}\left(\frac{H}{d_w}\right)^2, n(=d_e/d_w)$ is a drain spacing ratio. $T_h = \frac{C_h t}{d_e^2}$ is the horizontal coefficient of time and t is the consolidation time. $S(=d_s/d_w)$ is a diameter ratio of smear zone and $n(=k_h/k_s)$ is a permeability ratio of smear zone. H is the thickness of clay layer. The permeability of vertical drain and the coefficient of drainage resistance are expressed as k_w and L, respectively.

Pradhan's method

Pradhan et al. (1991) suggested formula given below for discharge capacity with degree of consolidation.

$$Q_{req} = \varepsilon_f \cdot U_h \cdot F_s \cdot z \cdot \pi \cdot C_h / (4 \cdot T_h \cdot 86{,}400) \quad (5)$$

$$T_h = -F(n) \cdot \ln(1/U_h)/8 \quad (6)$$

where $F(n) = n^2 \times \ln(n)/\ln(n^2-1) - (3n^2-1)/(4n^2), n = d_e/d_w$, ε_f is the final vertical displacement (0.25H), U_h is a horizontal degree of consolidation. Fs is a safety factor and z is the depth of PVD installation. C_h is a coefficient of horizontal consolidation (cm^2/day).

Large-Scale Discharge Capacity Test

Geotechnical properties of clay

The clay specimen used in this study to determine the discharge capacity of PVDs was obtained from reclamation site, Songdo, coastal area of Incheon, Republic of Korea. The value of moisture content is about 59.5%, specific gravity is determined as 2.70. The results of Atterberg limit tests indicated that liquid limit(LL) and plastic limit(PL) are 34.6%, 22.5%, respectively, and hence plastic index(PI) is 12.1%. Other consolidation properties are described in Table 2.

Table 2 Geotechnical properties of clay

Item		Unit	Value
Physical, Mechanical property	Saturated unit weight	t/m^3	1.7
	Gravity(G_s)	-	2.70
	Initial void ratio (e_o)	-	1.48
Consolidation index	Modified compress index(C_c)		0.32
	Remolded compress index(C_r)	-	0.0032
	Rate of strength increase(S_u/P_o')	-	0.279
	Coefficient of vertical consolidation(C_v)	cm^2/s	0.000156
	Coefficient of horizontal consolidation (C_h)	cm^2/s	0.003
	Vertical permeability(k_v)	cm/s	8.36×10-8
	Horizontal permeability(k_h)	cm/s	1.09×10-7
	Over consolidate ratio(O.C.R)	-	1.12
Vertical drain	Diameter of mandrel	cm	15
	Drain permeability	cm/s	0.013

PVD specimen

Six different types of PVD are used in this study to determine discharge capacity. As shown in Fig. 2, the core shapes of PVDs are different and named as A, B, C, D, E, and F types. All these PVDs are commercially available in the market. Physical properties of vertical drain are given in Table 3.

Table 3 Physical property of vertical drain

Type	Weight of core(gf/m)	Width (mm)	Thickness (mm)	Permeability of filter (cm/sec)
A, B	60(A), 120(B)	100±0.5	4±0.5	1.3x10-2
C	80	100±5.0	5.0	1.0×10-2
D	138.3	32(OD)	23.5(ID)	2.8×10-1
E	112.2	95±5	Over 6.5	1.0×10-2
F	128.5	102.1	6.45	1.1×10-2


(a) AType


(b) B Type


(c) C Type


(d) D Type


(e) E Type


(f) F Type

Fig. 2 Core Shape of Vertical Drain

Large-Scale Discharge Capacity Testing Apparatus

The layout of discharge capacity apparatus is schematically shown in Fig. 3. Once the discharge capacity is determined for specific PVD, then the required discharge capacity is decided. This testing apparatus is large enough to simulate the field condition in terms of overburden pressure by soil layer, and hydraulic gradient, also smearing effect and well resistance as well. This apparatus has a circular steel frame which diameter is 50cm and height is 120cm. The effective height of prefabricated vertical drain is 90cm because a tube height for loading weight has 30cm. This apparatus does have two water tanks, an inner and outer water tanks which can control hydraulic gradient by different water pressure, compressor, and subsidiary facilities. A clamp is placed at each position of upper and lower sides of testing apparatus to fix the drainage path in the .inlet and outlet. It protects that the clay inflows into the inside of vertical drain. A dial gauge is situated on the top of the apparatus to measure the settlement of soil. A circular pressure plate is placed on the top of soil specimen to take the pressure via rubber diapram which was fixed to the clamp. The water tank for outflow and inflow can control the hydraulic gradient(i) using different water pressure. Water is supplied to inside vertical drain from the outflow tank through the drain pipe connected to lower side of steel frame. It flows from bottom of steel frame through the vertical drain to upper drain pipe connected with outflow tank during testing as shown in Fig. 3.

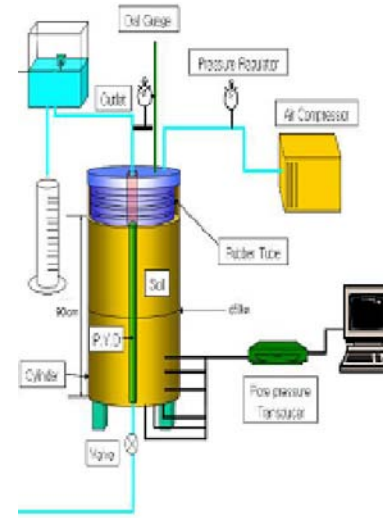

Fig. 3 Apparatus of Discharge Capacity Test

The performance of prefabricated vertical drains which installed in the field is greatly influenced by the speed of consolidation due to smearing effect regardless of the ground condition. In spite of the large influence, the permeability in the smear zone is not yet studied enough. The standard permeability test in this case is not clearly established yet. The soil sample was reconstituted to the field condition by means of the moisture content and saturated unit weight of soil. In the process of laboratory discharge capacity test preparation, pre-fabricated vertical drain is installed in the testing apparatus prior to fill the soft clay. In this way, the clay is not to infiltrate into the inside of vertical drain. The smearing effect is not considered in this study. The purpose of this study is to evaluate the discharge capacity of PVDs during the consolidation period of clay under the constant overburden pressure. The procedures of discharge capacity test with using the large-scale apparatus are shown in Fig. 4. The test conditions for lateral pressure, hydraulic gradient, drainage are also given in Table 4.

Table 4 Large scale discharge capacity test

Test condition	Value
Overburden pressure(kgf/cm^2)	0.5, 1.0, 3.0, 5.0
Hydraulic Gradient(i)	0.2, 0.5, 1.0
Drainage condition	One side drain


(a) Discharge capacity


(b) Upper part of discharge capacity apparatus


(c) Hydraulic gradient control device


(d) Installing lower part clamp


(e) Fixed lower part


(f) Filling clay specimen


(g) Installing loading plate


(h)Spread sand mat

Fig. 4 Procedures of discharge capacity test

Result of Discharge Capacity Test and Required Discharge Capacity

Influence of overburden pressure

The discharge capacity tests were conducted with using a large-scale apparatus in the laboratory to investigate the changing of discharge capacity with elapsed time and also for a given hydraulic gradient. Six different types of PVDs were used in this series of tests. The soft clay where A type vertical drain was installed, an initial discharge capacity was turned out to be about 46.7－52.7 cm^3/s with the overburden pressure of 0.5 kg/cm^2 and it is decreased as 27.22－28.1 cm^3/s under the overburden pressure of 5.0kg/cm^2. While in case of B type vertical drain, an initial discharge capacity was about 56－62.2 cm^3/s with the overburden pressure of 0.5 kg/cm^2, and then the discharge capacity was decreased as 29.4 － 30.7cm^3/s with the overburden pressure of 5.0 kg/cm^2. In case of clay soil where C type vertical drain was installed, an initial discharge capacity was about 53.5－61.2 cm^3/s with the overburden pressure of 0.5 kg/cm^2, and then it is decreased as 28.5－29.2 cm^3/s with the overburden pressure of 5.0 kg/cm^2. In case of clay soil where D type vertical drain was installed, an initial discharge capacity was about 64.9－70.8 cm^3/s with the overburden pressure of 0.5 kg/cm^2, and then it is decreased as 29.2－30.1cm^3/s with the overburden pressure of 5.0 kg/cm^2. It gives the second highest discharge capacity among six vertical drains. The similar variations of discharge capacity were also observed for the case of E and F types vertical drains. However, the degree of discharge capacity reduction with the increment of overburden pressure is relatively milder than those of other PVDs. Whereas F type vertical drain yields the highest discharge capacity in the early stage of consolidation, then it is decreased as similar discharge capacity as other cases.

All these results are shown in Fig. 5. From the test results shown in the figures, as increases the overburden pressure, the clay soil is being consolidated, and also lateral pressure to the PVD specimen is increased. Therefore, the discharge capacity is decreased. From the physical properties of various PVDs which described in Table 3, the size of opening space in the core of PVDs is proportionally related to the discharge capacity. The magnitude of discharge capacity with overburden pressure is somewhat comparable with the discharge capacity reported by Voldhuijzen (1986) and de Jager & Oostveen (1990) in Table 1.

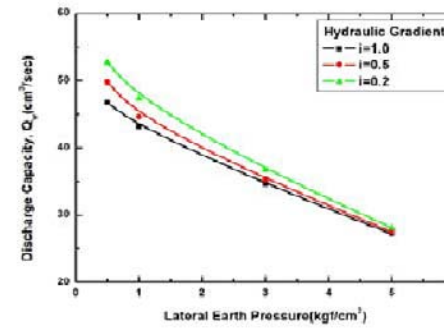

(a) A Type

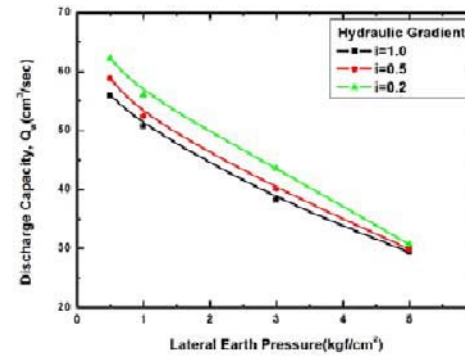

(b) B Type

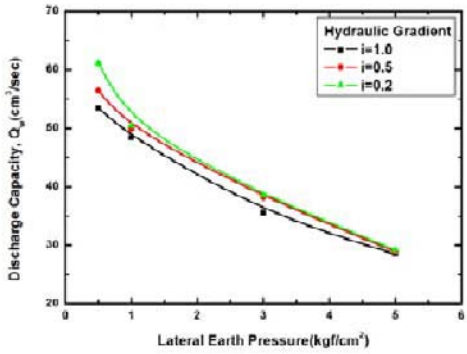

(c) C Type

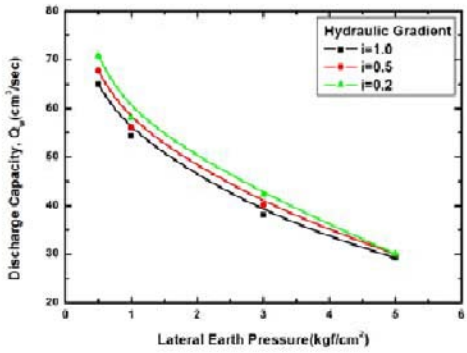

(d) D Type

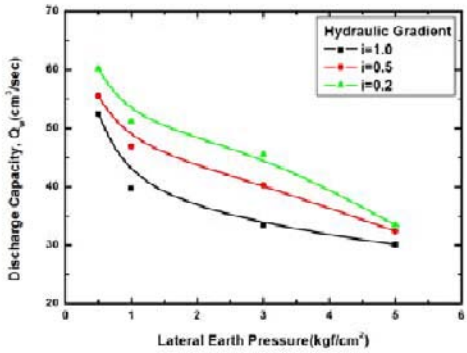

(e) E Type

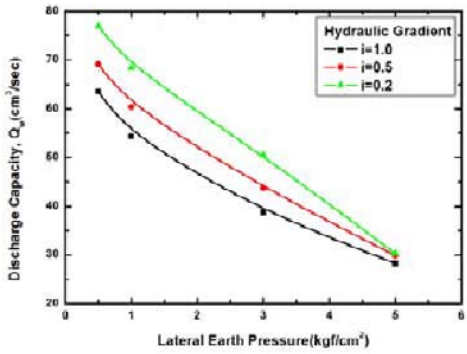

(f) F Type

Fig. 5 Variation of discharge capacity with overburden pressure

Influence of Hydraulic Gradient

The influence of hydraulic gradient to the discharge capacity of various vertical drains was also evaluated with respect to the overburden pressure. These results are graphically plotted in Fig. 6. The figures show that the discharge capacity decreases with increasing the hydraulic gradient. From the test results shown in Fig. 6a with the hydraulic gradient of 0.2, F type vertical drain yields the largest discharge capacity than that of other product. When the overburden pressure is low, the discharge capacities of vertical drains are greatly varied. However, as the overburden pressure increases, the difference of discharge capacities between the types of vertical drains is narrow down and finally it becomes the same value irrespective of the types of vertical drains under the overburden pressure of 5.0 kg/cm^2. Fig. 7b shows the test results with the hydraulic gradient of 0.5, the trend of discharge capacity with the types of vertical drains and overburden pressure is very much similar to the case of hydraulic gradient, 0.2. From the test results shown in Fig. 7c with the hydraulic gradient of 1.0, the discharge capacity of D type vertical drain gives the largest value. This means that the round type core gives less resistance for the flow of water and it has much larger core space than those of other drain types.

From the observation of tests results shown in Fig. 6, the variation range of discharge capacity decreases with increasing the hydraulic gradient. This trend indicates that the resistance of flow through the vertical drains increases with increasing the hydraulic gradient.

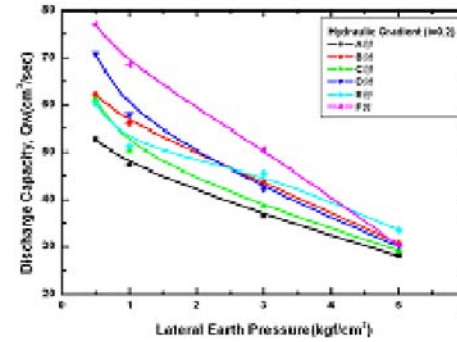

(a) Hydraulic gradient as 0.2

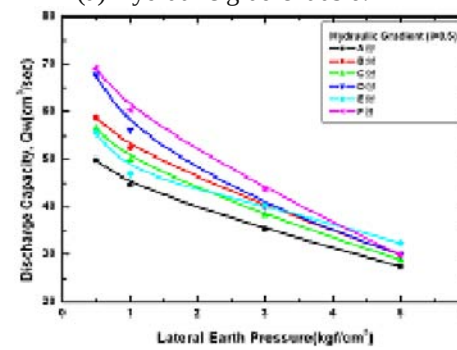

(b) Hydraulic gradient as 0.5

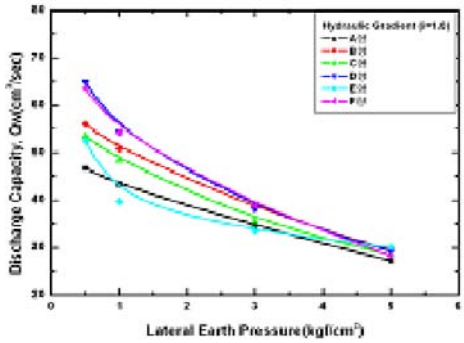

(c) Hydraulic gradient as 1.0

Fig. 6 Variation of discharge capacity with hydraulic gradient

Comparison Required Discharge Capacity with Laboratory Test Results

If the prefabricated vertical drain is ideal item to improve the soft ground, it should maintain the minimum required discharge capacity to consolidate the soft soil without any time delay. The discharge capacity of PVD tends to decrease while the soil is being consolidated due to decreasing of its permeability. In this study, the required discharge capacity with the time of 90% consolidation for various PVDs was estimated by the method suggested by Pradhan (1991). With considering Songdo construction site, overburden pressure, 0.5 kg/cm^2, and hydraulic gradient, 1.0 are applied in this study. The results of required discharge capacity with the time of 90% consolidation for various PVDs are shown in Fig. 7a. The figure shows that the require discharge capacities estimated for A, B, C, E, F types of PVDs at the time of 90% consolidation are almost the same value(average 13.4 cm^2/s) with an exception of D type. In case of D type vertical drain, the required discharge capacity is about 9.4 cm^2/s at the time of 90% consolidation. The size of opening space in the core of D type vertical drain is much larger than those of other types. This is maybe the cause of the difference in the required discharge capacity.

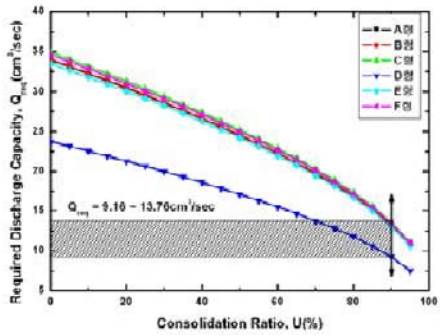

(a) At the time of 90% consolidation

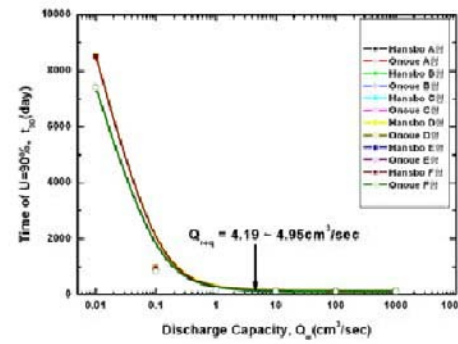

(b) Time delay of 90% consolidation

Fig. 7 Required discharge capacity for various PVDs

The required discharge capacity was determined by the methods proposed by Hansbo (1979) and Onoue (1988) with taking into account the time delay of 90% consolidation. The results of required discharge capacity with considering the time delay of consolidation for various PVDs are shown in Fig. 7b. The figure shows that the require discharge capacities estimated for A, B, C, E, F types of PVDs with considering the time delay of consolidation are the similar value(average 4.26 cm^2/s) with an exception of D type. In case of D type vertical drain, the required discharge capacity is about 6.19 cm^2/s with considering the time delay of consolidation. The large size of opening space in the core of D type vertical drain could induce much higher in the required discharge capacity than those of other PVDs types. Both Hansbo and Onoue methods give the similar values each other.

The required discharge capacities estimated (Fig. 7) by using the methods suggested by Pradhan (1991), Hanso (1979) and Onoue (1988) can be compared with the discharge capacities presented by previous studies in Table 1. The results shown in Fig. 7 indicated that the required discharge capacity at the time of 90% consolidation gives much higher value than that of the time delay of 90% consolidation. The theoretically estimated required discharge capacities in Fig. 7 are much lower values than those of the large-scale laboratory test in this study which is shown in Fig. 7b.

CONCLUSIONS

The discharge capacity was determined by using the large-scale laboratory apparatus for the different types of PVDs. The influence of overburden pressure and hydraulic gradient on the discharge capacity of various vertical drains were estimated. The required discharge capacity was theoretically determined at the time of 90% consolidation and the time delay of 90% consolidation. Finally, the results of discharge capacity and the required

discharge capacity were compared for various PVDs. Based on the results of laboratory and theoretically estimated discharge capacity for various PVDs, the following conclusions were drawn.

(1) As increases the overburden pressure, the clay soil is being consolidated, and also lateral pressure to the PVD specimen is increased. Therefore, the discharge capacity is decreased. A wide range variations of discharge capacity under the overburden pressure of 0.5 kg/cm^2 are observed with depending upon the types of PVD. It is indicated that the size of opening space in the core of PVDs is proportionally related to the discharge capacity at the lower level of overburden pressure. However, the discharge capacity is decreased with increasing the overburden pressure, finally it becomes almost the same value irrespective of the types of vertical drains under the overburden pressure of 5.0 kg/cm^2.

(2) From the observation of tests results, the variation range of discharge capacity decreases with increasing the hydraulic gradient. This trend indicates that the resistance of flow through the vertical drains increases with increasing the hydraulic gradient.

(3) The required discharge capacity estimated by theory at the time of 90% consolidation gives much higher value than that of the time delay of 90% consolidation. With comparison between the theoretical required discharge capacities and laboratory test results, the theoretically estimated required discharge capacities are much lower values than those of the large-scale laboratory tests.

(4) The discharge capacity of any type of PVDs used in this study is much higher than the required discharge capacity. This means that there is no necessary to use the heavy weight of core type PVD in the field. In other words, A type or B type PVD would be the most cost effective vertical drains in the ground improvement work.

REFERENCES

Korea Rural Research Institute (2006) Evaluation Report of Discharge Capacity with Vertical Drain for Construction Site at HwaJeon Industrial Area

Barron RA (1948) Consolidation of Fine-Grained Soils by Drain Wells, Trans, ASCE 2346: 221-228

Bergado DT, Manivannan R, Balasubramaniam AS (1996) Filtration Criteria for Prefabricated Vertical Drain Geotextile Filter Jackets in Soft Bangkok Clay, Geosynthetics International 3(1): 63-83

Hoedt Den, Hoeot Den G (1981) Laboratory testing of vertical drains. Proceedings of the 10th International Conference on Soil Mechanics and Foundation Engineering, Vol. 1, Stockholm: 627-630

Hansbo S (1979) Conslidation of clay by band-shaped prefabricated drains, Ground Eng 12(5): 16-25

Hansbo S (1986) Preconsolidation on soft compressible soils by the use of prefabricated vertical drains, Ann. des Travaux Publ, de Belgique 6: 553-562

Holtz RD, Jamiolkowsky M, Lancellotta R, Pedroni S (1989) Behavior of bent prefabricated vertical drains, Proc. 12th ICSMFE, Rio De Janeiro: 1657-1660

Onoue A (1988) Consolidation by vertical drains taking well resistance and smear into consideration, Soils and Foundations 28(4): 165-174

Oostveen JP, Troost GH (1990) Discharge index tests on vertical drains. In: Den Hoedt (Ed.), Proceedings of 4th International Conference on Geotextiles, Geomembranes and Related Products, Balkema, Rotterdam 2: 345-350

Pradhan TBS, Kamon M, Suwa S (1991) Design method for the evaluation of discharge capacity of prefabricated band-shaped drains. 9th ARC, Bangkok 1: 523-526

L–SHAPED GEODRAIN IN EMBANKMENT MODEL TEST AND NUMERICAL SIMULATION

M. Saito[1], S. Shibuya[2], J. Mitsui[3] and K. Hara[4]

ABSTRACT: An embankment is usually made of unsaturated soil. Unsaturated soil when properly compacted is stiff and strong, since it sustains the matrix suction. The soil suction disappears quickly in the process of wetting, which in turn brings about large deformation or even failure of the embankment. In order to prevent seepage flow into the embankment, and also accumulation of water behind it. Design for an L-shaped geodrain in the embankment is proposed in this paper. A numerical simulation was carried out to examine the efficiency of the L-shaped geodrain system. The analysis was based on the results of a seepage flow test performed using a decomposed granite soil.

KEYWORDS: geodrain, embankment, model test, numerical analysis, decomposed granite soil

INTRODUCTION

The geosynthetics are employed for many applications in hydraulic engineering (e.g., Heibaum et al. 2006). A catastrophic failure of Terr Armée wall reported recently by Shibuya et al. (2007) was triggered by heavy rainfall, which in turn weakened the fill material by saturation and also pushed the reinforced wall by the accumulated water pressure behind the wall. In such a case, horizontal drains (for example, see Tatta et al. 2006) are seemingly not efficient, or even worse, to prevent these causes of the wall failure from happening.

Based on this experience, an idea for preventing seepage flow into and behind the reinforced wall has come out in the second author's mind; that is an L-shaped geodrain system comprising a set of vertical and horizontal geocomposites may be installed in the fill.

At the outset, a numerical simulation was carried out to examine the efficiency of the L-shaped geodrain. The analysis was based on the results of a seepage flow test performed using a decomposed granite soil.

TESTS PERFORMED

Fig. 1 shows the configuration of seepage flow test. Decomposed granite soil was compacted in the rectangular chamber having the dimension of 200 cm in length, 40 cm in width and 100 m in height. The properties of the compacted decomposed granite soil are described as the soil particle density of 2.642 g/cm^3, the dry and wet density of 1.697 g/cm^{3}and 1.885 g/cm^3, respectively, the moisture content of 11.0%, the degree of saturation of 53%, and the porosity of 0.35 (e=0.54). The grading curve is shown in Fig. 2. Fig. 3 shows the result of compaction test. Note that the compacted model ground showed the degree of compaction of 87%.

As seen in Fig. 1, seepage flow can be initiated by

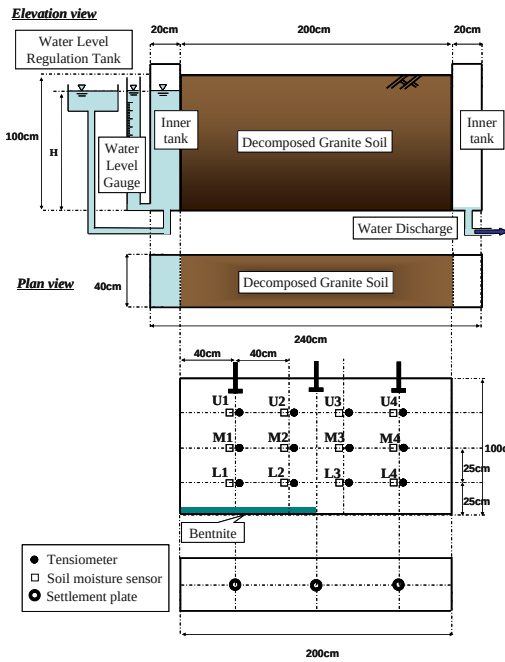

Fig. 1 Equipment for seepage flow test

[1] Assistant Professor, Research Center for Urban Safety and Security, Kobe University, JAPAN. Email: msaito@kobe-u.ac.jp
[2] Professor, Graduate School of Engineering, Kobe University, JAPAN. Email: sshibuya@kobe-u.ac.jp
[3] Graduate Student, ditto, JAPAN. Email: 074t130t@stu.kobe-u.ac.jp
[4] Chief Researcher, Taiyo Kogyo, also Graduate Student, ditto, JAPAN. Email: hk002996@mb.taiyokogyo.co.jp

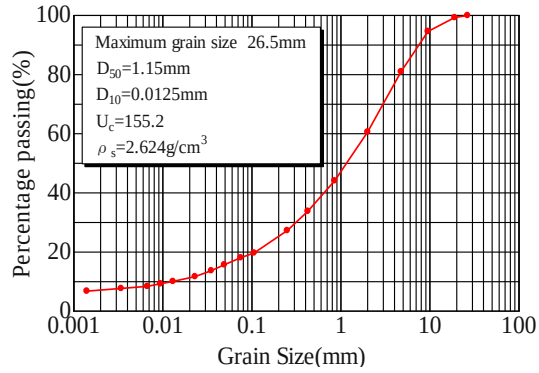

Fig. 2 Grading curve of decomposed granite soil

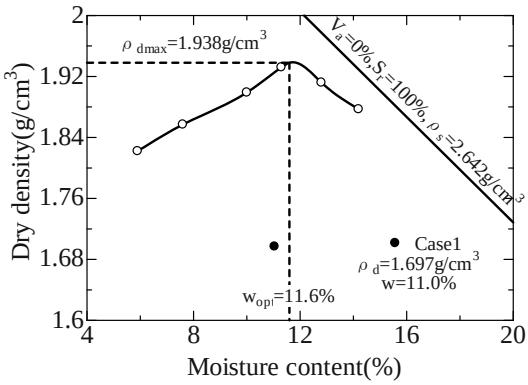

Fig. 3 Compaction curve

increasing the upstream water level against the fixed downstream water level. Instrumentations are arranged at twelve positions in the model ground, each in which the soil moisture and matrix suction were measured. Settlement was monitored at three points near the surface.

Fig. 4 shows the variation of the upstream water level with time. The upstream water level was increased to 90 cm from the chamber bottom, implying the hydraulic gradient of 90/200=0.45. The model ground was subjected to dewatering twice during the test.

TEST RESULTS

The settlement was almost zero throughout the test. Figs. 5 and 6 show the variations of pore pressure and the degree of saturation with time, respectively. The initial pore pressures in the model ground exhibited a considerable scatter so that some corrections were made for the measured pore pressures by assuming that the pore pressure distribution in an isotropic/homogeneous ground undertaking a steady flow is uniquely determined regardless of the soil properties. In this test, an instant about 20hrs after the initial filling may be regarded to have reached the steady state. Accordingly, the measured pore pressure at this state was each corrected to match the pore pressure from the numerical analysis. The trends for the measurements are reasonable except for M-4, in which the pore pressure showed no distinct drop on dewatering.

Note also that the degree of saturation Sw reached as much as 80%—90% observed at the lower part (L1-L4). Moreover, the S_w in the event of refilling reached a less value when compared to the initial filling, suggesting some changes of the soil properties.

NUMERICAL SIMULATION

Governing Equation

The following Richards' equation (Richards, 1931) is employed as the governing equation;

$$(C+\beta S_s)\frac{\partial \psi}{\partial t}=\nabla\cdot\left[\mathbf{K}\cdot(\nabla\psi+\nabla Z)\right] \qquad (1)$$

where C is the specific water capacity ($\doteq dS_w/d$), where is porosity and Sw is the degree of saturation, Ss is the specific storage coefficient, K is the hydraulic conductivity tensor, is the pressure head, and Z is the elevation head. Note that is equal to unity in the saturated zone with $S_w = 1$, and to zero in the unsaturated zone with $S_w \neq 1$. The K can be expressed in terms of the

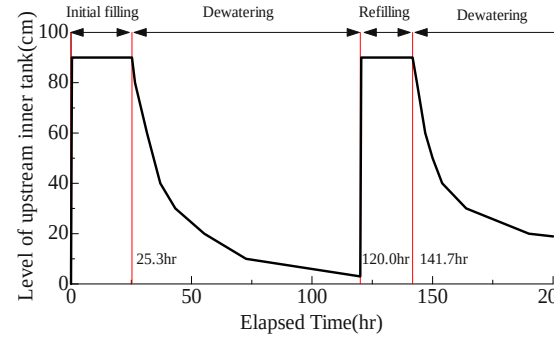

Fig. 4 Sequence of filling and dewatering

relative permeability k_r and the saturated hydraulic conductivity Ks, that is;

$$\boldsymbol{K}= k_r \square \boldsymbol{Ks} \qquad (2)$$

The boundary condition on Γ_1 for which the pore pressure head is defined, is given by

$$\psi = \psi_1 \quad \text{on} \quad \Gamma_1 \qquad (3)$$

On Γ_2, where flux q is defined in the following form;

$$q = q_2 = -\mathbf{n}\cdot\mathbf{K}\cdot(\nabla\psi+\nabla Z) \quad on \quad \Gamma_2 \qquad (4)$$

where n denotes the outwardly directed unit normal vector.

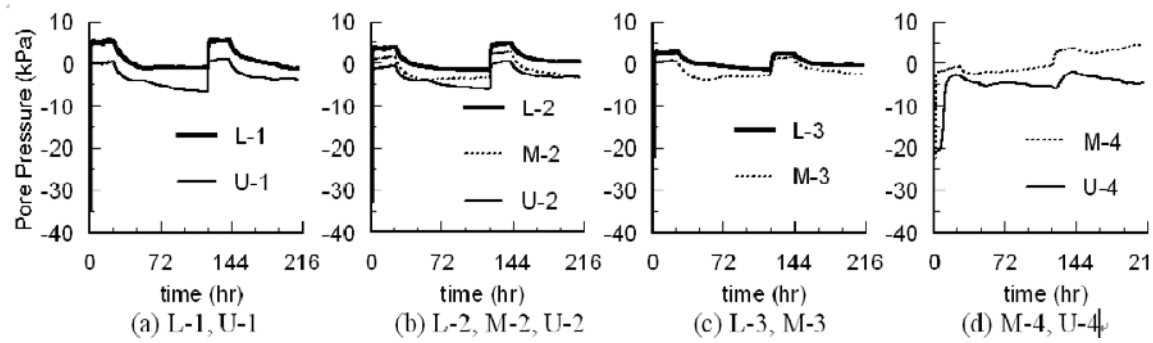

Fig. 5 Variation of pore pressure with time

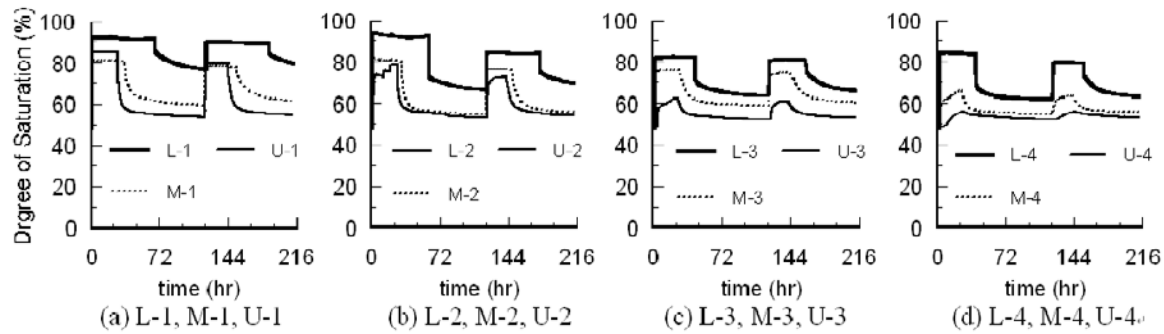

Fig. 6 Variation of the degree of saturation with time

Water Retention Curve

The relative permeability k_r is an essential parameter in the seepage analysis. This property is considered as a function of S_w, whereas the S_w is considered as a function of capillary pressure ψ_c ($\alpha - \psi$). Among many mathematical models previously proposed to describe the water retention curve, the van Genuchten equation (van Genuchten, 1980) is employed in the present study;

$$S_e = \frac{S_w - S_r}{S_f - S_r} = \left\{1 + (\alpha \psi_c)^n\right\}^{-m} \tag{5}$$

where S_e is the effective saturation, S_r is the residual saturation, S_f is the saturation at ψ_c =0, and α, n and m are parameters. The parameters, n and m, are both dimensionless, whereas α has the dimension corresponding to the reciprocal of the pressure head. The parameters n and m are not independent to each other, and they are related by

$$m = 1 - 1/n \tag{6}$$

The relative permeability and effective saturation are related as shown in the following (Maulem 1976);

$$k_r = S_e^{\varepsilon} \left\{1 - \left(1 - S_e^{1/m}\right)^m\right\}^2 \tag{7}$$

where ε is a parameter related to the degree of interconnection among voids. Generally, a value of 0.5 is used for ε. The water retention curve and relative permeability can be calculated if the parameters α, n, S_r and S_f are all known.

In general, the relationship between the degree of saturation and the capillary pressure exhibits a hysteretic curve against cycles of wetting and drying. An example of the hysteretic water retention curves at U-1 is shown in Fig. 7, in which the measured relationship is superimposed with the simulated curve. Simulation was achieved in a manner that the α, n, S_r and S_f were all identified by fitting the drying curve. In simulating the wetting curve, α was doubled in value while the values of n, S_r and S_f remained all constant (refer to Luckner et al. 1989). Table 1 shows the parameters employed for the seepage analysis in this study. The technique proposed by Scott et al. (1983) was used for estimating the scanning curves to describe the hysteretic water retention characteristics.

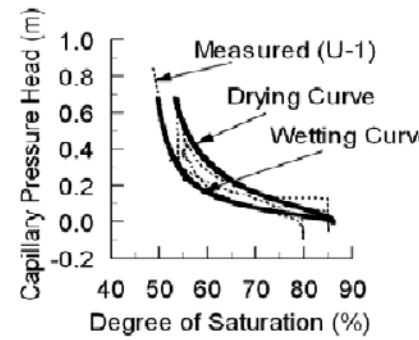

Fig. 7 Water retention curves (observation vs simulation)

Table 1 VG parameters

	Drying	Wetting
α (1/m)	8.45	16.9
n	2.001	2.001
Sr (%)	46	46
Sf (%)	86	86

SIMULATION MODE

Fig. 8 shows the idealized flow domain. Impervious boundaries are considered at z = 0 m and z = 1.0 m, q = 0 at the seepage surface boundary at x = 2.0m when $\psi < 0$, and ψ=0 when $q < 0$.

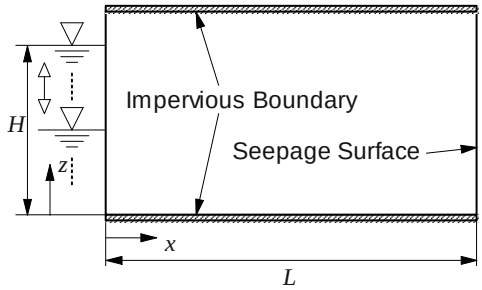

Fig. 8 Flow domain assumed in the numerical analysis

The upstream vertical plane at $x = 0$ m is the boundary to generate the water pressure varying with time. It was postulated that the water pressure rose linearly with time to reach the maximum value corresponding to H=0.9 m. Conversely, it was assumed that the H reduced with time in the event of dewatering by following the relationship shown below:

$$\frac{dH}{dt} = -\frac{Q_i(t,H)}{A} \tag{8}$$

where A represents the cross-section area of the water tank, and Q_i denotes the rate of water inflow into the model ground. The Q_i was not a priori given so that it was calculated by iteration.

The permeability of the model soil was taken as k=4.0 × 10^{-3} cm/s that was identified by making the calculated rate of water discharge in match with the maximum value measured at steady state. Note that the permeability in the vertical direction as measured in the laboratory was k=5.3×10^{-4} cm/s. Porosity is set to the measured value of 0.35. The number of elements in the analytical mesh is 40×20 with each element size of 0.05 m×0.05 m.

RESULTS AND DISCUSSION

Comparison of results between observation and analysis

Fig. 9 shows the variation of pressure head in the model ground at 21.5 hrs after the initial filling. The variations of pore pressure and the degree of saturation with time are shown in Figs. 10 and 11, in which the observations at L-2, M-2 and U-2 are compared against the results of numerical simulation. The response of pore pressure was successfully simulated. A trend for faster decrease of pore pressure compared to the observation suggests some reduction of the permeability at the second dewatering. Despite that the rise of S_w at refilling is overestimated by the analysis, the variation of the degree of saturation with time is also well simulated.

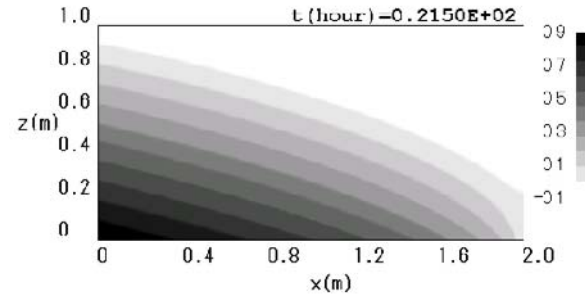

Fig. 9 Distribution of pressure head ψ (m×H_2O)

Fig. 12 shows a comparison of the rate of water discharge with time at x=2.0 m. Despite that the measurement was rather crude, the rate of discharge at refilling was definitely smaller in value compared to that at the initial filling. This trend matches well with the observation of the pore pressure response (see Fig. 10).

Based on the results shown in Figs.9－12, it may well be mentioned that the numerical analysis is capable of simulating the variations of pore pressure, the degree of saturation and the rate of water discharge with time associated with cycles of filling and dewatering.

NUMERICAL SIMULATION FOR GROUND SEEPAGE FLOW WITH AN L-SHAPED GEO-DRAIN SYSTEM

Numerical Analysis

As shown in Fig. 13, an L-shaped geodrain system is considered in the model ground with L=2.0 m, H=0.9 m and k = 4.0×10^{-3} cm/s. In the numerical analysis, the vertical drain having the thickness d=3.0 mm is mounted at the position of L_1=0.5 m.

The pore pressure head at steady state of seepage flow is shown in Figs. 14 and 15, in which the results of two cases using the geodrain permeability of k_d=1.0 cm/s

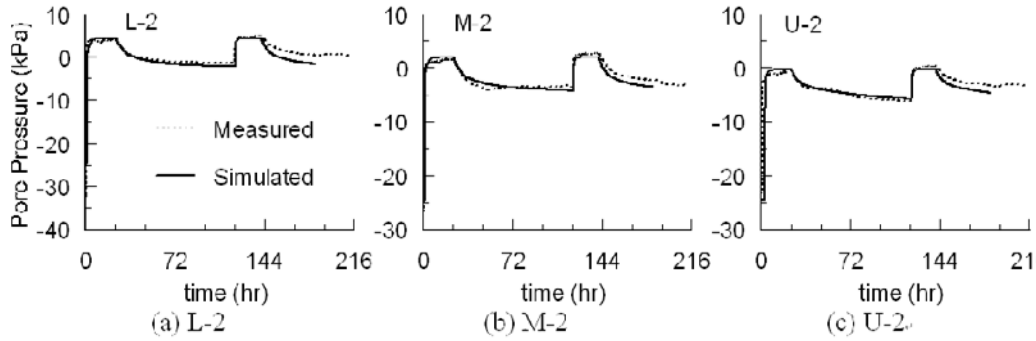

Fig. 10 Variation of pore pressure with time (observation vs simulation)

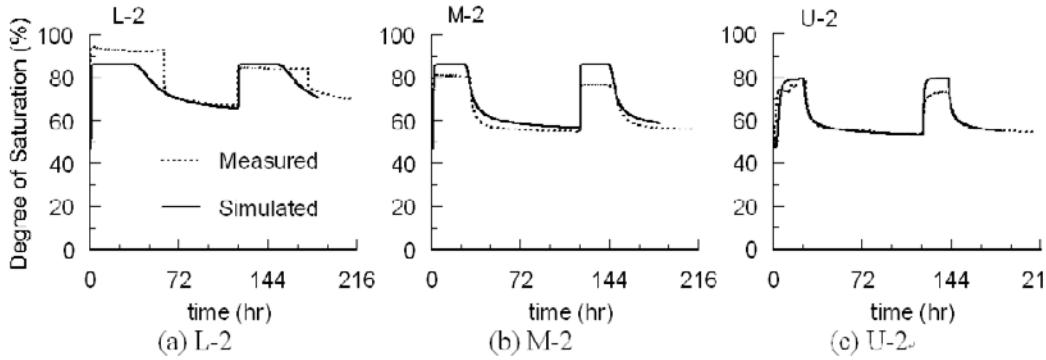

Fig. 11 Variation of S_w with time (observation vs simulation)

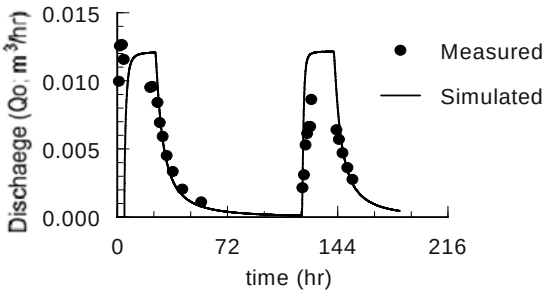

Fig. 12 Discharge from seepage surface

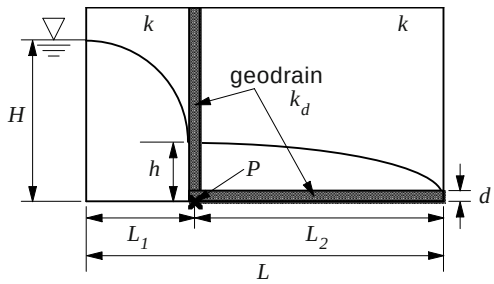

Fig. 13 Arrangement of L-shaped geodrain

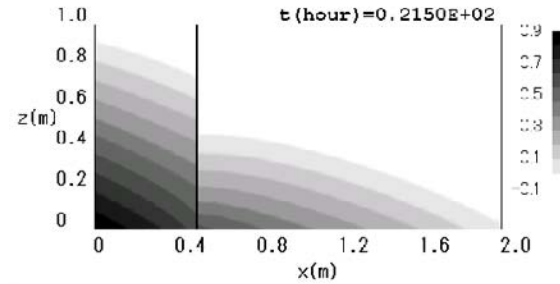

Fig. 14 Distribution of pressure head when k_d=1.0 cm/s

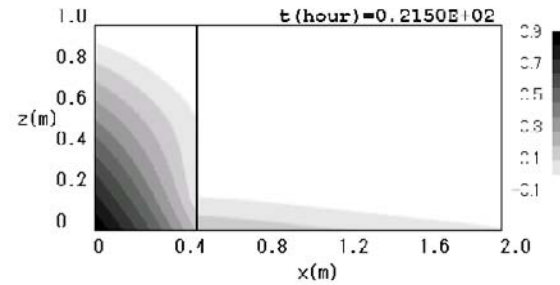

Fig. 15 Distribution of pressure head when k_d=10.0 cm/s

and k_d=10.0 cm/s are presented, respectively. The effect of the L-shaped geodrain system is significant in reducing the water level behind the vertical drain, *h*. Moreover, the *h* was much lower when the k_d is higher in value.

Design for an L-shaped geodrain system

As seen in Fig. 13, the rate of water inflow into the vertical drain, Q_1 can be derived after the theory of unconfined one-dimensional ground seepage flow, i.e.,

$$Q_1 = \frac{k}{2L_1}\left(H^2 - h^2\right) \tag{9}$$

On the other hand, the rate of water flow through the vertical drain may be approximated in the following:

$$Q_2 = \frac{k}{2L_2}h^2 + \frac{k_d}{L_2}dh \tag{10}$$

When the design value h_0 (i.e., the allowable water level behind the vertical drain) is considered for $h=h_0$, the design condition is given by observation and simulation (see Fig. 13).

$$Q_2 \geq Q_1 \tag{11}$$

In the meantime, the non-dimensional parameters α, β, γ are introduced;

$$\alpha = \frac{k_d d}{kH}, \quad \beta = \frac{h}{H}, \quad \gamma = \frac{L_1}{L} \tag{12}$$

Based on Eqs. 9 and 12, the α should satisfy

$$\alpha \geq \frac{1-\gamma-\beta^2}{2\beta\gamma} \tag{13}$$

When α and γ are both given, the parameter β when $Q_1=Q_2$ can be expressed in the following form:

$$\beta = \sqrt{\alpha^2\gamma^2+1-\gamma}-\alpha\gamma \tag{14}$$

Note that Eq. 14 needs only the geometric arrangements, together with the permeability, of the geodrain in a given field.

The result of numerical simulation is shown in Fig. 16, in which the pore pressure head at P (see Fig. 13) is examined for the relationship between α and β. Provided that the pore pressure head at P is equal to h, it is well demonstrated that the approximated solution using Eq. 14 is good enough to estimate the maximum water level behind the vertical drain.

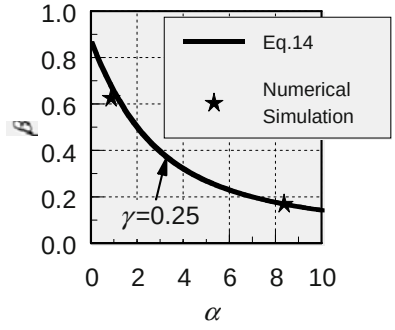

Fig. 16 Comparison of pressure head at P between

CONCLUDING REMARKS

It was successfully demonstrated in the seepage flow test using the compacted decomposed granite soil that the numerical analysis is capable of simulating the variations of pore pressure, the degree of saturation and the rate of water discharge with time associated with cycles of filling and dewatering. An L-shaped geodrain system is effective in reducing the downstream water level behind the vertical drain. A simple equation comprising the geometric arrangements, together with the permeability, of the geodrain is proposed for the design of the L-shaped geodrain in near future.

ACKNOWLEDGEMENT

The authors are very grateful to Dr. Chae J-G. for his support in preparing manuscript of this paper.

REFERENCES

Heibaum H, Furie A, Girard H, Karunarante GP, Lafleur J, Palmeria EM (2006) Hydraulic applications of geosynthetics, Keynote Lecture, Proc. of the 8th Inter. Conf. On Geosynthetics, Millpress 1: 79-120

Luckner L, van Genuchtn MTh, Nielsen DR (1989) A Consistent Set of Parametric Models for the Sub-surface, Water Resources Research 25: 2187-2193

Maulem Y (1976) A new model for predicting the hydraulic conductivity of unsaturated porous media, Water Resources Research 12: 513-522

Richards LA (1931) Capillary Conduction of Liquids through Porous Mediums, Physics 1:318-333

Scott PS, Farquhar GJ, Kouwen N (1983) Hysteretic Effects on Net Infiltration :163-170, In Advances in Infiltration, Am. Soc. Agric. Eng., St. Joseph, MI

Shibuya S, Kawaguchi T, Chae JG (2007) Failure of Reinforced Earth wall as attacked by Typhoon No. 23 in 2004, Soils and Foundations 46(2):153-160

Tatta N, Ito S, Kawauchi M, Matsumura T, Nakamura Y (2006) Behavior of a high airport embankment with horizontal drains, Proc. of the 8th Inter. Conf. On Geosynthetics, Millpress 2: 485-488

Van Genuchten MT (1080) A closed-form equation for predicting the hydraulic conductivity of unsaturated soils, Soil Science Society American Journal 44: 892-898

Proceedings of the 4th Asian Regional Conference on Geosynthetics
June 17 - 20, 2008 Shanghai, China

IN-SOIL HYDRAULIC TRANSMISSIVITY OF GEOSYNTHETIC DRAINS IN THE LABORATORY

K. Hara[1], J. Mitsui[2], K. Mitsumune[3], J.G. Chae[4] and S. Shibuya[5]

ABSTRACT: When geosynthetics such as plastic board drains are employed for drainage material in embankment, the drainage ability could be deteriorated owing to the sustained earth pressure, implying that the cross sectional area of the geosynthetics could be decreased by the compressive overburden stress. In engineering practice, it is thus of great importance to evaluate the in-soil performance of geosynthetic drains. In so doing, the in-soil hydraulic transmissivity of geosynthetic drains should be properly measured in the laboratory. In this paper, the hydraulic transmissivity of two types of plastic board drains was carefully examined in the laboratory by using fine-grained clay, poorly graded fine sand and well-graded granular material.

KEYWORDS: plastic board drain, transmissivity, in-plan flow, hydraulic gradient, in-soil, geocomposite

INTRODUCTION

Geosynthetics made of synthetic resin such as planar non-woven geotextiles and strip plastic board (PB) drains are often employed in earth fills and in soft clay foundations, with which drainage in the earth fill and consolidation of the foundation soil are grossly facilitated, respectively. It is surmised that the drainage capacity of these geosynthetics in the horizontal direction, i.e., in-plane hydraulic transmissivity, deteriorates to some extent due to reduction in cross-sectional area of the material when undertaking the earth pressure. It is also expected that the degree of deterioration in the hydraulic transmissivity is affected by the primary soil properties such as the grading.

In practical design, it is thus important to evaluate quantitatively the amount of deterioration of the material's transmissivity. In so doing, it is urgently needed to establish rational testing method for assessing in-soil transmissivity of geosynthetics. At present, in-plane hydraulic transmissivity of geosynthetics is usually evaluated by using an in-plane hydraulic transmissivity testing system after the standard plan described by the Japanese Geotechnical Society, JGS T-932 (plan). However, the testing system cannot generally evaluate in-soil behavior of geosynthetic specimen.

Accordingly, the in-plane hydraulic transmissivity of two types PD drains was measured in the modified in-soil test apparatus after JGS T-932 (plan). Discussion was made on the effects of the sustained pressure with and without the soil by using three kinds of soil showing different soil particle grading.

EXPERIMENT

The tests performed are conveniently categorized into *"normal test"* and *"in-soil test"* performed without and with soil, respectively. As seen in Table 1, the *"in-soil test"* was carried out using three kinds of soil conveniently called *"A"*, *"B"* and *"C"*. The mean diameter, D_{50}, the coefficient of uniformity, U_c and the coefficient of curvature, U'_c are shown in Table 1.

The *"normal test"* was carried out in an in-plane hydraulic transmissivity testing device of geosynthetics after the standard plan described by the Japanese Geotechnical Society, JGS T-932 (plan). As seen in Fig.1, the normal compressive stress was applied to the bare geosynthetic specimen by using an air-bag.

The *"in-soil test"* was carried out in the same testing device in which the geosynthetic specimen was sand-wiched in soils seen in Table 1. For example, Photos 1 and 2 show *"in-soil test B"*. The geosynthetic specimen was covered with a Poly Vinyl den Chloride (PVDC) film so that the water flows exclusively through the geosynthetic specimen.

[1] Technical Research Center, Taiyokogyo Corporation (Sun), Osaka, JAPAN. Email: hk002996@mb.taiyokogyo.co.jp
[2] Graduate student, Department of Civil Engineering, Kobe University, JAPAN. Email: 074t130t@stu.kobe-u.ac.jp
[3] Student, Department of Civil Engineering, Kobe University, JAPAN. Email: 0474128t@stu.kobe-u.ac.jp
[4] Research Fellow, Department of Civil Engineering, Kobe University, JAPAN. Email: chaie1976@yahoo.co.jp
[5] Professor, Department of Civil Engineering, Kobe University, JAPAN. Email: sshibuya@kobe-u.ac.jp

Two kinds of PB drains, called "PD-X" and "PD-Y" were tested in the current study. The PD-X is shown in Photo 3 and Fig. 2, whereas the PD-Y is shown in Photo 4 and Fig. 3. Table 2 shows some specifications of the PB drains.

Table 1 Soils used for *"in-soil test"*

Test name	Soil	D_{50} (mm)	U_c	U_c'
In-soil test A	kaolin	0.003	11.8	1.44
In-soil test B	Toyoura sand	0.175	1.5	1.04
In-soil test C	decomposed granite soil	0.49	191.9	4.28

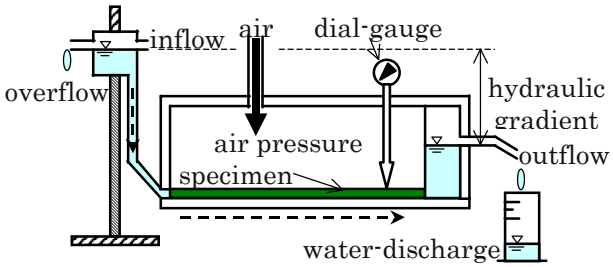

Fig. 1 Configuration of *"normal test"*

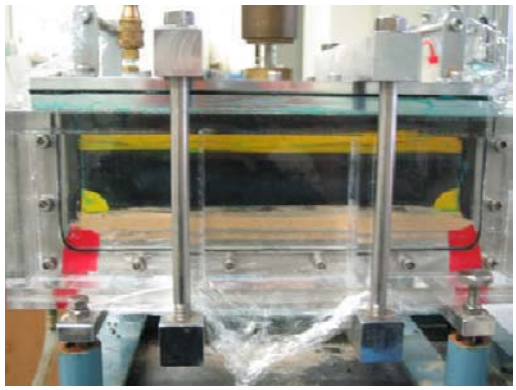

Photo 1 A snap for *"in-soil test B"*

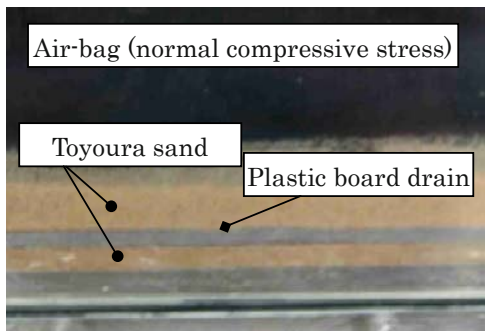

Photo 2 Geosynthetic specimen in *"in-soil test B"*

In all the tests, the PB specimen was subjected to incremental pressures of 20, 40, 100, and 200 kPa. The hydraulic transmissivity was examined at each stage by using the hydraulic gradients of 0.025, 0.05, 0.1, 0.2, 0.25, 0.5 and 1.0.

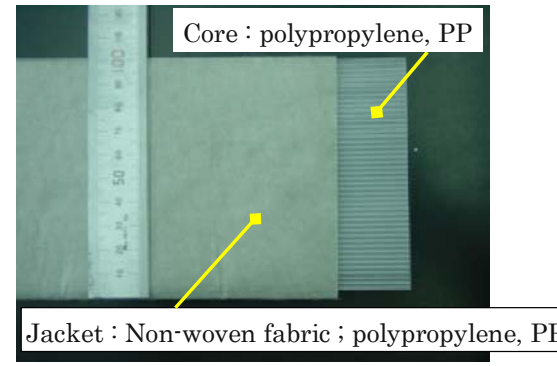

Photo 3 A snap for plastic board drain "PD-X"

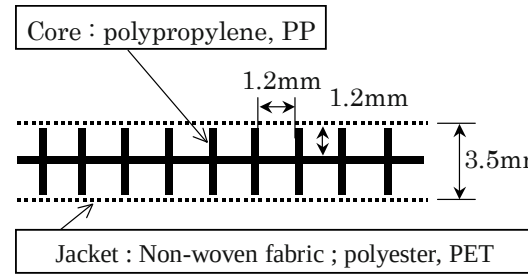

Fig. 2 A cross-section of "PD-X".

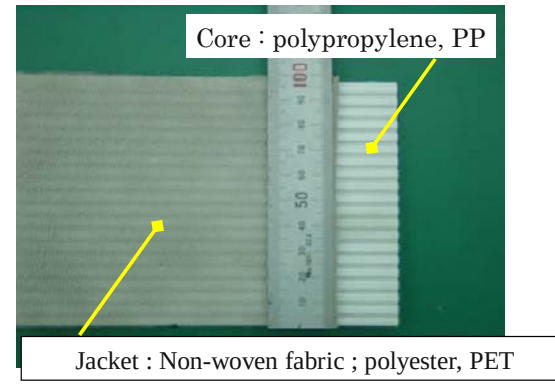

Photo 4 A snap for plastic board drain "PD-Y"

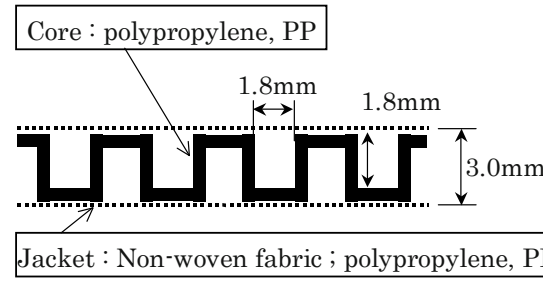

Fig. 3 A cross-section of "PD-Y"

Table 2 Form of geosynthetic specimens

Specimen name	Width of ditch	Depth of ditch	Jacket thickness
PD-X	1.2mm	1.2mm	0.3mm
PD-Y	1.8mm	1.8mm	0.2mm

RESULTS AND DISCUSSION

Definitions for Hydraulic Transmissivity

The hydraulic transmissivity, θ_h is defined by

$$\theta_h = \frac{Q}{W(\Delta h/L)} \tag{1}$$

where Q is the rate of discharge, W and L are the width and length of the specimen in the flow direction, Δh is the total head loss in the PB drain, and I(=$\Delta h/L$) is the hydraulic gradient applied to the PB drain.

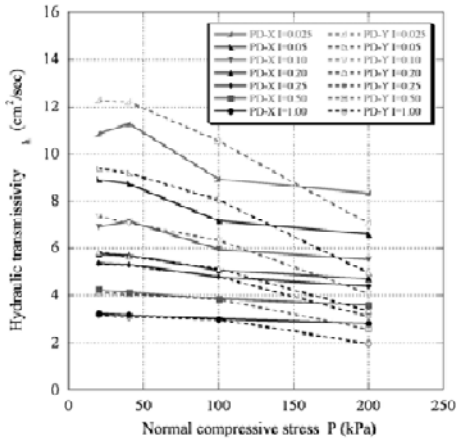

Fig. 4 Relationship between hydraulic transmissivity and normal compressive stress for

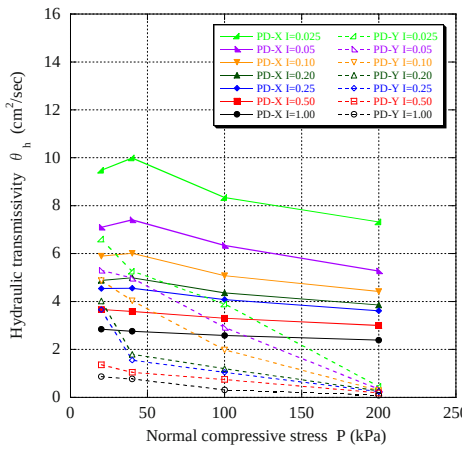

Fig. 5 Relationship between hydraulic transmissivity and normal compressive stress for *"in-soil test A"*

Comparison of In-plane Hydraulic Transmissivity

Fig. 4 shows the relationship between the in-plane hydraulic transmissivity and the normal compressive stress P in *"normal test"*, whereas the results of *"in-soil tests"* using kaolin, Toyoura sand and decomposed granite soil are shown in Figs. 5, 6 and 7, respectively. In each figure, the results of PD-X and PD-Y are denoted using solid and dashed lines, respectively.

As seen in these figures, the transmissivity of PD-X and PD-Y both decreased as the hydraulic gradient increased. Moreover, the pressure-dependency of θ_h was insignificant for PD-X, whereas the θ_h was greatly reduced as the sustained pressure P increased for PD-Y. In tests using PD-X, the pressure-dependency of θ_h was similar among three cases using soils A, B and C. Conversely, the transmissivity of PD-Y varied significantly depending on the soil type, noting that the transmissivity in *"in-soil test A"* using kaolin was almost zero at P=200 kPa, (see Fig. 5).

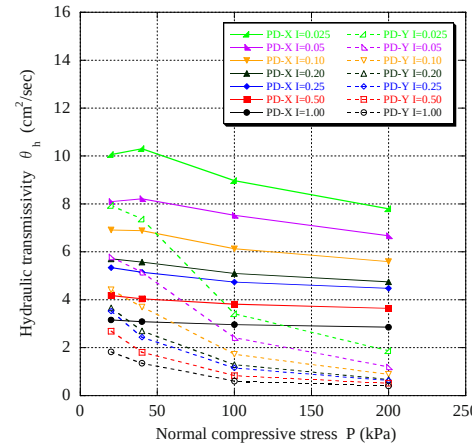

Fig. 6 Relationship between hydraulic transmissivity and normal compressive stress for *"in-soil test B"*

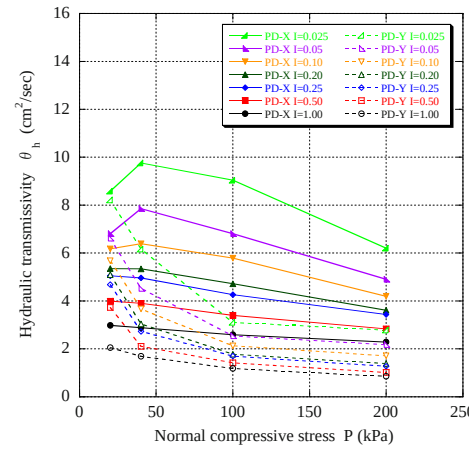

Fig. 7 Relationship between hydraulic transmissivity and normal compressive stress for *"in-soil test C"*

The difference between PD-X and PD-Y may be attributed to the specifications, i.e., the ditch of PD-Y is wider and deeper than PD-X, and the jacket of PD-Y is thinner than PD-X (see Table 2). Moreover, the rigidity of the jacket of PD-X is higher than PD-Y. Accordingly, the soil grains in *"in-soil tests"* of PD-Y penetrated deep into the PB drain as the *P* increased. It may be said that PD-X exhibits the structure for which the soil grains are hard to penetrate into the ditch than PD-Y.

As a result of it, even if these two PB drains, PD-X and PD-Y, exhibit the behavior similar to each other in *"normal test"*, they behaved quite differently in *"in-soil tests"* due to the different structure and the rigidity of the core material and the jacket, respectively.

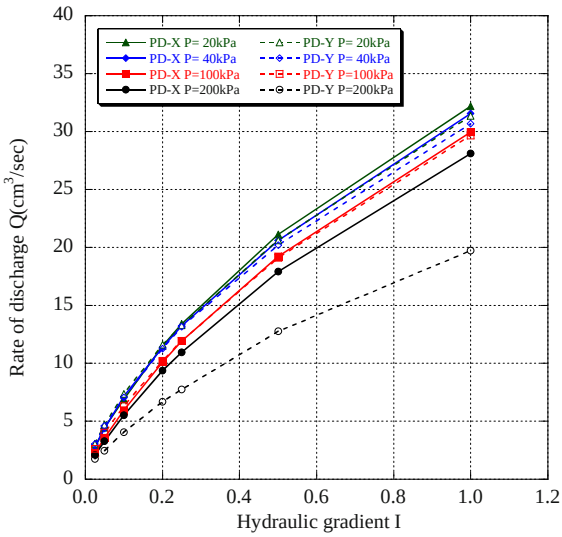

Fig. 8 Relationship between the rate of discharge and hydraulic gradient for *"normal test"*

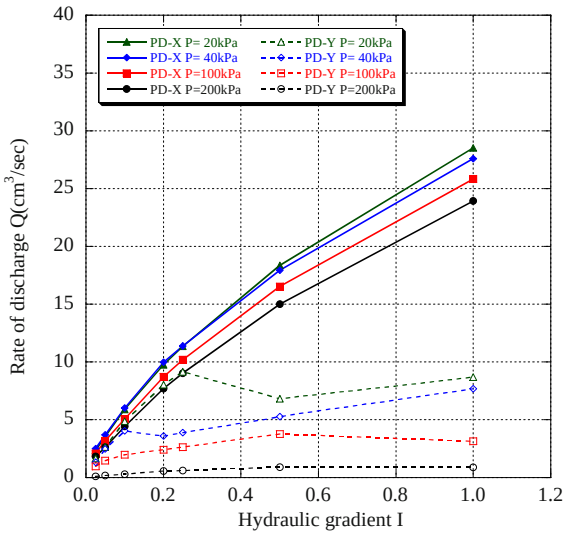

Fig. 9 Relationship between the rate of discharge and hydraulic gradient for *"in-soil test A"*

Relationship between the Rate of Discharge and Hydraulic Gradient

Figs. 8, 9, 10 and 11 show the relationship between the rate of discharge and the hydraulic gradient in *"normal test"* and three kinds of *"in-soil test"* performed by using two kinds of PB drains of PD-X and PD-Y, respectively. It should be stressed that the relationship between *Q* and *I* should be linear neither the flow friction loss nor the decrease in cross-sectional area of the PB drain occurs.

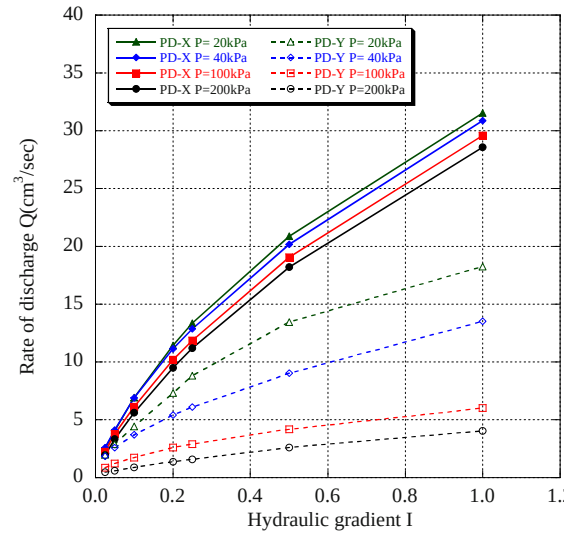

Fig. 10 Relationship between the rate of discharge and hydraulic gradient for *"in-soil test B"*

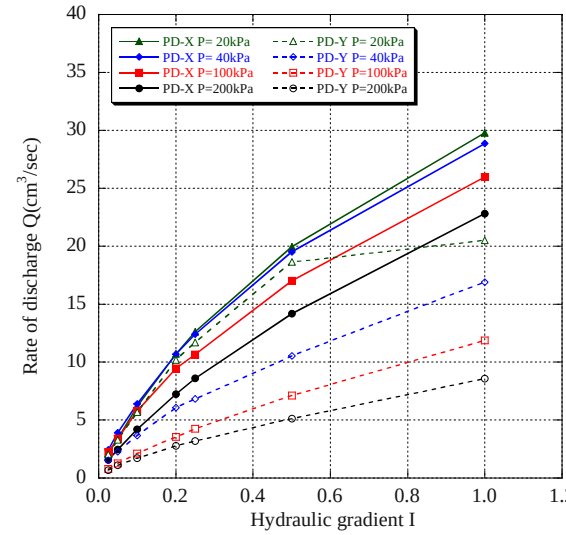

Fig. 11 Relationship between the rate of discharge and hydraulic gradient for *"in-soil test C"*

In tests using PD-X, the relationship between *Q* and *I* is similar between *"normal test"* and *"in-soil test B"*, suggesting that the rate of discharge was virtually

unaffected by Toyoura sand. Conversely, the rate of discharge was slightly reduced in tests using decomposed granite soil and kaolin (see Figs. 9 and 11). In particular, the rate of discharge decreased as the *P* increased in *"in-soil test C"*, implying that the decomposed granite soil having a large coefficient of uniformity tends to intrude into the core ditch.

In all the tests performed using PD-Y, the rate of discharge deteriorated greatly as the hydraulic gradient increased in value. The degree of deterioration was greater in the order of *"in-soil tests"* using kaolin, Toyoura sand, decomposed granite and the *"normal test"*. The dramatic deterioration observed in test using kaolin may be attributed to a large loss of cross-sectional area of the PB drain at higher *P*, since the jacket of PD-Y was not rigid enough to prevent the soil from intruding into the core space. Conversely, the trend may be prevented to some extent in other granular soils showing larger grains in size and wider grading. The results suggest that the jacket cannot be strong enough to resist against the intrusion of fine-grained soil when subjected to high pressures. In the case of granular soils, however, once some grains drop into the ditch, they protect further intrusion of soil grains in the ditch, resulting in less degree of deterioration as compared to fine-grained soil.

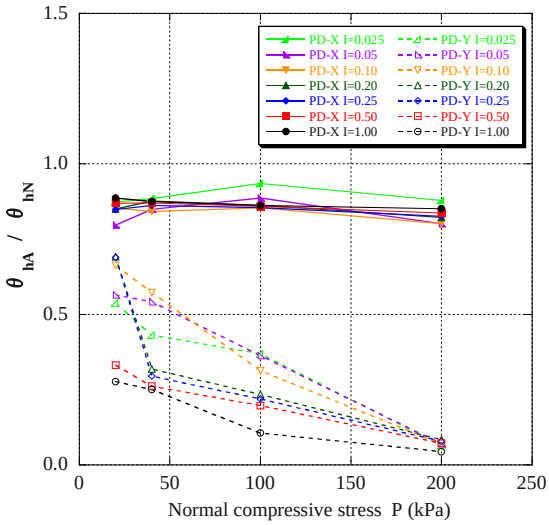

Fig. 12 Relationship between normalized hydraulic transmissivity and normal compressive stress for *"in-soil test A"* using kaolin

Comparison of Hydraulic Transmissivity between PD-X and PD-Y in In-soil Tests

Figs. 12, 13 and 14 show the hydraulic transmissivity of *"in-soil tests"* normalized by the corresponding result from the *"normal test"* plotted against *P*. As stated previously, the performance of PD-X is much better irrespective of the soil type. In particular, the transmissivity scarcely deteriorated in test using Toyoura sand (see Fig.13). On the other hand, the performance of PD-Y using kaolin was the worst by showing the transmissivity less than one-tenth of the *"normal test"*.

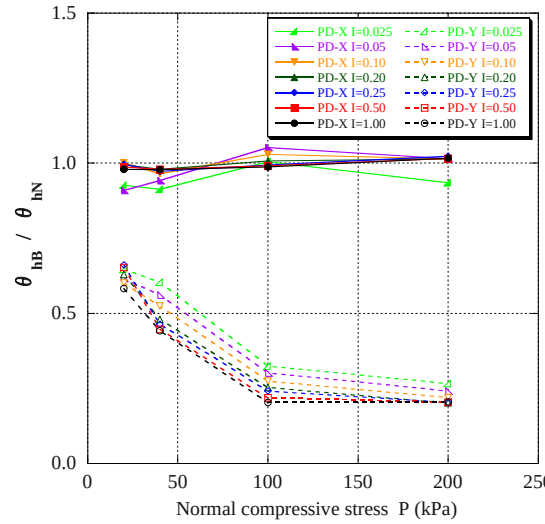

Fig. 13 Relationship between normalized hydraulic transmissivity and normal compressive stress for *"in-soil test B"* using Toyoura sand

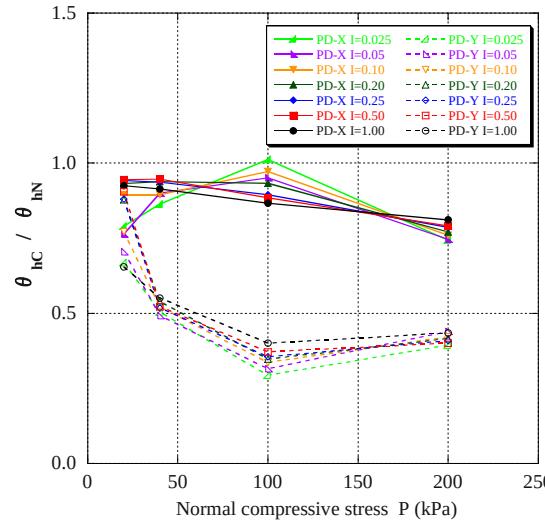

Fig. 14 Relationship between normalized hydraulic transmissivity and normal compressive stress for *"in-soil test C"* using decomposed granite soil

CONCLUSIONS

i) In-plane hydraulic transmissivity of plastic board drain was greatly affected by the existence of surrounding soil undertaking a sustained pressure, implying generally that it decreased as the pressure increased,

ii) the degree of deterioration of the in-plane hydraulic transmissivity depended on the soil type, together with the form of core as well as the rigidity of jacket, and
iii) the jacket should be rigid enough to resist against penetrating soil grains into the material.

REFERENCES

Ling HI, Jonathan TH, WU Nishimura J, Tatsuoka F (1989) In-plane Hydraulic Conductivity of Geotextiles. 4th Geosynthetics symposium, The Japan Chapter of the International Geosynthetics Society: 56-63

Kitajima T, Suwa Y, Pradhan T, Kamon M (1990) Factors affecting the discharge capacity of a prefabricated band shaped drain. 25th Geotechnical Research Meeting. The Japanese Geotechnical Society: 1717-1718

Park YM, Kim S, Jeon HY (2004) An evalutation on discharge capacity of perfabricated vertical drains using large scale test. Proceedings of the 3rd Asian Regional Conference on Geosynthetics, the Korean Geosynthetics Society and the International Geosynthetics Society: 330-337

Mitsui J, Hara K, Shibuya S (2006) Evaluating transmissvity (in-plane flow) of non-woven geo-textile and plastic drain. 41th Geotechnical Research Meeting, The Japanese Geotechnical Society: 1829-1830

Kohata Y, Tanaka M, Sato O, Hirai O (2006) Clogging evaluation on cross-plane flow performance of geotextile filter. Proceedings of the 8th International Conference on Geosynthetics (8IGS), The International Geosynthetics Society, Millpress 2: 561-564

Mitsui J, Hara K, Shibuya S (2007) Evaluating in-plane permeability of geosysnthetics in-soil. 42th Geotechnical Research Meeting. The Japanese Geotechnical Society: 1581-1582

Hara K, Mitsui J, Shibuya S (2007) Evaluating in-plane hydraulic conductivity of non-woven geotextile and plastic drain by laboratory test. The 5th International Symposium on Earth Reinforcement (Is Kyushu '07). New Horizons in Earth Reinforcement: 273-279

VACUUM-PVD COMBINATION WITH EMBANKMENT LOADING CONSOLIDATION IN SOFT BANGKOK CLAY : A CASE STUDY OF THE SUVARNABHUMI AIRPORT PROJECT

J. Saowapakpiboon [1], D.T. Bergado [2], J.C. Chai [3], N. Kovittayanon [4] and T.P. de Zwart [5]

ABSTRACT: A innovative improvement technique is currently applied for soft Bangkok clay combining capped PVD combine with vacuum pressure and embankment loading whereby the prefabricated vertical drains (PVD) are connected directly by PE tubes to a vacuum pump called " Vacuum-PVD System ". The method uses a surface soil layer as a sealing layer for leakage protection and there is no need to place air-tightening geomembrane sheets on the ground surface. This method has two advantages for situations of a) high air/water permeability layer exists near the ground surface, and b) combining vacuum pressure with embankment load. An actual field project combining PVD vacuum with embankment loading has just been completed. The performance data of the system during the improvement of the section EW-4, a part of the third runway of Suvarnabhumi International Airport, Thailand are presented and interpreted. The monitored data indicated that the system mobilized -60 kPa atmospheric pressure. This allowed for unprecedented loading and settlement rates during the construction of an embankment and achieved the required degree of consolidation within the specified time period.

KEYWORDS: improvement technique, Vacuum-PVD system, staged construction

INTRODUCTION

Vacuum consolidation was proposed in early 1950s by Kjellman (1952) and studies of vacuum induced consolidation continued up to the present (Holtz 1975; Choa 1989; Cognon et al. 1994; Bergado et al. 1998; Tang and Shang 2000; Chai et al. 2006a, b). Vacuum consolidation preloads the soil by reducing the pore pressure while maintaining constant total stress instead of increasing the total stress (Fig. 1). Fig. 1 clearly shows the increase of the effective stress as a result of the reduced atmospheric pressure in the soil mass. The net effect is an additional surcharge ensuring early attainment of the required settlement and an increased shear strength resulting in increased embankment stability. The Vacuum-PVD system is a new and innovative consolidation system based on the proven concept of vacuum consolidation. The vacuum drainage system (Fig. 2) is for advanced soil improve-ment whereby the vertical drains are connected via PE tubes to a vacuum pump (Cortlever et al. 2006). The vertical drains were specially developed CeTeau drains type CT-D911 which have a very high resistance against lateral pressure. This system has some big advantages over the standard vacuum drainage systems as follows:

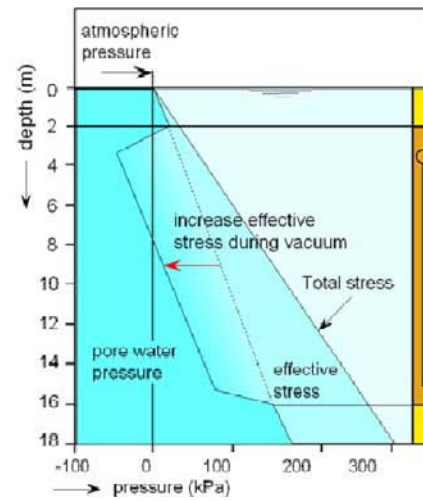

Fig. 1 Increase of effective stress

[1] Doctoral Candidate, School of Engineering and Technology, Asian Institute of Technology, THAILAND. Email: st103619@ ait.ac.th
[2] Professor, School of Engineering and Technology, Asian Institute of Technology, THAILAND. Email:bergado@ait.ac.th
[3] Professor, Department of Civil Engineering, Saga University, JAPAN. Email: chai@cc.saga-u.ac.jp
[4] General Manager, COFRA (Thailand) Co. Ltd., THAILAND. Email: @ceteau.com
[5] Project Manager, respectively, COFRA (Thailand) Co. Ltd., THAILAND. Email: @ceteau.com

- No liner needed that stay behind in the soil or has to be taken away
- Direct connection of every drain to vacuum pump without flow resistance
- No border trench needed
- No damage possible due to settlements
- Standard drain machines can be used
- No skilled labour needed
- Better control on functioning due to separate testing of the drain sections
- No drainage layer needed

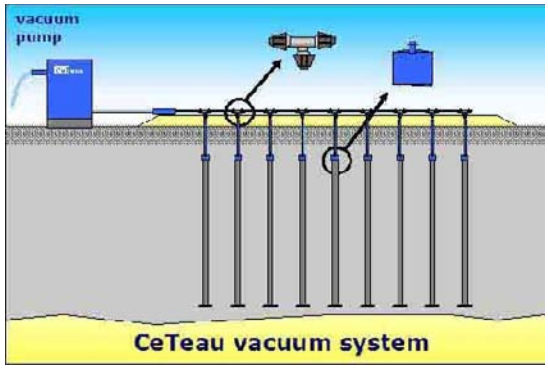

Fig. 2 Vacuum-PVD system

Vacuum-PVD SYSTEM

(1) *Structure of the Vacuum-PVD system*

A Vacuum-PVD unit consists of a piece of prefabricated vertical drain (PVD), a drainage hose and a cap connecting the PVD with the hose which it is connected by HDPE tubes as showed in Fig. 3. For the production shown in Fig. 2, the cap has a width the same as the PVD (106 mm), a length of 67 mm, and a thickness of 9 mm. The inside diameter of the hose is about 16 mm. The length of the PVD and the hose will be predetermined based on the information of site investigation and the required Vacuum-PVD will be manufactured in a factory and transported to the field. The Vacuum-PVD, the collection system, and the vacuum pumps are shown in Figs. 4 and 5.

(2) *Vacuum and embankment loading consolidation with Vacuum-PVD*

Consolidating a clayey deposit by vacuum pressure with PVD is illustrated in Figs. 6a and b. Fig. 6b shows the situation when there is a sand layer in the middle of a clayey deposit. To avoid vacuum pressure losses through this sand layer, a sealing sheet is pasted on the filter of the drain passing through the sand layer. Vacuum pressure was applied to the drain through the hose with a maximum value (p_{vac}) at just below the cap. The soil layer above the cap served as sealing layer of p_{vac} at the bottom to zero at the ground surface. The method of installation was the same as the normal PVD installation. An anchor plate was fixed at the end of the PVD and installed into the ground through a mandrel.

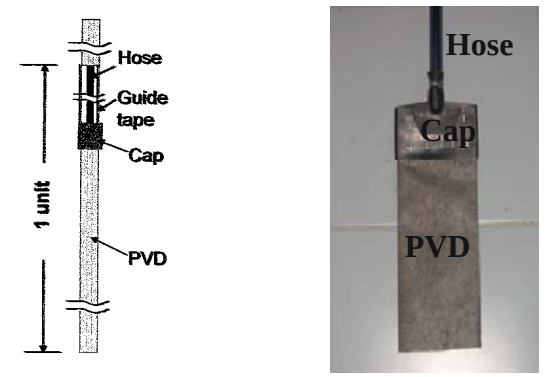

(a) Illustration (b) Actual Vacuum-PVD

Fig. 3 Structure of Vacuum-PVD

Fig. 4 Vacuum-PVD System

Fig. 5 Vacuum pump

The thickness of the surface sealing layer (H_s), can be estimated using a simple model, i.e., the vacuum pressure at the bottom of the layer is p_{vac} and zero at

the ground surface (Chai et al. 2006b)

$$H_s = \frac{p_{vac}}{\gamma_w Q_a} k_{air} A \quad (1)$$

where γ_w is the unit weight of water, k_{air} is the permeability to air flow of the sealing layer, A is the area of treatment, and Q_a is the capacity of a vacuum pump.

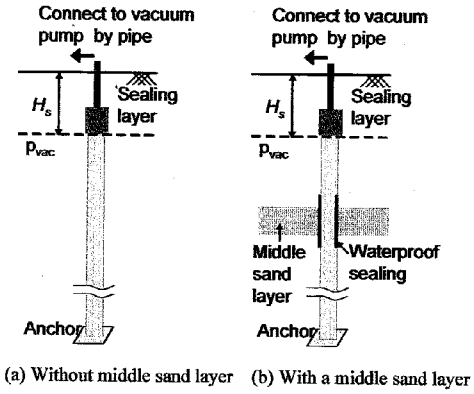

Fig. 6 Vacuum consolidation with CeTeau PVD

The increase of the effective stress for a conventional surcharge at time, t_1, can be written according to Eq. 2. When combining the same surcharge with vacuum consolidation the increase in effective stress can be calculated using Eq. 3.

$$\Delta\sigma'(t_1) = U(t_1)\cdot\Delta\sigma_s \quad (2)$$

$$\Delta\sigma'(t_1) = U(t_1)\cdot\Delta\sigma_s + U(t_1)\cdot p_v = U_{eq}(t_1)\cdot\Delta\sigma_s \quad (3)$$

In which $U(t_1)$ is the degree of consolidation at t_1, $\Delta\sigma_s$ is the surcharge, p_v is the vacuum pressure and $U_{eq}(t_1)$ is the equivalent degree of consolidation at t_1.

As $U_{eq}(t_1)$ will exceed $U(t_1)$ for all $t > 0$, the increase of the effective stress for a combination of surcharge and vacuum consolidation will always be more than for a situation with a surcharge only.

(3) *Settlement due to vacuum consolidation with Vacuum-PVD*

With the reduction of the consolidation period, it becomes increasingly important to monitor the development of the settlements with time and to accurately predict the final settlement in an early stage of the consolidation process as the time for corrective measures is generally limited. Asaoka (1978) has proposed a simple method to predict the final settlement based on settlement observations at fixed time intervals. By plotting consecutive readings $z(t)$ against $z(t+1)$ a line will be obtained which, over a large interval, can be represented by the linear function :

$$z_{t+1} = \beta z_t + A \quad (4)$$

where β = slope of the linear section of the best fit [-];
A = intersection of the extrapolated section of the linear fit with the Y-axis.

A few so-called Asaoka lines, representing various loading stages are been depicted in Fig. 7a.

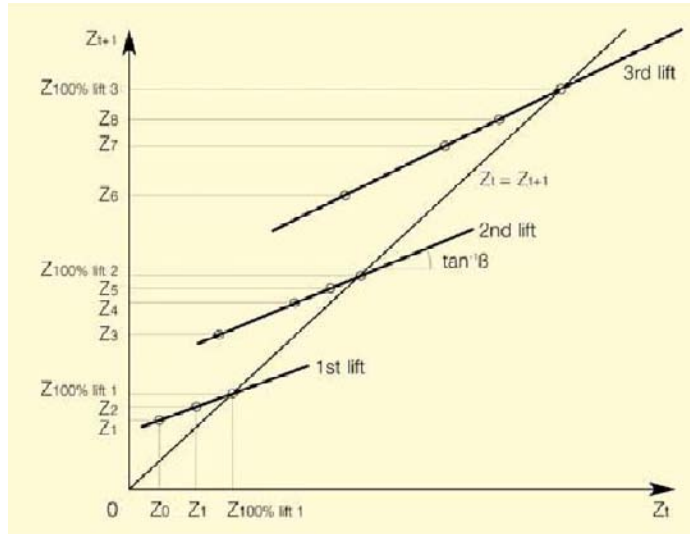

(a) Asaoka lines

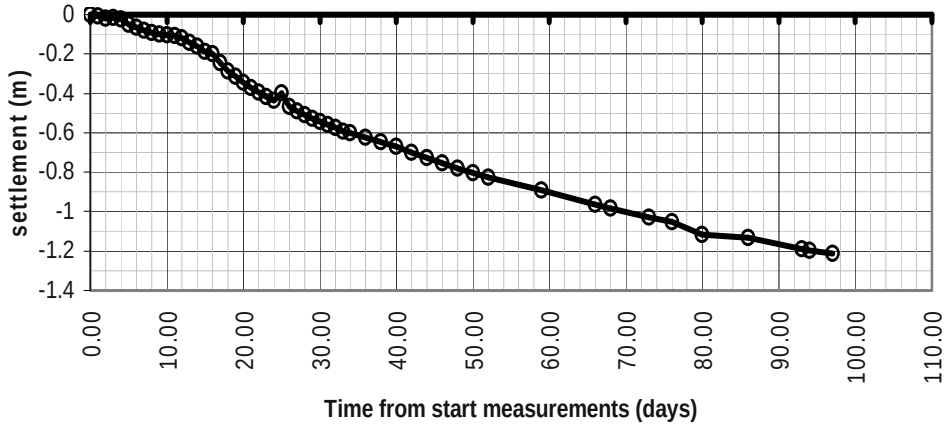

(b) Total settlement from Asaoka method

Fig. 7 Asaoka lines and Total settlement from Asaoka method

The intersection point of the extrapolated section of this straight line and the line $z(t)=z(t+1)$ will define the total final settlement at the moment full consolidation has been reached (see Eq. 5.

$$Z_{100\%} = \frac{A}{1-\beta} \tag{5}$$

The tangent of the plotted line can be related to the equivalent consolidation coefficient c_{eq} (consolidation coefficient accounting for the joint effect of the horizontal and vertical drainage of pore water) by applying the following formula:

$$C_{eq} = \frac{-5 \cdot H^2 \cdot \ln \beta}{12 \cdot \Delta t} \tag{6}$$

where H = length of drainage path (m)
Δt = time interval (s)

A FIELD PROJECT OF VACUUM AND EMBANKMENT LOADING CONSOLIDATION WITH VACUUM-PVD

(1) Description of the Project

A project combining vacuum and embankment loading consolidation with Vacuum-PVD at Suvarnabhumi Airport, Thailand was reported by COFRA (1996). The soil profile at the site can be divided into 8 sublayers as shown in Table 1 and Fig. 8. It consists of a 2.0 m thick weathered clay layer overlying very soft layer which extends from 2.0 m to 10.0 m depth (very soft clay 1 and very soft clay 2). Underneath the soft clay layer, a 2.0 m thick medium clay layer can be found. The light-brown stiff clay layer can be encountered at 15.0 m to 30.0 m depth. The groundwater level was found at about 0.50 m depth.

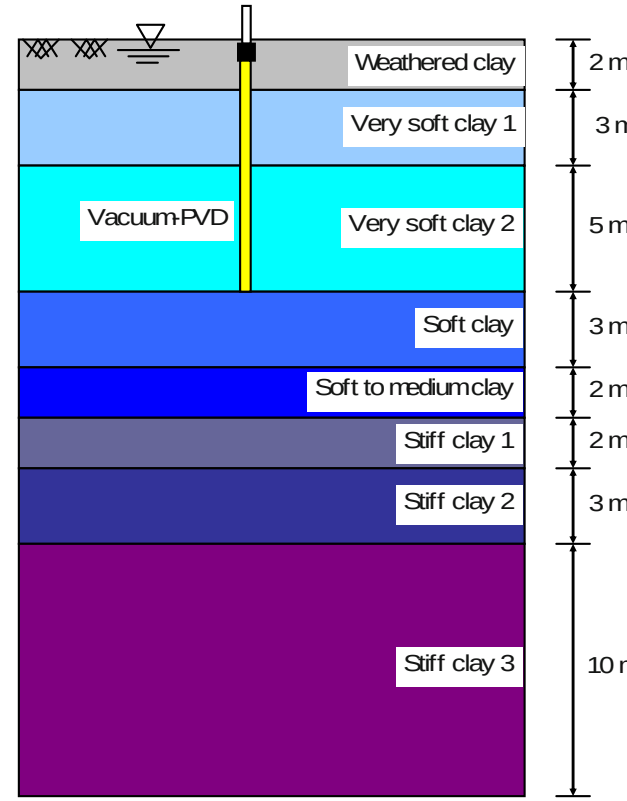

Fig. 8 Soil profile and the depth of Vacuum-PVD

In Table 2, the effective overburden pressure (*POP*) was derived from the given OCR value. The numbers are rounded and taken as an average value of each layer. The consolidation coefficient is estimated from an article by Athanasiu et al. (1999). In this article the C_v as function of the effective stress has been back-calculated from settlement data and from a case history on the terrain of the SBIA Project. The CR/C_a correlation is estimated to be 25.

Table 1 The stratigraphy at the site

Present surface	0.00 m	
Water level	-0.50 m	
Type	Top layer (m)	Bottom layer (m)
Top layer, weathered clay	0.00	-2.00
very soft clay1	-2.00	-5.00
very soft clay2	-5.00	-10.00
soft clay	-10.00	-13.00
soft to medium clay	-13.00	-15.00
stiff clay1	-15.00	-17.00
stiff clay2	-17.00	-20.00
stiff clay3	-20.00	-30.00

Table 2 The compressibility consolidation parameters.

Type	Unit weight [kN/m^3]	Compressibility			*POP* (kPa)	C_v_theory [m^2/year]
		RR	*CR*	C_a		
Top layer, weathered clay	18.50	0.035	0.350	0.014	30	-
very soft clay1	13.80	0.050	0.500	0.020	20	0.79
very soft clay2	14.00	0.042	0.420	0.017	30	0.79
soft clay	15.00	0.040	0.400	0.016	60	0.79
soft to medium clay	15.70	0.030	0.300	0.012	80	0.79
stiff clay1	18.50	0.008	0.080	0.003	300	-
stiff clay2	19.00	0.008	0.080	0.003	500	-
stiff clay3	20.40	0.000	0.000	0.000	500	-

Note:

POP = effective overburden pressure
CR= compression ratio
RR= recompression ratio
C_a = creep coefficient
C_v= vertical consolidation coefficient

The Vacuum-PVD was installed into 10 m depth with a spacing of 0.85 m and arranged in a triangular pattern (Fig. 9a, b). The instrumentation equipment is installed to monitor this system. Only the readings of the piezometers, the vacuum gauges on the pumps, the piezometer outside the drains and the settlement, are discussed in the analysis. All monitoring equipments installed at EW4 are given in Fig. 10. The following equipments are installed, namely: 2 piezometers (below 5.0 m from ground surface level), 8 settlement plates, and 2 settlement plates for internal use (0.5 m from ground surface level).

The following boundary conditions were used in the design: Installation time of drains=2 months, maximum pumping time=4 months, vacuum pressure of -60 kPa, depth of drains 10 m below ground present surface, 60 % consolidation requirement.

The embankment was 2.8 m (18 kN/m^3) and Foundation 1.0 m. Embankment was constructed in two phases, namely: Phase 1 (1.5 m, day 0) and Phase 2 (1.3 m, day 14). These assumptions are not based on calculations.

At the site, the work of installing Vacuum-PVD was carried out from May 7 to May 28, 2005. Installation date and initial reading date began on June 8, 2005 and ended on September 13, 2005 (vacuum and embankment loading consolidation). Before starting, a thorough soil investigation was done to check the movement of the settlement plates with the predicted settlements based on calculations of the consolidation process. The area that has to be treated was marked and the level was measured.

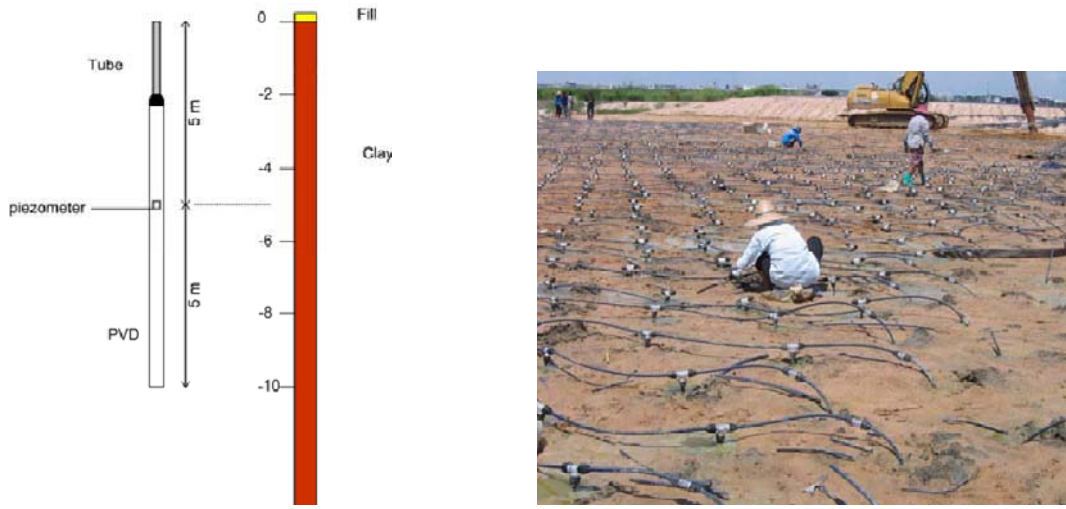

(a) The depth of the PVD and piezometer installation (b) The triangular pattern of the PVD

Fig. 9 The depth of the PVD and piezometer installation and the triangular pattern of the PVD

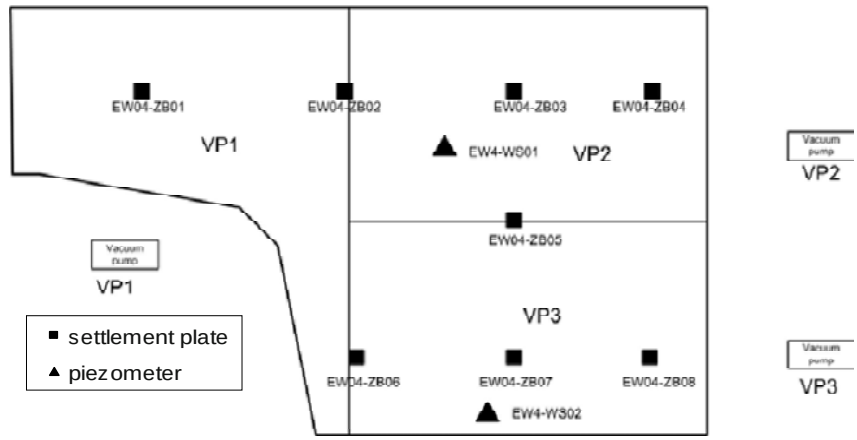

Fig. 10 Layout of the improved area and instrumentation points for EW-4

If the bearing capacity of the top layer was sufficient, the drain pattern can be set out. If the bearing capacity was not sufficient, a working platform of 0.5m thickness had to be made.

After setting out the drain locations, the installation was started. The drains were prefabricated on length before installation. The Vacuun-PVD, CT-D911, was supplied on rolls of 300 m. They were cut on a length which is 1 m shorter than the layer thickness that had to be consolidated. On one end, an anchor plate was connected to the drain. On the other end a 16 mm HDPE tube was inserted in the drain over a length of 0.5 m. The tube was connected to the drain with steel clips that were attached with electric powered equipment. The tube was able to resist 200 kPa pressure. The prefabricated drains were transported from a central assembly plant to the rigs.

The drains were pulled in at the bottom of the mandrel with a rope that was attached to the HDPE until the anchor plate touches the bottom of the mandrel. The mandrel was positioned above an installation point and pushed to the required depth and withdrawn. To be sure that the drain was not partly pulled back the end of the tube that was sticking out has to be measured. If the hole stays open, it was filled with clay slurry to assure that the drains were sealed of from the atmosphere. The crane was operated such that it cannot drive over the tubes to avoid damages. After completion of a determined section, the drains were connected to a central suction tube and tested for air tightness. The configuration of the tubing depends on the shaped and size of the area. After completion of the tubing system, it was tested and repaired if necessary.

Every 3,000 m^2 area was connected to a special vacuum pump that consists of a tank capable of resisting 150 kPa pressure. A 100 m^3 air pump and a 40—100 m^3 water pump were connected to the tank to get rid of the air, water vapour and pore water. The water was pumped on the treated area to increase the dead weight of the surcharge and avoid drying out of the top crust. When no surcharge was placed a maximum vacuum of 50 kPa was allowed to avoid formation of water vapour and other gases in the soil. Gases can block the permeability and thus decreased the rate of consolidation. After completion of 2.8 m surcharge, the full vacuum was applied that varied from -70 to -90 kPa at the tank to -50 to -60 kPa at the end of the drain. The pumps provided with a GSM warning system so that disturbance in the suction period was minimized. The pumps operated continuously (168 hours/week) and were tested every week during operation.

Settlement plates were placed between the tubes and were monitored. After completion, the permanent fill of 1.5m (settlement + final fill + surcharge) was placed. The settlements were measured during the filling stages and after completion of the surcharge until the required settlements were reached. During monitoring, -60 kPa vacuum was maintained in the vertical drains up to a minimum depth of 5 m and created 60% settlement (defined as the ratio of the current settlement to the project final settlement estimated from Asaoka method) while full surcharge and vacuum were applied to the soil, within a period of 6 months.

(2) Results of Measurement

The measured pressures between the start of the measurements and final reading as of 13 September 2005 are presented in this section which followed the construction time (Fig. 11). In this section, only the piezometer readings are given (Fig. 12). The pump pressures with no piezometer attached will be presented in the next section (Fig. 13). The vacuum has increased to -90 kPa under pressure on the pump and a more than -60 kPa inside the drains.

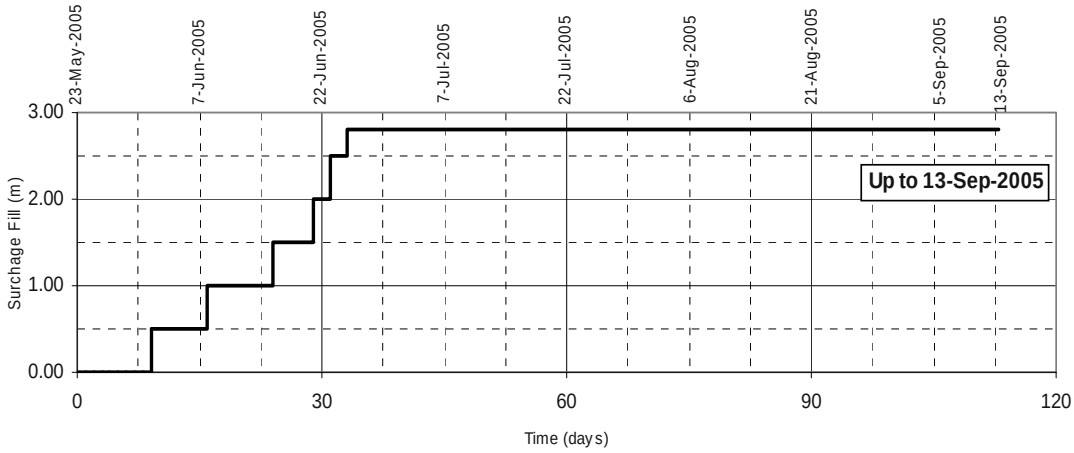

Fig. 11 Variation of total embankment height with time

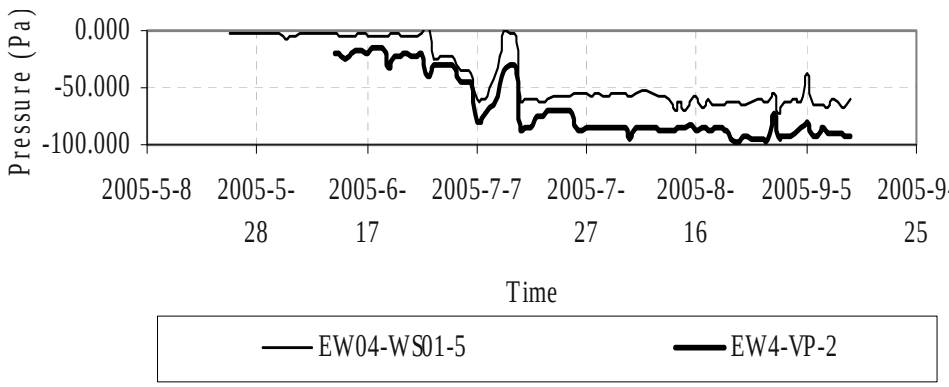

Fig. 12 Variation of vacuum gauge pressure with time with piezometer

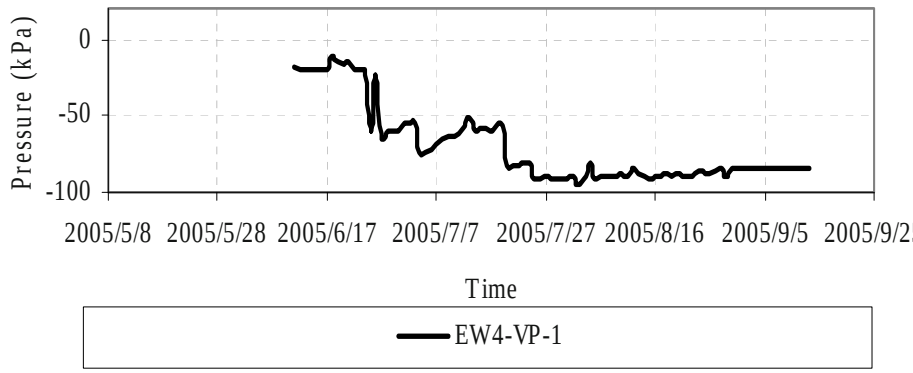

Fig. 13 Variation of vacuum gauge pressure with time with no piezometer

The latest readings of the pump and the piezometer show stabilized data with very high vacuum pressures ranging from -86 kPa to -92 kPa on the pumps at the time when the surcharge reached 2.8 m on 25 June 2005. The total time the pumps were running during this period, almost all pumps were running more than 99% of the time. The acceptance criterion shall be based on the degree of settlement (defined as the ratio of the current settlement to the projected final settlement estimated from the Asaoka method) with a value of no less than 60% while full surcharge and vacuum were applied to the subsoil. To explain how the degree of consolidation was calculated, a short theoretical paragraph is written below. With this theory, areas with a low vacuum pressure can be confirmed using a different degree of consolidation.

The consolidation theory by Terzaghi states that the local degree of consolidation $U_{(z,t)}$ is written as:

$$U_{(z,t)} = (\Delta u_0 - \Delta u_{(z,t)}) / \Delta u_0 \qquad (7)$$

The initial excess pore pressure Δu_0 is in this formula equal to the added load, $\Delta \sigma_v$. This means that in the initial situation, with a degree of consolidation of 0%, 0% of the added load is carried by the soil and 100% of the load is carried by the water. In this stage, no settlement has taken place. If a degree of consolidation of 100% is reached, 100% of the added load is carried by the soil, all the excess pore water has dissipated and all the settlement has taken place.

Reworking the formula with the initial excess pore pressure Δu_0 equal to the added load $\Delta \sigma_v$, the formula describing the degree of consolidation can also be written as:

$$U_{(z,t)} = (\Delta \sigma_v - \Delta u_{(z,t)}) / \Delta \sigma_v \qquad (8)$$

Eq. (8) shows that the degree of consolidation times the added load is equal to the actual percentage the effective stress increase in the subsoil ($\Delta \sigma_v - \Delta u_{(z,t)}$).

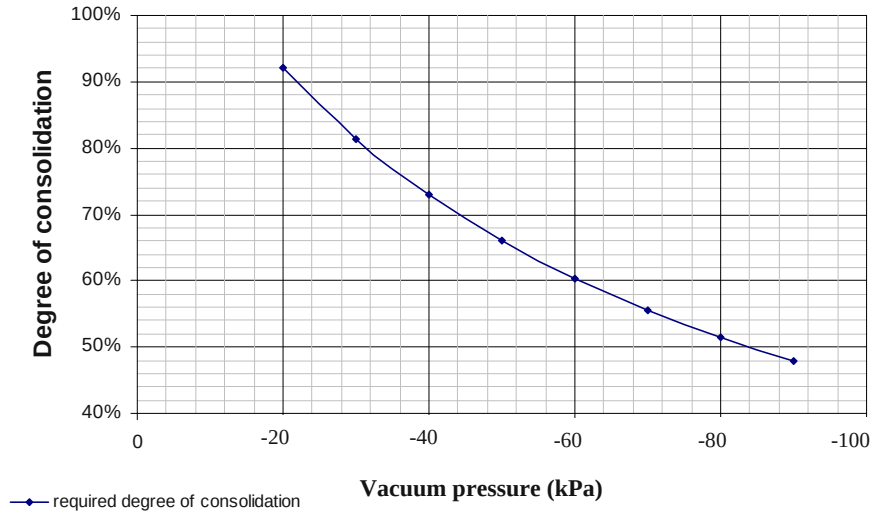

Fig. 14 Relationship between degree of consolidation and under pressure

If the required acceptance criterion with a degree of consolidation $U_{(z,t)}$ of 60% and a load $\Delta\sigma_v$ of 116 kPa is used, the excess pore pressure $\Delta u_{(z,t)}$ becomes 46 kPa. This means that 116-46 = 70 kPa of the load is carried by the subsoil and the increase of the effective stress $\Delta\sigma'$ in the soil is 70 kPa. Thus, it can be concluded that the aim of the soil improvement is to increase the effective stress in the soil by 70 kPa. If a lower vacuum pressure is applied to the subsoil than the required -60 kPa under pressure, the calculated increase in the effective stress can be used to calculate the needed degree of consolidation (Fig. 14) is as follows:

With the actual settlement and the Asaoka prediction of the final settlement the degree of consolidation can be calculated. Table 3 gives the summary of the Asaoka measurements.

The final settlement of EW4 has reached in between 0.91 m and 1.21 m with a degree of consolidation of 66% to 80% (Fig. 15). The settlement on settlement plates EW4-ZB06 to EW4-ZB08 was lower due to their location on a canal. Underneath the canal area less compressible material was present, reducing the settlement. All the settlement plates met the required degree of consolidation.

Table 3 Summary of the Asaoka calculations (values can vary due to incorporation of new measurements and the variability of the Asaoka method)

	Average vacuum on pump during last month [kPa]	Date measurement [-]	Final settlement [cm]	Final settlement based on the Asaoka prediction [cm]	Degree of consolidation [-]
EW4-ZB01	-87	13-9-2005	121	171	71%
EW4-ZB02	-87	13-9-2005	104	157	66%
EW4-ZB03	-89	13-9-2005	115	162	71%
EW4-ZB04	-89	13-9-2005	119	163	73%
EW4-ZB05	-89	13-9-2005	110	147	75%
EW4-B06*	-93	13-9-2005	91*	114	80%
EW4-B07*	-93	13-9-2005	93*	119	78%
EW4-B08*	-93	13-9-2005	101*	125	80%

- Settlement plate located on old canal (thickness of compressible material was less)

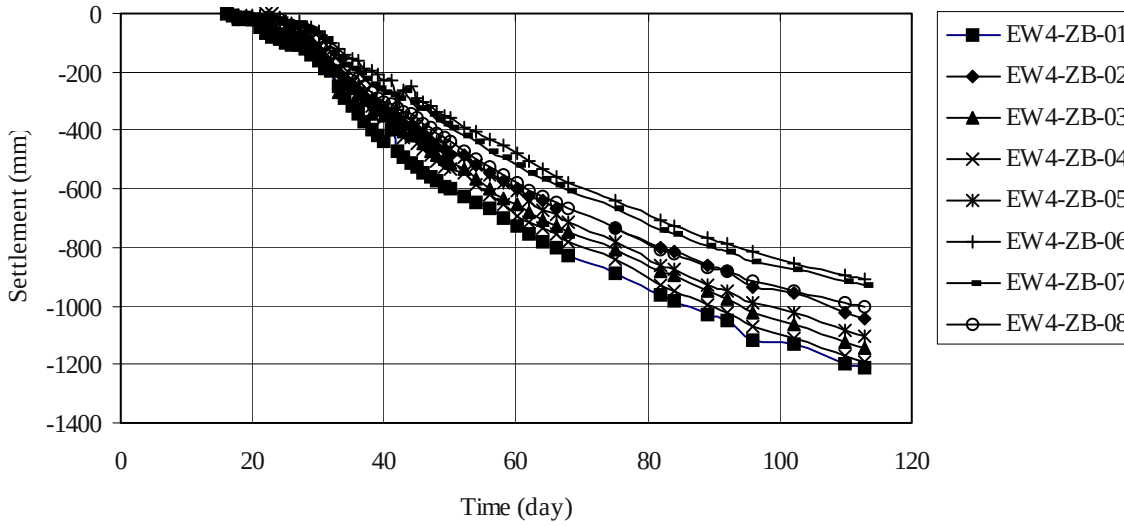

Fig. 15 Final observed settlement of each position of EW4

CONCLUSIONS

Based on the data and results of the analyses, the following conclusions can be made:

(1) The Vacuum-PVD System is a new improvement technique and was currently applied for soft Bangkok clay combining capped PVD with vacuum pressure and embankment loading whereby the prefabricated vertical drains (PVD) are connected by HDPE tubes to a vacuum pump. No need to place air-tightening geomembrane sheets on the ground surface.

(2) This method has two advantages for situations when: a) high air/water permeability layer exists near the ground surface, and b) combining vacuum pressure with embankment load.

(3) Average vacuum pressure of -50 to -60 kPa at PVD and -70 to -90 kPa at the vacuum pump were obtained.

(4) The final settlement 0.91 m to 1.21 m with a degree of consolidation of 66% to 80% were achieved.

(5) The Vacuum-PVD System reduced the time of consolidation by more than 50 %.

ACKNOWLEDGEMENTS

Heartfelt thanks are due to CeTeau FarEast and COFRA (Thailand) Co. Ltd. for supporting the research project. The cooperation of the Airports of Thailand (AOT) and the New Bangkok International Airport (NBIA) are highly appreciated. Lastly, many thanks also to Mr.Phatthana Pansaen who give information and data of field measurements.

REFERENCES

Asaoka A (1978) Observational procedure of settlement prediction. Soils and Foundations 18(4): 87-101

Athanasiu (1999) Analyses of Full-Scale field test results for the design of ground improvement at the New Bangkok International Airport. Geotechnical Engineering for Transportation Infrastructure. Barends et al. (eds). UK: Taylar and Francis.

Bergado DT, Chai JC, Miura N, Balasudramaniam AS (1998) PVD improvement of soft Bangkok clay with combine vacuum and reduced sand embankment preloading. Geotechnical Engineering Journal 29(1): 95-121

Chai JC, Carter JP, Hayashi S (2006a) Vacuum consolidation and its combination with embankment loading, Canadian Geotechnical Journal 43: 985-996

Chai JC, Miura N, Bergado DT (2006b) Preloading clayey deposit by vacuum pressure with cap-drain. Proceeding 21st Japanese Geosynthetic Symposium. Aomori, Japan

Choa V (1989) Drains and vacuum preloading pilot test. Proceeding 12th International Conference on Soil Mechanics and Foundation Engineering, Riode Janeiro. Brazil: 1347-1350

Cofra (Thailand) (1996) Design and Proposal for the Execution of a Test Field : Vacuum Consolidation for the Landslide Road System for Second Bangkok International Airport, Bangkok, Thailand

Cognon JM, Juran I, Thevanayagam S (1994) Vacuum consolidation technology: Principles and field experience. Proceedings Vertical and Horizontal Deformations of Embankments (Settlement'94), ASCE Special Pablication 40(2): 1237-1248

Corlever NG, Visser GT, De Zwart TP (2006) PVD ground improvement with vacuum preloading at Suvarnabhumi Airport. Proceedings International Symposium Geotechnical Aspects of Suvarnabhumi Airport, Bangkok, Thailand

Holtz RD (1975) Preloading by Vacuum: Current Prospects. Transportation Research Record. Washington, D.C., U.S.A. 548: 26-69

Kjellmann W (1952) Consolidation of clay soil by Means of Atmospheric Pressure. Proceedings on Soil Stabilization Conference, Boston, U.S.A.

Luger HJ, Nooy VD, Kolff AH (1999) Geotechnical design and behaviour of the Kertih Breakwater. Geotechnical Engineering for Transportation Infra-structure, Barends et al. (eds), Balkema

Tang M, Shang JQ (2000) Vacuum Preloading con-solidation of Yaogiang Airport runway Geo-technique 50(6): 613-653

Proceedings of the 4th Asian Regional Conference on Geosynthetics
June 17 - 20, 2008 Shanghai, China

THE PERFORMANCE OF ALTERNATIVE GEOCOMPOSITES FOR DRAINAGE UNDER LABORATORY AND FIELD CONDITIONS

C.A. Silva[1], E.M. Palmeira[2] and A.R.L. Silva[3]

ABSTRACT: This paper presents a study on the use of geotextile filter in combination with alternative drainage materials in geotechnical and geoenvironmental works. Laboratory and field tests were performed using water and leachate as fluids, respectively. The alternative drainage materials consisted of PET bottle caps, tire strips and whole tires. Laboratory tests consisted of transmissivity tests under stress and the field experiments consisted of monitoring the performance of instrumented domestic waste cells with granular and alternative drainage systems. The results obtained show the potentials of the use of alternative drainage materials in combination with geotextile filters.

KEYWORDS: geosynthetics, drainage, transmissivity, alternative materials, geocomposites

INTRODUCTION

The use of geosynthetics for drainage in geotechnical and geoenvironmental works has increased markedly during the last decades. By being manufactured these products present repeatable and reliable hydraulic properties, besides providing faster and cheaper construction conditions than traditional granular materials. The application of geocomposites for drainage can cover a wide range of engineering works such as drainage and collection systems in landfills, drainage of pavements, dams, retaining structures, agricultural applications, among others.

Normal stresses imposed to the geocomposite during construction and operation of the draining system can cause alterations on its hydraulic properties. High embankments can induce high normal stressed on the geocomposite. This is particularly so in the case of the use of such materials in the mining industry.

In some countries the cost of a geocomposite can be prohibitive, mainly due to the cost associated to its core element, particularly in small engineering works. Therefore, some alternative low cost or less stiff conventional core materials can be combined to geotextile filters to provide a cheaper final geocomposite product.

This paper investigates the performance of some alternative low cost geocomposite materials under laboratory and field conditions.

METHODS AND MATERIALS

Research Programme

The research programme consisted of laboratory and field tests on geocomposites or drainage systems made by the combination of a geotextile filter and different types of core materials. The alternative materials tested comprised PET bottle caps, tire strips and whole tires, depending on the experiment considered.

Transmissivity (θ) is one of the most important hydraulic properties of a geocomposite, being defined as the product of the in plane geocomposite hydraulic conductivity (k_p) by its thickness (t_G). Transmissivity tests under varying stress levels were performed in the laboratory, whereas in the field the performance of instrumented experimental waste cells was monitored for a period of two years. Clean deaired water was used in the laboratory, whereas raw leachate was employed in the field tests.

Tests in the Laboratory

Laboratory testing equipment

Transmissivity tests were performed to investigate the hydraulic performance of geocomposite materials under high normal stresses. The apparatus used was built at the University of Brasilia, Brazil, following the recommendations presented in ASTM D4716 (ASTM 1995) and is shown in Fig. 1.

[1] Research Student, Dept. of Civil and Environmental Eng, University of Brasilia, BRAZIL. Email: cassioasilva@unb.br
[2] Professor, Dept. of Civil and Environmental Eng., University of Brasilia, BRAZIL. Email: palmeira@unb.br
[3] Associate Professor, Dept. of Civil Eng., State University of Maranhao, BRAZIL. EMail: arls2005@ig.com.br

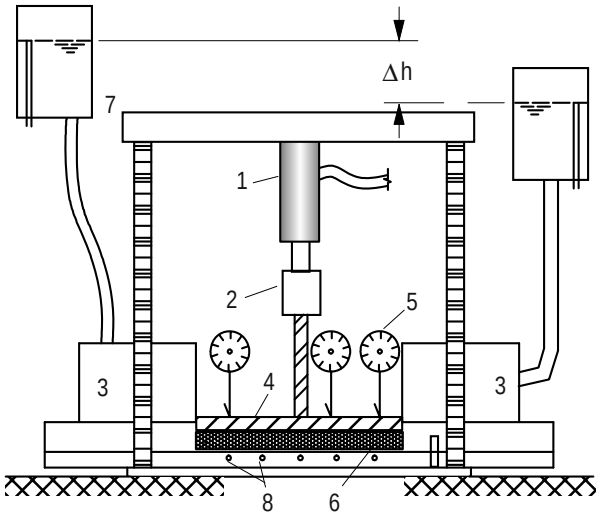

1 - Jack; 2 - Load cell; 3 - Lower water reservoirs; 4 -Loading platten; 5 - Dial gauges; 6 - Specimen; 7 - Upper reservoir; 8 - Ports.

Fig. 1 Equipment used in the transmissivity tests.

The geocomposite specimen is accommodated in a 42 mm high steel cell and the specimen dimensions are 300 mm × 300 mm. Two water reservoirs at different elevations provide water flow under a controlled hydraulic gradient. A rigid steel plate transmits the normal stress to the geocomposite specimen and rubber layers and silicone grease were used at the interfaces to avoid preferential flow along the specimen boundaries and to account for the influence of sagging effects. A jack connected to a hydraulic system provides the vertical load to the specimen which is measured by a load cell. Dial gauges allowed for the measurement of the compression of the geocomposite under stress. The loading system is capable of applying normal stresses to the specimen up to 400 kPa.

The hydraulic gradient of 0.5 use in the tests. Five ports installed along the side wall of the transmissivity cell allow the measurement of hydraulic water heads along the specimen length, which is useful to assess non uniformities of hydraulic properties of geosynthetics products (Gardonie Palmeira 1999).

Materials used in the laboratory tests

The alternative low cost geocomposites were formed by the combination of nonwoven geotextile filters and two types of core elements. One of the core elements consisted of PET bottle caps (Fig. 2) and the other was made of tire strips forming a grid like structure (Fig. 3). Table 1 summarises the geometrical and physical characteristics of the geocomposite materials tested. Besides being cheaper than conventional core materials, the utilization of these materials has a positive repercussion on environmental protection. It is well known that the disposition of tires in landfills can pose serious threats in case of fires or can favour the proliferation of insects and other animals that are harmful to human health. Besides, the use of bottle caps or tire strips also allows the investigation of the influence of the compressibility of the core material on the geocomposite hydraulic properties.

For the geocomposites with cores consisting of bottle caps (2.61 cm diameter, 1.45 cm high), the distances between the external faces of adjacent caps were equal to 0.6 cm, 4 cm and 10 cm (Figs. 2a to 2c). In the case of geocomposites with cores made of tire strips, the strips were in average 2 cm wide and 0.9 cm thick. The values of internal distances between strips (aperture sizes) for geocomposites GTS1and GTS2 were equal to 12 cm and 5 cm (Figs. 3a and 3b), respectively.

Table 1 Characteristics of the materials tested

Code	Combination of elements (see Notes)	Mass per unit area (g/m^2)	Thickness t_G (mm)
GCBC1	G1 – T1 – G1	2020	19.4
GCBC2	G1 – T2 – G1	1620	19.4
GCBC3	G1 – T3 – G1	850	19.4
GCTS1	G1 – P1 – G1	6080	22.0
GCTS2	G1 – P2 – G1	9095	23.0

Notes: Meaning of codes: GCBC = GeoComposite with Bottle Caps and GCTS = GeoComposite with Tire Strips; G1 = nonwoven geotextile made of polyester (μ = 200 g/m^2, t_{GT} = 1.9 mm); GCBC1 = 0.6 cm distance between caps external faces; GCBC2 = 4 cm distance between caps; GCBC3 = 10cm distance between caps; GCTS1 = 2 cm wide tire strips with 12 cm aperture size; GCTS2 = 2 cm wide tire strips with 5 cm aperture size.

Humphrey et al. (1997) studied the use of shredded tires having found deformations between 25% and 50% for normal stresses ranging from 48 kPa to 483 kPa. Other tests yielded hydraulic conductivities of tire shreds between 0.6 cm/s and 24 cm/s, for shreds sizes between 12 mm and 75 mm. Thus, tire shreds would certainly be permeable enough to be also considered as a core material for low cost geocomposites. However, in practice the manufacture of geocomposites with tire shreds as core would be considerably more complicate than those reported in this paper.

Additional information on the laboratory experiments can be found in Silva (2007).

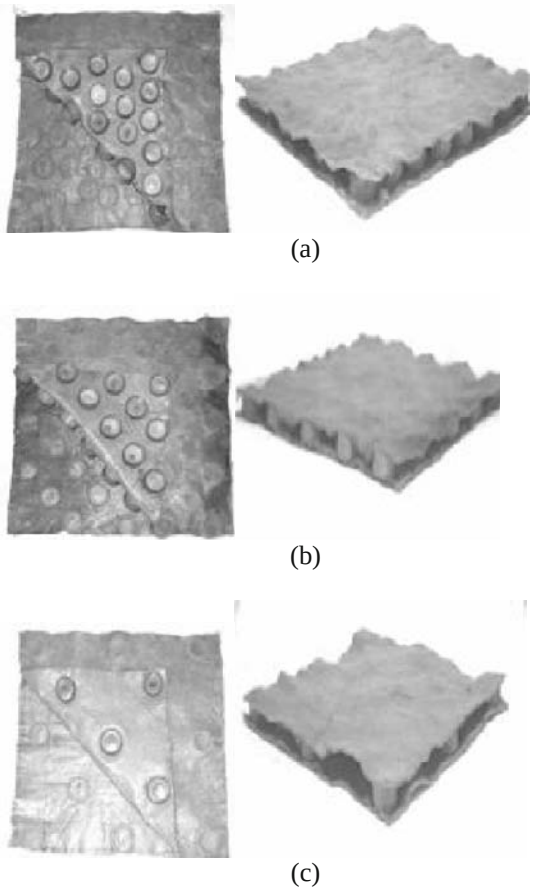

Fig. 2 Geocomposites with cores composed of PET bottle caps: (a) GCBC1, (b) GCBC2 and (c) GCBC3

Field Tests

The field experiments consisted of monitoring instrumented experimental waste cells filled with approximately 50ton of domestic waste. Therefore, the conditions were very different from those in the laboratory tests, particularly because in this case the fluid was leachate. The geometrical characteristics and a view of the cell during construction are presented in Fig. 4a and b. The drainage system at the bottom of the cell consisted of whole tires with a geotextile filter. The geotextile filter used was a nonwoven, needle-punched, geotextile made of polyester, with mass per unit area of 150 g/m^2 and thickness of 1.5 mm. The normal permeability and filtration opening size of the geotextile filter were equal to 0.4 cm/s and 0.15 mm, respectively. The drainage trench (Fig. 4a) in the middle of the cell base was filled with tire shreds (D_{90} = 45 mm, C_U = 1.5, where D_{90} is the diameter for which 90% in mass of the particles are smaller than that value and C_U is the uniformity coefficient). For comparison purposes, another instrumented waste cell was constructed with the same dimensions, but with a drainage layer at the bottom consisting of a 20 cm thick gravel layer (D_{85} = 65 mm, C_U = 1.2 and hydraulic conductivity equal to 24 cm/s).

The waste used to fill the experimental cells was obtained from a landfill 30 km away from the city of Brasilia, Brazil. Waste from the same origin was used to minimise the influence of waste variability on the test results. The waste average composition was: organic matter (49% in weight), plastics (18%), paper (13%), cardboard (9%), metals (2%) and others (9%). It should be noted the large amount of organic matter present, which is typical of Brazilian landfills (Junqueira 2000).

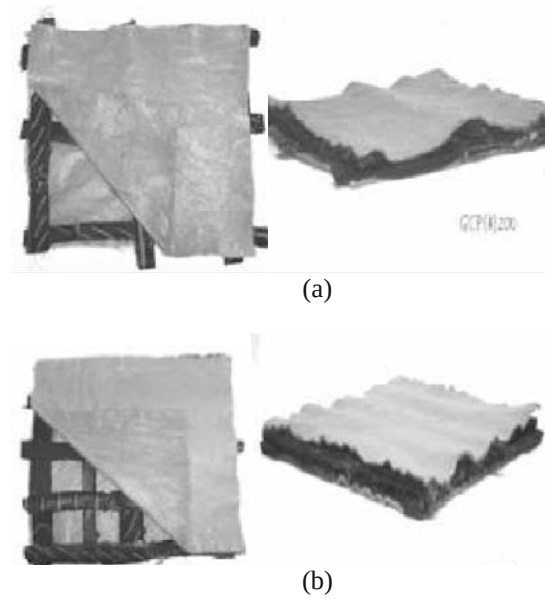

Fig. 3 Geocomposites with cores composed of tire strips: (a) GCTS1 and (b) GCTS2

The instrumentation of the waste cells consisted of settlement plates and temperature transducers installed at different locations (Fig. 4a). Measurements of effluent volume with time were also carried out as well as periodical chemical analysis of the leachate. A rain gauge measured the precipitation on the site, which allowed relating precipitation to leachate production with time.

Additional information on the characteristics of the materials used and test methodology can be found in Silva (2004).

RESULTS OBTAINED

Laboratory Tests

Figs. 5 and 6 present results of discharge capacity versus normal stress for the geocomposite materials tested. As expected, the discharge capacity decreases with increasing stress levels.

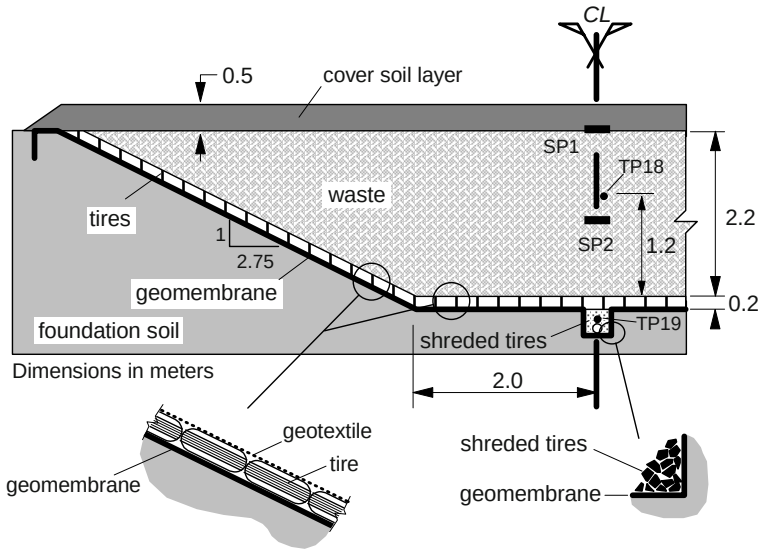

(a) Experimental cell cross-section

(b) View of cell construction before and after the geotextile installation

Fig. 4 Instrumented experimental waste cell.

For the tests on geocomposites with PET caps as core materials, a greater reduction of discharge capacity can be observed for GCBC2 and GCBC3 for normal stresses above 100 kPa (Fig. 5), associated with the compression of the caps. Geocomposite GCBC1 was rather insensitive to the range of stress applied due to the greater number of bottle caps per unit area in this case. The greater intrusion of the rubber membrane used in the tests in between bottle caps (sagging) in tests on geocomposites GCBC2 and GCBC3 was certainly also in part responsible for the smaller discharge capacities of these geocomposites in comparison to GCBC1.

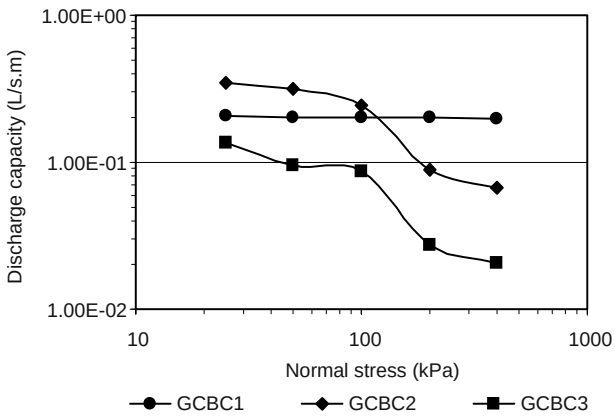

Fig. 5 Discharge capacity versus normal stress – Geocomposites with core composed of PET bottle caps

The results obtained for the geocomposites with cores made of tire strips are presented in Fig. 6. It can be seen that the discharge capacity of GCTS1 was influenced by the normal stress earlier in the test. This was due to the large spacing between the tire strips of this geocomposite in comparison to GCTS2.

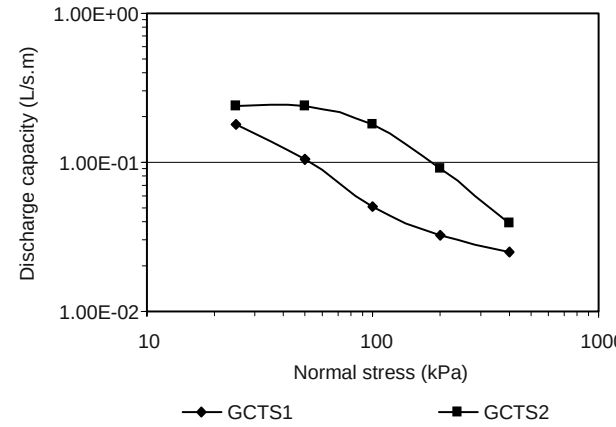

Fig. 6 Discharge capacity versus normal stress – Geocomposites with core composed of tire strips

The variations of geocomposite thickness with normal stress are presented in Figs. 7 and 8. These tests were compression tests only, using the transmissivity test apparatus, but without the use of the rubber layers, that would influence the results. For the geocomposites with cores formed by PET bottle caps, the greater the spacing between strips the larger the geocomposite compressibility, as shown in Fig. 7, which is consistent with the results obtained for discharge capacity. This was particularly so for geocomposite GCBC3. The results obtained for geocomposites GCBC1 and GCBC2 were close up to a normal stress of 200 kPa.

Fig. 8 presents the variation of geocomposite thickness with normal stress for the geocomposites with cores formed by tire strips. It can be seen that the rate of compression was greater up to approximately 100 kPa normal stress. This is in great part due to the initial accommodation of the core, because the thickness of the

tire strips was not uniform. This caused some gaps between the lower strip surface and the flat base plate of the testing cell, increasing core compressibility.

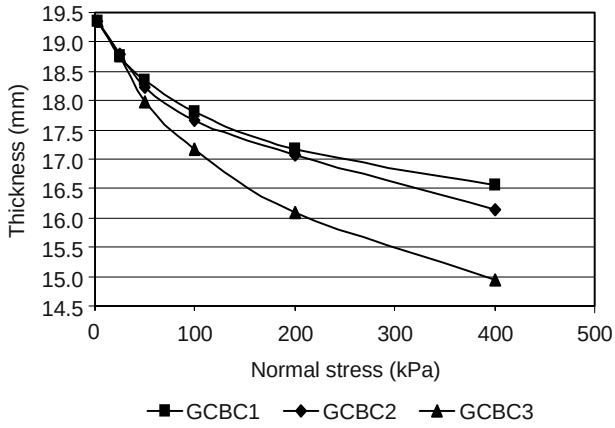

Fig. 7 Geocomposite thickness versus normal stress – Geocomposites with core composed of PET bottle caps

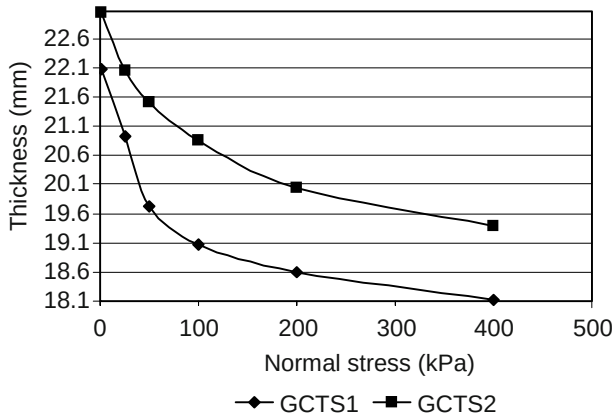

Fig. 8 Geocomposite thickness versus normal stress – Geocomposites with core composed of tire strips

Field Test Results

Fig. 9 shows results of cumulative effluent volume from the test cells versus time. It can be noted that the performance of the gravel drainage system and of the alternative drainage system (whole tires and geotextile) were very similar for the entire monitoring period.

The variations of normalised surface waste settlements versus time for both experimental cells are presented in Fig. 10. The normalised settlement was calculated dividing the vertical settlement at the top of the waste mass (ρ) by the initial waste thickness (H). Again, the development of waste settlements in both cells is very similar. The precipitation on the cells along the monitoring period is also depicted in Fig. 10. It can be noticed that a faster rate of waste settlement, as a result of greater waste degradation, takes place during the wet seasons, when infiltration of rain water in the cells is greater.

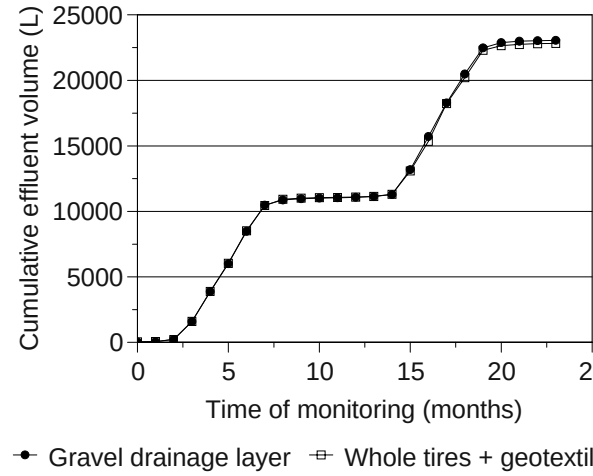

Fig. 9 Effluent volume from the experimental cells versus time

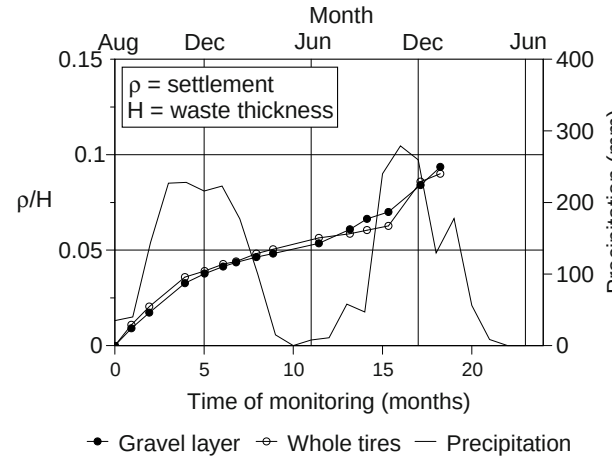

Fig. 10 Variations of normalised settlements versus time

Fig. 11 shows results of chemical analyses carried out on the leachate liberated by the experimental cells in terms of chemical oxygen demand (COD) values versus time. Some differences between results from each cell can be observed and probably were due to waste variability. However, during most of the observation period and particularly at the end of the tests the results obtained for both cells were not significantly influenced by the type of drainage system used. It is important to point out that for the conditions and duration of the experiments no signs of clogging of the geotextile filter was observed (Junqueira et al. 2006).

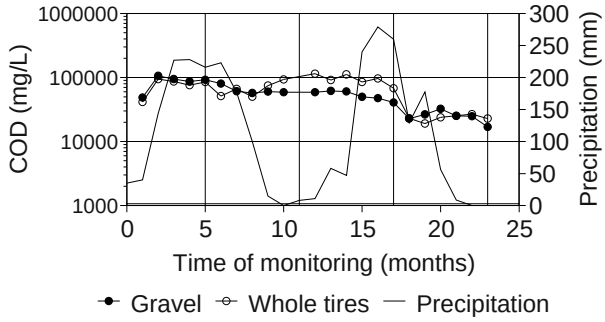

Fig. 11 Variation of chemical oxygen demand versus time

CONCLUSIONS

This paper presented results of laboratory and field tests on drainage systems consisting of the combination of geotextile filter and alternative drainage materials. The main conclusions obtained in the testing programme are summarised below:

- The transmissivity tests showed that the alternative geocomposite materials presented high discharge capacity, comparable to the results reported in the literature for conventional geocomposite products.
- The compressibility of the alternative geocomposite material depended on the nature of the core element used and on its geometrical characteristics.
- The results obtained also enhanced the fact that the use of less stiff cores in conventional geocomposites may cause significant reductions on the product final cost. These more compressible geocomposites could then be specified for works in which they would be submitted to low stress levels, which correspond to a significant fraction of the drainage works where geosynthetics have been employed.
- The performance of an experimental waste cell with a drainage layer consisting of whole tires and a geotextile filter was very similar to that of a cell with a conventional drainage layer made of gravel. The type of drainage system did not influence the chemical characteristics of the effluent. During the monitoring period (2 years) there was no sign of clogging of the drainage system of both cells.
- The combined use of alternative drainage materials and geotextile filters can yield to cheaper solutions for drainage systems, besides providing a better and more environmentally friendly use of some waste materials.

ACKNOWLEDGEMENTS

The authors are indebted to the following institutions for their support to this research programme: University of Brasilia, CAPES-Brazilian Ministry of Education, CNPq-National Council for Scientific and Technological Development, FAP-DF/Federal District Government and FINATEC/UnB.

REFERENCES

ASTM (1995) Test method for constant head hydraulic transmissivity of geotextiles and geotextile related products — ASTM D4716, ASTM Standards on Geosynthetics, USA: 48-51

Gardoni MGA, Palmeira EM (1999) Transmissivity of geosynthetics under high normal stresses, Geosynthetics'99, Boston, USA 2: 769-782

Humphrey DN (1997) Civil engineering applications of tire shreds. A short course lecture notes prepared for the California Integrated Waste Management Board, California, USA

Junqueira FF (2000) Analyses of domestic waste behaviour and draining systems with reference to the Joquei Club dump. DSc. Thesis, Graduate Programme on Geotechnical Engineering, University of Brasilia, Brazil: 288. (in Portuguese)

Junqueira FF, Silva ARL, Palmeira EM (2006) Performance of drainage systems incorporating geosynthetics and their effects on leachate properties. Geotextiles and Geomembranes, Elsevier Publishers 24(5): 311-324

Silva ARL (2004) A study on the behaviour of drainage systems of waste disposal areas under different scales. DSc. Thesis, Graduate Programme on Geotechnical Engineering, University of Brasilia, Brazil:329. (in Portuguese)

Silva CA (2007) Transmissivity tests on geocomposites for drainage. MSc. Thesis, Graduate Programme on Geotechnical Engineering, University of Brasilia, Brazil:106. (in Portuguese)

Proceedings of the 4th Asian Regional Conference on Geosynthetics
June 17 - 20, 2008 Shanghai, China

STRENGTH INCREASE OF PVD-IMPROVED SOFT CLAY UNDER STAGED EMBANKMENT LOADING

L. Ma[1], S.L. Shen[2] and X.W. Tang[3]

ABSTRACT: This paper present a case history of the performance of high sensitive Ariake clay under stage constructed embankment, on the bank of Rokkaku river, Saga, Japan. The subsoil was improved by prefabricated vertical drain (PVD) in the construction. The performance of subsoil, which improved by PVD, was investigated through field measurement and FEM analysis. The variation of physical properties of subsoil ware measured. Settlement and strength increase of subsoil are monitored and predicted. Field performance of embankment constructed on PVD-improved subsoil was analyzed using FEM. Combining FEM analysis and field measured results show that the undrained shear strength increased to twice of the original value and the stages construction could kept the stability high embankment.

KEYWORDS: embankment, settlement, shear strength, soft soil

INTRODUCTION

For the embankment constructed on soft clayey subsoil, the soft clay generally have large void ratio, high water content, high compressibility, low hydraulic conductivity, and low shear strength. Not only large vertical and lateral displacement of soft subsoil will happen during the construction of embankment but also sliding failure maybe occur due to the insufficient bearing resistance of soft subsoil. For this reason, embankment is constructed stage by stage to make subsoil consolidation under embankment loading and to make the soft subsoil acquiring strength from consolidation (Ladd et al. 1991). This paper presents a case history of a stage constructed embankment on soft Ariake clay. In order to speed up the consolidation, prefabricated vertical drain (PVD) was installed in soft subsoil to increase the vertical permeability of soft subsoil in the macro sense (Chai et al. 2001). Field measured and FEM analysis results show that the undrained shear strength increased with the height of embankment.

SITE AND SOIL CONDITIONS

The embankment was constructed on the Ariake clay and locates at the Shiroishi of Rokkaku river, Saga, Japan, as shown in Fig. 1. In this location the soft subsoil is the sediments under marine environment. Generally, the thickness of Ariake clay is from 10 to 20 m. It has been well documented that Ariake clay has a high sensitivity between 10－20 and at some place is even more than 1000. Its liquid limit is about 100% and plastic limit is around 65%. The generalized soil profile and soil properties of soft deposit at the field site are depicted in Fig. 2. The soil profile is consisting of a

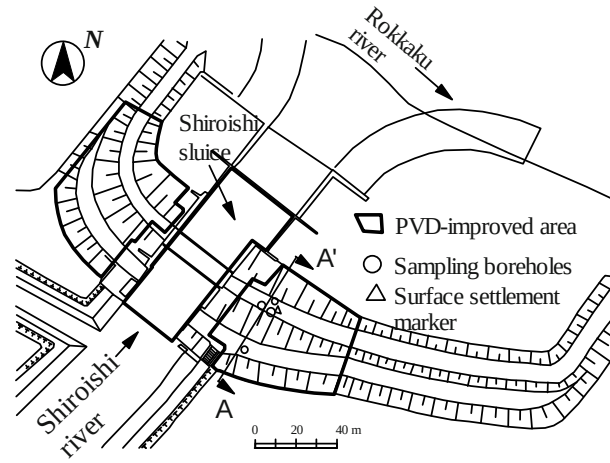

Fig. 1 Plan view of embankment and layout of instrumentation

[1] PhD. Student, School of Naval Architecture, Ocean & Civil Engineering, Shanghai Jiao Tong University, 1954 Hua Shan Road, Shanghai 200030, CHINA. Email: maleigeotechnical@sjtu.edu.cn
[2] Professor, ditto, CHINA. Email: slshen@sjtu.edu.cn
[3] Professor, Institute of Geotechnical Engineering Dept. of Civil Engineering Zhejiang University, 38 Zheda Road, Hangzhou, 310027, CHINA. Email:tangxiaowu@zju.edu.cn

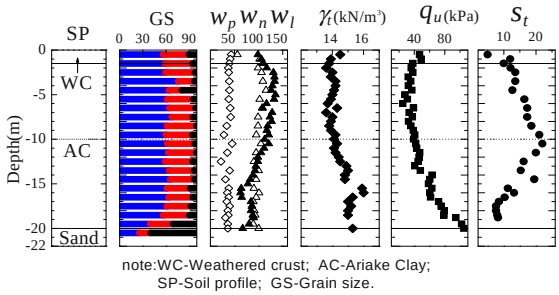

Fig. 2 Geotechnical profile and soil properties

thin weathered crust from 1 to 1.5 m thick overlying a soft high sensitive Ariake clay layer with the thickness of approximately 18.5 m. Below the Ariake clay is a layer of dense clayey sand, which has much permeability and strength. In the second layer, soft soil contains 56%—75% clay particles, 20%—36% silt particles, and 2%—8% sand particles. As shown in Fig. 2, the physical properties of soft clay have a big change in 10 m place, So that it was separated into two layers, the upper Ariake clay and the lower Ariake clay (Hanzawa et al. 1992). The water content of the upper layer is about 90%—140%, higher than its liquid limit. The lower layer is about 60%—90% lower than its liquid limit. Unconfined compressive strength of upper layer is between 20—40 kPa and 50—100 kPa for lower layer (Takeo Office 1996).

CONSTRUCTION OF EMBANKMENT AND FIELD INSTRUMENTATION

Fig. 3 plots cross sectional view of the embankments. As seen in the figure, the total height of embankment is 6.5 m. Before embankment construction, ground treatment methods were used. PVD was installed in a square pattern with the spacing 1 m, and to a depth of 20 m. A 0.5 m thick gravel sand mat was placed on natural subsoil, which was used as drainage boundary. The embankment construction procedure is depicted in Fig. 4. There are several stages in the construction. At the stage 1, the height of embankment reaches 3.3 m. In this stage, filling was compacted in a thickness of 20—30 cm. After stage 1, the subsoil consolidated for 75 days. Next stages are similar as the first one and the height of filling are 0.7 m, 1.5 m and 1.0 m respectively. After each stage, subsoil was also consolidated for a period. As plotted in Fig. 3, after stage 2 and stage 3, the subsoil was consolidatied for 70—80 days. From the beginning until end of the construction, the settlement of embankment has been monitored. At the same time, the physical and mechanical properties of the subsoil were tested in each stage. The location of bore hole is shown in Figs. 1 and 3.

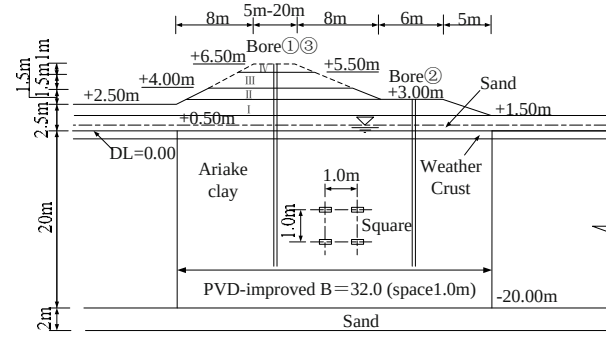

Fig. 3 Cross sectional view of embankment

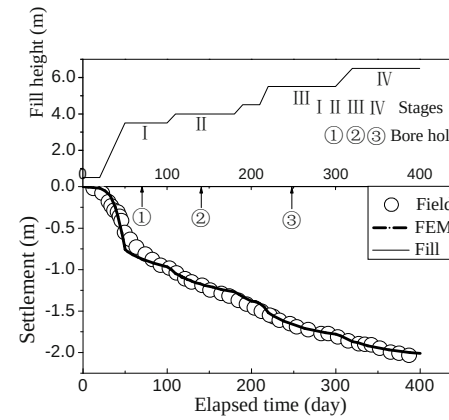

Fig. 4 Embankment construction procedure and settlement-time curve of the embankment

PREDICTION METHOD

Modeling the PVD-improved Subsoil

In order to analyze the behavior of PVD-improved soft subsoil under embankment loading, FEM was adopted. In the calculation, the effect of PVD-improvement was modeled as an equivalent value of vertical hydraulic conductivity (k_{ve}) was used proposed by Chai et al. (2001). The equivalent vertical hydraulic conductivity of PVD improved subsoil, k_{ve}, can be defined for the following expression (Chai et al. 2001):

$$k_{ve} = (1+\frac{2.5l^2}{\mu D^2}\frac{k_h}{k_v})k_v \quad (1)$$

where l=drainage length; D=diameter of unit cell; and k_h, k_v=horizontal and vertical hydraulic conductivity of soil layer, respectively. Parameter μ can be expressed as the following equation:

$$\mu = \ln\frac{n}{s} + \frac{k_h}{k_s}\ln(s) - \frac{3}{4} + \pi\frac{2l^2k_h}{3q_w} \quad (2)$$

where, $n=D/d_w$ (d_w=diameter of vertical drain); $s=d_s/d_w$ (d_s=diameter of smear zone); k_s=horizontal hydraulic conductivity in the smear zone; and q_w= discharge capacity of PVD in field.

FEM Analysis

The constitutive model of soft clay used in the analysis is the Modified Cam-clay. The model of the embankment material is linear elastic. The analytical domain of the ground with 28.5 m height and 232 m width was adopted. The determined model parameters for subsoil are list in Table 1. The displacement and drainage boundary conditions were set as: at bottom, both vertical and horizontal displacements were restrained, and bottom line (sand layer) was set as drained. Left and right vertical boundaries were undrained and the horizontal displacement of them was fixed. The ground surface was drained.

Strength Prediction Based on Constitutive Model

The undrained strength of the soft soil can be derived from constitutive model (Wood. 1990). The modified Cam clay (MCC) model is used in this study for soft clay. This model yields an undrained shear strength of soil as follows: (Wood 1990)

$$S_u = \frac{1}{2^{\Lambda+1}} M p_0^{'} (OCR)^{\Lambda} \tag{3}$$

$$p_0^{'} = (\frac{M^2 + \eta^2}{M^2})^{\Lambda} p^{'} \tag{4}$$

Where p' is the effective mean stress, η is the stress ratio q/p', p_0' is the corresponding effective mean stress on isotropic consolidation line, M is the slope of the failure line in (q, p') plot, OCR represents the overconsolidation ratio, and Λ equals (1-κ/λ), κ and λ are the slopes at void ratio versus logarithm mean effective stress plot during reloading, respectively.

Practically, Ariake clay is a structured clay with high cementation effect. Strictly, MCC is not suitable for the prediction. In this study, the author make a approximation that the Ariake clay was simply takes as in a quasi-overconsolidated state before yield, and after yield it is taken as in a normal consolidated state. The yield stress was taken as the preconsolidation pressure. Then, MCC was applied. This approximated may simulate the settlement and strength, but it maybe cannot simulate the pore pressure (Chai et al. 1994).

RESULTS AND DISCUSSION

Settlement

Fig. 4 plots settlement-time curve of the embankment. As seen in Fig. 4, at the beginning of construction the settlement of subsoil is very small. This is because of applied load is less than its yielding stress. Then, with the height of embankment increase, the settlement of subsoil increase too. This is due to applied pressure over the yield stress and consolidation level is on the normal consolidation level. At the end of construction, the settlement of embankment has reached 2 m and the total settlement of subsoil is 2.2 m. The FEM results for settlement of the embankment on natural subsoil and PVD-improved subsoil were also depicted in Fig. 4. FEM can predict field value fairly well. At the end of construction, the settlement of embankment simulated by FEM is also 2 m. However at several stages there are some different settlements between field measured data and FEM. It may be due to the approximate use of the constitutive model.

Variation of Physical Properties

Fig. 5 shows the distribution of water content with depth and As shown in Fig. 5, water content decreased with the stage of embankment; in stage 1, maximum decrease of water content was about 10%, the depth of water content decrease is about 8 m; in stage 3, the maximum decrease of water content is about 15% to a depth of about 16 m. Fig. 6 plots the variation of unit weight. As shown in Fig. 6, unit weight increased with the construction stage. The maximum increase is about 1 kN/m^3. The variation of unit weight with depth has the similar way as the water content. At the stage 3, it expands to 17 m.

Table 1 Soil parameters for the Shiroishi embankment

Soil layer	Depth	w(%)	Γ	λ	κ	k_h(10^{-3}m/day)	k_v(10^{-3}m/day)
B	2-0m	112.0	4.17	0.25	0.036	9.89	6.53
AC1	0~-6m	125.0	5.08	0.96	0.137	5.09	3.17
AC2	-6~-10m	112.0	4.60	0.67	0.096	2.28	1.35
AC2	-10~-12m	90.0	4.03	0.56	0.080	2.28	1.35
AC3	-12~-14m	62.0	3.30	0.44	0.063	1.91	1.09
AC4	-14~-18m	85.0	3.91	0.51	0.073	2.12	1.16

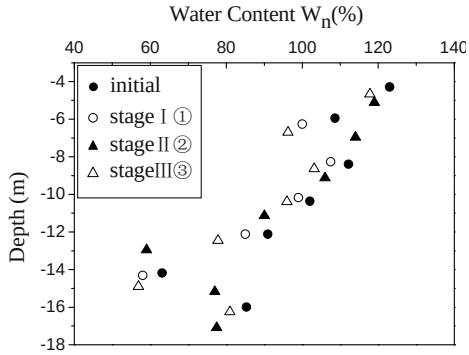

Fig. 5 Variation of water content

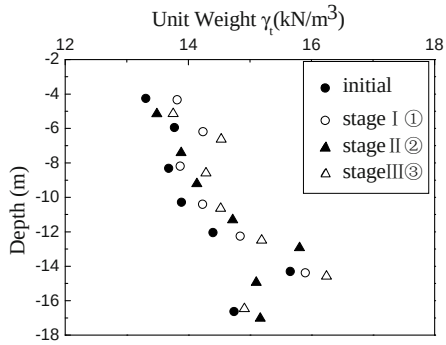

Fig. 6 Variation of wet unit

Variation of Strength

Fig. 7 plots the variation of strength after embankment construction. As shown in Fig. 7 the strength of subsoil is increasing during staged construction of embankment and the increment of strength is different after every stages. After stage 1, at depth 4 m the increment of strength reaches 20 kN/m^2. Meanwhile when depth increasing, the variation of strength increment shows a decrease. The variation of strength at stages 2 and 3 are in a similar way as these in stage 1. However the increment of strength reaches 40 kN/m^2. At the end of embankment construction, the strength of subsoil becomes twice as initial value. Fig. 7 also illustrates that MCC can predict the trends of strength even there was an approximation in application for this structured clay.

CONCLUSIONS

This study discussed the increase of undrained shear strength of soft Ariake clay improved by PVD under the staged embankment loading. The following conclusions can be drawn:

1. During the embankment construction, water content of Ariake clay subsoil decrease and unit weight increases. The variation of water content and unit weight decrease with the increase of the subsoil depth. This phenomenon reflects the embankment loading imposing on the subsoil changes with depth.
2. For the analyzed embankment, the increment of the strength during stage construction is about 40 kN/m^2 near the surface, and it decreases with the increase of the depth. At depth 17 m, the increase of the strength is about 25 kN/m^2. This phenomenon notes the embankment influence depth great than 17 m.
3. Based on the FEM simulated result and field measured data, it is confirmed that the method of PVD used improve clay ground under embankment is very effective.
4. The Modified Cam-clay can be used to predict strength increase of high sensitive soft clay under staged embankment loading with some approximate treatment.

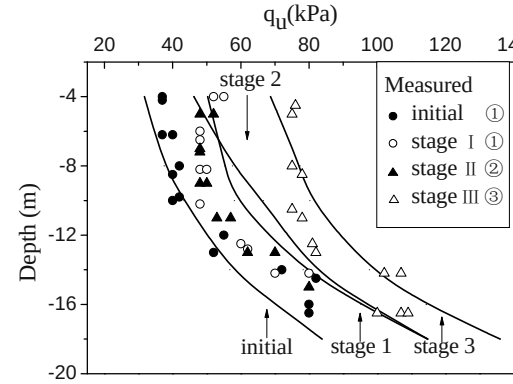

Fig. 7 Variation of strength after embankment construction

REFERENCES

Chai JC, Shen S L, Miura N, Bergado DT (2001) A simple method of modeling PVD improved subsoil. J. Geotech. and Geoenviron. Engng. ASCE 127(11): 965-972

Chai JC, Sakajo S, Miura N (1994) Stability analysis of embankment on soft ground. Soils and foundations 34(2): 107-114

Hanzawa H, Fukaya T, Suzuki K (1990) Evaluation of engineering properties for an Ariake clay, Soils and Foundations 30(4): 11-24

Ladd CC (1991) Stability evaluation during staged construction, Journal of Geotechnical Engineering, ASCE 117(4): 541-615

Takeo Office, the Ministry of Construction (1996) Research Report on Construction Countermeasures of Soft Clay Foundation of Dyke Embankment along the Bank of Rokkaku River, Saga, Japan: 229 (in Japanese)

Wood DM (1990) Soil behavior and Critical State Soil Mechanics: 112

RENOVATED VACUUM CONSOLIDATION WITH ELECTROOSMOSIS

Y.W. Jin[1]

ABSTRACT: With the renovated Vacuum Consolidation method, the water inside of the soil could be completely drained out. The design index, construction process, and monitoring of renovated Vacuum Consolidation method are detailly introduced. The soft soil ground could be consolidated effectively and quickly.

KEYWORDS: Electroosmosis, Drain board, Hand-form connect, Free-flow water, Soil-combined water

INTRODUCTION

The soft soil foundations were widely distributed in China littoral areas, with a high rate of containing water, high void ratio poor permeability and low bearing capability. This kind of soft soil must be improved before any construction engineering on it. The Vacuum Consolidation is one of the methods and applied in China from 1980's, but the mechanism of Vacuum Consolidation are not very clear. We renovated a new method named Vacuum Consolidation with Electroosmosis. With this new method, water can be drawn from free-flow water, pore water and soil combined water, while the soil combined water cannot be drawn by normal vacuum consolidation.

The mechanism of Vacuum Consolidation is to make negative pressure within the concretion area and depress the pressure of the area border, a pressure difference occurs between the inner soil and borderline, and then water seeping accordingly. With the time going, the pressure in the inner soil depress little by little, and such depressed pressure changes into the soil stress, the more deep vacuum, the more valuable stress applied, and of course result the better concretion. The vacuum loading could be applied in one times, and without any cut damage to the groundsill, that could save the time. Both vacuum loading and stack loading will result the groundsill fall down, and finally formed as boiler bottom, but the two methods have substaintial difference, which is under Vacuum loading, the soil within concretion area will press shift to the center of the area, thus result a better contractive and concretive performance than method of Stack loading under a same vertical deformation. Moreover, the method Vacuum Consolidate with Electroosmosis will have a better performance than Vacuum only.

DESIGN INDEX

Cancelled Sand Mat

For normal design of sand mat, the sand layer thickness no less than 200 mm, and could increase to 500 mm when needed. The sand mat can be cancelled in the project improved by Vacuum Consolidation with Electroosmosis.

Plastic Vertical Drain

Plastic vertical drain be disposed in order of correctitude triangle, distance is 1.0 m between each other. The insert deep is above 0.5 m of the silt layer, and can not enter the layer of sand. The upper board over 20 cm away from the ground surface, and be connected with hand-connect before burying with soil completely. The detail technique index as below table:

Table 1 Technique index of PVD

Core pipe	Material	Polyethylene, Polypropylene
	Width	100±2 (mm)
	Thickness	>4 mm
	Pull strength	>2.3 (kN/10cm)
	Water draining	>45 (cm^3/s)
Film	Material	Terylene, Polypropylene fabric
	Thickness	>0.48 (mm)
	Pull strength	>30 (N/cm)
	Upright water draining	>40 (N/cm)
	Infiltration	$>4\times10^{-3}$ (cm/s)

[1] General Manager , YiXing XinTai Earthwork Materials Co., Ltd., XinZhang street, YiXing Town, Jiangsu province, CHINA. Email: yxxintai@126.com

Vacuum Pre-compression Technique

Index of Vacuum Pre-compression is listed as follows:
(1) Vacuum of Drain board >80 kPa
(2) Weight bearing of groundsill >120 kPa
(3) Sinking < 300 mm
(4) Concretion >85%

The common process for the vacuum pre-compression is to insert PVD in the soft foundation areas with a certain distance by each other, then mat with 50 cm sand layer on the drain board, the PVC pipe wrapped with earthwork fabric were buried inside of the sand layer, and also be extended connecting with the vacuum pump. The entire sand layer be sealed with PE or PVC film for vacuum pumping. In generally, the vacuum degree inside of the film after pumping will be 0.008 MPa, but the drain board can only reach to 0.003 MPa, and also the sands will block the pipe , thus the vacuum degree could not keep continuing, part of the ground water will flow back to the deep earth under that situation, which will result the poor concretion in most cases.

Some properties of The renovated vacuum precompression are listed as below:
(1) Special designed hand-formed connect to connect with Drain board and Vacuum pipe, the sands will not enter the pipes and the vacuum system always keep stable. The vacuum system could be available till to bottom of drain board, and the water in deeps could be very quickly and effectively draw out, thus the soft foundation could be concreted in a quick manner and then shorten the engineering lead time.
(2) Using enhanced PE or PVC film, and weld sealing all the film connects.
(3)Renovated high performance drain board with electroosmosis.
(4) High speed vacuum pump.

Construction Technique

(1) The hand-formed connect is designed to solve the problem that drain board could not connect with vacuum pipe, and to prevent the sands enter into the pipes and vacuum block inside of the pipe, and also with hand-formed connect between drain board and vacuum pipe, the vacuum system could reach to the bottom of the board, as well as direct into the inner of deep soft earth.
(2) The connection of the outside fabric films is the key point to guarantee the vacuum sealing, so the fabric film connection should be welded properly, we use 1.2 PVC fabric film. Under films, we using special designed hand-formed connect and Φ32mm PE/PVC pipe, connected with pump. The Vacuum degrees after precompression will over 650 mmHg.
(3) Using enhanced high performance drain board, which with the high strength under vacuum. High pull strength fabric film could effectively prevent the sands enter into the pipes and make sure the effective vacuum system and free water draining inside of the pipes.
(4) The construction area and vacuum time depend on the draw rate of the vacuum pump.
(5) The specification of the film is shown in the Table 2.

Table 2 Specification of film

Thickness	Pull strength (Vertical/ Horizontal)	Elongation (Vertical/ Horizontal)	Right-angle Tear (Vertical/ Horizontal)
0.11－0.12 mm	8－10 Mpa	≥200%	≥30 N/mm

Monitoring and Inspection

(1) The purpose of the monitoring and inspection is to make proper adjustment for the engineering parameters, and guarantee the engineering quality and safety. And also to evaluate the soft foundation process effectiveness with the supporting data.
(2) Monitoring items: Ground surface sinking, Ground surface Horizontal shifting, Groundsill horizontal shifting, Hole water pressure, Ground layer sinking, Underground water table, Vacuum degree
(3) Checking frequency: Every 3 days during sand burying and drain board setting process; After starting vacuum pre-compression, check by every day, it can be changed to once per 3 days after 15 days, and then extend to by 7 days if minor variety of the data; During stack loading, check by every day, change to by 2 days after 3 days, and then extend to by 5 days if minor variety of the data; After stacking height reach to 1.7 m, check it by every week.

Construction Process

(1) The deposit position of the drain board should be numbered by row and column, the shift should less than 20 mm; The board Vertical shift should less than 1.5%; Keep integrity after board deposition, no tweak, no break and film tear; Anti-mud device should be installed at bottom of the tube, and make sure the mud not enter into the tube, improve the rube installation immediately if found the mud enter into the tube and quantity over 5% of the entire tube quantity; The deposit equipment should keep the length record for each plastic drain board.

(2) With the special designed hand-formed connect, upper board 30－50 cm sealing, sand stacking 20 cm on above, and completely sealing with fabric film, we can get a high vacuum system over 80 kpa. The drain board should not deform after setting in the soil, and keep free water draining even the groundsill deformed to S shape. Film strength should over 40 N/cm, and should not be damaged under high vacuum. The stacked sand height is about 30 cm－50 cm, and make cover the connect between drain board and vacuum pipe. The hand-formed connect is pre-processed a round hole in the factory.

(3) The concretion performance depends on the vacuum degree and time, the more high air draw speed, the more quick vacuum time. Our company's vacuum draw speed will be set over 4 m^3/minutes, one group of vacuum pump including two set of equipments (one of them is for back up), and effective area cover to 5000－6000 qu.m.

(4) Before apply the sealing film, clean up all the sundries from the sand layer such as conch, edged stone, and dig the holes (30*30*50) around the draining board which above the sand layer, connect the board and pipes with hand-formed connect, make sure the all connects be fasten, after that, bury with the sand to cover all of them, and then sealed with PVC film the outside. The films should be holt-felted into an integrated film with the size over the whole working area. The width of the hot-felt area should not less than 5 cm. After the 1st layer apply, check the film connect and fix any break holes. Using sand bags to hold the films after apply, and prevent it be tear or blow away by the wind. The worker should wear the soft-sole and away of damaging to the film during operating. The film after apply can also be fixed with a little vacuum pumping.

(5) The pipe device above the films including Outlet device, Connect pipe and Control valve. The Outlet device connect with inner film and out film, so it's critical for sealing completely, and there should has no any leakage after installation. In the vacuum pipes, install the back-valve and break-valve, which is used to smooth the vacuum pump process, and control the air-draw break time and keep the stability of the vacuum system.

(6) The bump's carry range above 32 m, the vacuum degree up to 730mmHg at free loading. One air-drawing set's working area could up to 1100 m^2, and could be adjusted base on the actually requirement. (will leave some Outlet on the films for back up)

(7) A standard vacuum meter is installed for each air-draw set to make a better control for the actual vacuum degrees. Install a vacuum detector under the bottom of the drain board and by every 2000－5000 m^2, the detector locates in the center of the board array, and also over 4m away from the engineering field edges. At end of the sub-pipe, install a vacuum detector, which should not be buried under the film.

(8) The density of the stack soil (general ground soil) should meet 18.0 kN/m^3 (conduct the density experiment by every 1000 m^2), the stack weight should not less than the design spec (1:1.5). During stacking process, special attention on the film damage and also the protection for the monitoring devices.

(9) The loading time will be made according to the monitoring data for the layer sinking, horizontal shifting and water gap pressure.

(10) Change to next loading lever once the loading concretion reach to 70%.

(11) After draining board and pipe installation, continue drawing vacuum 25－35 days, electroosmosis 10 days, and adjust per actual condition.

Some process are shown in the Figs. 1－4.

Fig. 1 Draining board installation

Fig.2 Vacuum system installation

Fig.3 Vacuum system installation

Fig. 4 Pre-compression and vacuum draw

Alert Values

Stop loading when the monitoring data over the following limit:
(1) Rate of the increased gap pressure and loading up to 0.5;
(2) Ground surface shift over 6 mm/day;
(3) Ground surface sink over 10 mm/day.

Safety Requirement

(1) Set safety hurdle and Alert board, reject any non-related peoples enter into the working area to prevent any possible accident.
(2) The operators should be aimed with safety measures when enter into the working areas.
(3) The anti-measures should be taken to prevent the groundsill shift damage when any alert for the gap pressure or slope shifting, and any enlarged trend for the ground surface shifting.
(4) Anti-measures: Add additional ½ loading on the sloping bottom and within 10m distance on the way of shifting.

SUMMARIZE

With the renovated vacuum precompression method, we can solve many common problems in current industry, expedite the soft foundation concreting, thus shorten the overall project lead time. This method is a real Chinese-invented with a good quality and low price, it applies for all kinds of soft foundation processing engineering such as railway, highway, port and dock, and rubbish disposal field, etc.

Landfill Engineering

GEOSYNTHETICS COVER SYSTEM FOR THE REMEDIATION OF A DISMISSED INDUSTRIAL SITE IN MILANO

D. Cazzuffi [1], P. Recalcati [2] and G. Tresso[3]

ABSTRACT: The paper describes a case history where an old factory site was redeveloped for a new intended use , following a reclamation of the related contaminated area; in particular, the design criteria followed to select geosynthetics that could be approved equivalent to the natural materials that were substituting (clay and gravel) are outlined , as well as the choice of the type of geosynthetics that could guarantee the stability of a top soil layer 0.40 m thick on a steep slope, allowing in the same time the presence of the trees planted on the slope itself.

KEYWORDS: landfill capping, GCL, drainage geocomposites, remediation technologies

FOREWORD

Following the end of activities of the Pirelli Tires and Cables industrial factory site "Pirelli Bicocca" North of Milano, the area was turned into a mixed urban quarter of around 10,000 inhabitants, with various cultural important infrastructures, such as the Arcimboldi theater (temporarily used to replace the theatre of La Scala during renewal works from 2003 to 2005) and several Departments of the Milano Bicocca University.

During the reconstruction works, one of the main problems to cope with was the landfilling of a stockpile of soil and debris coming from the preliminary demolitions and decommissioning of the industrial plants. Therefore, it was decided to create an artificial hill over 20 m high incorporating the total quantity of the wastes (280,000 m³ volume), covering an area of 15,000 m².

The site reclamation was designed by EcoAppraisal Srl – Tauw Group, with a contribution of Montana Srl, on behalf of Pirelli & C. Project Management, and the best sustainable alternative was that of landfilling the material on site and providing a permanent confinement from the surrounding environment.

The reclamation project, approved by the local authorities, involved the design with the aid of a risk analysis and the construction of a permanent capping of the total waste quantity.

The final destination of the hill, now called "Collina dei Ciliegi", is a city park; for this reason, a detailed study was carried out in order to define not only the capping system, but also the type and quantity of vegetation and trees to be planted.

The limited available area, and the resulting steep slopes of the hill (sometimes exceeding 30°), made the design of the capping system very challenging.

The use of traditional materials, such as compacted clay liners and gravel layers, was not possible; therefore, it has been necessary to identify the type of geosynthetics that could solve the engineering problems, giving the cover system the required level of safety and durability vs. time.

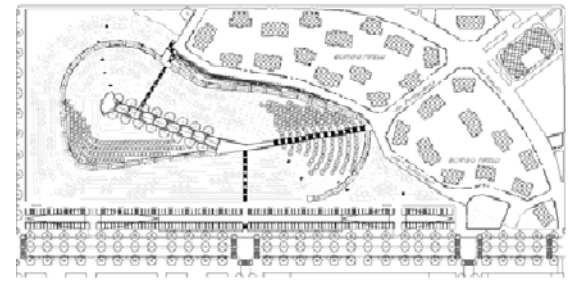

Fig. 1 Plan view of the reclaimed area

A detailed study was developed in order to allow the growth of medium-high trees with prevalent horizontal root apparatus in order to prevent the damage of the lining system. Although traditionally medium-high trees are not used for capping, plants were included in the environment impact plan and were considered mandatory from the municipality authorities for the overall acceptance of the project.

[1] CESI SpA, Geosynthetics and Environmental Geotechnics Office, Milano, ITALY. Email: cazzuffi@cesi.it
[2] Tenax SpA, Geosynthetics Technical Office, Milano, ITALY. Email: piergiorgio.recalcati@tenax.net
[3]Laviosa Chimica Mineraria SpA, Geosynthetic Clay Liners Division, Livorno, ITALY. Email: gtresso@laviosa.it

DESIGN CONSTRAINTS

In Italy, the construction and maintenance of non hazardous landfills must be designed in accordance with the National Act on 36, January 2003, derived from the European Council Directive 1999/31/EC.

In particular for the capping it is required a cover system consisting (from top to bottom) of:

- cover layer ≥ 1.0 m, whose function is mainly to allow the vegetation growth;
- drainage layer having a thickness ≥ 0.5 m;
- compacted clay layer (CCL) ≥ 0.5 m having hydraulic conductivity ≤ 1,00E-08 m/s;
- gas venting layer.

The slope geometry, quite steep and long size, made it impossible to follow strictly the proposed cover system. For example, it was not possible to place a compacted clay layer, and it was very difficult to lay down the required gravel drainage layer, guaranteeing — at the same time—its stability. The thickness of the cover layer was excessive too: a reduction to 0.40 m has been considered acceptable.

Therefore, the closure of the landfill was obtained by using a geosynthetic clay liner (GCL) in place of the CCL, and a drainage geocomposite in place of the gravel drainage layer.

GEOSYNTHETIC CLAY LINER SELECTION

The use of GCL in landfill capping could offer the following advantages.

First of all, the GCL is able, by swelling, to self seal any perforation that may occur, even after the landfill has been closed down. Second, in using at least one geotextile of a woven type, part of the bentonite is able to migrate through the geotextile and, when swells, automatically seals the joints between adjacent layers. This fact considerably simplifies the placement operation because it provides tightness through a simple overlap of the placed sheet edges.

The self-sealing capacity of GCLs is effective only in presence of small tears or holes, while large cuttings can remain partially open (see also Cazzuffi et al. 2005). Therefore, it is necessary to provide a proper mechanical protection to the GCL against puncturing and damaging by the coarse layer usually placed on top of the upper waste layer. Moreover, in order to be hydrated, the GCLs must be covered with at least 0.30 m of coarse soil.

Koerner et al. (1995) provide a method for assessing the technical equivalency of a GCL (Geosynthetic Clay Liner) to a CCL (Compacted Clay Liner).

In terms of steady flux of water, the Darcy's law is expressed by the following equation:

$$Q = v \cdot A = k \cdot i \cdot A = k \cdot \frac{\Delta h}{h} \cdot A \tag{1}$$

where

- Q (m³/s) is the total leakage
- v (m/s) is the filtration velocity
- k (m/s) is the permeability
- $i = h/h$ (m/m) is the hydraulic gradient
- A (m²) filtration surface

Considering a GCL and a CCL, it's possible to write the Darcy's law as follows:

$$\begin{aligned} Q_{GCL} &= k_{GCL} \cdot i \cdot A = k_{GCL} \cdot \frac{H + T_{GCL}}{T_{GCL}} \cdot A \\ Q_{CCL} &= k_{CCL} \cdot i \cdot A = k_{CCL} \cdot \frac{H + T_{CCL}}{T_{CCL}} \cdot A \end{aligned} \tag{2}$$

where

- H (m) is the hydraulic head
- T_{GCL} (m) is the thickness of the hydrated GCL
- T_{CCL} (m) is the thickness of the CCL

Therefore, in order to use a GCL instead of a CCL, the following condition should be verified:

$$Q_{GCL} \leq Q_{CCL} \tag{3}$$

that becomes

$$\left(k_{GCL}\right)_{required} \leq k_{CCL} \cdot \frac{H + T_{CCL}}{T_{CCL}} \cdot \frac{T_{GCL}}{H + T_{GCL}} \tag{4}$$

After having introduced the following assumptions:

- k_{CCL} = 1,00E-08 m/s
- H = 0.30 m (typical hydraulic head for landfills)
- T_{CCL} = 0.50 m
- T_{GCL} = 0.01 m (hydrated GCL thickness)

And the following condition should be verified:

$$\left(k_{GCL}\right)_{required} \leq 1{,}00\text{E}-08 \cdot \frac{0{,}30 + 0{,}50}{0{,}50} \cdot \frac{0{,}01}{0{,}30 + 0{,}01} = 5.23\text{E}-10 \text{ m/s} \tag{5}$$

As a conclusion, provided that the chosen bentonite geocomposite can guarantee an hydraulic conductivity $k < 5.23E\text{-}10$ m/s , it can replace a 0.50 m thick compacted clay layer (CCL).

The product selected on the base of these criteria is made up of two 150 g/m² woven geotextiles, which incorporate natural sodium bentonite (5 kg/m² minimum): the hydraulic conductivity of this product is in fact $k \leq 1.00E\text{-}11$ m/s (ASTM D 5887).

The two woven geotextiles are connected with diamond shaped polypropylene loop stitching, all separated and independent from each other. In this way any tear cannot

propagate, but remains confined to the loop where it occurs. Direct shear tests, performed at a nominal pressure of 55 kPa, provided an equivalent internal friction angle of 36°. The tensile strength of the selected GCL is 18 kN/m in both directions (EN ISO 10319).

DRAINAGE GEOCOMPOSITE SELECTION

The drainage geocomposite should be equivalent to a minimum thickness of 0.50 m gravel, characterized by a typical permeability of :

$$k = 1.00E\text{-}03 \text{ m/s} \quad (6)$$

The slope on which the geosynthetic should be laid is 1V/2H (p = 50%). This corresponds to an angle $ß$ = 27 °.

The typical flow equation (Darcy) is:

$$Q = k\,A\,i \text{ [m}^3\text{/s]} \quad (7)$$

The proposed thickness of the gravel drainage layer is: t = 0.50 m.

Therefore, the required flow rate corresponding to 1 meter width of the drainage layer is

$$q = k \times t \times 1.00 \times i \quad (8)$$

The hydraulic gradient along a slope, in the hypothesis of a steady flow, is equal the ratio between the difference in level (ΔH) and the length of drainage (L), that corresponds to the sinus of the slope angle:

$$i = \sin ß = 0.44 \quad (9)$$

Thus the required flow rate is:

$$q = 2.27E\text{-}04 \text{ m}^3\text{/s/m} \quad (10)$$

The most critical engineering property of a drainage geocomposite is its in-plane flow capacity under design loads and in presence of specific boundary conditions.

The design parameter used to quantify the in-plane flow capacity is either the flow rate per unit width of the geosynthetic or the hydraulic transmissivity (flow rate per unit width of geosynthetic and per unit of hydraulic gradient "*i*").

The flow rate per unit width is determined by measuring the quantity of water that passes through a test specimen in a specific time interval under a specific normal stress and a specific hydraulic gradient. The hydraulic properties are measured according to EN ISO 12958 with testing equipment derived from that originally used by Darcy to study the water permeability of soil.

In order to measure the drainage capacity of the geonets and of the geocomposites the test apparatus is capable of applying differing values for the hydraulic gradient "*i*", as well for the applied normal pressure, so as to simulate different possible operating conditions (varying overburden pressures). Transmissivity tests are usually performed at typical gradients corresponding to 0.1, 0.5 and 1.0.

If the value of i is different from the values of the flow rate diagrams in the data sheet, it is possible to evaluate the specific flow-rate for the hydraulic gradient immediately above the actual gradient by a formula suggested by Cancelli and Rimoldi (1989):

$$q_{i1} = q \cdot \sqrt{\frac{i_1}{i}} \quad (11)$$

with: q_{i1} specific flow-rate from the diagram [m²/s];
q specific flow-rate for the i gradient [m²/s];
i_1 the hydraulic gradient on the diagram of the geonet, immediately above the actual hydraulic gradient;
i actual hydraulic gradient.

As the required flow rate at a gradient i=0.44 is 2.70E-04 m³/s/m, the drainage geocomposite should be able to guarantee, at a gradient i = 0.50, a minimum water flow of:

$$q_{i=0.50} = q_{i=0.44}\sqrt{\frac{0.50}{0.44}} = 2.42\,E-0.4\,\text{m}^2/\text{s} \quad (12)$$

The drainage geocomposite used consists of a geonet core with two geotextiles laminated to both sides guaranteeing, at the specified conditions, a flow rate greater than 3.00E-04 m³/s/m; given the above, it was considered equivalent to the drainage layer foreseen by the Italian national regulation.

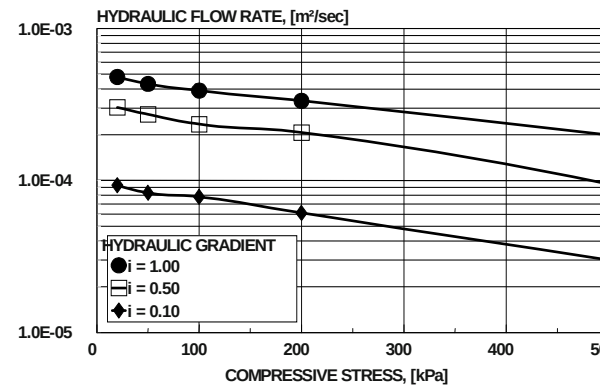

Fig.2 Transmissivity test result for the drainage geocomposite used

As the purpose of the drainage layer is not to develop an hydraulic head in the drainage layer itself, the hydraulic transmissivity of the geocomposite had to be compared with the quantity of water that can be calculated using the equation of the rainfall possibility relative to the hydrologic region of the waste disposal. Return times of 10 and 100 years, giving respectively rainfall intensities of 120 and 150 mm/hours for rainfall duration of 15 and 20 minutes, have been used. This verification was successful too.

STABILITY ANALYSIS

The capping system is subjected to a set of forces which, if not in static equilibrium, would trigger the sliding of the geosynthetic layers and/or of the topsoil layer. The free-body diagram for this analysis is shown in Fig. 3. The active force, that is the destabilizing one, has direction tangent to the slope and downward; it is calculated as the component along the slope of the weight W of the soil block, given by:

$$W = t \cdot L \cdot \gamma \tag{13}$$

where: t = thickness of the topsoil
L = slope length
γ = unit weight of the saturated topsoil

The component Fs along the slope is:

$$F_s = W \cdot \sin\beta \tag{14}$$

where: β = slope angle.

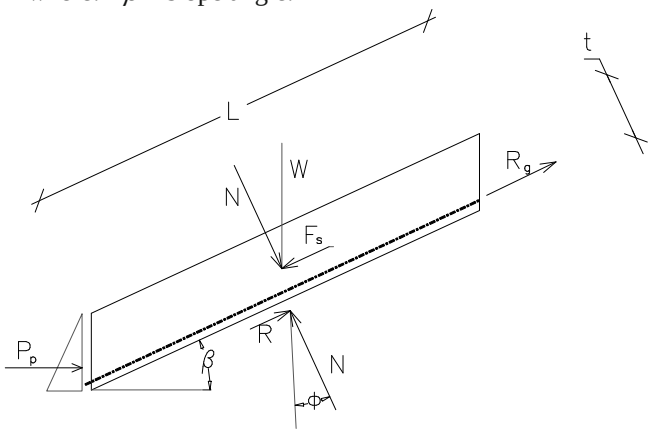

Fig.3 Free body diagram for the stability analysis of the capping system

The resisting forces are: the friction force R at the geocomposite — topsoil interface; the passive thrust at the toe; the strength of the reinforcement R_g.

The passive thrust at the toe has been reduced to 2/3 to take into account the fact that it's not possible to guarantee an adequate compaction and density of this soil.

The drainage geocomposite—GCL interface has a friction angle of about 18°. As the critical friction angle is lower than the slope angle, it is necessary to foresee the use of a reinforced geomat capable to transmit the required force to the cover layers in order to reach an adequate factor of safety.

It is then possible to calculate the required allowable tensile strength for the reinforcement, in order to ensure an adequate Factor of Safety F_S:

$$F_s = \frac{F_{resistamt}}{F_{active}} = \frac{R + R_g}{F_s} \tag{15}$$

$$R_g = FS \cdot F_s - R \tag{16}$$

The allowable tensile strength of the reinforcement has been assumed equal to the long term design strength for the geogrid.

L=slope length; t = topsoil thickness; W = topsoil weight; N=component of W normal to the slope; F_s = component of W along the slope; P_P = passive thrust at the toe; R_g = strength of the reinforcement; ϕ = friction angle of the critical interface; β = slope angle.

The peculiarities of this project, with steep slopes and minimal space for any anchorage, suggested the use of a reinforced geomat made up of the mechanical coupling of a geogrid (tensile strength of 55 kN/m) with a geomat. This kind of product ensures an optimal distribution of the stress state and, at the same time, prevents the danger of the topsoil layer sliding.

The stability of the cover system has been verified taking into account the load temporarily transmitted by the earth moving machineries that were thought to be used to spread the soil over the slopes. The verification have been done considering the surcharge transmitted by an excavator, 26 tons, having tracks size of 0.60 m × 3.79 m. The acting force has been modified, according to Italian regulations, to take into account the dynamic effect induced by the movement of the machinery. The increase in the required tensile strength in the geomat due to the temporary presence of the excavator was calculated to be less then 20 kN/m, and it was then considered acceptable in the short term.

SPECIAL CONSTRUCTION ASPECTS

As said in the Foreword, considering the presence of a highly populated area at a very short distance form the site, the landscape architects that were involved in the project had foreseen the presence of trees on the cover layer. The geometry of the slopes, as said before inclined at 27° on the horizontal, and the reduced soil thickness (0.40 m), could be a limitation in the growth of the trees. For stability reasons, it was not possible to increase the thickness of the soil to 1.00 m; the solution used was very easy and yet very effective; the existing surface was prepared before laying down the cover layers, by excavating some holes on the slopes. Particular care was taken during this operation to have always a minimum inclination downward of the slope, not to risk water could remain in the holes after they were waterproofed.

The holes were protected with one layer of nonwoven geotextile; the cover system, starting form the GCL, was then placed.

Moreover, intermediate transversal draining trenches were created along the slope to reduce the water runoff in the top soil layer.

Fig. 4 View of the landfill before the beginning of the works related to the capping system

Fig. 5 Excavation of the holes for the trees, and specific protection of the holes with a nonwoven geotextile

Fig. 6 Laying down of the drainage geocomposite (white) on the GCL (black)

Fig. 7 Laying down of the geomat reinforced with a geogrid over the drainage geocomposite

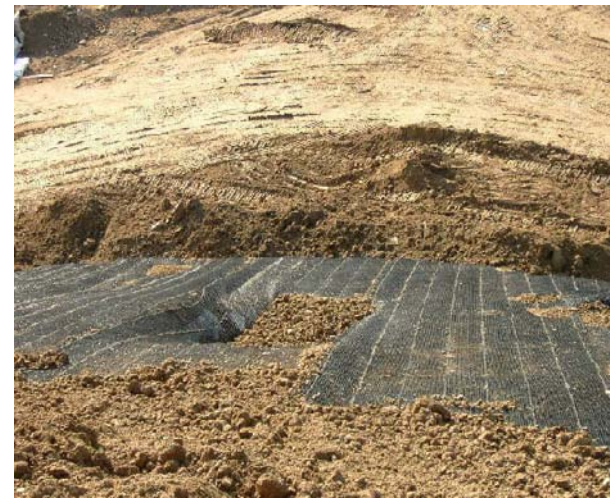

Fig. 8 Laying down of the topsoil layer. The hole previously excavated, where the tree will be planted, is clearly visible

Fig. 9 Intermediate transversal draining trench

Fig. 10 The aspect of the hill, just after trees have been planted

Fig. 12 Another view of the finished job; normal life is going on in front of the finished job

CONCLUSIONS

The project described in this case history represents an interesting example of the technical advantages that can be achieved through the use of geosynthetics instead of traditional materials. Moreover, it shows how a proper design, an adequate selection of materials and a careful installation can solve major problems. The example shown is particularly relevant as it demonstrates that it is possible to design capping systems with geosynthetics that respect the main technical requirements of the current European Regulations, even if geometrical and logistic conditions do not permit a full compliance with all aspects of the regulation.

REFERENCES

Bavestrelli A, Cazzuffi D, Recalcati P, Tresso G (2007) The use of geosynthetics for the reclamation of the Pirelli Bicocca area in Milano. Proc. Int. Symposium Geo-Environmental Engineering 2007, Grenoble, France: 59-64

Cancelli A, Rimoldi P (1989) Design criteria for geosynthetic drainage system in waste disposal. Proc. Sardinia '89. 2nd International Landfill Symposium, Porto Conte, Sassari, Italy: XXIII 1-27

Cazzuffi D, Crippa E, Villa C (2005) Laboratory tests and field observations on a geosynthetic clay liner (GCL) system installed as capping since seven years, Proc. Intern. Workshop “Hydro-Physico-Mechanics of Landfills”, Grenoble, France

Koerner RM, Gartung E, Zanzinger H (1995) Geosynthetic Clay Liners, Proc. Intern. Symp., Nuremberg, Germany, A.A. Balkema, Rotterdam

LARGE-SCALE SHEAR TESTS ON INTERFACE SHEAR PERFORMANCE OF LANDFILL LINER SYSTEMS

M. Kamon[1], S. Mariappan[2], T. Katsumi[3], T. Inui[4] and T. Akai[5]

ABSTRACT: Interface shear performance of various landfill liner systems were evaluated for landfill stability by conducting large scale shear tests. Testing program covers the interfaces between (1) geosynthetics (geomembrane (GM) sheet (HDPE and PVC) and non-woven geotextile) and subsoil, (2) geosynthetics and compacted clay liner (CCL), and (3) GM and geotextile. The focus of this paper is placed on interface shear performance under both as installed condition (dry for geosynthetics and optimum moisture content for CCL or subsoil) and saturated / wet condition, since landfill liner system is often subjected to saturated / wet condition due to the higher water retention capacity of CCL as well as the contact to leachate and/or groundwater. For geotextile-GM interface, there is no significant effect on the interface shear strength. The saturated CCL-GM interface had lower shear strength compared to the interface under as installed condition, although the shear performances of CCL-geotextile interface under both conditions are similar to each other. For the interfaces between geosynthetics and subsoil, the frictional resistance of HDPE with textures surface had a significant drop from 23 to 15 degree in the saturated / wet condition.

KEYWORDS: landfill liner, interface shear strength, water content, large-scale shear box test

INTRODUCTION

The liners and closure cover system of a modern municipal solid waste (MSW) landfill are constructed with layers of various geosynthetics, such as geosynthetic clay liner and/or geomembrane (hydraulic barrier), geonet (drainage layer), geotextile (filter) and geogrid (reinforcement). While geosynthetic clay liner and/or geomembrane function effectively as hydraulic barriers against leachate and infiltration, their interface peak and residual friction angles are lower than those of the soil alone. Such lower friction angle may present between geomembrane and other geosynthetics which could trigger much rapid failure during seismic loading conditions. The soil-geomembrane interface acts as a possible plane of potential instability of the system under both static and seismic loading (Ling and Leshchinsky 1997). Hence many researchers have discussed the interface shear strength of landfill liner materials (e.g., Stark et al. 1994, 1996; Gilbert et al. 1996; Daniel et al. 1998, Palmeira et al. 2002; Chiu and Fox 2004, Fox et al. 2004; Gourc et al. 2004). The focus of this paper is placed on interface shear performance under both as installed condition (dry for geosynthetics and optimum moisture content for compacted clay liner and subsoil) and saturated/wet condition. Landfill liner system, which is initially constructed under optimum moisture condition (OMC), is eventually subjected to saturated/ wet condition (SWC) due to the higher water retention capacity of CCL as well as the contact to leachate and/or groundwater. Thus, effect of the water content of the lining materials on the interface shear strength parameters should be carefully considered in the stability analysis of the landfill liner. This paper addresses a series of direct shear tests for the interface between (1) geosynthetics and (2) geosynthetic and soil under both OMC and SWC. Based on the test results, effect of the water content of the liner materials on the interface shear performance is discussed and summarized.

EXPERIMENTAL PROGRAM

Testing Apparatus

Fig. 1 shows the large scale shear box apparatuses used in the test. Bottom shear box size of 350×600 mm and top box size of 250×500 mm were employed for the test. 100 mm larger bottom box was set to allow 20% lateral displacement relative to top box length (500 mm)

[1] Professor, Graduate School of Global Environmental Studies, Kyoto University, JAPAN. Email: kamon@mbox.kudpc.kyoto-u.ac.jp
[2] Former Graduate Student, ditto, JAPAN. Email: vanan.nexus@gmail.com
[3] Associate Professor, ditto, JAPAN. Email: tkatsumi@mbox.kudpc.kyoto-u.ac.jp
[4] Assistant Professor, ditto, JAPAN. Email: inui@mbox.kudpc.kyoto-u.ac.jp
[5] Senior Research Scientist, Technology Research Institute of Osaka Prefecture, JAPAN. Email: akai@tri.pref.osaka.jp

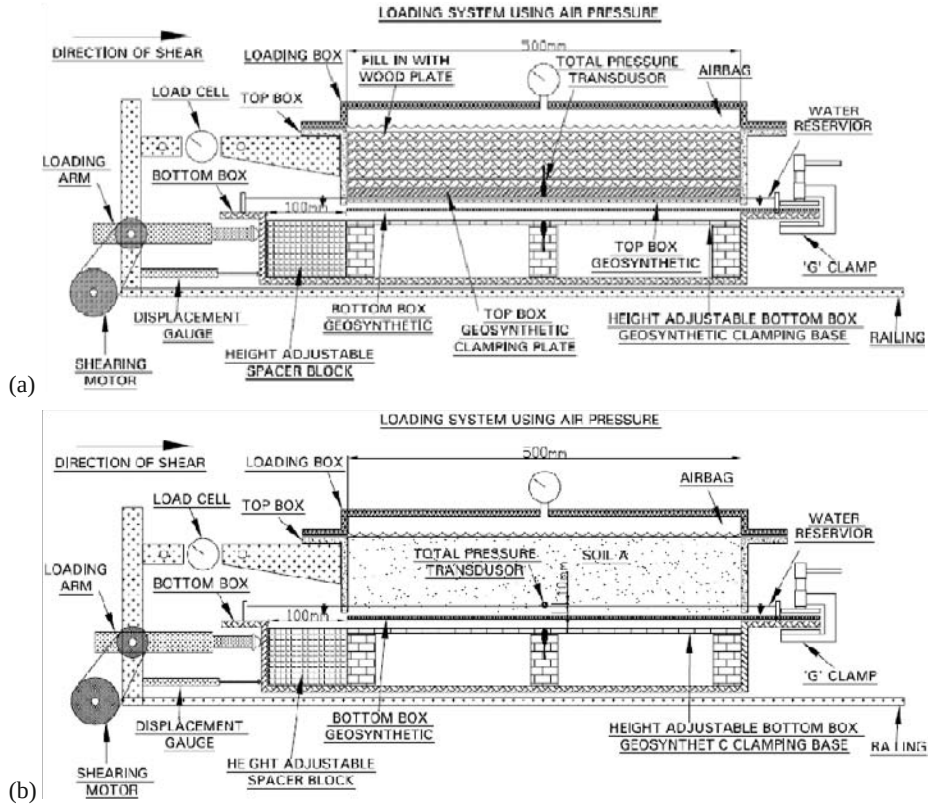

Fig. 1 Direct shearing test apparatus for the interface between geosynthetics (a) and geosynthetics and soil (b)

Table 1 Properties of geosynthetics used in the test

Materials		Geotextile	PVC sheet	HDPE sheet
Features		Non-woven type	Rear: Rough surface Front: Smooth surface	Smooth surface (Type-1) Blown film textured surface (Type-2)
Mass index	(g/m^2)	≥ 1,070 (JIS L1908)	≥ 1,940 (JIS L1908)	≥ 1,550 (JIS L1908)
Thickness	(mm)	10.0	1.5	1.5
Tensile strength	(N/mm)	≥ 16 (Weft, JIS L1908) ≥ 8 (Wrap, JIS L1908)	30 (JIS K6251)	544 (JIS K6251)
Elongation at break	(%)	≥ 55 (Weft, JIS L1908) ≥ 70 (Wrap, JIS L1908)	320 (JIS K6251)	790 (JIS K6251)
Tear strength	(N)	≥ 200 (JIS L1096)	N/A	289 (JIS K6252)
Penetration	(N)	≥ 1,000 (ASTM D4833)	N/A	≥ 539 (ASTM D4833)

Table 2 Physical properties of CCLs and native base soil

	Sand-bentonite mixture	Silt-bentonite mixture	Granite soil
Liquid limit (%)	47	69	–
Plastic limit (%)	23	35	–
Plasticity index	23	34	–
Particle density (Mg/m^3)	2.60	2.64	2.59
Maximum dry density (Mg/m^3)	1.90	1.68	2.06
Optimum water content (%)	10.5	17.5	9.0
Classification	Clay of low plasticity	Clay of high plasticity	Highly weathered granitic soil
Direct shear test			
Total cohesion (kPa)	77.0	43.1	31.4
Total friction angle (°)	34.3	35.8	45.5
CIU test			
Total cohesion (kPa)	5	4	5
Total friction angle (°)	15	22	30
Effective cohesion (kPa)	0	0	0
Effective friction angle (°)	33.5	28	35

during the shearing with the constant contact area of 250 ×500 mm. Constant shearing speed of 1 mm/min was employed with the normal vertical loads of 100, 200 and 300 kPa, which is equivalent to up to 20m-height landfilling based on the assumption that the wet density of the reclaimed waste is 15 kN/m^3. Testing methods

Table 3 Summary of test cases and results

Case	Material-1	Material-2	Dry/optimum moisture condition		Saturated/wet condition	
			Cohesion (kN/m^2)	Friction angle (°)	Cohesion (kN/m^2)	Friction angle (°)
Series 1: Geotextile-Geomembrane interface						
GT-H1	Geotextile	HDPE sheet (Type-1)	0.0*	7.6*	0.0*	7.3*
GT-H2	Geotextile	HDPE sheet (Type-2)	3.0	21.0	8.7	20.6
GT-PR	Geotextile	PVC sheet (Rear side)	11.3	18.6	6.1	18.2
GT-PF	Geotextile	PVC sheet (Front side)	26.3	16.9	0.0	22.3
Series 2: Soil-Geosynthetic interface						
SL-GT	Silt-bentonite mixture	Geotextile	0.0	15.2	0.0	19.0
SN-GT	Sand-bentonite mixture	Geotextile	0.0*	15.6*	0.0	20.6
GS-GT	Granite soil	Geotextile	0.0*	17.8*	9.9	18.6
SL-H1	Silt-bentonite mixture	HDPE sheet (Type-1)	0.0	15.3	0.0	5.2
SN-H1	Sand-bentonite mixture	HDPE sheet (Type-1)	0.0	13.7	0.0	6.1
GS-H1	Granite soil	HDPE sheet (Type-1)	0.0	15.6	0.0	19.8
SL-H2	Silt-bentonite mixture	HDPE sheet (Type-2)	0.0	24.1	0.0	9.1
SN-H2	Sand-bentonite mixture	HDPE sheet (Type-2)	0.0	24.5	0.0	10.9
GS-H2	Granite soil	HDPE sheet (Type-2)	0.0	23.0	26.8	15.2
SL-PR	Silt-bentonite mixture	PVC sheet (Rear side)	0.0	22.2	0.0	13.7
SN-PR	Sand-bentonite mixture	PVC sheet (Rear side)	0.0	19.7	2.4	10.5
GS-PR	Granite soil	PVC sheet (Rear side)	0.0	18.7	9.3	17.5
SL-PF	Silt-bentonite mixture	PVC sheet (Front side)	0.0	19.8	0.0	3.5
SN-PF	Sand-bentonite mixture	PVC sheet (Front side)	0.0	16.9	0.0	6.5
GS-PF	Granite soil	PVC sheet (Front side)	0.0	20.2	0.0	19.8

* Data have are published in Saravanan et al. (2006)

according to ASTM D3080-98, D5321-02 and D6243-98 were referred for the modifications of the shear box. To minimize the impact of the apparatus on the interface shear strength, the gap between the top and bottom boxes during shearing was kept 1 mm.

Materials

Geosynthetics

Geosynthetics most typically employed in the landfill liner were studied, namely non-woven geotextile, PVC (polyvinyl chloride) geomembrane sheet and two different HDPE (high density polyethylene) geo-membrane sheets (smooth surface HDPE sheet referred to "HDPE-1" and blown film textured surface HDPE sheet referred to as "HDPE-2"). The PVC geomembrane used has a rough rear and a smooth front. Both sides were subjected to the interface shearing. Basic properties of these geosynthetics are shown in Table 1.

Compacted clay liner and subsoil

Two different soil-bentonite mixtures were used as compacted clay liner materials; silt-bentonite mixture and sand-bentonite mixture. For these soil-bentonite mixtures, soil and sodium bentonite were mixed at dry mass ratio of 100:10 and compacted at optimum moisture content of 17.5% (silt-bentonite mixture) and 10.5% (sand-bentonite mixture). Compaction in the shear box was performed using a hand-held electric vibrating compaction machine. The compaction time was carefully calibrated for the minimum degree of compaction to reach more than 90% of the maximum dry density. As foundation soil, highly weathered granite soil compacted at its optimum water content of 9% was used. The basic physical and shear strength properties for these CCLs and granite soil are shown in Table 2.

Consolidated Isotropic Undrained (CIU) and small scale shear box tests were conducted on CCLs and compacted granite soil. The total cohesion, effective cohesion and friction parameters of the CCLs, along with the relevant shear box test results, are also listed in Table 2. A mixture of bentonite with sand shows similar cohesion to silt and bentonite mixture, however the sand mixture demonstrated higher frictional resistance from the CIU tests. The properties of highly weathered granite soil were sufficient to provide strong founding base.

Evaluation and Testing Cases

The interface test results indicate different kind of failures at different levels of relative displacement or horizontal strain. The maximum shear stresses ranged from 1% to 15% displacement relative to sample length or top shear box size of 500 mm. In order to consistently analyze the relative displacement and shear stresses associated with failure, the maximum shear stress was a selection of either maximum shear stress, or the maximum shear stress reached within 8% of relative displacement. The selected shear stress consists of a combination of peak and hardening residual shear stress within 8% of relative displacement. Based on the selection criteria, the use of peak or residual interface strength is proposed to be assessed within the prescribed horizontal strain value of 8%. This is due to some of the

test results presented in this paper have higher residual interface strength caused by horizontal strain hardening effect. Hence selection purely based on peak or residual interface strength in some cases could over or under estimate the interface resistance. Thus the selection of maximum shear stress within 8% horizontal strain was used as criteria in this research. The unit of 8% horizontal strain was selected as criteria of landfill liner failure limit, where potential geomembrane tearing which could lead to leachate pollution to the environment.

The selected shear stresses obtained were plotted against normal stresses to compute the failure envelope. To determine the total cohesion and total interface friction angle, best-fit linear plots were developed. The shear stress intersections were set to be through either axis or positive cohesion only. List of the test cases conducted and the interface shear strength parameters obtained are summarized in Table 3. Series 1 and 2 are designed to evaluate the effect of water content (OMC and SWC) on the interface shear performance between geotextile and geomembrane, and between geosynthetics and CCL / foundation soil, respectively. For SWC, the compacted soil samples were placed in a vacuum chamber with maximum negative pressure between 50 to 60 kPa for 48 hours to achieve the degree of saturation around 90% in the shearing zone.

RESULT AND DISCUSSION

Interface shear strength parameters under both saturated/wet condition (SWC) and optimum moisture condition (OMC) are presented in Table 3. By comparing interface test results under OMC and SWC, following differences were found.

For the interface between geotextile and geomembrane in Series-1, the test results had very little different between OMC and SWC. Only in the case GT-PF (geotextile / front side of PVC geomembrane) 30% higher frictional resistance and no cohesion were observed under SWC. However, it can be concluded that there is no significant effect on the geotextile/ geomembrane interface shear performance in the case that the whole landfill liner is saturated/submerged.

For the silt-bentonite mixture interfacing with geomembrane, the parameters obtained were lower for SWC compared to OMC of about 62%－195%. The HDPEs had frictional resistant lowered by 165%－95% and PVC geomembrane by 62%－88%. Fig. 2 shows the shear stress profile with the horizontal displacement/ strain for the interface between silt-bentonite mixture and HDPE-1 under both OMC and SWC. For OMC, the peak shear stresses were observed at the 1%－2% horizontal strain. For SWC, horizontal strain hardening effect was observed for all normal loads. These observations are also consistent with the silt-bentonite interfacing with HDPE-2 and PVC. For the silt-bentonite mixture interfacing with geotextile, 20% increment in frictional resistance was observed. The stress-displacement behaviors are similar to those of the interface with geomembranes.

For the sand-bentonite mixture interfacing with geosynthetics, the test results under SWC were similar to those of with the silt-bentonite mixture. However, the frictional contribution from the interfaces with sand-bentonite mixture was marginally higher than that of silt-bentonite mixture. In the initial prediction, sand-bentonite mixture was predicted to provide much higher frictional resistance as compared to silt-bentonite mixture. The test results were not as predicted due to the presence of bentonite in the sand and higher damages created on interfacing member during sharing by sand.

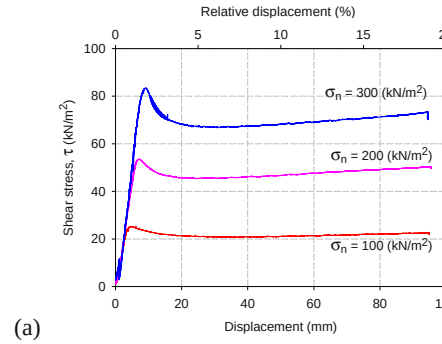

(a)

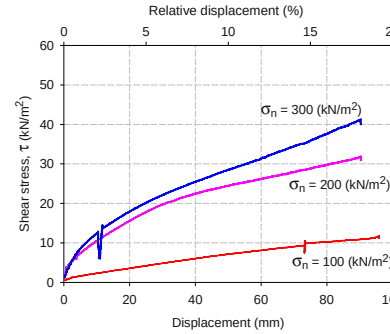

(b)

Fig. 2 Stress-displacement curves for the interface between silt-bentonite mixture and HDPE-1: (a) OMC and (b) SWC

Fig. 3 shows the stress-displacement curves for the interface between sand-bentonite mixture and HDPE-1 under SWC. Unlike the silt-bentonite mixture, the peak shear stresses were followed by the horizontal strain hardening for all normal loads. This behavior was observed for the interfaces between HDPE-2 and PVC.

The saturated interfaces were lower for geomembranes compared to geotextile. The HDPEs had frictional

resistant lowered by 125% and PVC geomembrane by 160%—463%. In the case of geotextile, 25% increment in frictional resistance was observed, although horizontal strain softening behavior was clear only under SWC for relatively larger normal loads, as shown in Fig. 4. These observations are similar to those for the silt-bentonite mixture.

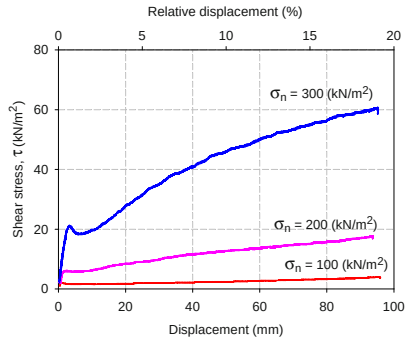

Fig. 3 Stress-displacement curves for the interface between sand-bentonite mixture and HDPE-1 under SWC

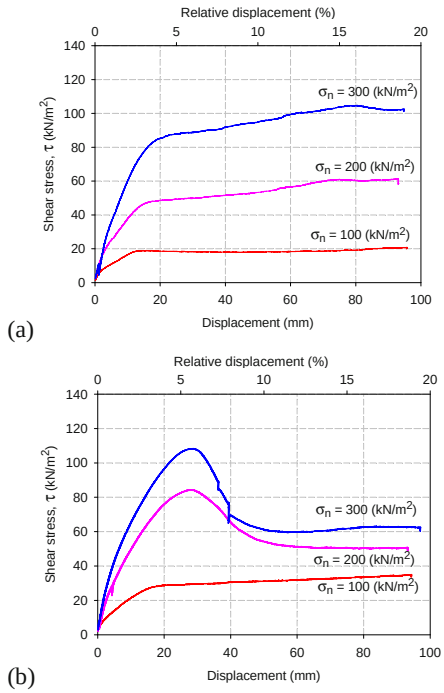

Fig. 4 Stress-displacement curves for the interface between sand-bentonite mixture and geotextile: (a) OMC and (b) SWC

Interface parameters of foundation granite soil with geotextile and geomembrane under SWC resulted in followings, compared to those under OMC:

- with geotextile: 4% higher;
- with smooth HDPE-1 geomembrane: 21% higher;
- with textured HDPE-2 geomembrane: 50% lower;
- with PVC geomembrane of both side: 2 to 7 % lower.

From the findings on granite soil, geotextile and smooth HDPE-1 geomembrane had higher frictional resistance compared to textured HDPE-2 geomembrane and PVC geomembrane under SWC. In the case of HDPEs, the frictional resistance of textured HDPE-2 geomembrane had significant drop from 23.0 degree under OMC to 15.2 degree under SWC, which is almost same to the frictional resistance of smooth HDPE (Type 1) geomembrane under OMC of 15.6 degree. As for PVC geomembrane only a drop of 2 to 7% was observed. Compared with CCLs, negative effect under SWC on the interface performance is less significant. This is probably because the presence of bentonite in CCLs affects the interface property a lot under SWC.

In all cases, geotextile had higher frictional resistance under SWC compared with OMC except the interface between geotextile and both sides of PVC geomembrane, where a significant drop of 30% in frictional resistance was observed between OMC and SWC.

CONCLUSIONS

This paper summarizes the interface shear performance of landfill liner components under as installed (optimum water content) condition and saturated/wet condition based on the test results of the modified large-scale shear test. The following remarks can be drawn:

(1) Interface shear performance between geotextile and geomembrane sheet is not affected by wetting or submerging

(2) Non-woven geotextile maintains or enhances the interface shear performance with both CCLs and foundation granite soil under saturated/wet condition.

(3) The saturated/wet CCL-GM interface had much lower shear strength compared to the interface under OMC. The peak shear stresses were not clear and horizontal strain hardening effect was observed under SWC. Especially, the frictional resistance of textured HDPE-2 geomembrane under SWC had significant drop from the value under OMC.

(4) For geotextile and geomembrane sheet, the frictional contribution from the interfaces with sand-bentonite mixture was marginally higher than that of silt-bentonite mixture.

5) Compared with CCLs, foundation granite soil is subjected to less significant influence on the interface performance under SWC. This is probably because the presence of bentonite in CCLs affects the interface property a lot under SWC. However, detail mechanisms accounting for these different behaviors are still unclear and should be further studied.

ACKNOWLEDGEMENTS

The authors wish to extend special thanks to Japanese Society for the Promotion of Science (JSPS) for their financial support for this research work.

REFERENCES

ASTM D3080. Standard Test Method for Direct Shear Test of Soils Under Consolidated Drained Conditions. ASTM International. West Conshohocken, PA

ASTM D5321. Standard Test Method for Determining the Coefficient of Soil and Geosynthetic or Geosynthetic and Geosynthetic Friction by the Direct Shear Method. ASTM International. West Conshohocken, PA

ASTM D6243. Standard Test Method for Determining the Internal and Interface Shear Resistance of Geosynthetic Clay Liner by the Direct Shear Method. ASTM International. West Conshohocken, PA

Chiu P, Fox PJ (2004) Internal and interface shear strengths of unreinforced and needle-punched geosynthetic clay liners, Geosynthetics International 11 (3): 176-199

Daniel DE, Koerner RM, Bonaparte R, Landreth RE, Carson DA, Scranton HB (1998) Slope stability of geosynthetic clay liner test plots, Journal of Geotechnical and Geoenvironmental Engineering, ASCE. 124 (7): 628-637

Fox PJ, Rowland MG, Scheithe JR (1998) Internal shear strength of three geosynthetic clay liners. Journal of Geotechnical and Geoenvironmental Engineering. ASCE. 124 (10): 933-944

Gilbert RB, Byrne RJ (1996) Strain-softening behavior of waste containment system interfaces. Geosynthetics International 3 (2): 181-203

Gourc JP, Reyes Ramirez R (2004) Dynamics-based interpretation of the interface friction test at the inclined plane. Geosynthetics International 11 (6): 439-454

Ling HI, Leshchinsky D (1997) Seismic stability and permanent displacement of landfill cover systems. Journal of Geotechnical and Geoenvironmental Engineering. ASCE 123 (2): 113-122

Stark TD, Poeppel AR (1994) Landfill liner interface strengths from torsional ring shear tests. Journal of Geotechnical Engineering. ASCE 120 (3): 597-615

Stark TD, Williamson TA, Eid HT (1996) HDPE geomembrane/geotextile interface shear strength. Journal of Geotechnical Engineering. ASCE 122 (3): 197-203

Saravanan M, Kamon M, Faisal HA, Katsumi T, Akai T, Inui T, Matsumoto A (2006) Interface shear stress parameter evaluation for landfill liner using modified large scale shear box. Geosynthetics, J Kuwano and J Koseki (eds.). Millpress. Rotterdam: 265-271

LEACHATE FILTER GEOTEXTILE AND APPLICATION FOR LAOGANG MUNICIPAL SOLID WASTE LANDFILL, SHANGHAI

T.W. Yee[1] and K.H. Wong[2]

ABSTRACT: The Laogang Municipal Solid Waste Landfill, Shanghai is situated in the eastern part of Laogang township in Nanhui district, about 60 km from the Shanghai city center. The landfill incorporated a double liner system at the base of the landfill for leachate control, a leachate drainage and collection system, and a leachate treatment system. The leachate drainage and collection system consists of a 600 mm thick layer of gravel with an embedded network of perforated pipes. A filter geotextile is placed above the gravel bed before solid waste is placed directly over the geotextile. A review of development of leachate drainage and collection systems as well as geotextiles for leachate filtration is included.

KEYWORDS: landfill, leachate, filter, geotextile, clogging

INTRODUCTION

The Municipality of Shanghai covers an area of 6,340km^2 with a population of more than 18 million and is administratively of equal status to that of a province. It is located on the coast of the East China Sea between the mouth of Chang Jiang (Yangtze River) to the north and the Hangzhou Bay to the south. Shanghai is the world's busiest port in terms of cargo throughput and ranks third busiest in the world, after Singapore and Hong Kong, in terms of container traffic. Shanghai is regarded as the center of finance and trade in China. Like all mega cities of the world, Shanghai also produces huge amounts of solid waste. It was estimated in 1994 that Shanghai generated 35,000 tons of municipal solid waste per day.

The Laogang Municipal Solid Waste Landfill of the Municipality of Shanghai, China is located in the eastern part of Laogang township in Nanhui district, about 60km from the city center of Shanghai. The landfill site is located on tidal land and occupies a total area of 361 hectares. At the end of 2002, the Shanghai Urban Appearance and Environmental Sanitation Bureau and the Shanghai Urban Construction Investment Development Corporation jointly invited its first international bidding for the fourth phase of the Laogang Landfill construction project. The project was won by a company set up by ONYX of France, CITIC Pacific of Hong Kong and Shanghai Chengtou Environmental Industries Development Co Ltd. The project involves investment, design, construction, operation, maintenance and transfer of management right. The design will incorporate a double geomembrane liner system, leachate collection and treatment system, landfill gas collection and management system, comprehensive environmental monitoring programs and modern landfill operations. Initial intake is estimated to be 6,300 tons per day with an anticipated total of 34 million tons of waste over a 20 years contract period. Fig. 1 shows the satellite view of the Municipality of Shanghai and the location of Laogang Municipal Solid Waste Landfill site.

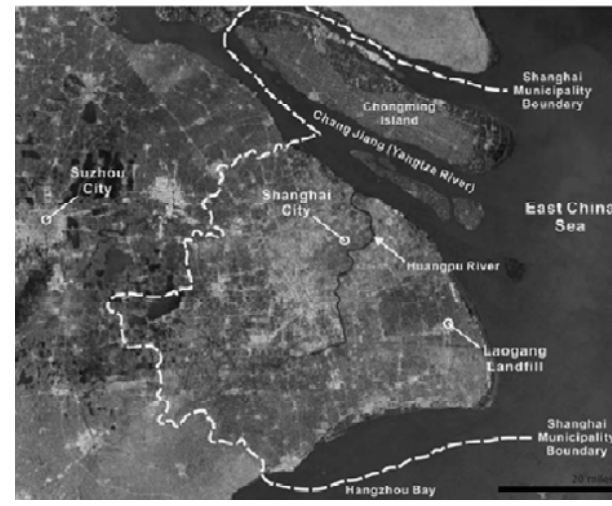

Fig. 1 Satellite view of the Municipality of Shanghai and the location of Laogang Solid Waste Landfill site

[1] Consultant, TW Engineering, MALAYSIA. Email: yeetackweng@yahoo.com
[2] Eric Kwok-Hung Wong, Hong Kong SAR, HONG KONG. Email: erickhwong@yahoo.com.hk

LEACHATE DRAINAGE AND COLLECTION SYSTEMS

Terminology

The Collins Essential English Dictionary defines landfill as “disposing of rubbish by covering it with earth”. It can mean the process or an area filled in by the process. Modern day landfill is engineered and defined as “a land disposal site employing a engineered method of disposing wastes on land in a manner that minimizes environmental hazards by spreading wastes in thin layers, compacting the wastes to the smallest practical volume and applying cover materials at the end of each operating day” (Rowe et al. 2004).

Leachate is termed as “a liquid produced from a landfill that contains dissolved, suspended and/or microbial contaminants from solid waste” (Rowe et al. 2004). Leachate is accumulated in landfill when percolation of water through solid waste dissolves soluble salts and gathers biodegraded organic compounds as well as possibly suspended solids to form a foul-smelling liquid.

Clogging is defined as “a build-up of biofilm, chemical precipitates and small (e.g. silt and sand) particles that are deposited in pipes and the granular material (e.g., sand or gravel), and geotextiles that are used in drainage systems” (Rowe et al. 2004). The build-up of such solids progressively reduces the hydraulic conductivity of the drainage system and consequently reduces its ability to drain leachate from the landfill.

Leachate

When water percolates through solid wastes that are undergoing decomposition, both biological materials and chemical constituents are leached into solution. Table 1 shows the typical data on the composition of leachate from new and mature landfills.

The potential for the formation of leachate can be assessed from a water balance perspective of the landfill. The water balance involves adding the amounts of water entering the landfill and subtracting the amounts of water consumed in chemical reactions as well as subtracting the quantity leaving as water vapor. The potential leachate quantity is the quantity of water in excess of the moisture-holding capacity of the landfill material. Fig. 2 shows the water balance perspective for assessment of leachate formation in a landfill; the amount of water out from below will equate to the amount of leachate collected.

Table 1 Typical data on the composition of leachate from new and mature landfills (Tchobanoglous et al. 1993)

	Value, mg/L[a]		
	New landfill (<2 years)		Mature landfill
Constituent	Range[b]	Typical[c]	(>10 years)
BOD_5 (5-day biochemical oxygen demand)	2,000－30,000	10,000	100－200
TOC (total organic carbon)	1,500－20,000	6,000	80－160
COD (chemical oxygen demand)	3,000－60,000	18,000	100－500
Total suspended solids	200－2,000	500	100－400
Organic nitrogen	10－800	200	80－120
Ammonia nitrogen	10－800	200	20－40
Nitrate	5－40	25	5－10
Total phosphorus	5－100	30	5－10
Ortho phosphorus	4－80	20	4－8
Alkalinity as $CaCO_3$	1,000－10,000	3,000	200－1,000
pH	4.5－7.5	6	6.6－7.5
Total hardness as $CaCO_3$	300－10,000	3,500	200－500
Calcium	200－3,000	1,000	100－400
Magnesium	50－1,500	250	50－200
Potassium	200－1,000	300	50－400
Sodium	200－2,500	500	100－200
Chloride	200－3,000	500	100-400
Sulfate	50－1,000	300	20－50
Total iron	50－1,200	60	20－200

[a]Except pH, which has no value.

[b]Representative range of values. Higher maximum values have been reported in the literature for some of the constituents.

[c]Typical values of new landfills will vary with the metabolic state of the landfill.

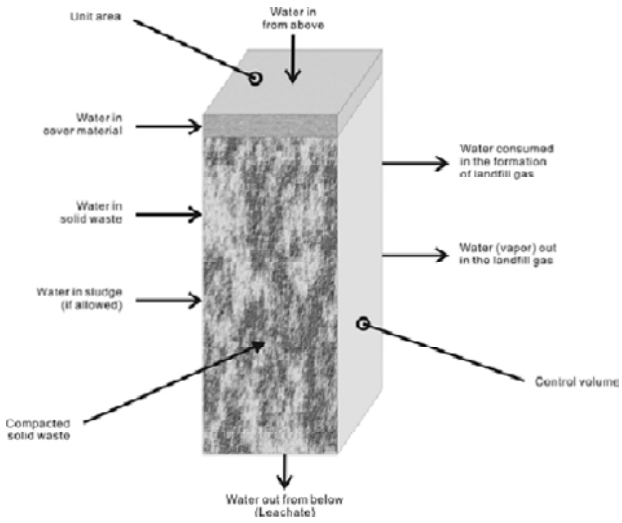

Fig. 2 Water balance perspective for assessment of leachate formation in a landfill (adapted from Tchobanoglous et al. 1993)

Development of Leachate Drainage and Collection Systems

The first recorded regulations to control municipal waste were implemented during the Minoan civilization a few thousand years ago. Solid waste from the capital, Knossos, were placed in large pits and covered in layers of earth at intervals (Tammemagi 1999). The basic method of landfilling has remained relatively unchanged up to the present day. Evolution of landfill design happened in response to problems encountered (Bouazza et al. 2002). Changes happened only when a problem was identified or issue reached a certain level of concern. One of the prime concerns has been on the drainage and collection of leachate. The objective is to prevent seepage of leachate from the landfill which would otherwise contaminate groundwater sources.

Development of leachate drainage and collection systems in landfill may be divided in three generations as follows:

- First generation—toe drains only
- Second generation—regularly spaced French drains
- Third generation—continuous granular drainage blanket

The first generation system was ineffective in controlling contaminant escape from landfill to underlying aquifers. The second generation drainage and collection system experiences leachate mounding once clogging develops in the drainage system. Rowe (1992) cautioned against the use because the confluence of flow near the collection pipe gives rise to high mass loading per unit time and hence increases the rate of clogging. The third generation of continuous granular drainage blanket which has perforated pipes regularly embedded within the drainage blanket and a suitably selected geotextile filter above the primary drainage layer yields a number of benefits over systems of earlier generations. Firstly, by lowering the height of leachate mounding, leachate seeps can be minimized. Secondly, by reducing the leachate head acting on the base of the landfill, the hydraulic gradient through the underlying barrier and advective velocity out of the landfill (both of which influences the movement of contaminant through a barrier) can be reduced to acceptable levels in many cases. Thirdly, by removing contaminant from landfill, the mass of contaminant available for transport will be reduced. Sand has been used as continuous drainage blanket in landfill. However, it is now recognized that sand is highly susceptible to clogging and hence uniform coarse gravel with an initial hydraulic conductivity of the order 10^{-2}m/s or higher is preferred (Rowe et al. 2004). Fig. 3 shows the three generations of leachate drainage and collection systems in landfills.

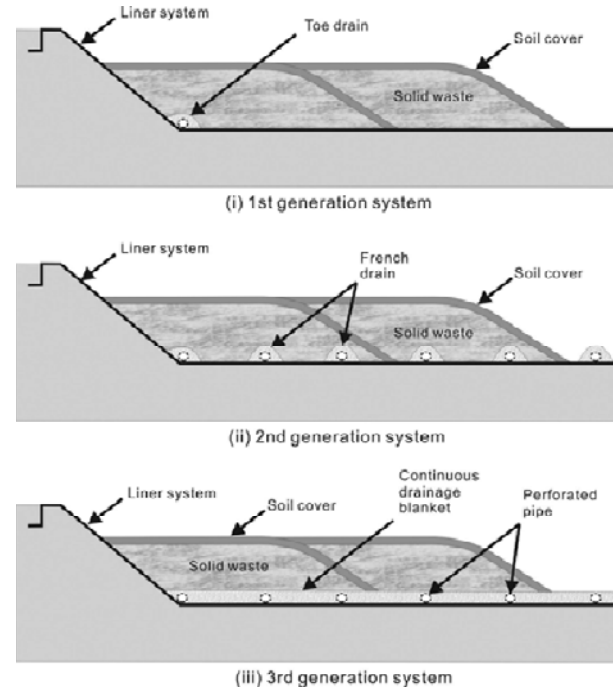

Fig. 3 Three generations of leachate drainage and collection systems

LEACHATE FILTER GEOTEXTILE

Role of Geotextile

The role of geotextile in a leachate drainage and collection system is to allow adequate leachate flow from the solid waste through to the drainage blanket and at the same time prevent or reduce clogging in the drainage gravel and pipe. The use of geotextile as a filter above

the drainage gravel has been reported to result in substantially less clogging than that observed in areas with no geotextile filter (Rowe et al. 2004). A comparison of clogging where the waste was in direct contact with the underlying drainage blanket with that where a woven, slit film, geotextile filter had been placed between the waste and the underlying drainage blanket at the Keele Valley Landfill, Ontario, Canada (Fleming et al. 1999) showed a significant difference in the upper unsaturated portion of the collection system (i.e., the portion influenced by the presence of geotextile filter). Where the geotextile filter had been used, between 0 and 20% of the pore space was filled with clog material whereas there was a 30 to 60% loss of void space in a comparable area where no geotextile was used. While the geotextile provided protection to the underlying gravel layer at the same time did experience some clogging.

Clogging of Geotextile

The study of Koerner and Koerner (1989) indicates a rough correlation between the TS/BOD levels of the leachate and the degree of clogging. Studies have shown that the magnitude of the decrease in hydraulic conductivity of the geotextile will depend on the openness of the pore structure of the geotextile, the flow rate and the concentration of the leachate. Table 2 shows the reduction of geotextile hydraulic conductivity for a range of different geotextiles permeated with leachate.

Selection of Geotextile

Koerner and Koerner (1995) recommended that for mild leachate, either a woven or nonwoven geotextile could be used in contact with the waste, provided it had properties that met the requirements given in Table 3.

Table 2 Decrease in hydraulic conductivity of geotextiles permeated with leachate (average COD: 3,000-4,000mg/l; BOD: 2,000-2,500mg/l; TSS: 300-600mg/l) at a rate of 2 x 10^{-5}m/s (Rowe 2004; adapted from Koerner et al. 1994)

Type of filter	M_A (g/m^2)	POA (%)	AOS (mm)	t_{GT} (mm)	Initial k_n (m/s)	Initial (s^{-1})	Equilibrium k_n (m/s)	Flow to equilibrium (m^3/m^2)
Uniform sand					4×10^{-3}		2×10^{-6}	119
Well-graded sand					6×10^{-4}		4×10^{-7}	170
W: Monofilament	200	32		0.7	3.4×10^{-3}	4.8	2.5×10^{-6}	51
W: Multifilament	270	14		0.8	1.9×10^{-3}	2.4	7×10^{-6}	51
W: Slit film	200	7		0.4	1.6×10^{-4}	0.4	8×10^{-8}	43
W: Monofilament	250	10		0.6	6.4×10^{-4}	1.0	5×10^{-8}	76
Special NW/W	740		0.3	6.3	1.5×10^{-2}	2.4	3.5×10^{-6}	102
NPNW	130		0.21	1.1	2.5×10^{-3}	2.1	6×10^{-8}	76
NPNW	270		0.18	2.4	3.6×10^{-3}	1.5	1×10^{-7}	93
NPNW	540		0.15	4.7	2.4×10^{-3}	0.5	2×10^{-7}	85
HBNW	120		0.165	0.4	2.4×10^{-4}	0.6	4×10^{-8}	76
NPNW	220		0.12	2.0	3.2×10^{-3}	1.6	1.5×10^{-7}	68

W denotes woven; NPNW denotes needle-punched nonwoven; HBNW denotes heat-bonded nonwoven.
M_A denotes unit mass of geotextile.
POA denotes percent open area of geotextile.
AOS denotes apparent opening size of geotextile.
t_{GT} denotes thickness of geotextile.
k_n denotes hydraulic conductivity.
Ψ denotes permittivity of geotextile.

Table 3 Recommended minimum values for geotextile filters for use with mild leachate and select waste over the geotextile (no hard or coarse material; for coarse and hard material over geotextile, the strength requirements may need to be increased) (Koerner and Koerner 1995)

Property	Woven monofilament geotextiles	Nonwoven needle-punched geotextiles
Mass, M_A (g/m^2)	200	270
Per cent open area (POA) (%)	10	-
Apparent opening size (AOS) (mm)	-	0.21
Grab strength (N)	1,400	900
Trapezoidal tear (N)	350	350
Puncture strength (N)	350	350
Burst strength (kPa)	1,300	1,700

Giroud (1996) has discussed the issue of geotextile clogging as part of a broad review of filter design. He tentatively recommends that sand and nonwoven geotextile filters should not be used even if the waste has been stabilized to produce low strength leachate by pretreatment. Rather, he recommends the use of monofilament woven geotextiles with a minimum filtration opening size (AOS) of 0.5 mm and a minimum relative open area (POA) of 15%, with a preference for a POA greater than 30%. The rationale for these recommendations arises from the observations that

- the specific surface area for monofilament woven geotextile is much smaller than that for nonwoven geotextiles and this decreases the surface area for biofilm growth,
- the woven filter structure allows more effective and rapid movement of fine material (i.e., material not intended to be retained) and leachate through the filter, and
- due to their compressibility, the filtration characteristics of a nonwoven geotextile vary with applied pressure.

However, Rowe (1998) would argue that the necessity to minimize clogging of filter geotextile may not apply to all design situations. Rowe (1998) would further argue that while excessive clogging is undesirable, the process of clogging also provides leachate treatment and, in doing so:

- decrease the potential for clogging at more critical zones (e.g., near collection pipes), and
- reduce the level of leachate treatment required after removal of leachate from the landfill.

LAOGANG SOLID WASTE LANDFILL PROJECT PHASE 4

Design for Leachate Drainage and Collection System

Fig. 4 shows the three dimensional cut-away perspective of the bottom and side slope liner and leachate collection layers for the Laogang Municipal Solid Waste Landfill Project Phase 4. The primary leachate collection layer consist of a 600 mm thick coarse aggregate layer sandwiched between a top leachate filter geotextile and a bottom nonwoven protection geotextile. Perforated HDPE pipes of nominal diameter 160 mm are embedded within the gravel layer in a network to collect the leachate for further treatment.

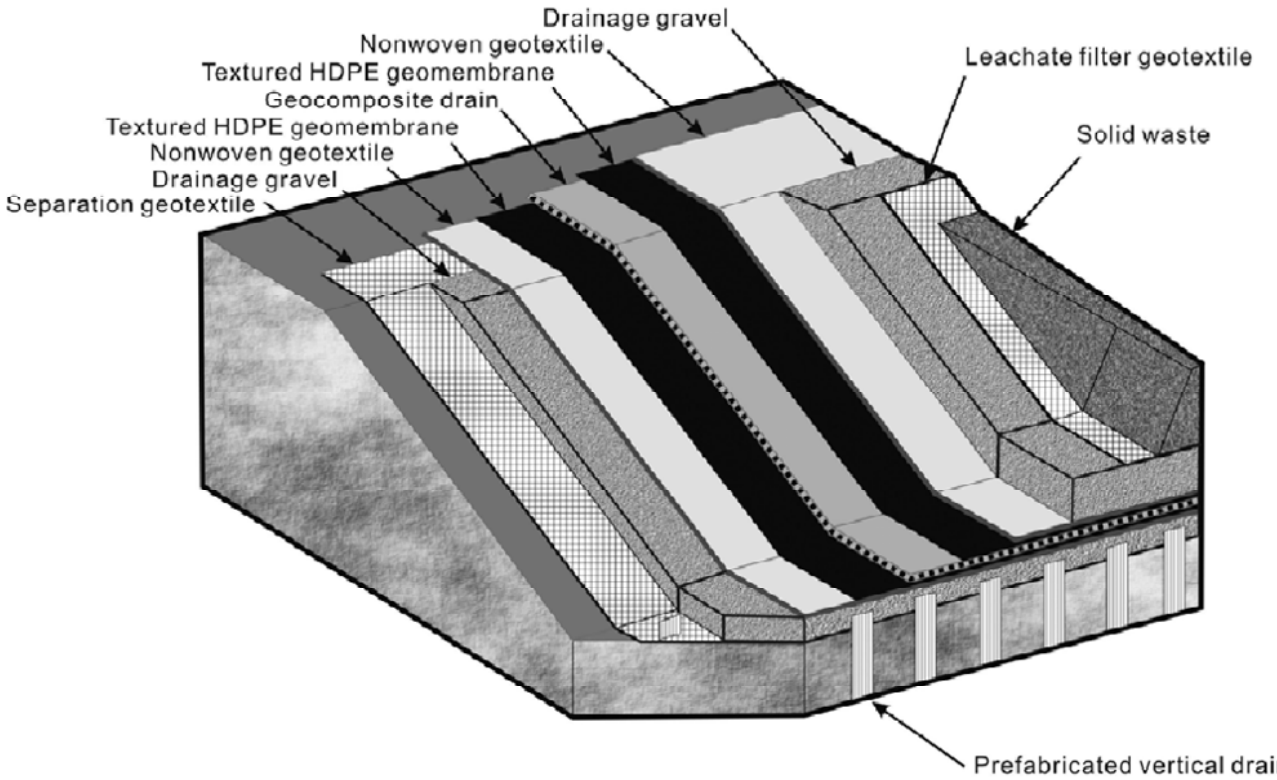

Fig. 4 Three dimensional cut-away perspective of bottom and side slope liner and leachate collection layers for the Laogang Municipal Solid Waste Landfill Project Phase 4

Table 4 Leachate filter geotextile specification for the Laogang Municipal Solid Waste Landfill Project Phase 4 and properties of supplied geotextile according to the manufacturer's datasheet

PROPERTY *(1)*	TEST METHOD	REQUIRED VALUES	GEOTEXTILE SUPPLIED
Grab Tensile Strength *(2)*	ASTM D4632	$\geq$ 800N	$\geq$ 1,130N
Grab Tensile Elongation *(2)*	ASTM D4632	$\leq$ 50%	15%
Trapezoidal Tear Strength *(2)*	ASTM D4533	$\geq$ 250N	$\geq$ 310N
Puncture (Pin) Strength	ASTM D4833	$\geq$ 300N	$\geq$ 560N
Permittivity	ASTM D4491	$\geq$ 0.5sec^{-1}	$\geq$ 0.95sec^{-1}
Apparent Opening Size	ASTM D4751	$\leq$ 0.43mm	$\leq$ 0.425mm
Percentage Open Area	CWO-22125	$\geq$ 10%	$\geq$ 10%
UV resistance *(3)*	ASTM D4355	$\geq$ 70%	$\geq$ 90%

Notes:
(1) All values are Minimum Average Roll Values (MARV) except UV resistance, which is the minimum value and Apparent Opening Size and Grab Tensile Elongation which are the maximum values.
(2) Measured in the weakest principal direction of the geotextile.
(3) Evaluation to be on 50mm strip tensile specimens after 500 hours exposure.

Specification for Leachate Filter Geotextile

Table 4 shows the leachate filter geotextile specification for the Laogang Municipal Solid Waste Landfill Project Phase 4. A total of 515,000 m^2 of woven monofilament polypropylene geotextile that conformed to the specification for the leachate filter geotextile was delivered to site over a time frame of four months. The properties of the supplied geotextile are compared against the specification in Table 4.

MQC for Leachate Filter Geotextile

The manufacturing quality control (MQC) requirement for the Laogang Municipal Solid Waste Landfill Project Phase 4 specifies that the manufacturer shall provide conforming Geotextile Roll Quality Control Certificates (GRQCC), tested at a minimum frequency of one per every 10,000 m^2 of geotextile supplied to the project. The GRQCC shall include all the specified properties in Table 4 except UV resistance. UV resistance Quality Control testing is required per formulation instead of per every 10,000 m^2 of geotextile supplied to the project.

Installation Process

Fig. 5 shows the installation of the liner system for the Laogang Municipal Solid Waste Landfill Project Phase 4.

Once the liner system and upper protection geotextile is laid, a layer of 600 mm thick coarse aggregate and embedded perforated pipes at specified locations are laid over. Then the leachate filter geotextile is laid over the coarse aggregate. Rolls of geotextile are unwrapped and unrolled over the coarse aggregate surface. Adjacent panels of unrolled geotextile are sewn together. Fig. 6 shows the landfill bottom liner and leachate collection system placed over with the leachate filter geotextile, ready for placement of solid waste.

Fig. 5 Installation of liner system for the Laogang Municipal Solid Waste Landfill Project Phase 4

Fig. 6 Leachate filter geotextile laid out and sewn together for the Laogang Municipal Solid Waste Landfill Project Phase 4

Fig. 7 shows the placement of the first batch of solid waste at the Laogang Municipal Solid Waste Landfill in 2005.

Fig. 7 Placement of solid waste directly over leachate filter geotextile for the Laogang Municipal Solid Waste Landfill Project Phase 4

Site Issues

The laying of leachate filter geotextile at the Laogang Solid Waste Landfill Project progressed relatively smoothly. Deliveries to site were done basically ahead of the actual work schedule and had to be placed in storage at site. Figure 8 shows the storage yard for leachate filter geotextile at the Laogang Solid Waste Landfill Project.

Fig. 8 Stockpile of leachate filter geotextile for the Laogang Municipal Solid Waste Landfill Project Phase 4

CONCLUSIONS

The following conclusions may be made:

- for effective leachate drainage and collection, continuous coarse gravel drainage blanket regularly embedded with perforated pipes is the preferred system,
- studies indicate that the use of geotextile as a filter above the continuous gravel drainage blanket helps to reduce clogging of the drainage blanket and embedded pipes, and
- the Laogang Solid Waste Landfill Project Phase 4 has employed amongst the highest international standards in the design of the leachate drainage and collection system.

REFERENCES

Bouazza A, Zornberg JG, Adam D (2002) Geosynthetics in Waste Containment Facilities: Recent Advances, Proceedings Seventh International Conference on Geosynthetics, Nice 2: 445-507

Fleming IR, Rowe RK, Cullimore DR (1999) Field observations of clogging in a landfill leachate collection system, Canadian Geotechnical Journal 36(4): 289-296

Giroud JP (1996) Granular Filters and Geotextile Filters, Proceedings Geofilters '96: 565-680

Koerner GR, Koerner RM (1989) Biological clogging of leachate collection systems, Durability and Ageing of Geosynthetics (ed. R.M. Koerner), Elsevier Applied Science, London: 260-277

Koerner RM, Koerner GR (1995) Leachate clogging assessment of geotextile (and soil) landfill for filters, US EPA Report, CR-819371, March

Rowe RK (1992) Integration of hydrogeology and engineering in the design of waste management sites, Proceedings International Association of Hydro-geologists Conference on Modern Trends in Hydro-geology, Hamilton: 7-21

Rowe RK (1998) Geosynthetics and the Minimization of Contaminant Migration through Barrier Systems Beneath Solid Waste, Proceedings 6th Inter-national Conference on Geosynthetics, Atlanta 1: 27-102

Rowe RK, Quigley RM, Booker JR (2004) Barrier Systems for Waste Disposal Facilities—2nd Edition, Spoon Press: London & New York: 587

Tammemagi H (1999) The Waste Crisis, Oxford University Press

Tchobanoglous G, Theisen H, Vigil S (1993) Integrated Solid Waste Management—Engineering Principles and Management Issues, McGraw-Hill: New York: 978

Proceedings of the 4th Asian Regional Conference on Geosynthetics
June 17 - 20, 2008 Shanghai, China

CASE HISTORY: KWAI CHUNG PARK VIADUCT AT GIN DRINKER'S BAY LANDFILL, HONG KONG

G. Ng [1]

ABSTRACT: One section, about 250 m of the Airport Railway Express linking the Chek Lap Kok International Airport and the city center runs through the Gin Drinker's Bay Landfill, which ceased operation in 1979. The site had no landfill lining system and existing subsoil drains were largely ineffective in intercepting migrating leachate. The gas content was considered a hazard so much so that the site, intended as Kwai Chung Park, was never opened to public. In addition, any concrete foundation built into the waste would have been susceptible to constant aggressive attack. Geosynthetics was introduced to mitigate environmental impact and to provide protection to viaduct concrete structures when excavation and construction began. This paper reviews the geosynthetics design, the material, the installation and the observable effectiveness eight years after completion.

KEYWORDS: geomembrane, geogrid, geotextile, geocomposite

INTRODUCTION

The Gin Drinker's Bay landfill was formed by way of public dump back in 1960's. At that time, environmental hazard was not a concern, let alone lining system. When the Airport Railway Express was conceptualized, the most feasible alignment was to have a section pass through the landfill, being the most viable location in between a cemetery hill on the North, the busy Kwai Chung Container Terminal on the South, the Kwai Chung Industrial area on the East and the Rambler Channel on the West. Other options would necessitate major rerouting and property relocations. Together with the natural elevation to cross the Rambler Channel, a decision was made to build the viaduct cutting through the landfill (Fig. 1). Kwai Chung Park Viaduct cost HK$300 million or USD 38 million (at 1995 value). The project kicked off in November 1994 and took 40 months to complete. Train was in operation in 1998 and a subsequent separated landfill restoration contract was implemented in 2000 to cap the entire landfill (Picture 1).

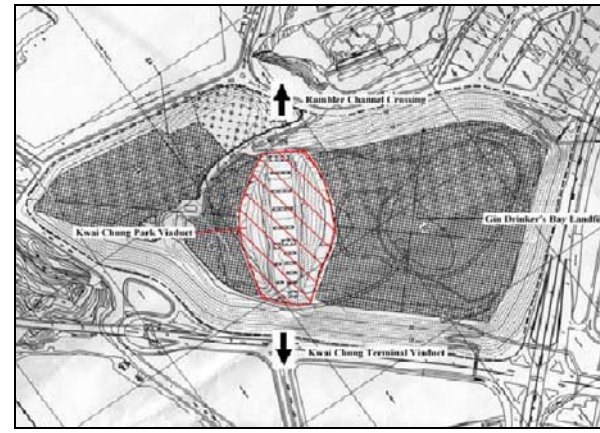

Fig. 1 Kwai Chung Park Viaduct layout in Gin Drinker's Bay landfill

Picture 1 Airport Express & Kwai Chung Park

SOLUTION

A capping system (picture 2) using geosynthetics was designed to encapsulate the exposed waste thereby reducing contact with the environment. The same system was extended to the pile caps and incorporated into each

[1]General Manager, G and E Company Limited, HONG KONG; Southeast Asia Area Manager, Tenax International BV, CHINA.
Email: nangary@i-cable.com

Picture 2 Kwai Chung Park Viaduct overview

pile. In doing so, the whole viaduct concrete structure was protected against leachate contact and any exposed waste as a result of excavation was kept away from external water, which would otherwise penetrate the waste and leach the contents into the groundwater. Adequate drainage and system stability was also put forward. Several different interconnected capping designs were adopted to cover the earthwork excavation and the concrete structure construction. The earthwork system covered the side slopes excavated from the crest of the landfill at +45 mPD to the railway formation at +20 to +25 mPD, in the shape of a mountain pass. The pile system referred to the protection of the pile caps and individual piles from the railway formation at +20 to +25 mPD level down to rock head at -10 to -36 mPD. The deepest pile had length in excess of 60 m. The platform system joined the capping and the pile system along the railway formation. A complete sealing was perceived.

CAPPING SYSTEMS

The earthwork system (Fig. 2; Picture 3) included four layers of geosynthetics: a bottom layer of geocomposite to collect seepage of leachate and under-ground water, an intermediate layer of 1.5 mm thick textured LLDPE geomembrane to prevent water infiltration, another geocomposite to drain away any accumulation of water on top of the geomembrane and a top layer of geogrid to stabilize the capping fill material.

All geosynthetics were selected with sufficient strength and frictional characteristics to maintain stability across the 1:3 slope, which has a run of over 70 m. A one meter trench at the crest of the slope served as the only anchorage. The system had to have several important features: it needed a large degree of flexibility to accommodate soft waste settlement; it had to be effective in intercepting and draining water; it had to provide sufficient interface shear friction to prevent various layers of geosynthetic from sliding against each other; and it had to offer resistance to hold the capping fill material from sliding.

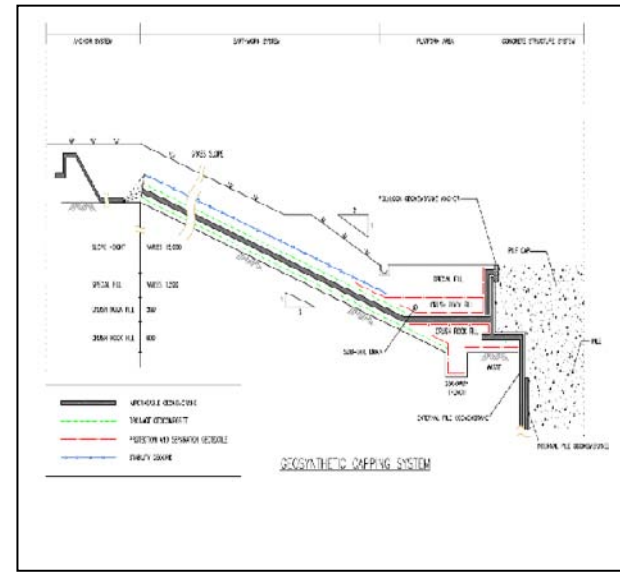

Fig. 2 Earthwork capping system

Picture 3 Earthwork capping geosynthetics

The pile system (Fig. 3; Picture 4) consisted of a double layer of 2.0 mm HDPE geomembrane. There were 52 piles of 2.20 m diameter and their depth varied from 30 m to 64 m. The internal lining layer had T-shape ribs (T-grip) on one side to ensure concrete bonding and the external lining layer had a smooth surface to minimize down drag resistance (negative skin friction). When soil settled, the membranes would slide against each other, minimizing damage to the concrete protection layer. There were 15 pile caps of various sizes. Underneath was a 2 mm smooth HDPE geomembrane extended to encase the underside and vertical face of the pile cap. Concrete embed was used at the termination. As such, all concrete structures were completely shielded.

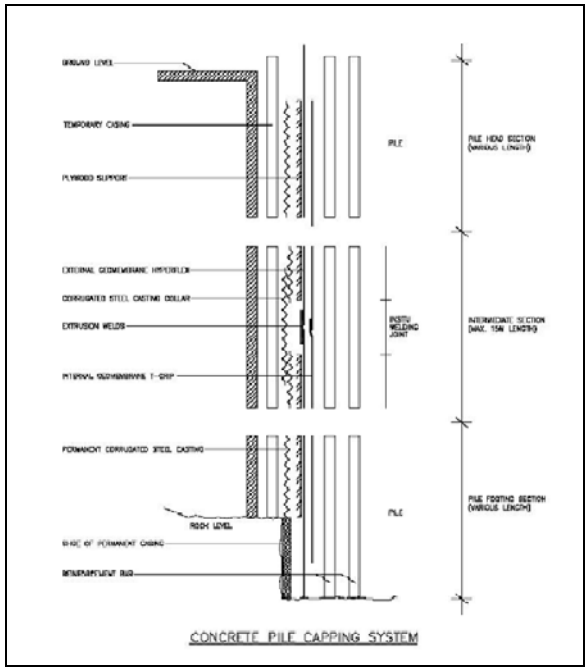

Fig. 3 Concrete pile capping system

Picture 4 Double lining inside the permanent casing

In between pile caps and the slope toe was the transition platform area. The capping system (Fig. 2; Picture 5) here resembled the earthwork system except that both geocomposites were replaced by drainage crush rock layer. In this situation, any water collected by the geocomposites were drained and buffered in the crush rock layer. Geomembrane thickness was increased to 2.0 mm in view of a higher risk of construction damage. Separation geotextile was used to cushion the geomembrane. There was, however, no need of a geogrid on the level platform. Along the toe of the slope, the 1.5 mm textured geomembrane was welded onto the 2.0 mm smooth geomembrane on the platform. This completed the impermeable barrier.

Picture 5 Transition platform capping geosynthetics

The 15 pile caps were in straight alignment linking the Kwai Chung Terminal Viaduct on the East towards Rambler Channel Crossing on the West. At each project interface, the lining system was necessary to maintain full coverage. Here the pile cap became the crest of the capping system sloping down to the toe, the site boundary. Space constrain had called for the adoption of a geogrid reinforced slope at the West end. This was to allow space to build a maintenance access road across the slope face. A 65º slope gave an extra 3 m width, which would otherwise not be available with conventional fill construction method. The capping lining system was installed under this reinforced structure following the earthwork lining design but to different level and contour (Fig. 4; Picture 6). Complication came at the lining layout along the transition where the upside capping lining merged with that of the downside at both the East and West project interfaces.

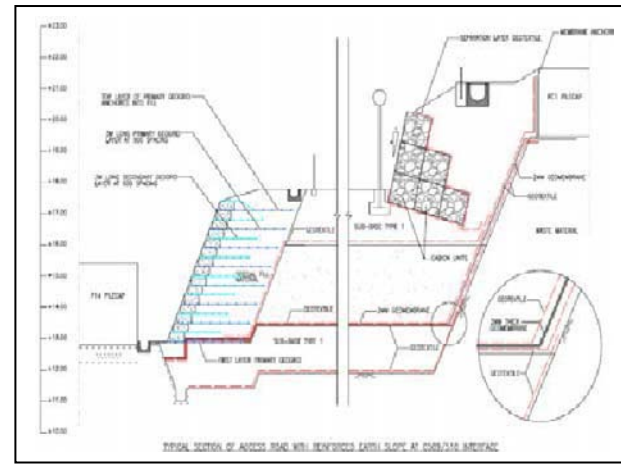

Fig. 4 Typical section of access road with reinforced fill slope

INSTALLATION

Pile double lining had to be pre-installed inside a permanent pile formwork. A corrugated tubular steel casing was taken as the permanent formwork to support the lining system. This had to be fabricated off site because of space congestion. Inside the casing, a 5 mm plywood lining was bolted onto the inside surface to receive the external HDPE liner. Tunnel rondelle was adopted to affix this liner. T-grip was then spot welded onto the external liner as temporary adhesion. A series of welding strength tests were conducted to determine method and location of welding. It was important to master the capability to hold the double lining in the formwork during transit and installation and yet to be able to disengage the two liner, effecting the negative skin function. Struts were sought to prevent detachment and collapse of double lining system during transit and storage. The maximum section length was 15 m for ease of handling and compliance to road transportation regulation.

Picture 6 Access road with reinforced fill slope

The lined formwork was lowered down the bore hole inside the temporary casing section by section. While the lower section was tucked at ground level, the upper section was hoisted and secured for section jointing. Here, extrusion welding was applied on each layer of liner. An extension lip was allowed to facilitate this operation. Stiff and rigid 2.0 mm HDPE permitted good workability. A steel collar was then screwed on the formwork to protect the jointing and to keep continuation of formwork. Each section was repeated in similar manner to reach full length of the pile. Perfect alignment was necessary to slip in the steel reinforcement cage. Any deviation from close tolerance would mean liner damage. Guide shoes were incorporated to direct the cage run between gaps of the T-grip ribs. In doing so, the T-grip was kept from collapsing during concreting. High precision and dedicated work were crucial.

Installation of capping geosynthetics was carried out primarily manually whereby each type of geosynthetics were cut, laid, properly connected and tested, panel-by-panel and layer-by-layer. Access limitation forbade any use of heavy lifting equipment. Temporary stability of the lining system was a problem at the Rambler Channel end where liners were installed in full height of over 10 m at an angle of 65º against waste material. Concerns were raised as to the effect of overstressing and excessive wrinkling during backfilling. Efficient work sequencing was set to cut down lining exposure time, thereby reducing risk of instability.

At the platform, the challenge came from the geomembrane interfacing work. This was the last part of the liner work, which could only commence after the pile system was completed. Works were complicated when liner had to be spread out from the pile prior to the construction of the pile cap. Special work sequencing was thought of to minimize possible construction damage.

MATERIAL

A bi-planar geocomposite with double sided non woven geotextile fulfilled the design strength, transmissivity and frictional characteristics. A uni-directional HDPE geogrid met the need for long-term design strength to hold the fill material from sliding on the nonwoven geotextile surface of the geocomposite. A textured HDPE geomembrane of 1.5 mm thickness was chosen for use on slopes, which was selected for its flexibility and strength needed to accommodate settlement and its frictional resistant surface needed for slope stability. An HDPE concrete protection liner T-grip was selected for use as the internal pile liner. It is made from HDPE of a thickness of 2 mm and has T-shape interlocks on one side running along the length of the pile at 100 mm spacing. The material's strengths include its toughness, its resistance to waste and leachate, its flexibility in fabrication and the possibility of engaging guide shoes between ribs when installing steel reinforcements. An HDPE geomembrane of 2 mm thick was selected for the external pile liner as well as for the platform. It was of the same thickness and properties as the T-grip and can be welded on to the internal liner by extrusion welding. A polypropylene geotextile was applied without any problem. Its inertness to waste offered reliability; its thickness at 4.4 mm was an ideal cushion to protect the geomembrane; and its high flow characteristic provided a good drainage and separation application.

Internal stability calculation using partial safety factor method was used to verify the suitability of the HDPE uni-directional geogrid in the reinforced slope construction. A secondary geogrid was put to optimize

surface stability. The same cushion geotextile was used to retain soil from being washed out of the geogrid. No surface treatment such as plastering or vegetation was applied. The geogrid was left exposed to the environment since (Picture 7).

Picture 7 Reinforced fill slope eight years after completion

CONCLUSION

At the time of installation, water running out from the geocomposite above the geomembrane along unfinished edges was noticeable after raining. Meanwhile, water was observed seeping out from the geocomposite below the geomembrane when rain subsided. This showed the desired drainage function and the geomembrane impermeability characteristics. During capping back-fill, no sliding of fill material had been encountered with the use of geogrid. Field and laboratory tests had demonstrated that The geogrid had no significant strength reduction as a result of UV exposure.

The capping soil was 1.5 m thick and the slope face was subsequently planted with grass, seedlings and whips. Sliding had never been recorded (Picture 8 & 9).

Picture 8 Vegetation on fill slope along the viaduct (1)

Picture 9 Vegetation on fill slope along the viaduct (2)

At the reinforced slope, very little deterioration to the exposed geogrid and geotextile were noticed. The slope stayed intact with no observable movement or distress. No differential settlement to the access road above the structure was noticeable.

To the pile lining, very little could be monitored. Inspection for possible lining damage prior to concreting was considered unsafe. From the record of concrete pour, consumption volume matched the anticipation. This indicated that there had been no concrete loss through the liner in the event damages had indeed taken place.

After Words

A request to re-visit the site in March 2005 was granted by the owner eight years after completion.

Vegetation was established quite well on all slope area, with some seedlings achieving over 5 m height. Full coverage of grass and ground cover were observed. The landscape appeared mature and no soil erosion or movement or settlement was noticed. All surface drainage did not show cracking and waterstop expansion joints remained intact. On the platform area, substantial settlements of up to 200 mm were seen at each end of the viaduct pile cap. One section of extrusion seam along the concrete embed where the HDPE geomembrane was welded onto the pile cap came off, signifying liner stayed integrity. Majority of the exposed seams were very strong and geomembrane was well protected by the geotextile against soil settlement down drag. No settlement was observed in all other areas. Exposed geomembrane and geotextile did not show signs of deterioration. There was no heavy ponding or soil penning which were signs of geocomposite malfunction.

This project covered only part of the landfill affected by the construction of viaduct. The whole landfill underwent restoration subsequently two years after the viaduct was in service (Picture 1). A lining system was installed only at the top plateau leaving side slope

surface drains to manage water infiltration. There was no continuity of lining systems in between the two phases of work. A drainage channel of about 2 m was allowed separating the two lining system to simplify the complexity of merging two systems. Trees were maturing on the slope in particular at the crest platform where the anchor trenches were. Structures constructed on slope such as access staircase and drainage channel did not seem to have dislocations. The geogrid did provide the sliding resistance.

Maintenance works are now primary horticultural in nature and drainage channel clearance. There was no leachate detection exercise until the whole landfill restoration work was eventually completed. The capping contractor has indicated little fluctuation volume of leachate. There were no observation wells within the viaduct vicinity. One could assume the same leachate quantity behavior. And surface drains were noticed to carry large quantity of water during rainy season. Information of gas monitoring shows insignificant amount. All these demonstrated satisfactory performance of the lining system.

The geogrid and geotextile in the reinforced slope were left fully exposed since completion. There seemed to be surprisingly little degradation (Picture 7). Geogrid samples were taken for tensile testing in 2005, after a continuous seven years of UV exposure. The results showed a remarkable 97% retaining of short-term strength.

ACKNOWLEDGEMENT

Thanks to Mass Transit Railway Corporation, Hong Kong for permission to write the article.

REFERENCE

Civil Engineering Department, Hong Kong Government. GEO Report No. 34, a Partial Factor Method for Reinforced Fill Slope Design

Civil Engineering Department, Hong Kong Government 1997. Endorsement Certificate No. RF1/97

GTM International, Wan Hin & Co Ltd 1996. CFE Joint Venture, MTRC Contract No. 509, Kwai Chung Park Viaduct, Project Interim Report

Koerner RM (2005) Design with Geosynthetics, 5th edition, Prentice Hall

Mass Transit Railway Corporation 1993 Drawings for Contract MTRC No. 509, Kwai Chung Park Viaduct

Tsinger LG, Giroud JP (1993) The Durability of HDPE Geomembrane, Geotechnical Fabric Report

Proceedings of the 4th Asian Regional Conference on Geosynthetics
June 17 - 20, 2008 Shanghai, China

EVALUATION OF TENSILE FORCE OF LINER SYSTEM WITH THE VARIATION OF HEIGHT OF INCINERATED ASH

S.F. Xu[1], H. Zhang[2], M.Y. Hu[3] and S. Imaizumi[4]

ABSTRACT: A liner system is installed on the bottom and the side slope of a waste landfill. Tensile forces can occur due to waste compaction which is transferred into the geosynthetics by friction. The long term design strength of the liner system placed on side slope in landfill may be determined by creep rupture strength, so it is very important to estimate the amount of tensile force created in the liner system, especially on the shoulder of liner system in course of filling. In this research, centrifugal model experiments and FEM analysis were conducted to study the variation of tensile force creating at the shoulder of liner system in course of filling. It is found that the tensile force creating at the shoulder of liner system increases remarkably with increasing height of incinerated ash.

KEYWORDS: liner system, shear stress, tensile force, FEM analysis

INTRODUCTION

The waste landfill should be designed that no leachate that may include hazardous materials flowing into surrounding ground and water over long period of years. A liner system is installed on the bottom and the side slope of a waste landfill to prevent the leachate from infiltrating into surrounding ground and polluting groundwater (Wang et al. 2004). The liner system has two layers of geomembrane with a thickness of 1.5 mm is typical one. The liner system is considered to experience various forces, such as tensile force induced by settlement of base ground (Knipschild 1984), thermal stress due to decrease of temperature (Imaizumi et al. 1999), lifting force by the wind (Zornberg et al. 1997), the tensile force by compaction work of disposed waste (Xu et al. 2003). The long term design strengths of the liner system are usually controlled by creep rupture within the design life, so it is very important for the design of the lifetime of liner system to determine the tensile force induced in components of liner system, especially on the shoulder of HDPE geomembrane in a progress of filling. But it is not clearly understood how the tensile force acting on the liner system due to the compaction work varies with increase of height of incinerated ash.

Many evaluation methods of the tensile force of the liner system have been presented by researchers, field tests and simulation tests were conducted to evaluate the tensile force in components of liner system by the compression of waste (Kanou et al. 1997; Gourc et al. 1997). The interface characteristics between different materials were obtained by direct shear tests (Katarzyna 2006; Mizyal et al. 1998), the calculation method based on the limit equilibrium of frictional force between materials (Koerner 1994) and the method of slope stability calculation on the basis of the direct shear test results (Briancon et al. 2002) were presented. But the studies on the variation of tensile force with the progress of filling were not conducted.

In this paper, the variation of tensile force creating at the shoulder of liner system in course of filling was studied.

INTERFACE FRICTION CHARACTERISTICS

Materials

Smooth surface HDPE geomembrane was used, its thickness, tensile strength and elastic modulus at 20℃ are listed in Table 1. Non-woven geotextile was used for

[1] Assistant professor,College of Civil Engineering and Architecture, Zhejiang University of Technology, CHINA. Email: xy20038@hotmail.com
[2] Assistant professor,College of Civil Engineering and Architecture, Zhejiang University of Technology, CHINA. Email: zhanghao@zjut.edu.cn
[3] Assistant professor,College of Civil Engineering and Architecture, Zhejiang University of Technology, CHINA. Email: huminyun@hotmail.com
[4] Professor, Energy and Environmental Science Graduate School of Engineering, Utsunomiya University, JAPAN, Email: imaizumi@cc.utsunomiya-u.ac.jp

protecting the HDPE geomembrane.

Incinerated ash from municipal waste was used to represent disposed waste in landfill. Particle-size distribution curve of incinerated ash is shown in Fig. 1. Water content of the incinerated ash was 41%.

Table 1 Mechanical properties of geosynthetics

Material	Thickness (mm)	Tensile strength (MPa)	Elastic modulus (MPa)
HDPEgeomembrane	1.5	35.3	484
Non-woven geotextile	10	1.4	6.5

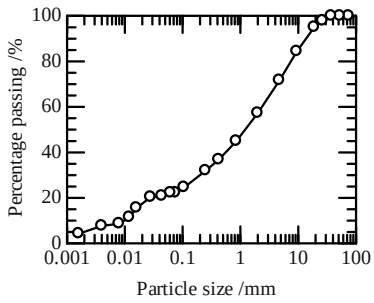

Fig. 1 Graining distribution curve of MSW

Description of Test Apparatus

The Interface friction characteristics are necessary to evaluate the tensile force of geosynthetics, so the shear test was conducted. Direct shear test apparatus (Fig. 2) is composed of two shear box, load and power system. The upper shear box having a dimension of 200 mm in length, 100 mm in width and 70 mm in depth can be filled with incinerated ash or non-woven geotextile. The lower box has a dimension of 350 mm in length, 200 mm in width and 50 mm in height.

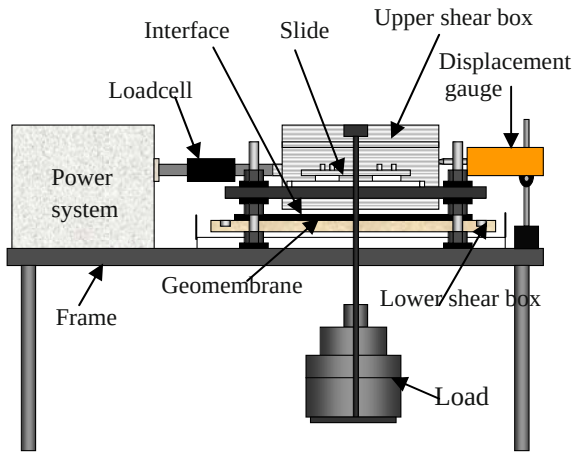

Fig. 2 Test apparatus

HDPE geomembrane was glued on the plywood board that was fastened to lower shear box with bolts. Power system caused shear force on the upper shear box. The rate of displacement of upper shear box was controlled to be 1 mm/min. Shear force was measured by loadcell that was set between power system and upper shear box. Displacement of upper shear box was also measured by displacement gauge. Then normal stress from 24.5 kPa to 98.0 kPa was applied on the upper polywood board.

Interface Friction Characteristics

The shear stress τ is a value that the peak shear force obtained from the relationship between relative displacement and shear force which is divided by shear area. Then the friction angle and cohesion are calculated by Mohr-Coulomb criterion:

$$\tau = c + \sigma_n \times \tan\phi \quad (1)$$

where c is cohesion (kPa); σ_n is normal stress on the interface (kPa); ϕ is friction angle between materials.

The friction angles between the incinerated ash and non-woven geotextile, HDPE geomembrane and non-woven geotextile are 12.5° and 19.7° respectively, but the cohesions are very small on the interface.

CENTRIFUGAL MODEL TESTS

Configuration of Model Landfill

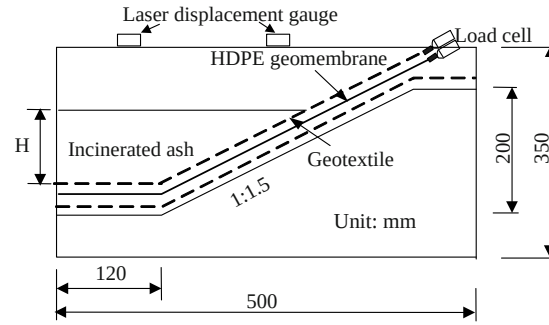

Fig. 3 Configuration of the centrifugal model

The model landfill as shown in Fig. 3 was placed in a steel container having a length of 500 mm, a width of 260 mm and a depth of 350 mm. The foundation and slope of the model landfill were made of gypsum. The slope of the model landfill is 1:1.5(V:H) with a height of 200 mm. Non-woven geotextile was then glued to the surface of the model landfill which was then covered by an HDPE geomembrane with a thickness of 1.5 mm. A protective layer of non-woven geotextile was spread over the HDPE geomembrane which was then covered

on the surface by incinerated ash. The model was accelerated to about 37 G in centrifuge. The tensile forces induced within the top non-woven geotextile and HDPE geomembrane were measured through load transducers which were fixed at the top of slope.

Testing Procedure

Incinerated ash was poured into model landfill. Its wet density was approximately 820 kg/m^3. Acceleration of the centrifuge was increased at a rate of 5 G/min to a maximum of 37 G, a 150 mm height in the model is equivalent with a 5 meter height of waste landfill in the prototype. The tensile forces of HDPE geomembrane and non-woven geotextile, the acceleration were recorded by computer at each 5 G interval in acceleration.

In order to investigate the relationship between the height of incinerated ash and tensile force creating at the shoulder of liner system, the height of incinerated ash was changed as 50, 100, 150 mm.

RESULTS OF TESTS

The results of testing are shown in Figs. 4 and 5. As the weight of the incinerated ash increases due to increasing acceleration, the incinerated ash is com-pressed, hence, the relative displacement is created at the interface between the incinerated ash and non-woven geotextile, which results in the tensile forces of non-woven geotextile and HDPE geomembrane through frictional resistance between materials. As shown in Figs. 4 and 5, the tensile forces of non-woven geotextile and HDPE geomembrane increase with increasing the gravitational acceleration for the constant the height of the incinerated ash.

Tensile forces also increase as the height of the incinerated ash is increased. The tendency of the graph depicting the increases in tensile force of non-woven geotextile, as a result of gravitational acceleration, and the tendency of the graph representing the increases in tensile force of HDPE geomembrane are almost identical (Fig. 6).

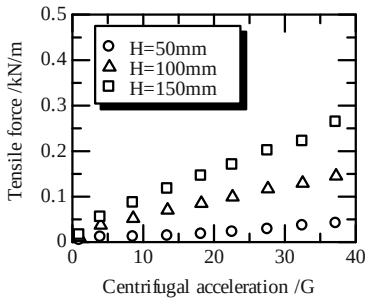

Fig. 4 Measured tensile force vs centrifugal acceleration (HDPE geomembrane)

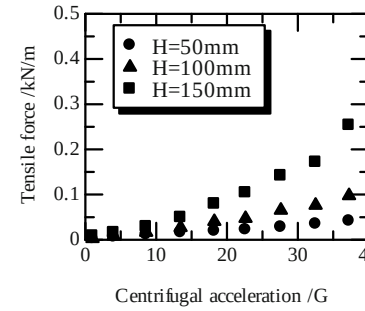

Fig. 5 Measured tensile force vs centrifugal acceleration (geotextile)

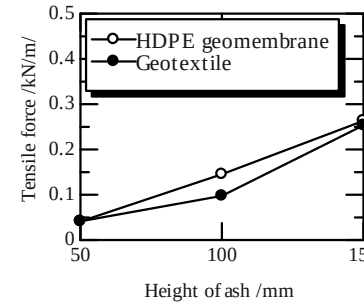

Fig. 6 Relation of the height of ash and tensile force (37G)

FEM ANALYSIS

Two dimensional FEM analyses were conducted. The finite element meshes and boundary conditions for the case where the height of incinerated ash is 150 mm are shown in Fig. 7. It is possible to displace freely between incinerated ash and steel container in the vertical direction, and the HDPE geomembrane and non-woven geotextile at the shoulder are fixed. The quadrilateral element and triangle element are used to model the incinerated ash. The interfaces between different materials are modeled by joint element.

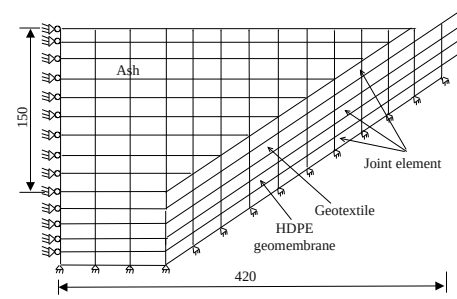

Fig. 7 Finite element mesh

Analysis Parameters

The friction angle and cohesion are 19.7° and 1.3 kPa respectively, the stress-strain response of incinerated ash is modeled by Duncan-Chang model (Duncan et al.

1970). The analysis parameters of interfaces are shown in Table 2.

Table 2 Analysis parameters

Interface or materials	k	n	R_f
Incinerated ash-geote	11.65	1.06	0.82
HDPE -geotextile	3.90	0.84	0.78
Incinerated ash	63.2	0.83	0.81

Analysis Results

The calculated tensile forces of HDPE geomembrane and non-woven geotextile are shown in Table 3 respectively. It is found that the calculated value of non-woven geotextile is close to the test value, the calculated values are 0.7—1.0 of the test value. The calculated values of HDPE geomembrane are larger than the test values, about 1.1-1.4 of the test values. The elastic modulus of HDPE geomembrane used for FEM analysis is data of 20℃, but the test temperature was 14℃ and HDPE geomembrane sensitive to environmental temperature. That is, the elastic modulus of HDPE geomembrane used is smaller than the test value, so the relative displacement between HDPE geomembrane and geotextile becomes smaller to make small in friction force, the deviation between calculated values and test values is generated.

Table 3 Comparison of calculated and experimental results (kN/m)

Height	FEM analysis		Experimental results	
(mm)	HDPE	Geotextile	HDPE	Geotextile
50	0.05	0.03	0.04	0.04
100	0.16	0.10	0.15	0.10
150	0.36	0.23	0.26	0.25

CONCLUSIONS

This paper describes the variation of tensile force creating at the shoulder of liner system in course of filling. From the results of test and analysis by FEM, the following conclusion can be obtained.

(1) The tensile force creating at the shoulder of liner system increases remarkably with increasing height of incinerated ash.

(2) The tensile forces of HDPE geomembrane and non-woven geotextile analyzed by FEM are consistent with those obtained by centrifugal model test in general. The calculated values of HDPE geomembrane are larger than the test values, about 1.1—1.4 of the test values. The calculated values of non-woven geotextile are about 0.70—1.0 of the test values.

REFERENCES

Wang XQ, Wang JQ (2004) Development and application of geomembrane liner system in solid waste landfills. Environmental protection science 30 (20): 24-26 (in Chinese)

Knipschild FW (1984) Selected Aspects of Dimensioning Geomembrane for Groundwater Protection Applications. Proc. of the Int. Conf. on Geo-membranes, 439-443

Imaizumi S, Kawamata K, Tsuboi M (1999) Study on Termal Stress within the Geomembrane Liner Induced by Temperature Decrease. Proc. of the 7th International Landfill Symposium: 115-122

Zornberg JG, Giroud JP (1997) Uplift of Geomembranes by wind-extension of equations. Geosyntetics International 4(2): 187-207

Xu SF, Imaizumi S (2003) The drag force evaluation of the liner sheet with a change of slope angle. Geosyntetics Engineering Journal: 49-54 (in Japanese)

Gourc JP, Fourier J, Berroir G, Stock R, Begassat P (1997) Assessment of lining systems behaviour on slopes. Proc. of the 6th International Landfill Symposium : 495-506

Kanou H, Doi Y, Imaizumi S, Tsuboi M (1997) Evaluation of geomembrane stress on side slope caused by settlement of wastes. Proc. of the 6th International Landfill Symposium: 525-534

Katarzyna ZA (2006) Shear strength parameters of compacted fly incinerated ash–HDPE geomembrane interfaces. Geotextiles and Geomembrane 24(2): 91-102

Mizyal I, Yildiz W (1998) Geomembrane-sand interface frictional properties as determined by inclined board and shear box tests. Geotextiles and Geomembranes 16(4): 207-219

Koerner RM (1994) Designing with Geosynthetic. Third Edition :545-550

Briançon L, Girard H, Poulain D (2002) Slope stability of lining systems—testal modeling of friction at geosynthetic interfaces. Geotextiles and Geomembrane 20(3): 147-172

Duncan JM, Chang CY (1970) Nonlinear Analysis of Stress and Strain in Soil. Journal of the Soil Mechanics and Foundations Division, ASCE 96 (SM5): 1629-654

Proceedings of the 4th Asian Regional Conference on Geosynthetics
June 17 - 20, 2008 Shanghai, China

EVALUATION OF CLAY GEOSYNTHETIC BARRIERS IN LANDFILL COVER SYSTEMS

H. Zanzinger[1]

ABSTRACT: Clay geosynthetic barriers (GBR-C) used in landfill capping systems have to provide sufficient low water permeability for the long-term even under critical conditions. The synthetic components need to be durable against thermal oxidation and they must also have enough strength to withstand the shear forces acting in slopes of landfill covers. Sufficticated oxidation tests like high-pressure autoclave tests as well as long-term shear creep tests have to be performed to come up with lifetimes for GBR-Cs of up to 100 years.
Most critical for a GBR-C is the question of dehydration. Long-term measurements in test fields and excavations show that desiccation can and must be avoided. Under extreme conditions no "self-healing" was found.

KEYWORDS: clay geosynthetic barrier, long-term shear strength, desiccation, cation exchange

INTRODUCTION

The essential effects on the durability of GBR-Cs are the durability against changes of the water content. This together with cation exchange is the most critical attack, which GBR-Cs in landfills have to withstand. Mainly in the summer months under high temperature stress bentonite in a GBR-C loses moisture. When reaching a critical suction, cracks will occur. There are two possibilities to prove the durability against moisture changes: Either one can show that the GBR-C will not dry out below the critical water content in a certain buried condition or it must be demonstrated that after dry/wet cycles the GBR-C will always reach a sufficient tightness again.

The paper discusses also the durability and ageing of the synthetics in a GBR-C. For their evaluation of laboratory tests have to be undertaken to simulate thermal oxidation and also shear creep of the com-ponents and of the composite.

CRITERIA FOR THE EVALUATION

According to German experience in the evaluation of GBR-Cs in landfill cover systems the following criteria will be givenfollowed:

- Mechanical robustness
- Construct ability
- Manufacturing and construction quality assurance
- Tightness against precipitation under consideration of temperature, mechanical loads and multiaxial deformations, overlaps, connections and intrusive constructions, load concentrations, micro organisms, plant roots, weathering, change of moisture content and ion exchange.

In the following the long-term durability of the synthetic components, long-term shear strength and desiccation behaviour of GBR-C will be discussed.

DURABILITY

The relevant ageing process for GBR-C, made of polyolefin's, is thermal oxidation. The chemical durability of polyolefin's is excellent, but the long-term behaviour depends strongly from on the use of stabilisers.

For the lifetime of GBR-C, the oxidative ageing process could anyhow be decisive. Shear creep rupture tests in hot water have limitations to simulate the oxidative ageing. In the application as barrier element ion a landfill capping oxidative ageing of the upper textile layer plays its role. Both thermal oxidations of the synthetic components as well as the shear creep rupture behaviour of the GBR-C have to be investigated independently.

Sodium bentonite will be changed by cat ion exchange within a few years into calcium bentonite. Egloffstein (2001) describes the influence of ion exchange on GBR-Cs. He used 0.1 to 0.3 mol/l $CaCl_2$-solutions and concluded that the hydraulic conductivity of a GBR-C with sodium bentonite increases due to ion

[1] SKZ - TeConA GmbH, Würzburg, GERMANY. Email: h.zanzinger@skz.de

exchange up to one order of magnitude. Prerequisite is, that the GBR-C has to be pre-swollen in the dry condition with deionised (DI) water.

All mineral liners need correctly designed surface layers and careful cultivation of the vegetation, as they have to be protected especially against root penetrations.

Uncovered GBR-Cs have principally to be protected against weathering influences like UV-radiation and rainfall. Before installation GBR-C need to be wrapped in water- and light tight packaging foils to avoid swelling and chemical degradation. After installation it must be sufficiently covered with soil on the same day, to avoid free swelling.

AGEING OF SYNTHETIC COMPONENTS

Ageing of needle punched or stitch bonded GBR-C means in regard of to long-term shear strength the oxidative degradation of the polyolefin fibres and yarns.

The prediction of long service life's of the synthetic components demands an immersion in hot water as well as an exposure in hot air. As the failure times will be dramatically reduced with increasing temperature, therefore often above 100°C will be tested. But the effectiveness of stabilisers above 100°C changes strongly and Arrhenius extrapolations to real service temperatures based only on such results are not allowed. One has to measure at lower temperatures than 100°C for considerable longer test durations. Müller et al. (2003) calls a test temperature of 80°C as the maximum temperature, which makes an Arrhenius extrapolation to service temperatures possible without changing the morphology in the materials.

Geotextiles (GTX) have large surface-volume-ratio and oriented morphology. The loss of antioxidants in GTXs runs relatively quick (few decades). For GTXs the induction period lasts longer as the time for the consumption of antioxidants. The fibres seem to have reasonable oxidation stability depending on the draw ratio of the fibres λ and the rate of oxygen supply r_{O2}. Müller et al. (2003) give an activation energy of 60 kJ/mol as lower boundary for this degradation process. Under such an approach – test temperature of 80°C and a service temperature of 15°C – the minimum test duration results in approximately one year, to extrapolate to a service life of e.g., 100 years.

The European standardization committee CEN/TC189 proposed to carry out the investigation of the oxidation resistance especially of GTXs in water under elevated oxygen pressure in high-pressure autoclaves. In this procedure the limiting oxygen diffusion can be avoided largely and the influence of migration of stabilisers and the influence of oxygen diffusion can be studied simultaneously. The test method allows both possibilities variation of test temperature and of oxygen pressure, to simulate accelerated oxidation behaviour. Tests in high-pressure autoclaves at elevated oxygen pressure show in contrast to tests in ovens no influence of the fibre surface on the oxidation behaviour. The antioxidant stabilisers will be consumed quicker, i.e., the oxidative reduction will be accelerated. The migration of antioxidants in the material keeps in comparison with atmospheric incubations nearly unchanged.

LONG-TERM SHEAR BEHAVIOUR

Short-term Shear Tests

Prove of transferable shear forces within the plane of a GBR-C takes place in a direct shear test using nail plates to transfer shear forces in the carrier and cover textiles. Under the influence of normal and shear forces the yarns and fibres will not only be loaded by tension but they will be hindered by normal loads to orientate along the direction of tension, to "de loop" or to open "knots".

Shear Creep

Long-term shear strength of a GBR-C depends on the creep behaviour of the used synthetics. Creep behaviour increases with increasing tensile loading, i.e., at low load ratios related to the maximum short-term strength of a fibre creep strain is small and time to failure is very long.

The reinforcing elements in GBR-Cs are not by all means oriented in the direction of loading; therefore it is difficult to predict how much in any respective case the tensile loading in a fibre of a GBR-C will be, especially since the mechanical properties are time dependent. Shear strength of bentonite increases with time due to ion exchange. Also the acting force of each single fibre changes with time, as by de looping, pull out or rupture of single fibres. Other fibres – till that less or unloaded – have to carry these forces. By fibre elongation due to creep further fibres can take over force portions. The effect is a reduction of the load ratio of each fibre.

Long-term Shear Tests

Hsuan and Koerner (2002) tested GBR-C, exclusively loaded with shear loads but without normal loads. As the technical expenditure and the needed time for the simulation of shear loading under different normal loads is considerable, one will be satisfied to find out, whether

for typical normal/shear loads the long-term behaviour is guaranteed. Zanzinger and Alexiew (2002) varied shear loads at normal loads of 20 kPa with the aim to get shorter rupture times with higher shear loading. Test temperature was 20°C. DI water was used and the stitch bonded GBR-C included sodium bentonite.

Thies et al. (2002) and Müller et al. (2004) followed a concept with “inclined plains” with inclinations of 2.5H:1V (normal load app. 50 kPa, shear load app. 20 kPa). Tap and DI water was used. The needle punched GBR-Cs have been made from HDPE and PP. Additionally the samples were equipped with and without thermal locking of the fibres in the carrier layer. Higher water temperatures have accelerated these shear creep tests.

Theoretically the transferable shear stress can be calculated by the determination of fibre strength and number of fibres per area. Under the use of reduction factors for e.g., creep and interaction coefficients an arithmetical allowable shear stress could be calculated. However investigations of Müller et al. (2004) have shown, that particular for needle punched GBR-C it is not allowed, to conclude with the help of reduction factors to long-term shear strength. That failure mechanism is more complex. Eventually the rupture of fibres in a short-term shear test is authoritative, but in a long-term shear test “de looping” of fibres could be decisive for the time till shear failure. GBR-C with higher peel strength had clear lower rupture times in long-term shear tests and those GBR-C made of PP had clear higher rupture times than those made of HDPE. Specimens without thermal locking did not fail partly even after years of testing. PP specimens behaved as well in quality better than HDPE specimens.

GBR-C specimens immersed in tap water underwent in short period an ion exchange. These GBR-Cs with calcium bentonite had extended rupture times. Testing in DI water is therefore the more critical test. But as in reality sodium bentonite changes anyhow into calcium bentonite a test in tap water is justified.

Tests at different test temperatures showed, that the rupture times of the specimens with thermal locking followed temperature dependence according to Arrhenius as the failure modus was rupture of the fibres. Which failure modus the GBR-C with “normal fixation” will follow is open, as up to now no failures were established.

In test set ups used by Zanzinger and Alexiew (2002), Trauger et al. (1996) and Koerner et al. (2000) in contrast to “inclined plains” (Thies et al. 2002) normal loads and shear loads can be applied independently. The consequence is the combination of both (Fig. 1): acceleration by elevated temperatures and variation of the shear loads to reduce the test duration. Using a shear creep rupture diagram any rupture time could be determined for a given shear stress.

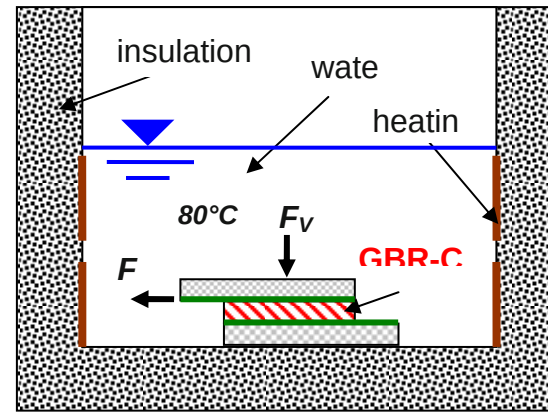

Fig. 1 Shear creep tests with a GBR-C (normal load σ and shear load τ and temperature ϑ can be varied)

DESICCATION BEHAVIOUR

Test Field Hamburg-Georgswerder

In 1994 two test fields with different GBR-Cs (needle punched or stitch bonded, filled with 3—3.5 kg/m² sodium bentonite) have been installed on the landfill Georgswerder near Hamburg, Germany. The concept was that the effects from desiccation and from root penetrations should occur in an early stage and with a high intensity. A usual cover height of the mineral liner is about 1 m. Cover height in the test fields was only 45 cm. After two dry periods high leakage rates occurred in both test fields in summer 1995 as assumed. Excavations in 1996 and 1998 (Melchior 2002) showed that the GBR-Cs were extremely de-hydrated. The moisture content of the bentonite varied between 55 and 100%. The bentonite showed clear crack structures. Ion exchange from sodium to calcium bentonite was nearly complete and penetrations of the GBR-C with vital roots were found. Laboratory tests in rigid wall permeameters proved, that the permittivities of exhumed samples from the years 1996 and 1998 increased by 4—5 orders of magnitude compared with the initial samples before installation. These laboratory tests confirmed the high leakage rates measured in the test fields. No “self-healing” of the GBR-Cs was noticed under those extreme conditions. Under certain conditions like new sodium GBR-Cs (Sivakumar Babu et al. 2001) or only slightly exchanged sodium GBR-Cs it could be the case. But for the test fields in Georgswerder this is invalid. The temperature stress there was that strong, that the bentonite was no longer able to close the cracks.

Excavations

Anyhow the test fields in Georgswerder should not be the scale, as the reality in German landfills is different. Within the last 10 years on many landfills in Germany excavations have been made. Sporer (2002) described eight excavations of landfill cover systems with cover heights between 50cm and 100 cm, 3—6 years old and all GBR-Cs—initially sodium bentonite—were exchanged in the meanwhile to calcium bentonite. Swell index was between 7 and 10 ml/2g. Water absorption (Enslin/Neff-test) was between 200% and 250%. Permittivities in rigid wall permeameters gave results between 5×10^{-8} s^{-1} and 1×10^{-7} s^{-1}, which could clearly be attributed to ion exchange. Despite of partly shallow cover heights no cracks have been determined in X-ray images. For the landfill Winkel/Bischoffswiesen with a cover height of 40 cm Heyer (2000) gave a permittivity of 5×10^{-8} s^{-1} of the exhumed sample. Heerten and Maubeuge (1997) report from excavations of three landfills. All GBR-Cs showed an ion exchange process. Tests in triaxial and in rigid wall permeameters gave permittivities between 10^{-9} and 10^{-8} s^{-1}. The cover heights were 60 to 100 cm. Heerten (2004) describes also an excavation at the landfill Tagewerben in autumn 2003 also after an extreme hot summer. That landfill is located at a very dry site (average annual precipitation of 500 mm/a), but the restoration layer was 140 cm thick. It was seen, that in the single layered GBR-C ion exchange was complete after 5 years period and the permittivity was 1.2×10^{-8} s^{-1}. A desiccation could not be established even after a very hot summer, as the moisture contents of the bentonite were still at 125%.

The so called “self-healing capacity” is less differentiated used for all conditions, which might occur in any landfill. Most is insinuated, that a GBR-C on a landfill is submitted to desiccation. In fact as a rule GBR-Cs are protected by a sufficiently thick soil cover of about 100 cm. For such application one can talk, that GBR-Cs are exposed to a certain temperature stress. A desiccation with cracks can not be talked on German landfills in general.

Wherever, the latest experience from exhuminations of four landfill final covers in USA is described by Meer and Benson (2007). They found, that not even a covering of the GBR-C with a soil layer 75 cm—100 cm thick or a polymeric geosynthetic barrier overlain by soil did ensure protection against ion exchange or large increase in hydraulic conductivity under North American climatic conditions. Only on two landfills cation exchange in the GBR-C was prevented either by the sodic condition of the surface layer in a landfill or by the humid condition and high precipitation in a landfill in Florida, USA.

Measurements on Site

Excavations can show the state of GBR-C. Test fields and lysimeter can give information on the behaviour of the system, which collect and register continuously all water balance data over years, to verify the check of the efficiency of GBR-C. Siegmund et al. (2001) described a 3 year old test field in Thuringia with a 8000 g/m² heavy calcium bentonite GBR-C, covered with 110 cm of soil. The GBR-C experienced only small changes in water content, so that there was no danger of dehydration. Further German test fields and lysimeters with GBR-C were installed among other things at landfill Aurach (Henken-Mellies 2005), in Essen (Heerten/Maubeuge 1997), in Lemförde (Blümel et al. 2006), in Munich (Military University), in Eschbelval at the landfill Deetz and at the landfills Kuhstedt and Dillinger Hütte (Arlst/Wolsfeld 2004). The measurements at the test fields show good system effectiveness far above 95%. System and material untightnesses were not found at these test fields after more than 7 years of service. Ion exchange took place always. The “degree of desiccation” depends on many factors such as load from soil cover, water reservoir of restoration layer, drainage layer, roots in the soil and properties of the adjoining layers (Sivakumar Babu et al. 2002).

Benson et al. (2007) gave a very detailed description of lysimeters in a landfill in Wisconsin, USA. Conventional GBR-Cs showed high percolation rates within 4—15 months after installation due to cation exchange and dehydration. After reconstruction with a composite GBR-C including a thin polyethylene foil the lysimeter was functioning satisfactorily.

Desiccation Tests in the Laboratory

Field tests are very time and cost intensive. On the other side single influences can’t often be separated from other influences occurring by chance, when all effects occur parallel. A reproducibility of field tests is difficult.

Sporer and Gartung (2002a) and Sporer et al. (2000) simulated with temperature induced desiccation tests (Fig. 2) the influence of water, water vapour and temperature on the moisture transport. They showed that the moisture transport takes place both up- and downwards. Water vapour is transported as a result of differences in water vapour pressure of the air in soil. Heat is transported as a result of temperature gradient. Without that, moisture transport moves only upwards. If temperature gradient increases, water moves along that gradient—therefore downwards. The second process becomes dominant as the drying temperature increases. According to that e.g., the lower GBR-C of a double-layer GBR-C

in an overlap will be supplied with moisture from the upper GBR-C. The upper GBR-C avoids therefore not the water movement from the lower layer but the water loss in the lower layer will be compensated by the water movement from the upper GBR-C downwards.

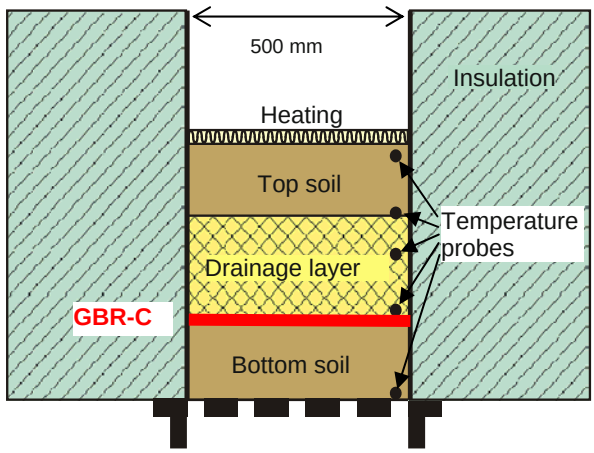

Fig. 2 Desiccation lab test (Sporer/Gartung 2002a)

Laboratory tests can't depict the complexity of reality, but the boundary conditions can be defined clearly. It is possible to compare different systems with each other. The test set up (Fig. 2) described by Sporer and Gartung (2002a) allows it, to depict complete cover systems. Desiccation will be caused through a unidirectional (vertical) temperature gradient. Moisture movement can happen up- and downwards. Ion exchange is possible. For a project specific system the critical water content for the desiccation of a GBR-C can be determined resp. time can be determined till critical water content during a dry period will be reached.

In further tests at MFPA Weimar desiccation stress on GBR-C was simulated in a permeameter (Heerten/Reuter 2002) by air circulation. The investigations gave critical water contents of 95% till 100% for GBR-C after ion exchange. Dry/wet-cycles of a sodium GBR-C in the same permeameter gave changes of the hydraulic conductivity of minimum 2 orders of magnitude.

Sporer and Gartung (2002b) found on a calcium GBR-C even after the first dry/wet-cycle large changes in swell index, which can't be explained by ion exchange but on irreversible changes in the structure of the bentonite. They came to the conclusion, that desiccation beyond a "critical water content" has to be avoided. The ability of bentonite to bind water depends on the structure and the type of clay minerals and its "history", i.e. it depends on the degree of desiccation and thus on the maximum water suction, which the clay has experienced during its "stress history".

SUMMARY

The essential proves for long service life's of GBR-Cs are the durability against desiccation and the long-term durability of the shear force transferable synthetic components. Furthermore the water permeability has to be shown.

For design considerations proves against sliding in the interfaces including internal shear strength have to be made. Thermal oxidation is the substantial ageing process of polyolefin geotextiles. Tests have to be undertaken in ovens respectively in high-pressure autoclaves.

Lifetime of GTXs depends on the time for the consumption of antioxidants but mainly on the induction time and the half-life during degradation of the mechanical properties.

Long-term shear strength of GBR-C depends on creep behaviour of the synthetic components. Shear strength of bentonite increases due to ion exchange. It is not allowed to conclude from short-term shear strength to long-term shear strength. Higher temperatures accelerate the testing of the long-term shear creep behaviour. Higher shear stress accelerates shear creep and shortens therefore testing time.

Finally it can be found out, that ion exchange and an extreme dehydration as in Georgswerder do not allow a "self-healing" anymore. Ion exchange is inevitable, but dehydration below a "critical water content" has to be avoided. Measurements on test fields show good system effectiveness of far above 95%. Numerous excavations prove, that in middle European climatic conditions in most cases a covering of GBR-C with minimum 100 cm and other favourable boundary conditions are sufficient, to avoid a desiccation. So that in many cases with the right choice of cover layers also the danger by root penetrations is reduced. Other signs for solutions, which have the aim of constructive changes of the GBR-C, like "safety against desiccation", "durable against roots" and insensitive to ion exchange are considerable more difficult to put into action as to arrange boundary conditions as such, that no damages of GBR-C can happen.

REFERENCES

Arlst KJ, Wolsfeld N (2004) Angepasste Oberflächen-abdichtungs-Systeme für Monodeponien der Stahlindustrie—2 Jahre Monitoring der 12 Test-felder am Standort Dillinger Hütte. Abfallwirtschaft in Forschung und Praxis, Band 132, Erich Schmidt Verlag, Berlin: 241-257 (in German)

Benson CH, Thorstad PA, Jo HY, Rock SA (2007) Hydraulic performance of geosynthetic clay liners in

a landfill final cover. Journal of Geotechnical and Geoenvironmental Engineering. ASCE July 2007: 814-827

Blümel W, Müller-Kirchenbauer A, Ehrenberg H, von Maubeuge K (2006) Experimentelle Nach-weise zur Funktionsdauer von Bentonitmatten in Oberflächen-abdichtungen für Deponien und Altlasten. The 22nd SKZ landfill conference. Würzburg (in German)

Egloffstein T (2001) Einfluss des Ionenaustausches auf die Dichtwirkung von Bentonitmatten in Ober-flächenabdichtungen von Deponien. The 7th German Geosynthetic Conference. Geotechnik special issue 2001, DGGT, Essen: 79-83 (in German)

Heerten G (2004) Bentonitmatten als mineralisches Dichtungselement im Umweltschutz. The 20th SKZ landfill conference. Würzburg (in German)

Heerten G, Maubeuge KP (1997) Auswirkungen von Wassergehaltsschwankungen in vernadelten Geo-synthetischen Tondichtungsbahnen auf ihre Wirk-samkeit als Dichtungselement. The 5th German Geosynthetic Conference. Geotechnik special issue 1997, DGGT, Essen: 193-200 (in German)

Heerten G, Reuter E (2002) Die Bedeutung der DIBt-Zulassungen für die Qualitätsanforderungen an Bentonitmatten heute und morgen. The 18th SKZ landfill conference, Würzburg (in German)

Henken-Mellies WU (2005) Long-term observations of alternative landfill capping systems—Field tests on a landfill in Bavaria. The 16th Nuremberg landfill seminar 2005, LGA (in German)

Heyer D (2000) Bentonitmatten als Dichtungselement in Oberflächenabdichtungssystemen von Deponien. The 16th SKZ landfill conference, Würzburg (in German)

Hsuan YG, Koerner RM (2002) Durability and lifetime of polymer fibers with respect to reinforced geo-synthetic clay barriers; i.e., reinforced GCLs. Zanzinger, Koerner & Gartung (eds.), Clay Geo-synthetic Barriers. Balkema, Netherlands: 111-117

Meer SR, Benson CH (2007) Hydraulic conductivity of geosynthetic clay liners exhumed from landfill final covers. Journal of Geotechnical and Geoenvironmental Engineering. ASCE. May 2007: 550-563

Melchior S (2002) Field studies and excavations of geosynthetic clay barriers in landfill covers. Zan-zinger, Koerner & Gartung (eds.), Clay Geosynthetic Barriers. Balkema, Netherlands: 321-330

Müller W, Büttgenbach B, Jakob I, Mann H (2003) Comparison of the oxidative resistance of various polyolefin geotextiles. Geotextiles and Geo-membranes 21 (2003): 289-315

Müller W, Seeger S, Thies M, Gerloff C (2004) Long-term shear strength of multilayer geosynthetics. The 3rd European Geosynthetics Conference, EuroGeo3: 429-434

Siegmund M, Witt KJ, Alexiew N (2001) Calcium-Bentonitmatten unter Feuchtigkeitsverän-derungen. The 7th German Geosynthetic Conference. Geotechnik special issue 2001, DGGT, Essen: 97-104 (in German)

Sivakumar Babu GL, Sporer H, Zanzinger H, Gartung E (2001) Self-healing properties of geosynthetic clay liners. Geosynthetics International 8(5): 461-470

Sivakumar Babu GL, Sporer H, Zanzinger H, Gartung E (2002) Desiccation behaviour of selected geosynthetic clay liners. Zanzinger, Koerner & Gartung (eds.), Clay Geosynthetic Barriers. Balkema, Netherlands: 295-302

Sporer H (2002) Exhumed clay geosynthetic barriers. Presentation at International symposium on clay geosynthetic barriers in Nuremberg, unpublished

Sporer H, Gartung E (2002a) Laboratory tests on desiccation of geosynthetic clay liners. Zanzinger, Koerner & Gartung (eds.), Clay Geosynthetic Barriers. Balkema, Netherlands: 331-338

Sporer H, Gartung E (2002b) Examinations on the self-healing capacity of geosynthetic clay liners. Zan-zinger, Koerner & Gartung (eds.), Clay Geosynthetic Barriers. Balkema, Netherlands: 339-343

Sporer H, Sivakumar Babu GL, Gartung E (2000) Desiccation tests on GCL. The 2nd European Geosynthetics Conference, EuroGeo2: 751-754

Thies M, Gerloff C, Müller W, Seeger S (2002) Long-term shear testing of geosynthetic clay liners. Zanzinger, Koerner & Gartung (eds.), Clay Geosyn-thetic Barriers. Balkema, Netherlands: 97-104

Trauger RJ, Swan RH, Zehong Y (1996) Long-term shear strength behavior of a needlepunched GCL. “Testing and Acceptance Criteria for Geosynthetic Clay Liners”, STP 1308, LW Well (ed.), ASTM, Philadelphia, USA: 103-120

Zanzinger H, Alexiew N (2002) Long-term internal shear testing on clay geosynthetic barriers. Zanzinger, Koerner & Gartung (eds.), Clay Geosyn-thetic Barriers. Balkema, Netherlands: 111-117

Proceedings of the 4th Asian Regional Conference on Geosynthetics
June 17 - 20, 2008 Shanghai, China

ABILITY OF CONCRETE ANCHORAGE FOR GEOMEMBRANE BARRIER IN LANDFILL

S. Imaizumi[1], T. Sekiya[2], K. Ozawa[3], K. Arakawa[4], H. Wakabayashi[5] and H. Tsujimoto[6]

ABSTRACT: In Japan, various types of geomembrane, such as HDPE, LLDPE, TPO(PE) and TPO(PP), are used as barrier sheet in waste landfill. The barrier sheet placed on the side slope is fixed on the berm and shoulder on the slope using concrete anchorage. In this study, small field tests to measure the anchor ability of concrete anchorage buried into trench for barrier sheet were conducted. Two types of gemembranes such as HDPE are LLDPE were used. The sectional size of concrete anchorage was changed as 1,600 cm^2 and 2,500 cm^2. The strength of wall and base of the trench was also changed by changing addition ratio of cement into loam. From the tests, it was found that (1) the maximum pull-out force was almost depend on the mass of concrete anchorage and (2) LLDPE sheet with low rigidity gave greater anchor ability than HDPE sheet with high rigidity.

KEYWORDS: geomembrane, liner of landfill, pull-out force, anchor ability

INTRODUCTION

In Japan, various types of geomembrane, such as High Density Poly-Ethylene (HDPE), Linear Low Density Poly-Ethylene (LLDPE), Thermo Plastic Olefin with Poly-Ethylene (TPO(PE)) and Thermo Plastic Olefin with Poly-Propylene (TPO(PP)), are used as barrier sheet in waste landfill. The barrier sheet placed on the side slope is fixed on the berm and shoulder on the slope using concrete anchorage.

About 10 years ago, the sectional size of concrete anchorage was about 900 cm^2. But this caused failure of anchorage due to the force by waste compaction work or thermal stress owing to decrease of the circumstantial temperature when the HDPE geomembrane with large thermal coefficients was used. So, Imaizumi et al. (1997) have conducted pull-out tests for HDPE geomembrane changing the sectional size of concrete anchorage and pointed out that a sectional area of 900 cm^2 was not enough. After then, the concrete anchorage with a sectional area of more than 2,500cm^2, usually 4,900 cm^2, has been employed.

Recently the use of geomembrane having medium rigidity, such as LLDPE, TPO(PE) or TPO(PP), has remarkably increased. Many engineers have thought that a sectional area of 4,900 cm^2 may be too much large and over-designed.

In this study, small field tests were conducted to evaluate the anchor ability of concrete anchorage buried into a trench for barrier sheet. Two types of barrier sheet with different rigidity, such as HDPE and LLDPE, were used. The sectional size of concrete anchorage was varied as 1600 cm^2 and 2500 cm^2. The strength of rear wall and base of the trench was also changed.

MATERIALS

Two types of geomembrane with a thickness of 1.5 mm, HDPE, and LLDPE were used as barrier sheet in the experiments. Nonwoven stapled geotextile with a thickness of 10 mm and a mass per unit area of 1,400 g/m^2 was used as the protective mat.

Table 1 shows properties of the geomembrane. The HDPE has about twice elastic modulus as large as LLDPE. But the thermal expansion coefficients of LLDPE and HDPE are same.

Table 1 Properties of geomembrane

Items	HDPE	LLDPE
Density ; g/cm^3	0.95	0.93
Tensile strength ; MN/m	574	453
Elastic modulus ; MN/m^2	480	220
Thermal expansion coefficient; $\times 10^{-4}$ /°C	2.0	2.0
Frictional coefficient	0.17	0.32

[1] Professor, Department of Energy and Environmental Science, Utsunomiya University, JAPAN. Email:imaizumi@cc.utsunomiya-u.ac.jp
[2] M.S. Student, ditto, JAPAN. Email:mt076620@cc.utsunomiya-u.ac.jp
[3] Senior Research Engineer, Geotechnical Engineering and Soil Environment Group, Kajima Corporation, JAPAN
[4] Research Engineer, ditto, JAPAN.
[5] Manager, Environmental Engineering Division, Kajima Corporation, JAPAN
[6] Deputy Manager, ditto. Engineer, ditto, JAPAN.

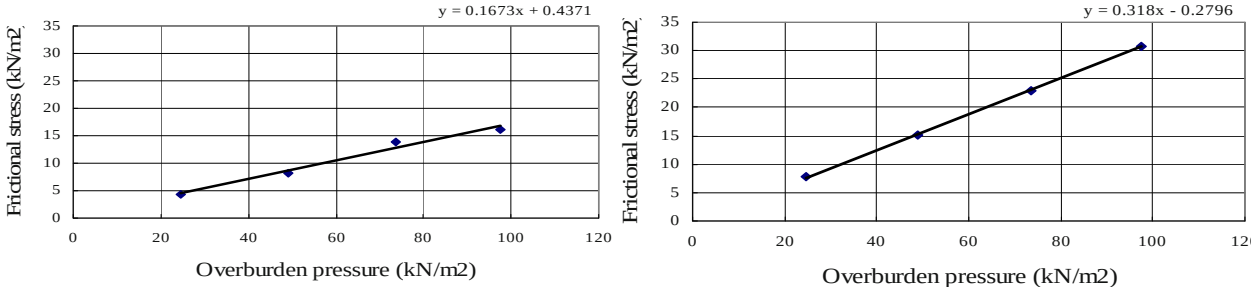

(a) HDPE (b) LLDPE

Fig. 1 Relation between the peak frictional stress versus overburden pressure on sheet/geotextil interface

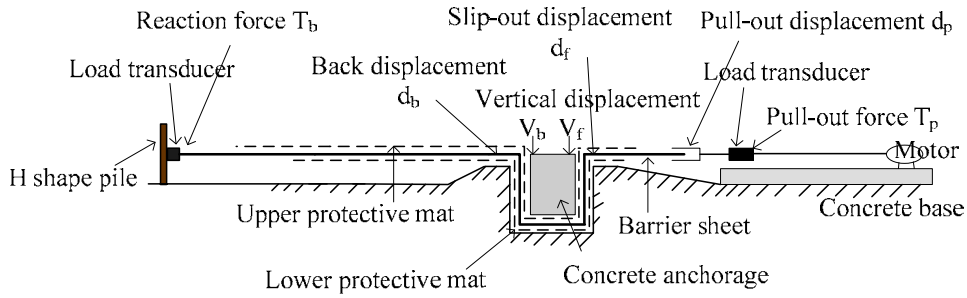

Fig. 2 Configuration of modeled concrete anchorage and instruments to measure the behavior

Fig. 1 shows relation between the peak frictional stress and overburden pressure obtained by direct shear tests for geomembrane/geotextile interface. In these tests, nonwoven stapled geotextile with a size of 195 mm×95 mm and geomembrane with a size of 280 mm×140 mm, which were glued on plywood with a thickness of 10 mm, were used. The overburden pressure was changed as 24.5, 49.0, 73.5 and 98.0 kN/m^2. In Fig. 1, the peak frictional stress has linear relationship with overburden pressure and an intercept (an adhesion) can be negligible. Therefore, the gradient of the relation was defined as a frictional coefficient. Obtained values are also listed in Table 1. HDPE has almost a half as small value as LLDPE.

OUTLINE OF PULL-OUT TESTS

Configuration

Fig. 2 shows a configuration of modeled concrete anchorage and instruments to measure the behavior of the barrier sheet and the concrete anchorage.

First, a trench with a bit larger sectional area than concrete anchorage was dug into modeled ground made from concrete. Then nonwoven stapled geotextile with a thickness of 10 mm and a width of 500 mm was spread as a bottom protective mat, and then barrier sheet overlying nonwoven geotextile was placed on the bottom protective mat. After assembling a plywood form, ready mixed concrete was placed in the trench to be anchorage with a given sectional area.

The electric motor with spiral bar in order to pull barrier sheet was fixed on the concrete base in front of the concrete anchorage. The toe of spiral bar was connected with barrier sheet through a load transducer. H-shape pile was buried at about 1.3 m backward from trench to measure reaction force.

As shown in Fig. 2, the measuring items are (1) pull-out force T_p at the front edge of barrier sheet, (2) reaction force T_b at the rear of barrier sheet, (3) pull-out displacement d_p at front edge of barrier sheet, (4) slip-out displacement d_f of barrier sheet at 50 mm front from the concrete anchorage, (5) back displacement d_b of barrier sheet at 50 mm back from the concrete anchorage, (6) vertical displacement v_f at front end of the concrete anchorage and (7) vertical displacement v_b at back end of the concrete anchorage. The temperature t_s on the surface of the sheet and circumstantial temperature t_c were also measured by thermo-couple.

The tests were performed as two series. The first (*A* series) was that the whole trench was made from concrete, and the second (*B* series) was that the front wall of trench was made from concrete and the base and rear wall of trench were made from cement mixed loam. In the *A* series test, sectional area of concrete anchorage with a width of 500 mm was changed as 1,600 cm^2 and 2,500 cm^2. In the *B* series tests, the sectional area of the concrete anchorage was 2,500 cm^2 but the strength of

cement mixed loam was varied by changing an addition ratio of cement as 7% and 10%.

Table 2 shows mass of the concrete anchorage and ratio, the value for refilled ground is a bit lower than that for sound (not refilled) ground. Judging from q_c, the cement mixed ground with an addition ratio of 7% or 10% can bear traffic service such as dumper.

Table 3 shows corn index q_c obtained by conducting cone penetration test against rear wall of trench in *B* series tests. Although the values of q_c at surface are almost same regardless of different of cement addition

Table 2 Mass of concrete anchorage (width is 500 mm)

A series tests

Sectional area	1,600 cm^2		2,500 cm^2	
Type of sheet	HDPE	LLDPE	HDPE	LLDPE
Mass (kg)	189.5	185.8	293.0	295.3

B series tests

Addition ratio of cement (%)	7	10
Type of sheet	HDPE	HDPE
Mass (kg)	321.5	306.5

Table 3 Average of cone index, q_c, of rear wall in ***B*** series tests (Unit; kN/m^2)

Addition ratio of cement (%)	7		10
Condition	Sound	Refilled	Sound
Up to 10 cm from surface	1637	1068	1568
Deeper than 10 cm from surface	1186	1068	1029

Procedure

After one week aging of concrete anchorage, only barrier sheet sandwiched by geotextile was pulled out by electric motor at a constant moving rate of 1.0 mm/min. During which, the forces T_p and T_b, horizontal displacements of barrier sheet d_p, d_f and d_b, and vertical displacements v_f and v_b of the concrete anchorage were measured through the load transducer and displacement transducer respectively, every 0.5 mm pull-out displacement at front edge of barrier sheet, and recorded on the data logger.

In the *A* series tests, the sheet, first, was pulled out in a condition as rear end of barrier sheet was not tied to H-shape pile (free-end condition). Then, the sheet was pulled out in a condition as rear end of barrier sheet was tied to H-shape pile through load transducer (tied-end condition). In the *B* series tests, the sheet was pulled out only in a condition as rear end was tied (tied-end condition).

RESULTS

Figs. 3 and 4 show the relationships between pull-out force T_p and reaction force T_b versus pull-out displacement d_p of barrier sheet. In the figures, T_{pf} means pull-out force in free-end condition, and T_{pt} and T_{bt} mean pull-out force and reaction force in tied-end condition, respectively.

When the rear end of sheet is free in *A* series tests, it is found from Fig. 3 that the pull-out force increases gradually with increase of pull-out displacement and

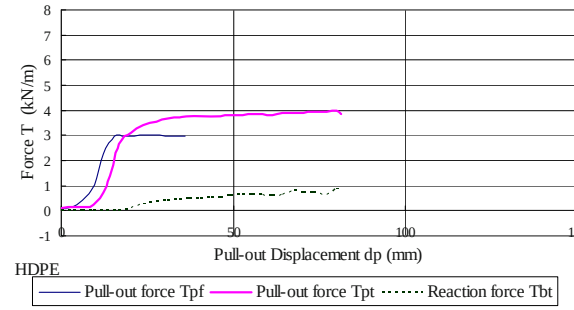

Sectional area; 1,600 cm^2 HDPE

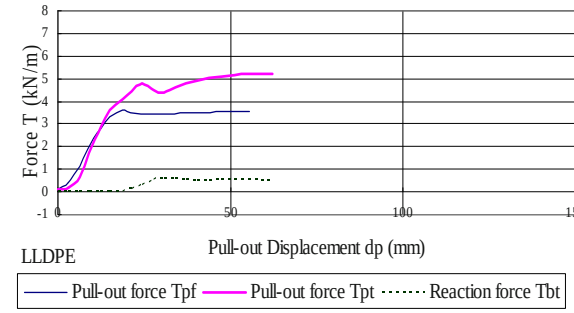

Sectional area; 1,600 cm^2 LLDPE

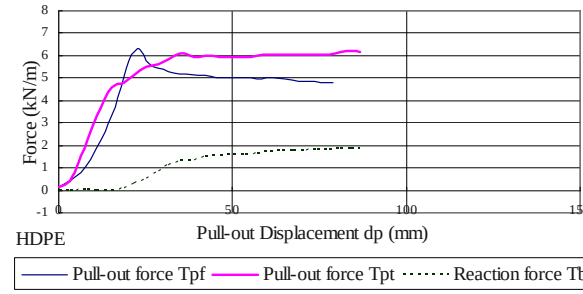

Sectional area; 2,500 cm^2 HDPE

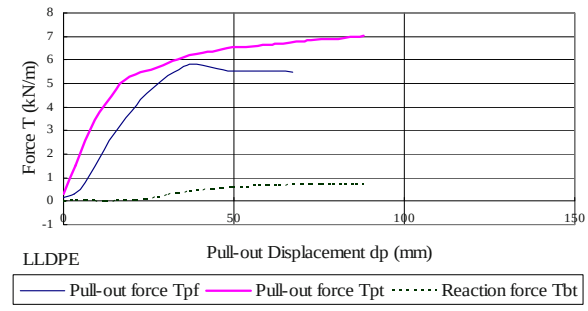

Sectional area; 2,500 cm^2 LLDPE

Fig. 3 Relationship between measured tensile force versus pull-out displacement (*A* series tests)

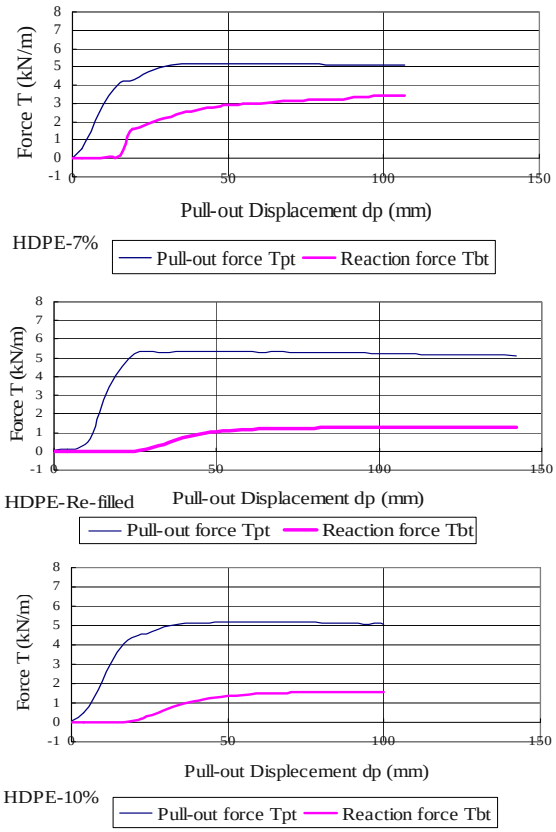

Fig. 4 Relationship between measured tensile force versus horizontal displacement (*B* series tests)

then shows the peak value followed by a little degradation.

When the rear end of sheet is tied to H-shape pile, it is found from Figs.3 and 4 that the pull-out force also increases with increase of pull-out displacement. However it does not show peak value but shows like yielding behavior before reaching the maximum value. And it is also seen that the reaction force mobilizes just when the pull-put force shows yield phenomenon and that the tendency of relation between reaction force versus pull-out displacement after yield point is very similar that of reaction force versus pull-out displacement.

Tables 4 and 5 are the list which summarizes the peak and final values of measurement about pull-out force and reaction force. Regarding the peak pull-out force in case of free-end condition of *A* series tests, the value for the concrete anchorage with a sectional area of 2500 cm^2 is 2.09 times and 1.59 times larger than that of a sectional area of 1600 cm^2, for HDPE and LLDPE respectively. The ratios are mostly equivalent to the ratio about the mass of concrete anchorage.

Fig.5 shows the relation between final value of pull-out force reduced by reaction force T_{pt} - T_{bt} in tied-end condition versus peak pullout force T_{pf} in free-end

Table 4 Summarization of measured tensile force in *A* series (Unit; kN/m)

Sectional area	1,600 cm^2		2,500 cm^2	
Type of sheet	HDPE	LLDPE	HDPE	LLDPE
Peak T_{pf} in free-end tests	2.98	3.59	6.22	5.72
Final T_{pt} in tied-end tests	3.75	5.21	6.18	7.02
Final T_{bt} in tied-end tests	0.87	0.50	1.86	0.70
Final T_{pt} - T_{bt} in tied-end tests	3.01	4.72	4.32	6.32

Table 5 Summarization of measured tensile force in *B* series (Unit; kN/m)

Addition ratio of cement	7 %		10 %
Type of sheet Condition	HDPE Sound	HDPE Refilled	HDPE Sound
Final T_{pt} in tied- end tests	5.01	5.02	4.99
Final T_{bt} in tied- end tests	1.67	1.33	1.56
Final T_{pt} - T_{bt} in tied-end tests	3.34	3.69	3.44

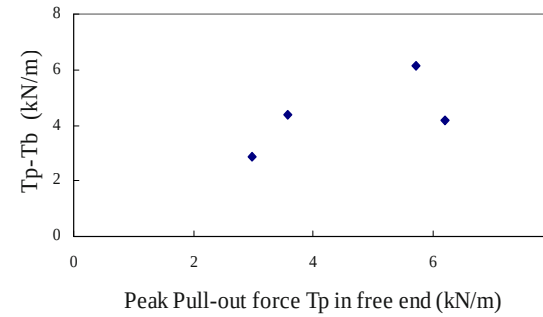

Fig. 5 Relation between final T_{pt} - T_{bt} in tied-end tests versus T_{pf} in free-end tests

condition. In the figure, both are almost equal. This suggests that the fluctuation of pull-out force after yield point depends on the change of reaction force.

From Table 4, it is found that peak pull-out force T_{pf} in free-end condition and pull-out force reduced by reaction force T_{pt} - T_{bt} in tied-end condition for LLDPE barrier sheet are greater than those for HDPE sheet. The frictional coefficient of LLDPE/stapled nonwoven geotextile is about twice as large as HDPE/stapled nonwoven geotextile as shown in Table 1. If the pull-out force in free-end condition is proportion to only the weight of concrete anchorage and frictional coefficient on interface of sheet and geotextile, the ratio of pull-out force for LLDPE to that for HDPE should be equal to the

ratio of frictional coefficients. But they were not consistent with together. It is considered that other factor may affect on pull-out force.

Comparing the final pull-out force reduced by reaction force T_{pt} - T_{bt} about HDPE sheet in case of *A* series (Table 4) with that in case of *B* series (Table 5), *A* series gave larger value. As described previously, the rear wall and base of trench in *A* series was made from concrete. Therefore, it can be said that the strength of rear wall of the trench sure affects on the pull-out force.

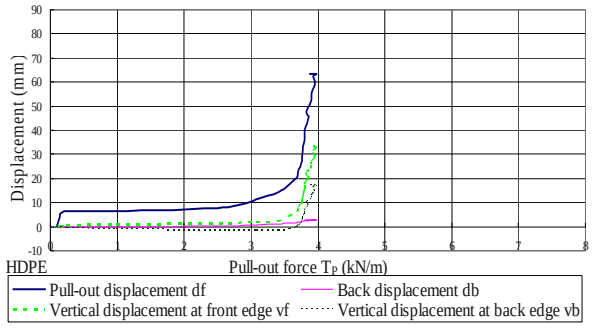

Sectional area; 1,600 cm^2 HDPE

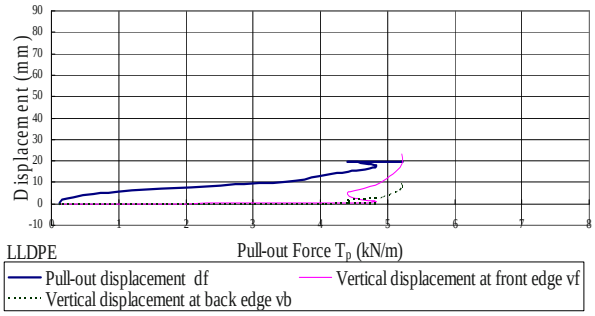

Sectional area; 1,600 cm^2 LLDPE

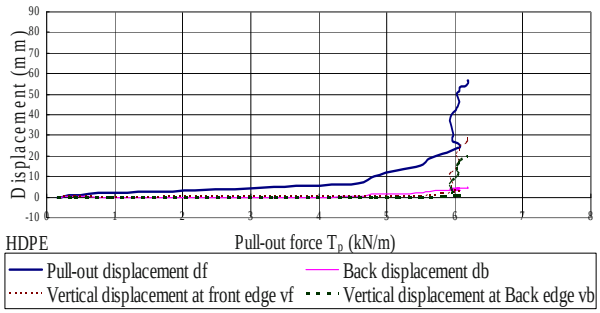

Sectional area; 2,500 cm^2 HDPE

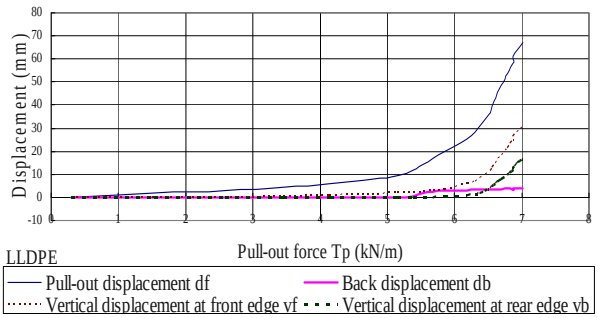

Sectional area; 2,500 cm^2 LLDPE

Fig. 6 Change of horizontal displacements of barrier sheet and vertical displacements of the concrete anchorage as pull-out force increases in *A* series tests

DISCUSSION ABOUT BEHAVIOR OF CONCRETE ANCHORAGE

Figs. 6 and 7 show the change of horizontal displacement d_f and d_b of barrier sheet, vertical displacement v_f and v_b of the concrete anchorage as pull-out force increases. Table 6 is a list of the pull-out force at a moment the displacement just mobilizes, which was read from Figs.6 and 7. From these figures and table, the behavior of concrete anchorage induced by pull-out

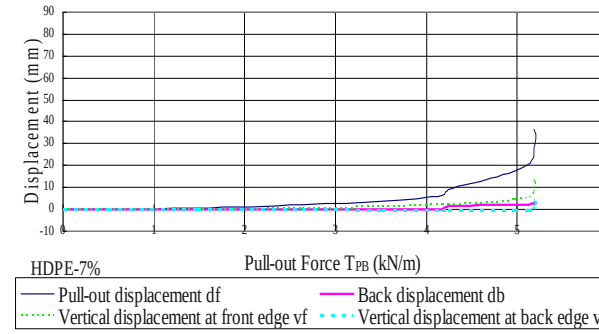

Sectional area; 2,500 cm^2 HDPE

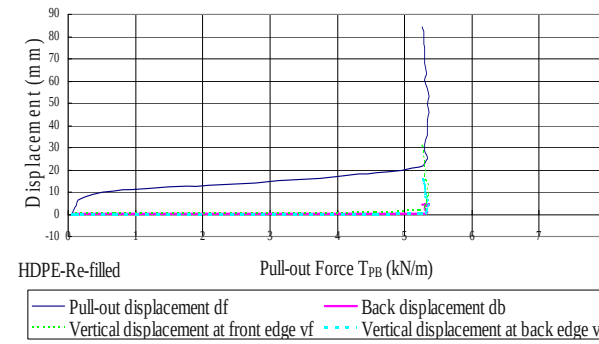

Sectional area; 2,500 cm^2 HDPE

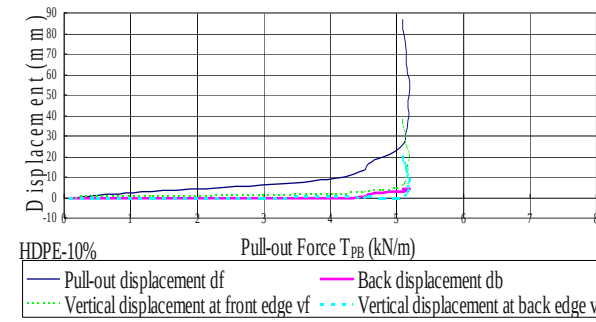

Sectional area; 2,500 cm^2 HDPE

Fig. 7 Change of horizontal displacements of barrier sheet and vertical displacements of the concrete anchorage as pull-out force increases in *B* series tests

force can be described as follows.

As the barrier sheet is pulled out at front edge, first, the sheet begins to slip out from concrete anchorage. In this phase, frictional force between the sheet and the protection mat under weight of concrete anchorage may contribute as reaction force. Second, the front of concrete anchorage rises up to rotate itself backward when the pull-out force reaches a certain force. In this phase, it is thought that rotational moment around the point of the back bottom of concrete anchorage, which is caused by weight of concrete anchorage, pull-out force and frictional force between the sheet and geotextile, is just balanced. But, third, this rotation will stop when the passive earth pressure of rear wall can mobilize completely due to further increase of pull-out force. Fourth, horizontal displacement of the barrier sheet at rear of concrete anchorage happens when more pull-out force works after rotation stops. At last, the back of concrete anchorage begins to rise up by further pull-out force.

Table 6 The value of pull-out force just when the displacement occurred (Unit; kN/m)

A series tests

Sectional area		1,600 cm^2		2,500 cm^2	
Type of sheet		HDPE	LLDPE	HDPE	LLDPE
Occurrence of	d_p	0.1	0.2	0.2	0.8
	v_f	3.6	2.0	2.8	3.9
	d_b	2.9	*	4.6	5.3
	v_b	3.7	3.8	5.7	6.0

* not measured

B series tests

Addition ratio of cement (%)		7		10
Types of sheet Condition		HDPE Sound	HDPE Refilled	HDPE Sound
Occurrence of	d_p	1.2	0.2	0.2
	v_f	3.1	3.8	2.8
	d_b	4.1	5.3	4.5
	v_b	3.2	5.3	5.1

CONCLUSIONS

The main results obtained in this study are as follows:

(1) The anchorage ability, i.e. the maximum pull-out force, of a barrier sheet seems to be proportional to mass of concrete anchorage.

(2) The barrier sheet with a higher rigidity as HDPE gives smaller anchorage ability than the barrier sheet with a medium rigidity as LLDPE.

(3) As the front of a barrier sheet is pulled, the front of concrete anchorage rises up to rotate backward. The rotation stops when the moment around the point of the back bottom of concrete anchorage induced by pull-out force, frictional force and passive earth pressure is balanced. But, the sheet behind the concrete anchorage may displace when further pull-out force works.

(4) The strength of rear wall of the trench affects anchorage ability.

ACKNOWLEDGEMENTS

This research was conducted as a cooperative work between Utsunomiya University and Kajima Corporation. The authors thank their financial support. They are also grateful to Mr. T Yoshinao for his helping the pull-out tests.

REFERENCE

Imaizumi S, Tsuboi M, Doi Y, Shimizu T, Miyaji H (1997) Anchorage Ability of a Geosynthetics Liner buried in a Trench filled with Concrete. Proc. of 6th International Landfill Symposium, III: 453-462

Proceedings of the 4th Asian Regional Conference on Geosynthetics
June 17 - 20, 2008 Shanghai, China

INTERPRETATION OF INSTALLATION DAMAGE OF GEOGRIDS BY CONSIDERING ENVIRONMENTAL CONDITIONS

H.Y. Jeon[1], A. Bouazza[2], S.D. Cho[3] and D. Cazzuffi[4]

ABSTRACT: We have compared the long-term performance of membrane drawn-type, warp/knitted-type, junction bonded-type, composite-type geogrid, and strip-type geosynthetic reinforcement from their total factor of safety calculated from the composite reduction factors. To evaluate these reduction factors, wide-width tensile measurements, installation damage, creep deformation, and chemical and biological degradation tests were performed. The total factor of safety for the geosynthetic reinforcements was calculated from the experimental results of these reduction factors. The long-term design strength of the geosynthetic reinforcements was calculated using equations contained in the Geosynthetic Research Institute Standard Test Method GG4. The reduction factor by creep deformation was determined to affect the long-term performance. Strip-type reinforcements and composite-type geogrids showed excellent long-term performance among the geosynthetic reinforcements studied.

KEYWORDS: geosynthetic reinforcements, long-term performance, reduction factor, total factor of safety

INTRODUCTION

Generally, installation damage, creep, temperature, chemical environmental factors, etc. are responsible for the reduction in the properties of geogrids, especially as regards their tensile strength,, and creep and installation damage are generally the prime factors. Therefore, many studies have been focused on these characteristics of geogrid reinforcement (Cazzuffi et al. 2001). In the current method of designing reinforced structures, the long-term design strength of the geogrids is determined by introducing the reduction factors that affect their long-term behavior for safety reasons (FHWA 1996). These reduction factors were considered independently, that is, the combined effect of the factors on the tensile property of the geogrids was not taken into account and this is the reason for their uneconomical and conservative design (Greenwood 2002). Recently, some studies have been conducted on the combination effect of creep and installation damage on the long-term design strength of geogrids, but most of the works were typical examples of such experimental studies (Pinho-Lopes et al 2002). In this study, the effects of the type of fill soils on the long-term behavior of the geogrids were evaluated by installation damage test and by considering the design criteria and construction conditions in Korea. The combined effect of creep and installation damage on the long-term tensile strength of the geogrids was also studied.

EXPERIMENTAL

Three types of PET woven geogrids with a PVC coating, 3 types of PET Warp Knitted geogrids with a PVC coating, 3 types of HDPE extruded and uniaxially drawn geogrids and 3 types of PET strip-razor bonded geogrids were used. Each type of geogrid was classified according to its ultimate tensile strength in order to evaluate the effect of the tensile strength of the geogrids on their resistance to installation damage. Three types of filling soils were used and maximum particle sizes of 40, 60 and 80 mm were used for all of the geogrids and gravel with a diameter of 25 mm was additionally used for geogrid samples B-2 and C-2. Fig. 1 shows the distribution curves of the soil size measured by sieving. The soils were classified as SW according to the Unified Soil Classification System. The soil in Test Site I has a density of 2.07 g/cm^3 and an optimum water content of 8.2%, while the corresponding values for the soil in Test Site II are 2.07 g/cm3 and 9.3% and those of the Soil in Test Site III are 1.94 g/cm^3 and 11.1%, respectively. Additionally, gravel with a particle size of 25 mm was used for geogrids B-2 and C-2. Visual observation of the

[1] Professor, Division of Nano-Systems Engineering, Inha University, Incheon, KOREA. Email: hyjeon@inha.ac.kr
[2] Professor, Dept. of Civil Eng., Monash University, Melbourne, AUSTRALIA. Email: malek.bouazza@eng.monash.edu.au
[3] Principal Researcher, Earth Structure & Foundation Eng. Res. Div., KICT, Goyang, KOREA. Email: sdcho@kict.re.kr
[4] Principal Researcher, Labs for Tests on Geosynthetics, CESI-PEC, Milan, ITALY. Email: CAZZUFFI@cesi.it

extracted geogrid was performed and then the samples were tested according to EN ISO10319. Creep tests were performed for the as-received samples and the installation-damaged geogrids. Two types of creep test conditions were separately selected according to the constituent material of the geogrid. Test temperatures were 20℃, 35℃ and 50℃, and the creep loads were 50% and 60% of the wide width tensile strength of the geogrid, respectively (Table 1).

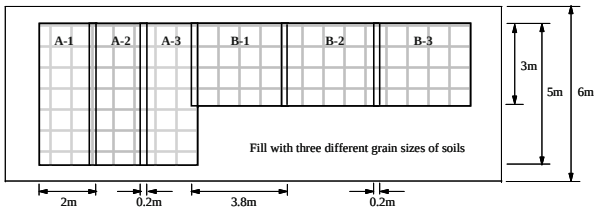

(Plan view of Test Sites I and II)

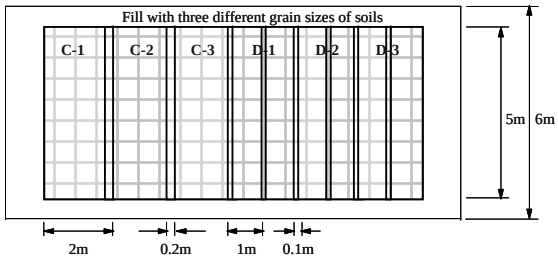

(Plan view of Test Site III)

Fig. 1 Schematic diagrams of installation damage field test

RESULTS AND DISCUSSION

Installation Damages with Filling Soils

To evaluate the effect of dmax on the characteristics of the installation damage incurred by the geogrids when they were used in reinforced earth structures with weathered granite backfill, the field installation test was performed. After the field installation damage test, the wide width tensile test was conducted for the extracted samples. The test was performed about 7 times for each geogrid and then the 5 results that showed the best fitting were averaged. The test results in terms of the SRR (Strength Reduction Ratio) are shown in Table 2. On comparing the results of Test I to those of Test II, it was observed that the results from Test II show a larger reduction in strength, whereas the aggregate contents in the fillers that were used in Tests I & II were almost the same (Fig. 2). This means that the angularity of the filler that was used in test I was sharper, so that more severe damage was caused. Table 2 shows the test results, which were obtained using weathered granite soil and aggregate with a diameter of 25 mm. It is clearly observed that the decrease in strength was accompanied by a decrease in the maximum tensile strain of the geogrid during the compacting of an up lift. Also, the average reduction in the tensile strength of the geogrids was 20% for geogrid B-2 with 25 mm filler; this value was closer to the value for the geogrid weathered by the granite soil with a dmax value of 40 mm, whereas the average reduction for geogrid C-2 weathered by the granite soil (d_{max}=40, 60 & 80 mm) was under 5%. Through the test results, it was confirmed that geogrids C and D, which were thicker and stiffer than geogrids A and B, were less damaged by installation stress.

Table 1 Specifications and tensile properties of geogrids

Test Site	Geogrid	Manufacturing Method	Wide-Width Tensile Property	
			Strength(kN/m)	Strain(%)
I & II	A-1	Woven PET-relatively flexible geogrid coated with PVC	66.2	10.6
	A-2		94.7	13.0
	A-3		109.1	11.4
	B-1	WIWK PET-relatively flexible geogrid coated with PVC	82.4	12.6
	B-2		104.9	13.3
	B-3		140.7	13.6
III	C-1	Extruded and uniaxial-drawn HDPE-relatively rigid geogrid	61.1	11.7
	C-2		82.3	12.1
	C-3		100.5	12.4
	D-1	PET flat ribs-relatively rigid geogrid welded (by?) laser	51.7	7.4
	D-2		81.5	7.0
	D-3		109.0	6.8

* PET : polyester, PVC : polyvinyl chloride
WIWK : Weft Insertion Warp Knitted, HDPE: High Density Polyethylene

Table 2 Results from wide width tensile tests for the damaged geogrids

Fill Material		Geogrid B-2 Test site Ⅰ			Geogrid C-2 Test site Ⅲ		
		Tensile strength (kN/m)	Peak strain (%)	SRR (%)	Tensile strength (kN/m)	Peak strain (%)	SRR (%)
Soil (Max. grain size, mm)	40	80.3	9.6	23.6	81.3	11.9	1.2
	60	67.9	8.5	35.5	80.2	12.2	2.5
	80	67.4	7.9	35.9	80.0	11.7	2.8
gravel (D 25 mm)		83.4	11.9	20.0	78.5	11.7	4.7

*SRR: Tensile strength reduction ratio of geogrids

Reduction Factor by Installation Damage

The reduction factors (RF_{ID}) of installation damage which were calculated are shown in Table 3. As shown in Table 3, the RF_{ID} of geogrids A and B are 1.35, 1.55 and 1.70 depending on the value of d_{max}, maximum particle size, whereas the RF_{ID} of geogrids C and D are

1.05 irrespective of the value of d_{max}. The RF_{ID} of geogrid B-2, which was obtained from the test conducted using aggregate with d=25 mm, is similar to that obtained using weathered granite soil with d_{max} = 40 mm, while geogrid C-2 in weathered granite soil shows good resistance to 25 mm gravel. And Fig. 3 shows the particle size distribution curves of filling soils.

Table 3 Estimation of partial factor for the installation damage of the geogrids

Relative stiffness	Geogrid	Filling material			
		Weathered granite soil (Max. particle size, mm)			Gravel (D25mm)
		40	60	80	
Flexible	A-1	(1.31, 1.32)	(1.39, 1.54)	(1.69, 1.70)	-
	A-2	(1.28, 1.26)	(1.54, 1.55)	(1.48, 1.59)	-
	A-3	(1.25, 1.35)	(1.31, 1.49)	(1.59, 1.69)	-
	B-1	(1.33, 1.33)	(1.46, 1.41)	(1.55, 1.54)	-
	B-2	(1.31, 1.35)	(1.55, 1.55)	(1.56, 1.69)	1.25
	B-3	(1.30, 1.33)	(1.44, 1.55)	(1.48, 1.58)	-
Rigid	C-1	1.03	1.05	1.05	-
	C-2	1.01	1.03	1.03	1.03
	C-3	1.02	1.03	1.05	-
	D-1	1.03	1.05	1.05	-
	D-2	1.01	1.04	1.05	-
	D-3	1.01	1.01	1.02	-
In case of A and B type geogrid, (No., No.) is the results of (Test site Ⅰ, Test site Ⅱ)					

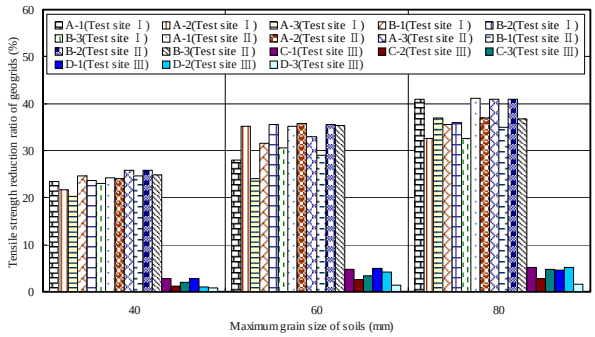

Fig. 2 Tensile strength reduction ratio of geogrids in field test site

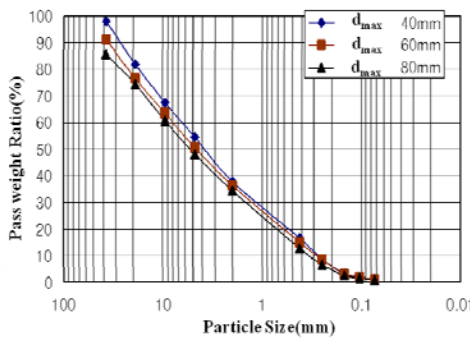

(a) Test site Ⅰ

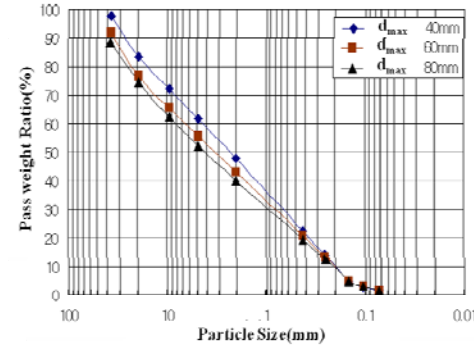

(b) Test site Ⅱ

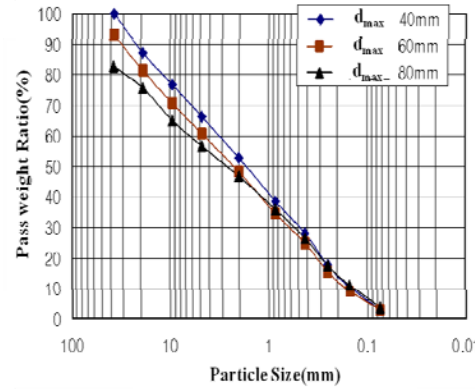

(c) Test site Ⅲ

Fig. 3 Particle size distribution curves of filling soils

Creep Deformation Behavior

To assess the creep behavior of geogrid B-2, the time-temperature superposition method was used. The shift factors for superposition were found to be -0.953 and -2.310 for the shift temperatures of 35℃ and 50℃, respectively, where 20℃ is the standard temperature. The creep strains of the as-received geogrid were 7.2% and 8.4% when loads of 50% and 60 % of T_{ult} were applied, respectively, as shown in Fig. 4.

This means that the as-received geogrids have good resistance against creep deformation. However, the creep of the damaged geogrid was 7.8% when a load of 50% of T_{ult} was applied, and when a 60% load was applied; there was no convergence in the creep curve. Therefore, it was determined that the proper creep load of the damaged geogrid was located between 50% and 60% of T_{ult}. In this study, the method defined by PWRC (2000) was used to determine the creep strength of the geogrids.

Table 4 shows the creep load and ratio of creep load vs. ultimate tensile strength of geogrid C-1, C-2. For these geogrids, creep load decreased with time after installation damage test but no significant cange between two geogrids.

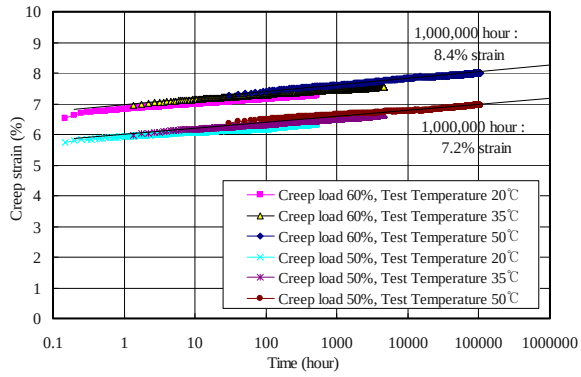

(a) as received

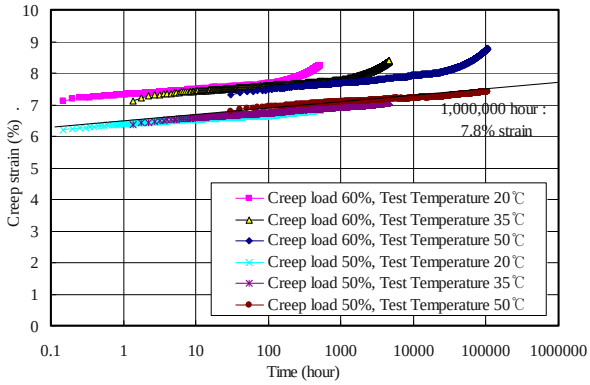

(b) damaged

Fig. 4 Creep strain curves of geogrid B-2 with creep load and test temperature

Table 4 Creep load evaluation of geogrids C-2 and C-3

Geogrid / Creep load	C-2			C-3	
	As received	After installation damage test		As received	After installation damage test (Weathered granite soil)
		Weathered granite soil	Gravel		
Creep load after 10^6 hours (kN/m)	31.4	30.4	30.4	38.2	37.3
Ratio of creep load vs. ultimate tensile strength (%)	38	37	37	38	37

The curve of the creep strain increment ratio (%) vs. the creep load ratio was also determined, in order to verify the validity of the creep strength. The creep load ratio refers to the ratio of the loading level to T_{ult}, and the creep strain increment ratio is calculated. A creep strain of 10% is referred to as the limit creep strain according to GRI-GG4. Fig. 5 shows the creep behavior of geogrid C-2 in the as-received condition.

The validity of the creep strength that was determined through these experiments was verified by plotting the creep strain increment ratio (%) vs. the creep load ratio, as shown in Fig. 6. Creep strength of the damaged geogrid *C* shows a decline of 2.6%—3.1% compared with the as received geogrid. Table 5 shows the RF_{ID} and RF_{CR} values which were used to evaluate the combination effect of these 2 factors.

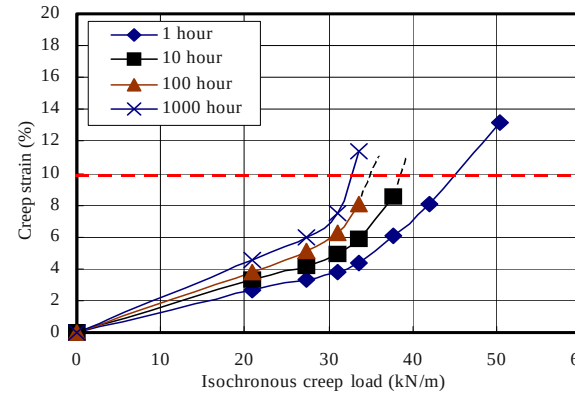

(a) Isochronous creep strain curves

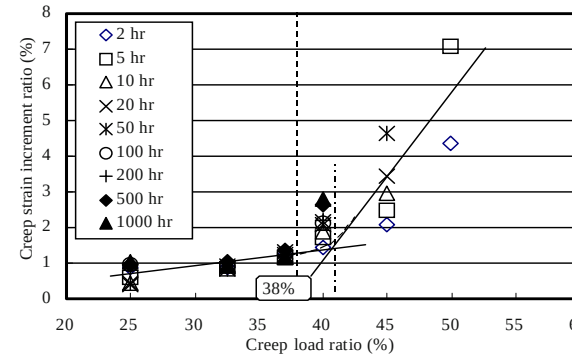

(b) Creep load ratio vs strain increase curves

Fig. 5 Analysis of creep curves for geogrid C-2

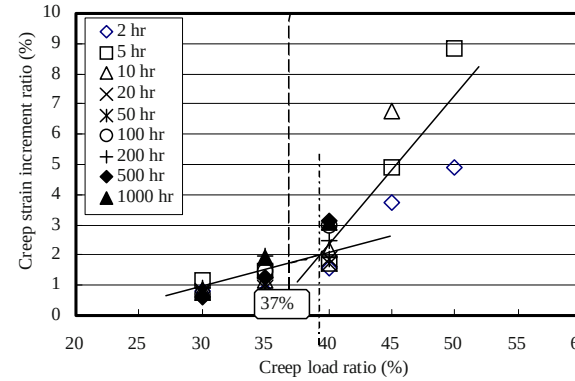

(a) geogrid C-2 (25 mm gravel)

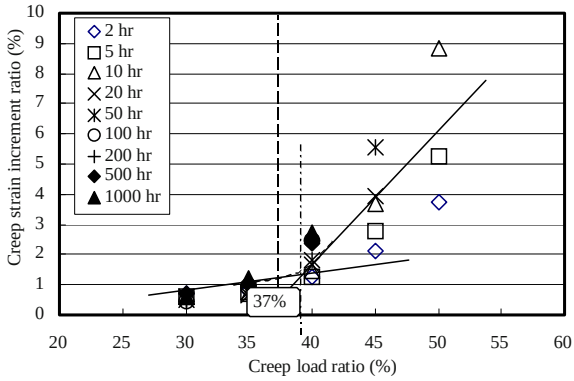

(b) geogrids C-2 and C-3
(80 mm granite weathered soil)

Fig. 6 Creep load ratio vs. creep strain increment ratio curves of geogrid C-2 after installation damage

Table 5 Reduction factor of geogrids

Filling Soil	B-2				C-2				C-3			
	GRI-GG4			*	GRI-GG4			*	GRI-GG4			*
	RF_{ID}	RF_{CR}	$RF_{ID}\times RF_{CR}$	RF_{DCR}	RF_{ID}	RF_{CR}	$RF_{ID}\times RF_{CR}$	RF	RF_{ID}	RF_{CR}	$RF_{ID}\times RF_{CR}$	RF_{DCR}
Granite Weathered Soil (80mm)	-	-	-	-	1.03	2.63	2.71	2.71	1.05	2.63	2.76	2.70
Gravel (25mm)	1.25	1.67	2.09	1.67～2.0	1.05	2.63	2.76	2.71	-	-	-	-

CONCLUSIONS

The reduction factors of installation damage (RF_{ID}) of the woven PET geogrid, for d_{max} = 40, 60 and 80 mm, are 1.35, 1.55 and 1.70, respectively, whereas those of the drawn HDPE geogrid and whole composite geogrid are both 1.07, the soil particle size. The reduction factor of installation damage of the PET woven geogrid is larger than that of the HDPE uniaxial-drawn geogrid, whereas the creep reduction factor of the HDPE uniaxial-drawn geogrid is about 50% larger than that of the PET woven geogrid. Using each reduction factor individually results in more conservative values of these factors than when the combination effect of these reduction factors is considered to calculate the long-term allowable strength of the geogrid.

REFERENCES

Cazzuffi D, Mongiovi L, Torresendi M (2001) Laboratory and Field tests for the Evaluation of Installation Damage of Geosynthetics in Reinforced Earth Structures, 15th ICSMGE, Istanbul: 1565-1568

FHWA(1996), Corrosion/Degradation of Soil Reinforcements for Mechanically Stabilized Earth Walls and Reinforces Soil Slopes, FHWA Publication No. FHWA-SA-96-072, Federal Highway Administration, Washington, D.C.

Greenwood JH (2002) The Effect of Installation Damage on the Long-term Design Strength of a Reinforcing Geosynthetic, Geosynthetics International 9(3): 247-258

Pinho-Lopes M, Recker C, Lopes ML, üller-Rochholz J (2002), Experimental Analysis of the Combined Effect of Installation Damage and Creep of Geosynthetics—New Results, Geosynthetics-7th ICG-Delmas: 1539-1544

ANALYSIS OF ENVIRONMENTAL CONDITION EFFECTS OF WASTE LANDFILL ON GEOMEMBRANE PERFORMANCE

H.Y. Jeon[1], K.Y. Lee[2], J.H. Kim[3] and C.R. Kim[4]

ABSTRACT: The effects of acidic and alkaline solutions to be considered waste on the chemical resistance of high density polyethylene (HDPE) geomembranes (GMs) were evaluated. Damaged and intact smooth/textured specimens were immersed in acidic, alkaline and distilled water (pH=4, 12, 8 and 7), and incubated at 20, 40, 60 and 80 °C respectively. Tensile stress of specimens was periodically determined by constant rate of load tensile testing apparatus while polymer structure was examined by a scanning electro-microscope. Damaged HDPE GMs showed excellent acidity-resistance as intact HDPE GMs. High temperature imparted flexibility in HDPE GMs which in turn showed lower tensile strength.

KEYWORDS: acidic and alkaline solutions, waste leachates, chemical resistance, acidity-resistance

INTRODUCTION

One of the concerns raised regarding the use of HDPE geomembranes is there susceptibility to stress cracking which, in turn, is a consequence of their high crystallinity.

Stress crack is an external or internal crack in a plastic caused by tensile stress less than its short-time mechanical strength (Koerner 2005).

Stress crack resistance, often estimated by environmental stress crack resistance tests, is an important performance parameter for HDPE GMs applied in landfills (Giroud 2005; Rowe 2002).

Conditions that can affect stress cracking include: level of loading, test temperature and environment, microstructure, polymer additives package, processing history and thermal history. Most of the waste in sanitary landfills in Korea is wet food waste and the waste whose solutions would have acidic or alkaline properties during the landfill periods.

In this study, we evaluated the slow crack resistance of HDPE GMs under such kinds of landfill conditions by stimulating alkalinity and acidity in laboratory.

EXPERIMENTAL

Geomembrane specimens were cut in machine direction (MD) and cross machine direction (CMD) using blanking die apparatus.

Notched specimens were made by cutting a control notch of 20% of the thickness of each specimen at cross section on the surface as suggested by ASTM D 5379-NCTL test.

This was carried out for original and treated samples, in which we measure the crack resistance in original materials and materials after the treatments.

For NCTL tests, samples were treated with pH 4 and 8 solutions under temperatures of 40°C and 60°C for the time being.

Test conditions are given in Table 1. The rupture time of stress crack resistance were measured in five specimens in each treatment at the end of test duration. The applied stress levels were ranged from 25% to 60% of yield stress at increments of 5%.

Table 1 Test conditions for NCTL test

pH	Chemical solution	Temperature (°C)	Test duration
4	HCl	40 and 60	1200 hours
8	NaOH		

Further, morphology of the surfaces of specimens was examined under a scanning electro microscope (SEM), before and after the NCTL tests.

[1] Professor, Division of Nano-Systems Engineering, Inha University, Incheon, KOREA. Email: hyjeon@inha.ac.kr
[2] Professor, Department of Civil Engineering, Dongseo University, Busan, KOREA. Email: civklee@gdsu.dongseo.ac.kr
[3] Master Student, Dept. of Textile Eng., Inha University, Incheon, KOREA. Email: hello3304@naver.com
[4] Master Student, Dept. of Textile Eng., Inha University, Incheon, KOREA. Email: 0116829590@hanmail.net

RESULTS AND DISCUSSIONS

To measure the chemical resistance after treatments done on GM samples, we performed stress—cracking test such as NCTL test.

Fig. 1 shows NCTL test results for GMs in pH 4 and 8 under 40°C and 60°C. Yield stress of 30% reported after 250 hours of failure time for the original materials.

By comparing the graphs in two diagrams of Fig. 1, no significant difference can be observed with pH 4 and 8 solutions. It implies that stress-crack behavior is independent with pH variations.

However, temperature variations are more sensitive to stress-crack behaviors as shown in Fig. 1 such as higher the temperature, lower the stress-crack resistant property. Thus, it is shown that no significant difference between CMD and MD directions as well as between S and T samples.

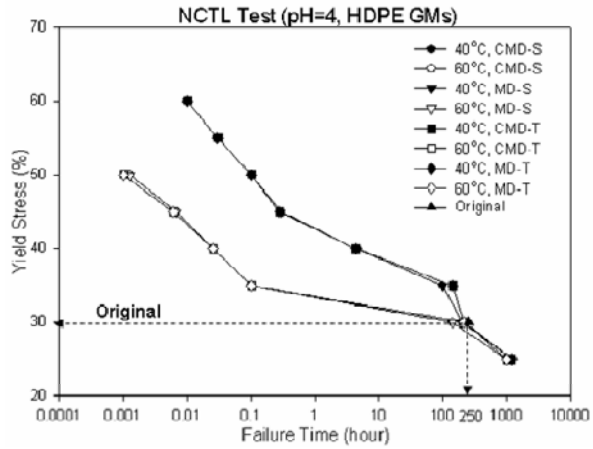

(a) pH 4

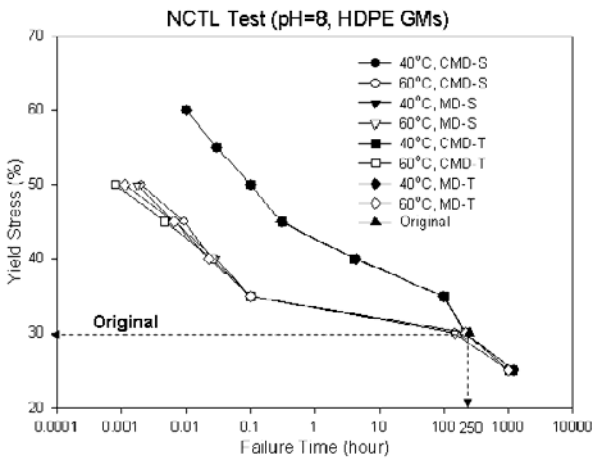

(b) pH 8

Fig. 1 The variations of yield stress (%) with failure time (hours). Condition: pH 4 and 8 temperature 40°C and 60°C. (Abbreviation for samples types: CMD-S: smooth cross machine direction; MD-S: smooth machine direction; CMD-T: textured cross machine direction; MD-T: textured machine direction)

According to the data of pH 8 at 60°C show very minimal deviations among their yield stress percentages of S and T samples as well as CMD and MD directions, up to about 0.5 hours time.

However, after yield stress lowered to 30% at 250 hours (same as original yield stress percentage), all tested samples treated under 40°C and 60°C temperatures came to a same line of behavior and yield stress percentage have reduced below 30% further.

Fig. 2 describes the percent yield stress versus failure time of cross machine direction HDPE GMs immersion in acidic (pH=4) and alkaline (pH=8) solution at 40°C, respectively.

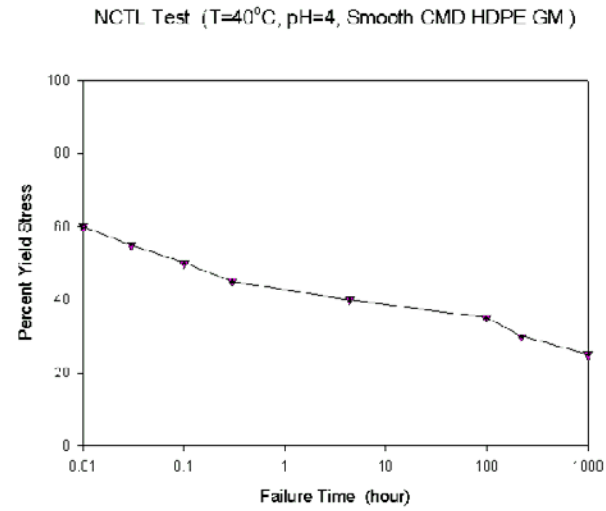

(a) pH 4

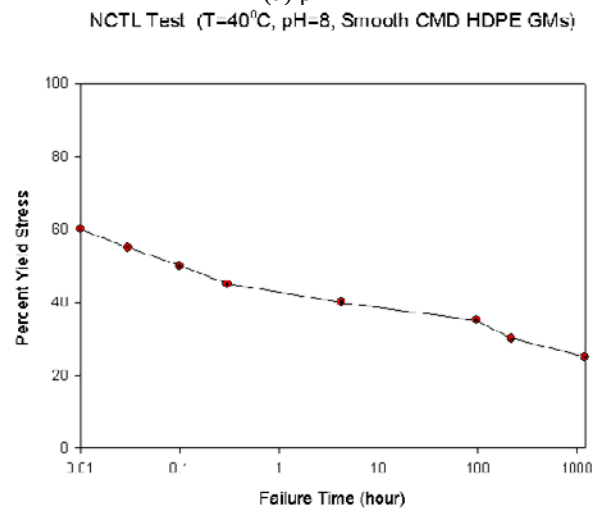

(b) pH 8

Fig. 2 Percentage yield stress versus the logarithm of the average failure time of smooth across machine direction (CMD) high density polyethylene (HDPE) geomembranes (GMs) at 40°C

No obvious differences were observed between alkaline (Fig. 3a) and acidic treatments (Fig. 2 b). This indicates that different types of HDPE GMs have the

similar stress crack resistance at the same temperature, in both acidic and alkaline conditions.

HDPE GMs have excellent acidity and alkalescency resistance.

Fig. 2 shows the percent yield stress versus failure time of cross machine direction HDPE GMs immersed in acidic solution (pH=4) and alkaline solution (pH=8) at 60°C, respectively.

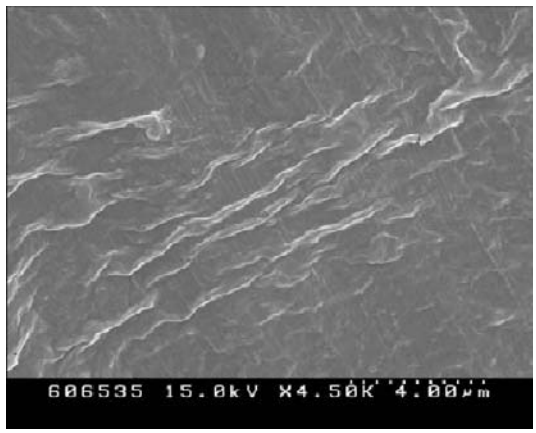

(a)

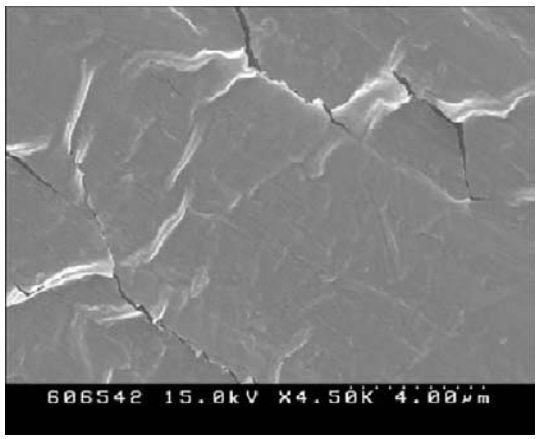

(b)

Fig. 3 SEM images of notched HDPE GMs at 80°C in alkaline solution (pH=12) after 120 days before (a) and after (b) tensile test

The surface appearance of notched (Fig. 3) and un-notch samples (Fig. 4) were obtained by SEM before and after the tensile tests (80 °C, 120 days). After being treated at higher temperatures for a period of 120 days their rupture loads and elongations of most samples changed dramatically.

There are obvious morphology changes after being treated, especially for notched samples, which have cracks on their surface after treatment (Fig. 3b). Similar crackes can also be seen on unnotched samples (Fig. 4 b).

Thus, visible surface micro cracks are indicated by image (b). Reason would be that due to the notch made on these samples, they cracked and failed under applied loads, but, un-notched samples do not show these types of cracks after the tensile test. The visible cracks indicated in Fig. 4 may cause to be occurred linear failures in the GMs.

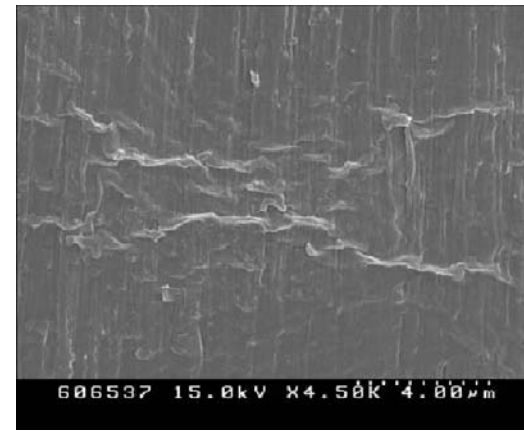

(a)

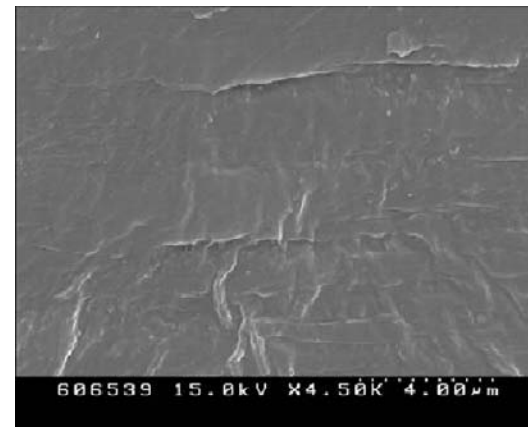

(b)

Fig. 4 SEM images of un-notched HDPE GMs at 80°C in alkaline solution (pH=12) after 120 days before (a) and after (b) tensile test

In Fig. 5 also, surface nature has changes, after treatments given under NCTL test, but, no visible surface micro cracks are indicated, after applying stresses. Therefore, damaging to the GMs is very important factor to be considered. It makes severe problems in load and elongation at yield and breaking and produce micro surface cracks, which will bring the GMs to a poor performance state.

In Fig. 5, we selected HDPE GMs at 60°C in alkaline (pH 8) solution, because, based on the observations made under stress-crack resistance test (as given in Fig. 3), 60°C gave lower stress crack-resistance properties compared to 40°C and therefore, we assumed that it may possible to occur micro surface cracks at 60°C on the treated samples.

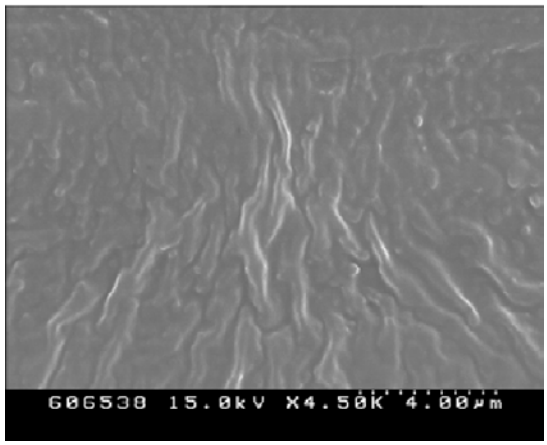

(a) before NCTL test

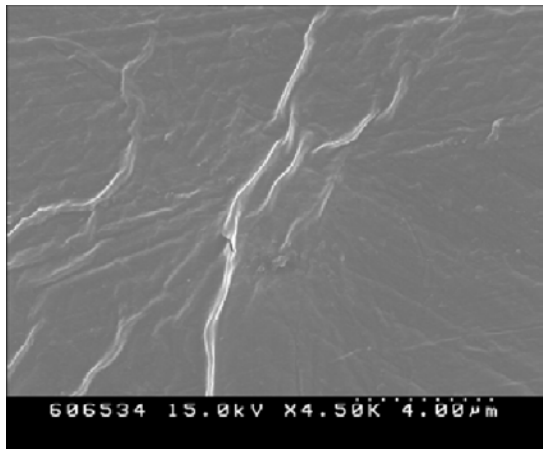

(b) after NCTL test

Fig. 5 SEM images of HDPE GMs at 60°C in alkaline solution (pH=8) before and after NCTL test

Thus, stress crack resistance property variations are independent of pH values. However, it is not possible to observe any micro cracks on the surface at that temperature. It implies that temperatures between 40°C and 60°C does not effect to create any cracks in the GM structure under acidic or alkaline pH solutions and results a good crack resistance under the mentioned conditions. One reason would be the high degree of crystallinity of HDPE, which compose of higher number of tie molecules, higher molecular weights and longer polymer chains.

CONCLUSIONS

Stress crack resistance is independent from pH variations, but significantly depend on temperatures such as higher the temperature, lower the stress crack resistance. Notched samples showed micro cracks on their surface and un-notched samples do not show any micro cracks under the tensile loads applied and tested conditions. Thus, temperatures between 40°C and 60°C does not effect to create any cracks in the GM structure under acidic or alkaline pH solutions and results a good crack resistance under the mentioned conditions.

ACKNOWLEDGEMENTS

This work was supported by grant No. RTI04-01-04 from the Regional Technology Innovation Program of the Ministry of Commerce, Industry, and Energy (MOCIE).

REFERENCES

Koerner RM (2005) Designing with Geosynthetics, 5th Edition, Person Education Inc., NewJersey, USA

Giroud JP (2005) Quantification of geosynthetic behavior, Geosynthetics International, 12 (1): 2-27

ASTM 5397-99 (2005) Standard Test Method for Evaluation of Stress Crack Resistance of Polyolefin Geomembranes Using Notched Constant Tensile Load Test.

Rowe RK, Sangma HP (2002) Durability of HDPE geo-membranes, Geotextile and Geomembrane, 20: 77-95.

VISUALIZATION OF CRACKS IN COMPACTED CLAYEY SOIL DUE TO USING X-RAY CT

T. Mukunoki[1], J. Otani[2], S. Camp[3] and J.P. Gourc[4]

ABSTRACT: The objective of this paper is to investigate the property change of compacted clayey soils for cover in the landfill subjected to moisture fluctuations and local deformation. Authors have tried to evaluate the crack behavior of compacted clayey soils due to punching loading without confining pressure. Based on the results of this study, mixing the rubber chips in the soil material was proposed as a new cover soil material. As consecutive study, conventional compacted clayey soils and compacted clayey soil with rubber chips were used for the following tests: the punching test and bending test with air compressing. At each level, the compacted clayey specimen is scanned using the X-ray computed tomography (CT) scanner and then, the density change in the specimen was visualized and evaluated quantitatively.

KEYWORDS: compacted clayey soil, cracks, landfill cover, X-ray computed tomography (CT)

INTRODUCTION

Impermeable liners prevent the contamination of environment from vicinity of landfills. Compacted clayey soils are commonly used as hydraulic barriers in waste containment systems such as in liners and covers for landfills (Koerner et al. 1997; Rowe et al. 2004; Camp et al. 2005). An advantage of using compacted clays as cover soil is to minimize infiltration of rainfall or snowfall through into the waste. However, the cover soil system is sometimes damaged by two predominant factors: (i) desiccation cracking due to moisture fluctuations, and (ii) cracking due to excessive local deformation.

This study focuses the factor (ii) and authors have performed to evaluate the crack behavior of compacted clayey soils due to punching and bending tests. Based on the results of this study, to mix the rubber chips in the soil material (Ashoke et al. 2004) was proposed as a new cover soil material. As consecutive study, conventional compacted clayey soils and compacted clayey soil with rubber chips are used for the described tests in the above. At each level, the compacted clayey specimen is scanned using the X-ray computed tomography (CT) scanner and then, the density change in the specimen was visualized and evaluated quantitatively.

Table 1 Specification of X ray CT scanner

Radiographic Field of Vision	150mm height600 mm
Number of display pixels	2048×2048
Resolution	0.1mm minimum
Scanning Time	2.5, 5 and 10 min
X-ray beam thickness	1.0 mm (minimum 0.3 mm)
Power of X-ray	300kV(2mA)
Maximum sample weight	981N
Scanning Operation	Translate/ Rotate system
X-ray beam form	Sector (spread 30 angle)
Detectors	176 channels

TEST METHODS

X-ray CT Scanner

Table 1 shows a specification of X-ray CT scanner. In this study, the voltage was chose 300 kV, the voxel number of a X-ray CT image is 2048×2048 and beam thickness was 1 mm (i.e., the dimension of a voxel is $0.07^2 \times 1.00$ mm^3).

An X-ray CT image is composed of CT-value with proportional to the material density; it is a digital image with a grey-scale image with 256 levels between black and white color. Black in the 2-dimensional (2-D) image indicates the lowest density area; meanwhile, white means the greatest density. All details to the CT image analysis can be referred in Otani et al. (2000).

[1] Associate Professor, Department of Civil Engineering, Kumamoto University, JAPAN. Email: mukunoki@kumamoto-u.ac.jp
[2] Professor, Department of Civil Engineering, Kumamoto University, JAPAN. Email: junotani@kumamoto-u.ac.jp
[3] Ph.D Student, ditto, JAPAN. Email: Sophie.Camp@ujf-grenoble.fr
[4] Professor, Lirigm, Universite de Joseph Fourier, FRANCE. Email: Jean-Pierre.Gourc@ujf-grenoble.fr

Materials

The compacted clayey specimen (referred as CCS, herein) had the optimum moisture content of 16 % and its liquid limit and plastic index are 43.6% and 24.3%, respectively. Mean diameter of tire chips is 2 mm. This study compares the physical compacted clay soil specimen with that mixing tire chips as proposed cover soil for the landfill. Table 2 shows the test cases.

Table 2 Test case

Test condition	Compaction energy (%)		Water content (%)		Tire chips mixing volume (%)	
	CE=100	CE=120	w_{opt}	w_{opt}+3%	5	10
UCP test	○	○	○	○	○	○

Punching Test

Punching test using CBR test apparatus was performed with unconfining condition (referred as UCP test). A diameter of a piston was 50 mm and loading speed was 1 mm/min. The specimens had a diameter of 150 mm and a height of 125 mm. The piston penetrates the specimen under zero over-burden pressure. All details for the punching tests can be referred from Mukunoki et al. (2006).

Bending Test

Fig. 1 illustrates the schematic of symmetric bending test. A cell was made of acrylic material to avoid reconstructing X-ray CT image with artifacts. In this study, disk specimen with a diameter of 150 mm and the thickness of 50mm was prepared to perform a symmetric bending test with stress controlled. Hollow disks with two different diameters were placed on the bottom of the mold and sponge was installed in the hollow part. A membrane rubber was placed on the disk specimen as shown in Fig. 1; therefore it was available to apply constant stress to the specimen through the membrane with air pressure. In this test, air pressure was applied step by step (e.g., 40, 60, 80 and 100 kPa)

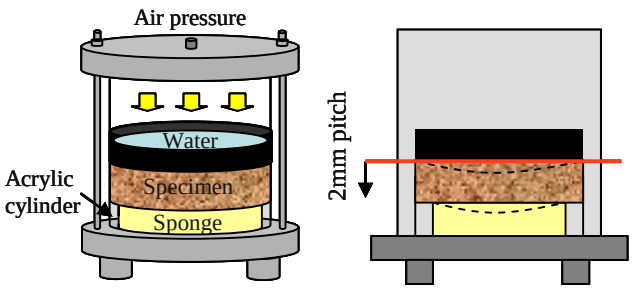

Fig. 1 Schematic of a bending test apparatus

RESULTS AND DISCUSSION

Punching Load Test

Load-displacement curve

Fig. 2 shows the relationship of load—displacement obtained from (a) punching load test for compacted clayey soil with optimum moisture content (16%) and (b) 19%. Compaction energy (CE) is 100% to make specimens. During scanning, specimen must be taken part from the loading system; therefore, stress release is caused in the specimen as shown in Fig. 3. However, the load went back on the previous load which CT scan was stated once so the affection of stress release is not significant in this test. Similar observation can be seen in Fig. 2 b but the curve to the specimen with moisture content (w) of 16 % shows a yield point obviously. The specimens with w of 19% has a yield point at the displacement of 7.0 mm and the load is 2.4 kN. On the

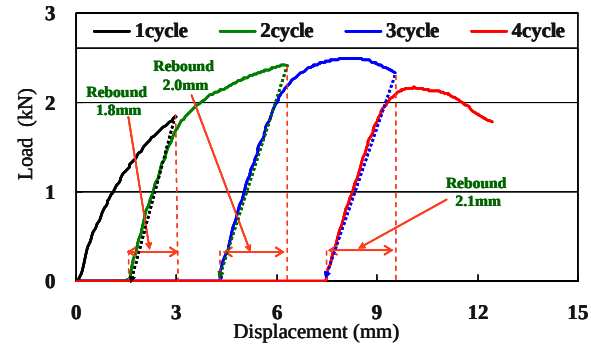

(a) Compacted Clayey specimen w_{opt} (16%)and CE=100%

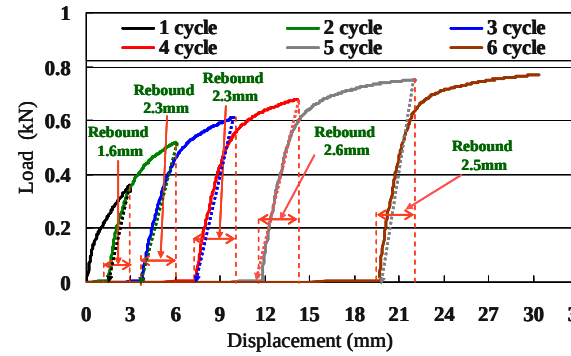

(b) CCS with w of 19% and CE=100%

Fig. 2 Load—displacement relationship obtained from punching load test

other hand, the CCS with 16% performs greater deformation than the CCS with 19%. The difference of only 3 % moisture content causes this difference of load—displacement behavior and this result indicates that the control of moisture content is important to keep stiffness and toughness of a cover soil. Fig. 3a, b show the CT images with respect to the comparison of moisture

content under CE of 100% at the specimen height of 120 mm. In Fig. 3a, b, cracks at the stage of 4th cycles in CCS with 16% as shown in Fig. 3a are connected each other and CCS was completely destructed; however, cracks in CCS with 19% still grew as shown in Fig. 3b. These images present the difference of toughness in each CCS visually.

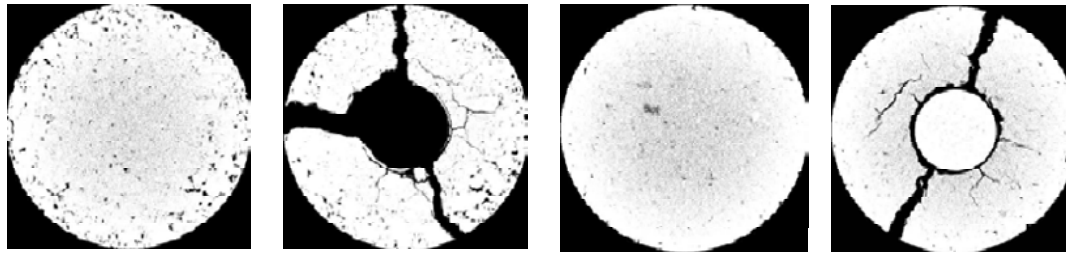

(1) Initial (2) 4th cycles (1) Initial (2) 4th cycles

(a) Compacted clayey specimen with w_{opt} (16%) and CE=100% at 4th cycles

(b) CCS with w of 19% and CE=100% at 4th cycles

Fig. 3 X-ray CT images of compacted clayey specimen due to loading in punching test

CCS with tire chips

Fig. 4a, b show the result for the case of using tire chips: (a) mixing ratio of 5% and (b) 10% in CCS with optimum moisture content 16% and 19%. The stiffness of CCS with 5% tire chips is slightly less than the CCS with 0 tire chips. Due to increase of load cyclic number, the degree of rebound of CCS with 5% tire chips is greater than the CCS with 0 tire chips. In case of 10 % mixing ratio of tire chips, the rebound behavior is obviously different and it is almost 2 times greater than the CCS with 5% tire chips for each cycle. Besides, the peak load is only 17 % less than the CCS with 5% tire chips. Fig. 5a, b show the CT images for the cases of using tire chips: (a) mixing ratio of 5% and (b) 10% in CCS with optimum moisture content 16%. at the specimen height of 60 and 120 mm. There is no significant difference between Fig. 5a, b as for generating large crack.

Bending Test for X-ray CT

CT images of the specimen for bending test

To evaluate the effect of defect part due to unbalanced settlement, two kinds of hollow cylinder disk were prepared under the symmetric bending test cell: a diameter of hollow is 130 mm. Fig. 5 show two-dimensional CT images of CCS with 130 mm of a diameter of a specimen. The CT image of CCS with 0 tire chips as shown in Fig. 6a has three large cracks. These are generated tensile stress due to loading. On the other hand, three smaller cracks can be seen on the center of the specimen as shown in Fig. 6b. Cracks did not generate in CCS with 10% tire chips like Fig. 6a. This indicates that the mixing tire chips would cause the reduction of tensile stress in the specimen and share stress would disperse in the clayey soil.

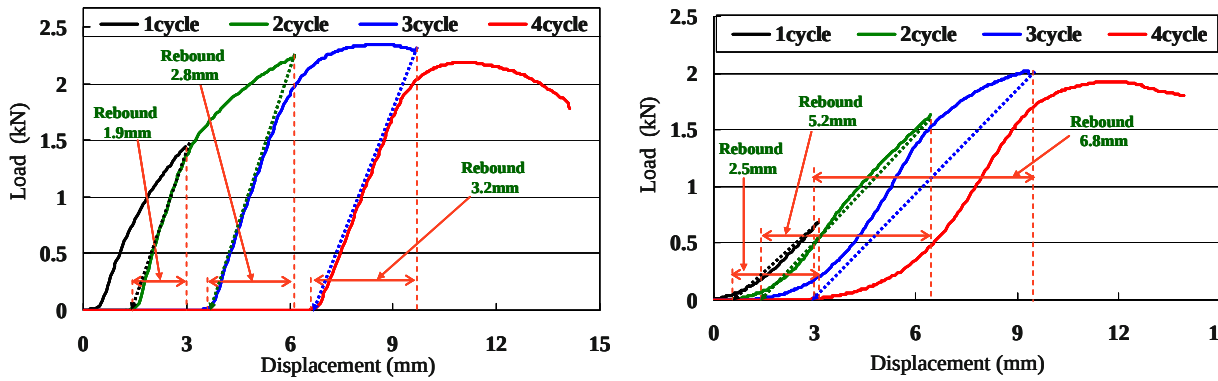

(a) Compacted Clayey specimen $w_{opt,}$ (16%) CE=100% and 5 % tire tips

(b) CCS with w of 19% and CE=100% and 10 % tire tips

Fig. 4 Load—displacement relationship obtained from punching test

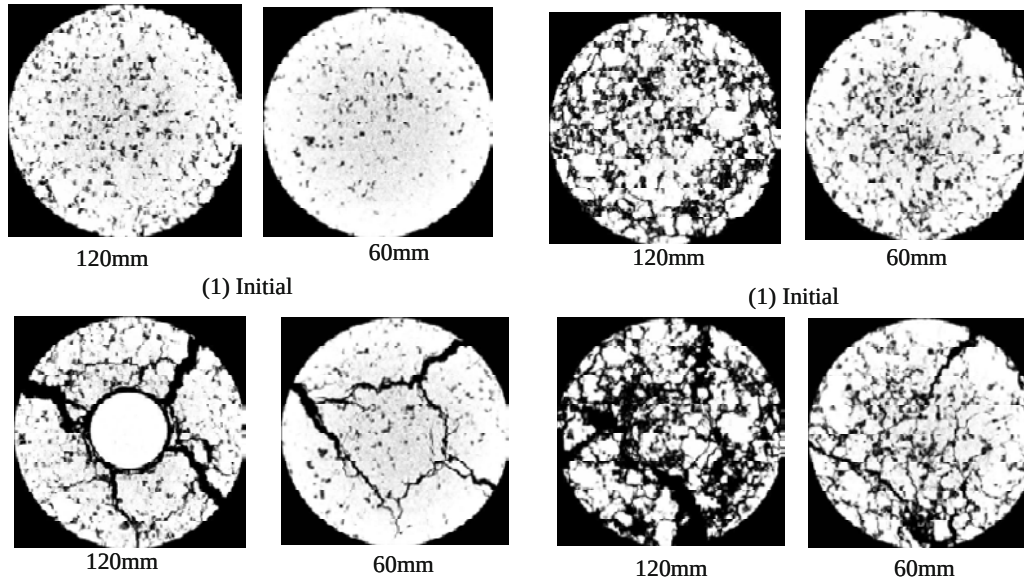

(a) Compacted Clayey specimen with w_{opt} (16%),and CE=100% and 5% tire tips

(b) CCS with w of 19% and CE=100% and 10 % tire tips

Fig. 5 X-ray CT images of compacted clayey specimen with tire tips due to loading in punching test

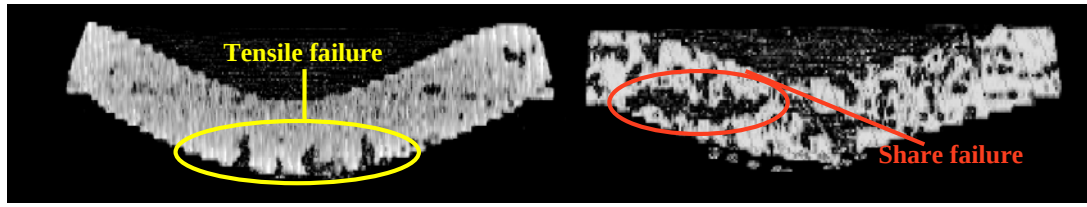

(a) Compacted clay (b) Compacted clay with tire tips

Fig. 6 Vertical cross section view of specimen with a diameter of 130 mm as Case 2

CONCLUSIONS

Punching tests under unconfining condition were performed on clayey soil with two different moisture contents and their specimens were scanned by X-ray CT scanner. Then, the method of the bending test for X-ray CT scanner were proposed in this study and the inner condition of specimens tested were visualized in this paper. The summaries are drawn as follows:

(1) Compacted clayey soil used in the site has excellent barrier performance and well-sufficient strength of soil;
(2) The deformation property of cover soil is affected with moisture content significantly; and,
(3) Mixing mass ratio of tire chips in the clayey soil does not perform to improve the stiffness but toughness well.

REFERENCES

Ashoke K, Karmokar H, Takeiti K, Yasuhara H, Kawai (2004) Evaluation of Leaching Possibilities from Used Tire Rubber Materials in Civil Engineering Applications, Proc. of Japanese Geotechnical Society conference

Camp S, Rey D, Kaelin JL (2005) Presentation of a new French site for storing very low level radioactive waste, Procs. of International Workshop, Hydro-Physico-Mechanics of Landfills, IRIGM, Universite de Grenoble, France: 1-4

Koerner RM, Daniel DE (1997) Final Covers for Solid Waste Landfills and Abandoned Dumps, Thomas Telford, ASCE Press

Mukunoki T, Otani J, Maekawa A, Camp S, Gourc JP (2006) Investigation of Crack Behavior on Cover Soils at Landfill using X-ray CT, Proc. of Advances in X-ray Tomography for Geomaterials: 213-219

Otani J, Mukunoki T, Obara Y (2000) Application of X-ray CT method for characterization of failure in soils, Soils & Foundations 40(2): 113-120

Rowe RK, Quigley RM, Brachman RWI, Booker JR (2004) Barrier system for waste disposal facilities, Spon Press

EXPERIMENTAL STUDY ON THERMAL STRAIN CREATING IN BARRIER SHEET IN WASTE LANDFILL

T. Harada[1], S. Nakai[2], K. Yamazaki[2], T. Kashiwagi[3], T. Nakajima[3] and S. Imaizumi[4]

ABSTRACT: Many types of barrier sheets are widely used in waste landfill in Japan. But these materials have high values of coefficient of thermal expansion comparing with other construction materials. This causes thermal stress in the barrier sheet when the circumstance temperature changes. Sometimes, it brings to serious problem such as tearing of sheet or failure of anchorage. So, it is very important to know how much the strain/stress is created due to the change of circumstance temperature. The authors constructed large model landfill site surrounding a bank with a height of 5m, and whole area of 1,600 m^2. Many types of barrier sheets, HDPE, LDPE, TPU and TPO were placed on the slope. Strain gages were pasted on the surface of the barrier sheets. Thermo-couples were also pasted to measure temperature of the barrier sheets. These data were automatically stored into the data-logger. Measurements were conducted for 2 years off and on. Measured strain level changed corresponding to the change of the temperature. The relationship between the temperature and the strain level of each barrier sheet were obtained. It is also measured in the corner and near the concrete structure. And it is found that strains are created isotropic even in the corner of the model landfill site.

KEYWORDS: barrier sheet, thermal strain measurement, model landfill site

INTRODUCTION

We have discharged a lot of waste in connection with everyday life and industrial activities. Today, the increasing waste becomes a big problem. The barrier sheet is installed in the landfill as seepage control work so that the circumference environment of a disposal site may not be polluted with leachate. Therefore, we are required to bring out the behavior of the barrier sheet to establish the safety of the liner system of the landfill. In this study, we make the model landfill site of a scale near the actual one. Then we settled many types of barrier sheets, and measure the strain level according to the circumstance temperature with strain gages for long time.

Then, we examine the behavior of the barrier sheets constructed in the model landfill site. And we aimed to check the safety and reliability of the seepage control work of the landfill.

OUTLINE OF EXPERIMENT

The area of the model landfill site is the rectangular shape of 45m×37.5m, and the surrounding dam height is 5m as shown in Figs. 1, 2 and 3.

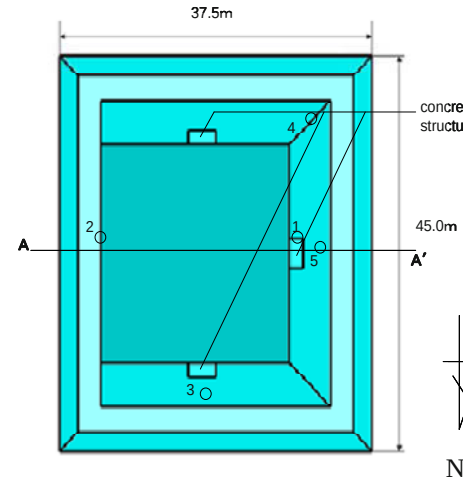

Fig. 1 Plan view of model landfill site

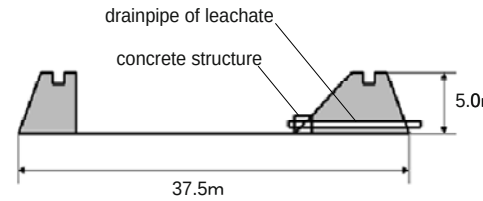

Fig. 2 Sectional view (A-A' section)

[1] Dr. Eng., Department of Civil Engineering, Bridgestone Corporation, JAPAN. Email:harad1-t@bridgestone.co.jp
[2] Dr. Student, Utsunomiya University Graduate School, JAPAN
[3] Eng., Department of Civil Engineering, Bridgestone Corporation, JAPAN
[4] Professor Department of Energy Environmental Science, Utsunomiya University Graduate School, JAPAN

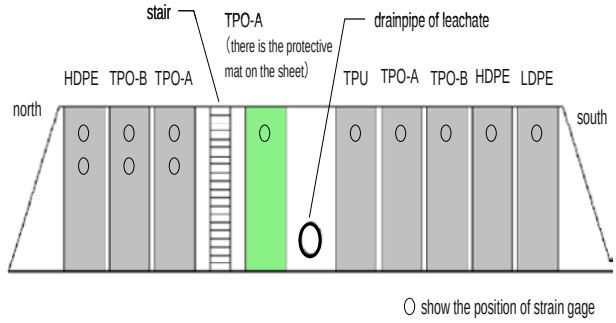

Fig. 3 Test site external view of outside slope

Inside of the test site there are 2 slopes and a straight wall. Also there are 3 types of concrete structures with drainpipes of leachate. The barrier sheets and lower protective mat were constructed in on the whole surface of inside of the test site and west side slope of outside. TPO (thermoplastic olefin)-A was used in the inside of the test site. Five types of barrier sheet, TPO-A, TPO-B, TPU (thermoplastic polyurethane), HDPE (high density polyethylene), and LDPE (low density polyethylene) were laid down in the west-outside slope of the test site. Their thickness is about 1.5 mm and their width is about 2.5 m, and the top and the bottom were fixed with concrete mass and steel plates.

The foil type strain gages which can measure the maximum expansion up to 15% were used. And the strain gages were set up in the positions of 1—5 of Fig. 1, and the round marks shown in Fig. 3.

Moreover, in order to measure the temperature on the surface of the barrier sheets, thermo-couples were stuck in the positions of measuring strain levels. And the measurement of the strain according to the temperature change was carried out divided in 2 times, 15 minute intervals in Winter—Summer (28th of February 13th of July) and 10 minute intervals in Summer—Winter (23th of July 31th of January).

Kinds and characteristics of barrier sheets which were evaluated are shown in Table 1.

Table 1 Characteristics of the barrier sheets

Kinds Characteristics	TPO-A	TPO-B	TPU	LDPE	HDPE
Thickness (mm)	1.56	1.58	1.61	1.54	1.56
Tensile strength (N/cm^2)	3522	1529	6474	3244	3314
Elongation (%)	730	730	520	740	750
1%secantelastic modulus(Mpa)	60	106	14	64	314
Linear xpansion coefficient (10^{-4}/C) (20℃—70℃)	2.2	2.0	1.8	2.5	1.9

EXPERIMENTAL RESULT

Relationship between Temperature and Strain

The related graphs of the temperature and the strain level were made. Horizontal axis shows the temperature, and vertical axis shows the surface longitudinal strain level.

As the one example, the change of strain during a day of the initial measurement (24th of July) is shown in Figs. 4 and 5. Fig. 4 shows the data of TPO-A and TPO-B. Fig. 5 shows the data of TPU, HDPE, and LDPE. Hereby, from Figs. 4 and 5 it can be said that the relationship between the temperature and the strain level is almost linear.

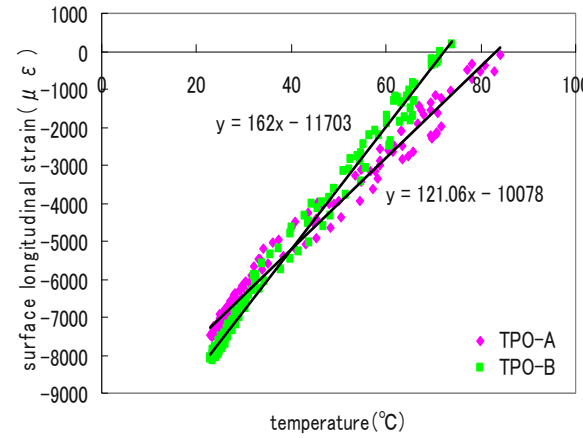

Fig. 4 Relationship between temperature and strain

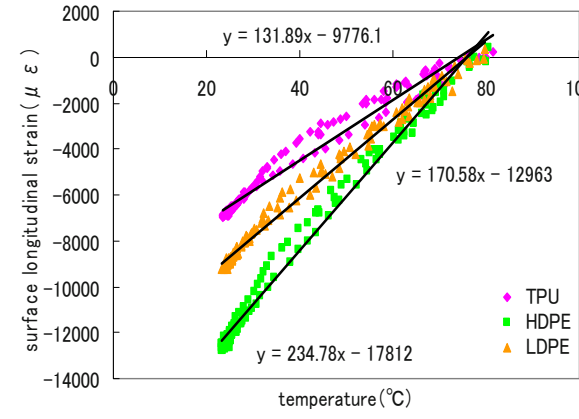

Fig. 5 Relationship between temperature and strain

At this time, paying attention to this slope of the approximated line, Fig. 6 was made. Horizontal axis shows the lapsed day, and vertical axis shows the slope which means the linear expansion coefficient.

Although there are slight variations, the slope can be considered to be almost constant.

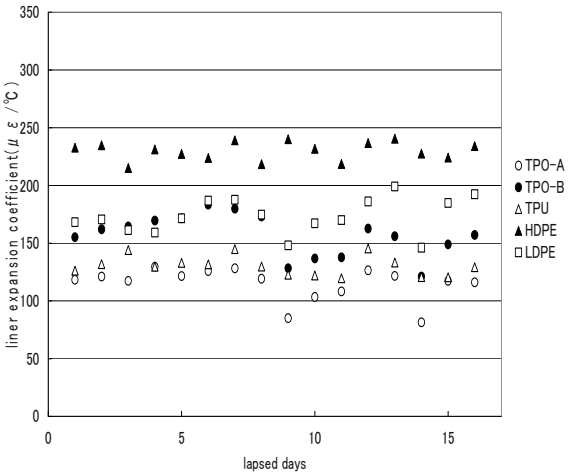

Fig. 6 Change of slope (linear expansion coefficient)

Then, they are shown in Table 2 and Fig. 7 that the comparison of the field analysis value that is the average value of the slope (linear expansion coefficient) and linear expansion coefficient requested separately by the laboratory experiment.

Table 2 Comparison of the linear expansion coefficient

	linear expansion coefficient ($\times 10^{-4}$/℃)	
	field analysis value	laboratory experiment value
TPO-A	1.15	2.2
TPO-B	1.55	2.0
TPU	1.30	1.8
HDPE	2.30	1.9
LDPE	1.75	2.5

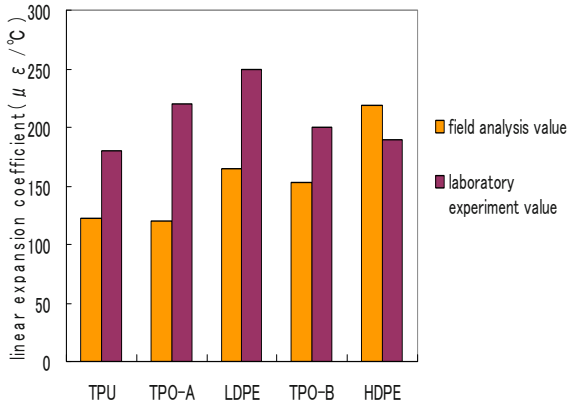

Fig. 7 Comparison of the linear expansion coefficient measured in the field and in the laboratory

Linear expansion coefficient depend on the field analysis were smaller than that of the laboratory experiment value excluding HDPE. We thought the reason is that the rigidity of the strain gage and the adhesive are larger than that of the barrier sheet. Even if modification arises on a sheet by change of temperature, since the rigidity of strain gage and adhesives are larger than that of the barrier sheet, modification work of the barrier sheet where the strain gage was stuck becomes smaller than free area. We think that the rate of reduction of the strain level is proportional to the rigidity of the barrier sheet. And as shown in table 1, rigidity of HDPE has brought the result of high value larger than laboratory experiment value.

Relationship between Laying Place and Main Strain

The strain of three elements of lengthwise, crosswise, and diagonal measured in the concrete structure, the corner, and the slope of the model landfill site with three element rosettes. Data were substituted for Eq. (1)—(3), and the level and the direction of the main strain level were calculated.

Maximum main strain:

$$\varepsilon_1 = \frac{1}{2}\left[\varepsilon_a + \varepsilon_c + \sqrt{2\left\{(\varepsilon_a - \varepsilon_b)^2 + (\varepsilon_b - \varepsilon_c)^2\right\}}\right] \quad (1)$$

Minimum main strain

$$\varepsilon_2 = \frac{1}{2}\left[\varepsilon_a + \varepsilon_c - \sqrt{2\left\{(\varepsilon_a - \varepsilon_b)^2 + (\varepsilon_b - \varepsilon_c)^2\right\}}\right] \quad (2)$$

Direction of main strain

$$\phi = \frac{1}{2}\tan^{-1}\left[\frac{2\varepsilon_b - \varepsilon_a - \varepsilon_c}{\varepsilon_a - \varepsilon_c}\right] \quad (3)$$

Here, it defines the tensile strain as plus and the compression strain as minus, the compression strain mainly resulted because the barrier sheet had been laid down while expanding in summer. Therefore, the shrinking strain becomes the largest “Minimum main strain”. Fig. 8 shows the appearance of the change in a day of the minimum main strain in the first day (24th of July) of the measurement in the concrete structure, the corner, and the slope. Also Fig. 9 shows the change of the temperature of the barrier sheet.

The change of the minimum main strain is almost corresponding to the change of the temperature, and minimum main strain shows minimum value in about 5 o'clock and midnight when the temperature is low.

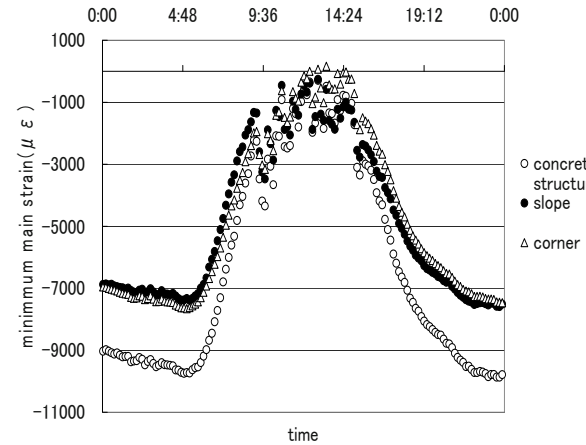

Fig. 8 The change of minimum main strain with time

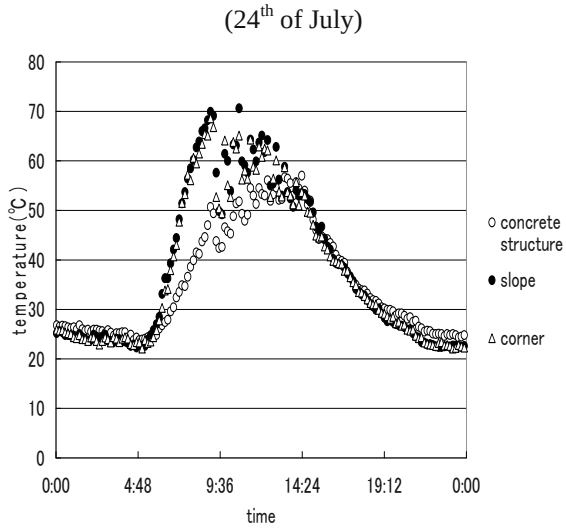

Fig. 9 The change of temperature with time (24th of July)

Figs. 10, 11and 12 shows the level and the direction of the main strain. It defines the negative direction of vertical axis as *a* direction, the positive direction of horizontal axis as *c* direction, and the element of lengthwise and crosswise are calculated based on the level and the direction of the main strain, and the minimum and the maximum main strain are plotted by centering on the starting point.

The oval was drawn by the way that passed by four plotted points, and it shows the level and the direction of the strain at the time. Figs. 10 and 11 show the strain of every three hours in the concrete structures on the date 24th of July, Fig. 12 shows the strain at midnight on the 4 days (24th, 28th of July and 2nd, 6th of August) in the concrete structures. Moreover, the straight lines that showed the average of a day of the calculated direction of the main strain were drawn in Figs. 10 and 11, and the straight lines that showed the average of all data of the direction of a main strain were drawn in Fig. 12.

Though the oval shown in Figs. 10, 11 and 12 has the change of the level, it has hardly changes of the shape and the direction. So we understand that the direction and the ratio of the main strain have hardly changed with time and with day.

Then, in Table 3, average of the direction and the level of minimum main strain, and the minimum value of the level are shown Moreover, the average in the direction of a minimum main strain at the position of the strain gage is shown in Fig. 13, it becomes 47.4° clockwise in the structures, 36.9° clockwise in the slope, 36.9° counterclockwise in the corner. Therefore the average and the minimum value of the main strain is the smallest in the concrete structure, and next it became the order in the slope, and in the corner.

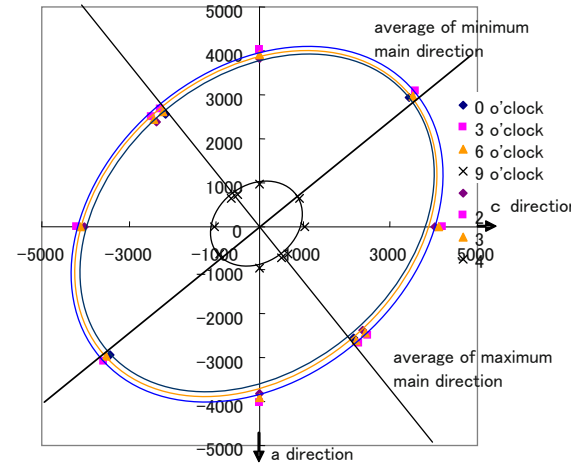

Fig. 10 The change of strain level (μ ε) and direction with time (0—9 o'clock)

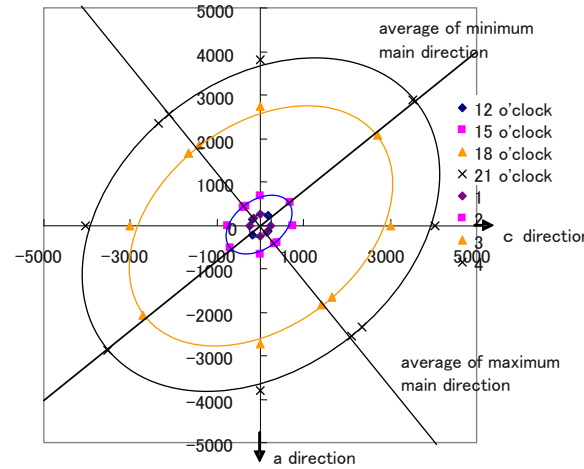

Fig. 11 The change of strain level (μ ε) and direction with time (12—21 o'clock)

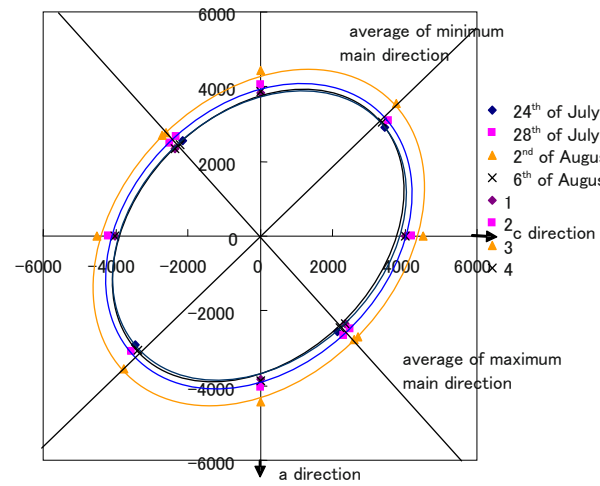

Fig. 12 The change of strain level (μ ε) and direction measured in 4 days (24th, 28th of July and 2nd, 6th of August)

Table 3 Level and direction of minimum main strain

	minimum main strain		
	minimum value(μ ε)	average(μ ε)	direction(average)(°)
concrete structure	-11249	-7101	-47.4
slope	-8818	-5550	-36.9
corner	-8702	-5348	36.9

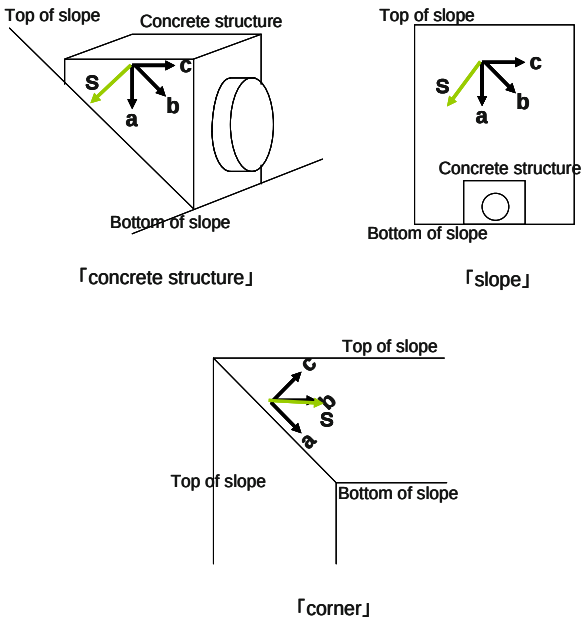

Fig. 13 The direction of main strain

CONCLUSION

The method which pursues the modification action of various barrier sheets using a strain gage was examined.

The modification action in various parts of the barrier sheet installed in the real scale model was measured.

When the strain is measured with the strain gage, the strain is measured small because the rigidity of the gage and the adhesive is larger than the rigidity of the barrier sheet. Therefore, the linear expansion coefficient of the requested barrier sheet tends to become smaller than the material characteristic values by the laboratory examination.

Conversion corresponding to the rigidity of the barrier sheet is required.

The direction of the main strain of the barrier sheet is almost constant.

REFERENCES

Kanno A, Takahashi S, Yoshino T : The analysis of stress and strain, Asakura Bookstore

Watanabe S: The strain gage and its application, Nikkan Industrial Newspaper Co

Proceedings of the 4th Asian Regional Conference on Geosynthetics
June 17 - 20, 2008 Shanghai, China

EVALUATING METHODS TO MODIFY THE CHEMICAL RESISTANCE OF GEOSYNTHETIC CLAY LINERS

T. Katsumi[1], H. Ishimori[2], and R. Fukagawa[3]

ABSTRACT: In order to reduce the barrier performance deterioration in bottom clay liners at waste containment facilities, this study investigated the effectiveness of (1) using manufactured modified bentonites, (2) prehydrating natural bentonites, and (3) confining natural bentonites at high effective pressure based on the hydraulic conductivity tests. The results showed that a modified bentonite of "multi-swellable bentonite" exhibited a low hydraulic conductivity of $< 1.0\times10^{-8}$ cm/s for NaCl solutions with molar concentration of ≤ 1.0 M, and a manufactured modified geosynthetic clay liner (GCL) of "dense-prehydrated GCL" exhibited an extremely hydraulic conductivity of $<1.0\times10^{-10}$ cm/s for any $CaCl_2$ solutions tested. Prehydrated bentonite, which is naturally prehydrated by absorbing the moisture in the underlying base layer, also exhibited a low hydraulic conductivity of $< 1.0\times10^{-8}$ cm/s for the permeation of any $CaCl_2$ solutions tested. Although the permeant solutions with high concentration and ionic valence increased the hydraulic conductivity of natural bentonite, higher confining pressures decreased the void ratio of the bentonite even for the chemical solutions so that the confined bentonite could exhibit a low hydraulic conductivity of $< 1.0\times10^{-9}$ cm/s even to the NaCl solutions and $CaCl_2$ solutions.

KEYWORDS: bentonite, chemical compatibility confining pressure, hydraulic conductivity, prehydration

INTRODUCTION

Clay liners used as bottom liners in waste containment facilities are required to have low hydraulic conductivities to prevent contamination of groundwater. Geosynthetic clay liners (GCLs) are factory-manufactured clay liners that consist of a thin layer of bentonite clay encased by geotextiles or glued to a geomembrane. GCLs have been considered as alternatives to current hydraulic barrier materials or as materials that can be combined with a compacted clay layer because they are cost effective, easy to install, and exhibit low hydraulic conductivity to water.

The low hydraulic conductivity of GCLs is due to the swelling of the bentonite, but bentonite has insufficient swelling against electrolytic solutions such as leachates from waste containment facilities. The barrier performance of GCLs directly exposed to leachates at waste containment facilities may deteriorate because the bentonite in GCLs has insufficient swelling against electrolytic chemical solutions. It has been reported that hydraulic conductivity values increased as the concentration of the electrolytic solution increased (Ruhl and Daniel 1997; Jo et al. 2001; Katsumi et al. 2007).

Because deterioration is due to such chemical attacks, many researchers have developed and proposed methods to improve the chemical resistance of GCLs. These methods include (1) to use chemically-resistant bentonites (Katsumi et al. 2004, 2007b; Kolstad et al. 2004; Onikata et al. 1996; Gates et al. 2004; Lo and Yang 2001), (2) to hydrate bentonites before prior to chemical solutions (Daniel et al. 1993; Lee and Shackelford 2005; Vasko et al. 2001), and (3) to confine bentonites with a higher effective stress (Katsumi and Fukagawa 2005; Petrov and Rowe 1997).

There are still few reports that the chemical compatibility and the hydraulic conductivity of (1) manufactured modified bentonites, (2) prehydrated natural bentonites, and (3) confined natural bentonites at high effective pressure were systematically investigated. This study focused on the effects of the electrolytic chemical solutions on the long-term barrier performance of these modified bentonites, which mean chemically-resistant bentonite, prehydrated natural bentonite, or confined natural bentonite. This paper systematically showed the results of the hydraulic conductivity tests using NaCl or $CaCl_2$ solutions, and discussed the effectiveness of these modified bentontes.

[1] Associate Professor, Graduate School of Global Environmental Studies, Kyoto University, JAPAN. Email: tkatsumi@mbox.kudpc.kyoto-u.ac.jp
[2] Research Fellow, Department of Civil Engineering, Ritsumeikan University, JAPAN. Email: ishimori@se.ritsumei.ac.jp
[3] Professor, Department of Civil Engineering, Ritsumeikan University, JAPAN. Email: fukagawa@se.ritsumei.ac.jp

EXPERIMETNAL CONDITIONS

Materials

To evaluate the barrier performance against chemical attack, three types of materials were used: (a) natural bentonite (NB), (b) multiswellable bentonite (MSB), (c) geosynthetic clay liner (GCL), and (d) dense prehydrated geosynthetic clay liner (DPH-GCL). NB and MSB used in this study were obtained from the same source, and MSB was produced mixed with propylene carbonate to activate the osmotic swelling. These bentonites are available in granular form. GCL was a GCL where powdered sodium bentonite is encapsulated between a polypropylene woven geotextile and a polypropylene nonwoven geotextile by needlepunching fibers. DPH-GCL contains a prehydrated powdered bentonite that is encapsulated between a polypropylene woven geotextile and a polypropylene nonwoven geotextile. Water content and particle density for each bentonite material are: (a) 7.62% and 2.65 g/cm^3 for NB, (b) 9.38% and 2.48 g/cm^3 for MSB, (c) 10.00% and 2.84 g/cm^3 for the bentonite in GCL, and (d) 62.47% and 2.73 g/cm3 for the bentonite in DPH-GCL, respectively.

Hydraulic Conductivity Test

For NB, MSB, GCL and DPH-GCL

The hydraulic conductivity tests were conducted according to ASTM D 5084. The tests were performed using flexible-wall permeameters with a cell pressure of 20—30 kPa and an average hydraulic gradient of 80—90.

The procedure was as follows. In order to prepare the specimen for the test, GCL and DPH-GCL were cut so that it had a 6 cm diameter. For the tests involving NB and MSB, the granular bentonite was loosely packed in a mold that had a 6 cm diameter and was 1 cm high. Then this molded specimen was sandwiched between two color filter papers attached with the woven geotextiles, and placed on the pedestals. The sides of this specimen were restrained with a rubber membrane. The membrane received a hydraulic pressure of 20—30 kPa by filling the outside cell with water, so that the solution could uniformly permeate through the specimen without leaking from the space between the side of the specimen and the rubber membrane. For specimens permeated with chemical solutions, the solutions were directly permeated from the influent point.

The flow volumes, the thicknesses and the hydraulic conductivity values of the specimen were measured over the testing duration. The thickness could be obtained by measuring a distance between the color filter papers, which side was colored with red ink, set up on the upper and the lower sides of the GCL specimen using a cathetometer. The hydraulic conductivity was calculated using a latest measured thickness. The hydraulic conductivity tests were continuously performed to check the change in the hydraulic conductivity with time. The representative value of the hydraulic conductivity to a solution was determined by considering the chemical equilibrium before the test was terminated, according to ASTM D 6766 “Standard Test Method for Evaluation of Hydraulic Properties of Geosynthetic Clay Liners Permeated with Potentially Incompatible Liquids”.

For prehydrated GCL

Prehydrated GCL was prepared using the apparatus as shown in Fig. 1. Toyoura sand was compacted at an optimum water content of 15% using a compaction test mold, which measured 10 cm in diameter, 12.7 cm in height, and 1,000 cm^3 in volume. The compacted soil was removed to an acrylic mold, which had a 10 cm diameter and 15 cm height, and was used as the base layer in the prehydration test. Next, a GCL was trimmed to a 10 cm diameter and then it was placed on the base layer with a confining pressure of 5 kPa. The acrylic mold with the base layer was placed in a water tank, which size is a 60 cm width×30 cm depth×35 cm height, with a water level of 1 cm as water supply source, and the tank was closed. Then this tank was placed in a constant temperature room controlled at 20 °C, and the GCL was cured for 7—31 days.

The GCL prehydrated in this prehydration test was cut into a diameter of 6 cm as the specimen for the hydraulic conductivity test. Here, the average of the water content of the specimen was indirectly estimated from the water content values of the remaining bentonite pieces after the trimming. The hydraulic conductivity of the prepared specimen was evaluated based on ASTM D 5084. Testing condition was the same as that in the hydraulic conductivity test with MSB and DPH-GCL.

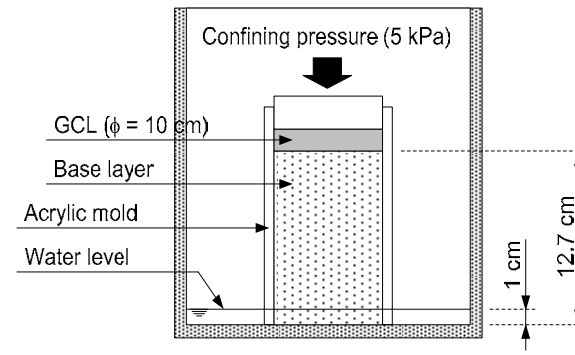

Fig. 1 Apparatus to prehydrate a GCL

For consolidated NB

To investigate the relationship between the void ratio and the hydraulic conductivity of the consolidated NB permeated with electrolytic chemical solutions, the consolidation of NB and the permeation of the solutions were conducted in fixed-ringed permeameters.

The procedure was as follows. The granular NB was loosely put in a fixed-ringed permeameter so that the thickness may become 1 cm, and then was hydrated with a permeant chemical solution. The NB was consolidated with a confining pressure for 24 hours. If the degree of the consolidation was more than 90%, the consolidated NB was permeated with the permeant solution with the same confining pressure and a hydraulic gradient of 80—90. The hydraulic conductivity test was continued until the termination criteria shown in ASTM D 5084 and D 6766 were satisfied. The void ratio and the hydraulic conductivity were calculated from the final thickness, which was measured by displacement gauge.

RESULTS

Manufactured Modified Bentonites

The hydraulic conductivities of two manufactured modified bentonites, MSB and DPH-GCL, are shown in Figs. 2 and 3. The hydraulic conductivities of NB and GCL were showed as reference values in these figures. The hydraulic conductivity of NB gradually increases for a NaCl solution with a stronger molar concentration. In contrast, MSB maintains a low hydraulic conductivity value of $k < 1.0\times10^{-9}$ cm/s up to a molar concentration of 1.0 M. However, when the molar concentration of the NaCl solution is 2.0 M, the hydraulic conductivity of MSB is nearly identical to that of NB. The MSB material's swelling is formed by propylene carbonate (PC) which is included in the MSB. PC can easily form a hydration shell by forming intermolecular hydrogen bonds between the outer limits of the hydration shells of the exchange cations. PC thereby can expand the space between adjacent clay layers. MSB activates the osmotic swelling of bentonite in fresh water as well as electrolytic chemical solutions, whereas in the latter NB cannot sufficiently swell.

The nonprehydrated GCL shows a low hydraulic conductivity for the deionized water, but the hydraulic conductivity of the GCL drastically increases for the permeation of a $CaCl_2$ solution with a strong molar concentration. The value becomes $k>1.0\times10^{-5}$ cm/s when the molar concentration of the $CaCl_2$ solution exceeds 0.2 M. In contrast, prehydrated DPH-GCL displays extremely low hydraulic conductivity values (k

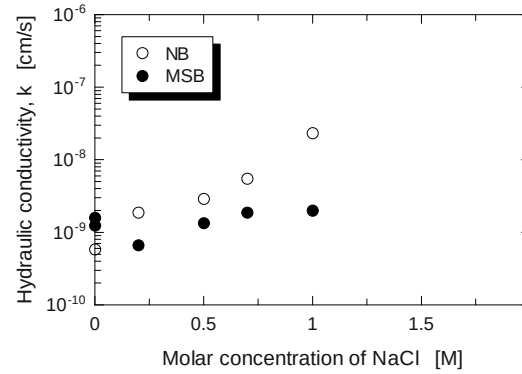

Fig. 2 Hydraulic conductivity of NB and MSB (Katsumi et al. 2007b)

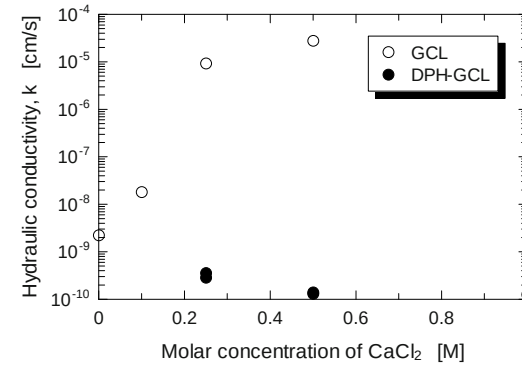

Fig. 3 Hydraulic conductivity of GCL and DPH-GCL (Katsumi et al. 2007b)

$\approx 1.0\times10^{-10}$ cm/s) for the $CaCl_2$ solutions, regardless of the tested $CaCl_2$ concentration level. The reason that DPH-GCL can exhibit an extremely low hydraulic conductivity is related to the prehydration effect and the consolidation effect of bentonite. It has been previously reported that prehydrated bentonite prevents a decreased barrier performance and void ratio upon exposure to chemical solutions. In addition, the effective pore space (the mobile water phase), which can pass permeant liquids, in the prehydrated bentonite is narrowed by the consolidation of a DPH-GCL in the manufacturing process. The consolidation of bentonite can increase the solid phase and immobile water phase relative to the mobile water phase so that the consolidated bentonite can obstruct the flow.

Prehydrated GCL

When GCLs are applied to bottom liners at waste containment facilities, they are naturally prehydrated because the bentonites in them absorb moisture in the underlying base layer on which they are installed. Fig. 4 shows the water content and the hydraulic conductivity of the GCLs prehydrated on the base layer as shown in

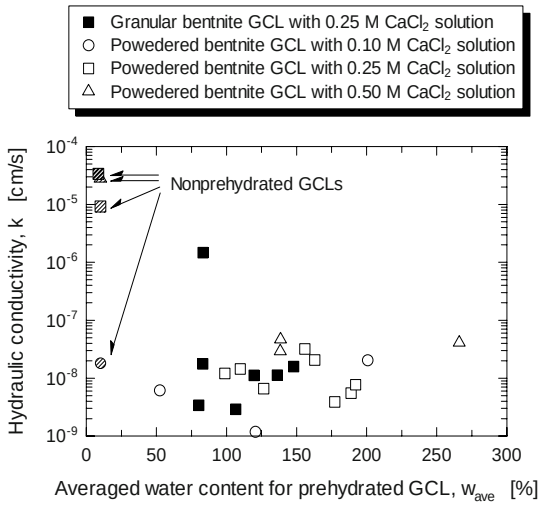

Fig. 4 Relationship between the hydraulic conductivity and the prehydration water content

Fig. 3, which simulates a prehydration process where an installed GCL at a real site was hydrated by absorbing moisture from base layer soil.

Fig. 4 shows the relationship between the hydraulic conductivity and the prehydration water content. Most of the prehydrated GCLs could exhibit the low hydraulic conductivity of $k \approx 1.0\times10^{-8}$ cm/s to any $CaCl_2$ solutions when the prehydration water content of GCL was more than 50%. However, one of the GCLs with granular bentonite exhibited the higher hydraulic conductivity of $k = 1.5\times10^{-6}$ cm/s than others. It may be because the granular bentonite makes it difficult to homogenously prehydrate GCLs. Even when one bentonite granular gets wet, it may not be easy for the pore water in the granular to freely disperse to another neighboring granular beyond the space between these granules. Even if the other parts are sufficiently hydrated and swelled with a high water content, the permeation of permeant liquids concentrates on the parts insufficiently swelled, which have a low water content, so that the hydraulic conductivity of the entire GCL becomes high. Therefore, the granular bentonite makes it difficult to be homogenously prehydrated, and the hydraulic conductivity of prehydrated GCLs with the granular bentonite is easily dispersed. It will be so difficult to estimate the barrier performance of prehydrated GCLs with the granular bentonite.

The difference between nonprehydrated GCLs and prehydrated GCLs was considered as follows. The prehydration treatment maintains an extremely low hydraulic conductivity even to the permeation of the aggressive chemical solutions such as $CaCl_2$ solutions. In particular, the effect of the prehydration treatment greatly appears in the hydraulic conductivity when the $CaCl_2$ solution with a high concentration permeates into the GCL. The swelling capacity of the nonprehydrated GCL is seriously decreased by the permeation of a $CaCl_2$ solution with a molar concentration of 0.5 M so that the hydraulic conductivity increases up to $k = 2.8\times10^{-5}$ cm/s. In contrast, if the GCL is prehydrated before exposing to the solution, the prehydrated GCL maintains a low hydraulic conductivity of $k \approx 1.0\times10^{-8}$ cm/s. Thus, it is concluded that prehydration effectively improves the chemical resistance of GCLs. The powdered bentonite more reliably improves the chemical resistance. It is difficult to definitely improve the chemical resistance of GCLs with granular bentonite by prehydration.

Consolidated NB

GCLs which are applied as bottom liners are confined by the load of the wastes buried. The bentonite in the GCLs is consolidated, and the void ratio is decreased. The consolidation of bentonite can increase the solid phase and immobile water phase relative to the mobile water phase, which means the effective pore space decreased, so that the consolidated bentonite can obstruct the flow even to electrolytic chemical solutions. The load of the wastes is one of the factors that affect the barrier performance of GCLs at real sites.

Figs. 5 and 6 show the relationship between hydraulic conductivity, the confining pressure and the void ratio. In these figure, the concentration of the permeant solution is arranged by the ionic strength, I:

$$I = \frac{1}{2}\sum c_i z_i^2 \qquad (1)$$

where c_i and z_i are the concentration and the valence of the i-th ion. The ionic strength is calculated from the concentration of the cations contained in the permeant solution because the cations are significantly dependent on the free swell and the hydraulic conductivity of bentonites.

The hydraulic conductivity of bentonite is decrerased with the confining pressure. In a low confining pressure, the hydraulic conductivity is strongly dependent on the ionic strength of the permeant solution. The solution with the strong ionic strength and the high ionic valence seriously increases the hydraulic conductivity due to insufficient swelling of the bentonite. In contrast, the hydraulic conductivities of the bentonites which were confined at the high effective pressure of 316 kPa were about $k \approx 1.0\times10^{-9}$ cm/s regardless of the type of the permeant solutions. It is because the solid phase and immobile water phase are relatively increased by the consolidation. Thus, the effective pore space which affects the mobility of the permeant liquid is narrowed.

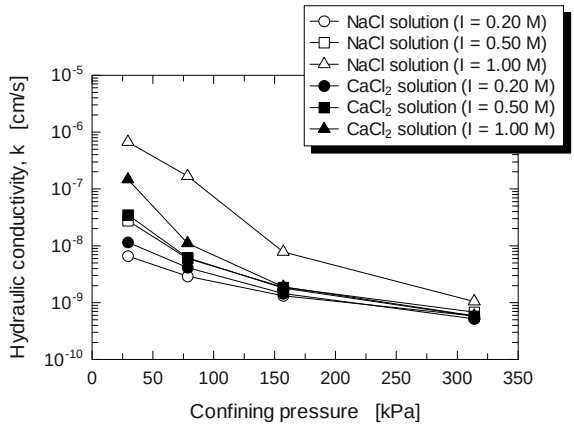

Fig. 5 Relationship between the hydraulic conductivity and the confining pressure

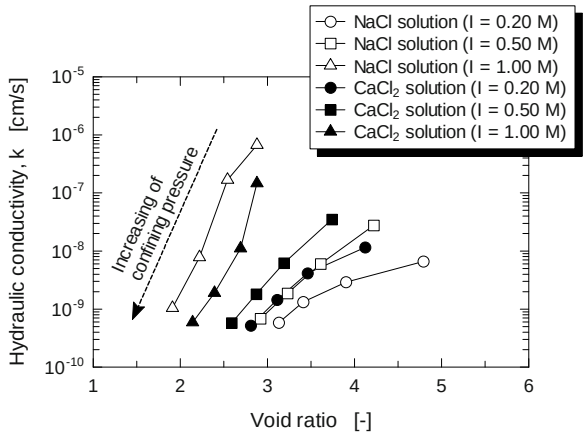

Fig. 6 Relationship between the hydraulic conductivity and the void ratio

Waste leachate is collected in the deepest parts of waste containment facilities. Although the possibility of the leakage of the waste leachate is considered high, GCLs which are installed in such parts are consolidated by the large load and expected to exhibit a low hydraulic conductivity.

The relationship between the hydraulic conductivity and the void ratio as shown in Fig. 6 is discussed. The relationship is strongly dependent on the concentration of the permeant solution. In the low concentration level, the bentonite can be sufficiently swelling so that the void ratio is large and the hydraulic conductivity is low. The permeant solution with the high concentration, however, decreases the swelling capacity of the bentoenite. Thus, the bentonite permeated with the solution having the high concentration level shows the low void ratio and the high hydraulic conductivity at a low confining pressure. When the confining pressure is increased from 29.4 kPa to 314 kPa, the hydraulic conductivity is decreased with the void ratio. The degree of this change, in particular, is remarkable in the high concentration level. For example, only one-order of the hydraulic conductivity decreased for the NaCl solution with the ionic strength of 0.2 M. In contrast, three-order of the hydraulic conductivity decreased for the NaCl solution with the ionic strength of 1.0 M. In conclusion, if the bentonite is consolidated by a high confining pressure, the bentonite can exhibit a low hydraulic conductivity even to chemical solutions with the strong concentration.

CONCLUSIONS

This paper presents the chemical compatibility and the hydraulic conductivity of (1) modified bentonites, (2) prehydrated GCL, and (3) confined natural bentonites at high effective pressure.

The hydraulic conductivity of a multi-swellable bentonite (MSB) is lower than that of natural bentonite (NB) for the permeation of a NaCl solution. MSB exhibits a good chemical resistance for NaCl solutions with a molar concentration of $\leqslant$1.0 M. The hydraulic conductivity of a dense prehydrated geosynthetic clay liner (DPH-GCL) is as low as $k = 1.0\times10^{-10}$ cm/s for $CaCl_2$ solutions with a molar concentration of $\leqslant$1.0 M. DPH-GCL also exhibits a more remarkable chemical resistance than ordinary geosynthetic clay liner (GCL).

Most of the prehydrated GCLs exhibit a low hydraulic conductivity of $k \approx 1.0\times10^{-8}$ cm/s against $CaCl_2$ solutions with concentrations between 0.1 and 0.5 M, when the prehydration water content of the GCLs are more than 50%. The prehydrated GCL exhibits a much lower hydraulic conductivity than the nonprehydated GCL. The prehydration treatment gives GCLs an extremely low hydraulic conductivity even to the permea-tion of the aggressive chemical solutions such as $CaCl_2$ solutions.

The hydraulic conductivity of bentonite is decrerased with the increase in confining pressure. In a low confining pressure, the hydraulic conductivity is strongly dependent on type of chemicals and the ionic strength of the permeant solution. In contrast, the hydraulic conductivities of the bentonites which were confined at the high effective pressure of 316 kPa were about $k \approx 1.0\times10^{-9}$ cm/s regardless of the type of the permeant solutions. Although bentonites do not have a capability of exhibiting a good barrier performance to chemical solutions with the high concentration level, the high confining stress may provide the narrow effective pore spaces which provide the free mobility of the permeants, and then the barrier performance may be improved. If the bentonite is consolidated by a high confining pressure, the bentonite can exhibit a low hydraulic conductivity even to chemical solutions with the strong concentration.

ACKNOWLEDGEMENTS

We are grateful to Professor Masashi Kamon (Kyoto University), Mr. Mitsuji Kondo, and Dr Masanobu Onikata (Hojun Co., Ltd.) for their insightful comments and discussions. Assistance with the experimental work was provided by former students of Ritsumeikan University, including Shinya Hasegawa, Shugo Numata, Masato Yokoi, Atsushi Ogawa, Satoshi Maruyama, and Kazuyoshi Hanamoto.

REFERENCES

ASTM D 5084. Standard Test Method for Measurement of Hydraulic Conductivity of Saturated Porous Materials using a Flexible Wall Permeameter, American Society for Testing and Materials

ASTM D 6766. Standard test method for evaluation of hydraulic properties of geosynthetic clay liners permeated with potentially incompatible liquids, American Society for Testing and Materials

Daniel DE, Shan HY, Anderson JD (1993) Effects of partial wetting on the performance of bentonite component of a geosynthetic clay liner, Geosynthetics '93, 3: 1482-1496

Gates WP, Nefiodovas A, Peter P (2004) Permeability of an organo-modified bentonite to ethanol-water solutions. Clays and Clay Minerals 52 (2): 192-203

Jo HY, Katsumi T, Benson CH, Edil TB (2001) Hydraulic conductivity and swelling of non-prehydrated GCLs permeated with single species salt solutions, Journal of Geotechnical and Geoenvironmental Engineering 127(7): 557-567

Katsumi T, Ogawa A, Fukagawa R (2004) Effect of chemical solutions on hydraulic barrier performance of clay geosynthetic barriers. Proceedings of the Third European Conference on Geosynthetics: 701-706

Katsumi T, Fukagawa R (2005) Factors affecting chemical compatibility and barrier performance of GCLs. Proceedings of the 16th International Conference on Soil Mechanics and Geotechnical Engineering, Millpress Science Publishers, Rotterdam, Netherlands: 2285-2288

Katsumi T, Ishimori H, Ogawa A, Yoshikawa K, Hanamoto K, Fukagawa R (2007a) Hydraulic conductivity of nonprehydrated geosynthetic clay liners permeated with inorganic solutions and waste leachates, Soils and Foundations 47(1): 79-96

Katsumi T, Ishimori H, Onikata M, Fukagawa R (2007b) Long-term barrier performance of modified bentonite materials against sodium and calcium permeant solutions, Geotextiles and Geomembranes. (accepted for publication)

Kolstad DC, Benson CH, Edil TB, Jo HY (2004) Hydraulic conductivity of a dense prehydrated GCL permeated with aggressive inorganic solutions. Geosynthetics International 11(3): 233-241

Lee JM, Shackelford CD (2005) Concentration dependency of the prehydration effect for a geosynthetic clay liner, Soils and Foundations 45(4): 27-41

Lo IMC, Yang X (2001) Use of organoclay as secondary containment for gasoline storage tanks. Journal of Environmental Engineering 127(2): 154-161

Onikata M, Kondo M, Kamon M (1996) Development and characterization of multiswellable bentonite. Environmental Geotechnics, AA Balkema Publishers, Rotterdam, The Netherlands: 587-590.

Petrov RJ, Rowe RW (1997) Geosynthetic clay liner (GCL)-chemical compatibility by hydraulic conductivity testing and factors impacting its performance, Canadian Geotechnical Journal 34: 863-885.

Ruhl JL, Daniel DE (1997) Geosynthetic clay liners permeated with chemical solutions and leachates. Journal of Geotechnical and Geoenvironmental Engineering 123(4): 369-381

Vasko SM, Jo HY, Benson CH, Edil T B, Katsumi T (2001) Hydraulic conductivity of partially prehydrated geosynthetic clay liners permeated with aqueous calcium chloride solutions, Geosynthetics Conference 2001: 685-699

Proceedings of the 4th Asian Regional Conference on Geosynthetics
June 17 - 20, 2008 Shanghai, China

FLOATING COVER FOR LEACHATE LAGOON AT HANGZHOU

M. A Sadlier[1] and X. H. Zhou[2]

ABSTRACT: The leachate lagoon at the Hangzhou Landill in China was giving rise to concern over odour and it was decided to install a geomembrane floating cover in order to control the odour. Some of the special features and considerations for the cover and lagoon were the irregular shape of the lagoon with a central berm at about half depth, the need to accommodate changes in leachate level and to control gas accumulations and release. The paper will discuss the design and construction aspects of the cover to meet these objectives.

KEYWORDS: geomembrane, floating cover, leachate, Hangzhou

GENERAL COVER PRINCIPLES AND DESIGN

The general principles of floating cover design and shape control are set out in Sadlier, Sieracke and Taylor (2001, 2002). It describes cover design for fixed level covers with gas collection and fluctuating water level covers for reservoirs as well as discussing the considerations for cover material selection. It does not discuss covers that combine fluctuating water levels with a requirement for gas collection that will require a composite cover design.

The main principle of floating covers built in an empty basin is that the effective span of geomembrane material that is required reduces as the water level rises. Ballast is therefore used to initiate the formation of trenches in the geomembrane which take up the slack.

The ballast is combined with two matching rows of floats which help by providing a lateral component to the floatation force which tensions the cover.

This system of cover tensioning functions well if no gas is produced under the cover.

Simple addition of perimeter gas collection to a cover of this design will result in problems with gas release. As wind direction changes the surface water on the cover will be driven towards the perimeter by the wind. With a cover without gas collection this water will eventually be released as the wind changes to another direction.

Fig. 1 A floating cover with tension from ballast and floats

[1] Geosynthetic Consultants Australia, Melbourne, AUSTRALIA. sadlier@attglobal.net
[2] Shenzhen Sheng Yi Environmental Co., Ltd., CHINA. shengyi@sz-shengyi.com

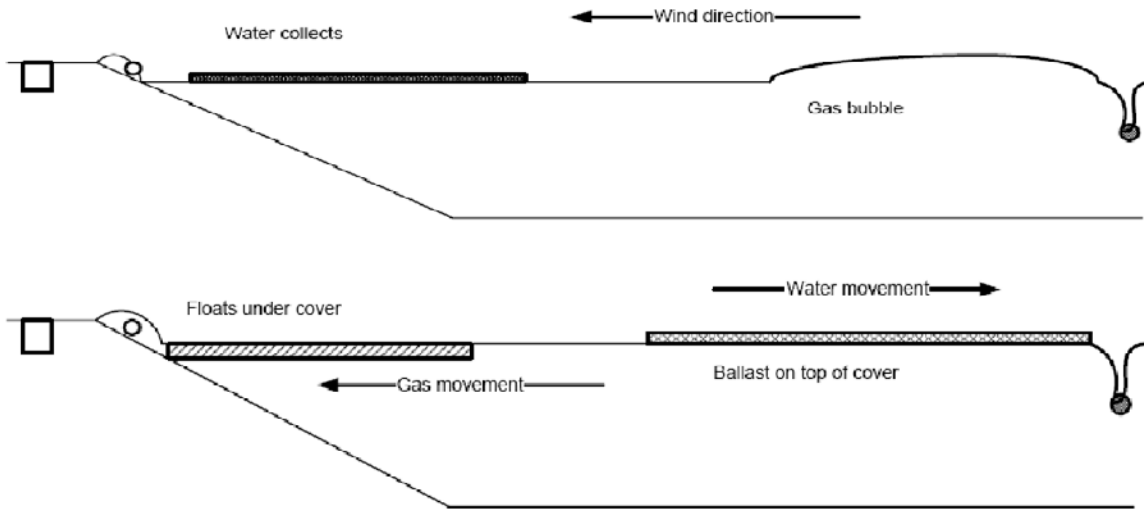

Fig. 2 Issues with management of surface water and gas under cover

However if gas is collecting under the cover the surface water at the perimeter will prevent the gas from moving to the perimeter and the resulting gas bubble will then prevent the water from moving away from the perimeter when there is a change in wind direction.

The established solution to this problem is to introduce gas release floatation under the cover near the perimeter gas collection and to combine this with additional gas control ballast near the centre of the cover. This allows the gas to release even if there is an initial collection of surface water and encourages the water to move to the ballast trench.

This works quite well for covers with a maximum span from perimeter to central ballast of about 70 metres. For larger spans some kind of modular approach is required.

Materials selection for the cover membrane is largely dependent on the extent to which the water level is expected to fluctuate and therefore cause the cover membrane to flex. Water supply reservoirs which fluctuate on a daily basis require very flexible materials such as reinforced polypropylene or Hypalon and fixed water level basins such as waste water lagoons can use a stiffer material such as HDPE. There are also materials of intermediate flexibility such as LLDPE and these different materials can be used to create composite covers with more flexible elements where required.

Fig. 3 Hangzhou Lagoon with central berm and perimeter bench

Fig. 4 Use of pontoon to deploy and seam panels

HANGZHOU LEACHATE LAGOON FLOATING COVER

The existing leachate lagoon at Hangzhou is at the base of the landfill and acts as a holding lagoon for the leachate treatment plant which is downstream from the lagoon. Leachate enters from channels via a settling tank and normally exits via outlets in the base of the lagoon.

The lagoon is trapezoidal in plan with a central berm at part depth to divide the lower portion into two lagoons.

The overall depth varies from 10 to 12 m with the sloping floor and the central berm is 5 m below the crest. The internal slopes are 1:2.

The main purpose of the cover is to reduce odour although there will be a secondary benefit in that the cover will prevent rainfall on the lagoon mixing with and adding to the volume of leachate.

Initial discussions with the landfill operators and owners indicated a desire for the cover to allow the leachate lagoon to be fully emptied on either one or both sides. This would have introduced great difficulties with balancing the cover across the berm and would probably introduce operational complexity by requiring water to be pumped as cover ballast from one side to the other.

Fig. 5 Matched ballast and floats

Fig. 6 Nearing Completion

It was eventually agreed to pursue a simpler solution based on the lowest operating level for the cover being the level of the central berm. The operating sequence will be that more leachate will enter the lagoon during the wetter summer months and that this will be drawn down by the treatment plant during the dryer months. On this basis the cover level is expected to fluctuate slowly on an effectively annual basis.

The design of cover adopted for the Hangzhou cover had the following features as shown on the sketch below:

a) A matched ballast and float system to control cover tension and shape.
b) Additional gas control ballast and under cover gas release floats.
c) Gas collection and release vents at the same locations as the under cover floats.

Since there is only limited leachate level movement expected the cover employed HDPE 2 mm thick.

The first construction method considered for the cover was to 'launch' the cover from one end. This would involve creating a fabrication platform at the chosen end and progressively fabricating the cover whilst pulling the whole cover forward to the other end. This can be very risky in strong winds.

The second method considered and adopted involves the use of a floating pontoon to provide a construction platform just above the leachate surface. The pontoon is made up of sections strapped together and is effectively two geomembrane panels wide for the full width of the leachate during construction. Each pontoon section is fabricated from timber framing, formply decking and polystyrene infill panels.

The geomembrane panels are welded into place progressively and the pontoon moved forward by ropes to keep it progressively in front of the completed panels.

There was also some discussion about whether it was better to have the leachate in the lagoon at the maximum or minimum level for construction. The maximum level requires the use of more pontoon area and the minimum level makes materials handling a little more difficult and dimension control also a little more difficult. It was decided to build the cover with the leachate level near the bench level.

CONCLUSION

An odour control cover has been successfully constructed over the existing leachate lagoon at Hangzhou using a HDPE geomembrane and a movable pontoon to assemble the cover over the leachate.

ACKNOWLEDGEMENT

This project was installed by Shenzhen Sheng Yi Environmental Co., Ltd with the assistance of Geosynthetic Consultants Australia.

REFERENCES

Sadlier M, Sieracke M, Taylor R. Luggage Point Water Re-use Lagoons, Geosynthetics 2001 Conference, Portland, OR, February 2001

Sadlier M, Taylor R (2002) Recent Developments in Polyethylene Geomembranes for use in Floating Covers 7th International Conference on Geosynthetics, September 2002

Proceedings of the 4th Asian Regional Conference on Geosynthetics
June 17 - 20, 2008 Shanghai, China

GEOGRID REINFORCED SOIL STRUCTURES TO INCREASE LANDFILL CAPACITY

J.W. Cowland[1]

ABSTRACT: Two geogrid reinforced soil structures have recently been used to successfully increase the capacity of a waste landfill in Hong Kong. A geogrid reinforced soil wall and a geogrid reinforced soil embankment have been constructed on the perimeter of the landfill to substantially increase the void space for waste. This paper summarises the design of the reinforced soil structures, the selection and quality control of the geogrids and fill material, and the facing details to prevent the outside face of the embankment structure being damaged during a possible hillside grass fire.

KEYWORDS: landfill, capacity, geogrid, reinforced soil structures, fire resistance

INTRODUCTION

The capacity of a solid waste landfill in Hong Kong has recently been substantially increased. This landfill was designed in 1993 for a capacity of 40 million tonnes of waste, and is now being operated and is about half full.

The landfill occupies a bowl shaped valley, which has a narrow opening at the downstream end leading onto a flat plain used for farming. The landfill is fully lined to contain leachate (Cowland 2000) and it has a leachate treatment system and an active gas control system. The waste will eventually fill the valley, with a maximum depth of 140 metres.

The capacity of the landfill has been increased by quarrying the valley to increase the void space. Using this excavated material, a geogrid reinforced soil wall was constructed across the narrow opening at the entrance of the valley in 2004, and a geogrid reinforced soil embankment was constructed along part of the landfill perimeter in 2006. These reinforced soil structures have increased the capacity of the landfill by about 5 million tonnes of waste.

The geogrid reinforced soil structures have provided an interesting case history. This paper summarises their design, the selection and quality control of the geogrids and the fill material, and the construction of the embankment structure. The outside face of the embankment has been designed to prevent the geogrids from being damaged during a possible hillside grass fire.

Geogrid Reinforced Soil Wall

A geogrid reinforced soil wall, 8 metres high, was constructed across the narrow opening at the entrance of the valley in 2003 and 2004 to increase the capacity of the landfill. This allows the placing of an extra 8 metres depth of waste across a large part of the 40 hectare landfill.

Geogrid Reinforced Soil Embankment

The rim of the valley bowl has a variable elevation, and in one location there is a 30 metre drop in the level of the top of the rim over a length of 300 metres. The capacity of the landfill was again increased in 2006 by the construction of a large geogrid reinforced soil embankment to fill this gap in the rim of the landfill. This structure is 30 metres high and 300 metres long, and allows the placing of an extra 30 metres depth of waste in this part of the landfill.

DESIGN

The purpose of the geogrid reinforced soil structures is to retain an extra height of waste within the landfill. They are lined on the waste side of the structure to contain leachate.

The wall was designed with vertical sides and the embankment was designed with sloping sides with in-termediate bencheGeogrid reinforced soil structures in Hong Kong are designed in accordance with the Guide to Reinforced Fill Structure and Slope Design (2002). The geogrid reinforced soil wall was designed in accordance with reinforced fill structure design.The reinforced soil embankment, with side slopes of 70°, was designed in accordance with reinforced fill slope design.

The waste loading on the side of the structures was

[1] Consultant, Geosystems Ltd, HONG KONG, CHINA. Email: cowland@netvigator.com

accounted for by using fill pressures and slope stability analysis, with the properties of waste as reported by Cowland et al. (1993).

It was decided that lining the side of the structures facing the waste would be carried out when the monitoring of the structures showed that settlement had mostly ceased. It was also decided that the side of the embankment facing away from the waste should be designed to resist the occasional hillside grass fires that occur in Hong Kong.

Wall and Embankment Dimensions

The 8 metre high wall was designed with vertical sides and is about 100 metres long.

The embankment follows and fills the dip in the rim of the landfill. In plan it follows a variable curve. It is 30 metres high for over 200 metres of its length; the rest being transition zones towards the higher edges of the dip.

The sides of the embankment are 70° to the horizontal, with 2 metre wide benches at a 7.5 metre vertical spacing. The top of the embankment is 5 metres wide, and the base about 40 metres wide on average.

Fill Material

During design, it was decided that granular fill material would be used to minimise the movements of the structures.

Geogrids

HDPE geogrids were chosen because of their good resistance to landfill leachate.

The design of the wall resulted in uniaxial geogrids with two different ultimate tensile strengths being used. Geogrids with a strength of 120 kN/m were used in the lower part of the wall and geogrids with a strength of 80 kN/m were used in the rest. These geogrids were placed in the soil with a vertical spacing of 400 mm and tied to concrete block facing units on the side of the wall facing away from the waste. The side of the wall facing the waste was formed with a geogrid wrap around arrangement.

The design of the embankment resulted in uniaxial geogrids with three different ultimate tensile strengths being used. Geogrids with a strength of 90 kN/m were used in the bottom third of the embankment, 60 kN/m in the middle third and 45 kN/m in the top third. These geogrids were placed in a wrap around arrangement with a vertical spacing of 400 mm.

Secondary biaxial geogrids were placed between the main uniaxial geogrids to help maintain alignment of the embank-ment faces. These secondary geogrids were attached to the centre of each wrap around and had a short penetration of 1 me-tre into the embankment.

A geotextile was placed inside the wrap around to keep the fill material in place (Fig. 1).

Fig. 1 Geogrid wrap around arrangement.

The long term design strength of the geogrids was determined from tests for tensile strength, installation damage, durabil-ity and creep. Geogrid creep characte-ristics were determined at 30°C as Hong Kong is located within the tropics.

Resistance to Grass Fires

In order to protect the side of the embankment facing away from the waste from the occasional hillside grass fires that oc-cur in Hong Kong, it was decided to place a 100 mm thick layer of gravel on this face. This was attached to the face using a steel mesh (Figs. 2 and 3).

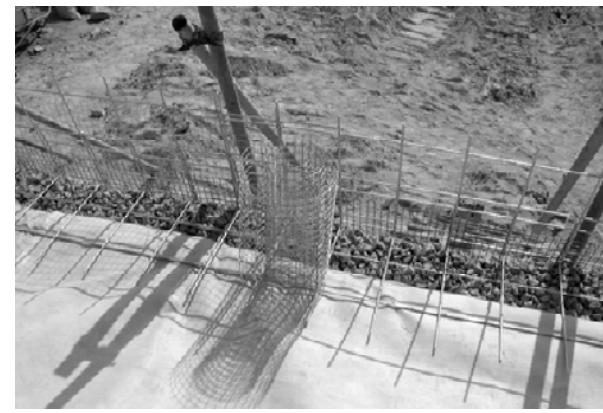

Fig. 2 Gravel facing for fire resistance

Fig. 3 Completed gravel facing

The gravel is intended to keep the temporary heat of a moving grass fire away from the geogrids.

The thickness of the gravel was chosen based on the work of Austin (1997), and was confirmed with a rudimentary fire test.

It was recognized that the effect of fire on a reinforced fill embankment is unlikely to cause structural failure. The maximum tension in the geogrids is within the embankment, some distance from the faces, where the geogrids will be protected from fire.

Only the wrap around portion of the geogrid on the faces is likely to be affected by a fire. In this location, after settlement of the embankment, the geogrids are not in tension and their localized removal would not cause structural failure. However, the absence of this portion of the geogrid would cause a serviceability problem with time as the compacted fill material would start to escape from the face of the embankment.

Therefore, protection of the wrap around with a flexible gravel facing was thought to be prudent. It was thought that a shotcrete facing applied in the early life of the embankment would be too rigid and might crack as the embankment settled.

CONSTRUCTION

Foundation

Hong Kong soils are saprolitic in nature and relatively strong. During excavation for the base of the embankment, small areas of weaker soils were removed and replaced by a thin concrete foundation.

Fill Material

The fill material was obtained from nearby excavations within the landfill, which has increased the void space for waste.

The excavation for the embankment was carried out in a profile of saprolitic soils and igneous rocks. The saprolitic soils were encountered first in the excavation and some consideration was given to changing the design of the reinforcement to util-ise these fine grained soils for the fill material. However, it was realised that the use of fine grained soils would increase the likelihood of unacceptable settlements of the embankment, especially if the fill became wet during placement.

It was then decided to use the igneous rock beneath the soil. This was reduced in particle size as much as possible during the excavation blasting, and then the rock material was passed over a vibrating screen with a screen opening size of 40 mm. The material that passed through the screen was a remarkably consistent sandy gravel that was perfect for the construction of a reinforced fill structure.

Geogrids

In addition to the factory quality control of the geogrids, samples were taken on site for testing. These samples were tested for ultimate tensile strength, and interface friction tests were carried out in a large shear box for each grade of geogrid against the fill material being used.

Compaction

The fill material was compacted using vibrating rollers. For the embankment, heavier rollers were used in the centre and lighter rollers near the edges.
Compaction control was achieved using a nuclear density gauge. Due to the consistent nature of the granular fill, the required compacted density was consistently achieved. In addition, this allowed a consistently good vertical alignment of the faces.

Monitoring

Monitoring of both the wall and the embankment movements was carried out by standard surveying techniques. Due to the use of good quality granular fill, and good compaction during placement, very little movement of either structure has occurred.

Lining

The wrap around arrangement on the side of the structures facing the waste has allowed the lining and drainage system to be placed directly on the face of the structure.

During design, it was decided that the lining and drainage system would not be installed until the movement monitoring confirmed that movement of the structures

had mostly ceased. In the event, little movement of the structures has occurred.

Completion

The reinforced soil wall across the narrow opening of the valley has been lined and the placing of waste against this wall commenced in early 2007.

By the middle of 2007, the lack of movement of the reinforced fill embankment indicated that waste could also be able to be placed against it. However, the operational filling requirement in this area is not for some time yet. Fig. 4 shows the embankment nearing completion.

Fig. 4 The embankment nearing completion

CONCLUSIONS

The use of geogrid reinforced soil structures, utilizing fill material excavated from within the landfill, has proved to be an economically feasible method to increase the capacity of waste landfills in Hong Kong. Figs. 5 and 6 show the completed embankment structure.

Fig. 5 Completed reinforced fill embankment on the side facing the waste

Fig. 6 Completed reinforced fill embankment on the side facing away from the waste

REFERENCES

Austin RA (1997) The Effect of Installation Activities and Fire Exposure on Geogrid Performance, Geotextiles and Geomembranes 15 (4-6): 367-376

Cowland JW, Tang KY, Gabay J (1993) Density and Strength Properties of Hong Kong Refuse, Fourth International Landfill Symposium, Sardinia, Italy: 1433-1446

Cowland JW (2000) The Use of Geosynthetics in Landfills in Hong Kong, Geosynthetics Asia 2000, Kuala Lumpur, Malaysia: 111-117

Guide to Reinforced Fill Structure and Slope Design (2002). Geotechnical Engineering Office, Government of the Hong Kong Special Administrative Region: 1-236

Proceedings of the 4th Asian Regional Conference on Geosynthetics
June 17 - 20, 2008 Shanghai, China

MODELING OF REHABILITATION OF UNREGULATED SOLID WASTE LANDFILLS

A. Edinçliler[1] and C. Altunel[2]

ABSTRACT: Unregulated solid waste landfills are causing severe environmental impacts for environment and human health due to the formation of leachates and landfill gas during decomposition of organic wastes. Common problems that usually be faced with these sites are visual pollution, air pollution, water pollution, soil contamination, spreading of waste, spreading of diseases, subsidence and odor. Therefore the rehabilitation of waste dumping sites has become a matter of importance for controlling these adverse effects. In this study, it is aimed to promote the rehabilitation of unregulated solid waste landfills and to provide guidance on how to effectively rehabilitate these sites so that off-site emissions from leachate and landfill gases are minimized. This study focuses on the geotechnical solutions to the problems associated with open waste dump sites. Full rehabilitation process includes shaping the waste body, surface water control, leachate management, gas management, final cover system with HDPE liner, settlement analysis, slope stability analysis and monitoring after closure. As a case study, data belongs to the unregulated solid waste landfill called Silivri are used. For the rehabilitation of the unregulated landfill, USEPA and Turkish Regulations are taken as major guidelines.

KEYWORDS: unregulated landfill, rehabilitation, HDPE fabric, geosynthetics

INTRODUCTION

Methods used for municipal solid waste (MSW) disposal in developed countries are generally landfilling whereas in Turkey predominantly is dumping. In landfilling method, waste is discarded at a designated area at the disposal site, then the material is systematically pushed and compacted by machinery, then regularly covered with soil or other suitable cover material. In dumping method, waste is discarded at an open disposal site and no precautions are taken for environment and human health.

The problems associated with open waste disposal sites which have not been rehabilitated include visual pollution, weed infestation, subsidence and the continued generation of leachate and landfill gases, including methane, a greenhouse gas.

Open waste disposal sites are classified as contaminated sites, which means that the land cannot be used for sensitive uses, such as for residential development. In urban areas, open waste disposal sites may be valuable for such uses as passive recreation or for local bushland regeneration projects.

There are particular problems with the rehabilitation of open waste disposal sites: there may be uncontrolled migration of landfill gas to the root zone of plants, leachate seepage, elevated temperatures in the root zone generated from organic waste deposits, and there may be the added complication of toxic wastes having been dumped at the site. Most of these problems can be resolved by good engineering practice such as leachate collection and removal system, final cover system and landfill gas collection and removal system Use of geosynthetic products as liner material can isolate the MSW and prevent contamination. The chemical resistance and flexibility of geomembranes and Geosythetics Clay Liners makes them technically superior to any other alternative for providing a positive barrier to the movement of fluids and gases.

This study focuses on the rehabilitation of open waste disposal sites and a case study namely, Silivri. The site has been used over the years for waste disposal by the municipality of Silivri. No precautions such as impermeable base liner and cover have been taken to isolate the waste and contamination. According to the data about the site a rehabilitation model proposed including, compaction of waste, surface water collection system, isolating the waste, leachate collection system and final cover system.

[1] Associate Professor, Department of Earthquake Engineering, Bogazici University, TURKEY. Email: aedinc@boun.edu.tr
[2] MSc Student, Department of Civil Engineering, Bogazici University, TURKEY. Email: cemaltunel@hotmail.com

OPEN WASTE DISPOSAL SITES

For the purposes of planning, it is convenient to classify waste disposal sites into a number of principal stages in the progression from open waste disposal sites to fully engineered, environmentally secure, sanitary disposal sites as follows; open waste disposal sites, controlled waste disposal sites, and sanitary landfills.

In reality each stage of landfill development is not discrete but a point on a continuum, involving progressively higher and more sophisticated levels of site engineering, operation, and management, all of which may be desirable or necessary but not always achievable in the short-term.

Open waste disposal sites which prevail in very low income countries are considered to be unacceptable but controlled disposal sites and engineered sanitary landfills can provide effective disposal of MSW in accordance with appropriate local health and environmental standards for low and middle income countries. The highest standards of engineered landfill, with multiple liners and leachate and gas treatment systems, are found only in the wealthiest countries in North-West Europe and North America (Thayumanavan et al. 2002).

Open waste disposal sites are generally sited on vacant plots of land and are sometimes developed on low-lying or marshy lands, often as a means of reclaiming land for subsequent development. They may be located adjacent to existing residential development because of constraints on availability of suitable land or, alternatively, may attract the development of communities involved in recycling activities. As a consequence of the proximity of residential communities, open waste disposal sites are often of small size, of limited capacity and pose high potential environmental risks due to the following factors (Ramboll 2003):

- They are unplanned;
- There is no control over waste inputs (both waste quantities and composition);
- There is no control over emission of pollutants released from waste decomposition.

Site Rehabilitation

Waste disposal sites, if not properly planned and filled, can cause major problems in the rehabilitation phase and in the long term. It is essential to investigate potential end uses of the area when a new waste disposal site is planned, or when extensions to existing sites are being considered. Rehabilitation process includes; shaping the waste body, surface water control, leachate management, gas management, final cover system, settlement analysis, slope stability analysis, and monitoring after closure.

Studies on Rehabilitation of Waste Disposal Sites

Starting from 1960s sanitary landfills are used in developed countries. Simultaneously, old waste disposal sites were started to be rehabilitated in those countries. Therefore, actually in developed countries rehabilitation is an “old” phenomenon. In contradicton, in developing countries like Turkey, although the number of sanitary landfills are increasing day by day still sanitary landfills are in minority. So, rehabilitation is still a “popular” subject for developing countries and there are lots of rehabilitation projects. A few examples are stated below.

Remediation of a previously closed waste disposal site, located in İzmir; one of the major cities in Turkey, performed by Durgunoğlu et al. (1998). The site had been used over the years for waste disposal by municipality without taking any precautions such as impermeable base liner and cover to isolate the waste. Remedial project for the site had been designed with the evaluation of the geotechnical model and contamination data to eliminate the existing and the further complications related to waste storage. The solid waste distributed over a large region within the storage space was planned to be compacted and stored in a limited area. The leachate collection system had been designed with the evaluation of hydrogeological conditions of the site and vicinity and a gas collection system had been proposed to eliminate the problems associated with the decomposition of the irregularity stored solid waste. The proposed design checked in terms of stability and settlement. The final storage scheme had been optimized with the evaluation of those analyses. A monitoring system consisting of settlement columns and piezometers had been proposed in the design to monitor the settlements and pore water pressures expected to occur during the construction of the compacted waste and are critical in terms of stability.

CASE STUDY

Istanbul is the biggest city of Turkey in terms of both population and economical size. It has 32 towns and one of them is Silivri which is 70 km. away from the city center of Istanbul in west direction. The size of the town is about 800 km^2 and has a population of nearly 40,000 which is a very small number when compared to the other towns of Istanbul. It has 8 municipalities, 27 village and 35 km. length coastal line that makes the city a touristic place in summer. During the summer season population of the city increases up to 150,000. Although tourism is a very important economical source for Silivri, general income level of people is low.

The average temperature of whole year in Silivri is 12.6 C° where the highest monthly temperature is seen in July as 22.2 C° and the lowest in January as 3 C°. The average precipitation of whole year in Silivri is 56.3 mm where the highest monthly precipitation is seen in December as 83.6 mm. and the lowest in August as 18.9 mm.

Silivri open waste disposal site was used between 1988 and 2004 (Fig. 1). Since January 2004, Silivri municipality started to dispose waste to a sanitary landfill in Çanta town that is far away from the city. But the site is still open and there are no precautions taken or any regulations applied to the site.

Fig. 1 A view from silivri waste disposal site

Silivri open waste disposal site is located near the center of the city. Residential area is just 250 m. away from the site. Also, animals around the site are in touch with waste which may cause diseases both for them and for people. Leachate formation can easily be observed around the site. Odor and visual pollution are other factors that affect environment. Therefore site selection was extremely wrong in terms of environment and public health. In order to diminish the danger, the site should be rehabilitated as soon as possible.

Average waste generation rate is 1 kg per capita per day in Silivri. During the active time 68,000 tons of waste was placed into the site. This is actually about 170,000 m^3 that was disposed over 21,250 m^2 area. The length of the disposal site is 170 m. where the width of it is 125 m. and the average depth of waste is about 8 m.

Due to the lack of industrial facilities, waste does not include industrial or hazardous components. Like all other lower income waste components, Silivri waste composed of mostly organics. In winters ash rate in the waste composition increases in an important amount because for heating people prefers generally coal. Other important components of waste are paper, plastics, glass and metals.

The geological parameters around the site are very important for modelling of rehabilitation. Soil layers under the waste are clayey sand, silty clay and clay respectively. Engineering properties of waste and soil layers underlying the waste shown in Table 2.

General information about Silivri and the disposal site is summarized in Table 3.

Table 2 Characteristics of waste and soil layers

Material	γ (kN/m^3)	C (kN/m^2)	Φ (°)
Waste	4	30	35
Clayey-sand	20	0	28
Silty-clay	19	25	0
Clay	18	30	0

Table 3 General information

Parameter	Value
Population of the town	40,000
Size of the town (km^2)	800
Waste production rate (kg /capita/ day)	1
Average temperature (C°)	12.6
Highest temperature (C°)	22.2 (July)
Lowest temperature (C°)	3 (Jan.)
Average precipitation (mm)	56.3
Highest precipitation (mm)	83.6 (Dec.)
Lowest precipitation (mm)	18.9 (Aug)
History of disposal site	1988
Width of disposal site (m)	125
Length of disposal site (m)	170
Size of disposal site (m^2)	21,250
Average depth of disposal site (m)	8
Highest point of waste (m)	10
Lowest point of waste (m)	5
Volume of waste (m^3)	170,000
Weight of waste (tons)	68,000
Groundwater table (m)	5
Nearest sewer system (m)	250

Waste Compaction and Re-shaping

As mentioned before, Silivri waste disposal site is an unregulated site, thus compaction and shaping was not done in the site. In order to decrease future settlement and increase the stability of our design, the waste should be compacted. Moderate compacted waste has a unit weight between 5 to 8 kN/m^3. As a result, assuming that 33 % volume decrease at the end of the compaction will satisfy the moderate compaction criteria. So, new waste

volume will be 115,000 m^3 instead of 170,000 m^3 and new unit weight will be 6 kN/m^3 instead of 4 kN/m^3.

Beside compaction, re-shaping the waste body is also important because another factor that affects the stability is the geometry of the waste body. According to information given before the edge slope of waste should be between 1H:3V and 1H : 5V and the top slope should be less than 4 percent. So, 1H:4V slope chosen for edge and 3 percent slope chosen for top. The cross-section of the re-shaped waste is shown in Fig. 2.

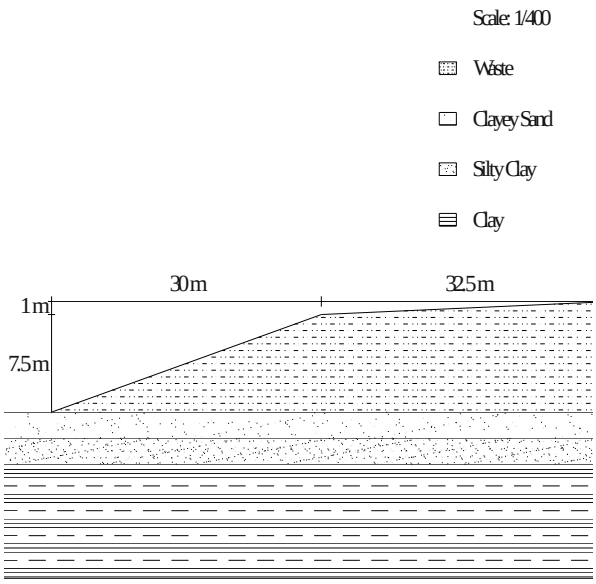

Fig. 2 Cross-section of the re-shaped waste

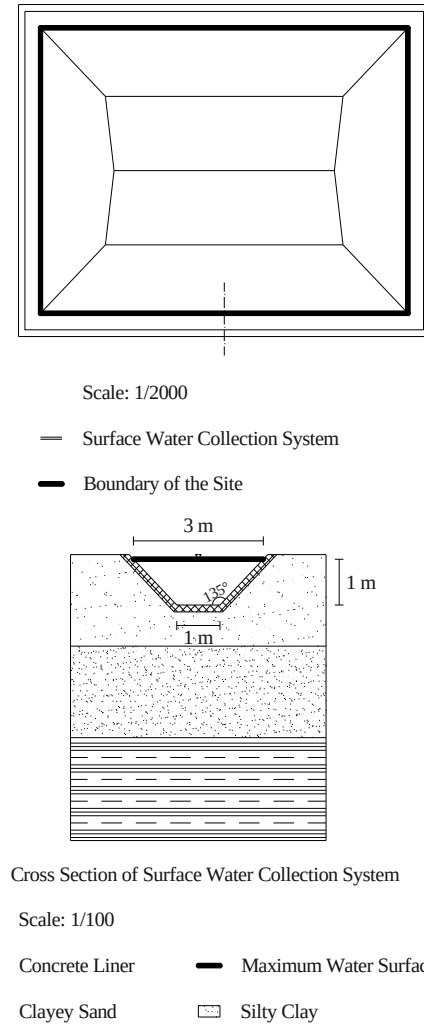

Fig. 3 Geometry of surface water diversion ditch

Surface Water Collection System

As stated above, the average precipitation of whole year in Silivri is 56.3 mm where the highest monthly precipitation is seen in December as 83.6 mm. and the lowest in August as 18.9 mm. According o this data, it is obvious that the region is not in a high precipitation zone. Therefore, standard surface water diversion ditch can be applied to the site. The geometry of the ditch is given in Fig. 3. The slope of the system chosen as 1 percent according to the Turkish Environmetal Ministry recommendations.

Because surface water is uncontaminated, surface water diversion ditches can be connected directly to municipal sewer system. Municipal sewer system is just 250 m. away from the site, therefore the idea to connect the ditches to sewer system is applicable and feasible.

Leachate Management

Leachate problem in Silivri waste disposal site can be eliminated in two phases, namely, establishing cut-off wall and leachate collection system around the site. First one should be constructed in order to prevent leachate seepage around the site, the latter one to collect and remove the leachate.

Cut-off wall is one of the most important part of the rehabilitation because it isolates the media under the waste in terms of permeability. Soil-bentonite backfill-type slurry walls are the most popular one because they are relatively inexpensive and easy to construct. Thus, in this study soil-bentonite wall with typical 2 % bentonite composition is preferred as cut-off wall. The ideal width of the wall is 90 cm. and the wall should be keyed into the underlying low permeability layer to prevent the interception. A detail of the cut-off wall is shown in Fig. 4.

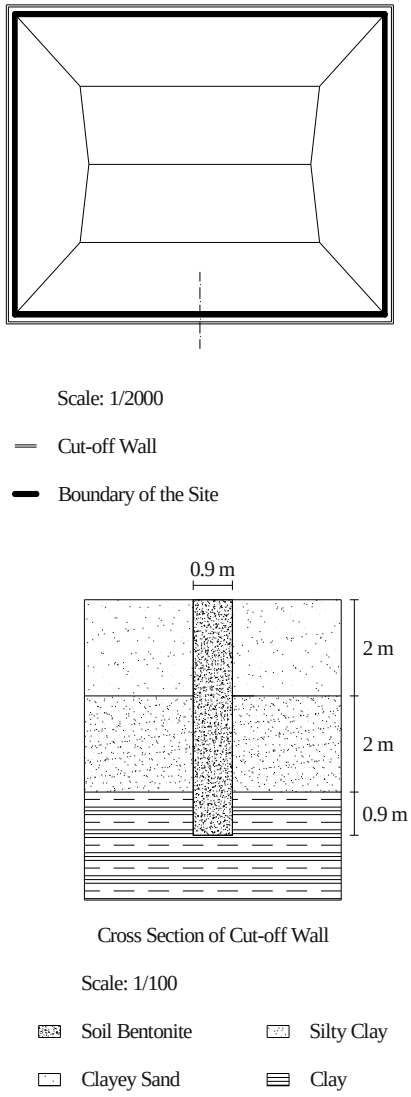

Fig. 4 Cut-off wall configuration

Leachate collection system should be installed around the waste disposal site. It is composed of vertical drainage layer and pipe system at the bottom of the layer. Drainage material is typically gravel but it should be rounded to prevent a probable damage that can be occured in the pipe system. The pipe system should be under the low-permeability soil level in order to collect all leachate formed under the waste. According to the Turkish Environmental Ministry, pipe size should be 200 mm. and it should be made up of high density polyethylene (HDPE). The slope of the system is 1 % like surface water collection system. The configuration of collection system is shown in Fig. 5.

Gas Management and Final Cover System

The management of landfill gas is not necessary on small and medium sized, rehabilitated dumps, because the biodegradable waste has already been by and large decomposed at these sites, and the amount of additional gas is therefore minimal and can be expected to decompose in the dump capping system. According to USEPA, disposal sites that have less than 111,000 tons of waste are not required to maintain gas system. As a result, gas management is not necessary for Silivri case because of the reasons stated above. So, final cover system should not include gas collection layer. The other parts of the final cover system take their places in the design according to the Turkish Environmental Ministry regulations.

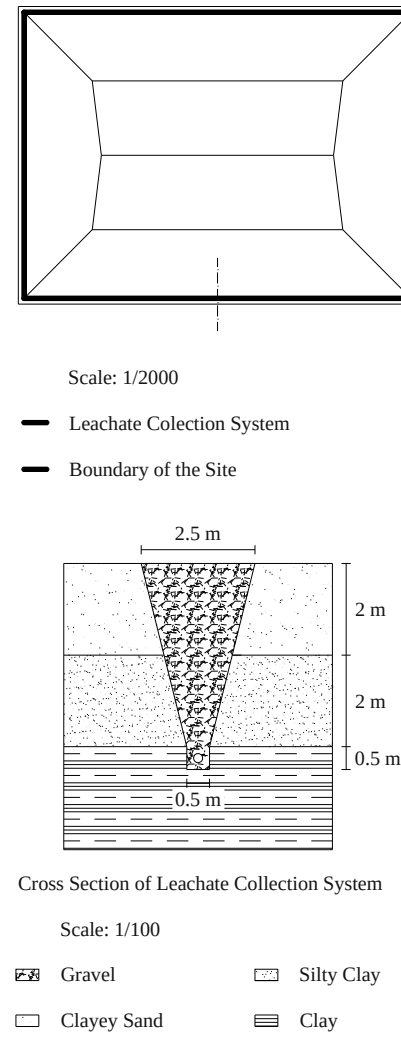

Fig. 5 Leachate collection system

Starting from bottom, the barrier layer which is composed of clayey-sand, the natural surficial soil of silivri, is 50 cm. thick. Then as an impermeable layer, 60 mil HDPE liner is used. Afterwards, the 30 cm. thick drainage layer which composed of gravel is applied. Finally, at the top clayey-sand is used as in the case of barrier layer with 100 cm. thickness. The configuration of final cover is shown in Fig.6.

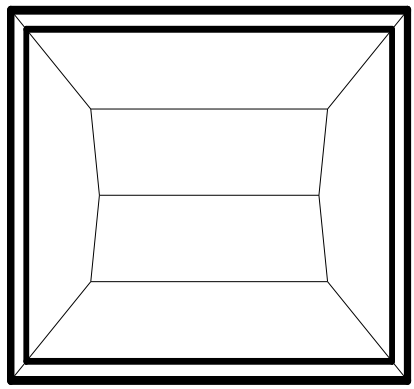

Scale: 1/2000

Boundary of the Site After Final Cover

Boundary of the Site Before Final Cover

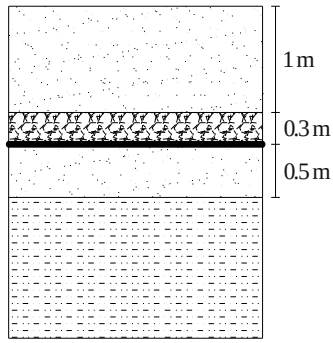

Cross Section of Final Cover System

Scale: 1/50

Waste

HDPE Liner

Clayey Sand

Gravel

Fig. 6 Final cover configuration

Settlement and Slope Stability

The settlement of the rehabilitated site in Silivri is calculated by Bjarngard and Edgers is used (Fig. 7). The vertical settlement of the waste body is calculated as as 0.47 m by using Bjarngard and Edgers approach.

The factor of safety for slope stability of the rehabilitated site in Silivri is calculated by Koerner and Hwu approach. The factor of safety for sliding is calculated as 1,73 by using Koener and Hwu approach.

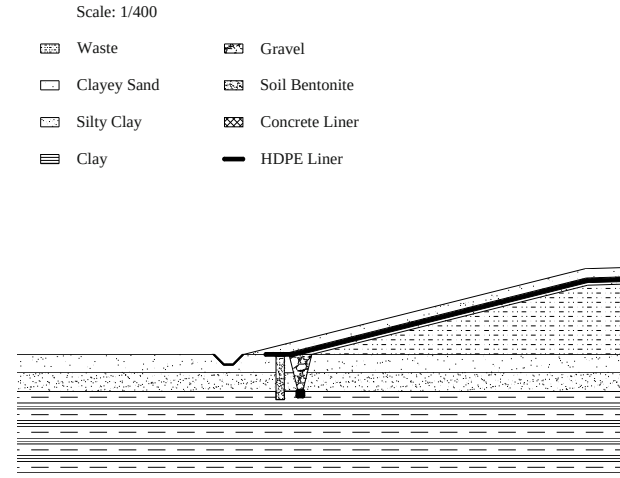

Fig. 7 Cross-section of rehabilitated site

CONCLUSIONS

The problems with Silivri waste disposal site may be eliminated in 5 steps. First of all, the waste is compacted and reshaped to increase the stability of the waste and decrease the future settlements. Secondly, in order to prevent surface water to diffuse the waste and increase the generation of leachate, diversion ditch is designed. Thirdly, for preventing leachate seepage around the site, cut-off wall is designed. Afterwards, to collect the leachate formed in the waste body, leachate collection system is designed. Finally, waste covering system is designed to isolate the waste. It is concluded that the calculated settlement value is reasonable for waste disposal sites compared with the literature.

REFERENCES

Thayumanavan S (2002) Gopalakrishnan and J Jesline, (editors), Open Dumps to Sustainable Landfills, Anna University

Ramboll-Erm (2003) Dumpsite Rehabilitation Programme, Tacis, Brussels

U.S. Environmental Protection Agency (1991) Solid Waste Disposal Faclity Criteria; Final Rule, Subpart C Operating Criteria 76-116

U.S. Environmental Protection Agency (1991) Solid Waste Disposal Faclity Criteria; Final Rule, Subpart F Closure and Post-Closure 322-349

Durgunoglu HT, Kulaç HF, İkiz S, et al. (1998) Remediation of an Existing Solid Waste Disposal Site, Contaminated and Derelict Land—GREEN 2, Thomas Telford, London

Proceedings of the 4th Asian Regional Conference on Geosynthetics
June 17 - 20, 2008 Shanghai, China

RELATIONSHIP BETWEEN SHORT-TERM COMPRESSION STRENGTH AND TRANSMISSIVITY PROPERTIES OF GEONETS

M.S. Mok[1], E. Blond[2], J. Mlynarek[3] and H.Y. Jeon[4]

ABSTRACT: This study deals with the relationship between short-term compression strength and transmissivity properties of geonets and its effect on the result of land filling design. The result shows that the compression behaviors undergo some plateau or roll-over region right after yielding point and this phenomenon will induce some significant decrease in hydraulic properties. Also, the hydraulic properties affected on designing results differently under low and high normal pressure conditions in case of bi-planar geonet. Large differences of q_{allow} values between the expected transmissivity value which comes from linear regression curve and true value especially in high normal pressure condition were observed. From these results it is assumed that when designing with geonet drainage material used in waste landfill, the loading condition must be considered and true transmissivity value which comes from the real hydraulic test should be used than expected values.

KEYWORDS: short-term compression strength, transmissivity, normal pressure conditions, linear regression curve, drainage material

INTRODUCTION

Geonets can be very useful as solutions for drainage in geotechnical and environmental engineering, for example municipal and very hazardous waste landfill and playground. A large number of product types of geonet with different properties may cover most of the usual applications in those construction sites.

In some cases the unit weight of waste case can be more times the unit weight of common soils and the size of the landfill can be very large than typical landfills. In those situations the geonet drainage layer may be subjected to very high normal stress.

Transmissivity of a geonet drain is known to be affected by various factors as follow:

(i) physical characteristics of the geonet,

(ii) intensity and duration of the applied vertical stress,

(iii) hydraulic gradient, and

(iv) presence of an various chemical and biological circumstances.

However, in most designing procedures some critical point such as a compressive behaviour of geonet is non-linear and the transmissivity. This non-linear phenomenon may cause a wrong designing value which can induce a failure of a system.

In this study, relationships between short-term compressive behaviour and in-plane flow capacity of a geonet are established from short-term compression test and transmissivity test. For the in-plane flow test, extensive transmissivity test are conducted under low and high normal loads to investigate the effect on flow rates of geonets. Also, its effect on designing with geonet drainage system was evaluated. In analysis, the ultimate flow capacity is reduced by a series of partial factors of safety to determine an available flow capacity for design.

Then this paper proposes an application of the true value which comes from transmissivity test result under high normal pressure would be considered when designing. This suggestion may increase the accuracy of the result of the design and can prevent any failure of the drainage system.

DESIGNING WITH DRAINAGE PRODUCT

Currently approach used to evaluate the service performance of geonet or geocomposite drains is described by Koerner (1998). This approach is more genetic in that it allows “reduction factors” to be applied to the transmissivity of the geonet or geocomposite measured in a short-term index-oriented test. In the

[1] Researcher, CTT Group/SAGEOS, Saint-Hyacinthe, Quebec, CANADA. Email: munsungmok@gmail.com
[2] Director, CTT Group/SAGEOS, Saint-Hyacinthe, Quebec, CANADA. Email: eblond@gcttg.com
[3] CEO, CTT Group/SAGEOS, Saint-Hyacinthe, Quebec, CANADA. Email: jmlynarek@gcttg.com
[4] Professor, Faculty of Nano-Systems Engineering, Inha University, Incheon, KOREA. Email: hyjeon@inha.ac.kr

design by function approach, a geonet or drainage geocomposite must meet the following equation:

$$FS = \frac{q_{\text{allow}}}{q_{\text{requried}}} \quad (1)$$

where FS = overall safety factor, q_{allow} = allowable flow rate of the geocomposite and q_{required} = required flow rate. In this equation, the required flow rate can be determined from previously well-documented methods. And for the allowable flow rate of the geonet or drainage geocomposite can be determined from the following equation. Table 1 shows the guidelines for the usual reduction factors values.

Table 1 Recommended reduction factor values for Eq. 2 determining allowable flow rate or transmissivity of geonets

Application Area	Reduction Factor Values in Eq. (2)			
	RF_{IN}	RF_{CR}	RF_{CC}	RF_{BC}
Sport fields	1.0-1.2	1.0-1.5	1.0-1.2	1.1-1.3
Capillary breaks	1.1-1.3	1.0-1.2	1.1-1.5	1.1-1.3
Roof and plaza decks	1.2-1.4	1.0-1.2	1.0-1.2	1.1-1.3
Retaining walls, seeping rock, and soil slopes	1.3-1.5	1.2-1.4	1.1-1.5	1.0-1.5
Drainage blankets	1.3-1.5	1.2-1.4	1.0-1.2	1.0-1.2
Infiltrating water drainage for landfill covers	1.3-1.5	1.1-1.4	1.0-1.2	1.5-2.0
Secondary leachate collection (landfill)	1.5-2.0	1.4-2.0	1.5-2.0	1.5-2.0
Primary leachate collection (landfill)	1.5-2.0	1.4-2.0	1.5-2.0	1.5-2.0

(Ref) R Koerner (2005), Designing with geosynthetics, 4th edition

$$q_{\text{allow}} = \frac{q_{\text{ultimate}}}{RF_{\text{IN}} \cdot RF_{\text{CR}} \cdot RF_{\text{CC}} \cdot RF_{\text{BC}}} = \frac{q_{\text{ultimate}}}{\Pi RF} \quad (2)$$

Where

q_{ult} = flow rate determined using ASTM D4716 for short-term tests between solid platens using water as the transported liquid under laboratory test temperatures,

q_{allow} = allowable flow rate to be used in Eq. 1 for final design purposes;

RF_{IN} = reduction factor for elastic deformation, or intrusion, of the adjacent geosynthetics into the geonet's core space;

RF_{CR} = reduction factor for creep deformation of the geonet and/or adjacent geosynthetics into the core space;

RF_{CC} = reduction factor for chemical clogging and/or precipitation of chemicals within the core space;

RF_{BC} = reduction factor for biological clogging within the core space;

RF = product of all reduction factors for the site-specific conditions.

Because of the tendency of polymer materials to undergo short-and long-term compressive creep, the flow capacity of geonet or drainage geocomposite under specific compressive loads must be considered. These short-and long-term creep properties are usually affected by its basic short-term compressive stress/strain behaviour. And eventually this property will affect on its intrinsic transmissivity. Due to these reasons, when drainage system using geonet or drainage geocomposite is conducted, the short-term compressive behaviour must be considered as a main factor.

SAMPLES AND TEST METHODS

Samples

Two types of geonets were used in this study. The first geonet (Sample A) is a 5.6 mm thick high density polyethylene (HDPE) traditional bi-planar geonet. The second type (Sample B) is also HDPE, and has 8.6 mm tri-planar. All these material are used for landfill cover and lining system drainage. Typical specifications for samples are provided in Table 2. Photograph of these samples are shown in Fig. 1. The reference list must be summarized at the end of the main text. Make sure reference information is complete and accurate in the following order: last names and initials of all authors; year of publication; title of paper, report, or book chapter; title of book or periodical; volume and issue numbers; name and location of publisher (for books), name and location of publisher or sponsor (for proceedings); and inclusive page numbers. The references are 5 mm hanging indentation.

Table 2 Basic properties of various samples

Property	Unit	Sample A	Sample B
Thickness	mm	5.6	8.6
Mass	g/m^2	920	1700
Carbon black	%	2.3	2.2
Density (final product)	g/cm^3	0.942	0.944
Crystallinity	%	56	55

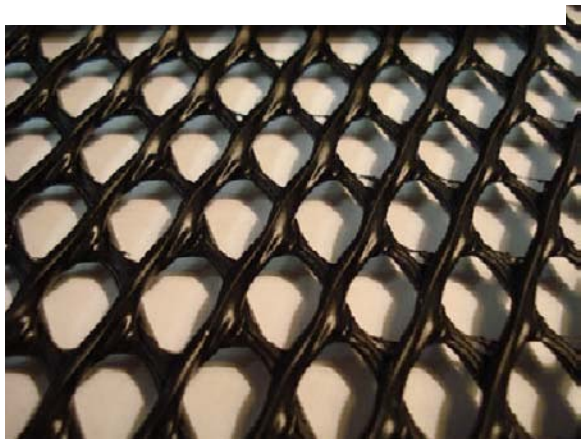

(a) Sample A

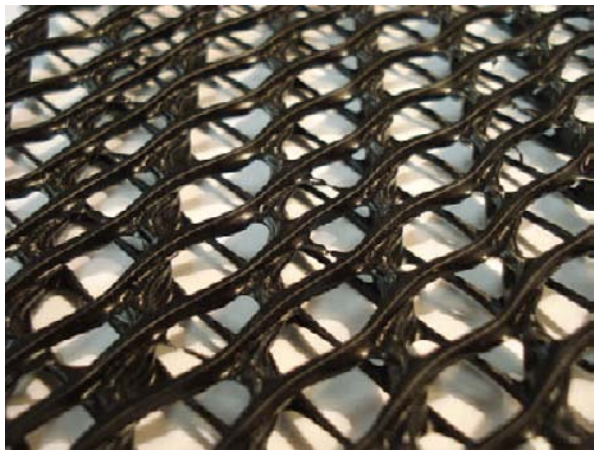

(b) Sample B

Fig. 1 Photograph of various geonets samples

Test methods

Short-term compressive test

Short-term compressive deformation test was performed using the procedures set forth in Standard Test Method for Determining Short-term Compression Behaviour of Geosynthetics (ASTM D6364). The geonet specimen is positioned between two rigid steel platens and compressed at a constant deformation rate of 1.0 mm/min. All tests for the basic short-term compressive were performed in tension at 23 ± 0.2^{o}C. For more precise and accurate temperature control, a heating platen was manufactured and applied through the tests. Fig. 2 shows these heating platens. Also to consider the landfill's severe site-specific conditions, modified test conditions were applied to the test; test temperature/ 23^{o}, 35^{o} and 50 ^{o}C, compressive deformation rate/ 0.1, 0.5, 1.0, 5.0 and 10 mm/min.

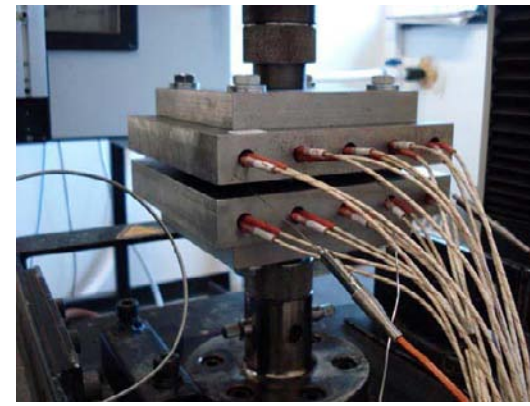

Fig. 2 Photograph of the heating platens

Transmissivity test

Relationships between in-plane flow capacity, confining stress and hydraulic gradient in a geonet were established from transmissivity testing equipment, for which there is a designated ASTM Standard Test Method (ASTM D4716; Test Method for Determining the (In-plane) Flow Rate per Unit Width and Hydraulic Transmissivity of a Geosynthetic Using a Constant Head).

The short-term flow test was carried out for each geonet sample at various normal stresses up to 2,000 (max.), and 3 hydraulic gradients ranging from 0.1 to 1.0. The water temperature normally ranged from 22 ^{o}C to 23^{o}C. A photograph test equipment and setup is presented in Fig. 2. Referring to the figure, hydraulic transmissivity is calculated utilizing the following equation:

$$\theta = \frac{Q}{B \times (\Delta h / L)} \tag{3}$$

Where, θ= hydraulic transmissivity (m^2/s), Q = volume of discharged fluid per unit time (m^3/s), L = length of the specimen (m), B = width of the specimen (m) and h = difference in the total head across the specimen (m). Fig. 3 shows transmissivity test equipment used in this study.

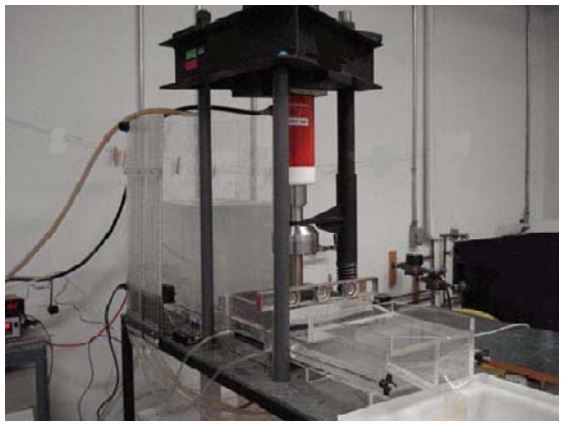

Fig. 3 Transmissivity test equipment

RESULTS AND DISCUSSION

Short-term Compressive Test

The relationship between normal compressive strength (kPa) and compressive strain (%) for each sample is displayed in Fig. 4. For the Sample A, it is quite clear that there exist a long range of plateau after yielding point which means the thickness will decrease without further normal pressure. This phenomenon is called a roll-over. And this advantage will advance the long-term flow capacity of the geonet. The graph of Sample B convincingly shows that there is no roll-over tendency. And this is considered that this behaviour is due to the different geometry. From the result, it is expected that with increasing compressive strength the transmissivity at a given stress decrease very signifi-cantly right after yielding point (roll-over) especially in Sample A.

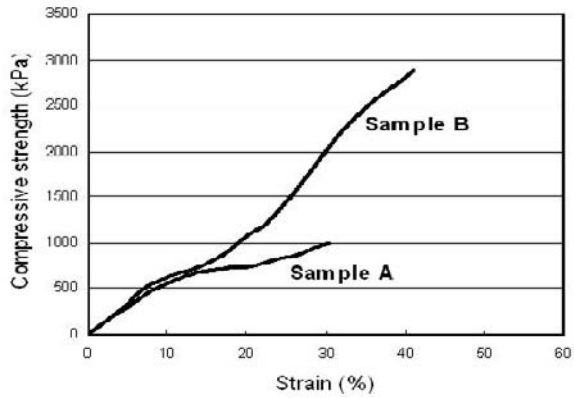

Fig. 4 Compressive behaviour of samples

Short-term Compressive Behaviours under Various Test Conditions

Figs. 13 ― 15 show all the results of compressive strength-strain behaviours which performed at various temperatures (23, 35 and 50°C) and various displacement rate (0.1, 0.5, 1.0, 5.0 and 10 mm/min). These results show that the compressive strengths decrease with increasing test temperature for both samples. Also for the various displacement rates, same tendencies were observed as for temperature variation. When the landfill's severe temperature conditions will be considered, this decrease in compressive properties may affect the long-term flow capacity of the geonet drainage very significantly. Consequently, the compressive strength/ stress behaviours should be considered very significantly during the designing the landfill drainage system especially for high normal pressure condition.

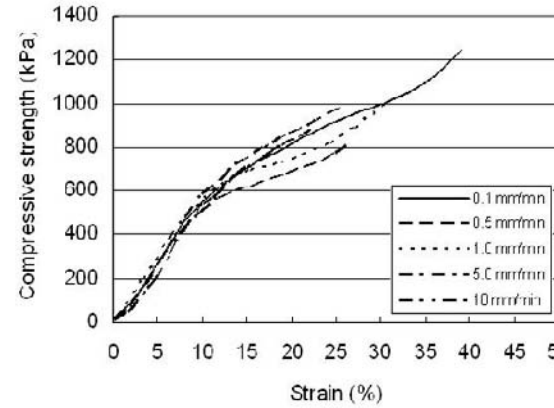

(a) Sample A

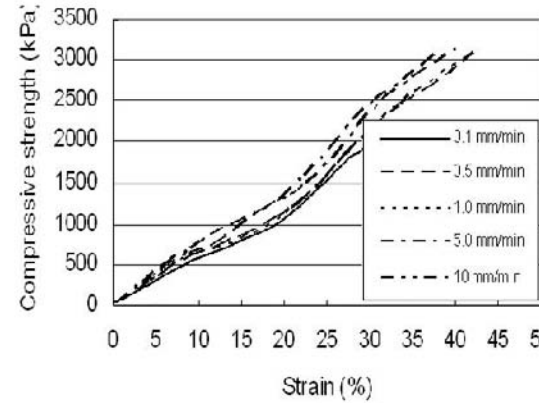

(b) Sample B

Fig. 5 Compressive behaviour under various displacement rates at 23°C

INFLUENCE ON TRANSMISSIVITY OF DIFFERENT NORMAL PRESSURE

The generic samples show different behaviour, the lines of transmissivity versus normal pressure drop rapidly for Sample A (bi-planar geonets) right after 500 kPa, show less decrease for Sample B (tri-planar) even up to 2000 kPa, that even extremely very high pressure. Fig. 8 explains these in-plane flow behaviours.

EVALUATION OF THE q_{allow} FOR EACH SAMPLES

The designing values of q_{allow} at different normal pressure conditions were estimated. These various pressure design considerations are as follow; low normal pressure (<500 kPa), expected high normal pressure using linear regression curve and also high normal pressure from true tested value. Figure 9 shows that at low normal pressure the expected value and true tested values are almost same, however beyond critical pressure (= 500 kPa) there are tremendous differences between the expected values and the true tested data. These differences of values may cause wrong designing procedure which induces a failure of the drainage system. From these results, the method for evaluating q_{allow} by using expected values is strongly not recommended for high normal pressure conditions. Table 3 also shows the result of the q_{allow}. In this table, the recommended reduction factors (1.5 for all factors) for primary leachate collection (Table 1) were used. The results of Table 3 show the large difference between the expected value and the true value for high pressure especially in Sample A.

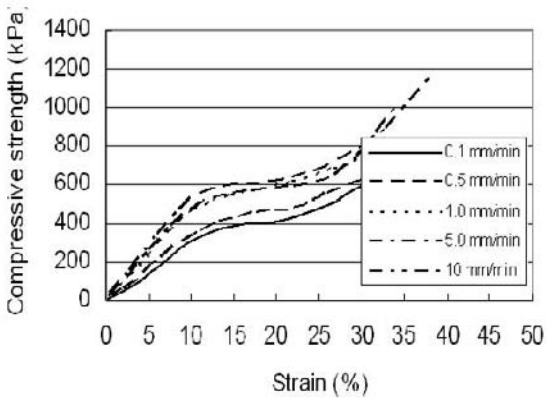

(a) Sample A

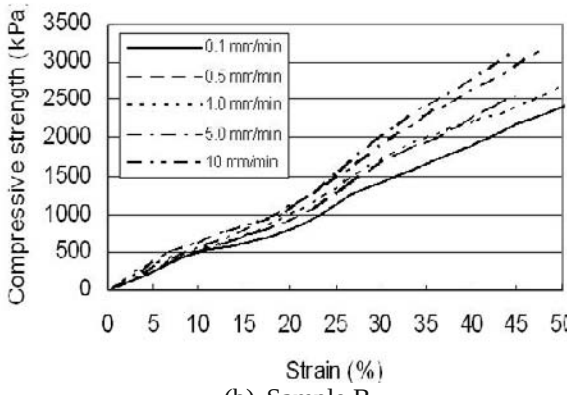

(b) Sample B

Fig. 6 Compressive behaviour under various displacement rates at 35°C

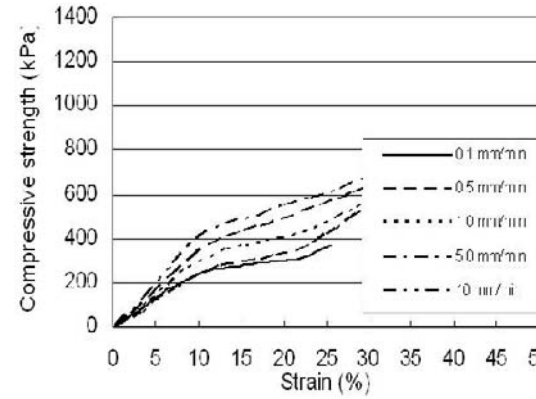

(a) Sample A

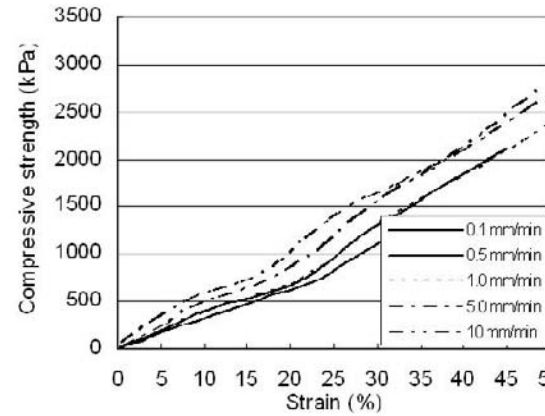

(b) Sample B

Fig. 7 Compressive behaviour under various displacement rates at 50°C

Table 3 Evaluation of the q_{allow} values

	Low pressure (100 kPa)		High pressure (800 kPa)	
q_{allow}	Expected value	True value	Expected value	True value
Sample A	1.28	1.29	0.83	0.37
Sample B	1.72	1.77	1.48	1.09

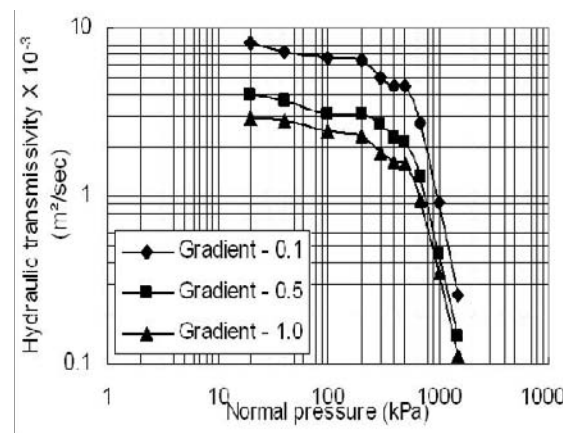

(a) Sample A

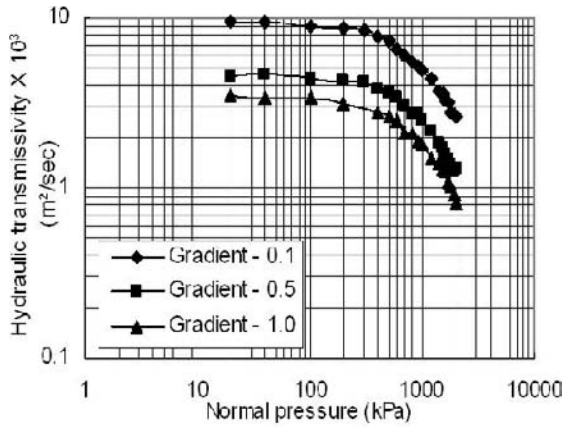

(b) Sample B

Fig. 8 Transmissivity of the samples

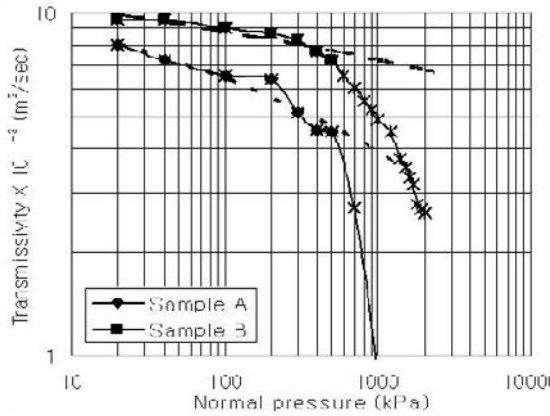

Fig. 9 Comparison between regression curves and true tested data

CONCLUSIONS

The purpose of this study was to evaluate effect(s) of various test parameters on the short-term compressive behaviour. Also the significance of the true tested vaules for the design which considering high normal pressure was evaluated. Based on the results in this investigation the following conclusions can be drawn:

(i) The preliminary results of the compression test confirm that for the Sample A (bi-planar geonets) there is a long range of roll-over region and this roll-over region will significantly affect on its transmissivity.

(ii) However, for the Sample B (tri-planar geonets) there is no roll-over region which means the trans missivity will decrease gradually by increasing normal pressure.

(iii) From the results which considered various test conditions (temperature and displacement rate), the effect of increasing test rate diminishes when test temperature level in short-term compression test is decreased (from 50°C to 23°C).

(iv) There were big differences between expected values from linear regression curve and true tested values when designing with geonets using its trans-missivity values to evaluate the qallow value especially in sample A for high normal pressure.

The authors recommend that the actual site-specific design configuration be considered especially in high normal pressure, as closely as possible, and these specific values should be obtained not from the expected values but from the real index or performance test.

REFERENCES

Fannin RJ (1995) Factors influencing the long-term flow capacity of geonets. Geosynthetics ’95: 267-280

Gardoni, MGA (1999) Transmissivity of geosynthetics under high normal stresses. Geosynthetics ’99: 769-782

Jarousseau C (2004) Drainage geocomposites: relation between water flow capacity and thickness in the long term, EuroGeo 3: 349-354

Koerner RM (2005) Designing with geosynthetics. 5th Edition, Prentice Hall, New Jersey, USA

Kolbasuk GM, Lydick LD, Reed LS. (1992) Effect of test procedures on geonet transmissivity results, Geotextiles and Geomembranes 11: 479-488

Narejo D (2004) Long-term performance consideration for geonet drainage geocomposites, GeoQeubec2004, Session 6D: 12-15

Proceedings of the 4th Asian Regional Conference on Geosynthetics
June 17 - 20, 2008 Shanghai, China

GAS PERMEABILITY OF HYBRID GEOSYNTHETICS FOR LANDFILL CAP COVER

M. Nishimura[1], T. Akai[2] and M. Kamon[3]

ABSTRACT: Landfill cap covers that suppress water infiltration to the waste and promote rapidly gas permeation at the same time are demanded. We have developed hybrid geosynthetics that consist of porous sheet and nonwoven geotextiles as landfill cap covers and their basic performances have been investigated by laboratory and field tests. In this study, gas permeability of porous sheets was evaluated by laboratory test. Field test was also conducted to examine gas permeability of the hybrid geosynthetics installed in the underground. In both tests, variation of substitution rate of nitrogen gas with time at both spaces divided by the sample was investigated, while nitrogen gas was introduced to one side of the spaces. As the results, it was clarified that porous sheets themselves are suggested to have sufficient fundamental characteristics on permeability of gases with chemically-inactive and sufficiently small in molecular size. It was also demonstrated that hybrid geosynthetics exhibits gas permeability even when installed in the underground.

KEYWORDS: landfill cap cover, hybrid geosynthetics, gas permeability, unsteady-state system, field test

INTRODUCTION

Appropriate cap covers with environmentally safe and secure features are necessary for landfill sites in which waste storage is finished (e.g., Robert MK and David ED 1997). In Japan, as landfill sites were considered to be a kind of in-situ bioreactor up to now, water permeable materials have been used for the landfill cap cover to accelerate stabilization by biodegradation of waste, and so-called "washing-effect" with meteoric water which commingles with breakdown products of the waste constituents to create leachate. However, recent advances on incineration technologies for reducing the waste have gradually lowered the necessity of the biodegradation process in landfill sites. In addition, since management cost rises as generating leachate increases, stricter countermeasure against environmental pollution risk is required.

On the other hand, degradation of constituents in landfill site produces several gases which arise from stored waste, and gas venting system is usually provided. As it also costs so much for maintenance and management of the system, and the time period until when redevelopment of the site becomes possible is so long, improved gas venting system is desired.

Under those situations, landfill cap covers that suppress water infiltration to the waste and promote rapidly gas permeation at the same time are demanded (Ishikawa et al. 2000). We have developed hybrid geo-synthetics that consist of porous sheet and nonwoven geotextiles as landfill cap covers and their basic performances have been investigated by laboratory and construction tests (Nishimura et al. 2006, 2007a).

In this study, fundamental characteristics on gas permeability of porous sheets were evaluated by laboratory test. Field test was also conducted to examine gas permeability of the hybrid geosynthetics installed in the underground. Since it is quite difficult to evaluate the gas permeability of inherently gas permeable materials in steady- state system, we adopted the experimental setups in unsteady-state system for each test and investigated variation of substitution rate of nitrogen (N_2) gas with time at both spaces divided by the sample, while N_2 gas was introduced to one side of the spaces.

TESTING CONDITIONS

Material Used

In this study, we used polyolefin porous film of 1.0×10^{-4} m in thick and coated fabric of 3.4×10^{-4} m in thick as porous sheets that exhibit waterproof and gas permeability. Triple-layered hybrid geosynthetics (shown in Fig. 1) was also produced from the polyolefin porous film and needle-punched nonwoven geotextiles (0.3 kg/m^2 in mass per unit area) which protect the porous film by laminating to both surfaces of the porous film.

[1] Researcher, Technology Research Institute of Osaka Prefecture, JAPAN. Email: m_nishimura@tri.pref.osaka.jp
[2] Senior Researcher, Technology Research Institute of Osaka Prefecture, JAPAN. Email: akai@tri.pref.osaka.jp
[3] Professor, Graduate School of Global Environmental Studies, Kyoto University, JAPAN. Email: kamon@mbox.kudpc.kyoto-u.ac.jp

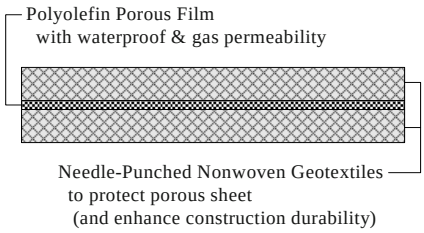

Fig. 1 Schematic illustration for hybrid geosynthetics used in this study

Laboratory Test

Fig. 2 shows the schematic of apparatus used in the laboratory tests. In our previous study (Nishimura et al. 2006), carbon dioxide (CO_2) gas which is one of the gases that can be produced from stored waste in the landfill sites had been used to examine gas permeability of porous sheets. However, in this study, we selected N_2 gas as a testing gas of laboratory test so as not only to examine on the same gas as was also used in the field test described below but also to check the effect of the difference in the type of gas on gas permeability of porous sheets.

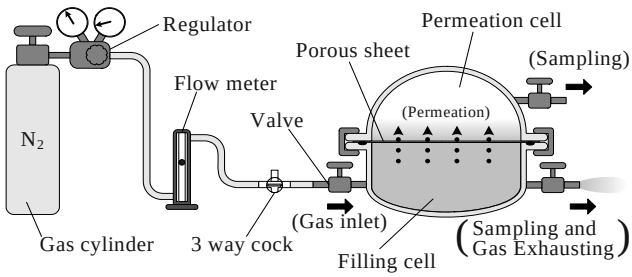

Fig. 2 Schematic of apparatus used in laboratory test

N_2 gas was introduced to "filling cell" with constant flow rate and permeated to "permeation cell" through the porous sheet while N_2 gas was partially exhausted from filling cell into the atmosphere with air which originally existed in the cell. Since filling cell was open system, both cells were kept under the atmospheric pressure. Thus N_2 gas permeated the sheet without total pressure gradient. Table 1 shows representative conditions in this laboratory test.

Table 1 Representative conditions in laboratory test

Gas permeation area of sample [m^2]		4.2×10^{-2}
Volume of cell [m^3]	Filling cell	4.0×10^{-3}
	Permeation cell	2.4×10^{-3}
Gas flow rate [m^3/s]		8.3×10^{-6}

Volume fractions of oxygen (O_2) gas, $f(t)$[-], at both cells were measured with time (t[s]) by pulling out the small amount of gas in the cell at regular time intervals and let it through the gas detector tubes (GASTEC Corporation). As original volume fraction of O_2 gas in the cell ($f(0)$[-]) was considered to be consistent with that in the atmosphere (0.209), substitution rate of N_2 gas, $x(t)$[-], was defined as

$$x(t) = 1 - f(t)/f(0) = 1 - f(t)/0.209 \quad (1)$$

and we evaluated the gas permeability of porous sheets by examining variation of substitution rate of N_2 gas with time.

Variations of substitution rate of N_2 gas with time were verified with polyolefin porous film and coated fabric. In addition, measurements were also carried out with LLDPE geomembrane of 1.5×10^{-3} m in thickness which was considered not to permeate the gas, and the case with no sample (blank) whose gas permeability was considered to be infinity for comparison.

Field Test

For application of hybrid geosynthetics to real landfill sites, it is assumed that soil layers are installed under and over the hybrid geosynthetics. To verify the gas permeability of hybrid geosynthetics installed in the underground, field test was conducted under three cases that (a) hybrid geosynthetics, (b) no sample (blank), (c) HDPE geomembrane of 1.7×10^{-3} in thickness, was installed in the underground. Fig. 3 shows the schematic illustration of experimental setup for the field test.

In the field test, N_2 gas was employed as a testing gas considering its safety and convenience, while CO_2 gas is not convenient to be supplied continuously into the underground in the outdoor field at well-controlled and relatively high flow rate because CO_2 is usually liquefied in the gas cylinder. N_2 gas was introduced to the center of the crushed stone layer with constant flow rate (8.3×10^{-4} m^3/s). Volume fractions of O_2 gas, $f(t)$[-], at several measuring points were measured with time (t[s]) by using O_2 gas sensors (MIJ-03, Environmental Measurement Japan Co., Ltd.) and gas detector tubes. Substitution rates of N_2 gas ($x(t)$[-]) at several measuring points with time were then derived from Eq. 1. Fig. 4 shows measuring points of volume fraction of O_2 gas.

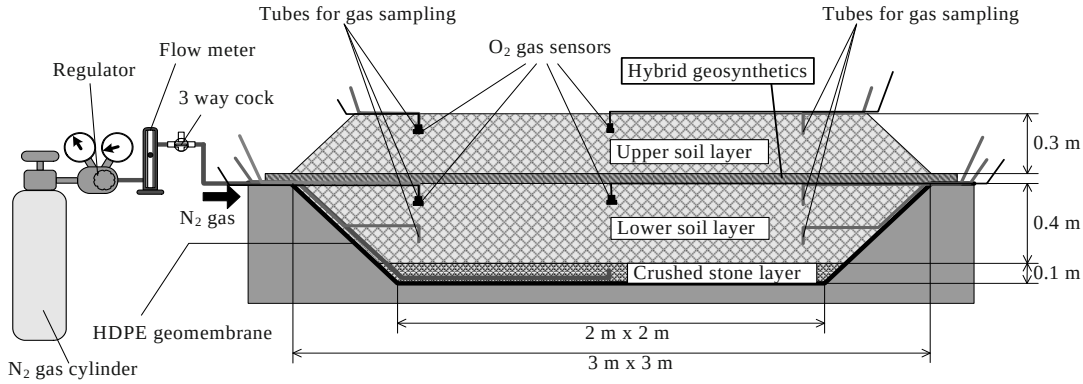

Fig. 3 Schematic illustration of experimental setup for the field test

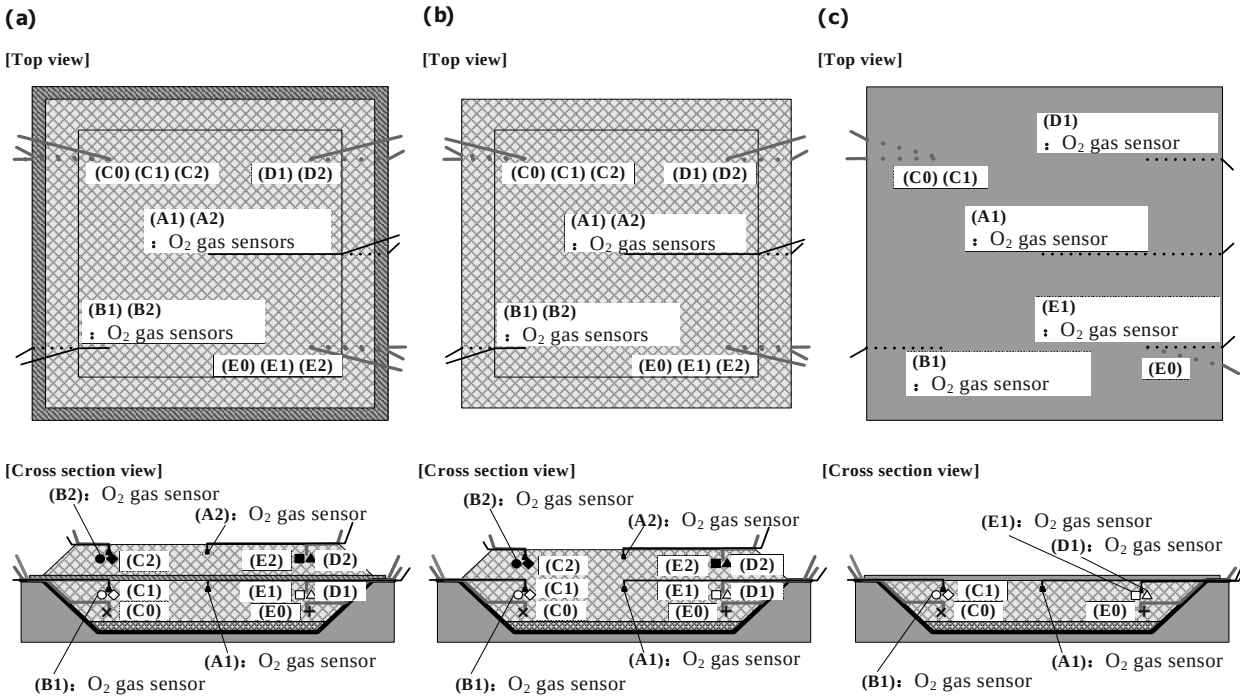

Fig. 4 Measuring points of volume fraction of O_2 gas in the field test: (a) hybrid geosynthetics, (b) no sample (blank), (c) HDPE geomembrane was installed

Three ponds were developed in the test field and their side walls and bottom were covered with HDPE geomembrane of 1.7×10^{-3} m in thickness not to leak gas out of the ponds. For each pond, single-sized crushed stone (S-30) was first installed on the bottom, and decomposed granite soil was then spread, flattened and compacted on this "crushed stone layer" to form "lower soil layer". After installing hybrid geosynthetics and HDPE geomembrane on the lower soil layer of pond (a) and pond (c) respectively, "upper soil layer" as a role of cover soil was accumulated on the hybrid geosynthetics of pond (a) and lower soil layer of pond (b). For the case that HDPE geomembrane was laid on lower soil layer (pond (c)), we did not install upper soil layer on HDPE geomembrane to observe the appearance of gas dome that could be formed with expanding of gas-impermeable geomembrane by introduced gas.

Figs. 5 and 6 show grain size distribution curve and compacting curve for decomposed granite soil used in the field test respectively. As had been revealed that gas diffusivity of soil layer is affected by the degree of compaction and water content of it (Nishimura et al. 2007b), both lower and upper soil layer were designed to be prepared within the hatching region in Fig. 6.

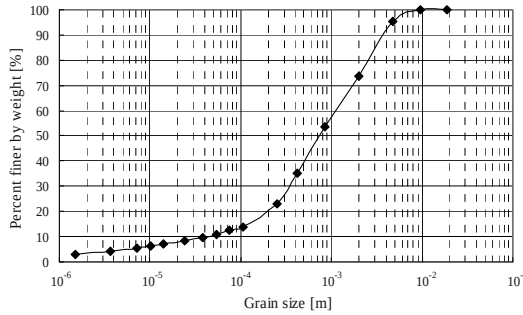

Fig. 5 Grain size distribution curve for decomposed granite soil

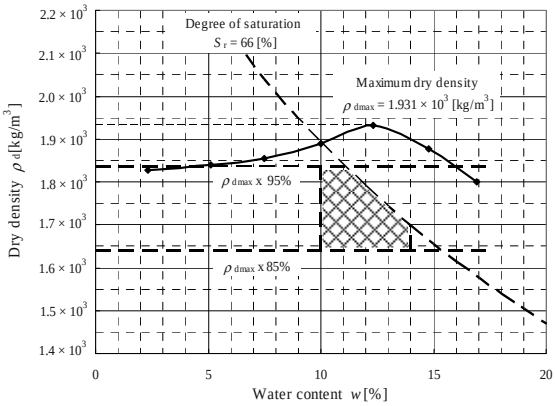

Fig. 6 Compaction curve for decomposed granite soil

RESULTS AND DISCUSSION

Substitution Rate of Porous Sheet

Fig. 7 shows variation of substitution rate of N_2 gas with time at (a) filling cell and (b) permeation cell for each case. Gas permeability of polyolefin porous film was almost equal to the blank condition without the sample. Coated fabric also exhibited gas permeability, though the performance on gas permeability was lower than that of polyolefin porous film. From these results, we employed polyolefin porous film as a porous sheet that constitutes hybrid geosynthetics used in the field test.

Furthermore, Fig. 7 exhibited similar trends which described above as those obtained in our previous study (Nishimura et al. 2006) using CO_2 gas with the same apparatus as shown in Fig. 2. Therefore it was supposed that porous sheets, especially polyolefin porous film, exhibit sufficient gas permeability at least for the gases of chemically-inactive and sufficiently small in molecular size.

Field Test Results

Fig. 8 shows pictures of the field test. Fig. 9 also shows variation of substitution rate of N_2 gas with time at several measuring points (shown in Fig. 4).

At first, substitution rate of N_2 gas at upper soil layer increased with time regardless of whether hybrid geosynthetics was installed. Therefore it was demonstrated that hybrid geosynthetics which consist of polyolefin porous film and needle-punched nonwoven geotextiles exhibits gas permeability even when installed in the underground.

Secondly, rapidity of increase in substitution rate varied depending on the measuring points even if they were on the same level in the soil layers. This tendency was significant in the lower soil layer. N_2 gas introduced was supposed to be diffuse faster along the interface between the soil layer and side wall of the pond than to the vertical direction through the soil layer.

In addition, at the pond that HDPE geomembrane was installed on the lower soil layer, HDPE geomembrane was gradually expanding as time advanced to be like a gas dome, which can be appeared in case failure in gas venting system occurs in the landfill site (shown in Fig. 8b).

Meanwhile, both time and difference of substitution rates at lower and upper soil layer, which correspond to concentration gradient, is considered to complexly influence diffusion/permeation process of N_2 gas. Furthermore, substitution rate varied depending on the measuring points in this large-scale experimental system.

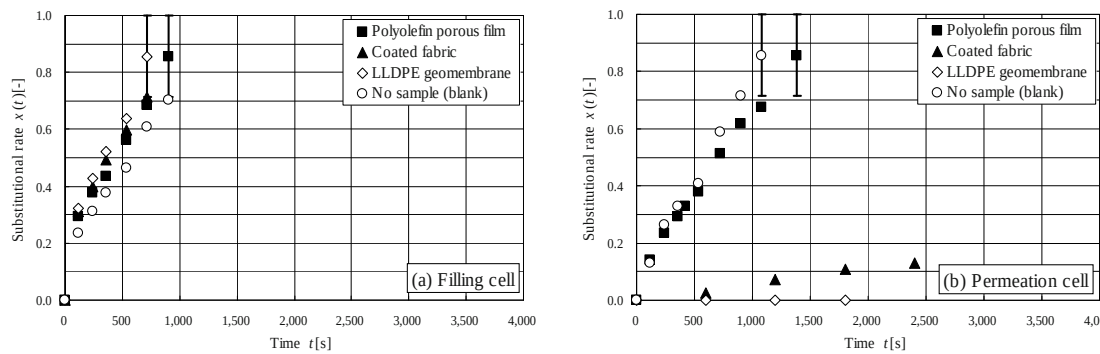

Fig. 7 Variation of substitution rate of N_2 gas with time at (a) filling cell and (b) permeation cell in the laboratory test

Fig. 8 Pictures of the field test: (a) hybrid geosynthetics, (b) HDPE geomembrane was installed

So it is difficult to discuss the gas permeability of hybrid geosynthetics installed in the underground only by comparing Fig. 9a and b. Thus we focused on substitution rates at the center of lower and upper soil layer for further consideration.

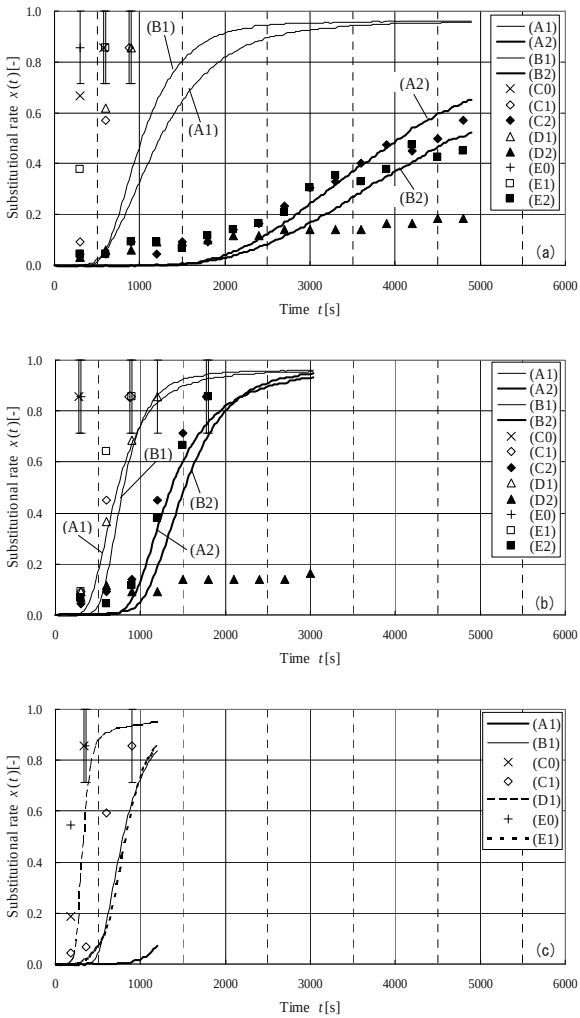

Fig. 9 Variation of substitution rate of N_2 gas at several measuring points with time for 3 cases in the field test: (a) hybrid geosynthetics, (b) no sample (blank), (c) HDPE geomembrane was installed

Fig. 10 shows relationships between substitution rates at the center of upper soil layer ($x_{A2}(t)$) and those in lower soil layer ($x_{A1}(t)$). The dashed line in Fig. 10 corresponds to the ideal condition that there is no difference in substitution rates of lower and upper soil layer and that gas permeation resistance of the total experimental system is assumed to be zero. Therefore, the deviation of experimental curves shown in Fig. 10 from the dashed line relates to gas permeation resistance for each system, and it was suggested that gas permeation resistance increased by installing hybrid geosynthetics when compared with the blank condition.

However, since experimental curves for the case that hybrid geosynthetics was installed rose sharply and $x_{A2}(t)$ was supposed to reach asymptotically close to 1 at the region where $x_{A1}(t)$>0.9, hybrid geosynthetics was expected to exhibit sufficient gas permeability even if substitution rate in the lower soil layer increased rapidly like this experimental system. On the other hand, substitution rate of lower soil layer in real landfill site is assumed not to increase so rapidly. Consequently, hybrid geosynthetics was considered to have sufficient gas permeability and be available to apply practically to landfill sites.

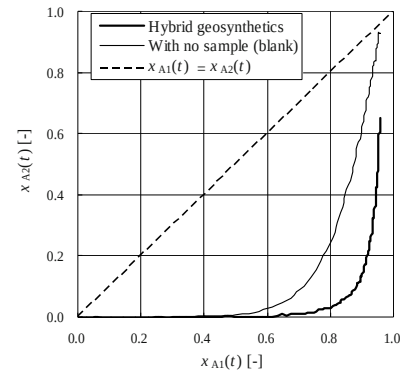

Fig. 10 Relationships between substitution rates at the center of upper soil layer ($x_{A2}(t)$) and those in lower soil layer ($x_{A1}(t)$)

CONCLUSION

Fundamental characteristics on gas permeability of porous sheets which constitutes hybrid geosynthetics for landfill cap covers were evaluated by laboratory test. Field test was also conducted to examine gas permeability of the hybrid geosynthetics installed in the underground.

Results in the laboratory test shows that porous sheets, especially polyolefin porous film, were suggested to exhibit sufficient gas permeability of gases with chemically-inactive and sufficiently small in molecular size. Thus polyolefin porous film was employed as a porous sheet that constitutes hybrid geosynthetics used in the field test.

From the results in the field test, it was demonstrated that hybrid geosynthetics also exhibits good characteristics on gas permeability even when installed in the underground.

ACKNOWLEDGEMENTS

This study was supported by Capping Working Group, Japanese Association of Geosynthetics. The authors wish to thank all members participating in this working group.

REFERENCES

Ishikawa M, Ueda S, Esaki K, Ohno F, Banno S, Maeda A (2000) Final Covers. In Committee on geo-membrane technologies, JCIGS (Edited), Handbook for Design and Construction of Landfill Site-Liner Technologies, Ohmsha, Japan: 119-122 (in Japanese)

Koerner RM, Daniel DE (1997) Introduction. In: Final Covers for Solid Waste Landfills and Abandoned Dumps, ASCE., USA: 1-39

Nishimura M, Akai T, Wada S, Nambu Y, Kamon M (2006) Characteristics and construction durability on hybrid geosynthetics for capping of landfill site. Geosynthetics Engineering Journal, Vol. 21, JCIGS., Japan: 285-290 (in Japanese)

Nishimura M, Akai T, Negishi K, Ishida M, Wada S, Nambu Y, Kamon M (2007a) Characteristics and construction durability on hybrid geosynthetics for capping of landfill site. Proc. of the 7th Japanese-Korean-French Seminar on Geo-Environmental Engineering, GEE07, Grenoble: 85-91

Nishimura M, Akai T, Wada S, Nambu Y, Asada T, Kamon M (2007b) Gas Permeability of Hybrid Geosynthetics for Landfill Cap Cover Installed in the Underground. Geosynthetics Engineering Journal, Vol. 22, JCIGS. Japan: 133-138 (in Japanese)

Proceedings of the 4th Asian Regional Conference on Geosynthetics
June 17 - 20, 2008 Shanghai, China

ANALYSIS OF TENSION OF GEOMEMBRANES PLACED ON LANDFILL SLOPES

S.J. Feng[1], and L.Y. Gao[2]

ABSTRACT: In engineered landfills, geomembranes are commonly used to isolate waste from the surrounding ground and groundwater in order to minimize the potential groundwater contamination. On the sides of a landfill, geomembranes are placed on prepared sloped surfaces and anchored at the crest level. Subsequent construction of a landfill includes the placement of soil cover and waste layers up various heights over these liners. This can result in application of substantial down-slope shear stresses on the geomembranes leading to development of significant geomembrane tension which is necessary to be studied so as to ensure the safety use. In this paper, three-states elastic-plastic model is presented to simulate the shear deformation property for the geomembrane-clay interface, and the governing differential equations of three states are got. Because the demarcation points among three states are unknown, the iterative computation method should be used to compute the tension of geomembrane. Finally, the important factors, including overburden height, slope gradient and geomembrane parameters, which influence the tension of geomembrane, are studied.

KEYWORDS: geomembane, interface, soften, tension, residual strength

INTRODUCTION

In engineered landfills, geomembranes are commonly used to minimize the potential contamination of the geo-environment. Since the landfills generally involve filling of a natural or man-made depression within the ground with wastes, these liners are provided at the sides and the bases of the facilities to form effective barriers to contaminant migration from waste into groundwater. This paper focuses on the placement of geomembranes over the side slopes with anchorage at the crest level. In practice, the compacted clay liners are constructed on the prepared slopes of the natural ground and then place the geomenbrane liners on the clay surface. Subsequent construction of the landfill includes the placement of soil cover and waste layers up to various heights above the geomembrane liners. It follows then that these geomembrane liners may develop substantial tensile stresses owing to the shear stresses exerted by the overburden soil and wastes on the slopes. Geomembranes have limited tesile strength and therefore, should be protected from high tensile stresses in order to ensure their long term integrity as barriers (Jayantha K, 2000; Koerner RM,1997).

To date, two approaches were predominantly employed to analyze this issue; namely, the limit equilibrium method as in traditional slope stability analysis (e.g.; Giroud and Beech 1989; Koerner and Hwu 1991) and the load-displacement analysis such as finite element method (e.g., Gilbert et al. 1993; Daniel and Koerner 1998), and finite difference method (Deng et al. 2007). In the first approach, the liner system is assumed to be at the verge of failure, and the tension which will develop within the liner is computed by considering the equilibrium of mobilized forces. The method ignores the stress-strain relationship of the liner interface. Due to the strain-softening nature of interface between geomembrane and clay, as the shear displacement increases, shear stress would first reach its maximum value, and then gradually decreases to the residual value. All of the above has made it obvious, that the gradual development of tension in the geomembranes can never be analysed using the limit equilibrium method. The second method is more general and rigorous, but requires detailed parameters representation of the slope and materials, and is time consuming. Except the two main methods, Jayantha (2000) presented a simplified analysis method, which was useful for design purposes. But in the analysis, the application of ideal elastic-plastic model in simulating the shear deformation characteristics of the interface would be inappropriate. The current paper develops simplified analytic solutions for the analysis of tension development in this type of geomembrane application, and in the model, the shear stress versus displacement relationship for interface between geomembrane and clay is divided into three states, including elastic one, softening one and residual strength one.

[1] Ph.D,Lecturer, Department of Geotechnical Engineering,Tongji University, CHINA. Email: fsjgly@mail.tongji.edu.cn
[2] Ph.D, Department of Building Engineering, Tongji University, CHINA. Email: xixi-gao@sohu.com

CALCULATION MODEL

As shown in Fig. 1, landfill side slopes are usually formed in several benches with intermediate berms providing anchorage for each lining segments. This figure shows the situation of the landfill slopes after filling with wastes. At present, the composite liner system including various materials like geomembranes, geonets, geotextiles and etc., which will serve specific functions such as drainage and filtering, may exist between the wastes and the clay base. During the construction of the lanfill, filling would take place by layers and blocks, successively covering each bench until the designed height is reached. Thanks to the high compressibility of wastes, shear stresses induced by the wastes settlement deformation are transferred through different interfaces in the composite lining system, and finally to the geomembrane-clay interface. For simplification, all overburden materials are seen as a single one, due to the fact that the friction angles at interfaces between geonets and geotextiles, and between gemembranes and the former two materials, are much greater than the one at the geomembrane-clay interface (Jayantha 2000). Thus, it is assumed that the normal stresses and shear ones prompted by overburden wastes would be acted directly on the geomembranes, without consideration of the shear function between geonets and geotextiles in the composite lining system (Zhang et al, 2004a, b).

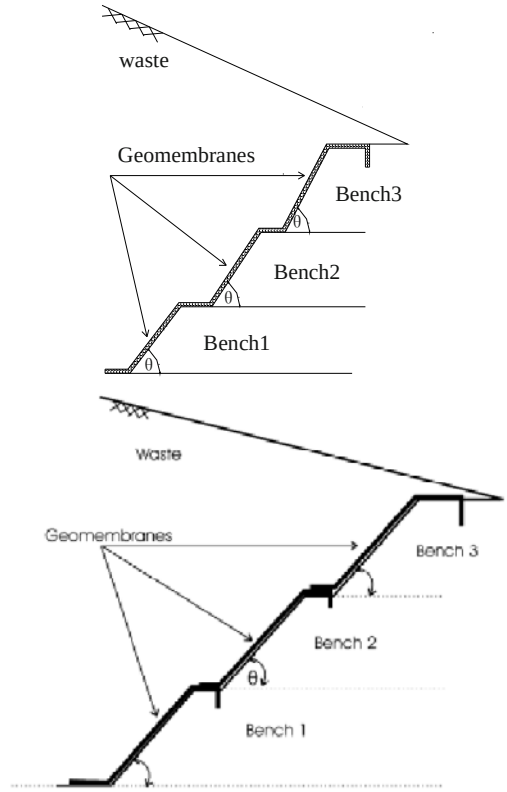

Fig. 1 Schematic diagram of geomembrane liner (Jayantha 2000)

A general idealization model featuring a single bench is shown in Fig. 2. Considering a small element of geomembrane as illustrated in Fig. 3. Assumption is that the geomembrane maintains elastic state, so the governing differential equations can be expressed as follows (Jayantha 2000):

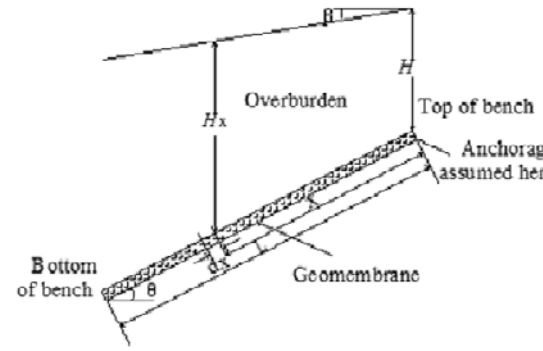

Fig. 2 General idealization of geomembrane liner Placement (Jayantha 2000)

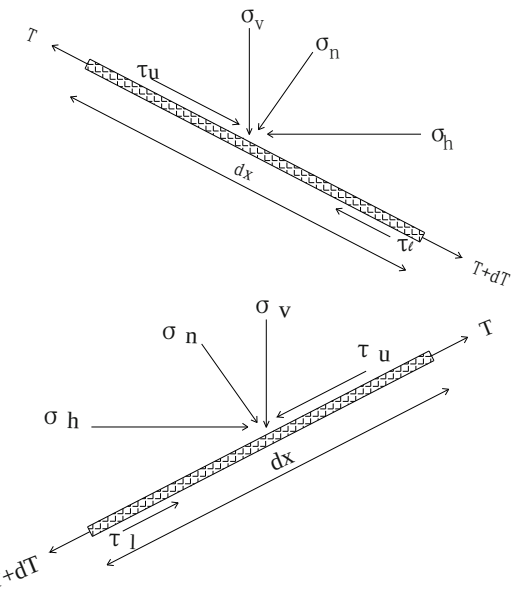

Fig. 3 Stresses on a small geomembrane element (Jayantha 2000)

$$\frac{\mathrm{d}T}{\mathrm{d}x} = \tau_l - \tau_u \tag{1}$$

$$\frac{\mathrm{d}u}{\mathrm{d}x} = \frac{T}{tE} \tag{2}$$

$$\frac{\mathrm{d}^2u}{\mathrm{d}x^2} = \frac{1}{tE}(\tau_l - \tau_u) \tag{3}$$

where u is the displacement of the geomembrane liner at distance x from the anchorage, T is the tension force of the geomembrane liner at distance x from the anchorage, t is the thickness of the geomembrance, E is the Young's

modulus of the geomembrane, τ_u is the shear stress on the upper interface at distance x from the anchorage, and τ_l is the shear stress on the lower interface at distance x from the anchorage.

With reference to Figs. 2 and 3, the vertical stress σ_v and horizontal stress σ_h above the liner can be assumed as:

$$\sigma_v = H_x\gamma = (H + x\sin\theta - x\cos\theta\tan\beta)\gamma \quad (4)$$

$$\sigma_h = K_x\sigma_v \quad (5)$$

where K_x is the coefficient of earth pressure at rest, H is the height of overburden wastes, β is the slope gradient of the waste top surface, θ is the slope gradient at bench surfacebottom, γ represents the average unit weight of overburden materials, it is assumed that the liquid pressure above the liner is not significant enough to take into account.

Assuming that the vertical and horizontal stress system represents the principal stress system for the medium above the liner, normal stress σ_n and shear stress τ_u at the upper side of geomembrane can be expressed by Eqs. 6) and 7 as

$$\begin{aligned}\sigma_n &= \sigma_v\cos^2\theta + \sigma_h\sin^2\theta \\ &= (K_x\sin^2\theta + \cos^2\theta)(H + x\sin\theta - x\cos\theta\tan\beta)\gamma\end{aligned} \quad (6)$$

$$\begin{aligned}\tau_u &= 0.5(\sigma_v - \sigma_h)\sin 2\theta \\ &= 0.5(1 - K_x)(H + x\sin\theta - x\cos\theta\tan\beta)\gamma\sin 2\theta\end{aligned} \quad (7)$$

The shear stresses on the lower interface will depend on stress-strain characteristics of geomembrane-clay interface. As a generally accepted conclusion of numerous tests conducted by many researches, the stress-strain relationship of the geomembrane-clay interface can be catalogued as the strain-softening type. In this paper, the three- states elastic-plastic model is put forward to represent the shear deformation characteristics of geomembrane-clay interface, as depicted in Fig. 4.

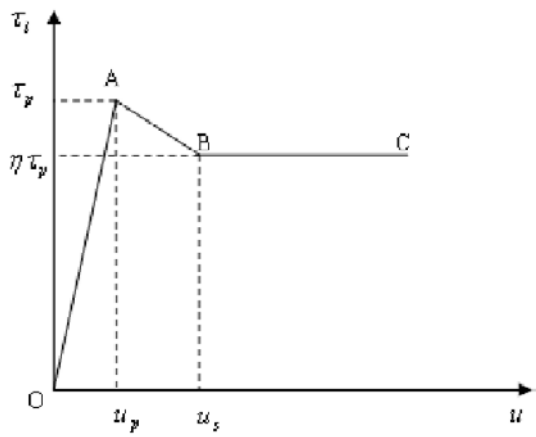

Fig. 4 Schematic plan of the shear stress versus displacement relationship for interface between geomembrane and clay

As illustrated in Fig. 4, line OA represents the elastic state, line AB the softening state and line BC the residual strength one. Shear stresses on the geomembrane-clay interface at different shear state can be expressed as:

$$\tau_l = k_p u, \qquad u \le u_p \quad (8)$$

$$\tau_l = (1 + k_s/k_p)\tau_p - k_s u, \qquad u_p < u \le [(1 + k_s/k_p - \eta)\tau_p]/k_s = u_s \quad (9)$$

$$\tau_l = \eta\tau_p, \qquad u \ge [(1 + k_s/k_p - \eta)\tau_p]/k_s \quad (10)$$

where k_{sp} is the slope of initial line OA (elastic state), k_{ps} is the slope of line AB (softening state),η is the ratio of residual to peak shear stress on geomembrane-clay interface, u_p is the deformation corresponding to peak shear stress, τ_p is the peak shear stress at the lower side of geomembrane, which can be expressed by the Mohr-Coulomb strength criterion as Eq. 11,

$$\tau_p = \sigma_n\tan\varphi_l + c_l \quad (11)$$

where φ_l is the friction angle of geomembrane-clay interface, c_l is the cohesion of geomembrane-clay interface.

SOLUTION TO GOVERNING EQUATIONS

Through respective substitution of the piecewise function representing the shear stress on the geomembrane-clay interface, into the governing equations for tensile stress of geomembrane, and in addition, through introduction of boundary conditions, displacements and tensile stresses for the three states, the elastic, the softening and the residual strength, would be obtained. Because the demarcation points among three states are unknown, the iterative computation method should be used to compute the tension of geomembrane. For easy calculation, non-dimensional forms of the governing differential equations are adopted, the chosen non-dimension variables are

$$\chi_p = \sqrt{\frac{k_p L^2}{tE}}, \quad \chi_s = \sqrt{\frac{k_s L^2}{tE}}, \quad u^* = \frac{u}{L}, \quad T^* = \frac{T}{tE},$$

$$H^* = \frac{H}{L}, \quad c_l^* = \frac{c_l}{\gamma L}, \quad \lambda = \frac{\gamma L^2}{tE}, \quad x^* = \frac{x}{L}.$$

$$\chi_p = \sqrt{\frac{k_p L^2}{tE}}, \quad \chi_s = \sqrt{\frac{k_s L^2}{tE}} \quad (12a)$$

$$x^* = \frac{x}{L}, \quad u^* = \frac{u}{L}, \quad u_p^* = \frac{u_p}{L}, \quad u_s^* = \frac{u_s}{L},$$

$$l_p = \frac{L_p}{L}, \quad l_s = \frac{L_s}{L}, \quad H^* = \frac{H}{L} \quad (12b)$$

$$T^* = \frac{T}{tE}, \quad c_l^* = \frac{c_l}{\gamma L}, \quad \lambda = \frac{\gamma L^2}{tE} \quad (12c)$$

where L is the length of the geomembrane on the slope.

Elastic State

By substituting Eqs. 7 and 8 into Eq. 3 and take the non-dimensional form as

$$\frac{\mathrm{d}^2u^*}{\mathrm{d}x^{*2}} - \chi_p^2 u^* = -\chi_p^2(C_p x^* + D_p) \tag{13}$$

In combination with the boundary conditions for elastic state, the solution is obtained as

$$u^*(x^*) = A_{1p}\cosh(\chi_p x^*) + B_{1p}\sinh(\chi_p x^*) + C_p x^* + D_p, (0 \le x^* \le 1) \tag{14a}$$

$$T^*(x^*) = A_{1p}\chi_p \sinh(\chi_p x^*) + B_{1p}\chi_p \cosh(\chi_p x^*) + C_p, 0 \le x^* \le 1) \tag{14b}$$

$$u^* = Ae^{\chi_1 x^*} + Be^{-\chi_1 x^*} - \frac{Mx^* + N}{\chi_1^2}$$

$$T^* = A\chi_1 e^{\chi_1 x^*} - B\chi_1 e^{-\chi_1 x^*} - \frac{M}{\chi_1^2}$$

where M, $A_{1p}N$, B_{1p},AC_p, and B D_p are calculation parameters.

Softening State

By substituting Eqs. 7 and 9 into Eq. 3 and take the non-dimensional form as

$$\frac{d^2u^*}{dx^{*2}} + \chi_s^2 u^* = \chi_s^2\left(C_s x^* + D_s\right)$$

$$\frac{d^2u^*}{dx^{*2}} + \chi_2 u^* = M_1 x^* + N_1 \tag{15}$$

In combination with the boundary conditions for softening state, the solution is obtained as

$$u^*(x^*) = A_{2s}\cos(\chi_s x^*) + B_{2s}\sin(\chi_s x^*) + C_s x^* + D_s, \quad (l_p \le x^* \le 1) \tag{16a}$$

$$T^*(x^*) = -A_{2s}\chi_s \sin(\chi_s x^*) + B_{2s}\chi_s \cos(\chi_s x^*) + C_s, \quad (l_p \le x^* \le 1) \tag{16b}$$

$$u^* = C_1\cos(\chi_2 x^*) + C_2\sin(\chi_2 x^*) + \frac{M_1 x^*}{\chi_2^2} + \frac{N_1}{\chi_2^2}$$

$$T^* = -C_1\chi_2 \sin(\chi_2 x^*) + C_2\chi_2 \cos(\chi_2 x^*) + \frac{M_1}{\chi_2^2}$$

where MA_{12s}, NB_{12s}, C_{1s}, and CD_{s2} are calculation parameters.

Residual Strength State

By substituting Eqs. 7 and 10 into Eq. 3 and take the non-dimensional form as

$$\frac{\mathrm{d}^2u^*}{\mathrm{d}x^{*2}} = C_r x^* + D_r \tag{17}$$

In combination with the boundary conditions for residual strength state, the solution is obtained as

$$u^* = \frac{C_r}{6}x^{*3} + \frac{D_r}{2}x^{*2} + A_{3r}x^* + B_{3r}, (l_s \le x* \le 1) \tag{18a}$$

$$T^* = \frac{C_r}{2}x^{*2} + D_r x^* + A_{3r}, (l_s \le x^* \le 1) \tag{18b}$$

$$u^* = \frac{M_2 x^{*2}}{6} + \frac{N_2 x^{*2}}{2} + C_3 x^* + C_4$$

$$T^* = \frac{M_2 x^{*2}}{2} + N_2 x^* + C_3 \tag{19}$$

where MA_{23r}, NB_{23r}, C_{3r}, and CD_{r4} are calculation parameters.

ANALYSIS OF GEOMEMBRANE TENSION

The tension of the geomembrane can be obtained based on the previous derivation and solution. Vulnerability occurs at the anchorage point of the geomembrane, where the tension is the greatest and failure is most likely to take place. The following analysis will mainly focus on the maximum tension in the geomembrane. For basic working condition, the parameters are taken as:

- the average unit weight of overburden materials γ= 1.5×10^4 kN/m^3
- the slope gradient of the waste top surface β= 15°
- the thickness of geomembrane t = 1.5 mm
- the shear stiffness of geomembrane-clay interface at elastic state K_s k_p= 1.0×10^7 Pa10^7 N/m^3
- the shear stiffness of geomembrane-caly interface at softening state K_p k_s = 8.0×10^6 N/m^{3}Pa

Once the plastic state is reached, the strength reducing factor is taken as 0.6, the friction angle of the interface as 12° and the cohesion as 0 kPa. There are a number of variables influencing the maximum tension of geomembrane, such as slope gradient, overburden wastes height and the non-dimensional variable λ, the following analysis will concentrate on those influencing factors. Fig. 5 illustrates the maximum tension versus slope gradient curve when K_x=0.5 and L=30 m. Under the same overburden height, the more the slope gradient goes, the more the maximum tension of geomembrane increases. As the overburden height mounts, the slope of the curve gradually increases.

Fig. 6 shows the relationship between the maximum tension and the non-dimensional variable λ under different landfill slope gradients. The maximum tension of geomembrane gradually increases as λ grows, in addition, the slope of maximum tension versus λ curve grows as the landfill slope increases. As soon as the slope gradient θ reaches 30^o, the pace of the maximum tension increment induced by slope gradient growth

slows down remarkably, clearly demonstrating that the residual strength state is reached for some parts of the grows as the landfill slope increases. As soon as the slope gradient θ reaches 30°, the pace of the maximum tension increment induced by slope gradient growth slows down remarkably, clearly demonstrating that the residual strength state is reached for some parts of the geomembrane-clay interface. With successive increment of the slope gradient θ, the residual strength state would basically dominant the geomembrane-clay interface, resulting in little maximum tension increment with θ.

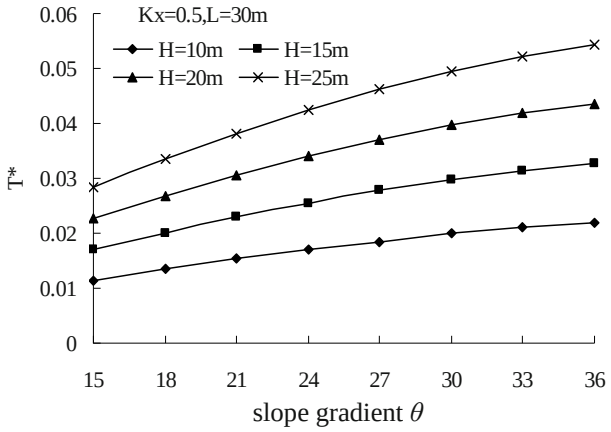

Fig. 5 Variation of maximum tension of geomembrane with slope gradient

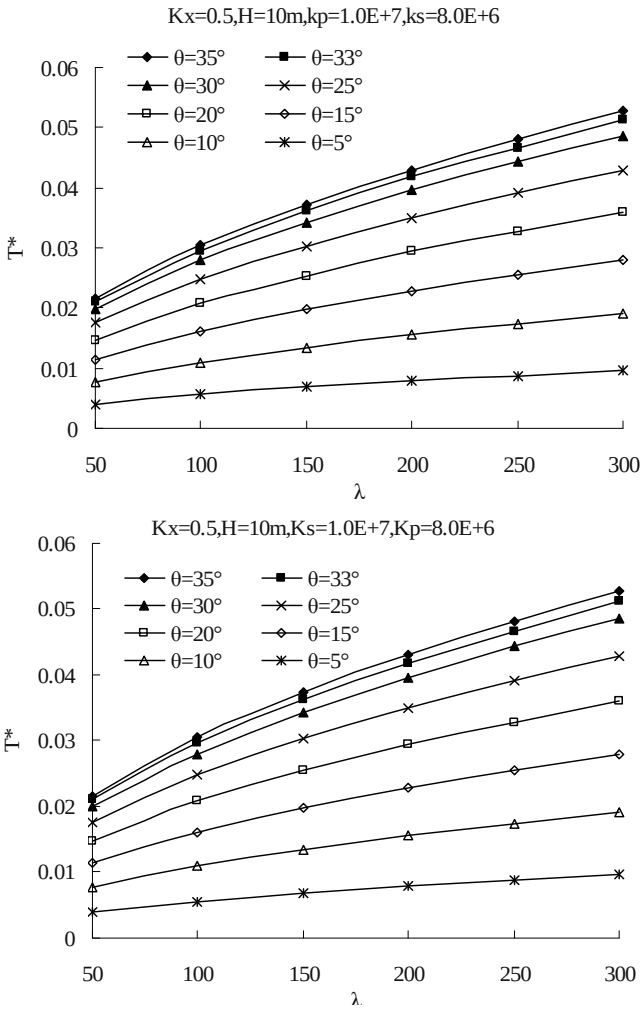

Fig. 6 Variation of maximum tension of geomembrane with nondimensional parameter λ

CONCLUSIONS

Three-statesThree-state elastic-plastic model is presented to simulate the shear deformation property for the geomembrane-clay interface, and the governing differential equations of three states are got. Because the demarcation points among three states are unknown, the iterative computation method should be used to compute the tension of geomembrane. As the landfill slope gradient increases, the maximum tension of geomembrane gradually grows. Once the slope gradient exceeds a certain value, the pace of the maximum tension increment induced by slope gradient growth slows down remarkably, clearly demonstrating that the residual strength state is reached for some parts of the geomembrane-clay interface. With successive increment of slope gradient, the residual strength state would basically dominant the geomembrane-clay interface, resulting in no maximum tension increment with slope gradient.

ACKNOWLEDGEMENTS

Much of the work described in this paper was supported by the National Natural Science Foundation of China under Grant Nos. 50708079， the research fund for the doctoral program of higher education (20070247041), Shanghai twilight program(2007CG23), the Program for Young Excellent Talents in Tongji University, and the Everbright Environment Innovation Fund. These financial supports are gratefully acknowledged.

REFERENCES

Daniel DE, Koerner RM (1998) Slope stability of geosynthetic clay liner test plots. Journal of Geotechnical and Geoenvironment Engineering 204 (7):628-637

Deng XJ, Kong XJ, Zou DG (2007) Calculation of tension in HDPE geotechnical membrane under complicated loads. Chinese Journal of Geotechnical Engineering 29 (3): 447-451 (in Chinese)

Gilbert RB, Long JH, Daly JJ (1993) Structural integrity

of composite geosynthetic lining and cover systems. Geosynthetics'93 Conference Proceedings Canada: 1389-1401

Giroud JP, Beech JF (1989) Stability of soil layers on geosynthetic lining systems. Geosynthetics'89 Conference Proceedings California: 35-46

Jayantha K (2000) Analysis of tension development in geomembranes placed on landfill slopes. Geotexiles and Geomembranes 18(1):47-61

Koerner R M (1997) Designing with Geosynthetics, 4th Ed. Prentice Hall, Englewood Cliffs, NJ, U.S.A.

Koerner RM, Hwu BL (1991) Stability and tension considerations regarding cover soils on geomembrane lined slopes. Geotextiles and Geomembraues 10(4):335-355

Zhang P, Wang JH, Chen JJ (2004a) Mechanical behavior of the interface between reinforcement and soil in pull-out tests on geotextiles. Journal of Shanghai Jiaotong University 38 (6):999-1002 (in Chinese)

Zhang P, Wang JH, Chen JJ (2004b) Analysis of tension and displacement of geomembranes placed on landfill slopes. Rock and Soil Mechanics 25 (5):789-792(in Chinese)

Daniel DE, Koerner RM (1998) Slope stability of geosynthetic clay liner test plots. Journal of Geotechnical and Geoenvironment Engineering, 204 (7):628-637

Deng XJ, Kong XJ, Zou DG(2007) Calculation of tension in HDPE geotechnical membrane under complicated loads. Chinese Journal of Geotechnical Engineering.29 (3): 447-451(in Chinese)

Gilbert RB, Long JH, Daly JJ (1993) Structural integrity of composite geosynthetic lining and cover systems. Geosynthetics'93 Conference Proceedings Canada: 1389-1401

Giroud JP, Beech JF (1989) Stability of soil layers on geosynthetic lining systems. Geosynthetics'89 Conference Proceedings. California: 35-46

Jayantha K (2000) Analysis of tension development in geomembranes placed on landfill slopes. Geotexiles and Geomembranes, 18(1): 47-61

Koerner RM (1997) Designing with Geosynthetics, 4th Ed. Prentice Hall, Englewood Cliffs, NJ, USA

Koerner R.M. and Hwu B.L.(1991). Stability and tension considerations regarding cover soils on geomembrane lined slopes. Geotextiles and Geomembraues 10(4):335-355.

Zhang P,Wang JH, Chen JJ (2004a) Mechanical behavior of the interface between reinforcement and soil in pull-out tests on geotextiles. Journal of Shanghai Jiaotong University 38 (6): 999-1002 (in Chinese)

Zhang P, Wang JH, Chen JJ(2004b) Analysis of tension and displacement of geomembranes placed on landfill slopes. Rock and Soil Mechanics 25(5): 789-792(in Chinese)

Proceedings of the 4th Asian Regional Conference on Geosynthetics
June 17 - 20, 2008 Shanghai, China

INFLUENCE OF WASTE AND SUBGRADE SETTLEMENT ON LANDFILL LINIER STABILITY AND INTEGRITY

C. Xu [1], Y.Y. Xiao [2], X.Y. Liao [3] and T.T. Chen[4]

ABSTRACT: The design of landfill on soft sub-grade should consider the stability of the waste and sub-grade. Because of the waste and subgrade settlements, the long-term integrity of the lining system also should be taken into account during the design period. A landfill built on soft soil foundation was analyzed, both global stability and local failure resulted from the loss of lining integrity due to the waste and subgrade settlement were considered here. Limit equilibrium technique was used as a method of assessing the global stability of landfill. Results presented in this paper demonstrate that traditional limit equilibrium technique is uncapable to assess local failure. The assessment of integrity requires knowledge of the interaction between components of the lining system and the waste body as it settles. Numerical model was used to assess local instability. The results show that the differential settlement of sub-grade influences the waste stability and the lining system integrity.

KEYWORDS: municipal solid waste (MSW) landfill, lining system, subgrade settlement, numerical analysis

INTRODUCTION

Geosynthetics are widely used as part of the barrier system in modern Municipal Solid Waste (MSW) landfill facilities. Geosynthetics are used in landfill on soft clayey soils not only to reinforce the stability of landfill but also to prevent the migration of leachate and the uncontrolled escape of landfill gas.

The design methods generally used are based on failure calculation or limit equilibrium concepts (Koerner and Hwu 1991). Failure can be defined in terms of two states (Jones and Dixon 2005): ultimate limit state, where there is a complete loss of stability or function (e.g. slope failure); and serviceability limit state such that the function of a structure is impaired (e.g., stressing of a landfill liner leading to increased permeability).

For landfill lining systems using geosynthetics, stability and integrity are both influenced by the shear strength between the various interfaces, i.e., geosynthetic/ geosynthetic and geosynthetic/soil. The shear strength developed at a geosynthetic interface is due to the waste overburden loads, waste settlement and consolidation (downdrag forces), and subgrade settlement. The mobilised shear strength will vary along the interface. Most geosynthetic interfaces are susceptible to strain softening, and a reduction in shear stress at displacements beyond peak strengths. This cannot be modeled by limit equilibrium approach.

Numerical modeling can be used to assess the shear stresses mobilized at strain softening geosynthetic interfaces for a range of waste properties. Long-term degradation controlled waste settlements plays an important role on lining system behaviour. Meibner and Abel (2000) presented results for numerical modeling of tensile stresses in a geomembrane basal and side slope liner resulting from waste degradation. Unfortunately, the model employed to represent the interface was not strain softening. Long et al. (1995) presented an approach to assess the integrity of all components in a lining system. But it is based on an assumption of waste settlement profile along the side slope. Jones et al. (2005) assessed the potential for loss of integrity due to geomembrane protection being compromised. But the approach used didn't consider the influence of subgrade settlement.

All of the above methods are capable of providing useful information that can be used to assess the stability and/or integrity of side slope lining system components during construction and subsequent degradation, and hence settlement of the waste body. However to date, none of the approaches can be used to assess the influence of subgrade settlement on landfill lining

[1]Prof., Ph.D. Key Laboratory of Geotechnical Engineering, Tongji University, CHINA. Email: c_axu@mail.tongji.edu.cn
[2]MS, CAAC New Era Airport Design& Research Institute Co. Ltd, Shanghai, .CHINA. Email: xiaoxiao1104@hotmail.com
[3]Ph.D Student, Key Laboratory of Geotechnical Engineering, Tongji University, CHINA. Email: liaoxingyue@gmail.com
[4]MS Student Key Laboratory of Geotechnical Engineering, Tongji University, CHINA. Email: titi88chen@yahoo.com.cn

stability and integrity. But landfills built on soft subgrade would have large differential settlements. This paper will present an investigation on the possibility of loss of protection to the geomembrane resulting from protection layer deformation and shear failure. In the analyses, the influence of waste and subgrade settlement will be considered.

NUMERICAL ANALYSIS

Numerical analyses were carried out using the finite difference code FLAC^{3D}, version 2.1 (Itasca). The analysis is illustrated using a conceptual case: a waste landfill built on thick soft subgrade in Shanghai area, as there's no suitable solid site available in Shanghai territory for waste landfill construction.

Model Construction

The model used in this paper simulates the behaviour of the strain softening geomembrane/geotextile interface in response to MSW landfill settlement. Shear strengths mobilised at the geosynthetic interface on the side slope and the base have been calculated in response to stresses induced in the lining system by the long-term settlement of the waste body and the soft subgrade. The material properties for the baseline conditions are given in Table 1. An elastic-plastic constitutive model was used for the waste and the subgrade soils with a Mohr–Coulomb failure criterion. The interface is assumed to be in a drained condition with zero pore water pressures.

Finite difference meshes used in the analyses are shown in Fig. 1. All zones within the mesh are free to move in any direction, with the exception of some boundaries. The boundary beneath the subgrade is fixed in both horizontal and vertical directions, and the boundaries on the side of the subgrade are fixed in horizontal directions. This represents the case where the geosynthetic elements of the lining system are underlain by soft clay subgrade. The model comprises a series of basal and side slope interfaces overlain by waste body.

Parameters Selection

The geometry of the conceptual model is supposed (see Fig. 1 and Table 1). The properties of the subgrade are present in Table 2, which are taken from Foundation Design Code of Shanghai (DGJ08-11-1999).

The waste physical and mechanical properties are determined by the waste components, compaction technique and its degration. Values of waste strength summarized by Jones et al. (1997) are for a range of different waste materials and test methods. The waste parameters used in this study are selected based on the test results of the waste of in Shanghai city and Zhejiang Province, China.

Interface shear strengths are modeled using the conventional parameters of friction angle (δ) and apparent adhesion intercept (α). The approach was presented by Jones et al. (2005). The interface frictional properties of the base interface are the results of laboratory tests carried out using a 300mm direct shear apparatus. The interface frictional properties of the side interfaces are the results of laboratory tests carried out using the tilt table device. We consider that the tilt table device can measure interface frictional properties between lining system components factually realizing the field condition of slope of landfill, where normal stress is low.

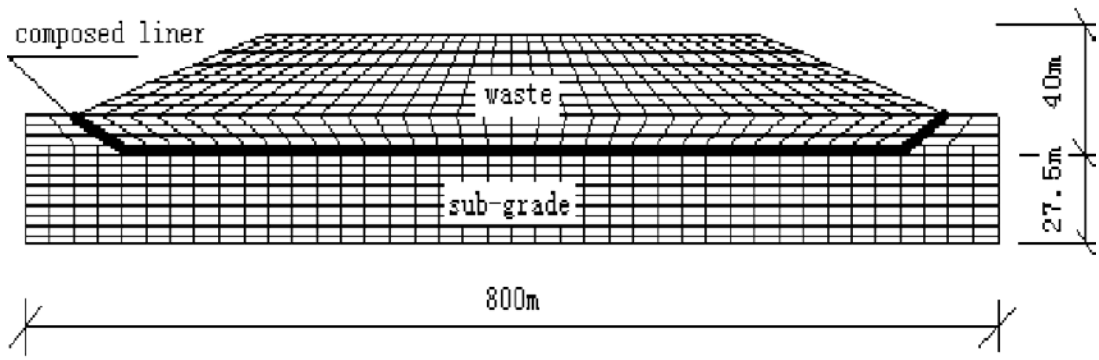

Fig. 1 Mesh layout and geometry of the example landfill

Table 1 Inputs for numerical analysis of baseline condition

Material	Property	Value
Geometry	Waste slope	1 in 3
	Side slope	1 in 2
	Waste height	40
	soft clay sub-grade depth	27.5
Subgrade (material beneath interfaces)	Young's modulus	$E = (1-2\mu^2/(1-\mu))E_s$
	Poisson's ratio	0.25
Waste	Young's modulus	500 kPa
	Poisson's ratio	0.3
	Density	1200 kg/m^3
	Friction angle	10
	Cohesion	15 kPa
Base interface	Interface shear stiffness	3000 kPa
	Interface normal stiffness	30000 kPa
	Peak friction angle	23.1°
	Peak cohesion intercept	3.2 kPa
	Residual friction angle	11.6°
	Residual cohesion intercept	2.5 kPa
Side slope interfaces	Interface shear stiffness	3000 kPa
	Interface normal stiffness	30000 kPa
	Peak friction angle	18.6°
	Peak cohesion intercept	0.26
	Residual friction angle	13.6°
	Residual cohesion intercept	0.23

Table 2 Properties of the example landfill subgrade soils

Soil layer No.	Soil Type	Thickness (m)	Bulk unit weight (kN/m^3)	$E_{s,0.1-0.2}$ (MPa)
2	Sandy silt	1.5	16.6	3.5
3	Mucky silty clay	7.5	18.2	4.0
4	Mucky clay	10.0	16.6	2.0
5	Clay	8.5	17.7	4.5
6	Silty clay	1.0	18.9	7.5
7-1	Sandy silt	4.5	18.5	12.0

COMPARISONS AND ANALYSES

Comparison of Limit Equilibrium and Numerical Analyses

The Limit Equilibrium (LE) analysis technique was used to assess stability of a landfill in the process of waste placement. The peak interface parameters on the base and the residual values on the side slope were used to account for the influence of waste settlement (Jones et al. 2005). The LE slope stability program QimStar Slope 1.0 was used to assess the stability of landfill. The results are presented in Table 3.

In case 1, the interface relative displacement and the mobilised shear stress along the side and base are small (see Fig. 2), so the calculated factors of safety from numerical analyses is still more than 1.2(see Table 4). The landfill is stable. But in case 2, the waste settlement (downdrag forces) and subgrade settlement are very large. It causes an integrity failure of the side slope lining system due to the loss of geomembrane protection through geotextile tensile failure or inadequate overlap between sheets, and would cause the rupture of any overlying drainage layer. This integrity failure mechanism cannot be predicted by the LE analysis.

Therefore, the concept of using peak shear strengths along the base and the residual strengths along the side slope seems to take account of waste settlement along the slope and would be expected to produce a conservative estimate of global stability.

Table 3 Calculated factors of safety from LE analyses

Case	Waste height (m)	Calculated factors of safety
Case 1	20	1.8
Case 2	40	1.2

Table 4 Factors of safety from numerical analyses

Case	Waste height (m)	Calculated factors of safety
Case 1	20	1.3
Case 2	40	<1.0

Subgrade Settlement

The subgrade settlement was considered in the numerical analysis in cases 1 and 2. Case 3 was added to simulate a condition the same as case 2, except for the subgrade condition. In case 3, the geosynthetic elements of the lining system are underlain by stiff and stable substrata. The calculated results of mobilized stress along the side interface in three cases are presented in Fig. 2. it is can be seen that mobilized shear stress in case 3 is less than that in case 2.

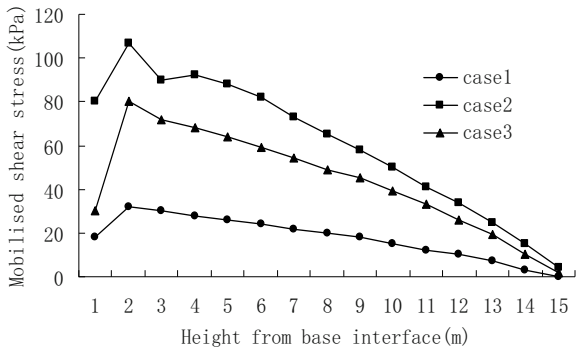

Fig. 2 Results of numerical analysis: Mobilised shear stress of side interface

Supposed that the waste height is 40m before the closure of the landfill, and the landfill foundation is composed of soft soils, the calculated settlement of subgrade cross the landfill is presented in Fig. 3. The results show that the settlement of subgrade under the landfill side is much smaller than that in the center. The differential settlement of subgrade would make the relative displacement in the lining system and between the lining material and soil around. This relative displacement can cause shear stress even more than the shear strength concerned. Therefore, The influence of the differential settlement of subgrade on the lining system stability and integrity should be considered in the design stage of waste landfill on soft subgrade.

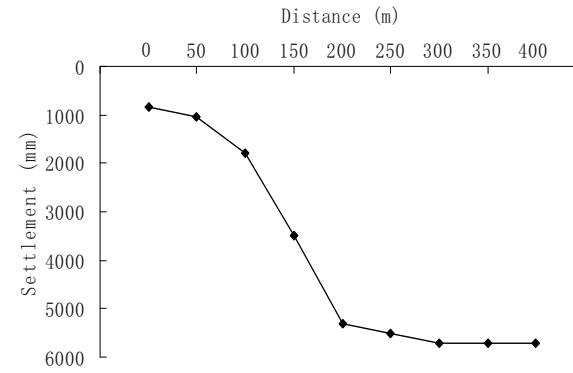

Fig. 3 Settlement vs. distance from the toe to the landfill center in case 2

CONCLUSIONS

Based on conceptual model of the landfill built on soft subgrade, an investigation into the interaction between waste and a geosynthetic landfill lining system has been undertaken to assess conditions of global stability and integrity failure. Stability has been assessed by both limit equilibrium analyses and numerical analyses. Strain softening behaviour of geosynthetic interfaces has been incorporated in the numerical model. The shear strength mobilized at the interface between geomembrane and geotextile components resulting from long-term waste settlement and subgrade settlement has been assessed.

Results show that Limit equilibrium analysis cannot be used to assess local instability of the lining system and the waste body on the side slope. Numerical analysis has demonstrated that waste settlement and subgrade settlement can result in slippage between lining components on the side slope even though the global stability factor of safety is adequate. Large displacements of the protection layer above the geomembrane can be considered and causes a local failure within lining system, as it would lead to loss of protection and hence integrity failure of the lining system. Numerical techniques that can model waste/barrier interaction and strain softening features of the interface should be used for such assessments. The design of WSM landfill on soft soils should consider the influence of the differential settlement of subgrade on the lining system function.

REFERENCES

David EB, Grahame F,Edward M (1995) Landfill settlement and the impact on site capacity and refuse

hydraulic conductivity. Waste Management & Research 13: 533-554

Jones DRV, Dixon N (1998) Shear strength properties of geomembrane/geotextile interfaces. Geotextiles and Geomembranes 16: 45-71

Jones DRV, Dixon N (2005) Landfill lining stability and integrity: the role of waste settlement. Geotextiles and Geomembranes 23: 27-53

Kocrner R, Hwu BL (1991) Stability and tension consideration regarding cover soils on geomembrane lined slopes. Geotextiles and Geomembranes 10: 335-355

Liu Z, Mei G, Zai J (2004) Calculation of oedometric modulus of soil and its application based on the routine soil test. Journal of Nanjing University of Technology 26: 5-8

Villard P, Gourc JP, Feki N (1999) Analysis of geosynthetic lining systems (GLS) undergoing large deformations. Geotextiles and Geomembranes 17: 17-32

ANALYSES OF GEOMEMBRANE AROUND CIRCULAR STRUCTURES

D. Gao[1], B. Zhu[2] and Y.M. Chen[3]

ABSTRACT: For the geomembrane around circular structures, a simplified model is presented to analyze its tensions and strains subjected to a differential settlement based on the conventional membrane theory. It is found that wrinkles will be induced in the geomembrane due to the negative in-plane compressive stress. Further, an improved analysis model was given based on the wrinkled membrane theory by introducing the concept of "variable Poisson's ratio". Calculated results using the simplified model and the improved model are compared. Parametric studies show that minimizing the differential settlement and using flexible geomembranes in the landfill, can limit the maximum tension in the geomembrane to allowable levels and reduce its behaved degree of wrinkles.

KEYWORDS: geomembrane, circular structure, differential settlement, tension, strain, wrinkle

INTRODUCTION

Geomembranes are commonly used materials in geotechnical and geoenvironmental engineering for separations. Such applications are landfill liners, landfill covers, liquid impoundment liners, etc. Usually, the geomembrane is supported by a compressible medium, such as soil and waste, and are often connected to the rigid structure (e.g. pipes, intake towers, water gate structures or manhole shafts) (Giroud and Soderman 1995). The compressible medium may settles due to degradation, its own weight or the overlying pressure applied on the geomemebrane. Thus differential settlement will be induced between the compressible medium and the rigid structure, which can result in tensions and strains in the geomembrane. If the tensions and strains exceed the tensile capacity of the geomembrane, tension cracks or tensile failure will develop in the geomembrane and the effectiveness of the liner served as a hydraulic barrier will be reduced.

The analyses of the tensions and strains in the geomembrane connected to rigid infinite long structures has been firstly reported by Giroud and Soderman (1995). Some engineering measurements have been suggested to decrease the tensions and strains in the geomembrane to allowable levels. It appeared that battering the structure's walls connected to geomembranes was an effective solution. Considering the length of the rigid structure is very large, the problem was two-dimensional (2D) and the geomembrane is in a plane-strain state. In a landfill, geomembranes are usually connected to rigid circular structures (e.g., gas venting well, monitoring well or manhole riser) (Fig. 1).

Fig. 1 Connection between geomembrane and gas venting well

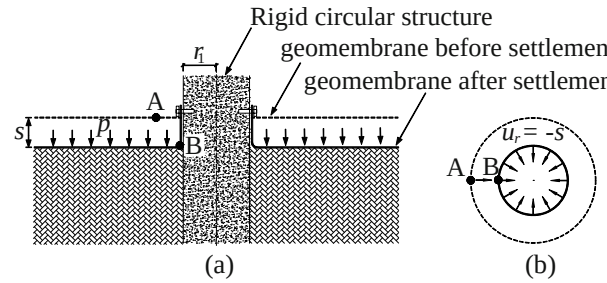

Fig. 2 Deformation of geomembrane around circular structure (a: vertical deformation; b: radial deformation)

If the geomembrane has a relatively small modulus or the overlying pressure is large enough, the geomembrane will almost remain in contact with the circular structure and the supporting soil due to a differential settlement, so that point A in the geomembrane may move to point

[1] Ph.D Student, Department of Civil Engineering, Zhejiang University, CHINA. Email:gaodengdeng@zju.edu.cn
[2] Ph.D, Department of Civil Engineering, Zhejiang University, CHINA. Email:binzhu@zju.edu.cn
[3] Professor, Department of Civil Engineering, Zhejiang University, CHINA. Email:chenyunmin@zju.edu.cn

B finally as shown in Fig. 2. As the circumference of the concentric circle passing point A is larger than that of the concentric circle passing point B, large in-plane compressive stress will be generated in the geomembrane close to the circular structure, which may induce out-of-plane large deformation in the geomembrane and wrinkles will be exhibited. Due to the complicated mechanism of wrinkles, any study and analysis model has not been given in existing literatures to deal with this axisymmetric problem considering wrinkles induced in the geomembrane. In view of this, the tensions and strains in the geomembrane around the circular structure subjected to a differential settlement are analyzed in this paper based on membrane theory and some useful conclusions are drawn.

SIMPLIFIED MODEL

Assumption

As shown in Fig. 2a, the surface of the medium supporting the geomembrane is assumed to be horizontal and the geomembrane is uniformly loaded by a vertical pressure p. The differential settlement s between the circular structure and compressible medium is uniform in the horizontal plane. The radius of the circular structure is r_1. The geomembrane has no bending stiffness and deforms sufficiently to remain completely in contract with the circular structure, thus, the total elongation of the geomembrane in the radial direction is equal to the differential settlement (Giroud and Soderman 1995). In addition, the tension-strain curve for the geomembrane is assumed to be linear.

It can be simplified as an axisymmetric problem: an infinite hollow geomembrane with the hollow radius r_1 laid between the overlying and underlying mediums. The inner boundaries are subjected to the uniform radial displacement u_r which is equal to s (Fig. 2b).

Fundamental Equations

In the conventional membrane theory (Huang 1985), the fundamental equations for the geomembrane element in axisymmetric deformations can be written as follows:

$$T_r = \frac{Et}{(1-\nu^2)}(\varepsilon_r + \nu\varepsilon_\theta) \tag{1}$$

$$T_\theta = \frac{Et}{(1-\nu^2)}(\varepsilon_\theta + \nu\varepsilon_r) \tag{2}$$

$$\varepsilon_r = \frac{du_r}{dr} \tag{3}$$

$$\varepsilon_\theta = \frac{u_r}{r} \tag{4}$$

$$\varepsilon_r = \frac{d}{dr}(r\varepsilon_\theta) \tag{5}$$

where T_r is radial tension, T_θ is circumferential tension, ε_r is radial strain, ε_θ is circumferential strain, r is radial distance from centre of geomembrane, v is Poisson's ratio for geomembrane, E is elastic modulus for geomembrane, t is thickness of geomembrane, and Et is stiffness of geomembrane.

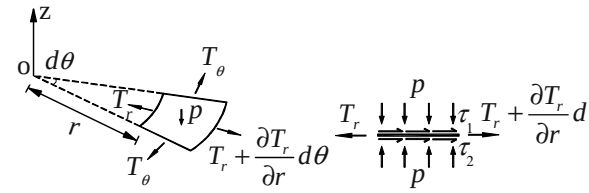

(a) (b)

Fig. 3 Analysis of geomembrane element (a: plane view; b: profile view)

As can be seen from Fig. 3, the force equilibrium equation for the geomembrane element is:

$$\frac{d}{dr}(T_r r) + (\tau_1 + \tau_2)r - T_\theta = 0 \tag{6}$$

where τ_1 is interface shear stress above geomembrane and τ_2 is interface shear stress below geomembrane. These stresses have the following values:

$$\tau_1 = p\tan\varphi_1 \tag{7}$$

$$\tau_2 = p\tan\varphi_2 \tag{8}$$

where φ_1 is friction angle between geomembrane and overlying medium and φ_2 is friction angle between geomembrane and underlying medium. Substituting Eqs. 1—4 into Eq. 6, the following equation can be obtained

$$\frac{d^2u_r}{dr^2}r + \frac{du_r}{dr} - \frac{u_r}{r} + ar = 0 \tag{9}$$

where $a = (\tau_1 + \tau_2)(1-\nu^2)/Et$. Eq. 9 can be solved by introducing two boundary conditions at $r = r_3$: $u_r = 0$ and $\varepsilon_r = du_r/dr = 0$, where r_3 is outer radius of the tensioned region in geomembrane. Its solution is:

$$u_r = -\frac{ar_3^3}{6r} + \frac{ar_3 r}{2} - \frac{ar^2}{3} \tag{10}$$

According to the previous assumption, the radial displacement u_r on the inner boundary of the hollow geomembane is equal to s, that is:

$$-\frac{ar_3^3}{6r_1}+\frac{ar_3r_1}{2}-\frac{ar_1^2}{3}=-s \tag{11}$$

For u_r points to the center, the minus sign appears in right part of Eq. 11. The value of r_3 in Eq. 11 can be calculated analytically as:

$$r_3=\sqrt[3]{A+\sqrt{B}}+\sqrt[3]{A-\sqrt{B}} \tag{12}$$

where $A=3sr_1/a-r_1^3$, $B=9s^2r_1^2/a^2-6sr_1^4/a$. Substituting Eq. 10 into Eqs. 1—4, the tensions and strains in the geomembrane can be determined as:

$$T_r=\frac{(\tau_1+\tau_2)\left[(1-\nu)r_3^3+3(1+\nu)r^2r_3-2(2+\nu)r^3\right]}{6r^2} \tag{13}$$

$$T_\theta=\frac{(\tau_1+\tau_2)\left[(\nu-1)r_3^3+3(1+\nu)r^2r_3-2(1+2\nu)r^3\right]}{6r^2} \tag{14}$$

$$\varepsilon_r=\frac{a}{6r^2}(r_3^3+3r^2r_3-4r^3) \tag{15}$$

$$\varepsilon_\theta=\frac{a}{6r^2}(-r_3^3+3r^2r_3-2r^3) \tag{16}$$

Compututional Example and Induced Wrinkles

A very low density polyethylene (VLDPE) geomembrane with thickness of 1 mm connected to the gas venting well in landfill is considered herein. The material properties of the geomembrane are selected as follows (Qian et al. 2001; Finley and Holtz 2002): The stiffness Et =170 kN/m, ν = 0.45, φ_1 = φ_2 = 30°. The radius of the gas venting well r_1 is 0.5 m. The thickness of the protective layer on the geomembrane is 0.6 m and the overlying pressure p is taken as 10 kPa. The differential settlement s between the underlying waste and the gas venting well is considered to be 0.05 m.

As can be seen from Fig. 4, the tensions and strains in the geomembrane reach the peak values at the edge of the gas venting well. It is interesting that the circumferential tensions in the geomembrane close to the gas venting well are negative, which means that the geomembrane in this region carries the in-plane compressive stress and wrinkles may be induced due to its poor resistance of the in-plane compressive stress, and this region is called the winkled region just as shown in Fig. 5. Outside of the wrinkled region, both of the radial and circumferential tensions are positive so that the geomembrane is in a bidirectional tensioned state and this tensioned region is also given in Fig. 5. Therefore, it may be more reasonable to divide the deformed geomembrane into the wrinkled and tensioned regions, and propose a new improved model to analyze the tensions and strains in the geomembrane considering the effects of wrinkles.

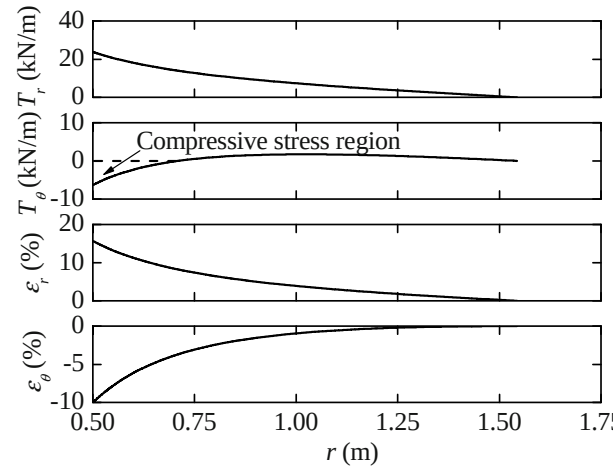

Fig. 4 Distribution of geomembrane tensions and strains based on conventional membrane theory

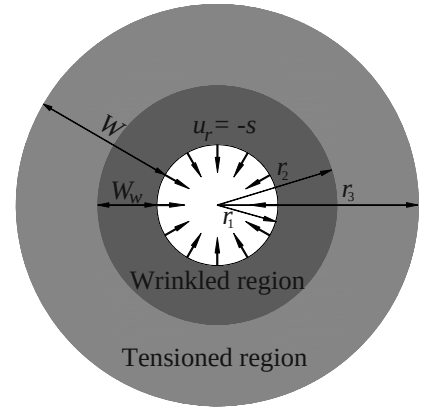

Fig. 5 Distribution of wrinkled and tensioned regions

IMPROVED MODEL CONSIDERING WRINKLES

Wrinkled Membrane Theory

The wrinkled membrane theory was developed by Stein and Hedgepeth (1961). The membrane considered therein is elastic, isotropic, has no bending stiffness and cannot carry compressive stresses. In this theory, if both principal stresses are positive, the membrane is in tension and thus will not be wrinkled. In a wrinkled membrane one principal stress must be zero and the other nonzero. A "variable Poisson's ratio" λ was defined for the "over contraction" behavior of a wrinkled membrane in the direction normal to the wrinkles.

Governing Equations Considering Wrinkles

According to the wrinkled membrane theory, the radial tension T_r is nonzero and the circumferential tension T_θ is zero in the wrinkled region. Substituting $T_\theta = 0$ into Eqs. 1 and 2, the stain-tension relationships of the wrinkled geomembrane can be rewritten as:

$$\varepsilon_r = \frac{T_r}{Et} \tag{17}$$

$$\varepsilon_\theta = -\lambda \frac{T_r}{Et} \tag{18}$$

where λ is the variable Poisson's ratio. At the edge of the wrinkled region connected to the tensioned region, λ must be equal to the real Poisson's ratio v.

Stain-displacement relationships and compatibility of the stains in the wrinkled region are the same as those in the tensioned region as shown in Eqs. 3—5. Substituting $T_\theta = 0$ into Eq. 6, it can be rewritten as:

$$\frac{d}{dr}(T_r r) + (\tau_1 + \tau_2) r = 0 \tag{19}$$

The solution of Eq. 19 is:

$$T_r = \frac{C_1}{r} - \frac{(\tau_1 + \tau_2) r}{2} \tag{20}$$

where C_1 is a constant. T_r should be continuous between the wrinkled and tensioned regions at $r = r_2$, where r_2 is outer radius of wrinkled region in geomembrane. The following equation can be obtained by combining Eqs. 13 and 20

$$C_1 = \frac{(\tau_1 + \tau_2)\left[(1-\nu) r_3^3 + 3(1+\nu) r_2^2 r_3 - (1+2\nu) r_2^3\right]}{6 r_2} \tag{21}$$

Substituting Eqs. 17 and 18 into Eq. 5 gives

$$T_r = -T_r r \frac{d\lambda}{dr} - \lambda \frac{d(T_r r)}{dr} \tag{22}$$

Combining Eqs. 20 and 22, the variable Poisson's ratio λ can be obtained as:

$$\lambda = \frac{-4C_1 \ln r + (\tau_1 + \tau_2) r^2 + 4C_2}{4C_1 - 2(\tau_1 + \tau_2) r^2} \tag{23}$$

where the constant C_2 can be determined by the equation $\lambda = v$ at $r = r_2$, that is:

$$C_2 = (\nu + \ln r_2) C_1 - \frac{1}{4}(1+2\nu)(\tau_1 + \tau_2) r_2^2 \tag{24}$$

The radial displacement u_r can be rewritten as follows from Eqs. 4, 18, 20 and 23

$$u_r = -\frac{\lambda T_r r}{Et} = \frac{\left[4C_1 \ln r - (\tau_1 + \tau_2) r^2 - 4C_2\right]}{4Et} \tag{25}$$

Introducing the two boundary conditions: (1) $u_r = -s$ at $r = r_1$; (2) $T_\theta = 0$ at $r = r_2$, the following equations can be obtained from Eqs. 14 and 25

$$(\nu - 1) r_3^3 + 3(1+\nu) r_2^2 r_3 - 2(1+2\nu) r_2^3 = 0 \tag{26}$$

$$C_1 \ln r_1 - \frac{1}{4}(\tau_1 + \tau_2) r_1^2 - C_2 = -Ets \tag{27}$$

Iterative solving Eqs. 26 and 27 gives the values of r_2 and r_3. Then, the tensions and strains in the wrinkled and tensioned regions can also be computed, respectively.

Results and Comparison

The example in previous section is recomputed based on the improved model. The computed tensions and strains in the geomembrane are shown in Fig. 6, the most difference compared to Fig. 4 is that the value of T_θ remains zero in the wrinkled region and is positive in the tensioned region. The width of the annular wrinkled region W_w is 0.22 m, and the width of the annular deformed region W is 1.06 m. Fig. 7 shows that the variable Poisson's ratio λ in the wrinkled region is larger than the real Poisson's ratio v = 0.45, which means that the geomembrane is "over contraction" in this region. The wrinkled degree of the geomembrane increases with the increasing value of the variable Poisson's ratio. The variable Poisson's ratio reaches the peak value at the edge of the gas venting well where the "over contraction" behavior of the membrane is greatest.

Using the simplified model and the improved model for r_1 =0.5 m, computed width of wrinkled and deformed regions as well as the maximum strain and tension are given in Table 1. The width of deformed region calculated by the improved model is somewhat larger than that by the simplified model, but the maximum strain and tension of the former are a little smaller than those of the latter. It may be concluded that the wrinkles could reduce the maximum strain in geomembrane in some degree. However, the wrinkles will also cause many problems so that they should be avoided or reduced in landfill engineering (Soong and Koerner 1999).

For the radius of the circular structure is infinite, the problem is almost a plane-strain one, and there is no wrinkle in the geomembrane. As shown in Table 1, the computed results by the simplified model are compared with those by Giroud and Soderman (1995). They are in good agreement with each other, which verifies the present model. For the geomembrane in an axisymmetric state (r_1=0.5 m), the maximum tension T_{max} and the maximum strain ε_{max} in the geomembrane are much more than those of a plane-strain one. Thus, more attentions should be paid to the geomembrane connected to the circular structure subjected to a differential settlement.

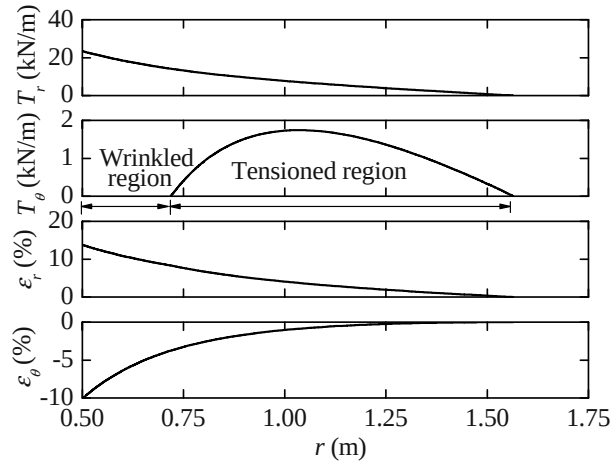

Fig. 6 Distribution of geomembrane tensions and strains considering wrinkles

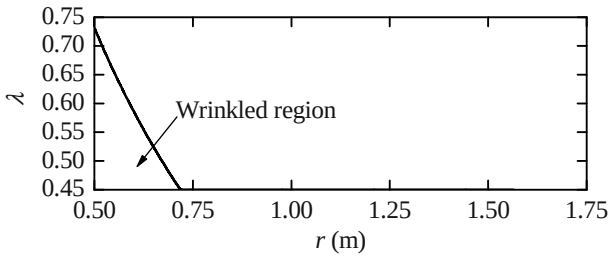

Fig. 7 Distribution of variable Possion's ratio in the wrinkled region

Table 1 Comparison of the computed results

Problems	W_w (m)	W (m)	ε_{max} (%)	T_{max} (kN/m)
Axisymmetric, r_1=0.5 m (Simplified model)	NL	1.04	15.65	23.77
Axisymmetric, r_1=0.5 m (Improved model)	0.22	1.06	13.79	23.44
Axisymmetric, $r_1 \to +\infty$ (Simplified model)	NL	1.36	7.36	15.69
Plane-strain (Giroud and Soderman)	NL	1.21	8.24	14.01

PARAMETRIC STUDIES

Three kinds of geomembranes (Polyvinyl chloride (PVC), LLDPE and HDPE) are selected in the analyses. The tensile stiffness Et is selected to be 76 kN/m, 170 kN/m, 540 kN/m, respectively.

Fig. 8 shows the effects of s on the width of the wrinkled region W_w and the maximum variable Poisson's ratio λ_{max}. It can be seen that the values of W_w and λ_{max} increase with the increasing of s. The stiffness of the geomembrane can influence W_w and λ_{max} heavily. The stiffer is the geomembrane, the larger the values of W_w and λ_{max} will be. Thus, the stiff geomembrane such as HDPE will exhibit wrinkles easier than the flexible geomembrane such as PVC and LLDPE, which have also been indicated by Giroud and Morel (1992).

Fig. 9 shows the effects of s on the maximum tension T_{max} and ε_{max} in the geomembrane. Values of T_{max} and ε_{max} increase rapidly with the increasing of s. The stiffness of the geomembrane can also greatly influence T_{max} and ε_{max}. The stiffer is the geomembrane, the larger T_{max} but the smaller ε_{max} will be induced. It can be explained, by the basic equation $\sigma = E\varepsilon$ or $T = Et\varepsilon$.

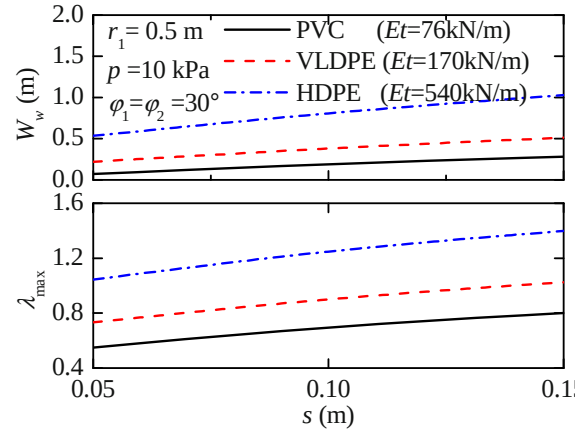

Fig. 8 Effects of differential settlement on width of wrinkled region and maximum Poisson's ratio

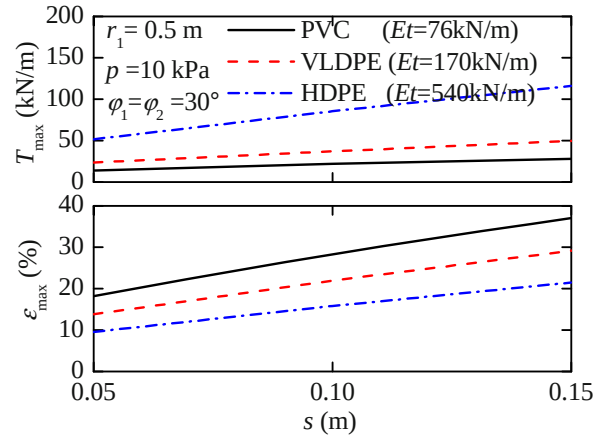

Fig. 9 Effects of differential settlement on maximum tension and strain in geomembrane

In landfills, it should limit the maximum tension and strain in the geomembrane to allowable levels and make efforts to reduce its wrinkled degree. According to the parametric analyses, two effective measures can be used in the engineering practices. One is minimizing the post-settlement of the underlying soil after laying the geomembrane to decrease the maximum tension and strain as well as wrinkled degree of the geomembrane. Dynamic compaction technique has been widely employed in landfills to improve the waste density (Van impe and Bouazza 1996). High leachate level and pore pressure exist within most of uncontrolled landfills in Asia. Lowering the high leachate level will cause a significant settlement in the landfill as a result of an increment to the self-weight stress. A field testing program for this measurement has been carried out in the Suzhou Qizishan Landfill in China. The other measure is using flexible geomembranes such as PVC, LLDPE and VLDPE geomembanes as the hydraulic barrier in landfills. Flexible geomembranes can exhibits high elongation and lower wrinkled degree, allowing them to conform to a large differential settlement. The three kinds of geomembranes mentioned above have been widely used in the final cover system of landfills (Qian et al. 2001).

CONCLUSIONS

For the geomembrane around the circular structure subjected to a differential settlement, a simplified model and an improved model respectively based on the conventional membrane theory and the wrinkled membrane theory are proposed to analyze its tensions and strains. The mechanism of wrinkles induced in the geomembrane is studied, and some parameters affecting the wrinkled degree as well as the tensions and strains are investigated. Following conclusions and discussions are drawn.

(1) The simplified model without considering wrinkles cannot analyze the actual deformation of the geomembrane. The wrinkled degree of the geomembrane can be shown by the width of the wrinkled region and the value of the variable Poisson's ratio computed by the improved model based on the wrinkled membrane theory.

(2) Compared with the plane-strain problem, larger tensions and strains will be induced in the geomembrane around the circular structure subjected to a same differential settlement.

(3) Minimizing the post-settlement of the underlying soil after laying the geomembrane can effectively limit the maximum tension and strain in the geomembrane to allowable levels and reduce its wrinkled degree. In addition, Flexible geomembranes should be used when a large differential settlement will be induced between the geomembrane and the rigid structure.

(4) If the geomembrane has a relatively large modulus or the overlying pressure is not large enough, the geomembrane cannot almost remain in contact with the circular structure and the supporting soil due to a differential settlement in practice. However, the proposed models considering the geomembrane are always in contact with the structure and the underlying medium are conservative, and it is benefit to be used in engineering practice.

ACKNOWLEDGEMENTS

This work were supported by the key fund of the National Natural Science Foundation (research grant: 50538080) and National Distinguished Young Scientist Foundation of China (research grant: 50425825).

REFERENCES

Finley CA, Holtz RD (2001) Investigation and modeling of two composite landfill covers. Geosynthet. Int 8(2):97-112

Giroud JP, Morel N (1992) Analysis of geomembrane wrinkles. Geotex. Geomembr 11:255-276

Giroud JP, Soderman KL (1995) Design of structure connected to geomembranes. Geosynthet. Int 2(3): 379-428

Huang KZ (1987) Plate theory. Tsinghua University Press, BJ

Qian XD, Koerner RM, Gray DH (2001) Geotechnical aspects of landfill design and construction. Prientice Hall, Upper saddle River, NJ

Soong TY, Koerner RM (1999) Behavior of waves in high density polyethylene geomembranes: a laboratory study. Geotex. Geomembr 17:81-104

Stein M, Hedgepeth JM (1961) Analysis of partly wrinkle membrane. Tech. Rep. NASA TN D-813

Van impe WF, Bouazza A (1996) Densification of domestic wast14e fills by dynamic compaction. Can. Geotech. J 33:879-887

NUMERICAL MODELING OF SMOOTH GEOMEMBRANE—SOIL INTERACTION SHEAR BEHAVIOUR BY DISTINCT ELEMENT METHOD

S. Kazempoor[1], A. Noorzad[2], A. Mahboubi[3] and A. Mirghasemi[4]

ABSTRACT: Geomembranes are one of the most widely used geosynthetics in various civil engineering applications. Their primary function is as a barrier to liquid. Smooth geomembranes are frequently used in combination with different soils, and due to their low surface roughness, are challenging to design to ensure adequate shear strength along the smooth geomembrane-soil interface. It is important to use the appropriate values of interface shear strength parameters in the design of slopes incorporating one or more geomembrane in contact with soils. This paper deals with study of smooth geomembrane-soil interfaces with distinct element method (DEM). The various factors that affect the interface shear behaviour are also studied. The models were conducted using direct shear box with PFC code that is a distinct element program. We tried to model the interface by DEM which is capable of modelling the interface and the obtained results show a good concordance with the experiments.

KEYWORDS: geomembrane, distinct element method (DEM), interface

INTRODUCTION

Geomembranes are commonly used as barriers in waste containment facilities and landfills due to various benefits associated with their use(s) and because of regulatory requirements. Geomembranes are also increasingly being used in reservoirs, ponds, lined canals and other geotechnical projects. Geotechnical engineers often characterize the shearing resistance along interface between geomembranes and soils using results from interface direct shear tests. The results of these tests are used in an analysis of stability against sliding along the given interface. Interface shear testing between soil and geosynthetics has now become an essential part of the design process in geotechnical and geo-environmental engineering.

In March 1988, a slope stability failure occurred at the Kettleman Hills Class 1 hazardous waste treatment and storage landfill at Kettleman Hills, California (Byrne et al. 1992). This failure developed by sliding along the interfaces within the composite multilayer liner system beneath the waste fill. The landfill failures given in Table 1 are attributed to low friction resistance at the interface between the geosynthetic and soil. These and other similar landfill failures have led to research into the interface friction behaviour for various interfaces at the liner and cap of the landfill. Many researchers have conducted research work on the interface shear behaviour of geomembranes and soils over the last 20 years. Interface shear strength of non-textured geomembrane and soil represents a significant portion of the research work conducted related to geosynthetics.

Table 1 Summary of Recent Landfill Failures

Year	Location	Quantity involved m^3	References
1988	N. America	490,000	Mitchell, et al. (1990)
1994	Europe	60,000	Koerner and Soong, (2000)
1997	N. America	100,000	Evans, et al. (1998) & Stark et al. (2000)
1997	Africa	300,000	Koerner and Soong, (2000)
1997	S. America	1,200,000	Koerner and Soong, (2000)

This paper deals with study of smooth geomembrane-soil interfaces with distinct element nethod (DEM). The various factors that affect the interface shear behaviour are also studied. The models are conducted using direct shear box with PFC code that is a distinct element program.

GEOTECHNICAL (ANALOGUE) SHEAR TESTS

A sand bentonite mixture was used having 3 % and 6% bentonite in combination with Ottawa sand. The grain size distribution for these materials is as shown in

[1] M.Sc of Geotechnical Eng, Dept of Civil Eng, PWUT, IRAN. Email: S_kazempoor@yahoo.com
[2] Assistance professor, Department of Civil Engineering, PWUT, IRAN. Email: ANoorzad@pwut.ac.ir
[3] Assistance professor, Department of Civil Engineering, PWUT, IRAN. Email: Mahboubi @pwut.ac.ir
[4] Associated professor, Department of Civil Engineering, Tehran University, IRAN.

the Fig. 1.

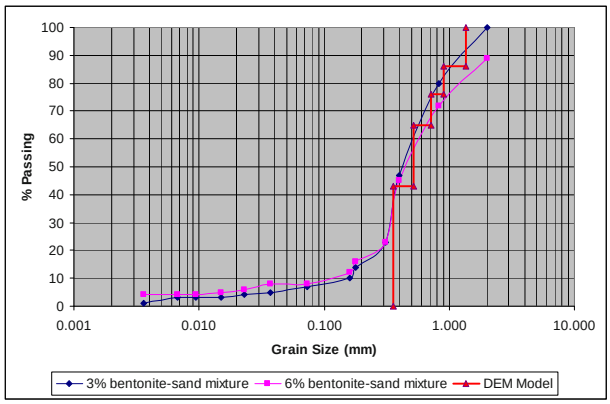

Fig. 1 The grain size distribution of materials

The geomembrane used in the present study was a 60 mil (1.5 mm thick) non-textured, high density polyethylene (HDPE) geomembrane manufactured by GSE Inc., Houston TX, USA.

The interface shear tests were conducted at the Geotechnical Engineering Laboratory of the University of Saskatchewan using a conventional direct shear apparatus (Clockhouse Engineering Ltd. England, Type-K12). A square base direct shear box (100 mm×100 mm) split horizontally at mid-height was used. The total height of the box was 79 mm. Normal stress is applied by placing dead weights on a hanger. Vertical and horizontal displacements are monitored using two Linear Variable Differential Transformers (LVDTs). The rate of shear displacement can be accurately controlled between 0.32 and 48.5 mm per hour. The direct shear box is capable of a maximum shear displacement of 14 mm. Although ASTM D5321-02 (ASTM, 2002) recommends a shear box having base dimensions of 300 mm×300 mm, the use of the box described above can be justified based on the fact that only a non-textured, smooth, geomembrane was used in the present study.

Direct shear testing was carried out on the various soils used (soils only) as well as on the several soil/geomembrane interface combinations. Each test series was performed under 4 normal stresses of 5, 12, 20 and 30 kPa. This range of normal stresses is representative of the range of normal stresses commonly encountered in landfill cover systems, lagoon liners and other common applications.

DISCRETE MODELLING OF DIRECT SHEAR TEST

In this study, to numerical modeling of the direct shear box test, we used the PFC^{2D} V 3.1 (Particle Flow Code, ITASCA Consulting Group).

The Distinct Element Method

The discrete method used is the Distinct Element Method (DEM) pioneered by Cundall. The DEM keeps track of the motion of individual particles and updates any contact with neighboring elements by using a constitutive contact law. The DEM runs according to an explicit time difference scheme. Each calculation cycle includes two stages: the application of a simple interaction law at all particle/particle or particle/wall contacts involving contact force and relative displacement; and the application of Newton's Second Law to determine the particle motion resulting from any unbalanced force. The DEM program used is PFC2D.

The particles are circular, their mechanical interaction is characterized using the soft contact approach. In this approach, although the particles are assumed to be rigid for purposes of shape definition, elastic deformation is allowed to take place at the contacts. The constitutive contact law used in simulations consists of two parts: a stiffness model—providing a linear elastic relation between contact force and contact relative displacement in normal and shear directions—and a slip model—enforcing a relation of Coulomb's type between shear and normal contact forces. Due to the dynamic formulation of the model, energy dissipation through frictional sliding may not be sufficient to reach a steady-state solution.

Additional dissipation can be introduced by using a local non-viscous damping force and moment in the particle equations of motion. This damping is controlled by a constant, which recommended valuẹfor quasi static problems will be used in the simulations presented hereafter.

The DEM is based on a granular model approach. Materials are built up by an assemblage of spherical particles, e.g., discs, spheres, or cylinders, which interact at common contact points in accordance with simple physical contact laws (e.g., Cundall & Strack 1979; Mora & Place 1998; Morgan 1999; Burbidge & Braun 2002). In the case of elastic-frictional contact laws, particles deform elastically under a defined load at a contact point generating a repulsive normal force (F_N) perpendicular to their contact plane. This normal force can be calculated from the particle normal stiffness value (k_N) and the magnitude of elastic deformation which is estimated from the amount of particle overlapping (Mindlin & Deresiewicz 1953; Cundall & Strack 1979; Cundall & Hart 1989; Morgan & Boettcher 1999). This concept applies to shear forces (F_s) as well. F_S increases until it exceeds the critical shear force ($F_{S\max}$)

$$F_{S\max} = C + \mu\ \sigma_N \qquad (1)$$

which leads to frictional sliding. In this case, slip along the contact occurs and F_S drops. σ_N defines acting normal force, C the cohesion, and μ the coefficient of friction for each single particle. The progressive breaking of contacts along discrete planes reproduces fracture and fault propagation (Strayer & Suppe 2002). The critical shear force leading to faulting is analogous to the critical shear stress that governs material strength (τ_{crit}) through the Mohr-Coulomb criterion

$$\tau_{crit} = C + \mu \ \sigma_N \qquad (2)$$

in natural systems (e.g., Morgan & Boettcher 1999). At the end of each time step, summation of all inter-particle contact forces (F_N) acting on a single particle enables the calculation of particle acceleration and thereby the new position of this particle using the Newtonian equation of motion (Cundall & Strack 1979).

As a consequence of the particle approach, material properties are attributed to each individual particle (μ_p) determining particle-particle interactions (Cundall & Strack 1979). Hence, macro-properties of a material package, e.g., "overall" coefficient of friction of a particle assemblage (μ), have to be calculated from shear box experiments (e.g., Morgan 1999). As we used cohesionless, elastico-frictional particles (C=0), the strength of the numerical assemblage is defined primarily by the coefficient of particle friction.

In addition, we implemented "electro-static" forces as a function of particle distance to simulate interactions between "clay" minerals equivalent to their geochemical or mineralogical behaviour in nature (e.g., Matthes 1983). These "electro-static" or so-called van der Waals forces are proportional to $\sim 1/r^6$, where r is the distance between the concerned particles (e.g., Gerthsen et al. 1982). As these 'electro-static' forces decrease with the power of 6 with particle distance they are relatively weak compared to frictional forces (e.g., Chen & Anandarajah 1996; Aplin et al. 1999). In addition, van der Waals forces can be approximated from the particle size if diameters are large compared to the distance between linked particles (Amahdi 2004). Therefore, we calculate "electro-static" forces only at direct contact points particularly between "clay" minerals where particles interact. In this case, inter-particle bonds are generated (e.g., ITASCA manual) which transmit van der Waals forces and moments between concerned "clay" particles. These bonds break up in accordance with the Mohr-Coulomb brittle criteria if the critical contact force is reached. As we are using only one type of "clay" particles up to now, the shear as well as normal forces are $F_{N,S-bond} = 1e8 \ N$ for these bonds. Simultaneously, normal and shear stiffness of these bonds are given as $k_{N,S-bond} = 1e8 \ \mathrm{N/m^2}$.

Model configuration

We developed a numerical shear box in accordance with analogue experiments which was a 2D cross section to 3D box shear apparatus. The bottom box with additional length in order to avoid the of surcharge fall. The top box was 10cm length with 4 cm height.

Approximately 8000 particles depending on the "sand" composition were generated randomly within the shear box to create a heterogeneous material layer and with Grain size distribution curve similar to laboratory test. Afterwards this particle assemblage was compacted due to increase of radii.

Two distinct initial states are generated, one is quite dense (void ratio e = 0.20) and another one quite loose (void ratio e = 0.27). Initial states are created by random deposition under gravity of the particles into the shear box. The top plate on the upper half of the box applies a vertical stress s = 30 kPa. During shear, the vertical displacement of the top plate is servo-controlled so as to keep the vertical stress s constant. The material is sheared at a low speed (v = 0.005 mm/s) in order to maintain a quasi static state, controlled by the calculation of the ratio of the mean unbalanced force to the mean contact force within the sample. This ratio keeps a value of the order of 10-5 all along the test.

The model configuration enabled the calculation of large strain rates equivalent to deformation rates that can be reached with analogue box shear tests. This type of simulation particle fracture was not allowed. In addition, fluids are not taken into account. Restrictions based on these model assumptions will be discussed below.

Geotechnical Shear Tests and DEM Observations

The simulation results in terms of macroscopic behavior are presented for the two initial densities. Some results are compared to the experimental ones obtained by Manoj Jogi. Fig. 2 shows the evolution of the ratio $t/s$of the shear stress on the horizontal split plane to the vertical stress and of the vertical displacement of the top plate of the box during shear. The maximum shear stress achieved by the dense sample is higher than the experimental value and, for a small displacement, this sample exhibits a stiffer behavior than the experimental one. The increase of volume observed during shear is significant of a dilatant behaviour. The loose sample provides a shear stress curve very similar to the experimental one and exhibits a contractant behavior. Even if a perfect plasticity state is not strictly reached, especially in the dense case, a residual friction angle of

about 23 degrees can be estimated. In conclusion, the simulations provide macroscopic results which are representative of loose and dense materials. Moreover, the response of the loose sample is quite close to the experimental one.

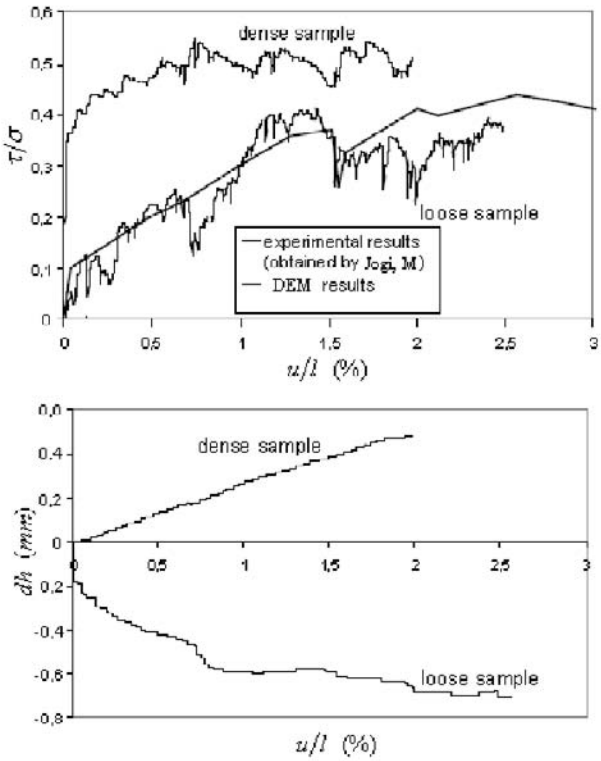

Fig. 2 Shear stress (Up) and vertical displacement (Down) during shear

CONCLUSIONS

Both experimental settings, numerical as well as analogue, supplied comparable results of coefficient of friction for dry "sand". In all dry experiments a typical strain hardening behaviour, characterized by a slight increase in the coefficient of friction pushing towards a mean friction value, could be observed.

The work briefly presented here is a part of a numerical study, in which main objective is to better understand the fundamental mechanisms governing the shear behaviour in granular materials. The results for direct shear appear a strong correlation between stress and strain rotations. During shear, there is a gain of contacts of normal direction corresponding to a compression direction, and a loose of contacts of normal direction corresponding to an extension direction. The contact forces distribution is strongly linked to the stress tensor. Due to interparticle friction, the contact force direction may be different of the contact normal direction. Thus, stress and strain principal directions may be different in a frictional material.

REFERENCES

ASTM D5321-02 (2002) Standard Test Method for Determining the Coefficient of Soil and Geosynthetic or Geosynthetic and Geosynthetic Friction by the Direct Shear Method, ASTM, West Conshohocken, PA, USA

Bulgern, William G (1982) Discrete System Simulation, Englewood Cliffe, Prentice Hall

Cundall PA (1994) Alternative User Interfaces for Programs That Model Nonlinear Systems, in Applications of Computational Mechanics in Geotechnical Engineering, pp. 343-352. Vargas et al., Eds. Rotterdam: Balkema

Cundall PA (1971) A Computer Model for Simulating Progressive, Large Scale Movements in Block Rocky Systems, Proc. Int. Symp. On Rock Fracture, Nancy France

FHWA (2001) Performance Test for Geosynthetic Reinforced Soil Including Effects of Preloading, FHWA-RD-01-118, McLean, VA 22101-2296

ICOLD (2005) Geomembrane Sealing Systems for Dams, Design principle and return of experience, Bulletin 78

Jiang MH (2006) Application of Discrete Element Method to Geomechanics, Dept. of Geotechnical Eng., Tongji University, China

Jogi M (2005) A Method for Measuring Smooth Geomembrane/Soil Interface Shear Behaviour Under Unsaturated Conditions, A thesis in Dept. of Civil Eng., University of Saskatchewan, SK Canada

Lanier J, Calvetti F (1997) Evolution of Microstructure in Granular Materials, Powders and Grains 97, RP Behringer & JT Jenkins (eds), Balkema, Rotterdam

Love AEH (1927) A Treatise of the Mathematical Theory of Elasticity, Cambridge University Press

Masson S, Martinez J (2005) Micromechanical Analysis of The Shear Behaviour of a Granular Material Using 2D Discrete Simulations of a Direct Shear Test, Laboratoire Ma2g, INSA Rennes

Olivari G (1989) Contribution of Micromechanics to Modelling the Behaviour of Granular Materials Response of Schneebeli's Material to a Cyclic Isotropic Loading, Powders and Grains, J Biarez and R Gourves (eds), Balkema, Rotterdam

PFC2D (1999) User's Manual, Itasca Consulting Group, Inc., Minneapolis, USA

Shimizu Y, Hart RD, Cundall P Eds (2004) Numerical Modeling in Micromechanics Via Particle Methods. Proc. of 2nd Inter. PFC Symposium, Kyoto, Japan

Thallak, G Sitharam (2000) Numerical simulation of particulate materials using discrete element modeling Dept. of Civil Eng., Yamaguchi University, Current Science 78(7)

NONLINEAR DIFFUSION OF SOLUTE IN SOIL COLUMN — TEST METHOD AND PRELIMINARY RESULT

Z.Z. Li[1], X.W. Tang[2], Y.M. Chen[3] and Y. Wang[4]

ABSTRACT: Nonlinear diffusion phenomena have been widely reported and the nonlinear character will inevitably be considered to obtain exact estimations of the migration of solute in the environment. A step-to-step diffusion test scheme based on the BTC method was put forward in this paper to investigate the change of diffusion coefficient with increasing solute concentration that is unclear in traditional test method. The obtained solute transport parameters were clearly linked to the solute concentration. Preliminary test on the transport of KCl in Kaolinite column was conducted and the results verified the existence of nonlinear diffusion. The partition coefficient decreased linearly with increasing KCl concentration while the diffusion coefficient increased a bit at first and then suffered a half reduction with double increase in KCl concentration.

KEYWORDS: nonlinear diffusion, soil column, potassium, Kaolinite

INTRODUCTION

Nonlinear diffusion phenomena have been widely reported in thermal conduction, air infiltration through polymer, reactional diffusion in chemical reactor, highly viscous liquid movement, wet edge movement in unsaturated soil, and so on (Prasad and Salomon 2005; Assis et al. 2006). As to the migration of solute in the environment, the nonlinear character will inevitably be considered to obtain exact estimations. Such features have been noticed by researchers recently. The diffusion coefficients of solute have been reported relevant with the solute concentrations (Lake and Rowe 2000). Others reported that the permeability of GCL increased with increasing solute concentration (Shackelford et al. 2000). Nonlinear adsorption has been incorporated into models/software to improve the correlation coefficient between the fitted curves and the test results (Do and Lee 2006). However, the predicted adsorption parameters (partition coefficient *Kd* or retardation coefficient Rd) were commonly found deviated from those obtained by equilibrium adsorption test. Little work has been taken into account of the nonlinear diffusion of solute in soil.

In this paper, the authors put forward a test scheme to determine the diffusion coefficient of potassium (K^+) in compacted Kaolinite. The obtained results were used to verify the nonlinear diffusion phenomenon of solute in soil column. Further in-depth study will be intended to be applied to estimating the migration of pollutant through porous media.

BACKGROUND

The diffusion coefficient can be predicted through several methods, including break through curves (BTCs), solute concentration profiles under permeable boundary conditions or nonpermeable boundary conditions etc. The break through curve method was adopted in this paper since the test procedure was easy to handle and the results were sequential, real-timed and prone to the adjustment of the test conditions or parameters.

Shackelford (Shackelford et al. 1989; Shackelford and Redmond 1995) has given the analytical solution of one dimensional solute transport problem. The exit solute concentration can be written as

$$\frac{c_e - c_i}{c_0 - c_i} = \frac{1}{2}\left[erfc\left(\frac{\sqrt{R_d L} - \sqrt{vt}}{2L^2\sqrt{Dt}} \right) + e^{\frac{vL}{D}} erfc\left(\frac{\sqrt{R_d L} + \sqrt{vt}}{2L^2\sqrt{Dt}} \right) \right] \quad (1)$$

where c_e= concentration of solute in exit of the soil column; c_0= solute concentration of the infiltration liquid; the c_i= initial concentration in pore liquid; D= diffusion coefficient; L= column length; R_d= retardation coefficient; t= diffusion time; v= infiltration velocity of pore liquid.

[1] Ph.D Student, Department of Civil Engineering, Zhejiang University, CHINA. Email: lazyhero@126.com
[2] Professor, ditto, CHINA. Email: tangxiaowu@zju.edu.cn
[3] Professor, ditto, CHINA. Email: cym@civil.zju.edu.cn
[4] Ph.D Student, ditto, CHINA. Email: wangyan850407@163.com

To obtain the required transport parameters (*Rd* and *D*), the least square principle was applied to fit the test data until the optimum correlation coefficient was obtained. Such work can be carried out on the Origin Pro7.5 platform using the nonlinear curve fit module.

APPARATUS AND TEST SCHEME

Apparatus

The authors assembled a test apparatus as shown in Fig. 1.

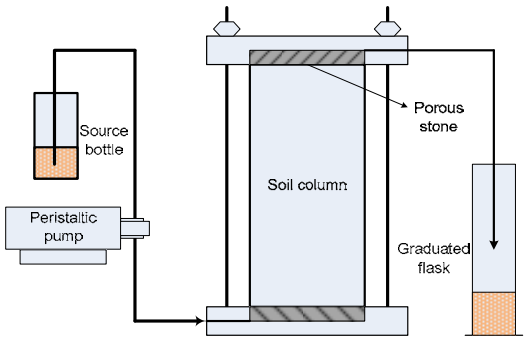

Fig. 1 Schematic view of the test apparatus

The peristaltic pump can transfer liquid without contacting with the pump and thus can avoid possible contamination of the solution. The soil column (4 cm height by 6.18 cm diameter) is placed in a test cell which is made of stainless steel and the porous stone is stable and resistant to salt solution. During the test, the source bottle was filled with solution containing fixed concentration of the target solute. The peristaltic pump was started to let the solution permeate through the soil column in constant velocity. The graduated flask was regularly replaced with cleaned empty flasks and the collected liquid was then sent to the Analyzing and Testing Center to determine the solute concentration.

Test Scheme

Step-to-step diffusion was previously used to describe the transport of atoms on the surface of semiconductor devices (Einstein 2002). In this paper, the authors proposed a similar conceptual test scheme to determine the transport parameters of solute in soil column. The concentration of the solute in source bottle was repeatedly adjusted to sequentially step-to-step increasing values as shown in Fig. 2. When the test was started, the deionized water was allowed to permeate through the soil column until the sample was totally hydrolyzed. And then the source concentration was shifted to C_{01} at time t_1 and kept constant until time t_2. The time t_1, t_2, t_3,… when the source concentration was increased depended on the duration required to make the solute concentration in soil profile equal to the source concentration C_{0i}.

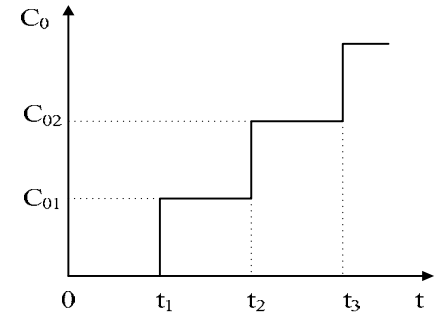

Fig. 2 Step-to-step increase in source solute concentration

This study was designed to investigate the change of diffusion coefficient with increasing solute concentration. However, in the traditional one-step BTC test, such relationship was unclear since the solute concentration in the soil profile varied with the distance from the source. In the case of low solute concentrations, the difference may be little. Once the source solute concentration was large and the unevenness of solute concentration in soil profile was obvious, the obtained transport parameters may be difficult to be linked to the solute concentration. Therefore the source concentration was shifted stepwisely with small increases to give clear linkage between D and C_0. Because the intervals in C_0 is restricted within a limited narrow range and the solute concentration in pore liquid is in the range of C_{0i}—C_{0i+1}, the midpoint of each step in concentration shift ($(C_{0i}+C_{0i+1})/2$) is assumed to determine the transport parameters as shown in Fig. 3.

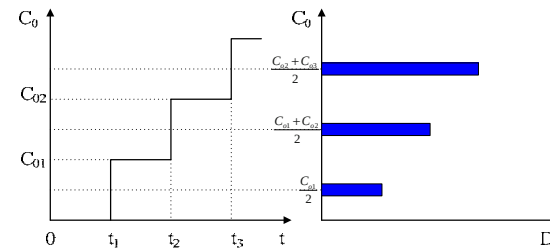

Fig. 3 Scheme of the relationship between solute concentration and predicted diffusion coefficient

EXPERIMENTS

Kaolinite (purchased from SinoPharm) was dried in an oven box at 105 °C overnight and then stored in plastic bags. The soil was prepared to obtain 15% water content (dry of optimum water content), stand overnight and then compacted into the soil column with Proctor compaction method. The dry density of the sample was determined as 1.33 g/cm^3. The sample was then installed into the apparatus and exposed to permeation with

deionized water to hydrolyze the clay mineral. KCl was chosen as the target solute. The permeation velocity was fixed as 1 rpm by the peristaltic pump (6.7×10^{-5} cm/s). The source concentration was increased from 0 to 0.1, 0.2, 0.4 M. The collected liquid was analyzed with atomic adsorption spectroscopy method to determine the concentration of potassium. Each step was continued until the exit solute concentration was equal to the inlet solute concentration. Two days was needed to complete such process in this study. The room temperature was fixed as 5—0 °C during the test.

RESULTS AND DISCUSSIONS

The test results were shown in Fig. 4. The test data were fitted with Eq. 1 with the previously described method. The obtained model constants and the correlation coefficients between data and fitted curves were shown in Table 1. The Rd and PL were fitted and the D and K_d were calculated based on R_d and PL:

$$D = vL / PL \tag{2}$$

$$R_d = 1 + \rho K_d / e \tag{3}$$

where e= pore ratio; ρ= dry bulk density.

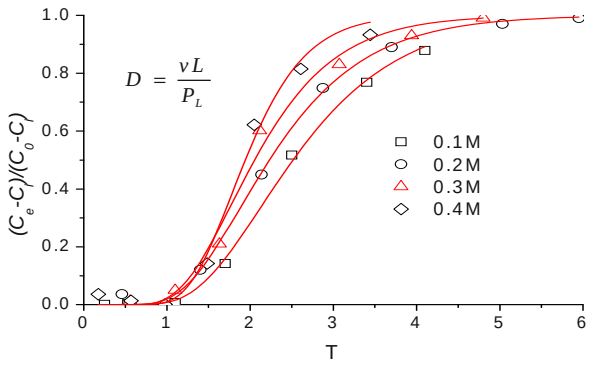

Fig. 4 Test results and fitted breakthrough curves (v=6.7×10^{-5} cm/s, L=4 cm, S=30 cm^2)

Table 1 Predicted transport parameters

C_0 M	0.1	0.2	0.3	0.4
R_d	2.718	2.417	2.198	2.025
PL	12.178	11.904	14.078	23.091
K_d	1.145	0.945	0.799	0.683
$D\times10^5$ cm^2/s	2.201	2.251	1.904	1.161
R^2	0.9987	0.9983	0.9905	0.9923

As shown in Table 1, the partition coefficient K_d decreased with increasing solute concentration from 1.145 to 0.683. And the diffusion coefficient D increased from 2.201E-05 to 2.251E-05 and then decreased to 1.904E-05 and 1.161E-05 cm^2/s. A double increase in solute concentration led to about half reduction in diffusion coefficient. Such phenomenon has not been reported and the results seem odd since the increased solute concentration was considered responsible for the increased permeability of soils (Peirce et al. 1987; Lo et al. 1994).

The relationships between K_d and C_0 and that between D and C_0 were further plotted in Fig. 5. The adsorption amount (Cs) was calculated as

$$C_s = K_d C_i \tag{4}$$

As shown in Fig. 5, the nonlinear adsorption behavior of K+ on Kaolinite was evident in this study.

The obtained D was larger than those reported in literature (Shackelford et al. 1989; Lake and Rowe 2000; Du et al. 2005). This is caused by the low bulk density and the high permeation velocity. Such features are always observed in the environment such as the movement of groundwater in loose soil stratums under difference in water heads or self gravities. Thus the predicted parameters may be applicable to estimating the transport behavior of solute/ contaminant in field conditions.

In addition, the decreased diffusion coefficient with increasing C_i might be caused by the increased adsorption amount (Cs) which could consume a certain proportion of solute during the transport process and would thus constrain the tendency of solute to be transferred downward by the pore water. Besides, the electrical double layer on the surface of Kaolinite will be changed to delay the movement of the solute in the presence of high concentration of KCl solution. Further investigations on the surface characteristics of Kaolinite in KCl solution will help to give the intrinsic diffusion mechanism.

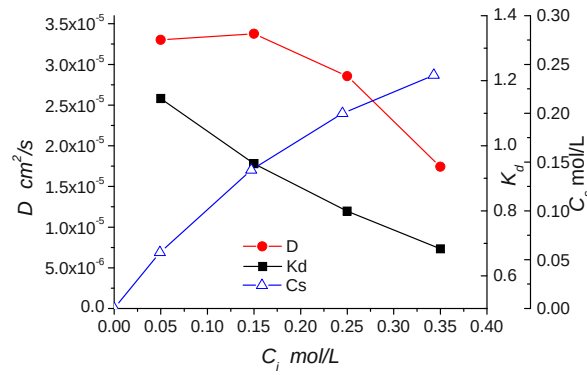

Fig. 5 Variation of D, K_d and C_s with C_i

CONCLUSIONS

A step-to-step diffusion test scheme based on the BTC method was put forward in this paper. The obtained solute transport parameters were clearly linked to the solute concentration. Preliminary test on the transport of KCl in Kaolinite column was conducted and the results verified the existence of nonlinear diffusion. The partition coefficient decreased linearly with increasing KCl concentration while the diffusion coefficient increased a bit at first and then suffered a half reduction with double increase in KCl concentration. Further study was necessary to reveal the mechanism of the decreasing diffusion coefficient.

REFERENCES

Assis PC, da Silva JrPC, da Silva LR (2006) Nonlinear diffusion equation and nonlinear external force: Exact solution. J. Mathemat. Phys 47: 103302

Do NY, Lee S (2006) Temperature effect on migration of Zn and Cd through natural clay, Environ. Monit. Assessm 118: 267–291

Du YJ, Hayashi S, Liu Y (2005) Experimental study of migration of potassium ion through a two-layer soil system. Environ. Geol 48: 1096–1106

Einstein TL (2002) Crossover between terrace- diffusion and diffusion step-to-step on vicinal surfaces: scaling function and analytic approximations. Surface Sci 521(3): 669-673

Lake CB, Rowe RK (2000) Diffusion of sodium and chloride through geosynthetic clay liners. Geotext. Geomem 18: 103-131

Lo IMC, Liljestrand HM, Daniel DE (1994) Hydraulic conductivity and adsorption parameters for pollutant transport. ASTM Spec. Tech. Publ 1142: 422-437

Peirce JJ, Sallfors G, Peel TA et al. (1987) Effects of selected inorganic leachates on clay permeability. J Geotech. Engin 113: 915-919

Prasad SN, Salomon JB (2005) A new method for the analytical solution of a degenerate diffusion equation. Advan. Water Resources 28(10): 1091-1101

Shackelford CD, Redmond PL (1995) Solute breakthrough curves for processed kaolin at low flow rates, J. Geo. Eng 121(1): 17-32

Shackelford CD, Benson CH, Katsumi T et al. (2000) Evaluating the hydraulic conductivity of GCLs permeated with non-standard liquids. Geotext. Geomem 18: 133-161

Shackelford CD, Daniel DE, Liljestrand HM (1989) Diffusion of inorganic chemical species in compacted clay soil. J. Contam. Hydrol. 4(3): 241-273

Geosystem Usage

UNDRAINED SHEAR STRENGTH PREDICTION AND STABILITY ANALYSIS OF GEOCOMPOSITE REINFORCED EMBANKMENT WITH CLAYEY BACKFILL

J.C. Chai[1], T. Hino[2], Y. Igaya[3] and A. Miyazaki[4]

ABSTRUCT: A method of predicting undrained shear strength (S_u) within a dual function geocomposite reinforced embankment with clayey backfill is described, in which the effects of discharge capacity (Q_w) of the geocompoiste, spacing ($2B$) between geocomposite layers, construction speed (V), and the coefficient of consolidation (C_v) of the backfill are considered. Then Q_w values of three geocomposites were measured by laboratory tests under the confinement of clayey soils. The test results indicate that to maintain a higher long-term (more than 1 month) confined in clayey soil Q_w value, a geocomposite must have a drainage core or tube. Then by referring the measured Q_w values, the effects of Q_w, $2B$, as well as V on S_u distribution within an assumed 5 m high embankment were investigated by the proposed method. With the predicted S_u values, the factor of safety (FS) of the assumed embankment has been investigated by Bishop's slip circle method, and the results demonstrate that a 5 m high embankment with clayey backfill can be successfully constructed using dual function geocomposite.

KEYWORDS: geocomposite, drainage, reinforcement, embankment, consolidation, factor of safety

INTRODUCTION

How to effectively treat the waste clayey soils generated from construction site or dredged from port is one of the geoenvironmental problems. On the other hand, there is a shortage of granular materials for embankment construction in Japan. Therefore, it is desirable to use waste clayey soils as embankment fills. Since the strength of waste clayey soil is low, in many cases, it can't be directly used as a construction material. A commonly used method is to mix cement or lime into the waste clayey soil to improve its engineering properties first, and then used in engineering constructions. There are reports of using this kind of method for airport construction (Tsuchida and Kang, 2003). One of the problems of this kind of method is the high pH values of the treated soil, which may have a negative geo-environmental impact. Another method is to use dual function (reinforcement and drainage) geocomposites. The drainage effect of geocomposite accelerates the self-weight induced consolidation and increases the undrained shear strength (S_u) of the clayey backfill, and the mobilized tensile force in the geocomposite further increases the stability of the embankment. There are reported case histories of the method (e.g. Tatsuoka and Yamauchi 1986). However, regarding design a dual function geocomposite reinforced embankment with clayey backfill, there are still issues need to be resolved, such as how to predict the distribution of S_u values within an embankment.

In this paper, firstly, a method of predicting S_u values within a dual function geocomposite reinforced embankment with clayey backfill is described. Then the results of confined in clayey soil discharge capacity tests of three geocomposites are presented. Finally, the factors influencing S_u values within an assumed 5 m high embankment and therefore the factor of safety (FS) of the embankment have been investigated.

UNDRAINED SHEAR STRENGTH (S_u)

To design an embankment with clayey backfill and reinforced by a dual function geocomposite, one of the tasks is to predict S_u values within the embankment during the embankment construction. The value of S_u of a soil is a function of effective stress, stress history and the mechanical properties of the soil. Ladd (1991) proposed an empirical equation to calculate S_u value in a ground as follows:

$$S_u = S \cdot \sigma_v^{'} \cdot (OCR)^m \quad (1)$$

[1] Professor, Department of Architecture and Civil Engineering, Saga University, JAPAN. Email: chai@cc.saga-u.ac.jp
[2] Lecturer, Institute of Lowland Technology, Saga University, JAPAN. Email: hino@ilt.saga-u.ac.jp
[3] Chief Engineer, Department of Civil Engineering, Saga Prefecture, JAPAN. Email:igaya-yutaka@pref.saga.lg.jp
[4] Chief Engineer, Department of Civil Engineering, Saga Prefecture, JAPAN. Email:miyazaki-atsushi@pref.saga.lg.jp

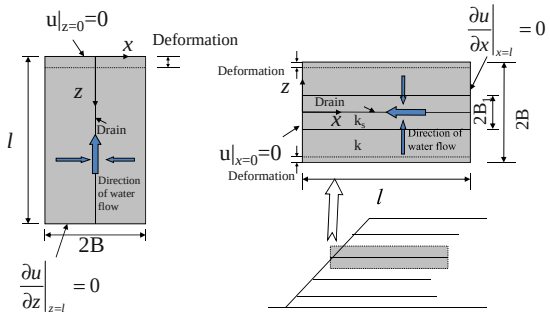

(a) Plan strain vertical drain **(b) Plan strain horizontal drain**

Fig. 1 Plane strain unit cells

where σ'_v is vertical effective stress, *OCR* is over-consolidation ratio, and *S* and *m* are constants. Ladd (1991) proposed that the range for *S* is 0.162 to 0.25 and for *m* is 0.75 to 1.0. For an embankment construction, *OCR* = 1.0, and to predict S_u, the value of σ'_v has to be evaluated first. Chai and Miura (2002) proposed a simple method for calculating the degree of self-weight induced consolidation of embankment backfill and it is summarized as follows.

Hird et al. (1992) extended Hansbo's solution (1981) for vertical drain consolidation under axisymmetric condition to plane strain condition. A vertical plane strain unit cell adopted by Hird et al. (1992) is shown in Fig. 1a. In the case of embankment construction, the geocomposite serves as a drain is placed horizontally. Fig. 1b shows a horizontal plane strain unit cell. Although the deformation patterns in Figs. 1a and b are different, both of them satisfy equal strain assumption, a basic assumption of Hansbo's solution. Therefore, equations derived for Fig. 1a case can be used for Fig. 1b case by using the corresponding notations adopted. With the notations in Fig. 1b, the average degree of consolida-tion at a distance of *x* from drainage surface (*x* = 0) is as follows:

$$U = 1 - \exp\left(\frac{-8T}{\mu}\right) \tag{2}$$

The expressions for *T* and μ are as follows:

$$T = \frac{C \cdot t}{4B^2} \tag{3}$$

$$\mu = \frac{2}{3} + \frac{2k}{B \cdot Q_w}(2 \cdot l \cdot x - x^2) + 2 \cdot \left(\frac{k}{k_s} - 1\right)\left(b_s - b_s^2 + \frac{b_s^3}{3}\right) \tag{4}$$

where *C* is the coefficient of consolidation of clayey soil, *t* is time, *B* is the half width of a plane strain unit cell, *k* and k_s are the hydraulic conductivities of clayey soil and smear zone around a drain, respectively, Q_w is discharge capacity of a geocomposite per unit width, *l* is drainage length, *x* is the distance from drainage surface, and $b_s = B/B_1$ (B_1 is the half width of the smear zone).

During embankment construction, backfill is placed layer by layer. To predict pore pressure variation during embankment construction by Eqs. 2 to 4, following assumptions are made.

(1) Approximate the construction process by stepwise loads.

(2) Take total load at *i* step as p_i, degree of consolidation at time t_i as U_i. At t_i, incremental load of *j* step Δp_j is applied, then for total load $p_j = p_i + p_j$, the degree of consolidation (U_{jo}) at t_i can be calculated as:

$$U_{jo} = \frac{U_i \cdot p_i}{p_i + \Delta p_j} \tag{5}$$

An imaginable time corresponding to U_{jo} (under load p_j) is:

$$t_{jo} = -\frac{B^2}{2 \cdot C}\mu \cdot \ln(1 - U_{jo}) \tag{6}$$

Using the moment (t_i) of applying p_j as a new origin for time, if the time from the new origin is t_j, then, time for calculating degree of consolidation at time t_j will be ($t_{jo}+t_j$). When the average degree of consolidation of each layer of an embankment at a given time is known, σ'_v and therefore S_u can be calculated.

For embankment construction, it can be considered that there is no smear zone (k/k_s =1, and B_l is not needed). Then with the method presented above, there are totally six parameters needed: Q_w; *C*; *k*; *B*; construction speed (*V*), and the constant *S* in Eq. 1 (*OCR* = 1, and *m* is not needed). Further *V* and *B* can be specified by design. Then remaining four parameters are, Q_w, *C*, *k*, and *S*. *S* is an empirical parameter and can be determined based on local experience. Finally, Q_w, *C*, and *k* must be measured by laboratory or field tests. Some test results on Q_w values of three geocomposites will be described in next section.

LABORATORY TEST RESULTS ON Q_w

Test Equipment

Q_w values provided by manufacturers are normally under the condition that the geocomposites are confined by rubber membrane or between two parallel plates (ASTM 2003). However, if using geocomposite for constructing an embankment with clayey backfill, there is a possibility that clayey particles enter the drainage channel through filter and influence Q_w value. The flow rates of three geocomposites were investigated under the confinement of clayey soil using a triaxial type discharge capacity test device (Fig. 2). During the tests, tap water was used and re-circulated by a micro-pump. The test

procedure has been described elsewhere (e.g., Chai and Miura 2002).

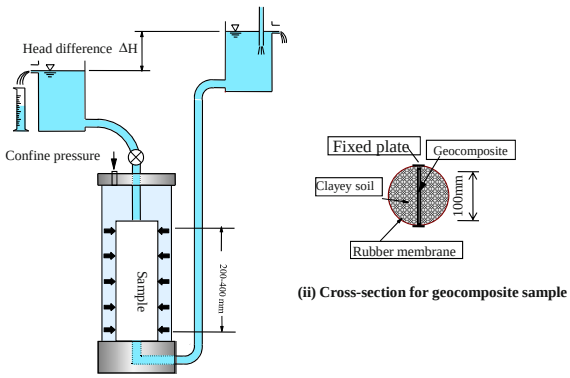

(i) Set-up

Fig. 2 Illustrations of test set-up

Materials

Geocomposite

Three geocomposites (A, B and C) were used and their structures and some of index properties are given in Fig. 3.

Fig. 3 Structures and index properties of geocomposites

Type	Sketch	Photo	Material	Unit weight
A	Non woven geotextile; Woven geotextile; 4.5 mm		polypropylene	678g/m^2
B	Non woven geotextile; 4.0 mm; PET tube		Non-woven geotextile: polypropylene Tube: PET filament spacing: 100 mm, inside diameter: 2 mm	281g/m^2
C	Non woven geotextile; Core; 7.0 mm		Non-woven geotextile: polypropylene Core: high density polyethylene	1010g/m^2

Clayey soils

Two types of clayey soils were used as confinement materials. One was remolded Ariake clay. Its liquid limit was 115% and plastic limit was 54%. The clay content (< 2 m) was about 48%. Another one was a mixture of the Ariake clay and decomposed granite passing through 1.2 mm sieve with a ratio of 1:2 by dry weight. It will be called mixed soil later. The liquid limit and plastic limit of the mixed soil were 61.6% and 33.7% respectively.

Test Results

For geocomposite A and B, the tests were conducted under the confinement of both the Ariake clay and the mixed soil, and for geocomposite C, the tests were conducted only under the mixed soil confinement. All the tests were conducted with a hydraulic gradient of 0.1. The confining pressures (σ) adopted were 10, 50, and 100 kPa. The test results are given in Figs. 4 to 6 for geocomposite A, B and C respectively. Generally, the flow rates reduced with elapsed time and increase of σ. It is considered that the reduction on the flow rate with elapsed time is mainly due to the clogging of the drainage paths caused by the soil particles entered the openings of the geotextiles. Geocomposite A, which does not have a drainage tube or core, had the lowest flow rate and C had the highest flow rate.

For geocomposite A (Fig. 4), when σ = 100 kPa, the flow rate was practically zero. Under σ = 10 and 50 kPa, at one month elapsed time, it became 0 to 2 m^3/year/m. The test with the mixed soil confinement showed a

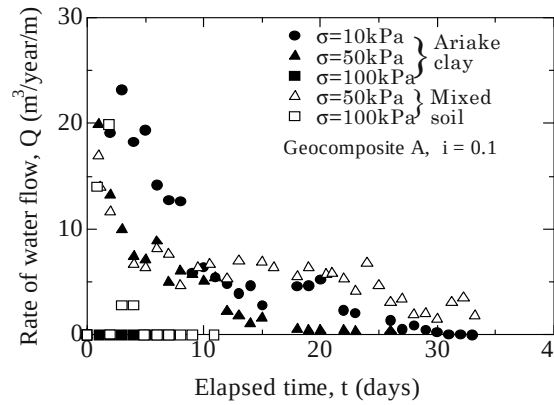

Fig. 4 Rate of flow of geocomposite A

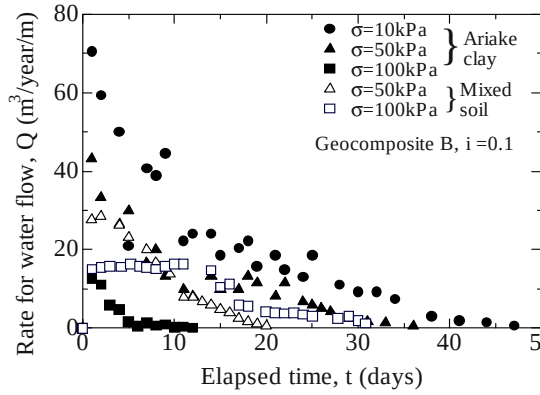

Fig. 5 Rate of flow of geocomposite B

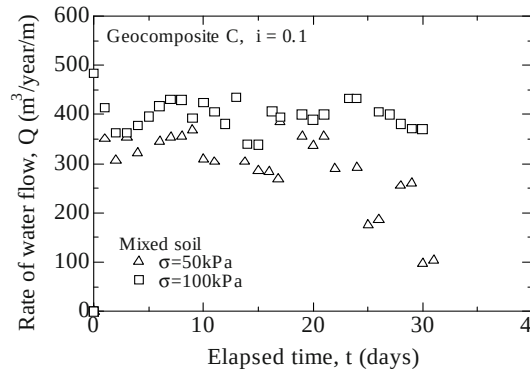

Fig. 6 Rate of flow of geocomposite C

higher long-term (more than one month) flow rate. Geocomposite B has one drainage tube per 0.1 m width and had higher flow rate than A. At one month of elapsed time, the flow rate is 0 to 10 m^3/year/m under σ = 100 to 10 kPa (Fig. 5). Geocomposite C has a drainage core and the reduction on flow rate with the elapsed time is less significant than A and B, and under σ = 100 kPa, within one month, the flow rate almost not reduced (Fig. 6). Also, the initial flow rates for σ = 50 and 100 kPa are almost the same (Fig. 6). Short-term (lasted for about 3 hours) test results indicate that for geocomposite C, when the confining pressure increased to more than 150 kPa, obvious reduction of the flow rate was observed and the flow rate of σ = 200 kPa was about 70% of that of σ = 100 kPa. This result indicates that the filter of geocomposite C is strong. Above discussions clearly indicate that to maintain a higher long-term (more than one month) flow rate under clayey soil confinement with a σ of more than 50 kPa, a geocomposite must has a drainage core and a strong filter.

The discharge capacity (Q_w) is defined as the flow rate under a hydraulic gradient of 1.0. If linearly converting the results given in Figs 4 to 6 to i = 1.0, at one month elapsed time, the range of Q_w will be 0 to 1,000 m^3/year/m.

STABILITY ANALYSIS

Conditions Assumed for Analysis

The geometry of a 5 m high embankment assumed for stability analysis is shown in Fig. 7. It is further assumed that the failure surface will not pass through the foundation. As shown in Fig. 7 the geocomposite is discontinued at the middle of the embankment. Although whether the geocomposite will be continued through the whole width of an embankment depends on the construction procedure, discontinuous assumption is in the safe side in term of stability analysis, in which the possible pullout failure of the geocomposite can be considered. Other assumed conditions are listed in Table 1. The Q_w values are selected referring the laboratory test results presented above. The basic value of 20 m^3/year/m is about the average values of geocomposite B at one month elapsed time for σ = 10 to 100 kPa. Regarding the allowable tensile force (T_a), the ultimate tensile strength provided by the manufacturers for geocomposite A, B and C are: 49.3 kN/m, 11 kN/m and 18 kN/m respectively. For geocomposite A, the test was conducted using a 200 mm wide strip sample with a strain rate of 1%/min. The failure strain was about 10%. For geocomposite B, the test was conducted using sample of 100 mm wide and 200 mm long (between clamps) with a strain rate of 100%/min. The failure strain was about 40%. For geocomposite C, it is mentioned that the test was conducted per ISO 10319 (ISO 1993) and the failure strain was 60%. Referring the above information, T_a values of 0, 5 and 10 kN/m are assumed. It is not intended to use Q_w and T_a values of a specific geocomposite, rather the analysis is try to provide some general information on the effect of Q_w and T_a on the stability of a dual function geocomposite reinforced embankment with clayey backfill.

Table 1 Parameters used for stability analysis

Parameters	Basic value	Range of variation
Discharge capacity of geocomposite, Q_w (m^3/m/year)	20	10 – 100
Spacing between geocomposite, 2B (m)	0.5	0.5 – 1.0
Coefficient of consolidation of backfill, C_v (m^2/day)	0.1	–
Speed of construction, V (m/day)	0.05	–
Hydraulic conductivity of backfill, k (m/day)	0.004	–
Total unit weight of backfill, γ_t (kN/m^3)	15.0	15.0 and 20.0
Allowable tensile force in geocomposite, T (kN/m)	5	0 – 10

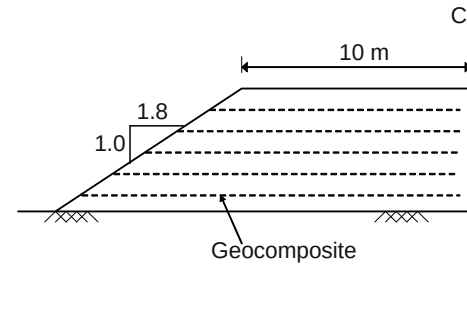

Fig. 7 Geometry of an assumed embankment

Predicted S_u Values Within the Embankment

With the method presented above and the values of parameters listed in Table 1, the distribution of S_u within the assumed embankment can be predicted using Eq. 1. In the calculation, the adopted value of constant S in Eq. 1 is 0.25.

Effect of Q_w and 2B

Fig. 8 shows the effect of Q_w and 2B (spacing) on S_u distribution at the end of construction. It can be seen that Q_w has a significant influence on S_u value. S_u increases with Q_w, but the increase rate reduced with the increase of Q_w. Increasing in spacing (2B) reduced S_u values.

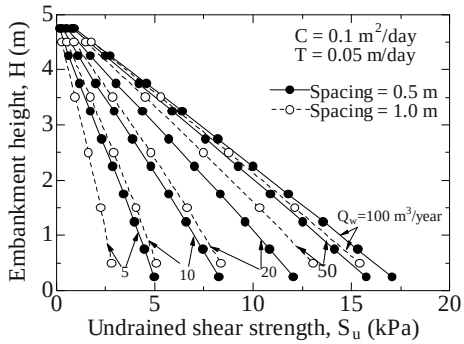

Fig. 8 Effect of Q_w on predicted S_u values

However, with the increase of Q_w value, the difference between $2B$ = 0.5 m and 1.0 m cases gradually reduced, which means that using a geocomposite with a higher Q_w value, a relatively larger spacing (e.g., $2B$ = 1.0 m) can be adopted and it may result in a more economic design.

Effect of construction speed (V)

Fig. 9 shows the distributions of S_u at the end of construction with three different V values. Reducing in V increases the time for self-weight induced consolida-tion and results in higher S_u values.

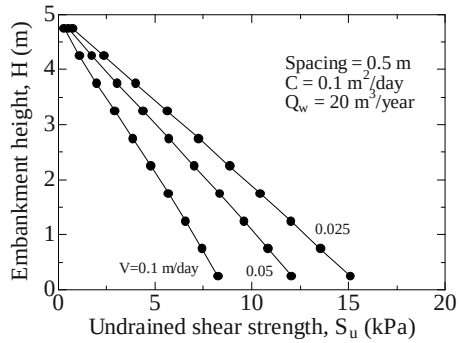

Fig. 9 Effect of construction speed on S_u values

Factor of Safety (FS)

With the predicted S_u values given in Figs. 8 and 9, and T_a values in Table 1, FS of the assumed embank-ment (not including foundation) was analyzed by using Bishop's slip circle method (Bishop 1955). The program used is ReSSA (2.0) (Leshchinsky 2001). Failure mechanisms of the reinforcement considered are (1) rupture and (2) pullout. In case of pullout failure, the interface shear resistance between a geocomposite and backfill soil was 80% of the corresponding shear strength of the backfill soil.

Effect of Q_w. and B

Fig. 10 shows the variation of FS with Q_w for $2B$ = 0.5 m (solid line) and 1.0 m (dashed line) cases. It can be seen that FS increases with the increase of Q_w, but the increment rate is gradually reduced. When Q_w > 50 m³/year/m, the increase rate is small. If taking FS > 1.2 as a basic requirement (JRA 1999), for not considering the reinforcement effect (T_a = 0), $2B$ = 0.5 m and $Q_w \geq$ 50 m³/year/m, and $2B$ = 1.0 m and $Q_w \geq$ 100 m³/year/m cases can satisfy the requirement. Comparing the FS of $2B$ = 0.5 m and 1.0 m cases, two points can be made. The first one is that with the increase of Q_w, the difference between FS values of $2B$ = 0.5 m and 1.0 m becomes smaller (the difference on S_u values becomes smaller, Fig. 8). The second one is that for $2B$ = 1.0 m case, the effect of T_a on FS is smaller than that of $2B$ = 0.5 m case because $2B$ = 1.0 m case has the less number of reinforcement layers.

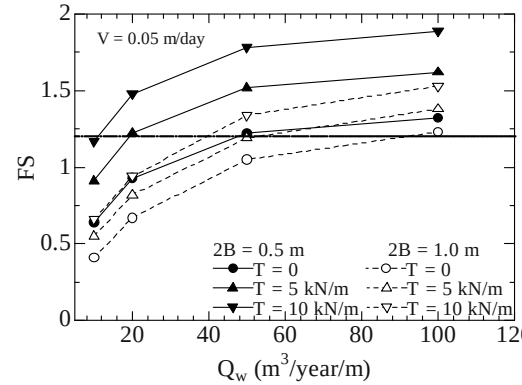

Fig. 10 Effect of Q_w and B on FS

Effect of construction speed (V)

The effect of construction speed on FS is shown in Fig 11. The slower the construction speed, the higher the FS value. For Q_w = 20 m³/year/m, without reinforcement effect, FS > 1.2 requirement can't be satisfied even for V = 0.025 m/day case. FS > 1.2 can be satisfied for V = 0.05 m/day and T_a = 5 kN/m case.

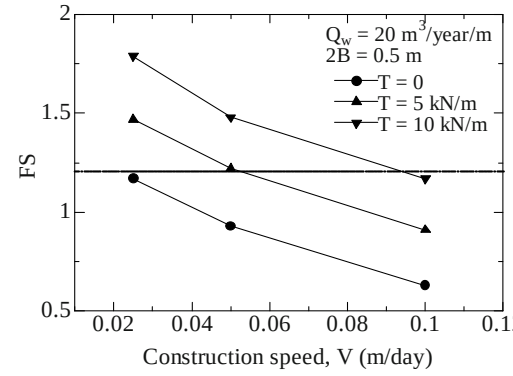

Fig. 11 Effect of V on FS

Effect of total unit weight (γ_t) of embankment backfill

The degree of self-weight induced consolidation is not influenced by γ_t (magnitude of load). Therefore, the vertical effective stress (σ'_v) within the embankment, and therefore S_u values (Eq. 1) in the embankment are linearly proportional to γ_t. However, increase on γ_t will increase driven force for slip failure. As a result, if not

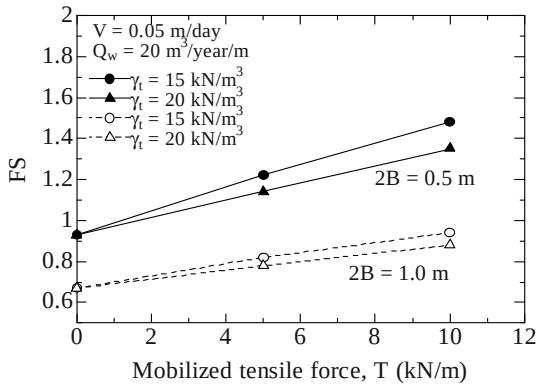

Fig. 12 Effect of γ_t on FS

considering the reinforcement effect, γ_t will not influence FS values. In case of considering the reinforcement effect, since the allowable tensile force (T_a) in the geocomposite not increases with increase of γ_t, the corresponding FS value will reduce. Fig. 12 compares F_S values of γ_t = 15 and 20 kN/m^3 cases. For T_a > 0 cases, F_S of γ_t = 20 kN/m^3 case is smaller. The larger the T_a value considered, the larger the difference.

CONCLUSIONS

A method of predicting undrained shear strength (S_u) within a dual function geocomposite reinforced embankment with clayey backfill is described. The results of laboratory discharge capacity (Q_w) tests for three geocomposites confined in clayey soils are presented. Referring the test results on Q_w, the S_u distribution within an assumed 5 m high embankment and therefore the factor of safety (F_S) of the embankment have been investigated. The detailed conclusions on the test and analysis results are as follows.

(1) Q_w values of geocomposites. The flow rates of the geocomposites reduced with increase of confining pressure and elapsed time. To maintain a higher long-term (more than one month) Q_w value, a geocomposite must have a drainage tube or core and a strong filter. The tests were conducted under a hydraulic gradient i = 0.1, and if linearly convert to i = 1.0, the range of Q_w values is 0 to 1,000 m^3/year/m at one month of elapsed time.

(2) Undrained shear strength (S_u). Regarding the effect of Q_w and spacing between geocomposite layers, B, on S_u, for the conditions investigated, it shows that when $Q_w \geq$ 100 m^3/year/m, the difference on S_u values for 2B = 0.5 m and 1.0 m becomes small, which implies that using a geocomposite with a higher Q_w value, a larger spacing (e.g., 2B = 1.0 m) can be adopted.

(3) Factor of safety (F_S). The analysis results indicate that with a requirement of FS > 1.2, even without considering the reinforcement effect (T_a = 0), 2B = 0.5 m and $Q_w \geq$ 50 m^3/year/m, and 2B = 1.0 m and $Q_w \geq$ 100 m^3/year/m cases can satisfy the requirement. When T_a = 0, the FS value is not influenced by the unit weight of backfill (γ_t), but for T_a > 0, FS reduces with the increase of γ_t.

REFERENCES

ASTM (2003) Standard guide for selection of test methods for prefabricated vertical drains (PVD), ASTM D6917-03, American Society for Testing and Materials, West Conshohocken, Pennsylvania, USA

Bishop AW (1955) The use of the slip circle in stability analysis of slopes, Geotechnique 5: 7-17

Chai JC, Miura N (2002) Long-term transmissivity of geotextile confined in clay. Proc. 7th Inter. Conf. on Geosynthetics, Nice, France (Ed. By Ph. Delmas and J. P. Gourc), Balkema Publishers 1: 155-158

Hansbo S (1981) Consolidation of fine-grained soils by prefabricated drains, Proc. 10th Int. Conf. Soil Mech. and Found. Engrg., Stockholm 3: 677-682

Hird CC, Pyrah IC, Russell D (1992) Finite element modeling of vertical drains beneath embankments on soft ground. Geotechnique 42(3): 499-511

ISO (1993) Wide width tensile test of geotextiles and geogrids. ISO 10319, International Organization for Standardization, Geneva, Switzerland

Japan Road Association (JRA) (1999) Guideline for slope and embankment stability measure, Geotechnical Engineering for Road Construction. Japan Road Association

Ladd CC (1991) Stability evaluation during staged construction. J. of Geotech. Eng., ASCE 117(4): 541-615

Leshchinsky Dov (2001) An example of using ReSSA in comples geometry of reinforced slope. ADAMA Engineering Inc., USA

Tatsuoka F, Yamauchi H (1986) A reinforcing method for steep clay slopes using a non-woven geotextile. Geotextiles and Geomembranes 4: 241-268

Tsuchida T, Kang MS (2003) Case studies of lightweight treated soil method in seaport and airport construction project. Proc. 12th Asian Regionla Conf. on Soil Mechanics and Geotechnical Eng., Leung et al. (eds): 249-252

GEOTEXTILE TUBE APPLICATION AS THE COFFERDAM AT THE FORESHORE WITH LARGE TIDAL RANGE FOR INCHEON BRIDGE PROJECT

S.M. Cho[1], B.S. Jeon[2], S.I. Park[3] and H.C. Yoon[4]

ABSTRACT: Design details and construction procedures of the large-scale geotextile tube works as the cofferdam of the temporary access road for Incheon Bridge constructions are introduced. 18.25 km long sea-crossing Incheon Bridge connects Incheon International Airport with the international free economic zone at New Songdo City in Incehon. Construction site is a foreshore which the tidal range is up to 9.27 m and the subsurface consists of soft silty clayey soil. There were so many difficulties in installation of the geotextile tube on the soft tidal flat due to huge differences in the water level between ebb and flow. The diameter of polyethylene tube is 4 m, or 5 m and the length of each tube is 50 m. Sands were used as a filling material instead of dredges soils which was originally planed to fill the tube. Hydraulic pumping of sand mixed water to the tube through multiple injection ports gave advantages to reduce the construction time and to maximize the tube size after the injection completion. Two sets of the 4 m diameter tubes were installed on the ground surface and 3 tubes of 5 m diameter were stacked on these tubes in sequence. Special featured sand filled fabric forms were spread at each stacked layer to increase the friction between the tube surfaces. Polyester geotextile mat was used as a scour protection apron and post piles fixed the mat to the ground. Various kinds of offshore equipment including flat barges were used and working schedule was planned according to the information of tidal range. Instrumentations have been also performed to monitor the behavior of the geotextile tube.

KEYWORDS: geotextile tube, cofferdam, Incheon Bridge, ebb and flow, instrumentation

INTRODUCTION

Geotextile tube method was introduced into Korea in the late 1990s. Submersed breakwaters to protect the waterfront against erosions were the first applications of this method in 2001 (Fig. 1). Temporary road made of geotextile tubes was used for bridge constructions on the river in the suburbs of Seoul in 2003 (Fig. 2).

Fig. 1 Geotextile tube breakwater at Yeongjin Port

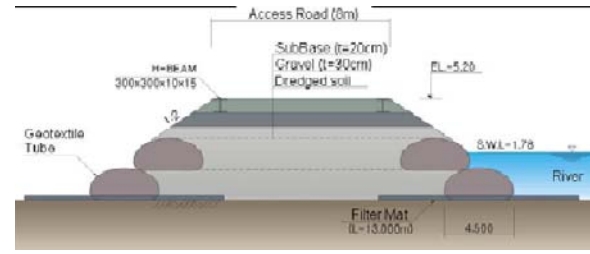

Fig. 2 Cross-section of temporary access road made of geotextile tube for Ilsan Bridge constructions

Geotextile tube is a kind of geotextile containers and it is filled with grain materials by hydraulic pumping. Hydration and cementation of the volume after the filling make the tube have the stability and help it resist external loads as a retaining structure in and out of the water. Sand, dredged soil, or, sludge has been commonly used as a filling material. Civil engineers have used increasingly in recent years geotextile tubes filled with sand for the retention and erosion protection of dredged material in the sea and the river.

[1] Director of TA Team, Ph.D., Incheon Bridge Construction Office, Korea Expressway Corporation, KOREA. chosmin@ex.co.kr
[2] Director of Construction Team, Incheon Bridge Construction Office, Korea Expressway Corporation, KOREA
[3] Head, Incheon Bridge Construction Office, Korea Expressway Corporation, KOREA
[4] Senior Manager, Incheon Bridge Site, DAELIM Industrial Co., Ltd., KOREA

Incheon Bridge has been constructed on the Yellow Sea to connect New Songdo City with the Incheon International Airport in Yeongjong Island. This 18.25 km long bridge will be the longest bridge of Korea in 2009 and will be also ranked as the 5th longest cable-stayed-bridge which has a main span of 800 m. Fig. 3 shows the bird's-eye-view of the bridge.

Fig. 3 Incheon Bridge

Both sides of this huge sea-crossing bridge located on the foreshore which difference of the sea level between the ebb and the flow is up to 9.27 m. Designer of the bridge determined to construct the left access side of the bridge to the island by the trestle and offshore equipment (Fig. 4). However, for the construction of the right side of the bridge, designers selected cofferdam for dry works (Fig. 5).

Fig. 4 Bridge construction using the trestle on the sea

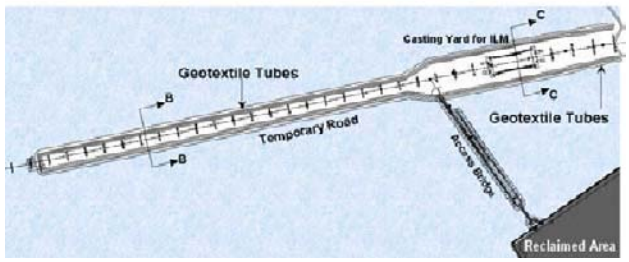

Fig. 5 Temporary road with the cofferdam for dry works

DESIGN OF GEOTEXTILE TUBE COFFERDAM

1,560 m long temporary road with geotextile tube cofferdams were planned to offer the dry work conditions for bridge constructions as shown in Fig. 5 (Korea Expressway Corporation 2007). This road is connected with the reclaimed area by the access bridge. Fig. 6 shows the cross section of the cofferdam.

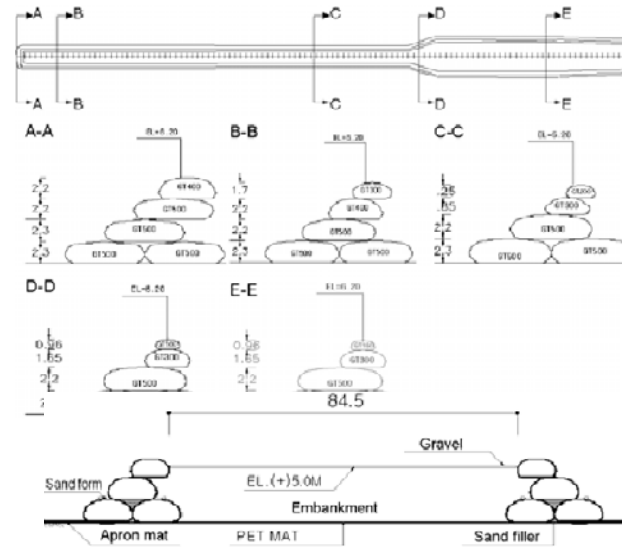

Fig. 6 Geotextile tube layers for the cofferdam

Material characteristics of the polyester geotextile for the tube are shown in Table. 1and 2 indicates the required properties of the geotextile for the tube suggested by US Army Corps of Engineers (Geosynthetic Research Institute 2001).

Table 1 Properties of the geotextile

Weight	900 g/m^2
Thickness	3 mm
Tensile Strength	> 200 kN/m
Elongation	13—14 %
Puncture Strength	20 kN
Permeability	10^{-2}—10^{-4} cm/sec

Table 2 Specification for geotextile tube (US Army)

Properties	Testing Method	Value
Tensile Strength (Wide)	ASTM D4595	> 100 lb/in
Tensile Strain (Wide)	ASTM D4595	< 15 %
Bursting Strength	ASTM D3786	> 1,200 psi
Tearing Strength	ASTM D4533	> 400 lb
Puncture Strength	ASTM D4833	> 350 lb
Seam Strength	ASTM D4844	> 600 lb/in
Permeability	ASTM D4491	> 0.1 l/sec
App. Opening Size	ASTM D4751	100 sieve
UV Resistance	ENV 12224	> 90%

Current velocity of the ebb and the flow is up to 0.9 m/sec and the ebb exposes the seabed (foreshore).

Height of the road ridge was determined to prevent the overtopping of the wave according to the Korean design specification for the port. And internal crest of the road embankment was designed to exceed the approximate highest high water (A.HHW) level. A.HHW elevation is 4.635 m. Fig. 6 indicates the elevation of the embankment crest is set to 5.0 m and the elevation of the top of the tube is set to 6.2 m. So, the tube cofferdam is 1.2 m higher than the internal embankment. Width of the temporary road is variable according to the zone. A-A, B-B, C-C are 34.0 m wide and E-E section has a width of 84.5 m.

Tubes were stacked up to 4 layers. Diameters of the tube are 3.0m, 4.0m, and 5.0 m. Prefabricated sand-packed mats were used between the upper tube and the lower tube to increase the friction at the interface of tubes.

Sand was selected as filler materials. Table 3 shows the preliminary test results to determine the filler material. Sand had the advantage of the reducing the filling time and the stabilization of the shape. Fig. 7 shows the tube height variation according to the elapsed time and the materials after the filling started.

Table 3 Comparison of the filler materials

Properties	Silty Clay	Sand
Grain Size (mm)	0.003—0.03	0.075—5.0
Shape Stability	Poor	Good
Injection Time to 1.2m height	10 hours	1 hour
Convergence Time	100 hours after the injection	30 hours after the injection
Effective Height	50% of the tube height	60% of the tube height

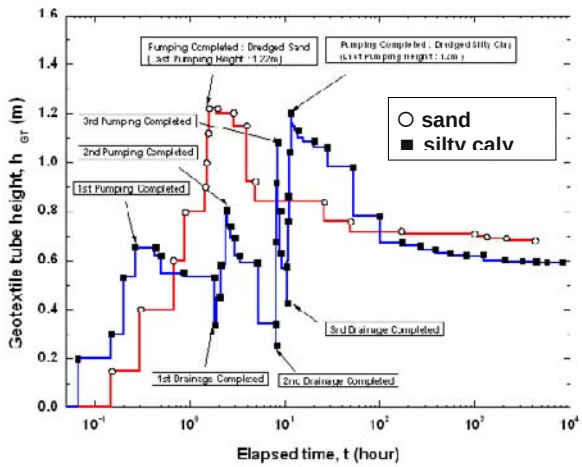

Fig. 7 Tube height variations according to the filler

Elevation of the seabed is from (-)2.5m to (-)0.7m. Subsurface soil consists of the silty clay and the sand. Weathered rocks and bedrocks appear beneath the soil layer (Fig. 8).

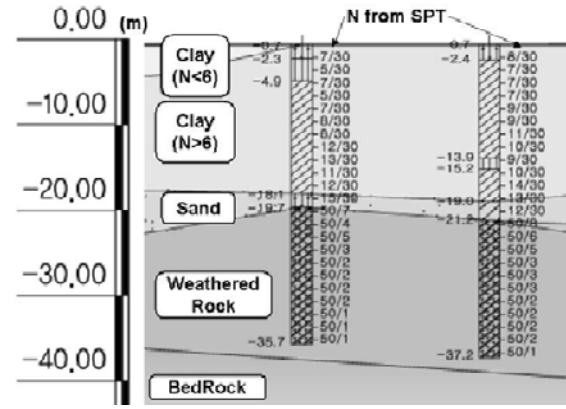

Fig. 8 Subsurface profile

CONSTRUCTIONS OF GEOTEXTILE TUBE

Prior to install geotextile tubes, scour aprons and base polyester (PET) mats were deployed on the site, the area was prepared using grading equipment including a small backhoe. Sand bags were laid on the mats to fix the aprons and mats against the currents. The location in which the geotextile tubes were to be placed had been marked off. Post pipes of 120 mm diameter were also installed on the seabed ground through the mats so that the geotextile tube can be fastened to them with straps to assure proper alignment during filling. Geotextile tubes were unrolled into position with the inlet ports facing upwards along the top centerline. Once the geotextile tube was deployed, it was secured to the previously installed post piles.

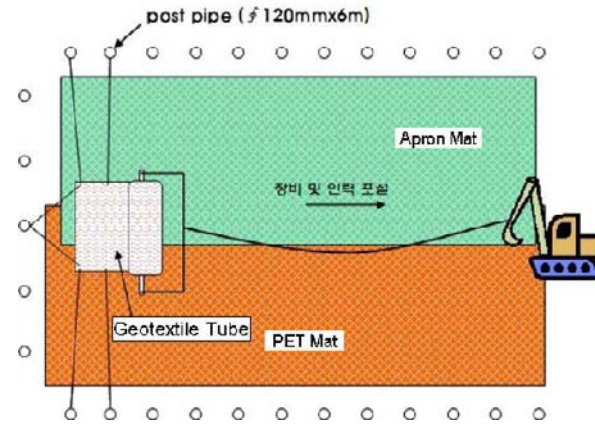

Fig. 9 Unroll of the geotextile tube on the scour apron and the PET mat

All these works of apron installations and tube deployments were carried out in the ebb conditions when the seabed revealed as shown in Fig. 10.

After the geotextile tube has been deployed, it started to fill the tube in the flood condition when the tube was in underwater.

Fig. 10 Geotextile tube deployments using post piles

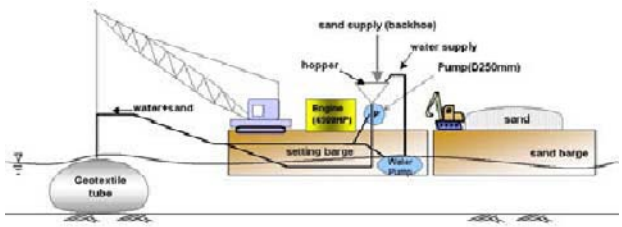

Fig. 11 Equipment combination for tube fillings

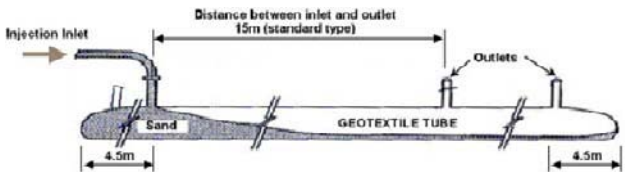

Fig. 12 Schematic diagram of the injection into the tube

Geotextile tubes generally contain several injection ports throughout the length of the tube. These ports are located at the top centerline and spacing between the inlet and outlet was 15m in this project. These ports are utilized for filling and also for relief of excess water.

80% of the filling material was water and rest of them was sand. Injections were continued to inflate the tube to the 80% of the tube volume. Injection pressure was controlled to be less than 0.3 kg/cm^2 to prevent the rupture of the tube.

Prefabricated sand form was used at the interface between upper and lower tubes (Fig. 13). Frictions at the interface can be increased thanks to this form. Gap between the adjacent tubes were filled with sands and sand bags.

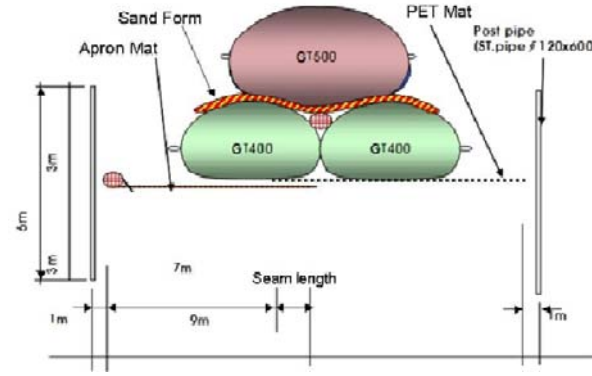

Fig. 13 Sand form installations

When the current was at the ebb and the seabed revealed, injections were stopped. So, injection works were performed in the underwater conditions, or the partly submerged conditions. Table 4 presented the injection results for the 5 m-diameter tube (50 m long) according to the submerged conditions.

Table 4 Injection results (D5.0m, L50m)

Conditions	Injection Time	Volume
Fully Submerged	4 hours	785 m^3
Partly Submerged	4 & 1/2 hours	785 m^3

Upon completion of the installation of the geotextile tubes, the injection ports were secured properly to assure that they did not become torn open during wave events.

After the completion of the injection, fully filled geotextile tubes continued to dewater and the solids consolidated for some time after the tubes had been filled. The duration of the dewatering and consolidation period can vary depending upon the type of geotextile utilized and the type of fill material that was pumped into the tube. Typically, coarse material will dewater much faster than fine material such as silty clay. From the preliminary tests, volume of the tube after the injection decreased gradually and it was getting stability. This convergence time to keep stabilized volume was 30 hours for the sand fill as shown in Table 3 and Fig. 7.

MONITORING INSTRUMENTATIONS

Strain gauges, piezometers, and displacement measuring instruments were installed at the geotextile tube to monitor the changes in stress and strain of the structure. Fig. 14 shows the instrumentation plan. Variations of the stress and pore water pressure in the tube, lateral displacement of the tube, settlement of the tube, and earth pressure below the tube were measured during the injection. Monitoring of the behavior continued after the injection.

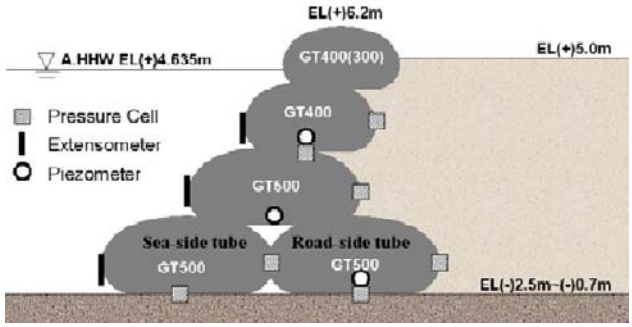

Fig. 14 Instrumentation sections (Univ. of Incheon, 2007)

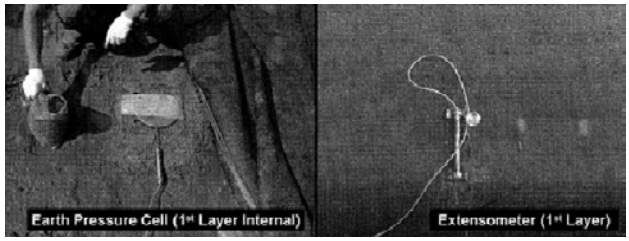

Fig. 15 Instrument Installations

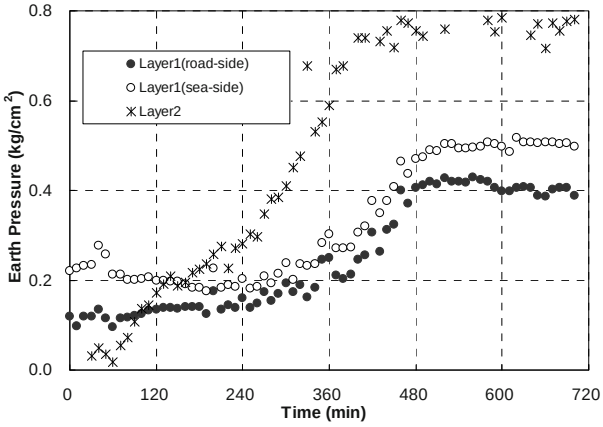

Fig. 16 Earth pressure changes in the tube

Fig. 16 presented the earth pressure changes of the tube during the 2nd layer tube injection in the underwater condition. Earth pressure in the 1st layer tube (road-side) was 0.12 kg/cm^2 before the beginning of the injection into the 2nd layer tube and it increased with elapsed time of the injection. Porewater pressure was excluded in this value. Earth pressure in the 1st layer tube after 6 hours inflations of the 2nd layer tube was 0.2 kg/cm^2 and it increased twofold at the end of the filling (0.4 kg/cm^2). Earth pressure beneath the sea-side tube of the 1st layer also changed from 0.22 kg/cm^2 to 0.51 kg/cm^2.

0.78 kg/cm^2 of the pressure was measured beneath the 2nd layer tube after the injection into the tube and Fig. 16 indicates that this pressure was distributed to the 1st layer tubes.

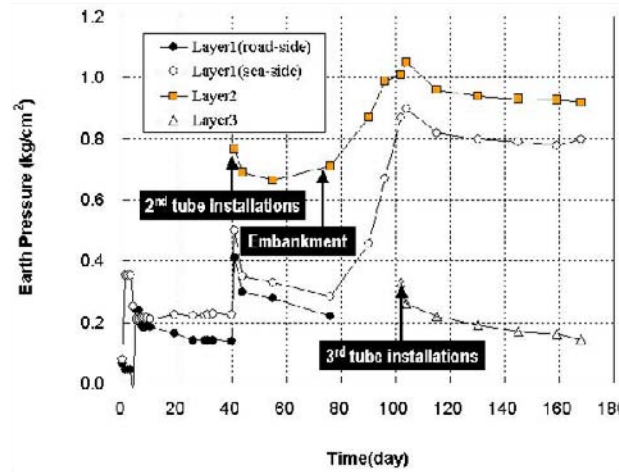

Fig. 17 Long-term variations of the earth pressure beneath the tube after constructions

When 41 days elapsed after the completion of the 1st layer tubes, 2nd layer tubes were installed. Temporary road embankment started after 76 days elapsed from the 1st layer tube completion. 3rd layer tubes were constructed after 102 days elapsed from the 1st layer tubes. Earth pressure beneath the 1st layer sea-side tube was 0.26 kg/cm^2 at the end of the injection and decreased to 0.23 kg/cm^2 after the 40 days passed. It increased up to 0.90 kg/cm^2 at the 3rd tube installation. Earth pressure beneath the 2nd layer tube was measured as 1.05 kg/cm^2 after the 3rd layer tube installation and it decreased to 0.92kg/cm^2. Earth pressure beneath the 3rd layer tube was 0.33 kg/cm^2 directly after the end of injection and it decreased gradually.

After considering measurement results, we found that earth pressure beneath the fully injected geotextile tube was about 40% of the predicted value. The height of the inflated tube didn't exceed 50% of the original diameter and the ground subsided as the injection proceeded. These caused low earth pressure under the tube. However, earth pressure beneath the 2nd layer tube showed 130% of the predicted value. These were due to

the concentration of the load on the centerline and small settlement of the 2nd tube. 1st layer tubes (sea-side and road-side) took the share of the 2nd tube's load and it prevented large subsidence of the ground.

Pore-water pressure in the geotextile tube increased slightly after the completion of the injection (Fig. 18).

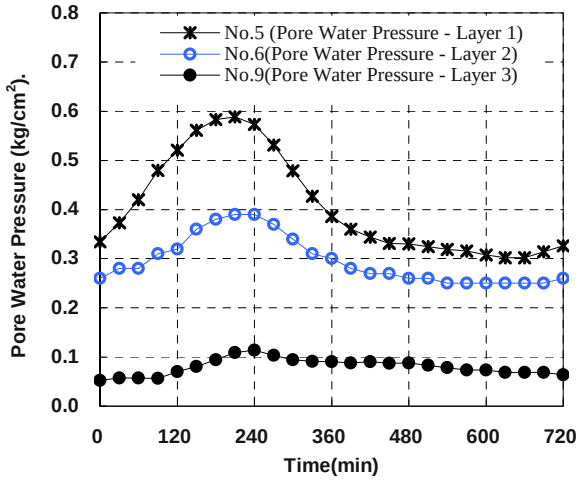

Fig. 18 Pore-water pressure in the geotextile tube after the construction

Fig. 19 shows the displacement of the tube. Maximum displacement was measured at the middle part of the tube in the circumferential direction. Axial displacement along the tube shaft was 70% of the circumferential displacement and the amount of 5% of the total displacement was reduced during 6 months after the installation. 80% of the reduced displacement was vanished in 15 days.

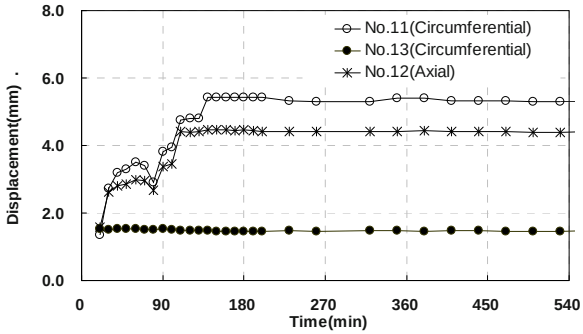

Fig. 19 Displacement of the 3rd layer geotextile tube during the construction

CONCLUSIONS

1,560 m long temporary road with 4 layered geotextile tube cofferdams were constructed on the foreshore which has 9.27 m difference elevation between the ebb and the flow. Brief descriptions of the design and construction procedure were introduced. Results of the field instrumentations to monitor the behavior of the geotextile tube were investigated. Earth pressure beneath the tube was different each other according to the tube position and elapsed time after the injection. Pore-water pressure and displacement of the tube were measured also.

ACKNOWLEDGEMENTS

Professor Shin's research group of the University of Incheon has carried out the preliminary tests and field instrumentations. Authors express gratitude to their efforts and contributions.

REFERENCES

Geosynthetic Research Institute (2001) Test Method, Properties and Frequencies for High Strength Geo-textile Tubes used as Coastal and Riverine Structures

Korea Expressway Corporation (2005) Design Report for Incheon Bridge Construction Project : Section 2

University of Incheon (2007) Research report: Geo-textile tube construction and Instrumentation for Incheon Bridge

CASE STUDY ON EARTH REINFORCEMENT USING SOILBAGS

Y.F. Xu[1] and J. Huang[2]

ABSTRACT: This paper presents an earth reinforcement method by soilbags and two case studies of its applications to pond filling-up and expansive soil slope protection in highway of China .The strength properties of soilbags are investigated through the unconfined compressive tests and bearing capacity tests on real soilbags in which medium grained sands and gravels were contained. It is found that soilbags have high strength when subjected to external forces, which is mainly due to the mobilized tensile force of the bags. The earth reinforced by soilbags has the advantages of improving the bearing capacity greatly for soft ground, resisting flexibly against deformation and being friendly to our environment with less noise during construction and no use of any chemical agents.

KEYWORDS: bearing capacity, earth reinforcement, retaining wall, soilbag, unconfined compressive strength

INTRODUCTION

Soilbags have long been used to reinforce dikes against floods and are used to build temporary structures in case of emergency (Kim et al. 2004). Soilbags, as new shore protection structures, especially at sandy coasts, are increasingly needed and widely used for flood emergency protection in dams and dikes, and also as construction elements for erosion control, bottom scour protection and scour fill artificial reefs, groynes, seawalls, breakwaters and dune reinforcement (Heibaum 1999; Restall et al. 2002; Saathoff et al. 2007; Shin and Oh 2007).

So far, soilbags have seldom been used for constructing permanent structures. The limited utilization of soilbags in constructing permanent struc-tures may be mainly due to a lack of mechanisms of the soil reinforcement by soilbags as well as the deteriora-tion of soilbags after a long termed exposure to sunlight (Matsuoka and Liu 2003). Matsuoka (2003) indicated that the bearing capacity of a foundation can be greatly improved if a part of the foundation is wrapped up with flexible reinforcement. Shao et al. (2005) and Huang et al. (2007) used soilbags to fill up ponds in highway in Jiangsu Province, China. Their field tests results show that solibags can effectively reduce the settlement of subgrade and cut down the engineering costs. However, limited studies on the unconfined compressive strength of real soilbags subjected to external forces have been conducted. In this paper, two case studies using soilbags in pond filling-up and expansive soil slope protection are presented.

MECHANICAL PROPERTIES OF SOILBAGS

Unconfined Compressive Strength of Soilbags

Unconfined compressive test is often used to determine the behavior of a material controlled under a constant rate, about 200 kg/min. The typical size of soilbags was 10 mm×40 mm×40 mm. The soilbags used for unconfined compressive strength tests were made of woven bags in which medium graded sands and gravels were contained. The soilbags were tamped and trimmed to a diamond shape so that their initial length, width and height would be easily measured before tests. The contained materials were medium sands and gravels with internal friction angles of 40º and 44º, respectively.

Soilbags were torn at the points such as contact points with the loading plate, the tailoring points and the maximum distortion points, where the external stress concentrated. The curves of measured compressive force versus settlement are shown in Fig.1. The curve of force-settlement relationship can be divided into two stages. At the early stage, the extension strain was less than the maximum extension strain of bags, the force was low and the contained materials were loose. The vertical settlement of soilbags increased rapidly with increasing extension strain of woven bags. As a result, the slope of the force-settlement curves is not high at the early stage. At the later stage, the slope of force-settlement curves is large. The extension strain was large enough to reach the maximum value. Contained materials in the bags were considerably compacted. The compressive force increased

[1] Professor, Department of Civil Engineering, Shanghai Jiao Tong University, CHINA. Email: yongfuxu@sjtu.edu.cn
[2] Section chief, Professor, Jiangsu Construction Headquarter of Highway Engineering, CHINA.

rapidly with the increase in the settlement of soilbags. This observation implies that during the late stage, even a large force is applied on the soilbag reinforced foundation, the settlement could be small. In other words, soilbags can be used to effectively reduce the foundation settlement. The measured stress-strain relationship of soilbags is shown in Fig. 2. The stress σ is vertical stress acting on the horizontal plane of soilbags, and equals to the vertical force divided by the horizontal area ($B \times L$), here B and L are the width and length of soilbags, respectively. The strain ε is vertical strain of soilbags.

The relationship between the unconfined compressive strength of soilbags and the tensile strength of woven bags is shown in Fig. 3. The unconfined compressive strength of soilbags linearly increased with the increase in the tensile strength T. The soilbags in which

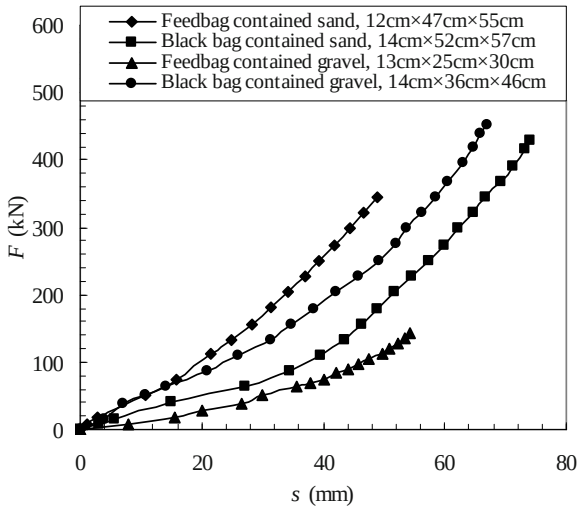

Fig. 1 Measured compressive force vs. settlement curves

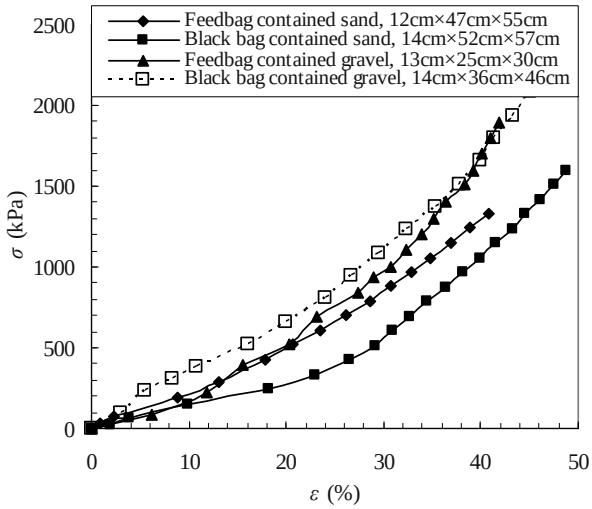

Fig. 2 The stress-strain curves of soilbags

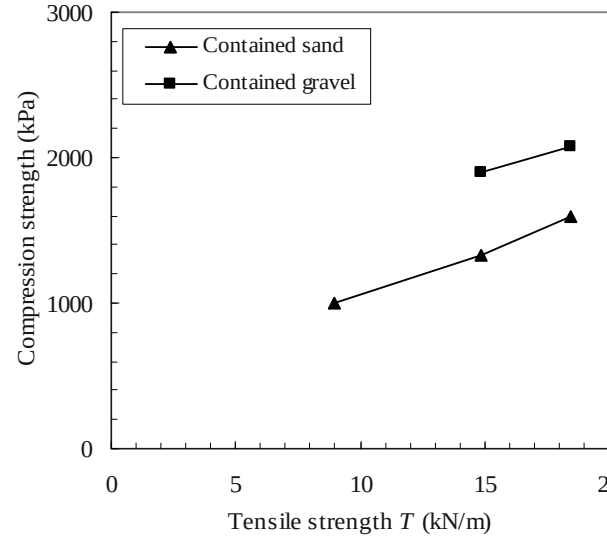

Fig. 3 Relationship between unconfined compressive strength and tensile strength

Fig. 4 Plate Load tests on soilbag reinforced foundation

gravels were contained have larger unconfined compressive strength than soilbags in which medium graded sands were contained. This is mainly because that the internal friction angle of the gravel is larger than that of the sand. During the unconfined compressive test, break of sand and gravel particles was observed.

Bearing Capacity of the Soilbag Foundation

Plate load tests were used to estimate the bearing capacity of the soilbag foundation under field loading conditions for a specific loading plate and depth of embedment. The plate load tests were carried out on a foundation reinforced by soilbags contained with sand, of which the internal friction angle was 33º. The test target is to validate the reinforcement of soilbags through measuring the bearing capacity (load) of real soilbag foundation, which is different from the conventional ones such as placing reinforcements (geotextiles, mattresses, strips, etc.,) horizontally installed in the grounds. In the

load tests, soilbags were kept to be 10 cm in height, 40 cm in width and length, respectively. The procedure of the bearing capacity tests is shown in Fig. 4. The diameter of the load plate is 0.5 m. The load was applied in stages and at each stage the load was maintained constant until the resulting settlement of foundation virtually ceases before applying the next load increment. When the settlement rate decreased to 0.5 mm/hr, the next load increment was applied. To measure the earth pressure between soilbags, the earth pressure transducers were installed in two different layers. The layout of the earth pressure transducers is shown in Fig. 5.

A series of bearing capacity tests were carried out on the real soilbag foundation. The slip surface of the soilbag foundation is similar with that of the soil foundation (Leshchinsky and Marcozzi 1990; Matsuoka 2003). It was observed that the soilbags were very solid and deformed similar to a footing foundation. The interparticle forces inside the soilbags are considerably larger than those outside (Yamamoto et al., 1995). This is because the external force acting on the footing induces a tensile force in the wrapping bags, and the tensile force thereafter acts on the contained materials inside the soilbags.

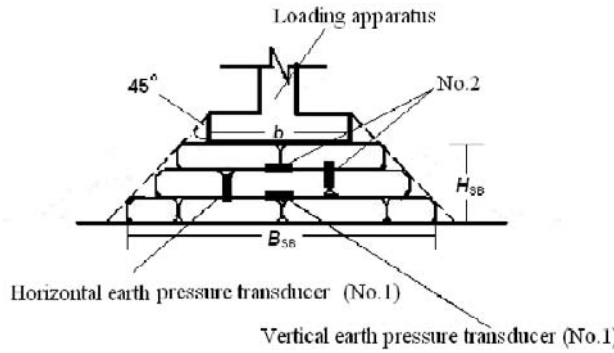

(a) Sketch map

(b) Installation of earth pressure transducer

Fig. 5 Earth pressure measurement between soilbags

The load-settlement curves of the plate load tests on real soilbag foundation are shown in Fig. 6. The vertical pressure, *p*, acts on the plate area. Soilbags are arranged as shown in Fig. 5a. The ultimate bearing capacity is determined according to the failure in the ground. From Fig. 6, it can be seen that the ultimate bearing capacity for the cases without soilbag, with 2 layers of soilbag, and with 3 layers of soilbag are 70 kPa, 160 kPa and 240 kPa, respectively. The bearing capacity of the soilbag reinforced ground is 2 to 3 times larger than that of the soil ground without soilbag.

The relationship between the bearing capacity and the height and width (length) of the soilbag foundation is shown in Fig. 7. In Fig. 7, B_{SB} and H_{SB} are the width (length) and height of the soilbag foundation, respectively, *b* is the width of the load plate. The relationship between the bearing capacity and the size of

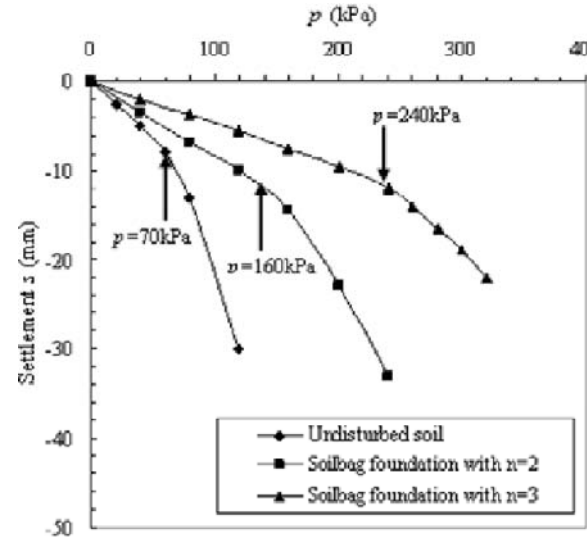

Fig. 6 Results of plate load tests

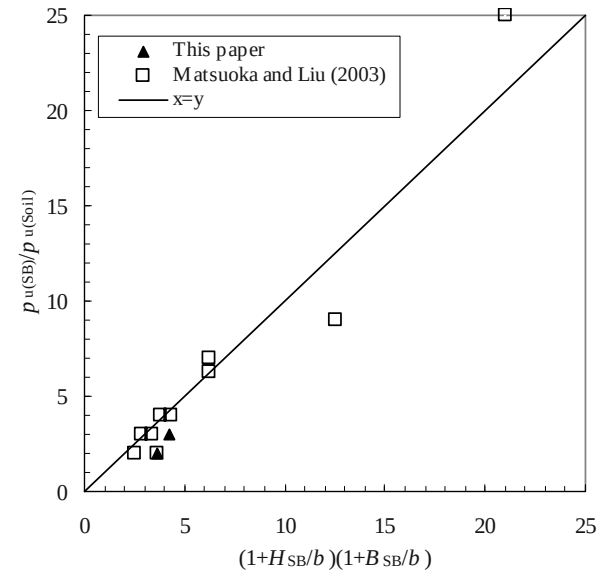

Fig. 7 Relationship between the bearing capacity and the size of the soilbag foundation

the soilbag foundation can be expressed by:

$$\frac{p_{u(SB)}}{p_{u(Soil)}} = \left(1+\frac{B_{SB}}{b}\right)\cdot\left(1+\frac{H_{SB}}{b}\right) \quad (1)$$

where $p_{u(SB)}$ and $p_{u(Soil)}$ are the ultimate bearing capacity of the soilbag foundation and undisturbed soil ground, respectively. The soilbag foundation is constructed by 2 layers at least according to Fig. 5a.

The earth pressure distribution in soilbags is shown in Fig. 8. In Fig. 8, σ_x and σ_z are the horizontal and vertical earth pressure between soilbags at the same plane. The solid line in Fig. 8 denotes the active earth pressure relationship, and the dashed line in Fig. 8 represents the earth pressure distribution at rest. The active earth pressure was calculated including apparent cohesion. It can be seen from Fig. 8 that the horizontal earth pressure is less than the active earth pressure and the earth pressure at rest is nearly constant. This phenomenon implies that soilbags were strongly confined by the tensile strength of bags, and could not laterally expand. The measured results of the earth pressure verify the reinforcement mechanism of soilbags.

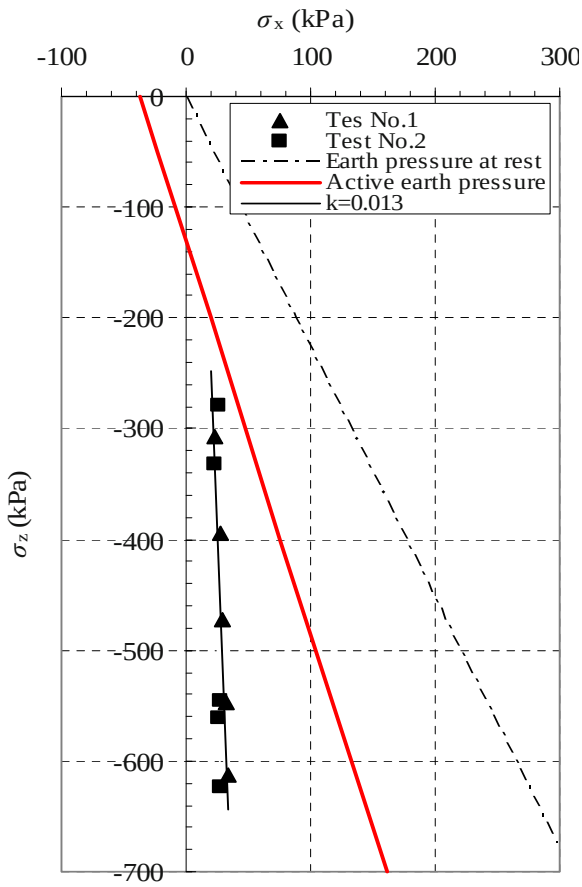

Fig. 8 Earth pressure distribution between soilbags

APPLICATION CASES OF SOILBAGS

Filling-up of Pond Using Soilbags

In the construction of highway in Jiangsu Province, extremely weak pond foundations were encountered where the ground was waterlogged and the construction machine could not stand on it. Initially the pond was designed to be improved by filling up crushed stones. However, this method is cost and usually results in large settlement. Finally, a new reinforcement method, the soilbag method was chosen to fill up the pond. In this case, one layer soilbags were first placed into the mucky ground, and the contained materials inside soilbags were natural soils with optimum water content. After the reinforcement by soilbags, the soft ground could even withstand a heavy construction machine like vibro-roller.

The design method of the pond filling-up by soilbags is shown in Fig. 9. Fig. 9a is the design of soilbags filled pond with a depth less than 3m, Fig. 9b is the design of soilbags filled pond with depth greater than 3 m, and Fig. 9c is for the important structure foundation, such as passage under road. The construction procedures are described as follows: (1) Excavate and remove the mucky soil from the pond bottom, (2) Compact the excavated foundation with vibrators and then place a layer of soilbags. The soilbags, having sizes of about 40 cm of length, 40 cm of width, and 10 cm of height, were made of natural soil with the optimum water content and polyethylene woven bags. They were connected mutually using high strength ropes and compacted thoroughly with vibro-roller. The compaction degree of the soil contained in woven bags was measured by the sand cone method, and was greater than 93%, which met the design requirement. (3) Place the second layer soilbags on the first layers and compacted soilbags using vibro-roller. After the construction of the two layers of soilbags, the natural soil was filled and rolled in a way similar to the tradition embankment filling materials. Since the confining stress σ of the subgrade soil is very small, its shear strength is therefore low. However, if soil is reinforced by woven bags, the shear strength of the soil would increase due to the tension force of the bags that is mobilized when the wrapped soil dilated under the traffic loading. This will lead to an increase in the bearing capacity of the subgrade foundation and the reduction in the settlement of subgrade soil. The effectiveness of this reinforcement method has been verified through a series of load tests on the soilbag foundation. The settlements of the subgrade plotted against the elapsed time are shown in Fig. 10. The settlement reaches the ultimate value much rapidly. The comparison of the ultimate settlement in the pond filled

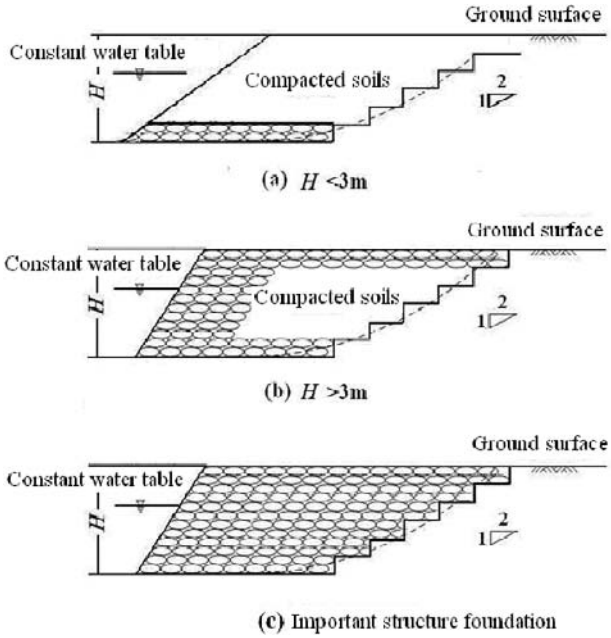

Fig. 9 Design of the pond by filling-up of soilbags

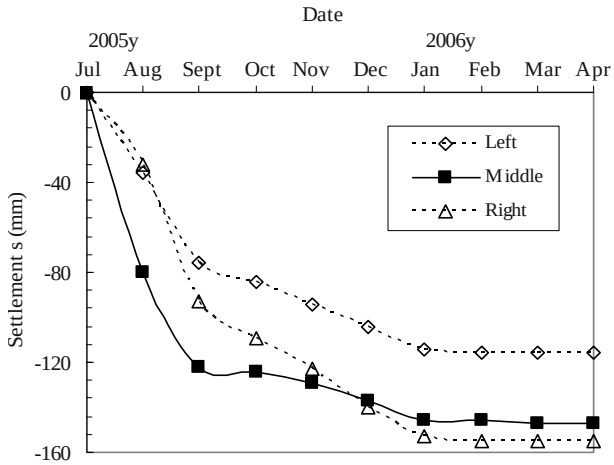

Fig. 10 Variation of measured settlement versus time of the soilbag subgrade

by soilbags and by crushed stone is shown in Fig. 11. It can be seen that the settlement reached more than 275 mm for the case reinforced by crushed stone, while reduced to less than 150 mm for the case reinforced by soilbags.

Slope Protection of Expansive Soil with Soilbags

Fig. 12 shows a case of construction of retaining walls using soilbags to protect the expansive soil slope. The retaining walls were constructed on the expansive soil foundation with a height of about 4 m, a total length of about 71m and an inclined angle of 30°. Four soilbags were connected in the lower part and the slope angle was 30° (Fig. 13). One soilbag has a length of 40 cm, width of 40 cm, and height of 10 cm. The materials inside the

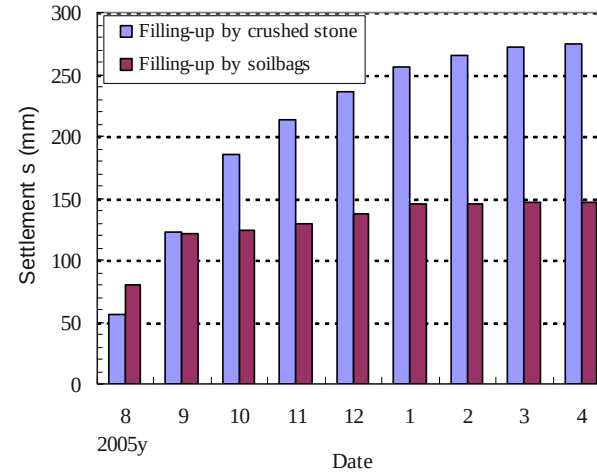

Fig. 11 Comparison of subgrade settlement in the pond between the case that filled by soilbags and the case that filled by crushed stone

Fig. 12 Retaining walls of soilbags to protect expansive soil slope

soilbags were natural soils with optimum water content. The woven bags were made of polyethylene. Soilbags were piled up and well compacted by vibrators layer by layer. Since the polyethylene bag was sensitive to sunlight, a thin layer of grass was cast on the outside surface of the wall, as shown in Fig. 13. In this project, about 2,000 soilbags were used and the construction was very silent because of no use of any heavy construction machines.

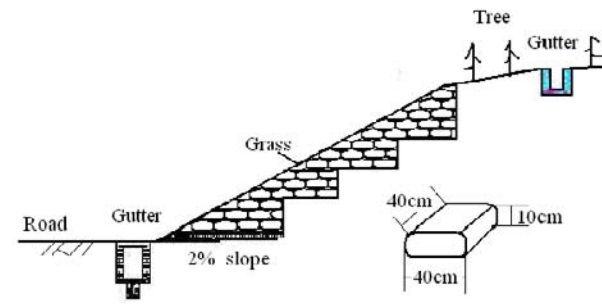

Fig. 13 Schematic design of a retaining wall using soilbags

CONCLUSIONS

From the tests and analysis presented in this paper, the merits of using soilbags as an earth reinforcement method in practice were discussed. Following conclusions can be drawn:

(1) Soilbags have high strength and little settlement when subjected to external load. This is due to the mobilized tension force of the bags upon external load.

(2) An apparent cohesion, *c*, which was induced in soilbags due to the tensile strength of the bags, significantly increased the compressive strength. The apparent cohesion, *c*, increased with the increase in the tension strength of woven bags and the internal friction angle of the contained materials.

(3) Soilbag reinforced foundation has high bearing capacity. The lateral earth pressure between soilbags is very low. The soilbags have high confining stress, which constrained the lateral displacement and reduced the settlement of the foundation.

ACKNOWLEDGEMENTS

The Communication Bureau of Jiangsu Province is acknowledged for its fund support. Lu MK, Gu XA, Dong Y of Changzhou Construction Headquarter of Highway Engineering, and Zhou BM of Jiangsu Construction Headquarter of Highway Engineering are also acknowledged for their help in the tests in situ. Shanghai Leading Academic Discipline Project (B208) is also acknowledged.

REFERENCES

Heibaum MH (1999) Coastal scour stabilization using granular filter in geosynthetic nonwoven containers. Geotextiles and Geomembranes 17: 341-352

Xu YF, Zhou BM, Tong LX (2007) Tests on soilbags. Journal of Highway and Transportation Research and Development (in Chinese): 84-88

Kim M, Freeman M, FitzPatrick BT et al (2004) Use of an apron to stabilize geomembrane tubes for fighting floods. Geotextiles & Geomembrane 22: 239

Leshchinsky D, Marcozzi GF (1990) Bearing Capacity of Shallow Foundations: Rigid vs. Flexible Models. Journal of Geotechnical Engineering, ASCE 116(11): 1750-1756

Matsuoka H (2003) A new interesting method of soil foundation. Kyoto University Press (in Japanese)

Matsuoka H, Liu SH (2003) A new earth reinforcement method by bags. Soils and Foundations 43: 173-188

Saathoff F, Oumeraci H, Restall S (2007) Australian and German experiences on the use of geotextile containers. Geotextiles & Geomembranes 25: 251-263

Shao JX, Huang J, Zhou BM, et al. (2005) Application of soilbags in subgrade engineering. Highway 7: 82-86 (in Chinese)

Shin EC, Oh YI (2007) Coastal erosion prevention by geotextile tube technology. Geotextiles and Geomembranes 25: 264–277

Yamamoto S, Matsuoka H (1995) Simulation by DEM for compression test on wrapped granular assemblies and bearing capacity improvement by soilbags, Proc. Of the 30th Japan National Conf. on SMFE: 1345-1348(in Japanese)

VERIFICATION OF VIBRATION REDUCTION CHARACTERISTICS WITH SOILBAG STRUCTURE

Y. Nakagawa[1], G.L. Chen[2], T. Tatsui[3] and S. Chida[4]

ABSTRACT: Soilbags are construction materials that contain soil or soil like materials in a bag with defined performance. Packs are standardized based on the tension strength, size and shape. The filler materials are specified by its internal friction angle. Its tolerance level against compression and shear stress is indicated based on the configuration. Authors have advanced the verification concerning the effect of reinforcement of soilbags by various experiments while the performance of soilbags is theoretically clarified thus.

Soilbags as the construction materials with defined performance quality are begin to be applied to the ground reinforcement or slope works so. On the other hand, it has been understood to have the effect of vibration reduction besides such the ground reinforcement characteristic in soilbag structure. The development of the method of vibration reduction that uses soilbag structure is advanced by this.

In this report, it introduces the verification experiments concerning the vibration reduction of soilbag structure and the application experiences to the construction works.

KEYWORDS: soilbag, vibration reduction, vibration measurement, Solpack method

INTRODUCTION

Noise of the road pavement and traffic vibration measures are nominated for a road environmental problem. As noise measure of the road pavement, a method with coarse graded asphalt concrete is used for the pavement outer layer. In contrast, as for the road traffic vibration measures, a method of construction to set up underground diaphragm walls is thought about. But it is it with large scale construction, and enormous expense is needed.

In this report, a method of reduce traffic vibration by laying soilbags in the letter of laminating under road is introduced. Soilbags have enough strength. On the other hand, pack materials repeat minute transformation by taking traffic load and soilbags have a function to absorb vibration energy. By making use of such properties of soilbags, the performance gain of the subgrade can be attempted by using stacked soilbags which have the effect of the ground reinforcement and the vibration reduction. By this, it is attempted slimming down of structure of pavement, reduction of total costs, and improvement of environment. In railway works, the gush of the mud caused by the vibration of the train can be suppressed by using stacked soilbags. And that leads to the performance gain in the railway foundations and the reduction of the maintenance costs.

PERFORMANCE EVALUATION TECHNICS OF SOILBAGS

Strength of Soilbag

When compression force acts on stacked soilbags, tension acts on pack materials. And confining pressure acts on filling materials. By this, soilbags occur by strength against compression pressure. When pack materials become not able to bear tension and breaks, soilbags reach destruction.

Fig. 1 shows schematic view about the shift of forces. When compressive pressure acts on, soilbags become go to be flat and the growth tension acts on pack materials. Furthermore, there is the property that is going to expand when the filling materials transform it. Tension produces in a bag and this tension acts on filling materials as confined pressure, because filling materials are confined with bags. Contact force between the particles of filling materials increase, and strong resistance is developed as soilbags. Soilbags have mechanism which increases

[1] Operating officer of planning and development branch, Techno Sol Co.,Ltd., JAPAN. Email: nakagawa@technosol.co.jp
[2] Operating officer (Head of Shanghai technical center), Techno Sol Co.,Ltd., JAPAN. Email: chen@technosol.co.jp
[3] Director (Head of Tsukuba technical center), Techno Sol Co.,Ltd., JAPAN. Email: tatsui@technosol.co.jp
[4] President, Solpack Association, JAPAN. Email: chida@chida-eng.jp

resistance by external force (Matsuoka et al. 2000).

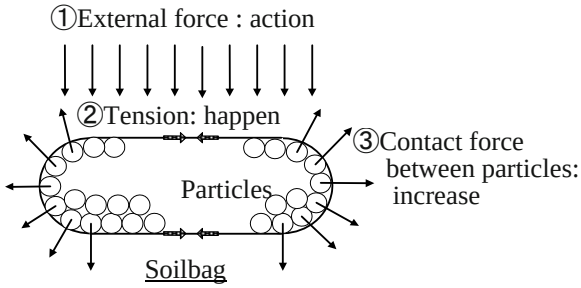

Fig. 1 Schematic view about the shift of forces

The compressive strength of soilbags is expressed with Eq. 1. Compressive strength of soilbags is in proportion to the tension of pack materials. And as much as the shape of the soilbags becomes thickness, strength increases. Therefore, strength of soilbags can be controlled by quantity of filling materials.

$$qu = 2 \cdot \frac{T}{B}(m \cdot Kp - 1) \cdot \left(\frac{m}{m+1}\right)^2 \quad (1)$$

qu: Strength against compression pressure
m: $m = B / H$
B: Load width of pressured surface
H : Thickness of soilbag
T: Tension strength of pack materials
Kp: Coefficient of passive earth pressure

Quality Inspections

The performance level of soilbags is calculated and tested. We can test the installation to verify the required performance is met or not.

Construction method of soilbags which is managed due to the below-mentioned item is named “Solpack method”. Below, it is stated “Solpack method”.

(1) Pack material（Strength, weather proof）
It is limited to the products certified by us.
(2) Property of the filler
It is necessary to find out the internal friction angle, before actual use.
(3) Specification of filler volume
The strength of soilbags is depended on the tension strength of the pack (T), strength constant of the filler (φ) and the volume of the filler. If T and φ are same, the strength is determined by the volume of the filler. Less the filler volume, the stronger soilbags is. It is important to control the filler volume. (When using our filler mould, the volume is controlled by adjusting the heights of the legs).
(4) Rules on Rolling Compaction
Add rolling compaction to soilbags to get the best of their potential performance. Apply rolling compaction according to the calculation result the relationship between number of rolling compaction and the dynamic modulos of deformation.

Fig. 2 Specification of filler volume
(Adjust the height of filling mould)

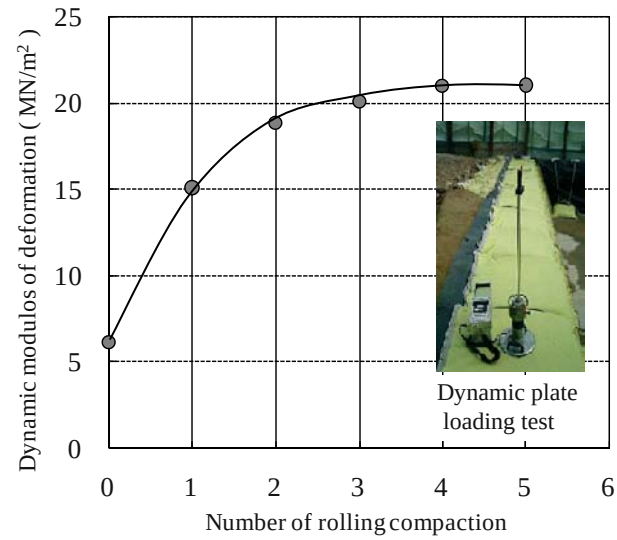

Fig. 3 Verification example of the dynamic modulos of deformation

Dynamic plate loading test (D.P.L.T.)

D.P.L.T. is followed by “Technical test regulation for the ground and rock mass, Chapter B 8.3 [Dynamic plate loading test] (TP BF-StB Teil B 8.3)”. This test is used as instant inspection of the dynamic modulos of deformation in construction management of an earth-work thing and road construction work.

The loading device consists of a 10 kg falling weight, which falls freely onto a set of steel springs and produces a load pulse with a peak of 7.07 kN and a pulse width of 18 ms.

In order to guarantee safe operation the falling weight is supplied with a transportation-lock pin and the guide rod with a stabilizer. To maintain the necessary constant drop height for every measurement a mechanism is mounted on the top of the rod to fix and release the falling weight.

CONSTRUCTION METHOD

In Solpack method, it must be constructed so that a target performance may be satisfied; construction and quality control are united.

Construction flow in Solpack method is shown in Fig. 4. By Solpack method, performance is shown by application of the performance display formula and quality inspection, and the grade of a required quality control changes with levels of a demand performance. Therefore, after taking into consideration importance, conditions of location, etc. of a structure, it is necessary to determine management frequency.

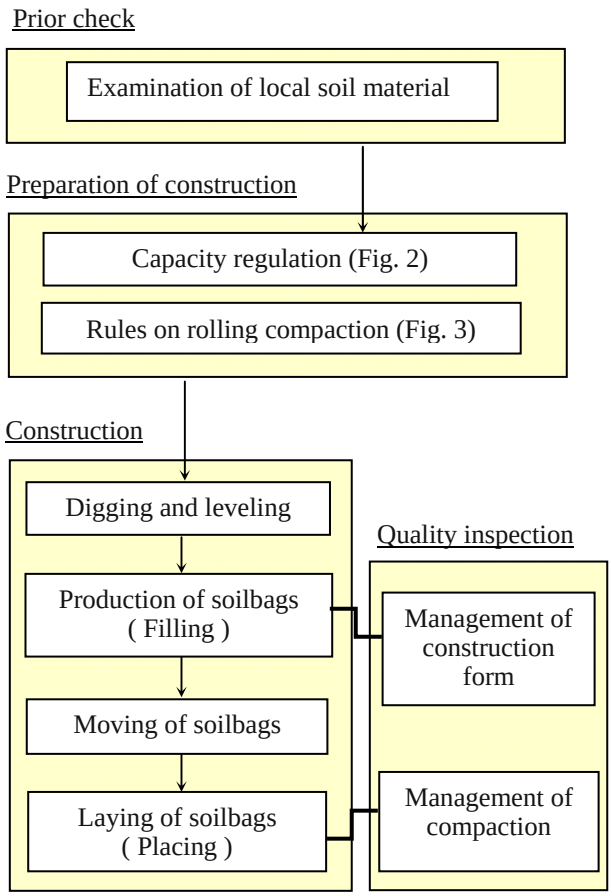

Fig. 4 Construction flow

Execution is mainly classified into three of the followings.

(1) Digging and leveling
(2) Production of soilbags (Filling)
(3) Laying of soilbags (Placing)

Digging and Leveling

In digging and leveling, the predetermined length shown in the design documents must be secured enough. And it has to be finished the foundation level (Fig. 5).

Fig. 5 Digging and leveling

Production of Soilbags

In production of soilbags, soilbags shall be produced so that efficient predetermined capacity may not be exceeded, using filling mould for soilbags.

The procedure of filling is shown Fig. 6.

Fig. 6 Production of soilbags (Filling)

Laying of Soilbags

About small sized soilbags, it covers by human power, and carries out using a crane or the bucket of back hoe. About large sized soilbags, it carries out using the hanging implement of the Rafter crane or the bucket of back hoe.

In case soilbags are laid, a crevice is making, laid in order in consideration of a spread width by compaction (Filling materials are compacted, and tension occurs in pack material by becoming flat accompanying it). If needed, in case the crevice between soilbags is filled up, it shall be carried out after compaction of soilbags.

And it must be compacted each layer using vibratory plate compactor.

Situations of placing and compaction are shown in Fig. 7.

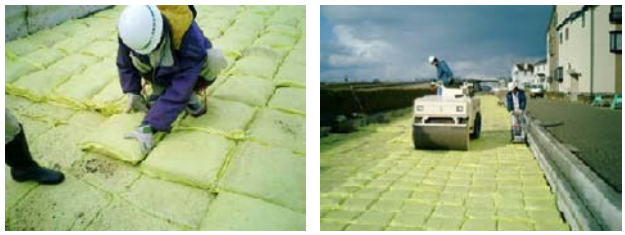

Placing Compaction

Fig. 7 Laying works

INSPECTIONS ABOUT VIBRATION REDUCTION WITH SOLPACK METHOD

Characteristics about Vibration Reduction

There is a function to absorb vibration energy to stacked soilbags. This is pack materials are elastic and to repeat minute deformation in turn, when soilbags catch the traffic load. It is able to reduce road traffic vibration by laying under the base course three or four layers soilbags which packed gravel materials. Because strength of soilbags is enough, stacked soilbags can prevent big damage of the road pavement (collapse, step, and sinking). In addition, by the load distribution effect of stacked soilbags, there is a stable property for vibration repeatedly. On this account, road pavement is stabilized with the progress the number of years after the service having maintained a vibration reduction function. And it can be maintained effect of vibration reduction for a long term.

Inspection of Vibration Reduction Effect

According to the research of past, when soilbags are received vibration to top and bottom direction, energy attenuation occurs by the fact that leveling and reconstructing are repeated. And, during soilbags which it adjoins contacting even if, transmission of vibration is little. Stacked soilbags show vibration reduction effect these two characteristics (pliability and individual characteristic) with.

Experimental models regarding the characteristics of vibration reduction of stacked soilbags are shown in Fig. 8. CASE1 is the model that arranged 3×3 lines of soilbags packed in crushed stone and stacked 4 layers. CASE2 is a general pavement model backfilled in crushed stone. It experimented these two cases, and compared vibration reduction. Experiment was done with the method of dropping the weight on the test models where the loading plate of thickness 10cm and width 80 cm is placed on. Acceleration sensors are arranged to examination models and measured acceleration at depth and horizontal directions when a weight dropped on.

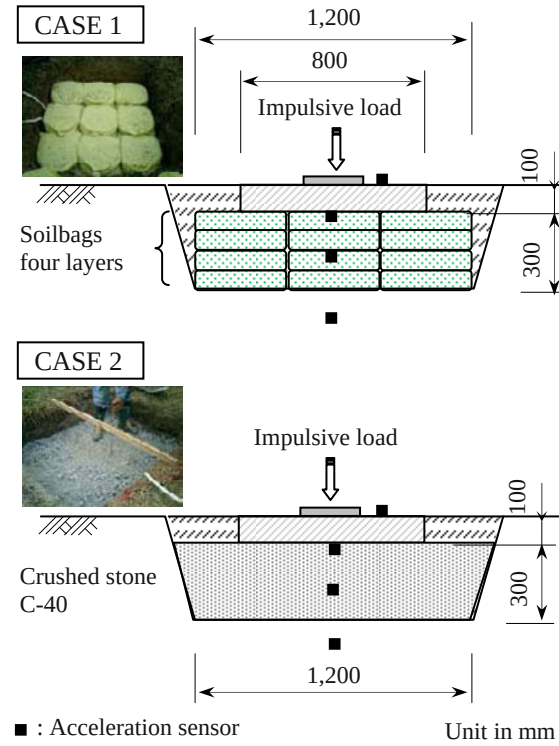

Fig. 8 Cross sections of examination model

Fig. 9 Impact loading device using the weight

Fig. 10 shows transmission rate of acceleration at the depth direction when dropping the weight from height of 10cm. Transmission rate of acceleration is shown with the value that divided acceleration measured at each position by acceleration of the loading point. According to this, as for transmission rate of acceleration at the depth direction, CASE1 shows small value than CASE2. Fig. 11 shows distance attenuation of vibration at the horizontal direction. Like the depth direction, CASE1 shows small value than CASE2.

Based on this result, it is found that soilbag structure is hard to transmit vibration and vibration reduction is large.

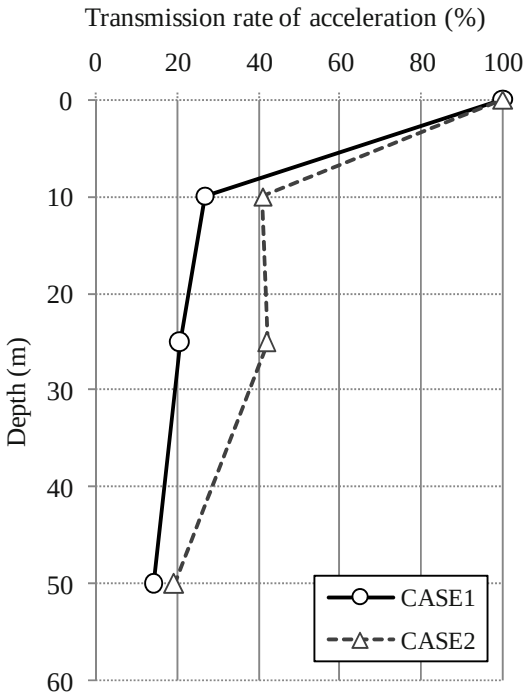

Fig. 10 Acceleration transmission rate of depth direction

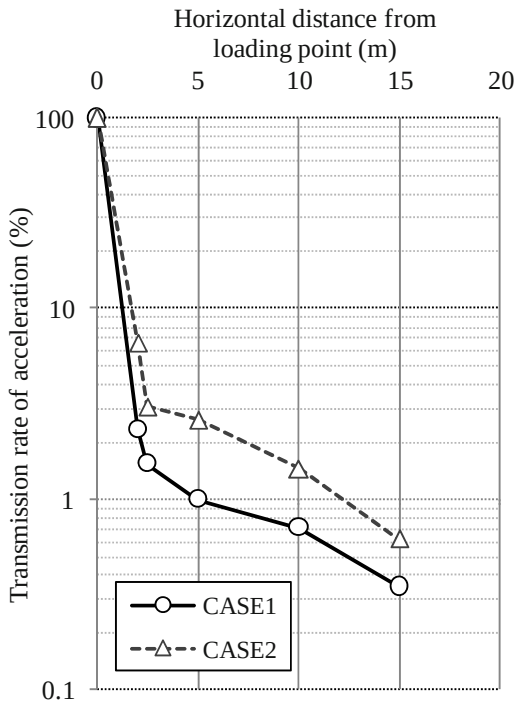

Fig. 11 Distance attenuation of acceleration

An application Example to Road Works

An example which vibration reduction characteristic of Solpack method is applied to road works is introduced. This road works is neighboring at houses, and Solpack method was adopted for the purpose of reducing traffic vibration to affect houses.

Structure of pavement which uses Solpack method is shown Fig. 12. Soilbags are laid 3—4 layers in the subgrade, and the width is 6.8 m. It is used recycled crushed stone for filling materials. On the other hand, as for normal pavement, recycled crushed stone was used for the subgrade without using soilbags.

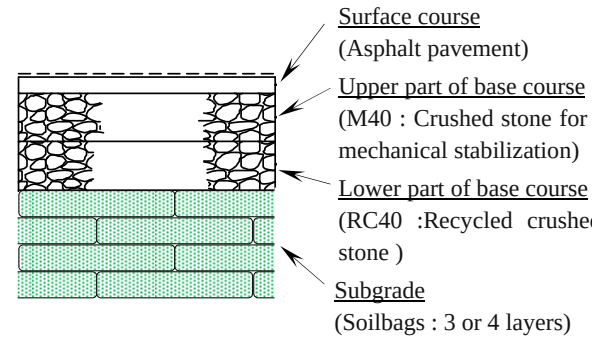

Fig. 12 Structure of pavement using Solpack method

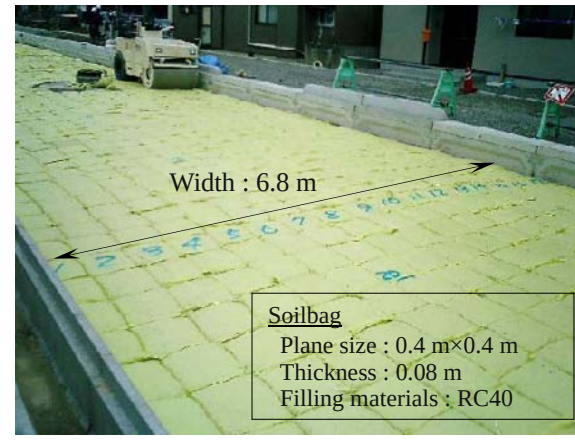

Fig. 13 A view of Solpack method

Vibration measurements were done by running a car on the base course. Transmission of vibration in road intersection direction was measured using vibration level-meters.

Table 1 and Fig. 14 show measurement results at the border of road, the border of road-housing site, and housing site when a dump-truck runs with 50 km per an hour. According to this, effect of vibration reduction approximately of 10 dB is verified at the pavement using Solpack method. However, difference by the number of layers of soilbags is small.

Next, measurement results at the case of small-car are shown in Table 2 and Fig. 15. Because vibration level is small about this case, the difference of vibration at the border of road. But, vibration reduction effect of the pavement using Solpack method is clearly in or near the housing site.

Table 1 Vibration level at the time of a dump-truck run

Locations of measurements	Distance from the border of roadway		
	0 m	4.5 m	14.5 m
Normal subgrade	66.0 dB	62.6 dB	59.6 dB
Soilbags 3 layers	57.7 dB	51.8 dB	50.7 dB
Soilbags 4 layers	53.2 dB	50.9 dB	49.6 dB

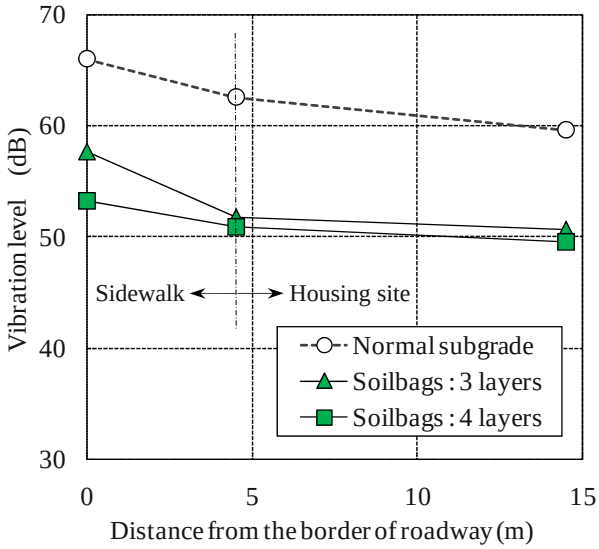

Fig. 14 Results of measurement
(A dump-truck runs with 50 km/h)

Table 2 Vibration level at the time of a small-car run

Locations of measurements	Distance from the border of roadway		
	0 m	4.5 m	14.5 m
Normal subgrade	52.5 dB	49.4 dB	48.3 dB
Soilbags 3 layers	48.8 dB	40.7 dB	39.0 dB
Soilbags 4 layers	51.1 dB	41.2 dB	43.0 dB

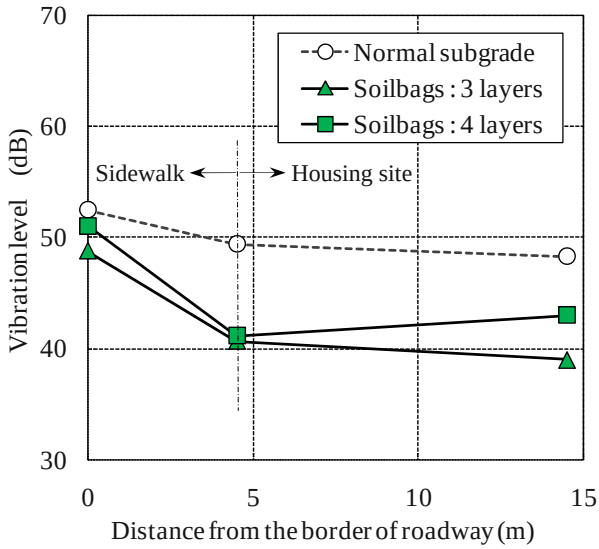

Fig. 15 Results of measurement
(A small-car runs with 40km/h)

CONCLUSIONS

The vibration reduction effect of Solpack method was identified by basic experiments and field inspections. Recently, Solpack method comes to be used as a vibration reduction method in construction field except road works so that it is shown in Fig. 16.

It is thought that elucidation of the vibration reduction mechanism and establishment of the design method that accepted a use are necessary, in future.

Railroad works Building foundations

Fig. 16 Application to other construction

ACKNOWLEDGEMENTS

This development has been supported by Solpack Association and carried out with many engineers by the cooperation of the construction worker. Authors would like to express thanks for their support.

REFERENCES

Matsuoka H, Chen Y, Kodama H, Yamaji Y, Tanaka R (2000) Mechanical properties of soilbags and unconfined compression tests on model and real soilbags, Proc. of the 35th Japan National Conference on Geotechnical Engineering 544: 1075-1076

Imaoka K, Matsuoka H, Ando T, Kitamura K, Ando H (2005) Reduction of traffic-induced vibration by soilbags, Proc. of the 40th Japan National Conference on Geotechnical Engineering 576: 1153-1154 (in Japanese)

Matsuoka H (1999) Soil Mechanics, Morikita Publication Co. Ltd. (in Japanese)

Yashima A, Sawada K, Seo Y, Minowa T, Tatsui T, Nakagawa Y (2005) The evaluation experiment of the slipping-down impact load applied to a Solpack-buffer system, Proc. of the 40th Japan National Conference on Geotechnical Engineering 1227: 2449-2450 (in Japanese)

Nakagawa Y, Sato M, Sakai M, Ootani Y, Teramoto H, Morimune Y (2005) Reduction Methods of Heat-island Phenomenon by Storage Type SOLPACK, Proc. of the 40th Japan National Conference on Geotechnical Engineering 1227: 2449-2450 (in Japanese)

APPLICATION OF STACKED SOILBAGS FOR SLOPE PROTECTION

G.L. Chen[1], Y. Huang[2], M. Sato[3] and S. Chida[4]

ABSTRACT: Generally, soilbags are widely used in temporary structures in the case of emergency or building constructions as a temporary engineering material. Previous applications are mostly based on experiences rather than the knowledge of its mechanical behavior and operation principles from the view of engineering mechanics. In this paper, the mechanism of soilbags is first addressed from the mechanical principles. Followed are an introduction of design concepts and applications for soilbags, including mechanical tests on single soilbags, researches and corresponding knowledge, and practical applications of stacked soilbags.

KEYWORDS: soilbags, slope protection, bearing capacity, strength, earthquake, material

INTRODUCTION

As used in common temporary engineering, a soilbag is simply filled with soils, whose working performance is not evaluated quantitatively. As a result of ongoing theoretical analyses and experimental researches on soilbags, however, new engineering performance and features are discovered (Matsuoka et al. 2000). This new finding has urged the applications of soilbags to permanent or semipermanent earth structures as a new type of earth reinforcement method. In addition, it also provides basis for setting material and construction demands in future performance-based design. In this paper, technical analysis and a performance evaluation method are first introduced with regard to soilbags. Then several practical applications are described in slope protections.

ENGINEERING DEFINITION OF SOILBAGS

Soil strength is generally determined by the external constraining forces. The soilbag considered in the paper is referred to as a woven bag which is filled with filling material (soils or materials analogous to soils). The strength of soilbags is reinforced by effective restraint on external forces and deformations due to tensile force of the woven bag. Performance of each soilbag can be definitely quantified. The compression strength, shear strength and deformation ability of a soilbag is depending on the tensile strength of the woven bag, internal friction angle and the soilbag volume (Japanese Patent 03187804).

PRINCIPLES OF SOILBAGS

Fig. 1 is a schematic view showing the reinforcement principles of performance-quantified soilbags. According to the figure, the traditional concept that external force is the main factor resulting in soil failure is disapproved. On the contrary, soilbags make use of external forces (various loadings) to obtain strength. Consequently, they are well-suited to various construction methods in work site even using low-cost filled-in soil materials. Besides, no matter a single soilbag or a soilbag group, the working performance is able to be quantitatively described like steel and concrete materials.

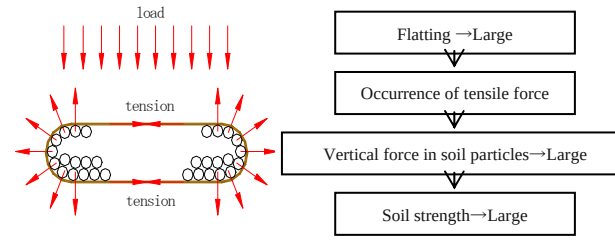

Fig. 1 Reinforcement principles of performance-quantified soilbags

[1] Manager, Techno Sol Co.,Ltd, JAPAN. Email: chen@technosol.co.jp
[2] Associate Professor, Department of Geotechnical Engineering, Tongji University, CHINA. Email: yhuang@mail.tongji.edu.cn
[3] President, Techno Sol Co.,Ltd, JAPAN. Email: sato@technosol.co.jp
[4] President, Solpack Association, JAPAN. Email: chida@chida-eng.jp

Fig. 2 shows the size and stress state of a soilbag. Eq. 1 is easily obtained according to the limit stress equilibrium state. Eq. 1 is used for quantifying soilbag performance in practical design. The concept was originated by Prof. Matsuoka at Nagoya Institute of Technology.

$$\sigma_{1f} = \sigma_{3f} K_p + 2\frac{T}{B}\left(\frac{B}{H} K_p\text{-}1\right) \tag{1}$$

in which,

$$K_p = \frac{1+\sin\varphi}{1\text{-}\sin\varphi} \tag{2}$$

where B and H are the width of compression surface and section depth of soilbags, respectively; T is the tensile strength of soilbag material.

Previous research showed that filling material reaches limit equilibrium state at the same time as a soilbag fails (Matsuoka et al. 2000). Moreover, load test results in the same research showed that the soilbag failure load may be over 40 times tensile strength of the woven bag.

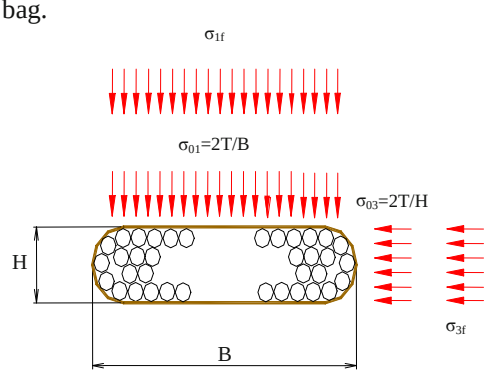

Fig. 2 Size and stress state of a single soilbag

SOILBAG MATERIAL AND FIELD MANAGEMENT

In work site, the following field management should be performed to ensure construction quality.

(1) Material Management of Woven Bags

Woven bags need sufficient tensile strength and durability. Woven bags are usually made of PE or PP material, which are particularly sensitive to ultraviolet rays. In principle, soilbags is inapplicable to the working environment with ultraviolet rays. Instead, it should be used in soils or in lightproof conditions.

(2) Physical Properties of Filling Material

Internal friction angle φ as well as other parameters should be obtained by laboratory tests when on-site dump is used.

(3) Packing Volume Management

From Eq. 1, the strength of single soilbag is determined by volume given the same T and φ. The smaller is the volume, the larger is the strength. Therefore, the filled volume should be controlled less than the limit value from the field management point of view.

(4) Rolling Management

On-site rolling is necessary in order to make full use of engineering performances of well-laid soilbags. Usually, relation curves of rolling number and dynamic deformation modulus are obtained through rolling before real construction. These curves will be used later to control the real rolling numbers.

DESIGN METHOD OF STACKED SOILBAGS

Technical features of a single soilbag have been introduced in the above sections. In real engineering, however, soilbags are mostly used in the form of stacked soilbags. This section will address on the design concept and requirements of construction details for application of soilbags in slope protection.

Retaining Wall Reinforced by Soilbags (Soilbag Wall)

Using soilbags in slope protection should ensure the strength of a single soilbag. In addition, adequate safety capacity should be guaranteed if calculated failure slip surface exists.

Fig. 3 illustrates the concept design of stacked soilbags used as a reinforced retaining wall.

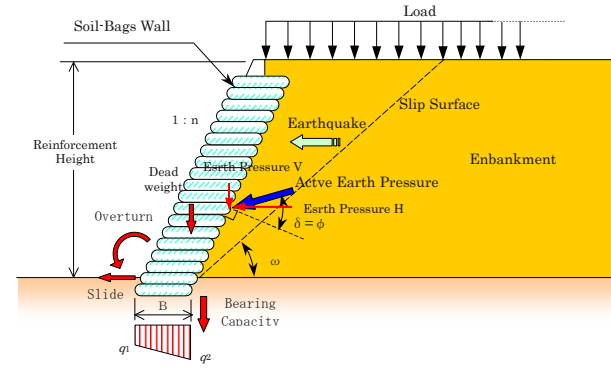

Fig. 3 Concept design of stacked soilbags

The use of stacked soilbags is a construction method developed for slope stability, making use of the design concept of semi gravity retaining walls and reinforced

soil retaining walls. In design, safety evaluation should be conducted on a single soilbag or a soilbag group in all aspects of loading, deformation, and environment. Checking computations should also be made on the safety of backfill and stability of slope or structures to satisfy operation function.

Fig. 4 shows a design flowchart of a soilbag wall. Generally, the design approach for soilbag walls may refer to the conventional concept of reinforced retaining walls, which is based on limit equilibrium methods and can be divided into three parts as follows: 1) internal stability analysis for possible failures within the reinforced soil blocks; 2) external stability analysis for possible failures behind and underneath the reinforced soil blocks; 3) compound stability analysis for possible failures behind and through the reinforced soil blocks.

In slope engineering, stacked soilbags are checked as a rigid body in terms of sliding, overturning, bearing capacity and overall stability. Calculation of earth pressures is started from the moving trend of the soilbag wall. The earth pressure acting on the wall should be considered as active earth pressure. Several linear slip surfaces are assumed at the base of slope. Then, the maximum active earth pressure and the corresponding slide angle are calculated. Stability of walls and bearing capacity of foundations can be evaluated with comparison of safety coefficient and design demand.

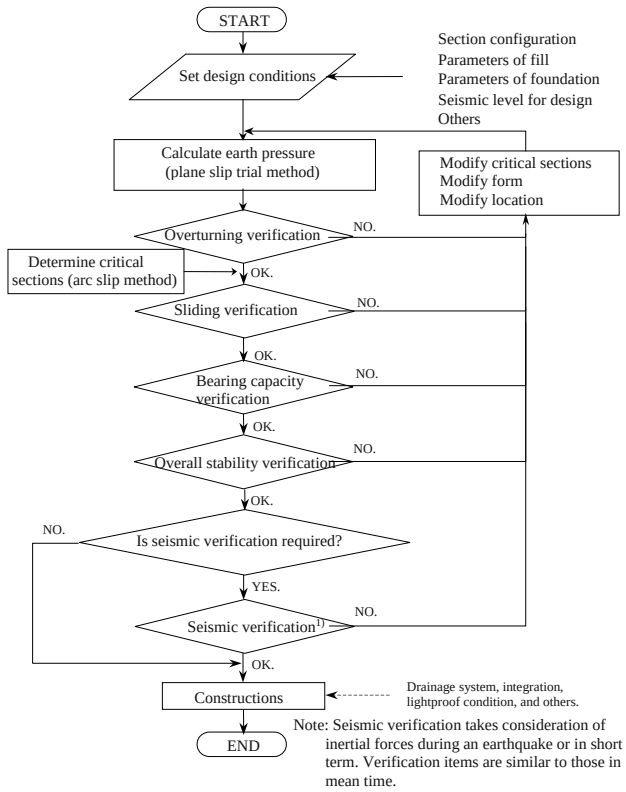

Fig. 4 Design flowchart for soilbag walls

Most important, the upper bound of friction coefficient is set as 0.6 for bottom surface of the wall from safety viewpoint. Besides, cohesive force of filling materials is not considered in principle.

For bearing capacity, no tension stress will be produced even the location of the resulting force exceeds the range of the bottom slab because a soilbag reinforce retaining wall presents advantages of a flexible structure. Therefore, it is assumed that tensile force is triangular distributed at the toe of the bottom slab. The foundation reaction is computed, being assumed to be distributed in all range of the bottom surface.

In addition, verification should be made on the compression strength of soilbags to ensure safety margin against foundation reactions.

In overall stability verification, circular slip method is adopted. Safety coefficient is determined assuming slip surface through base foundation and stacked soilbags. For stacked soilbags, upper loading may generate suspected cohesive forces in soilbags. So far, this value is taken as 5% of soilbag compression strength since it cannot be assessed quantitatively.

It should be noted that the loads on soilbag reinforced retaining walls may be different in the case of earthquake and in mean time. A number of factors should be taken account, such as the earthquake intensity, the inertial force induced by the wall weight, dynamic earth pressure of filled soil at the back of the wall, importance of the wall, and the difficulty for retrofit.

Large-scale shaking table test (wall height is about 5 m, and the slope of the wall surface is 1:0.3) has shown that stacked soilbags present characteristics of flexible retaining walls. The inertial force and the earth pressure will not occur in the same direction together during an earthquake. In addition, the maximum foundation reaction is less than twice of the wall weight during an earthquake.

However, researches on applicability of soilbag walls are still under going. For safety, inertial force and dynamic earth pressure during an earth are considered together in present design if seismic verification is required.

Requirements of Construction Details for Soilbag Walls

(1) *Necessity of integral soilbag walls*

Large-scale shaking table experiments, as mentioned before, has demonstrated that soilbag walls without integration also have sufficient stability against strong ground motions given surface slope of 1:0.3. In stability verification, suspected cohesive forces, however, may change with the force direction, wall height, and assembly form of soilbags. Hence, seismic horizontal

forces will be sustained by integrated polyethylene material without the contribution of the cohesive force.

(2) *Measurements against ultraviolet rays*

Woven bag is made of PE and PP or PET materials. They are resistless against ultraviolet rays despite of their high performance of acid-proof and lime resistance. Consequently, it should be ensured that soilbags are used in soils completely during service period. Generally, the following measures are adopted to ensure durability at least a decade.

a. Covering with light-proof cloth;
b. Retaining vegetation protection;
c. Use of concrete walls.

(3) *Settlement flexibility*

A soilbag consists of a woven bag and filling material. It may generate certain compression deformation according to the strength properties of filling material. Filling materials are, in common, crushed stones or on-site soils. Generally, the settlement of stacked soilbags does not exceed filling soils at the back of walls. Moreover, soilbag reinforced retaining walls present flexible features, which has good flexibility to deformation and settlement of walls.

APPLICATION CASES

Retrofit of a National Road (Seismic Hazard)

A slope of a certain national road was destroyed by a strong earthquake in Chuetsu area, Japan. In retrofit, a retaining wall with 4.6 m height was built using soilbags. Surface slope was 1:0.3. In order to glorify environment, soilbags were used as wall facing for vegetation restoration. Fig. 5 shows the design standard section. Photos in Fig. 6 illustrate the overview in construction and the construction processes.

Retrofit of a Skiing Field (Slope Hazard)

The slope of a skiing field was divided into upper and lower parts. Soilbag walls were built separately in two parts, which were 5.4 m and 5.9 m height respectively. In order to glorify the environment of the skiing field, soilbags were used as wall facing for vegetation restoration. Fig. 7 shows the design standard section. The design scheme adopts two columns of small soilbags. Fig. 8 shows the construction overview. Fig. 9 shows the related photos of the construction process.

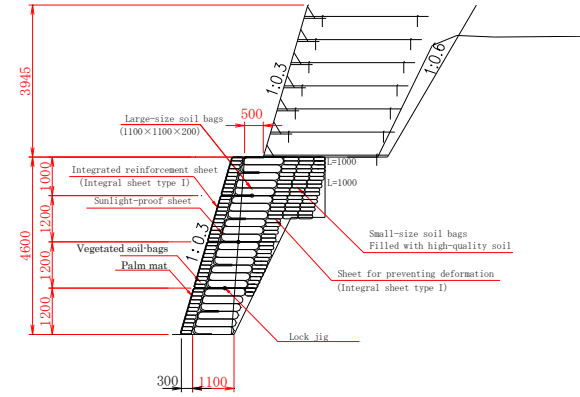

Fig. 5 Standard design section of a national road in Chuetsu area

Preparing for vegetation

Paving soilbags

Paving integrated high polyethylene material

Fig. 6 Construction processes for soilbag walls

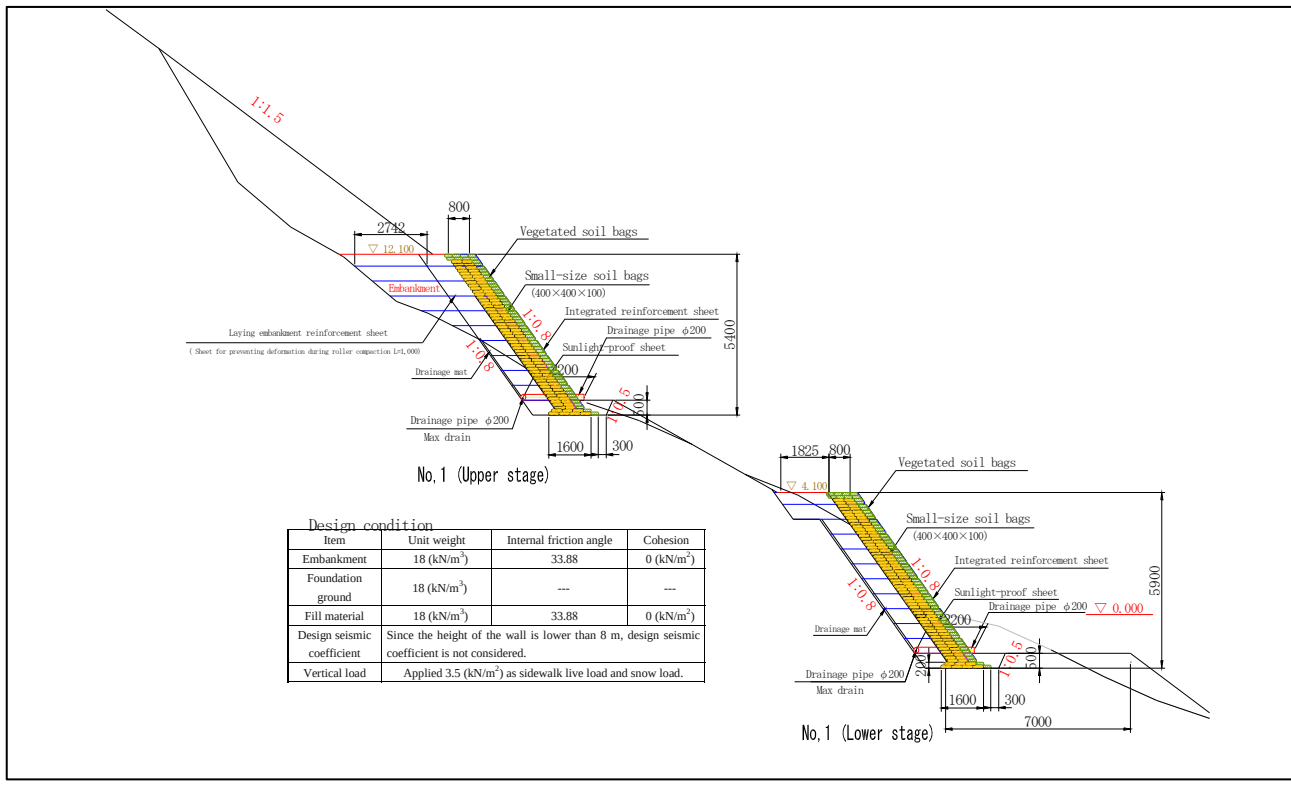

Design condition

Item	Unit weight	Internal friction angle	Cohesion
Embankment	18 (kN/m^3)	33.88	0 (kN/m^2)
Foundation ground	18 (kN/m^3)	---	---
Fill material	18 (kN/m^3)	33.88	0 (kN/m^2)
Design seismic coefficient	Since the height of the wall is lower than 8 m, design seismic coefficient is not considered.		
Vertical load	Applied 3.5 (kN/m^2) as sidewalk live load and snow load.		

Fig. 7 Design standard section of a skiing field

CONCLUSIONS

Technical feasibilities of reinforced retaining walls, which are composed by stacked soilbags, are validated theoretically and experimentally. A relative complete design system is also established. Compare to the other construction methods, using soilbag walls is able to significantly decrease soil treating at the back of a retaining wall, hence, reduce construction cost. Moreover, it is environment-friendly due to use of dump in site as filled-in materials.

It has been about eight years since research and development. It has been widely used in Japan and it is now spread in Asia and Africa.

No special construction equipment is needed. No special skilled worker is needed neither, as is benefit in the areas where manpower resources are abundant.

To improve the design system, further research and analysis are needed in terms of the design of soilbag compression strength, applicable height and slope.

Fig. 8 A view of the Project

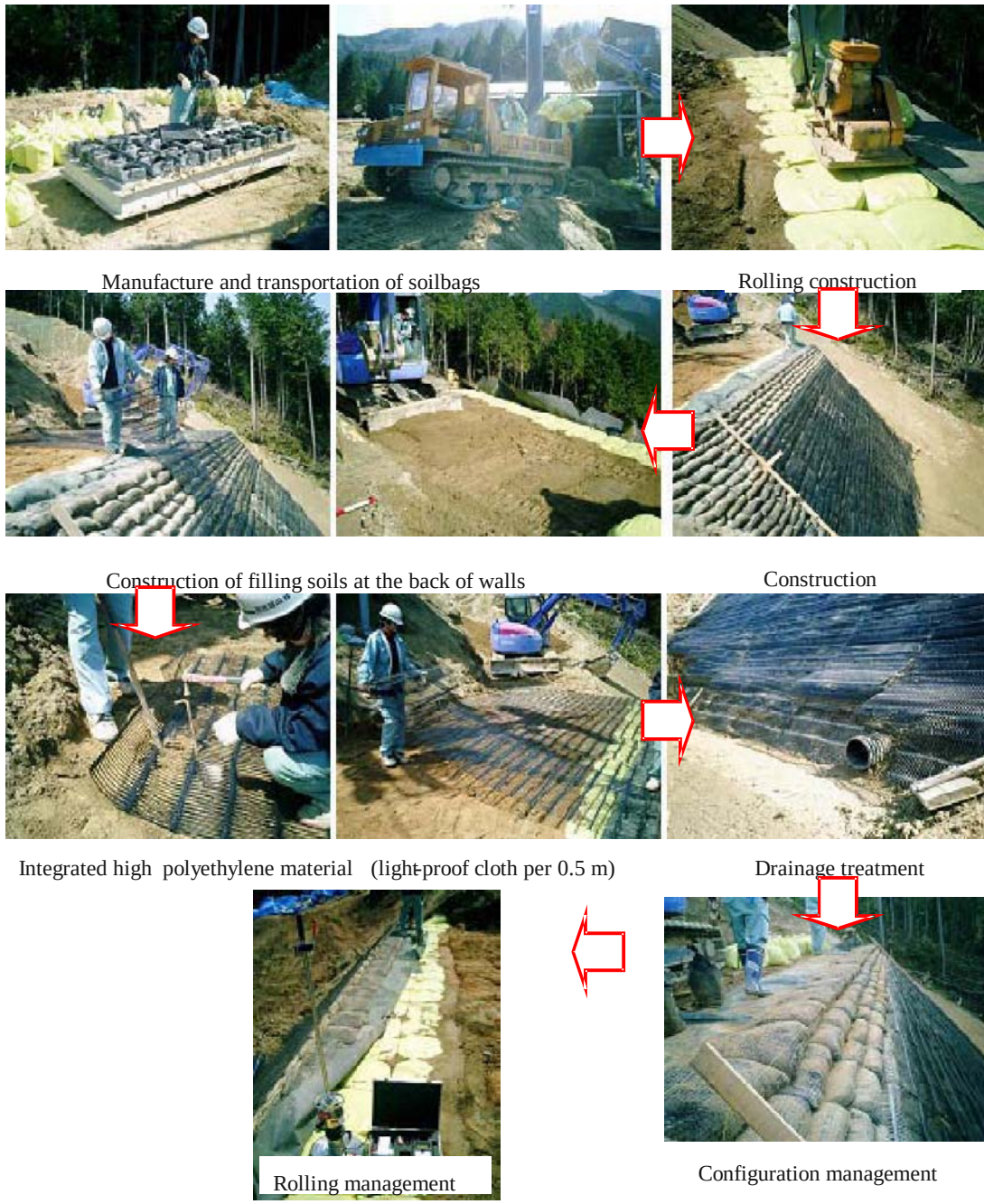

Fig. 9 Photos of the construction processes

REFERENCES

Matsuoka H, Chen Y, Kodama H, Yamaji Y, Tanaka R (2000) Mechanical properties of soilbags and unconfined compression tests on model and real soilbags, Proc. of the 35th Japan National Conf. on Geotech. Engrg 544: 1075-1076

Matsuoka H (2003) New approaches in geotechnical engineering. Kyoto: Kyoto University Press

NETIS Login number provided by New Technology Information System (CB-030011)

Co-research report of Ministry of Land, Infrastructure, Transport and Tourism, Building Research Institute and Nagoya Institute of Technology

MODELING GEOTEXTILE CONTAINER IN MARINE CONSTRUCTION USING GEOTECHNICAL CENTRIFUGE

C.Y. Tan[1] and S.H. Chew[2]

ABSTRACT: Given its flexibility, and erosion resistivity, geotextile containers are very suitable to be used as massive gravity structures in reclamation projects at deep water. Geotextile containers have become increasingly popular in many marine constructions. In a recent land reclamation project in Singapore, geotextile containers have been proposed as a solution for the containment of dredged material and at the same time, form part of the revetment structure in the project. These geotextile containers will be dumped into a maximum water depth of 25 m. Current experience on the use of geotextile containers is limited to installation depth of less than 20 m. Failure of geotextile container might occur due to excessive strain development during the construction stages. This study aims to investigate the strain development of the geotextile containers during the falling and landing process. Geotextile container is being modelled and tested in the geotechnical centrifuge in National University of Singapore. This centrifuge model is capable of reproducing the high stress level associated in the application of geotextile containers in this case. This paper reports on the model setup in centrifuge and the experimental procedure. The preliminary results are shown and discussed in this paper.

KEYWORDS: geotextile containers, centrifuge test, strain in geotextile

INTRODUCTION

Geotextile container is a form of single containment unit that is filled mechanically with sand, clay, or dredged material. Several geotextile containers can also be stacked or placed to form a bigger containment area. They have been successfully applied in hydraulic and coastal engineering in recent years such as shore protection, breakwaters, etc. (Pilarczyk 2000). In a reclamation project involving a lot of dredging of soft sediment and soft clay, dredged material often requires a specially designated containment area for disposal. Geotextile containers can be a good solution for the containment of such dredged material. One example is the use of geotextile container in Southern Island, Singapore to form a continuous perimeter bund for dumping ground of dredging spoils. Besides forming a perimeter bund, the filled containers can also be stacked to form part of the revetment structure in land reclamation projects.

In a recent land reclamation project in Singapore, geotextile containers have been proposed as a solution for the containment of dredged material and at the same time, form part of the revetment structure in the project. These geotextile containers will be dumped into a maximum water depth of 25 m However, the current experience on the use of geotextile container is limited to installation depth of less than 20 m. In addition, there are concerns on the placing accuracy of the geotextile container during installation at water depth of more than 20 m. Furthermore, the integrity of the units during release and impact, and the hydraulic stability of the whole structure are also concerned. At the moment, there is still lacking in theoretical basis for an accurate design model for such deep water case (Pilarczyk 2000).

The main obstacle in the application of the use of geotextile containers in containment bund is the lack of proper design criteria as compared to using rock and concrete blocks. Furthermore, due to the fact that the water depth in this project is much deeper than prior experience reported in literature, there is a concern on the long term performance of such system at this time. Thus, there is a need for research to get a better insight into the design and mechanism of such system.

An extensive research was initiated to investigate the design criteria, stability, and installation performance of geotextile containers. This paper presents an initial part of the study, focusing on the modelling the geotextile container in centrifuge.

[1] Doctoral Research Scholar, Department of Civil Engineering, National University of Singapore. SINGAPORE. Email:g0500497@nus.edu.sg
[2] Assistant Professor, Department of Civil Engineering, National University of Singapore. SINGAPORE. Email:cvecsh@nus.edu.sg

EXPERIMENTAL SETUP

The National University of Singapore's geotechnical centrifuge has been used for the model tests on geotextile container. This geotechnical centrifuge has a payload capacity of 40 g-tonnes and a maximum working g-level of 200 g (Lee et al. 1991). Figs. 1 and 2 shows a photograph of the experimental setup and the schematic diagram of the current experimental setup in centrifuge respectively. The strong box used for this experiment features an internal dimension of 420 mm× 420 mm×480 mm (L×W×H). The front sidewall of the container is made of Perspex plate, which allows observation to be done visually.

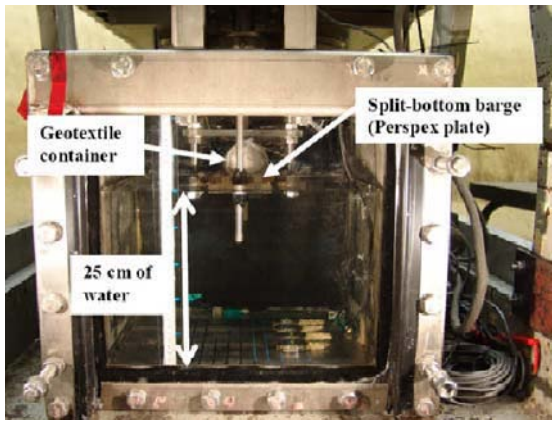

Fig. 1 Experimental set-up in the NUS Geotechnical Centrifuge

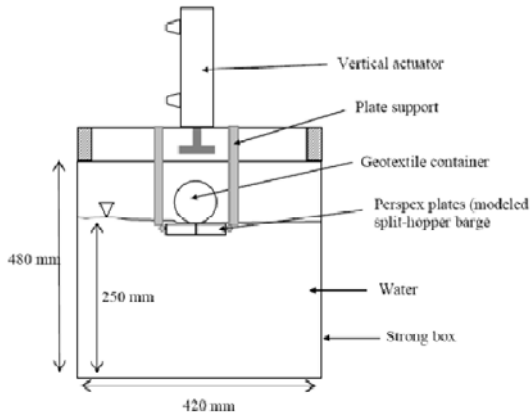

Fig. 2 Schematic diagram of experimental set-up

A split-bottom hopper barge has been modelled in the centrifuge. Two Perspex plates measuring 220 mm by 40 mm are used. These two plates are placed side by side, with both ends supported by 2 short end plates. The end plates are connected to the hydraulic piston, which allows the lowering of the plates and thus simulates the opening of the split bottom barge as shown in Fig. 3.

The model geotextile container used in this study has a diameter of 60 mm and length of 150 mm. This corresponds to a diameter of 6 m and length of 15 m in prototype as the experiment was conducted at an acceleration field of 100 g. The scaling relationships for a few parameters relevant to this experiment are given in Table 1. A summary of relationship between the model and prototype is shown in Table 2.

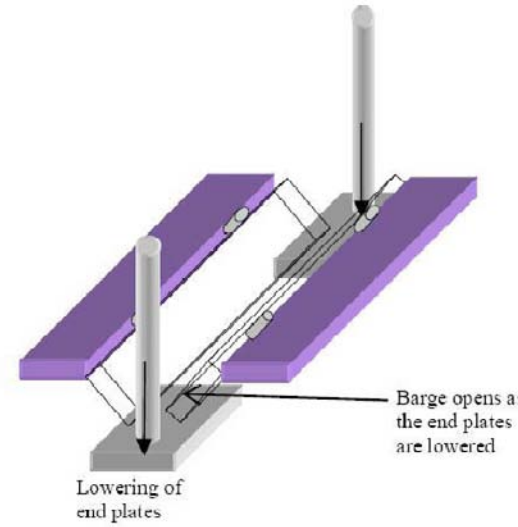

Fig. 3 Schematic drawing of model split-bottom hopper barge when the barge is opened

Druck PDCR81 miniature pore pressure transducers (PPT) were used to measure the variation in pore water pressure during the falling of geotextile containers in the centrifuge tests. The position of the PPTs that were installed in the geotextile container is shown in Fig. 4. Strain gauges were attached on the geotextile container to measure the geotextile strain and the corresponding tensile force in the geotextile container. The strain gauge used is resistance type strain gages. The method of attachment of strain gauges to the geotextile is adapted from Chew et al. (2000). Fig. 5 shows the position of strain gauges installed on the geotextile container.

Table 1 Scaling relationships applied in this centrifuge study

Parameter	Scale (model/prototype)
Linear dimension	1/n
Volume dimension	$1/n^3$
Strain	1
Mass	1/n
Time (dynamic)	1/n
Velocity (dynamic)	1

Table 2 Summary of relationship between model and prototype of geotextile container

Parameter	Prototype	Model
Diameter (m)	6.0	0.06
Length (m)	15.0	0.15
Volume (m^3)	424	0.0004

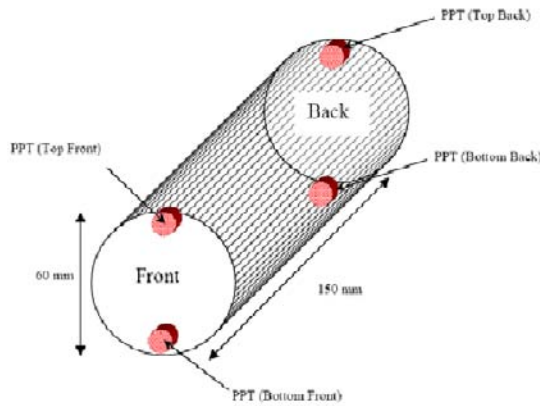

Fig. 4 Position of PPTs installed in a geotextile container

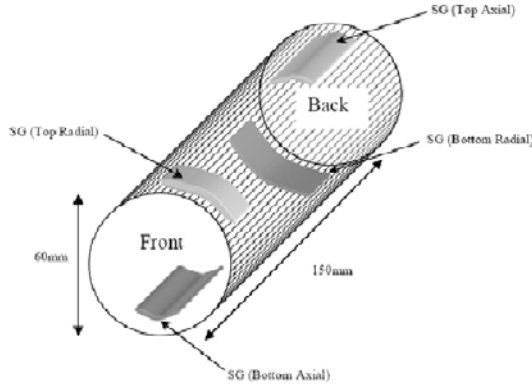

Fig. 5 Position of strain gages in a geotextile container

EXPERIMENTAL PROCEDURE

Firstly, the strong box was filled with water to a height of 25 cm (25 m in prototype scale). Secondly, the model geotextile container was prepared in 1 g, and then placed on the modelled barge. The barge can be adjusted accordingly to the height of water so that it is just right above the water surface. Extra caution has to be given on ensuring the amount of excess loose cables of various sensors on the geotextile container is sufficient for the falling process. With all sensors properly initialized, the model is being spun up slowly to 100 g. Upon reaching 100 g and stabilized, the modelled barge was "opened" and the model container will fall onto the bottom of strong box. Data logging of the sensors were done during the entire process barge opening and the falling of the container.

PRELIMINARY TESTS AND DISCUSSIONS

Sand was used as the fill material in the series of centrifuge modelling test presented in this paper. The type of sand used is uniform medium-to-fine River Sand imported from Australia. Key physical properties of the sand are summarized in Table 3.

Table 3 Physical properties of River Sand (after Chowdhury, 2003)

Properties	Values
Specific gravity	2.65
Maximum dry density, $\rho_{d,max}$ (kg/m^3)	1700
Minimum dry density, $\rho_{d,min}$ (kg/m^3)	1305
Maximum void ratio, e_{max}	1.03
Minimum void ratio, e_{min}	0.56
Mean grain size, D_{50} (mm)	0.25
Young's modulus, E (kPa)	10000
Permeability (m/s) (at 40% relative density, void ratio 0.84)	2.90×10^{-3}
Permeability (m/s) (at 78% relative density, void ratio 0.66)	6.21×10^{-4}

Test 1

The main objective of the first series of centrifuge test is to observe the falling process of geotextile container. In this series of centrifuge test, four PPTs where installed in a 6.0cm diameter geotextile container to monitor the position and the falling velocity of the geotextile container during the falling process. Two PPTs were installed at the front of the geotextile container and another two PPTs at the back of the geotextile container (Fig. 4). This geotextile container was filled up with 340 m^3 of sand, which is about 80% of the geotextile container's volume.

Fig. 6 shows the changes in the depth of the geotextile container as the barge releases the container into the water. The depth value is calculated based on the pore pressure measured by PPTs on the top portion of the containers during the falling process. On the x-axis, "time equals to 0" indicates the starting of barge opening. This fig. also shows that the geotextile container still stay on the barge for about 470 seconds after the start of barge opening.

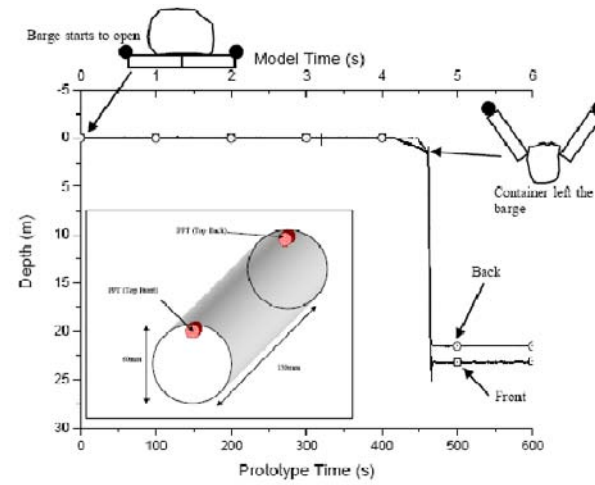

Fig. 6 Fall of geotextile container in Test 1 (based on top PPT)

The exact time where the geotextile container left the barge is shown in Fig. 7, which zooms in the detailed 20 seconds near the moment when it left the barge. It is clear that from Fig. 7, the top back portion of the container left at 460 seconds and the top front portion left more than 2 seconds later, at time 462.2 seconds. As for the time of impact, the top back portion hit the seabed at 464 seconds, while the top front portion reached the seabed at approximately 465.5 seconds. This seems to suggest that when the back portion of the geotextile container left the barge first and it pulls down the front portion, causing it to leave 2 seconds later. It also suggests that the back portion hit the ground 1.5 seconds earlier than the front portion. The spikes on the graph after the moment the container hits the floor indicated the impact experienced by the container and the PPT sensors. These data are considered as the excess pressure due to the impact and shall not be interpreted as the depth of the geotextile container.

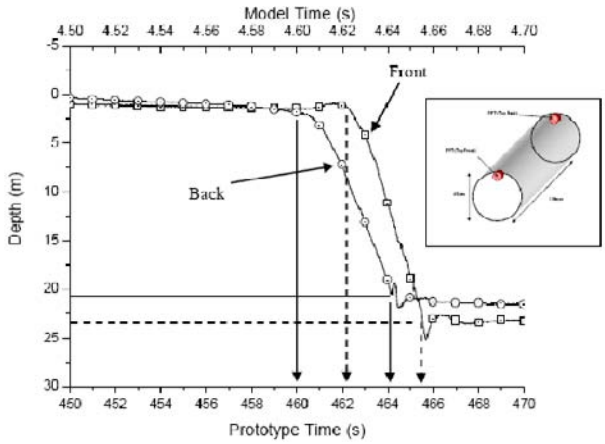

Fig. 7 Zoomed-in on the fall of geotextile container in Test 1 (based on top PPT)

Fig. 8 gives the picture of overall falling process from the PPTs at the bottom portion of the geotextile container and Fig. 9 shows the detailed 20 seconds of the fall. Fig. 8 is similar to Fig. 6 except that during the opening, the bottom portion seems to move gradually from 200 seconds to 400 seconds. From Fig. 9, it seems that the result of the bottom back PPT agreed with the result of the top back PPT that the container left the barge at 460 seconds and the container took 4 seconds to reach the seabed. The bottom front portion left the barge 2 seconds later at 462 seconds and hit the seabed at 465.5 seconds. Therefore, it is shown that the results of the top portion of the geotextile container match the results of the bottom portion of the container.

It is also observed that the impact recorded at the back of the container is much higher than the impact from the front (by comparing the magnitude of spikes during the impact from Fig. 9). This proves that the back portion which hits the floor first absorbed most of the impact of the fall.

By plotting the fall profile of the geotextile container in Fig. 10, it can be seen clearly that the back portion of the geotextile container left the barge earlier and hit the seabed earlier by about 2 seconds.

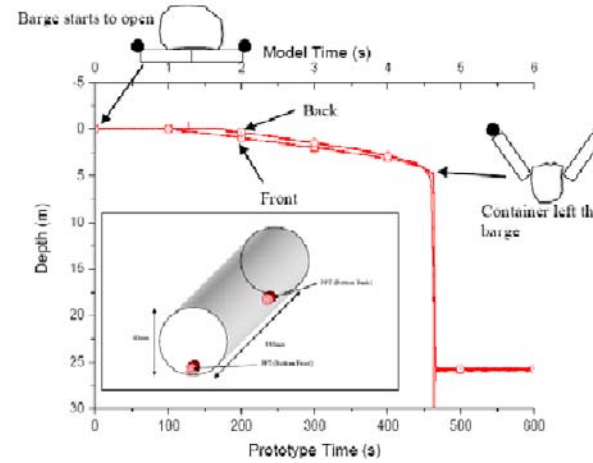

Fig. 8 Fall of geotextile container in Test 1 (based on bottom PPT)

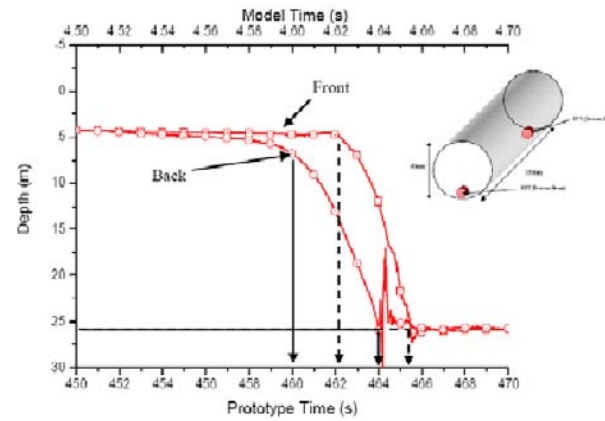

Fig. 9 Zoomed-in on the fall of geotextile container in Test 1 (based on bottom PPT)

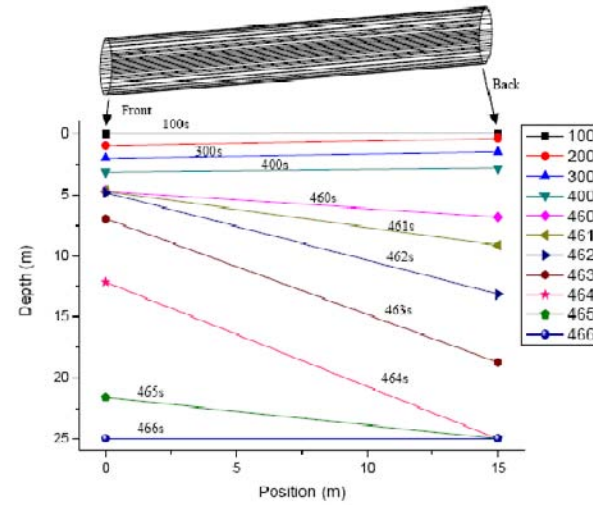

Fig. 10 Fall profile of geotextile container in Test 1

Test 2

The objective of the second series of test is to observe the strain development during the falling process of geotextile container. In this series of centrifuge test, the strain development in the geotextile before and during the falling, and at the impact were measured by strain gages installed on the geotextile containers. A 6.0 m diameter geotextile container was filled with dry sand of up to 70% of its volume capacity. The geotextile container was instrumented with two PPTs at the front portion and two strain gages at the bottom of the container (one each in axial and radial direction). The position of the geotextile container in the water is calculated based on the pore pressure measured during the falling process.

Fig. 11 shows that after 740 seconds, the container left the barge (with barge opening of 3.80 m) and hit the bottom of the strong box. It took only 6 seconds for the geotextile container to fall through the water and hit the bottom of the seabed. The detailed 50 seconds around the impact is shown in Fig. 12 where the results suggested that rotation could have occurred during the fall of the geotextile container.

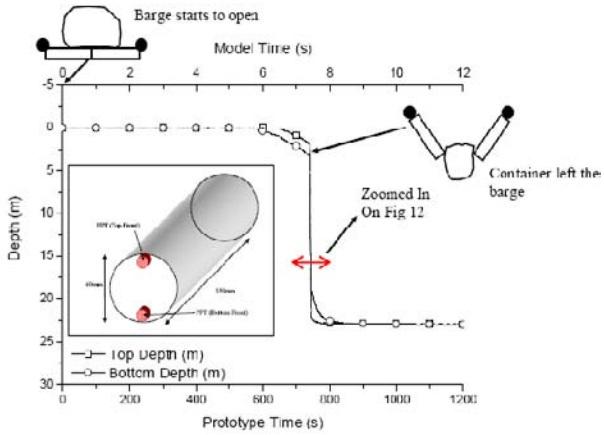

Fig. 11 Fall of geotextile container in Test 2

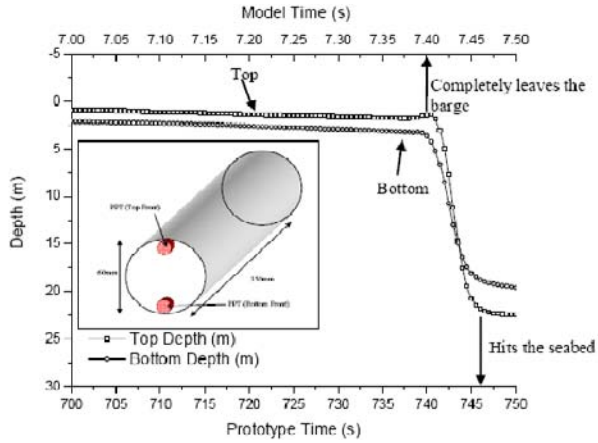

Fig. 12 Zoomed-in on the fall of geotextile container in Test 2

Fig. 13 shows that the strain in the bottom radial direction were increasing gradually once the barge opens but the strain in the bottom axial direction did not develop during this period of time. This clearly indicates that the geotextile is being stretched radially as the opening progresses. The strain in bottom radial direction reaches the peak strain of about 18,800 microstrain at prototype time of 735 seconds and followed by a decrease in the radial strain. The details at this particular time is zoomed-in and shown in Fig. 14.

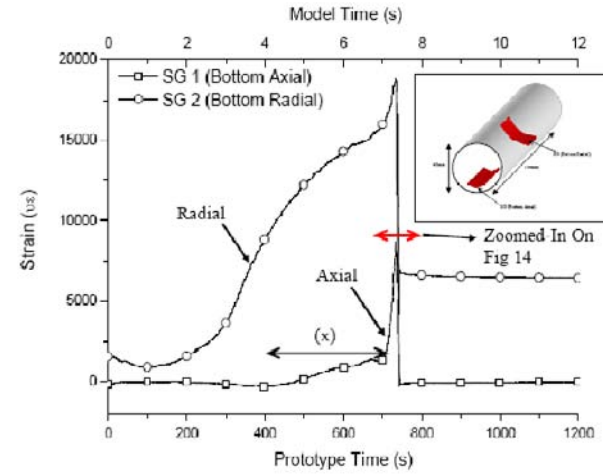

Fig. 13 Strain development of geotextile container in Test 2

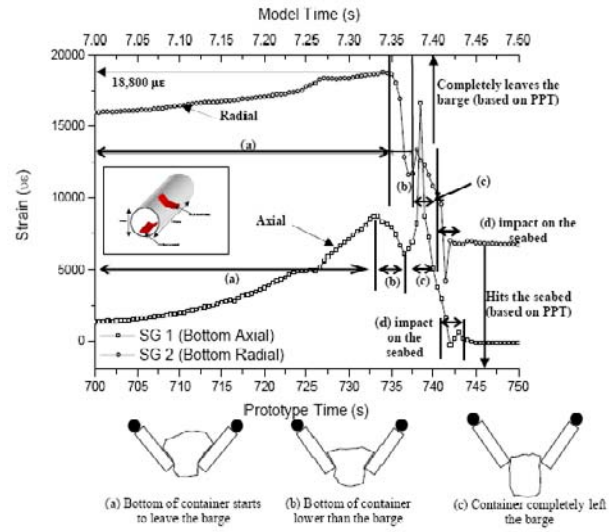

Fig. 14 Zoomed-in on the strain development of geotextile container in Test 2

Three period of time were identified: Zone (a) is when the bottom of container starts to leave the barge; Zone (b) is when the bottom of container is lower than the barge; and Zone (c) is when the container completely left the barge.

The reduction in strain in zone (b) could be due to the fact that the bottom part of the geotextile container has passed the opening of the barge, but the top portion was still clinched to the barge opening. Immediately after that, the container completely left the barge within the time range of 737.5 seconds to 740 seconds (zone (c)).

The time that the container left the barge as recorded by PPT was 740 seconds. The slight discrepancy in the time from 737.5 seconds to 740 seconds could be due to the fact that the PPT was located in the front portion while the strain gage in the radial direction was at the back portion of the container. Therefore, this result shows that the back portion of the container left the barge earlier than the front portion by about 1 to 2 seconds. As for the time of impact of the container on the seabed, the time ranged from 740 seconds to 742.5 seconds. This range is determined by the peak value recorded by the bottom radial strain gage before the strain became constant at 7000 microstrain. This result is consistent with that in Test 1.

On the other hand, the bottom axial strain remains almost zero during the first 400 seconds of the opening process of the barge (Fig. 13). From 400 seconds to 700 seconds, the axial strain picked up gradually to 1300 microstrain (marked as zone (x) in Fig. 13). This suggests that some non-uniformity has occurred along the length of the container. Further observations from 700 seconds to 732.5 seconds as seen in Fig. 14 confirmed that the geotextile container's was not uniform along the length as the axial strain developed rapidly, from 1300 microstrain to 8500 microstrain within 35 seconds. From 732.5 seconds to 736 seconds, a reduction of axial strain was recorded (marked as zone (b) in Fig. 14). This observation is consistent with radial strain, which also showed some reduction in strain before the container completely left the barge. After 736 seconds, the axial strain increased dramatically to a peak of 16,500 microstrain as seen in zone (c) of Fig. 14. This shows that the fall of geotextile container is not uniformly straight from the front to the back of the container. This could be due to uneven fill of material in the geotextile container had caused the container to fall unevenly into the bottom of the seabed. The time range of impact of the container based on the small peak in the axial reading is from 740.5 seconds to 743.5 seconds.

CONCLUSION

A series of centrifuge model tests has been conducted to model the falling process of geotextile containers into 25 m of water depth. The falling process and the strain development of geotextile containers were monitored. From the findings of this study, we can conclude the following:

i. Centrifuge modelling is capable of capturing key essential features of the falling and impact of the geotextile container.
ii. Non-uniform filling may lead to the results that the front and back part of the geotextile container may not hit the seabed uniformly at the same time.
iii. The results showed that in general, radial strain is high as the geotextile is being stretched during the barge opening process.
iv. Due to non-uniformity of the filling along the length of the tube, geotextile containers may not fall uniformly. This implies that the axial strain at certain location may be high.

ACKNOWLEDGEMENT

The authors wish to express their gratitude to the laboratory officers in the NUS Geotechnical Centrifuge Laboratory for their assistance in carrying out the centrifuge model test. The first author would also like to express his gratitude to the National University of Singapore for supporting his research and study via the NUS Research Scholarship.

REFERENCES

Chew SH, Wong WK, Ng CC, Tan SA, Karunaratne GP (2000) Strain Gauging Geotextile Using External Gauge Attachment Methods. ASTM STP 1379, USA

Lee FH, Tan TS, Leong CF, Yong KY, Karunaratue GO, Lee SL (1991) Development of geotechnical centrifuge facility at the National University of Singapore. Centrifuge 91: 11-17

Pilarcyzk KW (2000) Geosynthetics and Geosystems in Hydraulic and Coastal Engineering, Balkema, Rotterdam

APPLICATION OF GEOTUBES USED AS ENERGY DISSIPATER BEHIND A DAM

K. Jiang[1] and Q. Li[2]

ABSTRACT: This paper introduces a practical project which utilized geotubes as energy dissipater for scouring prevention. In the apron region downstream of a dam, rows of geotubes with diameter of 1.75 m (filled height 1.1 m) and length of 61 m were paved, which were overlain by protective geogrid gabions filled with broken stone. In order to prevent the foundation from being scoured, a lot of "small suspended geotubes" were installed at the end of apron. They were connected with the apron geotubes in place of traditional scouring protection trenches. The outer skin of geotubes was a geocomposite of woven and non-woven geotextiles. The geotubes are filled with local sand and gravel. The filling method is to spread geotextiles in place, then fill the soils and sew seams. The paper uses the fundamental principles of geotube for reference, and extends its scope of application, which may be referenced by similar projects.

KEYWORDS: geotube, energy dissipation, scouring prevention, small suspended geotubes

INTRODUCTION

Wang Jia Wan Rubber Dam, located on Hunhe River in region of Shenyang is a hydraulic structure for improving the natural landscape. The rubber dam is of pneumatic type. It has 6 openings, with height of 3.5 m and length of 401 m, and foundation which is a mixture of sand and gravel. After one year of completion, owing to its being unable to adjust its height, the 6th opening section was changed into water-filled type to control the river discharge. Because of insufficient capacity of the stilling pool located downstream of the dam, the apron behind the pool was lengthened and stabilized with the goal that the downstream would not be scoured severely.

LAYOUT OF PROJECT

To realize the purpose mentioned above, rows of geotubes were installed, filled with local sand and gravel, and were then overlain by protective geogrid gabions, thus forming a large flexible scour-resistant gravitational body. For preventing the foundation at the end of apron from being scoured, a series of "small suspended geotubes" were installed and connected with the geotubes in place of traditional scour protection trenches. The general layout is shown in Figs.1—3.

DESIGN OF GEOTUBES

The design of geotubes consists of design of the outline, filling method and analysis of stability under flow water.

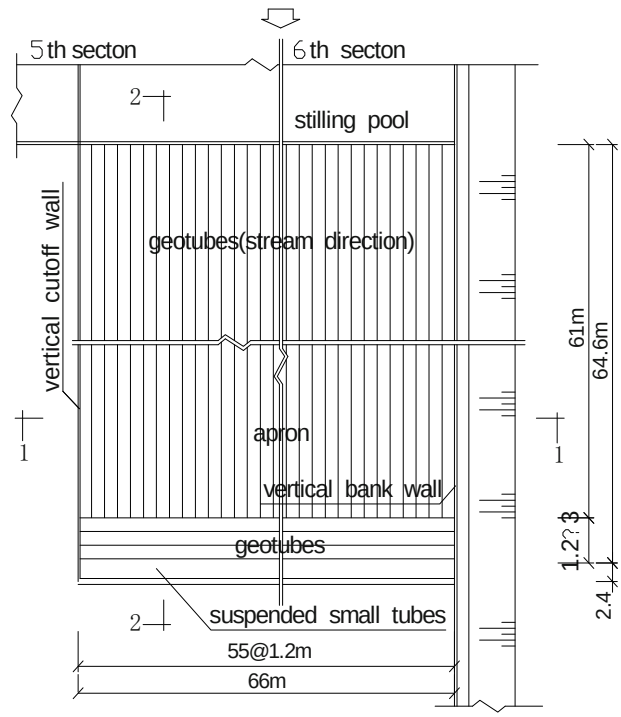

Fig. 1 Plan

[1] Professor, Liaoning Provincial Scientific Research Institute of Water Conservancy and Hydropower, CHINA. Email:jiang_717@hotmail.com
[2] Professor, Liaoning Provincial Scientific Research Institute of Water Conservancy and Hydropower, CHINA. Email:skyLiQu@126.com

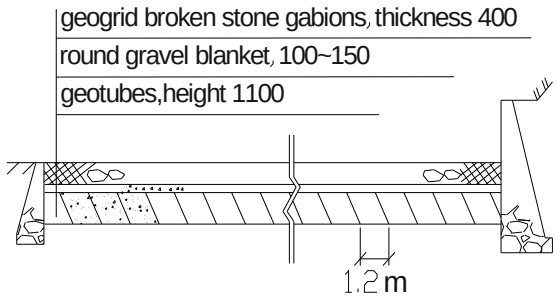

Fig. 2 Section 1-1

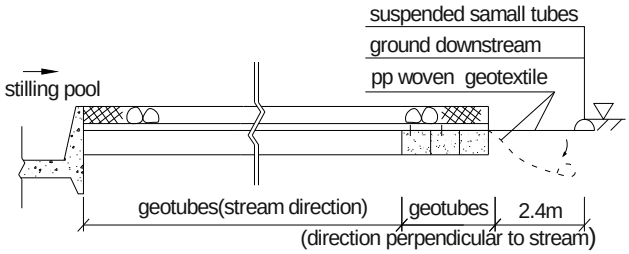

Fig. 3 Section 2-2

Design of the Outline

Theoretically, the greater volume of geotube per unit length is, the more stable it will be. In reality, there are other conditions need to be taken into consideration during design. Through comparison of various plans, it was decided to use the following parameters: height of geotubes 1.1 m, based width 1.2 m, circumference 5.5 m and length 61 m. The outlines are shown in Fig. 2.

Filling Method

The typical method is to pump sand slurry into the geotube through filling ports spaced at certain interval on its top. The outer skin of geotube is pervious. Water would drain out through the skin while the geotube is being filled, and the sand particles left within will consolidate into solid mass.

In our project, we first spread geotextiles on the ground, place the filling materials on it along longitudinal direction and then wrap it using the residual geotextiles on both sides to form a long tube, finally sew the seams using portable sewing machine. Close the two ends using the same method.

Outer Skin

Retention property of geotextile

The outer skin of geotube is composed of p.p woven and non-woven geotextiles. It must have the required strength and hydraulic property to retain the sand. For the geotextiles available in the market, their equivalent opening sizes (EOS) are 0.1 mm—0.6 mm for woven geotextiles and 0.05 mm—0.1 mm for non-woven geotextiles. The filling materials used is local sand and gravel; their gradation is listed in Table 1.

With information provided in Table 1, in order to prevent the deformation of the geotubes (mainly height reduction) due to loss of filling material particles, the equivalent opening sizes (EOS) of geotextiles and the characteristic diameter of filling materials have to meet the following criteria:

$$O_{95} \le nd_{85} \tag{1}$$

where O_{95}—EOS of geotextiles adopted;

d_{85}—characteristic diameter of filling material, here d_{85} = 32 mm;

n—a constant which is determined according to soil type, its gradation and type of geotextile, here n = 1 is adopted.

Tensile stress of geotextile

Geotube skins must have a certain tensile strength and durability. The stress analysis is very complicated. Since the fill materials are sand and gravel, they drain very fast and thus consolidate quickly; it is reasonable to use their drained strength in calculation. We will follow Palmerton's method (Lawson 2006). Also, the outer shape of geotube's cross section is assumed to be an ellipse.

Let the circumferential, axial and port connection stress

Table 1 Gradation of fill material (average value)

cobble			gravel		sand			silt	clay	fines	controlled dia.	effective dia.	coef. of non-unifermity	coef. of curvature
grain size (mm)														
>60	60-40	40-20	20-10	10-2	2-0.5	0.5-0.25	0.25-0.075	0.075-0.005	<0.005	%	d_{60}	d_{10}	C_u	C_c
%	%	%	%	%	%	%	%	%	%		mm	mm		
	5.08	25.73	12.55	18.33	23.68	9.53	4.1	1.05		5.0	14.52	0.38	37.08	0.24

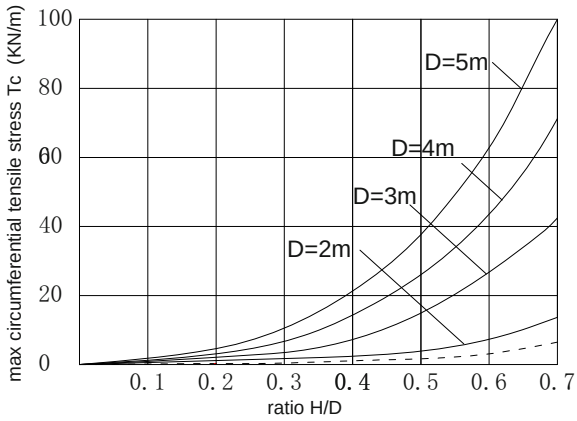

Fig. 4 Circumferential Tensile Stresses (Based on Palmerton's method)

be denoted by T_c, T_a and T_p respectively. Fig. 4 shows the max circumferential tensile stresses T_c when the calculated theoretical diameters of the filled geotubes D = 2 m, 3 m, 4 m and 5 m, using Palmerton's method (Lawson, 2006). When the max filled height $H = 0.6D$ and the theoretical diameter D = 1.75m, based on Fig. 4, max T_c = 6 kN/m. The magnitude of T_c around a filled geotube is a function of the curvature of outer skin. The magnitude is at its highest when the curvature is the highest, which occurs at both sides of the geotube. According to Palmerton, the max axial tensile stress is $T_a = 0.63T_c$, and the max port connection stress is $T_p = 0.3T_c$. The port connection is placed on top of the geotube, hence it is very important to use strong stitching threads and do well on the sewing.

The geotube's max T_c is obtained from Fig. 4, and strength of geotextile used in design should meet the following criteria:

$$[T_{max}]_c \geqslant F_s \cdot T_c \tag{2}$$

where: max—maximum value;

F_s—factor of safety, use F_s = 4—5,

hence the required strength of geotextile is

$$[T_{max}]_c \geqslant 4 \times 6 = 24 \text{ kN/m}.$$

Similarly, both $[T_{max}]_a$ and $[T_{max}]_p$ have to meet the condition shown in Eq. (2).

Stability of geotube under water flow

Geotubes in apron region submerge under water throughout the year and are subjected to stream scouring; hence we have to consider the stability of geotubes under water flow. Currently, research materials on this area are very rare. During analysis, an approximation may be used, i.e. we can use the principle of static equilibrium to find the forces exerted on the geotube and to calculate its stability.

The pushing force applied by stream on geotube:

$$F_p = C\frac{1}{2}\rho v^2 \cdot h \tag{3}$$

The friction between geotube and foundation:

$$F = fA(\rho_s - \rho_w)g \tag{4}$$

Friction requires:

$$F > F_p \tag{5}$$

The critical velocity v_{er} may be evaluated as:

$$v_{er} = \sqrt{2 \times \frac{\rho_s - \rho_w}{\rho_w} \times \frac{fAg}{hc}} \tag{6}$$

where: ρ_s, ρ_w —the density of sand fill and water respectively;

f—coefficient of friction between geotube and foundation;

A—contact area;

g—height of filled geotube;

c—a coefficient related to flow condition.

The calculated value of critical velocity based on equation (6) is v_{er} = 14 m/s.

The hydraulic model tests of the project gave the max stream velocity v_{max} = 3.48 m/s. That is a much smaller number compare to v_{er}, which means the stability is warranted. It should be noted that in the formula, both the depth of water over top of geotube and the dynamic effect of wave fluctuation are not considered. These two factors practically have certain influence on stability.

The protective gabions over geotubes

While under different situations such as static water, low velocity stream, high velocity stream or wave hitting condition, the answer to whether the geotubes need protection on the top, according to foreign technical papers, depends upon the following factors: (1) the stream velocity and wave height; (2) EOS of the outer skin $\leqslant d_{50;}$ (3) the discharge from skin $\geq$ 30 L/(m^2 • s); (4) if there is destructive effect on the geotubes from ice blocks or tree trucks carried along by flood. Through comprehensive investigation, it was decided to cover the geotubes with geogrid broken stone gabions.

Field Arrangement and Construction of Apron

In apron region downstream of stilling pool, along stream direction, 55 geotubes with individual length of 61 m are installed. At the end of those geotubes, another 3 geotubes with individual length of 66 m are installed

perpendicular to the stream direction. They are used for connecting the "small suspended geotubes". These geotubes are closely squeezed between cut-off wall and bank wall. They are filled with sand and gravel, sewn and compacted by light machine in place, following with round gravel paved on the top for protection, and overlain with geogrid gabions.

The outer skin geotextiles used are glued geocomposite of p.p woven and non-woven geotextiles both with a unit mass of 200 g/m^2. The tested tensile strength of the outer skin geotextiles is 40.5 kN/m in longitudinal direction and 28 kN/m in latitudinal direction, both larger than the required number. Since the goal of this project is to build a permanent structure, an anti-aging type geotextiles are used. The seams are sewn with 3 rows of high strength p.p threads.

DESIGN OF "SMALL SUSPENDED TUBE"

Estimate of Scour Depth

The residual energy of stream after passing through the stilling pool is reduced by the apron. Although it doesn't affect downstream severely, the establishing of cut-off wall or anti-scour trench is still needed for the stability of apron foundation. The scour-depth h_d can be estimated using the following formula:

$$h_d = \frac{0.66q\sqrt{2\alpha_0 - \frac{z}{h}}}{\sqrt{(\frac{\rho_s}{\rho_w} - 1)gd_{50}}(\frac{h}{d_{50}})^{\frac{1}{6}}} - h_t \qquad (7)$$

where q —discharge through the end of apron per unit length, here q = 12m^2/s;

h —- water depth at the end of apron;

z —- the position height where the velocity is the maximum (at the end of apron) in velocity distribution curve, when velocity is uniform, take $z = 0.5h$;

α_0 —the dynamic correction coefficient of velocity distribution at the end of apron;

d_{50} —- particle size obtained from grain size curve of river bed load;

ρ_s, ρ_w —density of river bed load and water respectively;

h_t —downstream water depth.

The calculated h_d = 4.16 m, which means the end of apron needs protection.

Design of Small Suspended Tubes

The small suspended tubes are made of high strength, flexible woven geotextiles with good anti-scour and deformable properties. The small tubes with diameter of 0.6 m are filled with sand and gravel.

When the stream flows through the end of apron and still has certain dynamic energy, the foundation beneath it will not be scoured due to the protection above it. On the other hand, the small tubes would be eroded and gradually sink down, the cross sectional velocity there would get adjusted, and finally enable the cross section to become stable. In comparison with the traditional scour-resistant trenches, even though they contain a great amount of large stones, the stones are dispersive, individual blocks and are very prone to being washed away during flood. The small tubes system, on the other hand, is a flexible integrated massive structure, which can deform consistently with foundation changes without loss of foundation soil. It can protect the foundation from being damaged, and it is very cost effective.

Selection of Material for Small Suspended Tubes

The small suspended tubes of p.p woven and non-woven geotextiles have unit mass of 620 g/m^2 and 150 g/m^2 respectively. The tensile strength of the non-woven geotextile is 140 kN/m.

CONCLUSION

This project uses rows of geotubes to build an apron downstream for a dam and uses broken stone geogrid gabions as its protective layer above. At the end of apron, a series of small suspended geotubes are installed in place of traditional scour protection trenches. Such a system completely utilizes and mobilizes the function of geotextiles. Reports like this are rarely published, it deserves further study from both theoretical and practical aspects. The project has been completed for nearly two years and the structure has subjected to floods with maximum unit width discharge up to q = 4m^2/s, yet no accident has occurred.

REFERENCES

Lawson CR (2006) Geotextile containment for hydraulic and environmental engineering, Proc. of the 8th International Conference on Geosynthetics, Yokohama, Japan

Lin G, Shu YM (2004) Design principle of construction of Geotubes, Proc. of the 6th Chinese Conference on Geosynthetics, Xi'an, Shanxi province

STUDY ON THE EXPERIMENT OF STABILITY OF UNARMORED FLAT GEOTUBE DIKE UNDER WAVE ACTION

C.R. Zhu[1], Y.M. Shu[2] and J.H. Jiang[3]

ABSTRACT: To study the stability of unarmored flat geotube dike subject to wave action, large scale model test has been performed. In the test, the archetypal geotube dikes with top width of 5.25 m, heights of 4.2 m, 6.3 m, 8.4 m, and slope ratios of 1.25, 1.5, 2.0, 2.5 were employed. The results of the test demonstrated that the stability of flat geotube dike under wave action decreases with the flatter wave increasing, while it decreases in the beginning and then increases with the slope ratio increasing. Empirical formula of safety factor was founded and compared by the results of critical wave heights obtained in the test.

KEYWORDS: geotube dike, wave pressure, model test, critical wave height, safety factor

INTRODUCTION

In China, the filling geotubes are applied to construct dikes for harbor and airport at coastal or for reservoir of water supply at estuary(Shu 2004). The shape of the geotube is flat rather than orbicular, seeing Figs. 1 and 2. Because of the different stability criterion of the two shapes of geotubes subject to wave action (The orbicular geotube destabilizes by overturning, the flat geotube destabilizes by sliding). So the criterion of orbicular geotube cannot be applied on the flat one(Lin and Shu 2005). There are a number of dikes or embankments constructed by filling flat geotubes in China, but there is few criterion based on experiment or analysis, the stability design of the flat geotube dike is usually dependent on construction experience. So it is very needed to study the stability of filling flat geotube dike subject to wave action.

EXPERIMENTAL SETUP

The model tests have been performed in the wave flume of the College of harbor and waterway of Hohai University. At one end waves were generated. At the other end a dike made of flat geotubes was built. The flume is 35 m long, 0.5 m wide, and 1.3 m high. The gathering and analyzing of data were done by computer automatically. The whole model was arranged as shown in Fig. 3. Where D_c is height of the dike, D is water depth in front of the dike, H is wave height, n is slope ratio of the dike.

Fig.1 Orbicular shape of geotube

Fig. 2 Flat shape of geotube

[1] Assistant engineer, Guangdong Provincial Investigation, Design and Research Institute of Water Conservancy and Electric Power, CHINA. Email:zcrjjh@163.com
[2] Professor, College of Water Conservancy and Hydropower Engineering, Hohai University, CHINA. Email:yimingshu2004@yahoo.com.cn
[3] Assistant, College of Water Conservancy and civil Engineering, South China Agricultural University, CHINA. Email:jjhzcr@163.com

The model geotube was sewed of PP geotextile and filled with sand. The length scale of 35 was applied to simulate three groups of dikes with height of 8.4 m, 6.3 m, 4.2 m and slope ratios of 1.25, 1.5, 2.0, 2.5.

Dikes were subject to regular wave by using constant wave steepness (1/20 and 1/25).

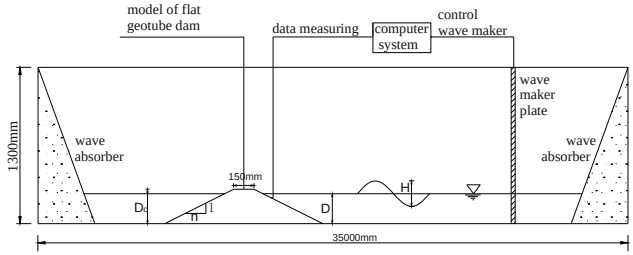

Fig. 3 Arrangement of model test

RESULTS AND ANALYSIS

Impacting Wave Pressure

The filling geotubes are usually applied to construct dike at coastal or estuary. Under these circumstances, wind makes water impacting and climbing up and down the slope of the dike. Horizontal wave pressure and uplift wave pressure are the main destabilizing loads of the geotube dike.

Horizontal wave pressure

Horizontal wave pressure distribution along the slope changes with slope ratios. The changes can be seen from the wave pressure measured along the slope in the test. The horizontal wave pressure of measuring point along a group of slope ratios (n=1.25, 1.5, 2.0, 2.5) is varied as shown in Figs. 4 and 5. Where water depth is 5.6 m, height of the dike is 8.4 m, wave height is 2.1 m, elevations of pressure measuring point are 3.5 m, 4.2 m, 5.6 m, 7.0 m, 7.7 m in the figures.

The horizontal wave pressure increases in the beginning and then decreases with the slope ratio increasing. The maximum pressure appears while slope ratio varying from 1.5 to 2.0. Subjecting to wave action with a certain wave steepness, there is a critical slope ratio corresponding to the maximum normal wave pressure on the slope (Jiang and Pan 1998).

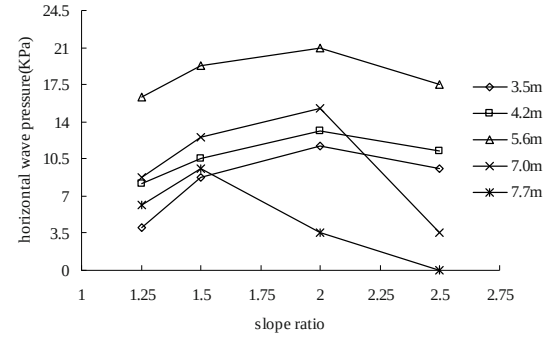

Fig. 4 Horizontal wave pressure with different slope ratios (H/L=1/20)

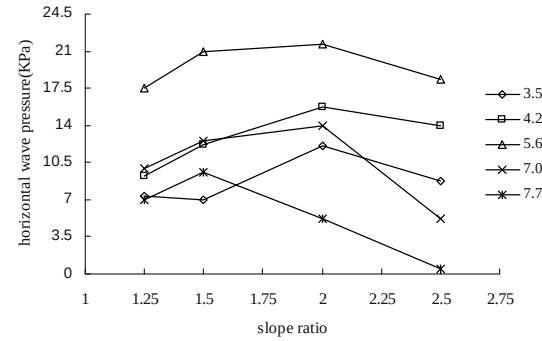

Fig. 5 Horizontal wave pressure with different slope ratios (H/L=1/25)

It is seen that the destroying action of flatter wave on the unarmored flat geotube dike is greater than the steeper wave from the test. Most of the horizontal wave pressure with wave steepness of 1/25 are greater than that of 1/20, and few of them is just the same or a little lower which may be caused by the measurement. The comparison of them is shown in Figs. 6 and 7. It is shown about 8.4 m -high dike subject to 2.1 m-high wave by using water depth of 5.6 m.

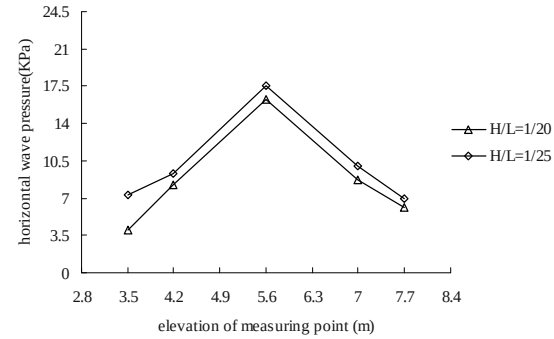

Fig. 6 Horizontal wave pressure of different wave steepness (slope ratio of 1.25)

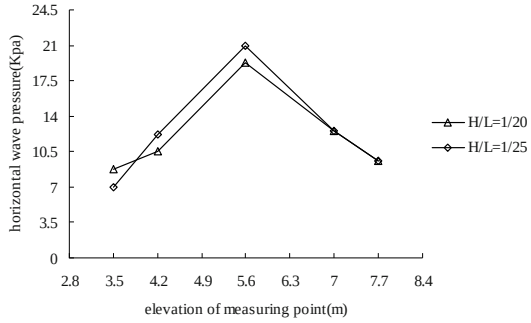

Fig. 7 Horizontal wave pressure of different wave steepness (slope ratio of 1.5)

Uplift wave pressure

The horizontal wave pressure is the major one of destabilizing forces, and it makes flat geotube to slide when it becomes greater than the stabilizing force. The uplift wave pressure makes the friction force decrease, and the contact areas among neighboring geotubes are reduced due to the uplifting of the geotube(Recio and Oumeraci 2007). Effect of wave steepness and slope ratio on the uplift wave pressure was studied in the test. It was seen that the top geotube of the dike slide first during the corruption of the dike from the test, so the uplift force at the bottom of the top geotube was investigated, three measuring points numbered 1, 2, 3 which arranged from upstream to downstream were applied.

The influence between wave steepness and uplift wave pressure is uniform with that of horizontal wave pressure. It is varied as shown in Figures 8 and 9. Uplift wave pressure distribution at the bottom of the flat geotube changes with slope ratios. The changes could be seen from the wave pressure of measuring points. It is varied as shown in Figs. 10 and 11, where the slope ratios are 1.25, 1.5, 2.0, 2.5, water depth is 7.7 m, height of the dike is 8.4 m, wave steepness is 1/20 and 1/25, wave height is 2.1 m.The uplift wave pressure decreases with the slope ratio increasing. In other words, the safety of the flat geotube dike decreases with the slope ratio increasing.

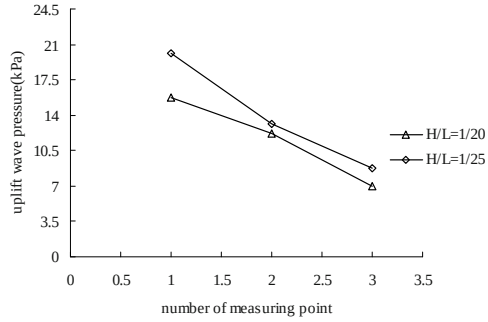

Fig. 8 Uplift wave pressure of different wave steepness (slope ratio of 1.25)

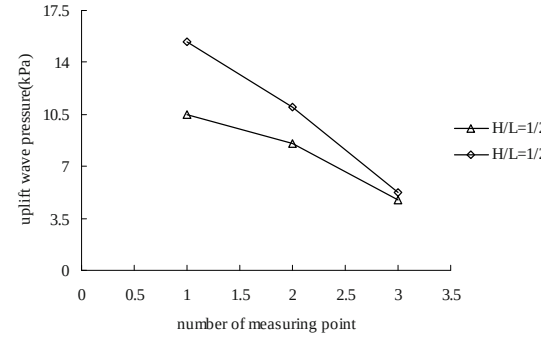

Fig. 9 Uplift wave pressure of different wave steepness (slope ratio of 1.5)

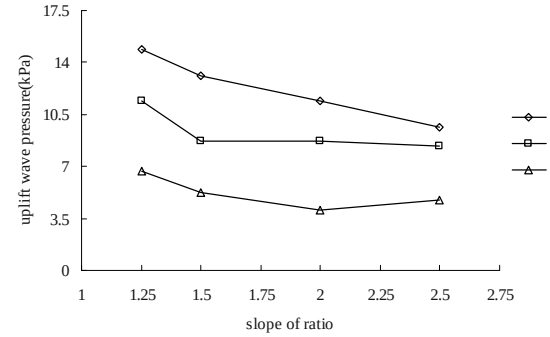

Fig. 10 Uplift wave pressure of different slope ratios (*H/L*=1/20)

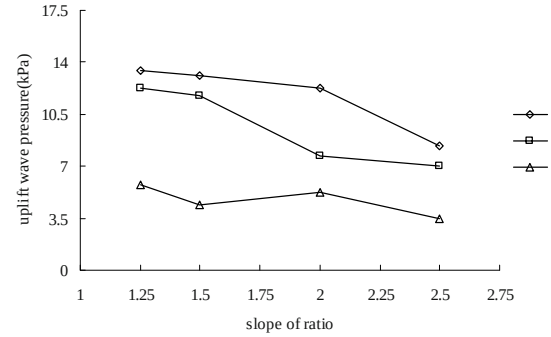

Fig. 11 Uplift wave pressure of different slope ratios (*H/L*=1/25)

Critical Wave Height

When a group of wave impact on the flat geotube dike, there is a certain wave which makes the top geotube to slide off the dike, and we call it the critical wave. In the test, critical wave heights of the geotube dike were studied under actions of different water depth and different wave. The critical wave heights are varied as shown in Tables 1—6. In the tables, the blanks mean that the wave produced under the water depth can't make the top geotube to slide, and the wave heights with brackets mean that the critical wave approach to that one.

Table 1 Critical wave heights of 4.2m-high geotube dike(H/L=1/20)

Water depth	*n*=1.25	*n*=1.5	*n*=2.0	*n*=2.5
4.2m			(1.4)—1.75	1.4—1.75
3.5m				

Table 2 Critical wave heights of 4.2 m-high geotube dike(*H/L*=1/25)

Water depth	*n*=1.25	*n*=1.5	*n*=2.0	*n*=2.5
4.2m		1.4—(1.75)	(1.4)—1.75	(1.4)—1.75
3.5m				

Table 3 Critical wave heights of 6.3 m-high geotube dike(*H/L*=1/20)

Water depth	n=1.25	n=1.5	n=2.0	n=2.5
6.3m	(2.1)—2.45	1.4—1.75	1.05—1.4	(1.75)—2.1
5.6m	2.1—(2.45)	2.1—2.45	1.4—1.75	1.75—2.1
4.9m			1.925—2.1	
4.2m				

Table 4 Critical wave heights of 6.3 m-high geotube dike(*H/L*=1/25)

Water depth	*n*=1.25	*n*=1.5	*n*=2.0	*n*=2.5
6.3m	1.75—2.1	(1.4)—1.75	(1.05)—1.4	(1.4)—1.75
5.6m	(2.1)—2.45	(2.1)—2.45	(1.4)—1.75	1.75—2.1
4.9m			1.925—2.1	
4.2m				

Table 5 Critical wave heights of 8.4 m-high geotube dike(*H/L*=1/20)

Water depth	*n*=1.25	*n*=1.5	*n*=2.0	*n*=2.5
8.4m	1.05—1.4	(1.75)~2.1	1.05—1.4	(1.75)—2.1
7.7m	(1.75)—2.1	1.75—(2.1)	1.75—(2.1)	2.1—2.45
7.0m	2.1—(2.45)	(2.45)—2.8	2.1—2.45	2.45—2.8
6.3m	2.45—(2.8)	2.45—(2.8)		
5.6m				

Table 6 Critical wave heights of 8.4 m-high geotube dike(*H/L*=1/25)

Water depth	*n*=1.25	*n*=1.25	*n*=1.25	*n*=1.25
8.4m	1.05—1.4	1.05—1.4	1.05—1.4	1.05—1.4
7.7m	(1.75)—2.1	(1.75)—2.1	(1.75)—2.1	(1.75)—2.1
7.0m	(2.1)—2.45	(2.1)—2.45	(2.1)—2.45	(2.1)—2.45
6.3m	(2.45)—2.8	(2.45)—2.8	(2.45)—2.8	(2.45)—2.8
5.6m				

From Tables 1 to 6, it can be seen that destroying actions of flatter wave on flat geotube dike is greater than the steeper one, the critical wave height deceases in the beginning and then increases with the slope ratio increasing. Water depth and the height of the dike are also relative to the stability of the dike. The stability of geotube dike decreases with the water depth increasing, and the reason may be that the higher water is easier to make wave up and over the top geotube, while the over wave is the main reason of the destabilization.

FORMULA OF SAFETY FACTOR

Main factors concerned with the horizontal wave pressure are wave height H, wave period T, wave length L, water depth D, height of the dike Dc, slope ratio n and water density ρ. Horizontal wave pressure P could be written by these factors as follows:

$$P = f\left(H,T,L,D,D_C,n,r\right) \tag{1}$$

Wave height H, wave period T and water density ρ are nondimensional each other, and could be defined as primary factor. Based on π criterion and considering the wave period criterion, the following can be gotten from Eq. 1:

$$P = \frac{\gamma H^2}{2\pi L} th\frac{2\pi D}{L} f_1\left(\frac{L}{H},\frac{D}{H},\frac{D_C}{H},n\right) \tag{2}$$

The safety factor of the top geotube is computed by horizontal wave pressure which considers uplift wave pressure as a part of it based on the critical limiting equilibrium criterion. The safety factor is computed as follows:

$$F_S = \frac{2\pi\gamma_S B\mu}{\gamma H}\frac{L}{H}\mathrm{cth}\frac{2\pi D}{L}\frac{1}{\xi\left(\frac{L}{H}\right)^{\alpha}\left(\frac{D}{H}\right)^{\beta}\left(\frac{D_C}{H}\right)^{\gamma}(n)^{\eta}} \tag{3}$$

where γ is density of water, γ_s is density of filling materials, B is width of the flat geotube along the direction of wave, μ is the friction coefficient between geotubes.

Based on the critical wave heights of the test, and regression analysis by statistic software of SPSS, empirical formula of safety factor was founded (A assumption was concerned that critical wave heights were average values of the two numbers in blanks of Tables 1—6) as follows:

$$1.25 \le n \le 2.0 \text{ ,}$$

$$F_S = \frac{2\pi\gamma_S B\mu}{\gamma H}\frac{L}{H}\mathrm{cth}\frac{2\pi D}{L}\frac{1}{1.464\left(\frac{L}{H}\right)^{1.685}\left(\frac{D}{H}\right)^{0.833}\left(\frac{D_C}{H}\right)^{-0.93}(n)^{0.32}} \quad (4)$$

$2.0 \le n \le 2.5$

$$F_S = \frac{2\pi\gamma_S B\mu}{\gamma H}\frac{L}{H}\mathrm{cth}\frac{2\pi D}{L}\frac{1}{1.679\left(\frac{L}{H}\right)^{1.711}\left(\frac{D}{H}\right)^{1.035}\left(\frac{D_C}{H}\right)^{-1.185}(n)^{-0.0227}} \quad (5)$$

In order to check accuracy of the Eq. 4 and 5, safety factors of the top geotube were computed by the two wave heights of each critical interval of Tables 1—6. The safety factors are drew in Figs. 12 and 13.

From Figs. 12 and 13, it can be seen that most of safety factors computed by the minor wave heights are greater than 1 and few of them is less than 1, while most of safety factors computed by the major wave heights are less than 1 and few of then is greater than 1. The results are primary correspondence with the phenomenon of the test.

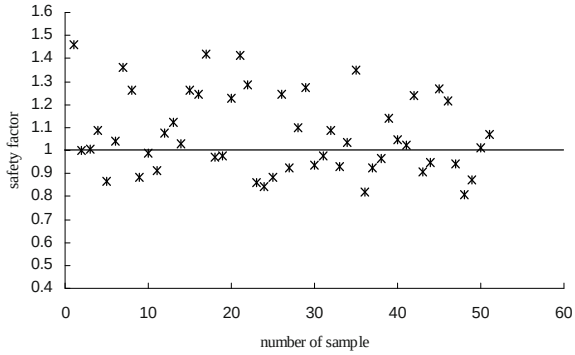

Fig. 12 Safety factors computed by the minor wave heights

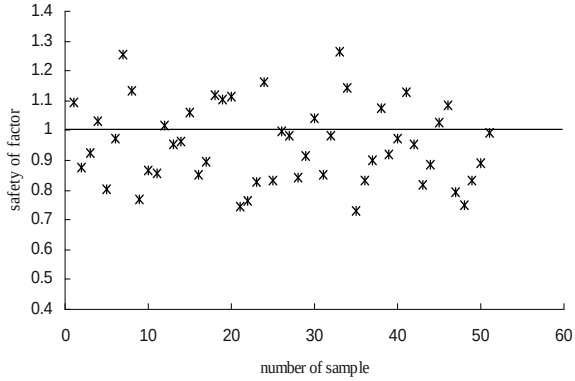

Fig. 13 Safety factors computed by the major wave heights

CONCLUSIONS

The stability of unarmored flat geotube dike subject to wave action was studied by model test. Effects of wave steepness and slope ratio on the horizontal wave pressure and uplift wave pressure were investigated in the test. Critical wave heights of geotube dike under different wave actions were obtained. The results demonstrate that the stability of flat geotube dike under wave action decreases with the flatter wave increasing, while it decreases in the beginning and then increases with the slope ratio increasing. The empirical formula of safety factor was founded upon the experimental data, and it was checked by critical wave heights of the test.

REFERENCES

Shu YM (2004) Field Experiment for Dike Soil at Yangtze River Estuary, Proceedings of the International Symposium on Engineering Practice and Performance of Soft Deposits, Japan 1:457-461

Lin G, Shu YM, Lin Y (2005) Principal of mud-filled bag embankment and practice, China yangtze river 36:25-27

Recio J, Oumeraci H (2007) Effect of deformations on the hydraulic stability of coastal structures made of geotextile sand containers, Geotextiles and Geomembrances (25):278-292

Zuo DQ, Theory and method of model test (1984) China water resource and electrical power press

Jiang ZY, et al. (1998) Experimental investigation on impacting pressure of wave on slope pavement, Chinese harbor engineering 1:22-27

Koerner GR, Koerner RM (2006) Geotextile tube assessment using a hanging bag test. Geotextiles and Geomembranes 24: 129-137

Pilarczyk KW (2000) Geosynthetics and geosystems in hydraulic and coastal engineering, published by Balkema, Rotterdike, Netherlands

Pilarczyk KW (1998) Dikes and revetments, published by Balkema, Rotterdike, Netherlands

Cantre S (2002) Geotextile tubes-analytical design aspects, Geotextiles and Geomembranes 20: 305-319

Proceedings of the 4th Asian Regional Conference on Geosynthetics
June 17 - 20, 2008 Shanghai, China

FLUME EXPERIMENT AND NUMERICAL ANALYSIS FOR BANK REINFORCEMENT WITH GEOCONTAINER

S.Q. Yang[1], Y.M. Shu[2] and X.C. Yang[3]

ABSTRACT: In China, dumped riprap is used for emergency elimination of bank collapse in large rivers. However, the riprap collapses due to washing and scouring in flood period. Geocontainer is applied to sustain river bank stable for a long time. In order to use geocontainer for practical emergency elimination of bank collapse, model experiment and numerical analysis about geocontainer are performed. The geometrical scale of model is 1:60. The formulae of sinking trace of the geocontainer have been deduced according to test data and it can be used to guide construction. The analysis software FLAC3D is used to analyze the stability effect of the geocontainer sustaining river bank under four water levels at Mahu dike in Yangtze river which collapsed in 1996. The result shows that the bank loses its stability under the fourth condition without sustained geocontainers and the bank stability can be kept with sustained geocontainers under the same condition.

KEYWORDS: bank reinforcement, geocontainer, numerical analysis

INTRODUCTION

Geocontainers are relatively new systems. They will be gradually applied in land reclamation, coastal engineering, channel dredging, breakwaters construction. Due to their large sizes, good suitable touch with river bed, geocontainers are applied to stop the river bank and bottom scoured and maintain the stable of the river bank.Studies about geocontainers mainly involved tensile stresses suffered by geotextile of geocontainer in the process of sliding from split barge. However, after sliding from the split barge they will drift to settling points according to the changing of water level and current velocity and studies about this problem are less at home and abroad.The stability of the bank slope will be improved by sustaining of the geocontainers after erosion taken place, seeing fig. 1. These will be studied as follows.

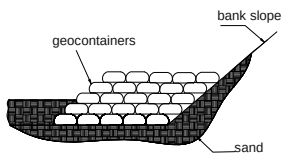

Fig. 1 Protecting the bank slope and bottom with geocontainers

MODEL EXPERIMENT

Based on the experience of length-width ratio, three kinds of geocontainers with different sizes are designed, being big-geocontainer, mid-geocontainer and small-geocontainer. The dimensions of them respectively are 35cm, 30cm and 25cm in model length corresponding to the actual length of 21m, 18m and 15m, and 50 cm, 41cm, 36cm in model circumference. Their actual volumes are $280m^3$, $200m^3$ and $160m^3$ respectively. Geotextile is made of polyhydrocarbonene woven fabric in flat yarn, of which the effective aperture meet the criteria of filter design. Model geocontainers are filled of sand with ρ =1.60g/cm^3.When the percentage of filling volume is 50%, the weight of model geocontainers are respectively 2.07 kg, 1.48kg and 1.18 kg.

Experiment Condition

The flume is recycled with rectangular section of 22m long, 1.3m high and 0.50m wide. There are a hydrostatic bar in the front, a rear door which is used to adjust water depth and a thin triangular weir which is used to measure flow-rate. Gravity similar criteria is

[1] Guangxi Electric Power Industry Investigation Design and Research Institute, CHINA. Email:ysqsxl@163.com
[2] Professor, College of Water Conservancy and Hydropower Engineering, HoHai University, CHINA. Email: yimingshu2004@yahoo.com.cn
[3] Student ,College of Transportation and Traffic, Jinlin University, CHINA. Email:yangxiaochao860327@163.com

adopted with geometric scale $\lambda_L = 60$, velocity scale $\lambda_v = \lambda_L^{1/2} = 7.75$.

Settling Geocontainers in Still Water

Firstly, geocontainers are dumped in still water, which are placed on two uniformly rectangles aquaplane contacting into 130°. Secondly, the board is opened slowly， and geocontainers are sliding from it. The project of landing position is coincidence with the initial dumping position in plane. The displacement and angle are nearly zero. This is the ideal conditions of the construction of geocontainers.

Dumping Geocontainers in Current Water

In order to study the geocontainer construction in a certain current, water velocity v =1～3m/s and water depth H=8～14m are designed. Three kinds of water depths and three kinds of velocities are selected, consisting nine working conditions. Considering dry sand being shipped from other place or dredged wet sand in actual construction, both cases of dry and wet sand are used.

The geocontainers of three sizes of are respectively dumped in water with depth of 13.3 cm,18.8cm and 23.3cm corresponding to actual depth of 8m,11m and 14m, and the velocities of flow are respectively 0.13m/s, 0.26m/s and 0.4m/s corresponding to actual velocity 1m/s, 2 m/ s and 3 m/s, those contain nine conditions.

Each geocontainer is dumped twice in the same condition, the average of the displacement s_1 and s_2 are recorded. The view is as shown in Figs. 2 and 3.

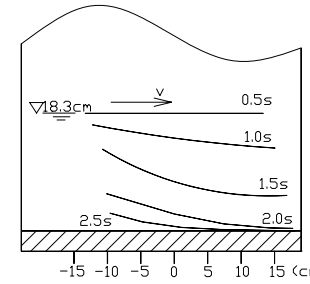

Fig. 2 The side view of dumped and settled spot

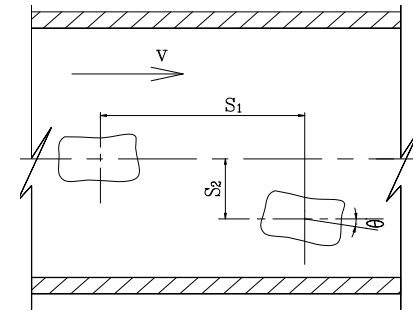

Fig. 3 The bird's-eye view of position changing with time

As shown in Fig. 3, s_1 is the displacement in the direction of water flow in process of sinking; and s_2 is the displacement in the direction of perpendicularity to water flow, and θ is the rotation angle in the horizontal plane. The experiment values of displacement and angle are measured in a variety of conditions as shown in Table 1 and Table 2.

Table 1 Experimental(Exp) and calculating(Cal) displacements and angles when the geocontainer is dry.

Sizes \ Condition		v_1=0.13m/s				v_2=0.26 m/s			
		h_1=13.3		h_2=18.3		h_1=13.3		h_2=18.3	
		Exp	Cal	Exp	Cal	Exp	Cal	Exp	Cal
Small	s_1/ cm	22	21.2	30	29.2	43	42.5	60	58.5
	s_2/cm	3	2.7	4	3.7	6	5.3	8	7.3
	θ/°	8	/	10	/	12	/	12	/
Middle	s_1/ cm	20	20.5	26	28.2	40	41	60	56.4
	s_2/cm	2.5	2.6	3	3.5	6.0	5.1	8	7
	θ/°	6	/	6	/	8	/	8	/
Large	s_1/ cm	16	17.2	22	23.7	38	34.5	48	47.4
	s_2/cm	2	2.2	2.5	3	5	4.3	6	5.9
	θ/°	4	/	5	/	5	/	5	/

Table 2 Experimental(Exp) and calculating(Cal) displacements and angles when the geocontainer is saturated

Sizes	Condition	v_1=0.13m/s				v_2=0.26 m/s			
		h_1=13.3		h_2=18.3		h_1=13.3		h_2=18.3	
		Exp	Cal	Exp	Cal	Exp	Cal	Exp	Cal
Small	s_1/ cm	6	5.3	8	7.3	12	10.6	16	14.6
	s_2/cm	0.8	0.7	1	1.1	1.8	1.3	2	1.8
	θ/°	4	/	5	/	4	/	4	/
Middle	s_1/ cm	5.5	5.1	8	7.0	11	10.2	15	14
	s_2/cm	0.6	0.6	0.8	0.9	1.5	1.3	1.8	1.8
	θ/°	3	/	5	/	4	/	5	/
Large	s_1/ cm	4	4.3	6	5.9	9	8.6	12	11.9
	s_2/cm	0.4	0.5	0.8	0.7	1	1.1	1.2	1.5
	θ/°	2	/	3	/	2	/	2	/

The following conclusion can be drawn from the experiment data:a) When the filling ratio is the same, the more the volume, the more the weight, and the smaller the s_1.b) When the velocity changes from 0.13m/s to 0.26m/s, the s_1 increases largely with the velocity increasing.c)When the velocity is the same, the more the water depth, the more the displacement.d) The landing angle in the horizontal plane is small. The maximum angle is about 10° with dry sand in container while landing angle can be omitted with wet container.

Based on the expermiment data and dimensional harmony principle, the formula can be drawn as follows.

$$s = P\frac{vh}{(\beta V)^{\frac{1}{6}}\sqrt{\frac{\rho_g-\rho_w}{\rho_w}g}} \tag{1}$$

$$s = 0.11k\frac{vh}{(\beta V)^{\frac{1}{6}}\sqrt{\frac{\rho_g-\rho_w}{\rho_w}g}} \tag{2}$$

In the same way S_2 is as the follows:

$$s_2 = \frac{1}{8}s_1 \tag{3}$$

Where k is coefficient of dry sand and wet sand and it gets 1.0 with dry sand or gets 0.25 with wet sand. v is flow velocity; h is water depth; ρ_w and ρ_g are the density of water and sand respectively ; g is gravity acceleration ; β is filling ratio; V is the volume of geocontainer.

To verify the accuracy of these formulae, volume of 740cm^3 , 920cm^3, 2592cm^3 and filling ratio of 50%, flow velocity and the water depth as shown in Table 1 and Table 2 are put into Eqs. 2 and 3, then the calculating displacement data can be gained as shown in Tables 1 and 2. Comparing the experimental and calculating results of Tables 1 and 2, it is seen that calculating results are close similar with experiment results. Therefore, Eqs. 2 and 3 are conformed with the experiment results.

NUMERICAL SIMULATION ANALYSIS

The stability effect of the geocontainer sustaining river bank is numerically analyzed by an example of Mahu dike in the Yangtze river.

Work Survey

Mahu dike is located in the Yangtze river near a curving section which is the turning of east-west to north-south. From the evolution of Yangtze River, the river gradually moved to south, and the south bank has been constantly eroded. The soil layer of slope has adverse geological conditions, and the parameters are as shown in Table 3. The geocontainers sustaining the slope is made of woven polyester with tensile strength of 222.48kN/m and 233.20kN/m respectively in weft and warp. The corresponding maximum elongation ratio is 13.1% and 13.6%. The density of the filling sand is 1800kg/m^3. The thickness of geotextile is 0.002m, elastic modulus 1.2GPa, friction angle 29°, cohesion 0.1MPa, tangentialstiffness 10000MPa/m, tensile strength 222.48 kN/m. The Slope model of before and after erosion are shown as Figs. 4 and 5.

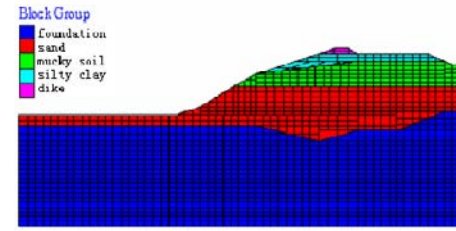

Fig. 4 Protecting the bank slope and bottom with geocontainers

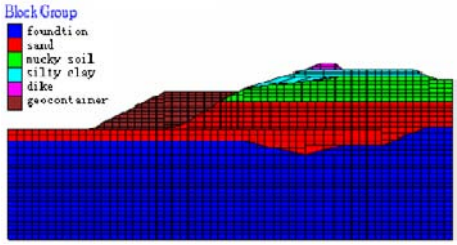

Fig. 5 Mahu dike model with sustained

Calculation Condition

The calculation simulate the stability of the scoured dike and the dike with sustained geocontainers under the changing water level and seepage action during six months. The water level was 20.72m on 9 July 1995 and descend to 15.8m on 18 August, and rose to 17.2m on 26 August, and descended to 8m in January 1996 with a drop of 10m. Inside the dike, there is always accumulating water with a level of 12 to 14m. The water level of the four condition in the numerical analysis is 20.7m,15.8m,17.2m and 8m respectively.

Calculation Results and Analysis

By calculating and comparing the indexes of displacements, minimum principal stresses, plastic zones and FOS, the result shows that the scoured bank loses its stability from stable state under the fourth condition and the bank stability can be kept with sustained geocontainers under the same condition. The five indexes of the scoured bank and sustained bank are shown as Table 4.

Table 3 Characteristics of foundation and soil layers

Characteristics	Density (g/cm^3)	Cohesion (kPa)	Friction (°)	Shear modulus (MPa)	Bulk modulus (MPa)	Coefficient of seepage (cm/s)	Porosity ratio
Mucky soil	1.82	16	6	2.6	7.8	$2*10^{-6}$	0.50
Silty clay	1.90	28	25	5	12	$3*10^{-5}$	0.40
Fine soil	1.70	0	33	7.25	16.7	$3*10^{-3}$	0.35
Limestone	2.30	25000	43	12300	21500	$1*10^{-8}$	0.15
Dike	1.85	31	26	4.2	10.2	$3*10^{-5}$	0.38
Geocontainer	1.80	0	30	8.8	19.2	$3*10^{-2}$	0.37

Table 4 Indexes of the scoured bank(SCB) and sustained bank(SUB)

	Z-disp (m)		X-disp (m)		Minimum principal stresses(MPa)		Fos		plastic zones(position and quantity)	
	SCB	SUB	SCB	SUB	SCB	SUB	SCB	SUB	SCB	SUB
1#	0.57	0.63	0.30	0.22	0.81	0.83	2.4	3.2	At the bottom 5 zones	Contact surface between geocontainer and bank 6 zones
2#	0.41	0.48	0.18	0.18	0.81	0.81	1.7	2.5	height of -15 m 9 zones	Contact surface between geocontainer and bank 12 zones
3#	0.46	0.54	0.21	0.19	0.82	0.81	1.8	2.7	height of 5 m 30 zones	Contact surface between geocontainer and bank 11 zones
4#	0.76	0.30	-0.68	0.09	0.81	0.81	0.98	1.6	Plastic zones breakthrough	Contact surface between geocontainer and bank 11 zones

Z-displacement (vertical direction) and X-displacement (horizontal direcion)

The Z-displacement is always uniform under stable state, but the X-displacement leaps when the river bank becomes instable.The z-displacement and the X-displacement under condition 1 are normal seeing Figs. 6 to 9.(displacement and condition is abbreviated to be ‘disp’ and ‘con’ in the figures)

Under condition 2 and 3 , with water levels changing from 20.7m to 15.8 and from 15.8m to 17.3m ,the Z-displacement and X-displacement of the scoured and sustained dike were similar with those of the condition 1.But under the condition 4 with water level changing from 17.3m to 8m the scoured dike loses its stability

while bank stability can be kept with sustained geocontainers. The displacements of the fourth condition are below, figs. 10 to 13.

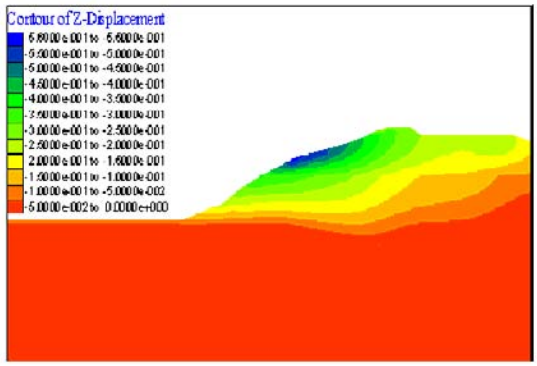

Fig. 6 Z-disp under con1 of scoured dike

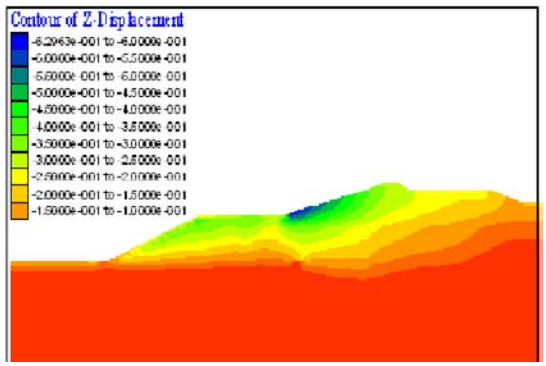

Fig.7 Z-disp under con 1 of sustained dike

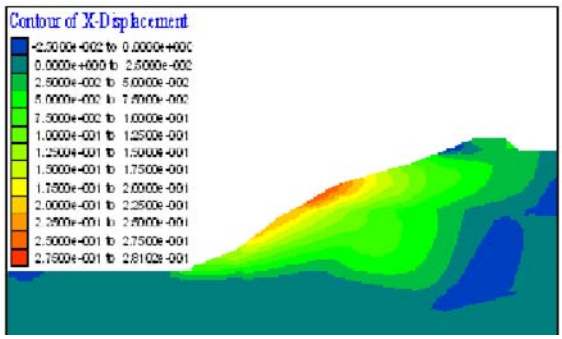

Fig. 8 X-disp under con1 of scoured dike

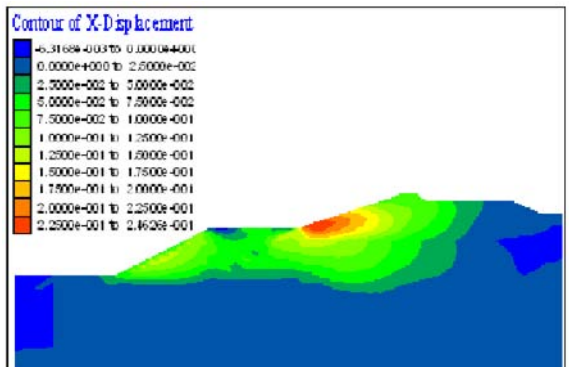

Fig.9 X-disp under con1 of sustained dike

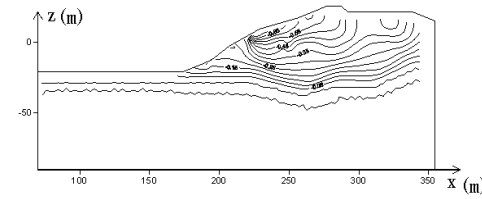

Fig. 10 Z-disp under con 4 of scoured dike

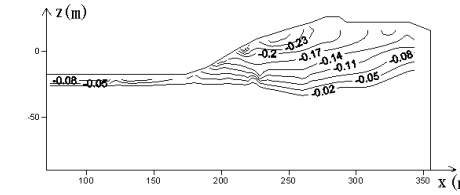

Fig. 11 Z-disp under con 4 of sustained dike

Under the first three conditions, variation laws for Z-displacement of the river bank no matter with geocontainers are the same. Merely, the maximum of Z-displacement of the river bank sustained with geocontainers is larger than that of the scoured bank. It is seen that the geocontainers stabilize the soured dike. However, under the fourth condition, the scoured bank lose its stability. The compare between the two Z-displacements can be seen in Figs.10 and 11. The maximum of Z-displacement of the river bank is 0.76 m and the other is 0.30 m.

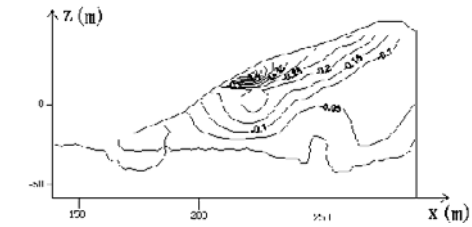

Fig. 12 X-disp under con 4 of scoured dike

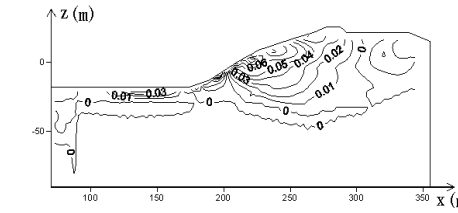

Fig. 13 X-disp under con 4 of sustained dike

Regarding to X-displacement, the maximum of X-displacement of the river bank sustained with geocontainers is smaller than that of the scoured bank. Under the fourth condition, the contour of the X-displacement is specially intensive. The maximum of X-displacement of the river bank is 0.68 m (see Fig. 12) and the other is 0.16 m (see Fig. 13).Under condition 4, from Figs.10 and 12, the maximum Z-displacement and

maximum X-displacement are 0.76 m and 0.68 m respectively. The ratio of X-displacement and Z-displacement has been up to 89.5%. The reverse osmotic pressure produced by descend of water level makes the X-displacement substantially increase. The maximum appears at the contacting surface between muddy soil and fine sand. Because the slope angle of sand layer is largest and anti-shearing strength of muddy soil layer is least, the deformation is large there. From Figs.11 and 13, the Z-displacement and X-displacement of the bank sustained with geocontainers are 0.30 m and 0.16m respectively and the ratio of X-displacement and Z-displacement has decreased to 50%.

Stresses

Generally the stress state of slope soil is compressive stress. If the minor principle stress is tension stress, the soil comes to failure. In output of FLAC, compressive stress is negative. So the maximum of output is considered .The stress unit of the output is Pa.

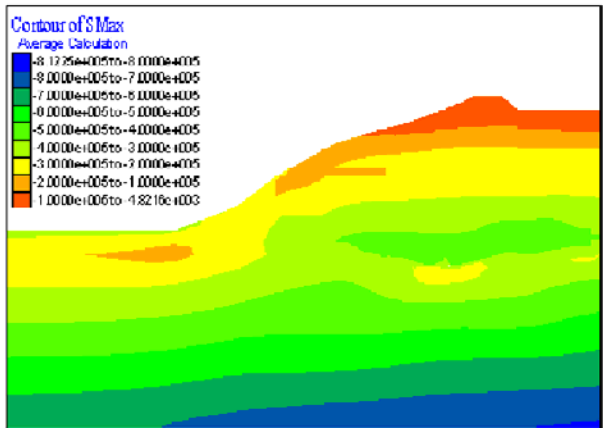

Fig. 14 Minor principle stress under con 1 of scoured dike

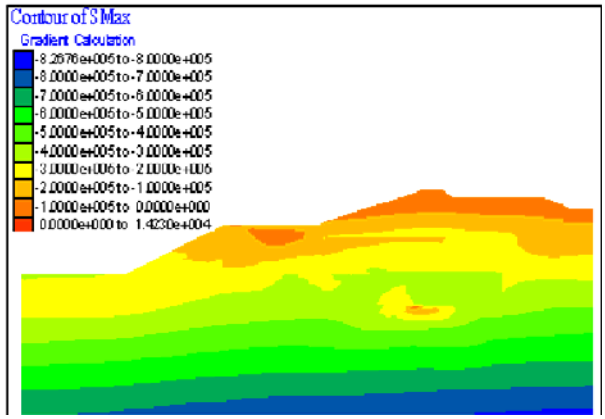

Fig. 15 Minor principle stress under con 1 of sustained dike

Under conditions 2, 3 and 4, the minor principle stresses are similar with that of condition 1, and the minor principle stresses of slope soil are about 0.81 MPa. No tension failure occurs.

Plastic Strain Area

Figs. 16 and 17 show the shear failure under con1—4:

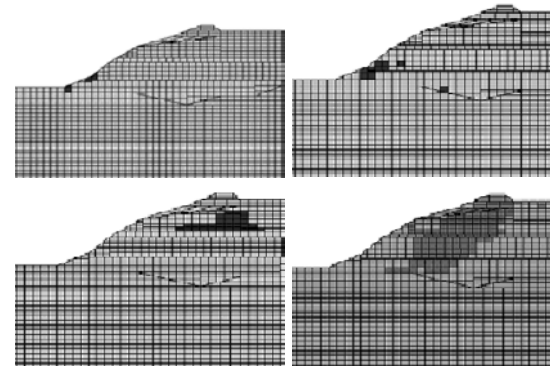

Fig. 16 Plastic state of the scoured dike under con1—con 4(from left to right, from up to down)

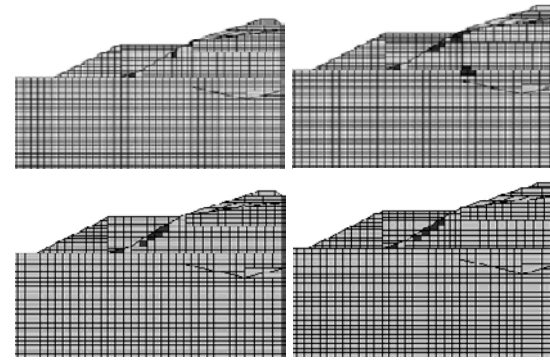

Fig. 17 Plastic state of the sustained dike under con 1—con 4(from left to right,from up to down)

From the above figures, it is seen that in first condition of dike sustained with geocontainers, there is a small amount of plastic strain region in the surface area of slope, and this doesn't exist before applying geocontainers, because the superposition of geocontainers and high water-level increases the local partial stresses.

In the second, third and fourth conditions, after the application of geocontainers, the stresse distributions are all improved, plastic strain region is smaller than that of scoured bank. Especially in the fourth condition, plastic strain regions are linked to moderate area in the scoured model, and the bank lose its stability. After geocontainers sustained, only some small-scale plastic strain region appears in the area of contact surface between geocontainers and bank slope.

Safety Factor of Strength Reduction

In FLAC software, anti-shear strength parameters of rock slope will be gradually reduced until it achieve the damaged state. When the safety factor of strength reduction Fos is more than 1, the analysis target is believed that it is in a stable state, when it becomes less than 1, destruction occurred. Fig. 18 shows the characteristic of Fos.

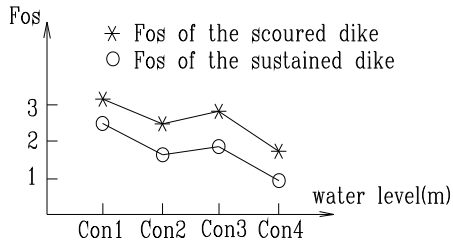

Fig. 18 Fos of scoured and sustained dike

Table 5 lists the model slope stability results in four kinds of conditions, with a method of strength reduction. Geocontainers increase the stability of the banks.

Table 5 Fos of scoured and sustained bank

Condition	SCB	SUB
1	2.4	3.2
2	1.7	2.5
3	1.8	2.7
4	0.98	1.6

CONCLUSION

The trace characteristic of geocontainer sinking in current is studied by experiments that containers with three sizes sink respectively under the conditions of three water depths and three water velocities. The formulae of sinking trace of the geocontainer have been deduced and it can be used to guide construction.

The stability effect of the geocontainer sustaining river bank is numerically analyzed by an example of Mahu dike in the Yangtze river. In short, geocontainers as slope protection measures, can prevent the bank from being scoured by water waves effectively and the stability of the bank slope will be improved by sustaining of the geocontainers after erosion taken place.Theoretically,it has proved geocontainer to be a good protection system and is expected to be gradually applied.

REFERENCES

Chen ZY, Sun YS (2000) Collapse mechanism of Yangtze River levee bank and engineering measures is explored, China Water Conservancy 2002(2):28-29

Pilarczyk KW (2000) Geosynthetics and geosystems in hydraulic and coastal engineering. Rotterdam: A.A.Balkema, Netherlands

Pilarczyk KW (1998) Dikes and revetments. Rotterdam: A.A.Balkema, Netherlands

Xu T (1982) Similarity theory and model test. China Agricultural Machinery Press, Beijing, China

Zhu LJ etc (2002) Experimental studies on the hydraulic characteristics of geo-textile sandbags. Proc. of 13th IAHR-APD Congress, Singapore 1: 157-162

Bezuijen A, Klein Breteler M (2002) Model tests on geocontainers, placing accuracy and geotechnical aspects. Proceeding of Geosynthetics-7th ICG, Delmas, Gourc & Girard: 1001-1006

Transportastion Applications

BEHAVIOR ANALYSIS OF REINFORCED SOIL RETAINING WALL UNDER CYCLIC LOADING

Y.Y. Kim[1], M.S. Yoon[2], S.J. Han[3] and S.S. Kim[4]

ABSTRACT: A reinforced soil retaining wall is defined as a vertical-walled structure formed by increasing the stability of the backfill of the retaining wall with the installation of reinforcement materials such as geosynthetics, geogrids and steel strips into the backfill. Reinforced soil retaining walls are flexible structures as the friction between soil and reinforcement materials, and the connection between parts of the wall and reinforcement materials allow it to resist earth pressures. Because of this flexibility, reinforced soil retaining walls are considered a distinguished seismic-resistant structure. Moreover, in recent years, the use of reinforced soil retaining walls as a railroad bed-bearing structure has increased. However, studies of reinforced soil retaining walls on the characteristic of the behavior of the walls caused by cyclic loading of trains have been carried out scarcely; accordingly, stability and reliability of soil retaining walls have not been sufficiently proved.

Experiments were conducted in this study by applying cyclic loading to a reinforced soil retaining wall, in an attempt to understand its behavior, depending on the magnitude and the location of cyclic loading. Formulas of vertical earth pressure and displacement were also suggested.

KEYWORDS: reinforced soil retaining wall, cyclic loading, geogrid, railroad roadbed

INTRODUCTION

A reinforced soil retaining wall is defined as a vertical walled-structure that is highly stable resulting from the installation of geotextiles including geogrids and band shape reinforcement materials between surcharge soil layers.

A reinforced soil retaining wall is a flexible structure as the friction between soil and reinforcement materials, and the connection between parts of the wall and reinforcement materials allow it to resist earth pressures. Because of this flexibility, reinforced soil retaining walls are considered a distinguished seismic-resistant soil structure. Tatsuoka (2006) has reported the excellence of reinforced soil retaining wall as a seismic-resistant soil structure. According to his case study, in 1995 during the Kobe earthquake, most of the gravity retaining walls, the most common type of a wall constructed to sustain railway roadbed at the time, were largely damaged or destructed by the earthquake. However, most of the few reinforced soil retaining walls sustained almost no damage.

Because of the excellent seismic-resistency of reinforced soil retaining walls, NCMA (National Concrete Masonry Association) and FHWA(Federal Highway Administration) established seismic design criteria for reinforced soil retaining walls, and interests in the application of reinforced soil retaining walls as a seismic-resistant structure or a railroad roadbed structure have been increasing internationally.

However, reinforced soil retaining walls have been restrictively applied to highways, housing, sports facilities, and shore protection. Also stability and reliability of a reinforced soil retaining wall to cyclic loading and long-term repeat loading are not sufficiently proved. Therefore, its application as a seismic-resistant structure or a railroad roadbed structure is minimal.

Bathurst & Raymond and Webster(1989) applied reinforced soil retaining wall to a railroad structure in their field testing. They reported that train's vibration lowered friction resistance between soil and reinforcement material and caused continuous displacement of the wall. Also, seismic design criteria of NCMA and FHWA is based on a quasi-static limit equilibrium analysis using the Mononobe-Okabe theory, so it is difficult to understand the actual behavior of reinforced soil retaining walls caused by dynamic loading.

In this study, behaviors of reinforced and unreinforced soil retaining walls were compared when cyclic loading

[1] CEO, E&S Engineering Co. Ltd., KOREA. Email: adm@eseng.co.kr
[2] Ph.D Student, Department of Civil Engineering, Hanyang University, KOREA. Email: ddingkko@hanyang.ac.kr
[3] Research Director, Expert Group for Earth & Environment Co., Ltd., KOREA. Email: hansj@ege.co.kr
[4] Professor, Department of Civil Engineering, Hanyang University, KOREA. Email: kimss@hanyang.ac.kr

was applied. Cyclic loading experiments on model railroad roadbeds supported by reinforced and unreinforced soil retaining walls were performed, and the behaviors and effects of a reinforced soil retaining wall against cyclic loading were analyzed by examining the correlation between settlement, strain of a geogrid, and horizontal and vertical earth pressures.

EXPERIMENTS

Characteristics of Surcharge Material

In this study, decomposed granite soil was used as a surcharge material. Mechanical properties of decomposed granite soil are listed in Table 1.

Table 1 Mechanical properties of surcharge material

Specific Gravity, G_s	2.65
Cohesion, c	0
Friction angle, (°)	27.5
Uniformity coefficient, C_u	14.1
Coefficient of curvature, C_c	0.4
USCS	SP
% finer of No. 200 sieve	16.6
Maximum dry unit weight, (g/cm^3)	1.85
OMC, (%)	15.7

Characteristics of Geogrid

In this study, polyester geogrids were used as a reinforcement material for the reinforced soil retaining wall. In order to estimate physical characteristics of a geogrid, external standard, thickness, and density were measured. Fig. 1 shows the direction of testing and the size of the grid. Physical characteristics of the geogrids used in this study are listed in Table 2.

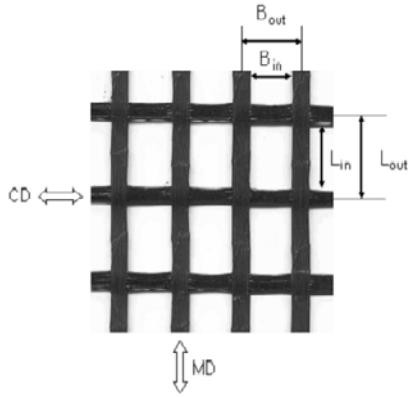

Fig. 1 Shape of geogrid

Table 2 Physical properties of geogrid

External standard				
Size of grid (mm)		Thickness of lib (mm)		Thickness of contact point (mm)
$L_{in}\times B_{in}$	$L_{out}\times B_{out}$	MD	CD	
19.2× 16.1	25.2× 25.2	1.3	1.1	1.4
Roll standard			Unit density (g/m^2)	Effective area ratio (%)
Roll width (m)	Roll length (m)	Roll weight (kg)		
2	50	45	450	51.3

Test Method

Preparation for retaining walls

Fig. 2 shows a section of the geogrid-reinforced soil retaining wall (GRS-RW) for cyclic loading test. A GRS-RW is made of four 25 cm thick decomposed granite soil layers and one upper macadam layer that is also 25 cm thick. The soil box is 1m in width, 1.4 m in length, and 1.5 m in height. A geogrid is installed on the soil box covering half of its width (70 cm).

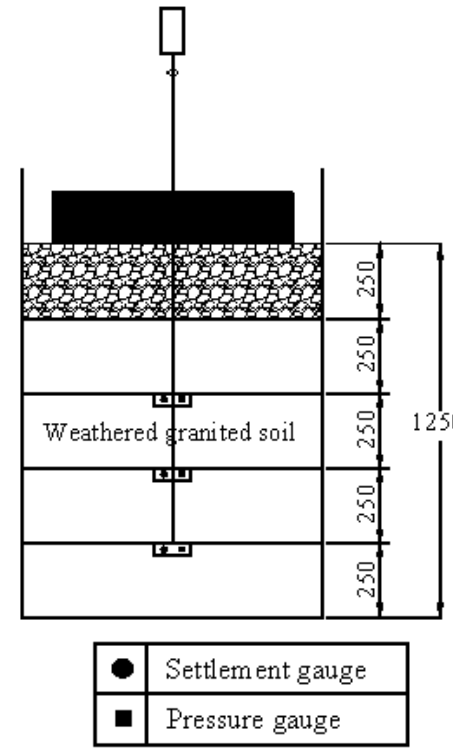

Fig. 2 Test section

Fig. 3 shows the test procedure. First, a geogrid with a strain gauge and surcharge materials in OMC were prepared. The surcharge materials were compacted to 25 cm in thickness maintaining a degree of compaction of 95%, and then a geogrid and a measuring instrument were installed. The geogrid was bolted onto the wall face. By repeating this procedure, 4 roadbed layers were set up, and finally the upper macadam layer 25 cm in thickness was set up. Cyclic load was applied by a load cell from loading a plate which is 27 cm in length and 80 cm in width.

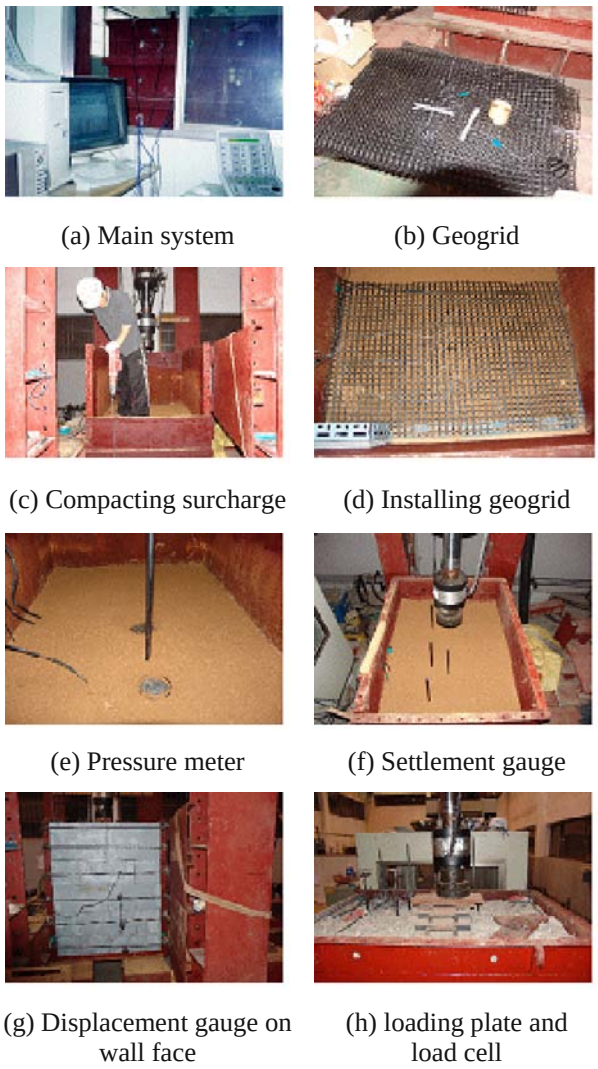

(a) Main system (b) Geogrid

(c) Compacting surcharge (d) Installing geogrid

(e) Pressure meter (f) Settlement gauge

(g) Displacement gauge on wall face (h) loading plate and load cell

Fig. 3 Test procedure

Installation of measuring instruments

The positions and kinds of measuring instruments were decided by considering the content and the purpose of the cyclic loading test. Fig. 4 shows the positions and the kinds of measuring instruments used in the test. The kinds of measuring instruments are listed in Table 2.

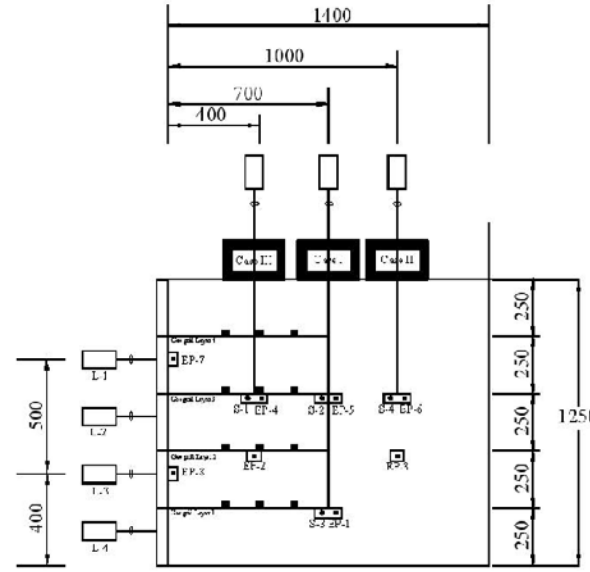

Fig. 4 Composition and position of measuring instruments

Table 3 Types and quantities of measuring instruments

Instrument	Qty	Term
Pressure meter	8	EP1—EP8
Horizontal displacement gauge	8	L1—L2
Settlement gauge	4	S1—S4
Strain gauge	12	ST1—ST12

Testing conditions

A cyclic loading test was performed on a GRS-RW and an unreinforced soil retaining wall. 3 loading tests were performed on a GRS-RW with different loading points. Test conditions are listed in Table 4. Distances from the wall face to loading points are shown in Fig. 4.

Table 4 Kind and number of measuring instruments

Test case	Loading point	Reinforcement	Remark
Unreinforced	0.7*H*	Unreinforced	*H* : Height of decomposed granite soil layer (1.0 m)
Case I	0.7*H*	Reinforced	
Case II	1.0*H*	Reinforced	
Case III	0.4*H*	Reinforced	

In order to prevent the retaining wall from failing, early static load, q_s, was decided to be 2.3 tonf by considering 7 tonf as a failure load which was obtained from a static loading test and 3.0 as a safety factor. Fig. 5

shows loading procedure for each case. First, a static load of 1.0 tonf was applied, and then additional 1.3 tonf was applied for about 100 seconds. Then step cyclic load of $1.1q_s$ (2.53 tonf) at Step I, $1.25q_s$ (2.88tonf) at Step II, $1.5q_s$ (3.45 tonf) at Step III, and $1.7q_s$ (3.91tonf) at Step IV were applied. In every step, cyclic load was applied at 3.5 Hz, 50000 times.

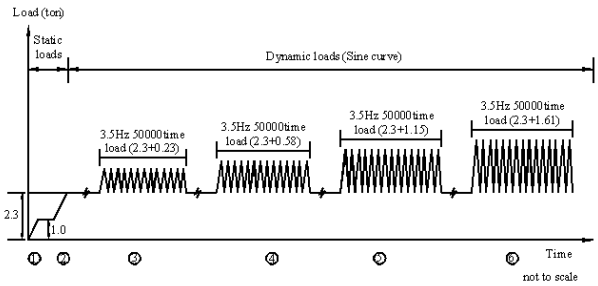

Fig. 5 Procedure of cyclic loading

TEST RESULTS

Vertical Stress Distribution

Fig. 6 shows the maximum plastic vertical stress distribution at $0.75H$ in height when the loading point is $0.7H$ away from the wall face. For the GRS-RW, vertical stress was much smaller than unreinforced reinforcement wall due to the dispersion effect by geogrid reinforcement at the straight bottom of the loading point (EP5). At a point near the wall face (EP4), maximum vertical stress on the GRS-RW was greater compared to that for the unreinforced soil retaining wall. Stress concentration occurred because tensile stress caused by cyclic loading transferred to the wall face which was connected to the geogrid by bolting. In this case, prediction equation for estimating vertical stress at the straight bottom of the loading point is as follows.

GRS-RW:

$$\Delta\sigma = 30.53 + 122.5\left(\frac{q_d}{q_{u(R)}}\right) \quad (1)$$

Unreinforced soil retaining wall:

$$\Delta\sigma = 15.39 + 30.3\left(\frac{q_d}{q_{u(R)}}\right) \quad (2)$$

where q_d is cyclic load, $q_{u(R)}$ is failure load obtained from static loading test, $q_d/q_{u(R)}$ is dynamic load increment ratio.

Also, vertical stress transferred to the wall face is relatively small and shows a linear behavior, because strain and tensile stress induced to the geogrid is in an internally stable state.

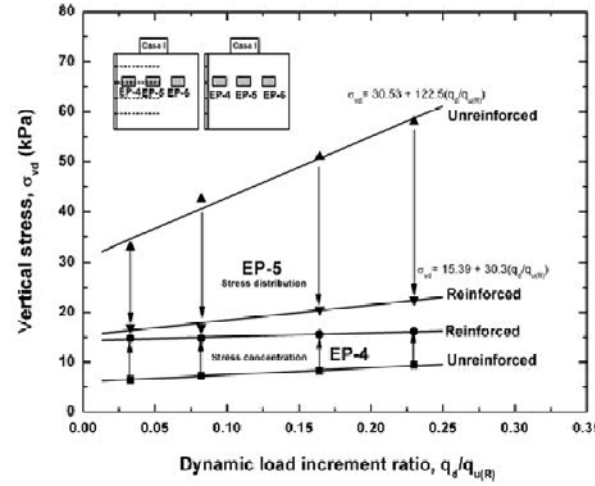

Fig. 6 Maximum vertical stress distribution according to dynamic load increment ratio

Fig. 7 shows the distribution of the maximum plastic vertical stress ratio ($\sigma_{vd(R)}/\sigma_{vd(u)}$), according to the dynamic load increment ratio where, $\sigma_{vd(R)}$ is maximum vertical stress for the GRS-RW, and $\sigma_{vd(u)}$ is maximum vertical stress for the unreinforced soil retaining wall. About 38%—51% of stress dispersion occurred at the straight bottom of the loading point EP4, and geogrid reinforcement had no effect outside the reinforced area (EP6). Vertical stress on the GRS-RW at EP4 was 2.2 times higher than that on the unreinforced soil retaining wall.

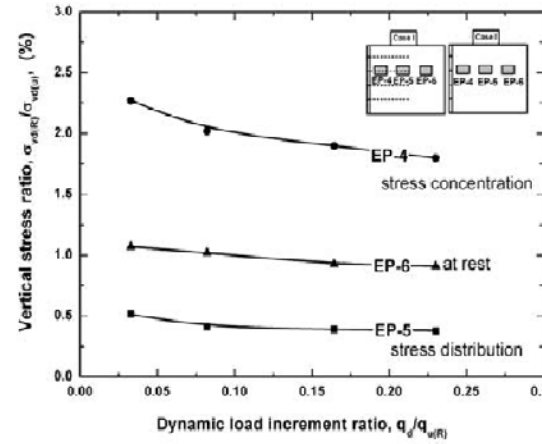

Fig. 7 Distribution of the maximum vertical stress ratio according to the dynamic load increment ratio

Settlement Distribution

In this study, final maximum plastic settlement from each loading step was measured to analyze the settlement behavior according to cyclic loading and whether the retaining wall was reinforced or not.

Fig. 8 shows the maximum plastic settlement of the

retaining wall according to the number of load cycles, n, and the dynamic load increment ratio. In order to express the maximum plastic settlement as a dimensionless coefficient, it was normalized by height of the decomposed granite soil layer, *H*. As the number of load cycles increased, the settlement increased rapidly after the early settlement occurred in the case of the unreinforced soil retaining wall, however, in the case of GRS-RW, the settlement increased slowly. Also, the critical number of load cycles, n_{cr}, which is a point where residual plastic settlement behavior begins to show, is decreased by geogrid reinforcement.

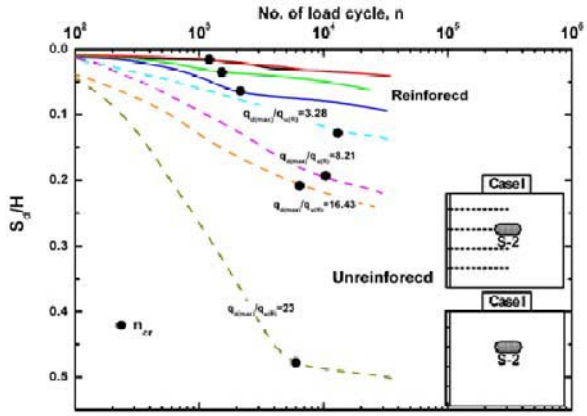

Fig. 8 Normalized settlement distribution according to the number of load cycles

Figs. 9 and 10 show the relationship between the dynamic load increment ratio and the normalized settlement for the GRS-RW and the unreinforced soil retaining wall when the loading point is 0.7*H* far from the wall face. As shown in Fig. 9, the inner plastic settlement in the case of GRS-RW was at its max at the straight bottom of the loading point, and the settlement was about 70% smaller than that of the unreinforced soil retaining wall. Also, as the dynamic load increment ratio increased, the settlement in the case of GRS-RW increased linearly, while that in the case of the unreinforced soil showed a nonlinear behavior. This is because of the stress dispersion effect caused by geogrid reinforcement. The settlement near the wall face of the GRS-RW was small because strain and tensile stress of geogrid was little and the GRS-RW was in an internally stable state. On the other hand, settlement near the wall face of the unreinforced soil retaining wall largely increased as the horizontal displacement of the wall face increased. In the case of the GRS-RW, compression occurred to geogrids at the straight bottom of the loading point because of the stress dispersion effect, and near the wall face, tensile strain induced by tensile stress occurred. Therefore, if geogrids are in an internally stable state, horizontal displacement of the wall face and settlement do not seem to affect the stability of the GRS-RW.

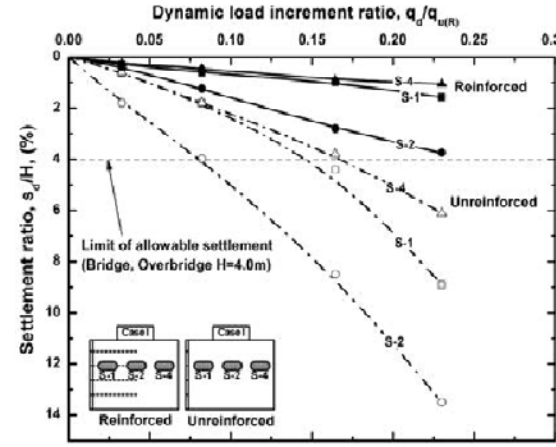

Fig. 9 Normalized maximum settlement according to dynamic load increment ratio

Fig. 10 shows the normalized settlement at the straight bottom of the loading point according to the dynamic load increment ratio. The settlement from the GRS-RW and the unreinforced soil retaining wall at the straight bottom of the loading point can be calculated using the follow equations.

GRS-RW:

$$s_d / H = -0.08 + 48.4\left(\frac{q_d}{q_{u(R)}}\right), \quad \left(\frac{q_d}{q_{u(R)}}\right) < 0.13 \tag{3}$$

$$s_d / H = -2.90 + 71.3\left(\frac{q_d}{q_{u(R)}}\right), \quad \left(\frac{q_d}{q_{u(R)}}\right) > 0.13 \tag{4}$$

Unreinforced soil retaining wall:

$$s_d / H = -0.07 + 16.8\left(\frac{q_d}{q_{u(R)}}\right) \tag{5}$$

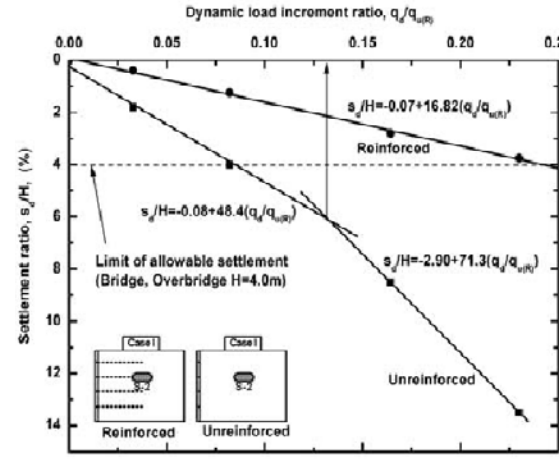

Fig. 10 Normalized maximum settlement distribution at the straight bottom of the loading point

CONCLUSIONS

In this study, laboratory cyclic loading tests were performed on the GRS-RW and unreinforced soil retaining wall, in order to understand the behavior of the GRS-RW under cyclic loading.

From this study, the following conclusions were obtained:

(1) In the case of the GRS-RW, vertical stress largely decreased because of the dispersion effect by geogrid reinforcement at the straight bottom of the loading point.

At a point near the wall face, maximum vertical stress for the GRS-RW was greater compared to that for the unreinforced soil retaining wall. Stress concentration occurred because tensile stress caused by cyclic loading transferred to the wall face which was connected to the geogrids by bolting.

(2) As the number of load cycles increased, the settlement increased rapidly after the early settlement occurred in the case of the unreinforced soil retaining wall, however, in the case of the GRS-RW, the settlement increased slowly. Also, the critical number of load cycles, n_{cr}, which is a point where residual plastic settlement behavior begins to show is decreased by geogrid reinforcement.

(3) The inner plastic settlement in the case of the GRS-RW was at its max at the straight bottom of the loading point, and the settlement was about 70% smaller than that in the case of the unreinforced soil retaining wall. Also, as the dynamic load increment ratio increased, the settlement in the case of the GRS-RW increased linearly, while the settlement in the case of the unreinforced soil showed a nonlinear behavior. From experimental equation, the settlement at the straight bottom of the loading point can be calculated.

REFERENCES

Tatsuoka F (2006) Geosynthetic-reinforcing technology for remedy works of soil structures damaged by earthquakes and heavy rainfalls. Korean Geo-synthetics Society. Conference Proceeding, Keynote lecture: 3-23

Bathurst RJ, Koerner RM (1989) Results of class a prediction for the RMC reinforced soil wall trials. the Appl. of Polymeric Reinf. in Soil Ret. Structures. Farrett PM, McGown, A, eds., NATO ASI Ser., E: Applied Sci., Vol. 14, Kluwer, 127-171; Engineering 128(10): 824-835

HIGH GEOGRID- REINFORCED SOIL RETAINING WALLS FOR A NEW AIRPORT

Y. Fujita[1], T. Sugimoto[1], M.Tsuda[2], Y. Nakamura[2], S. Kawahata[2], H. Funada[3], T. Yoshida[3], M. Ito[4] and K. Yoshida[4]

ABSTRACT: At the "Fujisan-Shizuoka Airport", which is now under construction, two high geogrid-reinforced soil retaining walls were constructed to preserve natural environment consisting of steep swamp areas in front of the walls. These areas are to be buried in the backfill if gentle-sloped embankments were constructed. The height of the walls is 21.1 m and 16.7 m. As the walls support the east side of the runway of the airport, it is required to ensure minimum residual displacements at the crest of the walls. A sufficient high seismic stability is another important design factor. To these ends, well-graded gravelly soil was selected as the backfill and the backfill was compacted very well to an average degree of compaction higher than 95%. The deformations of the walls under and after construction were monitored, which showed very small instantaneous and post-construction residual deformations of the walls. The recorded tensile strains in the geogrid also indicated a high stability of the walls.

KEYWORDS: geogrid, reinforcement, retaining wall, high backfill, airport, observation

INTRODUCTION

Shizuoka Prefecture is located in the middle of the Honshu Island in Japan, where major routes of overland traffic such as the Tokaido Shinkansen Line (bullet train) and Tomei Expressway, and has enjoyed its geographical advantages that lead to active social, economic and cultural developments (Fig. 1). Fujisan Shizuoka Airport (hereinafter referred to as the "Shizuoka Airport") is being constructed as an indispensable infrastructure to enhance the economy and attractiveness of the prefecture as well as to improve the access to the area, expand business chances, promote sports and cultural activities and serve as an emergency transportation center during disasters.

A number of precious plant species in the list of plants to be protected of the prefectural government were found growing in steep valleys near the eastern end of the planned runway where it was planned to construct embankments. It was decided to construct geogrid-reinforced soil retaining walls (GRS-RWs) near the two valleys to reduce environmental impacts and conserve as much as possible the moist habitat of the valleys. Considering that completed GRS-RWs are critical structures for the airport while they become as tall as 21.1 m and 16.7 m, careful and thorough investigation and design as well as construction management were conducted on the entire process. This paper describes the process of design and construction of these GRS-RWs, which are among the tallest ones in Japan.

Fig. 1 Location of the airport

OVERVIEW OF THE PROJECT

The Shizuoka Airport is a Class 3 airport located between Makinohara and Shimada cities and will have a 2,500 m long runway. The landfill project is being executed to open the airport in March 2009**.** The project involves large-scale embankment of soil, which amounts to 26 million m^3 in total, to a maximum embankment height of 75 m. Since the airport was planned to be constructed so as to be friendly to both people and natural environment, measures have been taken to protect the living environments of local residents as well

[1] Shizuoka Prefecture, JAPAN. Email: toshihiko1_sugimoto@pref.shizuoka.lg.jp
[2] Nippon Koei Co., Ltd., JAPAN. Email: a5054@n-koei.co.jp
[3] Kajima Corporation, JAPAN. Email: yt@kajima.com
[4] Maeda Kosen Co., Ltd., JAPAN. Email: m_ito@mdk.co.jp

as the natural environment. For example, pot-grown plantlets of native tree species were planted on embankment slopes, which have inclinations of 1:2 in V:H to restore the natural forest.

During the landfill project, precious species that were to be protected according to the prefectural government were found in two valleys near the eastern end of the runway located in a circle shown in Fig. 2. It was decided to construct GRS-RWs at these locations to as much as possible reduce environmental impacts and conserve the moist habitat of the valley.

Fig. 2 An artist view of the completed airport and locations of the GRS-RWs

PLANNING AND DESIGNING

Structure and Shape of the Embankment

The structure of the embankments for the airport was investigated based on environment protection policies: 1) minimizing the area of modification; and 2) restoring the natural environments in the modified areas as much as possible. For the former objective, it was decided that the planar structure of the airport has corners cut to a degree that the cuts do not adversely affect the basic functions of the airport (Fig. 3). It was also decided to construct GRS-RWs having steep face of 1:0.3 in H:V. These measures reduced the area of modification by 2 ha. For the latter policy, it was decided to vegetate the wall face of the GRS-RWs and the slopes of the embankments were greened by planting native tree species.

Design of GRS-RWs

As shown in Fig. 3, there are two valleys that needed environmental protection at the site. After a series of comparative investigations on workability, economy and environmental impacts of various measures, GRS-RWs were selected for both valleys. The related design issues are described below. Topographical and geological conditions at the site were thoroughly investigated as their thorough understanding was indispensable for stability as well as economic design of GRS-RWs. As shown in Fig. 4, gravel had deposited thick in “Valley 2”, and the gravel layer was judged to be able serve as the foundation ground of the GRS-RW. Since the shear strength of the gravel controls the length of geogrid reinforcement of the GRS-RW, in-situ direct shear tests were performed at the foundation of the wall. Since the wall was to be constructed on a slope of an inclination of about 35 degree, the site investigation for the design of the wall foundation was also conducted on the slope. The internal and external stability of the GRS-RWs under static and seismic loading conditions was examined by limit equilibrium-based stability analysis. The geogrid-reinforced soil retaining wall, having a wall height of 21.1 m and a width of 75.6 m, is one of the largest walls in Japan. The length of reinforcing materials (geogrid) is 22m, and the maximum design tensile strength is 87 kN/m.

The GRS-RW in “Valley 1” was completed in December 2006, and the overlying embankment is being constructed (September 2007). As shown in Fig. 4, the GRS-RW in “Valley 1” supports an overlying embankment as tall as 45 m. This is because there is a level difference of about 40 m between the design elevation of the shoulder of the airport embankment and the elevation of the foundation ground. In order to protect the environment, the dimensions of the embankment were designed so as to: 1) keep the bank slope inclination of 1:2.0 to enable reforestation; and 2) minimize the area of modification by construction a GRS-RW that can be greened. Curves were introduced into the planar shape of the embankment to mitigate stress concentration and reduce the volume of the embankment.

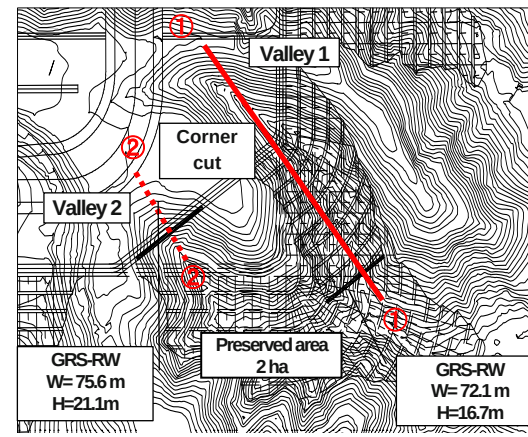

Fig. 3 Plan view of the airport at the eastern end of the runway (①—①and ②—② indicate cross-sections shown in Fig. 4)

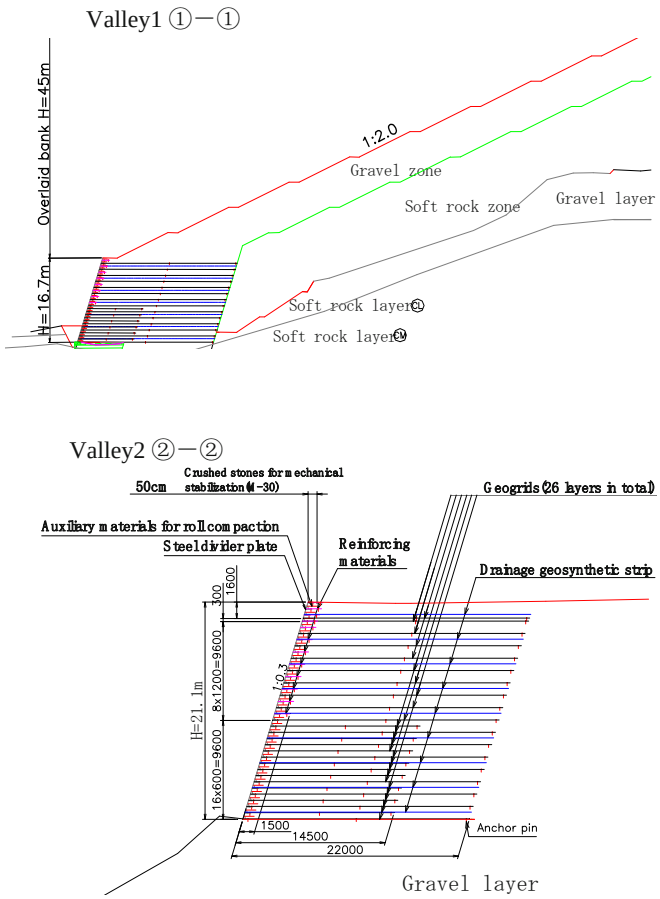

Fig. 4 Cross-sections of the two GRS-RWs

CONSTRUCTION

Backfill Materials

Of soils available at the site, a gravel soil (i.e., terrace gravel with cobbles) that had water content not exceeding 16% (gravel soil I) was selected as the embank-ment material. When well compacted, this gravel can exhibit the largest strength and a high resistance against erosion.

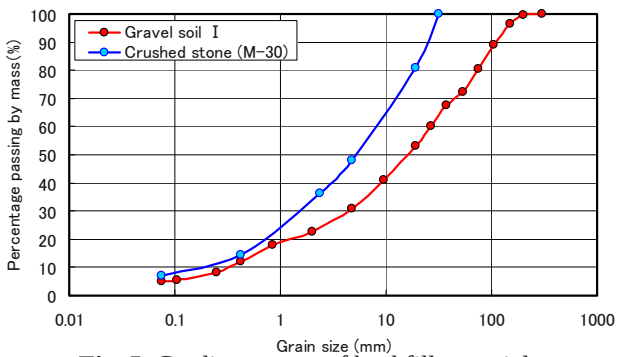

Fig. 5 Grading curves of backfill materials

A high-quality gravel, a crushed stone (M-30), was used in a zone with a thickness of 50 cm immediately behind the wall face for a high stability and a high permeability as well as a high workability. The grading curves of these backfill materials are shown in Fig. 5.

Geogrid

Geogrids type G-35 to 150, which have design tensile strengths of 20 to 87 kN/m, were used. Since the backfill materials contained gravel, the possible installation damage to these geogrids during operations of heavy compaction equipment was evaluated by field full-scale tests. The samples of the geogrids retrieved from roller-compacted test embankment were subjected to tensile tests (JIS L1908). It was confirmed that they meet the required strength. The wall was constructed using a L-shaped expanded metal framework having a vertical height of 60 cm for respective soil layers. The inside of the framework was covered with an inner liner of a non-woven geotextile to prevent the spilling out of sand. The behavior of the wall was monitored after installing each soil layer (35 in total) so that the location of the next framework can be adjusted.

Embankments

Geogrid-reinforced test fills were constructed in advance to determine these specifications. The compacted thickness of each soil layer was determined to be 30 cm based on a vertical spacing between geogrid layers, 60 cm or 120 cm. During the field compaction tests, vibrating rollers of 10 t and 18 t in weight were used. It was found that the 10 t roller was able to compact the backfill to a degree equivalent to that by the 18t roller, although the number of passing required to achieve a high compaction was larger. Moreover, lighter compaction machines were preferred than heavier ones in terms of preventing the wall face materials from falling forward during roller compaction. For these reasons, 10 t vibration rollers were selected. To compact crushed rock gravel in the zone immediately behind the wall face, where heavy compaction machines could not approach, 1 t vibrating rollers and vibrating compactors were used. In Valley 2, the embankment construction started in end December 2005, took about four months, and completed in end April 2006. Since the weather was generally fine during this period, it took about three days to finish one geogrid layer (60 cm) on average. Fig. 6 shows views of the entire GRS-RW in Valley 2 immediately after completion and one year after completion.

Immediately after completion　　One year after completion

Fig. 6 Entire view of the GRS-RW in Valley 2

Drainge of Rain Water and Ground Water

The GRS-RWs were designed so that no pore water pressure is built up inside by quickly discharging rain and seepage water from the existing ground. Perforated drainage pipes were buried along the boundary of the fill to the existing ground at the bottom of the embankment on both sides, and horizontal drainage geosynthetic strips (5 mm thick×300 mm wide) were arranged inside the embankment per 3 m^2 of wall face area (Fig. 7). A zone of crushed stone gravel immediately behind the wall face was also designed to smoothly drain water collected by the horizontal drainage strips as well as rain water from the embankment. During construction, temporary drainage shafts were arranged to discharge rain water from the crest of the embankment. At the center and the bottom of the wall face, where the water is finally discharged from the embankment, mat gabions and crushed stone gabions were arranged to prevent scouring .

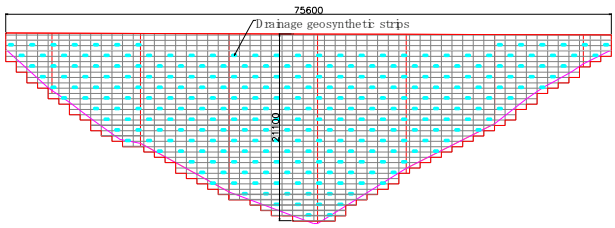

Fig. 7 Cross section of installed drainage geosynthetic strips

Quality Control Tests of the Embankment

The total density of the compacted backfill was measured by the sand replacement method at many locations in the zone consisting of crushed stone gravel immediately behind the wall face and by the RI method at many locations in the other zones consisting of gravel soil I. The RI test was performed once every 1,000 m^2 with 1 points per measurement. The maximum dry density, ρ_{dmax}, of the backfill, which is used to obtain the degree of compaction D_c, was determined by laboratory compaction tests of the backfill material per 10,000 m^3 of the embankment. Fig. 8 shows the histogram of D_c measured by the RI tests of the gravel soil I. The degree of compaction D_c exhibits a normal distribution with a mean of 97.5% and a standard deviation of 2.75% and with a variation coefficient of 3%, which fully satisfies the specified compaction criterion that all the measured D_c should be equal to, or larger than, 90%. It is to be noted that these very high measured D_c values were achieved not only by efforts to keep the specified compaction criterion, which is somehow too loose, but also by careful compaction works with a small lift of 30 cm with a sufficient number of passing of a 10 ton compaction roller in each soil layer. The shear strength of the compacted backfill increases significantly with an increase in from 90% to 100%. Therefore, these very high measured D_c values indicate that the completed GRS-RW has a very high stability exhibiting very small residual deformations (as shown below).

Plate bearing tests were conducted at two locations on the ground surface of roller-compacted embankment during construction. K-values measured by plate bearing tests were 212 and 255 kN/m^3 which are noticeably higher than those usually measured in stable natural subsoil (i.e., diluvial sand and gravel), equal to 130—200 kN/m^3. This result also shows that the compacted embankment is very still.

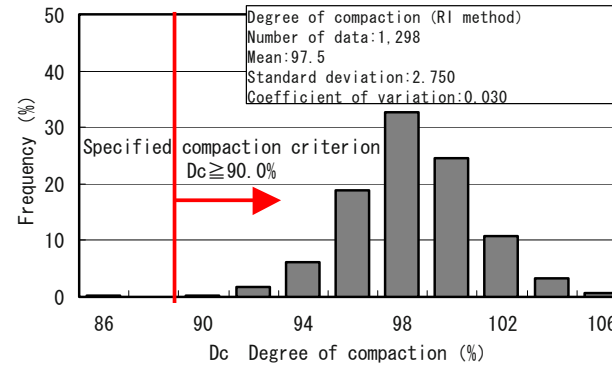

Fig. 8 Histogram of degree of compaction D_c

FIELD OBSERVATION

Instrumentation

Table 1 lists the measuring instrumentation installed in the GRS-RW and surrounding zones in Valley 2. Fig. 9 shows the positions of instrument installation in the GRS-RW in Valley 2. A differential settlement gauge and a borehole inclinometer were installed to monitor the embankment deformation. Three free field earth pressure cells and three piezometers were installed in the foundation ground of the embankment. Ten electric-resistant strain gauges were installed at a 2 m interval on

the longitudinal members of the geogrid at the third, 13th and 23rd layers from the bottom of the GRS-RW. Fourteen reflectors for electro-optical distance measurement were arranged on the front wall face to monitor vertical and horizontal displacements of the wall face. Filed observation has been conducted during the construction (from the end of December 2005 to the end of April 2006) and also after completion.

Table 1 Instruments installed for field observation

Place of installation	Instrument	Measurement item
Embankment	Differential settlement gauge	Settlement of the embankment
	Borehole inclinometer	Horizontal displacement of the embankment
	Free field pressure cell	Displacement of the foundation
	Piezometer	Earth pressure inside the embankment
Geogrid	Strain gauge	Strain of geogrid
	Electro-optical distance meter	Displacement of the geogrid at wall surface

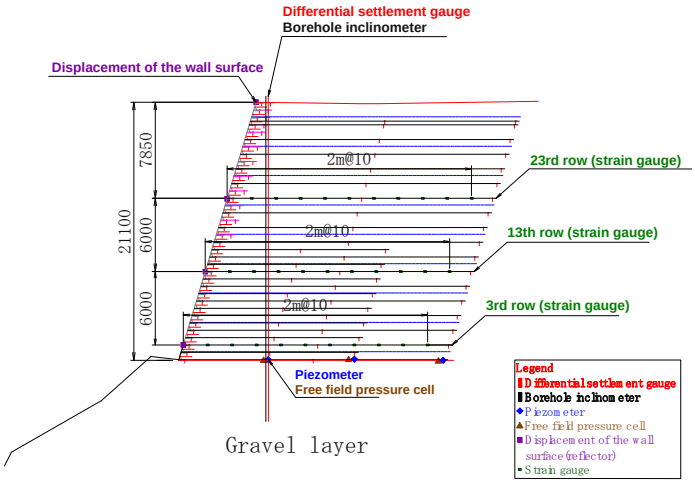

Fig. 9 Cross-section of the wall in Valley 2 showing locations of instruments installed for field observation

Results of Field Observation in Valley 2

Embankment

Fig. 10 shows the time histories of accumulated settlement at the transient crest during construction and the final crest after completion of the embankment. The settlement gradually increased during as the embanking progressed. It is to be noted that the total settlement was only 8 cm at the completion of the wall, which is only 0.4% of the total height, 21 m, of the wall. Furthermore, nearly no residual settlement has been observed after the completion of the wall. In particular, the settlement did not increase at all during rain falls with precipitation exceeding 150 mm.

The horizontal displacement both during construction and after completion is generally very small with a maximum displacement of only less than 1 cm. In particular, the measurements on July 27, 2006 and December 20, 2006 after the completion show that the displacements were kept nearly constant throughout the periods, showing that no increase in the residual lateral displacement in the GRS-RW. The fact that both settlement and horizontal displacement of the GRS-RW were very small is due likely to that the embankment was carefully constructed to achieve a high degree of backfill compaction as explained before. This result was also facilitated by an increase in the stability of the backfill by geogrid-reinforcing against vertical loading and lateral external spreading.

A number of piezometers installed in the foundation ground detected nearly no pore water pressure during and after the construction. This was likely because the horizontal drainage pipes installed inside the foundation ground and the pumping shafts, which were temporarily installed during construction, effectively discharged rain and underground water that seeped from the natural ground.

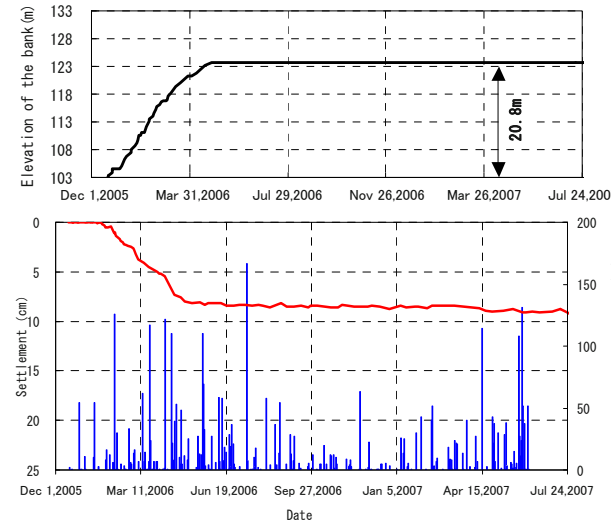

Fig. 10 Time histories of settlement of the embankment and precipitation, Valley 2

Geogrid and wall surface

Fig. 11 shows the time histories of strains that developed in the 13th geogrid layer. It may be seen that the strain increased throughout the entire embankment process and reached about 0.5% at the end of construction work. The strain was especially large at the location with a distance of 2 and 4 m from the wall face. This is because the shear stress directing outward are acting along the horizontal interface between the backfill and the reinforcement layer, which makes the tensile load in the geogrid at locations closer to the wall face larger. It is likely that this trend was facilitated by some

connection strength that can be activated at the connection between the metal framework placed at the wall face and the reinforcement layers: i.e., if the connection strength were too low, the outmost end of respective reinforcement layers became free end with zero tensile load, which would have made the tensile load in the geogrid at locations close to the wall face small, resulting in wall deformations larger than those actually observed. Despite the above, the largest tensile strain was as small as about 0.5%, which is much lower than the strain at tensile rupture, equal to 4.0%. The fact that the strains measured on January 26, 2007 and those measured a certain period after the completion are similar to those monitored at the time of completion shows nearly no creep deformation of the geogrid after the wall completion. It is considered that the creep failure of the geogrid layers is not likely during service.

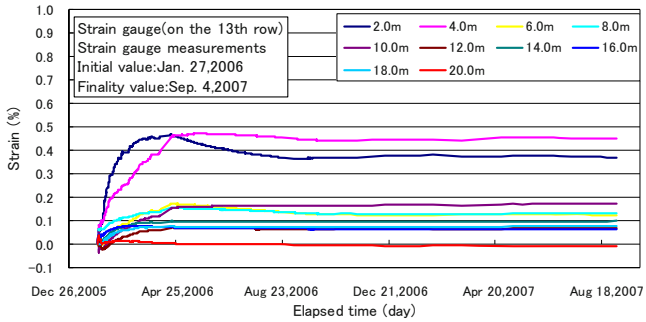

Fig. 11 Time histories of tensile strain of geogrids

Fig. 12 shows the time histories of the displacements of the wall face at the 13th soil layer.At the time of completion, the settlement (W2-H) became about 7 cm. The outward displacement (W2-Y) became about 5 cm, which is much smaller than the allowable limit, equal to 23.4 cm (i.e., 3% of the height at the said level from the wall bottom). The lateral displacement (W2-X) along the wall face was kept nearly zero throughout this observation. Nearly no displacements after the wall completion indicate that the GRS-RW is very stable.

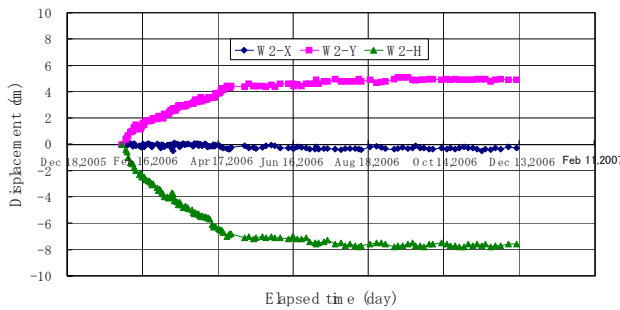

Fig. 12 Displacements at the wall face

CONCLUSIONS

In order to preserve precious plant species and the environment in and near the airport site, the area of landform modification was made minimum by constructing large-scale and two tall geogrid-reinforced soil retaining walls (GRS-RWs). The constructed GRS-RWs are largest among those constructed in Japan.

Careful investigation, design, and construction management enabled very stable GRS-RWs exhibiting nearly zero residual deformation after completion to be constructed. In particular, a high degree of compaction of the backfill achieved by compaction in a small lift and other relevant measures was an important factor.

ACKNOWLEDGMENTS

We thank the members of the Technological Committee for the Construction of the Shizuoka Airport (consisting of experts on civil engineering and pave-ment) and the Liaison Committee for Patrolling the Natural Environment of the Shizuoka Airport (consisting of experts on environment) for their precious advice on investigating bank structure. We also thank all persons involved for their advice and cooperation in surveying, designing and executing this project.

REFERENCES

Fujita Y, Sugimoto T, Koha T, Tsuda M (2007). Application of reinforced soil wall to high embankment in Mt. Fuji Shizuoka Airport (part 1). Proc. of the 42th Japan National Conference on Geotechnical Engineering. JAPAN

Takagi H, Sugimoto T, Nakamura Y, Kawahata S, Funada H, Yoshida T, Ito S, Tatta N (2007) Application of reinforced soil wall to high embankment in Mt. Fuji Shizuoka Airport (part 2). Proc. of the 42th Japan National Conference on Geotechnical Engineering. JAPAN

Fujinami T, Sugimoto T, Nakamura Y, Kawahata S, Funada H, Yoshida T, Ito M, Yoshida K (2007) Application of reinforced soil wall to high embankment in Mt. Fuji Shizuoka Airport (part 3). Proc. of the 42th Japan National Conference on Geotechnical Engineering. JAPAN

Kawaharazono M, Tobisu Y, Hirakawa D, Tatsuoka F (2006) Strength and deformation characteristics of sands and gravels for degrees of compaction larger than 90%. Proc. of the 3rd Kanto Regional Conference on Geotechnical Engineering. JAPAN

APPLICATION OF PREFABRICATED VERTICAL DRAINS TO THE CHANGI LAND RECLAMATION PROJECT, SINGAPORE

A. Arulrajah[1], M.W. Bo[2], J. Chu[3] and H. Nikraz[4]

ABSTRACT: The Changi East Reclamation Project in the Republic of Singapore involved the filling of approximately 200 million cubic of sand for the land reclamation of a total area of about 2500 hectares. Land reclamation was carried out using fill materials obtained from dredging granular material from the seabed at the borrow source. The ground improvement technique which involved combination of prefabricated vertical drain (PVD) with preloading was successfully applied in this project to improve the underlying compressible soils. The project comprises the installation of prefabricated vertical drains and the subsequent placement of surcharge to accelerate the consolidation of the underlying marine clay. In order to monitor the performance of ground improvement and to validate the performance of the prefabricated vertical drain system, several geotechnical instruments were installed to monitor the degree of consolidation at both area with PVD and area without PVD as control area. This paper provides a case study of the ground improvement works carried out with prefabricated vertical drains at the Changi East Reclamation Project and their subsequent performance assessment.

KEYWORDS: land reclamation, field instrumentation, ground improvement, prefabricated vertical drains

INTRODUCTION

From 1992 till mid 2004, the Changi East Reclamation Project in the Republic of Singapore involved the filling of approximately 200 million cubic of sand for the reclamation of a total land area of about 2500 hectares. The land reclamation works were carried out in 5 phases. Land reclamation was carried out using fill materials obtained from dredging granular material from the seabed at the borrow source. The combination of prefabricated vertical drain (PVD) with preloading ground improvement technique was successfully applied in this project to improve the underlying compressible soils. The project comprises the installation of prefabricated vertical drains and the subsequent placement of surcharge to accelerate the consolidation of the underlying marine clay.

In the entire project, a total of 142 million linear meters of vertical drains were installed making this one of the largest projects in the world in which prefabricated vertical drains were used. In order to monitor the performance of ground improvement and to validate the efficiency of the prefabricated vertical drain system several geotechnical instruments were installed to monitor the degree of consolidation at both area with PVD and area without PVD as control area.

Settlement gauges including deep settlement gauges were installed at the top of each sub layers whereas piezometers were installed at the centre of each compressible sub layer in order to monitor the settlement and pore pressure dissipation. Settlement and pore pressure were monitored with close interval in the first three months and wider interval at the later part of monitoring. Ultimate settlements were predicted using the field settlement results applying the Asaoka and hyperbolic methods.

This paper provides a case study of the ground improvement works carried out with prefabricated vertical drains at the Changi East Reclamation Project.

PREFABRICATED VERTICAL DRAINS

The prefabricated vertical drain (PVD) with preloading method was considered the most feasible one and this method was used in the project. The objective of using the vertical drains with preloading technique is to accelerate the rate of consolidation and to minimize future settlement of the treated area under the future dead and live loads. Soil improvement works is carried out in such a way that a specified degree of primary consolidation is designed to be attained within the desired time frame by improving the soil drainage system.

[1] Senior Lecturer, Swinburne University of Technology, Melbourne, AUSTRALIA. Email: aarulrajah@swin.edu.au
[2] Director (Geo-services), DST Consulting Engineers, Thunder Bay, Ontario, CANADA. Email: drmwbo@yahoo.co.uk
[3] Associate Professor, Nanyang Technological University, SINGAPORE. Email: CJCHU@ntu.edu.sg
[4] Associate Professor, Curtin University of Technology, Perth, AUSTRALIA. Email: H.Nikraz@curtin.edu.au

The primary use of prefabricated vertical drains is to accelerate consolidation to greatly decrease the duration of consolidation process caused by embankment built over soft soils. This will ensure that the final construction can be completed in a reasonable time and with minimal post construction settlement. Preloading increases the effective stress and reduces the compressibility of weak ground by forcing soft soils to consolidate. By doing so, the consolidation process also improves the strength of in-situ soft soils.

GEOTECHNICAL FIELD INSTRUMENTATION

Geotechnical instrumentation is the only means available of providing continuous records of the ground behavior from the point of instruments installation. Without a proper geotechnical instrumentation method or programme, it would be difficult to monitor at any point of time the current degree of improvement of the soil. By analyzing the instrument monitoring results, it is possible to determine the degree of consolidation of the foundation soil before allowing the removal of the surcharge load and it is possible to ascertain the achievement of required effective stress and to indicate the necessity for remedial action.

In order to study the performance of compressible soils under reclaimed fill, geotechnical instruments have to be installed. Various geotechnical field instruments were installed in instrumentation clusters to enable the instruments functions to complement each other. All instruments found in the instrument clusters were also extended and protected throughout the surcharge placement operations. In coastal land reclamation projects, instruments were installed either off-shore prior to reclamation or on-land after reclamation to the vertical drain installation platform level.

Field instruments suitable for the study of consolidation behavior of underlying soils and monitoring of land reclamation works included surface settlement plates, deep settlement gauges, multi-level settlement gauges, liquid settlement gauges, pneumatic piezometers, electric piezometers, open-type piezometers, water standpipes, inclinometers, deep reference points and total earth pressure cells. A total of 7246 geotechnical instruments were installed at the Changi East Reclamation Projects. Instrument monitoring was carried out at regular intervals so that the degree of improvement could be monitored and assessed throughout the period of the soil improvement works for the project. Instruments were monitored at close intervals of up to 3 times a week during sandfilling and surcharge placement operations.

INSTRUMENTATION ASSESSMENT

Assessment of degree of consolidation could be carried out by means of field instrument monitoring at regular time intervals. Degree of improvement can be monitored and assessed throughout the period. Two simple instruments that can assess the degree of consolidation are settlement plates and piezometers. Details on assessment of degree of consolidation have been discussed by Bo et al. (1997) and Arulrajah et al. (2005, 2004a, 2004b).

Degree of consolidation for settlement gauges can be computed based on the field settlement. Degree of consolidation is defined as percentage of magnitude of settlement that occurred at time *t* upon ultimate primary consolidation settlement as indicated in Eq. 1. From measured field settlement and predicted ultimate settlement, degree of consolidation can be estimated. Ultimate settlement can be predicted for marine clays treated with vertical drains and preload by the Asaoka (Asaoka 1978) or Hyperbolic (Tan 1995) methods.

$$U_s\,(\%) = S_t / S_\alpha \qquad (1)$$

where S_t = field settlement at any time *t*; S_α = ultimate settlement; and U_s (%) = average degree of consolidation.

Piezometers are utilized to measure the pore pressure in the soil. If regular monitoring is carried out to measure the piezometric head together with static water level, dissipation of excess pore pressure can be detected and thus degree of consolidation can be assessed. Average residual excess pore pressure is defined as ratio of excess pore pressure at time *t* upon initial excess pore pressure. Therefore degree of consolidation for a soil element, U_u can be defined as shown in Eq. 2.

$$U_u\,(\%) = 1 - (U_t / U_i) \qquad (2)$$

where U_u (%) = degree of consolidation for a soil element; U_t = the excess pore pressure at time *t*; and U_i = initial excess pore pressure which is equal to the additional load.

CASE STUDY AREA

Singapore marine clay at Changi is a quartenary deposit that lies within valleys cut in the Old Alluvium. The Case Study Area comprises of two distinct layers of marine clay which are the “Upper Marine Clay” layer and the “Lower Marine Clay” layer. The “Intermediate Stiff Clay” layer separates these two distinct marine clay layers.

The upper marine clay is soft with undrained shear strength values ranging from 10 to 30 kPa. Marine or

organic matter is found in the upper marine clay. The intermediate layer is a silty clay layer. The lower marine clay is lightly overconsolidated with an undrained shear strength varying from 30 to 50 kPa. It is not homogeneous but occasionally interbeded with sandy clay, peaty clay and sand layers. Below the lower marine clay is a stiff sandy clay layer locally known as Old Alluvium. The characteristics of the marine clay found at Changi, Singapore has been discussed previously by Bo et al. (1997, 1998) and Arulrajah et al (2004a, 2004b).

The Case Study Area consists of a Vertical Drain Area at which vertical drains were installed at 1.5 meters spacing to depths of 35 meters, as well as an adjacent Control Area where no vertical drains were installed. This enabled comparisons to be made between an area treated with vertical drains with an untreated area. Both the areas were treated with the same height of surcharge preload. Instruments were installed and monitored at both the Vertical Drain Area and the Control Area. The instruments in the Control Area were installed prior to reclamation in off-shore instrument platforms. These instruments were protected as the reclamation filling works commenced in the area. Fig. 1 shows the geological profile of the Case Study Area and the typical details of on-land and adjacent off-shore field instrumentation clusters.

Instruments in the Vertical Drain Area were installed on-land at the vertical drain platform level of +4 m CD just before or soon after vertical drain installation at 1.5 meter square spacing. Surcharge was subsequently placed to +10 m CD. The analysis of the instrumentation results was carried out for both the Vertical Drain Area and Control Area after a monitoring period of about 26 months which equates to a surcharging period of 20 months.

Fig. 2 shows the construction sequence of works at the Case Study Area. The profile of the field instrumentation elevations at the Case Study Area has been recently described by Arulrajah et al. (2005, 2004a, 2004b).

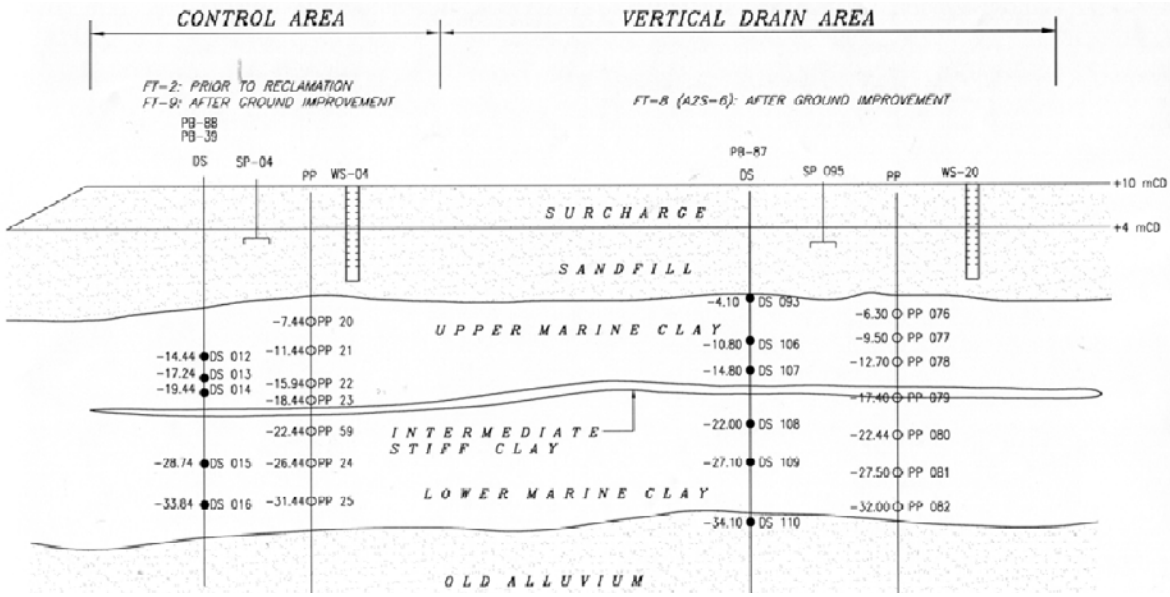

Fig. 1 Geological profile and details of field instrumentation at Case Study Area

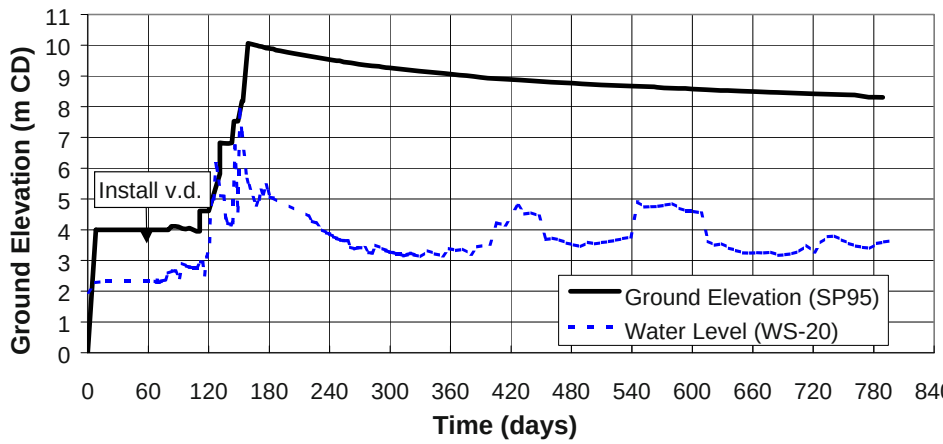

Fig. 2 Construction sequence of works at Case Study Area

Settlement Measurements

Fig. 3 indicates the magnitudes of settlements in the Vertical Drain Area. The deep settlement gauges that were installed in the different sub-layers indicate decreasing settlement with depth as would be expected. As expected, the Vertical Drain Area indicated much greater settlement magnitudes as compared to the Control Area. This indicates that the vertical drains are functioning. The settlement plates (SP-95) and the deep settlement gauge (DS-93) that were installed at the original seabed level gave similar reading for the magnitude and rate of settlement.

Fig. 4 compares the settlement plate results between the Vertical Drain Area and Control Area. The vast improvement of the Vertical Drain Area as compared to the Control Area is clearly evident in the figure. Fig. 5 compares the field settlement isochrones between the Vertical Drain Area and Control Area for various surcharge durations. As expected the magnitude and rate of settlement of the Vertical Drain Area is much higher than that of the Control Area.

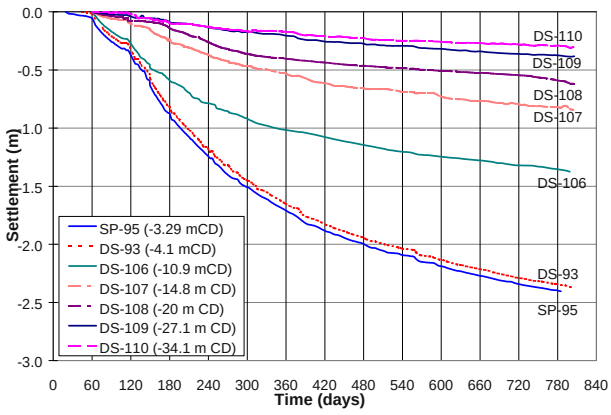

Fig. 3 Field settlement results at Vertical Drain Area

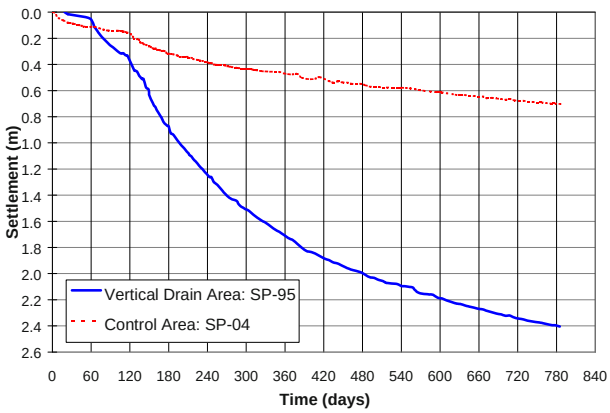

Fig. 4 Comparison of field settlement at Case Study Area

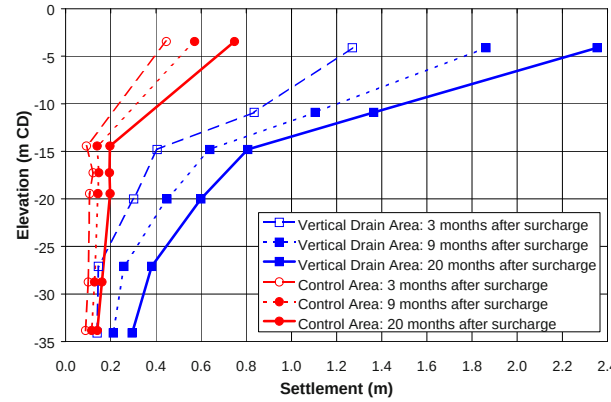

Fig. 5 Comparison of field settlement isochrones

Pore Pressure Measurements

The piezometer monitoring data in the Vertical Drain Area after correction of the piezometer tip settlement is shown in Fig. 6. Fig. 7 indicates the comparison of excess pore pressure isochrones between the Vertical Drain Area and Control Area at various periods after surcharge placement.

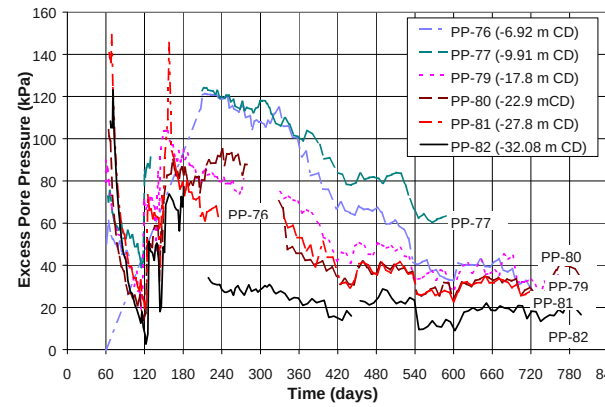

Fig. 6 Excess pore pressures at Vertical Drain Area

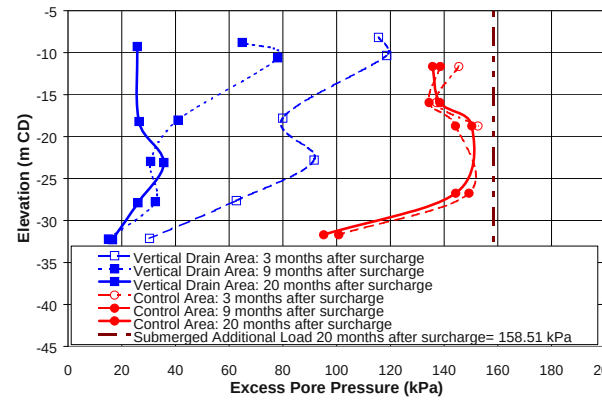

Fig. 7 Comparison of piezometer excess pore pressure isochrones

The rapid dissipation of excess pore water pressure with time is clearly evident in the Vertical Drain Area. The slow rate of dissipation of excess pore water pressure with time is also noted at the Control Area. It is evident that the degree of consolidation of the Vertical Drain Area is far greater than that of the Control Area.

Degree of Consolidation

The degree of consolidation was assessed from the settlement plates by the Asaoka (Asaoka 1978) and Hyperbolic (Sridharan & Sreepada 1981; Tan 1995) methods. The method of application of these methods for land reclamation projects on marine clay have been discussed by Arulrajah et al. (2004b) and Bo et al. (1997).

Fig. 8 compares the degree of consolidation as obtained from the settlement gauge and piezometer results. Table 1 compares the degree of consolidation as obtained by the observational methods at the Vertical Drain Area. It is seen that the methods give consistent results. The degree of consolidation of the piezometers was obtained from the isochrones of the piezometers. The degree of consolidation estimated from the pore pressure measurements is found to tie in well with that of the settlement gauges at the Vertical Drain Area which is about 80%. The degree of consolidation estimated from the pore pressure measurements in the Control Area is less than 20%.

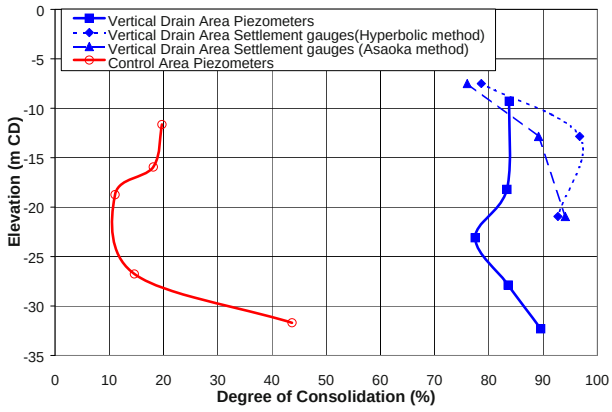

Fig. 8 Comparison of degree of consolidation between Vertical Drain Area and Control Area

Table 1 Degree of consolidation comparisons at Vertical Drain Area

	Asaoka	Hyperbolic	Piezometer
Ultimate Settlement (m)	3.000	3.005	-
Settlement to Date(m)	2.404	2.404	-
U (%)	80.1	80.0	80.0

CONCLUSION

The ultimate settlement predicted from the settlement gauges by application of the Hyperbolic and Asaoka prediction methods was found to be about 3 meters. The assessment of degree of consolidation is found to be in good agreement for the Asaoka, Hyperbolic and piezometer methods. The settlement gauges and piezometers indicate that the degree of consolidation of the Vertical Drain Area had attained a degree of consolidation of about 80%. The piezometers indicate that the Control Area had only attained a degree of consolidation of about 20%. The instrumentation results in the Vertical Drain Area indicates much higher degree of improvements as compared to the Control Area which indicates that the vertical drains are performing to improve the soil drainage system. In addition to the field instrumentation case study, this paper also discusses the methods of land reclamation and field instrumentation.

REFERENCES

Arulrajah A (2005) Field Measurements and Back-Analysis of Marine Clay Geotechnical Characteristics under Reclamation Fills. PhD thesis, Curtin University of Technology, Perth, Australia

Arulrajah A, Nikraz H, Bo MW (2004a) Observational Methods of Assessing Improvement of Marine Clay. Ground Improvement 8(4): 151-169

Arulrajah A, Nikraz H, Bo MW (2004b) Factors Affecting Field Instrumentation Assessment of Marine Clay Treated With Prefabricated Vertical Drains. Geotextiles and Geomembranes 22(5): 415-437

Asaoka A (1978) Observational Procedure of Settlement Prediction. Soil and Foundations 18(4): 87-101

Bo MW, Chu J, Low BK, Choa V (2003) Soil Improvement–Prefabricated Vertical Drain Techniques. Thomson Learning. Singapore

Bo MW, Arulrajah A, Choa V (1997) Assessment of degree of consolidation in soil improvement project. Proceedings of the International Conference on Ground Improvement Techniques. Macau: 71-80

Bo MW, Arulrajah A, Choa V (1998) Instrumentation and monitoring of soil improvement work in Land reclamation projects. 8th International IAEU Congress, Balkema, Rotterdam: 1333-1392

Sridharan A, Sreepada Rao A (1981) Rectangular Hyperbola Fitting Method for One-dimensional Consolidation. Geotechnical Testing Journal 4(4): 161-168

Tan SA (1995) Validation of Hyperbolic Method for Settlement in Clays with Vertical Drains. Soil and Foundations 35(1): 101-113

Proceedings of the 4th Asian Regional Conference on Geosynthetics
June 17 - 20, 2008 Shanghai, China

STUDY OF BEHAVIOUR OF BALLAST USING GEOSYNTHETICS

Satyendra Mittal [1], Ashok Kumar Sharma[2], B.V. Lokesh [3] and Ajay Dwivedi [4]

ABSTRACT: Well-built and maintained highways / railway tracks play major role in the development of any nation. The ballast and its engineering behavior have a key role to govern the stability and the performance of railway tracks. In present study, the effect of geosynthetic reinforcement on the (cumulative) plastic settlement, of point loaded strip footing on a thick layer of granular aggregate overlying different compressible bases has been studied under static loads and cyclic load tests. The prospective use of different types of geosynthetics to improve the performance of fresh and recycled ballast has also been investigated. The results show that inclusion of geosynthetics increases the coefficient of elastic uniform compression by around 38% and significantly increases the ultimate load carrying capacity.

KEYWORDS: ballast, geosynthetics, cyclic load, highways, railway tracks, ground improvement

INTRODUCTION

Many factors influence the safe and efficient operation of railroads throughout the world. The most important tasks of the railroad engineer are the design, installation, and maintenance of a highly stable track network that will reliably carry goods and passengers with safety and speed. The necessity of keeping a competitive edge against other means of transportation has increased the pressure on the railway industry to improve its efficiency and decrease maintenance and infrastructure costs. In case of ballasted railway tracks, the cost of substructure maintenance can be significantly reduced if a better understanding of the physical and mechanical characteristics of the rail sub-structure, in particular the ballast layer is obtained. The use of geosynthetics in construction can improve the functions of railway tracks (Indraratna et al. 1998; Raymond,1986, 1993).

The present paper deals with the static and cyclic load tests conducted on strip footing resting on ballast footing under dry and wet conditions. The ballast was overlying different compressible bases in tests. All the tests were repeated by using geosynthetics in between compressible bases and ballast. It has been observed that the geosynthetics improves the ultimate load carrying capacity by 17 % and 128 % in dry and wet conditions respectively. Similarly, the coefficient of elastic uniform compression increased by 38% and 36% in dry and wet conditions respectively by use of geosynthetics.

EXPERIMENTAL INVESTIGATIONS

Test set up

For this study, a footing of size 0.2 m×0.2 m was used and a large rigid steel tank of size 1.2 m×1.2 m and 0.45 m depth was used to investigate the ballast deformation and degradation under different conditions. The test tank was fully lubricated on all side to arrest friction. Fig . 1 shows a view of the tank used for study. The Fig. 2 shows the view of strip footing and loading arrangement adopted for study. Two dial gauges and a proving ring of capacity 5 tons was used to record the settlement and applying the load on footing respectively. A reaction frame made of steel was used to apply reaction on the test footing. Both dial gauges recorded the settlement and average of both values was used for plotting load V/s settlement curve. A hydraulic jack of 12-ton capacity was used to impart load on footing.

AGGREGATE USED FOR STUDY

Ballast was used for the experimental investigations. Ballast is a free draining granular material used as a load bearing material for railway tracks. It is composed of medium to coarse gravel sized aggregates (10-60 mm) with a small percentage of cobble – size particles. Ballast tracks are still the most common rail transportation structure due to its relatively low cost of construction

[1] Associate Professor, Department of Civil Engineering, I.I.T Roorkee-247667, INDIA. Email: smittfce@iitr.ernet.in
[2] Scientist, , Geotechnical Engg Division , CBRI Roorkee-247667, INDIA. Email:aksharma2002in@yahoo.co.in
[3] Post graduate student, Department of Civil Engg, I.I.T Roorkee, INDIA
[4] Technical Assistant, Geotechnical Engineering Division, C.B.R.I, Roorkee-247667, INDIA. Email:ajaydwivedi@gmail.com

and less possibility of maintenance. A thick layer of sand bed of height 0.25 m was poured into the tank. Over it another thick layer of gravel was poured. The gravel layer was around 0.15m height.

Fig. 1 View of the steel tank used for study

Fig. 2 View of dial gauges, proving ring and hydraulic jack setup over the strip footing

TESTS CONDUCTED

Static Loading Test—1 (Sand bed + ballast in dry condition)

The set up was made as stated above and load was applied incrementally. The first load of 6.25 t/m^2 is applied and the corresponding deflections were noted down with the help of dial gauges provided over the footing. The second load of 12.25 t/m^2 was applied over the footing and deflections were noted, the process was repeated and each load was applied at an interval of 6.25 t/m^2. This was done until the failure of aggregate occurred. The final readings were noted and recorded. The results in the form of loading intensity V/s settlement are shown in Fig. 3.

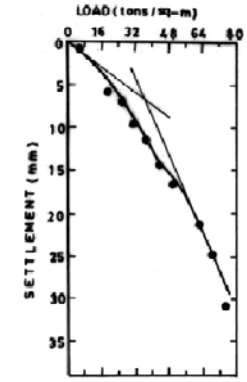

Fig. 3 Load V/s settlement curve for static load test – for sand bed +ballast in dry condition

Static Loading Test—2 (Sand bed + ballast + geo-synthetics in dry condition)

In this test set up (Fig. 4) the only difference was that a geosynthetic was placed in between the aggregate and the sand bed. After arranging the geosynthetic the load was applied incrementally and readings were recorded in the tabular form. Load was applied until failure occurred. The results are plotted as shown in Fig. 5.

Fig. 4 Geo-synthetic placed beneath the ballast and over the sand bed

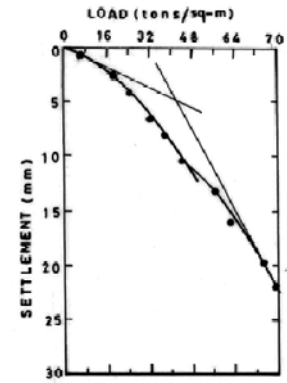

Fig. 5 Load V/s settlement curve for static load test – 2 for sand bed + ballast + geosynthetic in dry condition

Static Loading Test—3 (Sand bed + Ballast in Saturated condition)

In this test, the sand bed and ballast were used and they were kept in a saturated condition (Fig. 6) by allowing some water into the tank. The loading was applied in the saturated condition and values were recorded as in previous tests. The results are shown in Fig. 7.

Fig. 6 Ballast in the saturated condition

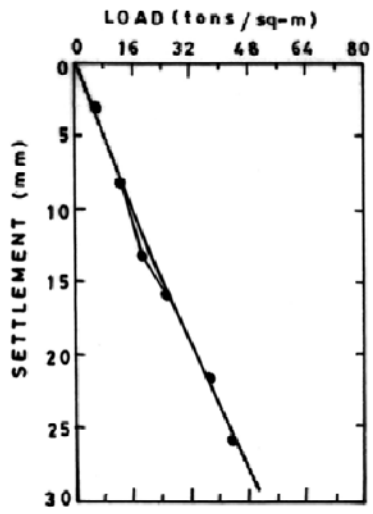

Fig. 7 Load V/s settlement curve for static load test – 3 for sand bed + ballast + geosynthetics in wet condition

Static Loading Test—4 (Sand bed + Ballast + geo-synthetics in saturated condition)

In this test, the sand bed, ballast and geosynthetics were used and they were kept in a submerged condition. The loading was applied in the saturated condition and values were recorded and plotted as shown in Fig. 8.

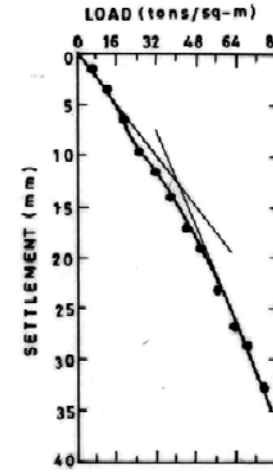

Fig. 8 Load V/s settlement curve for Static load test – 4 for sand bed + ballast + geosnthetics in wet condition

Cyclic Loading Test—1 (Sand bed + ballast in dry condition)

In the cyclic load test, load was applied in a cyclic manner. A load of 6.25t/m^2 was applied, dial gauge readings were noted down and load was decreased to zero and again load increased to 12.5t/m^2 was applied. This load was also withdrawn to zero and thus the entire test was done in the above manner till the test specimen failed. The test results are shown in Fig. 9.

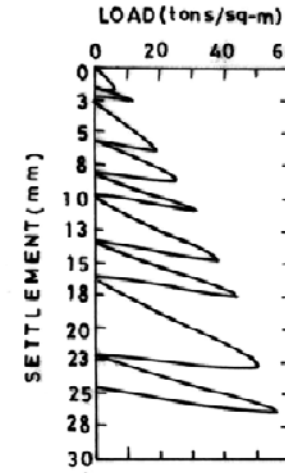

Fig. 9 Load V/s settlement curve for cyclic load test – 1 for sand bed+ ballast in dry condition

Cyclic Loading Test—2 (Sand bed + ballast + geo-synthetics in dry condition)

In this test, the geosynthetic was placed in between the aggregate and the sand bed. After arranging the geosynthetic in between the sand bed and aggregate, the footing was placed at the centre and hydraulic jack was

placed over it and a proving ring was placed over the hydraulic jack. The process of giving loading and removing was continued until the test specimen failed. The test results are shown in Fig. 10.

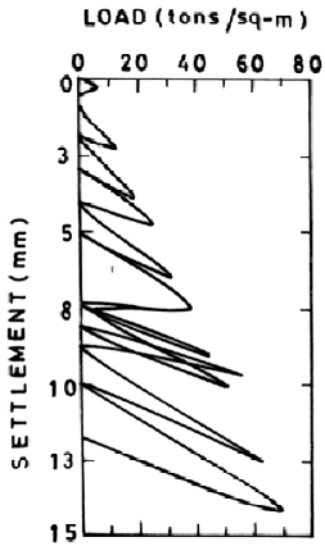

Fig. 10 Load V/s settlement curve for Cyclic load test – 2 for sand bed + ballast+ geosynthetic in dry condition

Cyclic Loading Test—3 (Sand bed + Ballast in Saturated condition)

In this test, the sand bed and ballast were kept in a submerged condition. Remaining all other things were same as in the previous tests. The test results are shown in Fig. 11.

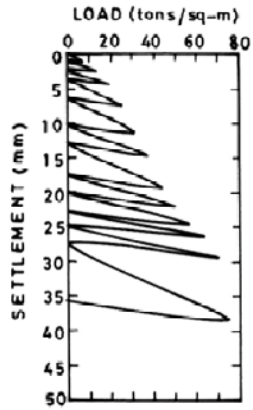

Fig. 11 Load V/s settlement Curve for cyclic load test – 3 for sand bed + ballast in wet condition

Cyclic Loading Test—4 (Sand bed + Ballast + geo-synthetics in Saturated condition)

In this test the ballast was placed over the sand bed, and geosynthetics were placed in between the ballast and the sand bed. The whole set up was kept in a submerged condition. The cyclic load was applied as in previous test. The test results are shown in Fig. 12.

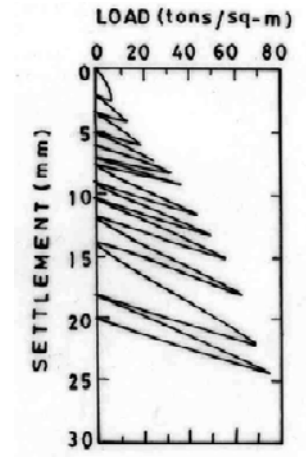

Fig.12 Load V/s settlement curve for cyclic load test – 4 for sand bed + ballast + geosynthetic in wet condition

COEFFICIENT OF ELASTIC UNIFORM COMPRESSION (C_U)

Load V/s elastic rebound plots have also been drawn using the values of cyclic loading tests. The typical plots out of various plots of cyclic load tests conducted in this study are illustrated vide Figs. 13—16 obtained from cyclic test results (Figs. 9—12). From these plots, coefficient of elastic uniform compression have been determined by taking the slope of the best fit line drawn from the values obtained for load V/s elastic rebound.

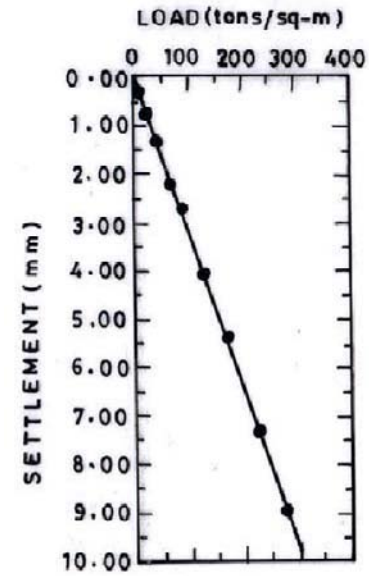

Fig. 13 Load V/s Elastic Rebound for cyclic load test – 1 for sand bed + ballast in dry condition

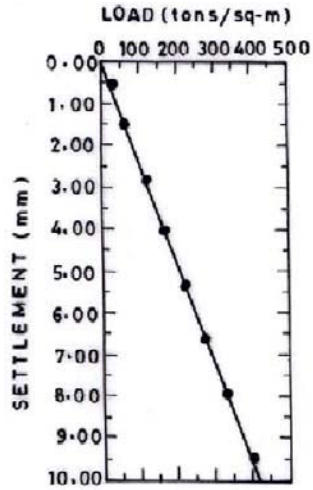

Fig. 14 Load V/s Elastic Rebound for cyclic load test – 2 for Sand bed + ballast + geosynthetics in dry condition

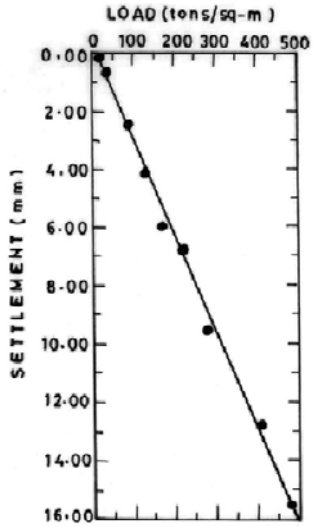

Fig. 15 Load V/s Elastic Rebound or cyclic load test –3 for sand bed + ballast in wet condition

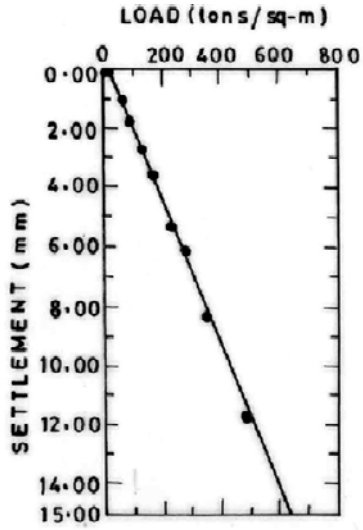

Fig. 16 Load V/s Elastic Rebound for cyclic load test – 4 for sand bed + ballast + geosynthetic in wet condition

RESULTS AND DISCUSSIONS

The results are summarized as below (Table 1). The static test results illustrated vide Figs 3, 5, 7 and 8 exhibit two different curves. The first curve is with higher rate of strain followed by the second curve with reduced rate of strain. This might be due to initial higher voids ratio of stone ballast. In static load test the tests in dry conditions indicate that nearly 17% of load carrying capacity increases by using the geosynthetics. While in the case of wet condition the load carrying capacity increased nearly by 128%. In Cyclic load test in dry condition, it was observed that nearly 38% of Coefficient of elastic uniform compression increases by using the geosynthetics, while in the case of wet condition this coefficient increased nearly by 36%.

Table 1 Summary of Test Result

Static Test, q_u (t/m^2)		Cyclic Test, C_u (t/m^3)		Reinforcement
Dry	Wet	Dry	Wet	
36	18	31034.48	30500	Without Goesynthetics
42	41	42500	39285.71	With Goesynthetics

Where q_u = Ultimate load carrying capacity and C_u = Coeff of Elastic Uniform compression (for plate size 200 mm×200 mm)

CONCLUSIONS

From this study, following conclusions are drawn:

1. By using the geosynthetics the load carrying capacity increases significantly.
2. The Coefficient of elastic uniform compression increases when a geosynthetic layer is laid in between the ballast and sand bed.
3. By using geosynthetics in rail tracks the flexibility of the ballast may increase and thereafter the performance of railway track may also improve.
4. The study shows that geosynthetics can help maintain the track integrity, enhance safety, reduce maintenance cost and improve operating revenues.

ACKNOWLEDGEMENT

The authors express their thanks for laboratory staff of IIT Roorkee and CBRI Roorkee specially Mr. AK

Mishra for extending their help in laboratory and computational works.

REFERENCES

Indraratna B, Ionescu D, Christie D (1998) Shear behaviour of railway ballast based on large scale triaxial tests. Journal of geotechnical and geoenvironmental Engineering : 439-439

Lokesh BV (2005) Study of Behaviour of Ballast using Geosynthetics, M. Tech project report, Dept. of Civil Eng., IIT Roorkee

Raymond GP (1986) Performance assessment of a railway turnout geotextile, Canadian Geotechnical Journal 23(4): 472- 480

Raymond GP (1993) Geo-textilefor railroad branch line upgrading. Proceedings on Geosynthetics Case histories, ISSMFE, Technical Committee 9: 122-123

Proceedings of the 4th Asian Regional Conference on Geosynthetics
June 17 - 20, 2008 Shanghai, China

STUDY ON THE MECHANISM OF EMBANKMENT REINFORCED WITH GEOTEXTILE BY FINITE ELEMENT METHOD

J.L. Liu[1], J.Q. Liu [2] and L.W. Chen[3]

ABSTRACT: The mechanism of road embankment reinforced with geotextile is studied with nonlinear finite element method. By comparative computing of the unreinforced road embankment with reinforced one, it is can be found that the lateral displacement of embankment decreased, the stability of embankment enhanced, the plastic zone connecting with embankment and foundation weakened, the value of plastic strain diminished and the area of plastic zone reduced when geotextile used in soft soil foundation, which indicated that the road embankment on soft soil foundation can be reinforced with geotextile effectively. In order to reinforce the embankment successfully, it is advised that the geotextile should be set on high-stress zone of foundation.

KEYWORDS: geotextile, embankment, lateral displacement, vertical settlement, stability analysis

INTRODUCTION

With the characters of reliable quality, convenient construction, high work efficiency, low cost and low degree of disturbance, geotextile had been used in reinforcement of soft soil embankment widely (Bergado 1994; Hinchberger and Rowe 2003; Xu Shuping and Liu Zude 2003; Yang GuoLin 2002).

Although geotextile has acted an important role in reinforcement of soft soils for years, the mechanism of reinforcement and the method of computation still need to be investigated and studied further (Bergado et al. 2002; Zhao Weibing et al. 1998). For many cases, the traditional limiting equilibrium method is usually used in practice (Bergado et al. 1994; Palmeira et al. 1998; Rowe and Soderman 1985). While the compatible deformation between geotextile and soil is not able to be reflected rightly by such a method. Basically, the distribution of pressure, settlement, stress field and strain field of the embankment changed because of reinforcement of geotextile, which can hardly be expressed by limiting equilibrium method reasonably. Furthermore, stability factor of the embankment obtained by limiting equilibrium method is usually too low (GB50290-98 Technical standard of China).

With the development of computer technique and finite element software, finite element method (FEM) has been used in analyzing stability of reinforced embankment gradually (Bergado et al. 2002; Hinchberger and Rowe 2003; Rowe and Mylleville 1990). Comparing with limiting equilibrium method, with FEM it is possible to reasonably investigate the compatible state of deformation between geotextile and soil, and can reflect the influence of geotextile on stress field or strain field effectively too. Then, to certain extent, the mechanism of embankment reinforced with geotextile can be effectively studied with FEM.

Based on the generalized formulation of two dimensional Biot's consolidation theory, the effect of geotextile used in soft soil foundation is studied by nonlinear FEM in this paper. The vertical settlement, lateral displacement and distribution of excess pore pressure of reinforced embankment are investigated. By comparative studies, the mechanism of embankment reinforced with geotextile is analyzed.

THE FEM MODEL OF REINFORCED EMBANKMENT

A typical profile of embankment with 18 m width, 4 m height and slope ratio of 1:1.5 is to be studied with nonlinear FEM, which basing on two dimensional Biot's consolidation theory. The depth of soft soil foundation is 8 m. The profile of the embankment is showed in Fig. 1.

According to the result of exploration, the soft soil foundation is divided into 3 soil layers along depth. The soil properties of each layer are shown in Table 1.

[1] Ph.D, Instructor, Department of Civil Engineering, Hefei University, CHINA. Email:alnile@163.com
[2] Graduate, Anhui Institute of Optics and Fine Mechanics, the Chinese Academy of Science, CHINA. Email:ljq1009p @163.com
[3] Ph.D, Instructor, School of Resource and Environmental Engineering, Hefei University of Technology, CHINA. Email: luwangchen8888@163. com

Geotextile is paved in sand bed, which located at the bottom of embankment. The thickness of sand bed is 0.3 m. The tensile strength of geotextile is *E*A=6500 kN/m. The interaction between geotextile and soil can be simulated with contact element. Fig. 2 showed the finite element mesh of embankment without geotextile, which divided by 15 nodes triangular element.

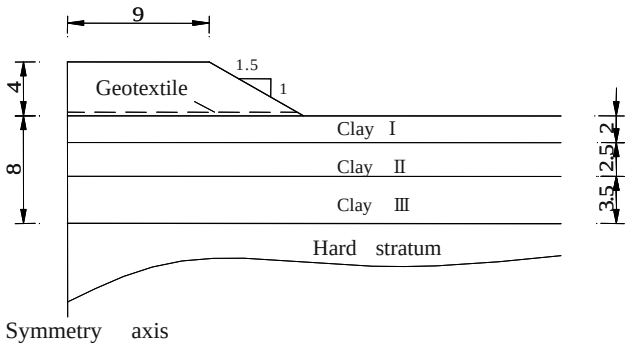

Fig. 1 The profile of the embankment (unit: m)

Table 1 The soil properties of each layer of foundation

Soil layer	Dry weight /kN.m^{-3}	Wet weight /kN.m^{-3}	k m/d	c' /kPa	ϕ' /^{0}	v	E /kPa
Embankment	16.0	20.0	1.0	4.0	24.0	0.30	2500
Sand-bed	17.0	18.0	1.0	1.0	22.0	0.30	1800
Clay I	16.0	19.5	3E-4	3.0	14.0	0.30	1200
Clay II	15.5	18.5	4E-3	2.0	18.0	0.33	800
Clay III	16.0	19.0	8E-4	6.0	26.0	0.25	1700

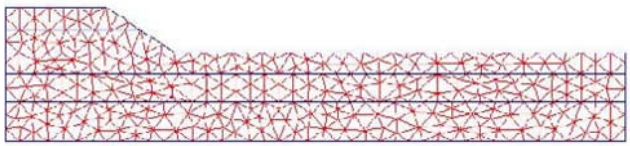

Fig. 2 The mesh of FEM model without geotextile

The embankment was constructed under the following progress: (1) Geotextile paved and the embankment filled to the height of 2 m, which cost 6 days. (2) In order to guarantee the stability of the embankment, 120 days were needed for the dissipation of excess pore pressure, which marked as the first phase of consolidation. (3) 8 days were spent to fill the embankment from the height of 2 m to 4 m. (4) At the end of construction, 550 days were needed for the dissipation of excess pore pressure, which marked as the second phase of consolidation.

Meanwhile, the stability of embankment at different construction stages can be calculated with shear strength reduction FEM. In this method the FOS of slope is defined as the shear strength reduction factor F_{trial} by which the origin shear strength parameters must be divided in order to bring the slope to the verge of failure (Cai and Ugai 2003; Duncan 1996, Dawson et al. 1999; Griffiths and Lane 1999; Zienkiewicz et al. 1975). The relationship between the factored shear strength parameters c_{r}, ϕ_{r} and the original strength parameters c, ϕ, are given by:

$$c_{\text{r}} = \frac{c}{F_{\text{trial}}},\ \phi_{\text{r}} = \arctan\left(\frac{\tan\phi}{F_{\text{trial}}}\right) \tag{1}$$

NUMERICAL RESULTS OF FEM ANALYSIS

With and without geotextile, the vertical settlement at the top surface of clay I is shown in Fig. 3. It can be obviously seen that the vertical settlements at the stage of consolidation is lager than that of corresponding construction stage, which indicated that the value of vertical settlement is controlled by dissipation of pore pressure in a certain degree.

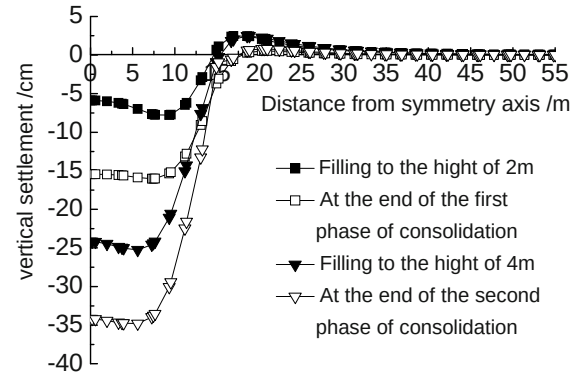

(a) unreinforced road embankment

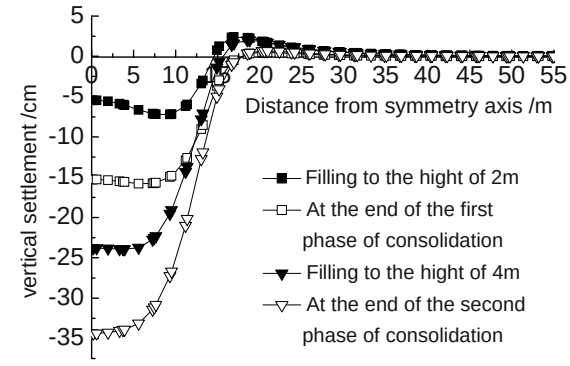

(b) reinforced road embankment

Fig. 3 The vertical displacements on the bottom surface of reinforced and unreinforced road embankment

However, according to the result showed in Fig. 3, there is not obviously different between the vertical settlement of reinforced road embankment and unreinforced one. The vertical settlement of embankment is

only homogenized by geotextile. In fact, the vertical settlement of embankment whether can be reduced by geotextile or not, has not achieved a common viewpoint among engineers. The vertical settlement of some engineering has been reduced by geotextile effectively, while there are also some other opposite examples. According to the result of XU Shao-man's research (1999), the influence of geotextile on vertical settlement of embankment is depending on the dimensi-onal effect of settlement and stress dispersion. The dimensional effect changed with different width of embankment, so it is difficult to estimate the influence of geotextile on vertical settlement of embankment simply.

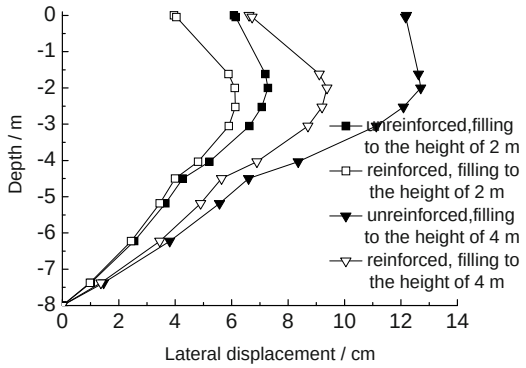

(a) at the phase of filling

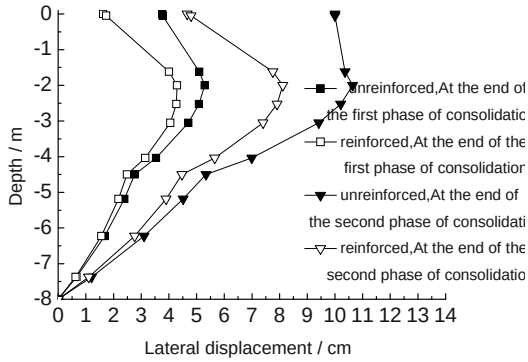

(b) at the phase of consolidation

Fig. 4 The lateral displacements on the toe vertical surface of road embankment

The lateral displacement of embankment under different construction stages are shown in Fig. 4. It can be found that, whether at filling stage or consolidation stage, the lateral displacement of reinforced embankment is smaller than that of unreinforced one obviously. That is to say, geotextile can reduce lateral displacement effectively, which has been verified by many engineering. This caused by the friction between soil and geotextile, which confined the development of lateral displacement, and homogenized the subsidiary stress of embankment too.

Fig. 5 showed the distribution of axis force along geotextile at different phase of construction. It can be found that the axis force of geotextile at the middle embankment is larger than that of the toe of the embankment. In a certain degree, the axis force of geotextile is generated by the friction between soil and geotextile, which is direct ratio with the value of normal stress. Therefore, at the zone of high normal stress, such as the place of the middle of embankment, axis force of geotextile become large. Therefore, in order to make use of geotextile successfully, it is advised that geotextile should be paved at the zone of high normal stress.

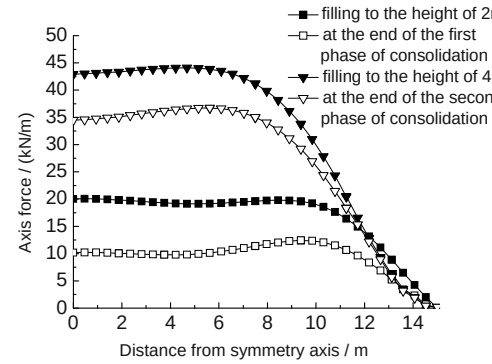

Fig. 5 Distribution of axial force along geotextile

While in the traditional limiting equilibrium method, it is assumed that the value of axis force unchanged along geotextile, which is unreasonable according to the result of FEM. Therefore, it is more rational to study the mechanism of reinforced embankment with FEM than limiting equilibrium method.

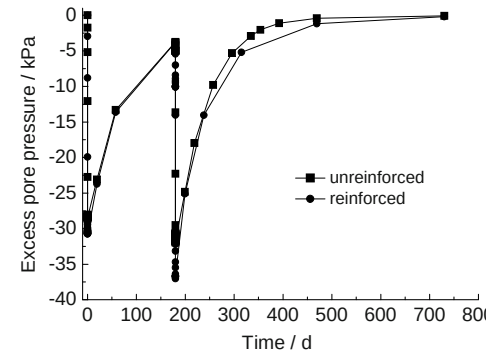

Fig. 6 The dissipation of the excess pore water pressure with time

Meanwhile, it also can be found that the axis force of geotextile at filling stage is bigger than that of consolidation stage from Fig. 5. At consolidation stage, the bearing capacity of soft foundation enhanced with dissipation of pore pressure, which inducing that the axis force of geotextile decreased. That is to say, the axis

force of geotextile assigned less with increasing of bearing capacity of foundation.

Fig. 6 showed the dissipation of excess pore water pressure with time at the place where depth -2m at the symmetric axis. It can be found that there is no influence on dissipation of pore pressure with geotextile or not. So, in order to expedite the dissipation of pore pressure, prefabricated vertical drains (PVDs) and geotextile can be combined using in soft soil embankment.

Table 2 The maximal settlements and FOS of embankment at different phase of construction

content	Filling to the height of 2 m			Filling to the height of 4 m		
	X_m/cm	Y_m/cm	FOS	X_m/cm	Y_m/ cm	FOS
unreinforced	7.29	7.77	1.452	12.70	25.24	1.081
reinforced	6.14	7.22	1.983	9.38	23.93	1.337
increment	-15.7%	-7.1%	33.4%	-26.1%	-5.2%	23.7%

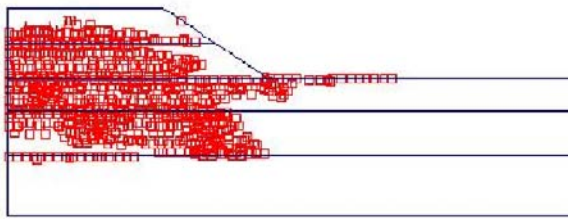

(a) unreinforced embankment

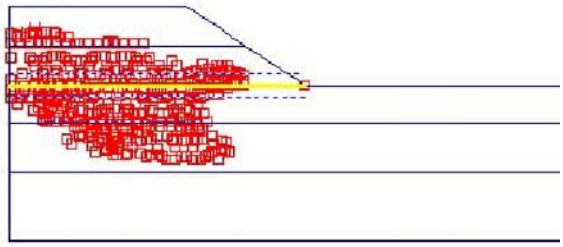

(b) reinforced embankment

Fig. 7 The plastic zone of reinforced and unreinforced embankment when filling to the height of 4 m

Table 2 showed the value of the maximal vertical settlement Y_m, the maximal lateral displacement X_m and factor of stability (FOS) of reinforced or unreinforced embankment at different phases of construction. The FOS of unreinforced embankment when filling to the height of 4 m is 1.081, which indicated that the unreinforced embankment almost arrived its critical state at the end of filling. Therefore, it is instability to filling on the soft foundation without geotextile. The FOS of embankment enhanced more than 20%, the maximal lateral displacement reduced more than 15% and the maximal vertical settlement reduced 6% when geotextile used, which verified the availability of geotextile directly.

The plastic zone of reinforced and unreinforced road embankment when filling to the height of 4 m is shown in Fig. 7. It is clear that, when geotextile used in the embankment, the plastic zone connecting with embankment and foundation weakened, the value of plastic strain diminished and the area of plastic zone reduced, thereby the FOS of embankment enhanced.

CONCLUSIONS

The effect of geotextile used in soft soil foundation is successfully investigated with nonlinear finite element method. From the study, the following conclusions and recommendations are drawn:

(1) The vertical settlement of embankment increased greatly at the phase of consolidation, which indicated that the value of vertical settlement is controlled by dissipation of pore pressure in a certain degree. There is not remarkable distinction on vertical settlement of embankment with geotextile or not in this study.

(2) The lateral displacement of embankment decreased, the FOS of embankment enhanced, the plastic zone connecting with embankment and foundation weakened, the value of plastic strain diminished and the area of plastic zone reduced when geotextile used in soft soil foundation, which verified the availability and efficiency of geotextile directly.

(3) The axis force of geotextile at the middle embankment is larger than that of the toe of the embankment. That's to say, geotextile act much effective role near the centre of the embankment. It is advised that the geotextile should be paved on zone of high normal stress.

ACKNOWLEDGEMENTS

Financial support provided by project of Hefei University (No. RC027) is gratefully acknowledged.

REFERENCES

Bergado DT et al. (1994) Performance of reinforced embankment on soft Bangkok clay with high-strength geotextile reinforcement. Geotextiles and Geomembranes, 13: 403-420

Bergado DT, Long PV, Murthy BRS (2002) A case study of geotextile-reinforced embankment on soft ground. Geotextiles and Geomembranes, 20: 343-365

Cai F, Ugai K (2003) Finite element analysis of slope stabilization. Proceedings of the twelfth Asian regional conference on soil mechanics and geo-technical

engineering, Singapore, August, 2003: 707-710

Duncan JM (1996) State of the art: limit equilibrium and finite-element analysis of slopes. Journal of Geotechnical Engineering, 122 (7): 577-596

Dawson EM, Roth WH, Drescher A (1999) Slope stability analysis by strength reduction. Geotechnique, 49 (6): 835-840

GB50290-98, Technical standard for applications of geosynthetics[S]. (in Chinese)

Griffiths DV, Lane PA (1999) Slope stability analysis by finite elements. Geotechnique, 49 (3):387-403

Hinchberger SD, Rowe RK (2003) Geosynthetic reinforced embankments on soft clay foundations: predicting reinforcement strains at failure. Geo-textiles and Geomembranes, 21:151-175

Palmeira EM, Pereira JHF, Silva D (1998) Backanalyses of geosynthetic reinforced embankments on soft soils. Geotextiles and Geomembranes, 16: 273-29

Rowe RK, Soderman KL (1985) An approximate method for estimating the stability of geotextile-reinforced embankments. Canadian Geotechnical Journal 22 (3): 392-398

Rowe RK, Mylleville BLJ (1990) Implications of adopting an allowable geosynthetic strain in estimating stability. Proceedings of the Fourth International Conference on Geotextiles, Geo-membranes and Related Products, The Hague: 131-136

Xu SM (1999) On the problems of soft cohesive ground under embankment reinforced by geotextile. Journal of Fuzhou University (Natural Science) 27(2): 76-80

Xu SP, Liu ZD (2003) Application of Biot's consolidation theory to improving soft ground by preloading method. Rock and Soil Mechanics 24(2): 307-310 (in Chinese)

Yang GL (2002) Research progress on reinforced earth. Mechanics in Engineering, 24(1): 9-17 (in Chinese)

Zienkiewicz O C, Humpheson C, Lewis RW (1975) Associated and non-associated visco-plasticity and plasticity in soil mechanics. Geotechnique, 25 (4): 671-689

Zhao WB et al. (1998) Study on calculational method of geotextile reinforced and plastic board-drained foundation. Chinese Journal of Geotechnical Engineering 20(3): 61-65 (in Chinese)

PRE-FAILURE PERFORMANCE AND FAILURE MECHANISM OF TWO TIER GEOSYNTHETIC REINFORCED SOIL WALL

C. Yoo[1] and S.B. Kim[2]

ABSTRACT: This paper presents the results of reduced-scale model tests on two-tier geosynthetic reinforced soil segmental walls with emphasis on the failure mechanism. A 1/5 scale 1-g model was created for an actual field wall, in which a tissue paper was used as the model reinforcement to represent geosynthetic reinforcement according to the similitude law. The model walls were brought to failure under their own gravitational loading during construction. The primary variable considered in the model tests was the offset distance between the upper and lower tiers. The observed offset distance of which the two tiers behave independently was found to be smaller than the computed based on the FHWA design guideline, suggesting some degree of conservatism in the FHWA design guideline. Practical implications of the finding are discussed.

KEYWORDS: geosynthetic reinforced walls, tiered wall, reduced scale model test, similitude law

INTRODUCTION

Geosynthetic-reinforced soil walls (GRS walls) have been well accepted in practice as alternatives to conventional retaining wall systems due to several benefits such as sound performance, aesthetics, cost and expediency of construction. This is especially true in Korea since its first appearance in the early 1990's. Although many geosynthetic-reinforced soil walls have been constructed and are performing well to date, there are many areas that need in-depth studies in order to better understand the mechanical behavior of GRS walls.

There are many situations where geosynthetic-reinforced soil walls are constructed in a tiered configuration for a variety of reasons such as aesthetics, stability, and construction constraints, etc. A previous numerical investigation by Yoo and Kim (2002), however, revealed that for cases with an intermediate offset distance as per the FHWA design guideline (Elias and Christopher 1997), the interaction between the upper and the lower tiers is significant causing larger wall deformation and reinforcements loads than what might be anticipated. Although in-depth studies are required to improve the current design approaches for GRS walls in tiered configuration, only a few studies are available on this subject (Leshchinsky and Han 2004; Yoo and Jung 2004; Yoo and Kim 2002; Yoo and Song 2006). In addition, most of the available studies concerns on either numerical investigation or performance under working stress condition. A study concerning the failure mechanism of GRS walls in two tier configuration is scarce. As the current design criteria addressed in the available design approaches, i.e., NCMA (Collins 1997) and FHWA (Elias and Christopher 1997) are somewhat empirical in nature, there exists an urgent need for evaluating the appropriateness of the design criteria adopted in the internal and external design calculations.

In this paper, the results of reduced-scale model tests on two tier geosynthetic-reinforced soil walls are presented, focusing on the failure mechanism. 1-g model walls were created for an actual field wall according to the similitude law so that the failure of the model walls could be brought under their own gravitational loading. The variations of pre-failure wall performance and the failure mechanism with the primary design factors, i.e., the offset distance and the reinforcement length, were then investigated. The appropriateness of the current design guideline, the assumed failure mechanism adopted in particular, was also examined.

REVIEW OF DESIGN GUIDELINES

NCMA Design Guideline

The NCMA design approach basically replaces the upper tier with an equivalent surcharge of which the magnitude is determined according to the offset distance D (Figure 1). External and internal stability calculations of the lower tier are performed assuming the lower tier

[1] Professor, Department of Civil & Engr., Sungkyunkwan University, KOREA. Email:csyoo@skku.edu
[2] Graduate Student, Department of Civil & Engr., Sungkyunkwan University, KOREA. Email:ksb9677@hanmail.net

being a single wall under the equivalent surcharge (q_{eq}). The upper wall is designed as if it were a single wall without taking into consideration of the possible interaction between the upper and the lower tiers. As for a single wall, the local stability calculations for the

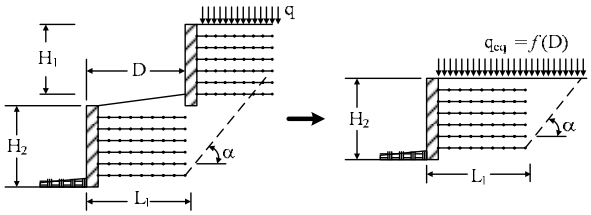

Fig. 1 Equivalent surcharge model (NCMA)

connection failure, local overturning, and internal sliding should be performed for both tiers. It should be noted that the same failure mechanism (surface) as adopted for a single wall is assumed for tiered walls. Details of the design procedure are available in Collin (1997).

FHWA Design Guideline

The FHWA design guideline requires determining the reinforcement length L that satisfies external stability requirements based on the following criteria (Fig. 2).

$D < H_2 \tan(90-\varphi)$: No interaction. Each tier is independently designed.

$D \le 1/20(H_1+H_2)$: Design for a single wall with a height of $H = H_1+H_2$.

$D > 1/20(H_1+H_2)$: For lower tier: $L_2 \ge 0.6H_2$

For upper tier: $L_1 \ge 0.7H_1$

where H_2 = lower tier height, H_1 = upper wall height, L_1 and L_2 = reinforcement length of upper and lower tier, respectively, and φ = internal friction angle of backfill.

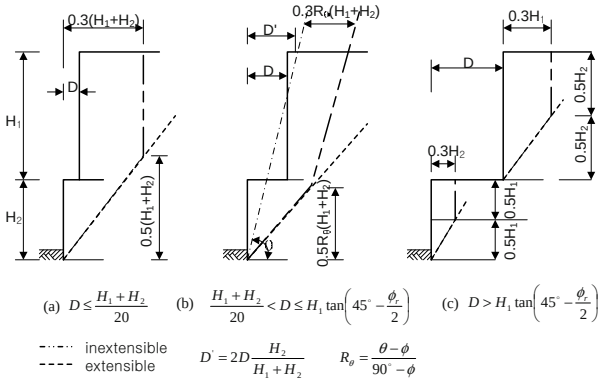

Fig. 2 Locations of maximum tension line (FHWA)

For internal stability calculations, additional vertical stresses at depths due to the upper tier are computed based on the criteria shown in Fig. 2. The location of the potential failure surface required for the pullout capacity calculation is selected based on the offset distance D (Elias & Christopher 1997). Note, however, that these criteria are geometrically derived and empirical in nature.

As shown, although the current limit-equilibrium method based design guidelines require to define the maximum tension line, i.e., failure surface, for internal stability calculations in particular, the criteria for the potential failure surface are rather geometrically derived and empirical in nature. The rational behind this criteria is limited.

EXPERIMENTAL PROGRAM

Reduced Scale Model Wall and Test Setup

A field wall reported by Yoo and Jung (2004), constructed at the Experimental site in Sungkyunkwan University, was selected as the prototype wall. The wall has an exposed height of 5 m and consisted of two tiers, i.e., a 3.4m high lower tier and a 2.2 m high upper tier. The primary reinforcement is a polyester (PET) reinforcement, having a tensile strength of 55 kN/m at strain of 12.5% with an average axial stiffness of J=500 kN/m.

Applying the similitude law to reduce the prototype wall to 1/5 scale results in a reduced model wall having the upper and lower tiers' height being 0.6 and 0.4 m, respectively with the reinforcement tensile strength of 1.4×10^{-2} kN/m. More specifically the similitude law defines the reduction ratio for the force term as Eq. 1.

$$\frac{F_m}{F_p} = \frac{M_m L_m T_m^{-2}}{M_p L_p T_p^{-2}} = \left(\frac{M_m}{M_p}\right)\left(\frac{L_m}{L_p}\right)\left(\frac{T_p}{T_m}\right)^2 \quad (1)$$

Where the subscripts *m* and *p* stand for model and prototype, respectively. *M*, *L*, and *T* indicate mass, length, and time, respectively. Based on Eq. 1, the reduction ratio for force was calculated to be 2.5×10^{-4}. yielding the tensile strength of model reinforcement of 1.4×10^{-2} kN/m.

Fig. 3 shows the cross section of the model wall, reduced from the prototype wall. As seen the reduced model wall has the upper and lower tier heights of 0.4 and 0.6 m, respectively, with an offset distance of 0.2 m. The model wall was constructed from the bottom up in a test box with no external support for the facing column, made up with a stack of wooden blocks of 3 cm (height)

× 5 cm (width) × 48 cm (length) with a pin type connection at two ends. The test box has dimensions of 1.5 m (height) × 1.8 m (length) × 0.48 m (width) and allows to test walls under conditions approaching an idealized plane strain condition. The toe of the wall was restrained horizontally. During construction each course of wooden block was placed first, followed by a 3 cm high fill placement by the raining technique. The friction between the backfill soil and sides of the test box was minimized by a combination of Plexiglas and lubricant.

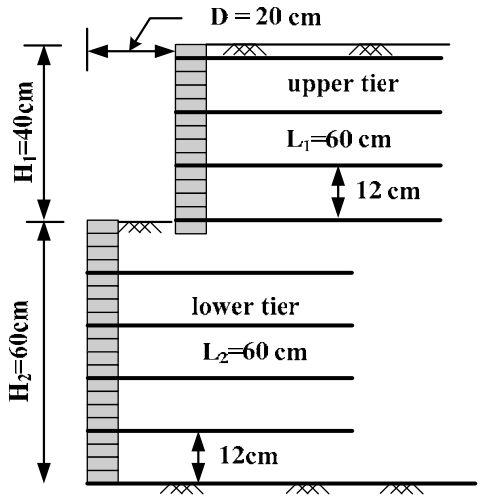

Fig.3 Model wall configuration (baseline)

Soil and Reinforcement

The model walls were constructed using fine sand (SP according to the Unified Soil Classification System) for which its grain size distribution curve is shown in Fig. 4. The effective size (D_{10}), uniformity coefficient (C_u), and coefficient of curvature (C_c) for the sand were 0.36 mm, 1.61, and 1.1, respectively. The raining technique was used to place the sand using a specially designed hopper system. To obtain consistent soil densities and placement conditions in the reinforced soil models, carefully controlled construction procedures were followed during the model preparation. These procedures included sand raining through air at controlled discharge rate and discharge height to give uniform backfill densities. The consistency of the placement density during raining was evaluated using small cans placed at different locations in the test box. The raining technique adopted in this study provided a uniform backfill relative density of approximately 70% with a unit weight of 17 kN/m^3. The shear strength parameters of the as-tested backfill were evaluated using a series of large scale direct shear tests with a shear box of 0.5 m × 0.5m in plan and 0.25 m in depth. The estimated peak internal friction angle at a density corresponding to the as-compacted state was approximately $\varphi_{ds} = 41°$. To bring the model walls to failure under their own gravitational loading it was essential to select a proper reinforcement which has the tensile strength similar to the computed model reinforcement tensile strength from the similitude law. The best choice at the time of the current study was a tissue paper having an ultimate tensile strength of 6×10^{-2} kN/m, estimated from in-air tensile tests at pre-set humidity at 20℃. As the in-air tensile strength of the tissue paper significantly varies with the relative humidity in the test environment (Rankilor 2004), efforts were made to keep the laboratory relative humidity constant for all tests.

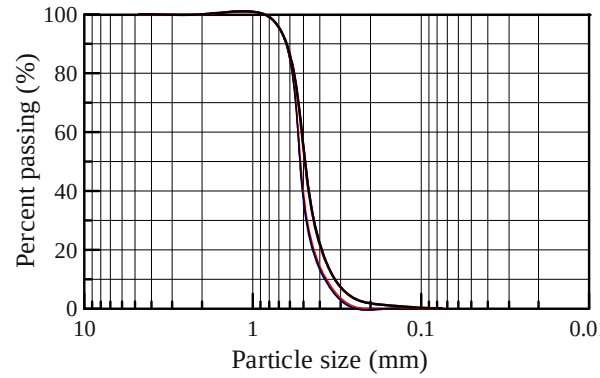

Fig. 4 Particle size distribution for sand backfill

Test Procedure

As the current study was aimed at examining the failure mechanism and relevant wall performance of the two tier wall at various boundary conditions, the main priority of the test procedure was to bring the walls to failure under their own gravitational loading without any surcharge. It should be noted that Rankilor (2004) has reported that the failure mode of a model reinforced wall under surcharge was different from that under its own gravitational loading.

The construction procedure of the test walls followed that in the field. For example, the 3 cm high wooden block was first placed at designated location, followed by raining the sand at 1.5 m discharge height. Layers of tissue paper reinforcement were then placed at designated locations. These steps were repeated until the model wall exhibited a sign of incipient failure. After placing the sand backfill a sufficient amount of time was allowed for the wall displacement to stabilize before a next backfill placement. Layers of colored sand was also placed at designated locations to monitor the failure surface. A total of five displacement-type potentiometers were placed on the lower tier facing to monitor the lateral facing displacement prior to failure. Fig. 5 shows a photograph of the model wall before failure

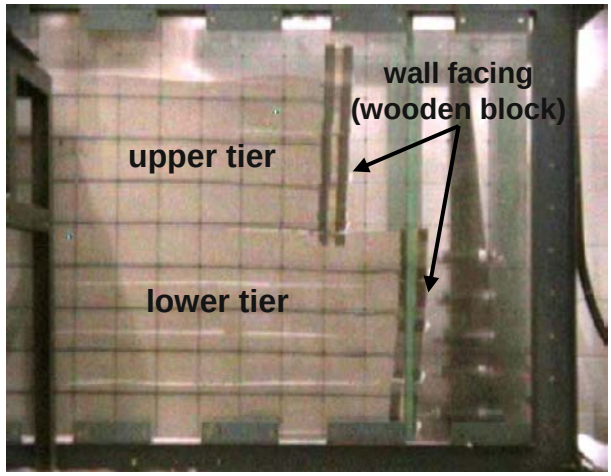

Fig. 5 Model wall before failure

Test Cases

A series of tests having different offset distances were conducted in the current study. The offset distance was selected as the key variable as the current design guideline, i.e., FHWA design guideline, categorizes three design cases in the external and internal stability calculations based on the offset distance.

Fig. 6 shows the details of the test cases. When conducting the tests all other variables were kept constant other than the offset distance. It should be noted that for pre-failure wall performance investigation the wall height was kept at $H_1 = 20\,\text{cm}$ and $H_2 = 60\,\text{cm}$, respectively for the upper and lower tiers, making the total wall height of $H = 80\,\text{cm}$ for all cases.

For investigation on the failure mechanism, however, the lower tier height was kept at $H_2 = 60$ cm while the upper tier height H_1 varied with the boundary condition, i.e., the offset distance.

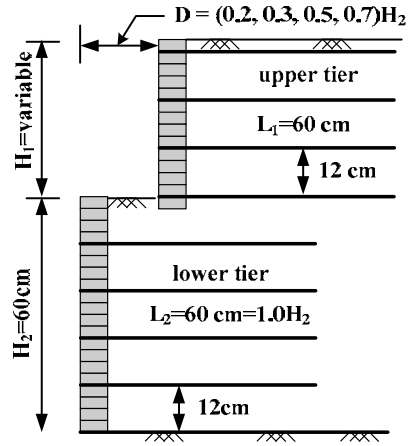

Fig. 6 Test cases (variable: offset distance)

TEST RESULTS

Pre-failure Behavior - Facing Displacement

Fig. 7 shows the variation of horizontal facing displacement profiles of the lower tier for the range of offset distances tested. Note that the results shown in this figure represent those when the wall construction was proceed to a total wall height of $H = 80\,\text{cm}$ to allow for direction comparison between the cases with different offset distances in terms of the pre-failure wall performance.

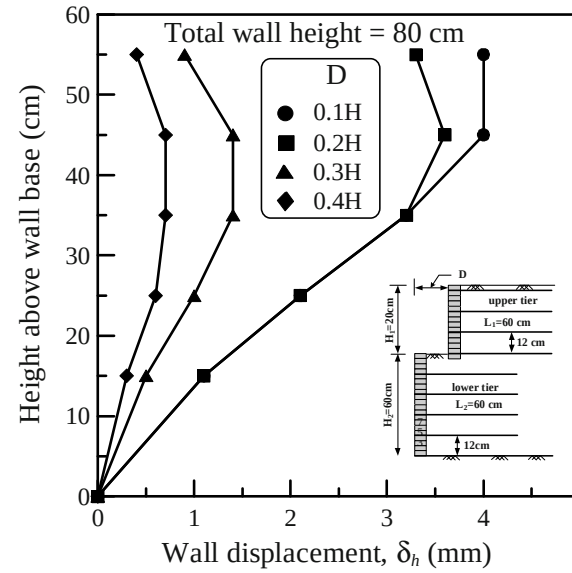

Fig. 7 Wall displacement profiles at *H*=80 cm

As shown although the magnitudes are small it is evident that an increase in the offset distance results in a decrease in the lower tier displacement δ_h. Also noticed is that the decrease in δ_h is more pronounced when *D* increases from 0.2*H* to 0.3*H* than any other changes in *D*, suggesting that a critical offset distance, in terms of pre-failure wall performance, is in the neighborhood of 0.2*H*—0.3*H*.

This trend can also be observed in Fig. 8, in which maximum wall displacements are plotted against the offset distance *D*. Note that all the cases tested *D*=(0.1—0.4) *H* in fact fall in the design category of "intermediate offset distance" as per the FHWA design guideline, for which the minimum upper and lower reinforcement lengths are prescribed as $0.7H_1$ and 0.6*H*, respectively.

The test results above, however, suggest that the pre-failure performance, i.e., wall performance at working stress condition, may vary with the offset distance for a given reinforcement layout, even for the same design category. This trend, as indicated by Yoo and Song (2006), is due primarily to the interaction between the upper and lower tiers, which is not well addressed in the

current design guideline. Further study is required in this area.

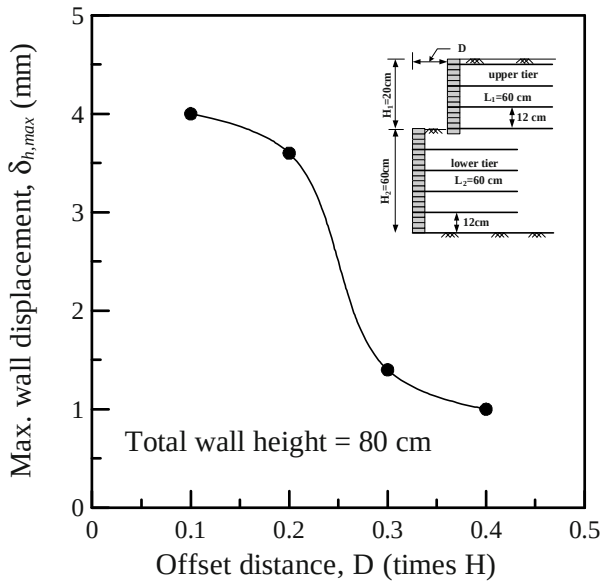

Fig. 8 Variation of maximum wall displacement with

Critical Height

For all tests conducted the critical height at which the wall collapse occurs were determined. The critical height (H_{cr}) in fact represents the degree of interaction between the upper and lower tiers for a given boundary condition.

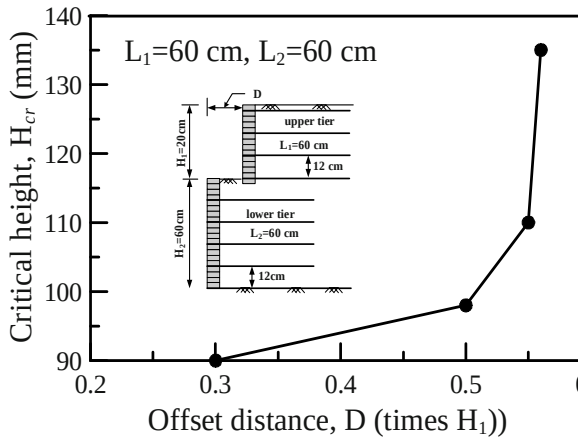

Fig. 9 Variation of H_{cr} with D

Fig. 9 shows the variations of H_{cr} with the offset distance D. In this figure the offset distance D is expressed in terms of the upper tier height (H_1) at the critical height. As would be expected, an increase in D results in an increase in the critical height. The rate of increase in H_{cr}, however, significantly increases when D reaches $0.5H_1$, after which no significant increase in H_{cr} with increasing D is evident, suggesting that the degree of interaction between the upper and lower tiers is significantly reduced when $D \approx 0.5H_1$. Note that according to the FHWA design guideline the critical offset distance beyond which the two walls are designed independently is $D \approx H_2 \tan(90-\varphi)$ in which no consideration for the upper tier height is considered. According to the FHWA design guideline, the critical offset distance would be approximately 70 cm, i.e., $D \approx 1.2H_1$ for the model wall. Although no further tests are conducted on cases with offset distances $D \geq 40\,\text{cm}$, the current design guideline appears somewhat conservative in considering the interaction.

Failure Mechanism

Fig. 10 shows photos captured at the event of failure for cases with different offset distances. Important observations are two fold. First, the failure surface tends to flatten as D increases, showing the failure surface initiates at the toe of the lower tier, then propagates into the reinforced zone of the upper tier. When D=40 cm however an isolated failure surface was developed in the upper tier with no failure surface developed in the lower tier, suggesting the two tiers acted independently. Only the upper tier failed for the case D=40 cm as the upper tier height was in fact larger than that of the lower tier. According to the criteria adopted in the FHWA design guideline the two tier are to behave independently when D=70 cm or larger, suggesting some degree of conservatism in the FHWA design guideline.

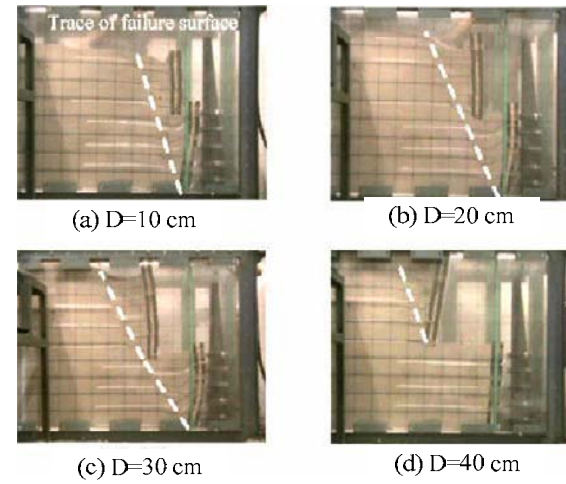

Fig.10 Observed failure patterns for different D

CONCLUSIONS

The pre-failure wall performance and the failure mechanism of two tier geosynthetic reinforced soil wall are investigated. A prototype wall was reduced based on the similitude law to create a 1-g reduced-scale model

wall. Tissue paper was used as reinforcement following the results of relevant calculation according to the similitude law. In the test the 1-g model walls were brought under their own gravitational loading. The primary variable was the offset distance of the upper and lower tiers.

The results of pre-failure wall facing displacement indicated that the facing displacement significantly decreases when $D > 0.3H$, suggesting that the critical offset distance, beyond which the interaction between the two tiers significantly reduces is, $D_{cr} = 0.3H$. Also shown is that the critical height for a given offset distance, i.e., the maximum wall height that can be constructed, becomes almost constant when $D > 0.5H_1$, suggesting that the interaction between the upper and the lower tier significantly diminishes when keeping $D \approx 0.5H_1$. Moreover, an isolated failure mechanism was observed in the upper tier with no failure surface developed in the lower tier when *D*=40 cm, suggesting the two tiers acted independently. The observed offset distance of which the two tiers behave independently is smaller than computed based on the FHWA design guideline, suggesting some degree of conservatism in the FHWA design guideline.

ACKNOWLEDGEMENTS

This work was supported by Grant No. R01-2004-000-10953-0 from the Basic Research Program of the Korea Science & Engineering Foundation. The financial support is gratefully acknowledged. A special thanks goes to my former graduate student who conducted the tests.

REFERENCES

Collin J (1997) Design Manual for Segmental Retaining Walls, 2nd Ed. NCMA, Virginia

Elias V, Christopher BR (1997) Mechanically Stabilized Earth Walls and Reinforced Soil Slopes, Design and Construction Guidelines. FHWA Demonstration Project 82, FHWA, Washington, DC, FHWA-SA-96-071

Leshchinsky D, Han J (2004) Geosynthetic Reinforced Multitiered Walls. J. Geotech. Engrg. ASCE 130(12):1255-1235

Rankilor PR (2004) The construction of self-loading micro-models of reinforced soil using ulta-weak reinforcement simultans. Proc. 3rd European Geo-syunthetics Conference. Munich, Germany: 649-654

Yoo C, Jung HS (2004) Measured behavior of a geosynthetic-reinforced segmental retaining wall in a tiered configuration. Geotextile and Geomembranes 22(5): 359-376

Yoo CS, Kim JS (2002) Behavior of Soil-Reinforced Segmental Retaining Walls in Tiered Arrangement. Journal of Korean Geotechical Society, KSGE 18(3): 61-72

Yoo C, Song AR (2006) Effect of foundation yielding on performance of two-tier geosynthetic reinforced segmental retaining walls—A numerical investigation. Geosynthetics International 20(3): 110-120

NUMERCIAL ANALYSIS OF GEOGRID AND PLASTIC DRAINAGE PLATE USED IN EXISTED RAILWAY ALTERATION PROJECT

P. Lv [1], W. Pang [1], L.J. Meng[1] and L.Q. Gao [2]

ABSTRUCT: To fit the demand of train speeding, existed railway should be widened, which causes the redistribution of the stress in the consolidated soft soil foundation that leads to unequal post-construction settlement, influences the stability of the roadbed. To eliminate above diseases, geogrid and plastic drainage plate usually be used. The paper uses FEM from aspects as layout manner, length, stiffness, interaction effect of geogrid, whether use plastic drainage plate and its span to analyze the stability of roadbed, max unequal post-construction settlement and consolidation time. The following conclusions are obtained: Geogrid apparently improves the roadbed slope stability of each stage, but has little effect on unequal post-construction settlement and consolidation; Plastic drainage plate apparently accelerates the consolidation and decreases the unequal post-construction settlement of roadbed. It has little effect on stability after consolidation; In roadbed widening project on soft soil foundation, geogrid and plastic drainage plate all have its work and should be used in combined way to perform the better engineering effect.

KEYWORDS: geogrid, plastic drainage plate, roadbed widening, FEM, unequal settlement, stability of roadbed

INTRODUCTION

With the China railway speeding plan, original roadbed should be widened. By summarizing completed and similar projects, main engineering diseases are unequal post-construction settlement and lacking stability of new widened roadbed. To avoid above diseases, geogrid and plastic drainage plate usually be used. The paper use finite element method (FEM) from aspects as length, layout manner, stiffness, interaction effect of geogrid, whether use plastic drainage plate and its span to analyze the effect on roadbed slope stability of each stage, the max unequal post-construction settlement and time for consolidation.

The initial condition suppose the roadbed and foundation have already consolidated after longtime work of self-weight and traffic load. The FEM calculation sequence coincides with the construction stage as listed in Table 1. Traffic loads simplified into uniform load according to related regulation.

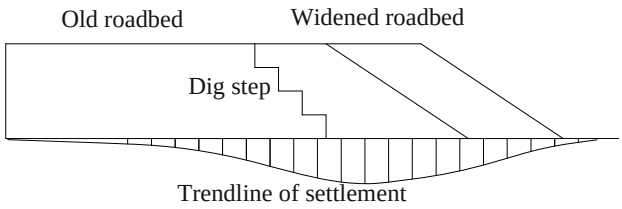

Fig. 1 Unequal post-construction settlement trend

Table 1 Construction sequence

Construction sequence	Time (Day)	No
Original roadbed simulation		Stage1
Shoulder excavation and replace peat of basement	10	Stage2
Fill to 2.0 m height	30	Stage3
Consolidation	180	Stage4
Fill to 3.0 m height	10	Stage5
Consolidation	60	Stage6
Fill to 4.0 m high	15	Stage7
Traffic load		Stage8
Consolidation	Decided by compute	Stage9

THEORY OF FEM ANALYZE

The paper use finite element method to perform analysis that based on the following theory.

[1] Lecturer, College of Construction Engineering, Shijiazhuang Railway Institute, CHINA. Email: lvpeng2941@126.com
[2] Lecturer, College of Architecture & Art, Shijiazhuang Railway Institute, CHINA. Email: dayu6601992@126.com

Equivalent Sand Well

The plastic drainage plate turn into equivalent sand well in FEM calculation (Jia and Chen 2004).

Simulation of Interface Interaction

An elastic-plastic model is used to simulate the behavior of interface elements, which represent the soil-geogrid interaction. Element is made up of ten nodes arranged in two parallel rows, each row of nodes represent the different material (Song & Chen 1996).

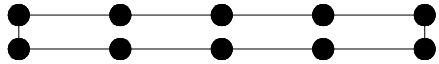

Fig.2 Interface element

The Coulomb criterion is used to distinguish between elastic or palstic behaviors, whether the interface remains in elastic state is decided by the shear stress τ given by the follow formula.

$$\tau \leq \sigma_n \tan \varphi_i + c_i \tag{1}$$

φ_i And c_i are the friction angle and cohesion of the interface, σ_n and τ are the normal stress and shear stress acting on the interface. During FEM calculation, coefficient R_{inter} used to represent the degree of soil-geogrid interaction. R_{inter}=1.0 means soil-geogrid combined rigidly and 0.0 means doesn't work together.

$$c_i = R_{\text{inter}} \cdot c \tag{2}$$

$$\tan \varphi_i = R_{\text{inter}} \cdot \tan \varphi \tag{3}$$

Shear Strength Reduction Method (SSR)

Shear strength reduction method (SSR) is carried out by FEM to perform the roadbed stability analysis. The factor of safety (FOS) is defined as the numbers by which the original shear strength parameters must be divided in order to bring the roadbed slope to the point of failure (Griffiths & Lane 1999).

$$FOS = \frac{\tan \varphi}{\tan \varphi_r} = \frac{c}{c_r} \tag{4}$$

FOS is the calculated factor of safety; φ and c is the initial parameter of soil, φ_r and c_r is parameters that reach critical failure state (Song 1997).

FEM MODEL

FEM analysis is according to construction sequence.

FEM and Geometry Model

Fig. 3 shows the soil layer distribution and dimension. Geogrid is placed at the dig step. Because the project is symmetric only right half is chosen for FEM analysis.

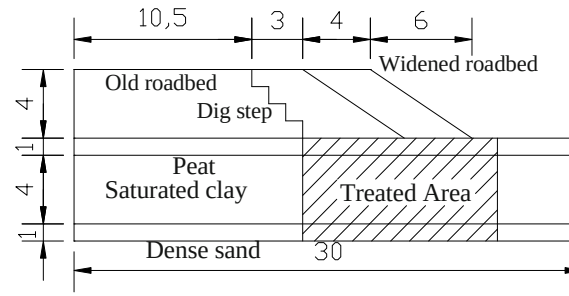

Fig. 3 Geometry model and soil distribution (m)

Meshed model shows in Fig. 4. The traffic load simplified into distribution load on the top of roadbed.

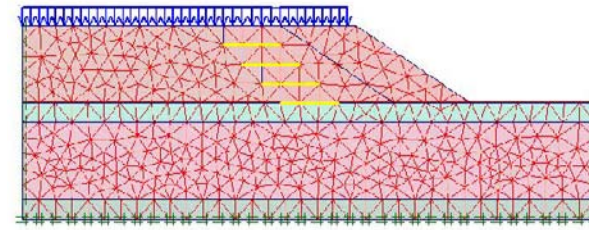

Fig. 4 FEM model

Boundary Condition of FEM Analyze

Boundary condition plays important role in FEM analysis. Combined with site geology investigation results, the bottom of model is dense sand so total displacement is fixed. Horizontal displacement of left edge is fixed because of symmetry.

Phreatic line is coincides with the ground water surface. In consolidation analysis the seepage edge of bottom and right side is free, but left edge is closed for symmetry reason.

Material Model and Parameters

Mohr-Coulomb model is used to describe the behavior of each soil.

For the reason that geogrid mainly bear tension stress and is in elastic state, it has been simplified into a linear-elastic model that only sustain tensile force, parameter EA is single used to describe the geogrid behavior. According to design the EA value is 600 kN/m in project (Song 1997).

Table 2 Soil parameters (Unit: SI)

Parameter	Clay	Dense sand	Peat	Roadbed filling
Dry soil weight	16.0	19.2	12	18.5
Wet soil weight	17.5	20.5	15	20.2
Permeability	0.002	0.2	0.002	0.001
Young's modulus	3200	15000	850	12000
Poisson's ratio	0.3	0.31	0.31	0.3
Cohesion	7	0	2	15
Friction angle	24	30	10	30

ENGINEERING EFFECT OF GEOGRID

The paper from aspects as layout manner, length, stiffness (EA), soil-geogrid interface effect of geogrid analyze the engineering effect.

Layout Manner of Geogrid

In formal design the geogrid is placed at each dig step and the length is 3.0 m. The paper compares the different layout manners.

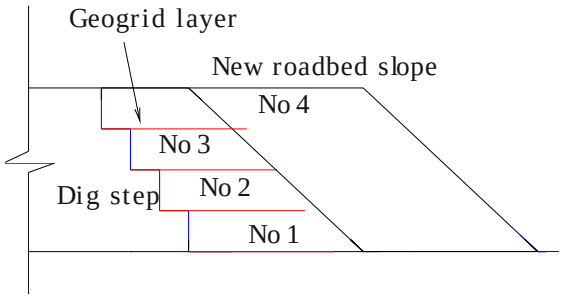

Fig. 5 Geogrid layout manner

Table 3 FOS of different geogrid layout manner

	Original design	No 1—3	No 1 & 3	No 2 & 3	No 1 & 4
Stage 3	1.337	1.337	1.292	1.198	1.307
Stage 5	1.251	1.251	1.229	1.207	1.198
Stage 7	1.219	1.183	1.152	1.183	1.193
Stage 9	1.318	1.273	1.255	1.236	1.227

Table 4 Max value of unequal post-construction settlement (mm) at top of roadbed

	Original design	No 1 — 3	No 1& 3	No 2 & 3	No 1 & 4
Settle-ment	78.4	79.1	79.9	80.2	79.5

Table 5 Consolidation time of post-construction

(Day)	Original design	No 1— 3	No 1 & 3	No 2 & 3	No 1 & 4
Time	479	491	503	499	494

From calculated results listed in Table 3 to 5, it can be seen that different geogrid layout manners can affect the behaviors of engineering.

Length of Geogrid

In original design the length of geogrid is 3.0m, the paper compare the condition with different lengths of 2.0 m, 4.0 m, 5.0 m and 6.0 m.

Table 6 Max value of unequal post-construction settlement (mm) at top of roadbed

	2.0	Original design	4.0	5.0	6.0
Settle-ment	87.3	78.4	78.2	77.9	77.9

Table 7 FOS of different geogrid length

Length (m)	2.0	Original design	4.0	5.0	6.0
Stage 3	1.225	1.337	1.402	1.403	1.403
Stage 5	1.198	1.251	1.263	1.267	1.268
Stage 7	0.978	1.219	1.224	1.226	1.226
Stage 9	1.079	1.318	1.327	1.328	1.329

Table 8 Consolidation time of post-construction

(Day)	2.0	Original design	4.0	5.0	6.0
Time	512	479	477	469	469

From calculated results listed in Tables 6 to 8, the length of geogrid should exceed a limit value, too short may leads to lack of stability and large unequal settlements of roadbed.

Effect of Soil-Geogrid Interaction

As pointed in Eq. 2 and 3 R_{inter} means the degree of soil and geogrid interaction. R_{inter}=1.0 means combines rigidly and 0.0 means does not work together at all. Value of R_{inter} determined by the filling material type, gravel usually takes value of R_{inter}=1.0 and peat is R_{inter}=0.0. The design value of R_{inter} is 0.66. The paper analyzes the effect of different R_{inter} (Liu and Wu 2003).

Table 9 FOS of different R_{inter}

	0.0	Original design	1.0
Stage 3	1.225	1.337	1.412
Stage 5	1.198	1.251	1.268
Stage 7	0.978	1.219	1.229
Stage 9	1.079	1.318	1.338

Table 10 Max value of unequal post-construction settlement (mm) at top of roadbed

	0.0	Original design	1.0
Settlement	86.8	78.4	74.1

Table 11 Consolidation time of post-construction

(Day)	0.0	Original design	1.0
Time	509	479	467

From calculated results listed in Table 9 to 11, the engineering behaviors decreased with the lack of soil-geogrid interaction.

ENGINEERING EFFECT OF PLASTIC DRAINAGE PLATE

To change the problem into plane strain analysis, the paper use theory of equality sand well to perform the FEM calculation. From results shown in Tables 12 to 14, it can be seen that plastic drainage plate can apparently accelerate consolidation and decrease unequal post-construction settlement. Too closer of plate can't develop the engineering behavior greatly, the reason is similar as the sand well has its influence radius.

Table 12 Max value of unequal post-construction settlement (mm) at top of roadbed

Span (m)	Without plate and geogrid	Only without plate	Original design	0.7	0.4
Settlement	129.4	127.2	78.4	77.2	76.3

Table 13 FOS of different plate span

Span (m)	Without plate and geogrid	Only without plate	Original design	0.7	0.4
Stage 3	1.174	1.205	1.337	1.341	1.341
Stage 5	1.089	1.168	1.251	1.252	1.252
Stage 7	0.965	1.078	1.219	1.221	1.222
Stage 9	1.011	1.318	1.318	1.320	1.321

Table 14 Consolidation time of post-construction

(Day)	Without plate and geogrid	Only without plate	Original design	0.7	0.4
Time	879	846	479	468	466

CONCLUSIONS

By summarizing FEM calculated results some conclusions can be obtained as follows.

(1) Engineering Effects of Geogrid. The geogrid has apparently improved the roadbed slope stability of each stage, but has little effect on unequal post-construction settlement and consolidation. Length, stiffness, interaction of soil, layout manner of geogrid all have its effect on engineering behavior and should choose suitable value for use.

(2) Engineering Effects of Plastic Drainage Plate. Plastic drainage plate has apparently accelerated the consolidation and decreased the unequal post-construction settlement. It has developed the roadbed slope stability at construction stage, but has little effect on stability after consolidation. Too large or small span of drainage plate can't apparently improve the engineering behavior.

In conclusion, geogrid and plastic drainage plate all have its advantages in roadbed widening project on soft soil foundation and should be used in combined way to perform the better engineering effect.

REFERENCES

Jia N, Chen RP (2004) Theoretical analysis and measurement for widening project of Hang-Yong expressway. J. Chinese Journal of Geotechnical Engineering 26(6): 755-760

Song EX, Chen ZY (1996) Soil-nail supporting and FEM analysis. J. Geotechnical Investigation and Surveying 2:1-5

Griffiths DV, Lane PA (1999) Slope stability analysis by finite elements. J. Geotechnique 49 (3): 387-403

Song EX (1997) Finite element analysis of safety factor for soil structure. J. Chinese Journal of Geotechnique Engineering 19(2): 1-7

Liu HL, Wu WJ (2003) Nonlinear finite element analysis of reinforced dike with geotextile. J. Rock and Soil Mechanics 24(1): 79-87

FEM ANALYSIS ON GEOGRID REINFORCED ASPHALT CONCRETE PAVEMENT

Y.Y. Fei[1] and Y.H. Yang[2]

ABSTRACT: In this paper, numerical calculation contrast analysis on the stress in asphalt pavement with and without reinforcement, as well as in different connective operation condition between geogrid and pavement is conducted. The results demonstrate that the optimum position varies with the different requirements of disease prevention. Geogrid can effectively improve stress condition when penetrating cracks are developed in base course. At the same time, the reinforcement mechanism and crack prevention function of geogrid are revealed, which show that geogrid reinforcement technology has priority to other methods.

KEYWORDS: geogrid, reinforcement, asphalt concrete pavement, FEM analysis

Asphalt concrete pavement is the main type of high-grade highway pavements. Cracking and rutting, which are common damages in this pavement, seriously affect the structure and service performance of the highway. So cracking and rutting are important problems that need to be solved on theory research and project practice of asphalt pavement (Han et al. 2000).

In recent years, many studies and tests have been done in project practices. Seen from these research results, geogrid can delay or decrease not only reflection cracking but also pavement rutting, and properly improve the fatigue life of semi-rigid base course (Yan 2003).

THE POSSSIBLITY OF GEOGRID APPLICATION IN ASPHALT CONCRETE PAVEMENT

Various methods are adopted to decrease pavement damages at home and abroad. Modified asphalt and SMA are widely used, but these two new techniques used in highway project have some drawbacks yet (Wang et al. 2003): (1) In common district special facilities and materials (high quality aggregate, additive for improving the property, filling) can not be provided, and the one-off investment is great. At the same time, their construction techniques needed add much more difficulties than normal methods, at present; (2) From the point of improving the cracking resistance, seepage prevention, segregation and diffusion of the pavement, it is not optimum to depend too much on adding elasticity and cohesion of asphalt binder, increase aggregate intensity and decrease compound void content; (3) Some questions relating to asphalt itself still demand to be solved, such as sunshine aging, high temperature softening, low temperature embitterment and shock fatigue. Geogrid has high tensile strength and modulus, with little long-term creep and good thermal stability. The geogrid whose surface is processed possesses better compatibility with asphalt, better material chemical stability and better grid restraining aggregate. So geogrid can strengthen the resistance ability against deformation of the surface when it is laid in or at the bottom of the asphalt concrete surface (Zhang et al. 2007). At the same time, since its area of spreading is quite large, the pressure, the secondary flexural-tensile stress, shear and temperature stress produced by the wheel load on the surface will be transferred to it to bear under the compatible conditions of surface deformation and these stresses will distribute within its covering scope. As a result, the anti-fatigue ability of the pavement will be improved and the anti-rutting and anti-swelling ability of it will also be reinforced (Cao et al. 2000). Many application examples have undergone economic benefit analysis and the results show it possesses obvious superiority. When the British Professor S.F.Brown introduced the application effect of Tensar geogrid applied in North America, Europe and Far East, he thought that geogrid could reduce rutting by 50%, delay reflection cracking and reduce the thickness of asphalt surface by 36% (Wang et al. 2004). Besides, abroad applications also show expenses can be cut down by 12%—16% in reinforced pavement if curing and rehabilitation with final service life are taken into account (Huntington et al.2000).

[1]Lecturer, Gansu Communications Institute of Technology, Lanzhou Gansu, CHINA. Email:feiyueying@163.com
[2] Professor, Civil Engineering Department, Lanzhou Jiaotong University ,CHINA. Email:yangyh@mail.lzjtu.cn

COMPUTATION MODULUS AND PARAMETER SELECTION

Computation Modulus

The pavement structure is considered as elastic layer system. Two conditions are considered in the paper, those are without cracking and with cracking according to the cracks in base course. The commonly used 6-layer structure in high-grade asphalt pavement is chosen in the pavement structure layers. In performing the FEM analyses, there are several kinds of models on connecting geogrid and asphalt pavement structure, including composite material model, membrane element and Goodman element etc. But it is difficult to evaluate reinforcement effect of geogrid correctly with these models. And according to the calculation experience, the relative slides are very small when Goodman element is used to analyze interface performance (Feng 2002). However, in practical application, slide often occurs between geogrid and structure layer. It shows a non-linear contacting state. The post element and contact element has been adopted to simulate geogrid and asphalt structure interface and the FEM analyses conducted and the function and effect of the reinforced asphalt concrete pavement illustrated by amount of calculation. Double circles vertical load is applied on the basis of *Specifications for Design of Highway Asphalt Pavement*（*JTJ014-97*）. Equivalent diameter: $2r$=2× 10.65 cm; the distance between two centers: 31.95 cm. Model load is applied at the corresponding line which represents loading situation at highway surface. Standard of axle load is single rut load 100 kN according to double wheel group; tire ground contacting intensity of pressure : p=0.7 MPa.

Material Parameter

Structural parameters of asphalt pavement are selected according to *Specifications for Design of Highway Asphalt Pavement*（*JTJ014-97*）.The elastic modulus of geogrid applied in this paper is 40GPa, and cross section is 0.0012 m^2 per meter. Interface spring parameters are defined as kz=ky=10^{13} N/m (Lin 2003). By stress convergence calculation, the size of subgrade is defined as 5m × 5m. Fig.1 indicates calculation structural diagram. Fig. 2 shows FEM mesh subdivision.

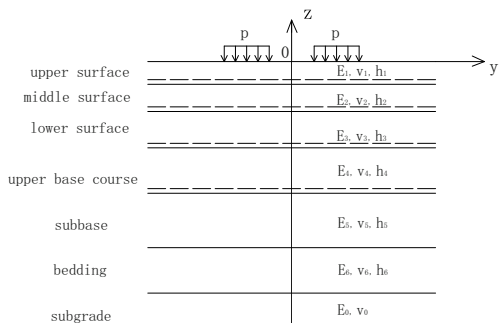

Fig. 1 Pavement structure and load schematic

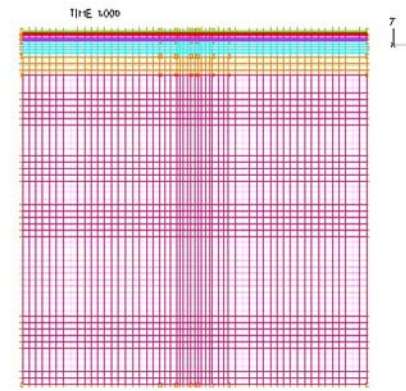

Fig. 2 FEM mesh schematic diagram

STRESS ANALYSIS ON PAVEMENT STRUCTURE REINFORCED BY GEOGRID

Without Penetrating Cracking in Base Course

Figs.3—6 are comparison graph of stress between the bottom of upper and lower surface when geogrids are laid in different structural layers of asphalt pavement.

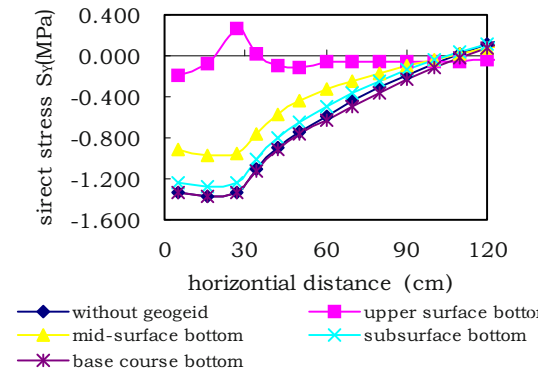

Fig. 3 Direct stress S_Y of upper surface bottom

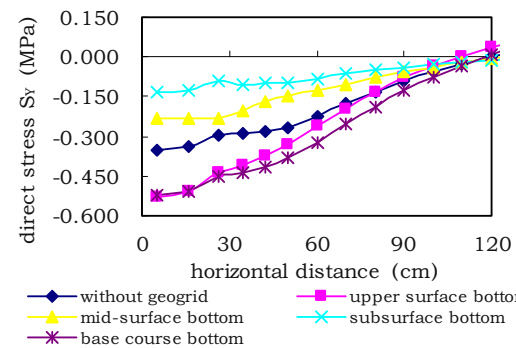

Fig. 4 Direct stress S_Y of subsurface bottom

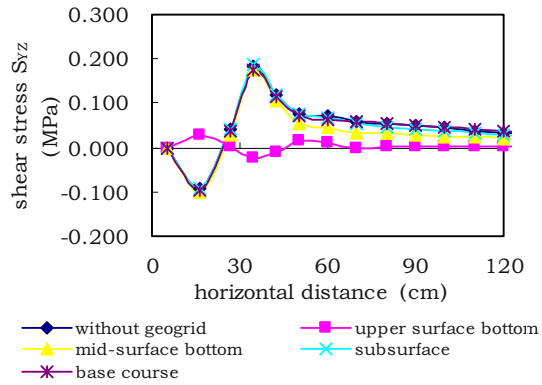

Fig. 5 Shear stress S_{YZ} of upper surface bottom

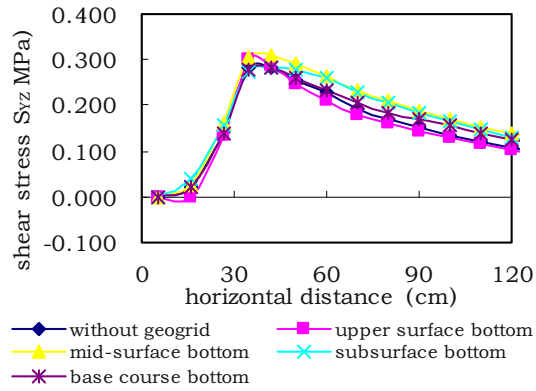

Fig. 6 Shear stress S_{YZ} of subsurface bottom

By FEM calculation, conclusions are drawn as follows:

(1) The great changes of each structural floor's direct stress S_Y has taken place when geogrids are laid in different structural floor of asphalt pavement. Geogrids, no matter laid at the bottoms of upper surface, middle surface or lower surface, can effectively decrease direct stress S_Y of upper surface bottom. But geogrid laid at the bottom of the upper surface acts more effectively. Maximum value of S_Y decrease from 1.37 MPa without geogrid to 0.08 MPa, and stress curves tend to flat. Reinforcing effect of geogrid is brought fully into play. At the same time, Fig. 3 shows that if the reinforced layer becomes farther from the upper layer of calculated layer, the reinforcement effect becomes weaker correspondingly.

Direct stress S_Y at the bottom of subsurface decreases obviously when geogrid is laid at the bottom of middle surface and subsurface, especially at the bottom of subsurface. Not only maximum value is reduced, but also all the direct stress S_Y at the bottom of subsurface is reduced. Thus it is clear that geogrids laid at the bottom of middle and subsurface can effectively improve direct stress S_Y of the bottom surface. The effect also becomes more obvious when the reinforced layer becomes nearer to the calculated layer. But geogrids take disadvantageous effect to the direct stress S_Y in the upper surface bottom layer when they are laid at upper surface bottom and base course one.

(2)The shear stress S_{YZ} at the bottom of upper surface decreases obviously when the bottom of the upper surface is reinforced. The maximum reduces from 0.186 MPa (without geogrid) to 0.013 MPa, but the changes of the shear stress S_{YZ} at the bottom of upper surface become less obvious with the depth of reinforced layer increasing. The change of the shear stress S_{YZ} at the bottom of subsurface is slight before and after the reinforcement is conducted. But Fig. 6 still shows that geogrid laid at the bottom of upper surface is advantageous to improve the shear stress S_{YZ} at the bottom of the subsurface.

(3) Geogrid, laid between asphalt concrete layers, can bond the materials at the upper and lower layers effectively and make the upper and lower structure layers of the pavement form one compound mechanical restraining system. The restriction areas hold back the aggregate movement and increase transverse binding force of the asphalt layer, thus every part of the asphalt layer ties up each other, which can prevent the movement of the asphalt layer and resist the happening of rutting.

(4) The larger dynamic friction is produced by the overall force loaded on geogrid. Since the geogrid itself can bear part of outside force, it makes bituminous mixture stress decease, thereby reducing stress of pavement structural layer. These make asphalt pavement tensile strength greatly improve and resist enough great tensile stress so that the pavement can not be destroyed. Even if the stress is concentrated at the tiny craze produced at partial area, the tiny craze can not be developed into crack since the geogrid carry over stress to disappear. Thus, the geogrid plays a role of delaying cracking.

With Penetrating Cracking in Base Course

The phenomenon of cracking often takes place due to temperature change, drying shrinkage and fatigue in the base course, especially the semi-rigid base course widely used at home. In the pavement structure, the crack in the base course can destroy the integration of the pavement structure and redistribute the stress of pavement structure. Assume that transverse crack appears in the base course and the surface is in good condition. The contrast analyses on stress in asphalt layers with load acting symmetrically at crack center and eccentric crack under two conditions: with or without reinforcement are conducted. (Assume that the geogrid is laid at the bottom of the lower layer).

The direct stress S_Y of asphalt pavement changing with depth is shown in Figs. 7 and 8.

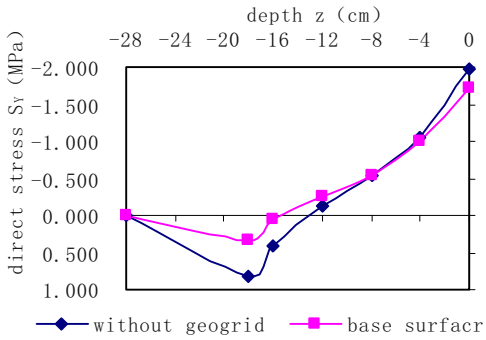

Fig. 7 Direct stress S_Y at different depth under symmetrical load

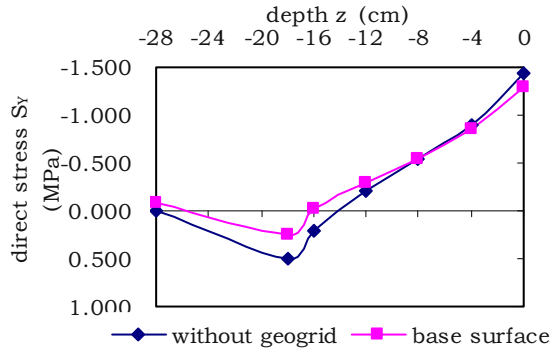

Fig. 8 Direct stress S_Y at different depth under unsymmetrical load

These figures show obviously that under the action of load, the tensile stress S_Y in the greater scope near asphalt layer is distributed linearly and it possesses the characteristics of flexural-tensile stress. The extreme value of stress at the bottom of the subsurface appears due to cracking. Geogrid plays an “interlocking” role for the mixture in the grid after geogrid is laid. Geogrid will be in the tensile state and tend to hold the two sides of crack together with stretching the two sides of the crack because of the flexural-tensile stress acted on them. It shows a bridge-toughening effect. This bridge effect is similar to the restraining effect acted by short fiber of short fiber composite materials against the extension of crack and it decreases the stress concentration around crack tip (Zhou et al. 1999). Besides, the damaging course to the asphalt concrete structure is different for the same geogrid with different reinforcement methods. Geogrid, which is laid near the bottom of the pavement structure, may work relatively earlier in restraining crack development; thereby it can take better effect to prevent cracking. As a result, geogrid should be laid over the crack and near the crack in order to protect structure from crack expanding upwards in the pavement structure.

STRESS AND HORIZONTAL DISPLACEMENT CAUSED BY CONNECTION OPERATION MODE AMONG GEOGRIDS, UPPER AND LOWER STRUCTURE LAYERS

In the practical project, the connection between geogrid and asphalt pavement structure layers is influenced by many factors, especially the measures adopted and technology used in construction.

The different connection condition between geogrid and asphalt concrete through the changes of stiffness coefficient ky of the connection spring in the horizontal direction in the contact element are simulated in the paper. The relatively small k_y (k_y=10^3 N/m) demonstrates no connection and complete slide existing between geogrid and asphalt concrete, yet this pavement situation hardly exists in practical structure. While the large k_y (k_y=10^{13} N/m) shows complete connection between geogrid and asphalt concrete and in this case, both can take effect altogether. But in fact, most conditions lie between the two mentioned-above condition. That is to say, the geogrid and asphalt concrete are at a state of semi-connection and semi-slide. The following research simulates the different connection conditions to conduct FEM analysis by changing spring stiffness coefficient k_y. In this case, geogrid is laid between the asphalt subsurface and base course surface. At the semi-connection state, k_y is 10^8 N/m while at the complete connection state, k_y is 10^{13} N/m.

Stress

Figs.9 and 10 show comparison sketches of stress produced by symmetrical and unsymmetrical loads in the base course with traverse cracking.

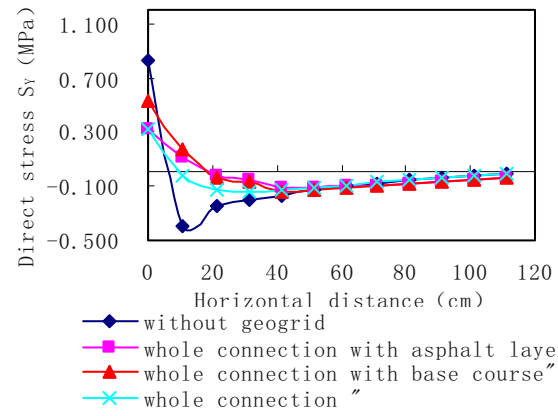

Fig. 9 Direct stress S_Y of different connection with symmetrical load

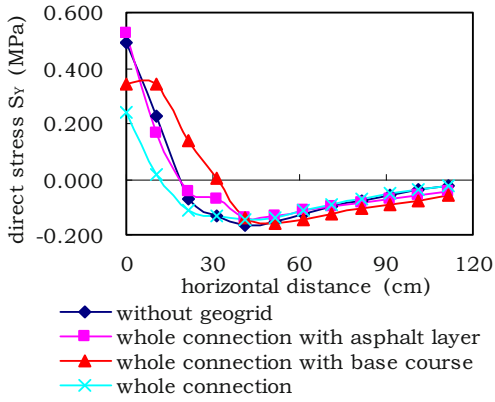

Fig. 10 Direct stress S_Y of different connection with unsymmetrical load

As shown in Figs.9 and 10, the stress S_Y distribution curves change obviously with the different connection condition. The changing scope largely lies on the area which is 0—40 cm from the wheel load center. When the geogrid and asphalt concrete are completely connected, the reinforcement effect becomes largest and the stress concentration around crack tip can be decreased effectively. But it is disadvantages to the bridge-toughening of geogrid when bad connection between geogrid and asphalt and full connection between geogrid and semi-rigid base course. It is essential to take active measures in the process of construction in order to ensure the complete connection between geogrid and upper and lower layer thus better reinforcement effect can be produced.

Horizontal Displacement

The comparison sketches of displacement arose by symmetrical and unsymmetrical loads in the base course with traverse cracking are shown in Figs.11 and 12.

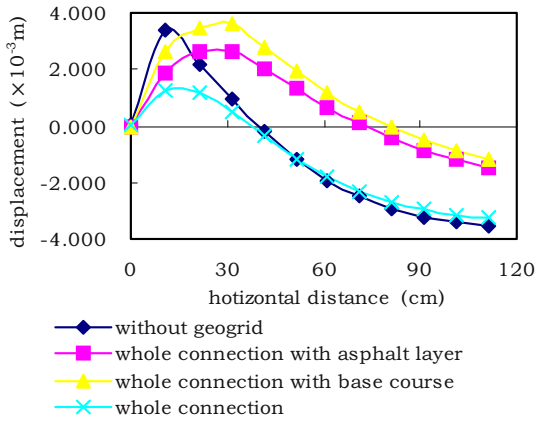

Fig. 11 Displacement of different connection symmetrical load

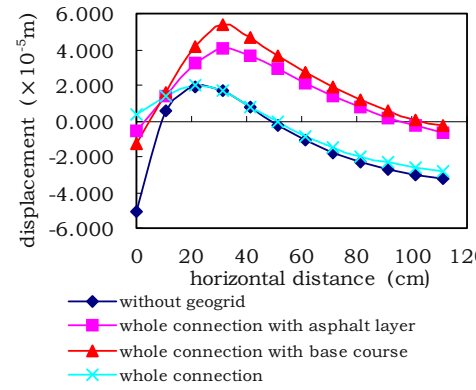

Fig. 12 Displacement of different connection with unsymmetrical load

It is shown that the displacement will increase greatly if the connection between geogrid and upper or lower structural layer is not good. Displacement decreases clearly only when they are fully connected. That is because geogrid restrains the displacement of granularity inside the asphalt mixture evenly and greatly reduces the stress concentration acted by interior load of the mixture when geogrid and asphalt structure are connected completely. At the same time, the interlocking frictional resistance of the geogrid grid against the granularity confines the movement of the granule inside the mixture, then decrease horizontal displacement.

CONCLUSIONS

(1) When there is no crack in the newly-built pavement, the stress influence on asphalt layers is different if geogrid is laid in various layers. As for the direct stress and shear stress at the bottom of the upper layer, the effect is most obvious when geogrid is laid at the bottom of upper layer. The effect decreases gradually with the increasing distances between the reinforced layer and calculation layer. When the reinforced layer lies in the bottom of the middle or the lower layer of the asphalt pavement, the geogrid can obviously reduce the stress at the bottom of the asphalt layer and evenly distribute stress in larger scope and finally prevent asphalt pavement cracking. But reinforcement laid below the calculation layer contributes little to stress. As a result, geogrid should be laid in the calculation structural layer or next to it for the sake of decreasing certain calculation layer stress of asphalt pavement.

(2) If transverse crack emerges in the base course, reinforced layer lying at the bottom of the asphalt layer can obviously reduce tensile stress at the bottom of the asphalt layer, particularly, it can effectively distribute the

stress concentration due to the base course cracking, thus decrease the damage rate of the pavement. Geogrid laid near the bottom of pavement layer can restrain crack relatively early, which well inhibiting the cracking. Therefore geogrid should be laid over the crack and on the base course surface in order to prevent crack from developing upwards.

(3) The connection between geogrid and asphalt pavement is very important. Reinforcement effect is largest when geogrid and asphalt concrete are connected completely. The full connection between geogrid and asphalt layer and semi-connection between geogrid and semi-rigid base course acts secondly. The bad connection between geogrid and asphalt while the full connection between geogrid and semi-rigid base course are most unfavorable for the geogrid to play in a bridge-toughening role. So it is essential to take measures in the process of construction to ensure the complete connection between geogrid and the upper and lower structure layer. Even under the limited or inconvenient circumstances in dealing with the upper surface of the base course, the connection between geogrid and asphalt surface should be ensured to try best.

REFERENCES

Cao DW, Hao DW, Han RM (2000) Mechanical Analysis on Geogrid-Reinforced Asphalt Concrete Pavement. Journal of Chongqing Jiaotong Institute 19(2):47—52

Feng GL (2002) Application Research of Settlement Criteria at Bridge Approach and Backfill Reinforcement at Back Wall of Abutment. Master Thesis, Tongji University, China.

Han RM, Yang YH, Wang BG (2000) Research on Geogrid-Reinforced Asphalt Concrete Pavement. Northwest Highway. Chengdu, China (2): 1-4

Huntington G, Ksaibati K (2000) Evaluation of geogrid-reinforced granular base. Geotechnical Fabrics Reports 1/2: 20-28

Lin PD (2003) Application of Reinforcement aterial to Alteration and Extension Project. Master Thesis, Harbin Institute of Technology, China

Wang HQ, MAO XZ (2003) Solving Focus Problem of Asphalt Pavement by Geosynthetics. China Highway 4: 18-20

Wang XQ, An JY, Wang Z (2004) Application of Geosynthetics to Asphalt Pavement and Its Design. Rock and Soil Mechanics. Rock and Soil magazine 25(7): 1093-1098

Yan HM (2000) Application of Glass Fiber Geogrid to Prevent Reflection Creaking in Newly-built Pavement. China Municipal Engineering 6:7-8

Zhang YF, Liu KP (2007) Application of Glass Fiber Geogrid in Highway Construction. East China Highway 2:64-66

Zhou ZG, Zhang QS, Zheng JL(1997) Bridge Effect of Geogrids Protecting Asphalt Pavement from Cracking under Traffic Loads. China Journal of Highway and Transport 12(7): 27-33

DYNAMIC FINITE ELEMENT ANALYSIS OF REINFORCED AND UNREINFORCED PAVEMENTS OVER SOFT CLAY

F.Y. Liu[1] and Y.Q. Cai[2]

ABSTRACT: In order to study the dynamic response of reinforced and unreinforced pavements on soft clay under traffic loading, cyclic triaxial tests were first conducted to investigate the effects of initial deviator stress, loading frequency, overconsolidation ratio, and cyclic stress ratio on softening behavior of clay. The empirical equation for softening of clay was proposed by regression analysis method. The equation was imported into FEM program through compiled subroutine. Dynamic response of unreinforced and geogrid reinforced pavements was studied by FEM in order to investigate mechanisms of reinforcement. The results indicated that softening behavior of clay had visible effect on the performance of unreinforced and reinforced pavements. Geogrid reinforcement can provide lateral confinement at the bottom of the base layer by improving interface shear resistance and improve stress distribution on subgrade layer. The effect of geogrid reinforcement was also shown to reduce surface deformation and nonuniform settlement.

KEYWORDS: traffic loading, reinforced pavements, softening behavior, mechanisms of reinforcement

INTRODUCTION

Observations show that the soft subgrade of the pavements may suffer high settlements that develop slowly after the main consolidation was completed under traffic loading. The high settlements degrade the pavements and ruts appear on the surface. Several methods may be used to increase the long term satisfactory performance of the pavements, one of which is the reinforcement.

Over the two last decades, with the availability of faster computers with larger data storage, it has been possible to perform finite element analyses with increasingly complex formulations. Burd et al. (1986) developed a large strain finite element model for the purpose of examining experimental results of reinforced unpaved roads. Barksdale et al. (1989) adapted an existing finite element model to predict the response seen in the experimental portion of their study. Hird et al.(1990) carried out a parametric study and concluded that sufficiently stiff and strong reinforcement may significantly reduce subsoil deformations and, for a subsoil of constant strength, the effect of reinforcement reduces with increasing depth. Miura et al. (1990) performed a finite element analysis of a reinforced paved road in support of a laboratory and field experimental program. The results from the analysis of reinforced and unreinforced sections showed general agreement with results from the laboratory test sections. Dondi(1994) used the commercial finite element program ABAQUS to model a geosynthetic reinforced flexible pavement. Three-dimensional (3D) static analysis was used. Wathugala et al. (1997) used the ABAQUS finite element program to formulate a finite element model of a geogrid reinforced pavement. The addition of the geogrid was shown to reduce the permanent rut depth by approximately 20% for a single cycle of load. Berg et al. (2000) showed in their review that geosynthetic membrane used to reinforce pavement system provides, under certain conditions, substantial load-carrying benefits to such systems. Perkins tested three different locations of the geogrid, while varying its stiffness, base thickness, and the subgrade strength. In his finite element simulations, Perkins performed a 3D analysis to duplicate the case of a test box. Ling et al. (2001，2003) used the two dimensional commercial finite element program PLAXIS to model the laboratory test previously conducted on a geogrid reinforced pavement system. They concluded that the associated and nonassociated rules gave similar results. Saad et al. (2006) performed a series of finite element simulations to evaluate the benefits of integrating a high modulus geosynthetic into the pavement foundation. It was found that placing the geosynthetic reinforcement at the base–asphalt concrete interface leads to the highest reduction of the fatigue strain. The placement of geosynthetic reinforcement in

[1] Lecturer, Department of Civil Engineering, Shanghai University, CHINA. Email:lfyzju@shu.edu.cn
[2] Professor, Department of Civil Engineering, Zhejiang University, CHINA. Email:caiyq@zju.edu.cn

thin bases is particularly effective.

Despite the extensive research on reinforced pavements in recent years, there have been very limited systematic studies on the cyclic behavior of reinforced pavements considering the degradation of soft clays. The initial elastic modulus is now widely considered a fundamental soil stiffness property in many routine designs and in back calculations using numerical analysis. While recent studies reveal the fact that the stiffness of soft clays may decay with increasing strain under traffic loading. This plays a vital role on the long-term performance of subgrade and needs to be considered in pavements design and numerical analysis. It necessitates the development of modified numerical models so as to address the long term behavior of reinforced and unreinforced pavements constructed over soft clays under traffic loading.

The purpose of this paper is to investigate the behavior of reinforced and unreinforced pavements under traffic loading through a plane strain dynamic finite element study. The degradation of the soft clays is also incorporated into the finite element model.

TESTING PROGRAM AND SOIL MODEL

Testing System and Materials

In order to simulate the behavior of reinforced and unreinforced pavements over soft clays exactly, the degradation behavior of soft clays should be firstly studied. The tests were performed using GDS two–way dynamic triaxial testing system, as shown in

Fig. **1**. Soil samples were taken from the construction site in Hangzhou. Samples were subjected to an isotropic effective confining pressure of 60 kPa for more than 24h

Fig. 1 GDS two–way dynamic triaxial testing system

to produce normally consolidated specimens. The initial deviator stress was ramped up to the target value for 1 min. Then cyclic loading was imposed in the vertical direction with a sinusoidal wave.

Table 1 Mechanical parameters of soft soils

I_p	I_L	e	c	Φ	G_s	ω
33	0.709	1.22	18.5 kPa	18.8°	2.744	0.48

Symbols and definitions for cyclic triaxial tests

Dynamic modulus Ed is defined as follows:

$$E_d = (q_{max} - q_{min}) / (\varepsilon_{dmax} - \varepsilon_{dmin}) \quad (1)$$

where ε_{amax} and ε_{amin} are the maximum and minimum strains in hysteresis loop, respectively; q_{max} and q_{min} are the deviator stress accordingly; The other parameters used are defined as follows: q is the deviator stress [=(σ1-σ3)], ε_d is the axial strain, σ_d is axial cyclic dynamic stress, σ_s is initial deviator stress.

The cyclic stress ratio S_c can be defined as follows:

$$S_c = \frac{\sigma_d}{2c_u} \quad (2)$$

where c_u is undrained strength of soil, and $c_u = 30.15\,\text{kPa}$ in this paper.

Degradation model

Since the lack of further studies on the mechanism of cyclic degradation of soft clays, it is not realistic to build up a model theoretically. Thus a mathematical model based on the test research may be an alternative. As loading frequency and cyclic stress ratio have little effect on the degradation of dynamic modulus, the effects of loading frequency and cyclic stress ratios are not included in the model for numerical modeling purposes Liu et al. (2007). The mathematical model can be presented as follows:

$$E_d = (A_1 + B_1\sigma_s)(\alpha_1 OCR^2 + \beta_1 OCR + \gamma_1) \times \varepsilon_d^{(C_1 + D_1\sigma_s)(\alpha_2 OCR^2 + \beta_2 OCR + \gamma_2)} \quad (3)$$

where σ_s is initial deviator stress, OCR is over-consolidation ratio, A_1, B_1, α_1, β_1, γ_1, C_1, D_1, α_2, β_2, γ_2 are parameters related to initial deviator stress and OCR. From regression analysis in this paper, the mathematical model of degradation can be expressed as follows:

$$E_d = (5.9401 + 0.0265\sigma_s)(-0.0804OCR^2 + 0.7425OCR$$

$$+0.3175)\times\varepsilon_d^{(-0.7460+0.0057\sigma_s)(0.0219OCR^2-0.1837OCR+1.1540)} \quad (4)$$

The comparison between calculated results and test results is shown in Fig. 2 and Fig. **3**.From the figures, it can be concluded that the predicted results considering degradation agree well with the measured results. Therefore, these results provide verification that the degradation model is reasonable.

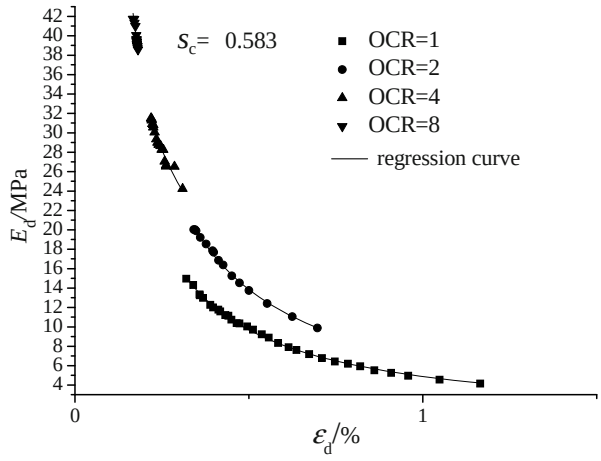

Fig. 2 Regression curve for $E_d - \varepsilon_d$ under different overconsolidation ratios

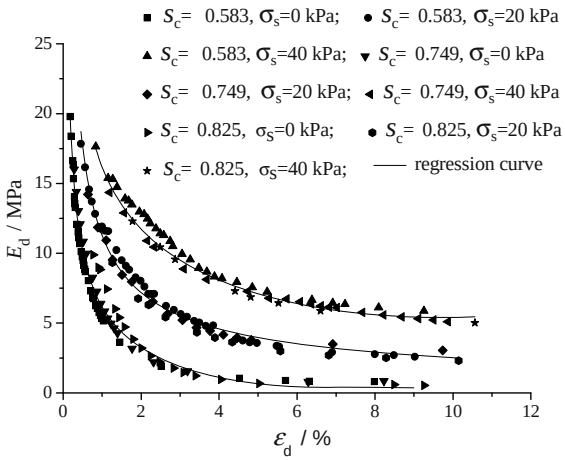

Fig. 3 Regression curve for $E_d - \varepsilon_d$ under different initial deviator stress load of 700 kPa is adopted in this study

FINITE ELEMENT MODEL CONSIDERATIONS

A two-dimensional (2D) analysis is adopted in this study. A load of one set of dual tires of 50 kN is considered. In the 2D analysis, the width of the contact area is 0.5 m. For a given point in the pavement system, the effect of the wheel load passage at that point can be reflected by a stress pulse (Terrel et al. 1974). A sinusoidal wave with a frequency of 2 Hz is used at peak

Due to the symmetry of geometry, boundary conditions and load, only half of the pavement system is considered, see Fig. 4. The subgrade is a 20 m thick clay layer lying on a rigid rock, which constitutes the lower boundary. The geogrid reinforcement lies between the embankment and the subgrade. Eight-node quadrilateral elements under plane-strain conditions are used for pavement, embankment and subgrade. The geogrid reinforcement is modeled with a three-noded bar element. The pavement layer is treated as linear elastic in this study. The constitutive relations of embankment and subgrade are simulated using Extended Drucker–Prager model. As the default value of Young's modulus in ABAQUS is unchangeable, a user subroutine is compiled to import the Eq. (4) into ABAQUS for subgrade. The geogrid is assumed to act as a linear isotropic elastic material. The side boundaries are assumed fixed only in the horizontal direction. The centerline of the load is 1.25 m away from the symmetric centerline. The size of time step is 0.01 s.

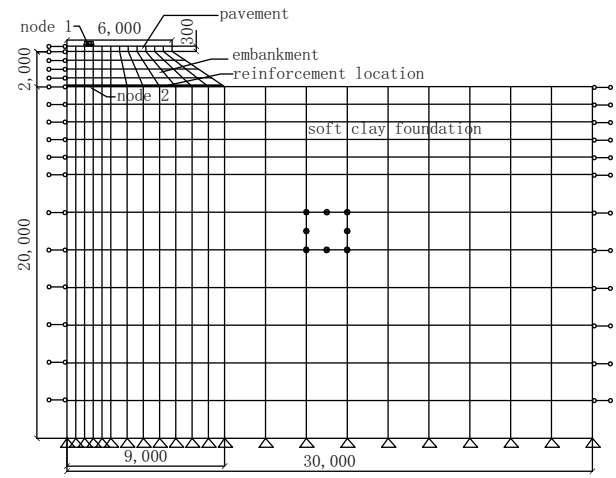

Fig. 4 Finite element discretization of the pavements

Table 2 Model parameters

name	density ($kg\cdot m^{-3}$)	Elastic modulus（MPa）	Poisson's ratio
pavement	2490	4134	0.3
embankment	1900	50	0.35
geogrid	1800	4224	0.42
subgrade	1850		0.42

RESULTS AND DISCUSSIONS

Fig. 5 shows a comparison of the vertical displacement responses of node 1 from reinforced and unreinforced pavements system. The horizontal ordinate N is the number of the load cycles and vertical ordinate δ is vertical

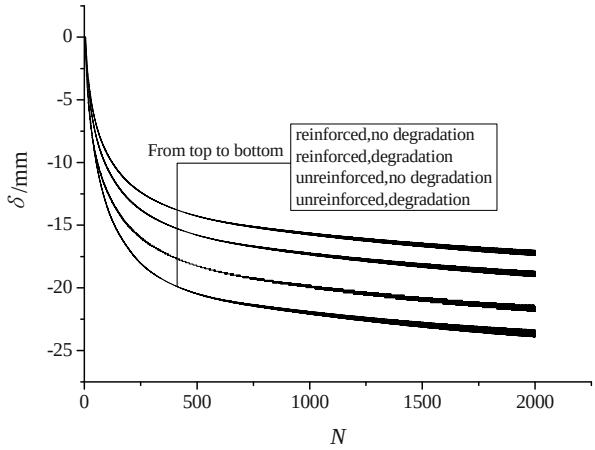

Fig. 5 Vertical displacement comparison of node 1

displacement. It is noticed from Fig. 5 that there is little difference in vertical displacement of node 1 between the reinforced and unreinforced pavements during the first few cycles. With the increasing number of load cycles, the reinforcement effect becomes more and more pronounced. As the degradation of clay is considered, the permanent vertical displacement of node 1 in reinforced pavements at the end of 2000 load cycles is 23.9 mm, while in unreinforced pavements, the displacement is 19.1 mm.The vertical displacement with reinforcement is 79.9% of that without reinforcement. The reduction of vertical displacement is due to the interaction between soil and geogrid. By interlocking soil, geogrids can provide confining effect on soil and therefore increase the modulus of soil. Geogrids can also reduce lateral sliding or displacement of soil. Such interactions results in less vertical deformation of the roadway surface.

The comparison of results considering degradation and no degradation are also shown in Fig. 5. Whenever reinforced or not, the permanent vertical displacement of node 1 when no degradation is considered is smaller than that considering degradation. Such observation indicates that the degradation has significant influence on the permanent vertical displacement of pavements system. There are many instances in engineering that the calculated vertical displacement is much less than the measured results. One of the important reasons may be that no degradation of clay is considered. Therefore, it is important to consider degradation in the study on dynamic response of road.

Fig. 6 and Fig. **7** show the variation of permanent vertical displacement along the top of the subgrade at peak load with increasing number of load cycles. Horizontal coordinate L is lateral distance from the symmetric central line. It is clearly seen that the zero displacement in the top of the subgrade goes away from central line gradually with the increasing number of load

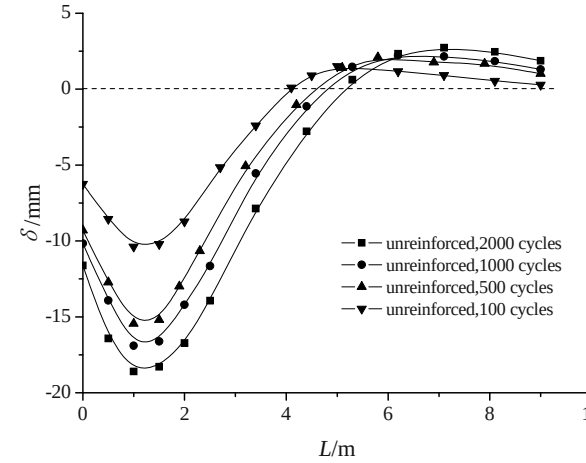

Fig. 6 Vertical displacement in the top of the subgrade under unreinforced condition

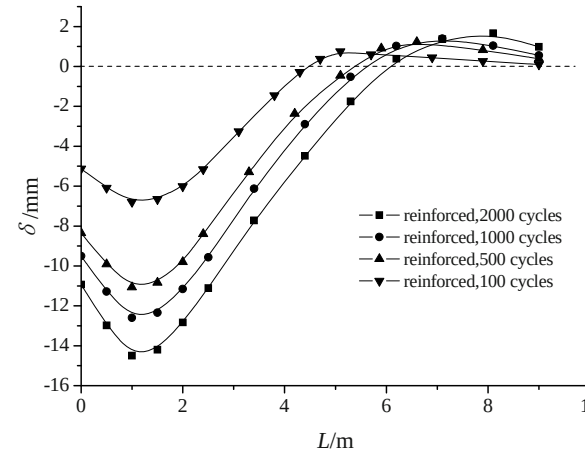

Fig. 7 Vertical displacement in the top of the subgrade under reinforced condition

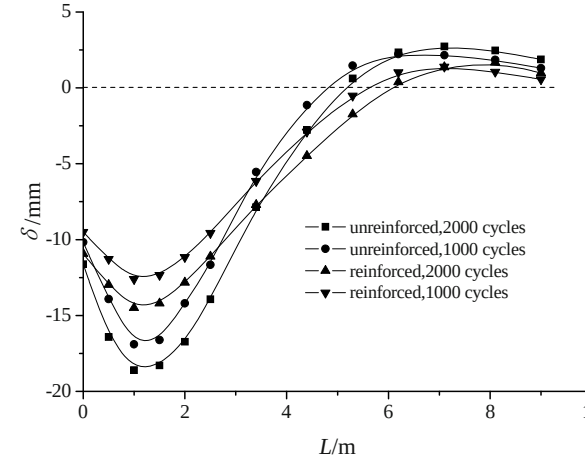

Fig. 8 Vertical displacement comparison of pavement

cycles. So does the maximal upheaval in the top of the subgrade. Fig. 8 shows permanent vertical displacement along the top of the subgrade at peak load. It is observed that the reinforced pavements have a flatter profile of

permanent vertical displacement than unreinforced pavements. The reason is that the vertical component of the tension membrane force can reduce the vertical stress acting on the subgrade and the reinforcement can also provide vertical confinement on the subgrade outside of the loaded area where heave happens.

Fig. 9 shows the variation of the TBR with the increasing load cycles. Traffic Benefit Ratio (TBR) (Berg et al. 2000) is a ratio of load cycles on a reinforced section to reach a defined failure or deformation state to the number of load cycles on unreinforced section, with the same geometry and material constituents, to reach the same defined failure state. Generally speaking, the bigger TBR is, the more significant the reinforcement effect is. During the first few load cycles, TBR is smaller. With the increase of load cycles, TBR increases rapidly and the reinforcement effect becomes more and more pronounced. It can be concluded from these observations that the reinforcement is more beneficial in reducing the long-term settlement of the pavements.

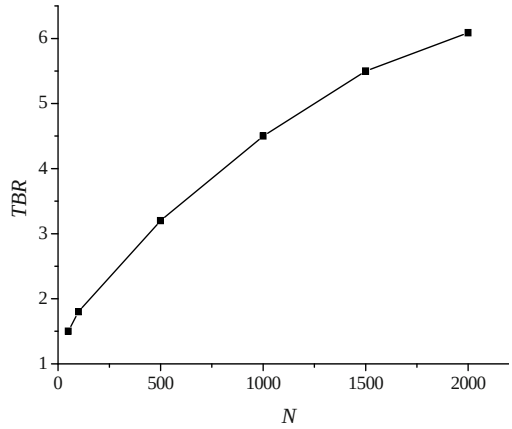

Fig. 9 Reinforcement effect versus cycles of load

CONCLUSION

A series of tests and finite element simulations are carried out to evaluate the benefits of integrating a high modulus geogrid into the pavement foundation. The simulations are conducted to investigate the beneficial effects of geogrid reinforcement to the vertical and horizontal displacement. The following conclusions can be drawn form the study.

1. Degradation will occur for soft clay under cyclic loading and the dynamic elastic modulus of the clay will decrease with the increase of axial strain.
2. The results of FEA show that the vertical displacement of the pavements system considering degradation of clay is larger than that without regard to degradation.
3. The reinforcement can reduce the vertical and horizontal displacement of pavements system. The reinforcement effect increases with the increasing load cycles.

REFERENCES

Barksdale RD, Brown SF, Chan F (1989) Aggregate base reinforcement of surfaced pavements. Geotextiles and Geomembranes 8 (3): 165-189

Berg RR, Christopher BR, Perkins SW (2000) Geosynthetic reinforcement of aggregate base course of flexible pavement structures, GMA White Paper, Geosynthetic Materials Association

Burd HJ, Houlsby GT (1986) A large strain finite element formulation for one dimensional membrane elements. Computers and Geotechnics 2 (1): 3-22

Dondi G (1994) Three-dimensional finite element analysis of a reinforced paved road. 5th Int. conf. on Geotextiles,Geomembranes and related products. 1. Singapore

Hird CC, Kwok CK (1990) Parametric studies of the behavior of a reinforced embankment. Proc. of the 4th International Conference on geotextiles, geomembranes and Related Products. The Hauge 1: 137-142.

Ling HI, Liu H (2003) Finite element studies of asphalt concrete pavement reinforced with geogrid. J. Eng. Mech 129 (7): 801-811

Ling HI, Liu Z (2001) Performance of geosynthetic-reinforced asphalt pavements. J. Geotech Geoenviron. Eng. 127 (2): 177-184

Liu FY, Cai YQ, Xu CJ, Wang Jun (2007) Parametric study of reinforced pavements on soft clay under traffic loading. Chinese Journal of Geotechnical Engineering 29(11): 1659-1664

Miura N, Sakai A, Taesiri Y, Yamanouchi T, Yasuhara K (1990) Polymer Grid Reinforced Pavement on Soft Clay Grounds. Geotextiles and Geomembranes 9 (1): 99-123

Perkins SW (2001) Numerical modeling of geosynthetic reinforced flexible pavements. FHWA/MT-01-003/99160-2, Department of Civil Engineering Western Transportation Institute, Montana State University, Bozeman

Saad Bassam, Mitri Hani, Poorooshasb, Hormoz (2006) 3D FE analysis of flexible pavement with geosynthetic reinforcement. Journal of transportation Engineering 132 (5): 402-415

Terrel RL, Awad IS, Foss LR (1974) Techniques for characterizing bituminous materials using a versatile triaxial testing system. ASTM STP561, American Society for Testing and materials,Philadelphia: 47-66

Wathugala G Wije, Huang B, Pal S (1997) Numerical simulation of geosynthetic-reinforced flexible pavements. Transportation Research Record 1534: 58-65

Proceedings of the 4th Asian Regional Conference on Geosynthetics
June 17 - 20, 2008 Shanghai, China

DEVELOPMENT OF ASPHALT OVERLAY FABRIC FROM JUTE AND ITS PERFORMANCE EVALUATION

M. Ghosh [1], P.K. Banerjee[2] and G.V. Rao[3]

ABSTRACT: A design concept of developing asphalt overlay (A/O) fabric made purely from jute and suitable for reinforcement and moisture barrier functions for low traffic road is described in this paper. A leno based woven construction was selected for the purpose. In-situ performance of the newly developed jute asphalt overlay (JAO) fabric within pavement and other two commercial A/O fabrics with different constructions was investigated. To this end, both the dry and hygrally treated samples of asphalt concrete beams (ACBs) with and without A/O fabrics were subjected to accelerated cyclic mechanical loading simulating the vehicular traffic. A comparison of crack propagation established the efficacy of JAO though it is weaker in respect of strength and modulus than one of the commercial A/O fabric used. An analysis of the fabrics exhumed from the tested ACBs revealed that JAO having grid like structure with suitable opening size help in creating proper interlocking among aggregates of the overlay and voids of the old pavement surface across the fabric within pavement and thereby the two layers of the pavement acts as a single body which resists crack growth much better beyond its level than sheet like A/O fabrics.

KEYWORDS: asphalt overlay fabric, jute, asphalt concrete beam, leno weave, grid like structure, cyclic mechanical loading

INTRODUCTION

In the context of development of infrastructure in India a very large exercise is currently underway for improving the network of roads all over the country. Among different geotextiles used in pavement rehabilitation, synthetic fibre asphalt overlay fabric is one which has been used extensively in developed countries. Traffic, temperature fluctuation and rainfall are three major factors responsible for pavement distress. The first two factors are responsible for generation and propagation of reflection cracking in the new asphalt concrete overlay and reflection cracking in new overlay allows rain water to percolate into the pavement structure weaken the underlying layers through rapid deterioration of the system. Asphalt overlay fabrics are used during rehabilitation of old cracked roads as crack-preventing system. Such fabrics are placed between new overlay and cracked pavement for preventing upward flow of crack from the old pavement to the new overlay.

The asphalt overlay fabric should be very stiff to hold the crack tips together and simultaneously be capable of absorbing asphalt so that a very strongly bonded and moisture-proof interface can be developed between the layers below and above the asphalt overlay fabric. A transition can be observed in selection of raw materials for asphalt overlay geosynthetics as well as their construction. Starting with non-woven polypropylene/ polyester paving fabrics, grids and composite structures (consisting of woven/knitted fibre glass/Kevlar grid and polypropylene non-woven fabric) are now commercially available in the market. The grid part would provide the necessary strength and stiffness to prevent deformation under load and the non-woven fabric part would impart the required asphalt-absorbency so that a very strongly bonded and moisture-proof interface can be developed between the layers below and above the asphalt overlay fabric. But, no standard asphalt overlay geosynthetics made up of natural fibres like jute has been produced so far though jute has better mechanical properties in many respects than conventional polypropylene or polyester fibres used for asphalt overlay products. Additionally, jute is eco-friendly, inexpensive and known to have good adhesion with asphalt as evident from the widespread application of bituminized jute fabric. Hence, it appears reasonable to propose that asphalt overlay fabrics can also be manufactured from jute.

[1] Post-doctoral Fellow, Department of Textile Technology, Indian Institute of Technology Delhi, INDIA. Email: mahuya.g@gmail.com
[2] Professor & Head, Department of Textile Technology, Indian Institute of Technology Delhi, INDIA. Email: pkbt1946@gmail.com
[3] Honorary Professor, Department of Civil Engineering, University College of Engineering, Osmania University, INDIA. Email: gvrao.19@gmail.com

Investigations related to suitability of jute to be used as raw material for asphalt overlay fabric have been conducted and reported elsewhere (Banerjee and Ghosh 2008; Ghosh 2006). To this end, thermal stability of jute in asphalt overlaying environment, compatibility of jute with asphalt as also its durability under hygral and enzymatic loads and the nature of jute-asphalt bonding were investigated. It was found that the strength of jute deteriorates by about 10% in hot asphalt. But, studies on jute-asphalt composites revealed that moisture damage of asphalt (matrix) and jute-asphalt interface up to the period of six months is not effective to deteriorate the mechanical property of jute encased within asphalt. Additionally, asphalt itself acts as protector for jute against bio-degradation. The co-existence of physical and chemical bonds between the two results in a very durable composite withstands hygral and enzymatic loads remarkably well. Hence, jute can be effectively used as raw material for asphalt overlay fabrics.

Consequently a 100% jute-based asphalt overlay fabric (JAO) of moderate capability suitable for low traffic roads has been developed and its in-situ performance within pavement in preventing reflective crack propagation under accelerated cyclic mechanical loading simulating traffic load investigated. Additionally, its efficacy to retard crack propagation after hygral loading, has also been evaluated through similar accelerated cyclic mechanical loading tests.

METHODOLOGY

Methodology for Preparation of JAO

An A/O fabric can retard or delay the crack propagation by holding the crack tips together. Evidently, the fabric should be firmly anchored with crack tips as well as the surrounding aggregates of the old pavement and the new overlay so that the concentrated stress generated at the crack tip due to loading can be transferred to the fabric and distributed over an area. Simultaneously, the fabric should have very high modulus so that fabric deformation remains marginal during load transfer—otherwise the whole pavement structure will disintegrate. Additionally, a moisture-proof fabric structure would help indirectly to prevent crack propagation by resisting water infiltration into the pavement structure.

It may be summarized that the asphalt overlay fabric should exhibit the following characteristics:

—A grid-like structure with suitable aperture size which would help in creating strong anchorage with the surrounding aggregates;

—This grid structure should have high modulus, i.e., moderately high breaking load with low breaking extension in both warp and weft directions to prevent deformation under load.

Additionally, the grid should be linked with an asphalt absorbent layer.

A leno-based construction made of thick and strong standard warp threads together with thin weft threads bound together by thin doup warp threads and plain woven bands of thick and strong weft and thin warp yarns inserted at proper intervals between two leno portions can yield a product, exhibiting very marginal crimp in the load bearing warp and weft ends and hence marginal extensibility in the ultimate fabric. Such a construction (Fig. 1) is proposed for the basic load bearing grid along with the required asphalt-absorbency imparted by the plain sections.

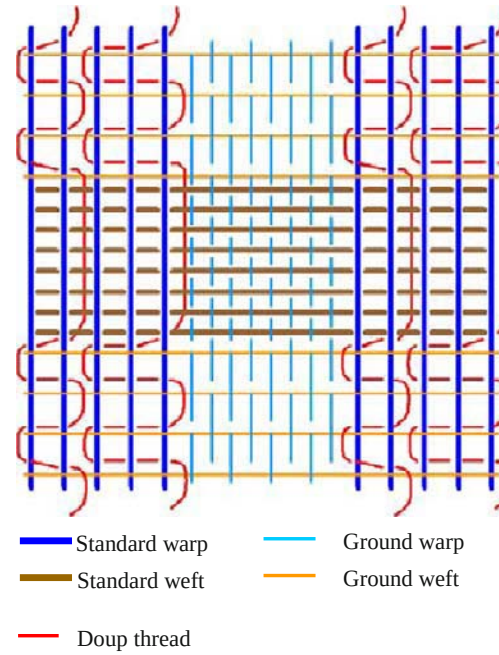

Fig.1 Structural construction of JAO

Performance Evaluation of JAO Fabric

The efficacy of a geotextile to retard the growth of reflection crack is influenced by a large number of factors such as the nature of traffic, crack spacing,overlay thickness and composition, location of geotextile, etc. (Lytton 1989). Hence, designing suitable tests for evaluating the performance of an A/O fabric can become a very complex issue. However a simplified approach adopted by Texas Transportation Institute involves determining the “fracture properties” of an overlay separately due to bending, shear and contraction. A linear combination of number of cycles to failure under these three modes have been found to relate very

well with field data pertaining to the growth of refection crack. It has also been suggested that "fracture properties" due to bending and shear are same. Hence, restricting attention to distress caused by mechanical and hygral loading reduces the focus of tests to bending and shear deformations only. Therefore, the evaluation of efficacy of JAO in retarding growth of reflection cracks due to mechanical and hygral loading can be carried out by designing cyclic mechanical loading tests involving bending and shear strains. Such cyclic mechanical loading tests can be designed in two modes namely three-point and four-point bending. Based on the concerned literature (Brown et al. 2001; Cho et al. 2004; Lytton 1989), a three-point cyclic mechanical loading test programme with semi-continuous support was planned to carry out on ACBs using a suitable MTS (Material Testing System) where the frequency and amplitude of loading could be so varied as to impose a strain rate well above that expected to be encountered on, for example a typical low traffic road, like district road in India.

Based on the literature as also requirements of accelerated test, mechanical loading domain was selected as below:

—Range of amplitude of loading: Min.: 28.79 % of breaking load of ACB in static loading. Max.: 71.21 % of breaking load of ACB in static loading;

—Ratio of minimum to maximum load during a test cycle: 0.1;

—Range of frequency of loading: Min.: 10.76 Hz Max: 19.24 Hz;

—Nature of loading: Sinusoidal.

The performance of JAO embedded ACB was tested employing the identified amplitude-frequency level combination. Simultaneously, unreinforced ACBs as well as those embedded with commercial products, namely, synthetic strain-relieving A/O fabric (PP nonwoven fabric, code named SGT) and asphalt-impregnated jute geotextile (code named JGT) were also tested under the same loading conditions to understand the effect of different types of A/O fabrics in prevention of crack propagation.

The effect of hygral loading was studied on unreinforced ACBs and ACBs embedded with JGT, JAO and SGT. To this end, beam specimens were subjected additionally to two different levels of hygral treatment by immersion under water for 15 and 30 days respectively. Subsequently, the ACBs were removed from water and subjected to the specific identified loading conditions obtained from the exploratory experimentation with JGT.

To understand the effect of construction of fabric in prevention of crack propagation the fabrics were exhumed from the tested ACBs and damage analysis was carried out.

EXPERIMENTAL PROCEDURE

Preparation of Jute Asphalt Overlay Fabric (JAO)

Two types of commercial jute yarns were chosen for weaving the fabric. The stronger one (742 tex), meant for the standard threads, was 1.4 mm thick having a breaking strength of 94 N (*CV* = 13.7%) and a breaking extension of 3.3 % (*CV* = 13.5%) while the thinner one (315 tex), meant for the doup and ground threads, was 0.75 mm thick having breaking strength of 32.7 N (*CV* = 19.5 %) and 2.3 % (*CV* = 12.1%) breaking extension. The actual photograph of JAO is shown in Fig. 2.

Fig.2 Actural photogragh of JAO (single layer)

Determination of Tensile Properties of Fabrics

Grab tensile test (ASTM D 4632-91) and Wide width tensile test (ASTM D 4595-86) were carried out on JAO and JGT, but only Grab tensile test was conducted on SGT for finding out their breaking load, elongation at break and Young's or E-modulus.

Evaluation of In-Situ Performance of Fabrics

Preparation of ACBs

Asphalt concrete mix used for the present study was a dense bituminous (or asphaltic) macadam (DBM) mixture with an asphalt content of 5.5%. The dimension of the ACBs was determined according to the particle size distribution of the aggregate mix. The maximum particle size of the main contributing section of the aggregate mix was 10 mm. The width and height of the

ACBs would be 7.5 times of the average particle size and the length would be 3 times of width. So the ACBs, as shown in Fig. 3, were prepared of dimension 225 mm (L)×75 mm (W) ×75 mm (H). A transverse notch of 5 mm depth and 3 mm base-width at the beam-centre was created to simulate a pre-existing crack in the old pavement. A/O fabric reinforcement was placed at 20 mm above the beam specimen-base for reinforced specimens.

Determination of breaking load of ACB under static condition.

For determining the breaking load of ACB with and without A/O fabric, under static loading condition, tests were conducted under 3-point bending mode using a loading frame. The deformation rate employed on ACB samples was 15 mm/min. From these tests, breaking load range of 1.08 kN to 1.47 kN was obtained and their average value was adopted as maximum load capacity of the ACBs.

Hygral treatment of ACBs

In extreme condition of monsoon in India, some areas become flooded for 2 to 3 weeks at a stretch. Hence, for investigating the effect of hygral loading on the performance of ACBs, some samples were kept immersed in water for 15 and 30 days before subjecting them to cyclic mechanical loading tests. The three levels of hygral load thus were “zero” time submerged under water (for simulating real life situation in seasons other than monsoon), 15-day water-submerged and 30-day water-submerged (for simulating flooded road condition during extremes of monsoon).

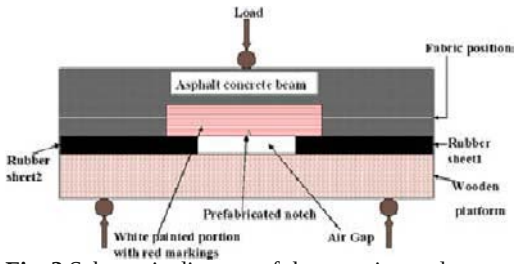

Fig. 3 Schematic diagram of the experimental set up for cyclic mechanical loading test of ABC

Cyclic mechanical loading test of ACBs

Before testing the ACBs on MTS, both the side surfaces of the beams were painted with white road-paint and marked with horizontal red lines at intervals of 5 mm up to 30 mm level above the beam-base to record the crack height with number of loading cycles during test.

The experimental set-up is shown in Fig. 3. Support was provided by two 20 mm thick layer of rubber pieces with a central gap of 50 mm and placed over a wooden base. This is to facilitate quick propagation of crack from and around the notch upwards in the event of a 3-point bending regime. The cyclic mechanical loading load was applied at the third point, as in a three-point bending test.

The crack propagation (i.e., crack height) with number of loading cycles was recorded by taking photographs with the help of a five mega pixel digital camera. In order to achieve a degree of confidence in the experimental data, tests for each combination of mechanical and hygral loading parameters were repeated and the average was chosen as the response value.

Determination of extent of damage in the exhumed A/O samples

A/O fabric samples were exhumed from the ACBs by softening the beam through heat. Subsequently, the asphalt coated fabric samples were cleaned several times with petrol so that the damages were clearly visible. Photographs of cleaned and dried samples were taken for damage analysis.

RESULTS AND DISCUSSIONS

Tensile Properties of JAO

The JAO was tested by subjecting it to Grab and Wide width tensile tests. The results of the tests are shown in Table 1. While comparing the breaking strength, elongation and modulus values of JGT and JAO, it is observed that JGT is stronger and stiffer than JAO and elongation is lower.

Grid Size

The fabric was woven in such a manner that the doup threads remained idle for eight cycles and were made to switch sides around the strands of standard ends for four cycles. During the eight cycles of plain weaving, the tension in the doup threads remained stable and the resultant grid created between pairs of columns of standard ends exhibit the range of 23 mm—20 mm in length direction and 15 mm—16 mm in width direction. However, during the subsequent four cycles, the tension in the doup threads rose sharply during the beating up process, creating openings within the two columns of strands as also between the neighbouring pairs of columns. The opening size created within the pairs of columns exhibit the range of 4 mm to 7 mm in length direction and 3 mm to 4 mm in the width direction.

Hence the resultant fabric exhibits a distribution of grids between small ones measuring 4 mm×4 mm to

large ones of 23 mm×16 mm.

Table 1 Tensile properties of asphalt overlay fabrics

Type of test	A/O fabric	Breaking load		Breaking elongation %		E-modulus MPa	
		Warp-way	Weft-way	Warp-way	Weft-way	Warp-way	Weft-way
Grab	JAO	0.98 kN	0.84 kN	9.4	9	104.9	96.1
	JGT	1.2 kN	1.19 kN	6.6	8.7	183.5	324
	SGT	0.56 kN	0.53 kN	88.2	71.8	28.4	37.2
Wide width	JAO	24.2 kN/m	24.8 kN/m	5.1	4.9	79.6	107.0
	JGT	25.6 kN/m	27.1 kN/m	2.9	4.9	343	263.9

Performance of A/O Fabrics in ACB under Cyclic Mechanical Loading and Hygral Loading

For testing the efficacy of the JAO, JGT and SGT fabrics in ACB vis-à-vis unreinforced ACBs, the load was kept at the critical value 0.78 kN while a moderate frequency of 15 Hz was chosen. This would permit a reasonable number of test cycles to failure, both from the point of view of accuracy as also test duration.

Experimental results reveal that under all experimental conditions, ACBs embedded with JAO do not exhibit any crack propagation beyond the level at which the JAO is placed within the ACB. Moreover, in many cases the crack initiated at the notch did not grow at all. A typical photograph of crack propagation in JAO reinforced ACB (Fig. 4) confirms this observation.

The ACBs embedded with JGT and SGT exhibited growth of crack well beyond the A/O layer (depicted in Fig. 5 and Fig. 6). The JGT appears to delay this growth better than the SGT.

The experimental data pertaining to hygral loading of unreinforced ACBs exhibit a sharp drop in resistance to crack propagation after a 15-day immersion while the 30-day immersed samples exhibit stiffening that matches that of the dry control sample. The JGT reinforced ACBs exhibit a trend that shows continuous improvement in resistance to crack propagation with increasing duration of hygral loading. However the JAO reinforced ACBs show the best results indicating no development of crack whatsoever, both after 15 and 30-day immersion.

Studies on the Exhumed A/O Samples

On visual observation, the JGT samples were found to have been extensively punctured, both when the ACB was subjected to low peak load and low frequency as also to high peak load and high frequency. However in the latter case some of the damaged portions are fairly large. The JAO sample also exhibits extensive damage although the nature of damage does not have any bearing to the peak load and frequency. The SGT sample on the other hand exhibits very large number of only pin holes surrounded by fused and darkened fabric portions.

The history of typical damages on the three types of A/O samples is listed in Table 2. It is observed from the Table 2 that the extent of crack propagation in both ACBs reinforced with the JGT samples is equal although the time (number of cycles) taken for the crack flow is much higher when the peak load and frequency are lower. The ACB reinforced with JAO sample on the other hand does not show any crack growth at all while the ACB reinforced with SGT exhibits easy growth of crack. Hence the extent of fabric damage or the absence of it does not have any bearing to crack growth. Moreover it is also evident that the raw fabric strength is not decisive in preventing crack propagation as the ACBs reinforced with weaker JAO do not show any crack growth whereas those with the stronger JGT exhibit prominent reflection crack.

Role of A/O Fabric in Preventing Growth of Reflection Crack

From the results of the experiments described in the foregoing, it is possible to conclude that ACBs reinforced by a grid like A/O fabric with flexible strands perform better in preventing crack propagation as compared to sheet like fabrics. Evidently the openings in the grid permit the aggregate particles from the overlay to pass through the grid openings and enter suitable voids in the damaged aggregates layer below the A/O fabric. On solidifying, these particles bridge the two

Table 2 Exhumed sample history of different A/O fabrics

Test conditions		Type of fabric	Observations			
Max. peak load (kN)	Frequency (Hz)		No. of installation damage	No. of cyclic mechanical loading damage	Length of crack (mm)	No. of cycles
0.42	12	JGT	8	0	30	15786
0.78	18	JGT	12	2	30	3184
0.78	15	SGT	Innumerable	0	30	6297
0.78	15	JAO	Not distinguishable from each other		0	19865

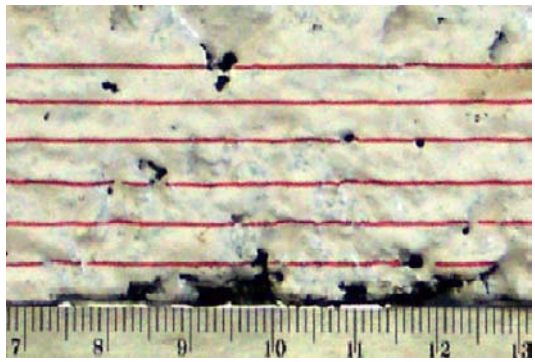

Fig. 4 (a) Front view of ACB with JAO before cyclic mechanical loading, at max. peak load = 0.78 kN, frequency = 15 Hz, No. of cycles = 19865

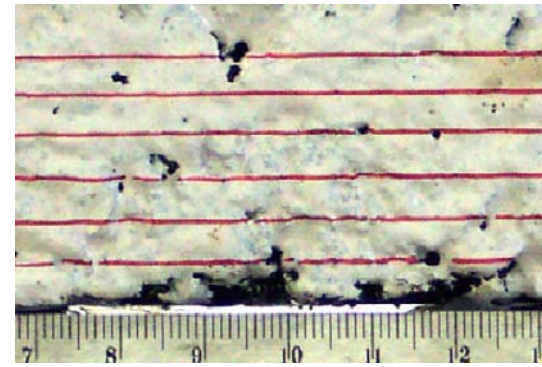

Fig. 4 (b) Front view of ACB with JAO after cyclic mechanical loading, at max. peak load = 0.78 kN, frequency = 15 Hz, No. of cycles = 19865

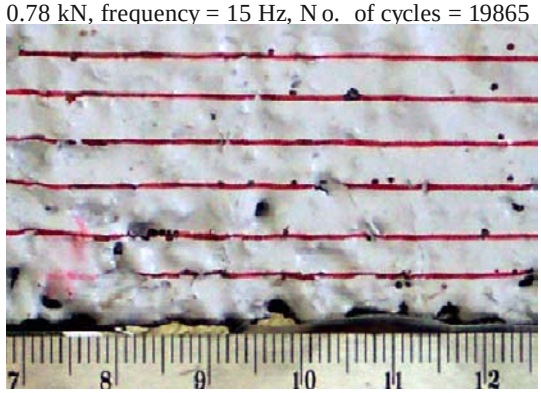

Fig. 5(a) Front view of ACB with JGT before cyclic mechanical loading, at max. peak load = 0.85 kN, frequency = 15 Hz, No of cycles = 7483

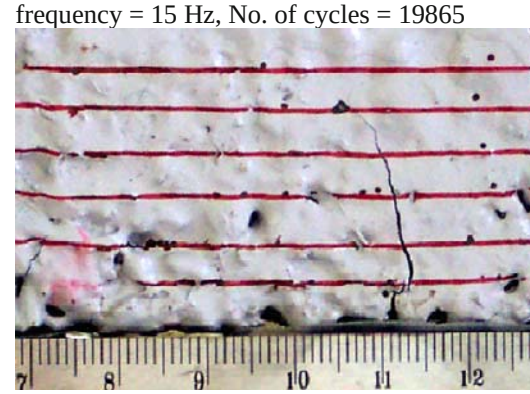

Fig. 5(b) Front view of ACB with JGT after cyclic mechanical loading, at max. peak load = 0.85 kN, frequency =15 Hz, No of cycles = 7483

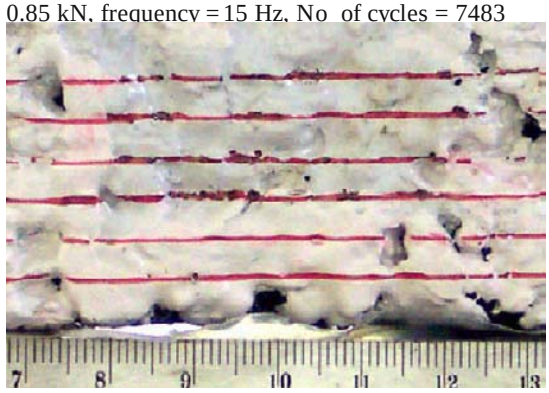

Fig. 6(a) Front view of ACB with SGT before cyclic mechanical loading, at max. peak load = 0.78 kN, frequency = 15 Hz, No. of cycles = 6297

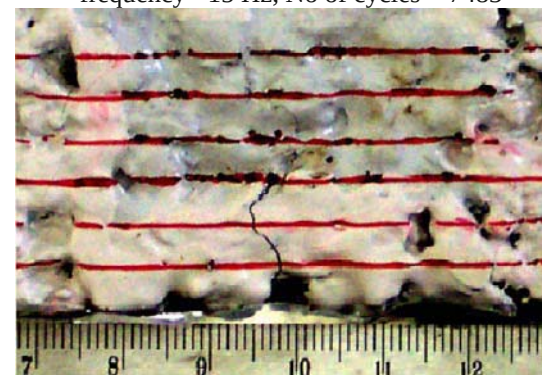

Fig. 6(b) Front view of ACB with SGT after cyclic mechanical loading, at max. peak load = 0.78 kN, frequency = 15 Hz, No. of cycles = 6297

layers of aggregate across the fabric permitting the entire beam to behave as continuum. Moreover such linkages across the fabric enable a better utilization of fabric strength during distortion. In the process of passing through the grid openings, some of the strands of A/O fabric do get damaged or are pushed apart. Nonetheless, the remaining load bearing strands contribute significantly to the overall strength of the beam as evidenced by lack of any crack growth observed from the experiments conducted.

The sheet like fabrics, whether the high strength low elongation JGT or the low strength high elongation SGT, did not permit proper interlocking of aggregate particles across the fabric. Some particles did puncture the JGT fabric at isolated points but could not lodge properly within the voids across, whereas the only damage experienced by the SGT fabric was due to localized melting of fibres caused by some of the hot particles of the aggregate. Consequently the performance of both these types of A/O fabrics has been inferior to that of the grid like fabric.

It is thus necessary to design an A/O fabric in the form of a grid in keeping with the particles size of the aggregate of the overlay so that wherever possible the particles of larger size can pass easily through the

openings of the grid and from a bridge with the cracked layer below, without causing significant damage to the fabric. Hence the pore size of the grid should be chosen keeping the larger particles of the aggregate in view.

SUMMARY AND CONCLUSION

A leno-based woven construction was chosen for developing A/O fabric of moderate capability made 100% out of jute which is suitable for low traffic roads. Grab and wide-width tensile tests were performed to asses the tensile properties of the newly developed JAO. Performance evaluation of JAO in preventing crack propagation within pavement was carried out by means of cyclic mechanical testing of dry and hygrally treated ACBs reinforced with JAO along with other two commercial A/O fabrics, viz. JGT and SGT. Following are the main findings and broad conclusions from the study:

(1)JAO exhibits a distribution of grid openings between small ones measuring 4 mm×4 mm to large ones of 23 mm ×16 mm.

(2) Though the strength and modulus values of JGT are higher than those of JAO, the latter performs much better in preventing crack propagation within ACB than the former under dry as well as under hygrally treated conditions. A grid like structure of JAO helps in proper interlocking among the aggregates of the overlay and the voids of the old pavement surface below the fabric. Consequently, the two layers above and below the A/O fabric behave as a continuous system. On the contrary, sheet-like structure of JGT and SGT do not permit proper interlocking across the fabric and consequently show very poor performance.

(3) Additionally, the opening size of the grids of an A/O fabric should be compatible with the larger aggregates of the AC mix used in pavement so that those particles can pass easily through the openings of the grid without causing significant damage to the fabric.

Hence, the following specific conclusions can be drawn:

(1) It is not the superior tensile properties but the suitable construction of the A/O fabric which plays main role in creating proper anchorage between overlay and old pavement surface and thereby prevents crack propagation into the overlay. A grid like structure of JAO is therefore more suitable for proper interlocking than sheet like fabric structures.

(2) The opening size of the grids of an A/O fabric should be compatible with the larger aggregates of the AC mix used in pavement and plays a vital role in maintaining integrity of the overlaid pavement system through assisting in creating proper interlocking with minimal fabric damage.

REFERENCES

American Society for Testing and Materials, Designation D 4632-91 (Reapproved 1996), Standard test method for grab breaking load and elongation of geotextiles

American Society for Testing and Materials, Designation D 4595-86 (Reapproved 1994), Standard test method for tensile properties of geotextiles by the wide-width strip method

Banerjee PK, Ghosh M (2008) Studies on jute-asphalt composites. Accepted for publication in J. Appl. Polym. Sci

Brown SF, Thom NH, Sanders PJ (2001) A study of grid reinforced asphalt to combat reflection cracking, Asphalt Paving Tech 70: 543-570

Cho SD, Kim NH, Lee DY, Kim JH (2004) A study on the performance of crack resistance for glassfibre-sheet reinforced asphalt pavement, in: Shim JB, Yoo C, Jeon HY (Eds.), Proceedings, 3rd Asian Regional Conference on Geosynthetics-Now and Future of Geosynthetics in Civil Engineering. Korean Geo-synthetics Society, Korea: 453-462

Ghosh M (2006) Development of Jute-Based Asphalt Overlay Fabric, Ph. D. thesis, 3rd and 5th Chapters, Indian Institute of Technology, Delhi, India

Lytton RL (1989) Use of geotextiles for reinforcement and strain relief in asphalt concrete. Geotext. & Geomem 8: 217-237

Geosynthetic-Pile Support Systems Sand Geocell Usage

GERMAN RECOMMENDATIONS FOR REINFORCED EMBANKMENTS ON PILE-SIMILAR ELEMENTS

M. Raithel[1], A. Kirchner[1] and H.G. Kempfert[2]

ABSTRACT: The construction of embankments on soft underground is a common problem. In recent years a new kind of foundation, the so-called "geosynthetic reinforced pile-supported embankment", was established. Until now the system behaviour can only be described analytically by simplified geomechanical models. Furthermore, there are simplified calculation procedures, which allow the dimensioning of the geosynthetic reinforcement. In the course of the revision of the EBGEO (German Recommendations for Geosynthetic Reinforced Earth Structures), new recommendations for soil reinforcements above pile-similar elements under static loading were worked out. These new developed analytical methods represent a new State-of-the-Art and enable a realistic and suitable approximation of the bearing behaviour of the composite structure.

KEYWORDS: embankments, pile-similar element, EBGEO

INTRODUCTION

Soil improvement and reinforcement techniques have undergone a significant development during the last decade, especially as a result of the increasing need to construct on soft ground providing economical solutions. Designing structures, such as buildings, walls or embankments on soft soil raises several concerns.

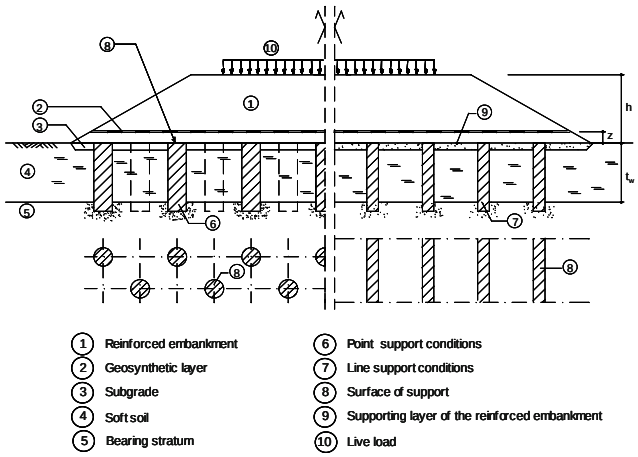

Fig. 1 Geosynthetic-reinforced pile-supported embankment

They are related to bearing capacity failures, intolerable settlements, large lateral pressure and movement, and global or local instability. A variety of techniques may be used to address the above concerns. These include pre-loading the soft soil, using light-weight fill, soil excavation and replacement, geo-synthetic reinforcement and soil improvement techniques. In recent years a new kind of foundation, the so-called “geosynthetic-reinforced pile-supported embank-ment” was established (Fig. 1). The pile elements (e.g., concrete piles, cemented stone columns, walls etc.) are placed in a regular pattern through the soft soil down to a lower load-bearing stratum.

Three possible support conditions are illustrated in Fig. 2. Piles are typically arranged in rectangular or triangular patterns in practice.

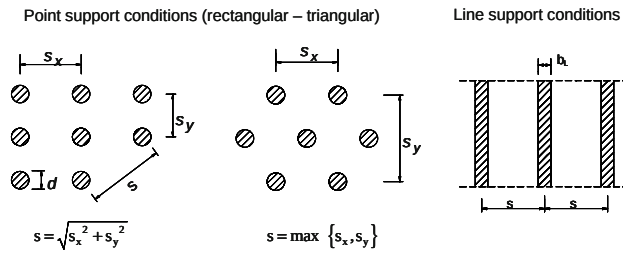

Fig. 2 Support conditions and definition of the distances

Above the pile heads, the reinforcement of one or more layers of geosynthetics (mostly geogrids) is placed.

In Germany the geosynthetic-reinforced pile-supported systems have been used for several appli-cations, especially for highway and railroad embank-ments (Alexiew and Gartung 1999; Alexiew 2001).

[1] Kempfert + Partner Geotechnical Consultants, Wuerzburg, GERMANY. Email: wue@kup-geotechnik.de
[2] Professor, Institute of Geotechnics, University of Kassel, GERMANY. Email: ks@kup-geotechnik.de

The systems have proved to perform well regarding both bearing capacity and serviceability if designed and constructed in an appropriate (Alexiew and Gartung 1999).

Until now the system behaviour can be described analytically only by simplified geomechanical models. Furthermore, there are simplified calculation procedures, which allow the dimensioning of the geosynthetic reinforcement (e.g. Hewlett and Randolph 1988; BS 8006 1995; Kempfert et al., 1997; Alexiew 2002). To examine the bearing mechanisms in the system and to derive a better analytical model, a research project has taken place at the Institute of Geotechnics, University of Kassel (Kempfert et al. 1999; Zaeske 2001; Zaeske and Kempfert 2002). The developed design procedure will be introduced soon into Chapter 6.9 "Reinforced earth structures on point- or line-shaped bearing elements" (Empfehlung 6.9 2003) of the new edition of the EBGEO (German Recommendations for Geosynthetic Reinforcement). This new analytical method represents a new State-of-the-Art. It is believed to be more precise and realistic than the "older" procedures available, which was confirmed by experiments (Zaeske 2001); at the same time it is more sophisticated and like other procedures available limited mostly to non-cohesive fills. An overview of common procedures today is given e.g. in (Alexiew 2002).

The general load transfer mechanisms, model test results and the new method of calculation and the construction recommendations for this kind of foundation as recommended in Chapter 6.9 of the EBGEO will be described shortly.

LOAD TRANSFER MECHANISMS

The stress relief of the soft soil results from an arching effect in the reinforced embankment over the pile heads and a membrane effect of the geosynthetic reinforcement. Due to the higher stiffness of the piles in relation to the surrounding soft soil, the vertical stresses from the embankment are concentrated on the piles, simultaneously soil arching develops as a result of differential settlements between the stiff pile heads and the soft soil between them. The 3D-arches span the soft soil and the applied load is transferred onto the piles and then to the bearing stratum. The redistribution of loads in the embankment depends on the systems geometry, the strength of embankment soil and the stiffness of "piles".

A modified stress-distribution theory was developed (Zaeske 2001). Additionally, a concept to take into account the supporting soft soil upwards counter-pressure between the piles in a deformation-related way was introduced including the tensile stiffness of reinforcement and the oedometric modulus of soft soil. Differential equations had to be developed to reflect this interaction (Zaeske 2001) (Fig. 3).

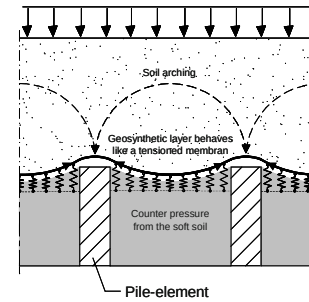

Fig. 3 Mechanisms of load transfer and interaction

RESULTS OF MODEL TESTS UNDER STATIC LOADING

Three-dimensional model tests in a scale of 1:3 were carried out to investigate the bearing and deformation behaviour and to check and verify the concept and theory mentioned above. A group of four piles was placed in a weak soil of peat in a rectangular grid, above which a reinforced or unreinforced sand fill was placed in different heights (Fig. 4).

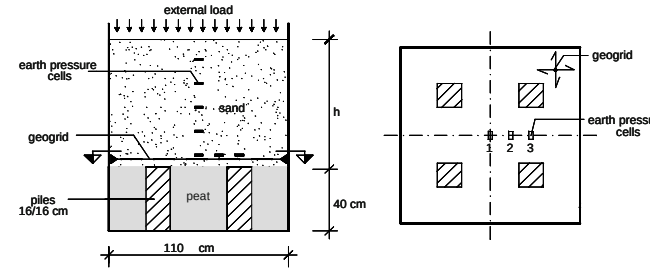

Fig. 4 Typical 1:3 scale test arrangement

The stress distribution in the reinforced sand layer was recorded by pressure cells. The part of the load carried by the piles was measured by load-cells and allowed a comparison with the measured stress field in the sand. Under static loading the dependency of the stress transfer on the geometric boundary conditions and the shear strength of the sand fill was verified.

Similar to field measurements, the strains in the geogrid were found to be relatively small, provided that reaction stress of the underlying soil between the rigid pile elements is mobilised. In addition to the model tests, numerical investigations with the finite element method (FEM) were performed for static conditions. The evaluation of the FE-calculations resulted in further information on the stress distribution in the reinforcing layer and the resulting load transfer onto the piles.

After these verifications, the new method became part of Chapter 6.9 of the new edition of the EBGEO

(draft) and is explained in the following chapter.

DESIGN RECOMMMENDATION EBGEO

The design procedure recommended in Chapter 6.9 of the EBGEO is divided into two steps:

In the first step the load/stress distribution in the embankment is evaluated without considering any geosynthetic reinforcement, which results in the vertical stresses on top of the piles ($\sigma_{zs,k}$) and on the soft subsoil between them ($\sigma_{zo,k}$). The analytical model is based on the lower bound theorem of the plasticity theory and results from pretended directions of the stress trajectories in the reinforced soil body. According to the numerical and experimental results the stress state in the reinforced embankment is divided into a zone, where the earth pressure at rest can be assumed, and an arching region, where the stress redistribution takes place (Fig. 5). Eq. 1 shows the differential equation derived from the equilibrium of forces of the three-dimensional soil element in radial direction (Fig. 6).

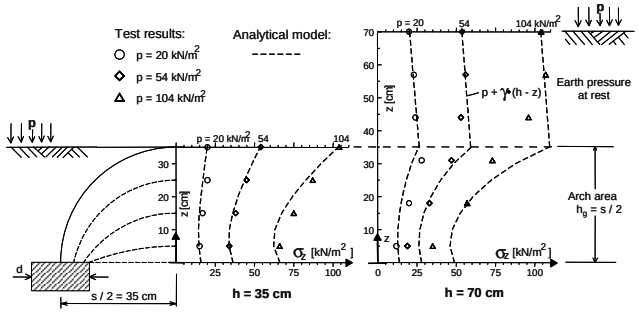

Fig. 5 Test results versus analytical model

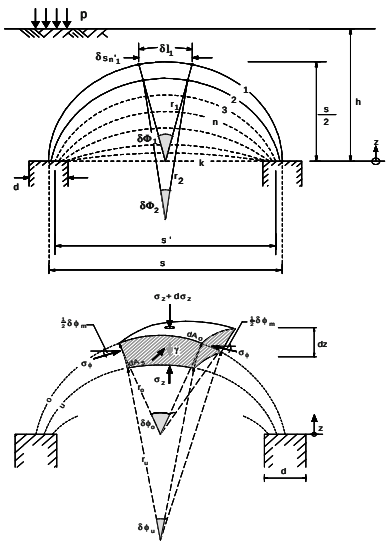

$$-\sigma_z \cdot dA_u + (\sigma_z + d\sigma_z) \cdot dA_o - 4 \cdot \sigma_\Phi \cdot dA_s \cdot \sin\left(\frac{\delta\Phi_m}{2}\right) + \gamma \cdot dV = 0 \qquad (1)$$

Fig. 6 "Arching" (Zaeske 2001; Zeaske and Kempfert 2002)

The solution of the equation gives the vertical stress $\sigma_z(z)$ inside the arch. The vertical pressure on the soft soil $\sigma_{zo,k}$ results from the limit $z \rightarrow 0$, Eq. 2. For more convenience, $\sigma_{zo,k}$ can also be derived from dimensionless design graphs (e.g., Fig. 7 for $\varphi'_k = 30°$). In the second step, the vertical pressure $\sigma_{zo,k}$ is applied to the geosynthetic reinforcement as external load.

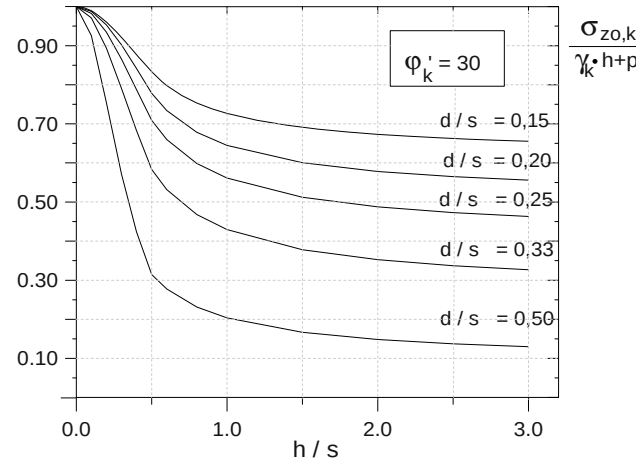

Fig. 7 Vertical stress $\sigma_{zo,k}$ on the soft soil

To predict the stresses in the reinforcement, an analytical model is applied based on the theory of elastically embedded membranes (Zaeske 2001). The maximum strain in reinforcement (i.e., the maximum tensile force) is concentrated in the band bridging two neighboured piles (despite the common engineering sense, it was confirmed by the experimental work as well). Therefore the analytical model assumes that the maximum stress in the geosynthetic membrane takes place within the width $b_{Ers.}$ and may be calculated based on a planar system (Fig. 8). Biaxial geogrids must be analysed both in x- and y-direction.

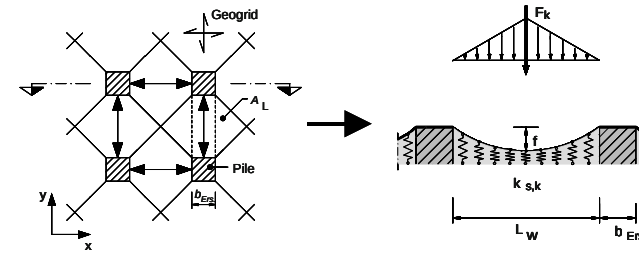

Fig. 8 Load transfer and simplified planar (2D) bearing system (Zaeske 2001; Zeaske and Kempfert 2002)

The resulting triangular vertical strip load F_k on the geogrid strip is calculated from the pressure $\sigma_{zo,k}$ and the loaded area A_L (Fig. 9).

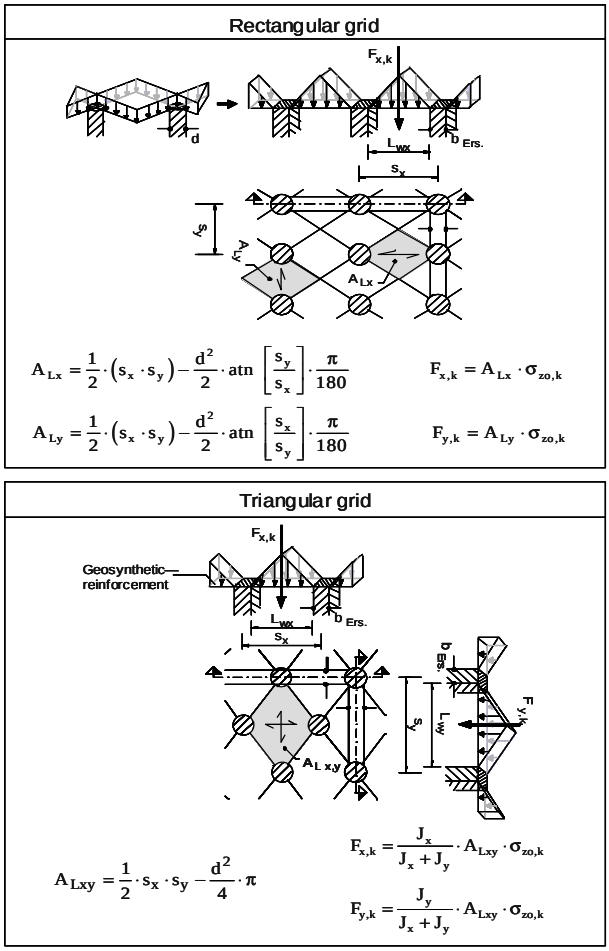

Fig. 9 Calculation of the resulting force F_k assigned to the load influence area A_L

The influence of the bearing effect of the soft soil between piles is considered by using a modulus of subgrade reaction.

The maximum strain in the geosynthetic reinforcement results from the tensile stiffness J_k of the geosynthetic, the modulus of subgrade reaction $k_{s,k}$ of the soft soil, the total vertical load F_k and the dimensions b_{Ers} and L_w. Since all geosynthetics tend to creep, the tensile modulus J_k is time-dependent and has to be red out from the real isochrones of the geosynthetic reinforcement; the latter is essential.

In Empfehlung 6.9 (2003), the value of σ_k can be taken from a dimensionless design graphs, see Fig. 10). Finally, the tensile force in the reinforcement $E_{M,k}$ (M = membrane) can be calculated directly as a function of the strain of the geosynthetic, Eq. 5. For two geosynthetic reinforcements the calculated force is divided with respect to the ratio of their tensile moduli.

By an inclined surface of the reinforced embankment geosynthetics are stressed by additional horizontal forces. The lateral thrust can be considered on the safer side assuming an active earth pressure condition without any support by "piles" or soft soil (Zaeske 2001, 2002).

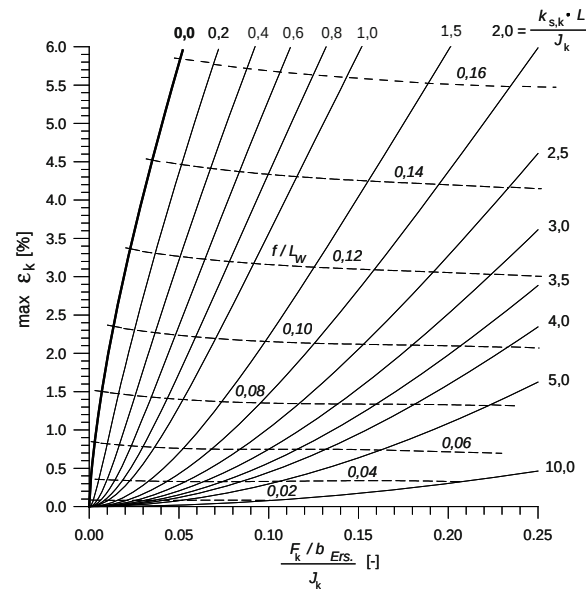

J_k	tensile stiffness of the geogrid	[kN/m]
L_w	clear distance = (s-d)	[m]
$k_{s,k}$	modulus of subgrade reaction	[kN/m³]

$$k_{s,k} = \frac{E_{s,k}}{t_W} \quad (3)$$

$b_{Ers.}$ width of support [m]

$$b_{Ers.} = \frac{1}{2}\cdot d\cdot\sqrt{\pi} \quad (4)$$

Stess in the reinforcement:

$$E_{M,k} = \varepsilon_k \cdot J_k \quad (5)$$

Fig. 10 Maximum strain in the geosynthetic reinforcement

CONSTRUCTION RECOMMENDATIONS

Based on German and international experience with geosynthetic-reinforced pile-supported embankments, practical reasons, experimental results and the validity of the analytical model following recommendations are established:

The center-to-center distance s and the pile diameter d of the piles resp. pile caps should be chosen as follows:

- $(s-d) \le 3.0$ m resp. $(s-b_L) \le 3.0$ m: in the case of static loads
- $(s-d) \le 2.5$ m resp. $(s-b_L) \le 2.5$: in the case of heavy live loads
- $d / s \ge 0.15$ resp. $b_L / s \ge 0.15$
- $(s-d) \le 1.4\ (h-z)$

The distance between the reinforcement layer and the plane of the pile/column/wall heads should be as small as possible, in order to achieve maximum efficiency of the geosynthetic membrane. However, it is recommended to have a safe distance (interlayer) between the lowest

reinforcement and the pile heads in order to prevent a structural damage of the reinforcement because of shearing at the edge of the pile heads.

- maximum two reinforcement layers;
- $z \leq 0.15$ m for single layer reinforcement;
- $z \leq 0.30$ m for two layers reinforcement;
- for two layers the distance between the geosynthetic layers should be 15 to 30 cm;
- design value of the tensile strength; $R_{Bd} \geq 30$ kN/m; ultimate strain ≤ 12 %;
- Overlapping is generally allowed, but only just above the pile (caps) and only in the secondary bearing direction; length of overlapping ≥ *d*.

PROJECT "RAILWAY HAMBURG – BERLIN"

As part of the improvement of the existing railway line Hamburg-Berlin, the section Büchen-Hamburg and the section Paulinenaue-Friesack were upgraded in 2003 by the German Rail company (Deutsche Bahn AG), to allow a train speed of 230 km/h. Due to very soft organic soil layers (peat and mud) and the insufficient bearing capacity of the embankment, an improvement of the railway embankment was necessary in this sections. As improvement method a reinforcement of the embankment with geogrids over columns, installed with the Mixed-in-Place method (MIP, can be characterized as a wet deep mixing technique) was executed (Fig. 11).

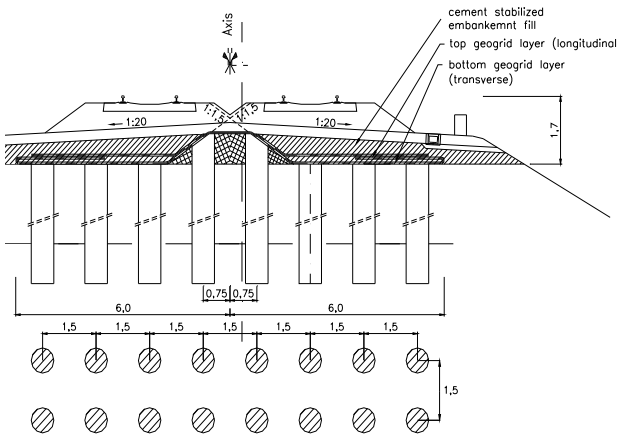

Fig. 11 Foundation system Section Büchen-Hamburg

Between two improved sections, better soil conditions are given, therefore no columns were installed. In this 75 m long part only a reinforcement of the embankment with two Geogrids was executed. In the sections with columns, underneath a 3—5 m fill of medium dense packed silty and gravely sand with slag and organic admixtures, very soft peat and mud layers, with a total thickness of 0.5—2 m, are present. The peat has a water content of 80%—330% and an organic content between 25% and 80%. Underneath these soft layers, slightly silty sand layers with a thickness up to 8 m are present, which are medium dense packed. At the base of the sand layers, boulder clay is present, which has a soft to stiff consistency and a water content of 10%—20%.

During the improvement work, a single track operation at 90 km/h was maintained. The operated track was secured by sloping the ballast bed, the protective layer and the embankment (Fig. 12). This made possible the construction of the geogrid reinforcement across the total embankment width. The MIP-columns were installed after the excavation of the protective layer. Prior to the setting of the MIP material, the columns generally were shortened to a level of 1.7 m below top of rail during the following excavation stage. The columns adjacent to the embankment axis, however, couldn't be shortened to 1.7 m below the rail level, which resulted in a cover of less than 1.5 m on top of the columns. Nevertheless, this option was favoured over a sheet pile wall, for instance, since the retracting of sheet piles could lead to unexpected settlements.

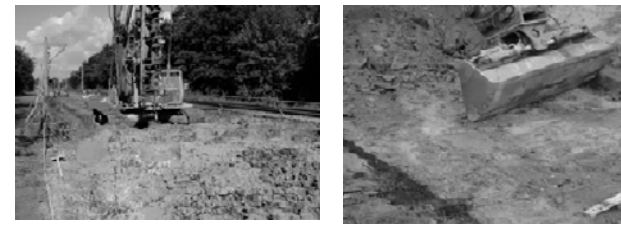

Fig. 12 Installation of MIP-columns (left), shortening of the MIP-columns (right)

The MIP-columns were installed using a single auger (Fig. 12). A cement slurry is injected continuously into the soil during the penetration as well as during the retrieval of the auger. Due to the rotation of the auger, the cement slurry is mixed with the soil. The MIP-technique is free of vibrations and displacements and therefore had no effect on the ongoing railway traffic on the other track. The cement columns (diameter 0.63 m) were installed in a square 1.5×1.5 m grid. The composition of the binder (water, cement and bentonite) and the water/binder ratio (approx. 1.0) was determined in laboratory tests on trial mixed samples. During the 1st improvement stage (track Hamburg-Berlin), approx. 800 l/m^3 binder were mixed into the soil. During the 2nd stage (track Berlin-Hamburg), the binder was mixed into the soil to the extent where a homogenous soil/binder mixture was obtained. This resulted in a variable, soil dependant binder quantity. The depth of the columns was determined on the basis of cone penetration tests prior to column installation.

On top of the MIP-columns two layers of Fortrac® PVA geogrid type M 400/30-30 were placed (Fig. 11). Since the geogrids are loaded in longitudinal direction only, the short-term tensile strength in transverse direction was put at only 30 kN/m, whereas the required short-term tensile strength in longitudinal direction was put at 400 kN/m.

The 1st geogrid layer was placed in transverse direction directly on top of the MIP-columns. This geogrid was rolled up near the embankment axis during the 1st construction stage, and later laid across the whole embankment in the 2nd stage. The 2nd geogrid layer was placed in longitudinal direction (Fig. 11).

To obtain a uniform bearing platform for the ballast bed, 2.5%—3% cement was added to the filling material. The top of this cement stabilization was roughened to ensure a sufficient friction with the upper protective layer. To avoid an influence of hydrolysis of the cement, polyvinylalcohol was used as geogrid material.

The settlement behaviour of the tracks was monitored by means of geodetic measurements of the outer rail of both tracks. The measurements were conducted in 3 measurement sections each 20 m in consisting of 5 measuring points with a spacing of 5 m. These measurement sections were set up at locations with unfavourable soil conditions. The results of the settlement measurements over 6 months of train operation are presented in Fig. 13. On both tracks the train speed was up to 160 km/h. The measurements show, that the track Hamburg-Berlin has settled up to 7 mm in a period of 6 months after reopening the track. This settlement can be considered as small since usually a settlement of 10 mm—15 mm will occur, due to compaction of the ballast bed, the protective layer and embankment, even if the soil conditions are favourable. Also, it has to be considered, that the geogrids have to deform slightly to become active.

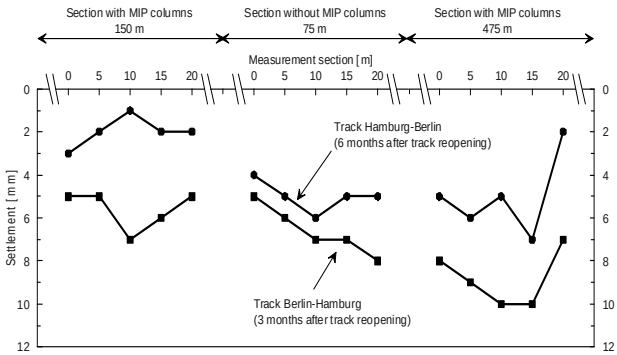

Fig. 13 Settlement measurements

REFERENCES

Alexiew D, Gartung E (1999) Geogrid reinforced railway embankment on piles—performance monitoring 1994-1998. Proc. 1st South American Symposium on Geosynthetics, Rio de Janeiro: 403-411

Alexiew D, Vogel W (2001) Railroads on piled embankments in Germany: Milestone projects. In: Landmarks in Earth Reinforcement. Swets & Zeitlinger: 185-190

Alexiew D (2002) Piled embankments design: methods and case studies. (Progettazione di rilevati poggiati su pali: metodologie ed esempi di casi reali). Proc. XV Italian Conference on Geosynthetics, Bologna, 16 October 2002

BS 8006 (1995) Code of Practice for Strengthened/ Reinforced Soils and Other Fills. British Standard Institution

Hewlett WJ, Randolph MF (1988) Analysis of piled embankments. Ground Engineering 21: 12-17

Kempfert HG, Stadel M, Zaeske D (1997) Berechnung von geokunststoff—Bewehrten Tragschichten über Pfahlelementen. Bautechnik, Jahrgang 75, Heft 12: 818-825

Kempfert HG, Zaeske D, Alexiew D (1999) Interactions in reinforced bearing layers over partial supported underground. Proc. of the 12th ECSMGE, Amsterdam, 1999. Balkema, Rotterdam: 1527-1532

Zaeske D (2001) Zur Wirkungsweise von unbewehrten und bewehrten mineralischen Tragschichten über pfahlartigen Gründungselementen. Schriftenreihe Geotechnik, Universität Gh-Kassel, Heft 10

Zaeske D, Kempfert HG (2002) Berechnung und Wirkungsweise von unbewehrten und bewehrten mineralischen Tragschichten auf punkt- und linienförmigen Traggliedern. Bauingenieur, Band 77

Empfehlung 6.9: Bewehrte Erdkörper auf Punkt—oder Linienförmigen Traggliedern, Entwurf September 2003 (2003). Kapitel 6.9 für die Empfehlungen für Bewehrungen aus Geokunststoffen (EBGEO) (Draft of Chapter 6.9 of the new edition of the German Recommendations for Geosynthetic Reinforcement)

DESIGN METHODS FOR PILE SUPPORTED BASAL REINFORCED EMBANKMENTS OVER SOFT CLAY

A.D. Gharpure[1], M. Korulla[2], P.V. Jayakrishnan[3], M. Scotto[4] and P. Naughton[5]

ABSTRACT: The piled embankment technique allows the time bound construction of high embankments with subsequent control of post construction settlements. A polymer based basal reinforcement is often used to span across the pile tops to distribute the load and maximize the economic benefits of piles installed in soft foundations. There are different methods for the design of piled embankments viz. BS 8006 Method, Russell Design Method, Empfehlung 6.9(Kempfert et al.) Method. BS 8006 assumes that all of the embankment loading will be transferred to the piles down to a firm stratum through the basal reinforcements. In the Russell design method a parameter called stress reduction ratio is defined as the average stress at the base of the embankment between the pile caps relative to the stress at the base of the embankment with no piles present. The Russell design method allows for both primary and secondary reinforcement to be installed. The third method is the German recommended procedure for designing embankments over piles. This design method calculates the tension in the reinforcement using the theory of elastically embedded tension membranes. The support from the subsoil is also considered in terms of the modulus of subgrade reaction. The present paper is an attempt to make a comparison between the three methods and to suggest the adaptability of each method in specific situations.

KEYWORDS: pile, embankment, basal reinforcement, soft soil

INTRODUCTION

When planning embankments over soft foundation soil, geotechnical engineers encounter the problems of poor bearing pressure, excessive differential settlement and lateral sliding instability. Many of these uncertainties associated with the soft soils have been engineered in the recent past with innovative ground improvement techniques. If the construction of the embankment has to be done over highly compressible clay deposits, basal reinforced pile embankment will pose distinct advantages over conventional consolidation methods .It enables the construction of embankment without much time lag and with minimum post construction settlements (Fig. 1).

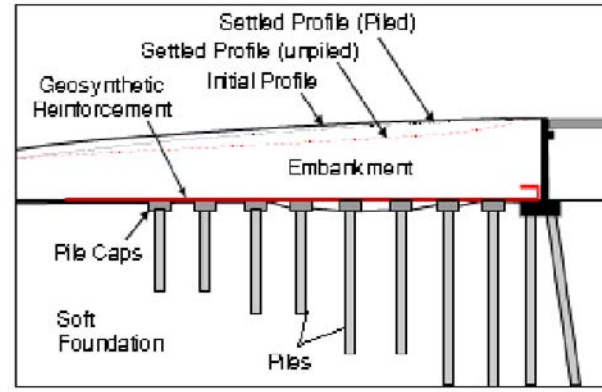

Fig. 1 Longitudinal section of typical geosynthetic reinforced piled embankment

In piled embankments, piles are installed through the soft subsoil deposit and generally rest on hard end bearing stratum. Over the pile, a polymeric reinforcement shall be placed to transfer the load of the embankment (partly or fully) to the piles (Figs. 2 and 3). It is

[1] COO, Maccaferri Environmental Solutions Pvt. Ltd., INDIA. Email: agharpure@maccaferri.co.in
[2] G.M –Designs, Maccaferri Environmental Solutions Pvt. Ltd., INDIA. Email: minikorulla@maccaferri.co.in
[3] Sr. Mgr –Designs, Maccaferri Environmental Solutions Pvt. Ltd., INDIA. Email: jaywdc@maccaferri.co.in
[4] International Geosynthetics Manager, Officine Maccaferri, ITALY. Email: moreno.scotto@infinito.in
[5] School of Engineering, Institute of Technology, Sligo, IRELAND. Email: patnaughton@eircom.net

approximated that the relative movement between sub soil and piled embankment will cause an arching action. This will transfer bulk of the load from embankment to the piles. Basal Reinforcements helps in making the system cost effective by increasing the pile spacing and decreasing the pile diameter by sharing the load. From a survey of various projects (Rutugandha . 2004) it was found that in conventional pile supported embankments, the percentage coverage of the pile caps over the total foundation area is 60%—70% and it can be reduced to 10%—20% by inclusion of a properly designed basal reinforcement.

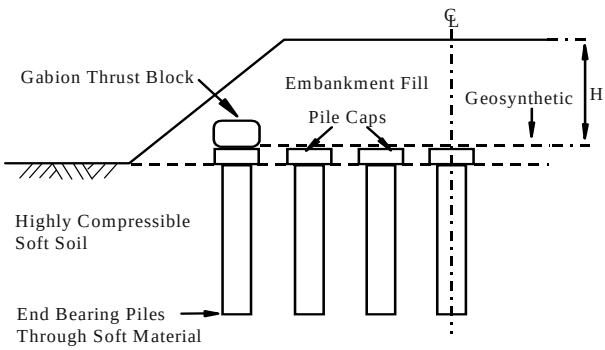

Fig. 2 Cross-section of a typical piled embankment (After Kempton et al. 1998)

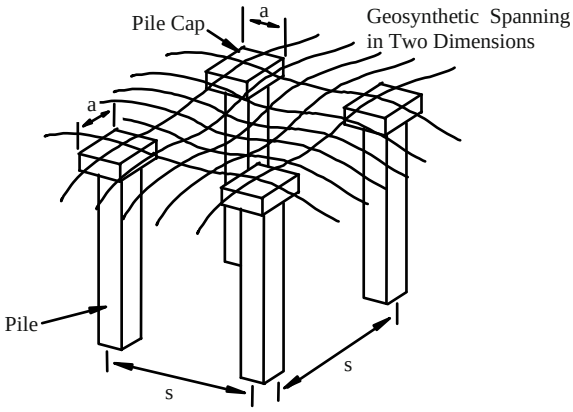

Fig. 3 Three-dimensional representation of a typical piled embankment (After Kempton et al. 1998)

Various design methods are available for the analysis of this complex soil structure interaction problem. It will be of great interest to compare the different methods to model the problem for analysis and design. Three design methods addressed in this paper are BS 8006 method, Russell et al design method and Kempfert et al design method.

DESIGN METHODS

BS 8006 Method

BS 8006, the code of practice for Strengthened and Reinforced Soils and other fills, Section 8 gives step by step simplified procedure for the analysis of basal reinforced piled embankments.

This method was initially developed by Jones et al (1990) and reported in a detailed way by various authors (Kempton et al. 1998; Scotto et al. 2006). Major steps are briefed as follows.

Design approach

An arching action will be developed between sub soil and the piled embankment due to differential settlement. This arching action is supposed to transfer bulk of the load from the embankment to the piles through the basal reinforcement**.**

Determination of vertical stresses

Degree of arching between the pile caps is assessed using Marston's formula for positive projecting subsurface conduits. Degree of arching will be expressed as a ratio of vertical stress exerted on top of pile caps (P_C') to the average stress at the base of the embankment (σ_V').

$$\left(\frac{P_C'}{\sigma_V'}\right)=\left[\frac{C_C a}{H}\right]^2 \tag{1}$$

where, C_C =Arching coefficient, a = width of the pile cap, H = Height of embankment.

The load transferred through piles is assumed as a function of the height of embankment in relation with critical height, 1.4 (s-a). The distributed load, W_T carried by the reinforcement between adjacent pile caps according to the critical height is given as follows,

For, H >1.4(s-a):

$$W_T=\frac{1.4sf_{fs}\gamma(s-a)}{s^2-a^2}\left[s^2-a^2\left(\frac{P_C'}{\sigma_V'}\right)\right] \tag{2}$$

For, $0.7(s-a)\le H\le 1.4(s-a)$:

$$W_T=\frac{s(f_{fs}\gamma H+f_q w_s)}{s^2-a^2}\left[s^2-a^2\left(\frac{P_C'}{\sigma_V'}\right)\right] \tag{3}$$

where, s = spacing between piles, f_{fs} = partial factor for soil unit weight, f_q = partial load factor for external applied loads, w_s = External surcharge loading and σ'_V = factored average vertical stress at the base of the reinforcement.

Load on the geosynthetic is assumed to be function of distributed load between pile caps and the resultant deflected shape of the geosynthetic.

Determination of basal reinforcement tension

Tension in the reinforcement T_{rp} is calculated from the distributed load on the geosynthetic in between the pile caps W_T and the strain in the geosynthetic ε.

$$T_{rp} = \frac{W_T (s-a)}{2a}\sqrt{1+\frac{1}{6\varepsilon}} \tag{4}$$

Partial factors are applied to the tension in the reinforcement for manufacture and extrapolation of design values, creep of the polymeric reinforcement, damage due to the installation process and environmental durability. The reinforcement need to be checked for resistance against lateral sliding. The reinforcement tensile load, T_{ds} needed to resist the outward thrust of the embankment is:

$$\mathrm{T_{ds}} = 0.5K_a(f_{fs}\gamma H + 2f_q w_s)H \tag{5}$$

Reinforcement tensile load should be generated at a strain compatible with allowable lateral pile movements (this avoids the use of raking piles). The length of the reinforcement should be enough to develop bond which will prevent the embankment to slide outwards over the reinforcement.

$$L_e = \frac{0.5K_a(f_{fs}\gamma H + 2f_q w_s) f_s f_n}{\gamma h\left(\frac{\alpha' \tan\phi_{cv}'}{f_{ms}}\right)} \tag{6}$$

where, L_e = minimum reinforcement bond length, f_{ms} = Partial material factor applied to $\tan\phi_{cv}'$, α' = Interaction coefficient relating the soil/reinforcement bond angle to $\tan\phi_{cv}'$.

Maximum strain in the reinforcement should be limited to ensure differential settlements do not occur at the surface of the embankment. The long term creep strain of the reinforcement should be kept to a minimum to ensure that the localized deformations do not occur at the surface of the embankment.

Russell Method

Russell's design method (Russell et al. 2003) considers that basal reinforcement shall be provided as both primary and secondary reinforcement. The primary reinforcement spans between adjacent pile caps, whereas secondary reinforcement covers the entire area to be supported. The stress reduction ratio is computed which is required to determine the uniformly distributed load over the reinforcement assuming no support and with some support from the subsoil. The tension in reinforcements is then calculated. Further, the compatibility of assumed design strains for both the reinforcements has to be checked with the actual strains.

Design approach

It is approximated that the uniformly distributed load on both primary and secondary reinforcement is calculated in proportion to a parameter called stress reduction ratio. Stress reduction ratio is defined as the ratio between average vertical stresses carried by the geosynthetic reinforcement to the average vertical stress due to embankment soil with no piles present.

Determination of stress reduction ratio

The stress reduction ratio S_{3D}, is calculated as:

$$S_{3D} = \frac{\sigma_{Base}}{\gamma H} = \frac{1}{\alpha\beta}\left[1-e^{-\alpha\beta n}\right] + \left[(1-n)+\frac{w_s}{\gamma H}\right]e^{-\alpha\beta n} \tag{7}$$

where

$$\alpha = \frac{4aH}{s^2 - a^2} \tag{8}$$

$$\beta = K\tan\phi'_{CV} \quad ; \ (K{=}0.5) \tag{9}$$

$$n = \frac{(s-a)}{2H}e^{\frac{\pi}{2}\tan\phi'_{CV}} \tag{10}$$

σ_{Base}= Average stress at the base of the embankment between adjacent pile caps, α = Diameter or width of the pile cap, s = centre to centre spacing of piles, H = Height of the embankment, w_s = uniformly distributed surcharge on the top of embankment, φ'_{CV} = effective angle of internal friction of the embankment fill.

Determination of uniformly distributed load on the reinforcement

Evaluate the uniformly distributed load W_T, on both the primary reinforcement and secondary reinforcement assuming no support and some support from the subsoil. When no support is assumed, the load on primary reinforcement and secondary reinforcement shall be related to vertical stress due to embankment soil, spacing between piles and size of the pile cap. When some support is assumed from subsoil, the vertical stress σ_{soil}, will be proportional to compressibility parameters apart from weight due to embankment soil, spacing between piles and size of the pile cap.

With no support from subsoil:

For, Primary Reinforcement

$$W_T = \frac{S_{3D}\gamma H(s+a)}{2a} \tag{11}$$

For, Secondary Reinforcement

$$W_T = \frac{S_{3D}\gamma H}{2} \tag{12}$$

With some support from subsoil:

For Primary Reinforcement

$$W_T = \frac{\left(S_{3D}\gamma H - \sigma_{soil}\right)\left(s^2 - a^2\right)}{2a(s-a)} \quad (13)$$

For Secondary Reinforcement

$$W_T = \frac{S_{3D}\gamma H}{2} \quad (14)$$

where

$$\sigma_{soil} = \frac{d_\circ}{m_v D} \quad (15)$$

$$x = \frac{\sigma_{soil}(s-a)}{S_{3D}\gamma H} \quad (16)$$

m_v = coefficient of volume compressibility of soil, D = Depth of subsoil, d_o = assumed deformation of subsoil due to the vertical load from embankment, x = distance over which the sub-soil supports the reinforcement between adjacent pile caps.

Determination of basal reinforcement tension

The tension induced in the primary and secondary reinforcement, T_{rp} is calculated as:

$$T_{rp} = \frac{W_T L_P}{2}\sqrt{1+\frac{1}{6\varepsilon}} \quad (17)$$

where

L_P =span of the reinforcement, ε = assumed design strain

Where no support is provided by the subsoil,

$L_P = (s\text{-}a)$

Where some support is provided by the subsoil,

$L_P = (s\text{-}a)\text{-}x$

Assumed design strain should be iterated to check the compatibility with the actual strain developed. Design the reinforcement for the ultimate tensile strength required for the reinforcement in longitudinal and transverse directions. The transverse reinforcement needs to be checked for resistance against lateral sliding. Reinforcement bond length at the extremities of the embankment is to be checked. Finally, Partial factors are applied to the tension in the reinforcement for manufacture and extrapolation of design values, creep of the polymeric reinforcement, damage due to the installation process and environmental durability.

Empfehlung 6.9—German Recommendations

The Empfehlung 6.9 (Kempfert et al. 2004) is the German recommended procedure for designing piled embankments. This method allows support from the subsoil to be included, if required. The design method calculates the tension in the reinforcement using the theory of elastically embedded tension membranes. Kempfert et al. (2004) have provided a dimensionless design chart for determining the tension in the reinforcement. Different situations of pile layouts like rectangular and triangular can be analyzed with this method.

Design approach

The load/stress distribution in the embankment is determined ignoring any geosynthetic reinforcement. Proceeding in this way the resulting vertical stresses are determined which acts on top of the piles and on the soft subsoil between them. The vertical pressure shall be applied to the geosynthetic reinforcement as external load. Finally, using the dimensionless design chart, the reinforcement tension is determined.

Determination of vertical stresses

The vertical stress on the subsoil is dependant on the embankment characteristics like geotechnical properties, height, loading on the embankment and pile characteristics like pile spacing and diameter. The design spacing of the piles(s) can be determined for different pile configurations like square, rectangular or triangular grid, Fig. 3.

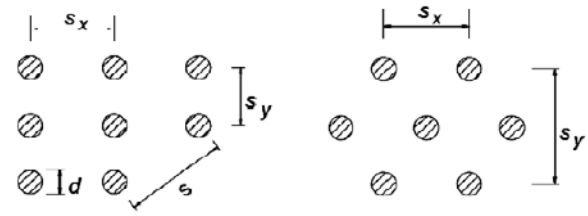

Fig. 3 Vertical, horizontal and design pile spacing. (After Kempfert, et al. 2004)

For a square or rectangular grid layout the pile spacing s can be determined as follows:

$$s = \sqrt{{s_x}^2 + {s_y}^2} \quad (18)$$

For a triangular distribution of piles the pile spacing s can be determined as follows:

$$s = \max\left[s_x, s_y\right] \quad (19)$$

Based on the pile spacing, the resultant vertical force acting on the reinforcement is calculated along the embankment and cross embankment direction by the method proposed by Kempfert et al. (2004).

Determination of basal reinforcement tension

The tension in the reinforcement is calculated using elastically embedded membrane theory. In Kempfert et

al. (2004) this is preformed using a dimensionless chart, Fig. 4. The influence of support from the soft soil between the piles is considered by using the modulus of subgrade reaction. Kempfert et al. (2004) suggests that the modulus of subgrade reaction, $k_{s,k}$ can be determined from the modulus of the subsoil, $E_{s,k}$, as follows:

$$k_{s,k} = \frac{E_{s,k}}{t_w} \tag{20}$$

where, t_w is the thickness of the soft soil layer.

In the dimensionless chart proposed by Kempfert et al. (2004) for determining maximum allowable strain in basal reinforcement, the inputs are vertical resultant force from embankment F_k, modulus of subgrade reaction $k_{s,k}$, long term stiffness of the reinforcement material J_k etc.

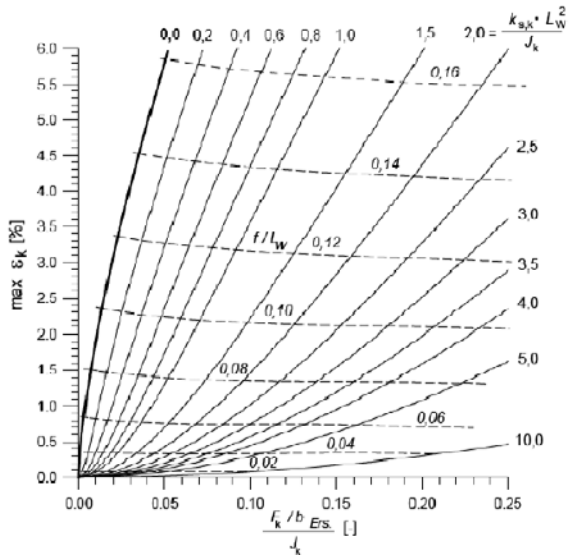

Fig. 4 Dimensionless design chart for determining the maximum allowable tension in the reinforcement. (After Kempfert, et. al, 2004)

The output from the dimensionless chart is the maximum allowable strain, ε_k (%), in the reinforcement and the ratio, f/L_W, Where, f=the maximum displacement of the reinforcement L_W = the clear spacing between pile cap edges in the longitudinal and cross embankment directions.

The tension in the basal reinforcement due to arching in the soil, $E_{M,k}$ can then be calculated as

$$E_{M,k} = \varepsilon_k j_k \tag{21}$$

COMPARISON OF THE METHODS

In calculating the load to be carried by geosynthetic, BS 8006 is not considering the reaction from the subsoil. By ignoring the contribution from the subsoil reaction, a major uncertainty is created about the vertical load the soft sub soil can carry in the long term without producing excessive settlement. Hence it is recommended to adopt a conservative approach when BS 8006 is selected for design of geosynthetic reinforced pile supported embankments. In shallow embankments soil arch may not fully develop and strain compatibility criteria may become critical when BS 8006 method is adopted. The initial tensile strain in the reinforcement is needed to generate a tensile load. BS 8006 specifies 6% strain as the upper limit for transferring all the embankment loads to the piles. For shallow embankments this upper strain limit may have to be reduced.

When comparing the Russell's method with BS 8006 method, there are more similarities than differences.

The Russell's method allows the inclusion of reaction from sub grade .So the method shall be considered a better way of modeling reinforced pile embankment problems compared to BS 8006 method.

In Kempfert method also the reaction from sub grade between the pile caps shall be considered when required. This method shall be suitable for different pile layout configurations.

CONCLUSIONS

Three different design methods for the analysis of basal reinforced pile supported embankments are presented in this paper. BS 8006 considers distributed load in the geosynthetic as a function of the embankment height. Russell's method is similar to BS method, but allows the inclusion of the reaction of the subgrade when required. Empfehlung 6.9, German Recommended procedure calculates the tension in the reinforcement using theory of elastically embedded tension membranes.

A number of other methods are available like Terzaghi (1943) and Hewlette & Randolph (1988). Numerical methods especially 3D models may give results close to the reality .However for practical reasons, simplified procedures like BS 8006 or Russell's method shall be used with enough precaution and conservative assumptions.

ACKNOWLEDGEMENTS

The authors would like to thank Maccaferri colleagues Mr. Vikramjiet Roy, Mr. Debiprasad Ghoshal, Mr. Gaurav Gupta and Mr. Vijay Dandage for their support and contributions for publishing this paper.

REFERENCES

BS8006 (1995) Code of Practice for Strengthened / Reinforced Soils and Other Fills, British Standard Institution, London: 122-150

Hewlett WJ, Randolph MF (1988) Analysis of piled embankments. Ground Engineering 21(3): 12-18

Kempton G, Russel D, Pierpoint ND, Jones CJFP (1998) Two- and three-dimensional numerical analysis of the performance of piled embankments. Proceedings of the 6th International Conference on Geosynthetics (6th ICG), 25-29 March 1998, Atlanta, USA 2: 767-772

Kempfert HG, Gobel C, Alexiew D, Heitz C (2004) German recommendations for Soil Reinforcement above Pile-Elements. EUROGeo3, Third Geosynthetic Conference, Munchen 1: 279-283

Russell D, Pierpoint N (1997) An assessment of design methods for piled embankments. Ground Engineering: 39-44

Russel D, Naughton PJ, Kempton GT(2003) A new design procedure for piled embankments. Proceeding of the 56th Annual Canadian Geotechnical Conference, Winnipeg, September 29 – October 1, Winnipeg, Canada, CD Rom

Rutugandha G (2004) Geosynthetic reinforced pile supported embankments." Thesis presented to the graduate school of the University of Florida in partial fulfillment of the requirements for the degree of Master of engineering University of Florida. http://etd.fcla.edu/UF/UFE0004884/gangakhedkar_r.pdf

Scotto M, Marchi GF, Schiavo M, Kempton G, Naughton P (2006) The use of geogrids in the construction of piled embankments on the new lines of the Italian high speed train. Proceedings of the 8th International Conference on Geosynthetics (8th ICG), 18-22 September 2006, Yokohama, Japan: 909-912

Terzaghi K (1943) Theoretical Soil Mechanics, John Wiley & Sons, New York

THEORETICAL AND NUMERICAL ANALYSIS ON GEOSYNTHETIC-REINFORCED AND PILE WALL-SUPPORTED EMBANKMENT

B.G. Chen [1], J.J. Zheng [2], S.W. Abusharar [3] and J. Chen [4]

ABSTRACT: The vertical reinforcement (pile walls) is combined with the horizontal reinforcement (geosynthetics) to provide an economical and effective solution for ground treatment of high embankments constructed on soft soil. Theoretical and numerical analyses were conducted to investigate the interaction among geosynthetics, pile walls and soft soil. The differential settlement between pile wall and soft soil will generate soil arching in embankment fill. Soil arching and tensioned membrane of geosynthetics are combined to transfer embankment loads from soft soil to competent substratum (such as bedrock) through pile walls, which minimize the yielding of the soft soil and potentially reduce the total and differential settlements. The soil arching efficiency, the pile wall efficiency, the differential settlement of the embankment, and the distribution of tension force in the geosynthetics have been analyzed with the consideration of four major influencing factors: the elastic modulus of the pile wall, the tensile stiffness of the geosynthetics, the height of the embankment fill, and the area ratio of the pile wall. Some conclusions are drawn as a reference for the design and construction of geosynthetic-reinforced and pile wall-supported embankment over soft ground.

KEYWORDS: geosynthetic, soil arching, efficiency, pile wall, embankment, settlement

INTRODUCTION

Construction of high embankment on soft ground is usually susceptible to bearing capacity failure, intolerable total and differential settlements, large lateral pressure and movement, and slope instability. A variety of techniques can be applied to solve these problems, such as overexcavation and replacement, preloading, using light-weight fill, horizontal reinforcement, and vertical reinforcement. However, some of these methods are limited due to complex conditions of strata, construction period, and economic condition.

When the vertical reinforcement is combined with the horizontal reinforcement, an economical and effective solution for ground treatment of high embankment can be provided, as reported by Luo et al. (2003), Chen et al. (2005), and Zheng et al. (2007). The main advantages associated with the use of this technique are as follows: (1) to fill embankment in a single stage without prolonged waiting times; (2) to significantly reduce differential and total settlements; (3) to reduce earth pressures between vertical reinforcements and transfer the embankment loads to a more competent stratum beneath the soft ground; (4) to avoid excavation and refill employed in typical situations.

The differential settlement between pile wall and soft clay will generate soil arching in embankment fill. Terzaghi (1936) analyzed the arching effect in sand generated by differential deformation. Hewlett (1988) verified the existence of soil arching by model tests, and analyzed the three-dimensional soil arching effect based on elasto-plastic theory and limit state. Chen (2004) improved the limit state method (Hewlett et al.1988) and proposed the formula for calculating the efficiency of pile. However, the effect of geosynthetics has not been considered in all these studies. Low (1994) studied the mechanism among embankment, geosynthetic and cap beam based on model tests and theoretical analysis, but the influence of material parameters on soil arching effect has not been considered, and the existing condition of soil arching effect is given by $H \geq 0.5s$ (H is the height of the embankment fill; s is the center to center spacing between pile caps). In fact, soil arching effect exists when the differential settlement between pile and soft clay occurs (Terzaghi 1943; Han et al. 2002; Liu 2003).

[1] Ph.D Candidate, School of Civil Engineering and Mechanics, Huazhong University of Science and Technology, CHINA. Email: baoguo_chen@126.com
[2] Professor, ditto, CHINA. Email: zhengjj@hust.edu.cn
[3] Ph.D Candidate, ditto, CHINA. Email: sariwaleed@hotmail.com
[4] Ph.D Candidate, Centre for Soft Ground Engineering, National University of Singapore, SINGAPORE. Email: chenj@nus.edu.sg

The interaction among the horizontal reinforcement, the vertical reinforcement, and the soft clay has been studied in this paper. The influences of the pile wall stiffness, the geosynthetic tensile stiffness, the embankment fill height, and the area ratio on the total and differential settlements, the efficiency, and the maximum tension force in geosynthetic are discussed in detail.

DEFINITION

Terzaghi (1943) defined arching effect as the transfer of pressure from a yielding fill mass onto adjoining stationary parts. When the settlement of soft ground is larger than the adjoining pile walls, the pressure on the soft ground under the yielding fill mass greatly decreased whereas the pressure on the adjoining pile walls increased, this was attributed to the shearing stresses between the yielding fill mass and the adjoining stationary fill mass, which resisted the descent of yielding fill mass located above the soft ground soil. If a geosynthetic layer is exist, it will stretch as the soft ground settles; the resulting hoop tension will reduce the net pressure on the soft ground and also resist the descent of yielding fill mass (Fig. 1). Due to the coupled effects, the differential settlement between the yielding fill mass and adjoining stationary fill mass will decrease along the height of embankment fill until it approaches zero. The zero differential settlement plane can be explained by equal settlement plane being limited below the embankment surface, where the height of embankment is effective height (h_e).

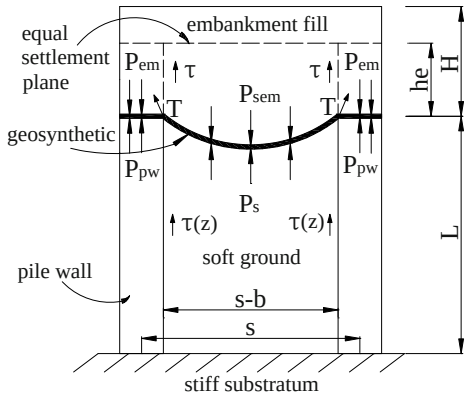

Fig. 1 Load transfer mechanism

The efficiency of soil arching (ESA) and efficiency of pile wall (EPW) are used to assess the degree of arching in embankment fill and load transfer, respectively. ESA and EPW are expressed as follows:

$$ESA = \frac{P_{em} b}{\gamma H s} \times 100\% \tag{1}$$

$$EPW = \frac{P_{pw} b}{\gamma H s} \times 100\% \tag{2}$$

where P_{em} is the mean pressure on the geosynthetics above the pile wall; P_{pw} is the mean pressure on the pile wall; γ is the unit weight of the embankment fill; H is the height of the embankment fill; b is the width of pile wall; s is the center to center spacing of pile walls.

THEORETICAL ANALYSIS

Analysis of Soil Arching

The development of the analytical framework for the analysis of geosynthetic-reinforced and pile wall-supported embankment is based on the following four assumptions:

a. The embankment fill and reinforced foundation soil system are assumed to be plane-strain conditions.
b. The interface between yield fill mass over the soft soil and the adjoining stationary fill mass on the pile wall is assumed to be vertical section.
c. The Rankine's theory of active earth pressure is applicable.
d. Assuming that the weight of geosynthetic is negligible.

The active earth pressure is induced by yield fill mass since the drag load is the action of yield fill mass on the adjoining fill mass. The equilibrium equation of vertical forces for the fill element above the pile wall is:

$$\begin{aligned}(P + dP)b = Pb + \gamma b dz + \\ 2[(\gamma z k_a - 2c\sqrt{k_a})\tan\varphi + c]dz\end{aligned} \tag{3}$$

where P is the mean earth pressure in the stationary fill mass; k_a is the coefficient of Rankine's active earth pressure, $k_a = \tan^2(45^\circ - \varphi/2)$; c is the cohesion of embankment fill; φ is the friction angle of embankment fill.

When $H < h_e$, the solution of Eq. 3 is given by:

$$P(z) = \gamma z + \gamma k_a \tan\varphi \cdot z^2/b + 2c(1 - 2\tan\varphi\sqrt{k_a})\, z/b \tag{4}$$

Assuming $z = H$, Eq. 4 then becomes:

$$P_{em} = \gamma H + \gamma k_a \tan\varphi \cdot H^2/b + 2c(1-2\tan\varphi\sqrt{k_a})H/b \quad (5)$$

When $H \geq h_e$, the solution of Eq. 3 is given by:

$$P(z) = \gamma z + \gamma k_a \tan\varphi[z^2-(H-h_e)^2]/b + 2c(1-2\tan\varphi\sqrt{k_a})(z-H+h_e)/b \quad (6)$$

Assuming $z = H$, Eq. 6 then becomes:

$$P_{em} = \gamma H + \gamma k_a \tan\varphi(2H-h_e)h_e/b + 2c(1-2\tan\varphi\sqrt{k_a})h_e/b \quad (7)$$

The vertical equilibrium of forces in embankment fill requires that:

$$P_0(z) = (\gamma z - mP(z))/(1-m) \quad (8)$$

Assuming $z = H$, Eq. 8 then becomes:

$$P_{sem} = (\gamma H - mP_{em})/(1-m) \quad (9)$$

where $P_0(z)$ is the mean pressure in yield fill mass over soft clay, P_{sem} is the mean pressure of yield fill mass on geosynthetic, m is the area ratio, $m = b/s$.

At the equal settlement plane, the settlements of yield fill mass equals to the adjoining stationary fill mass, this is given by:

$$W_{pw}(0) + S_{em} = W_s(0) + S_{sem} \quad (10)$$

where S_{em} and S_{sem} are the average deformations of embankment fill over pile wall and soft ground, respectively; $W_s(0)$ and $W_{pw}(0)$ are the average settlements of pile wall and soft ground at the pile wall top elevation, respectively.

The maximum differential settlement Δs at the pile wall top elevation is given by:

$$\Delta s = S_{em} - S_{sem} = \int_{H-h_e}^{H} (P(z)-P_0(z))/E_{em}\,\mathrm{d}z \quad (11)$$

and

$$\Delta s = W_s(0) - W_{pw}(0) \quad (12)$$

where E_{em} is the Young's modulus of the embankment fill, assuming that the modulus of the embankment fill over the pile wall equals to that over the soft ground.

In the design of road embankments, the height of embankment fill must be larger than the effective height of embankment to prevent differential settlement of the pavement ($H \geq h_e$). Assuming that embankment fill is cohesionless soil ($c = 0$), substituting Eqs. 6 and 8 into Eq. 11 gives:

$$\Delta s = \frac{\gamma k_0 \tan\varphi[H^3/3 - H(H-h_e)^2 + 2(H-h_e)^3/3]}{(1-m)bE_{em}} \quad (13)$$

Analysis of Geosynthetics

The deformed shape of geosynthetic is idealized to be a circular arc with a radius R, a subtended angle 2θ and a maximum displacement Δs midway between pile walls (Fig. 2).

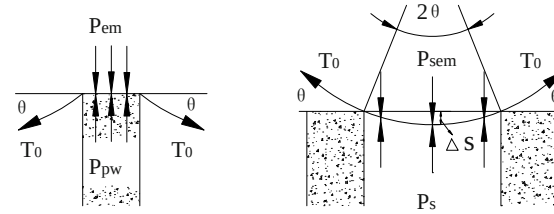

(a) geosynthetic on pile wall

(b) geosynthetic on soft ground

Fig. 2 Geosynthetics on pile wall and soft ground

By geometry:

$$\sin\theta = \frac{4\Delta s/(s-b)}{1+4[\Delta s/(s-b)]^2} \quad (14)$$

The vertical equilibrium of forces of geosynthetic (Fig. 2) is given by:

$$\begin{cases} P_{pw} = P_{em} + 2T_0\sin\theta/b \\ P_s = P_{sem} - 2T_0\sin\theta/(s-b) \end{cases} \quad (15)$$

where T_0 is the tension force in geosynthetic at the edge of pile walls, P_s is the mean pressure on the soft clay between pile walls.

Analysis of Interaction between Pile Wall and Soft Clay

Assuming that the substratum is bed rock and the distribution of negative skin friction is an inverse triangle. The negative skin friction is described as follows:

$$\tau(z) = \tau_u \cdot (L-z)/L \quad (16)$$

Assuming that the origin is at the top of pile wall and the positive direction of Z-axis is downward, the following equations can be derived based on the vertical equilibrium of forces of pile wall unit and soft clay unit.

$$\begin{cases} d^2W_{pw}(z)/d^2z = 2\tau/E_{pw}b \\ d^2W_s(z)/d^2z = -2\tau/E_s(s-b) \end{cases} \quad (17)$$

where, E_{pw} and E_s are the moduli of pile wall and soft clay, respectively.

The boundary conditions of displacement are given by:

$$\begin{cases} W_s(0) - W_{pw}(0) = \Delta s \\ W_{pw}(L) = W_s(L) = 0 \end{cases} \quad (18)$$

The boundary conditions of forces are given by:

$$\begin{cases} E_{pw}W'_{pw}(0) = P_{pw} \\ E_sW'_s(0) = P_s \end{cases} \quad (19)$$

Combining Eqs. 16, 17, 18 and 19, one obtains:

$$\begin{cases} W_{pw}(z) = 2\tau_u \cdot (z^2/2 - z^3/6L)/E_{pw}b + \\ \quad P_{pw}z/E_{pw} - 2\tau_u L^2/3E_{pw}b - P_{pw}L/E_{pw} \\ W_s(z) = 2\tau_u \cdot (z^3/6L - z^2/2)/E_s(s-b) + \\ \quad P_s z/E_s + 2\tau_u L^2/3E_s(s-b) - P_s L/E_s \end{cases} \quad (20)$$

Substituting Eq. 12 into Eq. 20 gives:

$$\Delta s = \frac{2}{3}\tau_u L^2 \cdot \left(\frac{1}{E_s(s-b)} + \frac{1}{E_{pw}b}\right) + \left(\frac{P_{pw}}{E_{pw}} - \frac{P_s}{E_s}\right) \cdot L \quad (21)$$

The vertical equilibrium of forces between the pile wall and the soft clay requires:

$$P_s = (\gamma H - mP_{pw})/(1-m) \quad (22)$$

Combing Eqs. 7, 9, 13, 14, 15, 21 and 22, using MATLAB program for calculating P_{em} and P_{pw}, which were substituted into Eqs. 1 and 2 for evaluating the efficiency of soil arching and pile wall.

Analysis of Theoretical Results

The results of theoretical analysis are shown in Fig.3 and Fig.4, the geometry and the material parameters are summarized in Table 1.

As shown in Fig. 3, ESA and EPW increase with increasing the stiffness ratio of the pile wall to the soft clay, but they are likely to approach limit values at a large stiffness ratio. EPW and ESA ranges from 44.04% —62.04% and 37.62%—54.55%, respectively when the stiffness ratio changes from 30 to 1E+04, and EPW is greater than ESA. Moreover, EPW and ESA increase with increasing the embankment height while the rates of increment decrease at a large ratio of the embankment height to the pile walls clear spacing, the discrepancy between EPW and ESA also decrease with the embankment height (Fig. 4).

Table 1 Material properties of the soil and pile wall

Materials	Parameters
embankment	C =0, φ =30°, γ =18 kN/m^3, E_{em} =12 MPa, H =4—12 m
pile wall	b =0.5 m, s =3 m, L =12 m, γ =24 kN/m^3, E_{pw} =66 MPa—22 GPa
soft clay	C =9 kPa, φ =6°, γ =16 kN/m^3, E_s =2.2 MPa

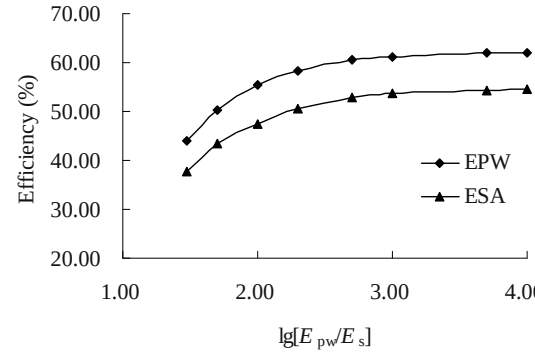

Fig. 3 Influence of stiffness ratio on efficiency

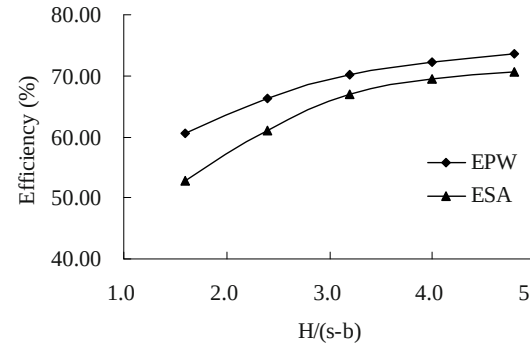

Fig. 4 Influence of different ratios of embankment height to the clear spacing on efficiency

NUMERICAL ANALYSIS

Numerical Modeling

In this study, the numerical modeling of geosynthetic-reinforced and pile wall-supported embankment is performed using PLAXIS. The plane strain state is assumed in the analysis. The embankment fill, soft soil, pile walls are assumed as Mohr-Coulomb elasto-plastic materials and geosynthetic is assumed as elastic material. A geogrid element is defined by five nodes as a 15-

noded triangular element is used for meshing the numerical model. The layout of pile wall as shown in Fig. 5a has been selected in the analysis herein for demonstrating the mechanisms of the problem. A numerical mesh is developed for a symmetry model as shown in Fig. 5b. The vertical sides of the model are horizontally restrained, and the bottom is fixed, Considering the typical dimensions of pile wall used in ground improvement, a diameter of 0.5 m is chosen for the pile wall. The typical center to center spacing of pile walls adopted in the simulation ranges from 1.5 m—6.0 m (the area ratio ranges from 33.3%—8.3%). Moreover, the stiffness of the pile wall ranges from 11 MPa—33 GPa，the tensile stiffness of geosynthetics ranges from 50 kN/m to 50 MN/m and the height of embankment fill ranges from 2 m—2 m. The 12m of soft soil is assumed to be underlain by a very stiff layer, such as bedrock so that there is no deformation at the bottom of the soft soil. Although multiple layers of geosynthetics can be placed within the embankment, one layer of geosynthetic herein is assumed for simplicity. All parameters used in the analysis of a control case are tabulated in Table 2.

Table 2 Material properties of the soil and pile wall

Parameters	Fill	Unit	Soft clay	Pile wall
Material model	M-C	-	M-C	Linear elastic
Type of material behavior	Drained	-	Drained	Non-porous
Unit weight	18.0	kN/m^3	16.0	24.0
Horizontal permeability	1.0	m/d	0.001	-
Vertical permeability	1.0	m/d	0.001	-
Young's modulus	14.0	MPa	2.2	1100
Poisson's ratio	0.3	-	0.35	0.2
Cohesion	1.0	kPa	9.0	-
Friction angle	30	°	6	-
Dilatancy angle	0	°	0	-
Interface reduction factor	0.8	-	0.4	-

Tension stiffness is 1000 kN/m, height of embankment fill is 4 m, area ratio is 16.7%.

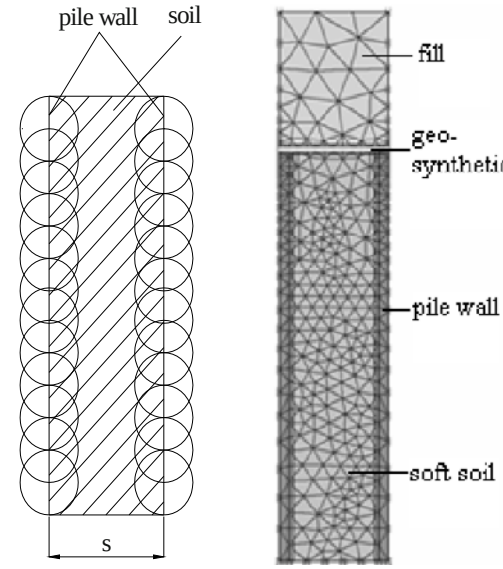

(a) pile wall layout (b) grid mesh

Fig. 5 FEM analysis model

Analysis of Numerical Results

The distribution of the tension force in the geosynthetic as a function of the distance from the center line of the pile wall is shown in Fig. 6. The numerical results indicate that the tension force is not uniform along the geosynthetic and the maximum tension force occurs near the edge of the pile wall. The deformation of geosynthetic is not uniform either and the maximum settlement occurs at the midpoint between pile walls (Fig. 7).

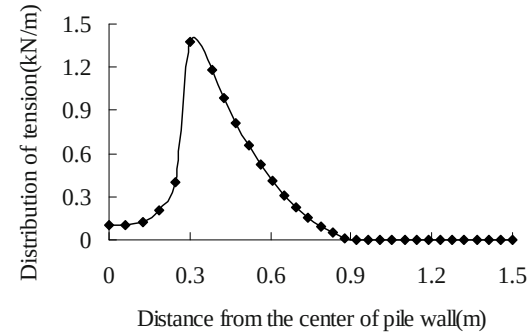

Fig. 6 Distribution of tension force in geosynthetic

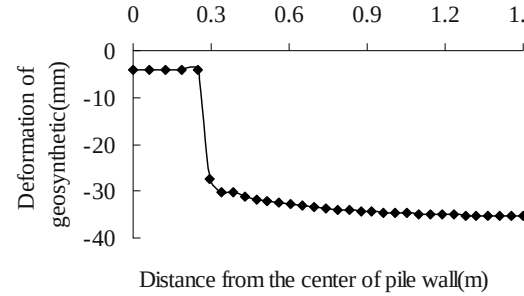

Fig. 7 Deformation of geosynthetic

The results obtained from the numerical simulation are compared with that obtained from the theoretical solution and summarized in Tables 3 and 4. It can be noted that the theoretical and numerical values of EPW and ESA increase with increasing stiffness ratio, but are likely to approach limiting values at large stiffness ratio and are close for a very large stiffness ratio. It can also be noted that the theoretical and numerical values of EPW and ESA increase with increasing $H/(s\text{-}b)$ and are in reasonable agreement.

Table 3 Comparison of results in the case of E_{pw}/E_s influence on EPW and ESA

E_{pw}/E_s	EPW (%)		ESA (%)	
	theoretical	numerical	theoretical	numerical
30	44.04	60.54	37.62	54.04
50	50.15	63.92	43.51	57.24
100	55.31	66.81	47.36	60.05
200	58.40	68.33	50.44	61.61
500	60.51	69.19	52.75	62.51
1000	61.28	69.51	53.62	62.83
5000	61.90	69.73	54.29	63.08
10000	62.04	69.77	54.55	63.11

Table 4 Comparison of results in the case of $H/(s\text{-}b)$ influence on EPW and ESA

$H/(s\text{-}b)$	EPW (%)		ESA (%)	
	theoretical	numerical	theoretical	numerical
1.6	60.51	65.95	52.75	58.72
2.4	66.35	70.41	60.94	62.79
3.2	70.09	72.86	66.89	65.06
4.0	72.28	74.65	69.42	66.70
4.8	73.49	75.82	70.73	67.70

The influence of elastic modulus of the pile wall, the tensile stiffness of the geosynthetic, the height of the embankment fill, and the area ratio on the total and differential settlements, EPW, ESA, and the maximum tension force in geosynthetic are plotted in Figs. 8—19, respectively.

The influence of the pile wall stiffness on the interaction of the embankment fill, geosynthetic, pile walls and soft clay are described in Figs. 8, 9 and 10, the stiffness of the pile wall ranges from 11 MPa to 33 GPa. The following may be noted:

a. The maximum total settlements decrease with increase of the elastic modulus of pile wall, and the maximum differential settlements increase with the elastic modulus of the pile wall, but these settlements are likely to approach a limit value at large stiffness.
b. EPW and ESA increase with the elastic modulus of the pile wall, and the variation trend is not obvious when the elastic modulus of the pile wall is greater than 1.1 GPa. The maximum EPW and ESA are about 69.77% and 63.12%, respectively.
c. The maximum tension force in geosynthetic increases with the elastic modulus of the pile wall, the increment of maximum tension force is slight when the modulus is less than 22 MPa or greater than 11 GPa.

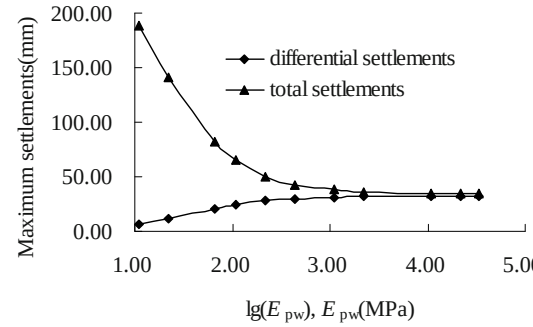

Fig. 8 Influence of pile wall stiffness on settlements

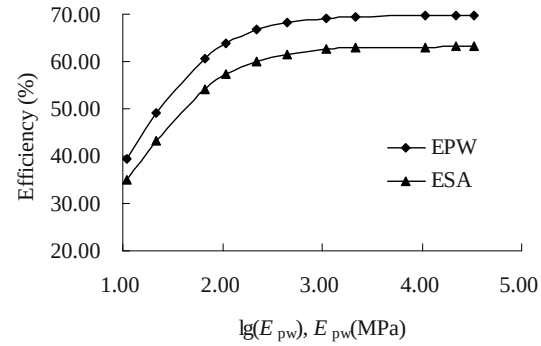

Fig. 9 Influence of pile wall stiffness on efficiency

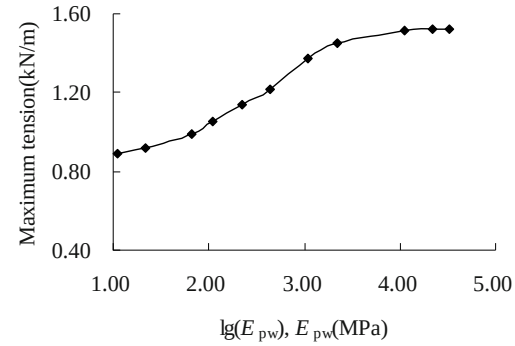

Fig. 10 Influence of pile wall stiffness on maximum tension force in geosynthetic

The influences of tensile stiffness of geosynthetic on the maximum settlements, EPW, ESA and the maximum tension force in geosynthetics are plotted in Figs. 11, 12 and 13, the tensile stiffness of geosynthetics ranges from 50 kN/m to 50 MN/m. The following may be noted:

a. The influence of geosynthetic stiffness on the maximum total settlement and differential settlement, EPW and ESA are not obvious.
b. With an increase of geosynthetic stiffness, the maximum settlements decrease slightly and the efficiency of pile wall and soil arching vary slowly.
c. The maximum tension force in geosynthetics increases with the tensile stiffness of geosynthetic, the increment of tension force increases with the tensile stiffness of geosynthetic.

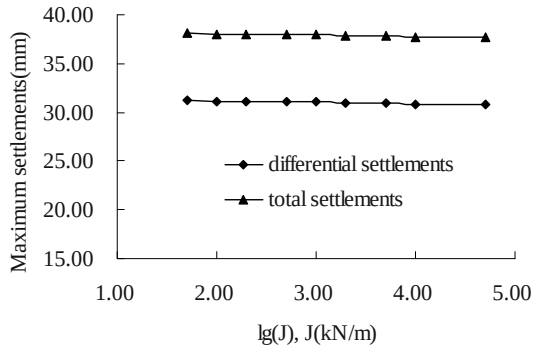

Fig. 11 Influence of geosynthetic stiffness on settlements

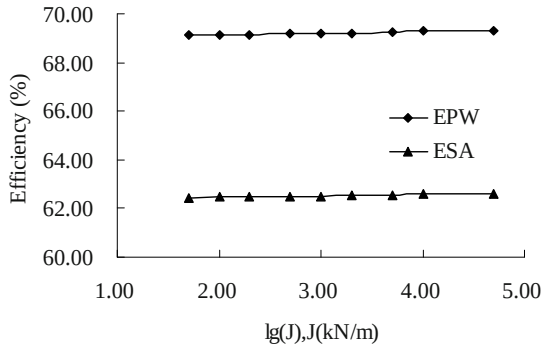

Fig. 12 Influence of geosynthetic stiffness on efficiency

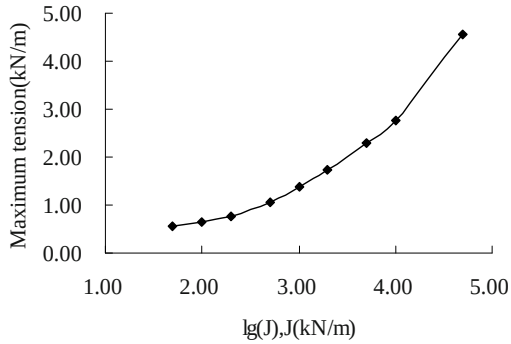

Fig. 13 Influence of geosynthetic stiffness on maximum tension force in geosynthetic

The influences of the height of the embankment fill on the maximum settlements, EPW, ESA and the maximum tension force in geosynthetics are plotted in Figs. 14, 15 and 16, respectively, and the height of embankment fill ranges from 2 m to 12 m. The following may be noted:

a. The total settlement and differential settlement increase with the height of the embankment fill.
b. EPW and ESA increase with the height of the embankment fill, and the increment of EPW and ESA decrease with an increase of the embankment height. The maximum EPW and ESA are 75.82% and 67.70%, and the maximum increments are about 20.55% and 18.92%, respectively.
c. The maximum tension in geosynthetics increases with the height of the embankment fill. The increment of maximum tension force increases with the height of the embankment fill.

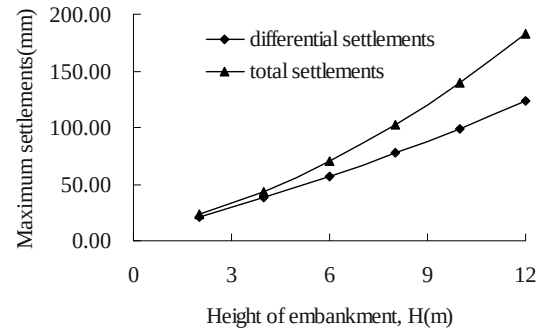

Fig. 14 Influence of height of embankment on settlements

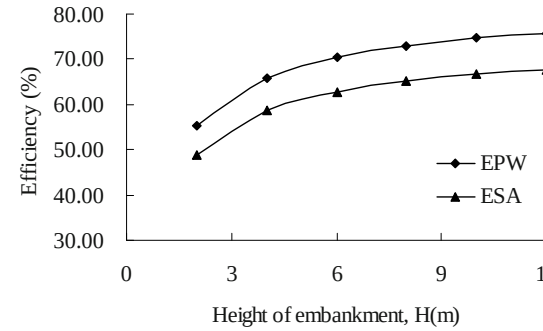

Fig. 15 Influence of height of embankment on efficiency

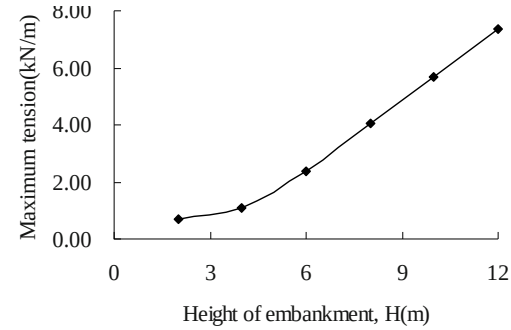

Fig. 16 Influence of height of embankment fill on the maximum tension force in geosynthetic

The influences of area ratio on the maximum settlements, EPW, ESA and the maximum tension force in geosynthetic are plotted in Figs. 17, 18 and 19,

respectively, and the area ratio ranges from 33.3% to 8.3%. The following may be noted:

a. The maximum total settlement and differential settlement decrease with an increase of the area ratio, but these settlements are likely to approach a limit value at large area ratio.
b. EPW and ESA increase with the area ratio. The stress on the soft clay is lower when the pile walls are spaced with smaller spacing.
c. The maximum tension force in geosynthetic decreases with an increase of area ratio, but is likely to approach the minimum or maximum values when the area ratio is greater than 33.3% or less than 10%.

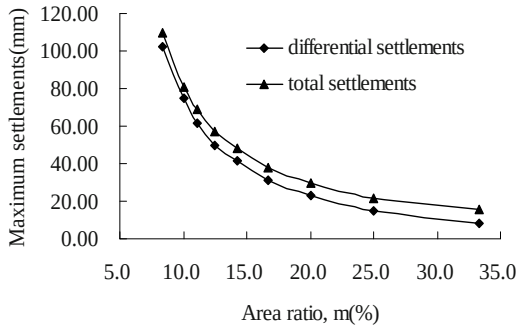

Fig.17 Influence of area ratio on settlements

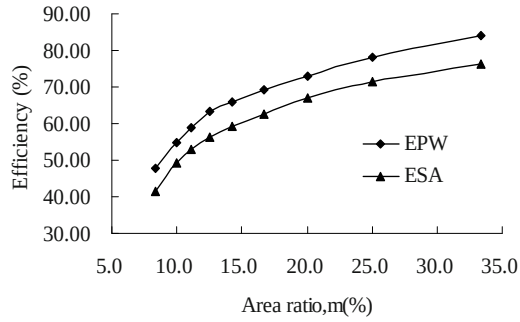

Fig.18 Influence of area ratio on efficiency

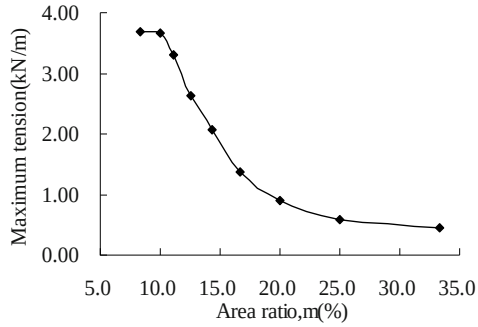

Fig.19 Influence of area ratio on the maximum tension force in geosynthetic

CONCLUSIONS

The distribution of tension force in the geosynthetic is not uniform along the geosynthetic and the maximum tension force occurs near the edge of the pile wall; the deformation of geosynthetic is not uniform either, and the maximum settlement occurs at the midpoint of geosynthetic between pile walls.

ESA and EPW increase with the elastic modulus of the pile wall, the height of the embankment fill and the area ratio, but the influence of tensile stiffness on ESA and EPW is not obvious.

Total settlement increases with the height of the embankment fill and decreases with an increase of the elastic modulus of the pile wall, the area ratio and the tensile stiffness of geosynthetics, but the influence of tensile stiffness of geosynthetics on the total settlement is slight.

Differential settlement increases with the elastic modulus of the pile wall and the height of the embankment fill, decreases with an increase of the area ratio. The influence of tensile stiffness of geosynthetics on differential settlement is slight.

Moreover, the maximum tension force in geosynthetics increases with the height of the embankment fill, the tensile stiffness of geosynthetics and the elastic modulus of the pile wall decrease with an increase of the area ratio.

ACKNOWLEDGEMENTS

This work is supported by National Natural Science Foundation of China (NSFC) (No. 50478090). The authors would like to express their appreciation to the financial assistance.

REFERENCES

Chen YM, Jia N, Chen RP (2004) Soil arch analysis of pile-supported embankments. China Journal of Highway and Transport 17(4):1-6

Chen RP, Jia N, Chen YM (2005) Mechanism and settlement analysis of pile-supported and geogrid-reinforced embankments. Chinese Journal of Rock Mechanics and Engineering 24(23):4358-4367

Han J, Gabr MA (2002) Numerical analysis of geosynthetic-reinforced and pile-supported earth platforms over soft soil. Journal of Geotechnical and Geoenvironmental Engineering 128(1):44-53

Hewlett WJ, Randolph MF (1988) Analysis of piled embankment. Ground Engineering 21(3):12-18

Liu JF (2003) Analysis on pile-soil stress ratio for composite ground under embankment. Chinese Journal of Rock Mechanics and Engineering 22 (4):674-677

Low BK, Tang SK, Choa V (1994) Arching in piled

embankments. Journal of Geotechnical Engineering 120(11):1917-1938

Luo Q, Liu JY, Zhang L (2003) Application of geosynthetic-reinforced sand blanket to settlement reduction of soft ground. Chinese Journal of Geotechnical Engineering 25(6):710-714

Terzaghi K (1936) Stress distribution in dry and in saturated sand above a yielding trap-door. Proc. 1st Int. Conf. Soil Mechanics. Harvard University, Cambridge 307-311

Terzaghi K (1943) Theoretical soil mechanics. John Wiley and Sons, New York, N.Y.

Zheng JJ, Chen BG, Abusharar SW (2007) Pile-soil stress ratio of two-directional reinforcement composite foundation. Journal of Huazhong University of Science and Technology (Natural Science Edition) 35(7): 110-113

Proceedings of the 4th Asian Regional Conference on Geosynthetics
June 17 - 20, 2008 Shanghai, China

CALCULATION TECHNIQUES AND DIMENSIONING OF ENCASED COLUMNS —DESIGN AND STATE OF THE ART

M. Raithel[1] and A. Kirchner[1]

ABSTRACT: Foundation systems with geotextile encased columns (GEC) have been used for soil improvement and primarily for road embankment foundations in Germany, Sweden and the Netherlands for almost 10 years (Raithel et al. 2004), but latterly they are also used in dike construction. In this paper, along with the development of the foundation and calculation systems and projects demonstrated, the essential main features of the calculation of the bearing and deformation behaviour are described.

KEYWORDS: geotextile encased column, GEC, dike construction, bearing behaviour, deformation behaviour

INTRODUCTION

With the foundation system GEC gravel-sand-columns are installed into a bearing layer to relieve the load on the soft soils. Due to the geotextile casing in combination with the surrounding soft soils the column has a radial support, whereas the casing is strained by ring tensile forces. To withstand the high ring tension forces, the geotextile casings are manufactured seamlessly. Due to the supporting effects of the casing, a special range of application, in opposite to conventional column foundations (i.e., granualar piles), is in very soft soils (undrained shear strength $C_u < 15$ kN/m²) like peat or very soft silt/clay as well as sludge. By a non-encased column, the horizontal support of the soft soil must be equal to the horizontal pressure in the column. By a GEC, the horizontal support of the soft soil can be much lower, due to the radial supporting effect of the geotextile casing.

As a result a stress concentration on the column head and a lower vertical pressure over the soft soil and therefore a large settlement reduction is obtained. The columns act simultaneously as vertical drains, but the main effect is the load transfer to a deeper bearing layer. In total, just minor settlements are resulting after the construction period, what is on the one hand referred to the settlement reduction because of stress concentration above the columns and the following stress reduction above the soft layers, on the other hand to the increasing stress activated through the effect of the columns as vertical drain, so that the bulk of the settlements can be compensated during the construction period. Furthermore the creep and respectively secondary settlements are reduced.

INTERACTIVE STRUCTURAL SYSTEM

The GEC are arranged in a regular column grid. Based on the unit cell concept, a single column in a virtual infinite column grid can be considered.

The effectiveness of a grid column foundation concerning a reduction of sinking and an increase of stability, basically depends on stress concentration above the head of column linked with an unloading of the soft layers, which is possible because of an arch action in the ballast covering.

In encased columns the stiffness circumstances between the columns and the surrounding soft layer is normally aligned in that way, that it results in a flexible and self regulating structural system at nearly equal settlement between column and surrounding soft layer. In the case of a yielding of the columns, the loads first have the possibility to relocate on the soft layers, causing a rising of the resistance of soil and allowing an interactive re-relocation (Raithel 1999). Indeed, this first leads to some lower load relocation and respectively stress concentration above the heads of columns in contrast to rigid pile-like elements in encased columns. At normal case there is no need for additional measures like geosynthetic reinforced bearing layers assessed to membrane forces above the heads of columns.

Generally, an analytical, axial symmetric model according to (Raithel 1999) and (Raithel and Kempfert 2000) is used for calculating and designing a geotextile encased column foundation, see Fig. 1. Based on the ring tension forces, it is possible to define the required stiffness of the geotextile casing by considering the product-specific factors of decrease (i.e., to considerate

[1] Kempfert + Partner Geotechnical Consultants, Wuerzburg, GERMANY. Email: wue@kup-geotechnik.de

the influences by creep, installation damage, type of connection, chemical offences, etc.) as well as the partial safety factor.

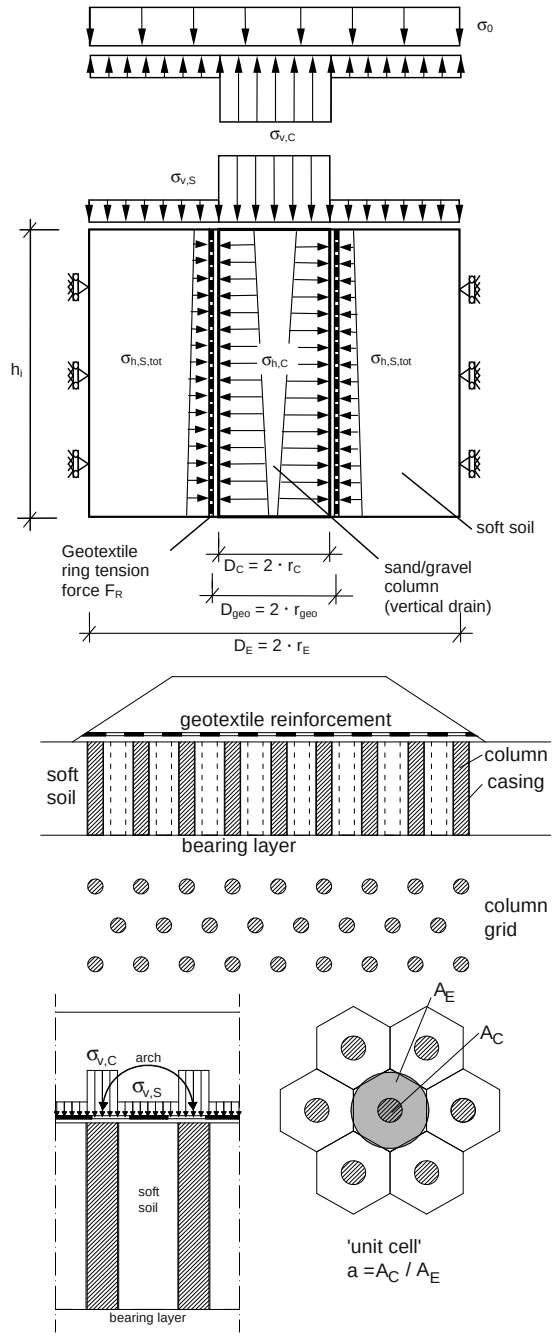

Fig. 1 Calculation model and schematic interpretations for the structural behaviour

PRODUCTION TECHNIQUES

Normally two installation methods are in practice. With the excavation method, an open steel pipe is driven into the bearing layer and the soil is removed by auger. By the vibro displacement method, a steel pipe with two base flaps is vibrated down to the bearing layer, displacing the soft soil. After that the geotextile casing is installed and filled with sand. After retrieval of the pipe under vibration a GEC filled with sand/gravel of medium density is produced. In Fig. 2 the vibro displacement method (right) and the excavation method (left) are shown.

Fig. 2 Excavation and substitution technique with double flap pipe (pictures: Möbius AG)

The excavation technique should especially be preferred in soils with great penetration resistances and respectively, if vibration action to border buildings, traffic facilities, etc. have to be minimised.

The advantage of the substitution techniques adverse the excavation technique is the faster and more economic production of the columns and the operational discharge of an initial tension in the soft layer. Moreover, no soils have to be extended and disposed.

PROJECT EXPERIENCES

In the mid-1990's, the first attempts were made to install encased sand columns. But the required techniques for installing a complete, self-regulating respectively interactive bearing system and the appropriate calculation models were developed since 1994. First bearing test on encased columns took place in Germany in 1994 and in 1996 the first foundation system "geotextile encased columns (GEC)" for widening an about 5 m high railroad embankment on peat and clay soils in Hamburg was carried out.

Meanwhile the appropriate calculation model to calculate the ring tension forces and the settlements as realistic as possible by considering the different interactions between soft soil, casing and column was developed. Up to now there are more than 20 reference projects in Germany, Sweden and the Netherlands.

Especially in road and railroad construction extensive experiences with the system GEC exist. By means of

measurements the effectiveness of the accomplished GEC foundations could be proved. As an example the ground improvement at the railroad Karlsruhe-Basel is shown in the following. The 1—2 m high embankment was founded on a approx. 7 m thick alternating sequence of peat, sludge and clay layers with stiffness between E_s=0.7 and 2.3 MN/m². To avoid vibrations at the existing rail track the columns (∅ 80 cm) were installed using the excavation method. The situation on site and typical measurements are shown in Fig. 3.

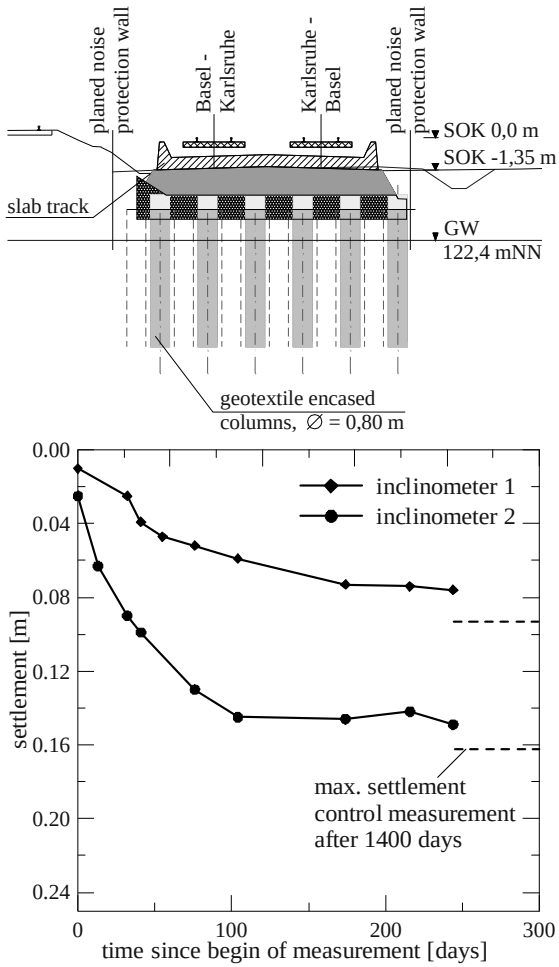

Fig. 3 Foundation and typical measurements at the project ABS/NBS Karlsruhe-Basel

In addition to using the foundation system in road construction there are meanwhile experiences in major hydraulic construction projects. Especially the area-extension of the airplane dockyard (EADS) in Hamburg-Finkenwerder by approx. 140 ha (346-acres) for the production of the new Airbus A 380 has to be mentioned. The area-extension is located in the "Mühlenberger Loch" adjacent to the west of the existing factory site. The area extension is carried out by enclosing the polder with a 2.4 km long dike to fill up in the area under buoyancy, see Fig. 4. The dike foundation was realized by about 60,000 geotextile encased columns with a diameter of 80 cm, which were sunk to the bearing layers with depth between 4 and 14 m below the base of the dike footing. This dike is the new main water protection dike of the airplane dockyard. Furthermore another 10,000 columns were installed to relocate the existing 'Finkenwerder Vordeich' towards the river Elbe and to avoid sludge replacement, to increase the stability and to decrease the settlements of the dike. Typical soil conditions are shown also in Fig. 4.

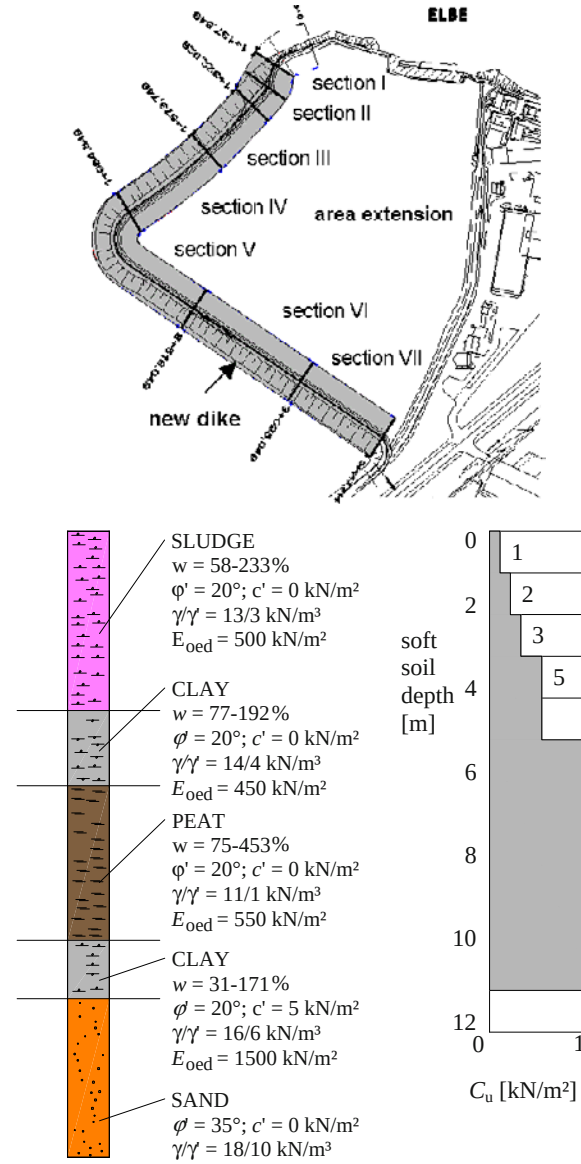

Fig. 4 Concept to reclaim land by the construction of a polder and typical soil boundary conditions

Due to the different soil conditions along the dike length 7 measurement cross sections were necessary. In a typical measurement cross section, 4 groups are placed, each containing one earth pressure gauge and one water pressure gauge above the soft soil layer, and two piezometers within the soft soil. In each cross section,

one horizontal and two vertical inclinometers are used for the examination of the deformation behaviour. The measured settlement in dike section VI is shown in Fig. 5.

Due to the foundation system GEC the dike could be constructed to a flood water save height of 7 m in a construction time of approx. 9 months. To complete the dike up to approx. 10 m, inclusive a cover of organic clay, a construction time of only approx. 15 month was necessary.

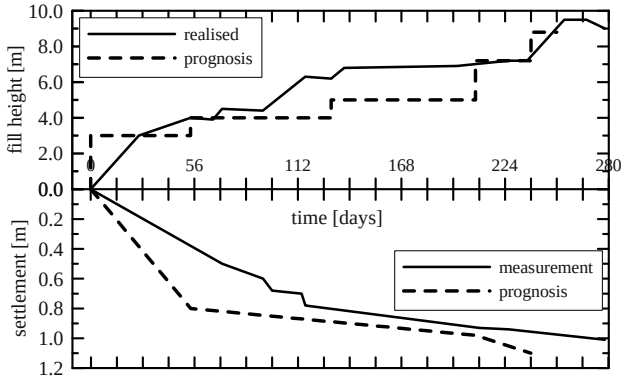

Fig. 5 Measured settlements, for example in section VI

SPECIAL ASPECTS IN CONCEPT AND DIMENSIONING OF A FOUNDATION WITH ENCASED COLUMNS

Through extensive measurements, especially at two test areas in the Netherlands and two test areas in Germany, there could be demonstrated, that the displacement columns were constricted until among the internal diameter of the pipe, because of the horizontal substitution stress by the application of the substitution technique with flap pipes.

To avoid a non-economic provision of the encasing and an underestimation of the appearing settlements, the diameter of the column, before loading by the construction proportional to the diameter of the substitution pipe, has to be considered in the dimensioning. Normally, this results from accretion of a consistent difference of diameter (if the case may be also lower and superior limit values) grounded on measurements of the constriction at comparable boundary conditions of production and soil types.

Additional numerical calculations can be made, whereas after the simulation of the displacement also the different constriction Δr_o in layered soils can be considered (see Figs. 6 and 7). But it is necessary to calibrate the calculation results to the available measured values, because the exact modelling of the production technique (displacement under vibration) also can be acquired hardly with numerical methods. So an additional factor according to measurements is used for the validation of the calculation values by the design.

For the numerical calculation shown in Fig. 7 the program PLAXIS was used. For the soft soil the Soft Soil Model (Cam-Clay type), for the sand and gravel of the column material the Hard Soil Model (modified Duncan/Chang model), was used. By the examination of a single column (according to the "unit cell concept") and the use of an axial symmetric calculation model the ring tension forces, the settlement and the constriction for the design can be determined.

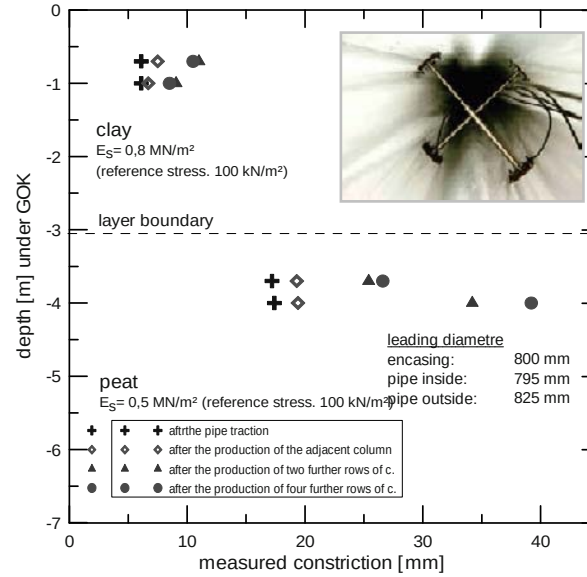

Fig. 6 Measured constriction of a column in layered soil

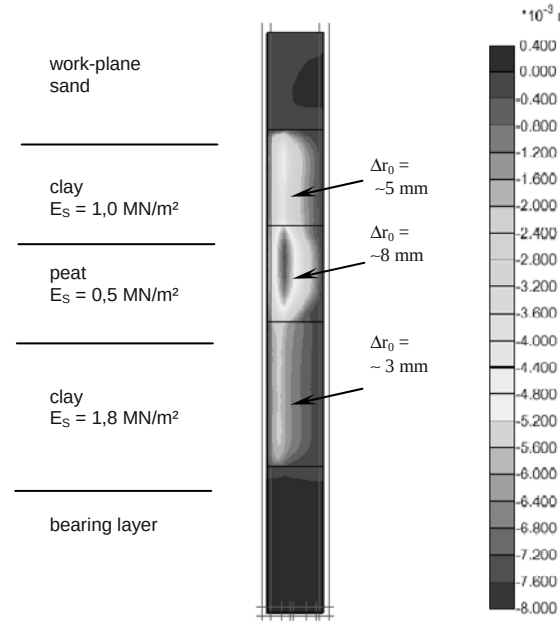

Fig. 7 Numeric (FEM) calculated constriction of a column (diameter 80 cm) in layered soil

During the sinking of the displacement pipe it gets down to a rising of the pore excess pressure and after its decrease an increase of undrained shear strength in the

soft layers. To quantify his influence to the stability in the soft layers, there were made extensive researches.

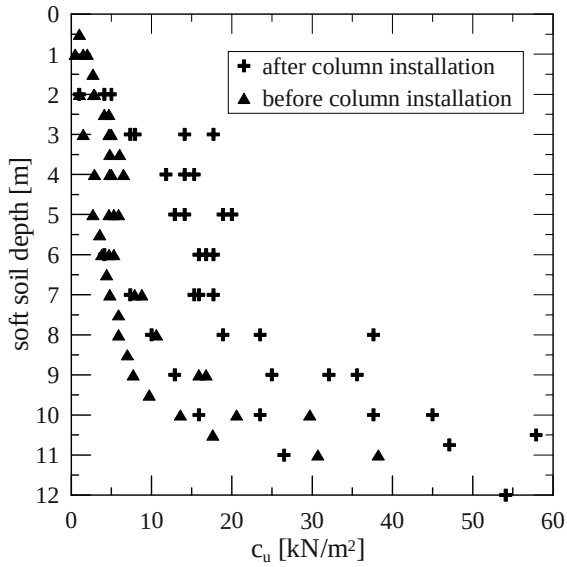

Fig. 8 Measured increase of undrained shear strength by displacement column installation (field tests)

In (Raithel 1999) there are results of in situ measurements described, which show, that at the beginning of the vibrating a rising of the pore excess pressure occurs, but the peak values were broke down rapidly. (Maybaum and Mühlmann 2002) are presenting results of big scale model tests and numeric calculations, which also show, that a continuous rising of the pore excess pressure occurs during the insertion. The peak values thereby occur directly in the region of the column, large-scale hydrodynamic conditional structure break-down, like e.g. a condensation in the soft layers, is not recognized. Comparative vane soundings show the not drained shear strength were meliorated through the inserting of the displacement pipe. In large-scale tests in consideration of a single column, there could be measured a melioration by the factor 1.5—2.0. In small-scale tests (Scale 1:10) considering a 15% column grid (A_C/A_E = 15%) there even could be measured an increasement with factors of 3—3.5 in consideration of the model laws.

In situ measurements for the development of the shear strength in practice shows also a minimal increasement of approx. 1.5—2.0 (see Fig. 8).

In the displacement technique it gets down to a lifting of the soft soil in the range of the columns, because of the substitution of the soft soil at the column installation. This effect has especially to be considered in the case of adjacent buildings, and can lead to, e.g., by the calculation of a dam filling, a decrease of the load, that has to be considered, because of the lesser filling amount until the reaching of the gradient.

Fig. 9 Small-scale model test (scale 1:10)

The ground heightening can apparently be observed in situ. For their quantification there were made extensive in situ measurements within a test area, but also small- and large-scale tests. In Fig. 9 the acquired heightening, which is established with small-scale tests (scale 1:10), is demonstrated exemplary for the production of the third range of columns. Because of the presented experiences the expected heightening can be appreciated with approx. 5%—10% of the soft layer.

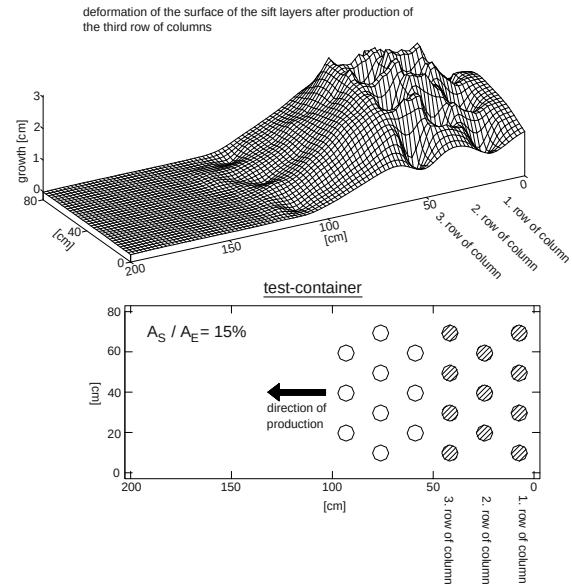

Fig. 10 Deformation of the surface of the soft layer after the production of the third row of column

LONG TIME SETTLEMENT BEHAVIOUR (CREEP)

The effectiveness of a grid-shaped column founda-tion in consideration of a settlement reduction, is essentially based on a stress concentration above the heads of columns, linked with an unloading of the soft layers, which is made possible because of an arch action in the ballast covering. The primary settlements thereby occur towards the laws of the consolidation theory, whereas an enormous acceleration of settlement is given, because of

the effect of the encased columns as big vertical drains. As a rule a big part of the primary settlements subsides during the construction period and can be compensated.

For the detection of the residual settlements there are to consider the primary settlements and also the secondary- and creep settlements.

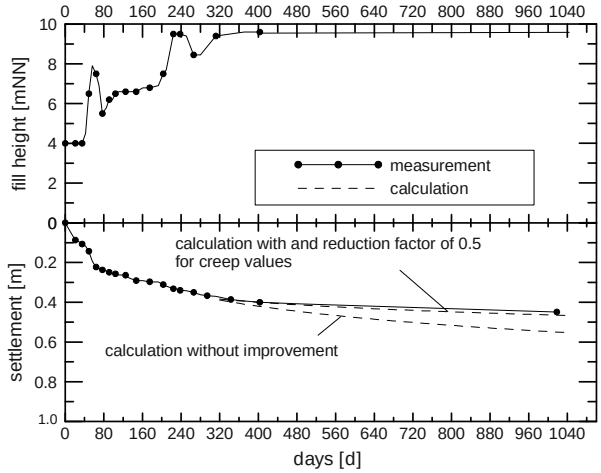

Fig. 11 Results from long-time measurements and calculations

In the literature (Edil et al. 1994) is described, that creep deformations result against these load change, which create the deformation. As the soft layer is less loaded, because of the stress concentration above the columns, so there is generally to count on a reduction of the creep settlement compared to the unimproved basement soil, because of the application of encased columns. Furthermore, the soft layer in consideration of the creep settlements underlies a stronger settlement than the column does. Hence, as a rule it gets down to a change in load relocation, because of the interactive load-bearing system and finally to a new equilibrium condition. Therefore, with a column foundation a further reduction of the creep settlements is reached, compared to the unimproved situation.

This effect could also be approved with measurement techniques in available long-time measurements. In Fig.11 measurement results of the dike foundation for the enlargement of the factory premises of the aircraft dockyard in Hamburg-Finkenwerder are demonstrated compared to calculational prognoses of the creep settlements. The outcome of this is, that by the approach of creep coefficients, which were declared and respectively differentiated for the unimproved basement soil (i.e., without column foundation), considerable bigger creep settlements were prognosticated in comparison to the measurement results. With a calculational prognosis using a correction factor of 0.5 for the creep settlements of the unimproved basement soil (see Eq. 1), the measurement results, in contrast, can well be reproduced.

$$s_k = R_{GEC} \cdot c_\alpha \cdot h_1 \cdot \log (t_{sk} / t_1) \qquad (1)$$

with:

s_k	creep settlement using GEC
R_{GEC}	Reduction factor by GEC = 0.25 to 0.5
c_α	creep factor
h_1	thickness of soil after consolidation
t_{sk}	time
t_1	end of consolidation

GERMAN RECOMMENTATIONS AND STANDARDS

At present, there is worked on the preparation of chapter 6.10 of EBGEO “Gründungsssystem mit geokunsts-toffummantelten Säulen” within the working group of the DGGT. A first concept of this recommendation is already available. Basically, here should be compiled recommendations for construction, calculation and realisation of geosynthetic encased column foundations. Comply with this regulations, the effectiveness of the foundation is ensured. The structure of the current concept comprises the scopes:

(1) Terms and definitions
(2) Effectiveness and application scopes
(3) Production technique
(4) Concept recommendations and construction notes
(5) Materials
(6) Details for calculation and dimensioning
(7) Test criteria, tolerances and quality control

REFERENCES

Edil TB, Fox PJ, Lan LT (1994) Stress-Induced One-Dimensional Creep of Peat; Advances in Understanding and Modelling the Mechanical Behaviour of Peat, Balkema, Rotterdam

Maybaum G, Mühlmann J (2002) Porenwasserdruck-Festigkeits- und Verschiebungsentwicklung bei Verdrängungsbohrungen in bindigen Böden. Syposium, Messsen in der Geotechnik, Institut für Grundbau und Bodenmechanik der TU Braunschweig, Heft 68

Raithel M (1999) Zum Trag- und Verformungsverhalten von geokunststoffummantelten Sandsäulen; Heft 6, Schriftenreihe Geotechnik, Universität Kassel

Raithel M, Kempfert HG (2000) Calculation Models for Dam Foundations with Geotextile Coated Sand Columns. Proc. International Conference on Geotechnical & Geological Engineering GeoEng 2000, Melbourne

Raithel M, Kirchner A, Schade C, Leusink E (2005) Foundation of constructions on very soft soils with geotextile encased columns—State of the art. ASCE-conference Geo-Frontiers 2005, Austin, USA

Proceedings of the 4th Asian Regional Conference on Geosynthetics
June 17 - 20, 2008 Shanghai, China

FORMULA OF PILE-SOIL STRESS RATIO IN PILE (SAND PILE)-NET (GEOGRID) COMPOSITE GROUND

L.R. Xu[1] and D.W. Lv[2]

ABSTRACT: Pile-net composite ground is a new method for ground improvement, which comprises both vertical piles and horizontal "net"— geosynthetic. In this kind of ground improvement method, net and piles as well as soil work together and perform compatibly, thus many advantages such as small settlement deformation, good stability and short construction period have been found in practical engineering and theoretical researches. And it has been concluded that the pile-soil stress ratio is an important parameter for design and research of pile-net composite ground, therefore based on the field research and measured data, combined with previous research, a calculation formula of pile-soil stress ratio in the pile-net composite ground, which is composed of sand piles and sand cushions reinforced with geogrid, was proposed with taking the effects of the reinforcement into account. And the comparison between calculated and observed field results showed this formula is applicable. In the later research, the interface friction coefficient (IFC) between reinforcements and soil should be considered in the formula to make it more perfect.

KEYWORDS: pile-soil stress ratio, pile-net composite ground, sand pile, geogrid, interface friction coefficient

INTRODUCTION

When embankments are constructed on soft ground, it is essential to improve the ground so as to keep it stable and limit its settlement. One of the efficient improvement methods is to drive piles into soft ground at first, then to lay horizontal "net" —geosynthetic— beneath the embankment. After improvement, net, piles and soil perform compatibly and work together to resist loads. This type of artificial foundation is called "reinforced piled embankment" (Jones et al. 1990), "Geosynthetic-reinforced and pile-supported composite foundation" (Yan et al. 2005) and called "pile-net composite ground system" by some scholars (Rao and Zhao 2002). The pile-net composite ground system comprises: (1) fill; (2) geosynthetic reinforced cushion; (3) pile-soil reinforcement region.

Pile-net composite ground has the comprehensive effectiveness of pile, mat, and drainage, squeezing denseness, reinforcement and prevention. It settles rapidly and has a small settlement deformation, and is especially applicable to quick construction of embankments and dams on natural ground. Recent works focus on studying the performance of pile-net composite ground by numerical analysis (Gabr and Han 2002) or field experiments (Bergado et al. 2002). The pile-soil stress ratio, i.e., the load sharing between a pile and the supporting soil, is a significant parameter which can reflect the performance of pile-net composite ground and related to the calculation of the stability, bearing capacity and especially settlement. Based on previous research, the pile-soil stress ratio of pile-net composite ground composed of sand piles and sand cushions with one-layer reinforcing net (geogrid) was researched in this paper. A calculation formula for pile-soil stress ratio of this type of pile-net composite ground was proposed. The comparison between pile-soil stress ratios calculated with those measured in Kunshan (located in the southern part of Jiangsu Province, P.R. China) trial embankment in Jinghu high-speed railway showed that the calculated results were relatively accordant with practical results. But the interaction effect between reinforcements and soil was not reflected in this formula, which leaded to the increasing difference between calculated and practical results in the late stage, so the formula should be perfected in later research.

DERIVATION OF THE FORMULA

Liu (2003) put forward a formula for pile-soil stress ratio of composite ground beneath embankments, which

[1] Dr. & Prof. School of Civil Engineering and Architecture, Central South University, Changsha 410075, CHINA. Email: lrxu@mail.csu.edu.cn
[2] PhD Student. School of Civil Engineering and Architecture, Central South University, Changsha 410075, CHINA. Email: cwdp2004@126.com

neglected the reinforcing effect. To simplify the deduction of the formula, he simplified the fill above the pile to the cylinder (inside fill cylinder) with the diameter d (d is equal to the pile's diameter), the fill above the soil around piles to the cylinder shell (outside fill cylinder) with the pile being the axis. By taking a micro unit from the inside fill cylinder to analyze its force, the stress in the plane of the top of piles (σ_p) is:

$$\sigma_p = \begin{cases} \dfrac{\gamma \cdot d}{4f \cdot k_i}\left(e^{4f \cdot k_i \cdot h/d} - 1\right) & h \le h_L \\ \dfrac{\gamma \cdot d}{4f \cdot k_i}\left(e^{4f \cdot k_i \frac{h_L}{d}} - 1\right) + \gamma\left(h - h_L\right)e^{4f \cdot k_i \frac{h_L}{d}} & h > h_L \end{cases} \quad (1)$$

where, γ is the fill gravity; f is the parameter relating to the internal friction of fill. f =tanφ, where φ is the internal friction angle of fill; k_i is the horizontal earth pressure coefficient. k_i = tan^2(45° − φ/2); h is the fill height; h_L is the fill critical height for the even subsidence plane and is relative to h, E (elastic modulus of fill), ΔS (pile-soil differential settlement), etc. The calculation method of h_L can be found in the reference (Liu 2003).

The above formula derived from the non-consideration of the reinforcing effect of geosynthetic, in fact when geosynthetic is embedded beneath the embankment, under the impact of the embankment load, the reinforcement produces tensile stress and restrains the lateral deformation by the frictional resistance. This equals to producing the lateral restraining stress that can increase the strength and modulus of composite ground and then deliver the top load to piles and decrease the load in soil around piles. Therefore, the reinforcing net can improve the pile-soil stress ratio in the plane of the top of piles (Meng et al. 2004).

In the following paragraphs, we will study the influence of the geosynthetic on the pile-soil stress ratio. Under the impact of the fill load, the flexible geosynthetic will be concaved. Its deformation can be shown in Fig. 1.

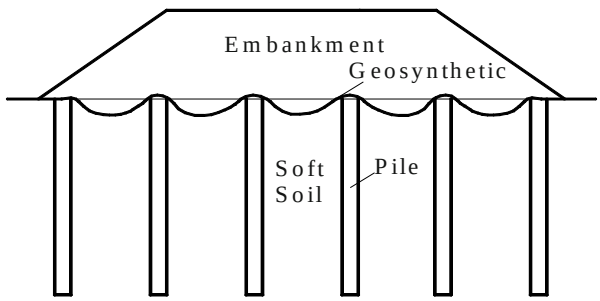

Fig. 1 Deformation of geosynthetic under embankment load

Take a unit from Fig.1, and further analysis performed as Fig. 2, for the geosynthetic beneath the embankment, the AB section above the sand pile is selected to be the calculation unit. Omitting the friction between geosynthetic and soil, the stresses on the unit include: (1) the downward compressive stress σ_p from the inside filling cylinder; (2) the upward compressive stressσ_p' from the sand pile; (3) the around slantingly downward tensile stressσ_g (has θ with the horizontal line).

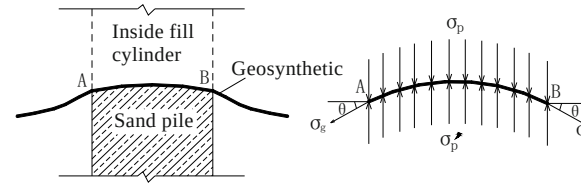

Fig. 2 Calculation unit of geosynthetic

The sand pile's cross sectional area is A_p. Then in vertical direction, the balance equation is:

$$\sigma_p' \cdot A_p = \sigma_p \cdot A_p + \sigma_g \cdot \pi \cdot d \cdot \sin\theta \quad (2)$$

modified as:

$$\sigma_p' = \sigma_p + \frac{4\sigma_g \cdot \sin\theta}{d} \quad (3)$$

where, $\sigma_g = E_g\varepsilon$; E_g is the tensile modulus of the geosynthetic (kN/m); ε is the strain of the geosynthetic in normal working condition.

The calculation of sinθ can be seen in Fig. 3. The simple maths theory puts out that the "θ" in Fig. 3 is equal to the one in Fig. 2.

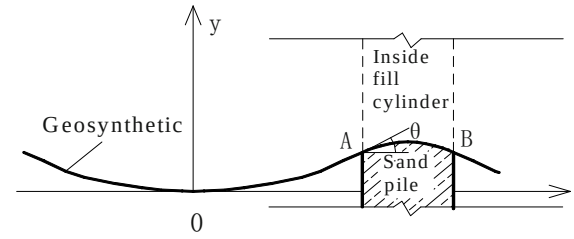

Fig. 3 Sketch map of θ

Under the embankment load, the flexible geosynthetic will be concaved in the range of soil around piles. The concaveness forms a catenary. When the deformation is smaller (i.e., pile-soil differential settlement is smaller), it can be regarded as a parabola (Jones

et al. 1990). Then in the coordinate system of Fig. 3, the equation of the parabola is:

$$y = ax^2 \tag{4}$$

The parabola passes the dot A (the same as the one in figure 2). The coordinate of A can be regarded as $x=L/2$, $y=\Delta S$. L is the distance between two adjacent piles and ΔS is the pile-soil differential settlement.

Substituting the coordinate of A to Eq. (4), it can be found that the uncertain coefficient "a" is equal to $4\cdot\Delta S/L^2$, so the parabola's equation is:

$$y = \frac{4\cdot\Delta S}{L^2}x^2 \tag{5}$$

The slope of the parabola at A can be drawn from Eq. 5:

$$y'\big|_{x=\frac{1}{2}L} = \frac{4\cdot\Delta S}{L} = \tan\theta \tag{6}$$

Thus:

$$\sin\theta = \sqrt{\frac{\tan^2\theta}{1+\tan^2\theta}} = \frac{4\cdot\Delta S}{\sqrt{16\cdot\Delta S^2 + L^2}} \tag{7}$$

Substituting Eq. (7) to Eq. (3), then:

$$\sigma_p' = \sigma_p + \frac{16\cdot\sigma_g\cdot\Delta S}{d\sqrt{16\cdot\Delta S^2 + L^2}} \tag{8}$$

Substituting Eq. 1 to Eq. 8, the stress in the top of piles can be gotten as follows:

$$\sigma_p' = \begin{cases} \dfrac{\gamma\cdot d}{4f\cdot k_i}\left(e^{4f\cdot k_i\cdot h/d} - 1\right) + G & h \le h_L \\ \dfrac{\gamma\cdot d}{4f\cdot k_i}\left(e^{4f\cdot k_i\frac{h_L}{d}} - 1\right) + \gamma\left(h - h_L\right)e^{4f\cdot k_i\frac{h_L}{d}} + G & h > h_L \end{cases} \tag{9}$$

where, $G = \dfrac{16\cdot\sigma_g\cdot\Delta S}{d\sqrt{16\cdot\Delta S^2 + L^2}}$.

Regarding the embankment fill and the geosynthetic as a whole, the forces imposed on it can be analyzed. The stresses include downward gravity and the upward stress from piles and soil around piles. Omitting the geosynthetic's gravity and height and the effect of pile-soil differential settlement, the balance equation in the vertical direction is drawn as follows:

$$\gamma\cdot h = m\cdot\sigma_p' + (1-m)\sigma_s' \tag{10}$$

where, γ is fill unit gravity, h is fill height, m is area replacement ratio of sand piles and σ_s' is the stress on the surface of the soil around piles.

Then Eq. (11) can be drawn from Eq. (10):

$$\sigma_s' = \frac{\gamma\cdot h - m\cdot\sigma_p'}{1-m} \tag{11}$$

Thus, the pile-soil stress ratio n in the plane of the top of piles can be deducted from Eq. 9 and 11:

$$n = \frac{\sigma_p'}{\sigma_s'} = \begin{cases} \dfrac{\left[\dfrac{\gamma\cdot d}{4\cdot f\cdot k_i}\left(e^{4f\cdot k_i\cdot h/d} - 1\right) + G\right](1-m)}{\gamma\cdot h - m\left[\dfrac{\gamma\cdot d}{4\cdot f\cdot k_i}\left(e^{4f\cdot k_i\cdot h/d} - 1\right) + G\right]} & h \le h_L \\ \dfrac{\left[\dfrac{\gamma\cdot d}{4\cdot f\cdot k_i}\left(e^{4f\cdot k_i\cdot h_L/d} - 1\right) + \gamma\left(h - h_L\right)e^{4f\cdot k_i\cdot h_L/d} + G\right](1-m)}{\gamma\cdot h - m\left[\dfrac{\gamma\cdot d}{4\cdot f\cdot k_i}\left(e^{4f\cdot k_i\cdot h_L/d} - 1\right) + \gamma\left(h - h_L\right)e^{4f\cdot k_i\cdot h_L/d} + G\right]} & h > h_L \end{cases} \tag{12}$$

Eq. 12 is the calculation formula proposed in this paper for pile-soil stress ratio of pile-net composite ground. In this formula, the variable "G" considers the reinforcing effect of geosynthetic. From the formula, this part makes the calculation result of pile-soil stress ratio bigger.

It must be pointed out that when there is pile-soil differential settlement beneath embankment, Eq. 10 is actually incorrect because its premise is the transfer of load is rigid (Priebe 1976), namely, the strain at the bottom of embankment is equivalent everywhere, but if the pile-soil different settlement is very little, Eq. 10 can be considered as an approximately equation. So the Eq. 12 is only applicable when the pile-soil differential settlement is not large. According to relevant studies (Jones et al. 1990; Liu 2003; Rao and Zhao 2002) and the authors' experience, the formula should be accurate enough if $\Delta S/L$ is less than 5%. The applicability of Eq. 12 will be detailedly discussed in the future research.

CASE

This trial embankment (See Fig. 4) of high-speed railway located in Taihu lake deposit plain of JiangSu province, P.R. China. And the strata belong to the Quaternary Holocene Lake Deposit Stratum. Sand piles improve the soft ground, the diameter of piles is 0.4 m and the distance between adjacent piles is 2.0 m, as is

shown in Fig. 5. The length of a pile is 15 m or 25 m. The height of embankment is 6.29 m, and geogrid reinforced sand cushion is imbedded beneath the embankment (Fig. 6). There were 3 observation sections. In each section, settlement plates, earth pressure gauges and flexible displacement gauges were embedded under the embankment. More details of the field observations can be obtained in the reference (Xu et al. 2005).

Fig. 4 The trial embankment

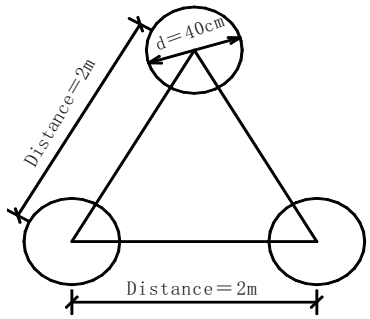

Fig. 5 Collocation of piles

Fig. 6 Displacement transducer of geogrid in sand cushion

According to Eq. 12, the pile-soil stress ratio in different time (for the different fill height h, pile-soil differential settlement ΔS and strain of the geogrid ε) can be calculated. The calculation parameters were presented in Tables 1 and 2. Only the parameters of Section I were listed because parameters of different sections were similar.

Table 1 Calculation parameters of Section I for pile-soil stress ratio (Invariable parameters)

φ (°)	E (MPa)	γ (kN/m^3)	d (m)	L (m)	m	E_g (kN/m)
30	10	20	0.4	2	0.0363	120

Table 2 Calculation parameters of Section I for pile-soil stress ratio (Variable parameters)

Date	h (m)	ΔS (mm)	ε
2003-5-24	0.3	5.7	0.004
2003-6-10	0.6	7.5	0.007
2003-7-3	1.05	10.6	0.007
2003-7-27	1.87	15.0	0.007
2003-8-6	2.22	15.4	0.008
2003-8-15	2.61	17.9	0.007
2003-8-29	3.24	18.6	0.009
2003-9-11	3.97	19.0	0.011
2003-10-14	4.49	20.2	0.013
2004-9-1	6.29	30.0	0.015

In this table, the internal friction angle φ of filling and the elastic modulus E is valued by the indoor experiments, in-situ tests and the experience; the values of ΔS and ε were obtained by field measurements.

Figs.7 and 8 compare pile-soil stress ratio curves calculated with measured at site in two sections.

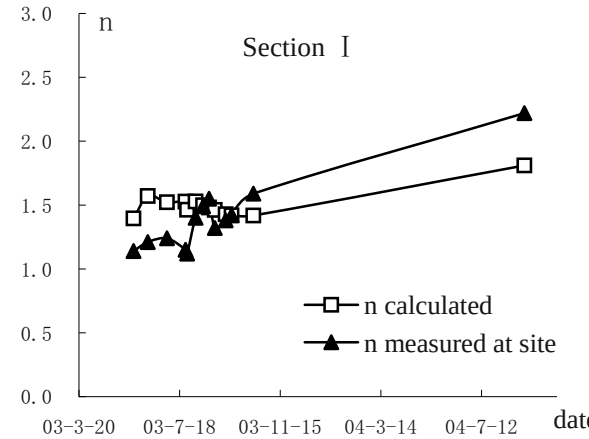

Fig. 7 Pile-soil stress ratio curves （Section Ⅰ）

From Figs.7 and 8, it is shown that the calculation results and the measured results of pile-soil stress ratios are close in the whole and the developing trend is correspondent.

The interaction effect between reinforcements and soil was not reflected in this formula, but in fact, the

interface friction has influence on the pile-soil stress ratio. During the interaction among pile, soil and net, the friction between geogrid and soil was gradually increasing, which made the pile-soil stress ratio increased, so in Figs.7 and 8, the calculated results were lower than the measured ones in late stage.

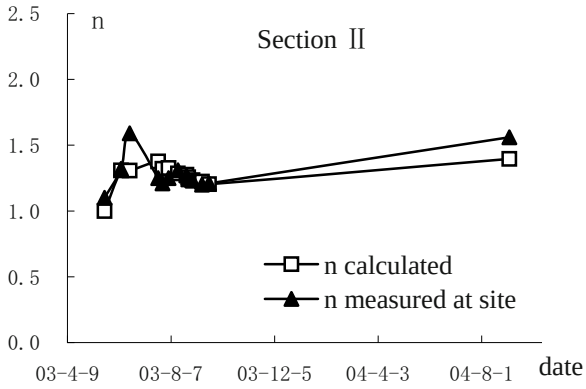

Fig. 8 Pile-soil stress ratio curves （Section Ⅱ）

CONCLUSIONS

Based on Liu's calculation formula (Liu 2003), this paper deduced the formula for pile-soil stress ratio of pile-net composite ground composed of sand piles and sand cushions with one-layer geogrid. Through comparison with the measured data, the reasonableness of the formula is testified. This formula can be the valuable reference in design and research. But the interaction between geogrid and soil was not reflected, which leaded to the increasing difference between calculated and practical results in late stage, so in the further research, the interface friction coefficient between reinforcements and soil should be considered to make the formula more precise.

ACKNOWLEDGEMENTS

The authors wish to acknowledge the financial help of National Natural Science Foundation of China (NSFC 50578159). We also acknowledge experts and technical personnel from the Fourth Survey and Design Institute of China Railway, China Tiesiju Civil Engineering Group Co. Ltd, Tongji University and Southwest Jiaotong University. They provided precious advice and help in field tests and observations.

REFERENCES

Bergado DT, Long PV, Murthy BRS (2002) A case study of geotextile-reinforced embankment on soft ground. Geotextiles and Geomembranes 20 (6): 343-365

Gabr MA, Han J (2002) Numerical analysis of geosynthetic-reinforced and pile-supported earth platforms over soft soil. Journal of Geotechnical and Geoenvironmental Engineering 1: 44-53

Jones CJFP, Lawson CR, Ayres DJ (1990) Geotextile reinforced piled embankments. Proc., Geotextile, Geomembranes and Related Products, Den Hoedt (ed.), Balkema, Rotterdam, ISBN90: 155-160

Liu JF (2003) Analysis on pile-soil stress ratio for composite ground under embankment. Chinese Journal of Rock Mechanics and Engineering 22 (4): 674-677 (in Chinese)

Meng QH, Xia YF, Xia YY (2004) The influence of the geogrid on the pipe-soil stress ration of composite-foundation. Soil Engineering and Foundation 18 (6): 52-54 (in Chinese)

Priebe HJ (1976) Design criteria for ground improvement by stone columns. Keller FmbH, Offenbach

Rao WG, Zhao CG (2002) The behavior of pile-net composite foundation. China Civil Engineering Journal 35(2): 74-80 (in Chinese)

Xu LR, Lü DW, Wang M, Gu SF (2005) Analysis on the settlement properties of soft ground improved by sand piles. Proc., Progress in Safety Science and Technology, Shaoxing, Zhejiang, China, V: 2180-2185.

Yan L, Yang JS, Han J (2005) Geosynthetic-reinforced and pile-supported earth platform composite foundation. Rock and Soil Mechanics 26(5): 821-826 (in Chinese)

PERFORMANCE OF ENCASED STONE COLUMNS AND DESIGN GUIDELINES FOR CONSTRUCTION ON SOFT CLAY SOILS

S. Murugesan[1] and K. Rajagopal[2]

ABSTRACT: One common approach for treatment of soft clay soils is the installation of stone columns. The load capacity of the stone columns depends very much on the shear strength of the surrounding soft clay soil. The stone columns help in both reduction of settlements and accelerated pre-consolidation of clay soil deposit. However, in case of extremely soft clay soils, the stone column formation may be difficult due to lateral spread of stones. The contamination of stone aggregate by the ingression of soft clay soil may inhibit the drainage function of stone columns. The geosynthetic encasement of stone columns is an ideal solution for enhancing the performance of stone columns in such conditions. The geosynthetic encasement helps in easy formation of the stone column and improves the strength and stiffness of the columns. This paper presents the results from a laboratory based studies on the performance of the encased stone columns. The laboratory studies consisted of load tests on stone columns with and without encasement in a clay bed formed in unit cell tank. The encasement was found to significantly improve the load capacity of the stone columns. Using the tension membrane theory for analysing the hoop strains in the geosynthetic encasement, design methodology has been developed for the selection of the geosynthetic material for use as encasement.

KEYWORDS: geosynthetics encasement, stone column, granular pile, ground improvement, soft soil

INTRODUCTION

Some problematic soils like soft clay deposits, peat soils, recent fills, marine clays, etc. posses problems in construction because of low bearing capacity, high compressibility, tendency for lateral flow, etc. These grounds need treatment for the improvement in their engineering behaviour as per the design requirements of the structure.

For flexible and lightly loaded structures lime columns or stone columns are the ideal form of ground improvement. The stone columns are best suited for the soft clay soils, peat and cohesive deposits and silty soils. The stone column (also called granular pile) is nothing but a vertical column element formed below the ground level with compacted and uncemented stone fragments or gravels. When the stone column is subjected to vertical loading, it undergoes significant vertical compression caused by the lateral straining or bulging of the aggregates. As the column simultaneously bulges and moves downward, the granular material presses into the surrounding soft soil and transfers stress to the soil through shear. This bulge, in turn, increases the lateral stress within the clay which provides additional confinement for the stone. An equilibrium state is eventually reached resulting in reduced vertical movement when compared to the unimproved soil (Greenwood 1970; Hughes et al. 1975).

One of the limitations of stone column technique is that it depends on the surrounding clay soil for the mobilization of load carrying capacity. The load capacity can not be improved more than 25 times the strength of the soft clay (Chummar 2000). Besides this, in soft clays the stone column installation itself may be difficult with loss of stones due to low confinement from the surrounding soft clay and the contamination of stone aggregate by the intrusion of soft clay soil will reduce the frictional strength of the aggregate and impede the drainage function of the column (McKenna et al.1975).

These drawbacks can be overcome by wrapping the individual stone columns with a suitable geosynthetic. The geosynthetic encasement helps in easy formation of the stone column and improves the strength and stiffness of the columns. Several advantages can be gained from encasement of stone columns like stiffer column, preventing the loss of stones into surrounding soft clay etc. as described by Raithel et al. (2002), Dimiter et al.

[1] Formerly Research Scholar, Department of Civil Engineering, Indian Institute of Technology Madras, Chennai – 600036, INDIA. Email: smgsoil@yaho.com
[2] Professor, Department of Civil Engineering, Indian Institute of Technology Madras, Chennai – 600036, INDIA. Email: gopalkr@iitm.ac.in

(2005) Murugesan and Rajagopal (2006), Kempfert and Gebreselassie (2006) and di Prisco et al. (2006).

In this paper the behaviour of these stone columns is investigated by model laboratory tests conducted in a unit cell tank having the stone column at the centre and the tributary soil surrounding it. This will represent a typical unit cell in the field among the grid of stone columns. From these tests the increased load capacity of the stone column is quantified based on the stiffness of the geosynthetic used for the encasement. The influence of the other parameters such as the diameter of the stone column and stiffness of the geosynthetic encasement are also investigated. The results from experimental investigations are analysed in detail through analytical models and design guidelines were framed from the analytical model and design charts have been presented in non-dimensional form relating various parameters involved in the design.

DESCRIPTION OF EXPERIMENTS

Materials Properties

The stone aggregates to form the stone columns in the present investigation were of granite chips, which are popularly used for the concreting and stone columns. They were uniformly graded and of size passing 10 mm sieve and retained in 2mm sieve. The angle of internal friction of stone aggregates as determined by the direct shear test is 41.5º. The unit weight of the stone fill in the stone column was maintained constant through out all the tests close to 1.6 gm/cc.

For encasing the stone column four different types of geosynthetics were used in the present study namely woven geotextile, nonwoven geotextile, soft grid - 1 with fine mesh and soft grid – 2 with coarse mesh. The tensile strength properties were determined from standard wide width tension tests (American Society for Testing and Materials, ASTM- D4595, 1986) and are listed in Table 1. As the geosynthetics were stitched to form the tube for encasing the stone column, the seam strength of the geosynthetic was also determined with geosynthetic specimens having a horizontal seam at mid length. In all the tension tests, the size of the geosynthetic specimen was 200 mm wide and 100 mm long. The failure observed in the junction peel test of woven and non woven geotextile was due to the tearing of the seam, whereas in the case of soft grids 1 and 2, the seam was intact and the sample yielded to a greater extent due to the high elongation of the material.

Table 1 Properties of geosynthetics used for the stone column encasement

Strength Properties	Woven geotextile	Nonwoven geotextile	Soft grid 1	Soft grid 2
Ultimate tensile strength (kN/m)	20	6.8	2.5	1.5
Ultimate seam strength (kN/m)	4.7	4.6	2.2	1
Initial modulus (seam) (kN/m)	17.5	12	9.6	1.5
secant modulus (seams) (kN/m)	15	12	4	1.5

Clay for the test was obtained from the lake beds. From the clay soil, normally consolidated clay, which was used for all the testing, was obtained by consolidating the slurry clay as per the following procedure. The clay was mixed with water thoroughly in a large tank (the quantity of water was such that the water content after mixing is approximately up to 1.5 times the liquid limit of the clay) to form slurry free from any lumps or flocks. This slurry was allowed to consolidate under a pressure of 10 kPa in a large tank by using dead weights and the settlement was monitored with the help of dial gauges. Drainage was permitted at the top and bottom by placing 75 mm thick sand layer sandwiched between suitable geotextile. The consolidation was prolonged for a period 8—10 days until the rate of settlement is less than 1 mm per day. This procedure yielded clay of uniform properties throughout the mass and the properties of the clay prepared by this procedure are listed in Table 2.

Table 2 Properties of clay

Properties	Values
Liquid limit	49%
Plastic limit	17%
Specific Gravity	2.59
Placement Moisture content	47 ± 1%
In-situ vane shear strength	2.5 kPa
Consistency Index	0.06
Dry unit weight	11.56 kN/m^3
Unified Soil Classification System	CL
Degree of Saturation	96%

Installation of Stone Column

All the load tests in the present study were performed on stone column installed in clay bed formed in a cylindrical steel tank (unit cell tank) of 210 mm diameter and 500 mm height. This tank will represent a typical unit cell in a grid of stone column with square pattern

spaced at 200 mm centre to centre or triangular pattern at 186 mm centre to centre. The schematic of the unit cell used is shown in Fig. 1. The clay bed is formed in the unit cell tank and the top of the clay surface is trimmed and levelled.

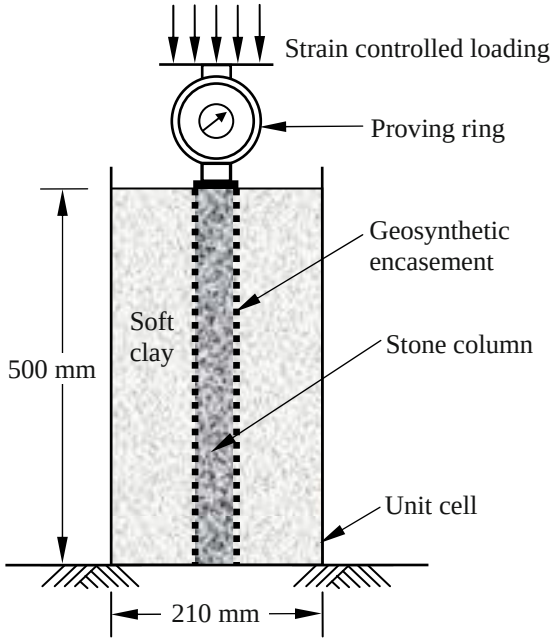

Fig. 1 Schematic of the load test on stone columns in a unit cell

The stone columns in the current study were installed by displacement method using a casing pipe having an outer diameter equal to the diameter of the stone column. The encased stone columns were installed by wrapping the geosynthetic around the casing pipe. The casing pipe along with a base plate having a circular groove to accommodate the casing pipe was pushed into the clay bed vertically at the specified location in the clay surface till it reaches the bottom of the tank. The base plate is to prevent the surrounding clay soil from entering into the pipe during the lowering of the casing pipe. The displaced clay during the installation was taken out and the surface of the soil was trimmed to its original level. The quantity of the stone aggregate required to form the stone column was pre-measured and charged into the casing pipe in layers of 50mm thickness. The stone aggregate was moistened before charging into the casing pipe in order to prevent it from absorbing the moisture from the surrounding clay. After placing each layer of stone aggregate, the casing pipe was lifted up gently (leaving the base plate and the geosynthetic encasement intact) to a height such that a minimum overlap of 15 mm between the bottom of the casing pipe and the stone fill within the casing pipe was always maintained. This is to prevent the necking of the geosynthetic encasement due to the lateral thrust by the surrounding clay. In the case of ordinary stone column, this method of installation ensures the continuity of the stone columns by preventing the clay soil from entering the casing pipe. Immediately after lifting the casing pipe, the stone aggregate was compacted with a tamping rod (10 mm diameter and 1 meter long) with 25 numbers of blows falling from a height of 250 mm. Each layer of aggregate was compacted using the same number of blows. The procedure was repeated until the entire height of the stone column was formed. The top surface of the stone column was levelled and any protruding geosynthetic was cut and trimmed flush with the surrounding clay surface.

Load Test on Stone Columns

After stone column installation the entire tank set up is placed in the loading frame and the loading is applied through strain controlled displacement of loading plate at a constant strain rate of 1.2 mm/minute. All the tests were done by loading only the stone column area to directly assess the benefits of encasement. The settlement in the stone column was measured with the help of a dial gauge at suitable intervals of time. The pressure on the stone column for various displacements was measured through a proving ring.

As the loading is quick it is essentially undrained loading, which simulates the field situation immediately after construction stage. Three series of tests were conducted by varying the diameter of the stone columns. First series of tests were conducted on the clay soil without any stone columns. Second series of tests were on Ordinary stone column without any encasement, (herein after referred as OSC) of three different diameters. Third series of test was on the geosynthetic encased stone column (herein after referred as ESC) with different diameter and different type of geosynthetic for the encasement. Load tests were conducted on ordinary stone columns (OSC) and the geosynthetic encased stone columns (ESC) to directly compare the relative performance and the increased load capacity due to the encasement. As the confinement effect is highly depend on the diameter of the specimen the tests were conducted on three different diameters of stone columns i.e., 50, 75 and 100 mm in order to predict the influence of the diameter of the stone column. The other parameter considered was the modulus of the geosynthetic used for the encasement; this was varied by using different types of geosynthetics for the encasement.

RESULTS AND DISCUSSIONS

Effect of Encasement of the Stone Column

A typical pressure settlement response is shown in Fig. 2. The figure shows the pressure settlement curves for the case of ordinary stone column and Encased stone columns encased with non woven geotextile, of three diameters, 50, 75 and 100 mm.

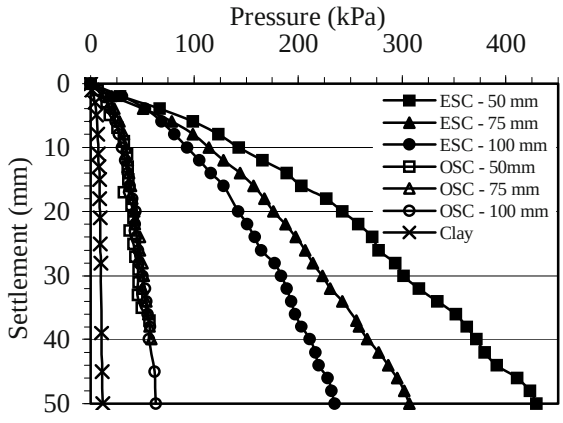

Fig. 2 Pressure settlement response of the stone columns encased in nonwoven geotextile

The ordinary stone columns show a clear catastrophic failure. Whereas the encased stone columns have shown elastic behaviour, and there is no remarkable failure, and the same was verified by plotting the log-log plot. The load carrying capacity of individual stone column for a settlement of 10 mm is increased by 3—5 folds. The ESCs behave like elastic semi-rigid flexible piles. The failure of ESCs could be due to the excessive settlement or bursting of the geotextile. In the case of ESCs the compression of the stone column was mainly due to the readjustment of the particle within the stone column and the elongation of the geosynthetic encasement. In the present study the failure was not observed even for the settlement of 50mm (i.e. 10% of the column length). The bulging was very much minimized which was observed from the exhumed stone columns after load tests, Whereas the OSCs underwent large settlement because of the excessive bulging occurring at the top end of the column. The bulging was observed from the mould prepared by filling the plaster of paris in the place of stones in the ordinary stone columns after exhuming the stones. Fig. 3 shows the load settlement response of the stone columns encased with woven geotextile for the three diameters (50 mm, 75 mm and 100 mm) of the stone column.

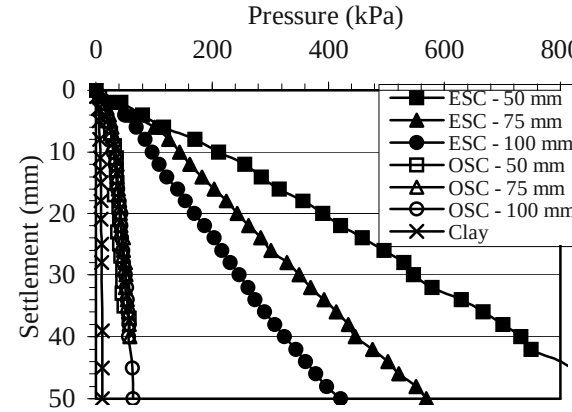

Fig. 3 Pressure settlement curves for stone columns encased in woven geotextile

Influence of the Diameter of the Stone Column

In the case of OSCs the load capacity is almost same for all the diameters. Whereas for the ESCs it could be observed from Figs. 2 and 3 that as the diameter increases the load capacity of encased stone column decreases. The load capacity is found to depend very much on the diameter of the stone column. Similar trend was reported by Murugesan and Rajagopal (2006) based on the numerical analysis also. The same trend of results was observed from the load tests conducted on the stone columns encased with woven geotextile for three different diameters. The variation of the load capacity at 10 mm settlement of the stone column with diameter of the stone column is shown in Fig. 4 for the case of OSC as well as for the case of ESCs with woven and non woven geotextile encasement.

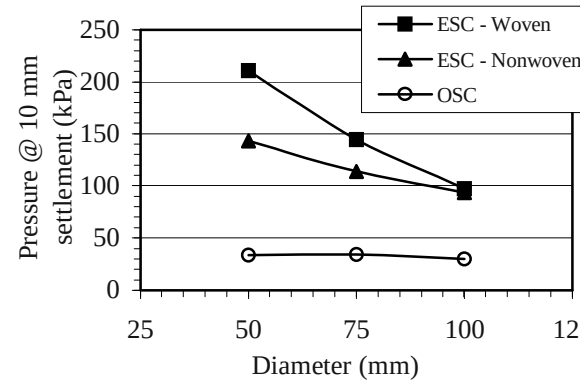

Fig. 4 Variation of the pressure corresponding to 10 mm settlement with the diameter of the stone columns

It is observed from the figure that the decrease in the load capacity is almost linear with the increase in diameter. The reason for the lesser load capacity is due to the lesser mobilization of lateral confinement in the large diameter stone columns.

Influence of Stiffness of the Geosynthetics

Fig. 5 shows the pressure settlement response of 75 mm diameter stone column encased with various geosynthetics.

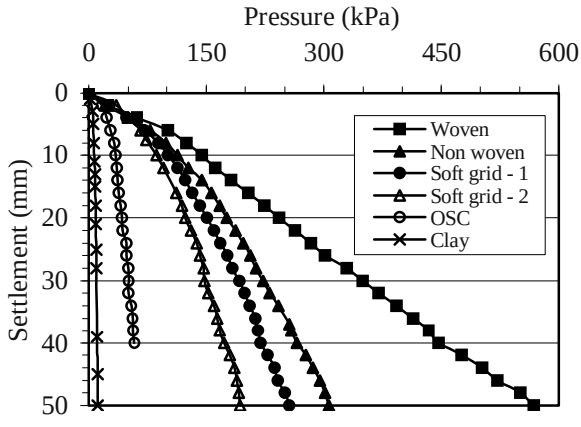

Fig. 5 Load settlement curve for 75 mm diameter stone columns encased with different types of geosynthetics

From the figure it is observed that the stone column encased with the woven geotextile is stiffer, next comes the nonwoven and the soft grids. This indicates that the load capacity of ESC is very much dependent on the modulus of the geosynthetic used for the encasement. This is in line with the conclusions given by Murugesan and Rajagopal (2006). The improved performance due to the higher modulus of encasement can be attributed to the enhancement of overall stiffness of the columns due to larger lateral stresses (confining stresses) mobilized in the column. As the lateral confining pressure by the geosynthetic is directly proportional to the secant stiffness of the geosynthetic stone columns with higher stiffness is having higher load capacity.

GUIDELINES FOR THE DESIGN OF ESC

Based on the results from this current research work, the following guidelines were developed for the design of geosynthetic encased stone columns. The bearing support from the soft soil is conservatively ignored in this methodology as the encased stone columns are specially suited for the case of extremely soft soils.

1. For the given pressure loading p_o from the structure suitable spacing (s) and diameter of the stone columns (d) are chosen. From the unit cell concept the load coming over the unit cell is assumed to be carried fully by the stone column.

Load on the stone column = Applied pressure, $p_o \times$ Area of the unit cell A

Area of the unit cell, $A = \pi\times(0.525s)^2$—for triangular grid

$= \pi\times (0.564s)^2$ —for square grid,

Load on stone column ≡ Load on the unit cell

$= p_o \times A$

Pressure on the stone column = Load on the unit cell/Area of the stone column, A_c.

2. The limiting stress on an ordinary stone column, σ_v without encasement is computed by using the equation

$$\sigma_v = (\sigma_{ro} + 4c_u) \; Kp_{col} \tag{1}$$

In which, σ_{ro} is the initial effective radial stress computed at an average depth of twice the diameter of the column, C_u is the undrained cohesion of the surrounding soft clay and Kp_{col} is the coefficient of passive pressure of the aggregates in the stone column.

3. The additional confinement p_c required is calculated as

$$p_c = \frac{(p_o - \sigma_v)}{Kp_{col}} \tag{2}$$

4. The corresponding hoop tension force in the encasement (T) can be estimated as, $T = \frac{p_c d}{2}$, where d is the diameter of the stone column.

5. The hoop strain ε_c in the encasement corresponding to the permissible settlement (δ) in the stone column is computed using the following equation,

$$\varepsilon_c = \frac{1-\sqrt{1-\varepsilon_a}}{\sqrt{1-\varepsilon_a}} \tag{3}$$

In which ε_a is the axial strain in the stone column. This value can be evaluated from the surface settlement of the stone column treated ground, δ

$$\varepsilon_a = \frac{\delta}{4\times d} \tag{4}$$

The effect of the surface loads was found to cause strains over a height of 4 times the diameter of the stone column ($4d$).

6. A suitable geosynthetic that can develop the long term allowable design tensile strength, T within a strain level of ε_c can be chosen for the encasement.

Based on the above design procedure developed for the encased stone columns, design charts have been prepared in non-dimensional form applicable for a range of realistic soil parameters, Fig. 6.

The area replacement ratio in this figure is calculated from the spacing, s and diameter of the stone column, d as

Area ratio = $0.907\times\left(\frac{d}{s}\right)^2$ —for triangular grid

Area ratio = $0.786\times\left(\frac{d}{s}\right)^2$ —for square grid.

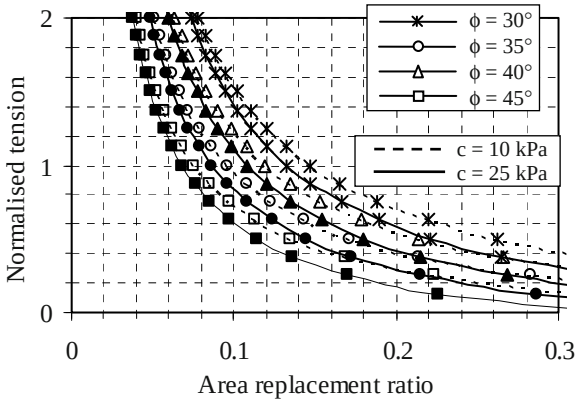

Fig. 6 Design charts for the geosynthetic encased stone columns

For the design of geosynthetic encased stone column, the design chart given in Fig. 6 be used with following steps

(i) For the assumed spacing and diameter of the stone column, calculate the area ratio.

(ii) For the properties of clay soil (c), friction angle of the stone aggregate (ϕ) and the area ratio, normalised tensile force [$T/(d \times p_o)$] required for the encasement is read from the chart. For other soil properties, linear interpolation may be used.

CONCLUSIONS

One of the methods of enhancing the axial load capacity of the stone columns installed in soft soils is encasing the individual stone columns with suitable geosynthetic. This encasement imparts lateral confinement to the stone column and also makes the stone column to act as end bearing elements. The behaviour of the geosynthetic encased stone columns was compared with the ordinary stone columns and found significant improvement. The major conclusions drawn from this study are as follows.

1. Pressure settlement response of geosynthetic encased stone columns generally shows linear behaviour not indicating any catastrophic failure unlike the conventional stone columns. The geosynthetic encasement increases the load capacity of the individual stone columns up to 3—5 time depending upon the stiffness of the geosynthetic used for encasement

2. The improvement in the load capacity due to encasement depends upon the diameter of the stone column. Lesser the diameter more would be the improvement. This is in line with the findings from earlier published literature.

3. The performance of the encased stone column also depends upon the stiffness of the geosynthetic used for the encasement.

4. Guidelines for the design of geosynthetic encased stone columns based hoop tension theory has been presented.

REFERENCES

American Society for Testing and Materials (1986) Standard test method for tensile properties of geotextiles by wide—width strip method. ASTM D4595

Chummar AV (2000) Ground improvement using stone columns: problems encountered. An International Conference on Geotechnical and Geological Engineering. Geo Eng. Melbourne, Australia

di Prisco C, Galli A, Cantarelli E, Bongiorno D (2006) Geo-reinforced sand columns: Small scale experimental tests and theoretical modeling. In: Proceedings of the 8th International conference on geosynthetics. Yokohama, Japan: 1685-1688

Dimiter A, Brokemper D, Lothspeich S (2005) Geotextile Encased Columns (GEC): Load capacity, geotextile selection and pre-design graphs. Geotechnical Special Publication. No. 130-142, GeoFrontiers: 497-510

Greenwood DA (1970) Mechanical improvement of soils below ground surface. Ground Engineering Proceedings Conference Organised by the Institution of Civil Engineers. London, June 1970: 11-22

Hughes JMO, Withers NJ, Greenwood DA (1975) Field trial of the reinforcing effect of a stone column in soil. Geotechnique 25(1): 31-44

Kempfert HG, Gebreselassie B (2006) Excavations and Foundations in Soft soils. Springer-Verlag Berlin Heidelberg, Netherlands

McKenna JM, Eyre WA, Wolstenholme DR (1975) Performance of an embankment supported by stone columns in soft ground. Geotechnique 25(1): 51-59

Murugesan S, Rajagopal K (2006) Geosynthetic-encased stone columns: Numerical evaluation. Geotextiles and Geomembranes 24(6): 349-358

Raithel M, Kempfert HG, Kirchner A (2002) Geotextile-encased columns (GEC) for foundation of a dike on very soft soils. Seventh International Conference on Geosynthetics, Nice: 1025-1028

ANALYSIS OF GEOSYNTHETIC REINFORCED STONE COLUMNS IN SOFT CLAY

R. Zhang[1] and S.R. Lo[2]

ABSTRACT: The paper presents the findings of a series of numerical studies on the behaviour of geosynthetic encased stone columns in very soft clay deposits and surcharged by embankment type loading. Observed settlement of a trial embankment built on very soft clay strengthened with stone columns indicated that the stone columns were not adequately effective in reducing settlement. Earlier work showed that the very softy clay could not provide adequate confining stress to the stones. For this reason, an alternative concept utilizing geosynthetic encasement was examined numerically. As the primary issue is the development of settlement with time after the completion of stone column installation, a fully coupled analysis was performed. To reduce the computational effort, a unit cell idealization was adopted. This study showed that the use of geosynthetic encasement has the potential of significantly enhancing the effectiveness of stone columns in very soft clay and the simplified analysis presented in earlier work is valid.

KEYWORDS: geosynthetic enforcement, soft soil, stone columns, coupled analysis

INTRODUCTION

Stone columns have been used as a ground improvement technique for a wide range of projects. Potential functions of the stone columns are increase in bearing capacity, reduction in post-construction settlement (by accelerating settlement rate), and reduction in total settlement. Design procedures for determining the bearing capacity of stone columns are well documented in FHWA (1983). The prediction of settlement is, however, less certain. For a road embankment section that leads to a piled abutment, the role of stone columns in limiting settlement is crucial. Applying a generous factor of safety to bearing capacity does not necessarily guaranteed compliance with settlement limit.

Stone columns may be used to support a column load in a manner similar to piles, i.e., the external load is applied to the top of a stone column and not to the surrounding soil. In a road embankment on soft clay situation, the stone columns function more as soil reinforcement and the mechanism is much more complicated. Immediately after the imposition of fill loading, most of the total stress is taken by pore water pressure in the clay and thus the stone columns only play a small role in resisting the fill loading. Indeed initial settlement will be small. It is only with dissipation of pore water pressure with time that the clay will settle and the weight of the fill will "arch over" to the stone columns. During this process, the stone columns will be strained both axially and radially, the latter leading to an increase in confining stress from the surrounding soil due to a cavity expansion mechanism. Some of the fill loading will still be transferred to the clay as effective stress and this also leads to increase in confining stress. Therefore, the mechanism involves the interaction of the stone columns and dissipation of pore water pressure of the surrounding soft clay. The latter is a coupled process between mechanical behaviour (as governed by effective stress principle) and flow of pore water (as governed by Darcy law).

REVIEW OF PREVIOUS WORK

Murugesan and Rajagopal (2006) presented an axi-symmetric unit cell analysis to demonstrate the effectiveness of geosynthetic encasement in improving the performance of a stone column. However the surrounding clay is characterized by a non-linear elastic model in terms of total stress. This makes it difficult to relate to the computed results to the actual time-dependent performance of such a system. Furthermore, the geosynthetic encasement appears to be modeled as isotropic and this will introduce an extra vertical reinforcing tube of unknown effects. Murugesan and Rajagopal (2007) presented 1g-model test to demonstrate the effectiveness of the geosynthetic encasement. However, the inherent scale effect and the rather atypical clay parameters reported (for example the clay had a

[1] PhD student, ADFA@UNSW, University of New South Wales, ADFA Campus, AUSTRALIA. Email: R.zhang@adfa.edu.au
[2] Associate Professor, ADFA@UNSW, University of New South Wales, ADFA Campus, AUSTRALIA. Email: R.lo@adfa.edu.au

vane shear strength of 2.5 kPa at 47% moisture content) make it difficult to translate the findings to a field problem.

Oh et al. (2007) reported the settlement performance of a 4 m high trial embankment constructed on soft estuarine clay improved by stone columns. The observed settlement at natural ground level (over a period of 457 days) of the stone columns treated section was only slightly less than that of the untreated section. The clay of this site, which is located in south-east Queensland, Australia, is very compressible, with compressibility Index, C_C, exceeding 1.5. It is noted that there is no stiff crust overlying the soft clay layer, and water table is at a depth of 0.5m. It is pertinent to note that such ground condition is not uncommon for estuarine deposits along the coast between northern New South Wales to south-east Queensland. It was hypothesized that the stone columns compressed "excessively" because the surrounding soft clay cannot provide adequate confinement.

In attempt to explain the unexpected observation of Oh et al. (2007) and to investigate the role of stone columns in very soft clay, Lo et al. (2007) conducted a numerical study of a unit cell arrangement as shown in Fig. 1 using a fully coupled analysis, and dimensions as shown in Table 1. It is important to note that the trial embankment reported in Oh et al. (2007) are not wide enough to allow modeling of a stone columns by a unit cell configuration, and hence the computed results could not be compared directly with field observation. However, the analysis did confirm that stone columns might not be adequately effective in reducing settlement. The effectiveness of encasement with geosynthetic was also investigated in the numerical study reported by Lo et al. (2007). In order to have the analysis conducted with commercial software CRISP, some simplifying assumptions were made. In essence the stone column is characterized as a Mohr-Coulomb elastic-plastic material with a non-associative flow rule, and with a Young's modulus given by:

$$E = 0.5\left(\frac{\sigma_{rs}(i)}{p_a}\right)p_a \qquad (1)$$

The above equation was deduced based on the Duncan Chang equation, by taken an average over the loading history, and neglecting some minor terms as explained in Lo et al. (2007).

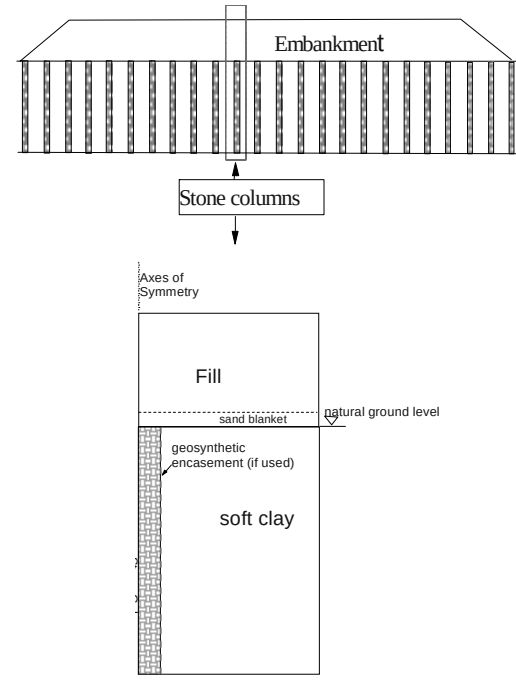

Fig. 1 Unit cell. (excerpted from Lo et al. 2007)

Table 1 Parameters for unit cell analysis

Items	Dimension(m)
Embankment elevation	4.0
Sand blanket thickness	1.0
Diameter of stone column	0.6
Unit cell radius	2.0
Depth of ground water table	0.0
Thickness of soft clay	10.0

The primary objective of this paper is to present a numerical analysis of a geosynthetic encased stone column that simulated, approximately, the construction history. This analysis removed the rather crude assumptions on the modeled of geosynthetic encased stone columns. This enables us to check the validity of the simplified analysis by Lo et al. (2007) and to gain further in-depth understanding of the mechanism.

GEOSYNTHETIC ENCASMENT

The benefits of using geosynthetic to encase or wrap geomaterials are well illustrated in studies on soil bag pile by Lohani et al. (2006). In this study, the geosynthetic was modeled as a cross-anisotropic Von Mises material with a hoop stiffness of 1000 kN/m. The stiffness in the vertical direction was assigned a low value (5% of the horizontal direction) so that it can not

provide any significant vertical support to the fill loading. This rather simple aspect of modeling was shown to be essential in the earlier work of Lo et al. (2007). So, the strength and stiffness of a stone column is dependent on effective confining stress provided by the geosynthetic hoop.

As shown in Fig. 2, the radial stress in acting on the stone column, σ_{rs}, can be expressed in terms of the radial stress of the surrounding clay, σ_r, and the hoop tension, T, in the geosynthetic encasement as illustrated in Fig. 2.

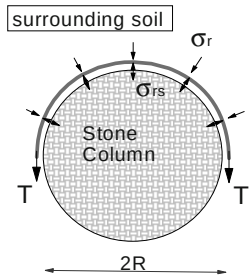

Fig.2 Hoop tension and radial stress in stone column. (Excerpted from Lo et al. 2007)

$$\sigma_{rs} = \sigma_r + T/R \tag{2}$$

Here R is the radius of the stone column. The second term can be viewed as the additional effective radial stress due to the geosynthetic encasement. Both T and σ_r can be decomposed into two parts; the initial value (i.e., after stone column installation) and the increase due to placement of fill and time dependent deformation. Therefore, Eq. 2 can be re-written as:

$$\sigma_{rs} = \sigma_r(i) + T(i)/R + \Delta\sigma_r + \Delta T/R \tag{3}$$

where (i) denotes the initial (as-installed) state, and "Δ" denotes increase due to loading.

The as-installed hoop tension, $T(i)$, is generally non-zero and dependent on the installation method. It is essential to have $T(i)$ included in the modeling. At the top zone, the value of $T(i)$ was limited by triaxial extension failure of the stones, and would increased with depth to a constant value, $T^*(i)$ at a depth z^*. When triaxial extension failure is not a factor, then $T(i)$ will be at an approximately constant value $T^*(i)$ depending on the installation technique. Therefore, the distribution of $T(i)$ is given in Fig. 3.

The condition of failure in triaxial extension means $\sigma_{rs}(i)$ is given by the following equation:

$$\sigma_{rs}(i) = K_p \sigma_{zs}(i) \tag{4}$$

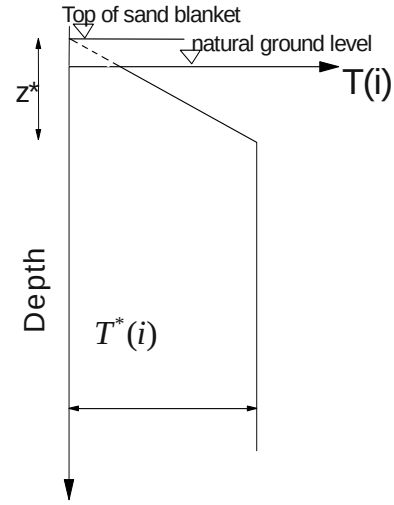

Fig. 3 Initial hoop tension. (Excerpted from Lo et al. 2007)

where σ_{zs} (i) is the in-situ vertical stress (due to self weight of stones), K_p = (1+sinϕ)/(1-sinϕ), and ϕ is the friction angle of the stones.

From Equation (3), the initial radial stress acting in the stone, σ_{rs} (i), is given by:

$$\sigma_{rs}(i) = \sigma_r(i) + \sigma_{rp} \tag{5}$$

$$\sigma_{rp} = 3.33T(i) \tag{5a}$$

σ_{rp} represent a "prestressing effective on the stones as a result of $T(i)$ locked-in by installation.

At a depth of z^*, both Eqs. 4 and 5 must be satisfied. Therefore, by taking water table being at natural ground level, z^* given by:

$$z^* = \frac{3.33T^*(i)/K_p - \gamma t_s}{\gamma'\left(1 - \rho K_0/K_p\right)} + t_s \tag{6}$$

where γ' = effective unit weight of stones, γ = bulk unit weight of stones, ρ = ratio of effective unit weight of clay to that of stones = 0.65, t_s = thickness of sand blanket = 1 m, K_o = at-rest earth pressure coefficient of the soft clay = 0.535.

Different level of $T^*(i)$, which simulate different level of pre-straining (or pre-stressing) of the geo-synthetic due to installation, can be assigned in the analysis.

FINITE ELEMENT ANALYSIS

A series of fully coupled analysis with modeling of construction sequence was performed by using the program AFENA. We also made minor modifications to

AFENA so that the geosynthetic encasement, installation effects and construction sequence can be better modeled.

Fill

The fill was modeled as a Mohr Coulomb elastic-plastic material with a non-associative flow rule. The parameters adopted for the analysis are given in Table 2 .

Soft Clay

The soft clay is modeled by the modified Cam-Clay model. In-situ stress was assigned based on an effective unit weight of 6 kN/m^3 and K_o = 0.535. The relevant soil parameters are given in Table 2.

Table 2 Soil Parameters.

Material	Parameter	Value
Fill	ϕ	30^o
	c	20 kPa
	ψ	5^o
	Young's modulus	3.0×10^{4}kPa
	Unit weight	20 kN/m^3
Soft Clay	M	1.1
	λ	0.65
	κ/λ	0.1
	e_{cs}	4.0
	k_z	2.3×10^{-10}m/s,
	k_r/k_z	2.0
Stone	ϕ	45^o
	c	5 kPa
	K	1000
	n	0.6
	r_f	0.7

Note:
ϕ = friction angle; c = cohesion; ψ = dilatancy angle; (M, λ, κ, e_{cs}) are parameters for modified Cam-Clay model; k = permeability; (K, n, r_f) are parameters for Duncan-Chang model.

Geosynthetic Encasement

The geosynthetic encasements are modeled as a Von-Mises cross-anisotropic element. The horizontal stiffness is taken to be 1000 kN/m. The axial stiffness was taken to be 5% of the horizontal stiffness in line with Lo et al. (2007). Poisson zero was taken to be zero to eliminate cross-coupling between axial and radial stress.

To eliminate the need for modifying the existing code to accommodate pre-stress and/or pre-straining effect, the influence of $T(i)$ was embedded indirectly into code via a stone column element.

Stone Column Element

The stones column was modeled as a free draining material. A stone column element is introduced into AFENA. This element is in fact a modified Mohr-Coulomb element with the following additional attributes:

- The tangential stiffness under is given by the Duncan-Chang Eqation.
- The stiffness under unloading is given by the initial Young's modulus using Janbu's Eqation.
- Loading is defined by increase inn stress ratio (not magnitude of stress component)
- The effect of $T(i)$, and thus σ_{rp} will be taken into embedded into the Duncan-Chang tangential stiffness Eq. of the Mohr Coulomb failure function.

The Duncan-Chang equation is as follows:

$$E = E_0 p_a \left(1 - r_f S\right)^2 \tag{7}$$

where E_0 (initial Young's modulus) and S is given by:

$$E_0 = K\left(\frac{\sigma_3}{p_a}\right)^n p_a \tag{8}$$

$$S = \frac{(\sigma_1 - \sigma_3)(1-\sin\phi)}{2\sigma_3 \sin\phi + 2c.\cos\phi} \tag{8a}$$

As the analysis is an increase analysis, we denote the lock-in stress due to (and in equilibrium with $T(i)$) by the superscript "*". Therefore, $\sigma_3 = \sigma^*_3 + \sigma_{rp}$, where σ^*_3 is the minor principal stress excluding the locked-in part stress due to $T(i)$. Eq. (7) can then be expressed as:

$$E_0 = K\left(\frac{\sigma^*_3 + \sigma_{rp}}{p_a}\right)^n p_a \tag{9}$$

This equation became approximate with loading as the radial direction is no longer that of σ_3. Using a similar argument Eq. 7a can be re-written as:

$$\begin{aligned} S &= \frac{(\sigma_1 - [\sigma^*_3 + \sigma_{rp}])(1-\sin\phi)}{2[\sigma^*_3 + \sigma_{rp}]\sin\phi + 2c.\cos\phi} \\ &= \frac{1}{2}\left(\frac{(\sigma_1 - [\sigma^*_3 + \sigma_{rp}])(1-\sin\phi)}{\sigma^*_3 \sin\phi + (\sigma_{rp}\tan\phi + c).\cos\phi}\right) \end{aligned} \tag{10}$$

Note that for $\sigma_z < \sigma_r$, it is an unloading situation despite $d\sigma_z > 0$ and Eq. (8) applies. Eq. 9 is used only under the condition of $\sigma_z \geq \sigma_r$, and $d\sigma_z > 0$. The benefit of the above "somewhat indirect" approach will be clear in the modeling of construction sequence. The parameters assigned in the analysis are given in Table 2.

Interface Modelling

In our analysis, the stone geosynthetic and soft clay interfaces were assumed to be full strength. This is because i) the installation of a stone column will automatically leads to an undulating surface, and ii) these interfaces are international nodes. Therefore preferential slippage cannot occur and there is no need to introduce any internal interface element.

CONSTRUCTION SEQUENCE

The following construction sequence was modeled.

(1) Initial in situ stress of soft clay deposit under green field condition
(2) Place sand blanket in 4 days
(3) Turn appropriate regions of soft clay into stone column elements and activate the geosynthetic elements.
(4) Build the embankment in a layer by layer manner
(5) Time-stepping for 10 years.

Note that the sand blanket needs to be placed first to form a platform to support the equipment for installing stone columns. Furthermore, step-3 automatically simulates the effects of $T(i)$ and associated σ_{rp} due to installation.

RESULTS OF FINITE ELEMENT ANALYSIS

It is pertinent to note that relevant soil parameters are assigned values identical to that of Lo et al. (2007) so that a meaning evaluation of the simplified analysis of Lo et al (2007) can be made. However, two different values of $T^*(i)$, 84 and 105 kN/m, were examined in this paper. These two values refer to the limiting condition when $z > z^*$. Furthermore, it provides some insight on the sensitivity of the computed results to $T^*(i)$.

Settlement

The development of settlement with time is compared in Fig.4 at the top of stone column. According to Lo et al. (2007), the settlement after 10 years for without-encasement stone column was 0.80 m The settlement of the encased stone column is reduced to about 0.225 m by encasing the stone column and inducing an adequate $T^*(i)$. It is also evident that the settlement is not particularly sensitive to $T^*(i)$.

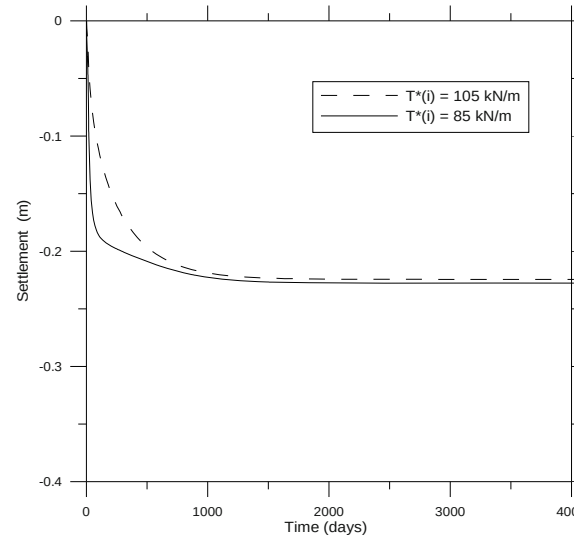

Fig. 4 Development of settlement with time

The settlement profiles at natural ground level and at top of the fill are shown in Fig. 5. The settlement profile presented in Fig. 5 shows a "bump" near the perimenter of the stone column at natural ground level. This bump increases with the pre-stress value $T^*(i)$. However, at the top of fill, the settlement profile was smooth and thus provides a high road surface.

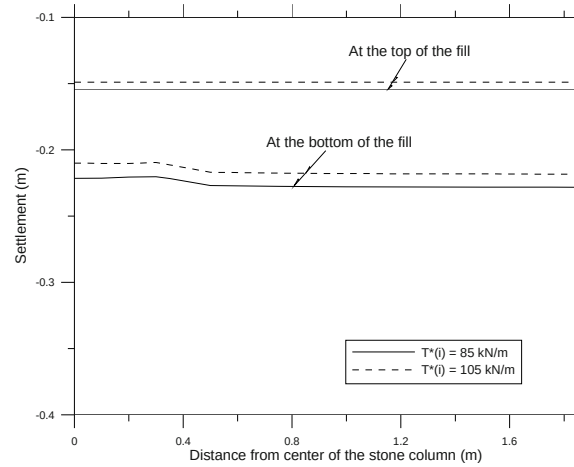

Fig. 5 Settlement Profile

The column force profiles at different time are plotted in Fig. 6. Evidently, the force taken by the stone column, and hence its contribution in supporting the embankment changes with time. This highlighted the need for a coupled analysis.

CONCLUSION

A numerical study was undertaken to examine the reinforcing role of stone columns in soft clay. The

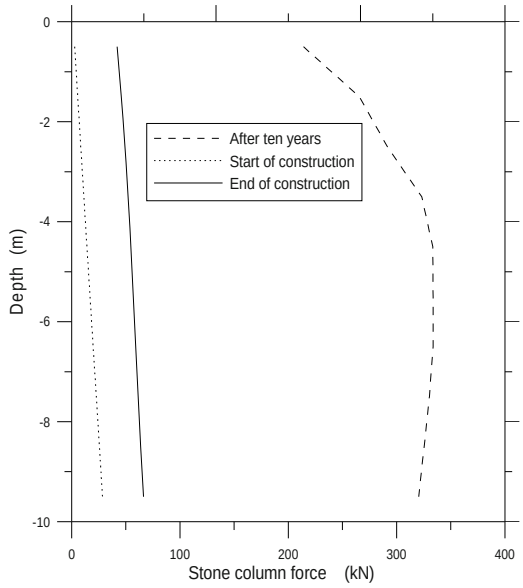

Fig. 6 Variation of stone column force with depth and time

analysis models the time-dependent interaction of the encased stone column and surrounding soft clay by a fully coupled analysis. The results showed that the effectiveness of using geosynthetic encasement in general and the validity of the simplified analysis of Lo et al. (2007). The results also demonstrate that the contribution of a stone column in supporting the embankment is time dependent because of mechanical and seepage coupling.

AKNOWLEDGEMENT

The research project related to this paper is sponsored by the one of the Cheung Kong oversea projects, Endeavour Australia Asia (China) Award.

REFERENCES

FHWA (1983) Design and construction of stone columns. FHWA Report No. RD-83/026: 194

Lo R, Mak J, Zhang R (2007) Geosynthetic Encased Stone Columns in Soft Clay. Proc of International symposium on earth reinforcement, Kyushu, Taylor and Francis 751-756

Lohani TN, Matsushima K., Aqil U, Mohri Y, Tatusoka F (2006) Evaluating the strength and deformation characteristics of a soil bag pile from full-scale laboratory tests. Geosynthetic International 13(6): 246-264

Murugesan S, Rajagopal K (2006) Geosynthetic-encased stone columns: numerical evaluation. Geotextiles and Geomembrances 24: 349-358

Murugesan S, Rajagopal K (2007) Model tests on geo-synthetic-encased stone columns. Geosynthetic International 14(6): 346-354

Oh EYN, Balasubramaniam AS, Bolton M, Surarak C, Bolton M, Chai GWK, Huang M (2007) Behavior of a highway embankment on stone columns improved estuarine clay. Proceedings of 16th Southeast Asian Geotechnical Conference, Malaysia 1: 567-572

NUMERICAL ANALYSIS FOR MECHANISMS OF A GEOCELL-REINFORCED BASE UNDER A VERTICAL LOAD

J. Han[1], X.M. Yang[1], D. Leshchinsky[2], R.L. Parsons[1] and A. Rosen[3]

ABSTRACT: Geocells have a three-dimensional cellular structure, which can be used to stabilize foundations in soft soil by increasing bearing capacity and reducing settlements. However, a considerable gap exists between the applications and the theories for the mechanisms of geocell-reinforced foundations. This paper presents a mechanistic analysis of a geocell-reinforced gravel base over soft subgrade under a vertical load using a three-dimensional numerical method. In this study, model tests on unreinforced and geocell-reinforced gravel bases on soft subgrade were modeled. The numerical results are compared reasonably well with the test data. In addition, the stresses and displacements in the bases and at the interface between the base and the subgrade and tensile stresses and shear stresses acting on the geocell sheets were examined.

KEYWORDS: geocell, subgrade, base, numerical analysis

INTRODUCTION

Geocells are manmade three-dimensional forms of geosynthetic (polymer) materials with interconnected cells infilled with compacted soil. Geocells have been successfully used worldwide to construct retaining walls and slopes or reinforce road bases. The key benefits of geocells used as base reinforcement are to confine fill inside the three-dimensional polymeric honeycomb cells to reduce its lateral movement and form a stiffened mattress to distribute applied loads to a wider area. Detailed review of geocells used as base reinforcement over weak subgrade can be found in the paper by Yuu et al (2008). A brief overview of the state of practice is given in the following section.

As summarized in Yuu et al. (2008), experimental studies have been conducted in three ways: (1) the use of triaxial cells (for example, Gourves et al. 1996) or resilient modulus cells (Mengelt et al. 2006) to investigate the confinement effect as increasing apparent cohesion or reducing long-term permanent plastic deformations; (2) the use of laboratory model tests to investigate the reinforcement effect as increasing bearing capacity and reducing settlements under static or dynamic loading (Rea and Mitchell 1978; Chang et al. 2007); and (3) the use o full-scale trafficking tests to investigate the overall effect as reducing rut depth and prolonging road life (Webster 1979).

Yuu et al. (2008) identified the following key influence factors on the performance of geocell-reinforced bases over weak subgrade: geometric variables of geocells, quality of infill soil, subgrade strength, and loading type and location.

As Yuu et al. (2008) pointed out, despite the effectiveness of the geocell system, the acceptance of geocells for base reinforcement of roads is limited due to lack of design methods. However, the lack of design methods results from limited understanding of the load transfer mechanisms, limited methods for quantifying the benefits, and limited full-scale performance data.

This study aimed to improve the understanding of mechanisms of geocell-reinforced bases over soft subgrade under a vertical load. In this study, model tests on unreinforced and geocell-reinforced bases over soft subgrade were modeled using the FLAC3D numerical software.

MATERIAL PROPERTIES AND MODEL TEST RESULTS

Background

The model tests conducted by Meyer (2007) on unreinforced and geocell-reinforced gravel bases over soft subgrade were used in this numerical analysis.

[1] Department of Civil, Environmental, and Architectural Engineering, the University of Kansas, Lawrence, KS 66045, USA. Email:jiehan@ku.edu
[2] Department of Civil and Environmental Engineering, the University of Delaware, Newark, DE19719, USA
[3] Formerly engineer, PRS Mediterranean, Europe-Israel Tower, 2 Weizmann Street, Tel Aviv, 64239, ISRAEL

Details on these model tests can be found in Meyer (2007). A brief description of these tests is provided herein. In Meyer's study, both sand and gravel were used as infill materials. In this study, however, only the test results based on gravel infill were used and are discussed below.

The model tests were conducted in a 2 m×2 m×2 m test box. The test sections include 1000mm thick subgrade, 50 mm thick sand layer for installation of earth pressure cells, a low strength nonwoven geotextile, 100 mm thick gravel, geocell-reinforced gravel at 100 mm, 150 mm, or 200mm thick, and 20 mm thick cover. The circular loading plate used in this study was 300 mm in diameter.

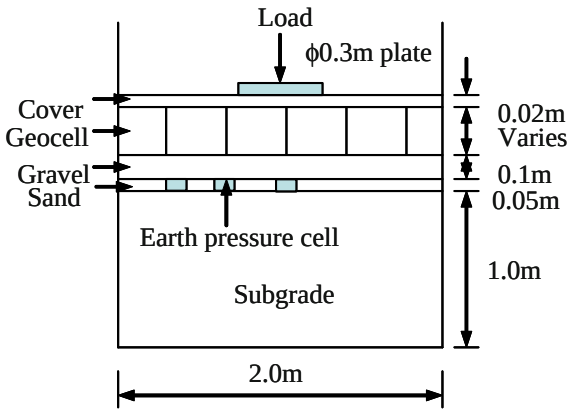

Fig. 1 Cross-section of test setup (modified from Meyer, 2007)

Subgrade

The subgrade used in these model tests was an artificially mixed soil called "Glyben", which is a mixture of bentonite and glycerine. The percent of bentonite used in the mixture was 53 to 54%. Meyer (2007) showed that this Glyben subgrade had an undrained shear strength of 15kPa and a dynamic deflection modulus of 4 MPa based on light dynamic drop plate tests. Rayhani and Naggar (2008) showed that the Glyben soil at the same percentage mixture had an undrained shear strength of 18.5 kPa and a maximum dynamic elastic modulus of 6.5—10MPa (average 8.0 MPa) at confining stresses of 30—300 kPa. Rayhani and Naggar (2008) also showed that the modulus was not that sensitive to the strain level when the shear strain was less than 0.1%.

Sand Layer and Geotextile

The thin sand layer was used for the placement of earth pressure cells. This sand layer was poorly graded and had the maximum particle size of 2mm and the friction angle of 38.9°. The nonwoven geotextile sheet was placed above the sand layer as a separator between the sand layer and the gravel base. Because this geotextile layer had a very low tensile strength, it is not expected to provide any reinforcement effect on the base.

Gravel Base

Gravel used in the model tests was well graded and had a maximum particle size of 36 mm, a coefficient of uniformity of 19.7, a coefficient of curvature of 1.8, and friction angles from 41° to 45° (Meyer, 2007). Gravel was placed above the nonwoven geotextile sheet as part of the base, inside the geocells as the infill material, and above the geocells as the cover.

Geocell

The geocells used in the model tests were provided by the PRS Mediterranean Ltd in Israel. The length and the width of the geocell mattresses were 2.00 and 1.06 m, respectively. The height of the geocells ranged from 100, 150, and 200 mm. The thickness of 200 mm for the unreinforced base corresponds to the height of the geocell at 200 mm. The perforated geocells consisted of HDPE with a density 0.95 g/cm³ (± 1.5%) having a cell length of 210 mm and a cell width of 250 mm. Single cells with a cell area of 26200 mm² were welded together to form a uniform geocell mattress. The cell walls were perforated with 10 mm diameter holes. The holes were arranged in horizontal rows which were staggered and separated 12 mm relative to the hole centers. The total open area was 16 % of the cell wall area. The surfaces of cell walls were textured with a multitude of rhomboidal indentations over the entire strip area at a surface density of 2200—3100 mm^2 and a depth of 0.35—0.85 mm.

The tensile stress-strain relationships of the same geocell materials were determined by five tensile tests conducted at a strain rate of 10%/minute (Han et al. 2008). The tensile stress-strain relation is presented in Fig. 2. The mean tensile stresses at strains of 2% and 5% were 5.0 and 8.2 kN/m, respectively and the mean ultimate tensile strength was 9.3 kN/m. The thickness of the geocell sheet was 1.778 mm. The tensile stiffness of geocell sheet at 2% strain was determined to be 250 kN/m based on the tensile stress-strain relationship.

Test Results

In the model tests, vertical displacements on the surface and earth pressures at the interface between the

base and the subgrade were measured (Meyer 2007). These test results will be presented and compared with the numerical results below.

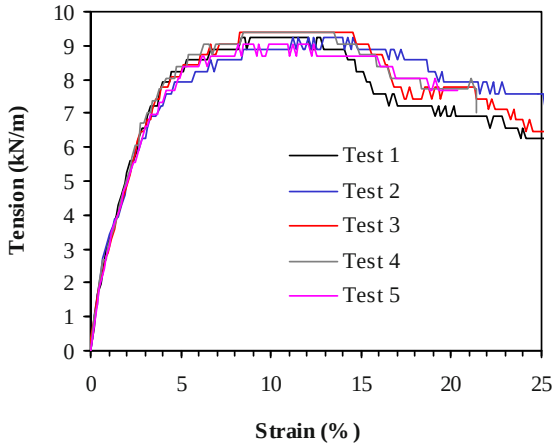

Fig. 2 Measured tensile stress and strain relation of geocell sheets (Han et al. 2008)

NUMERICAL MODELING

Models and Material Properties

FLAC 3D software (Version 3.1), a suitable tool to analyze three-dimensional polymeric honeycomb geocells, was used in this study. To investigate the interactions between geocells and infilled gravel and the performance of geocell-reinforced bases over soft subgrade, the model tests conducted by Meyer (2007) and based on the gravel infill were modeled and analyzed in this study. The mesh for the geocell-reinforced case is presented in Fig. 3 as an example. For the unreinforced case, no geocell was included in the model.

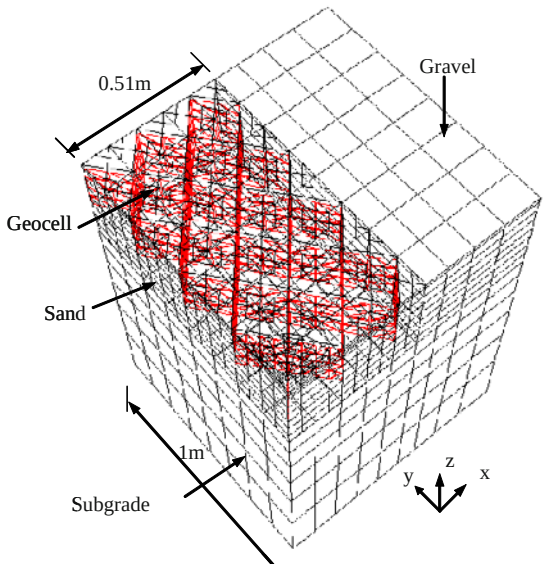

Fig. 3 Meshes and materials for numerical analysis

The subgrade, the thin sand layer, and the gravel base were modeled as a linearly elastic-perfectly plastic material with a Mohr-Coulomb failure criterion. The geocells were modeled using the linearly elastic structural (geogrid) elements provided by the FLAC3D software (Itasca 2006). The geogrid elements were used to form the geocells as shown in Fig. 3. The steel load plate with a diameter of 300 mm was modeled as an elastic solid material with a large elastic modulus. The low strength nonwoven geotextile was not modeled in the numerical analysis and is expected to have an insignificant effect on the results. The properties of these materials are provided in Table 1.

Table 1 Properties of materials used in the numerical analysis

Material	E (MPa)	ν	γ (kN/m^3)	c (kPa)	ϕ (^{o})
Subgrade	8	0.45	17	15	-
Sand	20	0.3	17	0	38.9
Gravel	50	0.3	17	0	43
Geocell	J = 250 kN/m, c_i = 0.8, k =71,000 kN/m/m				

Note: E = elastic modulus, ν = Poisson's ratio, γ = unit weight, c = cohesion, ϕ = effective friction angle, J = tensile stiffness of geocell sheet, c_i = interaction coefficient between geocell sheet and gravel, k = interface shear stiffness between geocell sheet and gravel.

The cohesion of the subgrade was selected based on the undrained shear strength determined by Meyer (2007). The elastic modulus of the subgrade was based on the test results of Rayhani and Naggar (2008). The friction angles of the sand and the gravel were chosen based on the test results in Meyer (2007). The moduli of the sand and the gravel in Table 1 were selected based on typical values. The tensile stiffness of geocell sheets were determined based on the tension-strain relationship from the tensile tests as discussed earlier. A typical interaction coefficient and an interface shear stiffness between geocell and sand were selected. Due to the symmetry of the model, only a quarter of the model was analyzed. The boundary conditions were fixed in the x or y directions but free in the z direction. The numerical models used the same dimensions as those in the experimental tests.

Numerical Results and Analyses

Vertical displacement

The measured and computed vertical displacements with the applied pressures under the loading plate are presented in Fig. 4. It is shown that the numerical results agree reasonably well with the measured ones. The

experimental and numerical results both show that the reinforced base by 100 mm geocell is equivalent to the 200 mm thick unreinforced base. An increase of geocell thickness increased the bearing capacity and reduced the vertical displacements of the bases.

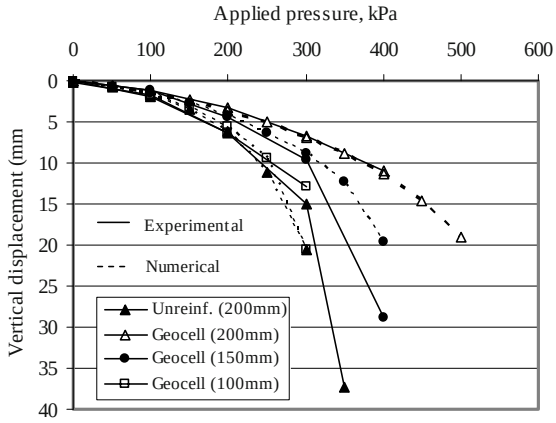

Fig. 4 Measured and computed vertical displacements of the loading plate

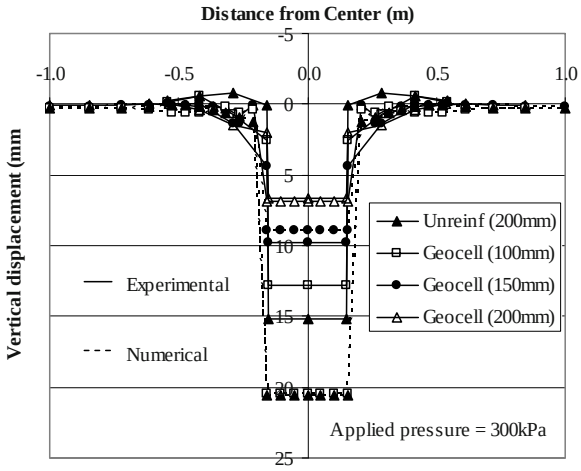

Fig. 5 Profiles of surface vertical displacements

Fig. 5 presents the profiles of the surface vertical displacements at the applied pressure of 300kPa. As discussed above, the computed vertical displacements for the unreinforced base and the geocell reinforced base with a cell height of 100 mm were larger than the measured ones. For the geocell-reinforced bases with a cell height of 150 or 200 mm, however, the computed vertical displacement profiles were close to the measured ones. In addition, the measured results showed that the unreinforced base had obvious heave near the plate but others did not.

The computed vertical displacements at the interface between the base and the subgrade are presented in Fig. 6. It is shown again that the 200 mm thick unreinforced base is equivalent to the 100 mm thick geocell-reinforced base in terms of the maximum vertical displacement at the interface of the base and the subgrade. The increase of the cell height reduced the maximum vertical displacement. In addition, the comparison of Fig. 6 and Fig. 4 shows that the majority of the vertical displace-ment (more than 70%) was induced by the compression and lateral movement of the subgrade.

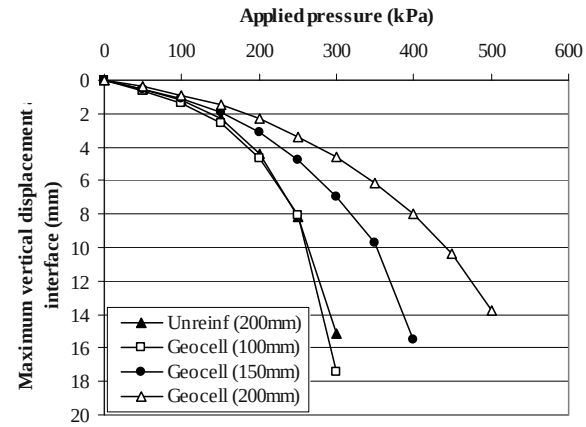

Fig. 6 Computed vertical displacements at the interface between the base and the subgrade

Horizontal displacement

Fig. 7 presents the variation of the maximum horizontal displacement at the interface between the base and the subgrade with the applied pressure. It is shown that the maximum horizontal displacement increased with the increase of the applied pressure. The use of geocell significantly minimized the horizontal displacement as comparing the 200 mm unreinforced base with the 200 mm geocell-reinforced base.

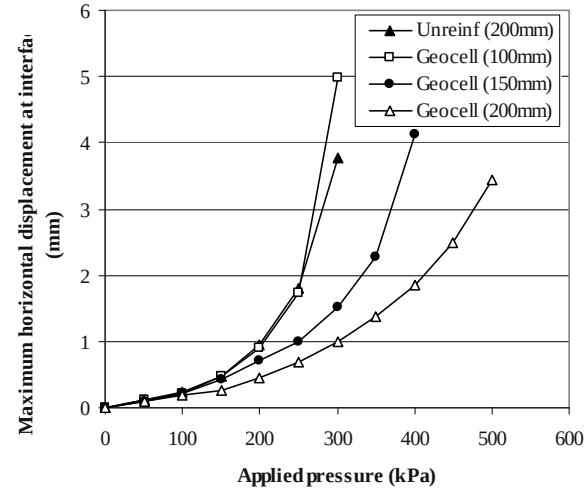

Fig. 7 Computed Maximum horizontal displacements at the interface between the base and the subgrade

Vertical stress

Fig. 8 presents the comparison of measured and computed vertical stresses at the interface between the base and the subgrade. The shape of the stress distribution is similar to that computed using the two layer elastic theory (Burmister, 1943). It is shown that the computed vertical stresses at the center were higher than those measured from the model tests. The increase of the geocell height reduced the vertical stresses at the interface. It is clearly shown that the inclusion of geocell significantly reduced the vertical stresses as the 200mm thick geocell-reinforced base compared with the unreinforced base at the same thickness. This reduction can be explained as the geocell provided extra confinement and increased the stiffness of the base. This phenomenon was found by the authors in another study (Han et al. 2008).

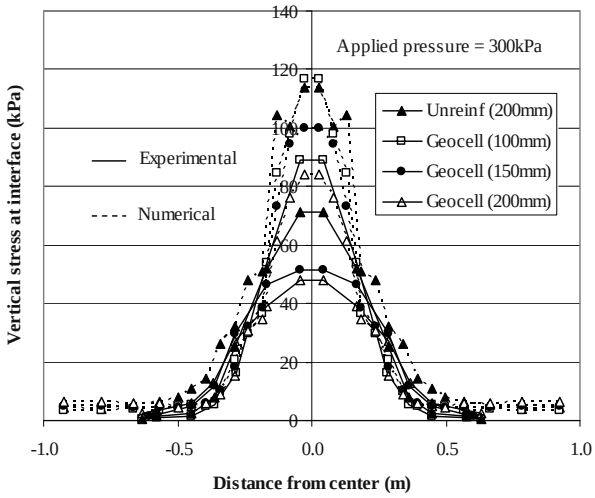

Fig. 8 Measured and computed vertical stresses at the interface between the base and the subgrade

Shear stress

The computed maximum shear stress at the interface between the base and the subgrade is presented in Fig. 9. It is shown that the shear stress for the unreinforced base was higher than that for the geocell-reinforced bases. In other words, the use of geocells reduced the shear stress at the interface between the base and the subgrade so that it reduced the chance for subgrade failure and increased the bearing capacity. In all the cases, the maximum shear stress at the interface was less than the undrained shear strength of the subgrade. In addition, the shear stress for the unreinforced base increased more rapidly with the applied pressure than the geocell-reinforced bases.

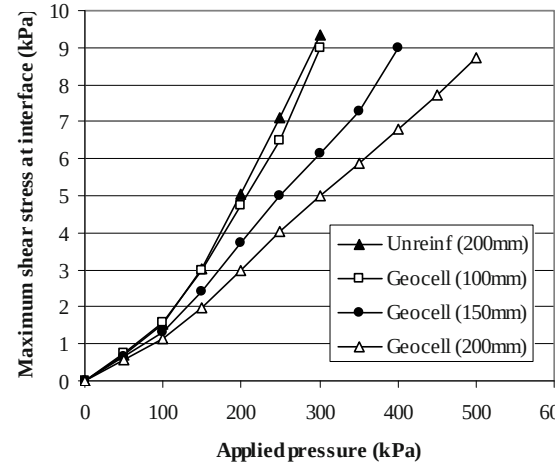

Fig. 9 Maximum shear stress at the interface of the base and the subgrade

Tension in geocell

The maximum tension in geocell was computed by the numerical method and presented in Fig. 10. It is shown that the maximum tension increased exponentially with the applied pressure and slightly exceeded the ultimate tensile strength of the geocell sheet at the last pressure. Because geocell sheets were modeled as linearly elastic structural elements due to the limitation of the software, the maximum tension was not limited by this ultimate tensile strength. In this study, however, the computed tension was slightly greater than the ultimate tensile strength at the last pressure; therefore, the overall results are still valid. Fig. 8 also shows that the geocell with a smaller height had higher maximum tension in geocell.

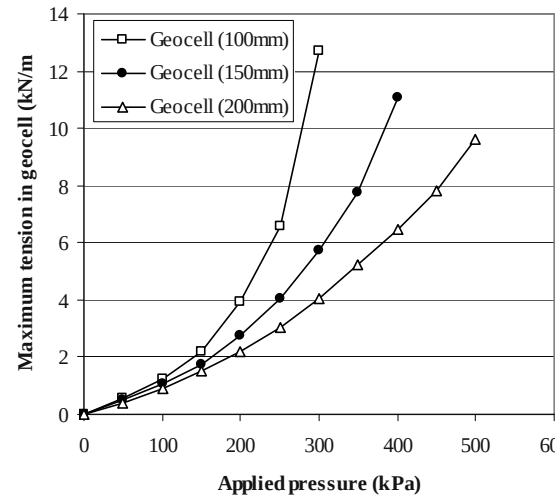

Fig. 10 Computed maximum tension in geocell walls

Interface shear stresses between geocell and gravel

Fig. 11 presents the maximum interface shear stresses between geocell walls and infilled gravel. It is shown that the interface shear stress increased approximately

linearly with the applied pressure and the geocells with different cell heights had almost the same interface shear stress response.

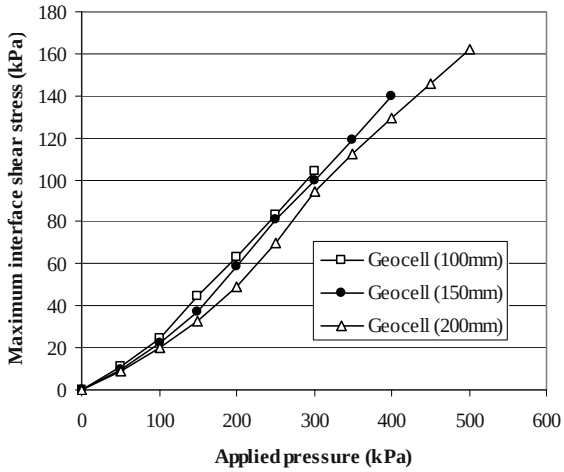

Fig. 11 Computed interface shear stresses at the interface between gravel and geocell wall

CONCLUSIONS

This numerical study shows that a 3D numerical model with linearly elastic-perfectly plastic constitutive laws can reasonably well simulate the behavior of geocell-reinforced bases over soft subgrade. The use of geocells can increase the bearing capacity and reduce the vertical and horizontal displacements and the vertical and shear stresses at the interface between the base and the subgrade. The maximum tension in the geocells increased exponentially with the applied pressure but decreased with the height of the geocells. Geocells at different heights had almost the identical interface shear stress response to the applied pressure.

ACKNOWLEDGEMENTS

This research was funded jointly by the University of Kansas, Transportation Research Institute from Grant # DT0S59-06-G-00047, provided by the US Department of Transportation – Research and Innovative Technology Administration and PRS Mediterranean, Inc. in Israel. Their support is greatly appreciated.

REFERENCES

Burmister DM (1943) The theory of stresses and displacements in layered systems and applications to the design of airport runways. Proceedings, Highway Research Board 23: 126-144

Chang DTT, Chang CH, Pai SW (2007) Investigation of bearing capacity and dynamic-elastic behavior of mechanical stabilizing of sandy subgrade using geocells. TRB 2007 Annual Meeting CD-ROM

Gourves R, Reffsteck P, Vignon JF (1996) Study of confinement effect in geocells. Geosynthetics: Applications, Design and Construction: 455-458

Han J, Yang XM, Leshchinsky D, Parsons RL (2008) Behavior of geocell-reinforced sand under a vertical load. Submitted for possible publication at Annual Meeting for Transportation Research Board, January

Itasca Consulting Group, Inc. FLAC3D Version 3.1 User's Guide, 2006

Mengelt M, Edil TB, Benson HH (2006) Resilient modulus and plastic deformation of soil confined in a geocell, Geosynthetics International 13(5): 195-205

Meyer N (2007) Determination of the bearing capacity of geocell reinforced soil over soft subgrade with static and dynamic plate load tests. Institute of Geotechnical Engineering and Mine Surveying, TU Clausthal, June

Rea C, Mitchell K (1978) Sand reinforcement using paper grid cells, Proceedings, Symposium on Earth Reinforcement, ASCE Annual Convention, Pittsburgh, PA: 644-663

Webster SL (1979) Investigation of Beach Sand Trafficability Enhancement Using Sand-Grid Confinement and Membrane Reinforcement Concepts, Report GL-79-20 (1). U.S. Army Engineer Waterways Experiment Station, Vicksburg, MS

Yuu J, Han J, Rosen A, Parsons RL, Leshchinsky D (2008) Technical review of geocell-reinforced base courses over weak subgrade. Submitted to Geo-Americas for possible publication

BEARING CAPACITY IMPROVEMENT OF ASPHALT PAVED ROAD CONSTRUCTIONS DUE TO THE USE OF GEOCELLS —FALLING WEIGHT DEFLECTOMETER AND VERTICAL STRESS MEASURESMENTS

A. Emersleben[1] and N. Meyer[2]

ABSTRACT: To evaluate the influence of a geocell layer on the load-deformation behavior of the soil large scale static load tests were carried out. Geocells with different aspect ratios made of different materials filled with sand had been tested. To simulate soft subgrade material an artificial mixed soil called “Glyben” was used. The test results showed that a geocell layer increased the bearing capacity of the infill materials and reduced the vertical stresses on the subgrade about 30 percent compared to an unreinforced soil. To verify the results of model tests, geocell reinforced, unreinforced and also hydraulic bounded base (HBB) in-situ test fields were carried out within different asphalt paved road constructions. After finishing the road construction vehicle crossing tests with a 40-tons truck and falling weight deflectometer measurements were carried out while the vertical stresses on the subgrade were measured by earth pressure cells. Compared to an unreinforced test section the stresses beneath the geocell layer were reduced by about 30 percent. Falling weight deflectometer measurements showed that the deflections measured in geocell reinforced test section were significantly smaller than in the unreinforced section. Back calculated layer modules were significantly higher in the geocell reinforced section compared to an unreinforced section.

KEYWORDS: geosynthetics, geocells, soft soil stabilization, soil reinforcement

INTRODUCTION

Geocells are honeycomb interconnected cells that completely encase the soil and provide all-around confinement, thus preventing the lateral spreading of the infill material. Due to the soil confinement the geocells increase the stiffness and the load-deformation behavior of gravel base layers and thereby reduce the deformation of the soil. Besides the soil-geocell layers act as a stiff mat, thus distributing the vertical traffic loads over a much larger area of the subgrade soil.

Several model tests (e.g., Dash et al. 2001, 2003; Sitharam et al. 2005) have shown the positive effect of geocells, made from different geogrids, on the load bearing capacity of soils. Meyer and Emersleben (2005a, 2005b, 2005c, 2006a, 2006b) and Mhaiskar et al. (1992) evaluated the influence of industrially manufactured geocells on the load-deformation behavior of soils.

The use of geocells to stabilize unpaved road constructions is far common, especially if qualified soils are not available near the construction site (Ben Kurari 2000; Forsman et al. 1998; Leytland et al. 2006).

The stabilization of gravel base layers of asphalt paved road constructions over soft soils with geocells is an alternative technique to reduce the deformations of the asphalt surface and to increase the stiffness of the main construction. Al Quadi et al. (2000) reported an increase of the modules of resilience of aggregate layers about 2 times due to the installation of geocells within an asphalt paved road construction.

This paper reported of the results of static load tests and in-situ field tests. By means of vertical stress measurements beneath the geocell layers and by means of falling weight deflectometer (FWD) measurements in geocell reinforced test fields the positive influence of geocells could be evaluated.

LARGE SCALE MODEL TESTS

Test Device

To evaluate the influence of geocells on the load bearing capacity of soil and the stress distribution large scale model tests were carried out in a test box with inside dimensions of 2 m length, 2 m width and 2 m

[1] Assistant Scientist, Ph. D. Student, Department of Geotechnical Engineering, Clausthal University of Technology, GERMANY, Email: ansgar.emersleben@tu-clausthal.de
[2] Professor, Department of Geotechnical Engineering, Clausthal University of Technology, GERMANY

height. Static load was applied over a loading frame. Vertical loads up to 150 kN can be applied. The loads were applied by a hydraulic jack and were transferred by steel plate with a diameter of 30 cm to the soil.

To measure the heave and settlement on the soil surface five inductive displacement gauges were installed in different distances to the center of the load plate.

For the determination of the stress distribution below the geocells, eight earth pressure cells were installed in a depth of 35 cm. The earth pressure cells (EPC) with a diameter of 5 cm and a maximum pressure capacity of 500 kN/m² were aligned in different distances to the center of the load plate.

Material

Soils

An artificial mixed soil called "Glyben" was used to simulate soft subgrade material. The soil consists of glycerin and bentonite. The soil parameters depend on the rate of mixture. The soil was mixed in small portions, filled in the test box and compacted. The main advantage of Glyben compared to other cohesive soils is that the soil parameters are constant for a long time because the water or glycerin content is not changing. The mixed Glyben got a undrained cohesion of c_u = 15 kPa and a friction angle of φ = 8°. The stiffness module from axial compression tests at relevant loads is about 5 MN/m².

Dry sand with a maximum particle size of 2 mm was used as infill material of the geocells as well as for the unreinforced tests. The coefficient of uniformity (C_u) was 3.2 the coefficient of curvature (C_c) was 1.03. The maximum and minimum void ratio of the sand is 0.45 and 0.34. The void ratio at infill density was 0.39. The friction angle at infill density was 38.9°. The sand was poured into the test box and compacted with a vibration plate compactor.

Geocells

Two different types of geocells were used in model tests. Geocell "Typ 1" was made from high density polyethylene (HDPE) with a density of 0.95 g/cm³. Single cells are 210 mm long and 250 mm wide. Single cells with a cell area of 262 cm² were welded together to form a uniform geocell mattress. The geocells have seam strength, depending on its height, of 1150 N (10 cm height), 1725 N (15 cm height) and 2290 N (20 cm height). The cell walls are perforated with 10 mm diameter holes. The total open area is 16 % of the cell wall area. The surface of cell walls is textured. Three different cell heights (h) of 10 cm, 15 cm and 20 cm were tested in the model tests while the equivalent cell diameter (d_0 = 23 cm) was constant in all tests.

Geocell "Typ 2" was made form thermally solidified nonwoven with a tensile strength of 20.7 kN/m. The peeled strength of the junction points is 10 kN/m and the shear strength is 13 kN/m. Three different cell diameters (d_0) of 16 cm, 22 cm and 30 cm were tested in the model tests at a constant cell height of h = 20 cm.

Test Installation

After the walls of test box were covered with foil and lubricant to minimize the friction between the soil and the infill material, the installation of the subgrade layer started. Glyben was filled in the test box in 10 cm layers up to a height of 1 m. Afterwards installation and adjustment of eight earth pressure cells were carried out. They were laid in a thin sand bed in different distances to the center of the load device, aligned and covered with sand. The layer thickness above pressure cells was selected to be equal in all tests. Distance between pressure cells and load plate was chosen to 35 cm. Extensive preliminary tests indicated that a minimum distance of 15 cm between pressure cells and lower edge of geocells was necessary in order to measure a representative stress distribution on the subgrade. On the subgrade material a nonwoven with low tensile strength at high strains was placed over the soil to separate subgrade and infill material. The geocells were then placed on the nonwoven. Geocells were stretched, adjusted with steel bars, filled with dry sand and compacted by a vibrating plate compactor. The load plate and displacement gauges were installed on the sand surface. The schematic experimental setup is shown in Fig. 1.

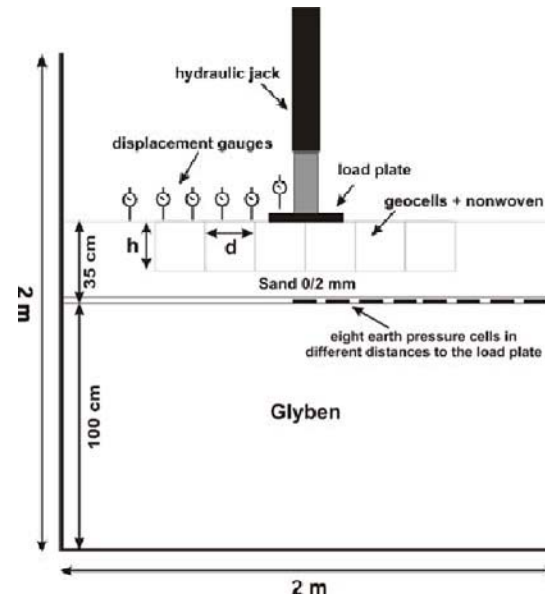

Fig. 1 Schematic diagram of test device

Static load was applied in steps. The number of applied load steps depended on the maximum bearing capacity of the soil. Every load step was applied until no more further settlement was observed.

TEST RESULTS

Load Carrying Capacity

The increase in load carrying capacity (*LCC*) due to the provision of geocell layer is represented with a non-dimensional load carrying factor *(LCF*), which is defined as the ratio of footing pressure with geocells at a given settlement $\sigma_{r,(s)}$ to the corresponding pressure on unreinforced soil at the same settlement $\sigma_{u,(s)}$.

$$LCF = \frac{\sigma_{r,(s)}}{\sigma_{u,(s)}} [-] \quad (1)$$

The calculated load carrying factors for two different test series are presented in table 1. Test series A was conducted with geocell "typ 1" to measure the influence of geocell height on the load-deformation behavior and test series B was carried out with geocell "Typ 2" to measure the influence of different cell diameters on the load-deformation behavior.

The load carrying factors were calculated up to load of 400 kN/m² respectively up to a settlement of 16 mm.

At this load/settlement the ultimate bearing capacity of the unreinforced sand was reached.

Table 1 load carrying factors, test series A, d = 230 mm

	s = 4 mm	s = 8 mm	s = 10 mm	s = 16 mm
h/d = 0.43	1.10	1.04	1.28	1.23
h/d = 0.65	1.55	1.37	1.64	1.47
h/d = 0.87	1.56	1.38	1.69	1.48

Table 2 load carrying factors, test series B, h = 200 mm

	s = 4 mm	s = 8 mm	s = 10 mm	s = 16 mm
h/d = 1.25	1.37	1.28	1.35	1.31
h/d = 0.87	1.33	1.22	1.32	1.26
h/d = 0.67	1.14	1.15	1.33	1.27

The load carrying capacity increases with increasing cell height and decreasing cell diameter. Depending on geocell height and diameter, the load carrying capacity could be improved up to 1.5 times due to a reinforcement of dry sand with geocells. Further improvement will occur at higher settlement and loads because the ultimate bearing capacity of unreinforced sand could not be increased while the ultimate bearing capacity of reinforced sand was not reached at a load of 400 kN/m².

Vertical Stresses

During static load tests vertical stresses on the subgrade were measured with eight pressure cells in different distances to the load plate. To avoid influences on the stress distribution resulting from measured peak stresses in single pressure cells the stresses of two pressure cells, which are adjacent to each other, were averaged according to Eq. 2.

$$\bar{\sigma}_{epc,i} = \frac{\sigma_{epc,i} + \sigma_{epc,i+1}}{2} \quad (2)$$

Vertical stresses were measured in every test. Exemplary the results of tests with 20 cm height and 23 cm in diameter geocells "Typ 1" are presented in Fig. 3 for different loads. Vertical stresses measured in the corresponding unreinforced test are presented in Fig. 2.

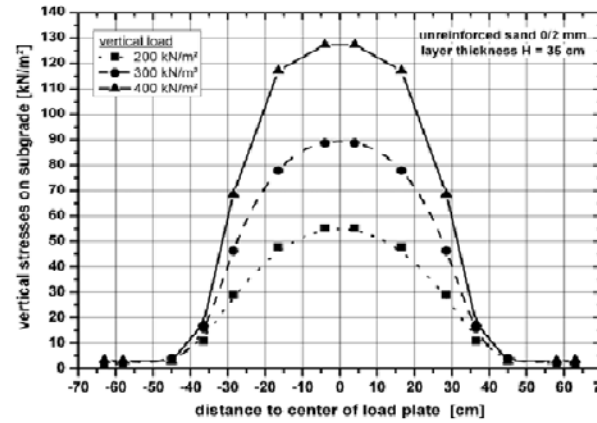

Fig. 2 Vertical stresses on subgrade, unreinforced soil

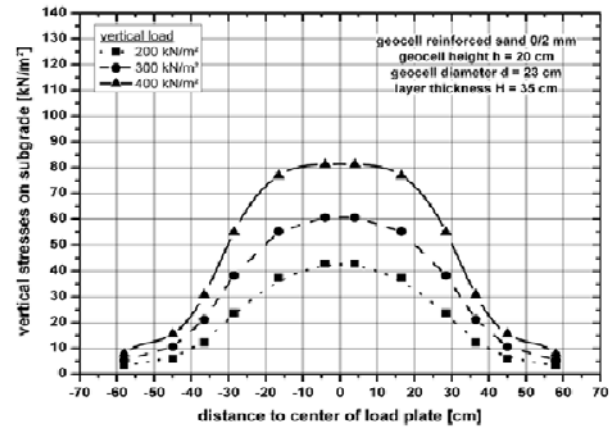

Fig. 3 Vertical stresses on subgrade, geocell "Typ 1" reinforced soil

The stresses which are measured in the unreinforced soil are significantly higher than those measured in the

geocell reinforced soil at the same load. A stress reduction between 30% and 36% can be observed depending on the applied load. Similar results were observed for different cell heights and cell diameters.

In the unreinforced soil the stresses are more concentrated in the area of the load plate while the stresses in the geocell reinforced soil are distributed over a larger area. These results indicate that the geocell layer acts like a stiff matt and diffuses the footing pressure over a larger area thus reducing the vertical stresses directly beneath the load plate. This effect increases with increasing load. Similar results were observed by Dash et al. (2003).

The influence of different cell heights and cell diameters on the magnitude of vertical stresses was marginal.

IN-SITU TEST FIELDS

To verify the results of large scale model tests, two different in-situ tests fields were carried out. Geocells were placed within the gravel base layers of two different asphalt paved road constructions. To measure the vertical stresses on the subgrade the test sections were instrumented with earth pressure cells. After the road constructions were finished vehicle crossing tests were carried out while the stresses on the subgrade were measured. In addition falling weight deflectometer (FWD) measurements were conducted.

Reconstruction of the Road K-23

The existing road K-23 consisted of a 20 cm thick asphalt layer in the upper part of the road. Below the asphalt layer there was a 15 cm gravel base layer. The underground consisted of sandy clay with low bearing capacity. At both sides of the street a drainage channel was located in small distance to the pavement over the whole length of the road to drain the water from the adjacent agricultural areas. The existing road had to be reconstructed since a large number of cracks have appeared on the road and lane grooves in the outer areas of the pavement have developed. Because of the low distance of the drainage channels to the street the lateral support of the pavement were insufficient, deformations of the outer road areas have taken place and ruttings have occurred due to traffic.

The main reconstruction concept of the existing road consists in the stabilization of the road foundations. In addition a new bituminous asphalt pavement is placed on the existing road surface.

First of all the existing asphalt layers were removed at the road sides on a width between 1 and 2 meters. After that, the gravel and the soil beneath the asphalt layers were replaced by a new 70 cm thick gravel layer with a maximum particle size of 32 mm. Approximately a 1 m wide band in the middle of the road was not built up newly. In this part of the road only the existing cracks were filled. When the gravel layers at the road sides were build up completely a 17.5 cm thick new asphalt pavement was applied over the whole width of the road.

In one part of the road an alternative road reconstruction was made, using “Typ 1” geocells. 20 cm high geocells with a diameter of 23 cm were installed in a length of approximately 500 m directly below the asphalt layer.

First of all the existing 20 cm thick asphalt course and the 40 cm gravel layer were removed until the subgrade was reached. Load plate tests on the subgrade gave an E_{v2}-value of 20 MN/m². After the subgrade was compacted earth pressure cells were installed on the subgrade. After the installation of earth pressure cells a new 15 cm thick gravel layer with a maximum particle size of 22 mm was build up and compacted. In one section geocells were placed and mounted on a nonwoven geotextile. They were filled with gravel until the old road surface was reached (Fig. 4). Another section was build up without geocells in the same way.

Fig. 4 Installation of geocell layer directly beneath the asphalt surface

A comparison of the three different rehabilitation sections can be seen in Fig. 5. Only test sections 1 and 2 could be instrumented with earth pressure cells.

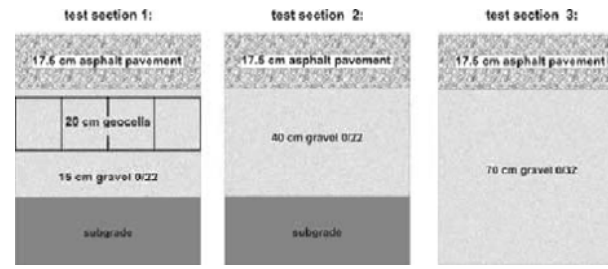

Fig. 5 Different reconstruction sections

After installation of gravel base course on the earth pressure cells plate load tests were carried out while the stresses on the subgrade were measured. The measured stresses in the geocell stabilized test section 1 were about 50% percent smaller than in the unreinforced test section 2.

In addition to plate load tests initial vehicle crossing tests were performed on 25 cm thick gravel layer. During crossing of a grader vertical stresses of 120 kN/m² were measured on the subgrade in the unreinforced test section 2 while only 75 kN/m² could be measured on the subgrade in geocell reinforced test section 1.

Vehicle crossing tests and vertical stress measurements

After the asphalt surface course was reconstituted further measurement was conducted. In this case controlled vehicle crossing tests were carried out on the asphalt course. A heavy truck with five axes and a weight of approximately 41 tons crossed the road at different speeds. During truck crossing the stresses in the underground were measured by the installed earth pressure cells. The stresses measured at a crossing speed of 40 km/h are presented in Fig. 6.

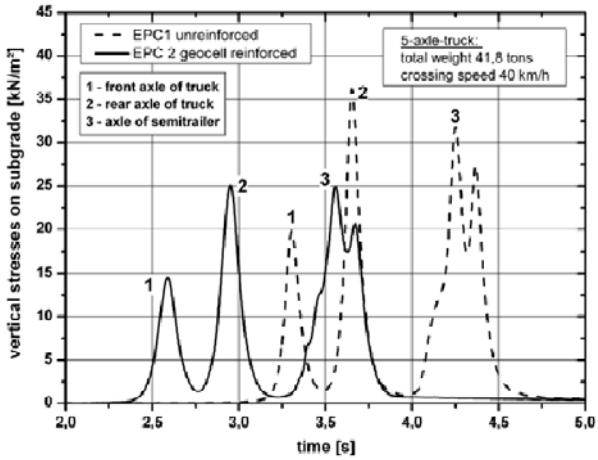

Fig. 6 Results of truck crossing tests, crossing speed 40 km/h

The measured peak values (1) and (2) resulted from the crossing of the single axle of the truck, the double peak values (3) result from crossing of semi trailer.

The results clearly confirmed the results of previous tests. The stresses which are measured in the geocell reinforced tests section are significantly lower than the stresses which are measured in the unreinforced section. The average stress reduction on the subgrade due to the installation of geocell layer in the gravel base layer is approximately 30%.

Similar results could also be observed at other crossing speeds. Both the stresses in the reinforced and also in the unreinforced sections decrease with increasing crossing speed.

Falling weight measurements (FWD)

In addition to vertical stress measurements falling weight deflectometer measurements were carried out after the road construction was loaded by traffic for a longer time.

Falling weight deflectometer (FWD) is a dynamic measuring instrument, which punctually notes the reaction of the pavement structure at a defined load impulse. To measure the pavement reaction a falling weight falls from a defined height in a rubber-puffer-system. The dynamic load impulse of 50 kN is transferred into the pavement structure by a load plate with a diameter of 30 cm. The magnitude and duration of the load impulse are corresponding with a truck passage.

The pavement reaction is measured on the road surface by nine geophones in form of deflections. The geophones are aligned in different distances to the load plate. The deflections and the form of the deflection hutch are the base of the evaluation of the bearing capacity and the stiffness of individual base layers and also for the total pavement structure (Fig. 7).

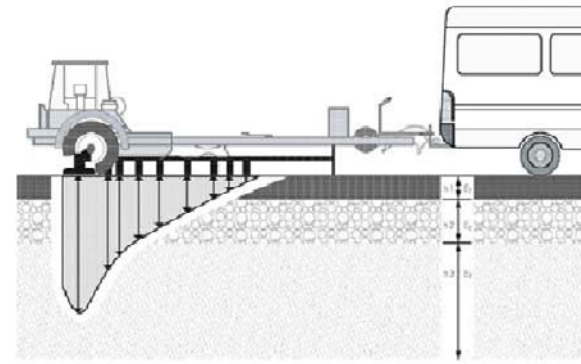

Fig. 7 Schematic diagram of falling-weight-deflectometer (FWD) measurements (FGSV, 2004)

To evaluate the influence of geocell layer within the mineral base course falling weight deflectometer measurements were carried out both in geocell reinforced section (test section 1, Fig. 5) as well as in the unreinforced section (test section 2, Fig. 5). Additional measurements were conducted in a test section with standard reconstruction of 70 cm gravel base course (test section 3, Fig. 5).

The average values of measured deflections and back calculated layer modules are presented inFig. 8.

The calculation of the represented layer modules takes place on basis of the theory of the elastic half space and multi-layer models (Ullitz, 1998).

The results show, that the highest deflections and lowest layer modules were measured in the unreinforced test section with a base layer of 40 cm gravel. Both the deflections and the layer modules of the unreinforced

test section with 70 cm thick gravel base layer and the geocell reinforced test section were very similar. The deflections of these test fields were about 15 percent lower, the layer modules were about 10 percent larger than those of unreinforced test fields with a 40 cm gravel base layer.

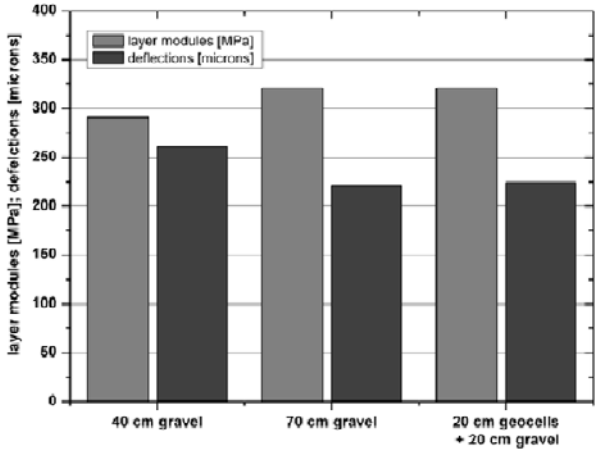

Fig. 8 Results of FWD-measurements

Therefore a stabilization of 40 cm mineral base course with 20 cm height geocells, placed in the upper part of the base layer, has a comparable effect with a 70 cm thick unreinforced gravel base layer in similar boundary conditions.

The conducted FWD measurements confirm the results of the vertical stress measurements.

Reconstruction of the Road K-637

To verify the results of large scale model tests and the results of in-situ field measurements during the reconstruction of the road K-23 a further test field was carried out.

The road K-637 had to be widened and stabilized, since the road should be used as access road during construction of a highway.

The main reconstruction concept of the existing road consists in a widening of the road shoulders of approximately 2 meters. In addition a new bituminous asphalt pavement is placed on the existing road surface. After the existing soil at the sides of the road were removed in a width between 1 and 2 meters until a depth of 50 cm was reached, a new 40 cm thick hydraulic bonded base layer (HBB) was placed in a layer of 20 cm thickness. When the HBB-layers at the road sides were build up completely 18 cm thick new asphalt pavement was applied over the whole width of the road.

The middle of the existing road was not built up newly. In this part of the road only the existing cracks were filled.

In one part of the road an alternative road reconstruction was carried out, using three different stabilization methods. Four test fields, each being 5 m long, were carried out. In one test field geocells are built in within the mineral base layer (test field 1, Fig. 9). A further road section (test field 3, Fig. 9) is stabilized with a 20 cm thick hydraulic bonded base layer. As a reference test field one section (test field 2, Fig. 9) remains unreinforced. In this section a 40 cm thick mineral base layer was build beneath the asphalt pavement. An overview of the test sections and their construction is shown in Fig. 9.

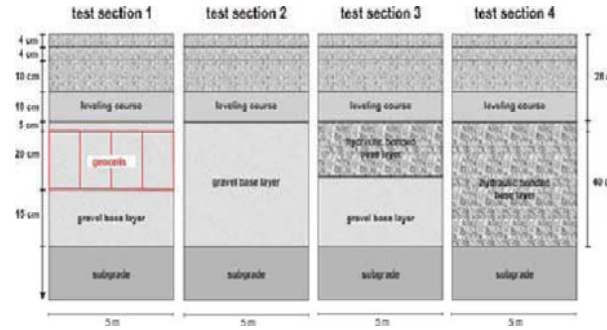

Fig. 9 Test section K-637

In test section 1, 2 and 3 dynamic earth pressure cells were installed directly on the subgrade material.

During and after the road construction vehicle crossing tests were carried out. The stress measurements during crossing tests verify the results of in-situ field tests during construction of the road K-23. The vertical stresses in the geocell reinforced section were about 30% lower than the stresses which were measured in the unreinforced test section. Because of its higher stiffness the 20 cm hydraulic bonded base layer could reduce the vertical stresses about 22% compared to the geocell reinforced test section. No stresses were measured in test section 4.

Falling weight deflectometer measurements were also carried out. The measured deflections in the geocell reinforced section were smaller than those measured in the unreinforced section. A further reduction could be observed in test section 3 and 4, because 20 cm and 40 cm thick hydraulic bonded base layers were placed beneath the asphalt pavement. With increasing height of HBB-layer the deflections were decreasing.

The highest back calculated layer modules could be observed in the HBB-layers while the modules of the unreinforced test section were the smallest. The modules of the geocell reinforced section are smaller than those of the HBB-layers but higher than the module of the unreinforced section.

If the vertical stress measurements and the FWD measurements are summarized, a very good agreement between the vertical stresses and deformations can be observed. With increasing layer modules the deformation and the vertical stresses are decreasing (Fig. 10).

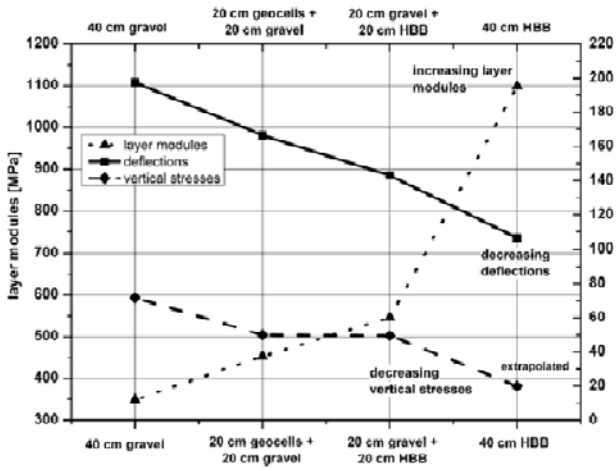

Fig. 10 Results of FWD measurements K-637

CONCLUSION

To determine the influence of a geocell layer on the load-settlement behavior and the vertical stresses on the subgrade large scale model tests were conducted. The results have shown that the geocell layer reduced the vertical stresses on the subgrade about 30%, distributed the vertical loads over a larger area and improved the bearing capacity of the infill material between 1.1 and 1.7 times.

In addition to the model tests two different in-situ tests fields were constructed during the reconstruction of the roads K-23 and K-637. Vehicle crossing tests have shown that in the geocell reinforced test sections the vertical stresses on the subgrade were reduced about 30% compared to the unreinforced section. FWD measurements have shown that the geocell layer increased the layer modulus of the gravel base layer and decreased the deflections on the surface.

The results of the in-situ tests confirmed the results of the large scale model tests. With increasing soil stiffness, e.g. due to an installation of geocells or a hydraulic bonded base layer, the vertical stresses on the subgrade and the deflections on the surface were reduced and the layer modulus were increased.

REFERENCES

Al-Quadi IL, Hughes JJ (2000) Field evaluation of geocell use in flexible pavements. Transportation Research Record (TRB) H 1709: 26-35

Ben Kurari K (2000) Implementation of geocells in low bearing capacity roads. Proceedings of the 2nd European Geosynthetics Conference, Bologna, Session 7A: 365-368

Dash SK, Krishnaswamy NR, Rajagopal K (2001) Bearing capacity of strip footings supported on geocell-reinforced sand. Geotextiles and Geomembranes, June, 2001, 19(4): 235-256,

Dash SK, Sireesh S, Sitharam TG (2003) Model studies on circular footing supported on geocell reinforced sand underlain by soft clay. Geotextiles and Geomembranes 21(4): 197-219

Forschungsgesellschaft für Straßen- und Verkehrswesen, FGSV Arbeitspapier "Tragfähigkeit" Teil C2 "FWD, Auswertung und Bewertung", AK 4.8.2, Entwurf Stand Februar 2004

Forsman J, Slunga E, Lahtinen P (1998) Geogrid and Geocell Reinforced Secondary Road over Deep Peat Deposit. Proceedings of the 6th International Conference on Geosynthetics 2: 773-778, Atlanta

Leytland IV, Aliver YA, Bubnovsky VV (2006) Experience on using plastic geocells in the construction of roads under conditions of the arctic of Russia. Proceedings of the 8th international Geosynthetic Conference: 705-708, Yokohama

Meyer N, Emersleben A (2005a) Mechanisches Verhalten von bewehrten Böden mit Geozellen. 9. Informations- und Vortragstagung über "Geokunststoffe in der Geotechnik", Sonderheft der Geotechnik: 49-55

Meyer N, Emersleben A (2005b) Mechanisches Verhalten von bewehrten Böden mit Geozellen. Symposium Geotechnik—Verkehrswegebau und Tiefgründungen, Schriftenreihe Geotechnik, Universität Kassel Heft 18: 93-112

Meyer N, Emersleben A (2005c) Einsatz von Geozellen im Verkehrswegebau. Tiefbau—Ingenieurbau—Straßenbau (TIS) Heft 11: 32-37

Meyer N, Emersleben A (2006a) Bodenstabilisierung mit Geozellen im Straßenbau. 21. Christian Veder Kolloquium (CVK) —Neue Entwicklungen der Baugrundverbesserung, Heft 28: 85-101 Technische Universität Graz (TUG)

Meyer N, Emersleben A (2006b) Stabilisierung von mineralischen Tragschichten mit Geozellen. Tiefbau Heft 11: 634-640

Mhaiskar SY, Mandal JN (1992) Soft Clay Subgrade stabilisation using Geocells. Geotechnical special publications 30: 1092-1103, New York, American Society of civil engineer ASCE

Ullidtz, Per: Modelling Flexible Pavement Response and Performance. Polyteknisk Forlag, Lyngby, 1998

Sitharam TG, Siressh S (2005) Behavior of embedded footings supported on geogrid cell reinforced foundation beds. Geotechnical testing journal 28(5): 1-12

Hydraulic Applications

DESIGN OF EARTH DAMS ALLOWING TEMPORARY OVERTOPPING BASED ON HYDRAULIC FAILURE EXPERIMENTS AND FLOOD ANALYSIS

K. Matsushima[1], Y. Mohri[2], S. Yamazaki[3], T. Hori[4], M. Ariyoshi[5] and F. Tatsuoka[6]

ABSTRACT: Every year a great number of small earth dams for agricultural irrigation are seriously damaged or totally fail because of flood overflow exceeding the drainage capacity of a spillway. To stabilize downstream slopes of earth fill dams against overflow, a new stabilization technology using geosynthetic soil bags with extended tails (GSET) was developed. GSET functions as a spillway for temporary flooding while it is designed to have a high seismic stability. A series of hydraulic failure experiments were performed on a 3.5 m-high and 2.3 m-wide full-scale GSET model with a downstream slope of 1:1.2 (V: H). The overflow was stepwise increased. Based on the test results, a flood stability design for GSET spillways allowing temporary overflow is developed. A design working example is presented based on an actual flood record. It is shown that the remedy work of an existing earth dam by means of a GSET-spillway is effective in particular with small earth dams with short-peak flooding.

KEYWORDS: overtopping, soil bag, flooding, spillway, remediation work

INTRODUCTION

There are approximately 210,000 reservoirs with earth dams constructed for agricultural irrigation that are lower than 15 m in height across Japan. Approximately 20,000 of these earth dams have deteriorated and need urgent but cost-effective repair. Moreover, every year a great number of dams are seriously damaged or even totally fail due to flood overflow exceeding the drainage capacity of a spillway and earthquakes, as typically seen in Photo 1. To substantially increase the stability of the slopes of such small earth dams against overflow and seismic loads, Matsushima et al. (2006a) proposed protecting the slope by stacking soil bags inclined downward at the back and anchored to the inside of earth dam with geosynthetic reinforcement (Fig. 1). This system, called geosynthetic soil bags with extended tails (GSET) spillway, is designed to properly function during emergency temporary flooding (Mohri et al. 2005; Matsushima et al. 2005a&b, 2006a & b, 2007a).

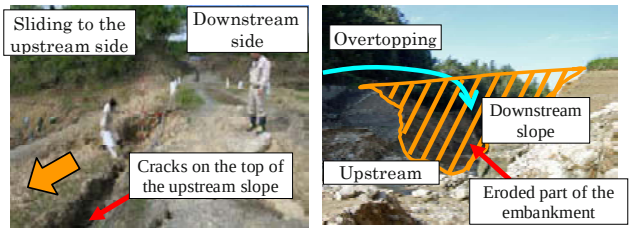

Photo 1 Failure of small earth dams: a) by the Niigata-chuetsu earthquake in 2004 in Kawaguchi town; and b) totally collapsed by heavy rainfall during Tokage typhoon No. 200423 in Awaji island

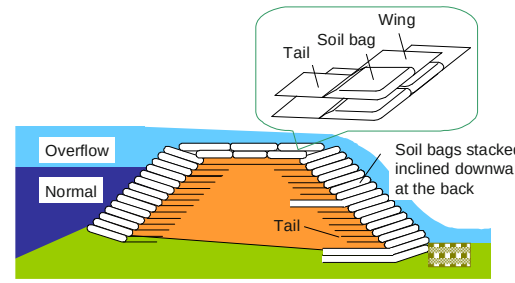

Fig. 1 Basic Spillway made of geosynthetic soil bags with extended tails (GSET) allowing temporary flooding (Matsushima et al., 2005a&b)

A soil bag system has a self-confining mechanism, in which the tensile force is mobilized in the soil bag sheet associated with compressive deformation of the backfill (Fig. 2: e.g., Matsuoka et al. 2001; Tatsuoka, 2004; Lohani et al. 2006). This mechanism increases the confining pressure in the backfill, resulting in an increase in the strength of the backfill. Therefore, large tensile force is developed in the geosynthetic soil bag by pre-compaction. It is considered that an stacked soil bag

[1] Researcher, Dept. of Geotechnical and Hydraulic Engrg., National Institute for Rural Engineering, JAPAN. Email: kenichim@affrc.go.jp
[2] Chief of laboratory of Soil Mechanics, Dept. of Geotechnical and Hydraulic Engrg., National Institute for Rural Engineering, JAPAN. Email: ymohri@affrc.go.jp
[3] Researcher, Mitsui Chemicals Industrial Products, Ltd., JAPAN. Email: yama820@affrc.go.jp
[4] Researcher, Dept. of Geotechnical and Hydraulic Engrg., National Institute for Rural Engineering, JAPAN. Email: thori@affrc.go.jp
[5] Researcher, Dept. of Geotechnical and Hydraulic Engrg., National Institute for Rural Engineering, JAPAN. Email: ariyoshi@affrc.go.jp
[6] Professor, Dept. of Civil Engineering, Tokyo University of Science, JAPAN. Email: tatsuoka@rs.noda.tus.ac.jp

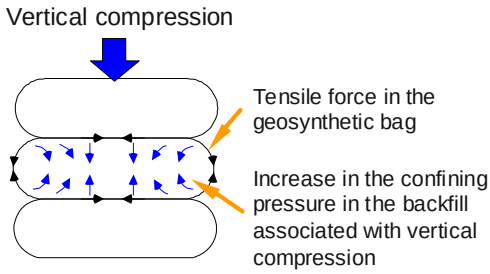

Fig. 2 Self-confining mechanism when the soil bags are vertically compressed

system can become stable against overtopping flow by the confining effect due to the weight of overlying soil bags. On the other hand, it is necessary to protect the outside face of the soil bags placed on the downstream dam against ultraviolet ray by means of, for example, vegetation, as seen in Photo 2.

ALLOWING OVERTOPPING

A GSET-spillway made of stacked soil bags is one specific type of stepped spillway (Fig. 1). Stream regimes on a stepped slope are categorized into the following three overflow levels with increasing overflow quantity (Fig. 3).

1) level 1(nappe flow; Fig. 3a), characterized by the formation of a nappe and an air pocket at each step with rich air entrained and napped on each soil bag step;
2) level 2 (skimming flow; Fig. 3b), characterized by the formation of an eddy at each step; and
3) level 3; formation of free fall at the top of the slope (Fig. 3c).

The stability of the GSET-spillway against overtopping in the respective regimes was investigated by performing hydraulic overflow-induced collapse tests on a 3.5 m-high and 2.3 m-wide full-scale GSET (Fig. 4; Matsushima, et al. 2007b). The downstream slope was 1H: 1.2V and the overflow level was stepwise increased. Fig. 5 shows the three overflow levels causing different

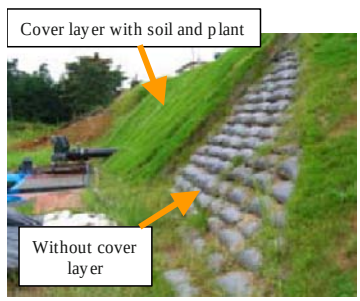

Photo 2 Vegetation to protect the soil bag slope from ultraviolet ray degradation

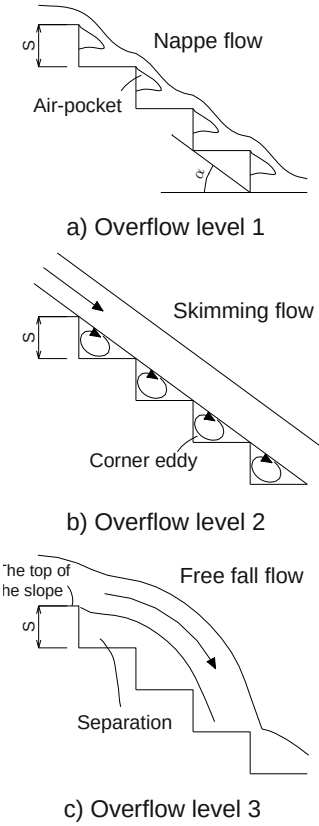

Fig. 3 Stream regimes of stepped spillways (after Hubert 1994)

damage patterns to the stepped slope observed in the experiments. At overflow level 2 (overflow depth h_{GSET}= 0.24—0.32 m; Fig. 5b), minor damage including sucking out a small amount of backfill material from the void between soil bag interfaces, perforations and surface attribution of the soil bags took place (Photo 3). The development rate of erosion in the reinforced slope of the earth dam model was slow. At overflow level 3, classified as free fall flow (h_{GSET}=0.32—0.58 m; Fig. 5c), serious damage by penetration of water flow into the soil bags occurred due to high energy of free falling

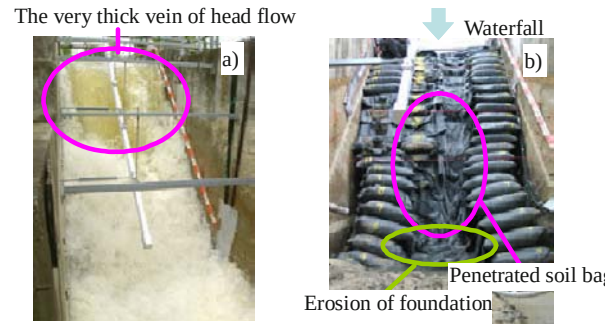

Photo 3 Minor or moderate damage: a) Evidence of backfill material sucked in the cell zone behind the stacked soil bags; and b) Attrition surface and perforations of soil bag surfaces

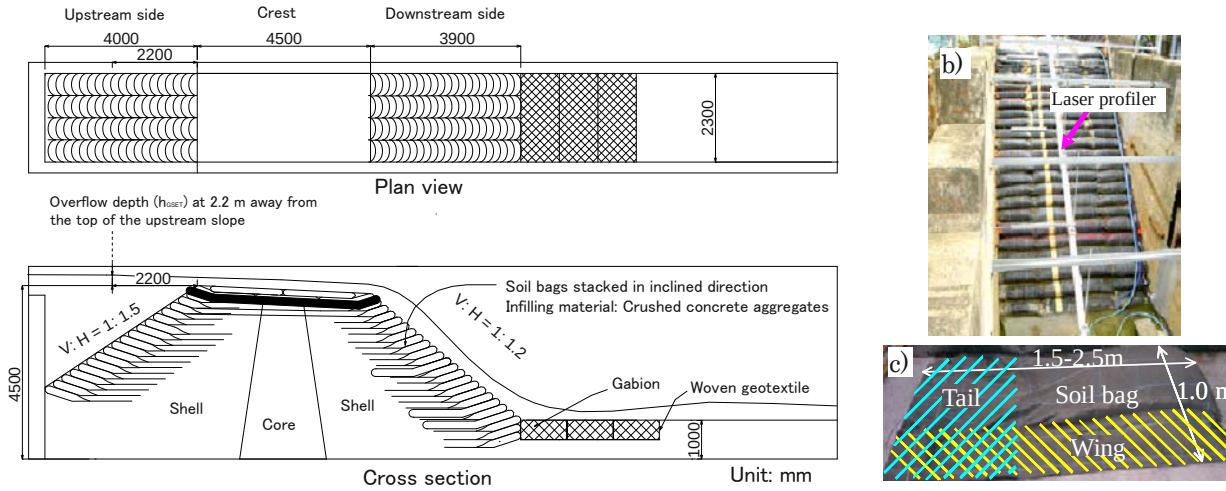

Fig. 4 Large-scale overflow-induced collapse test: a) plan view and cross section of full-scale small earth dam; b) downstream slope of the constructed GSET-spillway model; and c) a large soil bag integrated with wing and tail (Matsushima et al. 2007b)

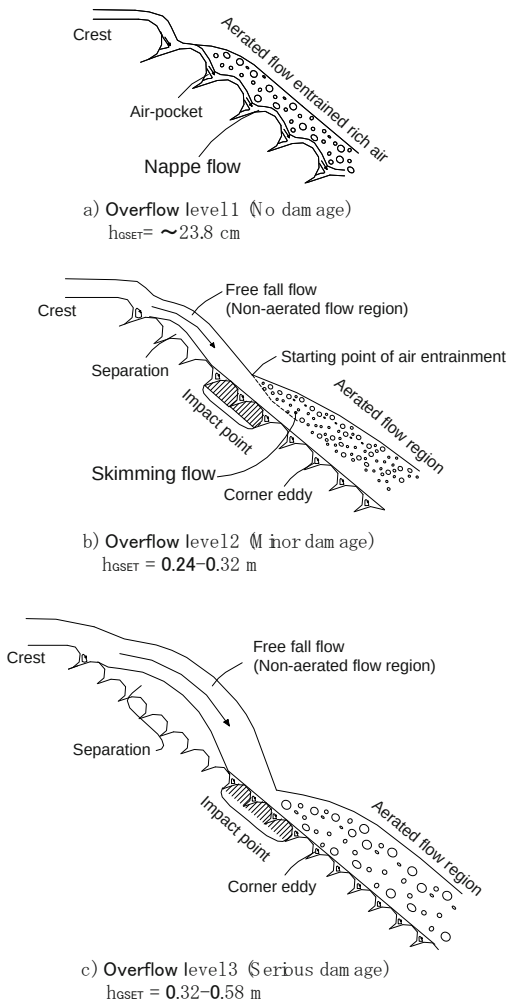

Fig. 5 Schematic diagrams of three flow regimes according to overflow level observed in the experiments

water. The development rate of erosion in the reinforced slope of the earth dam became significant. Photo 4 shows an erosion trace 225 min after the start of flow at h_{GSET} = 0.48－0.58 m.

Fig. 6 shows the hydraulic performance curve (i.e., a broken curve) of the GSET-spillway when subjected to overtopping flow (i.e., the boundary indicating allowable combinations of overtopping overflow depth h_{GSET} and duration) determined based the hydraulic test results (i.e., solid square data points). The allowable duration at level 2 overflow is very long due to a very low development rate of erosion, indicating that the stability of GSET-spillway can be maintained against temporary flooding at level 2. On the other hand, the allowable duration becomes much shorter when overflow level becomes 3 (h_{GSET}> 0.32 m) forming free fall flow. At overflow level 3 in a range of h_{GSET} from 0.32 m to 0.50 m, the stability of GSET-spillway becomes critical as the allowable duration becomes very short, less than 180 min.

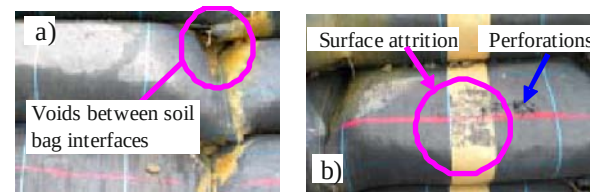

Photo 4 Overflow level 3 (serious damage): a) Stream regime on the downstream side at overflow level 3 with q= 0.652 m^3/s/m; and b) Erosion trace with the formation of a waterfall basin after final overtopping

PERFORMANCE DESIGN

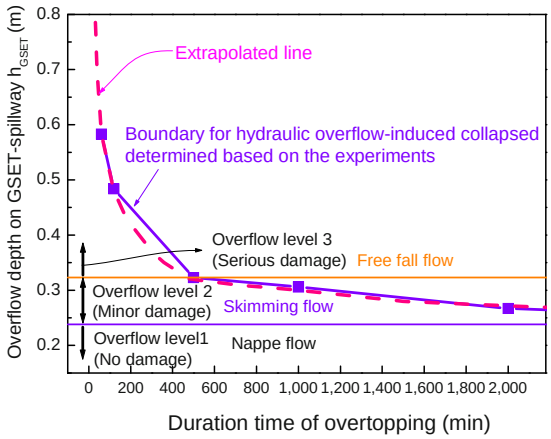

Fig. 6 Experimental performance curve of GSET-spillway

The performance design of the GSET-spillway in terms of flood stability is discussed in this section. Fig. 7a illustrates a remedy work of an earth dam by constructing a GSET-spillway added to an existing spillway having an insufficient drainage capacity. Fig. 7b shows the cross-sections of the existing spillway and GSET-spillway, where B is the width of the respective spillways; Δh is an elevation gap between the bottom levels of the existing spillway and GSET-spillway; and *DWL* is the design flood water level. As a working example to determine the width B_{GSET} of the GSET-spillway and the value of Δh, flood analysis of GSET-spillway was performed on a totally collapsed small earth dam by overtopping during Tokage typhoon No. 23 in 2004 in Awaji island (Photo 5). Table 1 shows the properties of this small earth dam. Fig. 8 shows the histories of rainfall at Gunke in Awaji island recorded by the Japan Meteorological Agency and overflow depth calculated by flood analysis. It may be seen that the estimated overflow depth h_{exist} largely exceeds the speficied *DWL* (h_{max}= 0.70 m) in the case without a GSET-spillway and the drainage capacity of the existing spillway is insufficient for this flood event. On the other hand, the duration of overflow with h_{exist} exceeding the specified *DWL* is short, within a couple of hours.

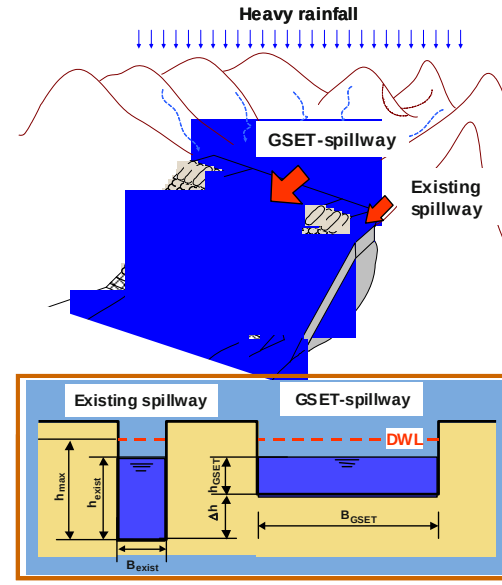

Fig. 7 Design example of remedy work by means of a GSET-spillway to increase the drainage capacity: a) overview; and b) cross-sections of the spillways

Fig. 9 shows the relationship between the over flow depth, h_{GSET}, and the width of GSET-spillway, B_{GSET}, for different elevation gaps between the bottom levels of the existing spillway and GSET-spillway, Δh. calculated by flood analysis using the same rainfall event. A flow coefficient of the GSET-spillway C_{GSET} = 1.5 obtained from the hydraulic test is used in this flood analysis. When the allowable overflow depth and duration for this flood stability design are specified to be, respectively, a range from 0.32 m to 0.50 m and 180 min as previously mentioned, the shaded area shown in Fig. 9a can satisfy

Table 1 Properties of the totally collapsed small earth dam analysed in this study

Width of the existing spillway B_{exist}	Flow coefficient C_{exist}	Basin Area	Full water reservoir area	Rate of run off f
3.5 m	1.796	0.2384 km^2	0.0013 km^2	0.8

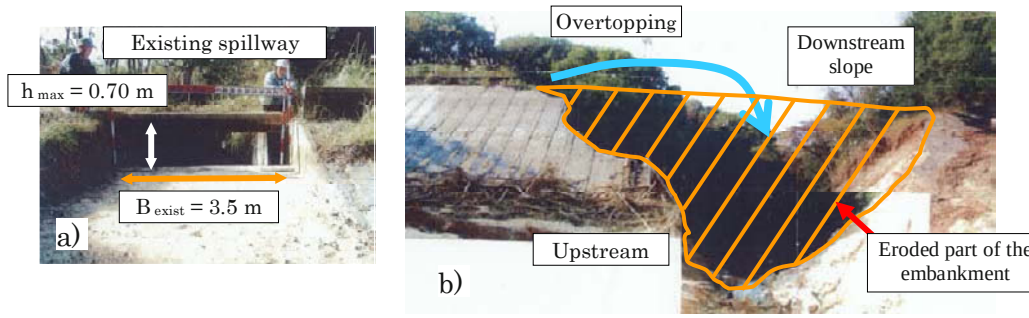

Photo 5 Small earth dams totally collapsed from heavy rainfall during Tokage typhoon No. 200423 in Awaji island: a) the existing s pillway with small drainage capacity b) Eroded dyke after overtopping

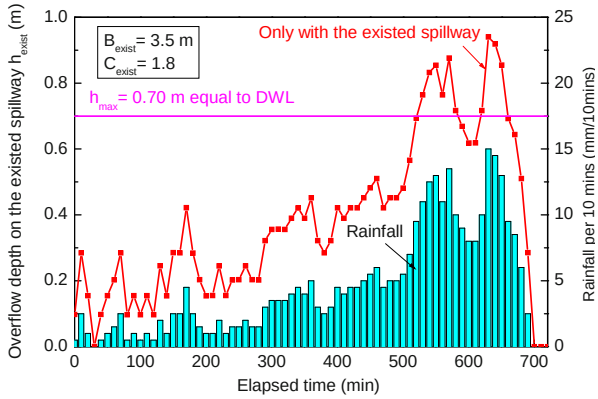

Fig. 8 History of rainfall and overflow depth h_{exist} during Tokage typhoon No. 200423 in Awaji island

the following conditions (a) & (b):

(1) The overflow depth h_{exsit} is less than 0.70 m for the *DWL*.

(2) The overflow depth h_{GSET} is less than 0.50 m.

(3) Duration when the overflow depth ranges from 0.32 m to 0.50 m is within 180 min.

Inside the shaded area, the minimum width of the GSET-spillway B_{GSET} is 4.0 m when Δh= 0.20 m at point A. To confirm whether the duration when the overflow depth ranges from 0.32 m to 0.50 m is within 180 min. (i.e., condition c) with the GSET-spillway having B_{GSET} = 4.0 m and Δh = 0.20 m, the time history of overflow depth h_{GSET} has been plotted in Fig. 10. It may be seen that this duration is equal to 122 min, lower than 180 min, satisfying condition c). When B_{GSET} is 12.5 m, a safer design results which allows only overflow level 2 (h_{GSET} <= 0.32 m) (Fig. 10).

CONCLUSIONS

The performance of GSET-spillway against overtopping was evaluated by performing hydraulic overflow full-scale tests inducing failure. Based on the above, a performance design of the GSET-spillway was proposed.

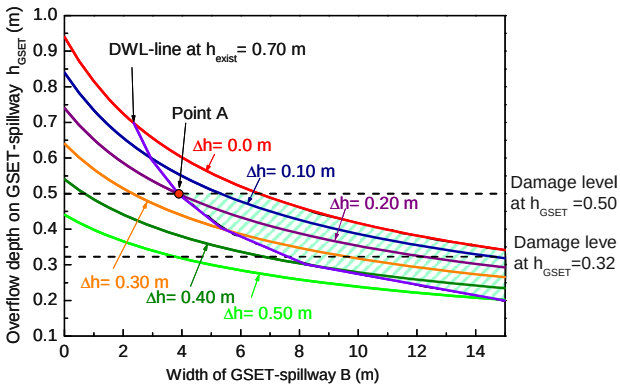

Fig.9 Relationship between the width of GSET-spillway B_{GSET} and overflow depth h_{GSET}

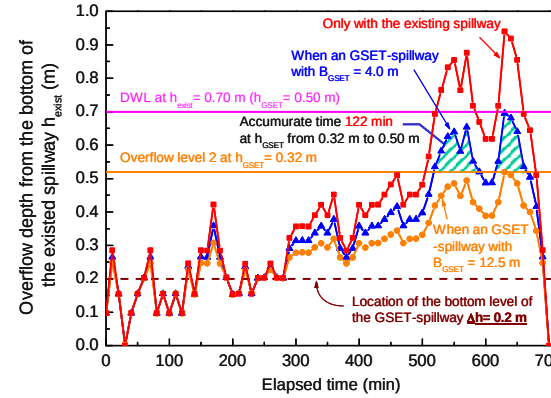

Fig. 10 History of overflow depth h_{exsit} at h= 0.20 m when GSET-spillway was applied to the totally collapsed earth dam

An example flood design of GSET-spillway was made based on analysis of allowable combinations of the overflow depth and duration. The following conclusions can be derived from the above:

(1) At overflow level 2 (skimming flow regime with an overflow depth h_{GSET} less than 0.32 m), the resistance of the GSET-spillway against overtopping flow is large enough with only minor damage.

(2) At overflow level 3 (free fall regime, h_{GSET}=0.32 — 0.58 m), the GSET-spillway can exhibit a high resistance only temporarily, for about three hours, because of a relative high development rate of erosion in the reinforced dam slope.

(3) The width of a practical GSET-spillway, B_{GSET}, is about 12.5 m when designed based on an allowable overflow depth h_{GSET} is less than 0.32 m. However, a smaller B_{GSET} can be employed if a temporary resistance against overflow depth h_{GSET}= 0.32 — 0.50 m is taken into account in the design.

The analysis shown in this paper indicates that the remedy work of an existing earth dam by means of a GSET-spillway is effective in particular with small earth dams that can be designed against with short-peak flooding resulting from a relatively small basin area.

REFERENCES

Hubert C (1994) Hydraulic design of stepped cascades, channels, weirs and spillways, Pergamon, First Edition, ISBN 08 041918 6

Lohani TN, Matsushima K, Aqil U, Mohri Y, Tatsuoka F (2006) Evaluating the strength and deformation characteristics of a soil bag pile from full-scale laboratory tests, Geosynthetics International 13(6): 246-264

Matsuoka H, Liu SH, Yamaguchi K (2001) Mechanical properties of soilbags and their application to earth

reinforcement, Proc. of the International Symposium on Earth Reinforcement 1: 587-592

Matsushima K, Yamazaki S, Mohri Y, Arangelovski G (2005a) Overflow model test of small dam with soil bags, Proc. of 40th Annual Symposium on Geotechnical Engineering: 1995-1996 (In Japanese)

Matsushima K, Yamazaki S, Mohri Y, Arangelovski G (2005b) Overflow Test of Small Earth Dam with Allowed Overtopping, Proc. of Annual Symposium on Irrigation, Drainage and Reclamation Engineering, CD-ROM (In Japanese)

Matsushima K, Yamazaki S, Mohri Y, Aqil U, Tatsuoka F (2006a) Structural features of earth dams allowing overtopping and a full-scale construction test, Proc. Annual Symposium on Irrigation, Drainage and Reclamation Engineering, CD-ROM (In Japanese)

Matsushima K et al. (2006b) Shear characteristics of geosynthetics soil bags stacked in inclined and horizontal directions, Proc. of 21st Geosynthetics Symposium (Japan Chapter of IGS): 145-152 (In Japanese)

Matsushima K, Aqil U, Mohri Y, Tatsuoka F, Yamazaki S (2007a) Shear characteristics of geosynthetics soil bags stacked in inclined and horizontal directions, Proc. 21st Geosynthetics Symposium (Japan Chapter of IGS): 145-152 (In Japanese)

Matsushima K, Yamazaki S, Mohri Y, Hori T, Ariyoshi M, Tatsuoka F (2007b) Large-scale overflow failure tests on embankments using soil bags anchored with geosynthetic reinforcements, Int. Sypo. on Earth Reinforcement Practice, IS Kyushu '07, accepted

Mohri Y, Matshushima K, Hori T, Tani S (2005) Damage to small-size reservoirs and their reconstruction method, Special Issue on Lessons from the 2004 Niigata-ken Chu-Etsu Earthquake and Reconstruction, Foundation Engineering and Equipment (Kisoko), October: 62-65 (In Japanese)

Tatsuoka F (2004) An approximiate isotropoic perfectly plastic solution for compresive strength of geosynthetic-reinforced soil, Geosynthetics International 11(5): 390-405

Yasuda Y, Ohtsu I (1999) Flow resistance of skimming flows in stepped channels, Proc. of 28th IAHR Congress, Grz, Austria, Session of B14 (CD-ROM)

EXPERIMENTAL STUDY ON THE INTERACTION MECHANISM BETWEEN GEOGRID AND EXPANSIVE ROCK BY PULL-OUT TEST

J.H. Ding[1], J.Tong[2] and C.G. Bao[3]

ABSTRACT: The interaction mechanism between geogrid and mid-weak swelling rock in the Project of South-to-North Water Transfers Projects is investigated by pull-out tests conducted at the modified laminated shear test apparatus. Quasi-friction angle and quasi-cohesion force of the interface are obtained through the experiments of two types of geogrids at different vertical loadings. Furthermore, the distribution law of interface frictional resistance at the different location of geogrid is analyzed. Finally, distribution of additional shear stress in soil induced by IFR is preliminary investigated.

KEYWORDS: expansive rock, geogrid, interaction, pull-out test

INTRODUCTION

Swelling rock is a kind of water-swelling and water-softening rock. In china, the engineers usually have to face the problem of swelling rocks(soils) in the engineering of roads, railways, airports etc., The problems caused by expansive rock (soil) in the South-to-North Water Transfers Project (SNWTP) emerged very frequently, and it is extremely hard to tackle with. The total length of trunk canal with relevant to the expansive rock (soil) in SNWTP is about more than 300 km. How to treat the expansive soil properly to maintain the stability of the cannal slope is the main technical.

Geogrid embedded in the soil is serviced as a high-tensile strength material to enhance the strength of soil and reduce the lateral deformation. The normal loading on the interaction between geogrid and soil induces the frictional force that restricts the deformation and movement of the geogrid. The interaction effect between the geogrid and soil exists not only on the interface between the two materials (contact skin, shear band), but also in a certain range near the interface, revealing the mechanism of the reinforcement.

In general, the methods to study the interaction properties mainly include laboratory direct shear test, pull-out test, torsion shear test, titled plate test and field full-scall test, etc. The direct shear test can be used to test the properties of the single shear plane between the reinforced material and the soil, while pull-out test can detect the interaction properties between the reinforced material and soil surround it. The two methods mentioned above are the principal research approaches which widely available in the engineering. There has been much research papers about the interaction between geogrid and sand or clay. However, there is few research on the reinforcement mechanism and effect for the special expansive soil(rock). In this paper, the interaction mechanism between geogrid and mid-weak swelling rock in the Project of SNWTP is analyzed by pull-out tests conducted on the laminated shear test apparatus. the quasi-friction angle and quasi-cohesive force of the interface are obtained, furthermore, the distribution of interface frictional resistance (IFR) at the different location of geogrid has been addressed.

PULL-OUT TEST

Test Apparatus

DHJ60 laminated shear test apparatus (made by Changjiang River Scientific Research Institute) comprises the vertical and horizontal loading system, shear box, stress and displacement acquisition system, etc. The performance index of DHJ60 laminated shear test apparatus is shown in Table 1. The apparatus is equipped with plane frame and hydraulic loading. Horizontal stress is strain-controlled mode with stepless speed at the range of 0.2—20 mm/min. The up shear box comprises 10 laminated rings, which number is from 1#

[1] Senior engineer, Key Laboratory of Geotechnical Mechanics and Engineering of the Ministry of Water Resources Changjiang River Scientific Research Institute, CHINA. Email:jhding1973@hotmail.com
[2] Eengineer, Key Laboratory of Geotechnical Mechanics and Engineering of the Ministry of Water Resources Changjiang River Scientific Research Institute, CHINA. Email:tongjun2007@yahoo.com.cn
[3] Professor, Changjiang River Scientific Research Institute, Ningbo Institute of Technology, ZheJiang University, CHINA. Email:bcgang@public.wh.hb.cn

to 10# from top to down. Rolling bearings between the laminated rings and lateral plane are employed to reduce the frictional force. The loading monitor transducers are employed to measure the horizontal and vertical force. The displacement of the laminated ring is measured by the resistant displacement transducer with the max. range of 100 mm.

Table 1 Performance of DHJ60 modified laminated shear test apparatus

General dimension (mm) 600×600×600	Max.loading (kN)		Max.disp. (mm)		shear velo. (mm/min)
Laminated ring(×10) (mm) 600×600×30	norm.	tan.	norm	tan.	0.2—20
Low shear box (mm) 600×600×300	1000	1000	100	120	

Test Material

Two type of uniaxial oriented HDPE geogrids (PE50 and PE80) are used in the pull-out test. Their mechanical properties are obtained by the unconfined tensile test, as shown in Table 2. The physical dimension of geogrid is listed in Table 3. Some longitudinal bars of the geogrid are labeled with the length of 15 cm beforehand, and are measured the elongation after the pull-out test. Total six nonstretch steel chords were fixed at three transverse ribs that embedded at the different position in the soil, the chords B1-1 and B1-2 is near to the pulling end and the B3-1 and B3-2 is the free end of geogrid. Copper pipes are used to protect the chords and reduce the friction between the soil and chords. The nonstretch chords are connected with dial gauges to measure the relative displacement between the soil and geogrid at different embedded position.

Table 2 Mechanical properties of the geogrid

Type of the geogrid	Tensile strength (kN/m)	Elongation (%)	Strength corresp. to 2%(kN/m)	Strength corresp. to 5% (kN/m)
PE50	52.32	11.98	15.81	29.83
PE80	85.10	10.55	30.37	55.23

The expansive rock was taken from Luwangfen, Xin County, Henan Province. Its basic physical and mechanical properties are presented in Table 4. The free expansion ratio is less than 62%, according the Standard GBJ112-87, it can be classified as mid-weak expansive rock. For the experiment soil sample, its particle size is smaller than 60 mm, water content is about 14% which same as natural content, and the dry density is 1.65 g/m^3.

Table 3 physical dimension of the geogrid (mm)

Types of geogrid	dimension		Long. rib		Trans. rib	
	length	width	Thick.	width	Thick.	width
PE50	231.0	17.10	0.91	5.72	2.55	16.97
PE80	265.4	16.65	0.84	5.70	4.16	17.26

Table 4 Basic property of expansive

Liquid limit w_L(%)	Plastic limit w_P(%)	Free Expansion Ratio(%)	c_{cq} (kPa)	φ_{cq} (°)
36.8—42.3	17.9—19.1	45—62	61.8	36.1

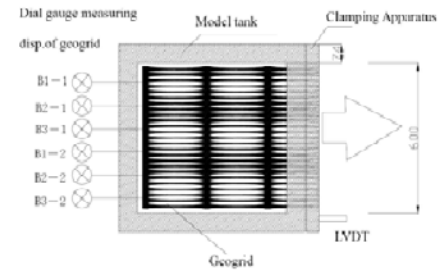

(a)

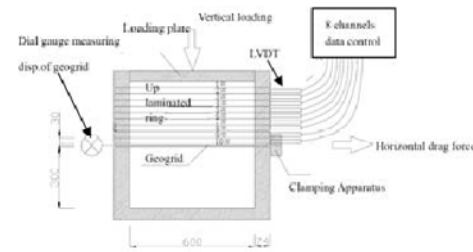

(b)

Fig. 1 schematic diagram for the pull-out test (a) plane; (b) cross-section (mm)

Test method

Soil sample is compacted with the specific water content and density. Afte the lower shear box is filled with the compacted soil. the geogrid with the displacement measurement chords is placed fully above the soil surface, and it have to be guarantee that the horizontal pull-out force is same direction with geogrids. Then fill the soil sample of the laminated rings layer by layer. At first, the expansive rock sample is consolidated at the specific vertical force, then the horizontal force is applied to start the pull-out test at the velocity of 0.3mm/min. The test process can be finished at one of the following standards: (1) horizontal force decrease to a stable value after reaching a peak value, (2) the free end of the geogrid moves at a constant velocity. The

schematic diagram of test apparatus are presented in Fig. 1.

Test Scheme

The factors that impacted significantly on the interaction mechanism between geogrid and expansive rock in pull-out test include vertical stress, pull velocity, soil water content, dry density, and geogrid strength, physical dimension, etc. The test scheme is shown in Table 5 and the pull velocity is 0.3 mm/min. The influence of the vertical stress and strength of the geogrid on the interaction frictional strength is investigated mostly, and the distribution laws of interface frictional resistance at different locations of geogrid are discussed. The distribution of additional shear induced by interface frictional resistance by the displacement is analyzed through the displacement of the laminated rings.

Table 5 Test Scheme

Num.	Vertical stress (kPa)	expansive rock		geogrid
		water content (%)	dry density (g/cm^3)	
1	50	13.8	1.65	PE50
2	100	14.2		
3	200	14.4		
4	300	13.6		
5	200	13.5		PE80

TEST RESULT AND ANALYSIS

Mechanism of the Interaction between Geogrid and Soil

When the geogrid embedded in the soil is subject to the tensile force, the deformation would occur at the direction of the imposed force. The frictional force that generates on the contact surface between the geogrid and soil can impede the relative movement. The frictional force distributes nonuniformly through the embedded direction with maximum value at the end applied the force, and transfers gradually to the free end by the increase of the horizontal force. When the frictional force at the free end reaches maximum value, the whole geogrid starts to move. Generally this moment is defined as the pull-out time. In practical engineering, the friction on reinforcement surface is assumed as uniform distribution to get a quasi-friction coefficient,

$$f = \mathrm{tg}\,\theta = \tau / \sigma_n \qquad (1)$$

where, θ is the quasi-frictional angle, σ_n is vertical stress, τ is the frictional force on the reinforcement surface, its average value is equal to $T/2A$, T is the horizontal force corresponding to pull out the geogrid，A is the contact area between geogrid and soil.

When fabricated geogrid reach the pull-out state, the relative displacement between geogrid and soil occurred, the interaction between geogrid and soil transfers from the static friction to the dynamic force and interlocking between the soil particle and geogrid. To stand against the passive resistance imposed by the transverse ribs and strength of the soil particle among the meshes, the horizontal pull force will increase until the soil mass yields failure. So the pull-out test process can be divided into two phases: the static friction phase and the sliding frictional stage, the mechanism of them is not completely same. In the first phase, there is only the friction acting on the interface; however, at the second phase, the soil particles outside the interface also yield displacement, rotation and shear, at last, the “indirect reinforcement” also takes effect.

The static friction strength and total interface strength is shown in Table 6. The τ_{max}-p curves of PE50 geogrid is presented in Fig. 2. It can be seen that at low stress condition, the static frictional strength at the geogrid and soil interface is only 27.6% of the peak strength, but the proportion of static friction rises with the increase of the vertical loading. When the vertical force equals to 200kPa, the static friction can be 78.1% of the peak value, once it exceeds 200kPa, the increasing extent will reduce. It can be deduced that the geogrid is easy to be pulled out and the soil particles have the tendency to adjust and reorganize when the overlying loading is relatively small, and with the interlock between geogrid and soil be going, the total interface friction strength can reach a great level at last. With the load’s augment, the interaction between the reinforcement and soil mainly displays the static friction, and the occlusion effect reduces.

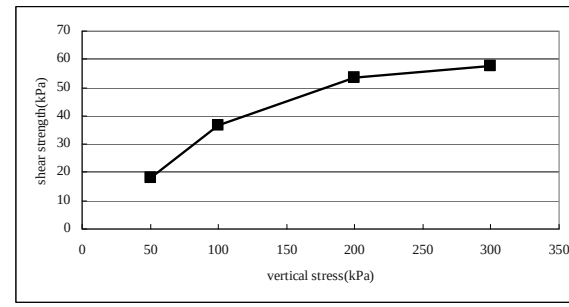

Fig. 2 τ_{smax} - p curves for PE50 geogrid

Characteristics of Stress Distribution on Geogrid-expansive Rock Interface

For macromolecule polymer materials, the pulling displacement at different position is comprised of two parts: one is the elongation subjected to a tensile force,

generally known as the extensibility, which mainly occurred at the clamp end; the other is the relative displacement between the geogrid and soil. Due to the thickness of the model sidewall (in present test the thickness of laminate sidewall is 74 mm), the geogrid at the given position is in unconfined state, so it is firstly pulled. However, the embedded geogrid is confined by the soil, so the tensile behavior is completely different from the unconfined situation, the geogrid's extensibility should be very small.

Table 6 Results for the pull-out test of geogrid

Types of Geogrid	PE50				PE80
V. loading (kPa)	50	100	200	300	200
Drag force corresp. to pull-out (kN)	4.1	6.3	12.2	13.2	12.3
Max. drag force (kN)	14.4	12.6	15.3	17.6	20.3
disp. of Geogid at the free end(mm)	32.13	33.68	22.20	19.17	24.93
Maximum disp. at the pull end (mm)	75.57	65.60	60.32	69.45	69.90
Max.interface static friction strength τ_{smax}(kPa)	17.94	36.73	53.43	57.79	54.73
Max.interface Friction strength τ_{max}(kPa)	65.02	76.44	68.45	78.59	92.23
τ_{smax} / τ_{max}(%)	27.6	48.1	78.1	73.5	59.34
Extensibility of geogrid(%)	0.3～0.9	0.3～0.6	0.5～0.6	0.3～1.0	0.9～2.0

The above suppose can be verified by the measurement of the label part of the geogrid's longitudinal ribs when the test finished. The extensibility of embedded geogrid PE50 is about 0.3%—1.0%, and that of the geogrid PE80 is slightly greater and can be reached to 0.9%—2.0%. The extensibility of both type of geogrid is far smaller than their ultimate elongation, and also, near the clamping apparatus, the geogrid extensibility is greater than that near the free end. It indicates that the distribution of the tensile force through the embedded depth is nonuniform; which decreases from the maximum value at the pull end to the free end. It can be explained by the nonuniform distribution of the interface frictional force.

Fig. 3 shows the variation of relative displacement with time at different embedded depth for the PE50 geogrid.

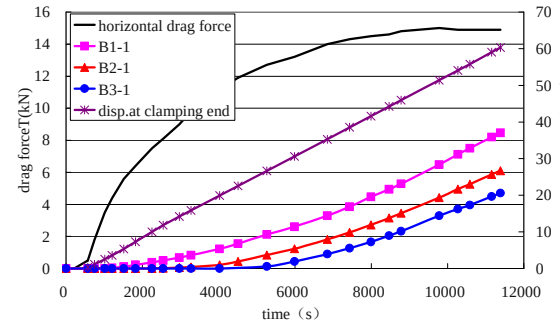

Fig.3 Time-history curve of the relative displacement between geogrid PE50 and soil at different embedded depth (σ_n=200kPa)

It can be obtained from Fig. 3 that the measuring point B1-1 nearest to the pulling end is firstly dragged to move and yielded relative displacement between geogrid PE50 and soil. Then the interface friction force transfers to the rear end gradually, and the measuring points B2-1 and B3-1 are observed to initiate moving subsequently until the whole body of the geogrid is dragged to move. When the pulling force approaches the peak value, the relative displacement progresses at uniform speed.

Distribution of Additional Shear Stress Induced by Interface Friction at Different Depth

As mentioned above, the "indirect reinforcement" can be explained by the Saint-Venant's Principle, It indicates that the additional stresses will come into being by a equilibrant system acted at any position of the object, but it only distributes in some area and reduce gradually to zero out of the area. "the stresses remote from the point of application of the load are not affected by the precise behavior of the structure close to the point of application of the load" (Saint-Venant 1855). Ding et al. (1999) analyzed and discussed the interaction mechanism between reinforcement and soil by numerical analysis. The concept of "the effective influence range of the reinforcement" is introduced to define the distribution behavior of additional shear stress induced by interface friction, which can be considered as the quantitative analysis of the "indirect reinforcement". So the reinforced space can be obtained. But the study in the paper was limited to theoretical analysis and lacked experimental validation. This test indicates the additional

shear deformation behavior by displacement variation of the ten laminated rings at different height.

Fig. 4 shows the distribution of lateral deformation of different laminated rings, some laws can be obtained as follows：(1) the shear deformation induced by friction is commonly small at millimeter level; (2) the maximum shear deformation generally occurred at the interface of the geogrid and soil, the farther the laminated ring from the interface, the smaller the shear deformation is; (3) when the overlying loading exceeds 200 kPa, the variation of the lateral deformation of the laminated ring at different height decreases.

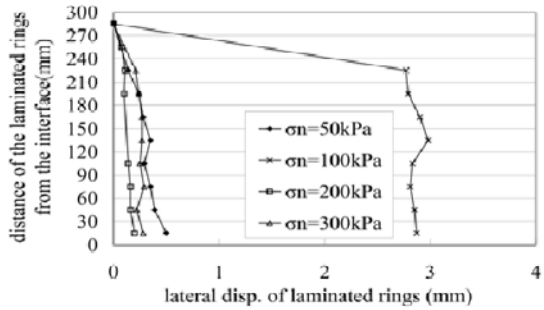

Fig.4 The distribution of lateral displacement of laminated ring corresponding to the maximum horizontal drag force

Fig. 5a shows the displacement of time-history curves for laminated rings with σ_n=50 kPa, 10# laminated ring locates at geogrid interface. Fig. 5b shows the time-history curves for 6#, 10# laminated rings and different measuring points of the geogrid including B1-1, B2-1 and B3-1. It can be seen that at the initial pulling stage of static resistance, 6# ring which is 120 mm away from the interface (not 10# ring nearest to the interface) yields the maximal displacement, while the test progresses to the sliding-friction stage, the displacement of 10# laminated ring increases to the maximum rapidly. But the maximum shear displacement under σ_n=200 kPa and σ_n=300 kPa occurred at 10# laminated ring all the time.

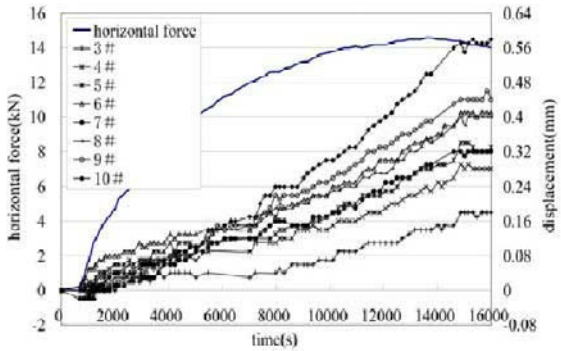

(a)

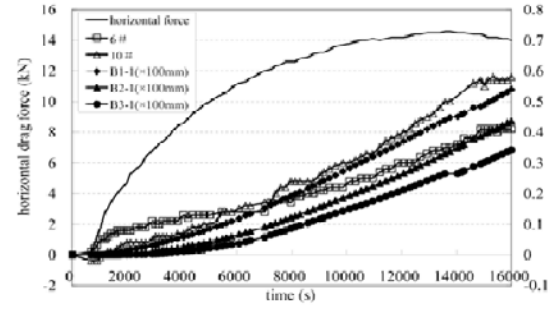

(b)

Fig.5 The time-history curves of laminated rings Displacement (σ_n=50 kPa)

The above experiment production validates the distribution of additional shear stress caused by the interface friction between the geogrid and soil. Nevertheless the value of “the effective influential range of reinforcement” can’t be determined quantitatively because of the limitation of the sample height and the up loading plate.

DISCUSSION AND CONCLUSION

In this paper, overlying loading and reinforced material have been taken into account among the influence factors for interface mechanical properties. Simple qualitative analysis on the interaction mechanism between geogrid and expansive rock in pull-out test is performed. More comprehensive experiment involves water content, dry density, pull-out velocity, dimension of geogrid will be bring forth in the other paper. Some conclusions can be received:

(1) The pulling process of the pull-out test can be divided into two stages: the static friction stage without relative displacement, and the sliding-friction stage with relative movement between geogrid and soil, the interface frictional distribution is nonuniform with time and space. The static friction under low pressure is much less than that under high pressure. The interlocking force between geogrid gridding and soil has significant influence on the behavior of interaction, especially under low stress.

(2) The displacement caused by tensile force consists of two parts: the tensile deformation of the geogrid (extensibility) and the relative displacement between the reinforcement and soil. The elongation of unidirectional geogrid is much less than the one under unrestricted tensile test.

(3) Interface friction will generate the additional shear stress, the concept of “the effective influence range of the reinforcement” shows the distributed area of the

additional shear stress, which reduces with the decrease of the vertical loading. If the vertical loading is greater than 100 kPa, the influential range may exceed 30cm.

REFERENCES

Bao CG (2004) Study on the interaction behavior of geosynthetic and soil in China, GeoAsia2004 proceeding of the 3rd Asian regional conference on geosynthetics, Seoul， Korea

Ding JH, Bao CG (1999) Analysis of mechanic mechanism for reinforced soil compound. The 8th proceedings of soil mechanic and geotechnical engineering. WangGuo Scholar Press 10: 441-444

Ma CM, Zhou YT, Miao HL (2004) Experimental Study on Interface Friction of Plastic Geogrid Reinforced Earth.China Railway Science 6: 36-39

Ma XL, Yang YH (2003) The Experimental Study on Soil Interaction Characteristics of Geogrid, Journal of Lanzhou Jiaotong University 8: 88-89

Nilay Tatlisoz, Tuncer B. Edil, Craig H. Benson etc (1998) Interaction between reinforcing geosynthetics and soil-tire chip mixtures, Journal of geotechnical 11: 1109-1119

Xu C, Zhao CF, Ye GB (2004) Research on interface between soil and geosynthetics. Journal of Tongji University 32 (3):307-311

Xu LR, Ling JM, Liu BC (2004) Experiment on Interface Friction Coefficient Parameters between Geogrids and Expansive Soil. Journal of Tongji University (Natural Science) 2: 172-176

Xu LR (2003) Study on the Interaction Parameters between Geogrid and Expansive Soil/Sand and Performance of Soft Ground Improvement with Reinforced-mat. Ph.D. thesis. Changshang Central South University

Zou JR, Liu TY, Leng WM (2005) The model test research on interaction of soil and geogrid. Journal of Railway Science and Engineering 3:51-55

HDPE LINED WATER RESERVOIRS FOR POWER GENERATING STATIONS

H.B. Ng[1]

ABSTRACT: An impervious High Density Polyethylene (HDPE) geomembranes have been successfully adopted as an alternative water barrier to conventional clay liners system of hydraulic reservoirs and ponds for few decades. With the ever-growing of population, the demand for more electric power capacity increases, hence bring to the need for more new high efficient generating stations and innovative methods of generating electricity from existing power plants. The HDPE geomembrane with outstanding mechanical properties and high durability provides a cost-effective solution as seepage control and leakage prevention to the reservoirs and dams. This paper highlights the manufacturing quality assurance and characteristic of the High Density Polyethylene (HDPE) geomembrane as waterproofing elements. Case studies on the application of HDPE geomembrane as an effective lining solution to the water reservoirs and dams for power generating stations are presented in this paper. Finally, discussion on the geomembrane installation and field quality assurance are also described in this paper.

KEYWORDS: HDPE, geomembrane, power stations, reservoirs, seepage

INTRODUCTION

Today, geosynthetic liners become an innovative and value-added solution to the protection of groundwater and surface water owing to their versatility, cost-effectiveness, ease of installation and outstanding mechanical and hydraulic properties, etc. Geomembranes materials are very low effective permeability ($<10^{-12}$ cm/s) flexible synthetic liners manufactured from base resins including high density polyethylene (HDPE), very flexible polyethylene (VFPE or LLDPE), chlorosulfonated polyethylene (CSPE, or Hypalon), plasticized polyvinyl chloride (PVC) and flexible polypropylene (fPP). Among the plastic materials utilized for geomembranes purpose, High density polyethylene (HDPE) geomembranes, with its superior hydraulic and mechanical properties in combination with its very low permeable characteristics, high longevity, outstanding chemical resistance and ultra violet light (UV) degradation resistance, are the most widely adopted geosynthetic lining materials for various containments and environmental engineering applications. Generally, HDPE geomembranes serve as impermeable barriers to prevent or limit the migration of liquids or water out of the containment.

This paper presents the successfully application of smooth high density polyethylene (HDPE) geomembrane as containment systems of water reservoir and storage pond in Thailand. The two case histories are currently among the largest water reservoirs and ponds used for power generation in the Thailand. The smooth HDPE geomembrane was introduced for these two project sites with the ultimate objectives: (a) to control and prevent seepage and leakage of water with the application of HDPE geomembrane liner due to its very low permeability, (b) to accommodate for potentially large settlement environment with the application of flexible membrane that exhibits outstanding mechanical properties, (c) an effective and economical solution to the water reservoirs and dams leakage and erosion problems due to its durability and outstanding ultraviolet light resistance, (d) an effective solution based on the proven track record in this type of application for more than two decades.

HDPE LINER FOR WATER CONTAINMENT

With the ever-growing of population, the demand for more electric power capacity increases especially due to the need for new generating stations and innovative methods of generating electricity from existing power plants. Until the mid of 1980s, the most commonly adopted liner was a conventional low impermeable clay soil layer of varying thickness and constructed by heavy mobile machineries and equipments. Geomembrane thus becomes an alternative lining system to clay liners, in which it is more economical, quicker and easier to install, and also out-performs clay liners that may desiccate and

[1] Technical Manager, GSE Lining Technology Co., Ltd., Bangkok, THAILAND. Email: hermannn@gseworld.com

crack over time due to the temperature effects. Geomembranes either alone or in conjunction with a concrete/brick cover can significantly increase the effectiveness of water containment or lining system. Not only erosion can be mitigated, but seepage and leakage problem shall be greatly reduced as compared to the conventional concrete lining system. It also provides a cost-effective and quality method of water-proofing the earthen water impoundments with aesthetic benefits. In addition, geotextiles are sometimes recommended to be laid underneath the geomembrane to serve as cushion and protection to the rocky or uneven and protruded subgrade, when necessary. Narejo et al. (1996) has proposed design methodology for the protection of geomembrane from puncture using nonwoven needlepunched geotextiles. Abramento M et al. (2006) reported on the necessarily of geotextile as mechanical protection of HDPE geomembranes in the Itiquira Dam Channel, which allowed for a rapid installation process with great effectiveness.

Todate, the most widely used lining systems are high density polyethylene (HDPE) geomembranes, which can be produced in various thicknesses and textured surfaces. The significant advantages of the 7 meters wide HDPE geomembrane includes its great flexibility, very low permeable, thermal stability, outstanding mechanical properties and UV light resistance, exceptional chemical resistance and durability, which makes it becomes an excellent liner candidate for hydraulic & water engineering applications. They have been successfully adopted in many water projects around the world, and working efficiently. N Ivy & C Mills (2002) reported that for over 20 years, HDPE geomembranes have been successfully applied to line ponds for power generating stations, inclusive of evaporation ponds or pumped storage ponds, etc. Hsuan and Koerner (1998) reported the predicted half-life of HDPE liners achieve 109 and 712 years at the respective 20^{o}C and 40^{o}C temperature. N. Ivy (2002) performed testing on 2.5 mm HDPE in both exposed and unexposed conditions after 20 years of service as containment for wastewater from a steam electric generating station. It is reported that no significant reduction in the primary physical properties was observed, that include tensile, tear, puncture, carbon black and density, except some reduction in OIT value caused by depletion of antioxidants.

In general, HDPE geomembrane can be designed for exposal or protected with a cover of soil or concrete. The outstanding UV-stabilized geomembranes can remain exposed for an extended period of time with no decline in their level of performance. However, as exposed geomembranes are relatively susceptible to damage from falling rocks, debris, machineries and vandalism, most reservoir liner systems are recommended to design with protection. The material can be easily unrolled and welded on site with hot wedge and extrusion techniques by skilled installation technician or qualified installers.

HDPE geomembranes as impermeable materials are widely used in a variety of applications in hydraulics engineering purposes, which include canal lining, tank linings, pond, lagoon, dams and water reservoirs, etc. It also provides a cost-effective and value engineering solutions for electrical power generation purposes, which includes disposal of spent fuel, storage of process water, cooling ponds, etc.

MANUFACTURING QUALITY ASSURANCE AND CHARACTERISTICS OF HDPE GEOMEMBRANE

High density polyethylene (HDPE) geomembrane is a flexible synthetic liner manufactured from poly-ethylene resin with a small amount of carbon black, UV stabilizers and antioxidants. There are two main manufacturing processes to produce HDPE geo-membranes, namely Round Die Co-extrusion (or blown film method) and Flat Cast Extrusion Processes. Both processes are capable to produce smooth and textured geomembranes. A high friction surface can be formed by creating a roughened surface on smooth HDPE sheet through the “texturing” process. This textured liner can be used to improve the stability of liner system and eventually maximize the available volume of the lined containment.

As a qualified manufacturer, a thorough quality assurance program for the geomembrane products is needed to be set up before the manufacturing process to ensure consistent production of quality materials that meeting both manufacturers’ requirements and the project specifications. The manufacturing quality assurance (QA) program generally consists of three stages, which starts with proper selection of highest quality raw materials, includes polyethylene base resins and masterbatch. All the raw materials have to meet the geomembrane manufacturer’s specifications and pass the acceptance of conformance tests prior to their utilization. A strict and thorough quality assurance program for the geomembrane products is also implemented during the manufacturing and before shipments of the finished products. The online manufacturing quality control carried out with state-of-the-art manufacturing process that provides feedback on the physical quality of the materials being produced. Besides that, an electrical spark detector is online to provide immediate notification of pinholes in the finished product. Rolls containing a pinhole are rejected from the standard

quality product.

Prior to the delivery, a series of QA laboratory tests shall be conducted to form the final examination on the finished products. The finished products are sampled for quality assurance tests in the laboratory as per the test frequency stipulated in the project specification, and compliance with the manufacturer's established minimum test frequency requirements. All the geo-membranes must pass through numerous industries standard or equivalent recognized tests and meeting manufacturer's minimum and project specifications.

In general, HDPE geomembranes manufactured from the round die coextrusion and flat cast extrusion processes show approximately the same in physical and mechanical properties.

SUCCESSFUL CASE HISTORIES

Two successful case histories on the application of HDPE geomembranes as primary barrier for water reservoir and storage pond of power plants in Thailand are presented in this section. Fig. 1 indicates the locations of the two project sites.

Fig. 1 The locations of project sites

Case History 1

The project site is located at Khorat province, which is about 250 km at the north east of Bangkok metropolitan, capital of Thailand. The project is a pumped storage hydropower plant used for power generation to supply electrical power to Khorat and the vicinity. The Lam Ta Khong hydropower plant is located at hilly terrain, mainly underlain by stiff to hard Silty Clay with interlayer of Sand and bedrock.

The project involved using of hydraulic power to generate the electricity current for the surrounding areas. Generally, the power generating station operates at or near ultimate capacity during the day time when the demand is the greatest, but the same plants have excess generating capacity at night. To build a new power plant is costly and takes years from design to completion of construction. As an alternative and value added to the construction of new power plants, the energy company has decided to look into innovative methods to better utilizing the full capacity of existing plant. Hence, pumped storage pond is designed to store excess nighttime capacity so that is may be used during the day time when the demand is greater. In fact, the pumped storage pond idea has been in use for over 30 years, but mainly relied on an available water source such as a dammed river or natural reservoirs.

The Lam Ta Khong Pumped Storage Project involves construction of the first pumped storage power plant in Thailand and aims at taking an advantage of surplus electricity from base load power plant during the low demand period to pump up water from the existing reservoir named Lam Ta Khong reservoir at lower elevation to be stored in the upper pond constructed on top of the plateau, which is about 370 m in relative vertical distance from each others, and the accumulated water shall be released thereafter to generate electricity during power peak demand hours. The completed pump storage type power station is capable to generate power capacity up to 1,000 megawatts (MW).

By utilizing geosynthetics in construction artificial reservoirs, they can be constructed in areas that lessen the impact on naturally occurring plants and animal life. To accomplish the task, a large reservoir is constructed at the upstream of higher elevation. The water is transferred using pumps from the lower reservoir at down stream and stored in the reservoir with impervious HDPE geomembrane system at the upstream, particularly during night time and/or when the electricity in used is of low capacity. The electricity generation shall only be conducted when the demand of power is increased, particularly during day time. There are water inlet and outlet at the bottom of the reservoir being used for the water pumping. The lined reservoir is located on a higher elevation underlain by stiffer soil and bedrock.

The total volume of the lined water reservoir is approximately 1.2 millions cubic meters with average storage depth of about 35 m. The configuration of the liner system from top to the bottom consists of 2.0 mm thick smooth HDPE geomembrane with geotextile as separator on the bituminous layer and concrete base. Table 1 tabulates the properties of HDPE geomembrane

used as liner to control the leakage problem.

Table 1 Material properties for 2.0 mm HDPE liner

Property	Test Method	Test Value
Thickness, mm	ASTM D5199	2.0
Density, g/cc	ASTM D1505	0.94
Tensile Properties	ASTM D6693,	
Strength at Break, N/mm-width	Type IV, Dumbbell, 2ipm	57
Strength at Yield, N/mm-width		30
Elongation at Break, %	G.L. 51mm	700
Elongation at Yield, %	G.L. 33mm	13
Tear Resistance, N	ASTM D1004	249
Puncture Resistance, N	ASTM D4833	703
Carbon Black content, %	ASTM D1603	2.0 ~ 3.0
Notched Constant Tensile Load, hrs	ASTM D5397	> 400 hrs.

The water reservoir was originally lined by using bitumen or asphalt coating laid on top of the concrete foundation. With the settlement of subgrade and foundation, the concrete base with bitumen coating cracked caused the leakage of the reservoir. Numerous remedial and repairing works were conducted before HDPE geomembrane was introduced to this project. There are about 400,000 m^2 of HDPE geomembranes utilized for the lining system of the pumped storage pond. With the using of HDPE geomembrane, the leakage problem is eventually resolved. Fig. 2 shows the geomembrane liner is under construction.

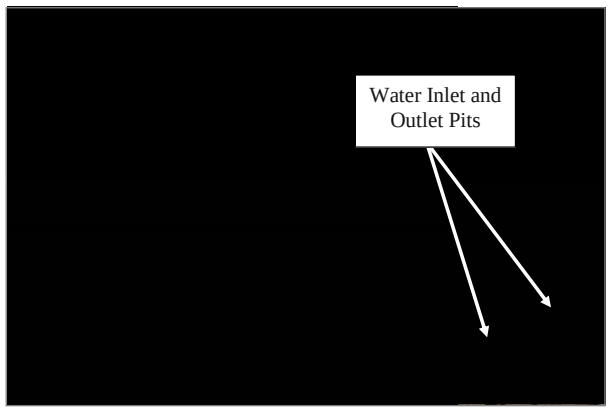

Fig. 2 The HDPE Lined Reservoir under construction

During the installation, a layer of nonwoven geotextile was laid as a separator on the existing bituminous layer to provide a better working platform for the lining works, particularly when under the hot sun during day time, the bitumen will be softened and melted, which cause to poor working platform condition and difficult for the machineries and workers to move around.

Case History 2

The Ratchaburi power plant project is located approximately 125 km at the west of Bangkok metropolitan, capital of Thailand. Ratchaburi power plant was built to run primarily on natural gas from offshore Myanmar (earlier known as Burma). The construction of this power plant is one of Asean's largest power stations with a planned generating capacity of 3,200 megawatts (MW).

The project involved construction of a waste (ash) pond with storage volume of about 700,000 cubic meter and a water reservoir or storage pond for turbine cooling purpose with capacity of about 1.02 millions cubic meters. The waste storage pond to store solid ash / waste, mainly gypsum, is measured about 15m deep and the water reservoir is about 30m in depth. In total, there are more than 500,000 m^2 of HDPE geomembranes deployed in these two storage ponds.

The Ratchaburi power plant is located on a relatively flat land and consists of soft alluvium soil mainly of Silty Clay and Clayey soils. The water containment structure from top to the bottom is mainly of 2.0 mm smooth high density polyethylene (HDPE) geomembrane as lining materials, geotextile as protection layer and 300mm of sand as drainage layer and working platform above the well compacted subgrade soil. The 2.0 mm thick smooth HDPE geomembrane was designed as primary liner for these containments. Fig. 3 shows the completed deployment of the waste storage pond and water reservoir.

Fig. 3 Overview of the Installed HDPE Lined Ponds

FIELD QUALITY ASSURANCE AND QUALITY CONTROL SYSTEM

The application of high quality geomembrane in associated with proper geomembrane installation and appropriate construction quality assurance (CQA) are crucial to the long-term performance of lining system. A CQA plan was normally developed before construction and implemented during construction to guide observation, inspection, testing as well as documentation of all field records.

Prior to the geomembrane deployment, the subgrade should be properly prepared by removing any sharp edges objects, debris and organics matters, and then well compacted to the desired density and strength. It is necessary to be extra careful during the installation process in order to prevent equipment or personnel from damaging the liner. In addition, the seaming of HDPE geomembrane always requires well-trained personnel and special equipments. It is also necessary to ensure the materials to be welded shall be wiped clean of moisture, dust and debris prior to the field welding. During the deployment of the initial geomembrane rolls, trial welds were conducted on the same type of materials used on this project. This is mainly to verify that seaming conditions are similar to operation condition and to ensure that the equipment functions properly. The trial welds are then subjected to destructive tests to qualify the welding and the equipment used before commencement on the field seaming works. Fig. 4 and 5 show the deployment and welding of geomembrane in progress.

Fig. 4 Deployment of geomembrane in progress

Thermal fusion wedge welding is commonly used as primary method for the field seaming of HDPE geomembrane. The extrusion welding technique is adopted only for non-linear seams, patches, pipe penetrations or areas that wedge welder is impractical. After the seaming works, a series of field installation quality assurance tests include non-destructive and destructive weld testing, were carried out in order to ensure the welding quality at site fully compliance with the design requirements as well as the equivalent recognized testing standards. The most common methods of non-destructive seam testing adopted in the Thailand industry are air-pressure testing and vacuum-box testing.

Fig. 5 Welding of geomembrane at project site

The thermal wedge welder creates a double-track weld, leaving an air channel in between these two weld tracks, which can then be used to non-destructively air pressure test the integrity of the seam. When the seam is completed, both ends of the air channel are sealed off and the seam is pressure-tested to determine its continuity. The non-compliance seams shall then be patched with extrusion welding techniques before retesting. The non-destructive vacuum-box testing is used to check the continuity of wedge weld seam, extrusion weld seams, repairs and patches that is not practical to conduct air pressure test.

Destructive seam testing is used to evaluate bonded seam strength, which involves cutting out a section of the seam and tested until failure is attained. Test strips are cut from the section and tested on site. The destructive samples are tested for shear-strength and peel-strength values, carried out in accordance to ASTM D 6392. The sampling frequency is, on average, one test location per 500 linear feet of seam for the entire project. The testing frequency may also be adjusted as per the engineer's instruction. In general, shear testing involves application of a tensile stress from the edge of one sheet, through the weld to the edge of the adjoining sheet. For the peel test, the overlapping portions of the sheet are pulled in opposite directions to observe weld separation

behavior. Fig. 6 shows the specimens for destructive tests of seam shear strength and peel strength tests.

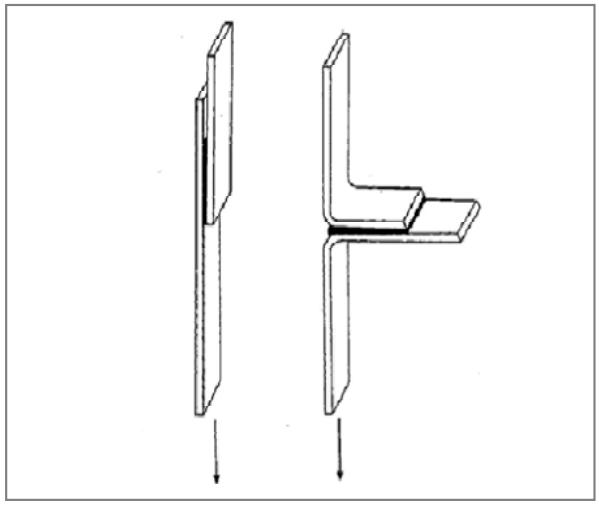

Fig. 6 Field destructive seam test specimens for : (i) Shear strength , (ii) T-peel strength tests

SUCCESSFUL CASE HISTORIES

An impervious HDPE geomembrane, which has been widely used as a barrier in various lining applications, particularly in geoenvironmental engineering works such as landfill, waste water treatment pond; industrial works such as tank for chemical and toxic water and also in the mining industry, now becomes a cost-effective and innovative lining solution for water reservoirs and storage ponds in power industry. HDPE geomembranes have a proven track record in these types of applications for more than two decades.

This paper presented the successfully application of HDPE geomembranes in hydraulic engineering works such as water reservoirs and waste pond for the power generation purpose in Thailand. The two case histories are currently among the largest water reservoirs and ponds used for power generation in Thailand. HDPE geomembrane generally serves as impermeable barriers to stop or limit the migration of liquids or water out of the containment. Owing to its specialty, 2.0 mm thick HDPE geomembrane was selected and had been successfully deployed and with acceptable leak-proofing performance in two large scale water reservoirs and storage ponds for power generation in Thailand.

A series of materials conformance tests conducted during the manufacturing process is always necessary in order to control and maintain the consistent quality of geosynthetic products supplied to the industry. HDPE geomembrane demonstrates not only on its durability and low permeability characteristics, it also provides outstanding mechanical properties and UV light resistance, which makes it becomes an effective lining material for hydraulic and water engineering applications. At last, the quality assurance and quality control program implemented during the field construction works was also discussed.

REFERENCES

Abramento M, Wickert F (2006) Use of Geotextile as Mechanical Protection of Geomembrane in Itiquira Dam Channel, Brazil. Proceedings of the 8th International Conference on Geosynthetics, Yokohama, Japan, September 2006: 623-626

Deopura BL, Chahar BR (2006) Geomembranes for Water Management. Proceedings of the International Seminar Geosynthetics in India – Present and Future (in Commemoration of Two Decades of Geo-synthetics in India), New Delhi , India, 8-10 November 2006: 92-102

Hsuan YG, Koerner RM (1998) Antioxidant Depletion Lifetime in High Density Polyethylene Geomembranes. Journal of Geotechnical and Geoenvironmental Engineering, ASCE 124(6): 532-541

Ivy N, Mills C (2002) Geosynthetics in Power Applications. GFR October/November 2002, 20(8)

Joaquim MG, Duarte (2004) Canals for Hydroelectric Power in Brazil, GFR April 2004, 22(3)

Koerner RM (1997) Designing with Geosynthetics (4th edition). Prentice Hall, Upper Saddle River, New Jersey 07458

Li Y, Zhou J, He S, Hou J (2006) Study on an Application of Geotech-Membrane in the leakage Prevention Works of Reservoirs of the Pumped Storage Power Station. Water Power, March 2006: 32(3) (In Chinese)

Narejo D, Koerner RM, Wilson-Fahmy RF (1996) Puncture Protection of Geomembranes, Part II: Experimental. Geosynthetics International 3(5): 629-653

Wilson-Fahmy RF, Narejo D, Koerner RM (1996) Puncture Protection of Geomembranes, Part I: Theory. Geosynthetics International 3 (5): 605-628

You G (2002) Polyethylene Geomembrane Liners in Containment Applications. Symposium on Ground Improvement and Geosynthetics, Bangkok, Thailand, 12-13 December 2002: 98-113

GEOGRID REINFORCEMENT ON HIGH EMBANKMENT/SLOPE APPLICATION IN JINPING POWER STATION PROJECT

Z.J. Dai [1], N.E. Wrigley [2], H. Zheng [3], M.F. Chen [4], Z.L. Feng [5] and S.H. Wang [6]

ABSTRACT: In order to build and then operate a new major dam and power station at Jinping, Sichuan Province, China, it was necessary to first construct an access road though mountainous terrain along the Yalong River. At one point this needed a 52.5 m high, soil-filled structure to support the road. Because of the proximity of the river a conventional slope could not be constructed. Various alternatives were considered, particularly stone and concrete retained structures. However, foundation properties were poor, cost was prohibitive and there were worries about the durability of such rigid structures in a region subject to seismic activity. The solution chosen after much deliberation was a geogrid-reinforced structure with a wrap-around face. When finished this would be the highest geosynthetic-reinforced structure in China. This paper describes the design and construction challenges faced and the solutions adopted for the successful completion of this project. Since successful completion of this structure the construction of a second steep slope, this time with a height of 66 m has been undertaken.

KEYWORDS: geogrids, reinforced soil

INTRODUCTION

High soil-filled structures are regularly needed when a road is constructed through mountainous terrain. Because of various site constraints such high soil-filled slopes cannot normally be built as conventional slopes. Either steep, reinforced slopes or retaining structures are required（Jewell 1991; Victor 2001; Zornberg 2004).

This was particularly true for one part of the Mianshagou section of the primary access road to the site of the Jinping Power Station in Sichuan Province of China. Here, the road would cross a steep gully, prone to rockfall, too close to the Yalong River to build an unreinforced slope. Also, if a suitable structure could be built this was one of the few places where a wide platform for a concrete plant could be constructed between the road alignment and the natural slopes. The site at the start of construction is shown in Fig. 1.

The question therefore, was: what type of reinforced or retained structure could be built economically?

GENERAL

Fig. 1 Start of Construction

Jinping Power Station, with a planned capacity of 8,000 MW, is a National Class 1 Hydraulic Power Station. It is located towards the head of the Yalong River which is a key site for development of hydraulic

[1] Engineer, BOSTD Geosynthetics Qingdao Ltd, CHINA. Email: techservice@bostd.com
[2] Director, NewGrids Limited, ENGLAND. Email: info@newgrids.com
[3] Engineer, BOSTD Geosynthetics Qingdao Ltd, CHINA. Email: techcentre@bostd.com
[4]Senior Engineer, Yellow River Engineering Consulting Co., Ltd. CHINA.. Email: lqs-mail@126.com
[5] Senior Engineer, Yellow River Engineering Consulting Co., Ltd. CHINA
[6] Senior Engineer, China Railway No.19 Bureau Group Corporation. CHINA

and electric resource. It is a national key project within the national strategies of western development, power transmission from west China to east China, and development of the national Hydropower Industry.

The whole area of the project of the Jinping power station has a complex geological condition and poor foundation. Because of the steep terrain the area for construction use is very limited and it is rightly said locally that “an inch of land is worth an inch of gold”. The local rock in Mianshagou is friable sedimentary material and it is subject to some seismic activity.

The sub-project that is the subject of this paper required a steep slope or stepped retaining wall of some 52 m in height. As well as providing a good alignment for the required 10.5 m road and the working platform needed for concrete preparation, this sub-project would also enable the re-use of a large amount of rockfill that would arise during construction of the road.

FACTORS TO BE CONSIDERED IN DESIGN

Space Available

It was calculated that a horizontal distance of 120.5 m in front of the road would be required for a conventional un-reinforced slope. As only about 1/3rd of this was available it was clear that a steep, reinforced slope or stepped retaining walls were needed.

Time Available

This road would be the primary access route for the whole of the construction and operation the Jinping Power Station. It therefore had to be completed before the main project could go ahead. As a result, its rapid construction was critical to the achievement of the overall main project timetable.

One factor the designers and construction team also had to bear in mind is the climate at this territory. Yalong River is at eastern edge of the Qingzang altiplano and it is dominated by westerly winds and a southwest monsoon. November to the next April is the dry season, with much sunlight, low humidity, a wide difference in temperature daily and just 5%—10% of the annual rainfall. Then May to October is the wet season, with less sunlight, high humidity, less difference in temperature daily and concentrated rainfall of 90%—95% of the annual total. It was therefore necessary for the foundation project for Mianshagou to be finished before the rainy season; otherwise the wet conditions would seriously hamper construction activities.

Foundation Bearing Capacity Available

Site investigation revealed that the upper 13m or so of the foundation was relatively recent gravel deposits. Underneath were layers of stiff clay and decomposed sandstone with some limitations on bearing capacity. Because of the height of the structure required, a design that gave no high localized foundation loads would be beneficial.

Seismic Conditions

With reference to “Seismic peak ground acceleration zonation map of China” and “Characteristic period of the seismic response spectrum zonation map of China” (scale 1：4,000,000) issued in 2001, the seismic horizontal peak acceleration for this construction area is 0.10 g. Therefore a good resistance to seismic loads was a requirement for the structures of this project.

ALTERNATIVE DESIGNS CONSIDERED

At the initial design stage for reinforcement of the Mianshagou slope, there were 3 designs considered, a mass stone built wall, a reinforced concrete wall, and geogrids-reinforced construction. Studies of the economical and technical aspects of these options revealed that there would be differences, as follows:

Structure Calculation

For stone built walls or reinforced concrete walls, both would need massive sections and extended work. Furthermore both would give high foundation loads. The geology survey of the site showed that the soft layer is too thick and the bearing capacity was insufficient for such designs. Piling these critical foundations would have been totally uneconomic. In contrast, design with a geogrid-reinforced steep slope would mean that there was no need for any large, rigid sections. Therefore peak bearing capacity requirements were greatly reduced. Calculations showed that sufficient bearing capacity was available with no special treatment.

Seismic Resistance

Stone built walls and reinforced concrete walls are rigid structures with poor resistance to seismic loads and they cannot accept associated foundation deformation. For geogrid-reinforced structures, the reinforced body is flexible and can adapt to foundation deformation. Also, because of the nature of their response to loading in

different speeds, geogrids, particularly those made from High Density Polyethylene (HDPE), have high strength properties in seismic loading conditions.

Drainage

The structure to be built would be at the bottom of a large gulley, with water infiltration both from rain and from within the mountain body. It would be necessary to drain this water effectively otherwise it would cause high internal water pressures and affect the stability of the structure.

As stone built walls and reinforced concrete walls have impervious faces high quality drainage systems must be built-in to the structure. Even these can be prone to blockage that is damaging to the structure.

With a geogrid-reinforced solution, using crushed rock fill, the whole structure is permeable and water in the structure body will drain through and out readily. Therefore there is no drainage problem and the slope is stable even where occasionally flooded.

Construction

Stone built walls and reinforced concrete walls both require lengthy construction programmes and the use of heavy equipment. Both involve time spent waiting for the concrete to cure to an adequate strenght at various stages before the next increase in height can be constucted.

For geogrid-reinforced structures, only a very simple construction procedure is required, with light materials and equipment and , importantly, a short contruction period. See Fig. 2.

Fig. 2 Construction of geogrid-reinforced slope

Cost Comparisons

The geogrid-reinforced solution adopted had a cost of RMB ￥4,167,201.00 (around USD556,000.00). Even without the cost of piling, it was estimated that the stone wall would have cost 13.5% more and the reinforced concrete solution 21% more than the geogrid solution.

Environmental Impact

The proposed green-faced steep slope would blend well into the natural environment of the river gorge of natural, steep, vegetated slopes. Also, the materials of construction: chemically inert geosynthetics and local crushed rock fill, could have no adverse impact on the river or locality.

Summary

Overall, it was clear that the geogrid-reinforced solution would offer a wide range of advantages over mass stone or reinforced concrete retaining walls. For all aspects of design, cost and performance it would give improvements over the other two solutions considered.

DESIGN AND LAYOUT OF GEOGRID-REINFORCED SLOPE

The project was designed by Yellow River Engineering Consulting Co., Ltd. In accordance with established Chinese practice. But because this structure was beyond established experience, E'Grid Plus software provided by BOSTD Geosynthetics Qingdao Co., Ltd was used for design and stability calculations for the structure. This software is based on the world-leading slope-stability software ReSSA from Adama Engineering of the USA.

The design solution chosen for the structure was a steep slope split into 4 tiers, 3 of 15m height and the top one of 7m height. The lower two tiers have face gradients 1:0.58 and the upper two have face gradients of 1:0.8. At the top of each tier there is a step back of 2 m. This form was chosen for structural and aesthetic reasons and also to facilitate future maintenance of the face by providing the steps for maintenance access and safety. Uniaxial HDPE geogrids were selected as the primary reinforcement of the structure. Different strengths and vertical spacings were used at different levels to meet the design requirements.

The overall design of the structure is illustrated in Fig. 3. The embedment length of the primary layers of geogrid needed for stability was 24 m. A stable face was ensured by the use of a “wrap-around” construction technique that is also illustrated in Fig. 3. With this technique the formwork for the face is layers of compacted sandbags, filled with local soil and appropriate seeds to form a green face to the finished structure. Each length of

primary reinforcement geogrid is wrapped up and around the outside of these sandbags to the level of the next layer of primary reinforcement. At that level it is turned back into the structure, joined to the next layer of primary reinforcement with a “bodkin joint” and tensioned. At each tier step the last length of primary reinforcement has a 3 m length buried in the fill of the step for anchorage.

Between layers of primary reinforcement there are layers of secondary reinforcement with 2 m embedment lengths at 330 mm vertical spacing. These ensure the local stability of the face, particularly in earthquake conditions. They also assist in achieving good compaction of the fill close to the face. Biaxial PP geogrids of 30 kN/m index strength were used for this duty.

One major reason for the choice of this form of structure was its suitability for use in seismically active areas. Because the different layers of reinforcement enclose the face and are joined to each other the whole structure is integrated together into a flexible whole.

The finished structure is shown in Fig. 4, where it can be seen that just months after construction vegetation was already becoming established on the face.

Fig. 4 Finished structure

DISCUSSION

When designing and building roads in mountainous terrain, embankments with natural side slope angles cannot often be used because of space constraints. Therefore bridges and retained-soil structures are widely

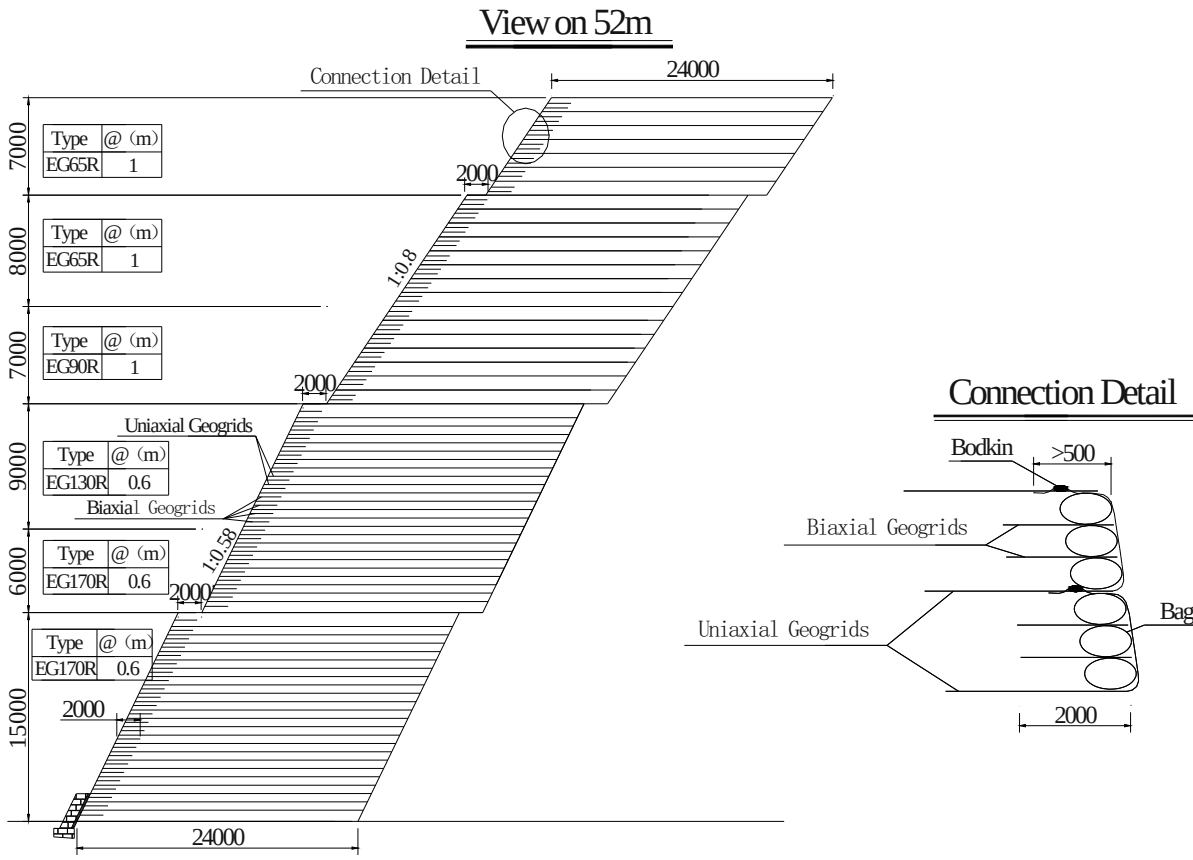

Fig. 3 Cross-section of geogrid reinforced structure

used to achieve acceptable road levels and alignments. In the project described in this paper the chosen solution was a geogrid-reinforced steep slope with a green face. Design studies had suggested that this would be the optimum solution for this project for all cost, engineering and environmental reasons.

As this would be the highest geosynthetic-reinforced structure in China at that time exhaustive studies were completed to ensure that it could be constructed safely and meet all the project requirements. These included design studies using world-leading software and investigation of the properties of available reinforcements. For the design to be valid it was important to ensure that all the design properties and factors, particularly the long-term strength of the reinforcement under creep loads and all other factors of its performance, were well understood.

The success of these studies is demonstrated by the fact that this structure has now stood for 2 years with no significant settlement. Road alignment and levels have been maintained throughout. As a result of the success of this structure two more such structures, but even higher than the one described here, have been included in the Jinping Project. At the time of writing this paper the second structure, which will have a height of 66m, is under construction and the third, which will have a height of 72 m, is under design. These structures will form the subject of future publications.

CONCLUSIONS

Compared with traditional gravity stone walls and concrete walls, geogrid-reinforced structures can have the following advantages and features:

(1) Geogrid-reinforced structures are flexible. If built with a flexible face they can safely adapt to a degree of foundation deformation. This flexible form of reinforcement also has a better anti-seismic capacity than rigid materials.

(2) Geogrid-reinforced structures can give substantial cost savings. The steep slopes that can be built minimize land-take and fill material requirements. Expensive treatment of foundations can often be avoided.

(3) A wrap-around structure with geogrids gives green faces easily, with significant benefits to the environment and society.

(4) The ease and speed of construction of geogrid-reinforced structures can significantly reduce project time-tables.

REFERENCES

Jewell RA (1991) Application of revised design charts for steep reinforced slopes, Geotextiles and Geomembrances 10(3): 203-234

Victor E, Barry R, Christopher RR, Berg (2001) Design of Reinforced Soil Slopes, Mechanically Stabilized Earth Walls and Reinforced Soil Slopes Design & Construction Guidelines, Ryan R. Berg & Associates, Inc., 2190 Leyland Alcove Woodbury, MN 55125 :223-274

Zornberg JG (2004) Advances in Geosynthetic Reinforced Soil Design, IGS News 20(3) :16-17

Proceedings of the 4th Asian Regional Conference on Geosynthetics
June 17 - 20, 2008 Shanghai, China

IMPROVEMENT OF ARCH ACTION AT CLAY CORE-WALL OF HIGH ROCKFILL DAM BY UNITED SEEPAGE CONCROL WITH GEOMEMBRANE

Y.L. Xing [1], Y.M. Shu [2], J.F. Hua [3], Y.H. Li[4] and W.Y. Zhou[5]

ABSTRACT: In this paper, the stress, strain, and seepage of a high rock-fill dam with clay core on the sand-gravel foundation is numerically simulated with FLAC^{3D} software. United seepage control with Geomembrane and disfigurement clay core in high rock-fill dam is a new design idea. The study result shows that the united seepage control measure not only can greatly lower the phreatic water surface in clay core but also can weaken the arch-action effectively which may result in horizontal cracks in clay core. In addition, the adoption of this kind of united seepage control measure can avoid the phenomenon that the maximum principal stress is less than pore pressure at the same elevation and improve the safety of clay core in mechanical and hydraulic ways.

KEYWORDS: high rock-fill dam, united seepage control, arch-effect improvement, numerical simulation

INTRODUCTION

In high rock-fill dam wall arch effect is due to the differences of the settlement amount and the settlement time of the different materials of both sides. For example, in the middle elevation of a dam with sand shell and clay core, the soil pressure measured at the two edges of the core is only the 30%—50% of the geostatic pressure. But the soil pressure measured in the dam shell is 1.9 times of the geostatic pressure (Wu et al. 1995). That shows the arch effect phenomena of the core-wall. The arch effect is dependent on the following factors: the differences of deformation modulus between the core-wall and the shell, the slope of core-wall, the height of the dam, the strength of the filling materials and the construction speed. Arch effect will lead to the decrease of the vertical stress in the core-wall, which may result in the occurring of the cracks. When the vertical stress in the core-wall is only 20%—50% of that in the adjacent shell, the horizontal cracks may occur(Gong et al. 2004). For the sake of eliminating the adverse impact of the cracks on the stability of the dam, the arch effect must be effectively weakened. In order to investigate the influence of united impermeable system on the arch effect in the core-wall of high rock-fill dam, Pubugou rock-fill dam in Sichuan province is taken as an as an example, of which a three-dimensional model is built to numerically simulate the stress, strain and seepage state with FLAC^{3D} software.

THE DESIGN BASIS OF UNITED IMPERMEABLE SYSTEM

To a rock-fill dam with high water level, the impermeable effect of a single impermeable system with clay core-wall or with geomembrane is not perfect. However, the united seepage control measure with geomembrane and clay core-wall system can effectively improved the seepage control efficiency and reduce the risk of local failure (Lin et al. 2004; SHU et al. 2006). That is because the impermeable geomembrane in the system can curtain off the core-wall and filter layer. In addition, the friction angle between geomembrane and soil or between geomembrane and filter layer is smaller than the friction angle between soil core and filter layer, which alleviate the arch effect of the core-wall. The united seepage control measure with geomembrane and clay core-wall system can not only enhance the impermeable effect, but also alleviate the arch effect.

IMPACT OF IMPERMEABLE SYSTEM ON ARCH EFFECT

The paper take Pubugou rock-fill dam which is

[1] Master, The water conservancy and hydropower, Hohai University, Nanjing, CHINA. Email:xingyuling623@163.com
[2] Professor, the water conservancy and hydropower, Hohai University, Nanjing, CHINA. Email:yimingshu2004@yahoo.com.cn
[3] Master, Yancheng Hydraulic Investigation and Design Institute, Yancheng, CHNIA. Email:jfhua_427@126.com
[4] Chengdu hydroelectric Investigation and Design Institute of SPC, Chengdu, CHINA. Email:xiali8765818@126.com
[5] Professor, Tsinghua University, Beijing, CHINA. Email:benben8765818@sina.com

assumed to adopt the united impermeable system as an example to perform a three-dimensional numerical simulation of the stress, strain and seepage state of the dam with FLAC^{3D} software. Then the analysis of the impact of the united impermeable system on the arch effect was conducted according to the simulated results.

Structure of Project and Mesh Generation

Pubugou rock-fill dam with a clay core-wall is built on a 75.4 m-deep covered layer of sandy gravel. The height of the dam and the depth of foundation is 184 m, 72 m respectively.

The three-dimensional model of the high rock-fill dam is established. The computational mesh of foundation and dam are shown in Fig. 1. Geomembrane is simulated with membrane element which can only bear tension stress. The different materials are connected by interface elements. Considering the geomembrane damage during construction, pores with the size of 10 mm×10 mm are set in an area of 4000m^2 (Gong B.N et al. 2004), as shown in Fig. 2.

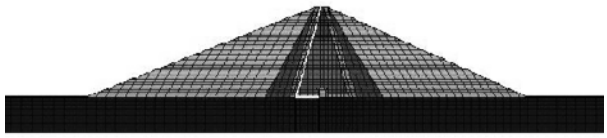

Fig. 1 Computation mesh of dam in largest section (with Geo.)

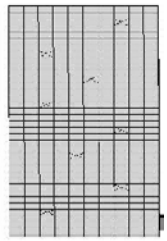

Fig. 2 Computation mesh of geomembrance and layout of holes

Constitutive Model of Structure and Parameters

Duncan-Chang hyperbolic constitutive model is adopted, and the model parameters are shown in Tables 1 and 2. Considering that the coefficient of permeability got from the permeability test is less than the actual value, The coefficient of permeability got from the test in the literature (Lin et al. 2004) was properly magnified as the calculation parameters.

Table 1 Stress-strain and seepage parameters for rock-fill dam with clay core-wall

materials	Density ρ/(kg·m^{-3})	Friction angle ϕ/(°)	Cohension C/kPa	damage than Rf	double logarithmic K
Foundation layer	147	38	0	0.64	780
Dam layer	230	43	0	0.68	1000
Transition layer	220	42	0	0.68	800
filter layer	220	40	0	0.65	700
Super core	200	22	1	0.74	390
Lower core	230	35	0.6	0.69	488
High plastic clay	200	16	5	0.86	125
Concrete cut-off wall	240	48	500	0	2.30e6
geo	/	40	0	/	/

Table 2 Stress-strain and seepage parameters for rock-fill dam with clay core-wall (continuation)

materials	double logarithmic n	Semi-logarithmic G	Semi - logarithmic F	Line D	Permeability coefficient k/(cm·s^{-1})
Foundation layer	0.42	0.32	0.08	7	2.5×10^{-2}
Dam layer	0.52	0.32	0.06	5	3×10^{-2}
Transition layer	0.52	0.33	0.08	7	2×10^{-2}
filter layer	0.54	0.35	0.08	7	1×10^{-2}
Super core	0.64	0.41	0.23	3.3	5×10^{-5}
Lower core	0.8	0.3	0.07	4.7	4×10^{-5}
High plastic clay	0.7	0.38	0.04	1.1	4×10^{-5}
Concrete cut-off wall	0	0.17	0	0	1×10^{-6}
geo	/	/	/	/	1×10^{-10}

Note: ($\lg(E_i/p_a)$, $\lg(\sigma_3/p_a)$) is double logarithmic coordinates; (v_i, $\lg(\sigma_3/p_a)$) is semi-logarithmic coordinates; ($-\varepsilon_r/\varepsilon_a$, $-\varepsilon$) is linear coordinates. In which: E_i is initial tangent modulus; p_a is atmospheric pressure; σ_3 is minimum principal stress; v_i is initial tangent Poission ratio; ε_a , ε_r is axial strain and lateral expansion strain in conventional triaxial test.

Simulation Results

In this paper, the post-construction condition and stable seepage condition are simulated respectively. The results of the stress-strain and seepage of the dam

adopting united seepage control measure with geo-membrane and clay core-wall in both two condition are attained, as shown in Figs. 3—5.

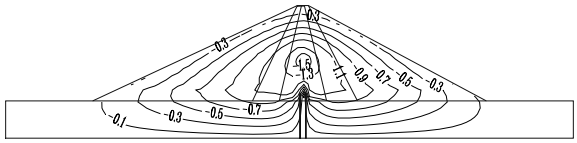

（a）without Geo.

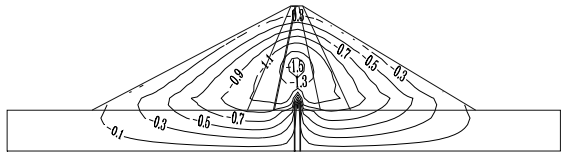

（b）with Geo.

Fig. 3 Settlement contour in post-construction condition without and with Geo.

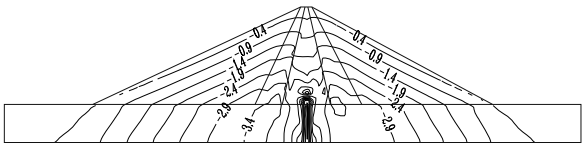

（a）without Geo.

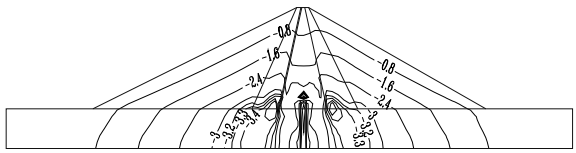

（b）with Geo.

Fig. 4 Contour of maximum principal stress in post-construction condition without and with Geo.

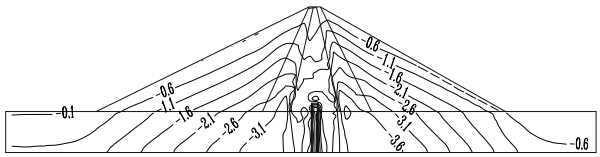

（a）without Geo.

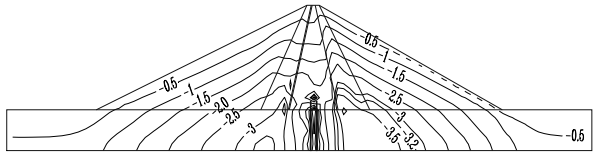

（b）with Geo.

Fig. 5 Contour of maximum principal stress in stable seepage condition without and with Geo.

ANALYSIS

(1) In the post-construction condition the largest settlement occurs at 75m height of clay core-wall (2/5 of height of the dam). The largest settlement value is less than 1% of the height of. the dam. In the stable flow condition, the changing trend of the settlement contour is similar to that of the post-construction condition, but it's settlement value is slightly larger than that of the post-construction condition. In the postconstruction condition the maximum principal stress contour is basically symmetrical about the wall, as double-arch shape, namely the contour in the interface of the shell and the core-wall is similar to the "hump". But the contour close to the core-wall has obvious subsidence trend. The large maximum principal stress is at the bottom of the clay core-wall. In the stable flow condition the double-arch shape of stress contours is more noticeable. This shows that arch effect phenomenon occur in core-wall of the dam. To demonstrate the reasonableness of the results of the calculation, the comparison of the maximum value of the settlement and the maximum principal stress in dam without goemenbrane between the calculation results and in the other literatures (Yang R 1995; Xu GA et al. 1997) is shown in Tables 3 and 4 .

Table 3 Settlement and the max of σ_1 in dam without Geo. in this calculation and in other literatures

condition	The largest settlement value /cm		
	This paper	literature [6]	literature [7]
post-construction	175	254	175
	Dam 2/5	Dam 2/5	Dam 2/5
stable flow	225	255	164
	Dam 2/5	Dam 2/5	Dam 2/5

Table 4 Settlement and the max of σ_1 in dam without Geo. in this calculation and in other literatures

condition	maximum value of σ_1 /MPa		
	This paper	literature [6]	literature [7]
post-construction	3.45	3.54	3.79
	Bottom of clay core-wall	Bottom of foundation	middle of foundation
stable flow	4.15	3.85	3.4
	middle of foundation	Bottom of foundation	middle of foundation

Note : The figures in Table 4 below the textual representation is the value of the field.

(2) In the stable flow condition the water level inside the core-wall with geomembrane is much lower than that of without geomembrane. From Fig. 6, we can see that the use of the united seepage control measure with geomembrane and clay core system has good impermeable effect. The seepage pressure contour line of which the value equal to 0 is the phreatic line. The phreatic line has depressed by 50% after adding the membrane. And the maximum seepage pressure at the bottom of the core-wall is just 55% of that without geomembrane. This significantly reduces the risk rate of failure of the clay core-wall with defect.

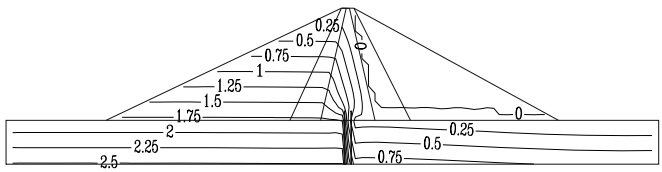

（a）without Geo.

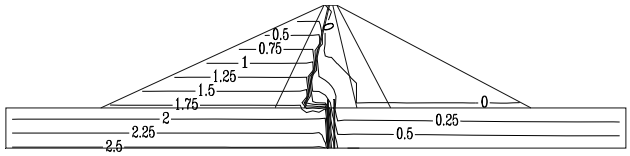

（b）with Geo.

Fig. 6 Seepage pressure contour in stable seepage condition without and with Geo.

(3) In the stable seepage condition the maximum principal stress inside the dam with a geomembrane is basically the same as that without it (as shown in Fig. 5). But the maximum principal stress value on the upstream surface of the core-wall with geomembrance increases compared to that without geomembrane, and the maximum increment is located at the height of 55 m of the dam, reaching a peak of 2.10 MPa. In the stable seepage condition the maximum principal stress on the upstream surface of the core-wall with geomembrane depresses with a lower speed, which indicates arch effect is improved.

(4) When the vertical stress inside the core-wall is less than the seepage pressure, which is caused by arch effect, hydraulic fracturing occurs and will lead to the horizontal cracks (WHITFIELD. B L 1996). Fig. 7 indicates that after adding geomembrane on the upstream surface of clay core-wall the stress inside the clay core-wall increases, and the seepage pressure inside the clay core-wall depresses duo to the impermeable geomembrane, which reduces the risk of hydraulic fracturing.

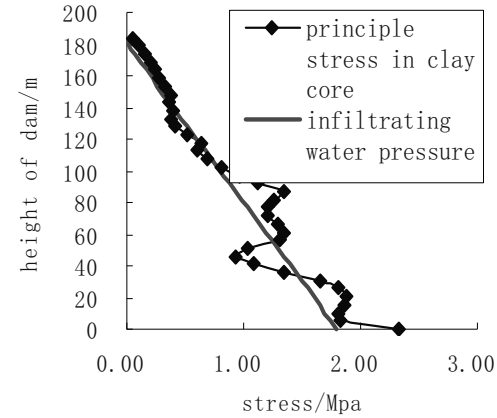

（a）without Geo.

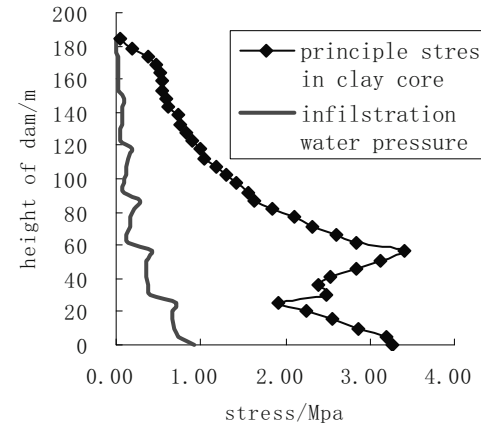

（b）with Geo.

Fig. 7 Comparison of σ_1 in core-wall upstream and seepage pressure without and with Geo.

CONCLUSION

(1) In the post-construction condition the largest settlement occurs at 2/5 height of the clay core-wall. In the stable flow condition the settlement value is slightly larger than that of in post-construction condition. The maximum principal stress contour in post-construction condition is basically symmetrical about the core-wall, as double-arch shape. Which indicates that arch effect phenomenon occurs inside clay core-wall. In the stable flow condition the arch effect in clay core-wall is more noticeable. The calculated value of the settlement and the principal stress value in this paper are in agreement with other literatures (Yang R 1995; Xu GA et al. 1997), which shows that this calculation model can be used to analyze the stress , strain and seepage of the dam.

(2) Adding geomembrane on the upstream surface of clay core-wall can effectively reduce seepage pressure, lower phreatic surface. That shows that even if there are shortcomings in geomembrane and gravel-soil of the

core-wall can not completely meet demand of impermeability, the united seepage control measure with geomembrance and clay core-wall system can still satisfy the demand of impermeability in macro level.

(3) Adding geomembrane on the upstream surface of clay core-wall not only effectively enhances the infiltration stability of the clay core-wall, but also alleviate arch effect of the maximum principal stress at the bottom of the upstream surface of the core-wall. Furthermore, the impermeable geomembrane can eliminate the phenomenon that the seepage pressure is lager than the maximum principal stress inside the clay core-wall. That causes the seepage pressure value become much smaller than the maximum principal stress inside the clay core-wall. So the risk of hydraulic fracturing is eliminated, which can ensure the security of impermeable core-wall both in mechanics and hydraulics ways.

REFERENCES

Gong BN, Tong L (2004) The analysis of arch effect in embankment dam project. Northeast Hydropower 22 (12) : 14-15

Lin DX (2004) Geomembrane Dam Design and Construction of a number of research. Dalian University of Technology

Shu YM, Li YH (2006) High embankment dam seepage control structure design method. Journal of Hohai University: Natural Science 34 (1): 60-64

The Commission of “Geosynthetics Application Handbook” preparation (2000) Geosynthetics Application Handbook (2nd Edition). Beijing: China Building Industry Publishing House

Whitfield BL (1996) Geomembrane appl ication for an RCC dam. Geotexts and Geomenbranes 24 (14): 253-264

Wu S, Zhang LM, Wu T (1995) The study for arch soil formation mechanism and conditions for the existence. Chengdu Science and Technology University Journal (2): 15-19

Xu GA, Wei ZG, Wu GS (1997) Pubugou Hydropower Station 3-D finite element calculation of seepage. Northwest Hydropower (2): 16-19

Yang R (1995) Pubugou high embankment dam 3D nonlinear analysis. The Application of Basic Science and Engineering Journals 3 (3): 260-2670

APPLICATION OF GEOSYNTHETICS FOR OFFSHORE BREAKWATERS AND COFFERDAMS

W.M. Kan [1] and A.M. Liu [2]

ABSTRACT: Several case histories are introduced to illustrate the application of prefabricated drains and geosynthetics to improve the soft soil foundations below breakwaters(offerdams). The foundations can be consolidated by the self-weight of the breakwaters (cofferdams), thus improving the strength of the foundations and ensuring the stability of the breakwaters (cofferdams). In the mean time, most of the settlement of the foundations can be completed during the construction of the breakwaters (cofferdams), which is significantly beneficial to rationally controlling the actual construction level of the breakwaters (cofferdams).

KEYWORDS: prefabricated drain, geosynthetic bedding, stability, settlement

INTRODUCTION

With the development of inter-tidal land and port construction in China, land resources become increasingly tight and as a result, more and more offshore artificial islands and land reclamation projects are being built. It is often necessary to build breakwaters (cofferdams) for these projects. However, along the lengthy coastal line of China, most of the shoals are composed of soft clayey soil of great thickness in regions like Tianjin, Guangdong, Shanghai, Ningbo and Lianyungang, where, when breakwaters (cofferdams) are built, the muck and mucky clay in the surface layer have to be removed first and then backfilled with rock material to form rubble mounds or hydraulic sand fill to form slopes. Such operations will not only generate a good quantity of engineering spoil but also increase greatly the demand for rock and sand materials. As a result, in regions short of rock and sand resources, more funds have to be invested in procurement and transportation of rock and sand material, thus increasing the construction cost on a large scale. If breakwaters (cofferdams) can be built directly on soft clayey soils, both the economic and social benefits will be considerable. By taking measures such as installation of prefabricated drains in soft soils, laying geosynthetics on the sand bedding against scouring and placing the core material by layers for the breakwaters (cofferdams), the soft soil foundations can be drained to consolidate under the self-weight of the breakwaters (cofferdams), thus improving the strength of the foundations and ensuring the stability of the breakwaters (cofferdams) during the construction of the breakwaters (cofferdams). After the completion of the breakwaters (cofferdams), the soft soil foundations will continue to drain and consolidate to further improve their strength, thus playing a positive role in stabilizing the trunk of the breakwaters (cofferdams) during the placing of backfill behind the breakwaters (cofferdams). Illustrations are made by the following examples of projects.

COMMON GEOSYNTHETICS FOR BREAKWATERS (COFFERDAMS)

The major geosynthetics used for the breakwaters (cofferdams) built on soft soil foundations are mainly prefabricated drains and geotextile. During the construction of breakwaters (cofferdams), the spacing of prefabricated drains will not be larger than 1.5 m and, if the daily settlement of the foundations is 20 mm, the daily discharge of water from the unit area improved by per piece of prefabricated drain will not be larger than 0.45 m^3 while the daily discharge of water by per piece of prefabricated drain of Model B should not be smaller than 2.16 m^3, completely meeting the functional requirements of the construction projects of breakwaters (cofferdams). As the soft soil in Tianjin area is generally not more than 20m thick, the prefabricated drains used are mostly prefabricated drains of Model B with their detailed properties as given in Table 1 and the geotextile used is mostly woven geotextile of continuous filament yarns. Geotextile with different properties may be selected and used according its function in breakwaters and

[1, 2] Tianjin Port Engineering Institute Ltd. of CCCC First Harbour Engineering Company Ltd., Tianjin 300222, CHINA

cofferdams of different structure formation and the properties of the geotextile commonly used in the breakwaters (cofferdams) built in Tianjin Port are as given in Table 2.

Table 1 Performance Index of Fabricated Drains of Model B

Description		Performance Index	Remarks
Material			Plastic core wrapped with non-woven geotextile filter
Sectional Dimensions (mm)	Width	100±2	
	Thickness	≥ 4.0	
Longitudical discharge capacity (m^3/s)		≥ 25×10^{-6}	At lateral pressure of 350 kPa
Permeability coefficient of filter (cm/s)		≥ 5×10^{-4}	After immersion in water for 24 h
Equivalent size of filter (mm)		<0.075	Calculated as O_{98}
Tensile strength of complete drain (kN/10cm)		≥ 1.3	With elongation of 10%
Tensile strength of filter (N/cm)	When dry	≥ 25	With elongation of 10%
	When wet	≥ 20	With elongation of 15% and immersion in water for 24 h

Table 2 Performance Index of Geotextile Commonly Used in Breakwaters (Cofferdams) in Tianjin Port

Description	Unit	Geotextile 1	Geotextile 2	Geotextile 3
Mass per unit area	g/m^2	≥260	≥340	≥600
Longitudinal tensile strength	kN/m	≥62	≥80	≥150
Transverse tensile strength	kN/m	≥45	≥56	≥105
Elongation at warpwise breakage	%		≤35	
Elongation at weftwise breakage	%		≤30	
Breaking strength when tearing by CBR	kN	≥6	≥8	≥11
Trapezoidal tearing strength	kN	≥1.1	≥1.4	≥2
Equivalent size at O_{90}	mm	≤0.3	—	≤0.3
Equivalent size at O_{95}	mm	—	0.07—0.4	—
Vertical permeability coefficient	cm/s	≥0.002	0.2—0.002	≥0.002

EXAMPLES OF PROJECTS

The soil in the surface layer in Tianjin Port region is mostly muck and mucky clayey soil, which is classified as very soft soil with high water content, high void ratio, low shear strength and low permeability. This layer of soil is the very soft soil of under-consolidated marine deposit with its underside level at about −9.0 m, below which is a layer of mucky clay and mucky silty clay of marine deposit with its underside level at about −14.0 m. The properties and the physical and mechanical indices of this layer of soil are slightly better. Further down from this layer of soil is the silty clay and silt of the limnetic facies with better physical and mechanical properties.

In recent years, breakwaters (cofferdams) of more than 30 km long have been built or are being built in Tianjin Port with varied types and forms, such as semi-circular breakwaters, breakwaters built with filled geotextile forms and cofferdams built with solidified soil in geo-forms. For all these breakwaters (cofferdams), prefabricated drains were installed to reinforce the weak and soft soil foundations and geotextile was laid over the sand bedding against the scouring by sea currents to ensure the drainage performance of the sand bedding, thus achieving the successful completion of these breakwaters (cofferdams).

East and South External Extensions of North Grand Breakwater for Tianjin Port

General profile

The East and South External Extensions of North Grand Breakwater for Tianjin Port are located in the sea beyond the existing North Breakwater for Tianjin Port,

which extends from the existing North Breakwater in the south and to the Ji Canal estuary in the north (Kan 2004). The sections of the first phase of the North Grand Breakwater, which were built with the semi-circular caissons, are the south external extension of 2 km long and the east external extension of 4.4 km long respectively. Considering the elevation of the original soil foundations and the variation of foundation settlement, the semi-circular caissons used for the extensions were blocks with widths from 11.6 m to 15.4 m and heights from 4.5 m to 6.7 m.The weight of each individual caisson was about 180t. The cross section of the extensions is as shown in Fig. 1. The sequence of construction was the placement of sand bags to build a low dam → placement of sand to construct the sand bedding of 1 m thick → installation of prefabricated drains of Model B (arranged in square grids with spacing of 1.5 m and driven to a tip level of −14 m) → laying of geotextile spread → placing of rock blocks to form the foundation bed of 1 m thick → installation of semi-circular caissons → placing of rock blocks to form the counter weight apron.

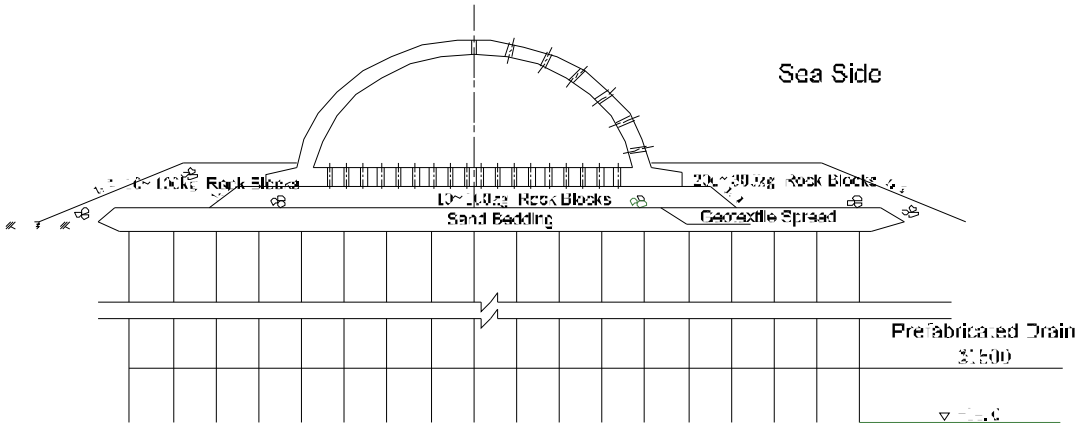

Fig. 1 Typical Cross Section of East and South External Extensions of North Grand Breakwater for Tianjin Port

Semi-circular caisson structure is favorably characterized by better self stability, low loads on foundations, rapid progress of construction, nice exterior appearance and low construction cost, etc. As a result, the semi-circular caissons were substantially used on the Yangtze Estuary Deepwater Channel Regulation Project. During the construction of the North Grand Breakwater for Tianjin Port, the installed prefabricated drains of Model B were used to consolidate the soft soil foundation with the self weight of the breakwater acting as the pre-load and the woven geotextile mats of continuous filament yarns of 260 g/m^2 was laid to provide effective protection for the draining sand bedding. With these measures, semi-circular caissons were successfully used on a large scale on muck and mucky foundations for the first time.

Result of soil improvement

With the installation of prefabricated drains, the drainage paths were shortened and the foundation soil developed greater consolidated settlement under the load of the breakwater. The settlement was between 64.3 cm and 85.0 cm and the rate of settlement was generally lower than 15 mm/d. The maximum lateral displacement of the surface layer of the soil mass on the two sides of the breakwater under the load of the breakwater was 20mm—30mm and the maximum rate of lateral displacement was lower than 4mm/d as shown in Figs. 2 and 3. As the soft soil under the breakwater was effectively improved and the strength of soil was enhanced to some extent, the soil foundation remained stable all the time during the construction of the breakwater and placement of fill material behind the breakwater.

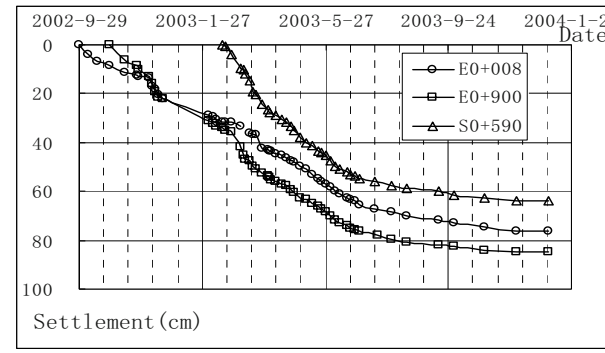

Fig. 2 Relationship of Settlement to Time at the Center of the Cross Section of the East and South External Extensions of North Grand Breakwater for Tianjin Port

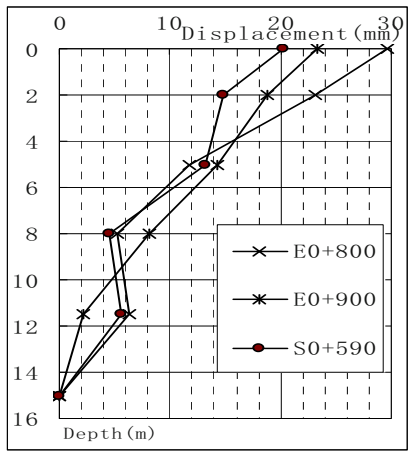

Fig. 3 Final Lateral Displacement at Different Depths of Soil Foundation of the East and South External Extensions of North Grand Breakwater for Tianjin Port

West Inner Levee of North Grand Breakwater for Tianjin Port

General profile

The West Inner Levee (First Phase) of North Grand Breakwater for Tianjin Port was 2000 km long and the level of structural safety was classified as Level Three (Kan 2005). The structural shape of the levee was a mound levee and the whole levee was made up of geotextile formed solidified soil armored with bagged concrete. The soft soil foundation was consolidated and improved by installed prefabricated drains of Model B and with the self weight of the breakwater acting as the pre-load while the woven geotextile spread of continuous filament yarns of 340g/m^2 was laid to provide effective protection for the draining sand bedding. The method employed to improve the soft soil foundation was the installation of prefabricated drains. The structural cross section of the west inner levee is as shown in Figs. 3 and 4. The sequence of construction of the levee was the placement of sand bags along the sides of the foundation trench to build a low dam → placement of sand to construct the sand bedding of 1m thick → installation of prefabricated drains of Model B (with spacing of 1.0 m and driven to a tip level of −15 m) → laying of geotextile spread → construction and placing of geotextile-formed solidified soil → laying of geotextile filter spread → placing of flaky stones and armor rocks and placing of geotextile formed concrete → placing of rock blocks on both sides.

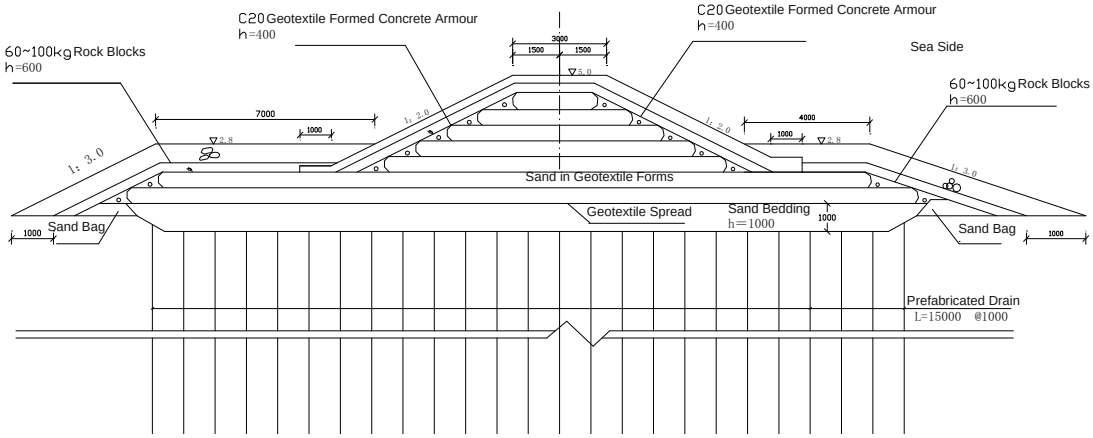

Fig. 4 Typical Cross Section of West Inner Levee of North Grand Breakwater for Tianjin Port

The major procedure to build geotextile formed solidified soil is to get soft soil directly from the sea bottom, which will be added with cement hardener to be mechanically mixed into uniform and flowing soil mixture and be filled into large geotextile forms that are placed in their designed position to become the geotextile formed solidified soil. The geotextile forms will be laid by layers one after another to be filled with the soil mixture and the solidified soil in geo-forms will eventually form the core of the offshore cofferdam. The technique, when being used, can not only cut down greatly the cost on construction materials but also minimize the damage by waves and currents to the cofferdam, especially the damage to the cofferdam during the construction of the cofferdam. When the technique is employed, it produces no pollution to the surrounding environment but can make full use of the mucky clay dredged from the basins and the waterways, thus reducing the contamination of the environment by the dredged spoil and meeting the requirements of environmental protection. Hence, the technique of solidified soil in geotextile-forms was successfully employed for the first time for West Inner Levee of North Grand Breakwater for Tianjin Port.

Result of soil improvement

With the installation of prefabricated drains, the drainage paths were shortened and the foundation soil developed greater consolidated settlement under the load of the breakwater. The settlement was between 60 cm and 100.7 cm and the rate of settlement was generally lower than 15 mm/d as shown in Figs. 3—5.

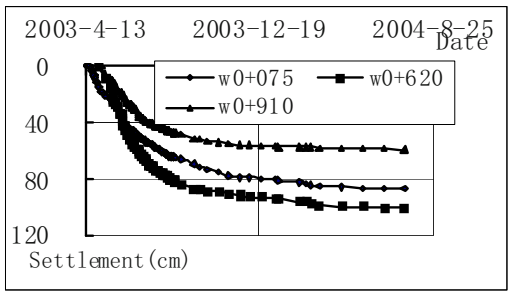

Fig. 5 Relationship of Settlement to Time at the Center of the Cross Section of the West Inner Levee of North Grand Breakwater for Tianjin Port

The maximum lateral displacement of the surface layer of the soil mass on the two sides of the breakwater under the load of the breakwater was 70—200 mm as shown in Figs. 3—6 and the maximum rate of lateral displacement was lower than 6 mm/d. The Employer, the Designer and the Contractor were immediately advised once the settlement and the rate of settlement exceeded the designed controlling value. The stability of the breakwater was maintained by way of readjustment of the rate of progress of the construction.

With the load of the cofferdam of geotextile formed solidified soil, the physical and mechanical properties of the foundation soil below the sand bedding were remarkably improved as shown in Table 3-1 and the vane shear strength was also increased significantly, especially the vane shear strength of the muck in the surface layer, which was increased from 5—6 kPa before the improvement to 25—38 kPa, with a increment of more than 300%, as seen in Figs. 3—7.

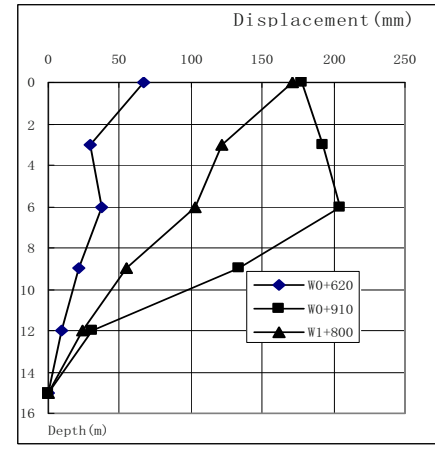

Fig. 6 Final Lateral Displacement at Different Depth of Soil Foundation of the West Inner Levee of North Grand Breakwater for Tianjin Port

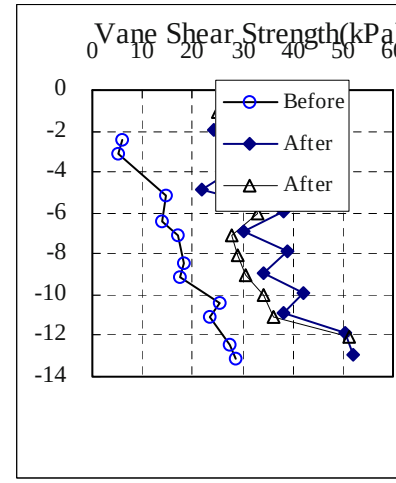

Fig. 7 Correlation Curves of Vane Shear Strength of Foundation Soil before and after Imposition of Loading by Cofferdam

Table 3 Comparison of Major Physical and Mechanical Properties of Foundation Soil Before and After Imposition of Load of Cofferdam Built of Geotextile Formed Solidified Soil

Name of Soil		w	ρ	e_O	I_p	I_L	c_q	Φ_q	c_{cq}
		%	g/cm^3				kPa	Degree	kPa
Muck	Before Improvement	63.7	1.62	1.747	25	1.55	5.2	0.1	11.1
	After Improvement	51.1	1.7	1.435	22.7	1.3	7.9	4.1	25.2
Mucky Clay	Before Improvement	44.7	1.78	1.225	20.4	1.15	10.3	2.2	16.9
	After Improvement	40.0	1.8	1.111	17.7	1.2	17.7	4.6	16.9

After the installation of the prefabricated drains, the soil foundation was effectively improved under the action of the self-weight of the cofferdam built with solidified soil in geotextile forms and the result of improvement was very significant. As the soft soil under the levee was effectively consolidated and the strength of the soil foundation was enhanced the levee remained stable all the time during placement of fill behind the levee.

Cofferdam for Secondary Subgrade on Artificial Island in Tianjin Port

General profile

The cofferdam for the secondary subgrade on the artificial island in Tianjin Port was located in the center of the planned artificial island and was the temporary access running through the artificial island, which was also the partition dam for reclamation to create conditions for the construction of the artificial island and will provide roads for transportation for the primary stage of development of the artificial island for the long term plan (Chen & Kan 2007). The cofferdam was totally 8.4 km long and the original elevation of the foundation did not vary very much, from 0—0.5 m. The cross-sectional formation of the cofferdam was as shown in Figs. 3—8. The sequence of construction of the cofferdam was the placement of sand bags to build a low dam → placement of sand to construct the sand bedding of 1 m thick → installation of prefabricated drains of Model B (with spacing of 1.0m and driven to a tip level of –14.0 m) → laying of geotextile of continuous filament yarns of 620 g/m^2 → placing of geotextile formed hydraulic fill and placing of flaky stones → placing of hill cut materials and armor blocks for penning → construction of surface layer. The design crown width of the cofferdam was 10 m and the elevation at the crown top was 5.6 m.

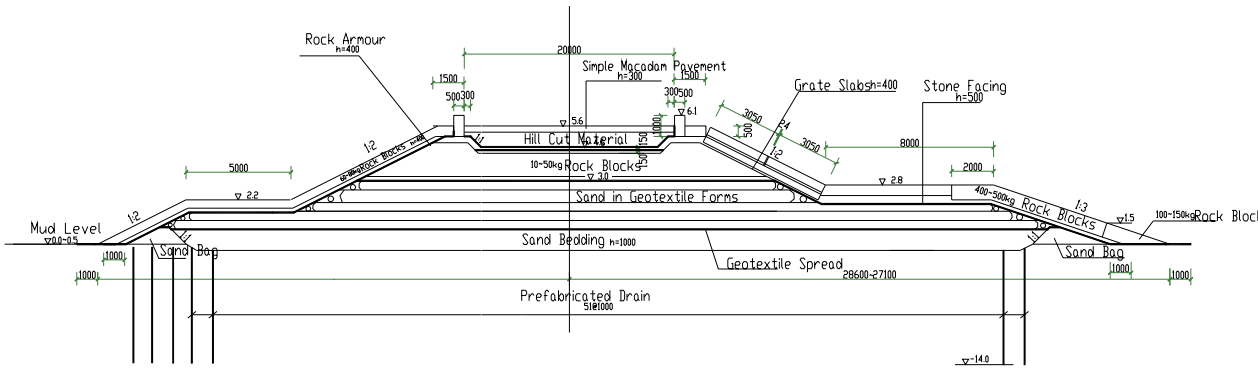

Fig. 8 Typical Cross Section of Cofferdam for Secondary Subgrade on Artificial Island in Tianjin Port

Result of soil improvement

With the installation of prefabricated drains, the drainage paths were shortened and the settlement of the foundation soil developed under the load of the cofferdam was from 116—135 cm and the maximum lateral displacement of the surface layer of the soil mass on the two sides of the breakwater under the load of the breakwater was 138—180 mm as shown in Figs. 3—9 and Figs. 3—10. As the soft soil under the cofferdam was effectively improved and the strength of soil was enhanced the soil foundation remained stable all the time during the construction of the cofferdam and placement of fill material behind the cofferdam. The rate of lateral settlement of the cofferdam was generally lower than 4mm/d. As the soft soil under the cofferdam was effectively consolidated and the strength of the soil foundation was enhanced to some extent, the cofferdam remained stable all the time during the construction of the cofferdam and placement of fill behind the cofferdam.

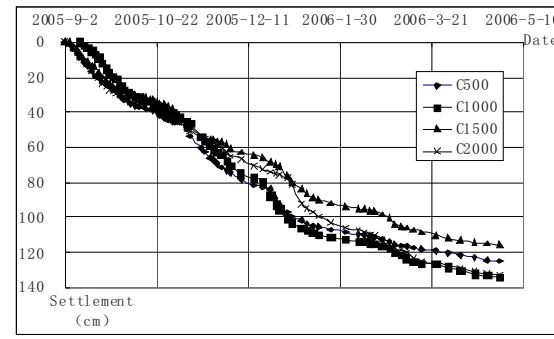

Fig. 9 Relationship of Settlement to Time at the Center of the Cross Section of the Cofferdam for the Secondary Subgrade on the Artificial Island in Tianjin Port

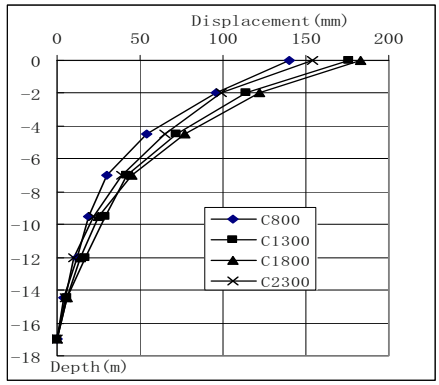

Fig. 10 Final Lateral Displacement at Different Depths of Soil Foundation of the Cofferdam for the Secondary Subgrade on the Artificial Island in Tianjin Port

Issues to Be Clarified

(1) The settlement in the above results of soil improvement was only the settlement of the breakwaters (cofferdams) during their construction, exclusive of the volume of "muck mixed sand" during the placement of fill, the "immediate settlement" during the installation of prefabricated drains and the compression of the breakwater (cofferdam) itself.

The surface of the original foundation was generally covered with a layer of flowing mud and slurry. When sand was placed to build the sand bedding, a considerable amount of placed sand got into the flowing mud and slurry. Though a sufficient amount of medium coarse sand was placed, the mud level wasn't increased accordingly. This settlement was about 50—60 cm according to the measured data of part of the project.

After the prefabricated drains were installed in the foundation, the under-consolidated muck or mucky clay in the surface of the foundation developed settlement under the load of the sand bedding and the self-weight of this layer of soil due to the shortening of the discharging paths and the settlement was about 25—35 cm.

As the settlement gauges were located below the underside of the breakwater (cofferdam), it was impossible to measure the amount of compression of the breakwater (cofferdam) itself and the settlement is different with different structural forms of the breakwaters (cofferdams).

(2) The results of underwater checking of several projects showed that the geotextile spread could better protect the sand bedding against scouring of sea currents.

(3) The final settlement of a soil foundation can be predicted according to the actual settlement curves of the foundation so as to provide reference for scientific and rational control of the actual construction level of the breakwaters (cofferdams).

CONCLUSIONS

There are varied types of breakwaters (cofferdams) that can be built on soft soils, such as semi-circular caisson breakwaters, breakwaters built with filled geotextile forms and cofferdams built with solidified soil in geo-forms. Better results can be achieved when prefabricated drains and geotextile spread are used to improve the soft soil foundations during the construction of the breakwaters (cofferdams).

(1) When prefabricated drains are installed in soft soil foundations for breakwaters (cofferdams), the soft soil foundations can be consolidated by the self-weight of the breakwaters (cofferdams), thus improving the strength of the foundations and, with placing of the fill by layers to build the breakwaters (cofferdams), ensuring the stability of the breakwaters (cofferdams) during their construction. After the completion of the breakwaters (cofferdams), the soft soil foundations continue their draining and consolidation to make the strength of the soil further increase, which plays also the positive role in stabilizing the breakwaters (cofferdams) during the placement of fill materials behind the breakwaters (cofferdams).

(2) The geotextile spread placed on the surface of the sand bedding can better protect the sand bedding against the scouring of sea currents.

(3) When prefabricated drains and geotextile spread are used to improve the soft soil foundations for breakwaters (cofferdams), most part of the settlement of the soft soil foundations can be completed during the construction of the breakwaters (cofferdams), which is significantly beneficial to rationally controlling of the actual construction level of the breakwaters (cofferdams).

REFERENCES

Chen YT, Kan WM (2007) Report on Measurement and Analysis of Construction of Cofferdam for Secondary Subgrade on Artificial Island in Tianjin Port, Tianjin Port Engineering Quality Testing Center, 2007 (Chinese)

Kan WM (2004), Observation and Preliminary Analysis of Settlement of Semi Circular Structures for North Grand Breakwater for Tianjin Port, Tianjin Port Engineering Institute, 2004 (Chinese)

Kan WM (2005) Report on In-Situ Observation and Measurement of Offshore Cofferdam Built with Solidified Soil in Geotextile Forms Tianjin Port Engineering Institute Ltd. of CCCC First Harbour Engineering Company Ltd., 2005 (Chinese)

Proceedings of the 4th Asian Regional Conference on Geosynthetics
June 17 - 20, 2008 Shanghai, China

RESEARCH ON AGEING RESISTANCE OF GEOTEXTILE

G.L. Ye [1], Y.L Xue [2] and W. Zhang [3]

ABSTRACT: Ageing of geotextile has attracted incessant attention from the engineering field. During the revision of Technical Specification for Application of Geotextile in Marine Works (JTJ239-98) published by the Ministry of Communications of China, artificially accelerated ageing tests in laboratory, natural insolating tests, measurement of underwater ultraviolet radiation energy, ageing tests of buried geotextile in sandy soil and tests of specimens sampled from practical engineering works were carried out for the monographic research on ageing resistance of geotextile. The paper is the summary of the test results, which can be of the reference for designers and contractors.

KEYWORDS: geotextile, ageing resistance, geosynthetics

FOREWORD

Synthetic materials have many properties meeting the engineering properties like filtration, dewatering, separation, reinforcing, anti-seepage and protection. As these synthetic materials are characterized by such advantages as being light weight, simple in installation, easy for transportation, low in price and abundant in sources, they have been widely used the world wide for nearly 30 years and have been reputed as a technical revolution in the 20th century.

The primary materials for geotextile are high molecular polymers and ageing of geotextile is resulted from the degradative reaction or the cross linking reaction of high molecular polymers because of the influence of extraneous factors as high molecular polymers are of chain-link structure. Among the ageing factors for geotextile, sunlight radiation is the most significant factor. But ageing of geosynthetics is a hidden danger for the safety of engineering works and, therefore, ageing resistance of geotextile has attracted the great concern of the engineering field (Yan et al., 2002; Wang & Gao 2003; Hu & Dong 2002).

During the revision of Technical Specification for Application of Geotextile in Marine Works (JTJ239-98) published by the Ministry of Communications of China, monographic research on ageing resistance of geotextile was carried out (Zhang & Ye 2005), which covered mainly the artificially accelerated ageing tests in laboratory, natural insolating tests, measurement of underwater ultraviolet radiation energy, ageing tests of buried geotextile in soil and tests of specimens sampled from practical engineering works. The correlativity of the result of artificially accelerated ageing tests with the result of natural insolating tests was also studied. This paper is the summary of the test results, which will be for the reference of designers and contractors.

AGEING RESISTANCE TESTS OF GEOTEXTILE

Ageing resistance tests of geotextile include two types of tests, one is artificially accelerated ageing tests and the other is the natural insolating tests.A lot of tests and research were carried out to investigate the ageing resistance of geotextile and the correlativity of the results of the two types of tests(Xue 2004).

Artificially Accelerated Ageing Tests

Six samples were taken from the selected testing materials.

Sample I: Ordinary woven fabric (230 g/m^2): The raw material is ordinary polypropylene filament yarn, which was woven into plain-woven fabric.

Sample II: Ordinary composite fabric with the smooth side facing up, which is ordinary polypropylene base fabric (230 g/m^2) with needle punched terylene composite cloth (150 g/m^2).

Sample III: The material for Sample III is the same as that for Sample II with the knap side facing up.

Sample IV: Anti-ageing woven fabric (230 g/m^2): The raw material is polypropylene filament yarn added with hindered amine light stabilizers, which is woven

[1] Tianjin Port Engineering Institute Ltd. of CCCC First Harbour Engineering Company Ltd., Tianjin 300222, CHINA
[2] Shanghai New Textile Industry & Appliances Company Ltd., Shanghai 200042, CHINA
[3]Tianjin Port Engineering Institute Ltd. of CCCC First Harbour Engineering Company Ltd., Tianjin 300222, CHINA

into plain woven fabric.

Sample V: Anti-ageing composite fabric with the smooth side facing up, which is the ageing resistant polypropylene base fabric (230 g/m^2) with needle punched terylene composite cloth (150 g/m^2).

Sample VI: The material for Sample VI is the same as that for Sample V with the knap side facing up.

The artificial accelerated ageing tester used in the tests was the home-made artificially accelerated ageing tester of Model UV-II for non metallic material while the fluorescent ultraviolet tubes were the USA made UV-B fluorescent ultraviolet tubes. An ultraviolet radiation tester of Model SUR-1 was used to measure the radiation energy in the ageing oven.

The relationship of the retention rate of the warpwise breaking tenacity of the six samples after accelerated ageing by ultraviolet radiation to the ultraviolet radiation energy is as shown in Fig. 1.

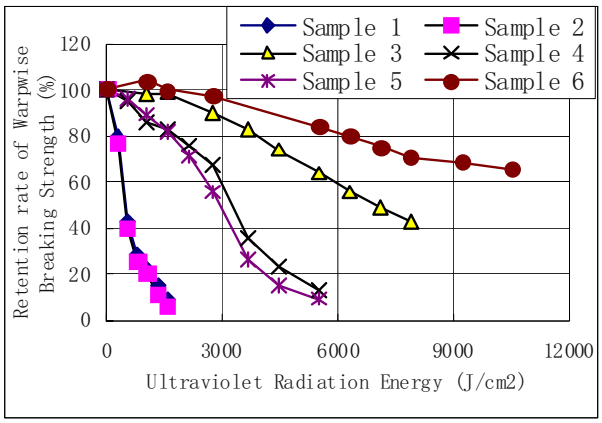

Fig. 1 Relationship of radiation energy to tenacity retention rate in accelerated ageing tests by ultraviolet radiation

The following conclusions can be reached after the artificially accelerated ageing tests.

(1) The ageing resistance of polypropylene geotextile added with hindered amine light stabilizers is higher than that of ordinary polypropylene woven fabric;

(2) The surface recombined terylene fiber has the function to keep out the ultraviolet radiation with significant physical protection effect;

(3) Under the conditions of accelerated ageing by fluorescence with higher ultraviolet radiation intensity, the effect of terylene fiber to keep out and absorb ultraviolet radiation is better than hindered amine light stabilizers;

(4) The ageing resistance of anti-ageing composite fabric with the knap side facing up is the highest among all the samples tested.

Natural Insolating Tests

Natural insolating tests were carried out on the six types of testing materials as given above. An ultraviolet radiation tester of Model SUR-1, which is the same type of tester used in the artificial accelerated ageing tests, was used to measure the solar radiation energy. The relationship of the retention rate of the warpwise breaking tenacity of the samples of different ageing time to the change of ultraviolet radiation energy is as shown in Fig. 2.

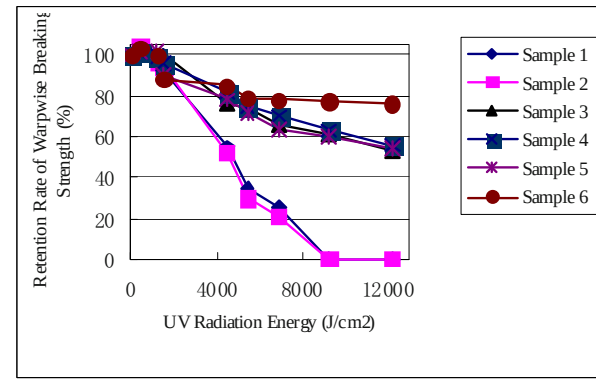

Fig. 2 Relationship of tenacity retention rate to ultraviolet radiation energy

The following conclusions can be reached after the natural insolating tests.

(1) The ageing resistance of polypropylene geotextile added with hindered amine light stabilizers is higher than that of ordinary polypropylene woven fabric;

(2) The surface recombined terylene fiber has the function to keep out the ultraviolet radiation with significant physical protection effect;

(3) With natural insolating, the effect of hindered amine light stabilizers is better than that of terylene fiber to keep out and absorb ultraviolet radiation, which is just contrary to the results of the artificially accelerated ageing tests;

(4) The ageing resistance of anti-ageing composite fabric with the knap side facing up is the highest among all the samples tested.

Study of Correlativity of Accelerated Ageing Tests and Natural Insolating Tests

With comparison of substantive curves, the relationship of the retention rate of the warpwise breaking tenacity to the ultraviolet radiation energy in both the artificially accelerated ageing tests and the natural insolating tests is very suitable for curve fitting by using Eq. 1 and the coefficients of correlation are all

more than 0.97. The parameters for the fitting-curve equation for various samples are tabulated in Table 1.

Table 1 Parameters for Fitting Curves of Various Samples

Parameter / Sample	Artificially Accelerated Ageing Tests			Natural Insolating Tests		
	a_1	b_1	Correlation Coefficient	a_2	b_2	Correlation Coefficient
Sample I	$4.4*10^{-4}$	1.18	0.98	$5.98*10^{-8}$	1.93	0.99
Sample II	$3.9*10^{-4}$	1.21	0.99	$3.79*10^{-9}$	2.26	0.99
Sample III	$2.13*10^{-8}$	1.95	0.99	$2.1*10^{-4}$	0.85	0.99
Sample IV	$9.63*10^{-8}$	1.96	0.98	$0.3*10^{-4}$	1.04	0.99
Sample V	$3.35*10^{-8}$	2.12	0.99	$2*10^{-4}$	0.86	0.99
Sample VI	$3.98*10^{-6}$	1.26	0.98	$8.31*10^{-3}$	0.38	0.97

$$y = 100 \times e^{-ax^b} \quad (1)$$

where y = Retention rate of warpwise breaking tenacity (%);

x = Ultraviolet radiation energy (J/cm^2);

a and b are constants to be determined by the values at the testing points.

According to Eq. 1 for fitting curves, when the breaking tenacity of the two types of geotextile being tested attenuates to the same degree (namely, $y_1 = y_2$), the corresponding values of the ultraviolet radiation energy for the two types of geotextile are reduced to the relationship as given in Eq. 2. The relationship between samples subject to different ultraviolet radiation energies in accelerated ageing tests and natural insolating tests is defined as the accelerating curve equation (namely, Eq. 2.

$$x_2 = A \times x_1^B \quad (2)$$

where x_2 : Atmospheric ultraviolet radiation energy when the ageing degree is the same (J/cm^2); x_1 : Fluorescent ultraviolet radiation energy when the ageing degree is the same (J/cm^2);

$$A = (\frac{a_1}{a_2})^{\frac{1}{b_2}}; B = \frac{b_1}{b_2}$$

a_1 ,b_1, a_2 and b_2 are the experimental parameters in the equation for the law of ageing under the artificially accelerated ageing and natural insolating conditions, which are as given in Table 1.

The coefficients of ultraviolet radiation for the above described samples are as given in Table 2.

It can be known from the analysis of the test results that, for Sample I and Sample II with lower ageing resistance, the atmospheric ultraviolet radiation energy is lower than the fluorescent ultraviolet radiation energy when the breaking tenacity of geotextile comes to the same degree of attenuation while, for the other four types of samples with higher ageing resistance, the atmospheric ultraviolet radiation energy is always higher than the fluorescent ultraviolet radiation energy. The difference is resulted from the different energy required for the degradation of different materials and the absorption of light energy by terylene fiber.

Table 2 Relationship of Ultraviolet Radiation of Various Samples

Parameter / Sample	A	B
Sample I	100.81	0.61
Sample II	165.15	0.54
Sample III	$2.0*10^{-5}$	2.29
Sample IV	$4.0*10^{-3}$	1.88
Sample V	$4.07*10^{-5}$	2.47
Sample VI	$1.84*10^{-9}$	3.32

The test results show that, when the breaking tenacity of the six types of samples reaches 50%, the serviceable time of the samples under the natural insolating conditions is 0.55, 0.55, 1.67, 1.90, 1.58 and 13.77 years separately, among which, the ageing resistance of Sample VI—anti-ageing polypropylene composite fabric with the knap side facing the light—is the highest. Hence, the serviceable life of geotextile under the natural insolating conditions can be more accurately predicted by way of accelerated ageing tests with fluorescent ultraviolet radiation on the basis of the above model of correlativity of the ageing law equation and the curves of acceleration.

FIELD TESTS OF AGEING RESISTANCE OF GEOTEXTILE

Measurement of Underwater Ultraviolet Radiation Energy

The ultraviolet radiation energy at different water depths was measured to obtain the pattern of variation of ultraviolet radiation intensity and to investigate the protection of geotextile by water depth.

The equipment used in the tests were ultraviolet radiation testers of Model SUR－1, a signal variation and acquisition device of Model QXY － 1 and a computer. During the tests, the ultraviolet radiation testers were placed at different water depths to measure the ultraviolet radiation. The tests were carried out twice in the swimming pool in Jiaotong University and at Hengsha Wharf respectively. It was fine and cloudless during the tests and the testing sites were not sheltered in any way. The average residual rates of radiation intensity measured at different water depths are as given in Fig. 3.

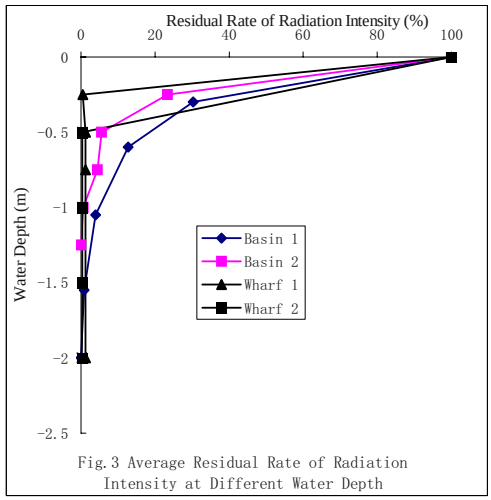

Fig. 3 Average Residual Rate of Radiation Intensity at Different Water Depth

In Fig. 3, the ultraviolet radiation attenuates rapidly with the increase of water depth, especially at Hengsha Wharf in the Changjiang estuary where the attenuation of ultraviolet radiation was more significant because of the high percentage of sediment in the water.

Ageing Resistance Tests of Geotextile in Water

At –2.0 m in a water area close to Hengsha Island in the Changjiang estuary, underwater ageing resistance tests were carried out on four types of geotextile, namely ordinary high strength woven fabric of polypropylene filament yarns, anti-ageing high strength woven fabric of polypropylene filament yarns, ordinary high strength woven and non-woven needle punched composite fabric of polypropylene filament yarns and anti-ageing high strength woven and non-woven needle punched composite fabric of polypropylene filament yarns. The duration of the underwater ageing resistance tests of the geotextile was 2 years and the test results are as given in Table 3.

The test results show that the strength of the geotextile placed under the water decreases with the extension of time but, generally, doesn't decrease very much. The annual strength loss of ordinary and anti-ageing geotextile is 1.01% and 1.16% respectively and, compared with the ageing rate of the geotextile in the natural insolating tests, the ageing rate of geotextile under the water is very slow. The serviceable life of the two types of geotextile is predicted to be 49.3 and 43.0 years respectively.

Ageing Tests of Buried Geotextile in Sandy Soil

Ageing tests were carried out on the ordinary and anti-ageing high strength woven fabric of polypropylene filament yarns buried in sandy soil at Hengsha Island in the Changjiang estuary. The thickness of sandy soil on the buried geotextile was 5 cm, 10 cm and 20 cm separately and the duration of the ageing tests was 450 days. The test results are as given in Table 4.

Table 3 Retention Rate of Warpwise Breaking Strength of Aged Geotextile in Water (%)

Category	Name of Sample	0 d	180 d	360 d	540 d	720 d
Ordinary Geotextile	High strength woven fabric of polypropylene filament yarns	100	98.49	97.49	97.68	97.8
	High strength woven and non-woven punched composite fabric of polypropylene filament yarns	100	101.46	100.56	97.59	98.2
Ageing Resistant Geotextile	High strength woven fabric of polypropylene filament yarns	100	97.68	98.92	96.48	97.29
	High strength woven and non-woven punched composite fabric of polypropylene filament yarns	100	98.18	96.99	98.33	98.12

Table 4 Retention Rate of Warpwise Breaking Strength of Aged Geotextile Covered by Soil (%)

Sample \ Time / Soil Thickness		0 day	90 days	180 days	268 days	450 days
Ordinary polypro-pylene filament yarn woven fabric	5cm	100	109.2	122.6	119.8	115.2
	10cm	100	117.8	121.2	126.6	125.4
	15cm	100	121.6	120.5	120.0	120.1
Anti-ageing polypro-pylene filament yarn woven fabric	5cm	100	108.1	112.0	113.3	112.4
	10cm	100	107.9	115.4	115.6	107.9
	15cm	100	108.2	112.2	115.7	116.9

It can be seen from Table 4 that, after the ageing tests of the buried geotextile ended in 450 days, the warpwise breaking tenacity of all the samples was higher than the original breaking tenacity of the tested geotextile. This is because the sandy soil had sheltered the buried geotextile from ultraviolet radiation and polypropylene material has the outstanding property against chemical and biological degradation. At this time no degradative reaction developed in the polypropylene as the samples in this period were still at the stage of physical change. The increase of strength was resulted from the spread of the macromolecular chain, recombination in the crystallization and non-crystallization regions and variation of orientation in polypropylene.

It can be known from the comparison of the results of the ageing tests of the geotextile placed under water and buried in sandy soil that sandy soil of 5 cm thick produces better sheltering effect against ultraviolet radiation than a water mass of 2.0 m thick. However, the testing period was very short and it is impossible to estimate the actual serviceable life of geotextile under such conditions. Comparing with the results of the underwater ageing resistance tests, the serviceable life of geotextile buried in sandy soil should be more than 50 years.

SAMPLING & ANALYSIS OF SPECIMENS FROM ENGINEERING WORKS

Pilot Dam for Waterway Regulating Works for Hanjiang River

The waterway regulating works for the Hanjiang River was located at a site (Groyne No.17) 2 km in the upstream of the Hanjiang River from Yicheng City. The pilot dam was originally designed to be totally 155 m long and 130 m of the dam was designed to be a section constructed with sand-filled geotextile bags. However, when the dam was built to 50 m long, the water level of the Hanjiang River rose rapidly by 1.6 m causing the dam of sand-filled geotextile bags submerged in the water by 1.4 m. A section of 22 m from the jetty head of the dam was destroyed by the water flow as armor rocks had not been placed in time. Armor blocks were then placed on the undestroyed section of 33 m to form the pilot dam. Construction of the pilot dam was commenced on March 11, 1989 and completed on June 18 the same year.

The geotextile used on the pilot dam was woven polypropylene fabric of 14×14 yarns/in^2 produced by Wuhan Huachang Plastics Plant. As the quantity of woven polypropylene fabric of 14×14 yarns/in^2 was insufficient, most of the sand bags were made of woven polypropylene fabric of 12×12 yarns/in^2. The technical performance indices of the geotextile are as given in the literature (Wang and Gao 2003）.

Sampling was made on the crown of the pilot dam. The protective course of 50 cm thick in the dam crown was basically intact but the base of slope caved in a little. After the protective course was removed, samples were carefully taken from the sand bags. After the samples had been taken, new woven fabric was placed to cover the sampling site, which was then reinstated with proper compaction. There were damage and holes in the samples of geotextile.

After the samples were taken from the site, six sets of specimens were tested for laboratory longitudinal and transversal stretching and trapezoidal tear. The detailed results of the tests are as given in the literature while the comparison of the test results is as given in Table 5(Yu, 2002).

Table 5 Test Results of Field Samples from Pilot Dam for Waterway Regulating Works for Hanjiang River

Description	Original Sample	Sample Taken 13 Years Later	Retention Rate of Strength (%)	Rate of Strength Loss (%)	Rate of Annual Stengthh Loss (%/y)
Mass per Unit Area (g/m^2)	113.9	131			
Thickness of Fabric (mm)	0.52 - 0.55	0.48			
Tensile Strength (N/5cm)	836	566	67.7	32.3	2.484
Breaking Strain ε (%)		12.0/11.0 - 13.5		84.3	1.542

Predicted serviceable life of geotextile with retention of 50% of strength: 20.1 years

The serviceable life of the geotextile at the sampling site was predicted to be about 20.1 years according to the test results. As the samples were taken from the dam crown where the conditions like weathering and sunlight were inferior to the conditions below the water, the sampling site was the worst located and there was damage resulted from the construction process. If the samples had been taken from other locations, the predicted serviceable life could be longer.

Waterway Regulating Works for Jiepai Reach of Changjiang River

The waterway regulating works for the Jiepai Reach of the Changjiang River began in 1994 and, after the works continued for 5 low water seasons, 14 groynes, 1 closure dike and 1 fish mouth type dividing dike were completed. Plenty of geotextile mattress and sand-filled geotextile bags were used on the project and, by March 1995, geotextile mattress of 1.26 million m^2 was placed to protect the foundation while sand-filled geotextile bags was installed to construct the works of 450 000 m^3. A total of 6 million m^2 of geotextile was used.

The polypropylene woven and non-woven fabrics used for the waterway regulating works for the Jiepai Reach of the Changjiang River were mainly produced and supplied by Changzhou Weaving & Knitting General Plant and Yichang No.5 Plastics Plant. The data and information available indicate that the quality of the products met all the design requirements.

Two spot tests were made on the geotextile used for the waterway regulating works at the Jiepai Reach of the Changjiang River. The first sampling and test were made in a large scale and the samples were taken in July 1999 and from six representative areas and locations where the working conditions were close to each other. Thus, the

samples were taken from Groynes No. 5, 7, 10 and 15, the fish mouth type dividing dike at Xinyuzhou and the closure dike, representing the geotextile used in the construction works from 1994 to 1999. All the samples were taken directly from under the mantle close to the water under conditions of not damaging the existing structures.

The second sampling was made on April 10, 2002 and the sampling site was at Groyne No. 7, which had been completed in May 1995. It had been in service for about 7 years when the second sampling took place. Samples were taken from the riverside and a location 20 m away from the river bank. The geotextile mattress was covered with sand bags, river sand and rocks. The mantle was about 50 cm thick. The geotextile samples taken from the geotextile mattress and sand bags were basically intact and the detailed test results are as given in the literature(Yu 2002). The annual strength loss and the predicted serviceable life of the geotextile calculated on the basis of the test results of the two samplings and the strength of the original samples were as given in Table 6.

Table 6 Test Results of Field Samples from Waterway Regulating Works for Jiepai Reach of Changjiang River

Description	Original Sample	Sample Teken 38 Months Later	Sample Teken 7 Years Later	Rate of Strength Loss (%/year)
Tensile Stength (N/5cm)	1140	1028	961	
Retention Rate of Strength (%)		90.1	84.3	1.542
Predicted serviceable life of geotextile with retention of 50% of strength:				29.2

The test results of the samples (Table 7) indicated that the retention rate of tensile strength of the geotextile buried for about 7 years on this project was 84.3% and it can be predicted from these results that the time for the geotextile to decay to the design strength (800 N/5cm) could be 15 years. The serviceable life of the geotextile when its tensile strength decays to 50% of its originally designed tensile strength is 29 years.

CONCLUSIONS

Synthesizing the analyses of the ageing resistance tests of the geotextile, sampling and analysis of samples taken from the engineering sites and the durable factors of geotextile as well as the measures taken to defer the ageing of geotextile, we can come to the following conclusions.

(1) Under the natural insolating conditions, ultraviolet radiation is the decisive factor causing the ageing of polypropylene geotextile; Composite geotextile with terylene fabric on the surface is capable of sheltering ultraviolet radiation and produces remarkable physical protection against ageing; and the ageing resistance of polypropylene geotextile added with hindered amine light stabilizers is superior to ordinary woven polypropylene fabric.

(2) Under the natural insolating conditions, the effect of hindered amine light stabilizers are better than that of terylene fiber to keep out and absorb ultraviolet radiation, which is just contrary to the results of the artificially accelerated ageing tests.

(3) The model of correlativity established on the basis of the ageing law equation and the curves of acceleration can be used to predict the results of the natural insolating tests by way of artificially accelerated ageing tests.

(4) Water mass and sandy soil both have the capability of sheltering geotextile from ultraviolet radiation and, according to the test results, sandy soil of 5 cm thick produces better sheltering effect against ultraviolet radiation than a water mass of 2.0 m thick. The serviceable life of polypropylene under both testing conditions should be more than 50 years.

(5) The serviceable life of geotextile predicted according to the results of field sampling and tests of the geotextile from the two engineering projects didn't exceed 30 years and the main cause for such results was the loss of strength of geotextile developed during the execution of the projects(Zhang and Ye, 2005).

(6) Ageing of geotextile may be deferred when ageing inhibitors are added in the raw materials of geotextile; and covering geotextile with sandy soil in engineering works can reduce or cut off sunlight to effectively protect the geotextile and defer the ageing of geotextile, thus prolonging the serviceable life of the geotextile.

REFERENCES

Yan J, Tao TK, Ding LF (2002) Field Observation Analysis of Geotextile Filter at Zhenjiang Section of Beijing-Hangzhou Grand Canal, Port & Waterway Engineering 2002(3)

Wang DW, Cao GZ (2003) Research on Aging Capability of Geosynthetics, Water Resources and Hydropower Engineering 2003(7)

Hu LW, Dong ZL (2002) Experimental Study of Filter Geotextiles Applied in Shenzhen River Project, Proceeding of the 5th Symposium on Prefabricated

Drainage Engineering, Ocean Press, Beijing, December 2002

Zhang J, Ye GL (2005) Analysis of Durability of Geotextile and Factors Affecting Durability of Geotextile, China Harbour Engineering 2005(1).

Xue YL (2004) Testing and Comprehensive Evaluation of Ageing Resistance of Geotextile, Shanghai New Textile Industry & Appliances Company Ltd., September 2004

Yu ZQ (2002) Report on Field Sampling and Testing of Geotextile Used on Engineering Works at the Hanjiang River and the Jiepai Reach of the Changjiang River, Tianjin Port Engineering Institute, October 2002

ANALYSIS OF ANTI-SLIDING MECHANISM OF GEOSYNTHETIC REINFORCED BEDDING COURSE

A.M. Liu [1], G.L. Ye [2] and C.Z. Huang [3]

ABSTRACT: The anti-sliding mechanism of geosynthetic-reinforced bedding course is proposed on the basis of theoretical deduction and analysis. Because of the tensile property of the geosynthetic-reinforced bedding course, part of the horizontal stress produced by the trunk of a breakwater is undertaken by the geosynthetic-reinforced bedding course to reduce the horizontal stress transmitted to the foundation soil, thus improving the overall stability of the foundation. A method to analyze the slope stability, which takes into consideration the anti-sliding performance of geosynthetic-reinforced bedding courses, was thus derived and was also verified by the results of field measurements and centrifugal model tests.

KEYWORDS: geosynthetic-reinforced bedding course, anti-sliding mechanism, stability analysis, horizontal stress.

FOREWORD

It has become a common understanding in recent years that, for projects with geosynthetic- reinforced bedding courses, the influence of the tensile stress borne by a geosynthetic- reinforced bedding course at the interface of soil mass upon the stability should be considered in the stability analysis. There are already a number of recommended methods for considering the tensile stress borne by a geosynthetic- reinforced bedding course at the interface of soil mass and for analyzing the corresponding stability(Liu et al. 1996; Shen 1998; Chen 2003; Huang et al., 2003). But, as the slide resistance of geosynthetic-reinforced bedding courses is related to multiple factors such as the height of fill material on top of the geosynthetic- reinforced bedding course, strength of foundation soil, tensile strength of the bedding course, etc., the anti-sliding mechanism of geosynthetic-reinforced bedding courses is not very clear. The anti-sliding mechanism of geosynthetic- reinforced bedding courses is further studied and investigated on the basis of the analysis of the results of field measurement and centrifugal model tests.

ANTI-SLIDING MECHANISM OF GEO-SYNTHETIC REINFORCED BEDDING COURSE

When a breakwater is built on soft soil and a geosynthetic- reinforced bedding course is built at the bottom of the breakwater, the anti-sliding mechanism of the geosynthetic- reinforced bedding course is as shown in Fig. 1.

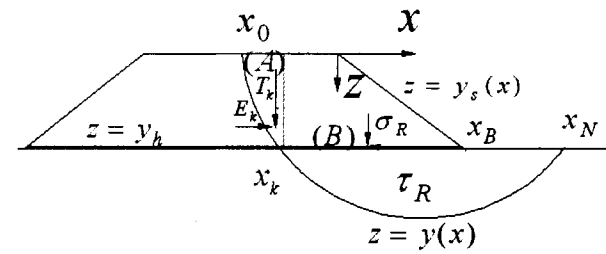

Fig. 1 Schematic Diagram of Anti-sliding Property of geosynthetic- reinforced bedding course

Assuming the surfaces of the breakwater to be $z = y_s(x)$ and the sliding plane to be $z = y(x)$, the part of the trunk of the breakwater and its foundation at $x_0 < x < x_N, y_s(x) < z < y(x)$ enveloped by the sliding plane and the slope of the breakwater will then be divided into (A) and (B) for calculation. It is first assumed that the geosynthetic- reinforced bedding course is of sufficient tensile strength and has a sufficient friction resistance between the bedding course and the underside of the breakwater trunk and between the bedding course and the surface of the foundation so that the geosynthetic reinforced bedding is not pulled broken or pulled out.

In Area (A), besides the gravity force, there should be also the horizontal force E_k and vertical shear force T_k at the interface between (A) and (B), which are generated by the trunk of the breakwater. In Area (B), besides the

[1, 2, 3] Tianjin Port Engineering Institute Ltd. of CCCC First Harbour Engineering Company Ltd., Tianjin 300222, CHINA

gravity force, there should be also the horizontal force E_k and vertical shear force T_k, which are generated by the trunk of the breakwater, as well as the axial tensile stress τ_R and the normal stress σ_R undertaken at each point by the geosynthetic reinforced bedding course. (If the geosynthetic reinforced bedding course is deemed not to bear any normal stress, then $\sigma_R = 0$).

In the trunk of the breakwater and its foundation, the stress components σ_x, σ_z, τ_{xz} should satisfy the equilibrium equation.

$$\left.\begin{aligned}\frac{\partial \sigma_x}{\partial x}+\frac{\partial \tau_{xz}}{\partial z}=0\\ \frac{\partial \sigma_z}{\partial z}+\frac{\partial \tau_{xz}}{\partial x}=\gamma\end{aligned}\right\} \tag{1}$$

At the sliding plane, $z = y(x)$, the relationship of stresses and the yield conditions should be satisfied.

$$\left.\begin{aligned}\sigma y'-\tau=\sigma_x y'-\tau_{xz}\\ \sigma+\tau y'=\sigma_z-\tau_{xz}y'\end{aligned}\right\} \tag{2}$$

$$\tau=\frac{1}{F_s}(c+\sigma\tan\varphi) \tag{3}$$

where, γ is the unit weight of soil while C, φ are the cohesive strength and angle of internal friction respectively.

As is well known, current methods for analysis of slope stability consider only the action of the trunk of a breakwater on its foundation but don't consider the reaction of the foundation on the trunk of the breakwater. Therefore, the earth pressure generated by the trunk of the breakwater is written $E_h=\int_{y_s}^{y_h}\sigma_x\,\mathrm{d}z$ as and $T_h=\int_{y_s}^{y_h}\tau_{xz}\,\mathrm{d}z$.

Based on the equilibrium equation, at any point in the underside of the geosynthetic reinforced bedding course, we have:

$$-\tau_{xz}\big|_{y_{h+}}=\frac{\mathrm{d}E_h}{\mathrm{d}x}-\tau_R \tag{4}$$

$$\sigma_z\big|_{y_{h+}}=\int_{y_s}^{y_h}\gamma dz-\frac{\mathrm{d}T_h}{\mathrm{d}x}+\sigma_R \tag{5}$$

It can be known from Eq. (4) that part of the horizontal stress, $\mathrm{d}E_h/\mathrm{d}x$, (distribution of earth pressure along the surface of the geosynthetic reinforced bedding course), generated by the trunk of the breakwater is borne by the geosynthetic reinforced bedding course, τ_R, while another part of the horizontal stress is transferred to the foundation, $\tau_{xz}\big|_{y_{h+}}$, after the horizontal stress passes through the geosynthetic reinforced bedding course. Assuming the proportion of the horizontal stress borne by the geosynthetic reinforced bedding course is $\eta_x(0\le\eta_x\le1.0)$, we then have

$$\left.\begin{aligned}\tau_R=\eta_x\frac{\mathrm{d}E_h}{\mathrm{d}x}\\ -\tau_{xz}\big|_{y_{h+}}=(1-\eta_x)\frac{\mathrm{d}E_h}{\mathrm{d}x}\end{aligned}\right\} \tag{6}$$

The tensile force taken by the geosynthetic reinforce bedding course at the sliding plane (intersecting point (x_R, y_R) between the geosynthetic reinforce bedding course and the sliding plane) is $T_R=\int_{x_k}^{x_B}\tau_R=\eta_x E_k$.

From Eq. 5, we have also $\eta_y(0\le\eta_y\le1.0)$.

$$\left.\begin{aligned}\sigma_R=\eta_y\frac{\mathrm{d}T_h}{\mathrm{d}x}\\ \sigma_z\big|_{y_{h+}}=\int_{y_s}^{y_h}\gamma\,\mathrm{d}z-(1-\eta_y)\frac{\mathrm{d}T_h}{\mathrm{d}x}\end{aligned}\right\} \tag{7}$$

When considering the balance of the moment of force and after calculating the moment at any point according to Eqs. 4 and 5, we have

$$\begin{aligned}&[(\sigma_z-\int_{y_s}^{y_h}\gamma\,\mathrm{d}z)(x-x_R)-\tau_{xz}(y_h-y_R)]_{y_{h+}}\\ &+[\tau_R(y_h-y_R)-\sigma_R(x-x_R)]_{y_h}\\ &=[\frac{\mathrm{d}E_h}{\mathrm{d}x}(y_h-y_R)-\frac{\mathrm{d}T_h}{\mathrm{d}x}(x-x_R)]_{y_{h-}}\end{aligned} \tag{8}$$

The total moment of force at the underside of the geosynthetic reinforced bedding course in the sliding mass is

$$\begin{aligned}&\int_{x_k}^{x_B}[(\sigma_z-\int_{y_s}^{y_h}\gamma\,\mathrm{d}z)(x-x_R)-\tau_{xz}(y_h-y_R)]\mathrm{d}x\\ &+\int_{x_k}^{x_B}[\tau_R(y_h-y_R)-\sigma_R(x-x_R)]\mathrm{d}x\\ &=-[E_k(y_h-y_R)-T_k(x_k-x_R)-M_{xk}]\end{aligned} \tag{9}$$

where $M_{xk}=[\int_{y_s}^{y_h}(y_h-z)\sigma_x\,\mathrm{d}z]\big|_{x=x_k}$

Eq. (9) indicates that the moment of force generated by earth pressure at the interface of (A) and (B) may be broken into two parts, i.e., one is the moment of force generated by the force transferred into the foundation, and the other is the moment of force generated by the force borne by the geosynthetic reinforced bedding course. There must be $\eta_t(0\le\eta_t\le1.0)$.

$$\begin{aligned}&\int_{x_k}^{x_B}[\tau_R(y_h-y_R)-\sigma_R(x-x_R)]\mathrm{d}x\\ &=-\eta_t[E_k(y_h-y_R)-T_k(x_k-x_R)-M_{xk}]\end{aligned} \tag{13}$$

$$\int_{x_k}^{x_B}[(\sigma_z - \int_{y_z}^{y_h}\gamma dz)(x-x_R)-\tau_{xz}(y_h-y_R)]dx = -(1-\eta_t)[E_k(y_h-y_R)-T_k(x_k-x_R)-M_{xk}] \quad (14)$$

It is obvious that the stress borne by the geosynthetic reinforced bedding course and its moment of force are just part of the earth pressure generated by the trunk of the breakwater and its moment of force while the earth pressure generated by the trunk of the breakwater and its moment of force can be obtained by the limit analysis theory. Therefore, if the method for stability analysis is required to satisfy the equation for the equilibrium of moments, the moments of force resulted from the force borne by the geosynthetic reinforced bedding course can be determined as long as η_t is determined.

The above analyses show that the property of geosynthetic reinforced bedding course to bear the tensile force makes part of the earth pressure by the breakwater taken by the geosynthetic reinforced bedding course, thus reducing the earth pressure being transferred to the foundation and improving the stability of foundation.

As a matter of fact, the anti-sliding property of geosynthetic reinforced bedding course lies mainly in its tensile property and the stability calculation is to reckon in the sum of the tensile stresses of the geosynthetic reinforced bedding course, $T_R = \int_{x_k}^{x_B}\tau_R = \eta_t E_k$, in the sliding mass according the above described anti-sliding mechanism. However, the sum of the tensile stresses is in fact just the part of the earth pressure, sustained by the geosynthetic reinforced bedding course, on the vertical plane at the intersecting point between the sliding plane and the geosynthetic reinforced bedding course.

ENGINEERING PRACTICE OF ANTI-SLIDING MECHANISM AND VERIFICATION BY MODEL TESTING

It is difficult to accurately determine the horizontal force, which is generated by the trunk of the breakwater and borne by the geosynthetic reinforced bedding course. The following discussions are made on the basis of the measured results from practical engineering projects.

In-situ Measurements at Breakwater Site in Huanghua Port and Analysis of Results of Centrifugal Model Tests

The surficial material in the foundation for the breakwater in Huanghua Port is soft cohesive soil with a considerable thickness, where geosynthetics were laid to form a geosynthetic- reinforced bedding course for the project. Tianjin Port Engineering Institute Limited of CCCC First Harbour Engineering Co. Ltd. carried out in-situ monitoring and measurements during the construction of the breakwater(Zeng 2002) and, when the placement of fill for the trunk of the breakwater was completed (Fig. 2), the distribution of tensile force of the geosynthetic reinforce bedding course along the cross-section of the breakwater was measured (The four cross sections of the breakwater for monitoring and measurements were identical to each other and only the thickness of the trunk of the breakwater is slightly different). The measured results of the tensile force in the geosynthetic reinforced bedding course and the calculated results of the earth pressure on the corresponding measured points are as given in Table 1. Furthermore, Hydraulic Engineering Department of Tsinghua University and China Communications Planning and Design Institute for Waterway Transportation carried out also the centrifugal model tests and the numerical simulation computation. The calculated results are also given in Table 1.

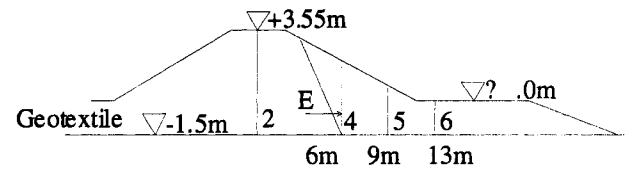

Fig.2 Schematic Diagram of Measuring Points for Measurement of Tensile Force of Geosynthetic Reinforced Bedding Course for Breakwater in Huanghua Port

At Measuring Points Nos.2 and 4, the measured tensile forces of the geosynthetic reinforced bedding course at Section 1-1 and Section 2-2 were about 50% of the earth pressure while the measured tensile forces of geosynthetic reinforced bedding course at Section 3-3 and Section 4-4 were obviously small. , which should be resulted from the poor takeup of the geosynthetic reinforced bedding course as the geological conditions at Section 3-3 and Section 4-4 were basically the same as that at Section 1-1 and Section 2-2 and the trunk of the breakwater was even slightly higher than the breakwater section at Section 1-1 and Section 2-2.

At Measuring Point No. 5, the measured tensile force of the geosynthetic reinforced bedding course was close to the earth pressure.

At Measuring Point No. 6, the average value of the measured tensile force of the geosynthetic reinforced bedding course was slightly higher than the earth pressure, indicating that the geosynthetic reinforced bedding course undertook also the horizontal force resulted from the lateral displacement of the soil mass.

Table 1 Measured Results of Tensile Force of Geosynthetic Reinforced Bedding Course and Calculated Results of Earth Pressure for Breakwater in Huanghua Port

	Measuring Point No. 2		Measuring Point No. 4		Measuring Point No. 5		Measuring Point No. 6	
	Measured Tensile Force (kN/m)	Calculated Value of E_k (kN/m)	Measured Tensile Force (kN/m)	Calculated Value of E_k (kN/m)	Measured Tensile Force (kN/m)	Calculated Value of E_k (kN/m)	Measured Tensile Force (kN/m)	Calculated Value of E_k (kN/m)
Section 1-1	15.3	26.0	6.60*	12.2	3.90	4.57	3.60	2.72
Section 2-2	11.2	23.0	5.20	10.3	5.60	3.41	3.80	1.85
Section 3-3	6.24	29.1	4.60	14.4	5.10	5.90	3.50	3.77
Section 4-4	6.70	27.0	4.20	12.9	3.90*	4.99	3.50	3.06
Average	9.86	26.3	5.40	12.5	4.60	4.72	3.60	2.85
Numerical Simulation	17.0		13.0		4.0		2.0	

(Note: E_k is calculated with Rankine's Equation for active earth pressure on the basis of the average value of the design high and low water level. The numerical value marked with* was achieved by interpolation with adjacent points.)

Analysis of In-situ Measured Results at East Breakwater Site in Qianwan Workboat Basin, Qingdao

When the fill for the trunk of the east breakwater in Qianwan Workboat Basin, Qingdao, was filled up to $\nabla + 2.5$ (Fig. 3), the tensile force of the geosynthetic reinforce bedding course was measured and the earth pressure at the corresponding locations was calculated (Zeng 2001). The measured tensile force of the geosynthetic reinforced bedding course and the calculated results of the earth pressure on the corresponding measured points were as given in Table 2.

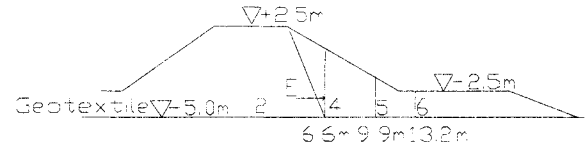

Fig. 3 Schematic Diagram of Measuring Points for Measurement of Tensile Force of Geosynthetic Reinforced Bedding Course at Section 1-1 of East Breakwater in Qianwan Workboat Basin, Qingdao

Table 2 Measured Results of Tensile Force of Geosynthetic Reinforced Bedding Course and Calculated Results of Earth Pressure on the foundation of East Breakwater in Qianwan Workboat Basin, Qingdao

	Measuring Point No. 2		Measuring Point No. 4		Measuring Point No. 5		Measuring Point No. 6	
	Measured Tensile Force (kN/m)	Calculated Value of E_k (kN/m)	Measured Tensile Force (kN/m)	Calculated Value of E_k (kN/m)	Measured Tensile Force (kN/m)	Calculated Value of E_k (kN/m)	Measured Tensile Force (kN/m)	Calculated Value of E_k (kN/m)
Section 1-1	11.0	43.6	9.50	30.7	9.20	16.6	6.00	5.90

At Measuring Points Nos. 2 and 4, the measured tensile force of the geosynthetic reinforced bedding course was obviously small, which was similar to the measured results of the geosynthetic reinforced bedding course at Section 3-3 and Section 4-4 of the breakwater in Huanghua Port. The measured tensile force of the geosynthetic reinforced bedding course at Measuring Points No. 5 was slightly higher than 50% of the earth pressure while the measured tensile force of geosynthetic reinforced bedding course at Measuring Points No. 6 was close to the earth pressure.

Analysis of Sliding Resistance

It should be first pointed out that the measured tensile force of the geosynthetic reinforced bedding courses as described above was obviously smaller than the tensile strength (the design tensile strength was 45 and 57.1 kN/m respectively). As a matter of fact, the tensile performance of the geosynthetic reinforced bedding courses hadn't been brought into full play because of the stability of the foundations. and the measured tensile

force of the geosynthetic reinforced bedding courses was certainly smaller. The centrifugal model tests for the breakwater in Huanghua Port proved that "the tensile force of the geosynthetics measured at the axial symmetry of the breakwater was 90 kN/m when the acceleration came to the ultimate acceleration (which was the acceleration at failure) ".

The results of the stability analysis indicated that the intersecting point of the riskiest slip arc with the geosynthetic reinforced bedding course was close to Measuring Point No. 2 and the vertical position of the center of the circular arc was basically identical with the height of fill in the breakwater. Considering that the method of stability analysis satisfied the equilibrium of moments, the moment arm of the geosynthetic reinforced bedding course to the center of the circular arc was the height of the fill while the moment arm of E_k to the center of the circular arc was about 2/3 of the height of the fill. When κ is written as the ratio of the moment of the tensile force of the geosynthetic reinforced bedding course to the center of the circular arc to the moment of E_k to the center of the circular arc, the ratio of the above said two projects was $\kappa = 0.56$ (average) and $\kappa = 0.38$ respectively and the average ratio of the five cross sections of the two projects was $\kappa = 0.53$.

Therefore, the anti-sliding mechanism of geosynthetic reinforced bedding course is rational that part of the earth pressure generated by the breakwaters is borne by the geosynthetic reinforced bedding course, thus reducing the earth pressure transferred to the foundation and improving the stability of the foundation. It is rational and authentic to adequately select η_t and consider the actual anti-sliding performance of geosynthetic reinforced bedding course by using $\eta_t E_k$.

ANALYSIS OF RESULTS OF STABILITY CALCULATIONS

It is easy to obtain methods for stability analysis that are commonly used in engineering projects, which take into consideration the anti-sliding performance of geosynthetic reinforced bedding courses, in accordance with the above described anti-sliding mechanism and limit equilibrium method. Actually, for a common method to analysis the stability of slopes, a calculation method, which considers the anti-sliding performance of the geosynthetic reinforced bedding courses can be obtained as long as the anti-sliding moment and the slip moment generated by the part of circular arc above the surface of a geosynthetic reinforced bedding course is multiplied by a coefficient of $(1-\eta_t)$ .For instance, the equation using the simplified slicing method, which takes into consideration the anti-sliding performance of a geosynthetic reinforced bedding course, is given below.

$$F_s = M_r / M_0 \tag{15}$$

$$M_\gamma = (1-\eta_t)\sum_{i=1}\int_{x_{i-1}}^{x_i}[w_{\gamma i}\tan\varphi_i + c_i(1+y'^2)](y-y_R)\,\mathrm{d}x + \sum_{i=k+1}\int_{x_{i-1}}^{x_i}[w_{\gamma i}\tan\varphi_i + c_i(1+y'^2)](y-y_R)\,\mathrm{d}x \tag{16}$$

$$M_0 = (1-\eta_t)\sum_{i=1}\int_{x_{i-1}}^{x_i} w_{\gamma i}(y-y_R)y'\,dx + \sum_{i=k+1}\int_{x_{i-1}}^{x_i} w_{\gamma i}(y-y_R)y'\,dx \tag{17}$$

Where, F_s is the safety factor, M_r, M_0 are the anti-sliding moment and the slip moment respectively, and w_{ri} is the gravity per unit width of slice i When $i \le k$, the sliding plane passes through the trunk of the breakwater.

The way that Eqs. 16 and 17 are written is to facilitate the calculation of the safety factors, which can be wholly rewritten respectively as

$$M_\gamma = \sum_{i=1}\int_{x_{i-1}}^{x_i}[w_{\gamma i}\tan\varphi_i + c_i(1+y'^2)](y-y_R)\,\mathrm{d}x + \eta_t F_s \sum_{i=1}^{k}\int_{x_{i-1}}^{x_i}[w_{\gamma i}y' - (w_{\gamma i}\frac{\tan\varphi_i}{F_s} + \frac{c_i}{F_s}(1+y'^2))](y-y_R)\,\mathrm{d}x \tag{18}$$

$$M_0 = \sum_{i=1}\int_{x_{i-1}}^{x_i} w_{\gamma i}(y-y_R)y'\,dx \tag{19}$$

Hence, it can be clearly seen that

$\sum_{i=1}^{k}\int_{x_{i-1}}^{x_i}[w_{\gamma i}y' - (w_{\gamma i}\frac{\tan\varphi_i}{F_s} + \frac{c_i}{F_s}(1+y'^2))](y-y_R)\,\mathrm{d}x$ is just the moment of force generated by the earth pressure from the trunk of the breakwater while

$w_{\gamma i}y' - (w_{\gamma i}\frac{tg\varphi_i}{F_s} + \frac{c_i}{F_s}(1+y'^2)$ is the distribution of lateral earth pressure along the sliding plane in the simplified slicing method. Based on the equilibrium of the horizontal force, we have,

$$\sum_{i=1}^{k}\int_{x_{i-1}}^{x_i}[w_{\gamma i}y' - (w_{\gamma i}\frac{\tan\varphi_i}{F_s} + \frac{c_i}{F_s}(1+y'^2))]\,\mathrm{d}x = E_k \tag{20}$$

The following factors should be taken into consideration when parameter, η_t, is determined.

Firstly, as the deformation of foundation makes the geosynthetic reinforced bedding course non-horizontal, it is noticed that the anti-sliding performance of the geosynthetic reinforced bedding course is mainly the axial tensile resistance. Part of the earth pressure should be transferred to the foundation soil.

Secondly, the takeup of the geosynthetic reinforced bedding course and the void space of the geosynthetics (like geogrid) should be considered. When the geosynthetic reinforced bedding course is not fully taken

up or there are voids in the synthetics, there is also part of the earth pressure transferred to the foundation soil.

Furthermore, the magnitude of the calculated value of a safety factor should be considered. The calculated results show that, when η_t is determined, the higher the safety factor is, the more significant the anti-sliding performance of the geosynthetic reinforced bedding course will be. This is because the total tensile force borne by the geosynthetic reinforced bedding course is $T_R = \int_{x_k}^{x_g} \tau_R = \eta_t E_k$ while E_k is the earth pressure when $\bar{c} = c / F_s$ and $\tan\bar{\varphi} = \tan\varphi / F_s$. When F_s is smaller (≤ 1.0), $\bar{c}$ and $\bar{\varphi}$ are enlarged, thus reducing E_k .As a result, the tensile force sustained by the geosynthetic reinforced bedding course is reduced and the anti-sliding performance of the geosynthetic reinforced bedding course becomes low as well. On the contrary, when F_s is greater (≥ 1.0) , the anti-sliding performance of the geosynthetic reinforced bedding course is enhanced. However, the fact is that, when F_s is greater (≥ 1.0) , the foundation generally deforms less and the geosynthetic reinforced bedding course must be poorly taken up, thus the part of earth pressure transferred to the foundation soil becomes greater and the anti-sliding performance of the geosynthetic reinforced bedding course becomes low.

The above three influential factors are so interrelated that, if the foundation deforms greatly, the geosynthetic reinforced bedding course must have been better taken p and the safety factor is relatively small.

The calculated results with the above method are compared with the results of the "Dutch Process" (simplified slicing method taking in the moment of force of the tensile strength of the geosynthetic reinforced bedding course) as given in Table 3.

Table 3 Comparison of Calculated Results of Safety Factors for Stability

Name of Project	Strength Index Adopted	Tensile strength of geosynthetic course kN/m	Safety factor without considering geosynthetic course	"Dutch Process"		$\eta_t = 0.5$		$\eta_t = 0.75$	
				Safety Factor	Increased by (%)	Safety Factor	Increased by (%)	Safety Factor	Increased by (%)
Breakwater for Huanghua Port	Vane shear strength	45	0.906	1.132	24.9	1.035	14.2	1.141	25.9
East Breakwater in Qianwan, Qingdao	Quick shear strength	57.1	0.950	0.992	4.42	1.048	10.3	1.086	14.3
North Breakwater in Qianwan, Qingdao	Quick shear strength	57.1	0.973	1.015	4.38	1.020	4.83	1.043	7.19
Cofferdam for Phase V of Nanjiang Port Area, Tianjin	Quick shear strength	50.0	0.911	0.976	7.13	1.002	9.99	1.060	16.4
Revetment for Huanghua Chemical Products Terminal	Vane shear strength	56.7	0.988	1.056	6.88	1.071	8.40	1.121	13.5

Note: Increment of strength of soil mass with the process of loading has been considered in the calculations.

The calculated results for the five projects given in above Table 3 are analyzed as follows.

If $\eta_t = 0.5$, it agreed with the anti-sliding performance $\kappa = 0.56$ of the geosynthetic reinforced bedding course for the breakwater for Huanghua Port according to the measured tensile force of the bedding course. At this point, the safety factor of the breakwater for Huanghua Port was reduced by 10.7% when compared with the result obtained by using the "Dutch process" while for the other four projects, the safety factors increased averagely by 8.4% when compared with the results derived without taking into consideration the performance of the geosynthetic reinforced bedding course and increased averagely by 2.7% when compared with the results obtained by using the "Dutch process".

When $\eta_t = 0.75$, the result obtained by using the "Dutch process" for the breakwater in Huanghua Port was basically identical with the calculated results derived with the method presented in this paper while for the other four projects, the safety factors increased averagely by 12.8% when compared with the results derived without taking into consideration the performance of the

geosynthetic reinforced bedding course and increased averagely by 7.1% when compared with the results obtained by using the "Dutch process". When the anti-sliding performance of the geosynthetic reinforced bedding course was not taken into consideration, the safety factors ranged from 0.906—0.988 and, after the anti-sliding performance of the geosynthetic reinforced bedding course was taken into consideration, the safety factors were increased to 1.043—1.141, which was identical with the actual stability of the foundations.

Therefore, it is safe to take $\eta_t = 0.5$ and credible to take $\eta_t = 0.75$.

Generally, the safety factors derived in accordance with the above methods of stability analysis for the anti-sliding mechanism of geosynthetic reinforced bedding courses have the following characteristics.

(1) With the same foundation conditions, the higher the trunk of the breakwater is, the greater the anti-sliding performance of the geosynthetic reinforced bedding courses will be. This is because, when the trunk of the breakwater is high, the greater the horizontal force generated by the trunk of the breakwater is, the greater the tensile force sustained by the geosynthetic reinforced bedding courses will be.

(2) The shallower the sliding plane is, the greater the anti-sliding performance of the geosynthetic reinforced bedding courses will be. This is because, when the trunk of a breakwater is determinate, the anti-sliding performance of the geosynthetic reinforced bedding courses changes a little with the depth of the sliding plane but the anti-sliding moment and the moment of sliding which do not reckon the anti-sliding performance will change significantly with the depth of the sliding plane. The deeper the sliding plane is, the greater the anti-sliding moment and the moment of sliding which do not reckon the anti-sliding performance will be.

CONCLUSIONS

1. Owing to the tensile property of the geosynthetic reinforced bedding course, part of the horizontal stress generated by the trunk of the breakwater is borne by the geosynthetic reinforced bedding course, thus reducing the horizontal stress transferred to the foundation soil and improving the overall stability of the foundation.

2. The measured results of the tensile force of the geosynthetic reinforced bedding courses on two practical engineering projects (with the measurements made at 5 cross sections) and the results of the centrifugal model tests and the numerical simulations proved that the anti-sliding mechanism presented in this paper is correct.

3. Assuming that the ratio of the earth pressure by the trunk of the breakwater to be borne by a geosynthetic reinforced bedding course is η_t, we can obtain a method for analyzing the slope stability that takes into consideration the anti-sliding performance of the geosynthetic reinforced bedding course. The commonly used methods for analyzing the slope stability can all be used to carry out the calculations which take into consideration the anti-sliding performance of the geosynthetic reinforced bedding course. It is only required that the anti-sliding moment and the sliding moment generated on the circular arc above the surface of the geosynthetic reinforced bedding course are multiplied by the coefficient of $(1-\eta_t)$.

4. The analyses of the calculated results of the 5 practical projects show that the calculated results achieved by using the method of stability analysis taking into consideration the anti-sliding performance of the geosynthetic reinforced bedding course, which was based on the anti-sliding mechanism of the geosynthetic reinforced bedding course given in this paper, reflect basically objectively the anti-sliding performance of the geosynthetic reinforced bedding course. The method is simple and practicable and the results of calculation can be directly comparable with that achieved by using the method (taking no consideration of the anti-sliding performance of the geosynthetic reinforced bedding course) specified in the Code for Soil Foundations of Port Engineering (JTJ250-98) and may be used directly for practical engineering works.

REFERENCES

Chen HJ (2003) Discussion on Methods for Stability Analysis of Geosynthetics on Soft Foundation below Dams and Breakwaters, Proceedings of Forum on National Geotexile Engineering in 2002, Modern Knowledge Press, November 2003

Huang CZ, Miao ZH, Yu ZQ, Sun WH (2003) Anti-Sliding Performance of Geosynthetic Reinforced Bedding Course and Method for Stability Analysis of Slopes, Proceedings of Forum on National Geotexile Engineering in 2002, Modern Knowledge Press, November 2003

Liu JF, Gong XN, Wang SY (1996) Method for Stability Analysis Taking into Consideration Anti-Sliding

Effect of Geosynthetics, Ground Improvement (published by Zhejiang University, China), 7(2)

Shen ZJ (1998) Limit analysis of soft ground reinforced by geosynthetics, Chinese Journal of Geotechnical Engineering, 1998(4):82-86

Zeng XT(2001), Report on Field Monitoring and Measurement of East Breakwater for Qianwan Workboat Basin in Qingdao, Tianjin Port Engineering Institute, September 2001

Zeng XT (2002) Report on Field Monitoring and Measurement of Breakwater for Huanghua Port, Tianjin Port Engineering Institute, August 2002

DRAINAGE STRUCTURE OF THE GEOSYNTHETICS PREVENTING THE BACK-DIKE SILTY SOIL FROM DISPERSED IMMERSION DESTRUCTION

B. Zhang[1], X.M. Qu[2] and A.L. Yuan[3]

ABSTRACT: The silty soil dike section takes about 1/3 of the total length of Songhua River dike. The serious dangers of the 1998 superflood all took place at these sections. The dispersed immersion destruction of the back-dike silty soil is one of the main destructive phenomena. This article presents the structures and designs of the geosynthetics preventing the silty soil dike from the dispersed immersion destruction with the danger removing and reinforcement projects of Songhua River dike.

KEYWORDS: Geosyntheticsgeosynthetics, silty soil, dispersed immersion, drainage structure

INTRODUCTION

At the time of the Songhua River flood in 1998, the dispersed immersion and slopeslide took place in many back-embankment sections of the Songhua River dikes made up of silty soil. For example, the famous Pangtou Pool breach in Zhao Yuan County is a burst by silty dike overtopping, while the dike turned out serious dispersed immersion and slopeslide 1.5 km from the breach, its main characteristic is the irregular scarp in the appearance and the slump slight slope at the back of the scarp, see Fig. 1. The silty soil at the foot of the slump slight slope is at the saturation state and at a very soft state in a certain depth. Since for a long time silty soil is suffering from freeze- thaw action in the winter and the rainfall erosion in rainy season, its density and internal moisture distribution are quite uneven and in its surface dispersed immersion scope, the down slope convergent seepage appeared and collapse and aperture formed in partial places. While silty soil f=20°—60°, k=10^{-3}—10^{-4} m/s, its anti-seepage gradient is very small, the allowable gradient is only 0.05 — 0.07, which almost has no cohesion, the washing resistance ability is very low and its allowable washing resistance speed is about 0.25—0.75 m/s, so under the current effect inside the dike, the dispersed immersion problem is very likely to happen. Because of the dispersed immersion and slopeslide, the effective section of back dike is reduced; it even reduces the height of levee crest, while the reduction of the section makes the dispersed immersion more serious, this vicious circle causes the burst of the dike. In the danger removing and reinforcement design of recent years, we take the geosynthetics as the drainage body to prevent the destruction of silt dike dispersed immersion.

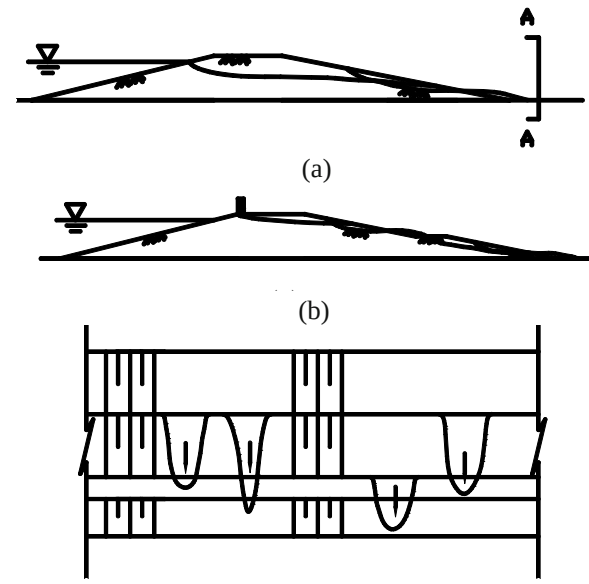

Fig. 1 Dispersed immersion destruction of the back-dike slope

MAIN GEOSYNTHETICS FOR PREVENTING THE DISPERSED IMMERSION DESTRUCTION

In the design of the drainage project, the geo-synthetics are all kinds of drain pipes, drainage board etc. In the danger removing and reinforced design of the Songhua River main stream silty dikes, they take not only the geosynthetics like geotextile, geomembrane and geocomposites made of geomembrane etc., but also new

[1] Professor, Heilongjiang Hydraulic Research Institute, Harbin, CHINA. Email: hljzhb@126.com
[2] Professor, Heilongjiang Hydraulic Research Institute, Harbin, CHINA
[3] Engineer, Heilongjiang Hydraulic Research Institute, Harbin, CHINA. Email: yuna19760822@163.com

materials like the soft drain pipe, complex drainage board, etc..

(1) The soft drain pipe is a kind of flexible pipe, which has a good property of suiting the foundation deformation and convenient for connection in construction. It takes the high tensile steel wire loop as the support, while the outside is enclosed with geotextile which has the function of reverse filter, moreover, the outside of the high tensile steel wire loop as the support is enclosed with PVC plastics, which is resistance to aging. As the drainage body of the silty dike, its main technical index should be seen at Table 1.

Table 1 The technical index of soft drain pipe

Property index	Unit	Index
Filtration coefficient	cm/s	$\geq 10^{-2}$—10^{-3}
Equivalent opening size	mm	0.17—~0.20
Internal diameter	mm	50—200

(2) The complex drainage board is one layer of geonet between two layers of geotextile like a sandwich. This kind of material has the functions of reverse filter, isolation and strong drainage. When the water enters into the interlayer, in the freeze- thaw condition, its function is very obvious. So it is a very ideal compound material when the drainage operation is needed in the silty dike. As the drainage body of the silty dike, its main technical indexes are at Table 2.

Table 2 The technical index of the compound drainage board

Property index	Unit	Index
Filtration coefficient	cm/s	$\geq 10^{-2}$—10^{-3}
Equivalent opening size	mm	0.10—0.15
Thickness	mm	≥10

DESIGN OF PREVENTING THE SILTY DIKE BACK SLOPE FROM DISPERSED IMMERSION DESTRUCTION

The main measure of preventing the silty dike back slope from dispersed immersion destruction is the drainage body design of the back slope and the ability of drainage body must be strong enough. In the reinforcement design of the main stream dike of Songhua River, it adopted the structure of geosynthetics drainage body.

The first principle of the design is to ensure the drainage ability of the drainage body and guarantee the seepage in the drainage body is unconfined seepage flow: and the second principle is to ensure the contacting seepage will not occur in the drainage body.

Design methods (Jie Liu 2005)

The size determination of the drainage body

For the horizontal drainage body, according to the seepage discharge entering into the drainage body, it should be calculated according to the Dupult formula:

$$q = \frac{k_2 h_3^2}{2L_3} \tag{1}$$

$$q = q_2 + q_3 \tag{2}$$

$$T_3 = 1.5h_3 \tag{3}$$

In this formula, q_2; q_3 represents separately the overall seepage discharge per unit width of the dike and is determined by the calculation of seepage discharge filed:k_3 and $h_3$are the seepage coefficients of horizontal drainage body and acting head separately: T_3 is the thickness of the drainage body. All the factors can be seen at Fig. 2.

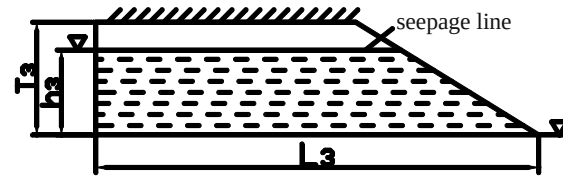

(a) Horizontal drainage body

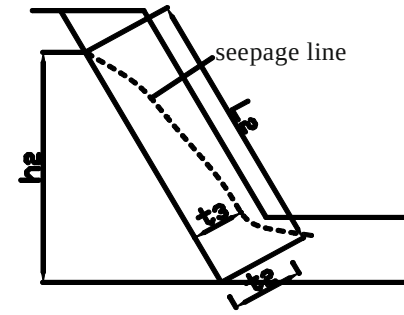

(b) Vertical drainage body

Fig. 2 Design factors of drainage body

If the seepage discharge and seepage coefficient of drainage body are known, we can fix the possible water head of the drainage body according to the following formula, that is:

$$h_3 = \sqrt{\frac{2L_3 q}{k_3}} \tag{4}$$

The seepage coefficient of the drainage body system is:

$$k_3 = 2.34 n^3 d_{20}^2 \tag{5}$$

In this formula: n is the porosity of the water drainage material: d_{20} is equivalent particle diameter (opening size).

For the vertical drainage, the drainage ability of the drainage body is determined by the following formula:

$$q_2 = k_2 i_2 A_2 = k_2 i_2 t_2 \cdot 1 = k_2 i_2 t_2 \tag{6}$$

Among them

$$i_2 = h_2 / L_2 \tag{7}$$

$$t_2 = \frac{q_2 L_2}{k_2 h_2} \tag{8}$$

Value $T_2 = 1.5 t_2$ (9)

In this formula: k_2, A_2 represents separately the seepage coefficient of the drainage body and the discharge area of the bottom seepage; T_2 is the vertical thickness of the drainage body:1.5 is the safety coefficient: L_2 is the length of the overflow section.

To ensure the contacting washing not occur, we need to check the possibility of contacting washing of the reverse filter layer and drainage body in the longitudinal current condition, that is:

$$J_K \le J_{K \cdot g} \tag{10}$$

$$J_K = (5 + 16.5 \frac{d_{10}}{D_{20}}) \frac{d_{20}}{D_{20}} \tag{11}$$

In this formula, D_{20} is the equivalent particle diameter of drainage body; d_{20} is the equivalent particle diameter of adjacent reverse filter layer: J_k is the hydraulic gradient between the reverse filter layer and drainage layers; $J_{k \cdot g}$ is the contacting washing allowable hydraulic gradient between the drainage body and silt soil.

THE STRUCTURE OF THE GEOSYNTHETICS PREVENTING THE DISPERSED IMMERSION OF SILTY DIKES

In the danger removing and reinforcement design of silty soil dikes after the Songhua River flood, in order to solve the dispersed immersion problem of the back dike, on the premise of meeting the above design requirements, we adopted the new type geosynthetics as the drainage body and have attained very good results in the application in the protection projects of Songhua River and Nenjiang dikes in Zhaoyuan County and Dumeng County of Heilongjiang province.

ts main structural forms should be seen at Figs. 3 and 4.

(a) Drainage at the back dike

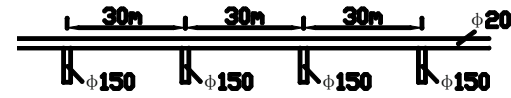

(b) The drainage plane layout of the back dike

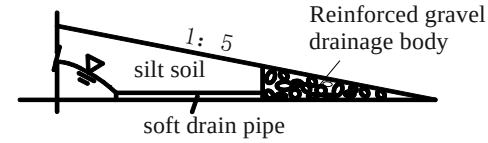

(c) Back-dike drainage enlarged drawing

Fig. 3 The soft drain pipe structure of silty soil dike back slope

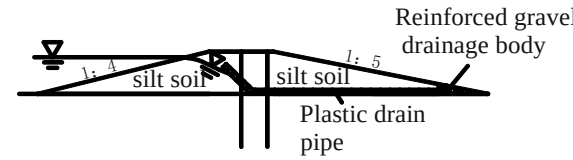

Fig. 4 The compound drainage board structure of silty soil dike back slope

CONCLUSIONS

The structures of the geosynthetics preventing the silty soil dike from the dispersed immersion destruction have been applied to the Songhua River and Nenjiang

River silty soil dike projects in Zhaoyuan County andDumeng County of Heilongjiang Province. The results can be concluded as below:

(1) The soft drain pipe and the complex drainage board applied to the back-dike can satisfy the drainage need of the silty soil by calculating and verifying.

(2) The long-term effect of the two kinds of structures needs more observation because they have not been proved in the flood.

(3) The durability of the soft drain pipe and the complex drainage board should be proved in the practical projects when they suffer the freeze-thaw cycle in winter.

REFERENCES

Liu J (2005) The control theoretical basis and engineering experience and lessons of the earth and rockfill dam Seepage. China Waterpower Press, Beijing

Wang Z (2002) The application of geosynthetic material at abroad. Modern Knowledge Press, Hong Kong

.

INTEGRATION AND DEMONSTRATION OF SAND DIKES ECOLOGICAL PROTECTION TECHNOLOGY

X.M. Qu[1], J.L. Shu[2] and F.P. Wu[3]

ABSTRACT: 1/3 of the main stream dikes of Songhua River are composed of silty soil. In 1998 the superflood of the Songhua River, a great deal of dangers came about from these dikes constructed with silty soil, this article focusing on the destructive condition of the "sand dikes" of Songhua River makes an integration of the Geocell Reinforced Gravel soil and 3D geonet technology and the ecological protection, and combining the engineering practice, it discuss a new ecological protection technology of the sand dikes.

KEYWORDS: sand dike, ecological protection, geocell, 3D geonet

INTRODUCTION

In 1998, Songhua River broke out the superflood that had never been seen for century, the sand dikes of the two banks of Nenjiang Rriver and Songhua River came about a great deal of danger and caused dike breach, which brought tremendous losses. After the flood, the main stream dikes were given thorough danger removing and reinforcement. But for the restriction of regional conditions, most of the country dikes, especially the sand dikes section built with silty soil are still in dangers. Most of them are suffering from the effect of wind and rain erosion and the winter freeze-thaw cycle. When the flood occurring, they have a difficulty in resisting the long time steeping and wave erosion, the embankment foundation downcutting, the failure slope, liquefaction, seepage and piping effect are liable to happen, even dike breach, which seriously weakens the flood protection ability of dikes. Therefore, the research on the new technology which is suitable for sand dike protection has become our first mission.

GENERAL SITUATION OF THE DEMONSTRATION PROJECT

Project Site Selection

Zhaoyuan county of Heilongjiang province is situated at Daqing oil field edge region of the downstream of Nenjiang River and the upstream of Songhua River main stream; it belongs to the Songnen Plain hinterland and has 110.41 km dikes, which protects 1.34 million mu area of land. For historical reasons, the dike flood prevention standards are very low. The trial demonstration project chooses the Songhua River stem dike Wang Yuncheng dike section, which is 2km away of the Zhaoyuan county western suburbs, this dike section is at the river bend position, when the flood coming, the current will erode the dike and also for the broad water surface before the dike and against wind and wave, it is easy to be stroked by wind and waves and becomes dangerous dike section.

Engineering Geology

The demonstration dike section geology situation possesses typical representation in the whole Songhua River dike protection, the embankment soil is silty soil, and the particle analysis is at Table 1.

Table 1 The soil sample particle analysis and organic testing chart of Wang Yuncheng dike section

Organic content %	Sediment percentage%	Soil particle proportion	Soil particle composition							Engineering classification
			Gravel	Sand				Silt	Clay	
			Fine	Coarse	Medium	Fine	Ultra fine			
			Grain diameter size（mm）							
			4－2	2.0－0.5	0.5 －0.25	0.25 －0.075	0.075 －0.05	0.05 －0.005	＜0.005	
			%	%	%	%	%	%	%	
0.34	21.5	2.65	1.5	10.	40.0	27.0	21.5			silty soil

[1] Professor, Heilongjiang Provincial Hydraulic Research Institute, CHINA. Email: hljzhb@126.com
[2] Engineer, Heilongjiang Provincial Hydraulic Research Institute, CHINA.
[3] Senior Engineer, Heilongjiang Provincial Hydraulic Research Institute, CHINA.

Slope Protection Scheme Selection

Traditional rivers dike protection can adopt slope protection project measures like dry pitching, fabricform and concrete panel etc to increase the anti scour capability of its dike slope surface. Towards this kind of condition of the trial project dike section, for the dike body is filled with silty soil and it is situated at the bottomland of the riverbed, the flood cross section is very broad, a great deal application of engineering measures is difficult to implement. According to the comparison of many schemas, we adopt ecological protection technology and combine new type geo-synthetics to construct ecological protection system and enhance the ability of beach protection and accretion promotion when the flood comes: prevent or reduce the erosion and scouring on sand dike surface by wind, waves and current, which not only safeguards the flood flowing safety of dike projects, but also improves the ecological environment. Ensuring the demonstration project upstream slope protection structure takes the following two slope protection schemes:

0+200—0+380 dike section adopts the geocell filled with gravel soil ecological slope protection

0+380—0+540 dike section adopts the 3D geonet grass ecological slope protection

ECOLOGICAL SLOPE PROTECTION TECHNOLOGY DESIGN

The Cross Section Design of Dike Body

As the material of constructing the dike is clayey sand, whose pervious bed thickness is 2—3 m, osmotic coefficient is approximately 1×10^{-4} cm/s， which is comparatively large. In addition, the anti scour capability of sand dike body is very low, its allowable anti scour flow velocity is 0.25—0.75 m/s， considering the seepage stability requirements and the current dike body shape, the design adopts the wide cross section dam type and a gentle incline ratio scheme. The design sizes of the dike body are: the design slope ratio of upstream slope ecological slope protection and downstream slope spraying grass slope protection are all 1:3, the levee crest and berm design width are all 6m, the design elevation of the levee crest is 131.30 m and the design elevation of berm is 129.30 m, the height difference of levee crest and berm is 2 m.(see Fig. 1).

The geocell filled with gravel soil ecological slope protection structure

The geocell is a kind of 3D network structure formed by the high molecular polymeric sheet through strength weld. Before using they are closely folding together, so as to make the transportation convenient. The geocell frame welding distance is 90 cm, the geocell frame height is 20 cm, and the folding length of it is 6 m. In the course of construction, after paving geotextile on the dike slope, pull the geocell into the network shape with manual work and fasten it on the dike slope with steel rivet. And fill the geocell with gravel and soil, so as to form the geocell filled with gravel soil ecological slope protection structure. Its structure design characteristics are:

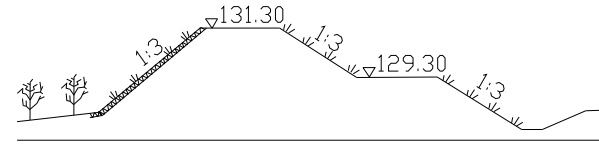

Fig. 1 Vegetation slope protection structure schema (Height: m Length: cm)

The Ecological Slope Protection Structure Design

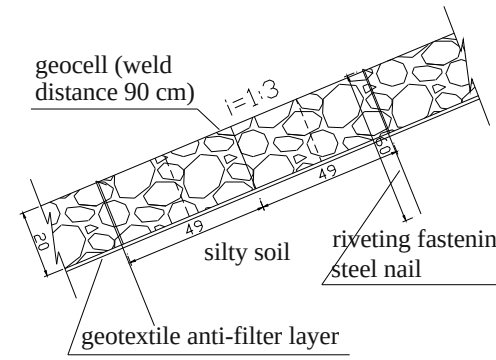

Fig. 2 Construction drawing of Geocell filled with gravel soil slope protection

(1) Adopting the geocell as the main frame can make full use of its good integrated slope protection capability. Put gravel soil into the geocell, the gravity stability of gravel will be interrelated with the wholeness of geocell, so as to achieve the goal of effective slope protection.

(2) The gravel soil put into every independent sealing geocell can ease the water erosion and slow down the scouring of the wind and wave on the slope surface, so as to attain the effect of slope protection stability.

(3)The grain diameter of graduation gravel in the geocell is 3—8 cm, the hole is silted with planting soil, the gravel surface can be grown green vegetation, the slope vegetation can react as reinforcing soil and slowing down the water scouring and the anti-filter of seeping water, at the same time, it increases the landscape effect.

(4) The plane flexibility of the geocell is very good; it can suit the influence of the freeze-thaw cycle on the

dike surface frost heave and thaw settlement deformation.

3D geonet grass ecological slope protection structure

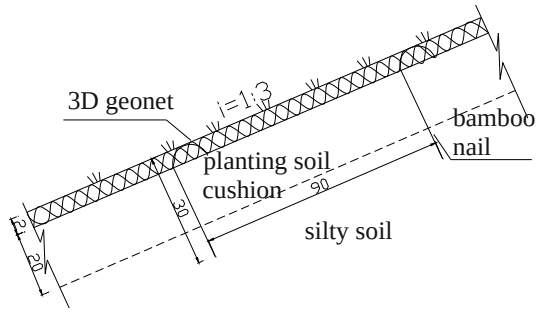

Fig. 3 Construction drawing of 3D geonet grass slope protection (cm)

3D geonet is composed of laminated plastic concav convex waveform nets. Its material is loose and flexible, and it leaves 90% space for soil filling, which can make the seed and surface soil stay in the stereoscopic graticule. For the geonet surface is of irregularity, it can make the wind and current produce innumerable whirlpool on the geonet surface to take the cushioning and dissipation of energy effect and prompt the carrier deposit in the geonet, this can effectively avoid the seed and seedling be lost through rain washing and greatly increase the vegetation coverage rate. Its structural characteristics are:

(1)Pave the 3D geonet on the after trimming dike slope and fasten them on the slope surface with bamboo nail riveting, then spray perennial seed on the slope surface and cover it with planting soil, watering and maintaining them to make them sprout and grow into lawn, after the root system and stem leaf have grown up, it will form an ecological slope protection structure with the 3D geonet together.

After the grass is in luxuriant growth, the plant root system can pass through the net pad unhindered and evenly and penetrate into the underground deeply for ten (scores of) centimeters and make the plant root system, geonet and soil form a solid compound whole. The 3D geonet and the plant root system can also take a role of the superficial layer integrated reinforcement on the dike slope. Therefore, this kind of compound system has a strong washing resisting ability, so it can fulfill the aim of effective protecting the side slope.

(2)The plant coverage can hold up rain and cushion the raindrop falling body kinetic energy, which make the soil on the ground surface be safe from the rain direct attack and prevent the formation of sink flow, the plant root system can enforce the wanter absorption capability of the soil, once meeting the rainwater, they can absorb quickly, even if the water flow is formed, it can also make the flow clear without soil through the anti-filter function of vegetation coverage.

(3)The raw material of the geonet is polyethylene, it is nontoxic and its chemical durability is reliable, burying under ground, its lifetime is over 50 years, even exposing under the sunshine, its lifetime can also be over 10 years. As the vegetation slope protection form, it has a much stronger washing resisting ability than the traditional sod slope protection. This kind of slope protection form can create protection effect with good economical and ecological benefit.

TRIAL ENGINEERING EFFECT

After the completion of the demonstration project of Wang Yuncheng dike section in Zhaoyuan county Heilongjiang province in June 2000, after over 6 years of observation, the two ecological slope protection of geocell filled with gravel soil and 3D geonet all achieve comparatively ideal effect. The ecological protection effect is very good and it has attained the expected aim. The vegetation on the geocell filled with gravel soil slope protection and 3D geonet grass slope protection are all growing luxuriant, their vegetation coverage all reach over 90%. (See Figs. 4—5)

Fig. 4 The effect picture of geocell filled with gravel soil ecological slope protection

Fig. 5 The effect picture of 3D geonet grass ecological slope protection

CONCLUSIONS

The integration and demonstration of sand dike ecological protection new technology develops the traditional engineering protection ideas; it takes the combination of engineering and ecological measures as its leading thoughts of technology research, in the process of constructing dike slope protection, it applies the new type geosynthetics, so it doesn't need large building machinery, the construction methods are suiting local circumstances and quite easy. At the mean time, the new type slope protection structure avoids some deficiencies of the traditional precast concrete panels slope protection, so it is an investigation of the new technology research of sand dike protection. The ecological protection technology research combines the natural conditions and regional characteristics of the two banks of rivers at cold areas. It improves the ecological environments and ensures the safe running of dike project. It suits the current basic condition of our country and is a kind of river sand dike protection system with the characteristics of low devotion and high reciprocation. According to the implement of the demonstration project, we got technological results with persuasion and provided valuable and practical technology for the dike project of sand dike construction of the Songhua River.

REFERENCES

Bao CG (1999) The Applied Technology of the Dike Project Geosynthetics, China WaterPower Press, China: 15, 137-139

Ecological Techniques and Case Histories

INTRODUCTION AND APPLICATION OF GEOSYNTHETIC IN QINGHAI-TIBET RAILWAY CONSTRUCTION

J.J Ge [1], J. Wei [2], L.M. Bao [3],X.M. Shi [4], L.H. Xuan [5] and X.L. LI[6]

ABSTRACT: The characteristics of nature, subgrade engineering design and construction are described along geermu-lhasa of the Qinghai-Tibet railway in the paper. Based on existing design, scientific research achievements and experimental studies, The Application of geosynthetics in the Qinghai-Tibet railway is introduced.

KEYWORDS: the Qinghai-Tibet railway, plateau permafrost, geosynthetics, application

INTRODUCTION

The total length of Qinghai-Tibet railway is 1956 km. Xining-Gelmud section (including Gelmud-Nanshankou section), which had been constructed in 1979, is 845 km long. The newly built Gelmud-Lhasa section locates in the hinterland of Qinghai-Tibet Plateau, crosses Qinghai province and Tibet Autonomous Region. Starting from Gelmud of Qaidam Basin, via Kunlun Mountain, Hoh Xil region, Fenghuoshan, Tanggula Mountain, Yasuta, Nagqu, Dangxiong, the railway ends in Lhasa, capital of Tibet Autonomous Region. The total length of Gelmud-Lhasa section is 1142 km (newly built section is 1110 km long, reconstructed section of Gelmud-Nanshankou existed lines is 32 km long) .There are 450 large and medium-size bridges summing up to 160.2 km, 10 tunnels totaling 9.6 km, 45 stations(43 newly built)totaling 57.9 km, and subgrade 914.30km. Length of railway above 4000 m elevation is 960km, maximum elevation of the railway in Tanggula Mountain is 5072 m, and length of railway passing through permafrost zone (continually frost time more than two years) is 546.3 km (Ge et al. 2007a, b). Qinghai-Tibet railway is the highest and longest plateau railway in the world, having the worst natural environmental conditions. Along the line, geological conditions are complicated, engineering technology is difficult, and environmental requirements are high. Three unprecedented confronted challenges are permafrost, alpine-hypoxia and ecological fragility.

SURVEY OF GELMUD-LHASA SECTION OF QINGHAI-TIBET RAILWAY

Topography and Landform along Gelmud-Lhasa Section of Qinghai-Tibet Railway

Areas passed by lines mainly belong to high-peneplain geomorphology. Hypsography gradually descends from west to east. Main mountain ridges passed by the railway are all east west trend. From north to south, there are mainly Kunlun Mountain, Hoh Xil, Fenghuoshan, Wuli Mountain, Kaixinling, Tanggula Mountain, Touerjiu Range and Nyaiqentanglha Range. From the north end of Gelmud-Lhasa Section Nanshankou, to Kunlun Mountain, natural slope is steep. However, in the middle section, except for Fenghuoshan and Kaixinling, terrain is flat and wide.

Development Conditions and Distribution Characteristics of Permafrost

Development conditions of permafrost

Main factors influencing permafrost include height, latitude, air temperature, geothermal gradient, groundwater and surface water, topography, landform, lithology, vegetation and geological structure.

Distribution characteristics of permafrost along qinghai-tibet railway

The development and distribution of permafrost along Gelmud-Lhasa Section are distinctly controlled by

[1]The first Railway Survey and Design Institute, Xi'an 710043, CHINA. Email:xlgjj_6@163.com
[2] The Institute of civil construction of Beijing Jiaotong University , Beijing 100044, CHINA. Email:zhengwei126@126.com
[3] The Institute for the economic planning of the Ministry of Railway,Beijing 100038, CHINA. Email:baolm@sina.com
[4] The Institute for the economic planning of the Ministry of Railway,Beijing 100038, CHINA. Email:xinming_shi@163.com
[5] The Institute for the economic planning of the Ministry of Railway,Beijing 100038, CHINA. Email:tdbxlh@sina.com
[6]The first Railway Survey and Design Institute, Xi'an 710043, CHINA. Email:lxl@163.com

three dimensional zonality, namely, vertical zonality caused by change of heat and water along with height; latitude zonality caused by heat difference between the south and the north; the zonality caused by different precipitation because of different distances from oceans and characteristics of atmospheric circulation.

While plateau permafrost is controlled by elevation, it also obeys zonality law. The lower bound of permafrost increases about 100—130 m with latitude processing every degree southward. At the same time, the temperature and depth of permafrost both obey altitude and latitude zonality law. Generally speaking, with elevation increasing 100 m in plateau, the average ground temperature decreases 0.8—0.9℃ and depth of permafrost increases 20m. At the same elevation, with latitude decreasing every degree southward, mean annual ground temperature (MAGT) increases 0.9—1.0℃ and depth of permafrost declines correspondingly.

Permafrost region in Gelmud-Lhasa Section of Qinghai-Tibet Railway approximately locates in 32°17′—35°3′ N，91°35′—94°10′ E area, and lies in hinterland of Qinghai-Tibet Plateau.

Climate

Regions passed by lines can be divided into three climate areas. From Gelmud to Naij Tal is plateau arid area, from Naij Tal to Kunlun Mountain Pass is plateau humid area, from Kunlun Mountain Pass to Tanggula Mountain Pass is plateau arid area, and from Tanggula Mountain to Lhasa is plateau semiarid area.

Regions passed by lines have high altitude, rarefied air and low atmospheric pressure. The mean annual atmospheric pressure at 4500 m is 580 mb, and atmospheric pressure at Tanggula Mountain Pass is the lowest, 544 mb.

Except for Gelmud and Lhasa, the mean annual air temperature is -2—-6℃, extreme maximum air temperature is 25℃, extreme minimum air temperature is -36—-45℃, mean annual gale weather days is 115—160, mean annual precipitation is 260—430 mm, mean annual evaporation is 1330—1760mm, and maximum snow cover depth is 14—40 cm.

MAIN PROBLEMS IN RAILWAY CONSTRUCTION IN PLATEAU PERMAFROST REGION

Construction of Gelmud-Lhasa Section of Qinghai-Tibet Railway is facing three difficult problems, namely, permafrost, alpine hypoxia and fragile environment.

Permafrost Problem

The main engineering geological problems include plateau permafrost, high seismic intensity and active faults. Engineering of this line is simple and the damage caused by active faults and high seismic intensity area is not severe, so the most important engineering geological problem is permafrost.

Frozen soil is one special soil whose composition, petrofabric, thermophysical-mechanical and physical-mechanical properties show different characteristics with ordinary soil. Seasonal thawing layer (active layer) of permafrost has seasonal freezing and thawing process every year, and generates a series of engineering geological problems which mainly include thawing settlement, frost heaving and harmful frozen soil geological phenomenon.

Thawing settlement

Massive ground ice often exists in the fine-grained soil nearby permafrost upper limit and in the coarse-grained soil which is filled with some fine-grained soil. Massive ground ice is prone to thaw if is affected by artificial activity, and the yielded settlement is the primary cause of subgrade deformation and failure.

Exchange and hydrothermal conditions of ground surface layer change after subgrade construction. The change may cause compression of basement soil layer or destroy ground surface soil. Depth of natural permafrost table will vary accordingly. When embankment is very low, because ground surface is destroyed, upper limit will descend. This may engender thawing of underground ice and sinking of subgrade. With the height of subgrade increasing, earth-fill increases the thermal resistance, and upper limit increases accordingly. The minimum height of embankment that can keep permafrost upper limit under subgrade changeless is called Critical Height of Embankment. When the height of embankment is larger than Critical Height of Embankment, upper limit will increase and subgrade is in a stable state; when the height of embankment is smaller than Critical Height of Embankment, upper limit will decrease and subgrade thawing settlement will occur accordingly.

Frost heaving

In low temperature permafrost areas, active layer is usually thin, and exists double direction freezing. Freezing is fast, so frost heaving is comparatively slight. In high temperature permafrost areas, active layer is usually thick and freezing is slow. If there is enough water in fine-grained clay layer, frost heaving is serious.

Harmful frozen soil phenomenon

Harmful frozen soil phenomenon is also called harmful cryogenic phenomenon. It means newly

formation and meso-and micro-topography caused by freezing and thawing of soil. They are unfavorable to engineering, mainly include ice cone, frost blister, freezing and melting solifluction, thermo-melting landslide and thermo-melting lakes.

Thermo-melting landslide, freezing and melting solifluction and thermo-melting lakes mostly distribute in flat terrace and high plain, centralizing in Chumar River high plain. After the thick underground ice under the slope thaws, the soil moves toward freezing and thawing interface and forms slumping under gravitation. Thermo-melting landslide and thermo-melting soli-fluction mostly happen in mountainous and hilly regions where there is underground ice, and develop best in south and north slopes of Fenghuoshan. Thermo-melting landslide can make buildings basement or slope instable.

Genesis of ice cone and frost blister can be divided into suprapermafrost water and subpermafrost water. They mostly distribute in Budongquan, Wuli Mountain, Kaixinling and Tanggula Road Pass.

Besides, in permafrost regions, because of influence of ground surface water and underground water, the ground is moist in long term, thermophilic and hydrophilous plants grow well, and there are peat accumulated piedmont slope or intermontane depression which is called frozen soil swamp (marshy wet land).

Environment Fragility Problem

Qinghai-Tibet Plateau is giant tectonic topographic unit whose elevation is highest in the world. Its particular natural characteristics and space distribution regulations engender unique plateau natural ecosystem. Qinghai-Tibet Plateau is original region of many famous rivers in South Asia and China. Wild animals living in Qinghai-Tibet Plateau are mostly precious plateau special species. They are the most valued wealth of human beings given by the nature. Therefore, in Qinghai-Tibet Railway construction, environment protect-tion appears very important and noticeable. To protect ecological environment of Qinghai-Tibet Plateau, Hoh Xil, Sanjiangyuan and Qiangtang National Natural Reserves have been established along the lines.

With the Qinghai-Tibet Railway construction, influences of artificial factors to plateau natural environment are gradually enhanced, and this will cause a series of environmental problems unavoidably. Permafrost, especially ice-rich frozen soil, is very sensitive to disturbance of ground surface. Some not large changes, such as vegetation destruction and current change can even cause permafrost irreversible changes and bring effect on subgrade stability. Therefore, environment protection must be specially noticed in railway construction of frozen soil areas. In view of engineering, environment protection is as well as very necessary to protect frozen soil and subgrade stability.

Alpine Hypoxia Problem

Regions passed through by Qinghai-Tibet Railway are all high-elevation areas. The length of section whose elevation is higher than 4000 m is about 960km, and the highest is Tanggula Mountain Pass, 5072 m.

Qinghai-Tibet Plateau has high elevation, rarefied air and cold climate. Plateau environment can bring great effects on human physiology, psychology and physical ability, cause human body a series of altitude physiological reaction and psychological changes, make physical ability and work efficiency drop notably. Because of alpine hypoxia, construction machinery efficiency decreases and faults increase.

APPLICATION OF GEOSYNTHETICS IN QINGHAI-TIBET RAILWAY

Brief Introduction to Application of Geosynthetics

In subgrade engineering design of Qinghai-Tibet Railway, there are the following adopted geosynthetics, and corresponding field test & study has been carried out on most adopted materials.

(1) Geogrid

It is mainly applied to high embankment (if fill height $H \geq 3$ m, geogrid paved below roadbed 2.2 m; if fill height $H \geq 6$ m, geogrid paved below roadbed 4.0 m) and cutting slope in high-ice content frozen soil, in order to solve uneven settlement of embankment, avoid longitudinal cracks, and enhance subgrade intensity. Because cutting slope has set up coarse-grained heat insulation replacement and filling soil layer of certain depth, considering inadequate compaction and initial temperature field evolution, reinforcement materials are set up to achieve slope reinforcement. In test engineering, transition sections of embankment and bridge also use geogrid reinforced cushion. Moreover, geogrid is also used in foundation treatment engineering of marshy frozen soil wet land. Subgrade reinforcement cumula-tively uses bidirectional plastics geogrid (30 kN/m) 328.5×10^4 m^2 and unidirectional plastics geogrid (25 kN/m)18.9×10^4 m^2.

Main technical capability index of subgrade reinforcement geogrid are: adopted polyester or warp-knitted glass fiber, bidirectional stress, tensile strength not less than 30 kN/m, corresponding maximum elonga-tion ratio not larger than 10%. At the same time, aiming at climate characteristics of Qinghai-Tibet Plateau,

geogrid is demanded to resist aging, resist frost (-45 ℃), and strength generally doesn't degrade after 200 freeze-thaw cyclings.

Besides, in design of reinforced earth retaining wall in south area of Anduo, geogrid is also used. It cumulatively uses HDPE geogrid $252.6\times10^4 m^2$, bidirectional warp knitted high tenacity polyester geogrid $87.8\times10^4 m^2$.

For geogrid, we carried out field test in Qingshuihe River area of Qinghai-Tibet Railway. Proving ground belongs to warm fine-grained frozen soil section, ground temperature is -0.5— -1.0 ℃, and the buried depth of permafrost table is 2—3 m. This is representative in the whole engineering of Gelmud-Lhasa Section of Qinghai-Tibet Railway. Monitoring work of settlement deformation, horizontal displacement and ground temperature has been done to analyze effects of embankment reinforcement and adaptability of reinforcement materials.

(2) Seepage-proof Composite Geomembrane

It is mainly applied to road cutting of high-ice content frozen soil and embankment of deep seasonal frozen soil. In order to prevent ground surface water infiltrating foundation and affecting frozen soil temperature field and water content, and to avoid thawing, transverse full-section laying is done under roadbed. Besides, aiming at the ordinary characteristic in non-permafrost regions, namely, foundation frost depth is large, in order to eliminate harmful frost heaving, composite geomembrane fault is used to prevent capillary water rising. Main technical index are: $750 g/m^2$, tensile strength≥15 kN/m, tearing strength≥ 0.42 kN, bursting strength≥2.6 kN, permeability coefficent≤10^{-11} cm/s, elongation rate 40%—80%. Furthermore, anti-aging and anti-freezing requests should also be satisfied. Accumulatively $179.6\times10^4 m^2$ seepage-proof composite geomembrane is used.

(3) Insulation Material

Thermal insulation materials mainly include EPS board, XPS board and PU board, which are used to protect permafrost foundation. It is a passive measure for obstructing external heat sources. Its essential is equivalent height of filling and its application scope is strictly confined to low embankment and road cutting. Heat pipe should be used when necessary. Most of the full lines adopt EPS and XPS. Test engineering makes comparative research on EPS and PU. Materials are required to have some compressive strength, low thermal conductivity and small water absorption rate. At the same time, in order to avoid influencing thermal insulation effect, plate joints should be reasonably processed.

Accumulatively, $6.9\times10^4 m^2$ XPS (thickness 0.08 m) and $18.7\times10^4 m^2$ PU (hickness 0.06 m) are used.

(4) Water-proof -Sheet

Mainly in order to prevent transference of freezing layer water and avoid moisture-heat exchange brought by water transference. The transference and exchange may cause instability of permafrost foundation. The measure assort with water-stop ridge to improve drainage conditions. Besides, in road cutting lot of exceptional section, some waterproof sheets are used whose utility is the same to seepage-proof composite geomembrane. SPRE waterproof sheet is mainly used in high-ice content frozen soil where there is cross slope and good permeability of layer above natural permafrost table. To prevent suprapermafrost water enter into basement, from water-stop ridge to natural permafrost table 0.5 m, SPRE is set up to cut off suprapermafrost water that flows toward subgrade, and accumulatively $121.8\times10^4 m^2$ SPRE is used. SBS waterproof sheet is mainly set up 0.2 m below roadbed in road cutting section and U-shaped side ditch bottom, and accumulatively $6.8\times10^4 m^2$ SES is used.

(5) Earthwork Mesh Cushion

To solve slope protection problem, considering environment protection requirements, test and study on grass planting on embankment slopes is carried out. Adopted base materials of test engineering are plane earthwork mesh cushion and three-dimensional earthwork mesh cushion. Effects are excellent according to field situation.

(6) Geocell

It is mainly used in flexibility protection tests of subgrade slope and soft foundation treatment engineering, and cumulative consumption is $17.6\times10^4 m^2$.

(7) Geotextile ($450 g/m^2$)

It is mainly used in anti-filter layer of infiltration ditches and scour protection engineering, and cumulative consumption is $2.3\times10^4 m^2$.

Application Effect of Geosynthetic Materials

Research results of several field investigations and test engineering show that, application of geosynthetic materials has achieved expected results, playing the role of protecting permafrost and improving embankment stability.

Research results of reinforced embankment test show that, in permafrost embankment, geogrid-reinforced layer plays obvious role in preventing embankment longitudinal cracks, restraining transverse cold cracks, increasing embankment integration and reducing uneven settlement. Tensile strength of reinforced embankment increases, and the ability of resistance to longitudinal crack is greatly increased as a result of enhancement of deformation coordination ability. The comparisons

indicate that because of uniform stress of soil, the space deformation of reinforced embankment is more uniform than that of non-reinforced embankment. Longitudinal cracks are not found, which indicates that reinforced layer plays some role in uniform distribution of embankment stress. In the finished design of Qinghai-Tibet Railway, embankments higher than 3 m in high-ice content region all adopt the measure.

From vertical deformation curves of reinforced embankment (DK1025+425) and non-reinforced embankment（DK1025+530）in Fig. 1, it is shown that they have the same tendency, that is, effect of reinforcement on solving vertical deformation problem is not obvious.

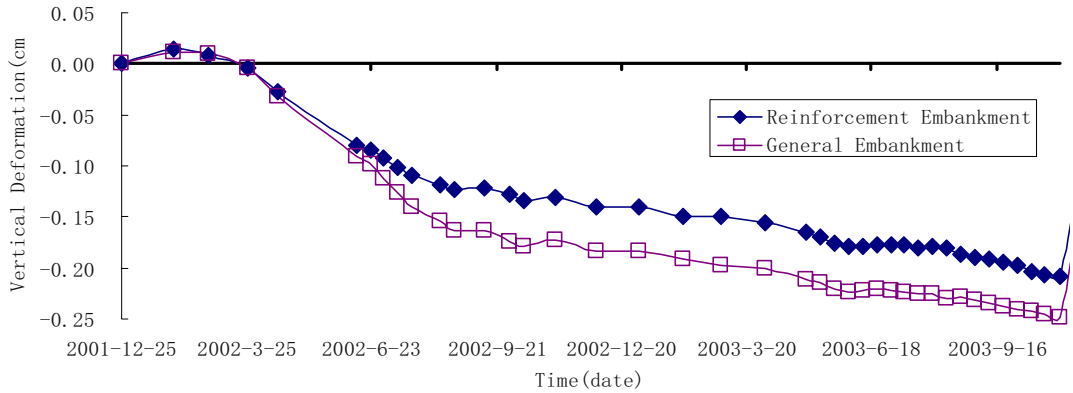

Fig. 1 Comparison on Vertical Deformation of Reinforcement and General Embankment

Analysis of horizontal displacement monitoring data shows that embankments all slowly move to the lateral. But with time process, the phenomenon gradually tends to be stable. Horizontal displacement of reinforced embankment is smaller than that of non-reinforced embankment.

Results of insulation materials research show that EPS thermal insulation board and PU thermal insulation board both have good effects. They play obvious role in effectively blocking heat sources such as radiation heat, therefore diminish influence of ground temperature on external air temperature variation. Monitoring data indicate that the temperature difference between the top and the bottom of thermal insulation board arrives at 5—10℃. But at the same time monitoring data in exothermic season indicate that when heat above thermal insulation layer dissipates normally, the heat below it cannot easily dissipate and this is unfavorable to permafrost protection, only a passive measure of protecting frozen soil. Thermal materials' capability index and construction technics results are also obtained from the test.

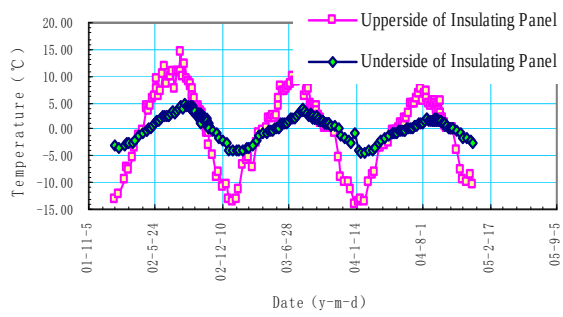

Fig. 2 The Temperature Variation Process of Fluctuate Thermal Insulation Panel（DK1024+525，PU: 6 cm）

Fig. 2 is the curve of ground temperature of PU board in top and bottom surface with time process in observation period. Fill height of the embankment is 2.5 m, and depth of PU board is 6cm, buried under embankment and 0.5 m distant from basement. From Fig. 2, in warm seasons, temperature above thermal insulation board is distinctly higher than that of below, temperature difference is large and insulation functions to prevent heat transferring downwards. In cold seasons, temperature above insulation board is lower than that of below, which indicates that insulation board also prevents cold energy transferring downwards and incarnates insulation board's characteristics of preventing heat and cold energy.

According to investigation results and cognition to permafrost, in low filling embankment and road cutting design, as a kind of thermal insulation material, XPS which has good thermal capability, durable capability and better compressive strength was used. Combining field ground temperature, hydrology situation and ice-content situation, passive measures are taken to fit active measures.

Roadbed slope flexibility protection and vegetation rebuilding techniques engineering results show that, geocell and earthwork mesh cushion play role in preventing slope stability, favor of slope stability and vegetation growing, and slope vegetation has thermal function. Photos 1 and 2 are slope protection situations

using geocell and earthwork mesh cushion in test engineering.

Photo 1 Slope Protection with Geocell

Photo 2 Slope Protection with Geomat and Artificial Grass

According to first-hand observed data of water-stop ridge and waterproof sheet (SPRE type), in the whole, waterproof sheets block suprapermafrost water, as Table 1 displays. From test results, moisture content of foundation soil by the two sides of water-stop ridge is larger in 7—9 months, mainly because of much rainfall, moisture content of layer above ground 2.0 m is larger than that of below. According to the difference (%) between upstream moisture content and downstream moisture content, in warm seasons (from the end of June to mid September), moisture content of downstream is smaller than that of upstream: at the depth of 1m, the difference is 2%—5.5%; at the depth of 2 m and 3 m, the difference is 0.5%—2.5%. It means that setting up vertical water-resisting materials under water-stop ridge can deaden suprapermafrost water flow into subgrade. Whereas, in cold seasons (from the end of September to early June of next year), moisture content of foundation soil by the two sides of water-stop ridge is approximately the same, and the difference is about 0.5%. In cold seasons, because ground temperature decreases, foundation soil is frozen and suprapermafrost water cannot flow.

Table 1 Moisture Comparison of Water-stop Ridge

Deep(m)	Moisture of Upstream Side （%）	Moisture of Downstream Side （%）
-1	17.4	15.6
-2	11.7	10.7
-3	10.7	9.5

Roblems in Application of Geosynthetics

Though theoretical analysis of reinforcement mechanism and test research have made great progress, especially in consolidation of soft foundation and high-steep slope, application and research of all kinds of geosynthetic materials in plateau permafrost high embankment should be deepen in the view of construction technology and engineering quality.

CONCLUSIONS

According to application analysis research of several geosynthetic materials (geogrid, seepage-proof composite geomembrane, insulation material, geocell) in Qinghai-Tibet Railway test engineering, various testing data indicate that application of geosynthetic materials to plateau frozen soil regions is feasible and valid.

REFERENCES

Ge JJ et al. (2007a) Survey and design convolve of Qinghai-Tibet railway (First draft). The First Survey and Design Institute of Railway

Ge JJ et al. (2007b) Research on science and technology convolve of Qinghai-Tibet railway (First draft). The First Survey and Design Institute of Railway

GEOGRID WRAPPED AROUND AND VEGETATED REINFORCED WALL APPLICATIONS IN THE VILLAGE OF OLYMPIC GAMES IN UNIVERSIADE 2005 IZMIR TURKEY

H.R. Yilmaz[1] and T. Eskisar[2]

ABSTRACT: 23rd University Olympic Games had been hold in Izmir in August 2005. This organization which is accepted as an important opportunity in most of the countries is achieved after great efforts of Izmir Municipality. As a part of this organization, a village for the athletes is constructed in a valley of Uzundere, Izmir. The apartment buildings, which are sold to individual buyers after the completion of the games, are spread out in a very wide area. In the slopes of the valley, green walls with geogrid reinforcements are used as a solution to form stable sides, prevent slope flows during precipitations, and other kinds of slides. Also, an aesthetical presentation of the village was a target to be attained. In order to achieve the goals of the project, geological, geophysical and geotechnical investigations are carried out. The heights of the geogrid reinforced retaining walls in the area are between 5.0 and 10.0 meters and they are constructed using uniaxial and biaxial geogrids with reinforced earth technique by a wrapping system and the geogrids are vegetated to get the green walls or in other words living walls. In this study the mentioned geogrid walls are explained both in the scope of construction and the costs. These applications are also accepted as interesting and cost effective by the Izmir municipality administrators.

KEYWORDS: geogrid, reinforced earth technique

INTRODUCTION

In this paper, it is intended to narrate the reinforced earth walls of the 23rd Olympic Games Village which is built in one of the widest valleys in Izmir. The completed green walls are totally more than thousand meters long at the moment. To make the statement much more clear, as an information, height and length of the walls can be given as, 7 meters high walls are 350 meters long, 6 meters high walls are 250 meters long, and 5 meters walls are 150 meters in length. These walls are constructed with reinforced earth technique using uniaxial and biaxial geogrids as reinforcements.

In general, as vegetable soil takes place in the thousands of sacks with seeds to form a green wall face, these green walls can be accepted as a wonderful solution to the traditional problems. These walls are a comparable and cost effective solution to those traditional reinforced concrete retaining walls with their low costs and expenses (Christopher and Holtz 1985; Holtz Christopher and Berg 1996; Ho and Rowe 1996). They are also very durable and their performances to dynamic effects are proved in a lot of projects all over the world (Cai and Bathurst 1995; Sandri 1997). It is important to know that these kinds of walls will become a major choice when understanding of their performance and economy is wide spread.

THE CONSTRUCTION OF GEOGRID REINFORCED EARTH WALLS

For preventing slope slides and retaining the lateral loads from very nearby new constructed buildings, these walls are constructed necessarily. As the publicity is another concern, aesthetical appearance of the walls is an important issue. Therefore vegetation technique could be an optional choice. It is known that this application could also be successful when wide areas of construction are in concern (Fuchs, 2006). There are many options to be used as a facing in retaining wall system (Gomes et al. 2006; Wills 2006). But, in this project the major point is to keep the natural view of the valley.

Depending upon the needs, the walls, which heights change from 5—10 meters, are constructed mostly in a stepped way. In the following lines brief construction information will be given to characterize the case significantly.

[1] Assoc. Professor, Department of Civil Engineering, Ege University, TURKEY. Email: yilmazrecep@yahoo.com
[2] R.A., Department of Civil Engineering, Ege University, TURKEY. Email: tugba.eskisar@ege.edu.tr

As the initial step, foundation soil of the retaining wall is excavated to the depth which is appointed by the official construction drawings. It is proper to mention that compaction and back filling is done, and drainage precautions are taken in every step of this project. First layer of the geogrid material is placed on the desired height of the project, and the first line of the geogrid rolls are not cut to make a wrap after completing the first slope of the wall (Fig. 1).

Fig. 1 Continuing lines of geogrid rolls in the field

In literature, this technique may be referred as wrap - around facing (Bathurst). It is important to lay the geogrid to the proper elevation and orientation of the material is checked by the site engineer. It is of great importance that the strength direction of geogrid is perpendicular to the wall surface. Then, as the face elements, sacks which contain both vegetal soil and seeds are used (Fig. 2).

Fig. 2 Sacks containing vegetal soil and seeds to form the face of the walls

The vegetal soil and seeds are filled in a closed station and carried to the site by loaders. The sacks are aligned one by one to form a clear cut appearance. Afterwards, another amount of soil is transferred by a bulldozer (Fig. 3). Layer by layer after the compaction of the ground and the placement of the sack, one slope of the wall is composed. Next, the left geogrid rolls of the first layer are lead to the top layer to form a wrap (Fig. 4). The valley is mainly surrounded by tiered geogrid walls which have 3 steps (Fig. 5). The top and the sides of the wall are vegetated by plants such as genista which is a strong surface coverer in hot climates (Fig. 6).

Fig. 3 Formation of a new layer

Fig. 4 View of the sacks wrapped around by the first layer of geogrids

Fig. 5 Three steps of the wall seen across the valley

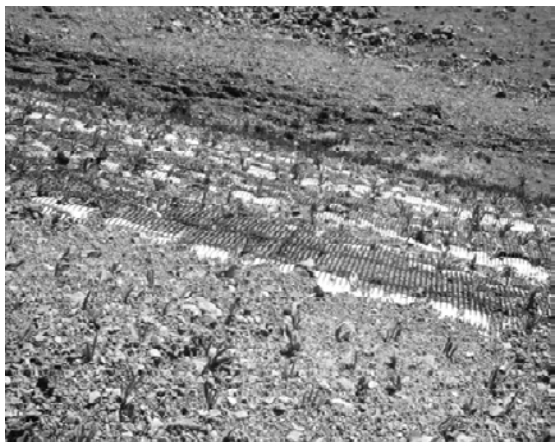

Fig. 6 Vegetation taking place

THE PROJECT DETAILS OF GEOGRID REINFORCED EARTH WALLS

Soil properties are approved to be sufficient after the complete site investigation. Therefore, the usage of the in situ soil as a filling is conformable. The technical details of the materials are as in Table 1 (Yılmaz et al. 2005).

Table 1 Geogrid (GG) and soil properties

Material	Properties
Soil	Kind of Filling: Spreading out and compaction with a small cylinder. Soil Cohesion: 0 Internal Friction: 30 Specific Gravity: 15
Geogrid (GG)	Roll Length: 50 -100 m Roll Width: 1.0-1.30 m Crib Strength: 27.60 kN/m Elongation in Max. Load: %12 Unit Weight: 0.30 kg/m^2

As it is appointed by the municipality administrators, for the construction of a 50 m^2 wall face, 8 hours of work per day is necessary to finish the construction on the determined period.

In this special production form of a retaining wall, the principles of a gabion wall and also reinforced wall techniques are used together with wrapping around the front faces using the reinforcement geogrids.

As an example, in a 7 m high reinforced earth wall 8 sacks per m^2 (wall surface) are used.

Table 2 is showing the geogrid application lengths for each row for a 7 m high wall.

In calculations for varying heights, the total geogrid need for the 6m high walls and 5 m high walls is found to be 56.20m^2/m and 41.76m^2/m, respectively.

Table 2 Application lengths of for each row of geogrid reinforcement

GG Row No.	Toe Support Length L(m)	Head Support Length D (m)	Slope Length Hc (m)	Total GG Length (m)
1	6.50			8.25
2	6.25			8.00
3	5.95			7.70
4	5.65			7.40
5	5.40	0.70	1.05	7.15
6	5.10			6.85
7	4.80			6.55
8	4.55			6.30
9	4.25			6.00
The distance between the two rows is 0.80 m.			Total m^2/m	64.20

THE UNIT AND TOTAL COSTS OF THE WALLS AND THE MATERIAL DEMAND

The material demand such as the sacks number, the amount of vegetated soil, seed, and the amount of geogrids are calculated and given in Table 3.

Table 3 Material demand for the walls with different heights

Wall Height (m)	7	6	5	Total
Sacks	27200	16800	8400	52400
V. Soil (m^3)	1190	735	370	2295
Seed (kg)	690	420	210	1310
Uni.Geogrid (m^2)	24000	12500	5300	41800
Bi.Geogrid (m^2)	5000	3000	1300	9300

THE RESULTS OF PRICE ANALYSIS

In order to pay the contractor, a detailed price analysis is prepared. As an example, the analysis made for the 10 m high wall is presented below comprising the material needed for a unit face and length of the wall. The prices and the effect of all of items to the prices as percentages are also given in Table 4.

Table 4 Demand list

Demand List	Quantitiy
Labor	
Engineer	1 person
Formen	1 person
Master Workman	1 person
Unskilled Workman	7 people
Machine Park	
Tracked Excavator	1
Transp. Car (Building Site)	1
Compaction Cylinder	1
Spade	6
Sack Filling Apparatus	2
Materials	
Uni. GG	81m^2/m
Bi. GG	24m^2/m
Sacks	8 per m^2
Vegetated Soil	0.35 m^3/m^2
Backfill. Material	Delivered for free
Seed	1kg/m^3

Demands for Unit Area

To complete the project on the desired time the appointed schedule is promulgated as 8 hours of work/day, production of 50 m^2 wall faces in 8 hours, etc. Needed labor is determined in this manner. Demands constituted for each item are given in Table 5. It is important to emphasize that all the materials except the geogrids are on unprofitable prices. If any other material is needed, it is to be added to the prices.

Table 5 Demands for unit area of 10m high wall production

Demands	Needed Labor	Prices ($/day)
Engineer	0.02 day/m^2	43
Formen	0.02 day/m^2	30
Master Workman	0.02 day/m^2	23
Unskilled Workman	0.14 day/m^2	19
Tracked Excavator	0.02 day/m^2	393
Transp. Car (Build.Site)	0.02 day/m^2	27
Compaction Cylinder	0.02 day/m^2	23
Uni. GG	8.5m^2/m^2	3.70
Bi. GG	2.4m^2/m^2	2.34
Sacks	8 per m^2	0.06
Vegetated Soil	0.35 m^3/m^2	11
Seed	0.35kg/m^2	9

If the demand for unit area is calculated properly then it can be distributed to the items of the wall cost and unit cost can be achieved. The evaluation of unit cost and the percentage in the costs of the materials and labor of the people in charge are given in Table 6.

Table 6 Wall Costs for 10 m high wall

Wall Cost	Unit Cost ($)	% in cost
Engineer	0.86	1.36
Formen	0.60	0.95
Master Workman	0.46	0.73
Unskilled Workman	2.66	4.21
Tracked Excavator	7.86	12.43
Transp. Car (Building Site)	0.54	0.85
Compaction Cylinder	0.46	0.73
Sacks	0.48	0.76
Vegetated Soil	3.85	6.09
Seed	3.15	4.98
Total labor cost (without GGs)	20.92	33.09
25% profit	5.23	8.27
Uni. GG	31.45	49.75
Bi. GG	5.62	8.88
TOTAL	63.22	100

In Table 6, the unit costs for a 10 m high wall with the consideration of the demand of labor which is different for workers, construction machines and materials needed for a unit wall production are calculated according to the daily need using appropriate prices and wages. The unit cost of labor without geogrids is 20.92$ and its percentage in the cost is 33.09 %. When geogrids are considered, total unit cost becomes 63.22$.

CONCLUSIONS

An interesting example of a cost effective geogrid wrapped around reinforced earth retaining wall application from Izmir is presented. As it is seen from the detailed material and labor costs, important benefits are derived in the local site by limiting the wall heights between 5—10 meters. In another literature, it is reported that the composition of a 10.7 m high, 200 m long project reduced the reinforcement needs about 35% when compared to conventional methods (Allen and Bathurst 2006). Also, composition of a tiered structure helps to pass higher elevations with working ease. Also, when compared to the conventional geotechnical materials, geogrid reinforcements can be installed

quickly and easily reducing overall construction time and costs. As it is seen from the tables presented in the previous chapters, the workman and machine requirements are at minimal stage. The only considerable point is the need for the workman having experience in geogrid materials. Besides, the vegetated sides form an aesthetical view which cannot be formed by any other construction type.

REFERENCES

Allen TM, Bathurst RJ (2006) Design and Performance of an 11 m High Block Faced Geogrid Wall, Geosynthetics, Eds. J. Kuwano & J. Koseki, Mill Press, Rotterdam: 953-956

Bathurst RJ http://geosyntheticssociety.org/source_ documents/Walls.pdf

Cai Z, Bathurst RJ (1995) Seismic Response Analysis of Geosynthetic Reinforced Soil Segmental Retaining Walls by Finite Element Method, Computers and Geotechnics 17(4): 523-546

Christopher BR, Holtz RD (1985) Geotextile Engineering Manual, US Federal Highway Administration, Washington, D. C., FHWA – TS – 86/203: 1044

Fuchs P (2006) Vegetated Retaining Walls Using Concrete Units and Geogrids Along the A8 Motorway in Austria, Geosynthetics, Eds. J. Kuwano & J. Koseki, Mill Press, Rotterdam: 957-960

Gomes ROM, Ribeiro LS, Vidal D (2006) Reinforced Soil Structure Trench with Geogrid and Head Wall Using Interlocked Concrete Blocks, Geosynthetics, Eds. J. Kuwano & J. Koseki, Mill Press, Rotterdam: 1057-1060

Ho SK, Rowe RK (1996) Effect of Wall Geometry on the Behaviour of Reinforced Soil Walls, Geotextiles and Geomembranes 14(10): 521-541

Holtz RD, Christopher BR, Berg RR (1996) Geosynthetic Design and Construction Guidelines, U.S. Federal Highway Administration, National Highway Institute, Washington, D. C., Publication No. FHWA-HI-95-038: 396

Sandri D (1997) A Performance Summary of Reinforced Soil Structures in the Greater Los Angeles Area after the Northridge Earthquake, Geotextiles and Geomembranes 15(4): 235-253

Wills PG (2006) The History and development of Incremental Block Wall Systems Utilising Geogrid Reinforcement, Geosynthetics, Eds. J. Kuwano & J. Koseki, Mill Press, Rotterdam: 1-15

Yılmaz HR, Aklık P, Eskişar T (2005) Case Study of a Geogrid Reinforced Retaining Wall in Universiade 2005 (İzmir) Olympic Games Village, Proceedings of the 2nd International Technical Textiles Congress, İstanbul, 13-15 July 2005: 596-601

Proceedings of the 4th Asian Regional Conference on Geosynthetics
June 17 - 20, 2008 Shanghai, China

LANDFILL BIOREACTOR FINANCIAL ANALYSIS—MONTEREY PENINSULA LANDFILL, MARINA, CALIFORNIA

S. Purdy[1] and R. Shedden[2]

ABSTRACT: The Monterey Peninsula Landfill, owned and operated by the Monterey Regional Waste Management District, is a municipal solid waste facility that is permitted under the State of California landfill regulations. In order to evaluate the potential cost benefits related to operating the site as a bioreactor, the District commissioned a consultant to determine the feasibility and benefits of changing their current operational procedures. The evaluation included a review of existing information and a detailed financial analysis and comparison between current practice and the operation of the site as a bioreactor. The results of the evaluation determined that the rapid degradation of refuse within a bioreactor will be beneficial for long-term health and safety, environmental protection, and methane gas generation.

KEYWORDS: bioreactor, enhanced methane generation, landfill, financial analysis

INTRODUCTION

The Monterey Peninsula Landfill (MPL) is a Class III sanitary landfill covering an area of approximately 126 hectares. The site is located in Northern Monterey County, California approximately 1.6 km east of State Highway 1 and 3.2 km north of the City of Marina. The MPL began accepting waste in 1966 and was constructed in a series of modules. The site currently receives approximately 209,000 metric tons of municipal solid waste per year delivered to the landfill by the general public and commercial haulers.

Disposal operations are currently focused in the Module 4 area, just to the east of the existing Materials Recovery Facility (MRF). Wastes are disposed of utilizing the area method of disposal, with waste lifts averaging 4.6 meters in thickness. Wastes are placed and compacted in thin layers on a working face sloped no steeper than 3:1 (horizontal:vertical). Soils for intermediate and working face cover, consisting generally of sands, are excavated from the upland plateau area south and east of the current landfill area. Sand has also been sold to local contractors for off site use.

The owner and operator of the MPL, the Monterey Regional Waste Management District (District), commissioned a consultant to conduct a financial cost-benefit analysis of their landfilling operation to determine the feasibility of operating the site as a bioreactor. A landfill that is operated as a bioreactor has many potential benefits. The more significant benefits include expedited methane generation and recovery, extension of landfill life due to enhanced refuse settlement, and improved leachate quality. The rapid degradation of the refuse within a bioreactor will be beneficial for long-term health and safety and environmental protection over the post-closure period of the landfill. The expedited methane generation will also provide the potential for additional beneficial uses of landfill gas.

The design and operation of a bioreactor landfill is different than the standard “dry tomb” landfill. For the design, the leachate collection system needs to be constructed to handle the increase in leachate generation due to liquid addition. The liner system itself may also require changes to ensure containment of the increased leachate quantities. The operational constraints involved with the liquid distribution system and landfill gas collection would also be considered in the cost benefit analysis. In order to provide the reader with a broad overview of landfill bioreactor technology, the authors have included a discussion on bioreactors in general, their benefits, and then present the financial analysis for the potential bioreactor at the MPL.

BIOREACTOR BACKGROUND INFORMATION

The information provided within this section is a summary of a “White Paper” presented at the Solid Waste Association of North America (SWANA) 5th Annual Landfill Symposium (Pacey et al. 2000). A

[1] Certified Engineering Geologist and Vice President, Vector Engineering, Inc., USA. Email: purdy@vectoreng.com
[2] Professional Engineer, Monterey Regional Waste Management District, USA. Email: rshedden@mrwmd.org

bioreactor landfill is a sanitary landfill that uses enhanced microbiological processes to transform and stabilize the readily and moderately decomposable organic waste constituents within 5—10 years of bioreactor process implementation. The bioreactor landfill significantly increases the extent of organic waste decomposition, conversion rates, and process effectiveness over what would otherwise occur within the dry tomb landfill. Stabilization means that the environmental performance measurement parameters (landfill gas composition and generation rate and leachate constituent concentrations) remain at steady levels, and should not increase in the event of any partial containment system failures beyond 5—10 years of bioreactor process implementation.

The bioreactor landfill requires certain specific management activities and operational modifications to enhance microbial decomposition processes. The single most important and cost-effective method is liquid addition and management. Other strategies, including waste shredding, pH adjustment, nutrient addition, waste pre-disposal and post-disposal conditioning, and temperature management, may also serve to optimize the bioreactor process. Successful implementation also requires the development and implementation of focused operational and development plans.

In effect, the bioreactor landfill is merely an extension of the accepted leachate re-circulation landfill option provided in the US Federal Landfill Regulations and adopted by the State of California. However, the bioreactor process requires significant liquid addition to reach and maintain optimal conditions. Leachate alone in some geographical areas such as the MPL may not be available in sufficient quantity to sustain the bioreactor process. Water or other non-toxic or non-hazardous liquids and semi-liquids are suitable amendments to supplement leachate (depending on climatic conditions and regulatory approval). Other process amendment strategies may also be included, subject to regulatory approval.

Shortly following closure of a bioreactor landfill, the landfill gas generation rate will usually be at its highest. It will then quickly decline over the next 5—10 years to a stable and relatively low and declining rate. Similarly, shortly after landfill closure, many leachate contaminant concentrations will change from levels regarded as highly polluted to much lower levels normally characteristic of extended stabilization. The leachate quantity at closure will be a finite amount, amenable to on-site treatment with limited need for off-site transfer, treatment, and disposal. In the event of post-closure partial containment system failure, the quality of the leachate generated from infiltration into a bioreactor landfill will be much better than other drier landfills.

Evidence suggests that bioreactor landfills can meet the prescribed regulatory requirements. A 1997 SWANA survey of 130 US bioreactor landfills indicates that most environmental and other relevant concerns have been resolved; information on leachate re-circulating landfills in existence worldwide is similarly positive.

Numerous benefits can be derived from a bioreactor landfill. These are situation-dependent and can affect different parties or stakeholders in different ways. They can accrue in the form of environmental, regulatory, monetary, and social benefits.

Some of the key benefits include 1) rapid settlement - volume reduced and stabilization within 5—10 years of bioreactor process implementation, 2) increased gas unit yield, total yield and flow rate – almost all of the rapid and moderately decomposable organic constituents will be degraded within 5—10 years of closure, and 3) improved leachate quality - stabilizes within 3—10 years after closure, and early land use possible following closure.

Key benefits for the maximizing of landfill gas capture for energy recovery projects include: 1) significant increase in total gas available for energy use which provides entrepreneurial opportunities, 2) potential increase in total landfill gas extraction efficiency (enabled over a shorter generation period), 3) increase in fossil fuel offsets due to increased gas energy sales 4) assistance in defraying landfill gas non-funded environmental costs, and 5) significant economy of scale advantage due to high generation rate over relatively short time.

Key benefits for increased landfill space capacity reuse do to rapid settlement during operational time period include: 1) increased landfill space capacity reuse due to rapid settlement during operational time period，2) increase in the amount of waste that can be placed into the permitted landfill airspace (effective density increase), 3) extension of landfill life through additional waste placement, 4) deferred capital and financing costs needed to locate, permit, and construct replacement landfill results in capital and interest savings, and 5) significant increase in realized waste disposal revenues.

Key benefits for improved leachate treatment and storage include: 1) low cost partial or complete treatment; significant biological and chemical transformation of both organic and inorganic constituents, although mostly relevant to the organic constituents, 2) reintroduction of all leachate over most of the operational and post-closure care period significantly reduces leachate disposal costs, and 3)

absorption of leachate within landfill available up to field capacity.

Key benefits for reduction in post-closure care, maintenance and risk include: 1) reduction in post-closure care, maintenance and risk, rapid waste stabilization (within 5—10 years) minimizes environmental risk and liability due to leachate and gas, landfill operation and maintenance activities are considerably reduced, post-closure landfill monitoring activities can be reduced, and reduction of financial package requirement.

Another major benefit of bioreactors may come from greenhouse gas abatement. Bioreactors can generally rapidly complete methane generation while attaining maximum yield. This can be combined with nearly complete capture of generated gas using the bioreactor landfill in combination with a landfill gas to energy project. With this approach, the high generation level and gas capture efficiency maximizes landfill greenhouse gas offset potential.

FINANCIAL ANALYSIS

General

In recent years, the waste industry has begun to recognize airspace as a real commodity and has started to explore ways to preserve it and make the best use of capacity. The increase in revenue due to increased density of waste is fairly easy to quantify. Another benefit easily quantified is increased site life in which closure and post-closure accruals can be spread over longer periods of time. Our analysis did not take into account the accrual of closure and post-closure costs. Also, expansion of the landfill gas to energy plant located on the MPL site, to utilize the increased gas production due to the bioreactor process, can easily be quantified and accounted for in the proforma.

Bioreactors have become an avenue to enhance the economics and environmental protection of a waste facility. Much research and several laboratory studies have been performed to show the benefits of bioreactors and recently, financial impacts are starting to be evaluated.

For the financial analysis conducted for the MPL, an anaerobic bioreactor option was compared to the typical dry tomb landfill operations currently conducted at the site. The new cell anaerobic bioreactor would involve the addition of liquids to the waste mass by means of a HDPE piping system and bio-solids added to the working face as the cells are being filled. The addition of liquids to the waste mass has also been referred to as leachate re-circulation. On average, the Monterey area receives less than 0.5 meters of precipitation a year. This amount of precipitation will produce some leachate, but probably not enough to operate a bioreactor at full capacity. Therefore, additional liquid beyond that collected in the leachate collection system may be needed to enhance the full bioreactor process. The District has additional water available from a dewatering system located on site. From previous bioreactor studies, the moisture content of the waste has to approach 40% to 45% to provide enough moisture to enhance and keep the bioreactor processes functioning (Reinhardt and Ham 1974).

Assumptions

The authors assumed that each bioreactor cell being constructed at the MPL would be on the order of 4 hectares. The total size of the permitted landfill footprint is assumed to be approximately 101 hectares. Total waste thickness was assumed to be on the order of 26 meters. The authors also assumed the site would operate 300 days per year. Total volume of the site was assumed to be just over 15 million cubic meters. Each 4-hectare cell would have a capacity on the order of 600 thousand cubic meters with one half of the cell consisting of floor area for leachate collection. Total incoming waste flow of 725 metric tons per day, an in-place density of 0.83 grams per cubic centimeter, and a gate rate of US $15.40 per metric ton were provided by the County. It should be noted that this exercise is a relative financial analysis.

The results of a literature search indicated that a 30 percent increase in the density of in-place waste (or in other words a 30 percent gain in airspace) for a properly operated bioreactor is very attainable (Reinhart and Townsend 1997; Harris and Schafer 2002), and (Hater and Barbush 2001). For conservatism, we assumed that over the life of a 4 hectare cell we would get a 20 percent increase in airspace.

According to Vogt and Augenstein (1999) and Pacey et al. (2000), gas production will increase substantially over standard Subtitle D cells. Hater and Barbush (2001) suggest at a minimum gas production will be 2 times that of normal production. The District provided gas generation data from the existing waste in-place. The authors used this data to calibrate the input parameters for the EPA Landfill Air Emissions Estimation Model to match existing conditions. Using the calibrated input parameters, the methane generation was estimated for future landfilling operations. For conservatism, the authors then used 1.5 times the normal production to estimate the incremental increase in methane gas

production following bioreactor implementation.

In regard to the power production, assumptions used were from documented information provided by the District and typical experience with landfill gas-to-energy projects. Capital expenditures for expanding power production capabilities were estimated from the District's and typical experience. Costs will be incurred for increasing well field efficiency, power generation sets, and yearly operation and maintenance costs.

Bioreactor investment can be estimated by applying capital costs to the entire site and to each additional cell. Costs attributed to the entire site were spread over the initial 20 year life of the facility similar to the accrual process. Some costs that were included in the start up operation were a leachate storage tank, odor control, gas system upgrades, etc. The authors did not include replacement cost of equipment pumps, piping, etc. beyond the original design. We included the capital costs to permit, install, and operate the completed bioreactor as designed. We also included some yearly maintenance cost estimates from previous experience.

Costs were also estimated for the development of each 4-hectare bioreactor cell. The liquid distribution piping systems were assumed as follows: 1) vertical perforated pipe spacing was assumed to be every lift of waste or on the order of 4.5 meters on center, 2) horizontal perforated pipe spacing was assumed to be 15 meters on center, 3) conservatively, perforated pipes were assumed to be surrounded by .17 cubic meters of gravel per 30 cm of pipe. Many bioreactor sites use revenue-producing backfill around pipes such as tire chips or glass.

We also conservatively assumed a substantial upgrade in the leachate collection system. The upgraded system was assumed to have a cushion geotextile with 60 cm of high permeability granular material. Other options such as substituting tire chips for 30 cm of the drainage layer could be used to lower this capital expenditure. Since more flow into the leachate collection and recovery system will occur, we assumed that the LCRS pumps would need to be upgraded. Costs were also included for extra geomembrane to piggy back over some pre-existing areas of the MPL that did not have geomembrane liner systems.

Estimated bioreactor yearly operation and maintenance (O&M) costs included personnel, analytical, monitoring, and equipment costs. Those costs were estimated from a literature search and from our experience.

Results

Table 1 presents the results of the financial analysis. In our analysis, the total increase in revenue per year due to bioreactor activities is a direct result of the increase in airspace and the generation of power. The financial benefits provided are partially offset by an increase in investment required in the technology and science of bioreactors and the increase in operational costs for the bioreactor system and other resultant maintenance items (odor control and health/safety programs). Our analysis assumes 15%—20% contingency on most capital, operation and maintenance costs.

There have been several benefits and risks excluded from this analysis because there is some uncertainty surrounding operation of the full-scale bioreactor. The potential benefits excluded are: reduced post-closure period, reduced heavy equipment, decreased air emissions, and deferral of cell construction and capping, since each constructed cell will have a longer individual life. The potential risks excluded are: change in construction costs for wider cells, allowing for flatter final grades, change in final slope grades resulting in loss of airspace (need flatter final grades for stability), and safety (wet working face, odors, fire and infectious waste).

CONCLUSION

The results of our analysis presented in Table 1 indicate a financial gain on the order of US 2 million dollars for implementation of a bioreactor system. Using what we believe are valid assumptions, the airspace recovery, increased density, and increase in landfill gas production can equate to a significant financial gain and longer life for the Monterey Peninsula Landfill.

Table 1 Revenue Increase with Bioreactor Option

Revenue / (Expense)	Years 1-20
Increase in Airspace	$3,950,802
Liquid Waste Revenue	$900,000
Power Production Revenue	1,870,282
Power Production Capital Costs	($160,127)
Power Production Maintenance & Operation Costs	($779,284)
Bioreactor Investment Costs (Entire Site Accrued Over 20 yrs)	($27,500)
Construction Costs – Module 4 (Cushion Geotextile and Gravel)	($910,271)
Design and Permitting Costs – Module 4	($100,000)
Yearly Bioreactor Operating, Piping, Maintenance, Costs, Etc.	($2,595,468)
Total Increase/Decrease in Revenue	$2,125,934

REFERENCES

Harris J, Schafer A (2002) Case History of Airspace Gain due to Recirculation, Proceedings, SWANA 7th Annual Landfill Symposium, SWANA, Silver Spring, MD, USA

Hater G, Barbush J (2001) Research and Design Issues for Data Collection in Landfill Bioreactors, Proceedings, SWANA 6th Annual Landfill Symposium, SWANA, Silver Spring, MD, USA

Pacey J, Augenstein D, Reinhart D, Morck R, Yazdani R (2000) The Bioreactor Landfill—An Innovation In Solid Waste Management, Proceedings, SWANA 5th Annual Landfill Symposium, SWANA, Silver Spring, MD, USA

Reinhart D, Ham R (1974) Solid Waste Milling and Disposal on Land Without Cover, U.S.E.P.A., Cincinnati, Ohio, PB-234 930

Reinhart D, Townsend T (1997) Landfill Bioreactor Design and Operation, Lewis Publishers, New York, New York, USA

Vogt G, Augenstein D (1997) A Comparison of Landfill Methane Recovery Models—a 19-Landfill Study, prepared for the Solid Waste Assoicatian of North America and the National Renewable Energy Laboratory of the USDOE. SWANA, Silver Spring, MD, USA

HIGH COST OF FAILURE

R.E. Belanger[1], C.B. Queja[2] and C. V. Zantua[3]

ABSTRACT: Geosynthetics used in waste containment facilities have occasionally encountered problems due to substandard geosynthetics, construction methodology, inadequate or inappropriate design, and poor operating practices. These problems are normally detected during construction or operational stages and the associated costs to correct them are many times higher than the original construction amount. This situation sometimes results in impacts to public health, loss of reputation and litigation. Fundamentally, through proper design, well planned material quality assurance (MQA) and construction quality assurance (CQA) most of the problems can be eliminated and consequently reduce or practically avoid the possibilities of damage to the natural environment and public health and safety. Vital collaborative participation of the key players in the industry: designer, MQA/CQA, and independent testing laboratories are important to a successful outcome. These coupled with administration and implementation of governmental statutes affecting the activities in all phases of waste containment projects will ensure attainment of the previously cited goals.

KEYWORDS: high cost of failure, MQC/CQA (QA/QC), public health & safety, environmental protection

INTRODUCTION

The main principle for developing effective treatment and disposal systems is to separate industrial and domestic wastes from the environment and the populace by using barriers or distance to reduce health hazards.

Through this effort, however, the potential hazards are just being transferred to new locations either solid waste or wastewater confinement and treatment facilities which still pose spectrum of risks to public health & safety and to the surrounding environment. The inevitability of these risks to happen had paved the creation and implementation of suitable measures involving control standards and regulations which cover largely the design, proper location, and efficient operation of wastes containment facilities (Bonaparte et al. 2002).

These measures were developed with high priority, and still being improved, in order to address and mitigate the negative impacts of these types of projects. In the Environmental Impact Assessment (EIA) system, installation projects as such are categorized as "critical projects" to denote the elevated potential hazards they pose to the community and the environment (Rowe 2005). The EIA system requires the project proponent to perform a comprehensive evaluation and documentation of all predictable impacts and the corresponding mitigating measures. The primary goal is to protect public health & safety and preserve the immediate environment.

Amongst the Environmental Protection Agency's (EPA) stringent requirements in the modern design of landfills and containment ponds is the inclusion of geosynthetics barriers and final cover systems to separate wastes and leachate from the immediate environment, i.e., soil and surface/subterranean water (Bonaparte et. al. 2002). From an engineering standpoint, these measures are adapted to provide protection and lessen contaminant impact.

However, for several reasons which are amply described by Bonaparte, and its mechanisms explained by RK Rowe (2005), failure of a system is inevitable. And clearly, the probability of this to occur is even higher for projects that never received proper attention with regards to appropriate MQA and CQA procedures implementation. Though some authors suggested that the percentage of the documented failures in geosynthetics projects is too small as compared with other structural projects, our viewpoint is not just limited to the statistics of the incidents occurred. The immediate and impending impacts of these failures to various stakeholders are not a matter of the frequency of their occurrences but rather the magnitude of their impact. A relatively minor problem could have a very detrimental effect to public or habitat.

[1] President, Precision Geosynthetic Laboratories, Anaheim, California 92801, USA. Email: rbelanger@precisionlabs.net
[2] Vice-President, Precision Geosynthetic Laboratories, USA. Email: cqueja@precisionlabs.net
[3] Sanitary & Environmental Engineering Consultant, Ph.D. Student, Miriam College, PHILIPPINES. Email: carmelo@zantua.net

It is often dissatisfaction of impacted individuals surrounding the facility that demand something be done to correct the problem. Steps in resolving project failures include: forensic exploration, refurbishment works, wastes placement delays, increased maintenance, legal procedures, cost of money, political consequences, loss of reputation of concerned entity. These equate to considerable economic liabilities to the concerned entities and always surpass the original cost of the project during construction or operation due to unique demand for extra expenditures and externalities.

When public health, safety and environmental protection are threatened, a High Cost of Failure (HCF) must be assigned to it independent of the other issues. This is in-line with our principal intention in the preservation of lives and our common environment (capital resources). However, because these entities are so precious on their own rights, by merely assigning a high "price-tag" will not suffice.

SCOPE

To some, owing to the nature of the entities affected, this failure can be perceived to be unquantifiable. It is difficult to put a price on nature whose functions and services are sometimes intrinsically unknowable and have yet to be discovered. Money value for environmental damage as compared with the essence of human life and well-being is trivial by comparison, or can not be equated at all. Nonetheless, in the practical perspective, for all intents and purposes, it is necessary to put an economic value on these "failures" as called upon by the current societal procedures in resolving this kind of issue. However, this paper will not be providing extensive or detailed valuing processes relating to the cost of failures. Instead, a little considered line-item in many waste containment projects, "third party laboratory testing & analysis" as part of the MQA and CQA with direct correlation to HCF will be emphasized. Since the functionality of the subject facilities is dependent on the capability of the materials used and engineering design applied to meet the projects criterion; the term "failure" utilized herein refers to un-attainment of any or all of these requirements, which is to ultimately protect the well-being of the populace and environment.

Because there are so many causative and influencing factors involved for failures to occur and tremendous engineering measures to mitigate them, our aim is central to the importance of the role of the key parties in the industry; i.e., design engineers, MQA/CQA & third party testing laboratories. The significant interaction within and among this group, as shown in Fig. 1, can profoundly decrease the possibility of HCF. As stated by the Geotechnical Resource Group (2004), on the factors contributing to numerous stability failures that, a continuing coordination and involvement amongst the persons involved in design, construction, and operations is important.

So far, we have positively envisaged the inter-connectedness of waste containment projects, HCF, and human-environmental well-being. The proceeding sections provided more details on this topic.

On the other hand, It is also worth mentioning here that the referenced material prepared by Bonaparte et al. 2002 (Assessment and Recommendations for Improving the Performance of Waste Containment Systems – performed under EPA Cooperative Agreement–CR-821448-01-0) was heavily utilized in this paper due to its contained exhaustive information that are relevant to our points of discussions. We hereby recommend that the said manuscript be consulted for more detailed and useful information.

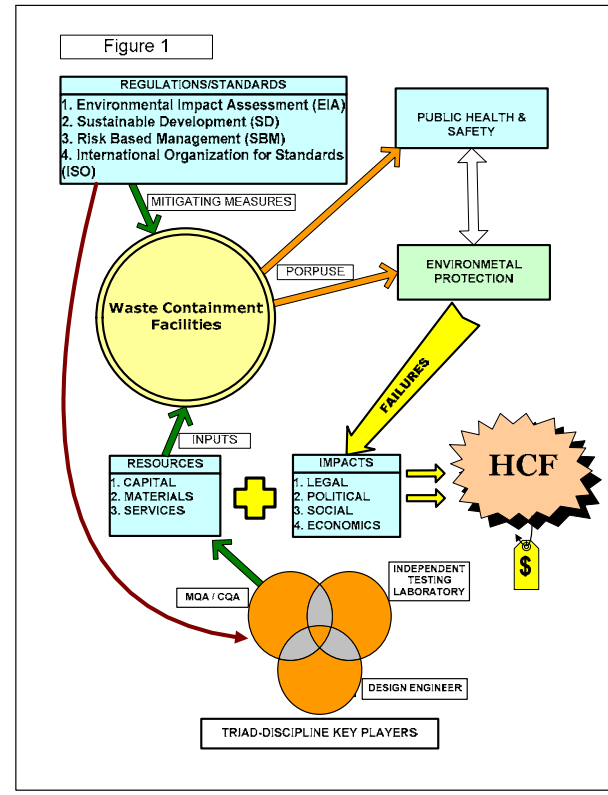

Fig. 1 Flow of Interactions Amongst the Important Key Players in the Geosynthetic Industry.

WHERE ARE WE NOW?

Vital details of the numerous and sometimes disastrous events of waste containment systems failures that have sporadically occurred elsewhere in the globe are not new to the knowledge of the geosynthetics and

construction industries. In the past and even in the most recent time, many problematic waste containment facilities involving geosynthetics have been noted to have encountered or are facing problems associated with the failure of liner systems and cover systems (Bonaparte et. al. 2002). Several slope stability problems were also adding to the number of landfill failure incidents evaluated. The degree of failure implications with different projects are so alarming that private/ governmental agencies and individuals have endeavored to scrutinize similar cases so as to understand the triggering mechanisms and trends governing them; evaluate pertinent externalities involved and to derived holistic resolution approaches out of these experiences. One good example is the comprehensive geotechnical and stability analyses for Ohio waste containment facilities conducted in 2004 by the Ohio EPA – Geotechnical Resource Group.

By so doing, various promising engineering solutions were suggested to address the issue. In congruent with this, better ways to effectively improve the overall design, construction methodology, and operations of the facilities are now cautiously being implemented. This integrative approach has contributed to the geosynthetic application projects in terms of attainment of optimum capital outlay, ease and effective operation, public health & safety, environmental protection, and various economic advantages.

WHAT IS CLEAR?

Even with the presence of all the necessary technical means, guidelines and controls that are accessible for use, landfill facilities failure incidents are still counting. Most of the failure events studied and reported by Bonaparte et al. 2002 (Appendix – F), demonstrated that the principal causes are attributable to: defective or substandard materials, poor workmanship, inappropriate construction methodology, and accidental damages incurred during construction. These problems are often times detected only during commissioning of the project or during operational stages. In some cases, the problems were caused by inefficient operational activities or poor management.

Those failures that resulted from substandard materials and/or poor workmanship as mentioned above could have been prevented or practically reduced to a manageable level should appropriate and adequate laboratory tests been performed as part of the QA/QC programs implementation. Little attention given or total disregards on the importance of prior independent laboratory analyses of the geosynthetics and field workmanship has lead to such unwanted experiences. Bonaparte et al. (2002) interestingly reported that some of the projects failed have utilized information from previous works completed by the same contractor/installer. Other projects made use of existing laboratory tests data or manufacturer's published data without undergoing laboratory validation procedures; and even worst, used inaccurate or un-conservative test methods or conditions. In the process, these were all extremely dangerous choices because they did not consider the number of factors that would essentially affect the design outcome and the quality of field workmanship and end-products. Obviously the importance was overlooked that every material being produced will have varying quality inconsistency throughout the production processes even with the same manufacturer.

Design associated problems were fifty one percent (51%) of the total number of failed facilities evaluated. In the conclusion, Bonaparte et al. (2002), lengthily lists the potential impacts to the immediate environment and severity levels of problems associated with landfill liner systems, cover systems, and impoundment liner systems failures. The paper also suggested varying problem prevention methods in various contexts, such as: design, CQA, material selection, technical specifications, training as well as other prevention methods. Design in this respect, is the analysis of the system in contact with open (natural) systems involving the intricate interaction of the geosynthetics to natural waters (subterranean run-off & leachate), soil-laden chemicals and external stresses such surface air velocity, type and weight of placement wastes, underground water and soil movement, and run-off abrasion effect capacities, and so on.

Clearly, in the course of the design process following a thorough material testing regime program shall not be discounted. The success of a landfill project can be achieved through the use of a verified or validated design and following it completely through the construction and operations stages. Compliance and acceptability of materials and finished work can be demonstrated directly by undergoing suitable laboratory testing and analyses. In this manner, design and laboratory testing through MQA/CQA must go hand-in-hand so as to assure the most plausible decisions. That is, to ensure attainment of the design efficiency and functionality of a waste containment facility to a certain degree in accordance with the site-specific criterion set forth.

By understanding that all the landfill problems seen in the past can practically be predicted and prevented; and that accumulated experience of the industry,

measures, control & standards are all at hand, what else is lacking so that this failure issue can be remedied or its impact weaken? The problem highlights that proactive or preventive measures are most often sacrificed and reactive steps are taken after the damaged has been done. Based on the lessons learned from the past, both material characteristics information and design numbers shall not to be guessed or referenced from other or previous projects. Nevertheless, it has been proven to be the case as pointed out previously. In addition, borrowing JP Giroud's statement (2006), "common sense or engineering judgment sometimes is not a viable reasoning option in scientific discipline decision-making".

Since most failures can be traced from or associated with uninformed decisions, is the question on ethical issue or professionalism among the key players valid? This question is a big challenge for the construction and geosynthetic industry to consider.

In terms of failures repercussions, previously mentioned, remedial actions incur additional monetary outlay precipitated from a ripple-effect. The extent of the resultant economic impact, however, is always dependent on the nature or severity of the problem and the required resources and effort to solve it. Generally, problems that are detected at the earlier stage of the project, i.e.; during construction, would probably be less costly to resolve than those discovered during operations. As reported by Bonaparte et al. (2002), "the cost of remedial efforts during the time of investigations ranged from below $10,000 for geomembrane holes identified during construction and more than several million dollars for repair of a liner system slope failure that occurred during cell operation".

Since some problems are can be anticipated in the successive phases of a project, a well planned and executed MCAQ/CQA can lessen the impact. For instance, poor quality or sub-standard geosynthetics are can be eliminated during the selection or design process through validation of the manufacturer's published data. The independent laboratory testing can confirm or determine quality variations that may occur during the production of the material. Also, timely and prudent implementation of the CQA during construction is a right venue for early detection of accidental damages or poor workmanship. Hence, the necessary repair can be applied quickly without causing so much delay.

WHERE DO WE WANT TO GO?

At the inception of a project, the economics involved largely influence decisions on the overall outcome of the project package and timing. During the phases of project design, construction, operation, and closure the fund appropriations are always "tightly" budgeted. Regardless of the extent of failure, any amount of failure will add up to another burden requiring sourcing effort for remedial funding and will be urgently necessary.

With this in mind, the aspiration to avoid or lessen the frequency or level of HCF as practicable is of paramount importance and must be adapted as the guiding principle in congruent with the overall quality program of a project. This further highlights the necessity to attain the intended purpose and functionality of landfill facilities. Nevertheless, we must recall that all of these, emanates from our original aim; i.e., to safeguard public health & safety and the conservation of the environment.

This interest must emerge as a common goal to every one involved. Yet, we can not attain our goals through our intentions alone and that appropriate actions must support this desire, as we may call it. Therefore, active and sincere participation of each discipline in all aspects of a project is very crucial.

In this endeavor, it is worthy to reiterate the grand role of the key actors whose commitment will make it happen. The essential interplay of this triad-discipline of Designer, MQA/CQA, and Independent Testing Laboratory as a group is very critical to ensure attainment of what is planned.

Through this interaction, our previous inquiry about professionalism and ethical dimension is intrinsically linked not only to the web of waste containment projects, HCF, and public-environmental well-being. Therefore, as the triad-discipline team works together with the intention to avoid or eliminate the HCF many problems can be prevented leading to successful landfill projects.

HOW DO WE GET THERE?

As we have seen in our previous discussions, none of the failure cases investigated was unpreventable. All the factors affecting the design, construction and operation of landfills can also be predicted similar to other even more complex and critical infrastructure installations such as: dams, bridges, and vertical structure installations. Assuming that the three key players are wittingly or unwittingly in agreement to end up with a successful project which we previously termed "intention"; what is that which is required from them to have it materialize is the corresponding appropriate "action". The action required must comprise of in-depth design with basis in the actual tested materials involved, rigorous administration and implementation of the

QA/QC (MQA/CQA) program during installation/ construction, and the application of best practices in the operation & maintenance of landfill systems.

However, this optimism would be difficult to realize, if not impossible, without the "will", which shall drive the entirety of this realm to reality. The "will" or determination would be a critical component that can be best played with government involvement. The state as we know has the sovereign responsibility to and for public interests and well-being. Thus, by putting to work all the purposely created regulations & standards could entail great influence in accomplishing the motive of this discussion. It is imperative to initiate a comprehensive monitoring and evaluation of landfill compliance that seeks for a new indicator of improvement/development that will supplement the now existing library of controls. This new database would incorporate both qualitative and quantitative measures of public health & safety, geosynthetics/construction industry capacity, and eco-logical health.

The above reasons represent a clear hint of what shall be done to handle HCF issues. And the contribution shall not just necessarily be coming from the intent, action and will of one entity or discipline, but of all who have a stake in the future of the still "young" geosynthetics industry. This approach will apparently harness, where appropriate, the talent and resources of the group through common ground for collaborative action. If largely implemented this will concretely address the dual challenge of managing the transition to "no or less" HCF and eventually effecting a paradigm shift amongst the key actors in the industry.

For the purpose of our discussions, let us focus on the three vital constituents of the industry, the Designer, MQA/CQA & Independent Testing Laboratories. Eventhough, we may agree that integration of a comprehensive testing plan to the overall QA/QC Plan of a landfill project is an important step that will enable accomplishment of the goal, but still, it is not an end in itself. It just reflects the intention. We still need to translate this intention into actions that are appropriate to our needs. To this, the key players' initiatives are put in to the scene. They must perform as a team for the proper administration and implementation of the quality plan.

From the manufacturing side, we have MQA that will ascertain the quality of materials to be used. An independent testing laboratory must be a part of the MQA to verify the data for design engineer's use. In this early stage of a project, we do realize that the "triad" is effectively collaborating to either evaluate or create a site-specific technical criterion. Take note of the term "site-specific" design. At the start of this paper, we have learned that some failure cases took place due to wrong assumptions or adoption of unverified manufacturer's published data. We shall take it here as a lesson learned so as not to mistakenly carry out on to new project applications. During design, the various geosynthetics can be qualified for their ability to achieve the design criterion and quality objectives. Laboratory and field tests information may be used to improve the design wherein a plausible decision for most economical design can be derived with confidence. In light of this, the necessary measures to avoid HCF must begin from choosing the right materials to be used.

In the course of the construction period, the group verifies the workmanship and monitors the materials characteristics variations due to exposure with varying natural stresses. The initial test reports generated from the material selection and design process, as database, are can be used as a tool in timely assessment of the integrity of the landfill systems. It could be effective, provided that the tests parameters used in the design were derived from the site-prevailing-conditions or conservative assumptions thereat.

During operational phase, the serviceability of the facility is dictated by the combination of: the life predicted for each material used, adequacy and appropriateness of design, overall quality of workmanship rendered during construction, and the operation & maintenance practices. Through proper design and well planned MQA and CQA most of the problems can be eliminated, saving the high cost of fixing the problems. Additionally, and likely more important than cost are damage to the natural environment and public health and safety. In this effect also, the industry will regain public confidence.

CONCLUSION

In relation to the foregoing, the following conclusions are hereby presented: (1) landfill system's failure always entails high remedial costs, (2) the causes and triggering mechanisms that affect the integrity of a landfill project are can be predicted and prevented to a practicable acceptable level, (3) a comprehensive testing regime via QA/QC (MQA/CQA) is one important aspect that determines the total and ultimate fate of a project, (4) the collaborative interaction of the key players: design engineer, MQC/CQA and third party testing laboratory in the geosynthetics/construction industry have a major role in the avoidance or reduction of unwanted system's failure in landfill projects, (5) the conceptual framework of collaborative approach showcased herein is applicable to all similar construction applications in achieving a successful project, (6) The

attainment of reducing HCF indirectly contributes in the achievement of various sustainable development principles, and (7) The role of related governmental involvement in spearheading activation of the EIA system and Sustainable Development principles are very imperative to the ever sought effective and efficient performance of the key players in the geosynthetics industry.

REFERENCES

Bonaparte, Rudolph et al. (2002) Assessment and Recommendations for Improving the Performance of Waste Containment Systems, Performed Under EPA Cooperative Agreement–CR-821448-01-0

De Havilland, Annette et al (2004) Geotechnical and Stability Analyses for Ohio Waste Containment Facilities

Edil, Tuncer B, Slope Stability Issues in Waste Disposal

Giroud JP (2006) Geosynthetic Engineering; Successes, Failures and Lessons; The Vienna Terzaghi Lecture in Yokohama September 18

Hsuan, Grace Y. Data base of field incidents used to establish HDPE geomembrane stress crack resistance specifications. 12th Geosynthetic Research Institute Conference

Koerner R, Soong TY (1999) Assessment of Ten Landfill Using 2D and 3D Stability Analysis Procedures. Proceedings of the 2nd Austrian Geotechnical Conference, H. Brandl. Ed. February 1999. Vienna, Austria

Koerner R, Soong TY (2001) Geosynthetic Reinforced Segmental retaining Walls. Geotextiles and Geomembranes 19: 359-386

Peggs, Lara, Elizabeth, Insurance—Construction Risk Management. GFR 22(7)

Raymond Gerald P, Giroud JP (1993) Geosynthetics case Histories. ISSMFE Technical Committee TC9 Geotextiles and Geosynthetics, March 1993

Rowe RK (2005) Long-Term Performance of Contaminant Barrier Systems. Geotechnique 55(9): 631-678

Scarborough, Jesse A (2005) A Tale of Two Walls; case Histories of Failed MSE Walls. Geo-Frontiers 2005 Conference Proceedings GSP 140

Seed RB, Mitchell JK, Seed B H (1990) Kettleman Hills Waste Landfill Slope Failure II: Stability Analysis. Journal of Geotechnical Engineering 116(4): 669-690

Yoo C, Jung HY (2006) Case History of Geosynthetic Reinforced Segmented Retaining Wall Failure. Journal of Geotechnical and Geoenvironmental Engineering 132(12): 1536-1548

Zang, JK, Anti-Competitive Conducts. China Experience. Development Research Center of the Sate Council, PRC 2004-6-22

CALCULATING THEORY OF SLOPE STABILITY INFLUENCED BY COMBINED UNDERGROUND AND OPEN PIT EXTRACTION

S.G. Sun[1], Q.F. Ran[2], D.L. Wu[3], J.C. Zhu[4], W.G. Duan[5] and S.J. Feng[6]

ABSTRACT: Aiming at rock mass deformation and failure character of slope, this paper mainly studies evaluating method of slope stability according to effect of combined underground and open pit extraction. Factor of underground mining was not considered in the past. Therefore, the conclusion was different from actual result. This paper relies on theory of random medium and starts from analysis of deformed stress of rock mass influenced by underground mining. Influencing feature of underground mining for slope rock mass is systematically analyzed. Then, evaluating theory and method for slope stability under combined mining effect is derived. By means of analysis result of theory and history-case, underground mining effect must be considered. Otherwise, result of calculation is not reasonable.

KEYWORDS: engineering extraction, mining influence, superimposition, slope stability

INTRODUCTION

In the course of extraction for all kinds of mines, a situation for combined underground and open pit mining existed. i.e., shallow ore is extracted by open pit mining and deep ore is extracted by underground mining. Open pit slope is situated in influenced zone of underground mining. Deformation and failure for slope rock mass are influenced by open pit mining, as well as underground mining. Deformation for slope rock mass was superimposed by combined underground and open pit mining. Thereby, all kinds of influence factors in open pit mining are considered in analysis of slope stability. Factor of underground mining ought to be added. Nevertheless, when this kind of problem was analyzed in the past, that strength of whole slope rock mass had only been decreased by underground mining was considered. It is neglected that the additional deformed stress acting on slope rock mass was produced by underground mining. Slope rock mass deformation was greatly produced. So, this influence factor ought to be considered in slope stability analysis. Stability of slope is really reflected on objectivity and over all fields. Therefore, this problem was studied and probed. Then the related calculating theories and methods in analysis were given.

BASIC PRINCIPLE

As show in Fig. 1, unbalance stress in slope rock mass is produced by open pit mining and other engineering environmental change （Bello Garcia 1997； and is also influenced by underground mining when underground and open pit mine extracted at same period. Underground mining produced two kinds of influences. One was great deformation of overlying rock mass of slope, which made it changeable that distribution of layer position and original rock stress. Thereby strength for whole slope rock mass was decreased. On other hand, internal stress state of rock mass produced essential change under its influence zone as underground mining produced deformation for overlying rock mass of slope. Deformed stress on different space position was not same. Meanwhile, the deformed stress will directly act on rock mass of slope, which increased deformation and failure of slope. Therefore, besides underground mining factor which decreased strength for whole slope rock mass was considered in the analysis of slope stability, deformed stress that underground mining produced for overlying rock mass of slope must also be considered. This paper would analyze the principle of calculation.

In Fig. 1, a unit body of ABCD is taken. Due to influence of underground mining, both sides of unit body produced unequal horizontal displacement, upper plane and lower plane of unit body produced unequal

[1] Department of civil engineering, North China University of Technology, Beijing, CHNIA. Email:ssg918@163.com
[2] Mine Bureau of Xiaolongtan, Yunnan Province, CHNIA. Email:ranqf.student@sina.com
[3] Mine Bureau of Xiaolongtan, Yunnan Province, CHNIA. Email:xltwdl@126.com
[4] Mine Bureau of Xiaolongtan, Yunnan Province, CHNIA. Email:xltyn@126.com
[5] North China University of Technology, Beijing, CHNIA. Email:duanweiguo456@163.com
[6] North China University of Technology, Beijing, CHNIA. Email:fsjiee@163.com

subsidence. The changes made unit body produce horizontal strain and vertical strain, as show in Fig. 2. Horizontal deformed stress was produced by underground mining as the following.

$$\sigma = E \cdot \varepsilon = E \cdot b \frac{d^2 W(\rho)}{d\rho^2} \qquad (1)$$

$$\sigma = E \cdot \varepsilon = E \cdot b \frac{d^2 W(\rho + \Delta\rho)}{d\rho^2}$$

where b—horizontal displaced coefficient; E—elastic modulus; ρ—polar coordinates; $W(\rho)$—subsidence value.

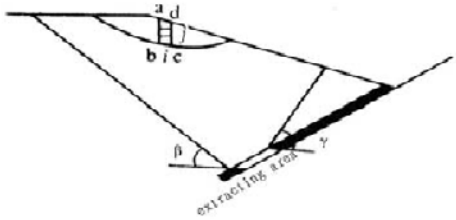

Fig. 1 relative position relationship of combined underground and open pit mining

Because subsidence of upper plane and lower plane of unit body was unequal, it produced vertical deformed stress. In general, under influence zone of underground mining, subsidence of any point of different depth far from surface was as following.

$$W(x, y) = \frac{W_{\max}}{R_x^2} \iint_A e^{-\pi(x^2+y^2)} \, dx \, dy \qquad (2)$$

where W_{max}—maximum subsidence value at the plane in depth z_i, A—extracting area. γ—unit weight;

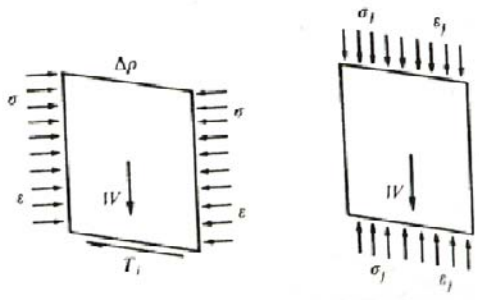

Fig. 2 Underground mining stress effect

In Fig. 2, resistant sliding force of unit body:

$$T_i = \Delta z_i \cdot \Delta\rho \cdot \gamma \sin\alpha_i \cdot \tan\phi + \Delta\rho_i(\sigma_{1i} - \sigma'_{1i}) \sin\alpha_i + \Delta z_i(\sigma_i - \sigma'_i)\cos\alpha_i \qquad (3)$$

Sliding force of unit body:

$$T'_i = \Delta z_i \Delta\rho_i \gamma \sin\alpha_i + \Delta\rho_i(\sigma_{1i} - \sigma_{1i}) \sin\alpha_i + \Delta z_i(\sigma_i - \sigma_i)\cos\alpha_i \qquad (4)$$

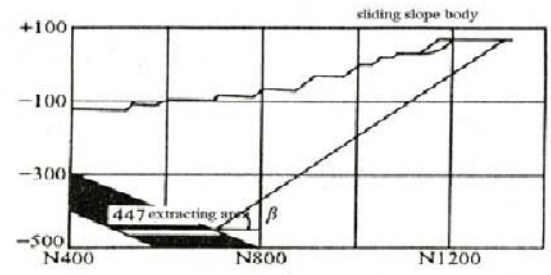

Fig. 3 Section diagram of hiding sliding slope body

Coefficient of safety about hiding sliding body was:

$$F = \sum_{i=1}^{n} \frac{\tan\phi\left[\frac{\gamma\cos\alpha_i + E(\varepsilon_{1i} - \varepsilon_{1i})}{\Delta z_i \cos\alpha_i} + \frac{E(\varepsilon_i - \varepsilon_i)}{\Delta\rho_i \sin\alpha_i}\right] + \frac{c}{\Delta z_i}}{\gamma\sin\alpha_i + \frac{E(\varepsilon_{1i} - \varepsilon_{1i})}{\Delta z_i \sin\alpha_i} + \frac{E(\varepsilon_i - \varepsilon_i)}{\Delta\rho_i \cos\alpha_i}} \qquad (5)$$

where γ—unit weight; α_i—Included angle between weight line and normal at middle of lower edge of unit body; ε_{1i}, ε_{1i}—Vertical strain value of unit body upper plane and lower plane respectively; ε_i, ε_i— Horizontal strain value of unit body's both sides respectively; c, ϕ, E—cohesion, angle of internal friction and elastic module respectively.

Because $\frac{\varepsilon_{1i} - \varepsilon^{n}_{1i}}{\Delta z_i} = \frac{d\varepsilon_1}{dz}$ and $\frac{\varepsilon_i - \varepsilon^{n}_{i}}{\Delta\rho_i} = \frac{d\varepsilon}{d\rho}$

Then Eq. 5 became:

$$F = \sum_{i=1}^{n} \{[\tan\varphi \cdot (\gamma\cos\alpha_i + E\frac{d\varepsilon_1}{dz}\cos\alpha_i + E\frac{d\varepsilon}{d\rho}\sin\alpha_i) + \frac{c}{\Delta z_i}] / [\gamma\sin\alpha_i + E\frac{d\varepsilon_1}{dz}\sin\alpha_i + E\frac{d\varepsilon}{d\rho}\cos\alpha_i]\} \qquad (6)$$

Eq. 6 is theoretical solution for slope stability when underground and open pit extraction at the same period. The $d\varepsilon/dz$ and $d\varepsilon/d\rho$ are calculated by following method.

The following parameter can be derived from Eq. 3:

(1) Horizontal strain along any direction (included angle between φ and axes x):

$$\varepsilon_\varphi = \varepsilon_x c_y \cos^2\varphi + \varepsilon_y c_x \sin\varphi + \frac{u_x i_y + i_x u_y}{2w_{\max}} \sin 2\varphi \qquad (7)$$

(2) Subsidence distribution coefficient along main cross-section of strike and dip:

$$c_x = \frac{[erf(\sqrt{\pi}\frac{x}{R_z})+1]-[\frac{erf(\sqrt{\pi}(x-L_x)}{R_z})+1]}{2} \quad (8)$$

$$c_y = \frac{[erf(\sqrt{\pi}\frac{y}{R_z})+1]-[erf(\sqrt{\pi}(y-L_y)/R_z)+1]}{2} \quad (9)$$

(3) Horizontal displacement:

$$\begin{aligned} u_x &= bw_{\max}[e^{-\pi\frac{x^2}{R_Z^2}} - e^{-\pi\frac{(x-L_X)^2}{R_Z^2}}] \\ u_y &= bw_{\max}[e^{-\pi\frac{y^2}{R_{z2}}} - e^{-\pi\frac{(y-L_y)^2}{R_z^2}}] \end{aligned} \quad (10)$$

(4) Curvature deformation:

$$\begin{aligned} k_x &= -2\pi\frac{w_{\max}}{R_z}[\frac{x}{R_z}e^{-\pi\frac{x^2}{R_Z^2}} - \frac{x-L_x}{R_Z}e^{-\pi\frac{(x-L_X)^2}{R_Z^2}}] \\ K_y &= -2\pi\frac{w_{\max}}{R_z}[\frac{y}{R_z}e^{-\pi\frac{y^2}{R_{z2}}} - \frac{x-L_y}{R_z}e^{-\pi\frac{(y-L_y)^2}{R_z^2}}] \end{aligned} \quad (11)$$

where: L_x, L_y—length along the strike and dip of slope respectively. The other parameter is same as above.

Derivative of horizontal strain along any direction is as follows:

$$\begin{aligned} \frac{d\varepsilon}{d\rho} &= \frac{d\varepsilon_x}{dx}c_y\cos^2\varphi + \frac{\varepsilon_y i_x\cos\varphi\sin^2\varphi}{w_{\max}} \\ &+ (\varepsilon_x i_y + u_x k_y)\cos^2\varphi\sin\varphi + \frac{d\varepsilon_y}{dy}c_x\sin^2\varphi \\ &+ \frac{\varepsilon_x i_y\sin\varphi\cos^2\varphi}{w_{\max}} + (\varepsilon i_y i_x + u_x k_y)\sin^2\varphi\cos\varphi \end{aligned} \quad (12)$$

The strain value can be calculated from Eqs. 7—10.

$$\varepsilon_1 = (i_x c_y\cos\varphi + i_y c_x\sin\varphi)/\tan\beta \quad (13)$$

where β—moving angle of rock layer.

Derivative of vertical strain to depth can be calculated as following method.

$$\frac{d\varepsilon_1}{dz} = \frac{k_x c_y\cos^2\varphi + k_y c_x\sin^2\varphi + \frac{i_x i_y}{w_{\max}}\sin 2\varphi}{\tan^2\beta} \quad (14)$$

The coefficient of slope stability is function of subsidence, horizontal displacement, horizontal strain, inclination and curvature deformation. Nevertheless, the deformed parameter above is not the same if it is situated in different space position of the overlying rock mass of slope Meanwhile, these parameter values are also decided by method of mining, geological structure and strength of rock mass etc. Therefore, if influence of underground mining is neglected, this obvious is unreasonable. Other evaluating methods of slope stability for underground mining influence are also as same as mentioned above.

CASE-HISTORY CALCULATION AND ANALYSIS

Summary of Landslide

E1000 zone in Fushun West Open Pit Mine produced a great landslide on March 30, 1986. The range of landslide zone was from E928 to E1096 along the strike, from N1087 to N1197 along the dip, and elevation from +75 to +33.7 m. The strike length from east to west was 168m, the dip width from south to north was 110 m，the difference of elevation was 41.3 m, the volume of landslide was $6.8\times10^5 m^3$.

Engineering geology character

Landslide occurred in surface soil of Quaternary period and Green argillaceous rock of Tertiary system，which included weathering green shale with the of thickness 12 m between them. Thickness of surface soil was 8—11 m. Green argillaceous rock is dip to north, which distribution is layer with shale. Bedding of landslide zone that is included many incompetent beds is great development. North side of sliding zone is F1 reversed fault.

Influence of open pit mining

Since 1982，the zone of slope gradually extracted to boundary of slope. 4-28 segment's artery moved to north. 4-28 segments was combined with 7-28 segment in February, 1986 as extracting 8m to north was extended. Because mining was extended, dip angle was increased. Stability of slope was influenced by open pit mining.

Influence of underground mining

Besides this zone slope was influenced by open pit mining, 447 slope in Shengli Mine extracted coal column of proof water between open pit and underground mine from May, 1985—1986 when open pit mining was extended. Range of underground slope was from E925 to E1250 along strike and elevation from -425 to -440 m. Fig. 3 shows the position relation between underground slope and open pit slope. Because of influence of underground mining, overlying rock mass of slope produced deformation and failure. The stability state of slope is influenced due to combined underground and open pit extracting. So, two main influence factors about underground and open pit mining would be considered in stability analysis and calculation of slope.

History-case Calculation

Landslide body was mainly at circular pattern (see Fig. 3), while boundary was that maximum crack of surface was as upper edge of landslide body and boundary of lower edge of lower toe of slope at 33.7 m. Upper surface sank 8 m in real measuring. Occurrence of plane was 180—188° and dip angle 36°. Lower part of landslide body moved 15 m to south and arose 1—3 m. In order to analyze influence about underground mining to stability of slope, the stability influenced by only open pit mining is analyzed, the parameters are shown in Table 1. Without water pressure effect and $d\varepsilon_1/dz$ being equal to zero, calculation and analysis were carried out. When friction angle of green argillaceous rock was 25°, coefficient of slope safety was 1. That was to say that slope stability was critical state. If influence factor of underground mining was added at this time, coefficient of slope safety was 0.82 according Eq. 6. Thereby, influence of underground mining can not be neglected. It is one of main factor to produce landslide.

CONCLUSIONS

This paper derived systemically theoretical method of slope stability evaluation under combined underground and open pit extracting. According to analysis result of theory and history-case, that influence of underground mining is one of main factors is obtained. During analysis of slope stability influenced by combined underground mining and open pit mining, two kinds of mining influencing factors ought to be considered. Otherwise, evaluating result is different from actual situation. The calculation method is suitable to evaluation and calculation not only for the state of slope stability in underground extracting and open pit extracting at the same period, but also suitable to that open pit mine first extracting and forming the slopes on a certain scale. Then the stability evaluation of slope is carried by influence of underground extracting. Moreover, it is also suitable to the stability valuation of hill zone slope carried out by underground mining influence in order to avoid or decrease economic loss. Therefore, before mining, evaluation of slope stability is great beneficial. Moreover, the theory and method is also suitable to that stability valuation for roadbed of railway or highway is carried out by influence of underground mining.

Table 1 Moving parameter of rock layer and mechanic parameter

Rock property	Thickness (m)	cohesion (kpa)	Angle of internal friction(°)	Specific gravity (10^3kg/m$^{3)}$	Elastic module （Mpa）
surface soil of Q.P	10	3.069	11	1.88	12
weathering green shale	12	3.942	11.78	2.00	910
green argillaceous rock		5.011		2.07	1000
moving parameter of rock	coefficient of subsidence	Extracting thickness (m)	Moving angle (°)	Extracting depth (m)	Dip angle (°)
	0.22	15	39	432.5	22

ACKNOWLEDGEMENT

The authors are grateful to the support of Beijing Municipal Education Commission project (KM2007 10009007) and North China University of Technology project.

REFERENCES

Adhikary DP (1997) A Study of The Mechanism of Flexural toppling Failure of Rock slopes. Rock Mechanics and Rock Enginering 30(2): 50-459

Bello Garcia A (1997) Parameter Optimization of Influence Functions in Mining subsidence. Inter. J. of Rock Mech. & Mining Sci 34(7): 45-50

Okubo S (1997) Local safety factor Applicable to Wide Rouge of Failure Criteria. Rock Mechanics and Rock Engineering 30(4): 30-36

Sun SG (1995) Effect of Combined Underground and Open Pit Mining and Deformation Mechanism of Slope; Chinese J. of Rock Mech. and Eng 15(5): 563-566(Chinese)

Dun SG (1999) Numeral Value Analysis of Slope Rock Mass Deformation Mechanism under Combined Mining Influence. J. of Univ. of Science and Technology Beijing 21(5): 417-420(Chinese)

VERTICAL ECOLOGICAL RESTORATION TECHNIQUE FOR THE HIGH-STEEP ROCK SLOPES OF HIGHWAY IN MOUNTAINOUS AREA

H. Zhu [1], D.H. Ruan [2] and S.Y. Qin [3]

ABSTRACT: The ecological restoration and revegetation of high-steep rock slopes is very difficult in highway construction in the mountain area. The traditional methods of revegetation such as borrowed-soil spraying, hydro seeding are very difficult to achieve good results. This paper presents the ecosystem, composed by green geonet which can be defined as geomask net and climbing plants, its structure, construction technology and short and long term ecological effect. The ecosystem was initially applied successfully as an ecological revegetation for high-steep rock slopes in China. It was observed over four years of project that it achieved a satisfactory ecological restoration result. The technical specification for vertical ecological restoration using geomask net with climbing plants as re vegetation for high steep rock slopes of highway in mountain area was complied with the support of the Hubei Hurongxi Highway Construction head office.

KEYWORDS: ecological restoration and revegetation, geo-mask net, climbing plants, high-steep rock slope

INTRODUCTION

The highway construction in the mountain area is a process of artificial interference and building on the natural environment in the mountain area. During the process of building, a large amount of rock slope, weathered rock slope, red sandstone slope can be found causing the original vegetation and ecosystems to be completely destroyed. What's worse, in this area is the soil is usually barren and natural recovery cycle of vegetation takes a very long time. If it is not protected in time, soil erosion will occur easily and thus induce undermining the road structure and endangering traffic safety. Both vegetation restoration and environmental protection are difficult problems for contractors and construction companies.

Many international research institutions are exploring suitable methods and technologies, such as role rock slope and poor soil slope green technology. If the slope rate is higher than 1:0.75, it is extremely difficult to use technologies such as borrowed soil spraying and hydro seeding vegetation and guarantee the long term effects. Moreover, these technologies require good fertile soil structure to make the plant growing nutrient matrix layer structure. This needs extensive borrowed soil forming taken from other places thereby causing a new excavation or the occupation of farmland destroying natural vegetation and creating new bare land. The vertical green technology of combining green geo-mask net with climbing plants is used by planting different climbing plants at the foot of the slope, on the top of the slope or on the grade slope of intermediate grade platform. This technology only needs a small mount of planting soil nearby and can be used in all kinds of slope rates, even on anti-vertical slope.

THE PRINCIPLE OF VERTICAL GREEN TECHNOLOGY

Vertical green technology of combining green geo-mask net with climbing plants is a new type of slope ecological protection technology developed by Yichang Bluet Environmental Engineering Ltd. By installing the Green geo-mask net on the surface of the rock slope, mainly using its porous structure, it provides growth stem for the vine plant growth. Meanwhile, the Green geo-mask net can prevent falling rock from the slope surface. The green geo-mask of the highway slope can improve landscape effects and can mitigate the vision fatigue of the drivers. The planting nutrition bed is on the bottom slope or the middle class of grade platform with backfilling with disinfection for improved soil. When planted the vine plants and flowers will have a long period of green, which is suitable for the local environment, in the planting nutrition bed. Accordingly, different vine plants are selected to suit different conditions. Eventually the plants will combine with each

[1] Senior Engineer, Hubei Nete Geosynthetics Ltd. CHINA.Email: 0717zhuhong@163.com
[2]Senior Engineer, Yichang Bluet Environment Engineering Ltd. CHINA
[3] Engineer, Yichang Bluet Environment Engineering Ltd. CHINA

other, forming a vine plant network structure on the surface of the rock slope. After natural evolution, the natural landscape will be restored with renewed ecological structure and ecological protection will be achieved. This technology has both the protection function and the natural landscape effect.

CONSTRUCTION PROCESS

Construction Technology

Construction procedure is list as follows:

Handling slope surface⟶ Installation of Green geo-mask net ⟶Fixing the planting nutrition bed ⟶ soil backfilling ⟶ Maintenance and management.

(1) Handling slope surface

Liquidate slope loose stones and debris table.

Consolidate the instability area by spraying concrete or repairing.

(2) Installation of green geo-mask net

Choose HDPE CE131 geonet as geo-mask net because it will be exposed over the slope. It is necessary to add anti-aging agents and flame retardants in the geomask net.

(3) Fixing green geo-mask net

If the slope is not weathered or weak weathered, the Green geo-mask net are fixed by φ10 diameter expansion bolts and metal gaskets which are bigger than the mesh size. If the slope is a weathered, strongly weathered or loose and broken, the green geo-mask net must be fixed by steel stick with 1.5 m×1.5 m spacing in the shape of winter sweet. It must be reinforced at every joint.

(4) The planting nutrition bed construction

The planting nutrition bed must be built by the foot of the slope in the shape of strip with 50 cm—80 cm wide and 50 cm—100 cm high. In that way, it can save the soil source and reduce the cost. In field construction, it can be built along the slope. While in the city it can be decorated by wall tiles. In order to prevent the salinity, compaction of the soil should install a small drain hole every 3 metres.

(5) Soil backfilling

Drainage pipe with geotextile or 5cm thick gravel layer in the bottom of the planting nutrition bed is used. The soil that is loose, fertile, and easy for plant growing are selected. It is a required to add some improved material and disinfectant treatment in soil. Taking account of the settlement of the soil after rain, generally the soil must be 5 cm—10 cm higher than the planting nutrition bed generally.

(6) Climbing plants cultivation

It is suggested to select 3—5 species of vine plants to adapt to the local environment. These are usually from different varieties of evergreen and deciduous flower vine plants. Then plant these about 20 cm apart. For a multi-platform slope, we can plant on both sides of the planting nutrition bed, drooping plants on the outside and climbing plants on the inside.

(7) Maintenance and management

(1) watering; (2) fertilization; (3) exception the weeds; (4) pest prevention; and (5) traction the purpose of traction are to guide climbers to entangle the geo-mask net to the setting direction. This will help the growth of the plants thus allowing the slope surface to be covered as soon as possible. Traction must be carried after planting.

Important Notes of Construction

(1) The main factions of geo-mask net are to provide the plant a framework for growth, to prevent gravel falling from the slope and to beautify the environment. Therefore, the geo-mask net must have a certain level of intensity, a porous structure and similar colors to the vegetation. Besides the advantages mentioned above, it has the quality of flexibility which means easy to install in the slope. Alternative metal net has high intensity but it can easily corrode and because of its strong thermal conductivity, it will decrease the growing speed of plants in summer.

(2) Depending on the local conditions native plants are recommended to chose. Before construction, research must be made about the distribution and the growth situation of local vine plants to decide the varieties to plant. The introduction of alien species must be done carefully to prevent the ecological catastrophe caused by biological invasions.

(3) Eco-rock slope protection works are generally on high steep slopes where poor conditions exist for construction. The geo-mask net is usually installed in very high places. Therefore special attention should be paid to construction safety measures. All construction workers must receive adequate safety training, be

equipped with proper safety equipment and must obey the strict rules of operating safely during the construction. One person should be responsible for the full-time security in work site. In large-scale civil engineering construction, it is very common to complete many jobs at the same time. The installation of the net must be isolated from other construction activities and completed separately.

(4) Construction is often affected by objective factors such as geographical and seasonal conditions. According to the actual situation, we can grow the plant in a mantle of nutrition in the nursery. After the completion of the building projects, the plants can be transplanted into the planting nutrition bed. This should increase the survival rate of seedlings, reduce conservation strength and overcome the impact of seasonal factors.

(5) The rationale of Vertical green technology of combining green geo-mask net with climbing plants is to restore ecosystems of the slope, beautify the environment, but not to resolve their own stability problems of slope. The prerequisite of this technology is the security and stability of the slope.

The Necessary Machinery Facilities

(1) Air compressor, Pneumatic hammer Mainly use to process the slope surface;
(2) Generator, electric hammer: for the geo-mask net installation and fixation;
(3) Small hoist (for the transportation of the construction materials and planting soil for multi-grade slope);
(4) Vehicle;
(5) Safety equipment.

THE DISPOSITION OF THE VERTICAL GREEN TECHNOLOGY

Selection of the Climbing Plants

Because of the impact of the construction site and environment, the Engineering ecological protection differs from urban gardening. Therefore, the choice of climbers must obey the following requirements:

(1) Wood vine plants;
(2) Strong adaptability and resistance of extensive management;
(3) Rapid growth that can cover rock slope as soon as possible;
(4) Strong ability of climbing, with well-developed root suckers or aerial root;
(5) Better landscape effects, mainly evergreen.

Principles of Climbing Plants Allocation.

1) According to local conditions, the plants which are selected should adapt to the local soil, climate conditions.
2) Preferred the native plants. After natural evolution the native plants will have adapted to the local soil, climate and other conditions. So it is easy for the plants to survive after planting to facilitate conservation and management and to prevent the risk of the introduction of alien species.
3) Principle of diversification of plant configuration. The evergreen, deciduous, vine spacing of planting flowers, rich cultivation levels reaching close to the surrounding natural landscape effect. Many varieties can be planted, and with plant competition the survival of the fittest may also promote the rapid growth of plants.Plant configuration should also be considered for the easy cultivation of plants for Green Project to provide adequate seed sources, cost savings and achieve a faster greening landscape effect. Small shrubs can be planted within the squad ball, woody flowers, rich green levels, enhanced visual effects.

Examples of Plant Configuration

Choice of the vine plant

The Yichang section of Shanghai—Chengdu expressway is a mountain highway. During the construction large excavations were carried out thus exposing rock slopes. This is now protected by vertical green technology of combining green geo-mask net with climbing plants. According to the research of the local wild vine plants and reference information, we chose the following vine plants in the implementation:

(10) Mucuna Sempervirens. It is a perennial evergreen vine plant of the legumes branch, which likes warm areas and resists the wet. It is widely distributed in south of China. It is a decorative plant with green leaves, purple fleshy, and flowering in April.

(2) Parthenocissus henryame

It is a vine plant of the Vitaceae branch with strong adaptability and a huge body. It grows fast with a lot of leafs which has a good covering effect. It is widely distributed and easy to reproduce. In autumn, the leaves will become red or orange in colour.

(3) Campsis Lour.It is deciduous vines plant of bignoniaceae branch, with aerial rooton its root. It clings to other plants, likes a warm, wet and humid environment. It has poly umbrella flowers or cone flowers inflorescence on the top. The corolla is funnel-shaped with bright red or orange color. It is the ideal vertical greening, landscaping flower varieties

(4) Pueraria thunbergiana Benth. It is a deciduous vine plant of legumes branch with a strong root system. It is lying on the ground or vine-entangled in the growth of other plants. The kudzu is strong, easily adapts to the soil, grows rapidly and spread strongly with dense branches. It is a good ground cover plant to protect the soil and water. The fallen leaves can improve soil fertility effect.

Configuration of liana plant

The project design was based on Four Seasons Evergreen. In the process of planting, we planted two Mucuna Sempervirens, one Parthenocissus henryame, one Campsis Lour and one Pueraria thunbergiana Benth every two meters. In the planting nutrition bed, we planted lobular privet ball, Lagerstroemia and GuiCong in 5m planting intervals.

August 2007, more than four years after the project implementation, various vine plants are growing well. All single-slopes are covered, and the Multi-grade slopes are covered by 90% coverage on average. Various plants mutually cling with each other. In spring and summer, the purple and red flowers are shining in the green leaves. In autumn, the plants are decorated by many fruits and in winter the evergreen vine is also beautiful. Therefore the landscape has many different characteristics throughout the year and plays the multiple role and function of ecological protection, ecological restoration and landscaping.

Liana plant growth in long- term

Some of the vine plants have their own suckers so they can climb without using stents, such as Parthenocissus henryame. In the project, we selected used a slope as an test case. In one region we installed geo-mask net. In another region we planted the same variety and specifications of vine plants without geo-mask net to compare its growth rate. The data is shown in Table 1.

(1) In the region with geo-mask net, the growth rate of several of vine plants, either drooping or climbing, was much higher than without geomask net region, even the Parthenocissus henryame whilst so doing, without the support of Parthenocissus tricuspidata.

(2) The growth rate of climbing plants is much higher than the growth rate of drooping plants. The liana plant likes to attach to other fork plants. If the fork plants are far away, it will choose the nearest plant to attach to. When there is nothing to attach to, it will lie on the ground and grow to the direction of other plants until it contacts with a clinging on plant. If it does not cling to the object, it will drop its vine and the growth rate will slow down gradually. Therefore, the use of geo-mask net will be able to make full use of the climbing characteristics of plants.

Table1 Liana Plant Growth Comparison (m/year)

Item	Climbing Plants		Drooping Plants	
	Geomask net	Without geomask net	geomask net	Without geomask net
Mucuna Sempervirens	11.5	5.0	3.7	1.0
Parthenocissus henryame	6.1	3.5	1.9	0.9
Campsis Lour	9.3	4.7	3.2	1.1
Pueraria thunbergiana Benth	10.5	7.3	2.9	1.45

CONCLUSIONS

The vertical green technology of combining green geo-mask net with climbing plants has already been successfully applied in Shanghai-Chengdu West Section Expressway, the Three Gorges Project and other important projects in China. The construction technology is simple, low cost and can easily be applied over a large area. It is particularly applicable to rock slope, slope shotcrete, rubble-stone retaining wall and other areas that other green technologies are unable to or are difficult to green. This will have the effect of ecological protection which can be widely used in rail, road, watering, municipal, mining and different engineering fields. It will produce very good social and economic benefits.

REFERENCES

Zhu H, Ruan DH (1998) treatment of container stockyard using stress distribution ability geonet. Proc.of sixth international conference on geosynthetics: 923-926

Paul NV Truong (1999) Vetiver grass technology for mine tailings rehabilitation.proc. of the first Asia-Pacific conference on ground and water bioengineering for erosion control slope stabilization: 315-325

INFLUENCES OF A RAINFALL ON THE STABILITY OF GRANITE RESIDUAL SOIL SLOPES

J. Gao[1] and J. Pan[2]

ABSTRACT: Observations showed that an overwhelming majority of landslides occurred during or after a rainfall. Infiltration of rainwater into slope would increase weight of the slope, change pore water pressure in the slope, and reduce shear strength of the soil. In an unsaturated soil slope, the matrix suction, which could be regarded as negative pore water pressure, was one of the major factors that influenced the stability of a slope. The influences of a rainfall on negative pore water pressures and the stability of a slope have been analyzed in this paper by simulating negative pore water pressure distribution of the slope under various rainfall intensities, with the help of a finite element software—GEO-SLOPE-SEEP/W. The importance of matrix suction to the stability of a slope was elaborated through the calculation of a granite residual soil slope project. Results showed that the safety factor of a slope was obviously underestimated if no matrix suction was considered. It differs much from the actual case.

KEYWORDS: granite residual soil, rainfall, matrix suction, negative pore water pressure, GEO-SLOPE-SEEP/W finite element simulation

SOFTENING AND DISINTEGRATION OF GRANITE RESIDUAL SOIL

Granite residual soil is the residual debris of granite after its physical and chemical weathering. In east of Yunnan-Guizhou Plateau in China, especially in Guangdong, Fujian, the southeastern Guangxi, the southern Hunan, and the southern Jiangxi, there is a wide distribution of granite. In the granite residual soil, the amount of particles greater than 0.5 mm and less than 0.074 mm is larger than that between 0.5—0.074 mm. And the total content of coarse soil particles is similar to that of fine soil particles, with a sector of 0.074 mm. The particle size range of granite residual soil decides its microstructure: the coarse soil particles are stuck together by parceling and padding of free oxides, and fine and silt sands are little in the skeleton, so the void ratio is large.

The natural state of a granite residual soil skeleton is like a rigid frame. When soil is to soak and cements is to dissolve, the rigid nodes of frames are gradually weakened and changed into hinge joints, causing a decrease of strength and an increase of compression in the soil. If there is a free-face, after cements completely dissolving and nodes completely destroyed, the soil near the free-face will disintegrate and collapse naturally. Apparently, if the soil is first disturbed by shrinkage, unloading, or other disturbances, some even most of its rigid nodes becoming hinge joints, and secondly immersed in water, it will soften and disintegrate faster. Some studies show that water-softening and disintegration of granite residual soil is a complex process and difficult to be judged in quantity. (Zhu 2002; Chen 2006; Liu et al. 2004). In order to analyze the influences of a rainfall to the distribution of negative pore water pressure and to the stability of a slope, assume that the residual soil in high saturated region, which is formed in residual granite soil slope, has completely softened and collapsed under a rainfall, and the shear strength of soil will be appropriately reduced.

NEGATIVE PORE WATER PRESSURES IN A SLOPE DURING OR AFTER A RAINFALL

Unsaturated soil is composed of soil particles and water and air. In the interaction between soil particles and water, soil particles demonstrate the compatibility, which is a retention to water. Its mechanism is very complex, but can be summarized as adsorption and capillarity, namely Matrix Suction in soil mechanics. And the retention of the solute in the soil solution to soil

[1] Graduate student, School of Civil and Traffic Engineering, South China University of Technology, CHINA. Email:cngaojian@gmail.com
[2] Associate Professor, School of Civil and Traffic Engineering, South China University of Technology, CHINA. Email:cvpan@scut.edu.cn

moisture is named Osmotic Suction (Yang 2001). Studies show that influence of osmotic suction on soil is usually less than that of matrix suction. Therefore, suction usually refers to matrix suction in soil mechanics. In unsaturated soil slope, the matrix suction can be regarded as negative pore water pressure. In recent years, people have understood the contribution of negative pore water pressure in enhancing the slope stability, and have developed several equipments and methods to measure negative pore water pressure (Xu et al. 2000). Therefore, in an analysis of the slope stability, it is reasonable to consider the shear strength provided by negative pore water pressure. This way is an extension of traditional limit equilibrium analysis method.

GEO-SLOPE-SEEP/W Finite Element Simulation

The ability of GEO-SLOPE-SEEP/W finite element software in simulating unsaturated seepage enables it to simulate extensive practical problems. The software can simulate water movement and the distribution of pore water pressure in the form of cloud pictures, in porous medium such as soils and rocks. It can also simulate and calculate problems such as rainfall seepage in slopes, water infiltration in penstocks, and instantaneous seepage in earth dams, and so on.

In order to study the influences of a rainfall on stability of residual soil slopes, this chapter analyzes an ideal simplified slope, considering only two layers of soil—granite colluvial deposit and weathered granite soil. And negative pore water pressure distribution of the slope is simulated under four kinds of rainfall intensities.

Conditions of the slope and rainfall: saturated hydraulic conductivity of the granite residual soil covering on the slope is 3.0×10^{-5} m/s; four rainfall intensities is respectively 1.0×10^{-5} m/s, 2.0×10^{-5} m/s, 3.0×10^{-5} m/s and 4.0×10^{-5} m/s.

Permeability conditions of granite residual soil of the slope: granite colluvial soil on the surface of the slope is unconsolidated; strongly weathering granite soil in the inner of the slope is integral. Comparing with granite colluvial soil, the permeability of completely weathering granite residual soil is much worse. Its osmotic coefficient changes more gently with the changes of negative water pressure.

Shape of the slope, division of grid and selection of water level: choose a simplified slope for analysis of rainfall seepage, to get the general distribution of negative pore water pressure in the slope under a rainfall. There are totally 550 soil units, the size of a single grid is 8.0 m × 8.0m or 4.0 m × 4.0m. The slope is 76 m in height, 170 m in length, with a water-level length of 60 m at the top and 56 m at the bottom. Analysis is done to

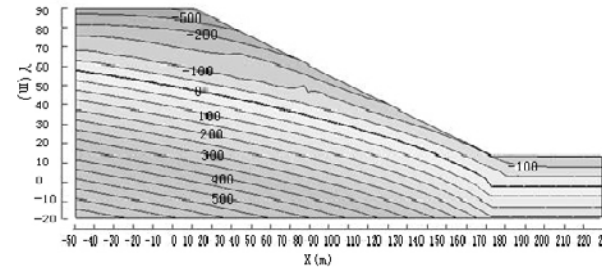

Fig. 1 Pore water pressure distribution of initialization condition in a slope

soil layer 32 m below the ground. The underground water level is 16 m below the ground. To simulate a stable groundwater seepage in the slope, on both side borders, of which the runoff is set up as 0, the constant head is assumed to be 60 m on the left and 0 m on the right.

Initial rainfall conditions: the intensity of initial rainfall is assumed to be 1.0×10^{-10} m/s for steady flow calculation in order to simulate the pore water pressure of the natural slope before a rainfall. As the intensity of initial rainfall is 5 orders of magnitude less than the simulated rainfall intensity, it can be regarded as a natural condition without any rainfall and it has little influence on the later calculation of slope under rainfall, so it can be used for initial rainfall conditions. In the whole calculation, changes of moisture evaporation and underground water table in the slope are not taken into consideration. The distribution of pore water pressure under initial conditions is shown in figure 1. Negative pore water pressure above the infiltration line increases linearly to -300 Kpa with depth of the slope.

Simulation Results of Seepage Flow in the Slope

Distribution rule of negative pore water pressure on the condition of sustained rainfall

Working condition 1: Assume rain falls vertically in the intensity of 1.0×10^{-5} m/s, and inclined 0.9×10^{-5} m/s. The pore water pressure calculation results in five conditions of rainfall duration at 2 hours, 4 hours, 8

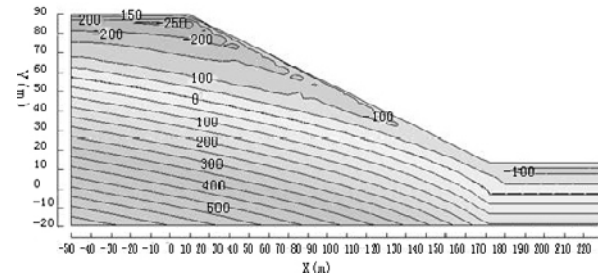

Fig. 2 Pore water pressure distribution after 2 hours of a rainfall

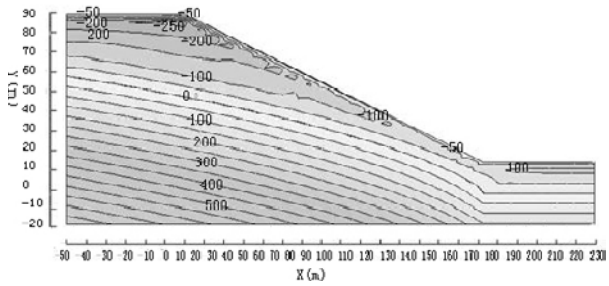

Fig. 3 Pore water pressure distribution after 4 hours of a rainfall

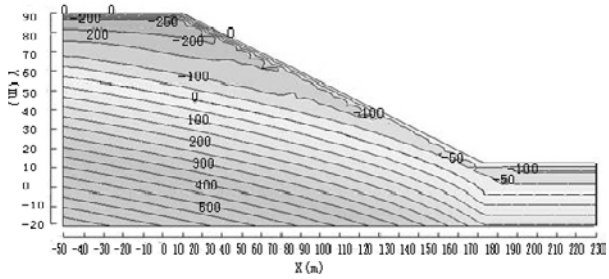

Fig. 4 Pore water pressure distribution after 8 hours of a rainfall

hours, 16 hours, and 24 hours are showed in Figs. 2—6.

After two hours rainfall, negative pore water pressure changed most largely in the top four meters below the slope top. Negative pore water pressure was -150 Kpa on the very top-level and -100 Kpa on the surface of inclined region; after four hours rainfall, negative pore water pressure on slope surface had become to -50 Kpa. After eight hours rainfall, negative pore water pressure on slope surface had gradually reduced to 0 Kpa, and a thin saturated layer was formed. When it rained for 16 hours, saturated zone in the crest had completely dispersed, and the 50 Kpa region became very obviously, about four meters thick. When it rained for 24 hours, the thickness of -50 Kpa region on the slope surface was about six meters. From Figs. 2—6, we could see it was on the surface that the negative pore water pressure changed most, and the main changes was in the first unit at thickness of 4 m on the crest. It stated that the influence of rainfall on the slope was limited.

Similar to condition 1, simulation could also be done with rainfall of 2.0×10^{-5} m/s, 3.0×10^{-5} m/s, 4.0×10^{-5} m/s, lasting 2 hours, 4 hours, 8 hours, 16 hours, and 24 hours. After analysis, we can see that the negative pore water pressure in the surface of slope is gradually reduced to 0 with infiltration of rainwater, and the maximum changes of negative pore water pressure is in a range of four meters on the surface of the slope. It shows that the influence of a rainfall on the slope is in a limited depth. When it rains less and sustains shorter, the influences on slope stability is less. With the continuous rainfall, the influences increases, but soil permeability in high saturated zone becomes strong, and the infiltration of rainwater flow away through the zone, therefore the influence is still very limited. From the conditions of 24 hours rainfall of different intensities, the depth of rainfall influence on negative pore water pressure is about 12 meters.

Distribution rule of negative pore water pressure after rainfall

Some of the landslides occurred after a rainfall, so it is of great importance to do research on pore water pressure after heavy rain. Assume that rainfall intensity is 4.0×10^{-5} m/s vertically and 3.0×10^{-5} m/s inclined, sustaining for 16 hours after the rain stopped.

From simulation results, we could see that 0.5 hours after the rain stopped, the saturated zone formatted in the slope, in a very short period of time, was gradually dissipated and formed many small saturated regions; 1 hour after the rain stopped, the saturated zone in the slope was almost completely dissipated, leaving many small saturation regions, and the negative pore water pressure in the slope failed to increase; 2 hours after the rain stopped, the saturated zone in the slope was completely disappeared, and negative pore water pressure did not increase, while part pressure continued to decrease; 4 hours after the rain stopped, the negative pore water pressure still did not increase significantly. It

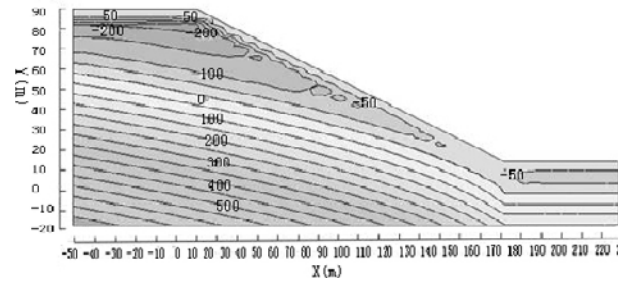

Fig. 5 Pore water pressure distribution after 16 hours of a rainfall

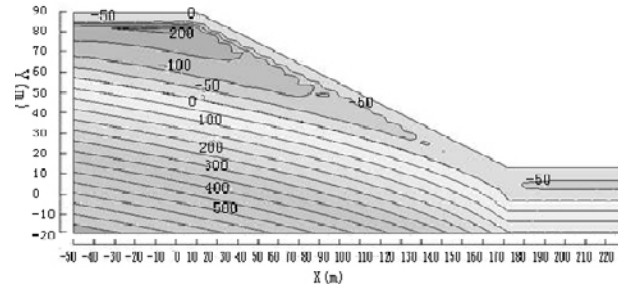

Fig. 6 Pore water pressure distribution after 24 hours of a rainfall

stated that after the rain stopped, the slope would maintain a high degree of saturation and low negative pore water pressure for a long time, all of which were not favorable to slope stability. Therefore, it is easy to understand why the slope still can slide after a heavy rainstorm stopped.

If the period between rainstorms is very short, its impact on the slope can be considered as a continuous rainstorm, and it has an enormous harm, thus the rainy season is a high-incidence season of slope undermining.

Distribution rule of pore water pressure in condition of $K_x = 2K_y$

In the granite residual soil slope, as a result of the stratified layers, horizontal permeability coefficient is larger than vertical permeability coefficient. Assume that granite residual soil is $K_x=2K_y$ in the slope, rainfall intensity is 3.0×10^{-5} m/s, lasting for 18 hours.

From cloud atlas, it could be found that compared with $K_y=2K_x$, the distribution of negative pore water pressure of slope was very similar at the first four hours. After 8 hours rainfall, saturated regions on the surface of slope went deeper for two meters to be connected through into a saturated zone, and its influence had reached eight meters below the surface; after 12 hours rainfall, a saturated zone formed on the slope surface, ranging from two to four meters in depth. The influence on the crest maintained 8 meters below the ground. After 16 hours rainfall, the thickness of saturated zone was 6 meters, and 50 Kpa pore water pressure region had been to emerge; after 18 hours rainfall, the rainfall influence depth was about 12 meters, a certain degree of constant head exposes out of ground to form a stream area, which was a fountain formed during the rainstorm, and there was a certain head pressure.

From a comparative perspective, when soil permeability coefficient becoming larger, saturated region in slope becomes to appear earlier and the infiltration of rainwater becomes faster, but with the appearing of saturation zone, soil permeability becomes strong in the region, and the infiltration of rainwater flow away through the high saturated zone, leading to that rainfall influence depth cannot increase significantly.

STABILITY ANALYSIS OF A GRANITE RESIDUAL SOIL SLOPE IN THE CONDITION OF RAINFALL

Outline of the Project

A granite residual soil slope is 35 m of a maximum height, with an average angle into 60 degree with the plane. On the foot of the slope is a hospital and other buildings. Therefore destruction of the slope will bring tremendous harm. And heavy rain often evoked pony size cyclical collapses around the crest of the slope.

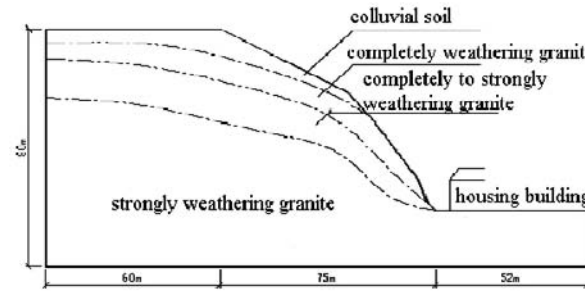

Fig. 7 The section of granite residual soil slope

Choose a less favorable profile, illustrated in Fig. 7, to do the stability analysis. Soil layers are composed mainly of weathering granite residual soil. On the layer of completely weathering granite soil of 10 meters thickness is a layer of granite colluvial soil of 4—5 meters thickness. Heavy rain will change the negative pore water pressure distribution in the slope, thereby affecting stability of the slope. The potential damage of such steep slope is mainly shallow slide.

Simulate Pore Water Pressure with Finite Element Software

Analyze the seepage of steady state and transient state based on finite element method. The distribution of negative pore water pressure of the slope before rainstorm is irregular; the biggest negative pore water pressure is -200 kPa. The minimum volumetric moisture content is 0.18 in the slope in the majority region of the slope above the saturation line, under which is saturated region, where the volumetric moisture content is 0.4.

Under 480 min rainfall, saturated thin layer appeared on the crest, and the main rainwater influence depth is about 4 meters. At the corner of the slope, there is a high water content. Volumetric moisture content is largest in colluvial deposit and still maintained at 0.18 in the rest region, showing that almost no rain penetrated into the deeper slope.

In the cloud picture of rainfall 720 min as shown in Fig. 8, saturated thin layer on the crest of slope disappeared, and -25 Kpa region distributed within surface layer of 2 m thickness in the slope. Region of volumetric moisture content 0.36 developed into the slope, stating that rainwater began to penetrate into the deeper of slope. Rainwater influence depth is about 12 meters in the soil, a little deeper on the crest of the slope. Part of massive infiltration of rainwater stayed in slope to infiltrate the soil, while the other part flowed away

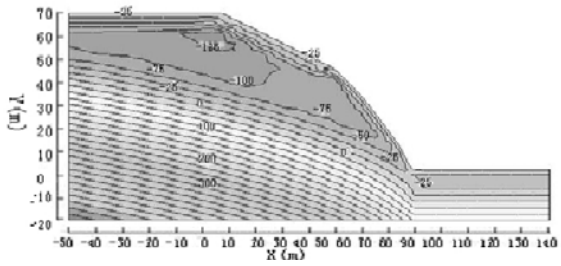

Fig. 8 Pore water pressure distribution under 720 min of a rainfall

along the surface of high saturation. After a heavy rain stopped, pore water pressure and volumetric moisture content change little in the slope, and slope will maintain a high degree of saturation and low negative pore water pressure for a long time, which is a disadvantage to the slope stability.

Results of the Analysis

Analyze the section plan illustrated in Fig. 7 with finite strip method, providing that vertical shear is 0 between strips, and seek security coefficient on the basis of moment balance. In the analysis, choosing the most dangerous circular slip surface, it can be found that all the critical slip surfaces pass through the foot of the slope (PAN and Zhang 2006).

In the first analysis, with matrix suction ignored, slope safety factor is 0.868. For the second analysis, considering matrix suction, slope stability safety factor is 1.073 by "total cohesion method" (Chen et al. 1997; Melinda et al. 2004), increasing 23.6 percent compared with 0.868. The slope safety factor calculated with matrix suction considered in is closer to reality. Therefore, for the high residual soil slope with high water table, influence of matrix suction should not be ignored.

CONCLUSIONS

Through simulation of negative pore water pressure distribution of a slope, influences of a rainfall on the stability of granite residual soil slope are studied in this paper. And through calculation of a granite residual soil slope project, contribution of matrix suction to the slope stability is elaborated. Conclusions are as follows:

1. With rainfall lasting, the slope safety factor is on a downward trend. After the cessation of rainfall, high saturation and low negative pore water pressure will remain for a long time, therefore the slope will be in danger long afterwards.

2. With increase of the soil permeability coefficient, saturated region in slope appears earlier, and the infiltration of rainwater becomes faster. But with appearance of the saturated region, soil permeability becomes stronger in this region, and the infiltration rainwater flows away through the high saturated zone, therefore the influence of the rainfall does not increase significantly.

3.In the calculation of granite residual soil slope, if matrix suction is not taken into consideration, the safety factor is obviously lower, inconsistent with the actual case. To calculate with measured matrix suction, slope safety factor is more close to the actual case.

REFERENCES

Chen YZ (2006) Stability analysis and strengthening comprehensive Study about Shitouling landslide of Water Supply Reconstruction Project from Dongjiang to Shenzhe. M.S. Thesis, Hohai University, Nanjing

Chen ZY, Zhang ZM, Chen YJ (1997) and ect. Unsaturated Soil Mechanics. Beijing: China Construction Industry Press: 144-148

Liu JJ, Xiong J, He X (2004). Geotechnical saturated-unsaturated seepage analysis under rainfall. Rock and Soil mechanics, 2004.11, 25 (by): 559-563

Melinda F, Rahardjo H, Han KK, Leong EC (2004) Shear strength of compacted soil under infiltration condition. Journal of Geotechnical and Geoenvironmental Engineering, ASCE 130 (8): 807-810

Pan J, Zhang NJ (2006) A project of some clay landslide measures in Shaoguan of Guangdong province. Journal of Shantou University (Natural Science) 21(3): 70-74

Xu J, Wang Z, Li WX (2000) Measurement technology for suction of unsaturated soil. Chinese Journal of Rock Mechanics and Engineering, 2000. 6, 19 (Supplement): 905-909

Yang XP (2001) Soil mechanics. Guangzhou: SCUT Press: 65-66

Zhu WB, Liu BC (2002). Forming and development process of soil landslide during rainfall. Chinese Journal of Rock Mechanics and Engineering 21 (4): 509-512

Proceedings of the 4th Asian Regional Conference on Geosynthetics
June 17 - 20, 2008 Shanghai, China

FAILURE OF SEGMENTAL RETAINING WALLS DUE TO THE INSUFFICIENCY OF BACKFILL PERMEABILITY

Abdolhosein Haddad[1] and Gholamali Shafabakhsh[2]

ABSTRACT: Segmental retaining walls (SRWs) reinforced by geogrids or geotextiles (primarily those with precast concrete block facing) are used extensively as retaining walls and bridge abutments in transportation networks in Iran. In spite of significant advantages of SRWs, like flexibility on soft foundations, seismic stability and their cost effective, there are some cases of SRWs failure because of neglecting basic geotechnical engineering principles in wall details. In an attempt to identify possible causes for the a 12 m height wall collapse, a comprehensive investigation was carried out including laboratory tests on the backfill, stability analyses on the as-built design based on the current design approaches and numerical slope stability analyses with pore pressure consideration. The investigation revealed that the inappropriate stability design and the bad-quality backfill were mainly responsible for the collapse. At last, practical significance of the findings from this study is also discussed for future similar projects.

KEYWORDS: segmental retaining wall, wall failure, slope stability, geogrid

INTRODUCTION

Failure plays an important role in engineering practices. For the engineer, knowledge of engineering failure is just as important as knowledge of its successes. Through the forensic study of failures, engineers can learn to avoid similar technical errors, allowing them to build more efficient, safer structures. A 12 m height segmental retaining wall system using geosynthetic reinforcement failed in Tehran capital of Iran in late Feb. 2006. This segmental retaining wall failure is analyzed with respect to the design, and construction to determine the causes of the failure. In an attempt to identify possible causes of the collapse, a comprehensive investigation was carried out, including soil mechanics laboratory tests for the SRW's backfill soil, stability analyses on the as-built wall based on the current design approaches and global slope stability with pore pressure analysis. Segmental retaining walls normally are designed to satisfy the internal, external, and local stability requirements of facing elements to ensure their long-term performance. The objectives of this paper are to identify the causes of the wall failure firstly and secondly to clarify the influence of insufficiency of backfill permeability on wall failure and finally illustrate consequences of neglecting fundamental principles of geotechnical engineering in the design and construction of geosynthetic reinforced soil retaining wall. To avoid any additional SRW failure, it is necessary to conduct a forensic study to explicate the common mistakes that have caused the collapse of the SRW and offer guidance for future engineering practices.

WALL DESCRIPTION

The wall was constructed for a newly developed urban highway in north part of Tehran. The landscaping and earthwork for the new highway required the construction of a 12 m high geosynthetic reinforced SRW. At this location, a 160 m long retaining wall was required, ranging in height from 5 to 12 m and 1750 m^2 in facing area to retain a natural slope. The wall was situated on a slightly sloping ground, immediately next to a 36 m wide highway away from the wall face. The highway eventually joins a main junction that is located approximately 30 m away from the wall. A typical sectional view of the tallest section of the wall, inferred from the information gathered from the site, is shown in Fig. 1.

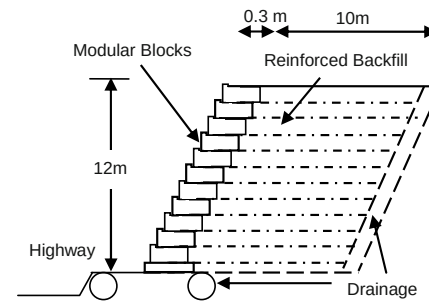

Fig.1 Wall geometry cross section

[1]Assoc. Professor, Department of Civil Engineering, Semnan University, IRAN. Email: ahadad@semnan.ac.ir
[2]Assoc. Professor, Department of Civil Engineering, Semnan University, IRAN. Email: ghshfabakhsh@semnan.ac.ir

Backfill Material and Geosynthetic

The safety of any structure is highly dependent on its material's stability and durability. Therefore, the selection of reinforcement and backfill soil for SRW's must consider the performance, service life, and the environmental conditions of the structure. Geologically, the original ground existing behind and under the embankment is composed of colluvial soil and weathered cemented soil and rock respectively. The colluvial layer is composed of clay and sandy gravel. The site investigation indicated that the reinforced backfill and retained soils were essentially the same being a completely decomposed sandy clayey soil available at the site. A number of laboratory tests were conducted to quantify relevant geotechnical properties of the select fill for use in a series of analyses using representative soil samples collected from different locations within the reinforced backfill and retained zones. As seen in the particle-size distribution curve in Fig. 2, the completely decomposed backfill soil contained over 38% of fines passing the number 200 sieve. According to the Unified Soil Classification System ASTM D2487, the soil was classified as SC, clayey sand, with a plasticity index of 16. The standard Proctor test ASTM D698 yielded a maximum dry unit weight of 21 kN·m^3 with an optimum water content of 15%. According to the physical tests, the backfill soil did not comply with the FHWA recommendation.

For determination of the saturated permeability and the shear strength parameters, specimens were compacted to the field density corresponding to 90% of its maximum dry unit weight obtained from the standard Proctor test. A series of falling head permeability tests yielded an average saturated hydraulic conductivity of Ks=1.0×10^{-6} m/s. In addition a series of large-scale direct shear tests using specimens of 300×300 mm in plan and 150 mm in height gave as compacted shear strength parameters of ϕ=27° and cohesion intercept of c=10—20 kPa. The natural soil classification and properties are shown in Table 1.

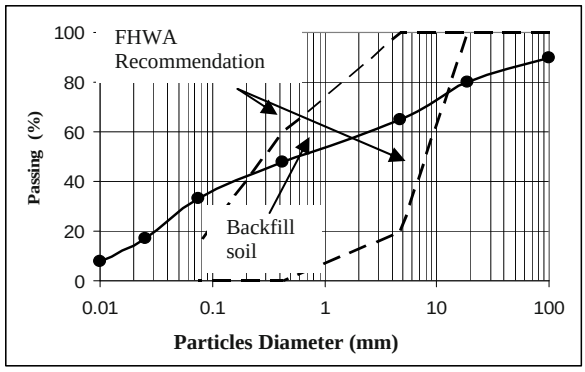

Fig. 2 Particle size distribution curve of backfill

Table 1 Natural soil properties

Layer	USCS	c (kPa)	ϕ (Deg)	k (m/s)
Colluvial-soil (Backfill)	SC/SM	10≅20	27	1×10^{-6}
Weathered soil & rock	SC/GC	25≅30	35	4×10^{-7}

The geosynthetic reinforcements used in Iran are predominantly flexible geogrid made of a variety of polymeric materials. Because of its complexity, the quality verifications of geogrid on site are always problematic. To identify mechanical characteristics of geogrid reinforcement layers, a series of rib tensile strength tests on the specimens recovered at the site were conducted in accordance with the test procedure as specified in GRI-GG1 _Test Method 1988. A loading rate of 10±3%/min was used as specified in GRI-GG1. According to the test results, the ultimate tensile strength and axial stiffness of approximately 90 kN/m and 800kN/m, respectively, were estimated. Because the tests were performed on geogrids obtained at the site, the measured tensile strength of 90 kN/m was thought to reflect possible decrease due to installation damage during construction.

The results of investigation indicated that 8—9 m long reinforcement layers were placed at a uniform vertical spacing of 0.6 m, thus satisfying the minimum reinforcement length 0.7H according to the currently available design approaches, i.e., National Concrete Masonry Association (NCMA -Collins 1997) and Federal Highway Administration (FHWA- Elias and Christopher 1997).

The wall facing was constructed using concrete modular blocks 450×450×200 mm (Length, Width and Height) with compressive strength between 18—20 Mpa. Visual investigation of the wall facing during the field investigation shows 5 cm set-back of the modular facing blocks was provided. A shear-key type connection between the modular blocks was used to transmit shear between the facing elements. Also crushed gravel was used to infill the spaces between reinforced backfill and retained soil. The crushed gravel was also extended to under the backfill to create a blanket drainage system without any filter layer. At this site the average ultimate bearing capacity of the foundation soil was approximately 800 kPa.

CAUSES OF FAILURE

Based on site observations and engineering studies for each failed case study, the causes of failure generally

can be distinguished as natural influences and professional mistakes. The wall failure occurred at the end of Feb. 1999. The highest section of wall (12 m) failed during a heavy rainstorm. Numerous worldwide studies have reported that intense rainfall has been the major factor responsible for many slope failures including reinforced earth structures, Huang (1994), Rahardjo et al. (2001) and Pando et al. (2005).

As seen in the photos taken after the collapse by the authors in Fig. 3, the collapsed portion of the wall extended approximately to 10 m, resulting in a total slid volume of soil over 350 m^3. In Fig. 4 the geogrid reinforcements and cracked modular blocks near the sliding zone are shown.

Fig. 3 Photo of collapse in the reinforced soil wall

Fig. 4 Wall failure-geogrid layers visible

A review of the original design was performed using the NCMA, Design Guidelines. Internal, external, facing stability and global stability were evaluated. The original design was based on the assumption that no hydrostatic forces would be acting on the SRW. A check of the original design was performed. This design check used the NCMA procedure in its entirety. Connection strength properties between the SRW units and reinforcement were based on laboratory tests provided by the manufacturer. The design section presented here is for the tallest section of wall measuring 12 m in height from leveling pad to top of the wall. For analysis, the available design/analysis program SRWall (Bathurst 2001) were used, which were developed based on the NCMA design approach.

The current limit equilibrium-based design approaches require allowable long-term design strengths (Ta) of the reinforcements; block interface and modular block/ geogrid connection strength properties for analysis. The allowable long-term design strengths for the geogrids were estimated based on the vendor provided information equal to 35kN/m. Because of the absence of the block interface and the geogrid/block connection properties, typical values based on NCMA (Collins 1997) and Chungsik Yoo et al. (2004) recommendations are used.

Wall Stability Analysis

The results of internal stability calculations that were shown in Table 2, indicate that the lower three layers do not meet the NCMA design requirement for tensile overstress (FS_{to}), exhibiting factors of safety well below the required minimum value of $FS_{to(min)}$ =1.0. Also the upper two layers do not meet the NCMA design factor of safty for pullout (FS_{po}).

Table 2 Internal stability results

Layer	Elev. (m)	Internal Stability		
		FS_{to}	FS_{Po}	FS_{isl}
1	0.3	0.64	10.2	1.23
2	0.9	0.85	11.4	1.45
3	1.5	0.97	9.51	1.67
4	2.1	1.15	8.3	2.41
5	2.7	1.2	7.84	2.73
…	…	…	…	…
14	8.1	12.1	2.21	4.21
15	8.7	13.5	1.87	5.31
16	9.3	14.2	1.45	7.12
17	9.9	15.3	1.21	8.19
18	10.5	>16	1.11	13.52
19	11.1	>16	0.95	19.32
20	11.7	>16		

FS_{to} = tension overstress factor of safety
FS_{po} = pullout factor of safety
FS_{isl} = Internal sliding factor of safety

Global Wall Stability Analysis

By considering the geometry of the SRW system and the failure mode, limit equilibrium based on global stability analyses were deemed necessary to identify causes of the failure. In order to simulate what actually occurred after the rainfall with a high degree of realism, the stability analyses were performed based on effective stresses with pore water pressures effects of the rainfall on wall. A series of steady state seepage analyses considering soil permeability, rainfall intensity and duration were first conducted assuming a non-deforming soil to determine a critical pore water pressure distribution during the event of the rainfall by Geo-Slope-SEEP/W Ver. 5 software. The results of this analysis are presented in Fig. 5. Then limit equilibrium-based slope stability analyses were carried out with Mohr-Coulomb failure criterion. This was done using a commercial software package GEO-SLOPE Ver. 5. The global factor of safety and failure surface of the wall are illustrated in Fig.6. The location of the failure surface was in fact in accordance with the traced failure surface based on the information gathered in the field.

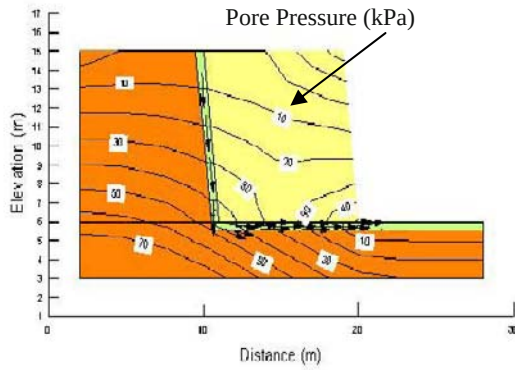

Fig. 5 Pore-water pressure distribution used in slope stability analysis

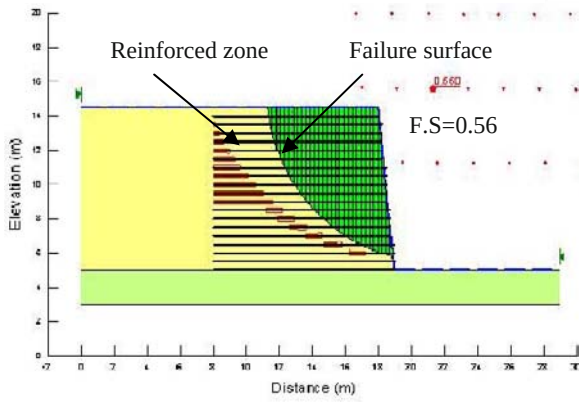

Fig.6 Failure surfaces obtained for wet case

The results of the slope stability analyses are presented in Table 3. The safety factor of SRW was larger than 1.2 in case of the dry case and was less than the required safety factor for wet case (after of the rainfall and backfill saturation).

Table 3 The results of Slope stability analysis

Method	Safety factor of SRW	
	Dry Case	Wet case
Bishop	1.90	0.56
Spencer	1.88	0.69

CONCUSIONS

In this study a comprehensive site investigation and slope stability analyses were conducted to investigate the causes of the collapse of a 12 m SRW. Based on the forensic diagnosis of the observed SRW failure, intense rainfall was the most important natural influence to causing the SRW failure. However, inadequate planning, inappropriate as-built design, the bad-quality backfill soil with a significant percentage of fines, available at the site and poor construction workmanship are responsible for the SRW failure.

The connection between the reinforcement and the facing of a SRW is an important component of the system that must be considered in both the design and construction of these systems. Also for tall SRWs or walls with complex geometry, global stability analyses should be carried out in design steps for various environmental conditions.

At last important lessons learned from the collapse is perhaps that the consequence of neglecting basic geotechnical engineering principles can result in a catastrophic collapse such as one that described in this paper.

REFERENCES

Bathurst RJ (2001) Design software for segmental retaining walls: SRwall ver. 3.2, National Concrete Masonry Association, Herndon, Va

Collin J (1997) Design manual for segmental retaining walls, 2nd Ed., National Concrete Masonry Association NCMA, Herndon, Va

Elias V, Christopher BR (1997) Mechanically stabilized earth walls and reinforced soil slopes, design, and construction guidelines. FHWA Demonstration Project 82, FHWA, Washington, D.C.

GRI test method (1988) GG-1: Single rib geogrid tensile strength. Geosynthetic Research Institute, Drexel Univ., Philadelphia

Huang CC (1994) Report on Three Unsuccessful Reinforced Walls, Recent Case Histories of Permanent Geosynthetic—Reinforced Soil Retaining Walls, Eds. Tatsuoka, F. and Leshchinsky D, AA Balkema Publishers, Rotterdam: 219-222

Pando MA, Ruiz ME, Larsen MC (2005) Rainfall-Induced Landslides in Puerto Rico: An Overview, Slopes and Retaining Structures under Seismic and Static Conditions, Geotechnical Special Publication 140, CD-ROM. ASCE

Rahardjo H, Li XW, Toll DG, Leong EC (2001) The Effect of Antecedent Rainfall on Slope Stability, Geotechnical and Geological Engineering 19: 371-399

Yoo C, Jung HS, Jung HY (2004) Lessons learned from a failure of geosynthetics-reinforced segmental retaining wall. Proc., 3rd Asian Regional Conf. on Geosynthetics, S Shim, C Yoo, HY Heon, eds., CIIR, Seoul, Korea: 265–274

DESIGN AND INSTALLATION OF ROCK FALL BARRIERS FOR THE POS SLIM PROJECT, MALAYSIA

Tiru Kulkarni[1] and Kenneth Choo[2]

ABSTRACT: Rock fall protection systems are a key element in the design and maintenance of infrastructure networks. These systems are generally categorized as either "active" systems (i.e.) where the system acts before the initiation of rock mass detachment , or "passive" systems (i.e.) where the system acts after the detachment of the rock mass.

Rock fall barriers comprise of a complex system of energy absorption devices that function as a passive rock fall mitigation mechanism. The design of such systems is based on a combination of site simulations and field crash tests. Due to recent developments in standardizing design and testing criteria for rock fall barriers, these systems are rapidly gaining acceptance due to reasons of site adaptability and economy. This paper deals with the various design and construction issues encountered on the Pos Slim rock project in Malaysia. The project is located in a geo-morphologically unstable region and involved several measures undertaken for the protection of a highway from unstable rock and soil slopes.

KEYWORDS: active and passive rock fall mitigation systems, rock fall barriers

INTRODUCTION

The concept of utilizing rock fall barriers is relatively new in Asia. Even in Europe, where these systems and applications are more common, the field of rock fall engineering is widely considered to be an evolving code of practice (i.e.) the design and installation of these systems depends largely on the experience and expertise of the engineer and the visualization of the problem (Bustamante; BS 8081-1989).

The main parameters affecting the design of a rock fall barrier system are:

(1) Falling energy;
(2) Falling velocity;
(3) Height of impact.

Falling energy and Falling velocity are related by the equation :

$$E = 0.5mv^2 + 0.5I\omega^2 \qquad (1)$$

where
m: mass of the block;
v : translational velocity of fall;
I : moment of inertia of the block;
Ω: angular rotational velocity.

Generally, for large block sizes the component of rotational energy (given by the factor $0.5*I*\omega^2$) is minimal, and can be neglected in practice.

Therefore,

$$E = 0.5mv^2 \qquad (2)$$

Falling velocity (i.e.) velocity of free fall can be estimated from the following Fig. 1.

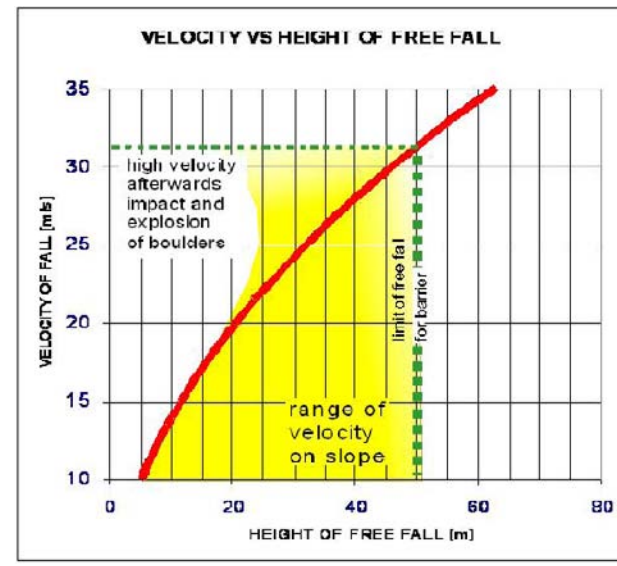

Fig. 1 Velocity vs height of free fall

The height of impact depends on:

(1) Morphology of the slope and;
(2) Trajectory of the block;

[1] Regional Manager, Maccaferri Asia Regional Headquarters, Kuala Lumpur, MALAYSIA. Email: kulkarni@maccaferri-asia.com
[2] Managing Director, Maraputra Sdn Bhd, Ipoh, MALAYSIA. Email: mrpsb1@streamyx.com

The trajectory of rocks which bounce while falling is more difficult to forecast as compared to unstable rock wedges which follow primarily a sliding pattern, as their trajectories are defined by the morphology of the slope.
A rock fall barrier is a complex system consisting of:

(1) Posts;
(2) Connection structures which act to transfer the energy to the energy dissipation devices;
(3) Energy Dissipation Devices which help in the dissipation of the generated energy on impact;
(4) Intervention structure which acts to catch the falling rock mass;
(5) Foundations and anchors.

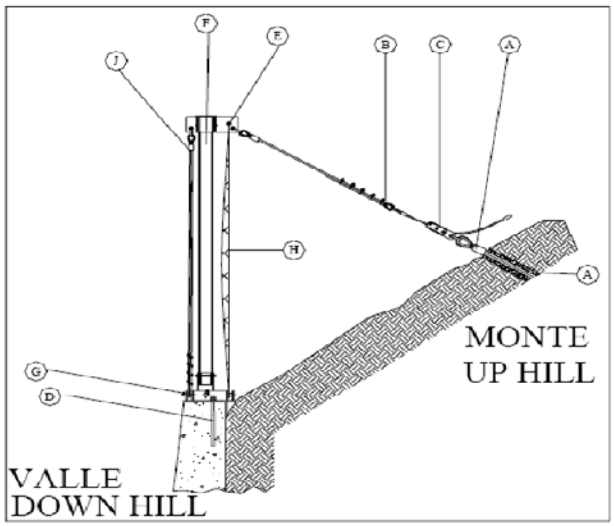

Fig. 2 Typical rock fall barrier

The mechanism of energy dissipation in a rock fall barrier is a complex process and very difficult to simulate and compute analytically. A live crash test is hence the accepted norm for certifying a stipulated capacity for the rock fall barrier.

THE POS SLIM PROJECT

The Pos Slim project involved slope stabilization works in Cameron Highlands, in the state of Pahang in Malaysia. The geology of Cameron Highlands comprises mainly granite rocks followed by small portions of metamorphic rocks and alluvium.

The geomorphology of this area is mainly dominated by denudational process as it is situated in a mountainous area and has constituent of deep highly weathered martial. Most parts, especially the exposed unprotected areas like slope-cut abandoned agriculture sites and slope-from agriculture sites, are highly affected by this process. Therefore, erosion feature such as rill gullies can be clearly seen, and as a consequence, in certain areas the phenomenon of mass movement is predominant as these features worsen. This can be clearly seen from the photo 1 and 2.

Photo 1 Actual site condition

The site was located between

(1) Northing 507975.593 and 508139.493 and;
(2) Easting 372754.721 and 372656.941 for the lower berm;
(3) Northing 508161.910 and 508337.210 and;
(4) Easting 372724.410 and 372638.040 for the upper berm;
(5) Total length of the site was 400 m.

Photo 2 Type of weathered slate formation prevalent at the site

Boreholes taken at five locations on the site showed a mix of stiff gravel and silt up to a depth ranging from 10 m—20 m followed by highly fragmented slate. Table 1 gives a summary of the borehole findings at the site.

Table 1 Bore hole test result

BH No.	0—10 m depth	10—20 m depth	20 m + depth
BH 1	Stiff sandy gravel	Weathered slate. End of BH @ 13.0 m due to bed rock	
BH 2	Stiff sandy gravel	Stiff sandy gravel	Stiff sandy gravel till 22.0 m. Weathered slate from 22.0 m. End of borehole @ 37.0 m due to bed rock.
BH 3	Sandy gravel	Stiff sandy gravel	Weathered slate. End of BH @ 22.1 m due to bed rock
BH 6	Stiff sandy gravel. End of BH @ 6 m due to bed rock.		
BH 7	Weathered slate. End of BH @ 4.5 m due to bed rock		

DESIGN OF THE ROCK FALL BARRIER

One of the first steps in the design of the rock fall barrier involved deciding the capacity and the height of the barrier. This involved a rock fall trajectory analysis carried out on a standard cross section at the site, whose results are shown in Figs. 3 and 4.

Using a Kolmogorov Smirnov distribution with a cutoff percentage of 95, the design kinetic energy was established at 146.99 kJ along with a design height of 1.287 m for the centre of gravity of the boulder.

Hence, keeping a minimum accepted Factor of Safety of 1.5, the capacity of the rock fall barrier proposed was 250 kJ with a design height of 2.0 m.

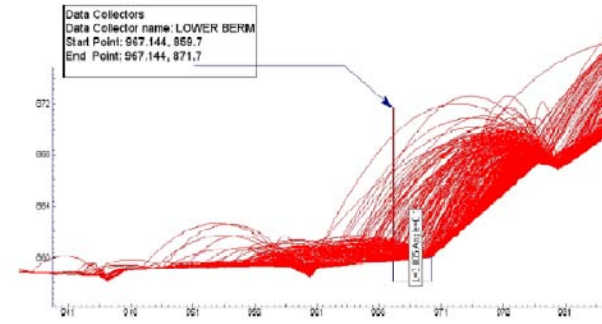

Fig. 3 Software result for trajectory analysis

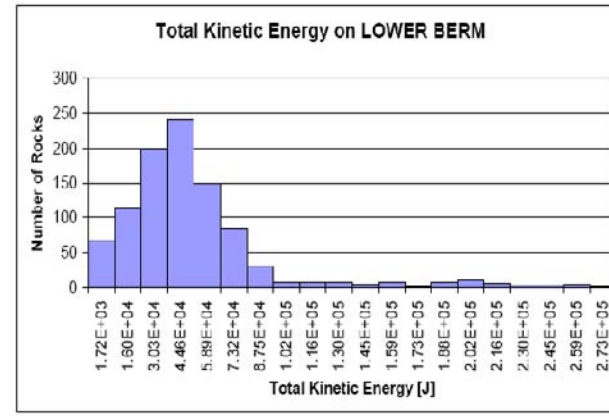

Fig. 4 Software result for kinetic energy

FOUNDATION AND ANCHOR DESIGN

The foundation design was carried out using a force vector analysis. Rakered micropiles were designed to resist a force of 213 kN.

There is no specific standard for micropile design. Relevant standards for individual design components were followed for the purpose of this design. These standards are BS 8081 and BS 449. Also referred was “Micro pile and anchor design” by Michel Bustamante.

The steps involved in the design were as follows:

(1) The force on each micropile was calculated using a Force Vector diagram, based on the measured upslope anchor force of 300 kN in the live crash test.

(2) The micropile was designed to resist this force considering the strata encountered for each borehole.

(3) The maximum micro pile length of 13 m (encountered for BH 2 & 3) was selected as the standard length for all micropiles.

FORCE VECTOR DIAGRAM FOR MICROPILES (NTS)

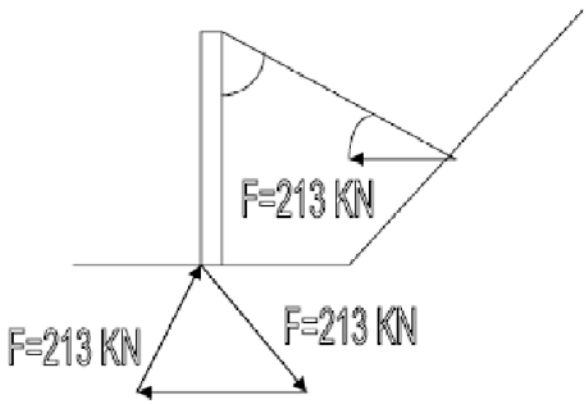

Fig. 5 Vector Force Diagram fro Micro Piles

Considering the anchorage angle as 45 degrees (w.r.t) horizontal plane, we get

Horizontal component of Force = 300 Cos 45
= 212.13 kN
Say 213 kN

From the force vector diagram, the components of the force on the micropiles are 213 kN each (equilateral triangle).

For Borehole 2 & 3

Consider pile diameter = 0.1 m

Tl = [Π * Ds1 * Ls1 * qs1 * 1000 (KN)]
+ [Π * Ds2 * Ls2 * qs2 * 1000]

Where Ds1 = α * Dq1
= 1.1 * 0.1
= 0.11

Ls1 =5 m (consider top 4 m as free length)
qs1 = 0.05 (refer Bustamante)
Ds2 = α * Dq2
= 1.2* 0.1
= 0.12
Ls2 = 4 m
qs2 = 0.20 (refer Bustamante)

Therefore,

Tl = 387.98
Say 388KN

Therefore FS = 388 / 213
= 1.82 > 1.5

Therefore OK

Therefore total micro pile length at BH 2
= 4 m + 5 m + 4 m = 13 m

Tendon design

Consider 40 mm rebar (min yield stress ζlim = 600 N / sq mm)

Assume sacrificial thickness 8 mm

Net diameter of rebar = 32 mm

Yield force of rebar = Π * D^2 / 4 * ζ lim
= 482 kN

FS = 482 / 213
= 2.26 >> 1.5

Hence OK

Provide 40 mm dia rebar for micropile.

Micro pile details

Diameter of micropile 100 mm
Diameter of bore 120 mm
Length 13 m

Anchors were designed on a similar methodology for a force of 300 KN.

Summary for anchors

Diameter of micropile 100 mm
Diameter of bore 120 mm
Length 14 m

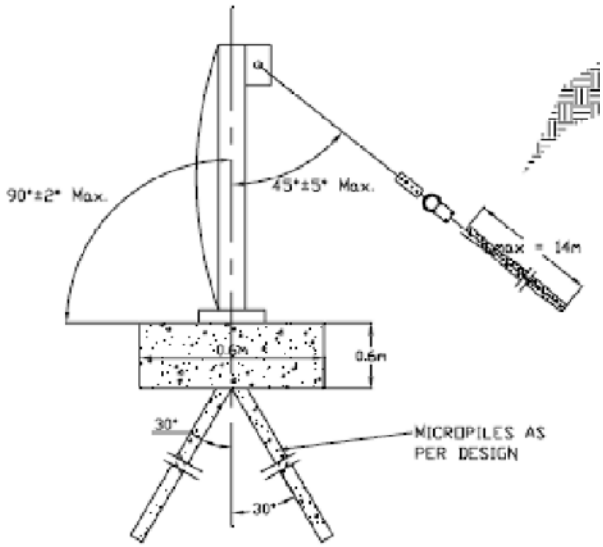

Fig. 6 Typical foundation details for rock fall barrier

CONSTRUCTION METHODOLOGY

Installation of rock fall barrier can be summarized in four easy phases as under:

Phase 1: Setting Out

The exact position must be accurately marked to ensure the alignment of the barrier complies with the requirement.

Phase 2: Positioning of Post

The post must be fixed to the base plate and properly adjusted vertically and horizontally to maximize the protection coverage area.

Phase 3: Positioning of Upper and Lower Rope

After properly positioning the post, the perimeter wire rope connecting all the post must be installed and tightened, this is to ensure that all post works as a monolithic structure to counter the falling force from the rock.

Phase 4: Fastening of Mesh Panel

The individual panels which act as the main barrier to the rock fall system will then be fixed between the post in two phases which is the main mesh panels and secondary mesh panels.

CONSTRUCTION ISSUES

Construction started in July 2007. Some of the issues encountered during construction were:

(1) Difficulty in drilling at 45° angle – Drilling proved to be very difficult due to the fragmented strata present at the site. The fragments would choke up the drill hole and slow down the progress. This was circumvented by bringing in high powered drilling rigs and increasing the number of drilling machines. In total, two mechanized drilling rigs were used for the project.

(2) Difficult topography and terrain – Simple tasks like provision of water for construction became difficult due to the location of the site. As there was no habitation nearby, temporary accommodation was constructed for the labourers on site. Frequent labour turnover caused delays, as the labour force was not used to working in such harsh conditions.

The construction and installation work for the entire stretch of 400 m was completed in October 2007, four months after commencement.

Some photos (Photos 3—6) showing construction work in progress

Photo 3 Installation of the Posts in Progress

Photo 4 Material sorting at site

Photo 5 A “monkey wrench” being used for tensioning the diagonal wire ropes

Photo 6 Installed barrier on the upper berm

CONCLUSION

The efficiency of a rock fall barrier is decided by it’s performance during a rock fall event. Since the construction of the barrier is quite recent, and there have been no rock fall events after it was installed it is difficult to comment on this aspect.

However, the design and installation of the rock fall barrier provided a number of engineering and project management challenges which were met successfully, thus completing a successful installation.

REFERENCES

Bustamante M. A Method for the Calculation of Anchors and Injected Micropiles

BS 8081-1989 : Code of practice for ground anchorages Add BS 449-1969: Specification for the use of structural steel in building

BIO-ENGINEERING APPROACH WITH JUTE GEOTEXTILE FOR SLOPE STABILIZATION

P.K. Choudhury [1], Arindam Das [2], D.N. Goswami [3] and T. Sanyal [4]

ABSTRACT: Jute is a natural eco-friendly biodegradable fibre. Its high tensile strength and high water absorption capacity along with some intrinsic properties has made it possible to develop varieties of products in the name of Jute Geotextile (JGT). A number of successful applications have been carried in the areas like road construction, river bank protection, slope stabilization, etc. In slope stabilization work, use of JGT with bio-engineering approach is an established practice in may countries. JGT in such application works initially as a protector against erosion and helps grow vegetation faster. On bio-degradation it adds nutrient to the soil. Three such important case studies for slope stabilization with JGT have been discussed with results in the paper.

KEYWORDS: jute geotextile, slope stabilization, bio-engineering approach

INTRODUCTION

Most of the construction project works on or around slope demand site specific protective measures for its stability as there is every possibility of collapse of the structure if the slope is unstable and subjected to erosion. There are number of techniques now in use to stabilize an unstable slope. A few examples are, bench terracing, fixing gabion wall, installation of masonry revetment walls, etc. In many cases it has been experienced that the denuded slope with an angle higher than the angle of repose generally fail quickly if the soil surface is not covered with a suitable erosion control material viz, geotextile in spite of adopting all possible geotechnical precautions. Bio-engineering approach has been found to be most successful technique to mitigate such soil related problem. In this process installation of geotextile is followed by seeding and plantation of saplings. As a result vegetation starts growing and the roots of vegetation take care of the soil which ultimately protects the slope from erosion, slides and other types of failure.

For controlling surficial soil erosion various types of geotextiles both natural and synthetic are available in the market. Natural geotextile are made from jute, coir sisal etc. Geotextile made of all these types of materials/fibres have been tried in India and abroad for erosion control and their performance were recorded. The results indicate that Jute Geotextile (JGT) is the best performer in this field .The market survey conducted by Homan in 1993 shows that natural fibre erosion control material contributes about 65% of the total market share. In fact, the capability of natural fibre in absorbing water and degradation with time (eco-friendliness) are its prime properties which give it an edge over synthetic geotextile .Second most property of natural fibre is its drapability. Due to high flexibility, the natural geotextile drapes easily and takes the shape of the contours of even undulated surface of the slope keeping no gap in between the soil and geotextile (Thomson and Ingold 1986). The intrinsic properties of jute fibre and the unique salient features of JGT has established its effectiveness in slope protection work. JGT when laid on the sloppy soil surface it acts as umbrella in one hand and reduces the impact of rainfall that could cause detachment of soil particles followed by run off on the other hand the thick diameter of yarn of fabric acts as mini check dam that arrests soil from flowing down the slope. Vegetation comes up within 2—3 months time and the fabric degrades after 1 year or so. During this process the slope is stabilized and area is covered with vegetation. The technique, termed as bio-engineering approach is highly effective for stabilizing slope of many kinds like, any road embankment, flood embankment, hill slope, over burden dump of mine spoil, etc. Some of the field applications along with their results discussed in the paper are the sufficient reasons to claim the supremacy of JGT.

[1] Incharge Geotech Cell, Indian Jute Industries' Research Association, Kolkata, INDIA. Email : geotex@ijira.org
[2] Junior Engineer, Indian Jute Industries' Research Association, Kolkata, INDIA. Email : geotex@ijira.org
[3] Civil Engineer, Indian Jute Industries' Research Association, Kolkata, INDIA. Email : geotex@ijira.org
[4] Geotech Advisor, Jute Manufactures Development Council, Kolkata, INDIA. Email : jmdc@jute.com/jmdcindia@vsnl.com

BIO-ENGINEERING APPROACH

Among many other methods in practice for soil erosion control and slope stabilization bio-engineering approach is one of the best choices. Bio-engineering is the utilization of vegetation, may be alone or in combination with geotechnical structures, to reduce the instability as well as erosion of slopes. This is considered as a basic part of the design and construction of earthen embankment. It provides the unique armouring on the slopes against erosion by reducing the surface run-off velocity and reinforces the soil.

Vegetation—Its Engineering Effect

Dislodged soil particles flows down the slope along with the run-off at a high rate eroding and destabilizing the structure if proper engineering measures are not taken that may be bio-engineering and or civil engineering. In bio-engineering domain plants have a number of effects on soil and slopes namely, hydrological and mechanical. The hydrological effects of plants are many such as interception (rain drops strikes the leaves before striking the ground soil), storage (leaves and stems hold water for some time before it eventually reaches the ground), infiltration (stems and shoots roughen and loosen the ground, enabling water to infiltrate more easily), etc. The mechanical effect of plant helps to reinforcing the slope by way of binding the loose soil with the deep rooted dense root network of the plants.

Role of Jute Geotextile in Bio-Engineering Approach

Open mesh woven JGT, a three-dimensional fabric when laid on the slope surface initially give protection against erosion by way of dissipation of impact of rain splash and acting as mini check dam due to the presence of thick yarn of the fabric placed across the slope. This check dam retains the dislodged soil particles along with the seeds spread over the slope. JGT is a excellent drapable fabric, this property is enhanced in wet state. Further, the yarns of fabric swells by around 20% when wet, that enables JGT to be more effective to act as check dam. Being hygroscopic in nature JGT creates a moist climate around the soil surface which is conducive to faster growth of vegetation. Within one or two months vegetation starts coming up and gradually the function of JGT initially intended becomes less and less necessary. Ultimately after about one year JGT colaces with the soil with the process of bio-degradation and adds nutrients to the soil. To be more clear it may be mentioned here that JGT and vegetation can be used in combination to perform a catching function. The capacity of JGT to retain soil is very high at first. With time jute decays, which weaken the fabric and its soil retaining capacity decreases. Eventually, JGT will fail to carry out any retaining function at all. In contrast, vegetations are not immediately very effective, but their capacity to retain soil increases as the plants grow and their root and shoot stems develop. When vegetation is fully grown it remains at about 100 percent relative strength. As the relative strength of JGT decreases, the relative strength of the vegetation increases and the soil-retaining function of JGT is handed over to vegetation .

Chemical Composition Physical Properties of Jute

Jute is a natural ligno-cellulosic bast fibre (Table 1) enriched in cellulose that facilitates absorption and retention of water. Some of its physical properties are shown in Table 2 for reference. Being textile grade fibre, it can be mechanically spun into desired quality yarn for manufacturing site specific fabric for use as geotextile to control soil erosion. A varieties of open mesh woven JGT has been developed and the technical specifications of some of these products are shown in Table 3.

Table 1 Chemical Constituents of jute fibre

Constituents	%
Cellulose	60—62
Hemi-Cellulose	22—24
Lignin	12—14
Others	1—2

Table 2 Properties of jute fibre

Specific gravity (gm/cc)	1.48
Co-efficient of static friction	0.45—0.54
Swelling in Water (Area wise)	40%
Water retention	70 %
Refractive Index	1.577
Specific Heat (Cal/g/°C)	0.324
Thermal conductivity (cal/sec/cm.°C/.cm^2)	0.91×10^{-4}
Thermal Cond. (M watt/metre. kelvin)	427.3
Heat of Combustion (Jules/g)	17.5
Ignition temperature (°C)	193

Table 3 Specifications Open Mesh Woven Jute Geo-textile

PROPERTIES	Type 1	Type 2	Type 3
Weight (g/m^2) at 20% M.R.	292	500	730
Threads/dm (MD×CD)	12×12	6.5×4.5	7×7
Thickness (mm)	3	5	6
Width (cm)	122	122	122
Open area (%)	60	50	40
Strength (kN/m) [MD×CD]	10×10	10 × 7.5	12×12
Water holding capacity (%) on dry weight	400	500	500

Cost wise JGT is the cheapest among all other geotextiles available in the market for such uses. For quite few years IJIRA with the support of JMDC (Jute Manufactures Development Council) and IJMA (Indian Jute Mills Association) has conducted a good number of field applications with success.

FIELD APPLICATIONS OF JUTE GEOTEXTILE

Sonarpur Slide Zone at Meghalaya (Fig. 1)

Location

The slide zone is located on NH 44 (Shillong to Agartala) at 142 km passing through Jayantia Hills in Meghalaya. The highway abuts hill slope on one side and the river Lubha at the toe of the down hill slope on the other. A massive land slide occurred in the monsoon blocking the highway upto a length of 200 meters.

Cause of land slide

The slope is geologically unstable comprising clay mixed up with disintrigated stones and grits. There are well defined seepage points on the slope, which saturate the overburden gradually after onset of the rain. The seepage water liquefy the clayey portion of the overburden and the slide of the weakened soil mass starts under favourable conditions.

Remedial measures undertaken

The authorities of Project Setuk, Border Roads Organisation (BRO) had done an excellent job for protecting the uphill slip deposits. The existing dump of debries was given a shape in different benches for allowing surface ran-off to flow to the adjacent water channel. Toe protection of every benching was done with sausage crate walls filled up with boulders at different levels.

Sausage crate walls were constructed as guide walls and drop walls in the main channel along which water flows and catch water drains were constructed to facilitate flow of seepage water. Shallow rectangular drains were constructed in different benches to drain off surface water.

Spoils covered with Jute Geotextile

The spoil deposits were covered with open mesh woven jute geotextile (292 gsm) at different benches and slopes. Broom grass seeds were sprinkled before laying the JGT for growth of vegetation on the slope.

Result of remedial approach

Grass seeds sprouted within 2—3 weeks after laying of JGT. Movement of clay and finer particles was totally checked and a vegetative cover has come up to stabilize the denuded overburden dumps.

Conclusion

The slide area where slope treatment was done with jute geotextile is in a good shape. The whole area is covered with plant and vegetation with green pasture on the slip over burden dumps indicating stabilization of landslide spoils.

Rambi Hydral Power Project (Fig. 2)

Location

Rambi Hydral Power Project is situated in the district of Darjeeling, West Bengal at 7.20 km down stream of Teesta Bridge. A barrage is under construction for this Hydral Project. It has a catchment area of 7755 sq.m. in the hilly terrain of Darjeeling hills adjacent to mighty river Teesta. Average annual rainfall in this area is 2875 mm. The area was subjected to land slides during rainy season and the project work was affected badly by the land slides.

NHPC Ltd., has undertaken this Hydral Power project with construction of a storage reservoir with a barrage and Power House. Since the project area is affected by land slides during rainy season the NHPC authorities had taken up erosion control measures on the slide area with the use of open weave Jute Geotextile of 730 gsm.

Remedial measures undertaken

The hill slope is comparatively stiff, slope angle ranging from 50º—75º. The soil is silty clay with admixture of stone boulders, shingles and pebbles. The affected hill area was prepared to proper slope by removing debris, stone boulders, etc. and by filling in large voids the slope irregularities were corrected. Geotechnical correction of the slope was made by construction of Rubble masonry revetment walls and breast walls at different levels for suitable heights. Necessary benching at different levels on the slope was done for the slope stability.

Slope covered with JGT

JGT was placed from the top of the slope after excavating trenches of section 500 mm×500 mm at the top bench. The JGT fabric was anchored in the trench and then it was rolled down on the slope to cover the whole area. An overlapping of 100 mm at sides and 150 mm at the end was provided in the JGT fabric. “U” shaped pins and bamboo pegs were fixed on the JGT to ensure proper anchoring of the fabric on the slope. A toe trench of section 500 mm×500 mm was also provided

and JGT was properly anchored in the trench. The trenches were filled up with stones and sand particles after laying of JGT.

Result of remedial measures taken up

After laying the JGT on the slope a layer of fertile soil of average thickness 50 mm was provided with admixture of grass seeds. The surface was finished uniformly after spreading of fertile soil over the JGT layer. The top surface was kept moist for 2—3 weeks till sprouting of vegetation started. The treated slope was fully covered with plants and vegetation within three months after laying of JGT. The roots of the plants and vegetation grown up had taken care of the slope soil and the whole area is fully stabilized after one year of laying JGT.

Conclusion

Open wave JGT is capable to retain the soil particles in position along the stiff slope and to render congenial condition for the growth of vegetation and plants by bio-engineering process.

Rescue Centre for Circus Animals at Khayerbari, Dist. Jalpaiguri, West Bengal (Fig. 3)

Location

Forest Department, Govt. of West Bengal had undertaken construction of a Rescue Centre for Circus Animals at South Khayerbari of Madarihat Range in the District of Jalpaiguri,West Bengal. The Rescue Centre is a circular enclosure and is set up in an open area of 4 acres. The diameter of the circular periphery is 142 metres having Animal cages constructed at the centre and comprises of open air enclosures around the cages. Outside fencing of the Rescue Centre is 6 m high Chain link fence fitted with M. S. Angle posts at 2 m intervals. After the peripherals fencing there is a deep trench 6.00 m wide and 3.60 m high. The side edge of this trench on the external end is protected with Rubble masonry retaining wall constructed along the trench abutting the peripheral fencing. Inside edge of the trench is natural earth of silty sand nature with admixture of grit, pebbles and shingles.

Problem

The retention of the earthen bank of the deep trench was posing a problem as the whole area was affected with rain cuts and erosion of soils.

Protective measures taken to retain the soil

The internal bank soil of the deep trench which is of non-cohesive nature was cut to slope 1：2.5. Open mesh Jute Geotextile (730 gsm) was laid on the slope with proper anchoring at top and bottom and fixed to the slope with bamboo pegs at suitable intervals. The JGT laid was covered by good quality of local earth of 50 mm (av.) thickness with admixture of manure to facilitate the growth of plant. Grass seeds were spread uniformly on the top soil surface and watered for 2—3 weeks. Germination of seeds started after two weeks and the whole surface treated with JGT was fully covered with grass and vegetation within 3 months.

Conclusion

JGT laid on the trench slope help retain the non-cohesive soil particles and prevented detachment of soil particles from the slope surface. Growth of vegetation ensured stabilization of soil on the trench slope. JGT, a bio-degradable natural geotextile, can be conveniently used for retention of non-cohesive soil particles on the slopes and help growth of vegetation in bio-engineering process.

Fig. 1 Slope Stabilization-Sonapur

Fig. 2 Slope Stabilization-Jalpaiguri

Fig. 3 Slope Stabilization-Rambi

REFERENCES

Choudhury PK, Chatterjee PK, Dutta U (1999) A Low Tech. Approach for Forests. 1st Asia—Pasific Conference on Water & Bioengineering for erosion control & slope stabilization

Juyal GP, Dadhwal KS (1996) Geojute for erosion control with special reference to mine-spoil rehabili-tation. Indian Journal of Soil Conservation, 24

Howell JH, Sandhu SC, Vyas N, Sheikh R, Rana SS (2006) Introducing Bio-Engineering to the Road Network of Himachal Pradesh. Journal of the Indian Roads Congress 67: 3

NEWLY TECHNOLOGY ON GEOTEXTILE APPLICATION IN THE IMPROVEMENT PROJECT OF THE DEEP-DRAFT CHANNEL OF YANGTZE ESTUARY

J.F. Zhu[1] and F.L. Zhou[2]

ABSTRACT: Yangtze Estuary has the character of big wind, high wave, rapid current and soft ground. Rock is short in this area. For conquering above disadvantages, it could only depend on technology innovation, cooperating R&D and continuously improvement and sophistication. An integrated Geotextile application's craftwork and relating technical equipments were developed based on above measures, Geotextile's technology updating, the development of new products and all partners participating. The partners in this project form a combining teamwork which include YEWCC, the Constructors, the Consultants, the Research institutes and the Geotextile Material Suppliers. The whole set technology and equipments have been the main factors that contributed to the extensive and successful application of the Geotextile in riverbed protection, bank structure and soft foundation improvement. The successful experience promotes the technology progress of water transportation construction industry as well.

KEYWORDS: geotextile application, soft mattress, sand-filled sack core, soft foundation improvement

BACKGROUND OF THE PROJECT

Yangtze Estuary is a delta characterized by ample flow and sediment and obvious tidal influence, runoff and tidal current interaction, muti-stage bifurcation, staggered shoal and channel, and the variability of river regime. A basic regime of Yangtze Estuary is characterized as three-stage bifurcation and four-river mouth split. In view of motion principle of water and sediment in common river mouths, estuarine circulating flow system is formed and fine sediment flocculation is produced due to the mixing of salt water with fresh water. So the estuarine turbidity maximum (ETM) zone and corresponding shallow water area are appeared in some stretches of the river mouth, Viz. "Sand Bar" sections. The water depth of these sand bar sections is shallower than that of the upstream and downstream (Fig. 1). The natural water depth at the mouth bar area is about 5.5—6.0 m.

Before the improvement project, the North Passage was opened up for 10,000 ton-class ship under the maintained water depth of 7.0 m. Only 15 ships with 9.5m load draft (equivalent to 15,000 DWT) can be passed through the North Passage using a tidal window every day. It could not meet the increasing turnover demand of Shanghai Harbor and JiangSu Province's Harbors which have more than 110 berths that were designed for calling the ships of 10,000 DWT or higher.

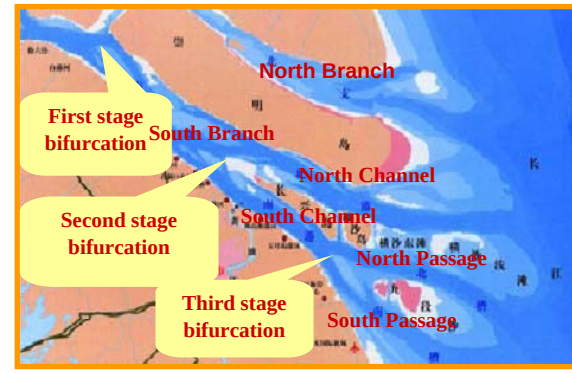

Fig. 1 the sketch map of Yangtze Estuary

Through long-term research since 1958, synthetically analyzing field measurements, results of physical model and numerical model, remote sensing photo as well as experimental data etc., the hydrodynamics including runoff and tidal current, wave and salt water intrusion are basically mastered, the formation mechanism and evolution characteristic of the mouth sand bar are basically grasped, the general river regime of Yangtze Estuary and riverbed evolution are understood. A scientific conclusion was made "under the condition that the general river regime of Yangtze Estuary is basically stable, North passage could be regulated ahead of other channels", which enable the feasibility for China to carry out the improvement project under the economic and technique condition of the end of 20th century.

[1] Senior engineer, Yangtze Estuary Waterway Administration Bureau, MOC, CHINA. Email:cjkhd@cjkhd.com
[2] Senior engineer, Yangtze Estuary Waterway Administration Bureau, MOC, CHINA. Email:zhoufl@cjkhd.com

The overall scheme for the improvement project was formulated as “making use of the ebb-dominated current, regulate the channel under mean water level, stabilize the diversion gap, build wide-spacing double training dikes and long groins, and combine with dredging works to achieve the designed water depth.” The project was divided into three phases to achieve the designed 8.5 m, 10 m and 12.5 m channel water depth respectively. The improvement project of the deep-draft channel of the Yangtze Estuary was commenced in January 1998. In September 2002 and November 2005, the first and the second phase projects were accepted by national government in sequence. The water depth of Yangtze Estuary navigable channel has improved from 7 m to 8.5 m, 9.0 m and 10.0 m. The third phase project is under construction.

ADOPTION OF GEOTEXTILE IN THE PROJECT

As an important integral part of the project, totally 141.484 km training dikes and groins has been constructed in Yangtze Estuary. For the advantage of low cost, convenient transportation, simplification of processing and anticorrosion, Geotextile plays an important role for foundation treatment, river bed protection and dike construction.

Application in Bed Protection Structure

The river bed of the Yangtze Estuary is mainly composed of silt and fine sand (D_{50}=0.086 mm), which are in high mobility under strong hydrodynamic influence and local topography is easy to change. Processing of the training dyke construction will result in change of the hydrodynamic conditions around the structure, which usually enhances the flow field alongside the structure, or produces surrounding current nearby the structure. All the changes of flow field will induce the scouring of the river bed around the structure. Therefore, no matter which type of structure is used, the bed protection structure must be adopted to control the river bed erosion, to insure the stabilization of the structure, and the cost will be easily controlled at the same time.

Traditional bed protection structure which was adopted in Yangtze Estuary area, such as platoon made by fascine with rock as ballast, due to its limitation of materials supply and construction efficiency, can not meet the demand of the construction intensity which will be over 20 km/year of construction speed of the regulating structures.

However, geotextile, characterized by its low cost and batch manufacture in plant, can substantially adapt to speedy the construction of bed protection works. Geotextile has the functions such as filtering and drainage, isolation, reinforcement, protection and anti-permeation, etc; it also has the availability to adapt the variational topography of river bed. Therefore, geotextile applied to bed protection is the only alternative for the grand project. The typical geotextile bed protection structure is shown in Fig. 2, which is named as “Geotextile Mattress”.

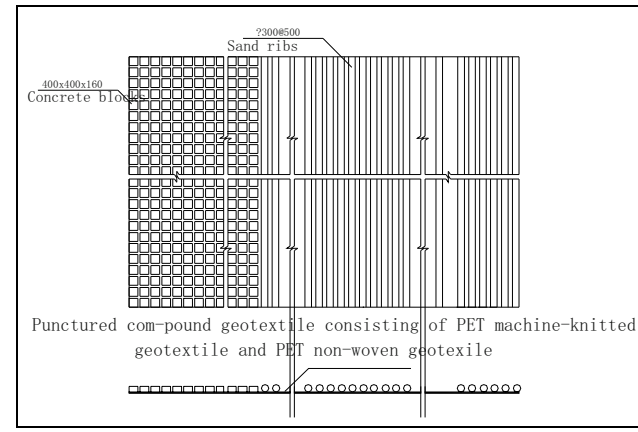

Fig. 2 Structure of bed protection mattress

Application in Sand Filled Sack Core

Some sections of the regulating structures are designed for shoals with shallow water, where the bearing capacity of foundation is good enough to support sloping type structure. In Yangtze Estuary, traditional rubble mound structure is uneconomical due to lack of rock. Sand filled sacks substitute in great amount for rock material and the sloping structure become feasible. Geotextile becomes the best choice for sand core loading material.

Application in Soft Soil Foundation Improvement

Comparing with the first phase project, some part of the second phase project has the characteristics of high structure height, large water depth, large wave pressure and low foundation bearing capacity. The wave height of Hs=3.32—5.90 m for 25 years recurrence interval in second phase project is much higher than the wave height of Hs=1.72—3.99 m of the first phase project. Some sectors of the structure have to be built on soft foundation consisting of mud under the high wave pressure force in second phase project. Results of the physical model tests and field investigation demonstrated that periodically lateral wave pressure on the structure will largely reduce foundation bearing capacity. To ensure the stability of the structure, foundation improvement is necessary.

Based on model and field tests results, sand quilt (filled sand in geotextile quilt) was introduced as horizontal drainage layer by layering on soft foundation. And paper piles were installed into soft foundation through the sand quilt. Using partial structures load (rubble mound) as preloading to accelerate soft soil drainage and consolidation. The typical cross section structure with improved foundation is shown on Fig. 3.

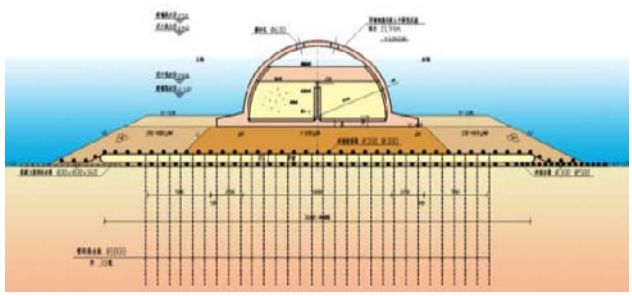

Fig. 3 Sketch of Semicircular Caisson Structure with Soft Foundation Improvement Measures

TECHNICAL PROBLEMS THAT SHOULD BE SOLVED FOR THE GEOTEXTILE APPLICATION IN THE PROJECT

River Bed Protection

For successfully apply geotextile in the river bed protection structure (Geotextile mattress), some technical problems were solved, including the procedures of material selection, structure design methods, construction techniques, and corresponding layering vessels and equipments.

The selection of geotextile type should meet the demand of isolating sand but allowing water seepage at the same time for soft mattress bed protection structure

The pore diameter and permeability coefficient of the geotextile material of mattress must meet the demand of sand isolation and water permeation. Its vertical and horizontal tensile strength must satisfy mattress layering construction. Extension coefficient of geotextile must adapt to the local topography changing under mattress and the deformation of structure's sedimentation. At the same time, it must have enough anti-pierce strength to secure the mattress perfection during construction of the dike structure. And the mattress must have the same service period as designed service life of regulating structures.

Geotextile mattress must insure to protect the mattress structure's stability

Geotextile mattress design including ballasting material design must insure to protect the mattress structure's stability under wave and current's effect during construction and service period. Mattress structure should minimize its interference with surrounding hydrodynamics and local river pattern, and should be convenient for construction.

Mattress structure can be divided into two parts: one part which is under the regulating structure called main mattress, and two sides of the main mattress are called supplementary mattress. The supplementary mattress must be able to adapt to the deformation of river topography due to scouring. The designed length of mattress should synthesize considering factors such as water depth, hydrodynamics, foundation characteristics, structure type, and so on.

In order to guarantee stability of mattress geotextile under effect of wave and current, the mattress should be added with ballasting material. After fulfill above requirements, the design of ballasting material should be lower enough to minimize its interference with local hydrodynamics and river pattern. The ballasting material should be reliable connected with mattress.

Mattress layering technique and corresponding equipments must meet the demand of serious construction conditions and huge engineering quantity.

Total amount of mattress in the project is above ten millions m^2, but the construction period is less than six years, so high efficient and reliable construction technique and corresponding equipments are required.

Sand-filled Sack Core

Selection of geotextile material

Required by design documents, the proportion of filling sand which particle diameter is larger than 0.075mm should be over 70%. So, the pore diameter and penetration coefficient of the geotextile material of sand bag must meet the demand of design requirement and speedy construction requirements. Its index of vertical and horizontal tensile strength, extension coefficient must satisfy the stress and deformation requirement during sand filling period. For the sand bag covered by rock filter layer, the geotextile material must have enough anti-pierce strength to secure the perfection of sand sack core during construction period. Geotextile material must be in favor of anti aging problem.

Sand bag's design

Basing on engineering experience, sand-filled sack core will directly face wave force action before being

protected by big sized rock or arcopode. The sand bag's structure design must sufficiently consider this factor. Meanwhile, the sand bag's structure design must in favor of structure durability.

Construction techniques and corresponding equipment

In this project, wave and tidal current are the main factors that affect sand filling construction. Especially when the top layer sand bag is filled, the construction efficiency will be reduced by tidal current. To meet the challenges of severe atmospheric conditions and vast construction quantity, special sand-filled sack core filling and layering vessel must be developed to increase construction efficiency and effective working days.

Soft Soil Foundation Improvement

The structure of sand quilt and paper piles driving techniques

The structure of sand quilt and paper piles driving techniques should ensure to obtain the least opening hole when paper pile penetrate sand quilt, so as to reduce sand loss. To achieve this aim, it is also needed to cover soft mattress on sand quilt in time after paper piles driven.

Sand quilt's filling and layering techniques

Sand quilt's filling and layering techniques must meet the quality and efficiency demand according to design document.

As horizontal drainage layer, the sand quilt must have enough thickness. Sand quilts should be connected together piece to piece to ensure drainage effect. So how to control and examine filling and layering quality becomes a key issue of construction techniques.

The construction techniques must meet the demand of working conditions and vast construction quantity.

In this project, it is needed to fill about 690, 000 m^3 sand quilt and install 600, 000 paper piles in six months. Construction condition is severe on open-sea. So the techniques and equipments must be redesigned to meet the above working demand, ensure construction quality, and increase efficiency to ensure enough preloading and consolidation period of soft foundation.

APPLICATION RESULTS

Participants of this project jointly focus on above key problems. It has achieved desirable results on the aspects including material selection, anti-aging research, technical index determination, construction techniques, quality inspection methods, special vessels and equipments development and so on.

Technical Index System

In accordance with the purpose of geotextile application, using position and loading characteristics, and in combination with availability of raw material and technology of manufactories, serial technical index system for different type geotextile material was developed. Table 1 is one example showing the index of one type of geotextile that is for soft mattress. The extension rate index mainly considers suitability to landform. The tensile strength index meets the requirement of construction load. Bursting strength and blistering strength are presented to conform to requirement of rock being dropped on it. Hole size and penetrability index are defined on the basis of river bed load grain size to ensure its functions as water drainage and sand holding.

Table 1 Technical Indices of 230 g/m^2 Polypropylene Filament Machine-Knitted Geotextile

Item		Unit	Index
Unit weight		g/m^2	$\geqslant 230^*$
Thickness		mm	>0.45
Tensile strength	vertical	N/50 mm	>3000
	horizontal	N/50 mm	>2900
Extension ratio	vertical	%	20—38*
	horizontal	%	16—32*
Trapezoidal tear strength	vertical	N	>900
	horizontal	N	>800
Bursting strength		N	>5000
Blistering strength		N	>500
Cone drop diameter		mm	<8.0
Hole size O_{90}		mm	$<0.08^*$
Vertical permeability parameter		cm/s	$>2\times10^{-3}$

Note: the index marked with "*" must be strictly complied, other indices could have 5% error.

Aging of geotextile caused by radiation of ultraviolet ray is one of the key factors that affect geotextile service life. For most sectors of this project, sufficient water depth becomes a natural barrier to resist ultraviolet ray. But for some sectors that built on shoal with shallow water, it is necessary to take anti-aging measure to protect geotextile. Checked by Guangzhou Anti-aging Research Institute and Changzhou Plastic Material Research Institute according to ASTMG53 standard, the anti-aging geotextile material special developed for this project can reach the design requirements. Compound punctured geotextile consisting of upper layer PET non-

woven geotextile and lower layer polypropylene machine-knitted geotextile is obviously better than solely polypropylene machine-knitted geotextile added with anti-aging agent, and much better than the geotextile without anti-aging agent.

Innovation of Construction Techniques

In this project, high precision GPS control network was established to provide position signal. With RTK GPS, the positioning accuracy can reach 5 cm. All the construction vessels are equipped with GPS receiving station. All working procedures including quality inspection is used GPS.

Soft mattress processing and layering technology

In this project, two type of ballasting methods are applied for soft mattress. One is sand ribs which are connected with soft mattress, the other is linked concrete blocks. Soft mattress with linked concrete blocks is mainly used in the position easy to generate 3D scouring topography deformation such as area around groins head and other location with complicated local hydro-dynamics, etc.

Concrete block is 400×400×160 mm in dimension. The concrete blocks is prefabricated using C20 concrete in precasting site, φ14 mm polypropylene rope is embedded in blocks to connect blocks.

Sand ribs (φ300 mm) under dike body are made of polypropylene filament machine-knitted in shape of cylinder. Sand ribs of supplementary mattress is sewed by polypropylene filament machine-knitted compounded with PET non-woven geotextile. All the sand ribs are fixed on soft mattress by polypropylene reinforced belt of 280 mm diameter.

Punctured compound geotextile and machine-knitted geotextile is usually 3—4 m wide. The length is determined according to the designed cross section, and usually is 50—140 m long. Reinforced belts in different scale and interval are stitched on single-list of geotextile material. Sewing method for mattress joining includes folded-sewing or T-shaped sewing. One kind of half-automated sewing product line is designed in first phase, it can meet the high-efficiency and quality demand.

Special soft mattress layering vessels equipped with broad operation platform, slide board, mattress layering position and control system were developed. With GPS and special positioning software, all the related construction data can be mastered real time on PC screen.

A great deal of survey of fixed cross section, denser observations of local sections and diving exploration were carried out during constructing. The results show that:

(1) Soft mattress prevents river bed under the coverage scope from scouring by current.

(2) Mattress can keep its stability under effect of wave and current.

(3) Optimized mattress structure with sand ribs and linked-blocks minimizes the influence of supplementary mattress on river bed evolution.

(4) Under the situation of scouring occurred in river bed outside supplementary mattress, the mattress can deforms along with river bed topography deformation.

(5) Mattress placed perpendicular to axial line of dike effectively improves the situation of non-uniform settlement of the dike body as well as the quantity of settlement.

Sand-filled sack core construction technology

At the beginning of the engineering implementation, the limited progress of the sand-filled bag dike core restricted the progress of subsequent working procedures. It is because the working vessels have to be moved and positioned several times when filling relatively more layers of sand-filled bag for dike core and placing the top filtering layer, which not only reduces effective operating time but also accumulates placing error.

To ensure construction progress and quality, Shanghai Navigation Channel Bureau and Shanghai Waterway Institute developed a new construction technique named as compound construction technique for multi-layer large-sized sand-filled bag and non-woven geotextile layer. The sand bags on middle layer and upper layer are sewn with filtering geotextile in plant, so it can be filled and layered in one time. The technique not only increases efficiency, but also avoids accumulated placing error. The woven geotextile between layers will not be exposed, and then the ability to resist wind and wave attacking on exposed sections is strengthened.

Practice since commencement shows that compared with traditional construction method rock-filled slope dike in Yangtze Estuary, sand-filled bag dike core structure adopted in first phase reducing the quantity of rock and the dike body load on foundation, improving dike body's capability to resist wave and wind attacking during construction period. Improved technique reduced difficulty of working on open-sea, and the constructing efficiency for per vessel in per day can reach 1400 m^3.

Sand quilt layering construction technology

Based on the construction technology of soft mattress layering and sand-filled sack core filling and placing, sand quilt filling and layering technology is developed. It mainly solves two problems that the head

of sand quilt drift driven by rotating current in construction site, and sand quilt filling thickness inspection method.

By summarizing field typical construction experience, interlayer and sand-filled ribs were added to sand quilt's head to increase head weight. Sand quilt layering working time is selected during low current speed period around tide slack to increase success ratio of layering. Sand filling quantity control method is adopted to guarantee sand quilt thickness, and combining diving probe check is taken to make selective rechecking.

Paper pile striking technology

According to design requirement, paper pile need to be driven into 10 m below sand quilt bottom. In this project, paper pile driving technology must solves the following three main problems: the first is how to smoothly pierce through sand quilt and keep the opened hole with minimal size, the second is how to ensure the driving depth, the third is how to reduce returning length of paper pile.

By summarized field typical construction experience, a 50 cm flat segment is added to original wedge-shaped end of the boring casing to let the soil quickly backfill the space when the boring casing is lifted, which can increase the friction force of paper pile and prevent the paper pile from returning. In order to minimize the open hole dimension, one blade type plate is used to pierce through sand quilt and foundation. Corresponding quality inspection methods is also developed to check paper pile returning length.

Innovation of Special Construction Vessels and Equipments

In this project, all the main working procedures use special designed large scale working vessels and construction craft. All these vessels are built adapting to the severe working conditions with large tonnage (2000—7000 tons) and strong anchor system. Every vessel is equipped with two RTK GPS receiving station for positioning (Figs. 4 and 5, Table 2)

High efficient mattress laying vessel

Based on the advanced placing method of the world, Shanghai Navigation Channel Bureau, No. 3 Navigation Fairs Bureau and No. 1 Navigation Fairs Bureau developed an advanced type placing vessels. The vessels are equipped with GPS and large sized incline board, which are special design for soft mattress. There are fifteen such kinds of vessels as main construction ship in this project. These vessels have some same advantages such as shallow waterline, strong capability to resist wind and wave, high efficiency (for per vessel in per day can lay more than 5000 square-meters mattress), high degree of mechanization and automation.

Fig. 4 Large scale mattress laying vessel

Large scale multi-layer large-sized sand-filled bag filling and laying vessel

To ensure construction progress and quality, Shanghai Navigation Channel Bureau and Shanghai Waterway Institute developed a new construction technique called compound construction technique for multi-layer large-sized sand-filled bag and non-woven geotextile layer after trial and error. In this technique, sand bag on middle layer and upper layer are sewn together with filtering geotextile in plant, so it can be filled and layered in one time, which not only increases efficiency but also avoids accumulated placing error. The woven geotextile between layers will not be exposed, so that the ability to resist wind and wave attacking in exposed sections is strengthened.

Paper pile driving vessel

Fig. 5 Paper piles striking vessel

Table 2 Summary of special construction vessel/facility

Vessel Type	Vessels Quan.	Construction efficient for one vessel per day		
		Unit	Ave.	Max
Mattress layering vessel	15	m^2	5372	10131
Sand-filled bag filling and laying vessel	3	m^3	1200	2000
Paper piles driving vessel	5	piece	1185	3900

Construction Quality Inspection Standard

In first phase project, by summarized field typical construction experience, a serial of construction quality inspection standards covering all the geotextile application procedures were drawn. The standards include material selection, sewing method, construction craft, quality check, etc. Before the second phase project commencing, these standards were revised in time based on the experience of first phase. During the second phase constructing period, soft foundation improvement quality inspection standard was added based on the field test data and experience. All these standards insured the smooth implementation of the geotextile application.

Consumption Amount of Geotextile

The amount of works related to geotextile application and consumption amount of geotextile are shown in Table3.

Table 3 Consumption amount of geotextile in Yangtze Estuary improvement project

No.	Item	Unit	First phase	Second phase	Sum
	Amount of works related to geotxtile application				
1	Geotextile soft mattress	million m^2	6.00	6.16	**12.16**
1.1	Soft mattress with concrete blocks blasting	million m^2	2.62	2.22	**4.84**
1.2	Soft mattress with sand ribs blasting	million m^2	3.38	3.94	**7.32**
2	Sand-filled sack core	million m^3	0.21	0.35	**0.56**
3	Sand quilt	million m^3	0	0.79	**0.79**
4	Paper pile	million	0	0.6	**0.60**
	Consumption amount of geotextile				
1	Geotextile material	million m^2	15.25	17.6	**32.85**
2	Reinforced geotextile belt	million m	16.66	21.6	**38.26**
3	Paper pile	million m	0	6.7	**6.7**

CONCLUSIONS

Application of geotextile in the Improvement Project of Deep-draft Channel of Yangtze Estuary is a consequent result of technical improvement on engineering design, construction technology and new type synthetic materials. We obtain a lot benefit during our engineering exploration which is depending on the adoption and implementation of advanced technology in this grand project. This project was selected as model engineering of geotextile application by Chinese government. Through the implementation of this engineering, we realized that there are still a lot of subjects need be further studied covering from theory and methods of design calculation, reasonable definition of physical and mechanical indices to scientific quantification of geotextile durability index, etc. The construction techniques also need be further improved and perfected. We want to cooperate with companies, institutes, etc. and experts all over the world to promote the development and application of new type geotextile material, and make more contribution to technical progress of civil engineering.

REFERENCES

Zhu JF, Jin L, Fan QJ (1999) The Geotextile Application in Yangtze Estuary Deepwater Improvement Project, Waterway Engineering 10: 87-94 (in Chinese)

Special Standard of MOC (2002, 2003) Standard of Quality Inspection Assessment for the Yangtze Estuary Deepwater Channel Improvement Project, and its Spplement

Fan QJ, Li NY (2004) Reason & Countermeasure Research for Northern Training Dike Partial Failure in the Second Phase Improvement Proect of Yangtze Estuary. China Harbour Engineering 2:1-8 (in Chinese)

Fan QJ (2005) Innovation, Source for the Success of the Yangtze Estuary deepwater channel improvement project. China Engineering Sciences No.1 (in Chinese)